

AGARD-CP-124

AGARD-CP-124

AD 771572

# AGARD

ADVISORY GROUP FOR AEROSPACE RESEARCH & DEVELOPMENT

7 RUE ANCELLE 92200 NEUILLY SUR SEINE FRANCE

AGARD CONFERENCE PROCEEDINGS No. 124

on

## Aerodynamic Drag

REPRODUCED BY  
NATIONAL TECHNICAL  
INFORMATION SERVICE  
U.S. DEPARTMENT OF COMMERCE  
SPRINGFIELD, VA. 22161

NORTH ATLANTIC TREATY ORGANIZATION



U.S. DEPARTMENT OF COMMERCE  
National Technical Information Service

AD-771 572

AERODYNAMIC DRAG

October 1973

N O T I C E

THIS DOCUMENT HAS BEEN REPRODUCED FROM THE  
BEST COPY FURNISHED US BY THE SPONSORING  
AGENCY. ALTHOUGH IT IS RECOGNIZED THAT CER-  
TAIN PORTIONS ARE ILLEGIBLE, IT IS BEING RE-  
LEASED IN THE INTEREST OF MAKING AVAILABLE  
AS MUCH INFORMATION AS POSSIBLE.

NORTH ATLANTIC TREATY ORGANIZATION  
ADVISORY GROUP FOR AEROSPACE RESEARCH AND DEVELOPMENT  
(ORGANISATION DU TRAITE DE L'ATLANTIQUE NORD)

AGARD Conference Proceedings No.124

**AERODYNAMIC DRAG**

*u*  
Papers, Discussion and Technical Evaluation of the Fluid Dynamics Panel Specialists'  
Meeting held in Izmir, Turkey, 10-13 April 1973.

## THE MISSION OF AGARD

The mission of AGARD is to bring together the leading personalities of the NATO nations in the fields of science and technology relating to aerospace for the following purposes:

- Exchanging of scientific and technical information;
- Continuously stimulating advances in the aerospace sciences relevant to strengthening the common defence posture;
- Improving the co-operation among member nations in aerospace research and development;
- Providing scientific and technical advice and assistance to the North Atlantic Military Committee in the field of aerospace research and development;
- Rendering scientific and technical assistance, as requested, to other NATO bodies and to member nations in connection with research and development problems in the aerospace field;
- Providing assistance to member nations for the purpose of increasing their scientific and technical potential;
- Recommending effective ways for the member nations to use their research and development capabilities for the common benefit of the NATO community.

The highest authority within AGARD is the National Delegates Board consisting of officially appointed senior representatives from each member nation. The mission of AGARD is carried out through the Panels which are composed of experts appointed by the National Delegates, the Consultant and Exchange Program and the Aerospace Applications Studies Program. The results of AGARD work are reported to the member nations and the NATO Authorities through the AGARD series of publications of which this is one.

Participation in AGARD activities is by invitation only and is normally limited to citizens of the NATO nations.

The material in this publication has been reproduced directly from copy supplied by AGARD or the author.

Published October 1973

533.6.013.12



*Printed by Technical Editing and Reproduction Ltd  
Harford House, 7-9 Charlotte St, London. W1P 1HD*

*ll*

## AGARD FLUID DYNAMIC PANEL OFFICERS

CHAIRMAN: Professor Dr L.G.Napolitano  
University of Naples, Naples, Italy

DEPUTY CHAIRMAN: Professor Dr D.Küchemann  
Royal Aircraft Establishment, Farnborough, Hants, UK

## PROGRAMME COMMITTEE MEMBERS

Professor A.D.Young (Chairman)  
Dept. of Aeronautical Engineering  
Queen Mary College, (Univ. of London)  
Mile End Road  
London, E.1  
England

Prof. Dr K.Gersten  
Inst. für Thermo- und Fluid-Dynamik  
Ruhr-Univ. Bochum  
463, Bochum-Querenburg,  
Postfach 2148  
Germany

Mr P.P.Antonatos  
Chief, Flight Mechanics Division  
Air Force Flight Dynamics Lab.  
Wright-Patterson AFB, Ohio 45433  
USA

Mr J.P.Hartzuiker  
Chief, Compressible Aerodynamics Department  
N.L.R.  
Sloterweg  
Amsterdam, Holland

M. l'Ing. General P.Carriere  
Directeur Scientifique de l'Aérodynamique  
ONERA  
29, Avenue de la Division Leclerc  
92320 Châtillon-sous-Bagneux  
France

Dr Ing. U.Sacerdote  
Ufficio Tecnico Studi Speciali  
Aeritalia  
Corso Marche 41  
10146-Torino  
Italy

Mr R.J.Templin  
Head, Low Speed Aerodynamics Section  
National Aeronautical Establishment  
National Research Council  
Ottawa K1A 0R6  
Canada

## PANEL EXECUTIVE

Mr J.A.Lawford  
AGARD NATO  
7 rue Ancelle  
92200 Neuilly-sur-Seine  
France

## FOREWORD

Current research and future prospects in the field of aerodynamic drag were presented and discussed at this Specialists' Meeting. Main emphasis was placed on subjects of practical value to the aerospace industry in relation to its need for accurate prediction and measurement of drag, and for its alleviation.

Twenty-seven papers were presented and discussed; the meeting concluded with a Round Table Discussion drawing out the main conclusions of the separate sessions.

Many of the papers were discussed after their presentation, but in accordance with a decision of the Fluid Dynamics Panel that a free discussion at that stage is preferable to one accompanied by the inhibiting effects of recording procedures, such discussions were not recorded and are not included in these proceedings.

The Specialists' Meeting was held at the Grand Hotel Efes, Izmir, Turkey, at the invitation of the Turkish National Delegates to AGARD.

CONTENTS

- iv -

AGARD FLUID DYNAMICS PANEL OFFICERS, PROGRAMME COMMITTEE  
AND FOREWORD

Page

iii

TECHNICAL EVALUATION REPORT

by S.F.J.Butler

vii

Reference

SESSION I – AIRCRAFT DRAG (GENERAL)

A SURVEY OF DRAG PREDICTION TECHNIQUES APPLICABLE TO SUBSONIC AND  
TRANSONIC AIRCRAFT DESIGN

by J.H.Paterson, D.G.MacWilkinson, W.T.Blackerby

1

AERODYNAMIC DRAG AND LIFT OF GENERAL BODY SHAPES AT SUBSONIC,  
TRANSONIC AND SUPERSONIC MACH NUMBERS

by F.G.Moore

2

ON SOME BASIC AND NEW ASPECTS ABOUT THE DRAG PROBLEM OF WINGS AND  
BODIES IN SUPERSONIC FLOWS

by A.Das

3

MEASUREMENTS OF THE DRAG OF SOME CHARACTERISTIC AIRCRAFT  
EXCRESCENCES IMMERSSED IN TURBULENT BOUNDARY LAYERS

by L.Gaudet and K.G.Winter

4

PROBLEMS OF ESTIMATING THE DRAG OF A HELICOPTER

by S.N.Wagner

5

AIRCRAFT DRAG PREDICTION FOR PROJECT APPRAISAL AND PERFORMANCE  
ESTIMATION

by S.F.J. Butler

6

SESSION II – WING DRAG

REMARKS ON METHODS FOR PREDICTING VISCOUS DRAG

by A.M.O.Smith and T.Cebeci

7

DRAG OF SUPERCRITICAL AIRFOILS IN TRANSONIC FLOW

by J.J.Kacprzyński

8

TRANSONIC DRAG DUE TO LIFT OF PLANAR JET-FLAPPED AIRFOILS

by H.Yoshihara, R.Magnus and D.Zonars

9

COMPARISON OF VARIOUS METHODS FOR CALCULATING PROFILE DRAG FROM  
PRESSURE MEASUREMENTS IN THE NEAR WAKE AT SUBCRITICAL SPEEDS

by J.Zwaaneveld

10

SESSION III – BASE DRAG AND SEPARATION

TRAINEE ET DECOLLEMENT

par M.Sirieix

11

NEW INVESTIGATIONS FOR REDUCING THE BASE DRAG OF WINGS WITH A BLUNT  
TRAILING EDGE

by M.Tanner

12

A STUDY OF FLOW SEPARATION IN THE BASE REGION AND ITS EFFECTS DURING  
POWERED FLIGHT

by A.L.Addy, H.H.Korst, R.A.White and B.J.Walker

13

- PREDICTION OF BUFFET ON-SET FOR AIRCRAFT – RECENT PROGRESS IN  
WIND TUNNEL-FLIGHT TEST DATA CORRELATION  
by R.C.McWherter 14

SESSION IV – INTERACTION EFFECTS

- ASSESSMENT OF THE INFLUENCE OF INLET AND AFTBODY/NOZZLE  
PERFORMANCE ON TOTAL AIRCRAFT DRAG  
by P.P.Antonatos, L.E.Surber, J.A.Laughrey and D.J.Stava 15

Paper No.16 withdrawn

- THE PROBLEM OF INSTALLING A MODERN HIGH BYPASS ENGINE ON A TWIN  
JET TRANSPORT AIRCRAFT  
by W.C.Swan and A.Sigalla 17

- THE DRAG RESULTING FROM THREE-DIMENSIONAL SEPARATIONS CAUSED  
BY BOUNDARY-LAYER DIVERTERS AND NACELLES IN SUBSONIC AND  
SUPERSONIC FLOW  
by D.J.Peake and W.J.Rainbird 18

- THE DRAG OF EXTERNALLY CARRIED STORES – ITS PREDICTION AND  
ALLEVIATION  
by P.G.Pugh and P.G.Hutton 19

SESSION V – HYPERSONIC DRAG

- DRAG IN HYPERSONIC RAREFIED FLOW  
by W.Wuest 20

- TRAINEE DE CORPS PORTANTS PILOTES A HAUTE ALTITUDE  
par J.Allègre, C.Matrand et M.F.Scibilia 21

- A REVIEW OF SUPERSONIC SPHERE DRAG FROM THE CONTINUUM TO  
THE FREE MOLECULAR FLOW REGIME  
by E.Vallerani 22

- THE INFLUENCE OF WAVE DRAG ON HYPERSONIC ENTROPY WAKE  
OBSERVATIONS  
by W.Merzkirch and A.Stilp 23

SESSION VI – TESTING TECHNIQUES AND FLIGHT/WIND TUNNEL CORRELATION

- DEVELOPMENT OF TECHNIQUES TO MEASURE IN-FLIGHT DRAG OF A US NAVY  
FIGHTER AIRPLANE, AND CORRELATION OF FLIGHT MEASURED DRAG WITH  
WIND-TUNNEL DATA  
by E.C.Rooney 24

- REVIEW OF DRAG MEASUREMENTS FROM FLIGHT TESTS OF MANNED AIRCRAFT  
WITH COMPARISONS TO WIND-TUNNEL PREDICTIONS  
by J.S.Pyle and E.J.Saltzman 25

- AN ASSESSMENT OF THE ACCURACY OF TRANSONIC DRAG MEASUREMENT IN  
A LARGE MODERN WIND TUNNEL  
by R.K.Fancett and T.Smith 26

- STING INTERFERENCE EFFECTS ON AFTERBODIES AT TRANSONIC SPEEDS  
by D.M.Sykes 27

	Reference
Paper No.28 withdrawn	
MESURES DE TRAINEE EN TUNNEL DE TIR par D.Bahurel et A.Desgardin	29
APPENDIX A – ROUND TABLE DISCUSSION HELD AFTER THE PRESENTATION OF PAPERS	A1
APPENDIX B – A SELECTION OF AGARD PUBLICATIONS IN RECENT YEARS	B1

VI

# TECHNICAL EVALUATION REPORT

by

S.F.J. Butler  
Ministry of Defence, UK

## 1 PREAMBLE

The AGARD Fluid Dynamics Panel organised a four-day Specialists' Meeting on 'Aerodynamic Drag' which was held at the Grand Hotel Efes in Ismir, Turkey, from 10th to 13th April 1973. The Programme Committee, which was led by Professor A.D. Young, F.R.S., Queen Mary College (U.K.), comprised Mr. P.P. Antonatos (U.S.A.), M.L'Ing.Gen.P. Carrière (France), Prof. K. Gersten (Germany), Mr. J.P. Hartsuiker (Netherlands), Dr. Ing. U. Sacerdote (Italy), and Mr. R.J. Templin (Canada). The members of the Programme Committee also undertook the duties of Session Chairmen. Prof. Young chaired the concluding round-table discussion, for which the panel consisted of the authors of the invited Reviews, Mr. J.H. Paterson (U.S.A.), M.M. Sirieix (France), Mr. P.P. Antonatos (U.S.A.), Prof. W. Wuest (German) and Mr. S.F.J. Butler (U.K.). The present author was invited by the Programme Committee to prepare the Technical Evaluation Report on the Conference. The advice of the Programme Committee in the preparation of this Report is gratefully acknowledged, but it must be stressed that the detailed views expressed are the sole responsibility of the writer.

Section 2 presents some basic considerations involved in the consideration of Aircraft Drag. The following Section deals jointly with the first two Sessions of the Conference (on General Aircraft Drag and Wing Drag), including the invited Review papers of Paterson<sup>1</sup> and Butler<sup>6</sup>. Section 4 concerns Base Drag and Separation (Session 3), including the Review contributed by Sirieix<sup>11</sup>. Interaction effects (Session 4), and the Antonatos Review<sup>15</sup> are considered in Section 5, whilst Section 6 deals with the essentially-distinct subject of Hypersonic Drag and the Wuest Review<sup>20</sup>. The conference ended with a Session on Test Techniques and Flight/Windtunnel comparisons (Section 7) and a round-table discussion reported in the full Conference Proceedings.

Some main conclusions and recommendations to the Fluid Dynamics Panel are contained in Section 8. A list of the Conference papers is appended for reference purposes.

## 2 GENERAL CONSIDERATIONS

A primary objective of research on aerodynamic drag is the development and proving of prediction methods in a form suitable for direct use by aircraft development teams and by those who have to assess the relative merits of alternative designs. Aircraft drag estimation methods are needed at various levels of sophistication and reliability<sup>6</sup> (Fig 1). Basic statistical analyses can form the basis of an acceptable forecasting procedure at the feasibility stage, although such an approach is essentially conservative and can lead to the perpetuation of low design standards, as well as being of little use when novel aircraft design concepts are under consideration. Of some significance is the ability to predict reliably the drag of a datum streamlined aircraft with fully-turbulent flow, against which achieved drag levels can be compared in a figure-of-merit approach. During the design development and refinement stage, the research aims include the achievement of drag design objectives and the limitation of drag growth. In this phase, drag predictions in practice must be prepared by a process of synthesis (rather than simple summation), within a format which can readily accommodate the changing sources of data. In the third stage, performance deficiencies must be rectified and the guaranteed performance predicted for a full range of operating conditions, involving analysis and interpretation of prototype flight-test data.

Fig 1. Three Stages of Drag estimation in Aircraft design

Stage	Feasibility	Development	Pre-production
Aims	Respond to market opportunity or military target	Meet objectives and control drag growth	Rectify design defects and estimate operational performance
Type of estimate	Quick approximate forecasts	Validated refined estimates	Guaranteed performance predictions
Design status	Outline sketch	Main features chosen	Frozen
Main data sources	General ( Theory Model Aircraft	Specific ( Theory Model General Aircraft	Specific (Theory Model Prototype

A flexible approach to drag prediction is particularly vital in the all-important research and development phase, preferably one in which a consistent framework is used based on aerodynamic theory, suitably supported by aimed research on specific key areas and validated by means of critical analyses of selected ad hoc model and aircraft test data. Although such a framework needs to provide for the progressive introduction of proven theoretical methods as these become available, the present Conference has confirmed that a comprehensive drag prediction method, valid for the current main

classes of aircraft and based entirely on theory, is not likely to be possible for a long time to come. Thus, careful judgement will continue to be needed in the choice of an optimum blend of prediction methods, if full advantage is to be taken of the data available from specialised and ad hoc research results. A clear need and opportunity thus exists for collaboration within AGARD to ensure that maximum benefit is obtained from national and industrial aimed research programmes relevant to drag estimation. This must include adequate attention to tunnel flow quality improvements and to flight and tunnel testing techniques. Moreover, the variety and difficulty of the theoretical problems which now present themselves are such that co-operation on an international basis seems essential to achieve a more optimal application of scarce original theoretical effort than applies at present.

In order to put matters into perspective, it is desirable to examine the relative magnitudes of the drag contributions due to different basic causes; illustrative drag breakdowns are given in Fig 2 of Paper 6. Although the relative magnitudes of the different components are obviously of importance in themselves, the order of uncertainty of each needs to be assessed, particularly where that contribution can be reduced or eliminated altogether by an informed design choice. Such considerations imply the need for a broad and persistent attack on the understanding of aircraft drag and its prediction. Taking full account of the present Conference, there can be few aspects of this subject with which we can afford to be satisfied at present. Above all, improved physical understanding and quantitative design methods must be sought for three-dimensional viscous supercritical flows and for shock-induced and other separated flows, before major improvements in aircraft drag prediction methods can reasonably be expected.

### 3 AIRCRAFT DRAG (GENERAL) AND WING DRAG

The review papers of Paterson, MacWilkinson and Blackerby<sup>1</sup> and Butler<sup>6</sup> may be regarded as complementary. Paterson concentrates on the application of available design methods to the prediction and understanding of the drag of subsonic and transonic transport aircraft, with particular reference to the exhaustive and impressive analysis undertaken in connection with the C5A. This review is an outstanding and mature contribution to the study of aircraft drag prediction. It shows what can be achieved, but also illustrates the effort and care which is necessary if a convincing conclusion is desired. On the other hand, Butler starts with a general analysis of the desirable features of future aircraft drag prediction methods suited to the computer age, including an assessment of the present limitations of theory. By way of contrast, the second half of this review comprises a set of cameos setting out current drag prediction practice as seen by U.K. specialists. These reviews together set the scene for the Conference and both contain material of strong relevance to other Sessions of the Conference. They form a natural starting point for a study of the Proceedings.

#### 3.1 Skin friction

No new thinking was evident on Reynolds number effects on skin friction. Paterson<sup>1</sup> tends to argue the need for further research to establish more firmly the variation of turbulent skin friction at elevated Reynolds numbers. The U.K. review<sup>6</sup> lays more emphasis on the manner in which two-dimensional skin friction data should be applied to swept and slender wings and to bodies. Paterson rightly stresses<sup>1</sup> the importance and difficulties involved in accurately predicting and limiting roughness and excrescence drag (see Section 3.6). There is the important complementary question of the problems involved in the practical estimation of the extent of laminar (and separated) flows to be expected on a specific flight vehicle, on which no progress was reported.

#### 3.2 Wing Sections

Paterson's paper<sup>1</sup> demonstrates the value of proven viscous design methods for profile drag and drag-rise prediction on conventional subcritical sections at moderate angles of incidence. There was general agreement on the need for extending such methods to deal adequately with the presence of shocks, flow separations and supercritical flow. Existing methods only offer acceptable accuracy for relatively-simple aerofoil problems; satisfactory methods are not yet available for more exacting problems, involving multiple aerofoils, bodies of revolution, or complex compressibility and shock interaction effects.

One important practical consideration arises because boundary-layer calculations usually end at the wing trailing edge and must be extended into the wake. Corrections to conditions far downstream by means of relationships such as those suggested by Squire and Young are no longer adequate. Smith and Cebeci<sup>7</sup> have considered the alternative approach of direct calculation of shear and pressure forces by integration around the aerofoil contour. At least as presented, this approach appears extremely sensitive to the assumptions applied near the trailing edge, resulting in unacceptable values for the pressure drag. No satisfactory explanation was advanced in the discussion following this paper, and an improved way of proceeding was not forthcoming. Smith however obtained more promising results, agreeing better with observations, by extending the boundary-layer calculations into the initial wake using mixing-length relations. This method is also applicable to bodies of revolution.

In a complementary paper, Zwaansveld<sup>10</sup> presented a detailed review of sectional drag calculation methods, including a new method for the treatment of the wake correction. The need for more accurate corrections for static pressure is confirmed and it is shown that this can be achieved by the application of integral relations with suitable choice of parameters. Because of the extreme sensitivity to local static pressure, particular care is shown to be needed in correcting wake drag surveys conducted close to the wing trailing edge.

One of the most interesting contributions related to the application of the jet flap to transonic speeds. It is generally accepted that the lift increment due to a jet flap in two-dimensional incompressible flow can be achieved with nearly-complete recovery of the jet thrust and with corresponding increases in lift/drag ratio. Larger drag penalties are known to be involved at transonic conditions, although the lift/drag ratio nevertheless may represent an improvement over that which may be achieved with elevated angles of incidence in the absence of a jet flap. In a particularly well-balanced paper, Yoshihara, Magnus and Zonars<sup>9</sup> discuss some jet flap experimental results obtained in the NAE High-Reynolds-Number facility and offer an extension to Spence's theory to allow representation of the observed effects of the upper-surface shock by means of a thickened boundary layer approaching the trailing edge and a thick wake flowing above the jet wake. At present, a priori knowledge of the upper-surface pressure at the wing trailing edge has to be assumed, together with a simplified variation of pressure in the wing wake towards the value appropriate to conditions downstream (any transverse variations being ignored). Further, in order to locate the shock and simulate the effect of the boundary layer on the effective wing camber, the pressure distributions on the upper surface behind the shock also form part of the assumed boundary conditions. The results show encouraging agreement with experimental observations, and it now remains to improve the method by incorporating self-sufficient procedures which will simulate to an adequate degree the principal viscous features namely, the shock-induced separation and the thickened wake flowing above the jet wake.

Theoretical effort has recently been concentrated on methods for supercritical aerofoil sections. However, as pointed out by Kacprzynski,<sup>8</sup> even the more elaborate methods do not feature the explicit use of design drag or drag-rise Mach number as objectives of the design process. Once an apparently-acceptable aerofoil shape has been derived by repetitive numerical experiment, its actual characteristics must be ascertained by calculations and tunnel experiments. Kacprzynski shows that economical isentropic calculations simulating some of the features of supercritical flows usually result in pressure distributions in reasonable agreement with experiment or more elaborate theory, and can yield acceptable predictions of drag-rise Mach number, though the exact position and strength of the shock may be somewhat in error. The possibilities of adapting such a method to allow the prediction of sectional drag are discussed; this would seem to require sounder physical understanding than is presently available.

The Conference failed to attract contributions relating directly to our ability to estimate the drag of wing sections in the presence of extensive flow separations (either due to shocks or to severe gradients) and no progress was reported in the important and challenging field of multiple-aerofoil theory.

### 3.3. Swept Wings

Unfortunately, there was no paper dealing specifically with drag prediction for a wing exhibiting three-dimensional viscous compressible flow. Perhaps the only major criticism which might be levelled against Paterson's paper is the reliance which is placed on strip theory and the rather superficial way in which three-dimensional features are treated. In the round-table discussion, Paterson and others stressed the desirability of developing such methods to the stage where supercritical flow and separations could be represented on a three-dimensional wing. The inviscid compressible flow about streamlined aircraft-like shapes can already be calculated and allowance can be made for viscous effects of moderate proportions. Provided effort is directed towards this aim, there are reasonable prospects of extending such methods to cope with essentially-shockfree mixed flows corresponding to the use of particular supercritical sections. As some allowance can be made for the presence of engine nacelles and interaction effects for an optimised configuration without significant flow separations, we would then be very close to the position where realistic drag targets could be predicted for the datum streamlined sweptwing aircraft central to a figure-of-merit approach. Thus, the importance of achieving a more complete treatment for the basic swept wing can hardly be over-emphasised. Especially for the small military aircraft, it is perhaps nearly as important to be able to predict the aerodynamic characteristics (including drag) at off-design conditions involving strong wing shocks and extensive flow separations, though more limited accuracy may be acceptable.

Drag prediction under high-lift conditions on a swept wing with multiple highly-deflected flaps is even more difficult. Unresolved difficulties in predicting sectional characteristics have already been mentioned. Further, the prediction of vortex drag is particularly unsatisfactory. There is no adequate means of calculating the spanwise loading, as the use of linearised theory implies a limit on the deflection angle of, perhaps  $15^\circ$ , and the vortex sheet is assumed to lie in the chordal plane of the wing. A theoretical approach is needed, suitably supported by experiment, which allows reliable calculations of the spanwise loading and hence the vortex drag, without the unrealistic simplifications required by linearised theory, possibly based on the non-planar theories which have been proposed.<sup>1</sup> Three-dimensional effects need to be allowed for in calculating the viscous drag, both to account for the modified chordwise loadings towards the tip and the root, and also to allow for the effects of the severe transverse pressure gradients on boundary-layer development. There are also pronounced three-dimensional flows between the individual aerofoils, which interact with the main flow around the complete wing. The supporting research needs to be of the highest standard.

### 3.4. Slender wings and low-aspect-ratio configurations

Slender-wing aerodynamics is a promising area for research on the application of the powerful computerised design optimisation techniques now becoming available. Das<sup>3</sup> discusses the results of an impressive study which has been conducted at DVLR Braunschweig. In the specification of the drag relations, naturally it has been necessary to employ empirical expressions for friction and base drag. After demonstrating that the drag estimation methods used generally yield good agreement with experiment for a range of slender shapes, Das applies variational methods to derive designs offering minimal wave drag due to volume (for different classes of bodies and wing), minimal wave drag due to

lift (for wings), and minimal vortex drag (for wings). Although not discussed fully in the Conference paper, Das has applied the same methods with some success to minimize the total drag of non-lifting slender bodies and thick slender lifting wings, experimental investigations broadly confirming the theoretical predictions. Further progress is limited by the deficiencies of theoretical methods for slender lifting bodies, and for slender wing-body combinations in the presence of vortex-shedding or compressibility effects.

The general position regarding the estimation of the vortex and wave drag of practical slender and low-aspect-ratio aircraft designs is less satisfactory. Thus, the estimation<sup>6</sup> of the vortex drag of slender aircraft with leading-edge separations relies essentially on empirical correlations; at supersonic speeds, the lift-dependent drag (including that due to wave drag) must be estimated similarly. For truly-slender configurations, wave drag calculations can be made, but it is by no means clear what degree of reliance can be placed on such methods when applied to practical aircraft-like shapes outside their strict region of validity. This is particularly relevant to the preliminary design of military strikefighter aircraft in their clean configuration, and is an area likely to profit by aimed research guided by theory.<sup>6</sup>

### 3.5 Bodies

Paterson<sup>1</sup> includes an empirical shape factor analysis demonstrating that, for typical fineness ratios, the drag of the fuselage of a large transport aircraft can be kept within 5% of that predicted by the ESDU Data Sheet method, even with a degree of rear-fuselage upsweep.

Moore<sup>2</sup> describes an interesting and valuable example of a fast and economical computerised design method for predicting the drag and lift characteristics of arbitrary missile-like body shapes over a practical incidence range (about  $\pm 20^\circ$ ) to a limited accuracy (usually 90%) at subsonic, transonic and supersonic speeds. Although most of the prediction methods incorporated are well-proven, a new procedure has been developed for the treatment of blunt-nosed bodies, whereby Newtonian and perturbation theories are combined to provide improved comparisons with experiment at comparatively-low mainstream Mach numbers (as low as 1.2), well away from the accepted limits for the application of Newtonian concepts. The main deficiency noted by Moore, not surprisingly, relates to the transonic flow regime, where an improved method is needed capable of dealing with blunt-nosed bodies having discontinuities along the ogive.

### 3.6 Excrescences

Paterson<sup>1</sup> correctly observes that most of the data currently used in the estimation of excrescence drag at cruise was obtained at low Mach numbers and at comparatively low Reynolds numbers, remaining largely unsubstantiated at the conditions appropriate to aircraft applications. However, an extensive research programme has been conducted over a period of years in the RAE Bedford 8ft tunnel to determine the drag of some 50 excrescence configurations immersed in the tunnel wall boundary layer, the tests covering a wide range of Mach numbers (0.2 to 2.8, excepting transonic conditions) and Reynolds numbers (up to  $100 \times 10^6$  at  $M=2$ ). This work was summarised by Gaudet and Winter<sup>4</sup> for the Conference in a form designed to encourage direct use by the aircraft designer. Considerable insight has been gained into boundary-layer/excrescence interaction, as a result of which a much better assessment of boundary-layer and Mach number effects will now be possible for many common types of isolated excrescences. As one could hardly hope to cover all possible excrescence and boundary-layer situations, attention should now be turned to multiple arrays of excrescences, apart from filling some gaps still apparent for certain classes of excrescences (such as rivets, aerodynamic fairings, inlets and outlets, and gaps in flying control surfaces). Careful model and flight research will be involved and this is a field where collaboration could bring considerable benefits to all.

The position is less satisfactory at high-lift conditions,<sup>6</sup> where excrescences not only cause parasitic drag but also often result in appreciable lift losses; the aircraft attitude or flap setting may well have to be increased in compensation, with additional indirect drag penalties. Even with care in design and development, direct and indirect excrescence drag can account for 10% of the drag at climb out. Surprisingly, this subject has received little systematic attention in the past; there is virtually no published drag information in the field of flap and slat engineering. Admittedly, model-scale simulation is not easy and extrapolation may prove difficult, since such excrescences are comparable in size with the boundary layer. Nevertheless, useful aimed research is certainly feasible, both at model scale and in flight. This is recommended as a much-neglected area with which AGARD should concern itself in future.

### 3.7 Helicopters

A concise and instructive review of this subject was presented by Wagner.<sup>5</sup> As designers aim at more efficient and economical helicopters capable of increased speeds and endurance, more emphasis must be placed on drag reduction. Significant associated benefits can include delays in the onset of blade stall and compressibility effects, as well as important reductions in the oscillatory loads on controls and in cockpit noise and vibration levels. The main source of drag increase with forward speed is shown to be fuselage parasitic drag. Unlike rotor lift/drag ratio, which can now be estimated with some confidence, the parasitic drag cannot be so estimated largely because of the shapes involved, although a measure of the effective parasitic drag area can be obtained by analysis of rotor power variations with forward speed. Wagner shows that the major parasitic drag contributions arise from the basic fuselage, the rotor pylon and the landing gear, although the contributions from minor causes certainly should not be neglected. Considerable advantages arise from an ability to conduct full-scale windtunnel tests for helicopter research, within the limits set by tunnel flow breakdown.

These include the possibility of measuring data free from scale effect and of isolating the contributions of particular components, as well as the avoidance of major problems associated with the design and provision of scaled model rotors. The general question of improved facilities for testing VSTOL models is a matter deserving, and already receiving, attention by AGARD.

#### 4. BASE DRAG AND SEPARATION

Flow separation phenomena and associated drag penalties lie at the heart of most of the avoidable elements of the drag of an aircraft. The performance in cruise, the climb-out characteristics, and the flying limits of an aircraft all are affected, if not determined, by flow separation considerations. It is hard to visualise how appreciable progress is to be made with drag prediction methods without substantial advances in this field, not only in general understanding but also in the provision of quantitative design procedures of a versatile type. It was, therefore, disheartening that no important advances in the treatment of twodimensional or threedimensional flow separations were discussed at this Conference. Bearing in mind the considerable time since the subject of flow separation was considered, it is recommended that this form the theme of an early AGARD Specialists' Meeting.

In his excellent review paper on drag and separation, M. Sirieix<sup>11</sup> stresses the basic importance of distinguishing between laminar and turbulent boundary layers in the consideration of separation effects. At least to a limited extent, it is possible to categorise turbulent separation phenomena by reference to the general unsteady characteristics associated with the flow. It is also helpful to differentiate in terms of the occurrence of fixed or free separation and reattachment conditions. The review paper considers the drag implications of different classes of separations and assesses available prediction methods. Unfortunately, despite all that has been achieved, a number of gaps still exist in the prediction of drag, even for twodimensional separations.

In order to improve our ability to cope with more general flow separation phenomena, on the one hand, it is fundamental and absolutely essential that improved calculation methods be available for compressible threedimensional viscous flows with attached turbulent boundary layers, and, on the other hand, that quantitative methods should be devised capable of dealing with the main types of flow separations. The latter will need to involve original theoretical developments, suitably supported and extended by high-quality experimental research. It may well prove difficult to achieve adequate simulation of the separation phenomena at model-scale conditions. Better ways will be needed to predict full-scale transition characteristics and flow separation boundaries. Improved understanding of shockwave/boundary-layer interaction will be essential.

The prediction of base flows and base pressures also leaves much to be desired. However, some progress is evident with semi-empirical methods (see also Section 5) providing grounds for future hope. There is reason to hope for substantial theoretical developments quite soon, through the application of improved boundary-layer and wake calculation methods. Thus, two specialised papers dealt with particular aspects of base flows.

The use of blunted aerofoils can have advantages at transonic conditions, provided the drag penalties can be reduced, for instance by the addition of splitter plates and wedges. Tanner<sup>12</sup> has extended his studies of this topic. He shows how the base drag penalty can be minimised by the use of a trailing-edge splitter wedge, so that the sectional drag returns close to the value achievable with a conventional sharp-edged section. It is argued that advantageous general aerodynamic characteristics can be obtained, without major drag penalties, by means of comparatively-minor changes to the wing profile. However, Tanner's investigations must be limited in value by the absence at present of test data at transonic speeds, confirming acceptable drag levels together with more attractive general characteristics.

Addy<sup>13</sup> has demonstrated that practical computerised methods can now be devised for the calculation of base and jet effects on bodies, provided recourse is made to detailed empirical modifications to extend available theories, especially as far as flow separation effects are concerned. Not surprisingly, Addy stresses the need for improved boundary-layer separation criteria to aid analysis of the complex situations encountered in practical designs. It is quite clearly shown how valuable and powerful a tool such a method can be to the design engineer in achieving better insight into the relative importance of, and interaction between, different design factors by allowing systematic numerical experimentation; provided that the essential features of the fluid dynamics have been incorporated faithfully. Such a program can also be of considerable assistance in the design of model research programmes. As such computer programs are devised and proved, they will increasingly feature in aircraft design and optimisation procedures of a semi-automated nature.

The prediction of the onset of buffet and drag with incidence are related topics of importance, especially in the design of small military aircraft. The interpretation and application of the results of model-scale investigations on buffet (using the procedure due to Mabey) has been studied by McWhorter,<sup>14</sup> including the effect of tunnel flow quality improvements deemed essential to allow meaningful predictions of aircraft buffet; following the further tunnel modifications (mentioned in the Preprint), a satisfactory reconciliation has been achieved with flight results. It seems a pity that no attempt was made in this paper to examine the link between tunnel flow and extrapolation problems for buffet investigations, and the prediction of aircraft drag in the presence of extensive flow separations from model-scale investigations.

The present position on drag and separation can perhaps be summarised by stressing again the need to develop general quantitative methods capable of dealing with threedimensional flow separation, with empirical modifications as necessary to achieve practical design procedures. The main potential benefit is expected to lie in an improved ability to design (at least in part) optimal practical configurations for which the full-scale behaviour can be estimated with more confidence. Of course, this will not remove the need for confirmatory model experimentation at the earliest possible point. As pointed out by Sirieix during the round-table discussion, improved understanding of model support effects could prove a valuable side benefit.

XII

## 5. INTERACTION EFFECTS

Airframe-propulsion system integration involves increasingly-important interaction effects for all classes of aircraft. The need for high-thrust supersonic aircraft and the advent of high-bypass-ratio fan engines have resulted in larger engines having greater impacts on the aircraft flow field and overall performance. The aircraft range factor may well not be improved, despite significant reductions in specific fuel consumption. Although it is generally agreed that airframe-propulsion interaction effects play an important role in determining the aircraft performance, as pointed out by Antonatos, Surber, Laughrey and Stava <sup>15</sup> it is difficult to determine their precise magnitude. Indeed, attempts so to do regularly lead to keen controversy between specialists at the interface between the aerodynamics and propulsion disciplines, as an apparent deficiency can arise from a variety of factors. Of basic importance is the use of a consistent and flexible accounting system,<sup>6, 15</sup> especially in the case of high-bypass-ratio engines. The degree of foresight achieved during the early stages of project formulation is often inadequate and so the book-keeping methods need to be revised and improved until they match the sophisticated model and flight-test techniques now feasible.

In the review paper, Antonatos <sup>15</sup> deals in appreciable detail with the series of inter-related model experiments which are necessary to study the effects of the main flow and geometrical factors, to assess the necessary corrections at model scale and to extrapolate the results to full-scale conditions and practical configurations. Sometimes, the estimated interference drag compounded by such an approach can be reconciled satisfactorily with aircraft flight-test results obtained under carefully-controlled conditions (see Section 7). However, there are often unexplained and serious differences between flight test results and predictions based on comprehensive model tests. As far as model testing is concerned, the adequate simulation of flow effects remains perhaps the most important technique problem to which a complete solution is not yet apparent.

It is certainly not possible in general to rely on theory to predict airframe-engine interaction effects, although existing theories are helpful in providing a framework within which to analyse experimental results and to develop empirical methods. A number of useful semi-empirical methods are consequently now available for preliminary design purposes <sup>6,15</sup>. However, early recourse to detailed specific research is certainly essential for each new project to determine acceptable engine arrangements. Threedimensional compressible flow theories should help in the future but need to be supplemented by quantitative methods for threedimensional boundary layers and separated flow regions (see Sections 3 and 4). In the meantime, the growing body of good-quality aimed research data in this field deserves careful analysis, preferably on a collaborative basis.

The selection of the airframe-engine general arrangement is complicated in practice by the need to consider a wide range of factors, embracing most of the aeronautical disciplines. In the case of the high-bypass-ratio engine, as applied to a near-sonic transport, the cruise drag can be affected decisively by a poor choice. Swan and Sigalla <sup>17</sup> examine in interesting paper the relative merits of conventional underwing and rear fuselage installations for jet transports, in comparison with unconventional overwing arrangements. Careful analysis supported by experiment is necessary to allow a reasoned initial choice of general configuration; this has to be followed by additional investigations to develop a near-optimum arrangement. Overwing installations are shown to offer worthwhile advantages in respect of lift augmentation and noise shielding. It is demonstrated that anticipated problems concerned with adverse effects on drag divergence speed and cruise drag can be alleviated by imaginative application of available theoretical design methods for subcritical flows, supported by suitable aimed research.

Some important interaction effects arise at wing-body and other junctions. There were no papers directly concerned with general junction-fairing design methods. The design of boundary-layer diverters for the constricted space between a nacelle and a body or wing surface is a related problem which has been relatively neglected. Peake and Rainbird's paper <sup>18</sup> forms an elegant study demonstrating how designers can recognise arrangements which may result in flow separation regions and the manner in which drag reductions can be achieved by a sensible approach to detailed design. This paper underlines the need for a better appreciation of threedimensional flow separations; it does not suggest how progress is to be made, particularly in developing quantitative methods.

The installed drag of external stores is a major component of the drag of a combat aircraft. Unless care is taken it can far exceed the sum of the free air drag of the stores and their supports; moreover, strong associated effects can arise on the general aircraft characteristics, including limitations to the flight envelope. Pugh and Hutton <sup>19</sup> show how this most complex problem can be approached by a systematic analysis of the reasons for the interference effects. Significant alleviation of drag can often be achieved merely by reducing the free-air drag of the stores and supports. There is also limited scope for the application of theory. Thus, for transonic and supersonic conditions, the drag of combinations may be reduced by the application of area-rule concepts. Once it is possible to calculate the flow field around an aircraft fitted with stores in compressible flow and estimate the boundary-layer development, it would seem feasible to predict the conditions appropriate to the onset of flow separations or supersonic flow. However, for the immediate future, we must agree with Pugh that simple semi-empirical methods for the prediction of installed drag are likely to prevail. The paper outlines

XII

a framework within which such analyses can be conducted. Much data already exist in this field, including a certain amount from systematic research; there is certainly scope for collaboration in the design of future research programmes and in the subsequent analysis. Economic considerations will tend to limit the amount of full-scale testing of a standard suitable to provide essential confirmatory comparisons with model test results. Recent flight/tunnel comparisons on the Buccaneer<sup>6</sup> should assist. Pugh rightly stresses that a sustained effort is justified on store installation drag, since the drag of combat aircraft may be reduced in this respect by an extent that could hardly be achieved in other ways.

## 6. HYPERSONIC DRAG

Despite limitations on research effort, considerable progress was reported in hypersonic drag prediction. The results are relevant to the flight of hypothetical future long-range aircraft, as well as to the re-entry stages of a space vehicle or strategic missile. As emphasised by Wuest<sup>20</sup> in an authoritative review paper, satisfactory simulation of full-scale behaviour usually can be achieved if both Reynolds and Mach number are reproduced, using a variable-density tunnel. Some problems are encountered due to different relaxation effects in tunnel and flight, suggesting a possible need for more attention to the quality of the tunnel flows. As illustrated by the particularly useful diagram of flow regimes included by Wuest (Fig 2 of paper 20), high-altitude flow is characterised by  $Ma_{\infty}/\sqrt{Re_{\infty}} > 0.01$ . Three main flow regimes can be distinguished, namely continuum flow  $Ma_{\infty}/\sqrt{Re_{\infty}} < 0.1$ , the rarefied transitional region, and free molecular flow  $Ma_{\infty}/Re_{\infty} > 3$ .

For simple shapes, reliable experimental data have been gathered over a wide range of Reynolds number and theories are now becoming available to explain the underlying flow phenomena.<sup>20</sup> Thus, Vallarani<sup>22</sup> presents detailed comparisons of sphere drag measurements with theory, demonstrating that predictions of sufficient accuracy can be made, provided use is made of empiricism. These studies are complemented by those of Wuest<sup>20</sup> for cylinders and cones, which reach similar conclusions.

In hypersonic rarefied flow, the drag can conveniently be divided into temperature-independent pressure drag, temperature-dependent pressure drag and friction drag. On blunt bodies, the pressure drag is dominant and rarefaction effects are small. For slender shapes, however, friction drag is of considerable importance, and shows significant dependence on rarefaction,<sup>20</sup> reaching a maximum value at a Knudsen number around 0.5. Although relaxation and radiation effects do not appreciably affect the pressure drag, they influence the general flow field, the shock stand-off distance and heat-transfer rates.

The position regarding predictions of the drag of realistic shapes is less favourable, although good agreement can be achieved in certain areas (see Allègre, Matrand, and Scibilia<sup>21</sup>). Theory sometimes shows a surprising degree of agreement with measurement, although the assumed flows are essentially unrepresentative (eg. strong interaction theory). Attempts to interpret measurements on complex shapes such as wing-body combinations and re-entry shapes generally indicate a need for further research. Low-density non-equilibrium flows are particularly complicated and difficult to predict at present.

Merzkirch and Stilp<sup>23</sup> have provided an interesting account of wake analysis at hypersonic speeds. Just as at low speeds, vortex drag and viscous drag can be differentiated by analysis of the wake, so, at hypersonic speeds, the viscous drag and the inviscid (entropy) components can be distinguished by means of schlieren visualisation of the latter component, which can then be associated with the wave drag of the body. In the present approach, the density distribution in the wake is inferred from knowledge or measurement of the bow shock geometry (in fact the latter could be used to estimate the drag directly, as shown by Pugh). If the wake density is thus prescribed, then the derived wave drag is in close agreement with that which results from a similar wake analysis with the density assumed to follow a Gaussian distribution (as proposed by Webb).

In the studies on 60° delta wings, described by Allègre, Matrand, and Scibilia,<sup>21</sup> the aerodynamic drag was found to be substantially increased in the transitional regime, where viscous and boundary-layer displacement effects predominate, relative to continuum flow. Under rarefaction conditions, close agreement is shown with strong interaction theory. Control presents important problems closely related to drag for aircraft-like shapes at hypersonic speeds. Allègre includes some comparisons between solid and fluid spoiler controls; the latter are shown to offer some advantages, including reduced control drag increments. At present, the results are somewhat specific, lacking systematic investigation of jet strength and geometry effects.

In view of the limited effort available for future research on hypersonic drag, such research must be selective, suggesting advantages from collaboration. Since calculation methods for simple shapes already tend to be complex, reliance will have to be placed on pragmatic approaches to drag prediction for more complex shapes. The most important areas for future research were indicated by Wuest in the round-table discussion. In the free-molecular regime, attention should be concentrated on gas-surface interactions. In the transitional regime, the main need appears to be an understanding of interaction effects for more complex shapes. Very strong viscous effects can be encountered in rarefied flow and the adequacy of windtunnel corrections is questionable. In the rarefied continuum regime, the key problem is the prediction of transition.

## 7. TESTING TECHNIQUES AND FLIGHT/WINDTUNNEL COMPARISONS

Since the admittedly-inadequate state of aerodynamic theory requires such heavy reliance to be placed on windtunnel model tests for drag prediction purposes, tunnel flow requirements, model test techniques and correction methods deserved earlier and more complete treatment at this Conference.

An authoritative review paper should have introduced this Session. Admittedly, the various review papers contained useful contributions relating to this subject area. Thus, Butler<sup>6</sup> includes brief outlines of the main issues, including observations on tunnel flow quality requirements, Antonatos<sup>15</sup> deals thoroughly with the test methods associated with engine/airframe interference problems, and Paterson<sup>1</sup> considers test technique aspects in the context of the analysis of specific aircraft research programmes. Those particularly interested in this subject are advised to consult these Reviews in the above order before commencing a study of the papers for this Session.

On the other hand, the Conference provided excellent coverage on flight-testing aspects and Paterson's paper should certainly be read from this viewpoint. Rooney also contributed an outstanding paper<sup>24</sup> on flight-testing methods and flight/tunnel comparisons. This paper would have been remarkable even had it been confined to the comparison of conventional (static), quasi-static, and truly dynamic measurement of drag in flight. It describes the use of sensitive accelerometers to measure accurately excess thrust in flight, together with improved and economical methods for assessing the installed thrust under dynamic conditions. The random scatter is acceptably low and good comparisons have been achieved between results obtained with the alternative flying techniques. Surprisingly, no problems appear to have arisen from dynamic effects on the thrust determination process. Obviously, the adoption of dynamic test techniques would result in great economies in flight test costs, as well as permitting a wider coverage of the flight envelope not possible with static techniques. However, in addition, Rooney includes comprehensive comparisons with corrected and extrapolated model test data, confirming Paterson's conclusion that good correlations can be achieved, provided the flight and model data are of high quality and properly corrected. Moreover, Rooney extends the range of the comparisons to cover supersonic speeds up to  $M = 2$  ( $68^\circ$  wing sweep), and also includes results for low-speed high-lift configurations at low wing sweep. Naturally, there are some areas where reconciliation is at present incomplete, particularly the minimum drag at supersonic speeds. Nevertheless, the overall agreement is astonishingly good.

In the next paper, by Pyle and Saltzman,<sup>25</sup> can be found a variety of flight research studies and flight-tunnel comparisons on unusual configurations. This paper will repay careful study, for it shows convincingly the advantages of a diagnostic and imaginative approach to flight research. The most significant results relate to base and boat-tail drag. Considerable differences are shown to exist between model and flight results, associated with the influence of tunnel and support interference and with scale effects (possibly including major variations in flow separation phenomena). The possible use of boundary-layer thinning to achieve boundary-layer flows at model scale more representative of flight deserves serious consideration.

Although it is true several Conference papers demonstrate that acceptable reconciliations can be achieved between model and aircraft tests, the difficulties associated with the correction and extrapolation of model tests (particularly as regards flow simulation effects) and of measuring drag in flight should not be underestimated. Antonatos<sup>15</sup> comments on the considerable difficulties involved in the conduct, analysis and interpretation of flight tests, if overall assessments are to be provided of the adequacy or otherwise of drag prediction methods for engine/airframe interaction effects; he stresses the need for supplementary flight investigations (such as detailed pressure plotting) to allow convincing treatments of critical flow regions. More general considerations of the problems of aircraft thrust and drag determination are included by Butler.<sup>6</sup> It can be agreed that important advances have been made recently allowing reliable assessment of installed thrust and accurate determination of (thrust-drag) margins under dynamic conditions in flight.<sup>6,24</sup> There is already a UK group actively preparing guide-lines for selected classes of engine/airframe combinations and this group could well serve as a focus for collaborative research within AGARD. Of course, it must always be borne in mind that it is one thing to perform a retrospective comparison of model and flight results, and quite another to prepare and guarantee drag predictions from aimed model-scale research for a new aircraft type.

Apart from the absence of a Review paper, already noted, unfortunately there were no specialist papers aimed directly at the principal tunnel flow quality and test technique problems for the main types of complete unpowered models of aircraft. It is certainly debatable<sup>6</sup> whether the quality of current transonic windtunnel flows can allow absolute drag determination of the desired standard; much the same applies for testing under high-lift conditions. At least, the problems of determining the drag of civil and military aircraft models close to transonic speeds deserved specific consideration.

Much interest was evident on tunnel-testing techniques, which prove demanding if accurate drag measurements are required. Support interference and, above all, engine-flow simulation techniques are accepted as major problem areas. There is a general feeling that insufficient attention has been paid in recent years to comparative tests on representative datum models and support systems; such research sponsored by AGARD would certainly receive strong support at working level and should be directed particularly at the above aspects.

A view on a particular aspect of rear sting interference was presented by Fancett and Smith,<sup>26</sup> the chosen test model representing a shell. Although they show that it is possible to reconcile, to a limited extent, drag measurements with variation of sting length by means of a semi-empirical approach, it is instructive that the residual variations still exceed 5% of the measured total drag at high subsonic speeds. Good overall agreement is obtained between corrected data and an independent set of data; however, Fancett explains that it has not been possible to conduct a critical examination of the latter.

In a companion paper, Sykes<sup>27</sup> discusses research studies on the effect of sting support geometry on base and boat-tail drag. The variation of base pressure with sting diameter/base diameter ratio is shown to be essentially different for cylindrical and boat-tailed bodies. The boat-tail drag is affected by the sting diameter/base-diameter ratio, although it does not depend greatly on the conical

flare shield. For subsonic speeds, a useful correlation is given relating the effects of sting length and flare angle on base pressure. This paper confirms the complex and sensitive nature of the interactions which can occur between a rear sting support and the local parts of a model. It underlines the need for a fresh assessment of support techniques and a generally-cautious approach by research teams to the problem of correcting model drag data for support interference.

The concluding paper, by Desgardin and Bahurel,<sup>29</sup> considers the problems involved in the analysis of data obtained from free-flight testing in a tunnel range. As long as detailed and accurate trajectory data is obtained, it is shown that computerised analysis techniques can readily be devised which allow the establishment of the variation of drag with incidence and speed to an acceptable accuracy. The new method has been applied successfully to the analysis of tests of specific body shapes in a hypersonic ballistic tunnel; typically, the drag coefficient has been established to an accuracy of 1% over a wide Mach number range.

## 8. CONCLUSIONS AND RECOMMENDATIONS

Ten main issues have been selected. Five relate to test facilities and methods, matters of vital importance in drag prediction. The other five are aimed at the main opportunity and problem areas.

- 1) There is an urgent need to provide a new generation of major transonic and low-speed windtunnels, capable of providing flows adequate to allow high-quality drag measurements at elevated Reynolds numbers;
- 2) Continued attention is needed to the simulation of high Reynolds number conditions at model scale, including the possible use of unconventional means such as controlled thinning of the model boundary layers;
- 3) Comparative research should be sponsored on datum model and support arrangements in selected major tunnel facilities at high subsonic and transonic speeds;
- 4) Critical research programmes should be arranged to develop an agreed appreciation of engine-flow simulation and auxiliary-test techniques for use in engine/airframe interaction investigations;
- 5) There should be collaboration in the codification of flight-test engine thrust determination methods and in the critical assessment of dynamic flight-test drag measurement techniques;
- 6) Twodimensional prediction methods already proven for conventional aerofoils should be extended to cope with supercritical flows, flow separations at elevated angles of incidences, and multiple high-lift configurations;
- 7) There should be an early AGARD Specialists' Meeting on Flow Separations; imaginative advances in the understanding and prediction of twodimensional and threedimensional flow separation phenomena are badly needed for incorporation in threedimensional viscous compressible flow drag prediction methods under development;
- 8) Collaboration should be arranged in good-quality drag measurements on common excrescence arrays at cruise and on representative excrescences at high lift;
- 9) Considerable scope exists for empirical analyses, guided by sound physical understanding, aimed at improved design and drag estimation methods related to engine/airframe and store-installation aspects;
- 10) The limited effort available for hypersonic drag research should be applied co-operatively to the main problems indicated by Wuest in the concluding discussion.

- XV -

XV

APPENDIX

CONFERENCE PAPERS

SESSION I - AIRCRAFT DRAG (GENERAL)

1. J H Paterson  
D G MacWilkinson  
W T Blackerby  
A survey of drag prediction techniques applicable to subsonic and transonic aircraft design.
2. F G Moore  
Aerodynamic drag and lift of general body shapes at subsonic, transonic and supersonic Mach numbers.
3. A Das  
On some basic and new aspects about the drag problem of wings and bodies in supersonic flows.
4. L Gaudet  
K G Winter  
Measurements of the drag of some characteristic aircraft excrescences immersed in turbulent boundary layers.
5. S N Wagner  
Problems of estimating the drag of a helicopter.
6. S F J Butler  
Aircraft drag prediction for project appraisal and performance estimation.

SESSION II - WING DRAG

7. A M O Smith  
T Cebeci  
Remarks on methods for predicting viscous drag.
8. J J Kacprzyński  
Drag of contemporary aerofoils in transonic flow.
9. H Yoshihara  
R Magnus  
D Zonars  
Transonic drag due to lift of planar jet-flapped airfoils.
10. J Zwaaneveld  
Comparison of various methods for calculating profile drag from pressure measurements in the near wake at subcritical speeds.

SESSION III - BASE DRAG AND SEPARATION

11. M Sirieix  
Trainée et décollement.
12. M Tanner  
New investigations for reducing the base drag of wings with a blunt trailing edge.
13. A L Addy  
H H Korst  
R A White  
B J Walker  
A study of flow separation in the base region and its effects during powered flight.
14. R C McWharter  
Prediction of buffet onset for aircraft—recent progress in wind tunnel—flight test data correlation.

SESSION IV - INTERACTION EFFECTS

15. P P Antonatos  
L E Surber  
J A Laughrey  
D J Stava  
Assessment of the influence of inlet and afterbody nozzle performance on total aircraft drag.
16. Withdrawn
17. W C Swan  
A Sigalla  
The problem of installing a modern high bypass ratio engine on a twin jet transport aircraft.
18. D J Peake  
W J Rainbird  
The drag resulting from threedimensional separations caused by boundary-layer diverters and nacelles in subsonic and supersonic flow.
19. P G Pugh  
P G Hutton  
The drag of externally carried stores - its prediction and alleviation.

20. W Wuest  
Drag in hypersonic rarefied flow.
21. J Allègre  
C Matrand  
M F Scibilia  
Trainée de corps portants pilotes à haute altitude.
22. E Vallerani  
A review of supersonic sphere drag from the continuum to the free molecular flow regime.
23. W Merzkirch  
A Stilp  
The influence of wave drag on hypersonic entropy wake observations.

SESSION VI - TESTING TECHNIQUES AND FLIGHT/WINDTUNNEL CORRELATION

24. E C Rooney  
Development of techniques to measure in-flight drag of a US Navy fighter airplane and correlation of flight measured drag with windtunnel data.
25. J S Pyle  
E J Saltzman  
Review of drag measurements from flight tests of manned aircraft with comparisons to windtunnel predictions.
26. R K Fancett  
T Smith  
An assessment of the accuracy of transonic drag measurement in a large modern windtunnel.
27. D M Sykes  
Sting interference effects on afterbodies at transonic speeds.
28. Withdrawn
29. D Bahurel  
A Desgardin  
Mesures de trainée en tunnel de tir.

XVII

A SURVEY OF DRAG PREDICTION TECHNIQUES  
APPLICABLE TO SUBSONIC AND TRANSONIC AIRCRAFT DESIGN

J. H. Paterson\*  
D. G. MacWilkinson†  
W. T. Blackerby\*\*

1-1

SUMMARY

Three aspects of aircraft drag prediction in the subsonic to transonic range are discussed:

1. Preliminary estimation procedures
2. Estimation using wind tunnel test data
3. Wind tunnel - flight correlation

Inaccuracies in the approach to use of flat plate skin friction, with appropriate shape factors, to predict profile drag are identified. Shape factor estimation may be inadequate due to use of obsolete empirical formulae, which are based on airfoil test data with mixed laminar - turbulent flow, and more significantly due to airfoils unrepresentative of current highly loaded designs with high viscous form drag. The success of new viscous flow solutions to predict drag and to interpret two-dimensional test data suggests that this approach will find increasing application in future work.

Reliance on wind tunnel tests to determine component interference is still necessary, in view of the lack of suitable theoretical viscous solutions in mixed flows.

Attempts to use low Reynolds number wind tunnel drag levels to predict full scale drag are shown to be reasonably successful, providing that careful testing techniques are employed, and correct interpretation of test data is made.

It is shown that full scale profile drag for the C-5A is predicted from wind tunnel data within a range 1 - 3% of flight data, using two alternative methods of scaling the results. The flight test data, analyzed in detail, confirm the predicted trends in profile drag with Reynolds number over a range from  $R_N = 40 \times 10^6/MAC$  to  $100 \times 10^6/MAC$ . Careful monitoring of the manufacturing tolerances during the development stage, together with these results, suggest that the effective surface distributed roughness levels are well within those values associated with smooth turbulent flow, and that the methods employed for estimating the total roughness drag increment are satisfactory.

NOTATION

$C_f$	Average flat plate skin friction coefficient	$C_L$	Lift coefficient
$R_N$	Reynolds number	$C_D$	Drag coefficient
SF	Component shape factor	$M_D$	Drag-divergent Mach number
$t/c$	Thickness/chord ratio	$C_{D_P}$	Profile Drag
$c$	Chord	AR	Aspect ratio
$c_l$	Section lift coefficient	$c_M$	Section pitching moment coefficient
$x/c$	Non-dimensional chord	$C_M$	Pitching moment coefficient
$C_p$	Pressure coefficient	$R_x$	Reynolds numbers based on distance from leading edge
$C_N$	Normal force coefficient	$\alpha_{FRL}$	Angle of attack of fuselage reference line
M	Mach number	$e$	Wing span efficiency
$c_{d_p}$	Section profile drag coefficient	$e$	Downwash angle
$\eta$	Non-dimensional semi-span station	$I_T/c$	Tail volume coefficient

Subscripts

W	Wing
A-h	Aircraft tail-off configuration

\*C-5A Flight Sciences Manager  
†Aircraft Development Engineer, Specialist  
\*\*Senior Aerodynamics Engineer

## 1. INTRODUCTION

Techniques for predicting subsonic and transonic aircraft drag at full scale Reynolds numbers can be classified broadly into three approaches:

- (1) Theoretical estimates requiring solution of the viscous flows around complete aircraft configurations.
- (2) Wind tunnel measurements at low Reynolds number, with extrapolation to full scale of the profile drag component using either semi-empirical flat plate skin friction or theoretical methods.
- (3) Empirical methods based on accumulated wind tunnel and flight test data on a variety of configurations, with parametric corrections to account for variations between one configuration and another.

In the past, during the preliminary design phase of a project prior to wind tunnel tests, drag estimates have generally been based on method (3), combined with an estimate of full scale profile drag. Today these estimates are more refined by inclusion of appropriate information from method (1). Method (1) however, is still under development and, although theoretical three-dimensional viscous flow programs are available for isolated components, procedures for solution of the viscous flows around complete airplanes are yet to be developed. In addition, most three dimensional viscous flow solutions are prohibitive from a cost point of view for preliminary design estimates, and thus the aerodynamicist is forced to rely on less expensive and less sophisticated procedures. In the future it is anticipated that improvements in computer technology and/or the development of integral methods will combine to produce the desired degree of sophistication.

As the airvehicle design proceeds from the preliminary design phase to the project definition phase, preliminary drag estimates are augmented by wind tunnel tests, when possible, and procedures for correcting low Reynolds number wind tunnel test data to full scale conditions. In this phase there are two primary sources of inaccuracy, namely, the wind tunnel data and the extrapolation procedures. Indeed, further inaccuracies in flight test data and compensating errors may have contributed to misleading evaluation of the degree of correlation which was achieved between wind tunnel and flight test data.

Each stage of the drag prediction process, as it applies to subsonic and transonic aircraft, will be reviewed in this paper to identify the sources of inaccuracy, as well as the degree of correlation with test data for the C-5A and C-141A configurations, achieved by various selected prediction techniques. The accuracy of drag predictions by any of the above methods or combinations thereof, is largely dependent upon our ability to predict profile drag, since this component accounts for approximately 60 percent of the cruise drag of current jet transports. It is appropriate therefore, to commence with a review of the methods of estimating profile drag of aircraft components, including empirical methods based on the flat plate approach and theoretical methods using trailing edge momentum considerations.

## 2. PRELIMINARY ESTIMATION PROCEDURES

### 2.1 Profile Drag

#### 2.1.1 Review of Flat Plate Skin Friction

The literature contains a vast amount of experimental data on plane surfaces at incompressible speeds. The experiments range from the early water tank towing experiments to modern wind tunnel tests using sophisticated measuring techniques. A significant number of tests are historical, having been conducted prior to 1950 by towing planks through water, primarily for use in ship design. Many of the early experiments are characterized by inconsistencies in testing and measuring techniques. Nevertheless, empirical skin friction formulae derived from these data have received widespread acceptance by hydro- and aerodynamicists. This is particularly true of the Karman-Schoenherr formula developed in 1932 and still widely used by aeronautical engineers. The authors (1) present a detailed review of the background testing and data on which this law is based. Comments will be confined to a summary of that review and will emphasize the principal findings which relate to the subject of this paper.

A selection of average skin friction test data from both water (open symbols) and air (solid symbols) experiments is shown in Figure 1. (References 2 through 13)

The intent of the study (1) was to identify the sources of inaccuracy from the voluminous test data available, and qualitatively assess the impact of these uncertainties on the correlation of drag predictions with wind tunnel and flight test drag results. The principal observations to be noted are:

- (1) Of the test data available, which form the historical background to Schoenherr's "mean line" analysis (7), significant scatter exists of the order of  $\pm 10\%$ , particularly over the Reynolds number range up to 40 million, where the majority of experiments were conducted. This range coincides with that for skin friction estimation on aircraft components, such as wings.
- (2) The basis for the variation of  $C_f$  with  $R_N$  in the range 100 to 300 million is solely from Kempf's water tank tests of 40 years ago. Beyond 300 million no basic data exist, although Schoenherr used Kempf's integrated results to extend these levels by his empirical formula to 450 million.

Tests in Water			Tests in Air		
Investigator/Description	Symbol	Reference	Investigator/Description	Symbol	Reference
Froude, 1872 - 16, 28, and 50 foot varnished planks.	○	(2)	Hughes, 1952 - NPL Tank; Composite curve for $l/b = 0$ .	---	(5)
Gebers, 1908 - 160, 360, 460, 652 cm planks.	□	(3)	Hughes, 1952 - NPL Tank; Composite curve for $l/b = 41.9$ .	---	(5)
Froude Tank, NPL, 1915 - 3, 8, 16 foot planks.	◇	(2)	Gibbons, 1915 - 9.5 foot glass plate.	▶	(9)
Gebers 1919 - 125, 250, 500, 1000 cm planks.	△	(4)	Wieselsberger, 1925 - 50, 100, 150, 200 cm planes.	■	(10)
Kempf, 1929 - Various plates, integrated by Schoenherr using the Schoenherr mean line.	▽	(6)	Jones & Williams, 1937 - CAT, 2 foot plank.	▲	(11)
Kempf, 1929 - Basic local $c_f$ data for iron plate, lacquered, waxed & polished; integrated graphically	⊙	(6)	Smith & Walker, 1959 - Flat plate, momentum defect method.	▲	(12)
Kempf, 1929 - Basic local $c_f$ data for iron plate rubbed smooth, integrated graphically	⊗	(6)	Smith & Walker, 1959 - Flat plate, floating element method.	◆	(12)
Washington Unpublished, 1932 - 20, 30, 40, 80 foot planks.	✱	(7)	Winter & Gaudet, 1966 - Sidewall of 8 x 8 foot RAE tunnel.	◀	(13)

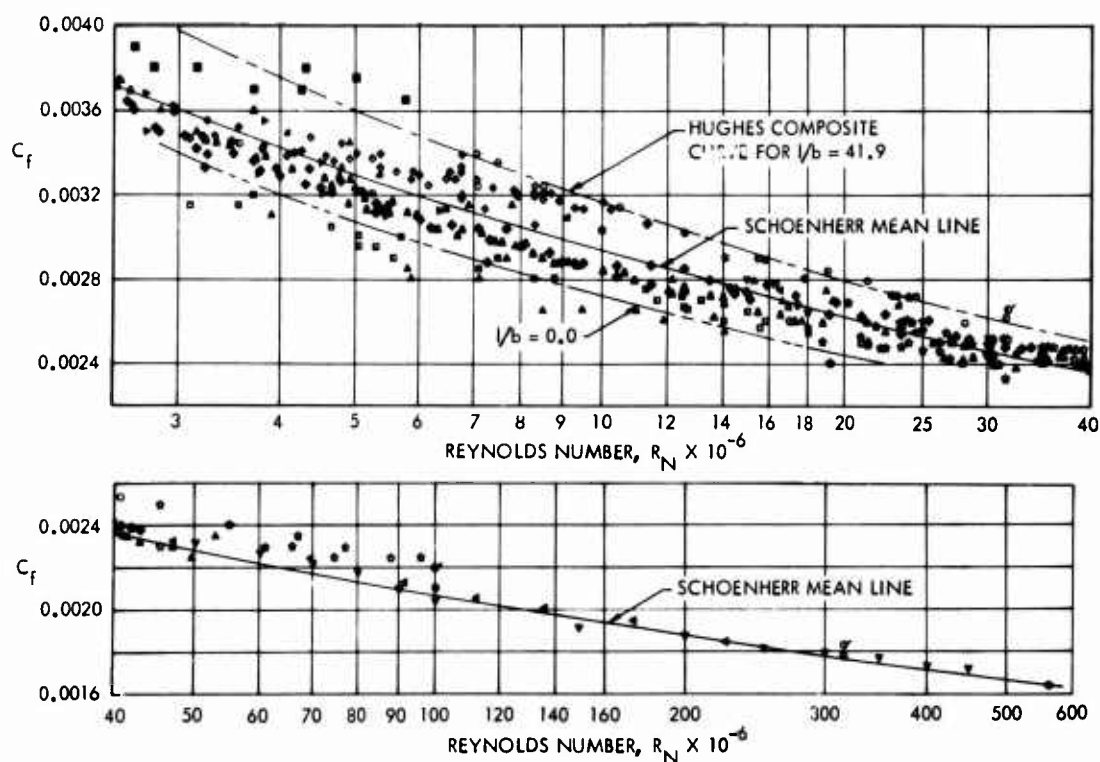


FIGURE 1. SUMMARY OF EXPERIMENTAL RESEARCH ON FLAT PLATE SKIN FRICTION

- (3) It is apparent from study of the experimental techniques and resulting data, that the magnitude of  $C_f$  in the Reynolds number range up to 30 million is conservative mainly due to 3-dimensional effects. This is confirmed by the work of Hughes (5), and to some extent by the data of Smith and Walker (12). In the range of  $R_N$  from 3 million to 40 million, the maximum difference in scale effect between all data is of the order of  $\pm 0.0002$  in  $C_f$ . This would represent a variation in predicted full scale profile drag of a typical transport wing when scaling wind tunnel data of approximately  $\pm 0.0005$  in  $C_D$ .
- (4) Although the Schoenherr mean line is a good representation of existing test data, substantiation of low and very high ( $R_N > 500$  million) Reynolds number skin friction is required by further research programs.

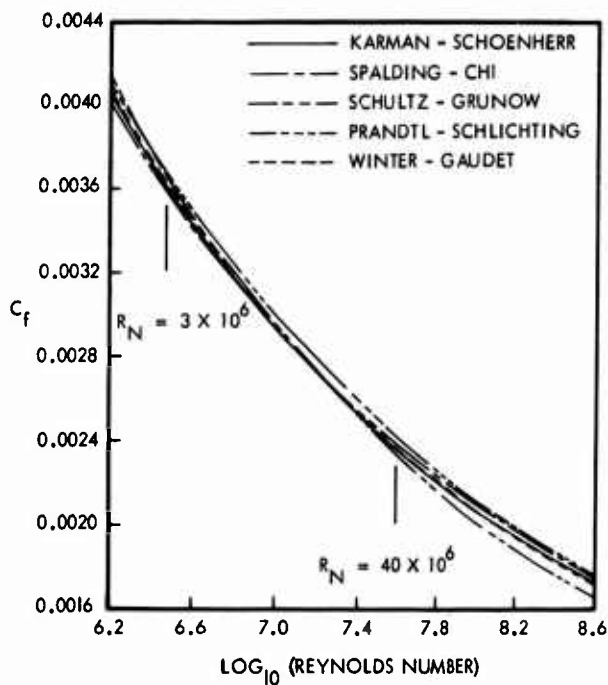


FIGURE 2. COMPARISON OF EMPIRICAL FLAT PLATE SKIN FRICTION FORMULAE FOR INCOMPRESSIBLE TURBULENT FLOW

Figure 2 shows a sample of mean  $C_f$  data for fully turbulent flow from five empirical skin friction formulae, mostly from analytical research on skin friction. None of these were evolved from a purely mathematical treatment of the flow over a flat plate; all contain some empiricism of the boundary layer parameters.

In order to extend the range of validity of resistance formulae based on the  $1/7$  power law, substitution of the universal logarithmic velocity distribution law was made. Schlichting obtained a modification to the Prandtl formula in this way. Calculations using the logarithmic velocity profiles become more cumbersome and therefore Schlichting derived an empirical curve fit given by:

$$C_f = \frac{0.455}{(\log R_1)^{2.58}} \quad (1)$$

This formula is shown plotted on Figure 2 as the Prandtl-Schlichting curve.

Based on the work of Von Karman, Schoenherr was able to deduce an empirical formula which approximated the mean line he had placed through a collection of experimental skin friction data. This has become the well known Karman-Schoenherr line:

$$\frac{1}{C_f} = 4.13 \log (R_1 C_f) \quad (2)$$

Schultz-Grunow (14) set out to investigate the application of the logarithmic laws of velocity distribution within the boundary layer of pipe flow to flow along a flat plate. He made very careful measurements using plywood and metal plates mounted in the wall of a wind tunnel. Two types of measurements were made: velocity distributions within the free boundary layer and resistance of the plates. One means of measuring friction was to directly weigh the drag on a movable rectangular plate mounted at various locations in a sector of the principal plate. This was very similar to the movable plate technique employed by Kempf in his pontoon test.

Schultz-Grunow's measurements showed that the velocity profile in the outer portion of the boundary layer of the plate deviates systematically upwards from the logarithmic velocity distribution law of a circular pipe. Based on his results, he repeated the derivation of the resistance formula and obtained the following formula:

$$C_f = \frac{0.427}{(\log R_1 - .407)^{2.64}} \quad (3)$$

The more recent paper written by Spalding and Chi (15) reviews some twenty theoretical treatments of the turbulent boundary layer on a smooth flat plate. The major characteristics of these theories were summarized and their predictions compared with available experimental data. The root-mean-square error for each was computed for evaluation purposes, and a new calculation procedure was developed based on the accumulated knowledge. Consideration was not limited to the incompressible case.

Use of the Spalding-Chi equations directly is somewhat tedious in that an iterative process must be used wherein the variation of local skin friction coefficient with Reynolds number is first determined and then the mean skin friction is computed for a given combination of local skin friction and Reynolds number. The variation of mean skin friction with  $R_N$  is shown for comparison purposes in Figure 2.

The final curve shown in Figure 2 is that due to Winter and Gaudet (13). Like the Spalding-Chi method, the solution of the Winter-Gaudet equations require an iteration process.

The maximum difference in scale effect from use of these formulae is about 0.00014 in  $C_f$  over a typical range of Reynolds numbers from  $3 \times 10^6$  to  $40 \times 10^6$ . Those two formulae most often used, namely the Prandtl-Schlichting and Karman-Schoenherr, however, produce an almost identical scale effect. Of more significance is the fact that most of these analytical treatments are based on test data with inherent scatter indicated in (1) above of  $\pm 10\%$  over this Reynolds number range.

## 2.1.2 Two-Dimensional Airfoil Profile Drag

Two aspects of the estimation techniques used in the calculation of two-dimensional airfoil profile drag are discussed. First, the empirical approach used in preliminary estimates is reviewed and some of the inherent limitations identified. Secondly, a theoretical approach is described and comparisons of theory and experiment are presented to establish the degree of correlation achieved.

It is assumed that for attached flow conditions,

$$c_{d_p} = c_{d_{p_{\min}}} + c_{d_{p_{c_l}}} \quad (4)$$

where  $c_{d_{p_{\min}}}$  is the minimum profile drag occurring at some optimum  $c_l$ , and  $c_{d_{p_{c_l}}}$  is the lift-dependent profile drag

which is primarily a function of airfoil thickness, camber, and trailing edge angle. Both terms depend on Reynolds number as a result of viscous modifications to the boundary layer and pressure distribution. For the purposes of this analysis, the first component in equation (4) can be further defined as

$$c_{d_{p_{\min}}} = (S.F.) \times 2C_f \quad (5)$$

where  $C_f$  is the skin friction of the equivalent flat plate with zero pressure gradient for the same transition location as the airfoil. Thus, in this analysis we define (S.F.), or shape factor, as the sum total of all the thickness and viscosity effects inherent in the airfoil characteristics and manifested as minimum form drag.

Hoerner (16) has shown, from a collection of early data, that the shape factor for sections with maximum thickness at 30% chord can be represented empirically by

$$(S.F.) = 1 + 2(t/c) + 60(t/c)^4 \quad (6)$$

where the second term represents the drag due to increase in local velocity over the section, or supervelocity. This can be shown for incompressible attached flow conditions to be

$$(t/c) = (\Delta v/v_o) = (1 - C_p)^{1/2} - 1 \quad (7)$$

The third term in equation (6) represents the viscous pressure drag effects.

Figure 3 presents a summary of a preliminary study in which the objective was to determine the method which provided the most realistic estimation of two-dimensional airfoil form drag as represented by the factor (S.F.) in equation (5). Where possible, sections of thickness close to 12% $c$  have been chosen, typical of the average values used on modern transport aircraft wings.

The experimental data shown in Figure 3 are derived from two sources: (1) NACA (17), and (2) Lockheed-Georgia (18), (19). It was found that most of the early NACA data are not ideally suited to accurate assessment of airfoil form drag. This is because the testing techniques employed favored either free transition or the application of an oversized roughness band applied around the leading edge. Hence, in the first instance correlation of measured drag with transition location was in most cases not possible and, in the second, accurate estimation of roughness drag was not attempted. For the present analysis, only transition fixed data has been used and corrected for an estimated transition strip drag of 10 counts, which is considered reasonable for the low range of lift coefficients pertaining to this analysis.

The Lockheed-Georgia data are taken from a research program on a series of airfoils derived from the basic C-5A section. Profile drag was measured by the wake traverse method. For the purposes of this analysis, it is sufficient to note that these airfoils generally conform to the principles of obtaining high loading characteristics by leading and trailing edge modifications and therefore differ somewhat to earlier, more conventional types. These data have been corrected for 8 counts of transition strip drag. This correction will be discussed later in more detail.

In addition to the experimental data, a number of estimates for the C-141 section at 0.389  $\times$  semispan and airfoil 8 (C-5A) of the Lockheed series are included.

These estimation methods are:

- (1) Supervelocity as in equation (7), using measured pressure data.
- (2) Thwaites' incompressible formula (20).
- (3) Lockheed-Georgia Subsonic Viscous Flow Program (21).

The large spread in value of (S.F.) at  $t/c = .12$ , indicated in Figure 3 is a result of parametric differences in camber, maximum thickness location and aft loading which all contribute to form drag. No attempt has been made to correlate the data for these effects. Certain features of the various methods are, however, noted;

- (1) In general, experimental form drag for the 12% airfoils lies within the range 30% to 50% of flat plate skin friction.
- (2) Estimates by the average supervelocity method for airfoil 8 and the C-141 section, using measured pressure data, are 10 - 15% lower than experimental data. The empirical result from Hoerner's equation also produces a low value of shape factor. (The use of a supervelocity method for three dimensional profile drag estimates will be discussed in subsequent paragraphs.)
- (3) The experimental results are in better agreement with the range of values given from the R.A.e.S. Data sheets (22).

The values of shape factor for the C-141A section from experiment, Thwaites and Lockheed theory agree within 5%, whereas the value predicted by the mean supervelocity process is 13% lower than the average of these figures. This indicates that assessment of the total airfoil form drag from viscous effects in attached flow conditions requires the application of the boundary layer methods typified by the Lockheed theory.

**Lift Dependent Profile Drag -** Assessment of airfoil profile drag variation with angle of attack for preliminary estimates is usually based on empirical correlation of wind tunnel test data from transition free and fixed tests. It is important to note that careful interpretation of test data is required in order to determine the true variation of profile drag, both skin friction and form components, with angle of attack. At full scale Reynolds numbers, only fully turbulent boundary layer conditions are pertinent; since low Reynolds number test data with free transition often produces an erroneous variation of drag with lift due to forward movement of the minimum pressure point, fully turbulent test data are required.

An example of the type of preliminary estimation procedure employed is given in Figure 4, where the drag due to lift variations with angle of attack are referred to the equivalent flat plate friction for any Reynolds number and transition condition. The results for a number of 4 and 5 digit series airfoils are shown as the ratio

$$(C_{fFP}/C_{fFP\ opt}) \text{ versus } \frac{(c_l - c_{l\ opt})}{(c_{l\ max} - c_{l\ opt})}$$

$c_{l\ opt}$  is assumed to be approximately  $10 y/c$ , where  $y/c$  is the ratio of maximum ordinate of the section camber line to the chord line. The data are applicable to partially laminar and fully turbulent sections with maximum thickness located at  $x/l \approx 0.30$ . The drag of 6 series sections are predicted reasonably well at  $(c_l - c_{l\ opt}) / (c_{l\ max} - c_{l\ opt}) \geq .30$ , i.e. beyond the laminar "bucket."

- NACA 63006
- ▲ NACA 63009
- NACA 63012
- ◆ NACA 64015
- ▼ NACA 65015
- \* NACA 2218
- x AIRFOIL 3
- AIRFOIL 8
- △ AIRFOIL 9
- AIRFOIL 10
- ▽ AIRFOIL 11
- ◇ AIRFOIL 12
- ▷ AIRFOIL 14
- ◊ AIRFOIL 16
- △ AIRFOIL 23
- ◇ AIRFOIL 24
- + AIRFOIL 26
- ◊ AIRFOIL 27
- ◊ AIRFOIL 28
- ◊ AIRFOIL 29
- ◇ C-141,  $\tau = .389$ , SUPERVELOCITY
- C-141,  $\tau = .389$ , THWAITES
- C-141,  $\tau = .389$ , WAKE TRAVERSE
- ◇ C-141,  $\tau = .389$ , THEORY
- ◇ AIRFOIL 8, SUPERVELOCITY
- ◇ AIRFOIL 8, THEORY

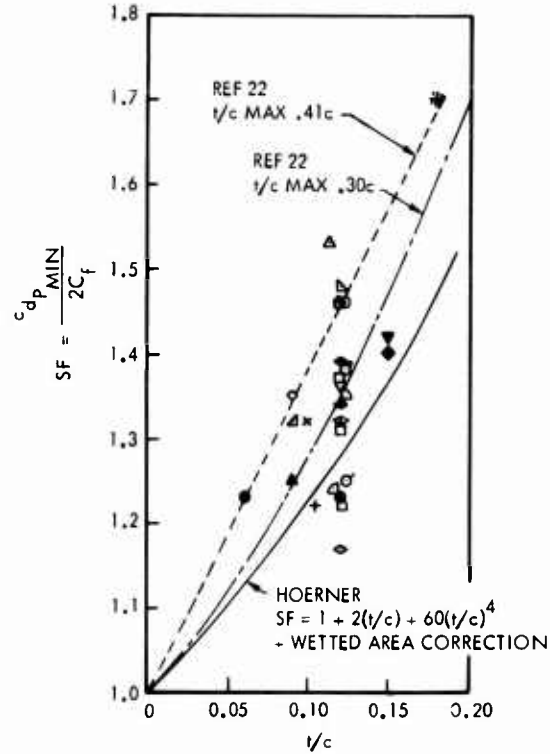


FIGURE 3. 2-DIMENSIONAL AIRFOIL SHAPE FACTORS. TRANSITION FIXED DATA

$$c_d = (C_l)_{OPT} \times [SF] \times [WF] \times \frac{C_f}{(C_l)_{OPT}}$$

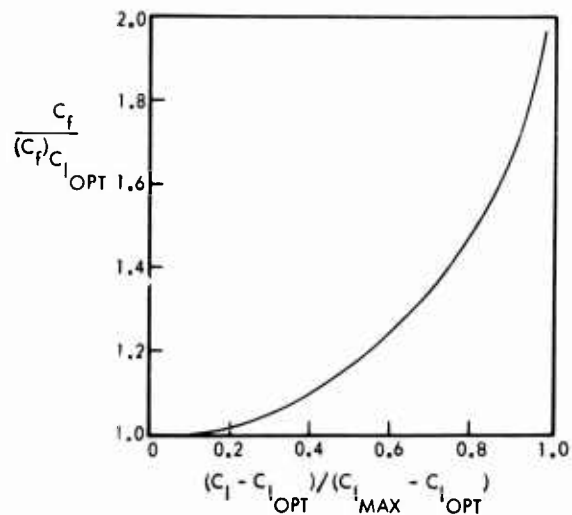


FIGURE 4. VARIATION OF SECTION PROFILE DRAG WITH LIFT

Two-Dimensional Viscous Flow Theoretical Program - In addition to the empirical estimation procedures available, the aerodynamic analysis of wings for modern subsonic aircraft demands analytical tools that are fast, inexpensive, and sufficiently accurate to discern subtle differences between project configurations. The analytical tools must be reliable and correlated so that their limitations are well established. All significant aerodynamic factors must be included in the analysis. One such program which is finding increasing use is a two-dimensional theoretical method for computing airfoil profile drag, already introduced briefly in the preceding paragraphs.

The two-dimensional viscous compressible pressure distribution program (TDVCP) (21) comprises potential flow and boundary layer theories and an iterative process that incorporates viscous effects into the airfoil pressure distribution.

The potential flow method used in this program is that of Weber (23). The Karman-Tsien compressibility relationship (24), is used to correct the incompressible pressure distribution for Mach number effects.

In the laminar portion of the boundary layer, only the momentum thickness up to transition is calculated. To calculate the development of the laminar boundary layer momentum thickness, the Thwaites formula with the Stewartson-Willingsworth transformation (25), (26), (27) is used. The displacement thickness in the laminar boundary layer region, which is used in the iteration scheme, is obtained from a parabolic extrapolation of the turbulent boundary layer forward to the leading edge of the airfoil. This assures a smooth airfoil for subsequent iterations. The program checks at each calculated point to determine whether the input fixed transition location has been reached, if laminar short bubble separation has occurred (28), or if transition is predicted by Michel's method (28).

The turbulent boundary layer is calculated by the theory of Nash (29), using the momentum thickness of the laminar boundary layer at the point of transition as a starting condition. A complete set of turbulent boundary layer parameters is calculated downstream to the airfoil trailing edge. For the incompressible case, this theory uses a modified Ludwig-Tillman skin friction law. The boundary layer is assumed separated if a local value of  $H$  equal to 2.4 is reached.

The boundary layer thickness effect is applied as a correction to the velocities in the solution obtained with the modified camber and angle of attack. The corrections to the velocities due to thickness are obtained by first calculating the potential flow on the basic thickness distribution of the original airfoil shape. Secondly, the potential flow is calculated on a body formed by adding the average boundary layer displacement thickness and the wake is taken as formulated by Powell (31). Finally, the difference in velocities obtained from the two solutions is applied as a velocity correction to the equivalent airfoil solution obtained with only camber and angle of attack viscosity corrections.

The newly defined airfoil having a revised camber, thickness and angle of attack is then used to determine an equivalent "inviscid" pressure distribution. The process outlined represents one step in an iterative process. The number of steps required to establish convergence varies with different airfoils, but five to ten iterations are usually sufficient. A convergence check on  $c_l$  is used to terminate the calculations.

Upon completion of the iterative process, the airfoil lift and pitching moment are integrated from the pressure distribution, and the two-dimensional drag is calculated by integration of the momentum integral equation along the wake by the method of Squire and Young (32) and application of the Stewartson transformation. This calculation is performed for both upper and lower surfaces and added to yield the two-dimensional drag.

New research is under way at Lockheed-Georgia by Goradia under NASA contract (33), to develop profile drag methods which account for asymmetric wake development pertaining to cambered airfoils at angle of attack. Data presented in the current paper, however, refer to the theoretical methods which use the Squire and Young momentum equation.

The two-dimensional drag rise Mach number prediction included in this program is keyed to the "rapid" drag rise Mach number as defined by  $dc_d/dm = 0.05$  at constant angle of attack. Using this drag-rise definition, Sinnott (34) following the observation of Nitzberg and Crandall (35) showed that the experimental drag rise Mach number agreed well with the occurrence of sonic conditions at the crest of two-dimensional airfoils. This observation has been utilized in the drag rise prediction method for two-dimensional airfoils of the Royal Aeronautical Society (36). The Lockheed program incorporates basically the RAeS method to calculate the drag rise Mach number. It has been extensively correlated (37) and found to predict lift, drag and pitching moment data that agree well with experiment for conditions of attached subsonic flow. The drag rise Mach number predictions agree well with experiment when used in conjunction with pressure distribution criteria (37). It is appropriate at this point to show some of these results to illustrate both the accuracy and limitations of the program. Most of the experimental data were obtained from tests (18) (19) in the two-dimensional facility of the Aircraft Research Association in England.

Figure 5 shows a comparison of the predicted viscous pressure distribution with experiment for airfoil 3 at a lift coefficient of about 0.42 at  $M = 0.64$  and  $R_N = 6.8 \times 10^6/c$ . This airfoil has a slightly "peaky" characteristic with very little aft loading. Agreement between theory and experiment is good, but the program underestimates the uncambering effect of the boundary layer. Figure 6 shows a similar comparison for airfoil 12 which is a peaky, aft loaded, advanced technology, airfoil. The agreement between theory and experiment is quite good, even in the highly loaded aft portion of the airfoil.

1-8

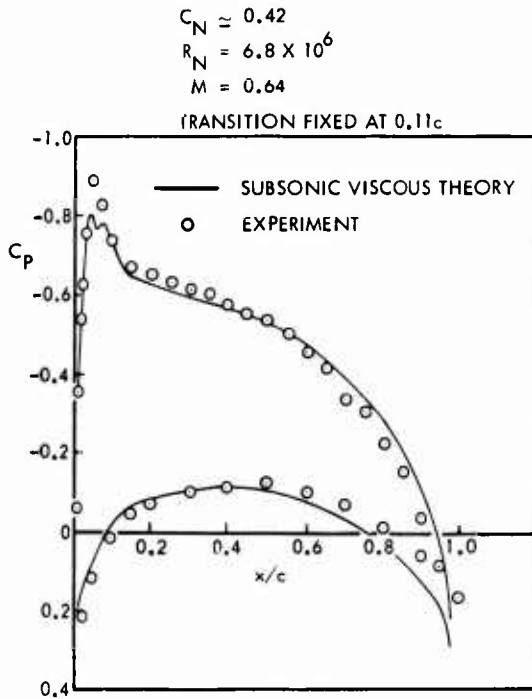


FIGURE 5. COMPARISON OF THEORETICAL AND EXPERIMENTAL PRESSURE DISTRIBUTION FOR AIRFOIL NO. 3

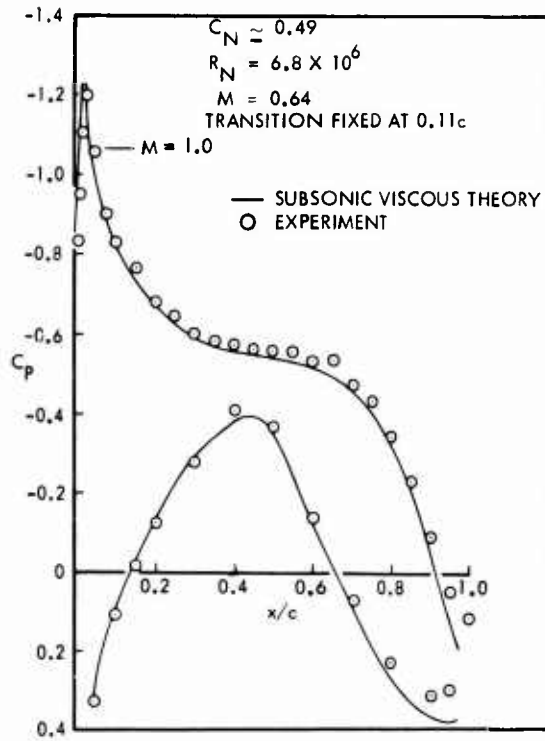


FIGURE 6. COMPARISON OF THEORETICAL AND EXPERIMENTAL PRESSURE DISTRIBUTION FOR AIRFOIL NO. 12

Figure 7 shows a summary of the force data for airfoil 3 at  $M = 0.64$  and  $R_N = 6.8 \times 10^6$ . The dashed lines are the inviscid potential flow lift and pitching moment data for the airfoil. The solid lines are the predicted viscous data estimated by theory. The symbols are experimental data from the test program mentioned above. This figure shows how the viscous iterative scheme moves the predicted data from the potential flow value towards the experimental results. There is still some disagreement between the viscous prediction and experimental data, which may be due to damping mechanisms in the iterative scheme, or to the experimental technique.

The amount of disagreement varies from one airfoil to the next as shown in Figure 8, which presents a similar set of predicted and experimental force data for airfoil 12. In this case, the agreement between theory and experiment is better than for airfoil 3.

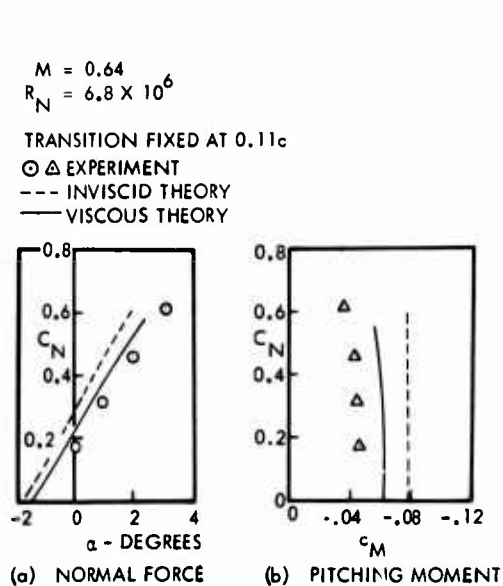


FIGURE 7. COMPARISON OF THEORETICAL AND EXPERIMENTAL FORCE DATA FOR AIRFOIL 3

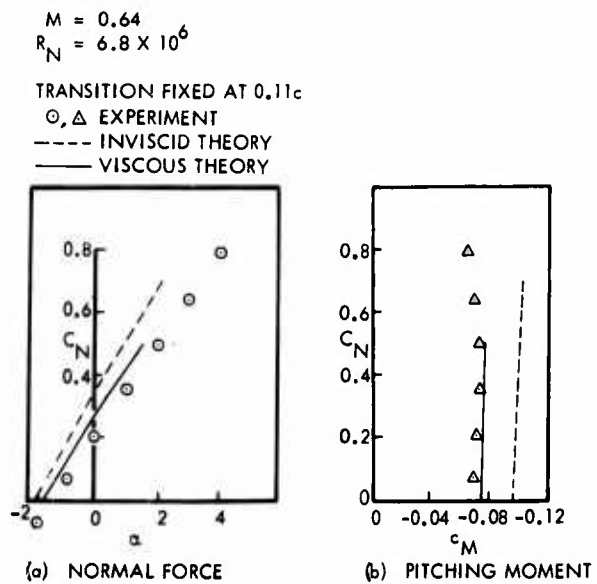


FIGURE 8. COMPARISON OF THEORETICAL AND EXPERIMENTAL FORCE DATA FOR AIRFOIL 12

Figure 9 shows predicted  $c_l$  vs  $c_d$  for airfoil 3, for transition at 11% chord. The experimental free transition point was at approximately the same location and the experimental drag values agree closely with predictions. Of further significance is the fact that the shape of the  $c_l$  vs  $c_d$  polar is accurately predicted up to the  $c_l$  where supersonic flow appears on the airfoil.

The predicted variation of drag with Reynolds number for airfoil 3 at  $M = 0.75$  and  $\alpha = 0$  is shown in Figure 10 for transition at 2% chord and 11% chord. The free transition test data shows a movement of transition with increasing Reynolds number up to a point between 2% and 11% chord at  $R_N = 5.5 \times 10^6$  where the transition point apparently stabilized. For higher Reynolds numbers, the drag follows the predicted curve closely. These data show the predicted variation of drag with Reynolds number to be correct.

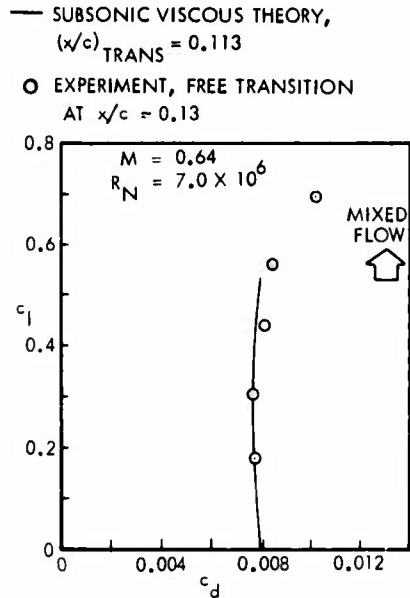


FIGURE 9. COMPARISON OF THEORETICAL AND EXPERIMENTAL DRAG CHARACTERISTICS FOR AIRFOIL 3

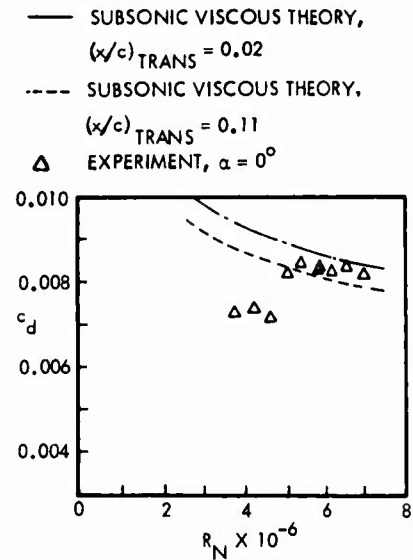


FIGURE 10. DRAG VS  $R_N$  FOR AIRFOIL 3

Substantiation of the variation of drag with increasing Reynolds number is shown in Figure 11 for NACA 65<sub>215</sub> - 114 airfoil where experimental transition locations were known. Again, agreement is good, particularly at the lower Reynolds numbers. The agreement at high Reynolds numbers is essentially the same as that shown by Osborne (38).

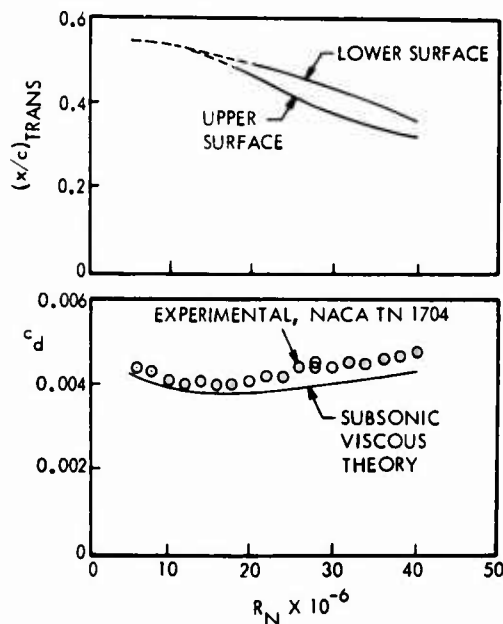


FIGURE 11. DRAG VS. REYNOLDS NUMBER FOR KNOWN TRANSITION LOCATION, NACA 65<sub>(215)</sub> - 114 AIRFOIL

Figure 12 shows the same data on airfoil 3 as were shown in Figure 10, but with the addition of fixed transition data from the same test. The fixed transition data has a higher drag level than the analytical prediction for transition at 2% chord. Also, the fixed transition drag level is about 0.0008 in  $c_d$  greater than that of free transition at the higher Reynolds numbers. These observations indicate that roughness drag due to the transition strip was present in the fixed transition data. This was supported by the fact that the roughness diameter was double the calculated boundary layer height at the same location for the higher Reynolds numbers tested.

The momentum thickness magnification effect developed by Nash (39) was applied to the calculated boundary layers for transition at 2% and 11% chord respectively, to produce the predicted drag plus incremental roughness drag curves shown in Figure 13. These two curves were intended to bracket the conditions of transition at the oversize roughness strip or transition ahead of the roughness strip. Agreement between the prediction and experiment is good. At the lower Reynolds number, the experimental data matches the curve based on laminar flow to the roughness strip, which is compatible with the transition location implied by the free transition data.

- ROUGHNESS STRIP AT 0.11c
- △ FREE TRANSITION
- SUBSONIC VISCOUS THEORY,  $(x/c)_{TRANS} = 0.02$
- SUBSONIC VISCOUS THEORY,  $(x/c)_{TRANS} = 0.11$

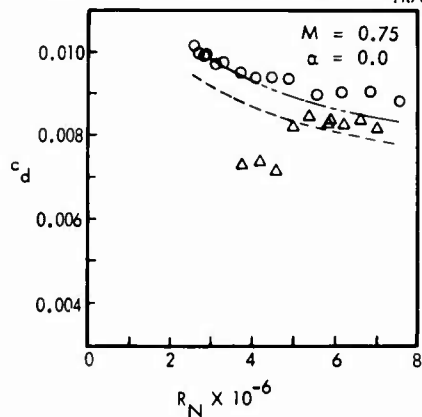


FIGURE 12. CORRELATION OF THEORETICAL AND EXPERIMENTAL DRAG FOR AIRFOIL 3

- EXPERIMENTAL, ROUGHNESS AT 0.11c
- SUBSONIC VISCOUS THEORY,  $(x/c)_{TRANS} = 0.11$  PLUS ANALYTICAL ROUGHNESS DRAG
- SUBSONIC VISCOUS THEORY,  $(x/c)_{TRANS} = 0.02$  PLUS ANALYTICAL ROUGHNESS DRAG

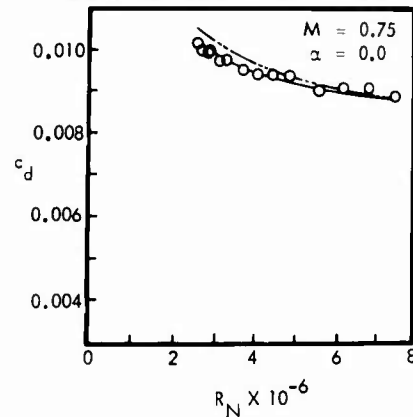


FIGURE 13. CORRELATION OF EXPERIMENT WITH THEORY ALLOWING FOR ESTIMATED ROUGHNESS DRAG

Figure 14 shows an analysis of a Lockheed-California Airfoil (No. 4) that was also tested at ARA. The test data are from a free transition test at  $M = 0.649$  and Reynolds number of  $2.5 \times 10^6$ . Theory predicts separation of the lower surface at  $c_l$  values less than 0.2 and separation of the upper surface at  $c_l$  values above  $c_l = 0.55$ . These two separation conditions are reasonably well supported by the experimental data. The free transition prediction shows that transition moves from 70% chord at  $c_l = 0.25$  up to 14% chord at  $c_l = 0.55$ . The experimental data, however, shows little variation in drag and follows the predicted  $c_d$  vs  $c_l$  curve for transition at 14% chord almost exactly. On the basis of this comparison, it was decided that extensive regions of laminar flow at low  $c_l$  conditions were not obtained in the experiment.

These examples serve to illustrate how analytical methods can be used to examine trends in experimental data and to increase confidence in use of data where certain subtle difficulties such as roughness drag, local separation, etc., could have made the data unusable.

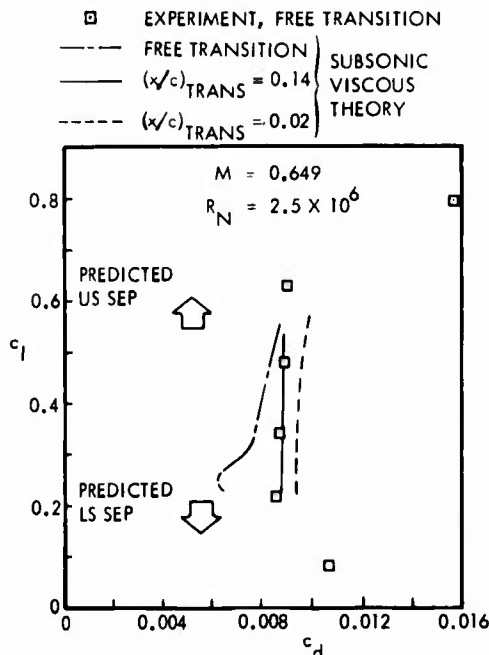


FIGURE 14. COMPARISON OF THEORETICAL AND EXPERIMENTAL DRAG CHARACTERISTICS FOR CALAC AIRFOIL NO. 4

The drag rise Mach number predictions are based on reasonably well established methods (36) but it is considered worthwhile to illustrate some capabilities and limitations identified from correlation studies. Figure 15 shows the predicted and experimental  $M_D - c_l$  boundary for airfoil 3.

This airfoil is 10% thick and is designed to carry most of the loading on the forward part of the airfoil, with a small leading edge peak. The result is that the airfoil has a relatively flat lower surface and considerable curvature in the mid-chord region of the upper surface. This airfoil has a modest drag rise Mach number which is limited by the upper surface conditions at all positive lift coefficients. The agreement between theory and experimental drag rise Mach number is good.

Figure 16 shows the theoretical and experimental drag rise Mach number data for airfoil 27 which has a flat top design pressure distribution with all of the loading on the aft part of the airfoil, at the design lift coefficient of 0.2. The theoretical drag rise boundary is composed of two lines which intersect at about  $C_l = 0.35$ . The upper line represents the  $C_l - M_D$  boundary for drag rise due to the airfoil upper surface while the lower line represents the boundary where drag rise is caused by the lower surface. Again, the agreement between theory and experiment is good.

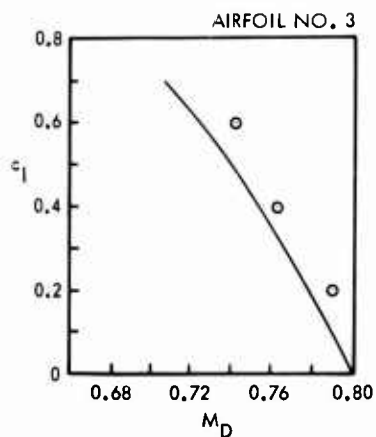


FIGURE 15. CORRELATION OF THEORETICAL DRAG DIVERGENCE MACH NUMBER AND EXPERIMENT

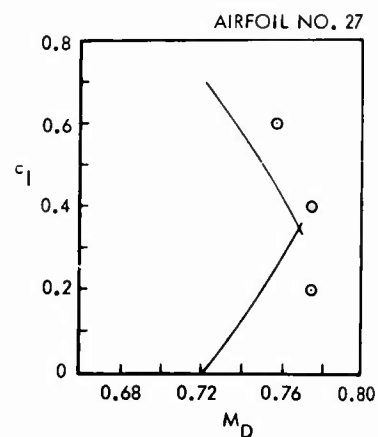


FIGURE 16. CORRELATION OF THEORETICAL DRAG DIVERGENCE MACH NUMBER AND EXPERIMENT

Airfoils 28 and 31 were designed to study the effect of lower surface pressure distribution shape on drag rise Mach number. Both airfoils have the same upper surface. Airfoil 31 has the minimum  $C_p$  on the lower surface at the crest and airfoil 28 has the minimum  $C_p$  ahead of the crest, somewhat similar to a peaky upper surface pressure distribution. Figure 17 shows that while the predicted  $M_D$  boundaries for the lower surface differ by a small amount, the experimental  $M_D$  for the peaky type lower surface is 0.025 greater than the prediction. Of significance is the fact that the high  $c_l$  drag rise Mach number, which is determined by the peaky type upper surface, also exceeds the predicted  $M_D$  by 0.025. This comparison illustrates that suitable pressure distribution shape criteria can lead to airfoil performance that exceeds the predicted  $M_D$  boundary.

Figure 18 shows experimental and theoretical  $M_D$  boundaries for airfoil 13. This airfoil has a peaky type pressure-distribution, but the shape of the recompression region aft of the peak is more triangular than peaky in nature, so the airfoil drag rise falls somewhat short of the predicted  $M_D$  boundary. This airfoil as well as the comparison in Figure 17 is presented to illustrate the need for pressure distribution shape criteria (37) as a necessary supplement to the predicted  $M_D - C_l$  data.

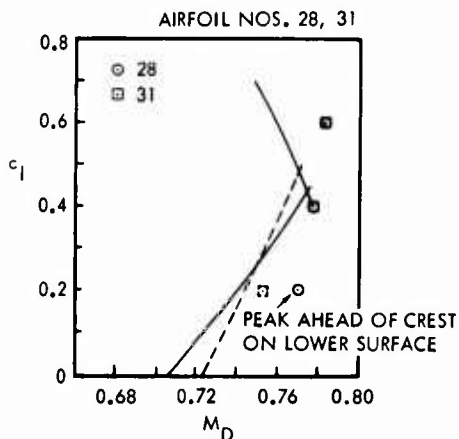


FIGURE 17. CORRELATION OF THEORETICAL DRAG DIVERGENCE MACH NUMBER AND EXPERIMENT

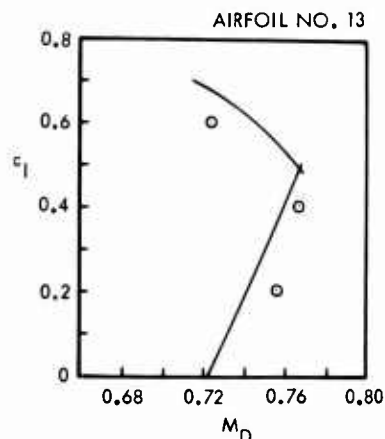


FIGURE 18. CORRELATION OF THEORETICAL DRAG DIVERGENCE MACH NUMBER AND EXPERIMENT

### 2.1.3 Wing Drag

The calculation of finite wing profile drag is accomplished by a strip theory analysis using the basic section data either from empirical estimates or theory. For the purpose of this program, the boundary layer crossflow components are neglected. It has been shown that if the crossflow components of the boundary layer on a swept wing are neglected, then the best approximation to the development of the boundary layer can be made if the boundary layer parameters are calculated in the effective direction (40). For a theoretical approach, the computer program uses a set of streamwise section ordinates for selected spanwise stations. The sweep angles of each constant percent chord line are used to convert the ordinates into effective swept sections. The problem is then reduced to one of calculating the pseudo - two dimensional boundary layer and profile drag as described in the previous section. Streamwise corrections to  $C_D$  are obtained using the

method of Cooke (41). Finally, the streamwise section drag data are integrated across the wing by strip theory to produce total wing profile drag. An example of C-141 wing profile drag, computed for four Reynolds numbers is given in Figure 19. This shows both the scale effect on  $C_{D_{P_{MIN}}}$

and some dependence on Reynolds number of the lift-dependent profile drag.

Wing drag-rise prediction is now discussed, using as an example the C-5A wing. A strip theory analysis of the drag rise Mach number of the C-5A wing is shown in Figure 20(a), (b), (c). The plots of  $c_l$  (available and actual) are shown for  $M = 0.75, 0.77,$  and  $0.80$  respectively. The  $c_l$  available at a given Mach number was obtained from the predicted section  $M_D \sim c_l$  boundaries. The wing  $C_L$  was increased until the local  $c_l$  distribution just touched the  $c_l$  available line. The corresponding  $C_L$  was taken to be that value at which drag rise would occur for the wing at that Mach number.

Following this procedure for three Mach numbers, a wing  $C_L \sim M_D$  boundary was constructed as shown in Figure 21. The flight test  $M_D \sim C_L$  boundary for  $dC_D/dM = 0.05$  is shown. Near the design  $C_L$  of 0.45, the predicted  $M_D$  boundary is exceeded because the wing develops a good peaky type pressure distribution and even at off design conditions, the benefits of the peaky pressure distribution are quite significant.

$M = 0.7$   
TRANSITION AT 0.02C

SYMBOL	$R_N \times 10^{-6} / MAC$
○	3.96
□	7.2
△	25.0
⊙	45.0

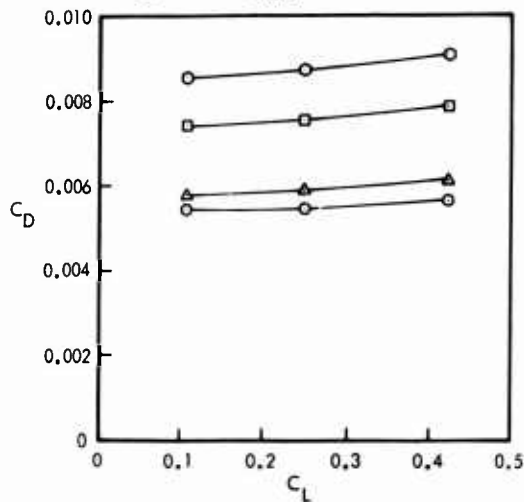


FIGURE 19. PREDICTED WING PROFILE DRAG

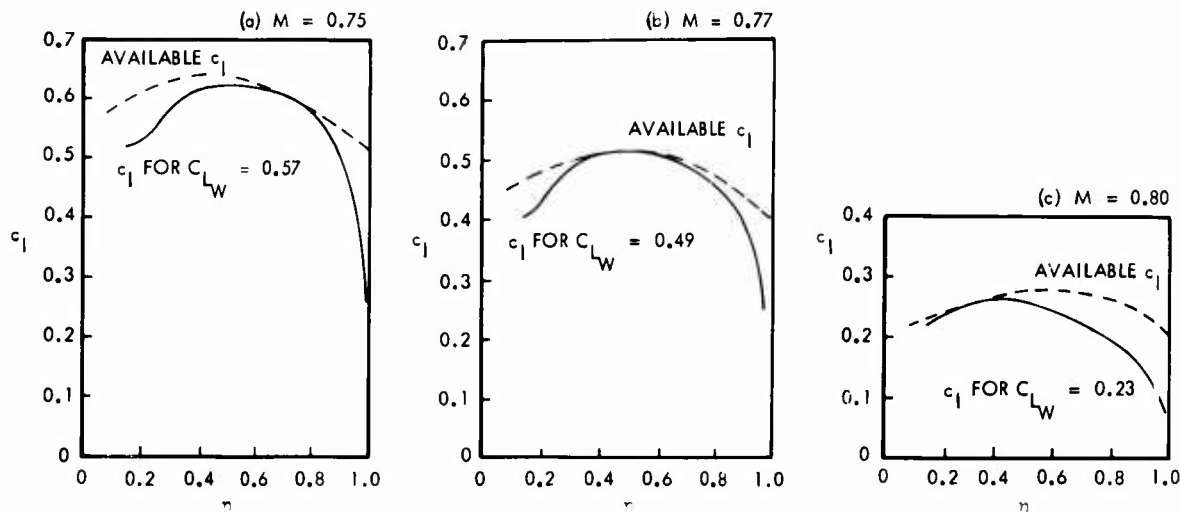


FIGURE 20.  $c_l$  FOR DRAG DIVERGENCE ON THE C-5 WING

2.1.4 Bodies

Preliminary estimates of fuselage drag in incompressible attached flow conditions are based on established methods for equivalent bodies of revolution; in the case of transport configurations with parallel center sections, and cambered fore-and-after bodies, careful design of these contours can minimize excess pressure drag to acceptable levels.

A number of wind tunnel test results on different types of fuselage have been selected to correlate with the empirical method as shown in Figure 22. Only data where model support corrections were known are used. Also, transition was fixed in all cases near the nose of the model. Minimum profile drag was estimated by Young's method for axisymmetric bodies,

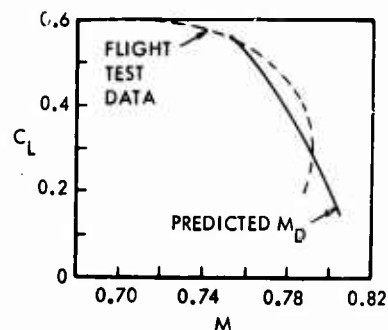


FIGURE 21. COMPARISON OF PREDICTED AND FLIGHT DRAG DIVERGENCE FOR THE C-5A

given in RAeS Data Sheets (42). The shape factor was derived by referring this drag level to the equivalent flat plate value from the Karman-Schoenherr formula. The favorable form drag over the center parallel section is accounted for by arbitrarily defining the overall fineness ratio as  $d_{\max}/l_A + l_B + 2d_{\max}$ . The figure shows incremental pressure drag to increase significantly above  $d_{\max}/l \approx 0.1$ , but even for a typical fineness ratio of 0.15 the incremental pressure drag is only about 5% above the idealized level. Actual transport designs indicated by the horizontal arrows show that even with upswept afterbodies, the excess pressure drag can be maintained within this figure, approximately equal to 3-5 aircraft drag counts.

### 2.1.5 Other Components

The profile drag of other components are estimated using essentially the same methods as outlined above. These include empennage, pylons and discrete protuberances such as wheel well fairings. Nacelle drag is treated independently in later sections.

### 2.2 Induced Drag

Induced drag due to trailing vortices on a finite span wing is calculated by the method of Glauert (43). Preliminary work may require detailed parametric trade studies to optimize wing span loading for satisfactory levels of  $(-C_{MO})$ ,  $C_{L_{MAX}}$  and cruise induced drag. A number of

computer programs are in use to calculate wing-body span load distributions as a basis for vortex induced drag estimation. These include the following, which represent an increasing degree of accuracy and sophistication.

- (i) Vortex Collocation Lifting Surface Theory for Planar Wing-Body Configurations (44).
- (ii) Non-Planar Vortex Lattice Program for Arbitrary Configurations (45).
- (iii) Linearized Wing-Body Interference Program (46).

A typical example of the capability of these programs is shown in Figure 23, where results from program (ii) are compared to test data.

### 2.3 Trim Drag

The change in configuration drag required to trim an aircraft about its center of gravity is defined as

$$C_{D_{TRIM}} = \Delta C_{D_i} + \Delta C_{D_{TAIL}} \quad (8)$$

where  $\Delta C_{D_i}$  is the increment in wing-body induced drag due to compensating, by wing lift, the tail load required to trim the aircraft, and

$$\Delta C_{D_{TAIL}} = \Delta C_{D_{P_{TAIL}}} + C_{D_{i_{TAIL}}} + C_{L_{TAIL}} \tan \epsilon \quad (9)$$

Note:  $C_{D_{P_{TAIL}}}$  is normally included in the airplane profile drag build-up and not in the trim increment.

ARROWS INDICATE ACTUAL TRANSPORT FUSELAGE DESIGNS. SHADED AREA DENOTES EXCESS PRESSURE DRAG DUE TO NOSE FINENESS RATIO AND AFTERBODY SWEEP.

$$\left(\frac{d_{MAX}}{l}\right)_{EFFECTIVE} = \frac{d_{MAX}}{l_A + l_C + 2d_{MAX}}$$

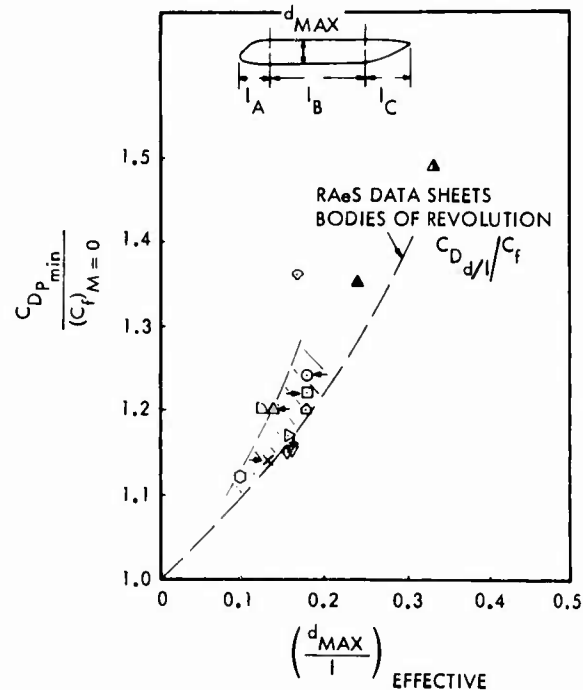


FIGURE 22. SUBCRITICAL FUSELAGE PROFILE DRAG

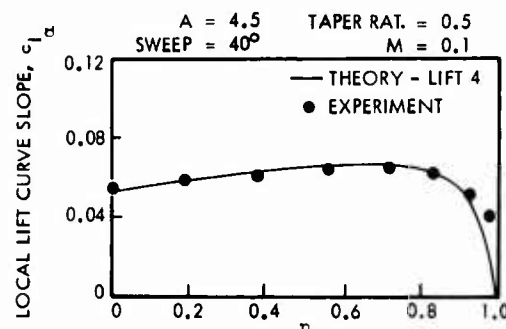


FIGURE 23. COMPARISON OF LIFTING SURFACE THEORY WITH EXPERIMENTAL DATA FOR A SWEEP WING

1-14  $\Delta C_{D_i}$  In preliminary estimation procedures, the most important component to recognize is the wing induced drag effect, which can be derived from the change in tail load required to trim by

$$C_{L_{TAIL}} = \frac{C_{M_O} + C_{L_{A-h}} \left( \frac{dC_m}{dC_L} \right)_{A-h}}{l_T/c} \quad (10)$$

Thus, estimation of  $C_{M_O}$  and  $dC_m/dC_L$  are required for the wing-body configuration. The non-planar vortex lattice program calculates wing-body lift and pitching moment characteristics for this process. Examples of the correlation between theory and experiment for a subsonic transport configuration are shown in Figure 24.

More refined trim drag estimation through recognition of the generally small changes in the tail components can be obtained by use of established techniques for estimating profile drag and wing downwash (47).

#### 2.4 Interference Drag

Aerodynamic interference between aircraft components in close proximity is fundamentally the result of increased superelevations, pressure gradients and boundary layer confluence at the junctions, and may lead to premature separation in some cases. While theoretical viscous flow methods for predicting wing-body interference have not been developed, potential theory can provide guidance in the initial shaping of junctions, thereby reducing the required amount of experimental development efforts. In the preliminary design stage, interference drag, other than the effects of the fuselage and pylon-nacelle on wing induced drag, is usually taken to be negligible at the Lockheed-Georgia Company, with the assumption that this goal can be achieved during the normal wind tunnel phase by appropriate filleting, as shown during the development of the C-5A configuration (48). This goal is not always achieved, however, or even attempted by some design teams, as witnessed by several aircraft development programs during recent years.

Other component interference, for example, pylon/nacelle/wing and empennage interference is minimized as far as possible by designing for smooth area distributions and optimum contouring to avoid excessive superelevations and adverse pressure gradients. The favorable effects of installing pylon/nacelles under wings will be dealt with in some detail in later sections.

#### 2.5 Correlation of Predicted and Wind Tunnel Wing Drag

The wing drag component can be expressed as

$$C_{D_{WING}} = C_{D_{P_{WING}}} + \frac{C_L^2}{\pi A R e} \quad (11)$$

where  $C_{D_{P_{WING}}}$  is the profile drag, including variations away from the optimum  $C_L$  for minimum drag, and  $C_L^2/\pi A R e$  is the vortex induced drag comprising the net effects of a non-elliptic span load distribution.

During preliminary calculations of the configuration drag, a number of approaches to the estimation of profile drag are available as already indicated in previous sections. Examples of some of these are given in Figure 25(a), (b), (c). The data are from three Lockheed-Georgia transport configurations, the C-141A, the C-5A and an advanced transport design study LGX-124. The tests were conducted with transition fixed, and data for  $M = .700$  have been chosen to represent subcritical conditions, although at off-design  $C_L$  some degree of supercritical flow is inherent in the test results, and this must be borne in mind when reviewing the comparisons. Test data for "wing-alone" is obtained by subtracting fuselage-alone results from wing-fuselage data.

Five methods have been investigated for estimating profile drag;

1(a)  $\bar{C}_f \times (SF)_{Ref (16)} + \frac{C_L^2}{\pi A R e}$ , where  $e$  is calculated from experimental span load distributions, and  $\bar{C}_f$  is the spanwise integration of the local chord values of  $C_f$ .

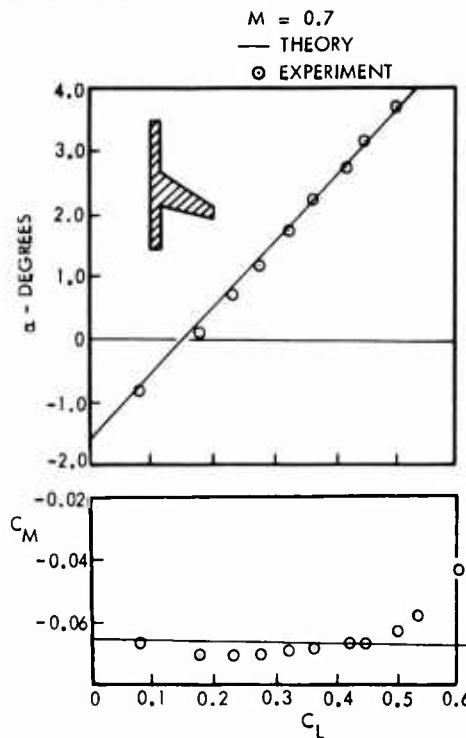


FIGURE 24. CORRELATION OF LIFTING SURFACE THEORY WITH EXPERIMENT

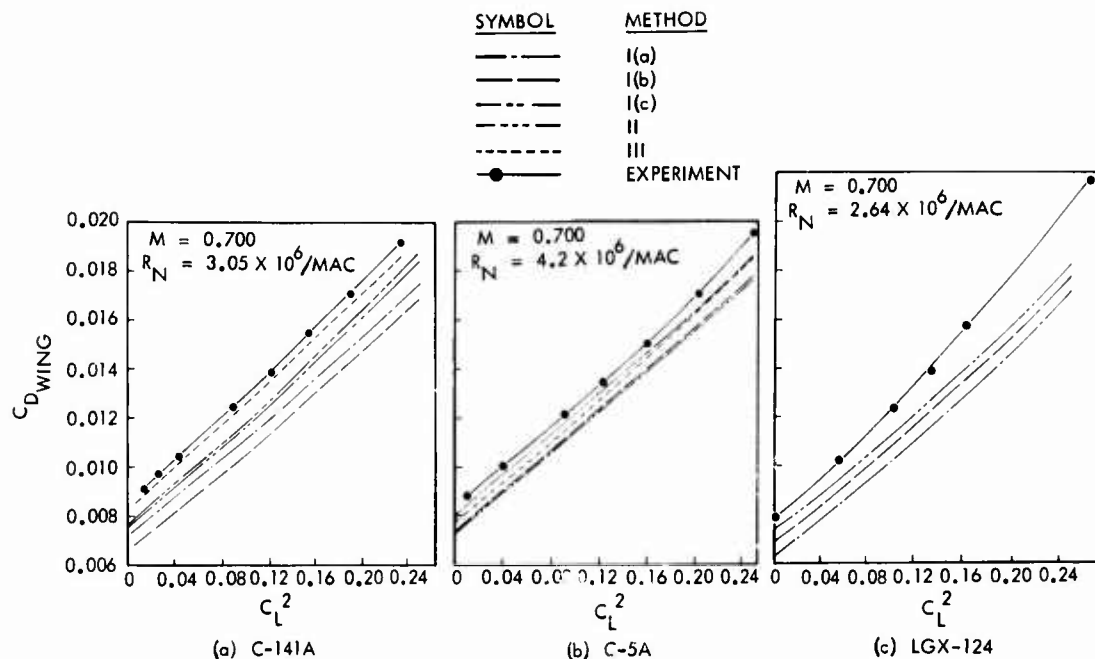


FIGURE 25. WING DRAG PREDICTION

- I(b) As I(a), with shape factors from average superelevation based upon measured pressure distributions.
- I(c) As I(b), with  $C_f$  based on the Reynolds number of the mean aerodynamic chord.
- II Profile drag from the subsonic viscous flow program (Section 2.1.2) using test pressure data as input.
- III Profile drag from the subsonic viscous flow program using geometrical data as input.

Comparisons of the test data with estimates reflect the degree of wing-body interference for each configuration, as well as the accuracy of each estimation method. For the C-141A configuration, Figure 25(a) some excess profile drag was known to be present, even though this is a high-wing configuration. Methods I(a), (b), and (c) appear to disagree by 10% at typical cruise  $C_L$ , whereas methods II and III predict  $C_{D_p}$  and the variation of  $C_D$  with  $C_L$  within 3% of the experimental results. These differences essentially reduce to the estimated values of  $C_{D_p \text{ MIN}}$  from each method. The shape factors

derived from methods I(a) and (b) are less than the implied shape factor from III, again indicating that the viscous theory accounts for substantially more form or pressure drag than the other methods. It is interesting to note that one of the common methods of estimating wing flat plate skin friction, I(c), by representing the wing Reynolds number by the MAC value, gives closer agreement to III. This approach is satisfactory only for wings with moderate taper ratios (49).

The comparison for the C-5A studies, Figure 25(b), show similar results. The test data for the LGX-124, Figure 25(c) a low wing configuration, show a non-linear variation of  $C_D$  with  $C_L^2$ , indicating excess profile drag and some separation problems at high  $C_L$  due to non-optimized wing-body junction design. Consequently, methods I(a), (b), and (c) (II and III unavailable) predict optimistic drag at cruise for these configurations.

### 3. PREDICTIONS BASED ON WIND TUNNEL TEST DATA

#### 3.1 Introduction

Aircraft configuration development is usually planned to include a series of low and high speed wind tunnel tests, with the initial series at the project definition phase in order to substantiate the early drag predictions. The uncertainties regarding early project estimates on absolute level of subsonic profile drag, viscous drag creep in the subcritical range, and drag-rise onset are defined, and development of the configuration for minimum interference proceeds through a series of flow visualization studies, and an analysis of the aircraft component drags supplemented by theoretical methods where appropriate.

Use of wind tunnel test data to predict total configuration drag at full scale conditions is one method in use by industry teams. Unfortunately, many early attempts at this method have failed due to accumulated errors in the model testing techniques and empirical scaling processes. Experience gained during these programs, together with the introduction of refined testing techniques and development of new theoretical methods are together helping to identify the true nature of the problem and incidentally to highlight the limitations of existing test facilities.

### 3.2 Wind Tunnel Testing Techniques

The evaluation of high speed model data free of interference from the support system has been a continuing problem to aerodynamicists during recent years. One system, favored by the Lockheed-Georgia Company based on experience gained during the C-5A program, is illustrated in Figure 26. This concept avoids the use of a rear-mounted support sting and the problems related to interference of the complex flows in the vicinity of rear fuselages and empennages.

The model is supported by a forward mounted, load bearing, thin blade from the lower fuselage, (A), through a support sting situated below the model. This configuration measures the combined model load,  $L_M$ , and the interference terms  $L_{I_{S-M}}$  and  $L_{I_{B-M}}$ , the interference of the sting on the model and blade on the model, respectively. The sting interference term,  $L_{I_{S-M}}$ , is obtained by extrapolating respective load data at each of four different sting displacement distances to an infinite displacement of model and sting,  $D \rightarrow \infty$ . The second configuration is designed to obtain the interference of the blade on the model,  $L_{I_{B-M}}$ . For these tests, the model is mounted on an auxiliary load bearing dorsal strut. Tests can be made to measure both total model plus blade load, plus dorsal interference load,  $L_{I_{D-M}}$

$$(B) \quad L_B + L_M + L_{I_{M-B}} + L_{I_{B-M}} + L_{I_{D-M}}$$

and with a metric dummy blade only, where the blade load plus interference of the model on the blade is measured,

$$(C) \quad L_B + L_{I_{M-B}}$$

Without the dummy blade installed, the total load measured is the model plus interference of dorsal on model

$$(D) \quad L_M + L_{I_{D-M}}$$

Thus, interference free data,  $L_M$ , is obtained from  $D - B + A + C$ .

One example of the net blade interference term, shown in Figure 27 is seen to be unfavorable to the model and to have a significant effect on the measured induced drag, amounting to approximately 6 aircraft drag counts at cruise  $C_L$ .

The other important aspect of testing models for drag prediction is the correct simulation of the full scale boundary layer characteristics on the model surfaces. Ideally, we require to simulate a boundary layer growth which represents a smooth fully turbulent condition. The method of artificially fixing transition is essential when full scale drag prediction is attempted from wind tunnel data. However, very careful and systematic tests are required to ensure that correct interpretation of drag levels can be made.

In subcritical flows it is customary to trip the boundary layer close to the wing leading edge. Braulow et al (50) has shown that it is possible to obtain essentially a zero drag penalty due to transition strip providing narrow, sparsely distributed, bands of roughness are used. The roughness size for a given wind tunnel Reynolds number is determined according to the criterion  $R_k \geq 600$ , the critical roughness Reynolds number based on the roughness height,  $k$ , the velocity at the top of the roughness,  $U_k$ , and the kinematic viscosity at the top of

#### STING INTERFERENCE EFFECTS ON MODEL

$$A. \quad L_{I_{S-M}} + L_M + L_{I_{B-M}}$$

FROM PLOT 1/D  $\rightarrow 0$

#### BLADE INTERFERENCE ON MODEL

B. DORSAL STING, MODEL & BLADE METRIC.

$$L_B + L_M + L_{I_{M-B}} + L_{I_{B-M}} + L_{I_{D-M}}$$

C. DORSAL STING WITH METRIC DUMMY BLADE ONLY.

$$L_B + L_{I_{M-B}}$$

D. BLADE OUT.  $L_M + L_{I_{D-M}}$

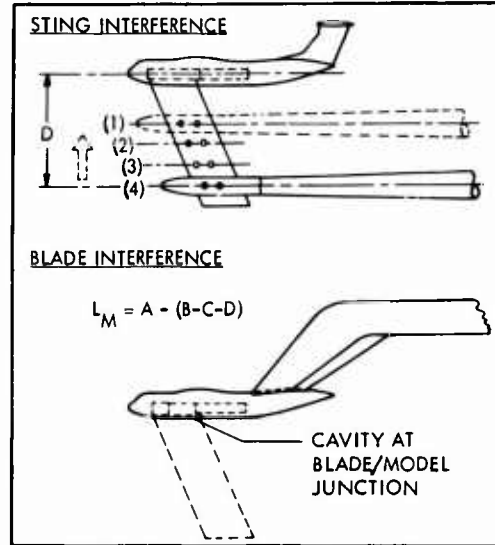


FIGURE 26. SUPPORT INTERFERENCE EVALUATION

□ BLADE OUT  $L_M + L_{I_{D-M}}$

-x- (DERIVED)  $L_M + L_{I_{D-M}} + L_{I_{B-M}}$

△ MODEL & BLADE METRIC  $L_B + L_M + L_{I_{M-B}} + L_{I_{B-M}} + L_{I_{D-M}}$

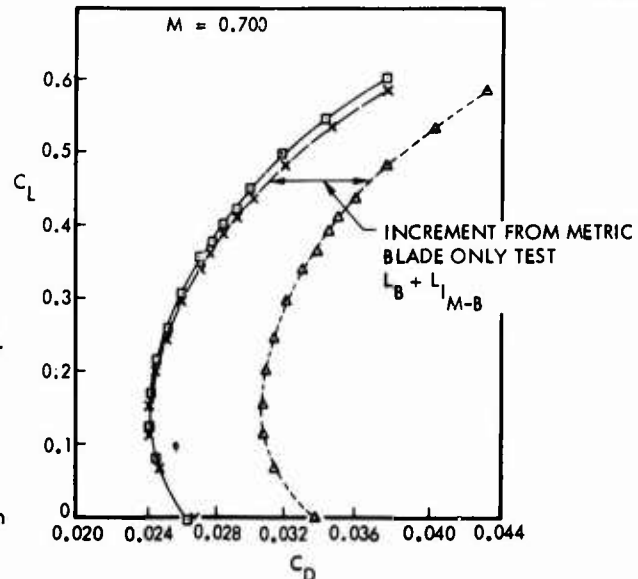


FIGURE 27. BLADE INTERFERENCE EVALUATION

the roughness,  $\nu_k$ . Results of systematic tests on a C-5A model are shown in Figure 28. Transition was fixed by 0.05 inch wide bands of sparsely distributed balltini beads of the same size across the span at constant distance from the leading edge, according to the criterion that  $R_{X'} \geq 0.1 \times 10^6$ .

For a given Reynolds number and roughness size, transition was monitored by sublimation tests to determine the exact transition location on the wing. The results show that at  $R_N = 4.2 \times 10^6 / \text{MAC}$  a plateau was obtained representing a fully fixed condition and that no measurable drag increase was obtained over a roughness size range from .0021 inches to .0045 inches. Beyond this size the roughness height approaches the boundary layer thickness and a drag increase is obtained. As Reynolds number is decreased the width of the plateau also decreases and it is seen that for a given roughness size, transition begins to move downstream of the band. It is important to note that unless sublimation checks are made at each condition, low Reynolds number tests can produce an erroneous variation of drag with roughness size which can be incorrectly interpreted as "roughness" drag.

In the supercritical flow range the problem of high Reynolds number simulation becomes far more complicated. This was first identified by Paterson (51) during the C-141A flight test program and has subsequently been confirmed by a number of papers on the subject, notably that of Pearcey, Osborne and Haines (52). For attached flow conditions, a number of conflicting features are apparent in the simulation process. Recognizing that transition must be fixed to avoid the extent of laminar flow varying with Mach number and  $C_L$ , a forward location will inevitably produce boundary layer thicknesses at the wing shock location and trailing edge which are non-dimensionably greater than full scale. The problem is compounded if there exists a type B flow condition (52), where incipient rear separation is present, so that we have conditions where interaction of a shock induced bubble with the rear separation are aggravated by low Reynolds number transition fixing methods. There is no precise way to avoid this problem, other than detailed experimental analyses through pressure surveys and flow visualization to identify the type of flow condition relevant to the particular wing design. In the case of the C-141A, the subcritical flow condition is characterized by a strong adverse pressure gradient and a rear separation tendency which is very sensitive to changes in upstream boundary layer thickness. It is pertinent to note that this characteristic is becoming increasingly identified in the new generation of highly loaded 'supercritical' wings. For the C-141A Paterson (53), (54) has shown that the low wind tunnel Reynolds number condition exhibits, at drag-rise conditions, a rear separation which extends rapidly forward to the shock with increasing Mach number or angle of attack, resulting in a retarded shock movement. This is illustrated in Figure 29. Due to the over-thickened model boundary layer, however, a compensating and over-riding effect is the less favorable trailing edge pressure recovery, leading to a net premature drag rise.

One method of possibly achieving a closer correlation of the drag-rise characteristics is to locate the roughness band further aft, but ahead of the transition free shock location to reduce the discrepancy between model and full scale trailing edge boundary layer thicknesses. Paterson (53) investigated the possibilities of this technique and showed that it provided closer agreement with flight test results. However, this technique does not guarantee that transition remains fixed ahead of the shock at all Mach

- 1 FULLY TURBULENT ON UPPER & LOWER SURFACES
- 2 FULLY TURBULENT ON LOWER SURFACE, PARTIALLY LAMINAR ON UPPER
- 3 FULLY TURBULENT ON LOWER SURFACE, NEAR-FIX ON UPPER
- 4 FUSELAGE FIXED

1-17

$$M = 0.767, \quad C_L = 0.475$$

$$\begin{aligned} \circ R_{N'} &= 2.1 \times 10^6 / \text{MAC} & R_{X'} &= 0.2 \times 10^6 \\ \triangle R_{N'} &= 2.8 \times 10^6 / \text{MAC} & R_{X'} &= 0.27 \times 10^6 \\ \times R_{N'} &= 3.5 \times 10^6 / \text{MAC} & R_{X'} &= 0.33 \times 10^6 \\ \diamond R_{N'} &= 4.2 \times 10^6 / \text{MAC} & R_{X'} &= 0.40 \times 10^6 \end{aligned}$$

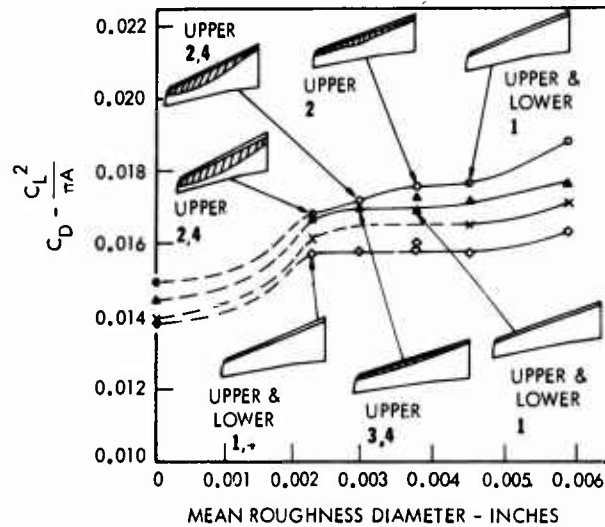


FIGURE 28. RESULTS FROM TRANSITION INVESTIGATION ON THE C-5A MODEL.

- U/S GRIT, 0.075c, 0.0025"
- + U/S GRIT, 0.40c, 0.0040"
- U/S GRIT, 0.50c, 0.0040"
- ◇ TRANS FREE

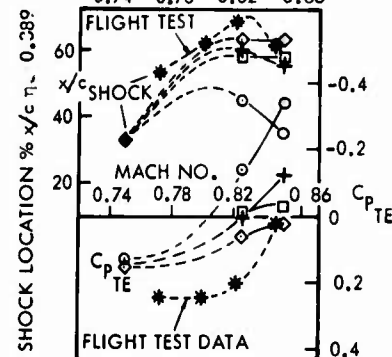
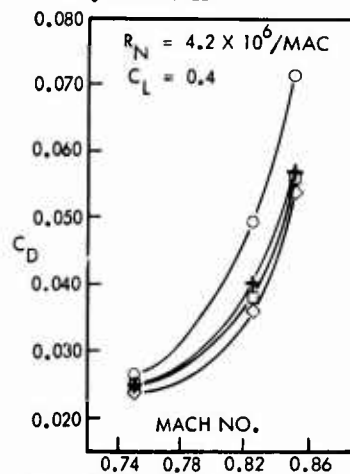


FIGURE 29. EFFECT OF TRANSITION LOCATION ON DRAG RISE CHARACTERISTICS

1-18

number and  $C_L$  combinations. An example of the improvement in agreement between wind tunnel test data and flight test results is shown in Figure 30. To minimize discrepancies in aerodynamic loads for the C-5A, the technique was introduced of fixing transition at a location near the leading edge and re-energizing the boundary layer ahead of the shock by means of vortex generators. This procedure was first correlated using a C-141A model and C-141A flight test results of shock location and then used on the C-5A wind tunnel tests. Although this served the development purposes of the C-5A, it too suffers from the fact that it is to some extent configuration oriented, and to adequately cover the complete range of Mach number and angle of attack, the location of the vortex generators must be varied so that they are always ahead of the shock, a prohibitive if not impossible testing technique. The method is, of course, not suitable for drag prediction because of the "over-thinning" effect of the vortex generators on the boundary layer and the resulting spurious interaction of the boundary layer and shock.

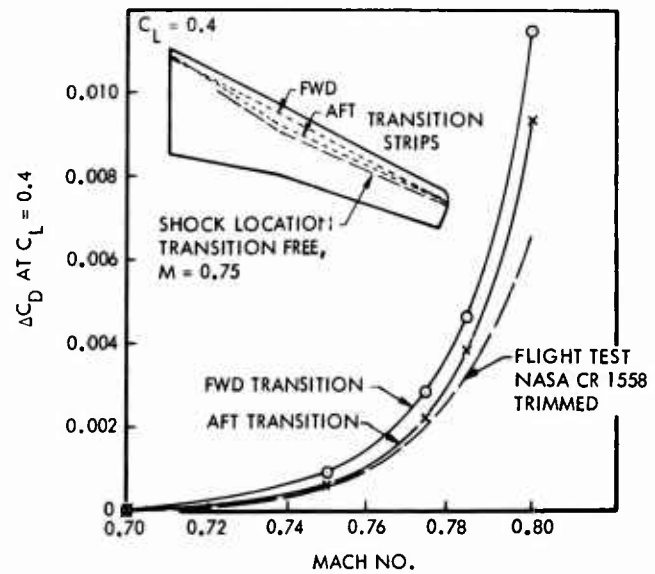


FIGURE 30. C-141A DRAG RISE CORRELATION

### 3.3 Examples of Interference Drag Measured in the Wind Tunnel

The inadequacies of theoretical methods to determine interference drag can be judged by a review of some examples of wind tunnel measurements on component interference. Two items are singled out for detailed discussion. The first is that due to an upswept afterbody and the effects of other components on the pressure drag of the afterbody. Figure 31, shows estimated and experimental data for a fuselage with an upswept afterbody and the effects of adding wheel fairings located on the parallel section of the fuselage ahead of the afterbody. The experimental drag of the isolated fuselage (obtained from a blade-mounted model of the C-141A) closely approximates the estimate at angles of attack beyond  $3^\circ$ , where attached flow exists, while at negative angles of attack separation on the afterbody causes the drag to increase 20 counts above the estimate. The wheel fairings cause additional drag at negative angles of attack; flow visualization studies indicated the drag increase to be due to separation of the flow at the base of the fairings.\* The apparent drag increment due to adding the fairings increases with angle of attack indicating an additional interference effect on the afterbody, because its boundary layer becomes separated, due to non-optimum wheel-fairing/afterbody contours. Afterbody pressure drag was computed from a static pressure survey for the fuselage-wheel fairing configuration. These results (shaded) show a similar trend of drag with angle of attack to the force balance data; however, a significant difference in level exists due to the fact that the estimate for the wheel fairing drag assumes attached flow conditions.

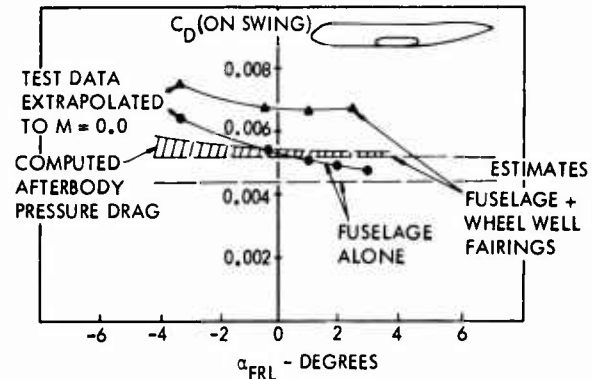


FIGURE 31. THE EFFECTS OF WHEEL WELL FAIRING ON FUSELAGE PROFILE DRAG

Afterbody pressure drag for three model configurations is shown in Figure 32. Here, the addition of the wing shows a reduction of the afterbody pressure drag, whereas adding a fin and horizontal T-tail increases the interference drag on the afterbody by 18 counts at cruise angles of attack. A polar plot of the static pressure variation around the aft fuselage at a station halfway along the aft facing afterbody surface showed that adding the wing to the fuselage-wheel fairing configuration resulted in increased suction at the top center line ( $\theta = 0^\circ$ ) and maximum half breadth ( $\theta = 90^\circ$ ) locations due to the imposed downwash field in the cross flow plane. The positive pressure increase on the lower surface is more significant as far as pressure drag is concerned due to the rapid pressure-area change on the fuselage underside, resulting in a favorable interference effect on afterbody pressure drag as indicated in Figure 32. The effect of adding the

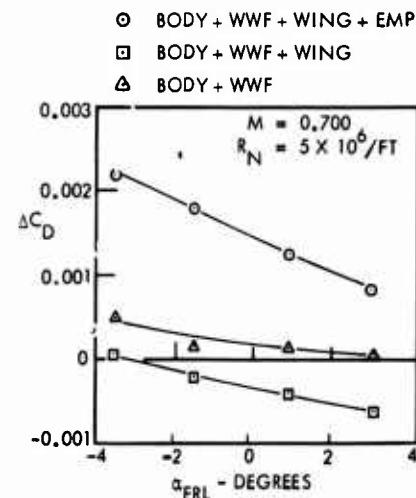


FIGURE 32. COMPONENT INTERFERENCE EFFECTS ON AFTERBODY PRESSURE DRAG

\*A modified wheel-fairing developed on the basis of flow visualization studies, reduced the drag 6 aircraft drag counts, however, it was not incorporated in the production configuration.

empennage is to create a large increase in suction on the afterbody, resulting in a more adverse transverse gradient at fuselage stations in the vicinity of the fin maximum thickness location. It is possible that reduction of this interference drag could be obtained by modifying the dorsal fillet to minimize the fin superevelocities.

Some indication of a favorable scale effect on the afterbody pressure drag interference term is shown in Figure 33, however, it is insignificant at cruise angle of attack.

The second item to be discussed in detail is that of wing/pylon/nacelle interference and the approach used in minimizing this component in wind tunnel tests. Considerable experience of this problem has been gained during the C-5A program, and also on the L-500 project.

The major elements of the wing/pylon/nacelle flow field for an underwing installation are shown in Figure 34. Prediction of the full scale installed pylon/nacelle drag is a complex problem dependent on mutual interference of nacelle inlet flows, nacelle afterbody flow and power effects and the wing stagnation field. These effects are measured on wind tunnel models in the normal development phase of a project.

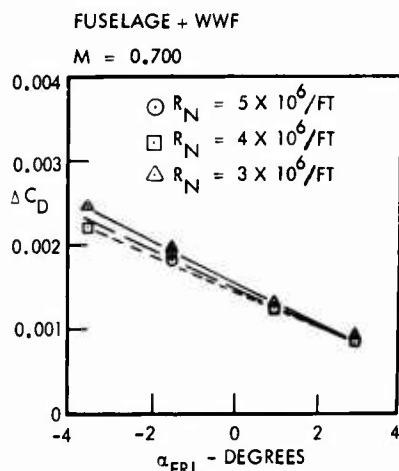


FIGURE 33. REYNOLDS NUMBER EFFECT ON AFTERBODY PRESSURE DRAG

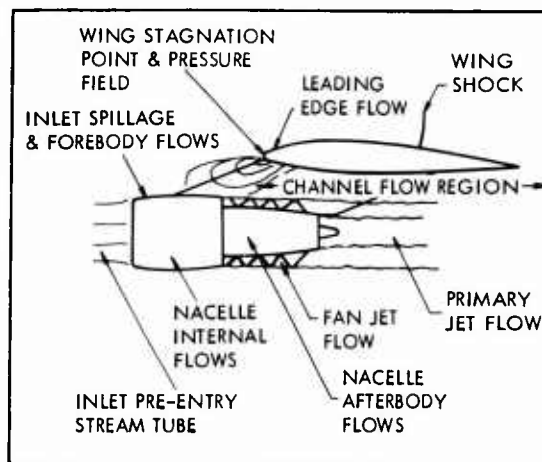


FIGURE 34. MAJOR ELEMENTS OF WING/ PYLON/NACELLE FLOW FIELD

Summary curves of the net interference of an installed pylon/nacelle are shown in Figure 35 from optimization tests on the L-500 project, for a free flow nacelle. For positions of the nacelle exhaust plane relative to the wing leading edge,  $X/C$  greater than approximately 0.20, it was found that favorable interference was obtained with increasing vertical displacement  $Z/D$  up to 1.1. Only at forward nacelle locations,  $X/C < 0.20$ , was it beneficial to move the nacelle up toward the wing to obtain highly favorable results.

The effects of simulated power have been investigated in detail on a large L-500 semispan model (55). To gain a better understanding of nacelle/pylon/wing interference effects, an analysis was made of the component force changes due to interference and how the total forces are distributed between the nacelle/pylon and wing. For this study, the 3/4 length duct configuration,  $K10N6$ , was selected. Figure 36 shows overall nacelle interference effects for the complete aircraft configuration. Interference effects on the nacelle are mostly unfavorable except in the range of fan pressure ratios 1.0 - 1.1. The component of interference on the wing is, on the other hand, highly favorable, but reduces with increasing fan pressure ratio. Because of the nacelle effect, the total favorable interference diminishes at a faster rate with increasing fan pressure ratio, from -12 counts to about -6 counts at the full scale value of 1.475.

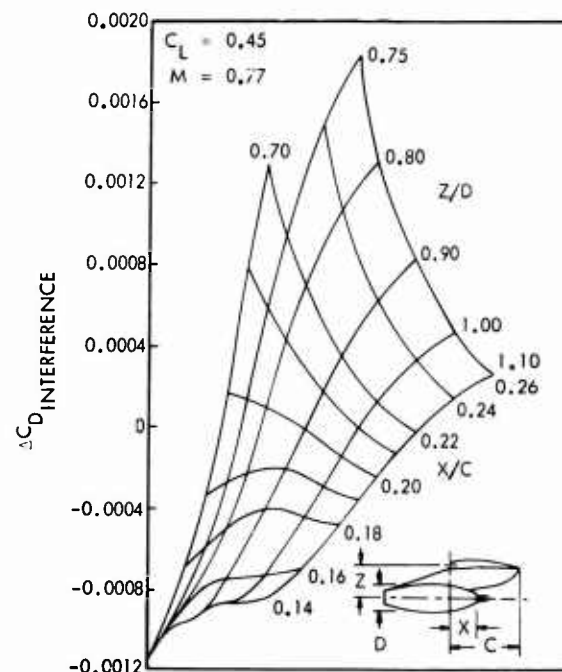


FIGURE 35. FLOW-THROUGH NACELLE POSITION EFFECT ON AIRPLANE DRAG,  $C_L = 0.45$

From the same analysis, Figure 37 presents a correlation of the results from a free flow nacelle test with the data from the powered nacelle test at a fan pressure ratio of 1.475. This indicated generally good agreement of the angle of attack effects on total wing/pylon/nacelle interference between the two techniques for this nacelle configuration.

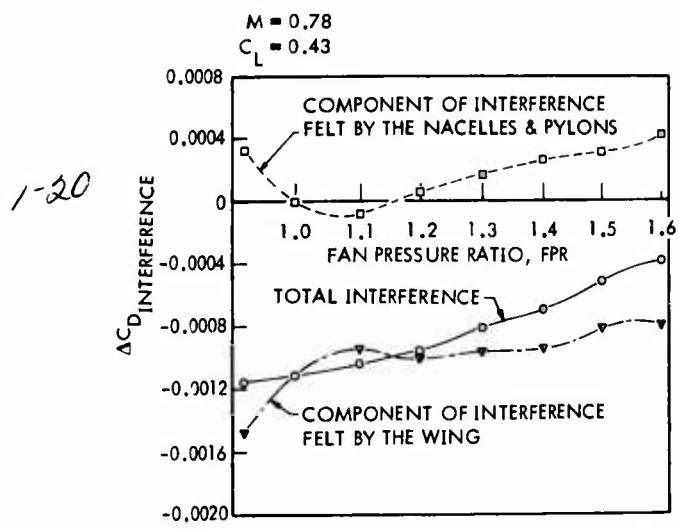


FIGURE 36. EFFECT OF FAN PRESSURE RATIO ON INTERFERENCE DRAG COMPONENTS, L-500 SEMI-SPAN POWERED MODEL

3.4 Extrapolation of Wind Tunnel Test Data to Full Scale Conditions

The technique of testing a wind tunnel model with transition artificially fixed implies that use can then be made of the classical skin friction laws for smooth turbulent flow to predict the full scale level of drag. Examination of the component drag equation for an aircraft suggests it is easy to identify possible primary or secondary scale effects on all the terms. However, we shall emphasize the effects on the primary terms, namely the minimum measured profile drag,  $C_{D_{P_{min}}}$ , the lift dependent profile drag,  $C_{D_{P_{C_L}}}$ , and the

summation of the individual profile drag estimates for each component,  $\Sigma C_{D_{P_{min}}}$ . Thus, scale effects on the excess profile drag due to interference are included.

The principal assumption upon which predicted full scale drag is based is that

$$\left( \frac{C_{D_{P_{min}}}}{C_f} \right)_{\text{WIND TUNNEL}} = \left( \frac{C_{D_{P_{min}}}}{C_f} \right)_{\text{FULL SCALE}} \tag{12}$$

This implies that form drag over and above flat plate skin friction reduces with Reynolds number, since  $C_f$  at full scale is less than  $C_f$  in the wind tunnel. Excess profile drag is assumed to remain constant over the Reynolds number range of interest.

Results of some studies on scale effects on profile drag of a typical transport wing are shown in figure 38. As introduced in an earlier section, methods under the heading (I) are from preliminary estimation procedures, using shape factors from either Reference (16), or from average super-velocity calculations. Also shown in Figure 38 are the wing profile drag from methods II and III using viscous theory. The average wing shape factor showing the degree of form drag above flat plate skin friction is shown to differ by 30% at low Reynolds numbers. The implications of these differences in Reynolds number corrections from wind tunnel to full scale are a maximum difference of 7 counts in full scale drag level. The maximum difference in scale effect from methods I(c) and II, or III is however, only 3 counts for the wing. A corresponding total aircraft figure is estimated to be of the order

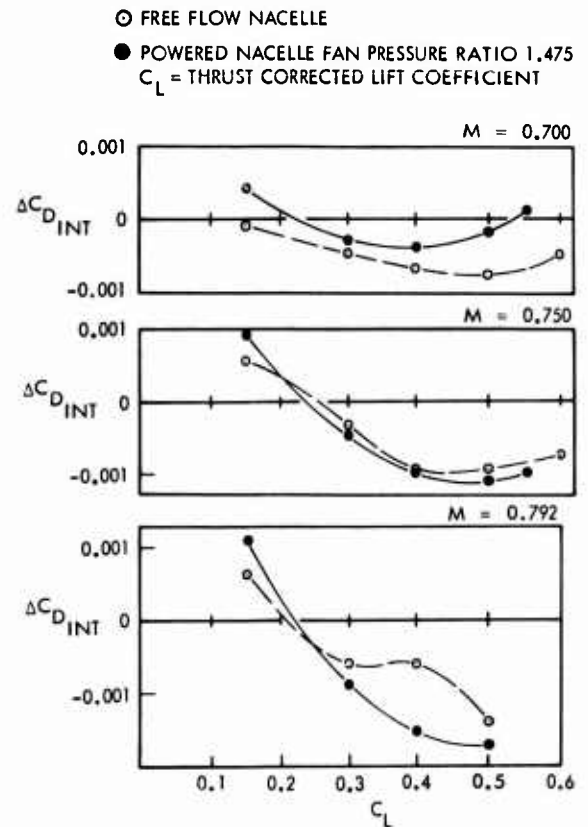


FIGURE 37. WING/PYLON/NACELLE INTERFERENCE - AIRCRAFT DRAG

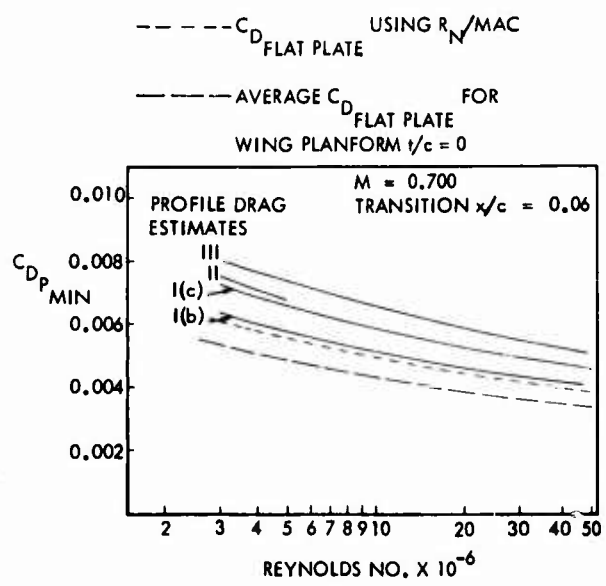


FIGURE 38. SCALE EFFECTS ON MINIMUM PROFILE DRAG OF A TRANSPORT WING

of 5 counts between these methods. It is interesting to note that the results from method III, in which profile drag was estimated by the theoretical viscous method using ordinate data, indicate that shape factor is constant over the whole Reynolds number range, confirming one of the basic assumptions in the scaling process.

1-21

#### 4. CORRELATION OF C-5A PREDICTED & FLIGHT TEST DRAG

##### 4.1 Introduction

Preceding sections discuss, in general terms, some of the approaches to preliminary estimation of drag in the subsonic range. Wind tunnel testing techniques in current use are also described. The use of wind tunnel data for full-scale prediction requires, in particular, that account be taken of:

- (i) Reynolds number effects on profile drag,
- (ii) The difference in transition locations on the model and full scale aircraft,
- (iii) Differences in the surface roughness between the highly polished wind tunnel model and the aircraft.

In the case of the C-5A these and other corrections are necessary to determine a realistic drag level at full scale conditions. The following is a detailed discussion of the model corrections, leading to the analysis of flight test drag data, and finally a correlation of predicted and flight drag at both subcritical and cruise conditions.

##### 4.2 Corrections to C-5 Wind Tunnel Data

###### 4.2.1 Wind Tunnel Facility Correlation Corrections

Subsequent to the high-speed wind tunnel development program on the C-5A, a study was initiated, sponsored by USAF Aeronautical Systems Division and NASA Ames Research Center, to establish data correlation between various transonic facilities using the high speed C-5A 0.0226 scale model (56). An appraisal of the data from the various facilities was made through analyses of the force measurements and facility flow characteristics. This indicated that a number of corrections could be applied to the basic model data in order to explain the various facility discrepancies. These corrections, confirmed by detailed calibration measurements, can be summarized as follows:

	$\Delta C_D$	
	$C_L = 0$	$C_L = 0.45$
Buoyancy	+0.0003	+0.0003
Mach Number	-0.00015	-0.00016
Wall Effects	0	-0.00023
Inertial Effects	+0.00045	+0.00045
High Order Interactions	<u>+0.00015</u>	<u>+0.00005</u>
Total	+0.00075	+0.00041

These corrections are applied to the wind tunnel data in this analysis.

###### 4.2.2 Reynolds Number Correction

Various methods of estimating scale effects on profile drag are discussed in Sections 2.5 and 3.4. The scale effect on  $C_{Dp}$  is defined as the increment between the estimated profile drag at the wind tunnel Reynolds number and the mean cruise flight Reynolds number of the aircraft assuming a fixed transition location. For the C-5A, the mean cruise Reynolds number is  $55 \times 10^6 / MAC$ .

Two methods of estimating and scaling profile drag are used for the C-5A analysis. These are, referring to Section 2.5, method I(c), in which profile drag is estimated by a shape factor based on su, ervelocity of each component and the Karman Schoenherr flat plate skin friction law, and method II or III, which uses the subsonic viscous flow theory. Method I(c) gives a correction of  $\Delta C_D = 0.0061$ , while methods II or III indicate a correction of 0.0066.

###### 4.2.3 Transition to Leading Edge

Section 3.2 points out that the method of fixing transition on the C-5A model resulted in no measurable drag on the model due to the roughness band. The transition strip was placed at a constant distance of 0.8 inches from the wing leading edge ( $R_x = 0.4 \times 10^6$ ), 2 inches from the fuselage nose, 0.4 inch from the leading edge of the fin, tailplane and pylons, and on the nacelles it was placed 0.8 inch from the lip externally and 0.4 inch internally. Since transition on the airplane at flight Reynolds numbers is assumed to occur at the leading edge of all the components, a correction must be applied to the wind tunnel data to simulate transition at the leading edge. This correction is estimated to be  $\Delta C_D = +0.00135$ .

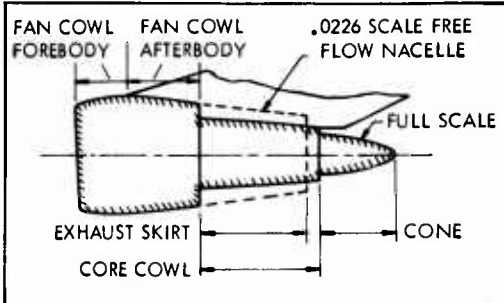
1-22 4.2.4 Pylon Nacelle Drag

Section 2.4 describes some of the techniques for measuring pylon nacelle interference drag in wind tunnel tests.

For the C-5A performance calculations, the division of airframe drag and nacelle drag was defined as the intersection line of the pylon and nacelle (see Figure 39). Isolated nacelle drag was accounted for in the engine thrust levels, and assumed independent of the wing/pylon/nacelle mutual interference effects. Isolated nacelle drag consists of the following:

- (i) Afterbody Pressure Drag
- (ii) Forebody Additive Drag
- (iii) Internal and External Skin Friction Drag

COMPONENT	PROFILE DRAG		INTERFERENCE PRESSURE DRAG	
	MODEL	AIRCRAFT	MODEL	AIRCRAFT
EXTERNAL	+0.00104 <sup>(A)</sup>	+0.00056		
INTERNAL	+0.00074 <sup>(B)</sup>			
FAN COWL FOREBODY			(+0.00086) <sub>I</sub>	
FOREBODY ADDITIVE			(+0.000165) <sub>I</sub> <sup>(C)</sup>	(+0.00025) <sub>I</sub>
FAN COWL AFTERBODY			(-0.00024) <sub>I</sub>	(-0.00055) <sub>U</sub> <sup>(D)</sup>
EXHAUST SKIRT			(-0.00023) <sub>I</sub>	
TURBINE COWL CONE				



SUBSCRIPT I REFERS TO INSTALLED VALVES  
 SUBSCRIPT U REFERS TO UNINSTALLED VALVES

MODEL ESTIMATE = (A) + (B) + (C) + (D) = 0.002495

FIGURE 39. C-5A MODEL AND FULL SCALE DRAG COMPONENTS

The C-5A high-speed model nacelle fan cowl contours were identical to the full-scale nacelle. Downstream of the fan cowl, the model nacelle contours represented the boundary between the supersonic exhaust flow of the fan and the external local flow, as shown in Figure 39. Tests conducted on a 0.057 scale powered nacelle semispan model indicated that the hard boundary free flow nacelle provided good simulation of the actual powered flow characteristics and interference effects.

Afterbody pressure drag is defined as the total pressure-area force, due to external flow, which acts on the aft-facing area of the isolated nacelle. This is a function of Mach number and fan nozzle pressure ratio. During early studies of the afterbody pressure drag for the isolated full scale nacelle, an estimated value of 5.5 aircraft drag counts was applied to engine thrust levels. Although this procedure was correct so far as the isolated nacelle was concerned, data was compiled from subsequent wind tunnel tests to confirm that the installed effects of the nacelle were favorable to the aircraft drag. Figure 40 presents nacelle centerline static pressure characteristics showing the effect of the wing lower surface positive pressure field on the installed nacelle. Figure 41 shows the afterbody pressure drag versus angle of attack, and also confirms the technique for simulating powered nacelle effects by using a "hard boundary" modified afterbody free flow nacelle. Thus all installed effects were assumed to be inherent in the model and full-scale drag polars, and only the isolated afterbody drag was accounted for in performance calculations, as shown in Figure 39. The model full-scale contours of Figure 39 indicate that a further pressure-area term existed due to the exhaust cone not represented on the model. This was assumed to be also favorable but was neglected resulting in some very small degree of conservatism in the prediction.

Forebody additive drag results from incomplete recovery of inlet diffusion momentum over the forward facing portion of the nacelle lip and external cowl. For the C-5A, the cruise mass flow ratio  $A_0/A_{max}$  was 0.65, with a corresponding nacelle exit  $C_p = +.20$ . For the high-speed force model, a slightly higher mass flow ratio was obtained, resulting in an average exit  $C_p = -.005$  at cruise Mach

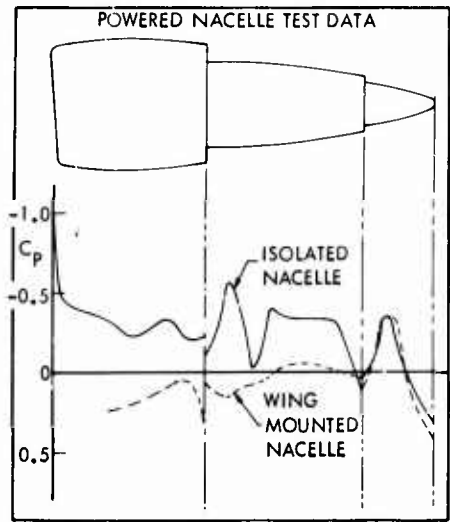


FIGURE 40. EFFECT OF WING PROXIMITY ON NACELLE PRESSURE DISTRIBUTION

numbers. For model correction purposes, the estimated forebody additive drag for an isolated nacelle assumes that the interference effects of the wing flow field occur independently of the mass flow ratio, and are assumed to be included in the model drag polars.

Internal drag calculations were made for the C-5A model nacelles corresponding to the model test conditions. Figure 42 presents summary plots of the forebody additive and internal drag components as functions of nacelle exit pressure coefficients.

The external model nacelle profile drag was estimated using standard methods. Figure 43 presents a summary of the C-5A nacelle drag increments necessary to achieve compatibility of the model drag and full-scale thrust for correct performance calculations.

#### 4.2.5 Roughness Drag

The term "roughness drag" is used to describe parasite drag in excess of the basic skin friction and form drag, due to manufacturing tolerances, fasteners, protuberances, antennae, vents, probes, surface waviness, and skin surface grain structure and finish. Drag estimates for these items are generally based upon the data of Wieghardt (57), Hoerner (16), and Schlichting (58). The majority of these data were obtained at relatively low Reynolds numbers and Mach numbers; data for Reynolds numbers in excess of  $20 \times 10^6$  and Mach numbers high enough to produce mixed subsonic and supersonic flow are not generally available. Although these data are the primary source of roughness drag estimates and thus have received broad acceptance throughout the industry, they remain largely unsubstantiated at full scale conditions of Reynolds number and Mach number.

Notwithstanding the shortcomings of these data, they can be and are used to evaluate roughness drag by judicious application combined with computed or experimental data on local flow velocities and boundary layer conditions. When the roughness item height is large compared to the momentum thickness of the boundary layer ( $h \geq 10\theta$ ), the boundary layer effects are minor and the pressure or form drag of the item predominates. For small roughness elements, where  $h \leq 2\theta$ , boundary layer effects predominate. Roughness elements falling between these limits require a rational application of all known factors.

The effects of small isolated protuberances are the most difficult to quantify. Fasteners fall into this category and, depending on the fastener patterns and distribution, may tend to act more as a distributed roughness than isolated elements. Fasteners can become a very significant drag item if not properly controlled and for this reason most modern transport airplanes use flush fasteners. Even here, however, manufacturing and production tolerances result in protrusions and depressions of the order of  $\pm 0.0005$  to  $\pm 0.0010$  inch, depending on the method of fastener installation, i.e., machine versus manual. These actual tolerances are significantly less than those specified by the aerodynamics requirements document. Boundary layer calculations for a typical wing section indicate the thickness of the laminar sublayer to be 0.0005 inch at the front beam and 0.002 inch at the rear beam, thus it would not be expected that these fastener tolerances would contribute a significant drag increment. In addition, modern paints and painting techniques tend to minimize flow disturbances due to fasteners by the inherent smoothing action of the paint application.

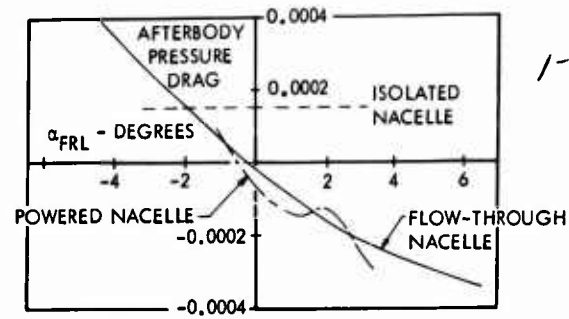


FIGURE 41. FAN COWL AFTERBODY PRESSURE DRAG

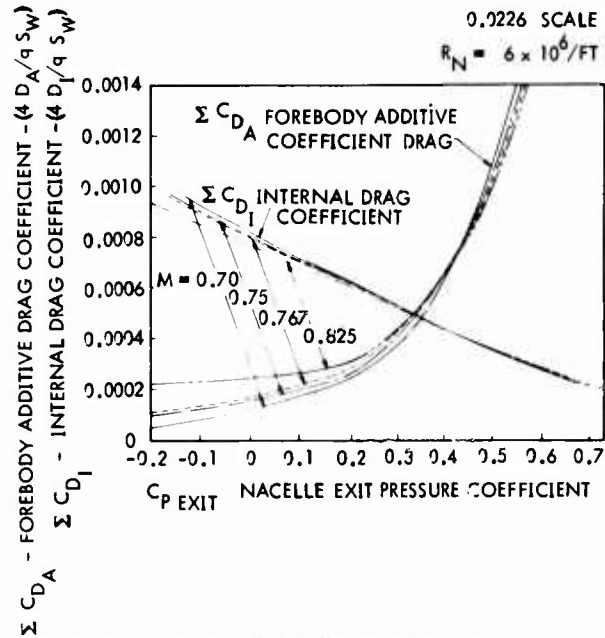


FIGURE 42. C-5A FOREBODY ADDITIVE AND MODEL NACELLE INTERNAL DRAG

- INBOARD NACELLE (X2) } FAN COWL FOREBODY
- OUTBOARD NACELLE (X2) } FAN COWL FOREBODY
- △ INBOARD NACELLE (X2) } FAN COWL AFTERBODY
- △ OUTBOARD NACELLE (X2) } FAN COWL AFTERBODY
- INBOARD NACELLE (X2) } EXHAUST BOUNDARY SKIRT
- OUTBOARD NACELLE (X2) } EXHAUST BOUNDARY SKIRT

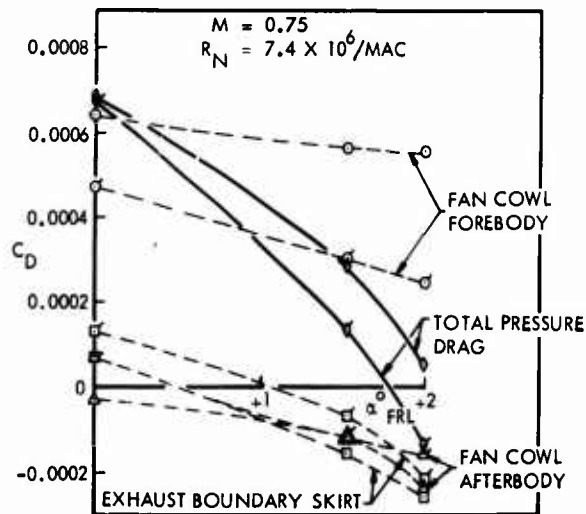


FIGURE 43. C-5A MODEL NACELLE PRESSURE DRAG COMPONENTS

1-24 To achieve an acceptable level of roughness drag a concerted effort must be made throughout the design and development phase of a project. This requires the coordination of the requirements of the aerodynamicist, the ingenuity of the designer, and the skills of the toolmaker, the master model maker and the production staff, to arrive at the desired goal. To assure orderly progress of this effort, the aerodynamicist must establish a target roughness drag level, prepare an aerodynamic smoothness requirement specification, and continuously monitor estimated roughness drag levels as the design develops. In this way, reasonable compromises between conflicting requirements can be made and design changes necessary to achieve the target drag level can be properly evaluated on the basis of overall system economics. For the C-5A the target drag level was established as 0.0007 in  $C_D$  or 5 percent of the estimated full-scale profile drag. Although considerable improvement in the estimated level of roughness drag between the first preliminary design estimate and the final production configuration estimate was achieved as a result of continuous surveillance of roughness sources, it was not possible to achieve the target drag level. Figure 44 presents a comparison of the final estimate and the target levels for the major contributors to roughness drag. Examination of these data show that elimination of one item, the drag of the exposed flap tracks, would have reduced the estimated drag level almost to the target amount. Design studies were conducted to evolve a scheme for just this purpose, however, complexity and potential maintenance problems combined to negate incorporation on the production configuration. The validity of the estimated roughness drag increment will be discussed in a later section of the paper dealing with wind tunnel - full scale correlation studies.

Item	$\Delta C_D$ (Counts)		Item	$\Delta C_D$ (Counts)	
	Estimate	Target		Estimate	Target
<b>General</b>			<b>Fuselage</b>		
Antennae	.535		Doors	.250	
Anti-Collision Light	.010		Waviness	.046	
CDPIR Installation	.024		Air Conditioning I/O System	1.350	
Windshield Wiper	.160		Nose Radome & Vent	.115	
Total	.729	.500	Leakage (Pressurization)	.500	
<b>Wing</b>			Negative Pressure Relief Vents	.200	
Skin Joint Steps & Gaps	.291		Wheel Well Fairing Vents	.056	
Aileron Spacer Gaps	.245		Wheel Well Fairing Slip Joints	.020	
Step at Slat T.E.	.150		Wheel Well Fairing Surface	.072	
Discontinuities at Slat Segment Ends	.500		APU Exhaust Outlet	.020	
Slat Actuator Doors	.010		Fuselage Doubler	.250	
Step at Spoiler T.E.	.210		Wing Root Fairing Slip Joints	.029	
Spoiler Gaps	.340		Visor Door - Fuselage Joint	.186	
Wing Tip Lights	.002		Kneeling Blisters	.200	
Static Discharge Wicks	.060		Total	3.294	3.100
Anti-icing Air Exhaust	.022		<b>Empennage</b>		
Steps and Gaps Around Flaps	.200		Skin Joints	.094	
Exposed Flap Tracks	1.600		Spacer Gaps	.452	
Exposed Bearings	.250		Bullet Base	.007	
Gear Boxes	.200		Total	.553	.500
Flap Trolley Bumps	.400		<b>Pylons</b>		
Total	4.480	2.878	Steps and Gaps	.022	
			Total	.022	.022
			<b>TOTAL</b>	9.075	7.000

FIGURE 44. ESTIMATED AND TARGET ROUGHNESS DRAG INCREMENTS

The following is a list of the corrections applied to the C-5A wind tunnel data for correlation with the flight test data.

C-5A Correction of Model Drag to Full Scale	
Model Drag at $M = 0.7$ , $C_L = .45$ Trimmed at 30% MAC	.02935
Corrections ( $\Delta C_D$ ):	
Reynolds No. - Method Ic	-.0061
- Method II, or III	(-.0066)
Model Transition to Leading Edge Transition	+.00135
Roughness	+.0009
Nacelle (Nacelle Drag Included in Engine Net Thrust)	-.0025
Support Tare and Interference	+.0001
Wind Tunnel Facility Correlation Correction	+.00041
Total Correction	-.00584
Full Scale Prediction	.02351
Full Scale Prediction (with Method II, or III Reynolds No. Corr.)	(.02301)

### 4.3 Analysis of Flight Test Drag

#### 4.3.1 Aerodynamic Consideration

1-25

As used in this analysis, the components which constitute total drag are illustrated in Figure 45; thus an aircraft flight drag coefficient may be expressed as:

$$C_D = C_{D_{P_{min}}} + C_{D_i} + C_{D_{trim}} + C_{D_{P_{CL}}} + C_{D_{P_C}} \quad (13)$$

where

$C_{D_{P_{min}}}$  = Minimum profile drag comprising skin friction and pressure drag on all aircraft components plus drag due to surface roughness. This includes form drag and interference of all external items on the aircraft, protuberances, steps, gaps, surface distributed roughness, and leakage drag.

$C_{D_i}$  = Vortex drag corresponding to the spanwise distribution of lift.

$C_{D_{trim}}$  = Trim drag, the additional drag associated with the change in component loads, due to the tail load required to offset the pitching moment for a given c.g. position.

$C_{D_{P_{CL}}}$  = Lift dependent profile drag.

$C_{D_{P_C}}$  = Compressibility drag; wave drag and shock-induced separation drag, especially significant at off-design conditions. In this correlation the induced drag and trim drag reflect Mach effects and therefore  $C_{D_{P_C}}$  is defined as the compressibility effect on profile drag.

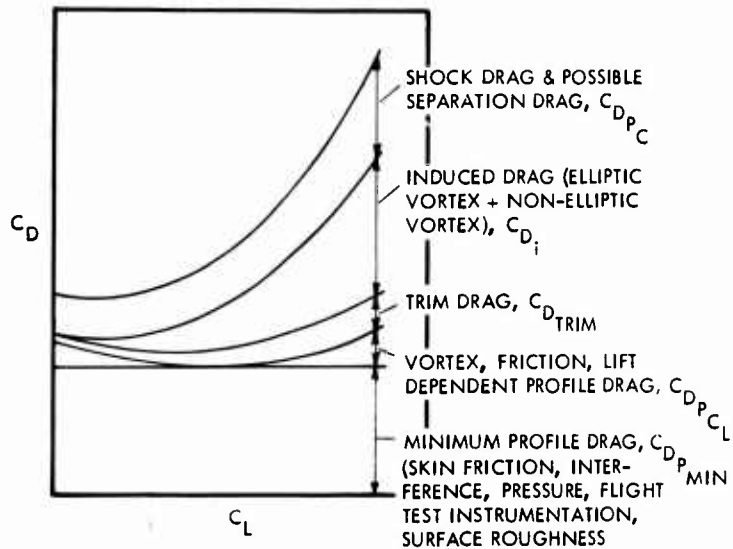


FIGURE 45. BREAKDOWN OF TYPICAL SUBSONIC JET AIRCRAFT DRAG POLAR

Flight test measured drag are made equivalent to wind tunnel data at the same  $C_L$ ,  $M$  and  $R_N$  by correcting for air-frame flexibility and center of gravity location, and by accounting for the drag of all external items such as flight test instrumentation, which is not represented on the wind tunnel model. In equation form:

$$C_{D_{rigid\ equiv}} = C_{D_{flex}} + \Delta C_{D_{rigid-flex}} + \Delta C_{D_{trim\ c.g.}} - C_{D_{inst}} \quad (14)$$

where

$C_{D_{flex}}$  = Measured flight test drag

$\Delta C_{D_{rigid-flex}}$  = Flexibility drag at flight test conditions

$\Delta C_{D_{trim\ c.g.}}$  = Incremental drag between trimmed drag at flight test c.g. location and normalized c.g. location

$C_{D_{inst}}$  = Drag of external flight test modifications for instrumentation

Each of the drag components and the corrections necessary to determine rigid aircraft drag are discussed as the data are developed for correlation.

#### 4.3.2 Flight Test Program

The C-5A aircraft was recently flight tested under a rigorously supervised program combining the efforts of the Lockheed-Georgia Company, the USAF Aeronautical Systems Division, the USAF Flight Test Center and the General Electric Company. Two in-flight photographs of the C-5A are shown for interest in Figures 46(a), (b). Flight testing of the C-5A aircraft was conducted at Edwards Air Force Base, California during the period 5 June 1969 through 15 January 1970. Performance data

suitable for aircraft drag evaluation were obtained from four-engine level-flight speed-power tests. Ten such flights were made covering an altitude range of 5000 feet to 40,500 feet, a gross weight range of 439,000 pounds to 702,000 pounds and a speed range from  $M = 0.28$  to  $M = 0.816$ . This represented a Reynolds number range from  $37 \times 10^6 / MAC$  to  $105 \times 10^6 / MAC$ . Lift and drag coefficients were computed from measured parameters using the following equations:

$$C_L = W \cos \gamma - F_N \sin [\alpha_{FRL} + i_T] \quad (15)$$

$$C_D = F_N \cos [\alpha_{FRL} + i_T] - W \sin \gamma \quad (16)$$

where

- $W$  = weight  
 $F_N$  = net thrust  
 $\alpha_{FRL}$  = angle of attack  
 $\gamma$  = angle of climb  
 $i_T$  = angle between thrust line and fuselage reference line  
 $q$  = dynamic pressure  
 $S$  = wing area

Figure 47 shows, diagrammatically, the lift and drag vectors on a typical aircraft such as the C-5A.

#### 4.3.3 Thrust Determination

The evaluation of full scale drag is primarily dependent upon the accuracy inherent in the determination of installed propulsive system net thrust. The computation of net thrust for the installation of the TF39 engine on the C-5A aircraft comprises a synthesis of drag, engine airflow and thrust calculations, which have been empirically calibrated from the results of both model scale and full scale test programs. These procedures are outlined in some detail by Poland and Schwanebeck (59); for the purposes of this paper only a brief summary of procedures and results is necessary.

Due to the large gross thrust and ram drag of highly efficient turbofan engines, such as the TF39, relative to net thrust, accurate and consistent determination of these quantities is essential to the evaluation of engine net thrust. This is accomplished by the selection and calibration of computational procedures based on experimental values for pressure and temperature in engine exhaust nozzles. Nozzle coefficients constitute the basis of this calibration and provide a common denominator for comparative evaluation of test data for different facilities, engines and test conditions.

Pylon-net thrust is defined as:

$$\begin{aligned} \text{Pylon net thrust} = & \Sigma + \text{fan nozzle gross thrust} + \text{core nozzle gross thrust} - \text{ram drag} \\ & - \text{pylon and core cowl scrubbing drag} - \text{plug scrubbing drag} \\ & - \text{forebody and afterbody pressure drags} - \text{fan cowl friction drag} \end{aligned}$$

The pylon scrubbing drag is for that portion of the pylon which lies within the streamtube determined for fully expanded fan exhaust flow.

In order to assure compatibility of the results from several test facilities and the various individual tests involved, several precautions were taken to minimize data discrepancies.



FIGURE 46. C-5A IN-FLIGHT PHOTOGRAPHS

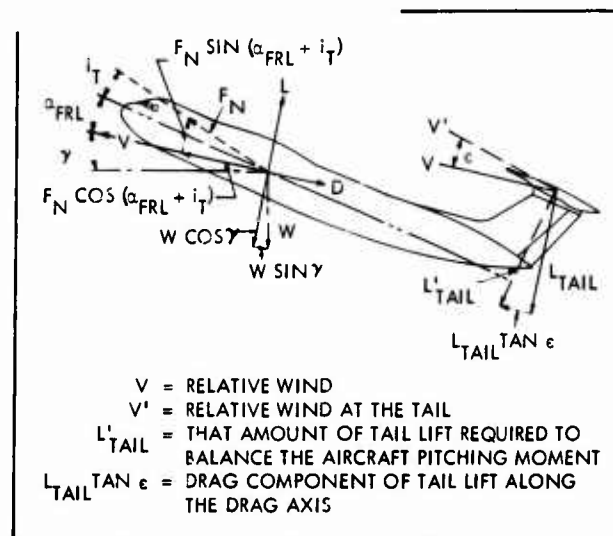


FIGURE 47. SKETCH OF JET AIRCRAFT LIFT AND DRAG VECTORS

1. The production configuration for the nozzle and nacelle contours was adopted as the reference configuration for all performance testing of the TF39 engines and for nozzle/nacelle models, thus avoiding any requirement to adjust test results for differences in nozzle and/or nacelle geometry.
2. Production engines assigned to both the performance flight test program and to the altitude cell test program were designated as Calibrated and Instrumented (C & I) engines and were supplied with nominally identical pressure and temperature instrumentation, avoiding any requirement to adjust experimentally derived nozzle coefficient data for differences in sampling errors which might occur if the instrumentation were not identical.
3. The inlet bellmouths used for all outdoor static tests were of identical General Electric design and manufacture and were provided with nominally identical instrumentation. Nozzle static pressures were used in combination with nozzle total pressures and temperatures to compute airflow and thrust.
4. Nozzle coefficients were defined on the basis of total pressure at the nozzle throats in order to avoid discrepancies in coefficient level due to differences in instrumentation sampling errors and internal viscous losses for differences in hardware.

1-27

The results of tests of a number of C & I engines in the Lockheed Engine Test Stand, the results of General Electric tests on their number 4 Engine Test Stand at Peebles, and the results obtained from the altitude cell test at Air Force Arnold Engineering Development Center were used to establish the final nozzle coefficients.

Three independent checks of the thrust calculation procedure have been made from analysis of flight test data for a C-5A equipped with C & I engines.

The first check was obtained by securing the C-5A to the test beds of the Edwards Air Force Base Static Thrust Calibration Facility and comparing calculated thrust to measured thrust on a point by point basis. The results are shown in Figure 48 for total thrust and average engine thrust respectively. The agreement is better than  $\pm 1$  percent of average engine thrust or less than  $\pm 0.5$  percent of the full scale thrust stand capacity.

Flight testing of the C-5A included a survey of inlet flow using an inlet rake to measure both total and static pressures and total temperatures. Airflow was also determined throughout the program by the summation of engine nozzle flows from measured nozzle pressures and temperatures. Figure 49 shows excellent agreement in the airflow obtained from these two sources, thus adding assurance to the validity of the nozzle coefficients, which are used for both airflow and gross thrust calculations. The third objective confirmation of in-flight thrust calculations was obtained from airplane drag calculations for sawtooth climbs and descents. The drag coefficients obtained from the calculation of net thrust during Normal Rated Thrust climbs and Idle Thrust descents are compared to the drag coefficients obtained from level flight speed-power tests in Figure 50. In the past, data scatter has generally tended to negate the potential usefulness of this type of comparison, however, for the C-5A the climb and descent data describe a  $\pm 2$  percent scatter band around the level flight speed-power test results.

The excellent agreement of test results from different test facilities plus the flight-test confirmation of consistency for thrust and airflow calculations provides assurance that the full scale drag data for the C-5A are a valid set for the purpose of wind tunnel flight test correlation studies.

#### 4.3.4 Corrections to Flight Data

(a) Center-Of-Gravity Location - Center-of-gravity locations for the various flight test points vary from a forward location of 19.5% MAC to an aft location of 36% MAC. In order to eliminate the variation in drag caused by varying amounts of trim required, the data are corrected to a common center of gravity location of 30% MAC. Wind tunnel data, for a range of horizontal stabilizer settings and varying Mach numbers are used to establish this correction. Figure 51 is an example of the effect of varying the trim center-of-gravity location on the C-5A drag for constant trimmed lift coefficients at  $M = 0.700$ .

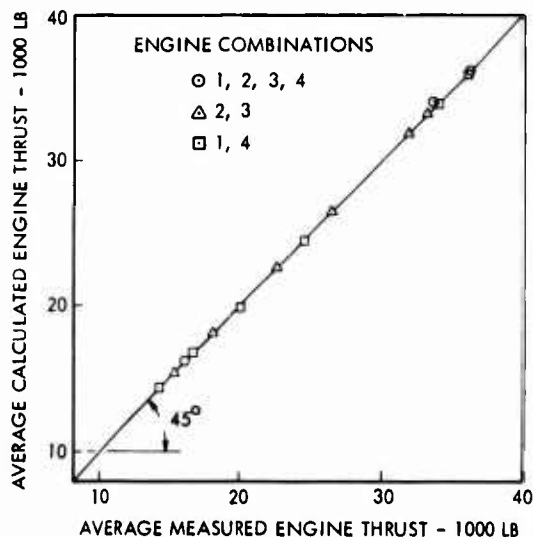


FIGURE 48. C-5A STATIC THRUST COMPARISON ON E.A.F.B. THRUST STAND

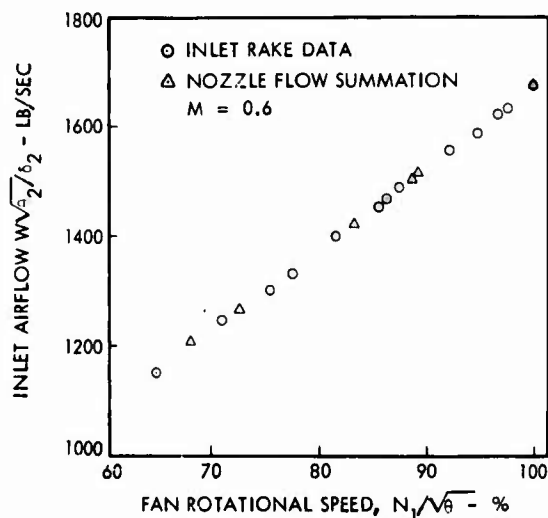


FIGURE 49. FLIGHT TEST COMPARISON OF INLET FLOW CALCULATIONS

(b) Flight Test Instrumentation Drag - A number of external configuration changes were made to the flight test aircraft to provide various items of flight test equipment. Drag due to these changes is subtracted from the flight measured drag. Pre-flight test estimates were made for each item separately, using existing methods, and are tabulated below. These estimates were substantiated by USAF Aeronautical Systems Division and Flight Test Center personnel.

Item	$C_D$
Nose boom and airspeed system	.000043
Trailing cone and cable	.000064
Takeoff and landing cameras	.000061
Tail bump skegs	.000196
Water ballast dump holes	.000021
Nose straps	.000037
Total	.000422

(c) Flexibility - Flexibility, or aeroelastic effects, as they are applied in this analysis, refer to the elastic deformation of the structure caused by aerodynamic and inertia loads. The distortions of the aircraft structure result in an overall redistribution of the aerodynamic loads and corresponding shifts in aircraft center of pressure. Of particular importance is the deformation of the wing. Under the influence of aerodynamic lift, the wing deflects upward along its elastic axis. For swept wings this results in a reduction in local airfoil section angle of attack compared with the unflexed wing.

This aerodynamic twisting or "wash out" of the wing reduces the local load on the wing with the greatest reduction occurring at the tip. At a constant wing angle of attack, the integrated load is less than that of the unflexed wing, and this lift loss is retrieved by increasing the aircraft angle of attack. Figure 52 illustrates this characteristic for the C-5A wing. As can be seen, substantial changes in the shape of the span load distribution occur in order to maintain a constant trimmed lift coefficient of 0.5. Dynamic pressure values of 400 pounds per square foot are typical of the higher Reynolds numbers tested. The rationale for including flexibility effects in the analysis is apparent from Figure 52. The C-5A wind tunnel model wing was designed with the rigged wing twist distribution, corresponding to the rigid or  $q = 0$  data, and therefore considerable variations from this base configuration occur in the flight results. Even had the model been designed with the incremental twist of some selected flight condition, the excursions in flight conditions to either side of the selected flight condition would necessitate corrections for aeroelastic deformation.

Other components of the airframe, such as the fuselage and empennage, also deform under aerodynamic loading, however, their effects on drag are considered secondary to those of the wing and therefore are not considered in this analysis. The effects due to the wing flexibility are three-fold: the changes in span load distribution produce (1) corresponding changes in the induced drag and (2) corresponding changes in local lift coefficients for the flexible wing relative to the rigid wing, which affects the wing profile drag; and (3) the changes in load distribution are accompanied by relocation of the wing center of pressure which alters the trim tail load and the associated trim drag. These are considered separately below.

- NORMAL CLIMB 25000 FT
- △ NORMAL CLIMB 35000 FT
- IDLE DESCENT 25000 FT
- ◆ IDLE DESCENT 35000 FT

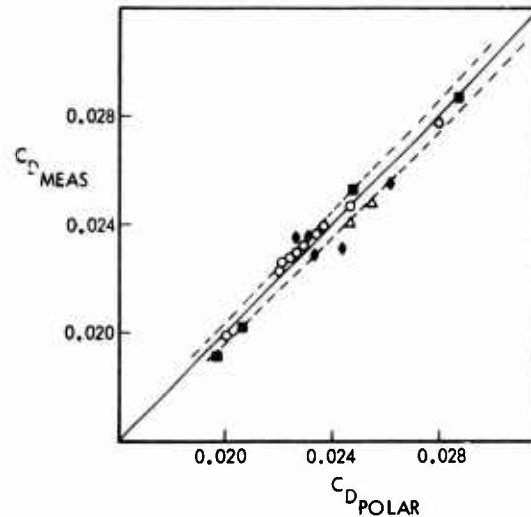


FIGURE 50. FLIGHT TEST DRAG COMPARISON - SAWTOOTH CLIMBS AND DESCENTS, CLEAN CONFIGURATION

$$M = 0.7$$

$$R_N = 4.2 \times 10^6 / \text{MAC}$$

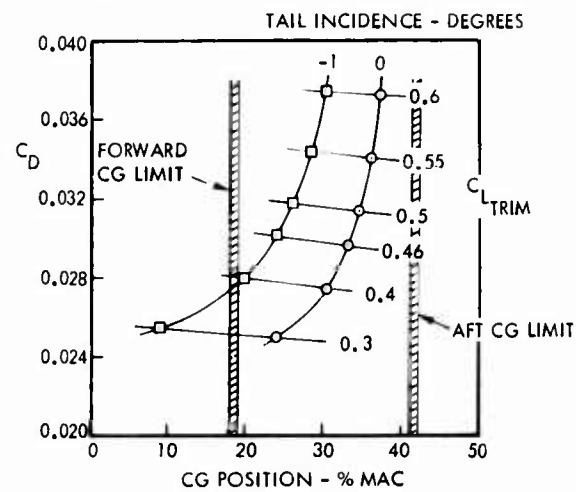


FIGURE 51. C-5A MODEL DRAG VERSUS CG POSITION

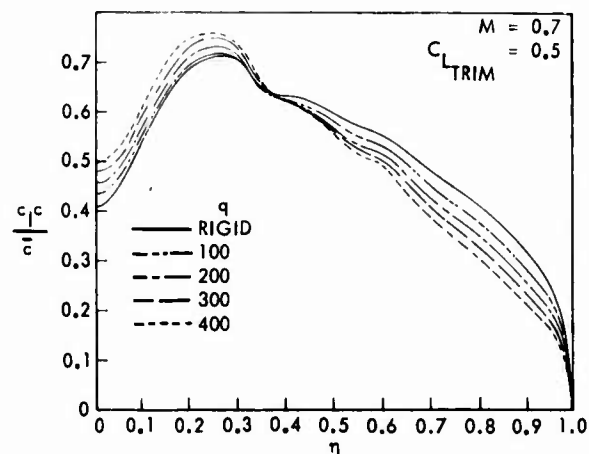


FIGURE 52. EFFECT OF FLEXIBILITY ON C-5 SPANWISE LOAD DISTRIBUTION

### Vortex Induced Drag

As mentioned earlier in Section 2.2, vortex induced drag comprises elliptic and non-elliptic vortex drag.

$$C_{D_i} = \frac{C_L^2}{\pi A e} \quad (17)$$

The span efficiency factor is calculated using lifting line theory after Glauert (43). This method is used to evaluate the induced drag over the range of lift coefficients and Mach numbers of interest. Figure 53 presents the variation of wing span efficiency with lift coefficient for a range of Mach numbers. These data are based on rigid loads data determined from wind tunnel pressure tests. The effect of wing distortion due to aeroelasticity on wing induced drag is determined by calculating the flexible spanwise load distribution and the associated value of  $e$ . The reduction in load near the wing tip tends to reduce the efficiency factor; however, this effect is more than offset by the increase in load on the inner wing and fuselage. Typical results at  $M = 0.700$  are shown in Figures 54 and 55.

Figure 54 shows the variation in wing span efficiency factor as a function of dynamic pressure for a range of lift coefficients. The incremental effect on induced drag depicted in Figure 55 is then found from the following:

$$\Delta C_{D_i} \text{ rigid-flex} = \left( \frac{C_L^2}{\pi A e} \right)_{\text{rigid}} - \left( \frac{C_L^2}{\pi A e} \right)_{\text{flex}} \quad (18)$$

### Wing Profile Drag

The second effect of the wing deformation is due to the local changes in wing section angle of attack. This produces changes in local lift coefficient and thus influences the wing profile drag. The magnitude and sign of the change at any local wing station depends on the spanwise location, the amount of distortion present, and the proximity of the local lift coefficient to the section design value.

In order to ascertain the incremental change in wing profile drag due to aeroelastic effects, it is first necessary to compute the profile drag of a rigid wing. The subsonic viscous flow program described in Section 2.1.2 is used for this purpose. It is recognized that this theory is not valid where mixed flow exists, and that for a large number of flight test points such conditions are present. Data from the two dimensional airfoil wind tunnel test program introduced in Section 2.1.2 for an airfoil representing a C-5A mid semi-span section, are used to define the section drag variation with lift above the critical  $C_{l_c}$ .

Profile drag polars are first generated for various wing stations using section ordinates. In this manner, the effects of actual thickness and camber variations of the C-5A wing are included. These polars are then used with the rigid and flexible local lift coefficients for a particular flight condition to obtain the increment in local profile drag due to the aeroelastic deformation.

The total wing incremental profile drag is obtained by strip integration:

$$C_{D_p} \text{ wing rigid-flex} = \int_0^1 \frac{\Delta C_{d_p} C}{C_{\text{ave}}} \quad (19)$$

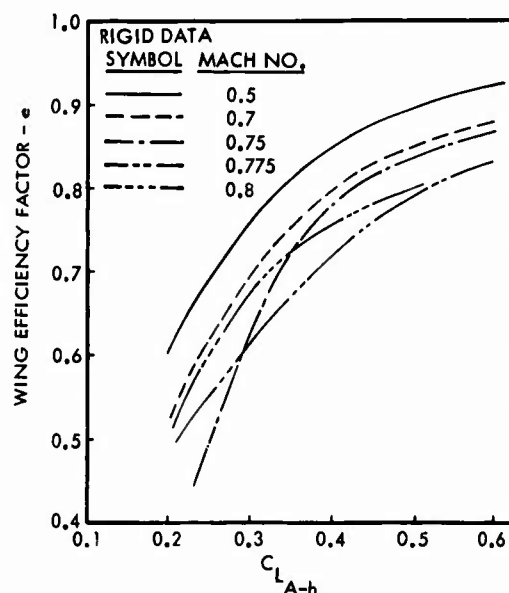


FIGURE 53. EFFECT OF  $C_L$  AND MACH NO. ON C-5A WING EFFICIENCY FACTOR

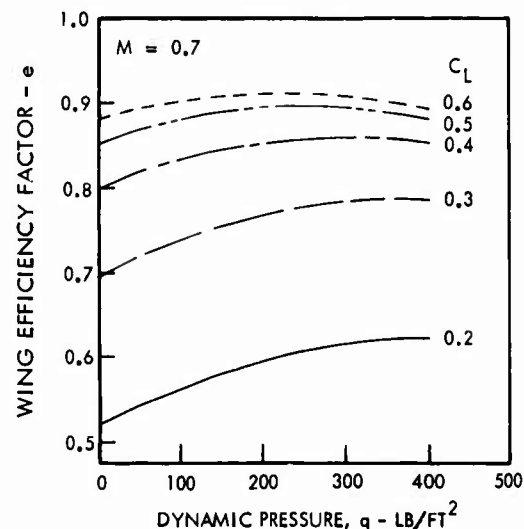


FIGURE 54. EFFECT OF FLEXIBILITY ON C-5A WING EFFICIENCY FACTOR

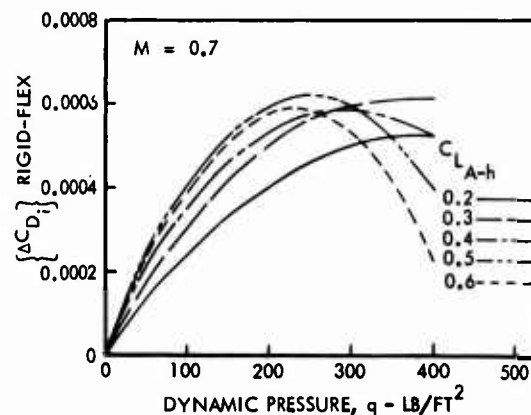


FIGURE 55. EFFECT OF FLEXIBILITY ON C-5A WING INDUCED DRAG

Figure 56 presents the increment for the C-5A wing as a function of lift coefficient and dynamic pressure. It is interesting to note that both the induced drag and wing profile drag increments due to flexibility are favorable effects on the C-5A.

A better understanding of the profile drag increment may be obtained by referring to Figure 52, where it can be seen that outboard stations experience a reduction in lift as the wing flexes. Thus, the section drag for these stations tends to reduce from the rigid case. Just the opposite occurs inboard. A typical spanwise variation in the profile drag increment, rigid minus flexible, is shown in Figure 57. The positive increments outboard have a larger influence than the negative inboard increments, and for the C-5A, the integrated result is a favorable drag reduction for the flexible case. This favorable effect is obviously configuration dependent and the C-5A results are not necessarily representative of other configurations.

#### Trim Drag

Finally, consideration is given to the flexibility effect on trim drag. The changes in spanwise load distributions on a swept wing due to aeroelastic effects, shift the location of the wing center of pressure thus altering the tail load required to trim the aircraft. For the C-5A, the redistribution of span loading, such as shown in Figure 52, results in a reduced tail load and slight changes in downwash angle. The changes must be recognized in the trim drag components. Thus

$$\Delta C_{D_{\text{trim}} \text{ rigid-flex}} = \Delta C_{D_{i \text{ trim}} \text{ rigid-flex}} + \Delta C_{D_{i \text{ tail}} \text{ rigid-flex}} + \Delta (C_{L_{\text{tail}}} \tan \epsilon) \text{ rigid-flex} \quad (20)$$

Below are tabulated a summary of typical trim increments due to flexibility:

M	$C_L$	q(PSF)	$\Delta C_{D_{\text{trim}} \text{ rigid-flex}}$
.6943	.4764	185.5	.000066
.7488	.4400	247.	.000123
.756	.2131	389.	.000338
.7747	.3498	330.	.000226

The net flexibility correction, accounting for the component effects described above is computed to be 0.00071 in  $\Delta C_{D_{\text{rigid-flex}}}$  at  $M = 0.700$ ,  $C_L = 0.45$ .

(d) Lift, Mach Number and Reynolds Number Effects - Before proceeding into the actual correlation, a brief summary is given of the method of treating the flight test results for the effects of three major variables,  $C_L$ , Mach number and Reynolds number. Preliminary studies during the post-flight analyses of the flight test data indicated that drag creep on the C-5A was essentially zero up to about  $M = 0.75$ . Thus it was felt that any scale effect in the data would become apparent by plotting the low speed data versus  $C_L^2$  as in Figure 58. The data were grouped by Reynolds Number and a different symbol used for each grouping so that mean lines could be faired through each set. A comparison of the incremental scale effect taken from this figure and that of a pre-flight test estimate, is shown in Figure 59. The estimated scale effect was based on combining the Karman-Schoenherr skin friction law with form factors derived by the supervelocity method. Agreement between the flight and predicted scale effect are satisfactory especially in view of the fact that these flight results are uncorrected for flexibility. It was therefore assumed that the flight data exhibited scale effects, and that normalization of all the data to a common Reynolds Number of  $55 \times 10^6 / \text{MAC}$  would permit a more reasonable assessment of the  $C_L$  and Mach Number effects.

Each flight test drag value was corrected for all known factors (c.g. location = .30 MAC, instrumentation drag, flexibility and Reynolds number =  $55 \times 10^6 / \text{MAC}$ ). Plots of  $C_D$  and  $C_L$  versus Mach number were made for each flight. A cross plot of these data was then constructed and is presented in Figure 60. The result shown in Figure 60 is a matrix of drag polars for various Mach numbers representing an initial attempt to find the  $C_L$  Mach number relationship for the C-5A flight data.

An iterative technique was then employed to arrive at the final best fit to the data. This was facilitated by a computer program devised to accept an input drag polar matrix and correct each flight test point to its nearest nominal  $C_L$  and Mach number. Additional points were also created to assist in the fairing of drag curves by correcting the flight test points to the nearest  $C_L$  and Mach number above and below the nominal value. From the output of this program a new matrix of drag polars could be developed and compared with the input polars. When the deviation between the two were sufficiently small

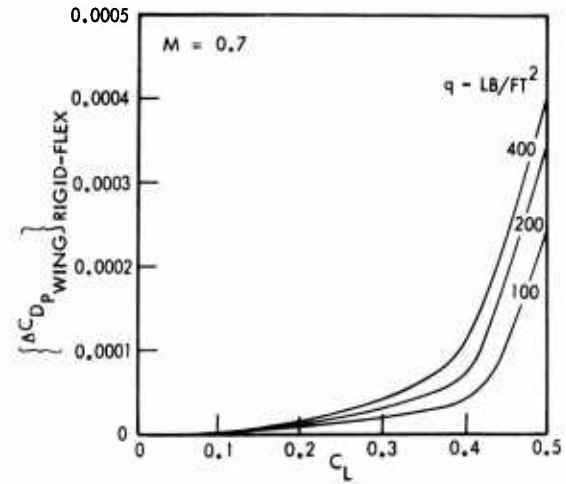


FIGURE 56. C-5 WING PROFILE DRAG INCREMENT DUE TO FLEXIBILITY

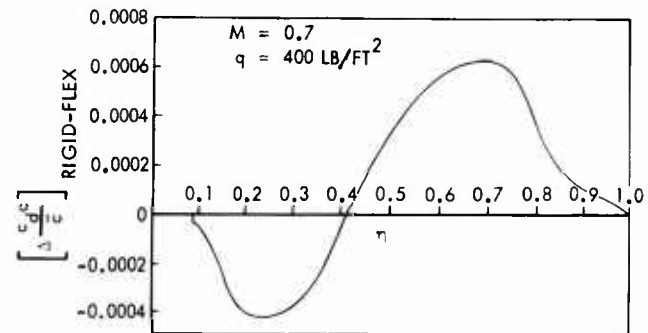


FIGURE 57. SPANWISE VARIATION OF C-5A WING PROFILE DRAG DUE TO FLEXIBILITY

to be insignificant, the process was complete. The final set of drag polars thus determined is presented in Figure 61. A distinction is made between the primary points, or those which are nearest to the nominal Mach numbers, and the secondary points which were created to fill in gaps and assist with curve fitting.

NOTE: (1)  $C_{D_{TEST}}$  CORRECTED TO CG = 30% MAC  
AND FOR FLIGHT TEST EQUIPMENT  
(2) HIGH MACH NUMBER TEST POINTS NOT INCLUDED

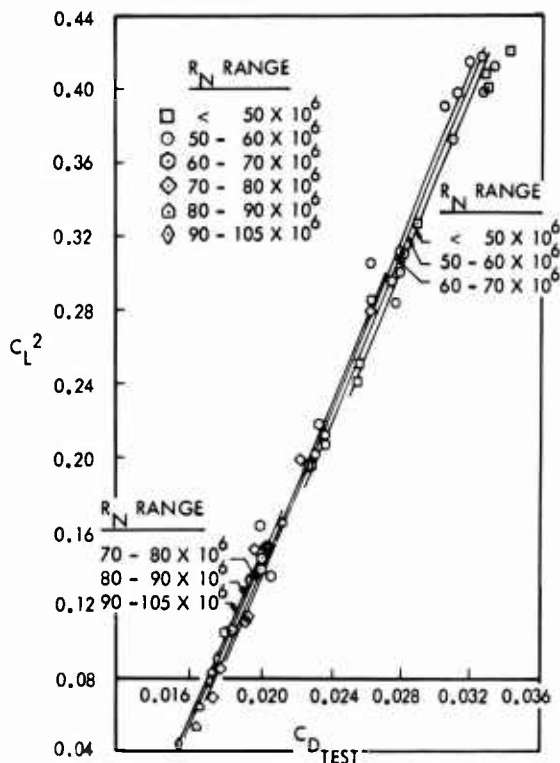


FIGURE 58. EFFECT OF REYNOLDS NUMBER ON  $C_L^2 - C_D$

$$\Delta C_D = \text{INCREMENTAL } C_D \text{ FROM THE NOMINAL VALUE AT } R_N = 55 \times 10^6 / \text{MAC}$$

$$= C_{D_{R_N}} - C_{D_{R_N = 55 \times 10^6}}$$

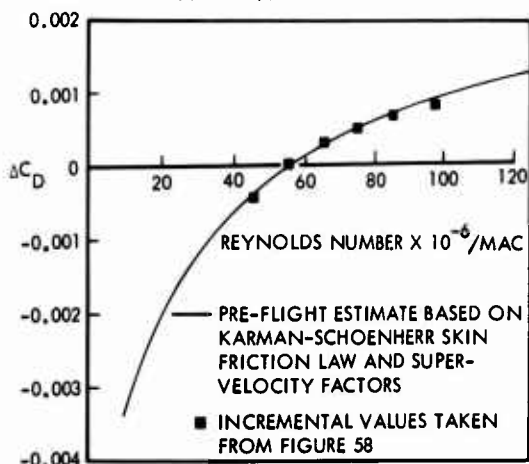


FIGURE 59. COMPARISON OF PRELIMINARY FLIGHT TEST SCALE EFFECT WITH EMPIRICAL ESTIMATE

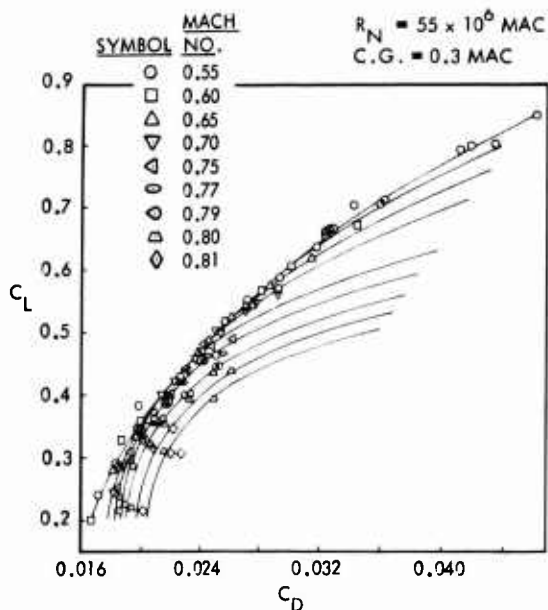


FIGURE 60. C-5A FLIGHT TEST DRAG NORMALIZED TO A CONSTANT REYNOLDS NUMBER - INITIAL DRAG POLAR

NOTE:  
SOLID SYMBOLS ARE FOR  $M_{TEST}$  VALUES NEAREST TO NOMINAL MACH NOS.  
OPEN SYMBOLS ARE POINTS CORRECTED TO NEAREST MACH NOS. ABOVE AND BELOW  $M_{TEST}$ .

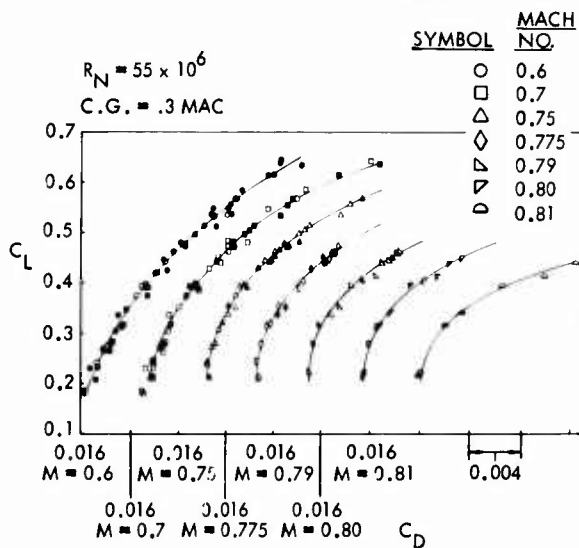


FIGURE 61. C-5A RIGID DRAG POLARS - FINAL ITERATION

#### 4.4 Correlation Results

Results from correlation studies of predicted drag from wind tunnel tests, and flight test data, are now presented for the C-5A configuration. Figure 62 compares drag polars at  $M = 0.700$  at a Reynolds number of  $55 \times 10^6 / \text{MAC}$ . The flight data, transferred from Figure 61 represent the equivalent rigid aircraft condition. The wind tunnel test data are corrected by the methods described in Section 4.2. Two methods of scaling the model data are used to correlate with the flight results. In Section 3.4, it is shown that the difference in Reynolds number correction from use of Method I(c), and the revised method based on calculated wing profile drag from viscous theory, was 5 aircraft drag counts. Section 4.2.5 indicates a target level of 7 counts for the aircraft roughness drag, and an actual estimated value of 9 counts attained during the final development phase. This number represents 6.8% of the total configuration profile drag.

Figure 62 indicates very close agreement between the predicted drag polars and flight test data. The correlation of airframe profile drag  $C_{D_P}$  is of more interest, and is shown in

Figure 63. The flight test data are again for the equivalent rigid aircraft, and normalized to a Reynolds number of  $55 \times 10^6 / \text{MAC}$ . All the flight data points shown are from the Mach number range  $0.65 \leq M \leq 0.725$ . Agreement of  $C_{D_P}$  is within 1% for Method I(c) and 3% for Method II.

The magnitude of predicted  $C_L$  for minimum  $C_{D_P}$  appears to be slightly higher than the flight test value, but the discrepancy is only 0.025 in  $C_L$ .

The variation of profile drag with  $C_L$  is generally in close agreement over the  $C_L$  range from 0.20 to cruise values in the region of 0.45. The discrepancies at higher  $C_L$ 's must be viewed as accumulated errors in either flight test data, where the high  $C_L$  range exhibits greater scatter, or further unknown errors in the wind tunnel data such as support interference inaccuracies, transition fixing, or tunnel flow and interference errors. The agreement in values of  $C_{D_P \text{ MIN}}$  and  $C_{D_P}$  is, nevertheless, considered to be substantially better than many previously published wind tunnel-flight correlations.

Figures 64, 65, and 66 are presented in order to examine Reynolds number effects and the overall accuracy of the flight data. Two of the figures present total flight test drag (64, 65) and one the profile drag comparisons (Figure 66). The rationale for presenting alternative sets of data in this analysis is to find what, if any, differences are introduced by the flexible corrections. The methodology employed to generate and present the flight data in all figures is the same. Initially, having determined the  $C_L$  - Mach number variation in the flight data, it is possible to normalize all the flight test points to one common  $C_L$  and  $M$  condition. In this instance no assumption is made regarding Reynolds number effects and the drag values thus obtained are plotted against Reynolds number. For comparisons of total  $C_D$ , the data have been normalized to  $C_L = 0.46$  at  $M = 0.7$  and for the profile drag case, the data are normalized to the minimum profile drag level at  $M = 0.7$ . High Mach number test points have been included in order to show as many points as possible. Where the test Mach number is greater than the drag rise Mach number, the symbols are solid. Test points having values of  $C_L > 0.53$  have been eliminated for these figures, since separation effects at high  $C_L$ 's tend to produce excessive scatter in flight measured drag.

As can be seen by comparing Figures 64 and 65, the flexibility corrections tend to reduce the amount of scatter in the flight data, and have no apparent effect on observable Reynolds number trends. The scale effect noticeable in the total drag is also apparent in the minimum profile drag of Figure 66. For comparison, a curve representing the estimated variation of minimum profile drag with Reynolds number is superimposed on Figure 66.

The method chosen for the estimated scale effect is Method I(c) of Section 3.4. By resorting to either Method II or III, a slightly larger scale correction would apply. Statistical analyses of the data of Figure 66 show that the scatter in the flight data averages  $\Delta C_D = \pm 0.00045$ , which represents only  $\pm 3.5\%$  of the total flight profile drag or about  $\pm 2.0\%$  of cruise drag.

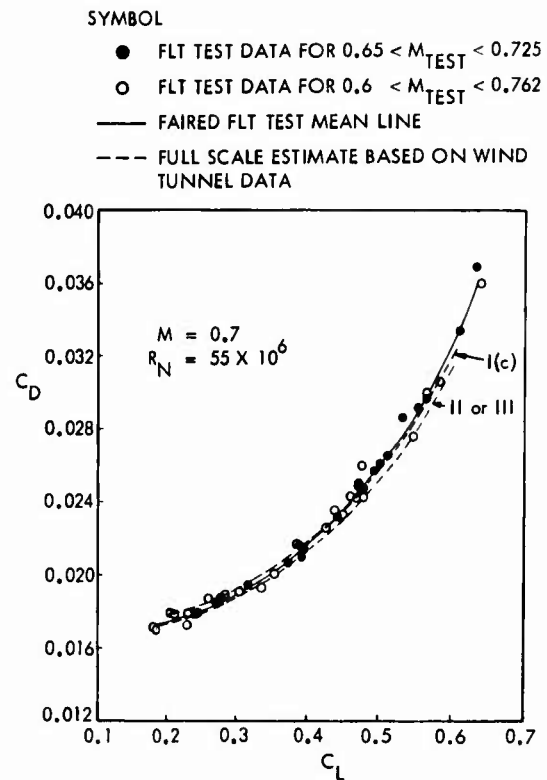


FIGURE 62. CORRELATION OF C-5A PREDICTED AND FLIGHT TEST DRAG AT  $M = .7$

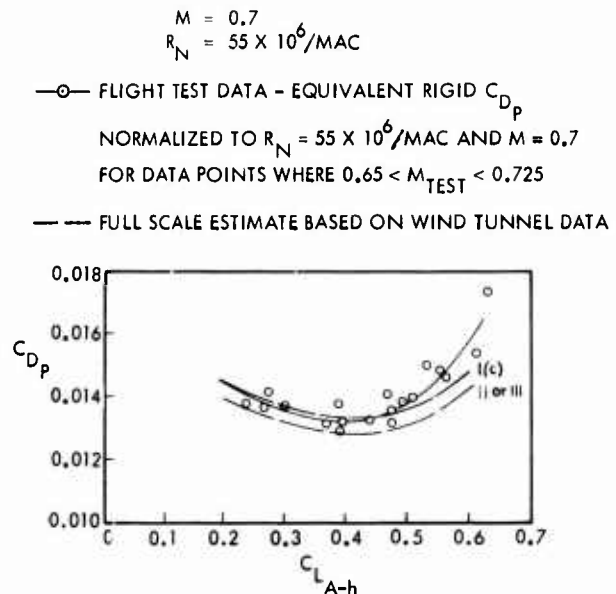


FIGURE 63. CORRELATION OF C-5A PREDICTED AND FLIGHT TEST PROFILE DRAG

ALL FLIGHT TEST DATA NORMALIZED TO  $M = 0.7$ ,  
 $C_L = 0.46$   $CG = .30$  MAC

SYMBOL

- FLIGHT TEST DATA FOR  $M_{TEST} \leq M_{DRAG RISE}$
- FLIGHT TEST DATA FOR  $M_{TEST} > M_{DRAG RISE}$

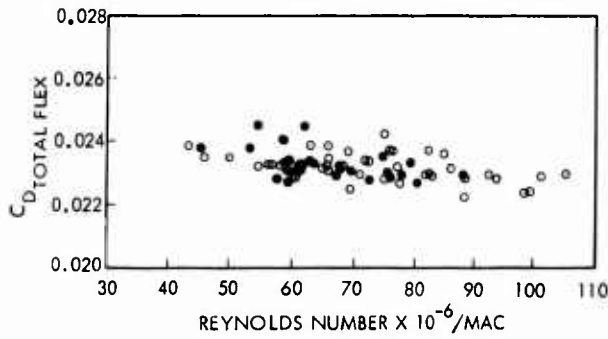


FIGURE 64. C-5A FLEXIBLE FLIGHT TEST DRAG

The trends of profile drag with Reynolds number, shown in Figure 66, indicate that the variation of this component up to values of  $R_N = 100 \times 10^6/MAC$  are in close agreement with estimated Reynolds number effects based on theoretical methods available. It would appear therefore that the overall skin friction of the aircraft is representative of smooth turbulent boundary layer conditions, and that the effective surface distributed roughness drag of the configuration is always less than estimated for "critical" roughness based on Nikuradse's experiments. Information given in Section 4.2.5 confirms that with the strict monitoring process on tolerances during the development stage, together with the benefits of paint sprayed surfaces distributed roughness drag is not encountered and the results confirm the absence of a "terminal" value of skin friction drag.

Figure 67 compares the C-5A drag-rise characteristics from prediction based on wind tunnel data, and flight test. Flight characteristics for both the flexible and rigid aircraft are shown, indicating a small difference in drag rise due to flexibility. The correlation of the rigid aircraft drag rise Mach number, based on the definition  $dC_D/dM = .05$ , indicates agreement within  $\Delta M_D = .001$  between the predicted and flight test characteristics. In the low Mach number range,  $0.70 < M < 0.77$ , however, a favorable reduction in the drag creep characteristics at full scale conditions is noted. This is believed to be due in part to a favorable Reynolds number effect on the viscous form drag, due to the method of fixing transition in the wind tunnel, as indicated in Section 3.2. Other contributions to this discrepancy must be attributed to the complex problems of simulating high Reynolds number flows in mixed flow conditions, as outlined in Section 3.2.

##### 5. CORRELATION OF C-141A PREDICTED AND FLIGHT TEST DRAG

In this section some preliminary results from the C-141A drag correlation program are presented. Under the sponsorship of NASA, Langley, this study included retesting of a C-141A model to obtain wind tunnel data as complete and reliable as possible. This work is not yet complete and therefore, only preliminary results are presented here. The C-141A flight data shown here are taken from Reference (60) where an analysis, similar to that described for the C-5A, was reported.

Two sets of estimates based on wind tunnel tests are included in this correlation; one set is taken from pre-flight wind tunnel results, and the other from a recent high speed test at the NASA Langley 8 foot facility (1). Again, scale corrections are considered using Method III of scaling profile drag, to show a range of estimates. No correction for full scale roughness drag has been applied. Figure 68 shows the C-141A profile drag variation with lift coefficient from flight test compared

ALL FLIGHT TEST DATA ARE EQUIVALENT RIGID RESULTS  
 NORMALIZED TO  $M = 0.7$ ,  $C_L = 0.46$   $CG = 0.30$  MAC

1-33

SYMBOL

- FLIGHT TEST DATA FOR  $M_{TEST} \leq M_{DRAG RISE}$
- FLIGHT TEST DATA FOR  $M_{TEST} > M_{DRAG RISE}$

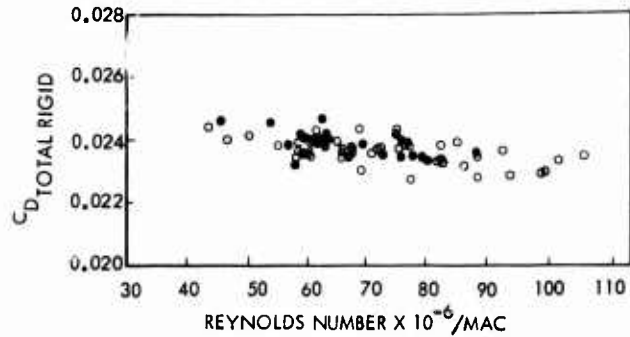


FIGURE 65. C-5A EQUIVALENT RIGID FLIGHT TEST DRAG

ALL FLIGHT TEST DATA NORMALIZED TO  $M = 0.7$   
 $CG = 0.3$  MAC

SYMBOL

DATA

- FLIGHT TEST DATA FOR  $M_{TEST} \leq M_{DRAG RISE}$
- FLIGHT TEST DATA FOR  $M_{TEST} > M_{DRAG RISE}$

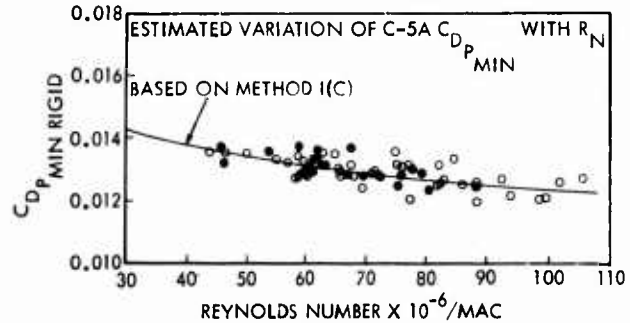


FIGURE 66. CORRELATION OF C-5 EQUIVALENT RIGID FLIGHT TEST PROFILE DRAG WITH THE RIGID ESTIMATE BASED ON WIND TUNNEL DATA

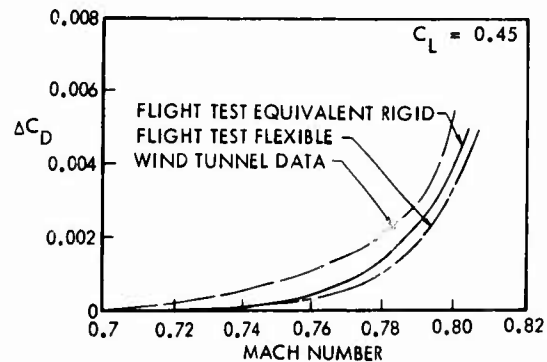


FIGURE 67. C-5A DRAG RISE COMPARISON

1-34

with the wind tunnel based estimates. The flight data points have been normalized to  $M = 0.7$  and  $R_N = 32.5 \times 10^6 / MAC$ .

Excellent correlation is shown with the Langley data except at the higher lift coefficients. The deviation at high  $C_L$  may not be as large as shown here in view of the fact that only a few flight points are available in the high  $C_L$  region and the fairing of the flight test mean line may be questionable. The earlier set of wind tunnel estimated data was based on model testing with transition fixed by a wide band (0.4 inches) of densely distributed carborundum particles. This technique was used extensively in the past and there is all likelihood that transition was overfixed, resulting in excess pressure drag due to overthickening of the boundary layer. Apparently this is the case since the 1 ft dependent profile drag from this test differs significantly from both the flight results and the Langley data. Also, a significant roughness drag correction due to the transition strip was applied to the data. In the case of the Langley test, the C-141A model transition fixing technique was intended to prevent these problems, and followed that developed for the C-5A.

It is shown that the  $C_L$  for minimum profile drag and the value of minimum profile drag are essentially the same for the flight test data and for the prediction based on the Langley wind tunnel data. The scale correction used to extrapolate the wind tunnel data to full scale was based on Method II. Use of a smaller scale correction from Method I(c) would cause a deviation in  $C_{Dp, MIN}$  of about

5 drag counts, and the predicted levels would be higher by 5 drag counts.

Figure 69 shows a scale effect correlation of the C-141A minimum profile drag. The flight test results (60) have been normalized to the lift coefficient for minimum profile drag at  $M = 0.7$  in order to examine Reynolds number effects. The mean curve through the data and the accuracy bands placed on the figure are from Reference (60), where a statistical analysis of the flight test data was reported. The mean line does not represent any of the five scaling techniques as was the case for the C-5A data, rather it is a statistical best fit of the data. However, the variation of  $C_{Dp}$  with  $R_N$  based

on Method II is presented on the figure as a comparison. The agreement between the two is within 1.5 drag counts over the flight range of  $R_N$  which is only about 1% of profile drag.

In Reference (60) consideration was given to the accuracy of the flight test data by assessing the overall accuracy of the mean curve and the corrections made to the flight data, a process of examining the flight test scatter. It was estimated that the overall inaccuracy of the flight data should be no larger than  $\Delta C_D = \pm 0.00074$  or  $\pm 3.3$  percent

of drag at cruise. Statistical analyses showed that the scatter in the flight data averaged  $\pm 3.7$  percent of cruise drag, which agrees with the estimate very closely.

## 6. AERODYNAMIC SMOOTHNESS

The chart shown in Figure 70 presents the familiar correlation of aircraft effective skin friction drag for subcritical flight test conditions. The data points shown are all for large subsonic aircraft, including commercial jets, military cargo turboprop and jet transports, and bomber aircraft. The majority of the data for jet transports lies close to an effective skin friction line of  $C_f = 0.0030$ . Three turboprop cargo aircraft with rear loading capability and, consequently, upswept afterbodies exhibit values of  $C_f$  in the 0.0050 to 0.0060 range. Data for the C-5A indicate a relatively high degree of aerodynamic cleanliness giving  $C_f = 0.0027$ . This is confirmed by the trends of the individual flight test data points with Reynolds number, presented in the previous section.

CLEAR SYMBOLS - RIGID FLIGHT TEST DATA

- LANGLEY DATA CORRECTED TO FULL SCALE
- AMES 088 DATA CORRECTED TO FULL SCALE

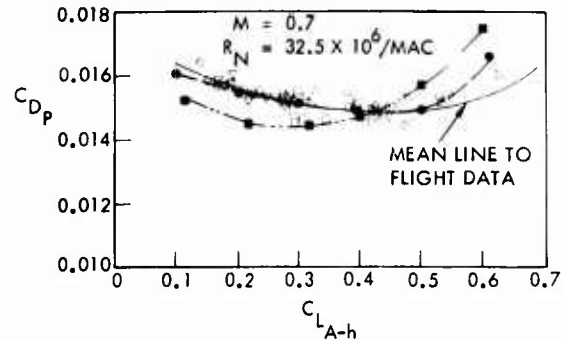


FIGURE 68. CORRELATION OF C-141 PREDICTED AND FLIGHT TEST PROFILE DRAG

- LANGLEY TEST } CORRECTED TO FULL SCALE
- AMES TEST } USING ESTIMATE, METHOD II
- ESTIMATED OVERALL MAXIMUM ERROR AT APPROX CRUISE CONDITIONS,  $\pm \Delta C_D = .00074$
- STANDARD DEVIATION,  $2\sigma = \pm \Delta C_D = .00078$

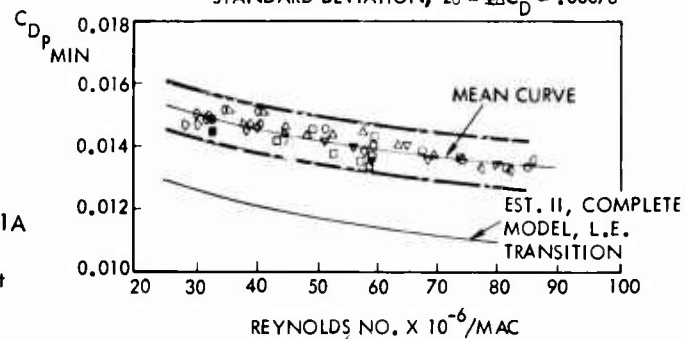


FIGURE 69. CORRELATION OF C-141 MINIMUM PROFILE DRAG

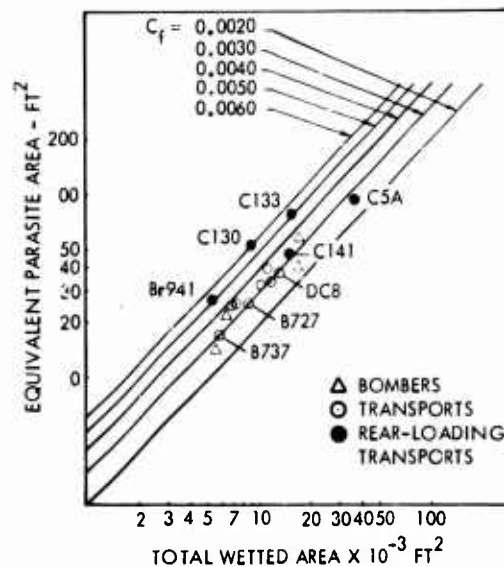


FIGURE 70. SUBSONIC PARASITE DRAG

It appears that effective skin friction for subsonic transports can be reduced to levels approaching  $C_f = 0.0025$  and possibly lower if meticulous care is taken in detailed aerodynamic design during the development stage.

## 7. CONCLUSIONS

This survey has presented some of the main features and problems of subsonic drag estimation from an industry point of view. In particular, experience gained on the development of large multi-engined transport aircraft has been outlined with details of preliminary estimation methods, wind tunnel testing techniques, and the degree of correlation obtained between predictions based on wind tunnel data and flight test data.

Some of the principal conclusions to be noted are:

1. Semi-empirical methods of estimating wing profile drag are generally inadequate at the project design stage of a new aircraft, and should be supplemented when possible by viscous flow solutions using potential and boundary layer theories. Use of the "flat plate x shape factor" approach can give inaccuracies for two reasons, (a)  $\pm 10\%$  scatter in test data upon which several semi-empirical formulae are based, and (b) inadequate definition of the true shape factor accounting for the exact degree of form drag at minimum drag conditions, and at angle of attack. In this respect, correlation of estimated shape factor is rendered difficult due to use of empirical formulae based on mixed laminar-turbulent flow measurements, and results in discrepancies of 10 - 15% depending on the type of airfoil camber and loading design. A requirement exists for research on skin friction beyond about  $300 \times 10^6$  based on component length, where very little test data has been obtained to substantiate Schoenherr's mean line extrapolation. This is of particular importance with regard to prediction of transport fuselage drag, where length Reynolds numbers of up to  $600 \times 10^6$  are considered.
2. The viscous flow solution, using potential flow and boundary layer theories, has proved to be a valuable tool in both predicting airfoil profile drag and interpreting test data. Minimum profile drag,  $c_{d_p \text{ MIN}}$ , is shown to be predicted to within 2% from detailed correlation studies of test data. Although limited to subcritical attached flow conditions, reasonable agreement is shown for the lift-dependent profile drag up to moderate values of  $c_l$  for a wide range of airfoil designs, ranging from "conventional" to highly loaded peaky and aft cambered designs. Procedures for computing profile drag in the presence of unsymmetrical or separated boundary layers and in supercritical flows remain to be developed. Prediction of drag-rise Mach number for conventional airfoils is satisfactory, using established criteria; for airfoils with both upper and lower surface "critical" boundaries, suitable pressure distribution shape criteria to supplement the standard methods are essential.
3. Further research is required on component interference, particularly wing-fuselage. Although adequate methods are available for prediction of individual wing and fuselage drag for most conventional transport designs, no satisfactory methods exist for estimating three-dimensional interference in viscous flows, and heavy emphasis is still given to ad-hoc wind tunnel testing at low Reynolds number, supplemented by potential flow methods and empirical "guidance" techniques.
4. Considerable effort has been made recently, and will continue, on improving the confidence level of wind tunnel data for use in predicting full scale drag. This approach has not always proven fruitful in the past, very often due to inadequate quality of model testing techniques, and erroneous interpretation of test data. Very detailed and systematic tests are required to ensure that good data is obtained and that the full limitations of low Reynolds number testing are appreciated. A method of fixing transition for the subsonic region has been demonstrated, but no completely satisfactory method exists for predicting full scale drag-rise characteristics in mixed flows. Evaluation of the type of wing shock-boundary layer and trailing edge flow characteristic is required before a reasonable interpretation can be made of the likely scale effects on drag-rise Mach number.
5. Detailed correlation studies of the C-5A cruise drag have been made, using predictions based on wind tunnel data and flight test results. These data are presented with emphasis on the wind tunnel corrections necessary for a valid correlation, and the accuracy of the flight-measured thrust levels. Confidence in the powerplant thrust measurements was demonstrated through the excellent agreement of test results from different test facilities and the flight-test confirmation of consistency for thrust and airflow calculations. Statistical analysis of the flight data indicated a scatter of  $\pm 3.5\%$  of profile drag. It is shown that predicted subcritical minimum profile drag agrees within 1 - 3% with rigid airframe flight test data. The variation of profile drag with  $C_L$  is also in good agreement. This degree of correlation confirms that use of low Reynolds number test data, carefully measured, and use of standard scaling methods are adequate for the purposes of predicting full scale drag. Agreement of drag-rise Mach number, based on the definition  $dC_D/dM = .05$  is within 0.001 in  $M_D$ . The most notable difference in wind tunnel and flight drag-rise is in the nature of the subcritical drag creep, which is assumed to be due to a favorable scale effect associated with the method of fixing transition in the wind tunnel.

1-36

6. Experience on two large transport aircraft, the C-141A and the C-5A, demonstrates that a strict monitoring procedure to minimize manufacturing surface "roughness" results in full scale profile drag representative of smooth turbulent flow over Reynolds number ranges up to  $100 \times 10^6 / \text{MAC}$ . This suggests that the effective surface distributed roughness drag is less than that predicted for a "critical" roughness based on the Nikuradse sand grain criterion. The correlation of predicted profile drag, based on wind tunnel tests, with flight data, confirms that the methods in use for estimating this increment are reasonably accurate for this aircraft configuration.

#### REFERENCES

- (1) Unpublished Work under Contract NAS1-10045 (Correlation of Full Scale Drag Predictions with Flight Measurements on the C-141A Aircraft).
- (2) Froude, W.: Experiments on Surface Friction Experienced by a Plane Moving Through Water, British Association Reports, 1872.
- (3) Gebers, F.: Ein Beitrag Zur Experimentellen Ermittlung des Wasserwiderstandes gegen bewegte Koeper, Schiffbau, Vol. 9, 1908.
- (4) Gebers, F.: Das Aehnlichkeitsgesetz bei im Wasser geradlinig fortbewegter Platten, Schiffbau, Vol. 22, Nos. 29-33, 35, 37-39, 1919.
- (5) Hughes, G.: Frictional Resistance of Smooth Plane Surfaces in Turbulent Flow, New Data and a Survey of Existing Data, Trans. Inst. Naval Architects, Vol. 94, No. 4, Oct. 1932, pp 287-322.
- (6) Kempf, G.: Neuerge Ergebnisse der Widerstandsforschung, Werft Reederei U. Hafen, June 1929.
- (7) Schoenherr, K. E.: Resistance of Flat Surfaces Moving Through a Fluid, Trans. Soc. Naval Architects and Marine Engineers, Vol. 40, 1932, pp. 279-313.
- (8) Falkner, V. M.: The Resistance of a Smooth Flat Plate with Turbulent Boundary Layer, Aircraft Engineering, Vol. 15, No. 169, March 1943.
- (9) Gibbons: Skin Friction of Various Surfaces in Air, Annual Report of the N.A.C.A., 1915.
- (10) Wieselsberger: Untersuchungen ueber den Reibungswiderstand stoffbespannter Flaechen, Ergebnisse der Aerod, Versuchsanstalt Goettingen, Vol. 1.
- (11) Jones, R.: and Williams, D. H.: The Profile Drag of Aerofoils at High Reynolds Numbers in the Compressed Air Tunnel, ARC R&M 1804.
- (12) Smith, Donald W.: and Walker, John H.: Skin-Friction Measurements in Incompressible Flow, NASA TR R-26, 1959.
- (13) Winter, K. B.; and Gaudet, L.: Some Recent Work on Compressible Turbulent Boundary Layers and Excrescence Drag, Agardograph 97, 1966.
- (14) Schultz-Grunow, F.: New Frictional Resistance Law for Smooth Plates, NACA TM 986, 1941.
- (15) Spalding, D. B.; and Chi, S. W.: The Drag of a Compressible Turbulent Boundary Layer on a Smooth Flat Plate With and Without Heat Transfer, J. Fluid Mechanics, Vol. 18, Part 1, 1964, pp 117-143.
- (16) Hoerner, S. F.: Fluid Dynamic Drag
- (17) Abbott, I. R.; Von Doenhoff, A. E.; Stivers, L. S.: Summary of Airfoil Data, NACA Rept. 824, 1945.
- (18) Moulden, T. H.; Hecks, K.; Bennett, J. A.: Development of Conventional-Type Two-Dimensional Airfoils for High-Subsonic Operation (1967), Lockheed-Georgia Report ER-9846, May 1969.
- (19) Moulden, T. H.; Hecks, K.; Goradia, S. H.: Development of Conventional-Type Two-Dimensional Airfoils for High-Subsonic Operation (1968), Lockheed-Georgia Report ER-9857, May 1969.
- (20) Thwaites, B.: Incompressible Aerodynamics, Clarendon Press, Oxford, 1960.
- (21) Blackwell, J. A.; Bennett, J. A.: A Subsonic Viscous Flow Method for Analysis of Two-Dimensional Airfoils and Swept Wings, Lockheed-Georgia Report ER-10,706, May 1970.
- (22) RAeS Data Sheets, Wings 02.04.02, 03.
- (23) Weber, J.: The Calculation of the Pressure Distribution on the Surface of Thick Cambered Wings and the Design of Wings with Given Pressure Distribution, ARC R&M 3026, 1957.

- (24) Shapiro, Ascher H.: *The Dynamics and Thermodynamics of Compressible Fluid Flow, Volume I*, The Ronald Press Company, New York, N.Y. 1953, pp 347.
- (25) Thwaites, B.: *Approximate Calculation of the Laminar Boundary Layer*, *Aero Quarterly* Vol. I, p 245, 1949.
- (26) Stewartson, K.: *Correlated Incompressible and Compressible Boundary Layers*, *Proceedings of the Royal Society, (A)* Vol. 200, p 84, 1949.
- (27) Illingsworth, G. R.: *Steady Flow in the Laminar Boundary Layer of a Gas*, *Proceedings of the Royal Society, (A)* Vol. 199, p 533, 1949.
- (28) Cebeci, T; Smith, A. M. O.: *Calculation of Profile Drag of Airfoils at Low Mach Numbers*, *J. Aircraft* Vol. 5, No. 6, November - December 1968, pp 535-542.
- (29) Nash, J. F.: *A Practical Calculation Method for Compressible Turbulent Boundary Layers in Two-Dimensional and Axisymmetric Flows*, Lockheed-Georgia Aerospace Sciences Lab Research Memo ER 9428, 1967.
- (30) Preston, J. H.: *The Calculation of Lift Taking Account of the Boundary Layer*, ARC R&M 2725, 1953.
- (31) Powell, B. J.: *The Calculation of the Pressure Distribution on a thick Cambered Aerofoil at Subsonic Speeds Including the Effects of the Boundary Layer*, ARC C.P. No. 1005, June 1967.
- (32) Squire, H. B.; Young, A. D.: *The Calculation of the Profile Drag of Airfoils*, R&M 1818, November 1937.
- (33) Unpublished Work by S. Goradia - Lockheed-Georgia Company under NASA Contract.
- (34) Sinnott, C. S.; Osborne, J.: *Review and Extension of Transonic Airfoil Theory*, ARC R&M 3156, 1961.
- (35) Nitzberg, G. E.; Crandall, S.: *A Study of Flow Changes Associated with Airfoil Section Drag-Rise at Supercritical Speeds*, NACA TN 1913, 1949.
- (36) Royal Aero Society: *A Method of Estimating Drag Rise Mach Numbers for Two-Dimensional Aerofoils*, Transonic Data Memo 6407, 1964.
- (37) Burdges, K. P.: *A Synthesis of Transonic, 2-D Airfoil Technology*, Lockheed-Georgia Company ER 11011, 1971.
- (38) Osborne, J.: *A Comparison Between Predicted and Measured Profile Drag for a Two-Dimensional Aerofoil at Incompressible Speeds Over a Large Range of Reynolds Number*, N.P.L. Aero Note 1052, ARC 28720, 1967.
- (39) Nash, J. F.; Bradshaw, P.: *The Magnification of Roughness Drag by Pressure Gradients*, *Journal of the Royal Aeronautical Society* Vol. 71, January 1967.
- (40) Nash, J. F.; Tseng, R. R.: *The Three-Dimensional Turbulent Boundary Layer on an Infinite Yawed Wing*, *Aeronautical Quarterly*, 1970.
- (41) Cooke, J. C.: *The Drag of Infinite Swept Wings with an Addendum*, ARC CP 1040, 1969.
- (42) RAeS Data Sheets, Bodies .02.04.01, 02.
- (43) Glauert, H.: *Elements of Aerofoil and Airscrew Theory*, Cambridge University Press, London, 2nd Edition, 1947.
- (44) Martin, G. H.: *Vortex Collocation Lifting Surface Theory for Subsonic Compressible, Potential Flow*, Lockheed-Georgia Company ER 8814, 1967.
- (45) Blackwell, J. A., Jr.: *A Non-Planar Vortex Lattice Program (RAX-LIFT 4) for Calculation of Aerodynamic Characteristics for Arbitrary Aircraft Configurations at Subsonic Speeds in or Out of Ground Effect*, Lockheed-Georgia Company IDC E-74-701-70, 1970.
- (46) Stevens, W. A.: *A Linearized, Aerodynamic Analysis of Wing-Body Combinations - Part I: Subsonic Flow*, Lockheed-Georgia Company, ER 11287, 1972.
- (47) USAF Stability and Control DATCOM, Section 4.4.1 *Wing-Body Combinations at Angle of Attack*, 1969.
- (48) Paterson, J. H.: *Aerodynamic Design Features of the C-5A*, SAE Paper 670847, Los Angeles, Oct. 2 - 6, 1967.
- (49) Ross, R.: *Turbulent Skin Friction for Tapered Wings*, *AIAA Journal of Aircraft*, Vol. 8, No. 10, October 1971.
- (50) Braslow, A. L.; Hicks, R. M.; Harris, R. V.: *Use of Grit-Type Boundary-Layer-Transition Trips on Wind Tunnel Models*, NASA TND-3579, 1966.

- (51) Paterson, J. H.: Scale Effects on Shock-Boundary Layer Interactions, Unpublished presentation to Division Advisory Group, USAF Aeronautical Systems Division, November, 1965.
- (52) Pearcey, H. H.; Osborne, J.; Haines, A. B.: The Interaction Between Local Effects at the Shock and Rear Separation - A Source of Significant Scale Effects in Wind-Tunnel Tests on Aerofoils and Wings, NPL Aero Note 1071, ARC 30477, 1968.
- (53) Paterson, J. H.: Proposed Investigation of Scale Effects on Shock-Boundary Layer Interactions, Interdepartmental Communication - Lockheed-Georgia Company, December 1965.
- (54) Paterson, J. H.: Effects of Reynolds Number on the Aerodynamic Characteristics of Transonic Aircraft, Course on Transonic Aerodynamics, Space Institute of University of Tennessee, March 1968.
- (55) Stone, F. R., Jr.: Analysis of Wing/Pylon/Nacelle Interference Drag on an L-500 High Speed Semi-Span Powered Nacelle Wind Tunnel Model, Lockheed-Georgia Company, ER-11218, 1972.
- (56) Treon, S. L.; Steinle, F. W.; Hageman, J. R.: Data Correlation from Investigations of a High-Subsonic Speed Transport Aircraft Model in Three Major Transonic Wind Tunnels, AIAA Paper N.69-794, July 1969.
- (57) Wiegardt, K.: Increase in Turbulent Skin Friction Caused by Surface Irregularities, Armed Services Technical Information Agency Translation No. 103.
- (58) Schlichting, H.: Boundary Layer Theory, Fourth Ed., McGraw-Hill Book Co., Inc., 1960.
- (59) Poland, D. T.; Schwanebeck, J. C.: Turbofan Thrust Determination for the C-5A, AIAA Propulsion Joint Specialists Conference, San Diego, June 1970.
- (60) Paterson, J. H.; Blackerby, W. T.; Schwanebeck, J. C.; Bradlock, W. F.: An Analysis of Flight Test Data on the C-141A Aircraft, NASA CR-1558, 1970.

AERODYNAMIC DRAG AND LIFT OF GENERAL BODY SHAPES  
AT SUBSONIC, TRANSONIC AND SUPERSONIC MACH NUMBERS \*

2-1

by

Frankie G. Moore \*\*  
Naval Weapons Laboratory  
Dahlgren, Virginia  
USA

SUMMARY

Several theoretical and empirical methods are combined into a single computer program to predict drag, lift, and center of pressure on bodies of revolution at subsonic, transonic, and supersonic Mach numbers and for angles of attack to twenty degrees. The body geometries can be quite general in that pointed, spherically blunt, or truncated noses are allowed as well as discontinuities along the nose. Particular emphasis is placed on methods which yield accuracies of ninety percent or better for most configurations but yet are computationally fast. To handle the blunt nosed configurations, a new procedure has been employed: that of combining modified Newtonian theory with perturbation theory.

Theoretical and experimental results are presented for several projectiles and the comparisons meet the general accuracy requirements above. The combined perturbation - Newtonian theory gave pressures which compared better with experiment than any existing approximate technique in the lower supersonic speed regime.

LIST OF SYMBOLS	$x, r, \theta$	cylindrical coordinates with $x$ along axis of symmetry and in calibers and $\theta=0^\circ$ in leeward plane
$C_A$ total axial force coefficient		
$C_{Af}$ axial force coefficient contribution from skin friction	$x, y, z$	rectangular coordinates with $x$ along axis of symmetry and in calibers
$C_{AW}$ axial force coefficient contribution from expansion and shock waves	$x_{cp}$	center of pressure in calibers from nose unless otherwise specified
$C_{D0}$ zero lift drag coefficient; $C_{D0} = C_A$	$x_p$	distance to centroid of planform area in calibers from nose
$C_{dc}$ crossflow drag coefficient	$\alpha$	angle of attack
$C_{f\infty}$ mean skin friction coefficient based on free-stream Reynolds number	$\beta$	angle between tangent to body surface and axis of symmetry
$C_M$ pitching moment coefficient about nose unless otherwise specified (positive nose-up)	$\gamma$	ratio of specific heats ( $\gamma = 1.4$ )
$C_N$ normal force coefficient	$\delta$	angle between a tangent to the body surface and freestream direction
$C_p$ pressure coefficient; $C_p = (P - P_\infty) / (1/2 \rho_\infty V_\infty^2)$	$\delta^*$	angle which the nose makes with the shoulder of the body (degrees)
$d_B$ base diameter (calibers)	$\eta$	ratio of drag coefficient of a circular cylinder of finite length to that of a circular cylinder of infinite length
$l$ body length (calibers)		
$M$ Mach number		
$P_r$ Prandtl number	$\theta_c$	cone half angle
$R$ body radius (calibers)	$\rho$	density
$R_N$ Reynolds number - $(\rho V l) / \mu$	<u>Subscripts</u>	
$S_w$ wetted surface area of body	$\infty$	freestream conditions
$S_p$ planform area of body	$a$	afterbody
$T_w$ wall temperature	$B$	boattail
$u, v, w$ velocity components in cylindrical coordinate system	$BA$	base
	$n$	nose
$V$ total velocity - $V = \sqrt{u^2 + v^2 + w^2}$	$r$	reference conditions (reference length is the afterbody diameter = $d_r$ )
$Vol$ volume of body		

\* Research partially sponsored by Naval Ordnance Systems Command under ORDTASK 35A-501/090-1/UF 32-323-505

\*\* Research Scientist in Ballistics Division of the Surface Warfare Department

2-2

## 1. INTRODUCTION

There are many methods available in any particular Mach number region to compute drag and lift on various body shapes. These methods range in complexity from exact numerical to semi-empirical and the body shapes vary from simple pointed cones to complex multi-stage launch vehicles. However, attempts at combining the various methods above into an accurate and computationally fast computer program have been scarce. Saffell, et al<sup>1</sup> developed a method for predicting static aerodynamic characteristics for typical missile configurations with emphasis placed on large angles of attack. However, the drag was computed by handbook techniques<sup>2</sup> and slender body theory was used for the lift and pitching moment. As a result, poor accuracy for body alone aerodynamics was obtained using this method.

Another method which computes drag and lift throughout the Mach number range is the GE "Spinner" program<sup>3</sup> designed specifically for projectiles. This program, which is based on empirical correlations as a function of nose length, boattail length, and overall length, gives very good accuracy for most standard shaped projectiles. However, its use as a design tool is somewhat limited in that the drag of a given length nose is the same no matter what ogive is present or if there are discontinuities present along the nose. The same statement applies to the boattail since a conical boattail of from 5° to 9° is assumed no matter what the boattail shape is. Moreover, no pressures can be computed by the GE program and no attempt has been made to include nonlinear angle of attack effects.

It is apparent then, from the above discussion, that there is a definite need for an analytical method which can take into account nose bluntness and ogive shape, discontinuities along the body surface, as well as nonlinear angle of attack effects. The theory should be accurate enough to replace preliminary and intermediate wind-tunnel testing but yet should be computationally fast enough so it can be used as an efficient design tool.

The method presented herein for accomplishing the above task relies heavily on analytical work and to a lesser degree on empirical data. As such, it is believed to be the first such program with major emphasis on analytical as opposed to empirical procedures. Some of the methods had to be modified to handle the general geometries of interest and this will be discussed later.

The body shapes considered assume the nose may be pointed, truncated, or have a spherical cap. There may also be two ogives present with a discontinuity in shape between the two. The afterbody consists of a cylinder followed by a boattail or flare as shown in Figure 1.

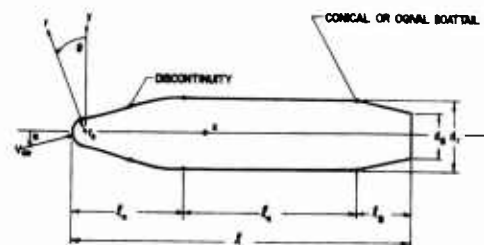


FIGURE 1 TYPICAL BODY GEOMETRY

## 2. ANALYSIS

### 2.1 Wave Drag

Wave drag results from the expansion and compression of the air as it flows over the body surface. Compression of the air is seen in the form of shock waves which first occur around Mach number 0.7 to 0.9 depending on the body shape. The methods used to calculate this form of drag differ significantly in transonic and supersonic flow and thus will be discussed individually below.

#### 2.1.1 Supersonic Flow

There are several methods available for calculating the supersonic pressure distribution but only two hold promise of meeting our requirements on speed of computation and accuracy as set forth in the introduction. These methods are the second order perturbation theory of Van Dyke<sup>4,5,6</sup> and the second order shock expansion theory<sup>7</sup> modified for blunt bodies in reference 8. Since the major interest of the present work is in the lower supersonic speed regime, the perturbation approach is chosen because it is more accurate than shock expansion theory at these Mach numbers. If the nose is pointed with slope less than the freestream Mach lines, then the perturbation theory is sufficient to calculate the entire pressure distribution. Since the above references 4, 5, and 6 give a detailed discussion of the perturbation theory, it will not be repeated here. If the nose is blunt, the perturbation theory is combined with modified Newtonian theory as discussed below.

The modified Newtonian pressure coefficient is

$$C_p = C_{p0} \sin^2 \delta \quad (1)$$

where the stagnation pressure coefficient behind a normal shock is

$$C_{p0} = \frac{2}{\gamma M_\infty^2} \left\{ \left[ \frac{(\gamma+1) M_\infty^2}{2} \right]^{\frac{\gamma}{\gamma-1}} \left[ \frac{\gamma+1}{2\gamma M_\infty^2 - (\gamma-1)} \right]^{\frac{1}{\gamma-1}} - 1 \right\} \quad (2)$$

According to reference 9, if the nose is truncated then the pressure on the truncated portion is only about ninety percent of the stagnation value given by eq. (2) so that for a truncated nose:

$$C_p(o,r) = C_{p0} = \frac{2}{\gamma M_\infty^2} \left\{ 0.9 \left[ \frac{(\gamma+1) M_\infty^2}{2} \right]^{\frac{\gamma}{\gamma-1}} \left[ \frac{\gamma+1}{2\gamma M_\infty^2 - (\gamma-1)} \right]^{\frac{1}{\gamma-1}} - 1 \right\} \quad (3)$$

On the other hand, if the nose has a spherical cap it can be shown that:

$$\delta = \sin^{-1} [\sin\beta \cos\alpha - \cos\beta \cos\theta \sin\alpha] \tag{4}$$

where  $\tan \beta = dr/dx$ . Then combining eqs. (1) and (4) one obtains for a spherical nose cap:

$$C_p(x, \theta) = C_{p0} [\sin^2\beta \cos^2\alpha - \sin 2\alpha \sin \beta \cos \beta \cos \theta + \cos^2\beta \cos^2\theta \sin^2\alpha] \tag{5}$$

where  $C_{p0}$  is given by eq. (2).

Assuming that the pressure coefficient over that portion of the body where the local slope is small can be calculated by perturbation theory, the only question that now remains so far as the supersonic Mach number region is concerned is where does the modified Newtonian theory end on the surface and where does the perturbation theory begin. To determine this match point, recall that the slope of the body surface must be less than the Mach angle to apply perturbation theory, that is  $\delta \leq \sin^{-1} (1/M_\infty)$ . Thus, the upper limit of the perturbation theory is

$$\delta = \sin^{-1} (1/M_\infty) \tag{6}$$

Using this relation in eq. (4) and assuming a spherical nose cap there is obtained for the coordinates of the point below which Newtonian theory must be applied:

$$r_u = r_n/M_\infty [\sqrt{M_\infty^2 - 1} \cos \alpha + \sin \alpha] \tag{7}$$

$$x_u = r_u \tan \alpha + r_n [1 - 1/(M_\infty \cos \alpha)]$$

It is important to note here that if  $x > x_u$  Newtonian theory may still be applied but if  $x < x_u$  perturbation theory cannot be applied.

The limiting angle of eq. (6) corresponding to the coordinates of eq. (7) is shown in Figure 2 as the upper curve. Note that very large cone half angles can be computed using the perturbation theory at the lower Mach numbers. However, as shown by Van Dyke<sup>4</sup> the loss in accuracy of perturbation theory increases rapidly as the angle  $\delta$  is increased. Realistically, since at an angle of  $25^\circ - 30^\circ$  the error is still slight the maximum angle  $\delta$  for which perturbation theory is applied should not exceed these values. Based on these accuracy considerations, the Newtonian theory should be applied for  $\delta$  values outside the solid line boundary of Figure 2 and perturbation theory within the boundary. Now the match point, which for the present work will be defined as the point where the pressure coefficients of the Newtonian theory and the perturbation theory are equal, can be determined as the solution proceeds downstream. For body stations downstream of the match point, perturbation pressures are used in the force coefficient calculations whereas for  $x$  values along the surface less than that at the match point, Newtonian pressures must be used.

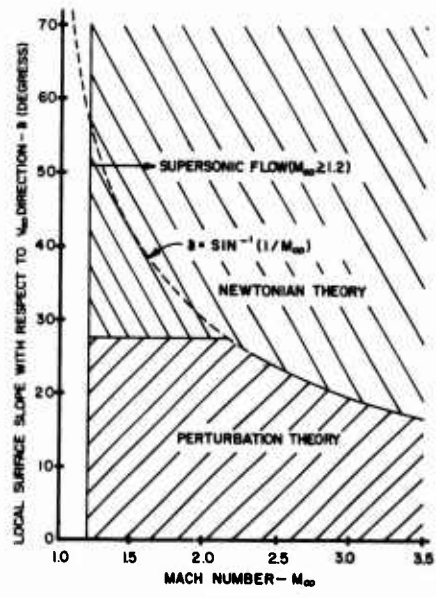


FIGURE 2 BOUNDARIES OF PERTURBATION AND NEWTONIAN THEORY

2.1.2 Transonic Flow

If the flow is transonic, the available theories for the wave drag calculations are limited. Here the main limitations are in body shape because there does not appear to be a theoretical method available which can handle the blunted nose or the discontinuities along the body surface. Wu and Aoyoma<sup>10, 11</sup> have developed a method which handles tangent-ogive-cylinder-boattail configurations at zero angle of attack but no general nose geometries can be used as is the case in supersonic flow. Thus the approach of the present paper will be to calculate the wave drag for tangent ogive noses of various lengths throughout the transonic Mach number range and to estimate the wave drag of the more complicated nose geometry based on these results. It is true that the accuracy here is not consistent with that of the supersonic work; but it appears from the results (as will be discussed later) that this approach is justified, at least for noses with slight blunting ( $r_n/r_b \leq 0.3$ ).

Figure 3 gives the axial force coefficient for tangent ogive noses as a function of nose length and Mach number as computed by the nonlinear-linear stretching method of Wu and Aoyoma. For a given nose length and transonic Mach number, one can obtain the axial force from these curves by interpolation. If pressure coefficients are desired, the general program of Wu and Aoyoma must be used.

For the boattail wave drag, again the work of Wu and Aoyoma<sup>11</sup> is used where the pressure coefficient along the boattail is given by:

$$C_p(x) = -2/5 \frac{(x_1 - C)}{\sqrt{(\gamma+1) M_\infty^2/3}} \left[ \frac{1}{25} \frac{(x_1 - C)^2}{(\gamma+1) M_\infty^2/3} - \frac{1 - M_\infty^2}{(\gamma+1) M_\infty^2} \right]^{1/2} - (dr/dx)^2 \tag{8}$$

2-4 where  $x_1$  is measured from the shoulder of the boattail and

$$C^2 = 25 (\gamma+1) M_\infty^{2/3} \left\{ \frac{1}{2} \frac{1 - M_\infty^2}{(\gamma+1) M_\infty^2} + \left[ \frac{5}{4} \left( \frac{1 - M_\infty^2}{(\gamma+1) M_\infty^2} \right)^2 + \frac{2}{M_\infty^{2/3}} \frac{1 - M_\infty^2}{(\gamma+1) M_\infty^2} \left( \frac{3}{2} \frac{dR/dx}{\sqrt{\gamma+1}} \right)^{2/3} + \left( \frac{3}{2 M_\infty \sqrt{\gamma+1}} \frac{dR/dx}{} \right)^{4/3} \right]^{1/2} \right\}$$

Eq. (8) can be integrated numerically to obtain the boattail wave drag.

## 2.2 Skin Friction Drag

For large caliber projectiles and missiles, the boundary layer will generally be turbulent over about ninety percent of the projectile body. Thus, for simplicity, it will be assumed that the entire boundary layer is turbulent. Further, it will be assumed Prandtl number one and zero pressure gradient so that the method of Van Driest<sup>12</sup> can be used. According to Van Driest the mean skin friction coefficient can be obtained from:

$$\frac{0.242}{A (C_{f_\infty})^{1/2} (T_w/T_\infty)^{1/2}} (\sin^{-1} C_1 + \sin^{-1} C_2) = \log_{10} (R_{N_\infty} C_{f_\infty}) - (1+2n)/2 \log_{10} (T_w/T_\infty) \quad (9)$$

$$\text{where } C_1 = \frac{2A^2 - B}{(B^2 + 4A^2)^{1/2}}; \quad C_2 = \frac{B}{(B^2 + 4A^2)^{1/2}}; \quad A = \left[ \frac{(\gamma-1) M_\infty^2}{2 T_w/T_\infty} \right]^{1/2}; \quad B = \frac{1 + (\gamma-1)/2 M_\infty^2}{T_w/T_\infty} - 1$$

The variable  $n$  of eq. (9) is the power in the power viscosity law and is 0.76 for air. Once the mean skin friction coefficient has been determined from eq. (9), the viscous axial force coefficient is:

$$C_{A_f} = C_{f_\infty} S_w/S_T \quad (10)$$

## 2.3 Base Drag

Much theoretical work has been performed to predict base pressure (references 13 - 17). There is still no satisfactory theory available, however, and the standard practice has been to use empirical methods. This is the approach taken here. Figure 4 is a mean curve of experimental data from references 13, 14 and 18 through 24. This data assumes a long cylindrical afterbody with fully developed turbulent boundary layer ahead of the base. There could be deviations from this curve due to low body fineness ratio, boattails, angle of attack, Reynolds number and surface temperature. Each of these effects will be discussed below.

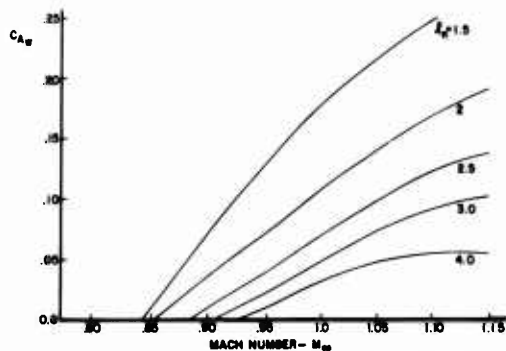


FIGURE 3. TRANSONIC WAVE DRAG OF TANGENT OGIVES.

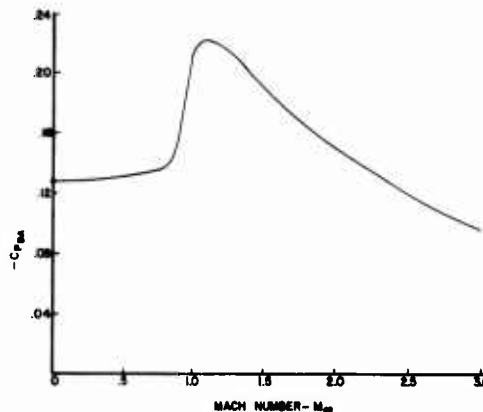


FIGURE 4. MEAN BASE PRESSURE CURVE

The minimum length of most projectiles is about four calibers. According to references 18 and 24, the base pressure at low supersonic Mach numbers is essentially unaffected by changes in body length if the fineness ratio is greater than four. This is not true at high supersonic and hypersonic Mach numbers as shown by Love<sup>12</sup>. But since the main interest is for  $M_\infty \leq 3$  the effect of overall fineness ratio on base pressure can be neglected.

In addition to the above, Love shows that the nose shape has little effect on base pressure for high fineness ratio bodies. Thus, for bodies of fineness ratio of four or greater the effect of nose shape and total length on base pressure can be neglected.

The base pressure is significantly altered by the presence of a boattail so that this change must be accounted for. Probably the most simple method to do this is an empirical equation given by Stoney<sup>23</sup>.

$$C_{A_{BA}} = -C_{P_{BA}} (d_B/d_T)^3 \quad (11)$$

Eq. (11) can be used throughout the entire Mach number range where  $C_{pBA}$  is the base pressure given by the curve of Figure 4.

It has been shown in many works<sup>17,25</sup> that the base pressure is essentially independent of Reynolds number,  $R_N$ , if the boundary layer ahead of the base is fully developed turbulent flow. A turbulent boundary layer usually occurs for  $R_N$  of 500,000 to 750,000 depending on the roughness of the body surface. The minimum  $R_N$  ahead of the base one would expect to encounter on the present bodies would be about 1,000,000. Moreover, most practical body shapes have various intrusions and protrusions, such as on the fuze of a projectile, which tends to promote boundary layer separation. In view of these practical considerations, Reynolds number effects on base pressure may safely be neglected (the same arguments also hold for surface temperature).

The effect of angle of attack on base pressure is to lower the base pressure and hence to increase the base drag. For bodies without fins, the amount of this decrease is dependent mainly on freestream Mach number. If  $\alpha$  is given in degrees then an empirical relation for the change in base pressure coefficient due to angle of attack is given by

$$[\Delta C_{pBA}]_{\alpha} = -(0.012 - .0036M_{\infty}) \alpha \quad (12)$$

Eq. (12) was derived from a compilation of experimental data presented in Figures 7 through 15 of reference 18. The base drag coefficient now becomes, in light of eqs. (11) and (12):

$$C_{A_{BA}} = - [C_{pBA} - (.012 - .0036M_{\infty})\alpha] (d_B/d_T)^3 \quad (13)$$

#### 2.4 Inviscid Lifting Properties

At supersonic Mach numbers the inviscid lift, pitching moment, and center of pressure are calculated with the hybrid theory of Van Dyke. This method is adequate for small angles of attack where viscous effects are negligible. At subsonic and transonic Mach numbers the lifting properties are more difficult to obtain. For subsonic velocities the lift could be calculated by perturbation theory<sup>25</sup> but since projectiles rarely fly at Mach numbers less than 0.7, a formulation on this basis was not justified. An alternative would be slender body theory but the accuracy of this approach is inadequate. In light of the above reasoning, a semi-empirical method for normal force characteristics was derived based on nose length, afterbody length, and boattail shape. This method was then extended through the transonic Mach number range since the state-of-the-art in transonic flow does not allow one to handle the general body shapes or flow conditions.

The total inviscid normal force acting on the body may be written

$$C_{N_{\alpha}} = (C_{N_{\alpha}})_n + (C_{N_{\alpha}})_a + (C_{N_{\alpha}})_B \quad (14)$$

where the subscripts n, a, and B stand for nose, afterbody, and boattail respectively. The first term of eq. (14) can be approximated by

$$(C_{N_{\alpha}})_n = C_1 \tan \delta^* + C_2 \quad (15)$$

where  $C_1$  and  $C_2$  are given in Figure 5 as a function of Mach number. This relationship was determined empirically from the cone results of Owens<sup>27</sup>. It is approximately correct for  $l_n > 1.5$ , cone bluntness up to 0.5, and  $M_{\infty} < 1.2$ . Here the angle  $\delta^*$  in eq. (15) is the angle which the nose makes with the shoulder of the afterbody.

The normal force coefficients of the afterbody and boattail can be obtained from Figures 6 and 7 respectively. Figure 6 was derived analytically in the transonic Mach range from the method of Wu and Aoyama<sup>11</sup> and in subsonic flow from the experimental data of Spring<sup>28</sup> and Gwin<sup>29</sup>. In the work of Spring and Gwin above, the normal force of the nose plus afterbody was given but the nose component can be subtracted off by the use of eq. (15). The boattail normal force coefficient was given by Washington<sup>30</sup>, but he stated that there was not enough data available in subsonic and transonic flow. Hence the data of Washington was supplemented by the 175mm Army projectile<sup>31</sup> and Improved 5"/54 Navy projectile<sup>32</sup> data to derive the general curve of Figure 7.

Although slender body theory may not be adequate for predicting the normal force coefficient, it appears to predict the center of pressure of the nose and boattail lift components at subsonic speeds reasonably well. According to slender body theory the center of pressure of the nose is:

$$(x_{cp})_n = l_n - \frac{(Vol)_n}{\pi R_T^2} \quad (16)$$

and of the boattail:

$$(x_{cp})_B = l_n + l_a + l_B - \frac{(Vol)_B}{\pi R_T^2} \quad (17)$$

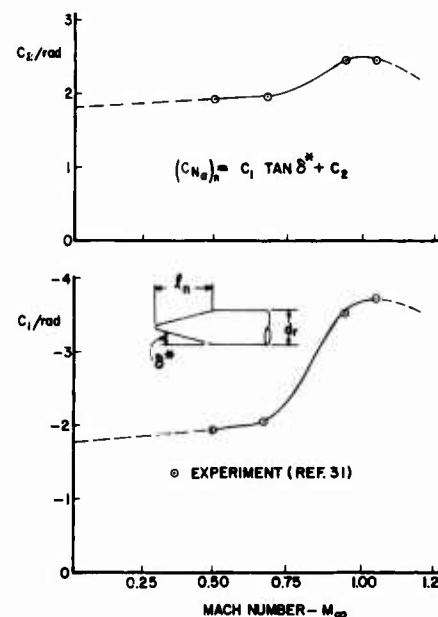


FIGURE 5 CONSTANTS TO DETERMINE  $(C_{N_{\alpha}})_n$  FOR  $M_{\infty} < 1.2$

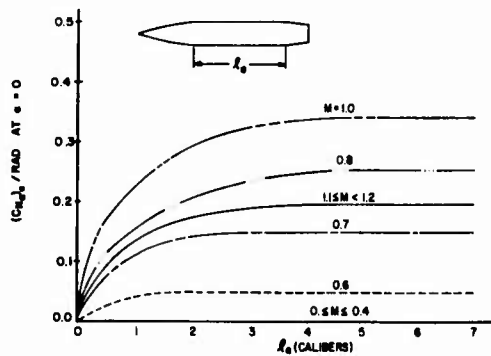


FIGURE 6 INCREASE IN  $(C_{N\alpha})$  AT SUBSONIC AND TRANSONIC MACH NUMBERS DUE TO AFTERBODY.

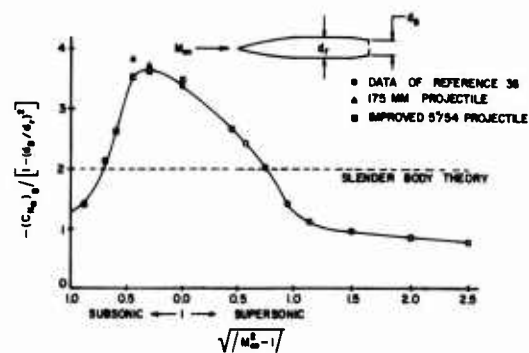


FIGURE 7 DECREASE IN  $C_{N\alpha}$  DUE TO BOAT-TAIL

The center of pressure of the afterbody normal force was calculated analytically by the method of Wu and Aoyama in transonic flow and assumed to have the same value in subsonic flow. Figure 8 is a plot of  $(x_{cp})_a/l_a$  versus afterbody length measured at the point where the afterbody begins. Now knowing the individual lift components and their center of pressure locations, one can compute the pitching moment about the nose as:

$$C_{M\alpha} = - [(C_{N\alpha})_n (x_{cp})_n + (C_{N\alpha})_a (x_{cp})_a + (C_{N\alpha})_B (x_{cp})_B] \quad (18)$$

### 2.5 Viscous Lifting Properties

Strictly speaking, the previous discussion on inviscid lifting properties gave  $C_N$  and  $C_{M\alpha}$  at  $\alpha = 0$  only. If  $\alpha > 0$ , there is a nonlinear contribution to lift and hence pitching moment due to the viscous crossflow of velocity  $V = V_\infty \sin \alpha$ . Allen and Perkins<sup>33</sup> list these contributions as:

$$(C_N)_{vis} = \eta C_{d_c} S_p/S_r \alpha^2 \quad (19)$$

$$(C_M)_{vis} = -\eta C_{d_c} S_p/S_r x_p \alpha^2 \quad (20)$$

where  $\eta$  and  $C_{d_c}$  are given in Figure 9. Note that the crossflow drag coefficient is here taken to be a function of Mach number only and the crossflow Reynolds number dependence is not accounted for. The center of pressure of the entire configuration should then be:

$$x_{cp} = - \frac{C_M + (C_M)_{vis}}{C_N + (C_N)_{vis}}$$

### 2.6 Summary

Figure 10 gives a summary of the various methods used in each particular Mach number region to compute static aerodynamics. As may be seen, major emphasis has been placed on analytical as opposed to empirical procedures.

## 3. RESULTS AND DISCUSSION

### 3.1 Numerical Techniques

A computer program was written in Fortran IV for the CDC 6700 computer to solve the various equations discussed in the analysis section by numerical means. The various methods used for each individual force or moment component are the same as those discussed in the references and will not be repeated here. However, mention should be made of the fact that the step size used in the hybrid theory of Van Dyke was considerably smaller than he suggested, particularly for a blunt nosed body or behind a discontinuity. For example, for the most complicated body shapes as many as 200 points were placed along the body surface. Also slight oscillations in the second order solution were found behind a corner although Van Dyke does not mention these details.

Quite often, it was necessary to evaluate an integral numerically or to compute the value of a function and its derivative at a given point. The integration was carried out using Simpson's rule; the interpolation and differentiation using a five point Lagrange scheme. Both methods have truncation errors which are consistent with the accuracy of the governing set of flow field equations.

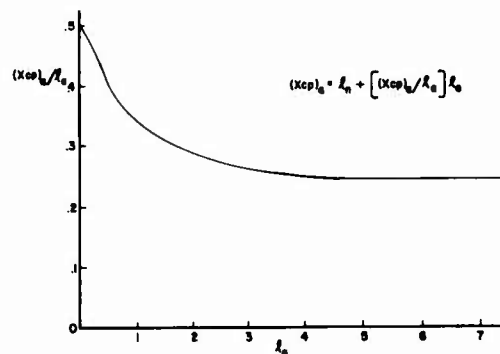


FIGURE 8 CENTER OF PRESSURE OF AFTERBODY LIFT FOR  $M_{\infty} = 1.2$

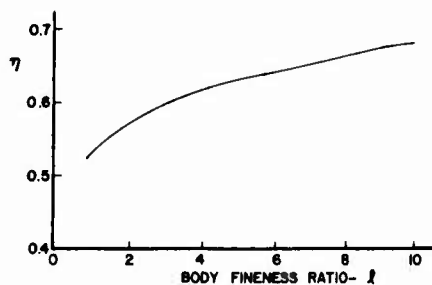
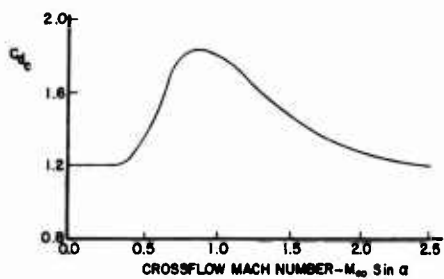
FIGURE 10-A. DRAG PROPORTIONALITY FACTOR- $\eta$ 

FIGURE 10-B. CROSSFLOW DRAG COEFFICIENT

FIGURE 9 DRAG PROPORTIONALITY FACTOR AND CROSSFLOW DRAG COEFFICIENT

COMPONENT	MACH NUMBER REGION		
	SUBSONIC	TRANSONIC	SUPERSONIC
NOSE WAVE DRAG	—	Wu and AOYOMA PLUS EMPIRICAL	2 <sup>ND</sup> ORDER VAN DYKE PLUS MODIFIED NEWTONIAN
BOATTAIL WAVE DRAG	—	Wu and AOYOMA	2 <sup>ND</sup> ORDER VAN DYKE
SKIN FRICTION DRAG	VAN DRIEST II		
BASE DRAG	EMPIRICAL		
INVISCID LIFT and PITCHING MOMENT	EMPIRICAL	Wu and AOYOMA PLUS EMPIRICAL	TSIEN 1 <sup>ST</sup> ORDER CROSSFLOW
VISCOUS LIFT and PITCHING MOMENT	ALLEN and PERKINS CROSSFLOW		

FIGURE 10 METHODS USED TO COMPUTE BODY ALONE AERODYNAMICS

The computational times depend on how complicated the body shapes are and the particular Mach number of interest. The longest computational time for the most general body shape computed was less than half a minute for one Mach number. For most configurations the average time is about fifteen seconds per Mach number for  $M_\infty \geq 1.2$  and about five seconds per Mach number for  $M_\infty < 1.2$ . This assumes of course that a table look-up procedure is used in the transonic region where the curves of Figure 3 are input as data sets as opposed to solving the nonlinear partial differential equation of transonic flow. If the aerodynamic coefficients of a given configuration are desired throughout the entire Mach number range, an average execution time of two minutes is required for most configurations (ten Mach numbers).

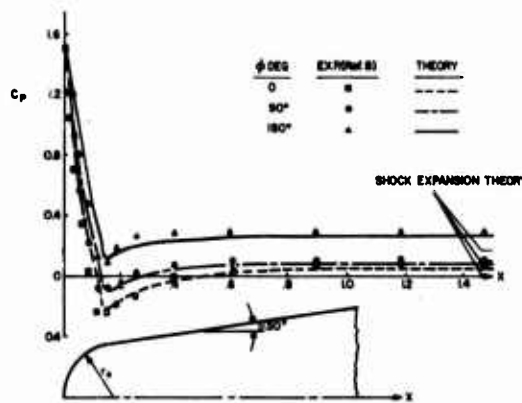
A detailed discussion of the computer program, along with a listing, is given in a report of the present work as reference 34.

### 3.2 Comparison with Experiment

The only new method presented in the current work is the combined perturbation - Newtonian theory for blunt bodies. It is thus of interest to see how the pressure coefficients along the surface compare with experimental data. Figure 11 presents a typical comparison at  $M_\infty = 1.5$ . The experimental data is taken from reference 8 which combined modified Newtonian theory with shock expansion theory to compute forces on blunted cones. The asymptotes of the pressure coefficient in each of the planes computed by the method of reference 8 are also indicated on the figures. As seen in the figure, the present theory predicts the aerodynamics much better than shock expansion theory at  $M_\infty = 1.5$ . For the very same blunted cone at  $M_\infty = 2.96$  (not shown) the present method gave values for the pressure and force coefficients which were about the same as those of shock expansion theory. The reason for this is that the basic perturbation theory was derived assuming shock free flow with entropy changes slight; hence the theory should be most accurate in the lower supersonic speed regime. On the other hand, shock expansion theory was derived assuming a shock present and so one would expect this method to be better than perturbation theory as  $M_\infty$  is increased. Apparently, the crossover point is around  $M_\infty = 2.5$  to 3.0 so that for the major portion of the supersonic speed range of interest in the present analysis, perturbation theory is more accurate.

Another interesting point in Figure 11 is the discontinuity in slope of the pressure coefficient curve which occurs at the match point. This is because in the expansion region on the spherical nose the perturbation pressure decreases much more rapidly than the Newtonian theory and, as a result, the overexpansion region, which occurs at low supersonic Mach numbers, is accounted for quite well. Note that the match point is different in each plane around the surface ( $x \approx 0.11$  to 0.14).

One of the questions which arises in the development of a general prediction method pertains to accuracy. To answer this question, force coefficients for several cases were computed embracing variations in nose bluntness, Mach number, angle of attack, and afterbody length. These cases are presented in Figures 12 through 15 along with experimental data.

FIGURE 11 COMPARISON OF THEORY AND EXPERIMENT FOR BLUNTED CONE;  
 $\alpha = 0.55, M_\infty = 1.5, \theta = 8^\circ$

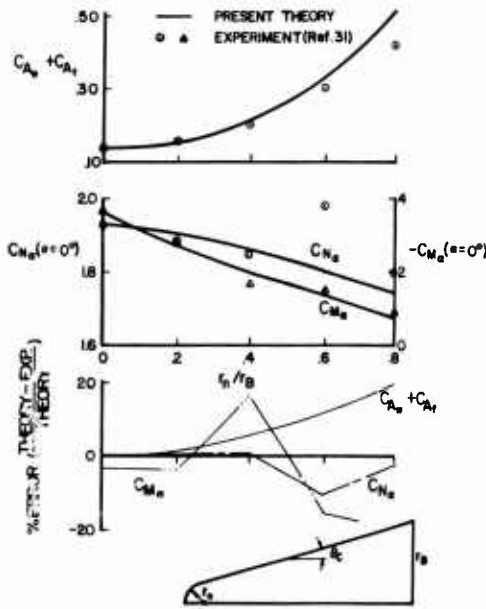


FIGURE 12 COMPARISON OF THEORY AND EXPERIMENT FOR A BLUNTED CONE;  $M_{\infty} = 1.5$ ,  $\theta_c = 10^\circ$ .

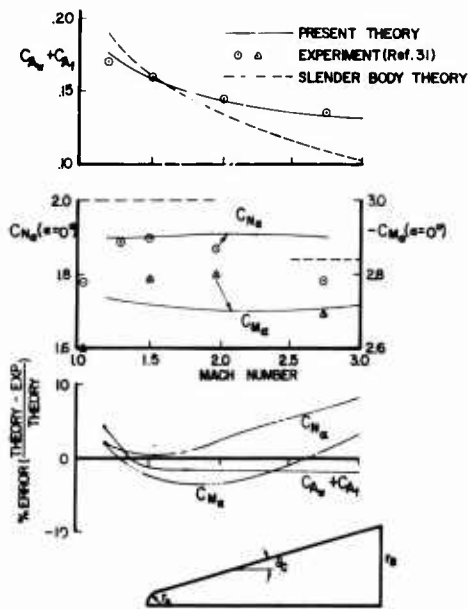


FIGURE 13 COMPARISON OF THEORY AND EXPERIMENT FOR BLUNT CONE;  $\theta_c = 10^\circ$ ,  $r_n/r_B = 0.2$ .

The first of these cases (Figure 12) gives the axial force coefficient, normal force coefficient, derivative, and pitching moment coefficient derivative as a function of nose bluntness for a simple blunted cone configuration. Note that the axial force coefficient includes only the wave plus skin friction components because the base drag was subtracted out of the given set of experimental data. An important point here is that very good accuracy is obtained, even for large bluntness ratios. For example, with bluntness  $r_n/r_B = 0.6$ , the force coefficients are in error by less than fifteen percent. This tends to verify that a combined perturbation - Newtonian theory can be used successfully for blunt configurations even at low supersonic Mach numbers.

The next figure, Figure 13, compares the theoretical static aerodynamic coefficients with experiment as a function of Mach number for a blunted cone with bluntness ratio of 0.2. Also included in Figure 13 is the slender body theory. As seen by the error comparisons at the lower part of the figure, accuracies of better than ten percent can be obtained throughout the supersonic Mach number range for the force coefficients.

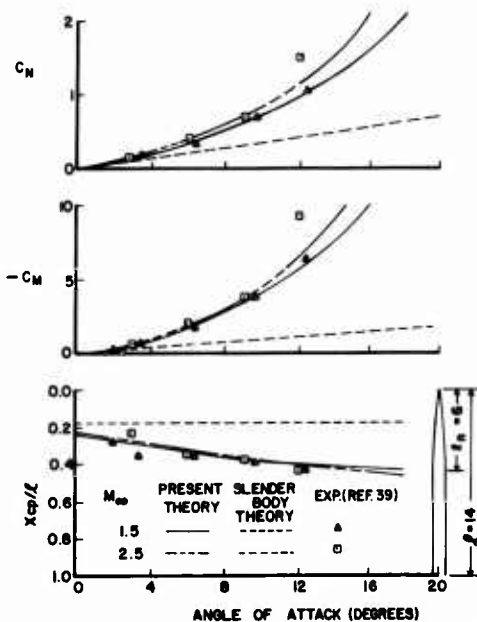


FIGURE 14 COMPARISON OF THEORY WITH EXPERIMENT FOR TANGENT OGIVE-CYLINDER.  $L = 14$  CALIBERS

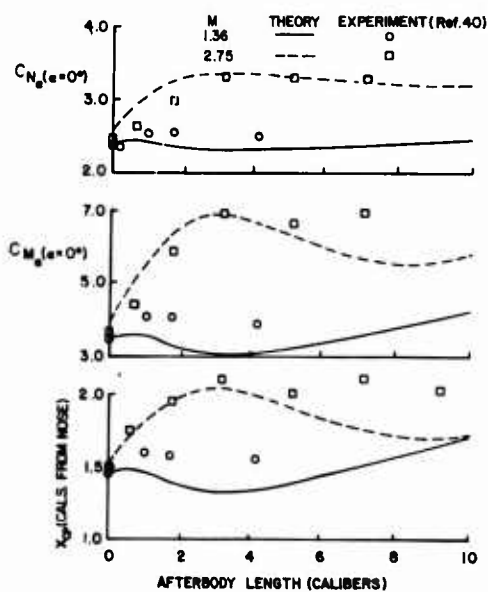


FIGURE 15 COMPARISON OF PRESENT THEORY WITH EXPERIMENT AS A FUNCTION OF AFTERBODY LG. (2.83 CALIBER TANGENT OGIVE NOSE).

The third variable of interest is angle of attack. Figure 14 presents the results for a tangent ogive cylinder of nose length six calibers and total length fourteen calibers. Two Mach numbers are considered,  $M_{\infty} = 1.5$  and  $M_{\infty} = 2.5$ . Again the results are good, except at very large angles of attack. 2-9

The final variable of interest, afterbody length, is examined in Figure 15. The nose of the body is a 2.83 caliber tangent ogive. For zero afterbody length, the theory agrees with experiment very well. However, as the afterbody length increases the theory underestimates the afterbody lift at the lower supersonic Mach numbers for short afterbody lengths and at the higher Mach numbers for long afterbody lengths. This loss in lift predicted by the inviscid theory was also found by Duford<sup>35</sup> and he attributed it to boundary layer displacement effects. Even so, the present theory is superior to slender body theory which gives zero lift due to an afterbody.

To summarize the previous four figures, one could say in general that accuracies of ninety percent or better can be obtained for force coefficients of most configurations. However, for extreme cases, such as very large nose bluntness or angle of attack, the accuracy will be decreased and the amount of this decrease can be approximated from Figures 12 through 15.

The theoretical zero lift drag curve of the 5"/38 RAP projectile<sup>36</sup> along with three sets of experimental data<sup>37</sup> and an NWL empirically derived curve are shown in Figure 16. Note that the experimental data varies by about thirty percent for  $M_{\infty} < 1$  and by ten percent for  $M_{\infty} > 1$ . The theoretical curve tends to support the BRL data subsonically and the NOL and NWC data supersonically. The numbers in parenthesis are the factors by which the drag curves must be multiplied throughout the flight of the projectile to match actual range firings. The NWL empirical curve is the curve which is actually used in range predictions due to the failure of experimental data to predict an adequate drag curve. This empirical curve was derived from actual range firings. It should therefore be slightly high because of yaw induced effects. The important point here is that for this particular shell, the theory agrees better with actual range firings than any of the sets of experimental data.

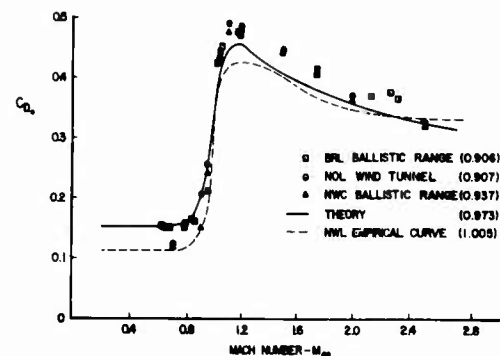


FIGURE 16 ZERO LIFT DRAG CURVE FOR 5738 RAP PROJECTILE

Figure 17 gives the static aerodynamic coefficients for the 5"/54 RAP projectile<sup>38</sup>. The 5"/54 RAP has a nose length of about 2.5 calibers and a boattail of 0.5 and is 5.2 calibers in length. As seen, excellent agreement with experimental data is obtained for the drag coefficient throughout the entire Mach number range. Fair agreement is obtained for normal force coefficient and hence pitching moment and center of pressure. The comparison for the lifting properties is Mach number dependent: in the low supersonic region the theory is consistently about ten percent low on normal force whereas at high supersonic speeds it compares very well with experiment. The reason, as already mentioned, is the failure of the inviscid theory to predict afterbody lift correctly at low supersonic Mach numbers. At subsonic and transonic Mach numbers, the theory does about as well as could be expected considering there was a considerable amount of empirical work in that region.

For boattailed configurations, such as the 5"/54 RAP, it was found necessary to account approximately for the thick boundary layer on the boattail. This was done by viewing the unpublished shadow graphs obtained in conjunction with the work of reference 32. Apparently, a maximum boattail angle of six degrees can be allowed before boundary layer separation takes place. In addition, the boundary layer displacement thickness accounts for another about 1/4 - 1/2 degree decrease in the effective boattail angle. These two results were used to determine effective boattail angles on all boattailed configurations. Without this approximate accounting of the boundary layer effect on the boattail shape, the lifting properties would have been in error by an additional ten percent for boattailed configurations.

Figure 18 presents theoretical results for a more complicated projectile design. The nose is about sixty percent blunt with two different ogive sections. The overall length is 10.58 calibers with a 0.66 caliber boattail, 7.24 caliber afterbody and 2.68 caliber nose. The only experimental data available for this extreme case is at  $M_{\infty} = 1.6$  (unpublished). Excellent predictions are made by the theory at this Mach number, although it is not expected to be that good in subsonic and transonic flow.

#### 4. CONCLUSIONS

1. A general method has been developed consisting of several theoretical and empirical procedures to calculate drag, lift and pitching moment on bodies of revolution from Mach number zero to about three and for angles of attack to about twenty degrees.
2. Comparison of this method with experiment for several configurations indicates that accuracies of ninety percent or better can be obtained for force coefficients of most configurations. This is at a cost of about \$30.00 for ten Mach numbers in the range  $0 \leq M_{\infty} \leq 3$ .
3. A second order axial perturbation solution can be combined with modified Newtonian theory to adequately predict pressures on general shaped bodies of revolution. This is true for Mach numbers as low as 1.2 even though Newtonian theory was derived for high Mach number flow.
4. A first order inviscid cross flow solution is not sufficient to predict afterbody or boattail lift at low supersonic Mach numbers. However, when account is made for the boundary layer, markedly improved results for boattail lift was obtained.

5. There is still no adequate theory available in transonic flow which is computationally fast and accurate and can consider blunt nosed configurations with discontinuities along the ogive. Thus more research needs to be directed along these lines.

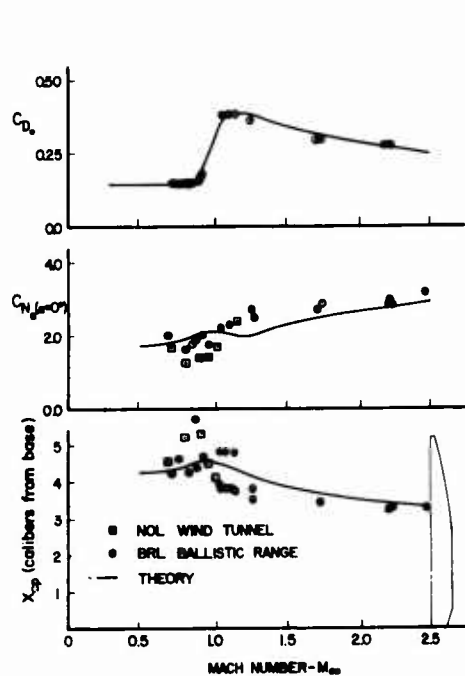


FIGURE 17. COMPARISON THEORY AND TEST DATA FOR 5754 RAP PROJECTILE.

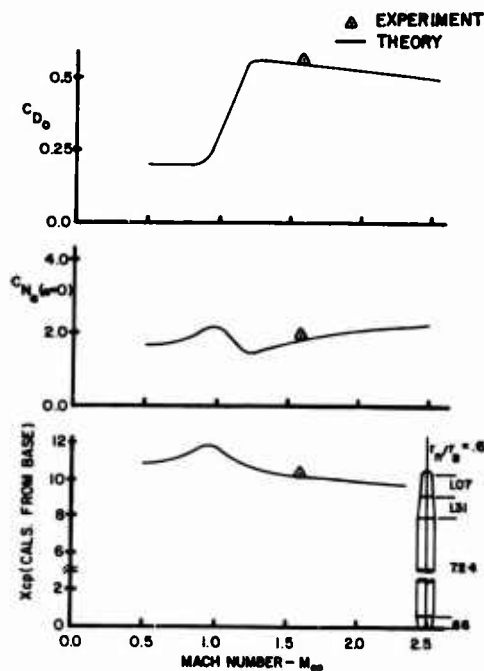


FIGURE 18. AERODYNAMICS OF GENERAL BODY SHAPE

#### 5. REFERENCES

- Saffell, B. F., Jr.; Howard, M. L.; Brooks, E. N., Jr: "A Method for Predicting the Static Aerodynamic Characteristics of Typical Missile Configurations for Angles of Attack to 180 Degrees", NSRDC Report 3645, 1971.
- Dougllass Aircraft Co., Inc.: USAF Stability and Control DATCOM, Revisions by Wright Patterson Air Force Base, July 1963, 2 vols.
- Whyte, R. H.: "'Spinner' - A Computer Program for Predicting the Aerodynamic Coefficients of Spin Stabilized Projectiles", General Electric Class 2 Report, August 1969.
- Van Dyke, M. D.: "A Study of Second-Order Supersonic Flow Theory", NACA Report 1081, 1952.
- Van Dyke, M. D.: "Practical Calculation of Second-Order Supersonic Flow Past Nonlifting Bodies of Revolution", NACA TN-2744, July 1952.
- Van Dyke, M. D.: "First and Second-Order Theory of Supersonic Flow Past Bodies of Revolution", JAS, Vol. 18, No. 3, March 1951, pp. 161-179.
- Syverson, C. A.; Dennis, D. H.: "A Second-Order Shock-Expansion Method Applicable to Bodies of Revolution Near Zero Lift", NACA Report 1328, 1957.
- Jackson, C. M., Jr.; Sawyer, W. C.; Smith, R. S.: "A Method for Determining Surface Pressures on Blunt Bodies of Revolution at Small Angles of Attack in Supersonic Flow", NASA TN D-4865, November 1968.
- Tetervin, Neal: "Approximate Analysis of Effect on Drag of Truncating the Conical Nose of a Body of Revolution in Supersonic Flow", NOL TR 62-111, December 1962.
- Wu, J. M.; Aoyama, K.: "Transonic Flow-Field Calculations Around Ogive Cylinders by Nonlinear-Linear Stretching Method", U. S. Army Missile Command Technical Report No. RD-TR-70-12, April 1970. Also AIAA 8th Aerospace Sciences Meeting, AIAA Paper, 70-189, January 1970.
- Wu, J. M.; Aoyama, K.: "Pressure Distributions for Axisymmetric Bodies with Discontinuous Curvature in Transonic Flow", U. S. Army Missile Command Technical Report No. RD-TR-70-25, November 1970.
- Van Driest, E. R.: "Turbulent Boundary Layer in Compressible Fluids", JAS, Vol. 18, No. 3, 1951, pp. 145-160, 216.
- Love, E. S.: "Base Pressure at Supersonic Speeds on Two-Dimensional Airfoils and on Bodies of Revolution with and without Turbulent Boundary Layers", NACA TN 3819, 1957.
- Chapman, D. R.: "An Analysis of Base Pressure at Supersonic Velocities and Comparison with Experiment", NACA TR 1051, 1951.
- Cartright, E. M., Jr.; Schroeder, A. H.: "Investigation at Mach Number 1.91 of Side and Base Pressure Distributions Over Conical Boattails without and with Jet Flow Issuing from Base", NACA TM E51F26, 1951.
- Kurzweg, H. H.: "Interrelationship Between Boundary Layer and Base Pressure", JAS, No. 11, 1951, pp. 743-748.
- Crocco, L.; Lees, L.: "A Mixing Theory for the Interaction Between Dissipative Flows and Nearly-Isentropic Streams", Report No. 187, Princeton University, Aero. Engr. Lab; 1952.
- Bureau of Naval Weapons: "Handbook of Supersonic Aerodynamics", NAVWEPS Report 1488, Vol. 3, 1961.
- Reller, J. O., Jr.; Hamaker, F. M.: "An Experimental Investigation of the Base Pressure Characteristics of Nonlifting Bodies of Revolution at Mach Numbers from 2.73 to 4.98", NACA TN 3393, 1955.

20. Peck, R. F.: "Flight Measurements of Base Pressure on Bodies of Revolution with and without Simulated Rocket Chambers", NACA TN 3372, 1955.
21. Fraenkel, L. E.: "A Note on the Estimation of the Base Pressure on Bodies of Revolution at Supersonic Speeds," Royal Aircraft Establishment TN No. AERO 2203, 1952.
22. U. S. Army Missile Command: Engineering Design Handbook: Design of Aerodynamically Stabilized Free Rockets, AMCP 706-280, 1968.
23. Stoney, W. E., Jr.: "Collection of Zero-Lift Data on Bodies of Revolution from Free-Flight Investigations", NASA TR R-100, 1961.
24. Kurzweg, H. H.: "New Experimental Investigations on Base Pressure in the NOL Supersonic Wind Tunnels at Mach Numbers 1.2 to 4.24", NOL Memo 10113, 1950.
25. Krens, F. J.: "Full-Scale Transonic Wind Tunnel Test of the 8-Inch Guided Projectile", NWL TR-2535, 1971.
26. Karamcheti, K.: Principles of Ideal-Fluid Aerodynamics, John Wiley and Sons, Inc., New York, 1966.
27. Owens, R. V.: "Aerodynamic Characteristics of Spherically Blunted Cones at Mach Numbers from 0.5 to 5.0", NASA TN D-3088, December 1965.
28. Spring, D. J.: "The Effect of Nose Shape and Afterbody Length on the Normal Force and Neutral Point Location of Axisymmetric Bodies at Mach Numbers from 0.80 to 4.50", U. S. Army Missile Command Report No. RF-TR-64-13, 1964.
29. Gwin, H.; Spring, D. J.: "Stability Characteristics of a Family of Tangent Ogive-Cylinder Bodies at Mach Numbers from 0.2 to 1.5", U. S. Army Missile Command, Report No. RG-TR-61-1, 1961.
30. Washington, W. D.; Pettis, W., Jr.: "Boattail Effects on Static Stability at Small Angles of Attack" U. S. Army Missile Command Report No. RD-TM-68-5, 1968.
31. Whyte, R. H.: "Effects of Boattail Angle on Aerodynamic Characteristics of 175mm M437 Projectile at Supersonic Mach Numbers", U. S. Army Munitions Command Technical Memorandum 1646, September 1965.
32. Ohlmeyer, E. J.: "Dynamic Stability of the Improved 5"/54 Projectile", NWL Technical Report in publication.
33. Allen, J. H.; Perkins, E. W.: "Characteristics of Flow Over Inclined Bodies of Revolution", NACA RM A 50L07, 1965.
34. Moore, F. G.: "Body Alone Aerodynamics of Guided and Unguided Projectiles at Subsonic, Transonic, and Supersonic Mach Numbers", NWL TR-2796 (in publication).
35. Buford, W. E.: "The Effects of Afterbody Length and Mach Number on the Normal Force and Center of Pressure of Conical and Ogival After Bodies", JAS, No. 2, 1958, pp. 103-108.
36. Chadwick, W. R.; Sylvester, J. F.: "Dynamic Stability of the 5-Inch/38 Rocket Assisted Projectile", NWL Technical Memorandum No. K-63/66.
37. Moore, F. G.: "A Study to Optimize the Aeroballistic Design of Naval Projectiles", NWL TR-2337, September 1960.
38. Donovan, W. F.; MacAllister, L. C.: "Transonic Range Tests of 5-Inch/54 Rocket Assisted Projectile (Inert)", BRL MR 2107, July 1971.

## ON SOME BASIC AND NEW ASPECTS ABOUT THE DRAG PROBLEM OF WINGS AND BODIES IN SUPERSONIC FLOWS

by

Arabindo Das  
Dr.-Ing., Head of Theoretical Aerodynamics Dept.  
Institut für Aerodynamik der DFVLR  
33 Braunschweig, Flughafen  
Germany

## SUMMARY

With the objective to determine optimum shapes of slender wings and bodies for minimum total drag in supersonic flows a comprehensive theoretical and experimental analysis of the problem has been carried out in the Institute of Aerodynamics of the DFVLR, Braunschweig. The paper presents some of the results which have been obtained until now. The theoretical formulae for the various drag components which are necessary for a variational problem of drag minimization have been reviewed, summarized, partly modified or extended, and finally compared with experimental values.

Based on the linearized mass flux concept already known in the literature a modified boundary condition leads to a certain improvement in the results of the linear theory. A simplified treatment of the modified linear theory is presented.

A unified approach to the problem of minimization of wave drag due to volume and wave drag due to lift yields very simple analytical results. The optimum body shapes show a certain dependence on Mach number. For minimization of vortex drag the necessary wing twist yields a remarkable improvement, which could also be verified by experiment.

While the known friction drag formulae from the literature have been checked with experimental values, the problem of base drag of axial symmetrical bodies has not been completely solved as yet; theoretical work on this topic is being continued.

Finally for minimizing the total drag of wings and bodies under some prescribed conditions an optimum matching of the geometric and aerodynamic parameters has been outlined.

NOTATIONS

Geometric data

$b = 2s$	maximum span of a wing
$b_o$	maximum width of a body cross section
$d$	profile thickness or body diameter
$d_o$	maximum thickness of a profile or maximum diameter of a body
$F$	wing or body surface
$h_o$	maximum height of a body cross section
$\bar{k}$	$\frac{1}{2}$ trailing edge thickness parameter
$l$	chord length or body length
$l_o$	reference basic length of bodies with cut off rear part
$l_i$	maximum chord length of a wing
$r$	radial distance
$R$	radius of a body
$R_o$	maximum radius of a body
$s(\xi)$	local half cross width of a wing
$\bar{s}(\xi) = s(\xi)/s$	dimensionless half cross width of a wing
$s = b/2$	half span width of a wing
$S(\xi)$	local cross section area of a body or wing
$S_o$	maximum cross section area of a wing
$\bar{S} = S/l^2$	dimensionless cross section area
$S_w$	wing area
$S_f$	friction surface area
$S_B$	base area
$V_o$	volume of a body or wing
$\bar{V}_o = V_o/l^3$	dimensionless volume
$x; y; z$	cartesian coordinates
$y_c(x)$	contour coordinate of a profile
$\alpha$	geometrical angle of incidence
$\bar{\alpha}$	angle of incidence at the wing center line
$\bar{\alpha}_T$	reference angle of incidence at the trailing edge of the center line
$\delta_r = b_o/l; d_o/l$	thickness parameter
$\psi; \bar{\psi}$	angular coordinates
$\theta_S$	peripheral-parameter of the cross section of a body
$\hat{\kappa} = S_w/s l_i$	area ratio based on the reference area of a delta wing
$\kappa^* = \bar{S}(1)/2\bar{V}_o$	base area parameter
$\lambda_o = h_o/b_o$	ratio of the axes of an elliptic cross section
$\xi=x/l; \eta=y/s$	dimensionless coordinates
$\tau_m$	mean thickness
$\bar{\tau}_m = \tau_m/l_i$	dimensionless mean thickness

Aerodynamic data

$a_n; \bar{a}_n$	coefficients for fixing source or doublet-distributions
$b_n$	coefficient for fixing spanwise distribution of circulation
$c_a$	lift coefficient of a chordwise wing-strip
$\bar{c}_a$	lift coefficient of a crosswise wing-strip

$c_L = L/q_\infty S_w$
$c_D = D/q_\infty S_w$
$c_D^* = D/q_\infty S_o$
$c_{DV}^*$
$c_{DW}^*; c_{DW}^*$
$c_{Do}^*; c_{Do}^*$
$c_{Dl}^*; c_{Dl}^*$
$c_{DL}^*; c_{DL}^*$
$c_{Di}$
$c_{DB}^*$
$c_{DF}^*; c_{DF}^*$
$\hat{c}_D = c_D S_o/V_o^{2/3}$
$c_f$
$c_p$
$D$
$f(x)$
$h(\xi)$
$K_o, K_o^*$
$K_l$
$K_i$
$L$
$Ma_\infty$
$m = \beta s/l_i$
$p$
$q_\infty = \frac{1}{2} \rho_\infty V_\infty^2$
$Re_\infty = V_\infty l/\nu$
$T$
$T_w$
$u; v; w$
$V_\infty$
$V$
$\alpha_h$
$\alpha_i$
$\beta = \sqrt{Ma_\infty^2 - 1}$
$\gamma = \frac{c_a(\eta) l(\eta)}{2b}$
$\epsilon$
$\kappa$
$\nu$
$\rho$
$\hat{\sigma}$
$\sigma'$
$\sigma$
$\psi$
$\phi$

total lift coefficient
total drag coefficient of a wing
total drag coefficient of a body
fore drag coefficient of a body
total wave drag
wave drag coefficient due to volume
wave drag coefficient due to lift
drag coefficient due to lift
induced drag coefficient due to vortex formation
base drag coefficient of a body
friction drag coefficient
drag coefficient based on volume
friction coefficient
pressure coefficient
aerodynamic drag of wing or body
source strength
doublet strength of a lifting wing
wave drag parameter due to volume
wave drag parameter due to lift
induced drag parameter
total lift of a wing or body
Mach number
relative slenderness parameter
static pressure
dynamic head of onflow
Reynolds number of onflow
static temperature [°K]
wall temperature [°K]
perturbation velocity components
onflow velocity
local velocity in the perturbation field
induced flow deflection due to doublets or bound vortices
induced flow deflection due to free vortices
Mach number parameter
circulation about a local chord of a wing
an infinitesimal quantity
adiabatic exponent
dynamic viscosity of a flow medium
medium density
mass flux
doublet strength
parameter of a wing shape
perturbation potential
total potential in a flow field

Indices

$c$	contour
$l$	lower surface
$u$	upper surface
$\infty$	onflow

3-2

## 1. INTRODUCTION

The general gas dynamic equation derived from the conservation equations of a flow field is quite nonlinear and as such offers exact solutions in few cases only.

A linearization of this equation is often resorted to, in order to obtain explicit formulae for the aerodynamic forces on a moving body and of these the explicit drag formula can be used for optimization of body shapes. Original contributions of various authors to the linearized theory are well known in text books and in the literature and a few of these have been cited in references [1] to [33] of the present paper.

The linearized theory confined to the domain of small perturbation flow fields possesses some inherent inaccuracies due to the linearization itself, and also because of the simplification of the boundary condition by which the distribution of the singularities are fixed. In many cases the latter causes more error than the former. A linear theory may be considered as a standard reference whose basic equations possess a unified order of accuracy with regard to the fulfilment of the conservation theorems.

Besides the problem of pressure drag which can be treated by the potential theory, the problem of friction drag and base drag is equally important. While theoretical treatment of friction drag can be found in the contributions [34] to [37] some survey papers on base drag, references [38] to [40], reveal the limited advancement in this field. Having explicit formulae for pressure and friction drag one can find out optimum shapes of nonlifting and lifting wings and bodies giving minimum total drag.

This topic has been treated in detail in the Institute of Aerodynamics of the DFVLR, Braunschweig, being based on theoretical and experimental analysis. The results obtained during the last five years have been reported in references [41] to [48]. The present paper summarizes a few basic and new aspects which could be concluded from these results and it will indicate a logical approach to determine body shapes for minimum total drag with the body shapes depending on the onflow Mach numbers.

The fundamental physical considerations for aerodynamic optimization are outlined in [49], while some general mathematical methods on this subject are presented in [50].

## 2. A MODIFIED TREATMENT OF THE LINEAR THEORY

A supersonic flow field under small perturbations is described in the literature by the following set of equations:

Perturbation potential field

$$\beta^2 \varphi_{xx} - \varphi_{yy} - \varphi_{zz} = -0 \left[ \epsilon_1(Ma_\infty, \varphi, \kappa) \right] \approx 0 \quad (2.1)$$

Boundary condition

$$\vec{v} \cdot \text{grad } F = 0 \quad (2.2a)$$

$$\text{or usually } \vec{v} \cdot \text{grad } F = 0 \left[ \epsilon_2(Ma_\infty, \delta, \alpha) \right] \quad (2.2b)$$

Pressure coefficient

$$c_p = \frac{p-p_\infty}{\frac{1}{2} \rho_\infty v_\infty^2} = - \left[ 2\varphi_x - \beta^2 \varphi_x^2 + \varphi_y^2 + \varphi_z^2 \right] \quad (2.3)$$

The boundary condition, Eq (2.2a) being essentially a kinematic relation is formally correct but does not uniquely define the mass flux relation, which in the usual linear theory may deviate from its exact value. The boundary condition is usually further simplified as indicated in Eq (2.2b) inducing more error. However the criterion of mass flux can be introduced into the boundary condition satisfying at the same time the required kinematic relation. The linearized mass flux criterion first introduced by G.N. WARD [7] is uniformly valid in a small-perturbation flow field yielding for the continuity condition the same degree of accuracy as the linearized potential equation itself.

### 2.1 The linearized mass flux criterion

The mass flux  $\rho v$  in a compressible flow field can be obtained by expanding the density  $\rho$  as a Taylor series in powers of the pressure change  $dp$ . From [7] it follows for the perturbation mass flux

$$\rho \vec{v} = |\rho_\infty v_\infty| \left\{ i + \nabla \varphi - \vec{v}_\infty \vec{v}_\infty \cdot \nabla \varphi / a_\infty^2 \right\} + \dots \quad (2.4)$$

$$\text{with } \nabla \varphi = i \varphi_x + j \varphi_y + k \varphi_z$$

Using the linearized expression for the local sound velocity

$$a^2 \approx a_\infty^2 - (\kappa-1) v_\infty^2 \varphi_x \quad (2.5)$$

Eq (2.4) The linearized mass flux ratio can be directly expressed as:

3-4

$$\hat{g} = \frac{\rho \vec{V}}{|\rho_{\infty} V_{\infty}|} = \left\{ \frac{a}{a_{\infty}} \right\}^{\frac{2}{\kappa-1}} \cdot \frac{\vec{V}}{V_{\infty}} \approx [i(1-\beta^2 \varphi_x) + j\varphi_y + k\varphi_z] + \dots \quad (2.6)$$

The dimensionless mass flux  $\hat{g}$  satisfies the following expression

$$\text{div } \hat{g} = - [\beta^2 \varphi_{xx} - \varphi_{yy} - \varphi_{zz}] = 0 \quad [\varepsilon_1 (Ma_{\infty}, \varphi, \kappa)] \quad (2.7)$$

So, instead of Eq (2.2a) one can introduce the following boundary condition for the body surface:

$$\hat{g} \cdot \text{grad } F = 0 \quad (2.8)$$

With Eq (2.8) the physical condition of zero mass flow through the surface will be satisfied with the same order of accuracy as with the linearized Eq (2.1) itself. This problem was analyzed further in detail in our group [42] leading to some modified formulae for the flow field. In the following a simple and concise treatment of the modified linear theory will be presented, the approach differing essentially from [42], in which somewhat lengthy and involved mathematical methods were resorted to.

## 2.2 Two-dimensional flow

For a two-dimensional flow the set of equations describing the flow field are:

$$\beta^2 \varphi_{xx} - \varphi_{yy} = 0 \quad (2.9)$$

with  $\varphi$  as the normalized perturbation potential, where the total potential of the flow field is given by

$$\Phi = V_{\infty} (x + \varphi) \quad (2.10)$$

The boundary condition, Eq (2.8), yields

$$\hat{g} \cdot \text{grad } F = \hat{g}_i \cdot dy_c - \hat{g}_j \cdot dx_c = 0 \quad (2.11)$$

The physical significance of this expression is depicted in Fig. 1. Eq (2.11) with Eq (2.6) yields

$$(1 - \beta^2 \varphi_x) dy_c - \varphi_y dx_c = 0 \quad (2.12)$$

The solution of the potential equation, Eq (2.9), for two-dimensional flow is well known:

$$\varphi(x,y) = \begin{cases} F_1(x - \beta y) & \text{for } y > 0 \\ F_2(x + \beta y) & \text{for } y < 0 \end{cases} \quad (2.13)$$

Inserting the expression for  $y > 0$  in the boundary condition, Eq (2.12), one gets for the upper surface:

$$\frac{dy_c}{dx} = \beta^2 F'_1(x_c - \beta y_c) \frac{dy_c}{dx} - \beta F'_1(x_c - \beta y_c) \quad (2.14)$$

The right hand side of this equation represents a total differential of the expression for  $y_c$  denoted by

$$F_1(x_c - \beta y_c) = F_1(x^*) = -\frac{y_c}{\beta} (x_c) + C \quad (2.15)$$

where for pointed bodies with  $y_c(0) = 0$  the constant C disappears. Eq (2.14) yields further

$$F'_1(x_c - \beta y_c) = F'_1(x^*) = -\frac{y'_c}{\beta(1-\beta y'_c)} (x_c) \quad (2.16)$$

with  $y'_c = dy_c/dx$ . From Eq (2.13) and Eq (2.16) it follows for the upper region ( $y > 0$ ) of the perturbation flow field using the correlation between  $x$  and  $x_c$  over  $x^*$  and  $\beta$

$$\varphi_x(x,y) = F'_1(x - \beta y) = F'_1(x^*) = -\frac{y'_c}{\beta(1-\beta y'_c)} (x^*, \beta) \quad (2.17a)$$

$$\varphi_y(x,y) = -\beta F'_1(x - \beta y) = -\beta F'_1(x^*) = -\frac{y'_c}{(1-\beta y'_c)} (x^*, \beta) \quad (2.17b)$$

The pressure coefficient in a two-dimensional flow field is given by

$$c_p(x,y) = -\frac{2u(x,y)}{V_{\infty}} = -2\varphi_x(x,y) \quad (2.18a)$$

and hence

$$c_p(x,y) = \pm \frac{2y'_c}{\beta(1 \mp \beta y'_c)} (x^*, \beta) \quad \begin{cases} \text{upper signs for } y > 0 \\ \text{lower signs for } y < 0 \end{cases} \quad (2.18b)$$

With  $\beta y'_c \ll 1$  Eq (2.18b) is identical with the Ackeret solution [1]. A comparison of the results according to Eq (2.18b) and after the Ackeret solution has been carried out for a profile in [43] as shown in Fig. 2.

### 2.3 Axially symmetric flow

For axially symmetric supersonic flow fields the equation of perturbation potential has the form

$$\beta^2 \varphi_{xx} - \varphi_{rr} - \frac{1}{r} \varphi = 0 \quad (2.19)$$

and the modified boundary condition introduced is:

$$\hat{g} \cdot \text{grad } F = 0 \quad (2.20)$$

The solution of Eq (2.19) is already known, namely

$$\varphi(x,r) = -\frac{1}{2\pi} \int_0^{x-\beta r} \frac{f(x_1) dx_1}{\sqrt{(x-x_1)^2 - \beta^2 r^2}} \quad (2.21)$$

with

$$\hat{\phi}(x,r) = V_\infty (x + \varphi) \quad (2.22)$$

as the total potential of the flow field. The boundary condition, Eq (2.20), yields

$$\hat{g} \cdot \text{grad } F = 2\pi R \hat{g}_1 dR - 2\pi R \hat{g}_r dx = 0 \quad (2.23a)$$

as illustrated in Fig. 1. From Eq (2.6) this takes the form

$$(1 - \beta^2 \varphi_x) dR - \varphi_r dx = 0 \quad (2.23b)$$

or

$$R'(x) = \frac{dR}{dx} = \frac{\varphi_r}{1 - \beta^2 \varphi_x} \quad (2.24)$$

The expression for  $\varphi_x$  and  $\varphi_r$  derived from Eq (2.21) and inserted into Eq (2.24) gives

$$RR'(x) = -\frac{\beta^2}{2\pi} \int_0^{x-\beta R(x)} \frac{f'(x_1) RR'(x) dx_1}{\sqrt{(x-x_1)^2 - \beta^2 R^2(x)}} + \frac{1}{2\pi} \int_0^{x-\beta R(x)} \frac{f'(x)(x-x_1) dx_1}{\sqrt{(x-x_1)^2 - \beta^2 R^2(x)}} \quad (2.25)$$

The right hand side represents a total differential of the expression for  $R^2(x)$  denoted by

$$\frac{R^2(x)}{2} = \frac{1}{2\pi} \int_0^{x-\beta R(x)} f'(x_1) \sqrt{(x-x_1)^2 - \beta^2 R^2(x)} dx_1 \quad (2.26)$$

This expression connects the body geometry with the source distribution  $f(x)$ . For  $\beta R(x) \ll 1$ , Eq (2.26) reduces to the usual relation of the slender body theory, namely

$$S(x) = \pi R^2(x) = \int_0^x f(x_1) dx_1 \quad (2.27a)$$

or

$$f(x) = S'(x) \quad (2.27b)$$

For axially symmetric flow the Eq (2.3) is to be used for static pressure distribution, which gives with  $x^* = x - \beta r$

$$c_p(x,r) = \frac{1}{\pi} \int_0^{x^*} \frac{f'(x_1) dx_1}{\sqrt{(x-x_1)^2 - \beta^2 r^2}} + \frac{\beta^2}{4\pi^2} \left\{ \int_0^{x^*} \frac{f'(x_1) dx_1}{\sqrt{(x-x_1)^2 - \beta^2 r^2}} \right\}^2 - \frac{1}{4\pi^2 r^2} \left\{ \int_0^{x^*} \frac{f'(x_1)(x-x_1) dx_1}{\sqrt{(x-x_1)^2 - \beta^2 r^2}} \right\}^2 \quad (2.28)$$

If the linear source distribution  $f(x)$  is known, Eq (2.28) represents an explicit expression for the pressure distribution

Some pressure distributions on cones and axially symmetric parabolic body based on Eq(2.26) and Eq (2.28) have been calculated and compared in [42] as demonstrated in Figs. 3 and 4 showing improvements in the results.

### 3. AERODYNAMIC DRAG OF WINGS AND BODIES IN SUPERSONIC FLOWS

34  
Knowing the perturbation potential in the flow field one can calculate the pressure drag on the body either by applying momentum theorem on a control surface surrounding the body or by integrating the pressure components acting in the axial direction of the body. In case of two-dimensional profiles or nonlifting bodies where vortex drag is absent both methods yield the same results giving explicit expressions for the wave drag. In case of lifting bodies the method of momentum integral on a control surface is to be chosen to separate the wave drag from the vortex drag. In the following the expressions for wave drag of nonlifting and lifting wings and bodies are summarized, the basic expressions being already known from the literature.

#### 3.1 Wave drag of wings and bodies

##### Two-dimensional profiles

Integrating the pressure components in the x-direction one obtains for the wave drag:

$$c_{DW} = \frac{1}{l} \int_0^l \left\{ c_{pu} \cdot \frac{\partial y_u}{\partial x} - c_{pl} \frac{\partial y_l}{\partial x} \right\} dx \quad (3.1)$$

Using Eq (2.18) for  $c_p$ -values one gets

$$c_{DW} = \frac{2}{\beta l} \int_0^l \left\{ \frac{y_u'^2}{1-\beta y_u'} + \frac{y_l'^2}{1+\beta y_l'} \right\} dx \quad (3.2)$$

This drag formula contains the factor  $(1-\beta y')$  in the denominator and as such deviates a little from the conventional formula. If one retains only the second order terms the wave drag due to volume and due to lift can be separated in the usual way giving for  $y_{u,l}' = -\alpha(x) \pm y_d'$ :

$$c_{DW} = c_{D0} + c_{D1} = \frac{4}{\beta l} \int_0^l \left\{ y_d'^2(x) + \alpha^2(x) \right\} dx \quad (3.3)$$

##### Three-dimensional nonlifting bodies and wings

The wave drag of axially symmetric nonlifting bodies can be obtained from the perturbation potential of the source field. The expression for the wave drag due to linear source distribution  $f(\xi)$  has been derived in [2], [6] and [12] yielding for a body with finite base area

$$\frac{D_0}{\rho_w l^2} = -\frac{1}{2\pi} \int_0^1 \int_0^1 f'(\xi) f'(\xi_1) \ln|\xi-\xi_1| d\xi d\xi_1 + \frac{f(1)}{\pi} \int_0^1 f'(\xi_1) \ln|1-\xi_1| d\xi_1 + \frac{[f(1)]^2}{2\pi} H_0(1) \quad (3.4)$$

Where  $H_0(1)$  depends on the shape of the base area

$$\begin{aligned} H_0(1) &= 0 && \text{for pointed and cylindrical bases,} \\ H_0(1) &= \ln 2 - \ln \beta \bar{R}(1) && \text{for circular bases of boat-tail bodies} \end{aligned} \quad (3.5)$$

For elliptical bases the expression for  $H_0(1)$  is given in [17] and [41].

The above expression for wave drag can also be used as a first approximation for slender bodies and wings of general cross-sections provided that the evaluation of  $H_0(1)$  is carried out after the method given by M.J. LIGHTHILL [12].

For slender wings one gets

$$H_0(1) = \bar{k} - \ln \left( \beta \frac{s}{l_1} \right) \quad (3.6)$$

The  $\bar{k}$ -values depending on the distribution of surface slopes at the trailing edge are given in [12] and [41].

##### Lifting wings of zero thickness

The perturbation potential due to a wing with lift can be calculated using source, vortex or doublet distributions. The three singularity distributions are interrelated through their dependence on the perturbation potential:

$$\begin{aligned} \text{Source strength} \quad q(x) &= 2 \frac{\partial \phi(x)}{\partial n} \\ \text{Doublet strength} \quad h(x) &= \frac{\Delta \phi(x)}{2} \\ \text{Vortex strength} \quad \bar{\kappa}(x) &= 2 \frac{\partial h(x)}{\partial x} \end{aligned} \quad (3.7)$$

A linear theory for moderately slender wings with lift has been developed by ADAMS and SEARS [16] using doublet distributions on the wing plane. The expression for the wave drag due to lift comes out as in [41]: 3-7

$$\frac{D_i}{\rho_\infty s^2} = \frac{\beta^2 s^2}{8k_i^2} \left[ -\frac{1}{2\pi} \int_0^1 \int_0^1 \sigma''(\xi) \sigma''(\xi_1) \ln|\xi - \xi_1| d\xi d\xi_1 + \frac{\sigma'(1)}{\pi} \int_0^1 \sigma''(\xi_1) \ln|1 - \xi_1| d\xi_1 + \frac{[\sigma'(1)]^2}{2\pi} \cdot H_1(1) \right], \quad (3.8)$$

where

$$\frac{s}{l_i} \sigma'(\xi) = \frac{s}{l_i} \frac{\partial \sigma}{\partial \xi} = 2 \bar{c}_a(\xi) \frac{s(\xi)}{s} \quad (3.9)$$

denotes the lift-loading on a crosswise strip of local span width  $2s(\xi)$  and

$$H_1(1) = 2 \ln 2 + \sum_{n=1}^N (n+1) \left\{ \frac{b_{2n+1}}{b_1} \right\}^2 + \frac{1}{2} - \ln \frac{\beta s}{l_i} \quad (3.10)$$

The  $b_n$ s originate from the type of lift distribution along the span of the wing expressed by

$$\gamma(n) = \bar{\alpha}_T b_1 \sum_{n=0}^N \frac{b_{2n+1}}{b_1} \sin(2n+1)\bar{\gamma} \quad (3.11)$$

with  $\eta = y/s = \cos \bar{\gamma}$  and  $\bar{\alpha}_T$  as a reference incidence angle of the wing center line at the trailing edge.

Finally the connection between  $\sigma'(\xi)$  and the doublet strength  $h(\xi)$  is given by the relations in Eq (3.7) yielding:

$$\Delta c_p(\xi, \eta) = 4 \frac{s}{l_i} \cdot \frac{\partial \tilde{h}}{\partial \xi}(\xi, \eta) \quad (3.12)$$

where  $\tilde{h} = h/V_\infty s$  denotes the dimensionless doublet strength and the local  $\eta$ -values on a crosswise strip is given by  $\eta = y/s(\xi)$ . It follows from Eq (3.9) and Eq (3.12):

$$\sigma'(\xi) = 4 \int_{-1}^{+1} \frac{\partial \tilde{h}}{\partial \xi}(\xi, \eta) \cdot d\eta \quad (3.13)$$

The wave drag formula, Eq (3.8), due to lift of wings is completely analogous to the wave drag formula, Eq (3.4), due to volume if one puts

$$\begin{aligned} f(\xi) &\equiv \sigma'(\xi) \\ H_0(1) &\equiv H_1(1) \end{aligned} \quad .$$

### 3.2 Vortex drag of wings and bodies

The vortex drag of wings with lift can either be calculated from the strength of the bound vortices and the induced downwash from the free vortices or from the momentum or energy contents in the induced field at the Trefftz-plane. For lifting wings this yields:

$$\frac{D_i}{\rho_\infty s^2} = -\frac{2}{\pi} \int_{-1}^{+1} \int_{-1}^{+1} \frac{\gamma(\eta) \frac{\partial \gamma}{\partial \eta_1}}{n - \eta_1} d\eta_1 d\eta \quad (3.14)$$

where the circulation about a local chord is denoted by

$$\gamma(\eta) = \frac{c_a(\eta) l(\eta)}{4s} \quad (3.15)$$

With  $\gamma(\eta)$  given by the expression in Eq (3.11) one gets for the vortex drag:

$$\frac{D_i}{\rho_\infty s^2} = \pi \bar{\alpha}_T^2 b_1^2 \left\{ 1 + \sum_{n=1}^N (2n+1) \left( \frac{b_{2n+1}}{b_1} \right)^2 \right\} \quad (3.16)$$

Since

$$\sigma(1) = 2\pi b_1 \bar{\alpha}_T = \frac{c_L \hat{k}}{s/l_i} \quad (3.17)$$

Eq (3.16) takes the form as derived in [41]

$$\frac{D_i}{\rho_\infty s^2} = \frac{[\sigma(1)]^2}{4\pi} \left\{ 1 + \sum_{n=1}^N (2n+1) \left( \frac{b_{2n+1}}{b_1} \right)^2 \right\} \quad (3.18)$$

### 3.3 Friction drag of slender bodies and wings

For a given flight condition normally the Mach number and the Reynolds number of the onflow are prescribed. If the Reynolds number of the flow is high and the laminar region at the nose is quite small, one can approximately assume that the boundary layer is turbulent on the whole length of the body or wing.

Based on the method of L. PRANDTL and H. SCHLICHTING [34] various approaches have been developed, [35] till [37], to calculate compressible turbulent boundary layers.

The skin friction of a flat plate in fully compressible turbulent boundary layer has been derived in [35] and [36] giving

$$c_f = \frac{0.455}{T_w/T_\infty} \left[ \log \frac{Re_\infty}{(T_w/T_\infty)^{2.8}} \right]^{-2.58} \quad (3.19)$$

where for an adiabatic surface

$$\frac{T_w}{T_\infty} = 1 + \sqrt[3]{Pr} \frac{\kappa-1}{2} Ma_\infty^2 \quad (3.20)$$

With  $\sqrt[3]{Pr} = 0.89$  one gets

$$\frac{T_w}{T_\infty} = 1 + 0.178 Ma_\infty^2 \quad (3.21)$$

#### Friction drag of wings

The friction drag of a flat plate of delta-like shape can be based on the average Reynolds number  $\overline{Re}_m = V_\infty l_m / \nu$  with  $l_m = l_i/2$ . For turbulent boundary layers Eq (3.19) yields:

$$c_{WR} = 2c_f = \frac{0.91}{(1+0.178 Ma_\infty^2)} \left[ \log \frac{\overline{Re}_m}{(1+0.178 Ma_\infty^2)^{2.8}} \right]^{-2.58} \quad (3.22)$$

#### Friction drag of bodies

The turbulent friction drag of a slender body with general cross-section shape is given by the approximate formula

$$c_{DF}^* \overline{S}_o = \frac{D_F}{\rho_\infty l^2} = \overline{c}_f \overline{S}_f \quad (3.23)$$

with  $\overline{c}_f = c_f (1 + \delta_{\max}/2)$  to account for the velocity increase on the surface due to thickness effect, and where  $c_f$  is calculated from Eq (3.19) based on the Reynolds number  $Re_\infty = V_\infty l / \nu$ . The dimensionless friction surface is being denoted by  $\overline{S}_f = S_f / l^2$ .

For general body shapes with elliptical or circular cross-sections one gets

$$\frac{D_F}{\rho_\infty l^2} = \int_0^1 c_f \overline{U}(\xi) d\xi \quad (3.24)$$

where the periphery of the cross-section  $S(\xi)$  can be expressed as  $\overline{U}(\xi) = U(\xi)/l$ , with

$$U(\xi) = \sqrt{\pi S(\xi)} \left[ 1.5 \left( \sqrt{\lambda_o} + \frac{1}{\sqrt{\lambda_o}} \right) - 1 \right] = \sqrt{\pi S(\xi)} \cdot \theta_S \quad (3.25)$$

where  $\theta_S$  denotes the bracketed term, and  $\lambda_o = h_o/b_o (< 1)$  is the ratio of the axes of the elliptical cross-section. With  $\overline{c}_f$  as an average value of the friction coefficient over the body length, one gets

$$\frac{D_F}{\rho_\infty l^2} = \overline{c}_f \theta_S \sqrt{\pi \beta} \bar{V}_o \int_0^1 \left( \frac{\overline{S}(\xi)}{\beta^2 \bar{V}_o} \right)^{\frac{1}{2}} d\xi \quad (3.26)$$

The dimensionless volume  $\bar{V}_o$  being prescribed.

### 3.4 Base drag of bodies

The base drag of three-dimensional bodies has to be evaluated from experimental data since a complete theoretical treatment of the base flow behind bodies is still lacking. Systematic base pressure measurements have been performed by a number of investigations yielding correlation curves of the base drag depending on

Mach number and Reynolds number. In [33] to [40] many of these results are reviewed, and a large number of references are cited. Theoretical work in this field is still being continued by various research groups.

3-9

The results of the foregoing analysis on pressure drag and friction drag have been compared with experimental values for a large number of slender wings and bodies giving acceptable agreement. A few of the results are shown in Figs. 5 to 8. The condition of small perturbation is the most important criterion that must be satisfied to assure the validity of the pressure drag formulae. Having now the explicit formulae for the drag components these can be utilized to minimize the drag components and also the total drag under prescribed conditions.

#### 4. WING AND BODY SHAPES FOR MINIMUM PRESSURE DRAG

In order to determine body shapes for minimum wave drag certain prescribed auxiliary conditions must be satisfied.

For nonlifting bodies and wings these include some of the parameters like volume, length, maximum cross-section, base area etc. at a given flight condition. For lifting wings the auxiliary conditions consist in prescribing the total lift and the center of pressure at a given flight condition.

The minimization of the wave drag can be carried out by applying variational methods as was done in [19], [20] and [21]. In both cases under consideration one has to deal with isoperimetric problems. A complete general treatment of such problems has been given in [41]. An outline of the treatment is given in the following:

##### 4.1 Minimization of wave drag due to volume of wings and bodies

Based on the expression for wave drag given in Eq (3.4) one has the following set of variational problem:

$$\frac{D_0}{q_\infty k^2} = F_0 [f'(\xi), f'(\xi_1), f(1), \xi, \xi_1] \rightarrow \min. \quad (4.1)$$

Auxiliary conditions (prescribed)

For  $\beta R(\xi) \ll 1$

$$\text{Base area: } \int_0^1 f(\xi) d\xi = \bar{S}(1) \quad (4.2)$$

$$\text{Volume: } \int_0^1 \xi \cdot f(\xi) d\xi = \bar{S}(1) - \bar{V}_0 \quad (4.3)$$

This isoperimetric problem can be described by a single expression as follows

$$J_0 [f(\xi)] = \left\{ \frac{D_0}{q_\infty k^2} + \lambda_1 \int_0^1 \xi \cdot f(\xi) d\xi + \lambda_2 \int_0^1 f(\xi) d\xi \right\} \rightarrow \min. \quad (4.4)$$

where  $D_0$  is to be expressed by Eq (3.4), and  $\lambda_1$  and  $\lambda_2$  denote the usual Lagrange multiplier.

The application of variational methods to this problem yields, as shown in [41], the following Euler equation

$$\frac{1}{w} \int_0^1 f'(\xi_1) \ln|\xi - \xi_1| d\xi_1 - \frac{f(1)}{w} \ln|1 - \xi| + \lambda_1 \frac{\xi^2}{2} + \lambda_2 \xi + C_0 = 0 \quad (4.5)$$

If the end conditions  $f(0)$  and  $f(1)$  are fixed through the prescribed conditions the Euler equation yields the solution of the extremal problem.

Expressing the source distribution in a series form

$$f(\vartheta) = a_0 \vartheta + \sum_{n=1}^N a_n \sin n\vartheta \quad (4.6)$$

where  $\xi = (1 - \cos\vartheta)/2$ , the Euler equation (4.5) will be satisfied, provided  $N$  does not exceed the value  $N = 2$ . The coefficients  $a_n$  will be obtained from the auxiliary conditions.

Knowing the source distribution the equivalent body shape can be obtained from Eq (2.26) giving

$$\bar{S}(\vartheta) = \frac{1}{2} \int_0^{\vartheta^*} f(\vartheta_1) \sqrt{(\cos \vartheta_1 - \cos \vartheta)^2 - 4\beta^2 R^2(\vartheta)} d\vartheta_1 \quad (4.7)$$

with 
$$\xi^* = \xi - \beta R(\xi) = \frac{1 - \cos \psi^*}{2} \quad (4.8)$$

From Eq (4.6) it follows

$$f'(\psi_1) = a_0 + a_1 \cos \psi_1 + 2a_2 \cos 2\psi_1 \quad (4.9)$$

The general expression for optimum body shape having minimum wave drag due to volume is

$$\begin{aligned} \bar{S}(\psi) = \frac{a_0}{2} \int_0^{\psi^*} \sqrt{(\cos \psi_1 - \cos \psi)^2 - 4\beta^2 R^2(\psi)} d\psi_1 + \frac{a_1}{2} \int_0^{\psi^*} \cos \psi_1 \sqrt{(\cos \psi_1 - \cos \psi)^2 - 4\beta^2 R^2(\psi)} d\psi_1 \\ + \frac{a_2}{2} \int_0^{\psi^*} 2\cos 2\psi_1 \sqrt{(\cos \psi_1 - \cos \psi)^2 - 4\beta^2 R^2(\psi)} d\psi_1 \end{aligned} \quad (4.10)$$

As a special case of very slender bodies with  $\beta R(\psi) \ll 1$ , Eq (4.10) yields

$$\bar{S}(\psi) = \frac{a_0}{2} (\sin \psi - \psi \cos \psi) + \frac{a_1}{4} \left( \psi - \frac{\sin 2\psi}{2} \right) + \frac{a_2}{4} \left( \sin \psi - \frac{\sin 3\psi}{3} \right) \quad (4.11)$$

One can easily recognize that the second term in this expression is identical with the von Kármán-ogive and the third term with the Sears-Haack body. The first term appears in order to match arbitrarily given base areas to a given volume. Eq (4.11) yields:

$$\begin{aligned} \bar{S}(1) &= \pi \left( \frac{a_0}{2} + \frac{a_1}{4} \right) \\ \bar{V}_0 &= \pi \left( \frac{3a_0}{16} + \frac{a_1}{8} + \frac{a_2}{16} \right) \end{aligned} \quad (4.12)$$

Prescribing the base area through the relation  $\bar{S}(1) = 2\kappa^* \bar{V}_0$  where  $\bar{V}_0$  is a given dimensionless volume and introducing a further auxiliary condition,  $\bar{S}''(1) = 0$ , to provide uniqueness of the problem assuring at the same time finite surface curvature at the trailing edge it follows for the unknown coefficients  $a_n$  of a boat-tail body

$$\begin{aligned} a_0 &= \frac{\bar{V}_0}{\pi} \left( 8\kappa^* - \frac{32}{5} \right) \\ a_1 &= \frac{\bar{V}_0}{\pi} \left( \frac{64}{5} - 8\kappa^* \right) \\ a_2 &= \frac{\bar{V}_0}{\pi} \left( \frac{48}{5} - 8\kappa^* \right) \end{aligned} \quad (4.13)$$

Von Kármán-ogive:

$$\bar{S}(1) = 2\bar{V}_0; \quad a_0 = 0; \quad a_1 = \frac{8\bar{V}_0}{\pi}; \quad a_2 = 0 \quad (4.14)$$

Sears-Haack body:

$$\bar{S}(1) = 0; \quad a_0 = 0; \quad a_1 = 0; \quad a_2 = \frac{16\bar{V}_0}{\pi} \quad (4.15)$$

For flat wings with  $\kappa^* = 0$  it follows

$$\bar{S}(1) = 0; \quad a_0 = -\frac{a_1}{2} = -\frac{6.4}{\pi} \bar{V}_0; \quad a_2 = \frac{9.6}{\pi} \bar{V}_0 \quad (4.16)$$

Some optimum shapes of nonlifting bodies according to Eq (4.10) to Eq (4.16) are presented in Figs. 9 and 10 showing slight dependences of the body shapes on the onflow Mach number. The use of source expressions in the auxiliary conditions Eq (4.2) and Eq (4.3) gives rise to small errors which can be compensated by correcting for the deviation in volume or base area. In contrast to the Sears-Haack bodies these bodies possess sharp noses.

#### 4.2 Minimization of wave drag due to lift of wings

The expression for wave drag due to lift given in Eq (3.8) together with the auxiliary conditions leads to the following variational problem.

$$\frac{D_1}{q_\infty s^2} = F_1 \left[ \sigma'(\xi), \sigma'(\xi_1), \sigma'(1), \xi, \xi_1 \right] \rightarrow \min. \quad (4.17)$$

Auxiliary conditions (prescribed)

$$\text{Total lift} \quad \int_0^1 \sigma'(\xi) d\xi = \frac{L}{q_\infty s^2} = \frac{c_L S_W}{s^2} \quad (4.18)$$

$$\text{center of pressure:} \quad \int_0^1 \xi \cdot \sigma'(\xi) d\xi = \bar{\xi}_D \cdot \frac{c_L S_W}{s^2} \quad (4.19)$$

Thus the variational problem takes the form

$$J_1 [\sigma'(\xi)] = \left\{ \frac{D_1}{q_\infty s^2} + \lambda_1 \int_0^1 \xi \cdot \sigma'(\xi) d\xi + \lambda_2 \int_0^1 \sigma'(\xi) d\xi \right\} \rightarrow \min \quad (4.20)$$

where  $D_1$  is to be taken from Eq (3.8) and  $\lambda_1$  and  $\lambda_2$  denote Lagrange multipliers. The formulation of this variational problem due to lift is surprisingly analogous to that of the thickness problem.

The Euler Equation of the variational problem takes therefore the same form as in Eq (4.5) of the thickness problem, yielding

$$\frac{1}{\pi} \int_0^1 \sigma''(\xi_1) \ln |\xi - \xi_1| d\xi_1 - \frac{\sigma'(1)}{\pi} \ln |1 - \xi| + \lambda_1 \frac{\xi^2}{2} + \lambda_2 \xi + C_1 = 0 \quad (4.21)$$

If the end condition  $\sigma'(0)$  and  $\sigma'(1)$  are fixed, the Euler equation (4.21) alone will yield the optimum loading  $\sigma'(\xi)$  on crosswise strips of the wing.

Setting

$$\sigma'(\xi) = \bar{a}_0 \psi + \sum_{n=1}^N \bar{a}_n \sin n\psi \quad (4.22)$$

Eq (4.21) will be satisfied if  $N$  is limited to  $N = 2$ . The  $\bar{a}_n$ -values are obtained from the prescribed auxiliary conditions. It follows:

$$\begin{aligned} \pi \left( \frac{\bar{a}_0}{2} + \frac{\bar{a}_1}{4} \right) &= \frac{c_L \hat{\kappa}}{s/l_1} \\ \pi \left( \frac{5\bar{a}_0}{16} + \frac{\bar{a}_1}{8} - \frac{\bar{a}_2}{16} \right) &= \bar{\xi}_D \frac{c_L \hat{\kappa}}{s/l_1} \end{aligned} \quad (4.23)$$

and hence

$$\begin{aligned} \bar{a}_0 &= \frac{2}{\pi} \frac{c_L \hat{\kappa}}{s/l_1} \cdot \bar{s}'(1) \\ \bar{a}_1 &= \frac{4}{\pi} \frac{c_L \hat{\kappa}}{s/l_1} \{ 1 - \bar{s}'(1) \} \\ \bar{a}_2 &= \frac{4}{\pi} \frac{c_L \hat{\kappa}}{s/l_1} \{ 4 - 8\bar{\xi}_D + \bar{s}'(1) \} \end{aligned} \quad (4.24)$$

As optimum lift distribution along  $\xi$ -direction one gets:

for  $\sigma'(1) = 0$  (Gothic, Ogee)

$$\sigma'(\xi) = \frac{4}{\pi} \frac{c_L \hat{\kappa}}{s/l_1} \left[ \sin \psi + 2(1-2\bar{\xi}_D) \sin 2\psi \right] \quad (4.25)$$

for  $\sigma'(1) = 1$  (Delta)

$$\sigma'(\xi) = \frac{2}{\pi} \frac{c_L \hat{\kappa}}{s/l_1} \left[ \bar{s}'(1)\psi + 2 \{ 1 - \bar{s}'(1) \} \sin \psi + \{ 4 - 8\bar{\xi}_D + \bar{s}'(1) \} \sin 2\psi \right] \quad (4.26)$$

These optimum distribution are illustrated for  $\bar{\xi}_D = 0.6$  in Fig. 11 for two wing planforms. Integrating  $\sigma'(\xi)$  over  $\xi$  yields the optimum geometric parameter  $\sigma(\xi)$  where according to slender wing theory [41] the following dependence exists:

$$\sigma(\xi) = 2\pi b_1 \bar{s}^2(\xi) \bar{a}_1(\xi) \quad (4.27)$$

$$\bar{a}(\xi) = \bar{a}_1(\xi) + \bar{a}_h(\xi) \quad (4.28)$$

where  $\bar{a}_1(\xi)$  and  $\bar{a}_h(\xi)$  denote flow deflections at the center line of the wing caused by the free vortex system and the bound vortex system respectively. Now knowing the wing planform  $s(\xi)$  it is easy to determine the required wing camber  $\bar{a}(\xi)$  for optimum lift distribution. The distribution of  $\sigma(\xi)$  is

illustrated in Fig. 12 for two values of the parameter  $\sigma'(1)$  or  $\bar{\sigma}'(1)$ . The distribution of  $u(\xi, \eta)$  in the spanwise direction will be determined from the wing twist necessary to suppress the vortex drag.

#### 4.3 Minimization of vortex drag due to the lift of wings

For lifting wings with finite span the formation of vortex sheets in the downstream flow is unavoidable and it is wellknown that an elliptic distribution of lift loading over the span makes the induced drag a minimum. For slender flat wings it is difficult to obtain this optimum distribution without wing twist as concentrated vortices are likely to form at the leading edges contributing to increased vortex drag. So for minimizing the vortex drag of slender wings the formulation of the variational problem looks as follows:

For the vortex drag as in Eq (3.18) to be a minimum it is required that

$$K_1 = \left\{ 1 + \sum_{n=1}^N (2n+1) \left( \frac{b_{2n+1}}{b_1} \right)^2 \right\} \rightarrow \min. \quad (4.29)$$

To prevent concentrated vortex shedding at the leading edges the local velocity there must be tangential to the surface, requiring:

$$\Delta c_p (\eta = \pm 1) = 0 \quad (4.30)$$

with

$$\Delta c_p(\xi, \eta) = 4 \frac{\alpha}{\Gamma_1} \frac{\partial}{\partial \xi} \left\{ \bar{w}(\xi) \bar{a}_1(\xi) \sum_{n=0}^N b_{2n+1} \sin(2n+1) \bar{\psi} \right\} \quad (4.31)$$

For slender wings this is equivalent to setting [41]:

$$E = 1 + \sum_{n=1}^N (2n+1) \frac{b_{2n+1}}{b_1} = 0 \quad (4.32)$$

These two requirements must be simultaneously fulfilled at a prescribed flight condition and leads to the following variational problem as has been shown in [33]

$$\frac{\partial}{\partial b_{2n+1}} (K_1 + \lambda E) = 0 \quad (4.33)$$

with  $\lambda$  as Lagrange multiplier. The solution of Eq (4.33) comes out as

$$\frac{b_{2n+1}}{b_1} = - \frac{4}{(N+3)(N-1)} \quad \text{with } N \geq 3 \quad (4.34)$$

The Eq (4.34) fixes the wing twist for a given incidence angle  $\alpha_T$  at the trailing edge preventing the formation of concentrated vortices at the leading edges. The pressure and lift distribution over the span of a delta wing for different N-values are shown in Fig. 13. For  $N \rightarrow \infty$  the pressure distribution approaches that of a flat plate. For  $N = 7$  the lift distribution on the span is almost elliptic and the pressure peaks are not high, so that the adverse pressure gradients for the wing boundary layer in this region are kept within limits.

## 5. AERODYNAMIC DRAG OF WINGS AND BODIES WITH OPTIMUM SHAPES

The aerodynamic shapes or load distributions for minimum drag being fixed it is now easy to determine the drag values of wings and bodies from Eq (3.4) and Eq (3.8).

### 5.1 Minimum wave drag due to volume of wings and bodies

The wave drag of wings and bodies due to volume is given by:

$$\frac{D_o}{\rho_0 a_0^2} = \left\{ -\pi a_0^2 \ln 2 + \frac{\pi}{4} a_1^2 + \frac{\pi}{2} a_2^2 + \pi a_0 a_1 - \pi a_0 a_2 + \frac{\pi}{2} a_0^2 H_0(1) \right\} \quad (4.35)$$

From this it follows for the wave drag coefficients in supersonic flow regime:

von Kármán ogive

$$c_{Do}^* \bar{S}_o = \frac{16}{\pi} \bar{V}_o^2 \quad (4.36)$$

Sears-Haack body

$$c_{Do}^* \bar{S}_o = \frac{128}{\pi} \bar{V}_o^2 \quad (4.37)$$

Boat-tail bodies with circular base

$$c_{Do}^* \bar{S}_o = \bar{V}_o^2 \left[ (8.17\kappa^{*2} - 21.28\kappa^* + 16.67) - \frac{1}{2} \ln \left( \frac{2}{\pi} \beta^2 \bar{V}_o \kappa^* \right) \{ 10.19\kappa^{*2} - 16.30\kappa^* + 6.52 \} \right] \quad (4.38)$$

Flat bodies (wings)

$$c_{Do} \bar{S}_W = \frac{128}{\pi} \bar{V}_o^2 K_o \quad \text{or} \quad c_{Do} = \frac{128}{\pi} K_o \bar{r}_m^{-2} \cdot \frac{s\hat{\kappa}}{l_i} \quad (4.39)$$

$$\text{with} \quad K_o = 1 - 0.16 \left( 2 \ln 2 + 3 - \bar{k} + \ln \frac{\beta s}{l_i} \right) \quad \text{and} \quad \bar{r}_m = V_o / S_W l_i \quad (4.40)$$

Comparison of the theoretical and experimental drag values of some optimum shaped bodies and wings at zero lift are shown in Fig. 14 and Fig. 15.

### 5.2 Minimum wave drag due to lift of wings

The wave drag of wings due to lift is given by the expression

$$\frac{D_1}{q_\infty s^2} = \frac{\beta^2 s^2}{l_i^2} \frac{\pi}{8} \left\{ -\bar{a}_o^{-2} \ln 2 + \frac{\bar{a}_1^{-2}}{4} + \frac{\bar{a}_2^{-2}}{2} + \bar{a}_o \bar{a}_1 - \bar{a}_o \bar{a}_2 + \frac{\bar{a}_o^2}{2} H_1(1) \right\} \quad (4.41)$$

which according to [41] can be written as

$$c_{D1} = \frac{1}{2\pi} \beta^2 c_L^2 \hat{\kappa} \cdot K_1 \cdot \frac{s}{l_i} \quad (4.42)$$

where  $K_1$  is determined from the Eq (4.41) after inserting the  $\bar{a}_n$ -values.

### 5.3 Minimum vortex drag of wings

The vortex drag of twisted wings preventing the shedding of concentrated rolled up vortices is obtained from the Eq (3.18) where the  $\bar{b}_n$ -values are taken from Eq (4.34). It follows:

$$c_{Di} = \frac{1}{4\pi} K_1 \frac{c_L^2 \hat{\kappa}}{s/l_i} \quad (4.43)$$

with  $K_1$  as given in Eq (4.29).

For  $N \rightarrow \infty$  Eq (4.29) together with Eq (4.34) yields  $K_1 = 1$ , and hence the vortex drag coefficient for a plane delta wing reduces to:

$$c_{Di} = \frac{c_L^2 \hat{\kappa}}{4\pi s/l_i} = \frac{c_L^2}{\pi \Lambda} \quad (4.44)$$

which is identical with the induced drag due to elliptic load distribution over the wing span. The twist increases the vortex drag a little above the theoretical minimum value for an elliptic distribution but keeps it quite below that of a flat delta wing with rolled up vortices at the leading edges. This fact is demonstrated by comparing the induced drag values of twisted and flat wings as shown in Fig. 16.

## 6. OPTIMUM COMBINATION OF AERODYNAMIC AND GEOMETRIC PARAMETERS OF WINGS AND BODIES FOR MINIMUM TOTAL DRAG.

It is outside the scope of this paper to treat this problem in detail, however, an outline of the method will be indicated for the treatment of nonlifting and lifting wings and bodies in order to obtain minimum total drag or highest lift/drag ratios for lifting wings.

### 6.1 Optimum slenderness ratio of bodies and wings with given volume in supersonic flows

The total drag of a slender body or of a wing without lift can be expressed by summing up all the drag components. This yields

$$\text{General body:} \quad D = D_o + D_f + D_B \quad (4.45)$$

Expressed in terms of drag coefficients, one gets:

$$c_D^* S_o = \frac{128}{\pi} K_o^* \frac{V_o^2}{l_i^4} + \bar{c}_f \theta_S I_S \sqrt{V_o} \sqrt{l} + c_{DB} \cdot S(1) \quad (4.46)$$

$$\text{with } I_S = \sqrt{\pi} \int_0^1 \left\{ \bar{S}(\xi) / \bar{V}_o \right\}^{1/2} d\xi \quad \text{known from the distribution of the cross-section area } \bar{S}(\xi) / \bar{V}_o.$$

Flat body (wing)  $D = D_o + D_f$  (4.47)

or  $c_D S_W = \frac{128}{\pi} K_o \frac{V_o^2}{\ell_i^4} + 2 \bar{c}_f \hat{\kappa} s \ell_i$  (4.48)

for a given volume  $V_o$  and friction coefficient  $\bar{c}_f$  the total drag depends on the length  $\ell$  of the body or wing.

Problem statement for nonlifting slender bodies:

<u>Prescribed</u>	<u>To be determined</u>
Mach number $Ma_\infty \rightarrow \beta$	optimum length $\ell_{opt}$
Reynolds number $Re_\infty + c_f$	optimum slenderness ratio $\ell/d_o$
Volume $V_o$	minimum drag $D_{min}$
Base area $S(1)$	
Volume distribution $S(\xi)$	
Cross section shape $\rightarrow \theta_s$	

6.2 Optimum lift coefficient and optimum slenderness ratio of wings with given total lift in supersonic flows

The total drag of a lifting wing can be written as:

$$D = D_o + D_i + D_{i'} + D_f \quad (4.49)$$

Expressed again in terms of drag coefficients this yields:

$$c_D S_W = \frac{128}{\pi} K_o \hat{\kappa} \bar{\tau}_m^2 \beta \frac{s}{\ell_i} \cdot \frac{(c_L S_W)}{\beta c_L} + \frac{1}{2\pi} K_i \hat{\kappa} \beta \frac{s}{\ell_i} \cdot (c_L S_W) \cdot \beta c_L + \frac{1}{4\pi} K_i \hat{\kappa} \frac{(c_L S_W)}{\beta \frac{s}{\ell_i}} \cdot \beta c_L + \frac{\beta c_{DF}}{\beta c_L} (c_L S_W) \quad (4.50)$$

with  $\beta s/\ell_i$  and  $\beta c_L$  as the two variable parameters, whose optimum are sought.

Problem statement for lifting wings with thickness:

<u>Prescribed</u>	<u>To be determined</u>
Mach number $Ma_\infty \rightarrow \beta$	optimum lift coefficient $(\beta c_L)_{opt}$
Reynolds number $Re_\infty + c_f$	optimum slenderness ratio $(\beta s/\ell_i)_{opt}$
Lift $L$ or $(c_L S_W)$	optimum wing area $(S_W)_{opt}$
Lift distribution $\sigma'(\xi)_{opt}$	optimum camber $\bar{a}(\xi)_{opt}$
Planform $s(\xi) \rightarrow \hat{\kappa}$	optimum twist $\alpha(\xi, \eta)_{opt}$
Mean thickness $\bar{\tau}_m$	maximum lift/drag ratio $(L/D)_{max}$
Volume distribution $S(\xi)_{opt} \rightarrow K_o$	
Wing twist parameter $N \rightarrow K_i$	

The optimum values of the parameters looked for can be easily obtained by differentiating the drag expressions in Eq (4.46) and (4.48) with respect to the parameter  $\ell$  for nonlifting bodies, and the drag expression in Eq (4.50) with respect to  $c_L$  and  $s/\ell_i$  for lifting wings and equating the results to zero.

Some results of such optimizations are demonstrated in Figs. 17 and 18 showing quite acceptable results. The optimum slenderness ratios of nonlifting boat-tail bodies for minimum fore drag at various Mach numbers and different friction coefficients are displayed in Fig. 17. For lifting wings Fig. 18 shows the optimum combinations of lift coefficient and slenderness ratios at given mean thicknesses  $\bar{\tau}_m$  and given friction coefficients  $c_f$ . Experimental verification of these results is illustrated in Figs. 19 and 20.

7. CONCLUSION

The theoretical and experimental analysis on the drag problem at supersonic speeds described in this paper shows to what extent the linear theory for small perturbation flow field can be applied to estimate the wave drag due to volume of slender wings and bodies at zero lift as well as the induced drag and wave drag of lifting wings. The linear theory yields acceptable results in the domain of its validity. The approximate expressions for the friction drag can also be well utilized. Applying the theoretical expressions for the drag components, optimum aerodynamic shapes of wings and bodies for minimum total drag have been calculated.

Comparison of the theoretical and experimental results, not all of which could be presented here, reveal that advancements on two basic problems are still lacking - namely a linear theory of the lift problem and the base drag problem of general slender bodies, as well as a non-linear theory of lifting wings and bodies comprising the effect of accentuated vortex shedding at higher incidences and the effect of compressibility at higher Mach numbers - the two effects being basically different.

## REFERENCES

- 315
- [1] Ackeret, J. Über Luftkräfte auf Flügel, die mit größerer als Schallgeschwindigkeit bewegt werden. Zeitschrift Flugtech. 16 (1925), S. 72-74.
  - [2] v. Kármán, Th. Moore, N.B. The Resistance of Slender Bodies Moving with Supersonic Velocities with Special Reference to Projectiles. Trans. Amer. Soc. Mech. Engrs. 54 (1932), S. 303-310.
  - [3] Prandtl, L. Theorie des Flugzeugtragflügels im zusammendrückbaren Medium. Luftfahrtforschung 13 (1936), S. 313-319.
  - [4] Schlichting, H. Tragflügeltheorie bei Überschallgeschwindigkeit. Luftfahrtforschung 13 (1936), S. 320-335.
  - [5] Lighthill, M.J. Supersonic Flow Past Bodies of Revolution. ARC-Report R u. M No. 2003 (1945).
  - [6] Ward, G.N. Supersonic Flow Past Slender Pointed Bodies. Quart. Jour. Mech. and Appl. Math. 2, Part 1 (1949), S. 76-97.
  - [7] Ward, G.N. Linearized Theory of Steady High Speed Flow. University Press, Cambridge (1955).
  - [8] Robinson, A. On Source and Vortex Distribution in the Linearized Theory of Steady Supersonic Flow. Quart. Jour. Mech. Appl. Math. I (1948), S. 408-432.
  - [9] Puckett, A.E. Supersonic Wave Drag of Thin Wings. Jour. Aero. Sci. 13 (1946), S. 475-480.
  - [10] Keune, F. Oswatitsch, K. Nichtangestellte Körper kleiner Spannweite in Unter- und Überschallströmung. Zeitschr. f. Flugwiss. 1 (1953), S. 137-145.
  - [11] Weber, J. Some Notes on the Zero-Lift Wave Drag of Slender Wings with Unswept Trailing Edge. ARC R u. M No. 3222 (1961).
  - [12] Lighthill, M.J. The Wave Drag at Zero Lift of Slender Delta Wings and Similar Configurations. Jour. Fluid Mech. 1 (1956), S. 337-348.
  - [13] Lomax, H. The Wave Drag of Arbitrary Configurations in Linearized Flow as Determined by Areas and Forces in Oblique Planes. NACA TIB 4620 (1955).
  - [14] Jones, R.T. Properties of Low-Aspect-Ratio Pointed Wings at Speeds Below and Above the Speed Sound. NACA Report No. 835 (1946).
  - [15] Jones, R.T. Leading Edge Singularities in Thin Airfoil Theory. Jour. Aero. Sci. 17 (1950), S. 307-310.
  - [16] Adams, M.C. Sears, W.R. Slender-Body Theory-Review and Extension. Jour. Aero. Sci. (1953), S. 85-98.
  - [17] Kahane, A. Solarski, A. Supersonic Flow about Slender Bodies of Elliptic Cross Section. Jour. Aero. Sci. 20 (1953), S. 513-524.
  - [18] van Dyke, M.D. First and Second-Order Theory of Supersonic Flow past Bodies of Revolution. Jour. Aero. Sci. (1951), S. 161-178.
  - [19] Haack, W. Geschosßformen kleinsten Wellenwiderstandes. Lilienthal Gesellschaft Bericht 139 (1941), S. 14-28.
  - [20] Sears, W.R. On Projectiles of Minimum Wave Drag. Quart. Appl. Math. 14 (1947), S. 361-366.
  - [21] Ferrari, C. Sulla determinazione del proietto di minima d'onda. Teil I Alli d. R. Accad. d. Sci. di Torino 74 (1938), S. 675-693. Teil II do. 75 (1939), S. 61-96.
  - [22] Adams, M.C. Determination of Shapes of Boattail Bodies of Revolution for Minimum Wave Drag. NACA TN 2550 (1951).
  - [23] Harder, K.C. Rennemann, C. On Boattail Bodies of Revolution having Minimum Wave Drag. NACA TR 1271 (1956).
  - [24] Lord, W.T. Brebner, G.G. Supersonic Flow past Slender Pointed Wings with Similar Cross Sections at Zero Lift. Aero. Quart. 10 (1959), S. 79-102.
  - [25] Jones, R.T. Theoretical Determination of the Minimum Drag of Airfoils at Supersonic Speeds. Jour. Aero. Sci. 19 (1952), S. 813-822.
  - [26] Jones, R.T. The Minimum Drag of Thin Wings in Frictionless Flow. Jour. Aero. Sci. 18 (1951), S. 75-81.
  - [27] Grant, F.C. The Proper Combination of Lift Loadings for Least Drag on a Supersonic Wing. NACA Report 1275 (1956).
  - [28] Cohen, Doris. The Warping of Triangular Wings for Minimum Drag at Supersonic Speeds. Jour. Aero. Sci. 24 (1957), S. 67-69.
  - [29] Brebner, G.G. Some Simple Shapes to Produce Low Lift-Dependent Drag on a Slender Delta Wing. ARC C.P. 428 (1957).

- [30] Roper, G.M. Use of Camber and Twist to Produce Low-Drag Delta or Sweptback Wings, without Leading-Edge Singularities at Supersonic Speeds. ARC R u. M No. 3196 (1961).
- [31] Munk, M.M. The Minimum Induced Drag of Airfoils. NACA TR 121 (1921).
- [32] Hayes, W.D. Linearized Supersonic Flow. North American Aviation Co., Report AL-222 (1947).
- [33] Smith, J.H.B. K.W. Mangler The Use of Conical Camber to Produce Flow Attachment at the Leading Edge of a Delta Wing and to Minimize Lift-Dependent Drag at Sonic and Supersonic Speeds. ARC R u. M No. 3289 (1963).
- [34] Schlichting, H. Boundary Layer Theory. McGraw-Hill, New York (1960).
- [35] Monaghan, R.J. A Review and Assessment of various Formulae for Turbulent Skin Friction in Compressible Flow. ARC C.P. No. 142 (1953).
- [36] Cope, W.F. The Turbulent Boundary Layer in Compressible Flow. ARC R u. M. No. 2840 (1943).
- [37] Wilson, R.E. Turbulent Boundary-Layer Characteristics at Supersonic Speeds - Theory and Experiment. J. Aer. Sci. Vol. 17 (1950), S. 585-594.
- [38] Carpenter, P.W. et al. Survey and Evaluation of Supersonic Base Flow Theories. NASA CR 97 129 (1968).
- [39] de Krasinski, J.S. A Study of Separated Base Flow Behind Bodies of Revolution in Supersonic Streams. Part I: Review of Physical and Theoretical Aspects of Base Flow. IIAE-INF-01-65 (1965).
- [40] Schmidt, W.R. Zusammenstellung experimenteller Unterlagen zum Heckwiderstand von Flugkörpern im Transschall- und im Überschallbereich und Vergleich mit theoretischen Berechnungsmethoden. Dornier System Bericht EFB-Nr. 132/72 (1972).
- [41] Das, A. Über die Berechnung der optimalen Form von schlanken Flugkörpern bei Überschallgeschwindigkeiten. Habilitationsschrift. T.U. Braunschweig (1967). Jahrbuch 1968 der DGLR (1968). S. 261-285. Instituts-Bericht 66/32 (1966).
- [42] Wellmann, J. Der Einfluß der Machzahl auf die Konturformen von Körpern mit minimalem Wellenwiderstand bei Überschallanströmung. Dissertation T.U. Braunschweig (1972). Instituts-Bericht 71/8 (1972).
- [43] Puffert, W. Berechnung der Druckverteilung an zweidimensionalen Tragflügelprofilen nach den linearen und nichtlinearen Theorien der Überschallströmung. Diplomarbeit T.U. Braunschweig (1971).
- [44] Das, A. Krux, P. Wellmann, J. Zum Widerstandsproblem schlanker Körper bei Nullauftrieb in Überschallströmung. Z. Flugwiss. 19 (1971), S. 62-76.
- [45] Das, A. Schroeder, H.-H. Untersuchungen über das Auftriebsproblem schlanker Tragflügel bei Überschallströmung. Z. Flugwiss. 19 (1971), S. 265-281. Investigations into the Lifting Problem of Slender Wings in Supersonic Flow. RAE Library Translation No. 1677 (1972).
- [46] Das, A. Köster, H. Der Überschallwindkanal des Forschungszentrums Braunschweig der DFVLR. Z. Flugwiss. 17 (1969), S. 231-242.
- [47] Köster, H. Experimentelle Untersuchungen über die linearen und nichtlinearen Anteile der aerodynamischen Beiwerte eines schlanken Rumpfes bei Überschallanströmung. DLR-FB 72-42 (1972).
- [48] Wellmann, J. Vereinfachung von Rechnungen am schiefen Verdichtungsstoß. DLR-FB 72.11 (1972).
- [49] Küchemann, D. Aircraft Shapes and their Aerodynamics for Flight at Supersonic Speeds. Proc. 2nd Int. Cong. Aero. Sci., Zürich (1960), S. 221-252.
- [50] Miele, A. Editor Theory of Optimum Aerodynamic Shapes. Academic Press, New York/London (1965)

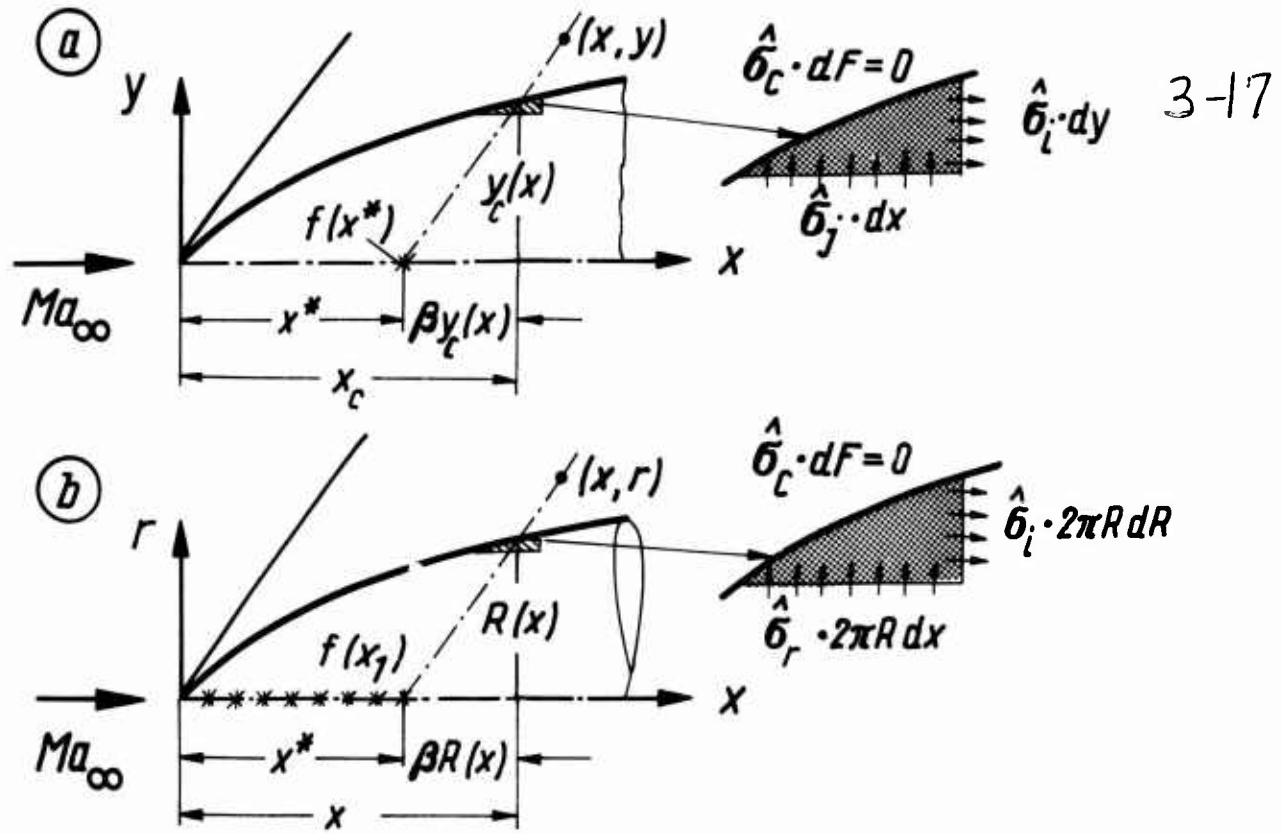


Fig. 1: Modified boundary conditions for (a) a two-dimensional profile and for (b) an axially symmetric body according to the linearized mass flux concept.

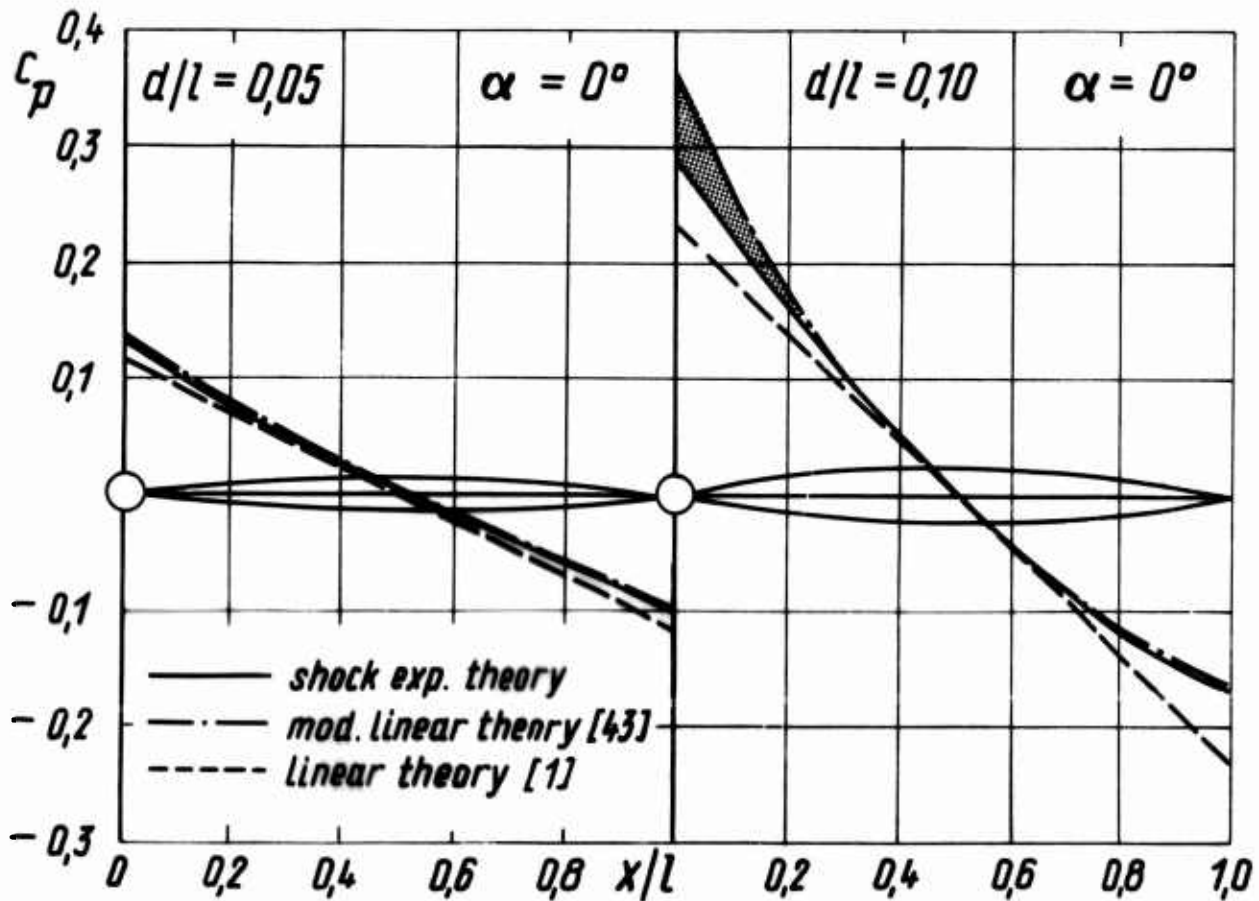


Fig. 2: Pressure distribution at Mach number  $Ma = 2$  on the surface of parabolic profiles of different thickness from linear and non-linear theories of supersonic flow.

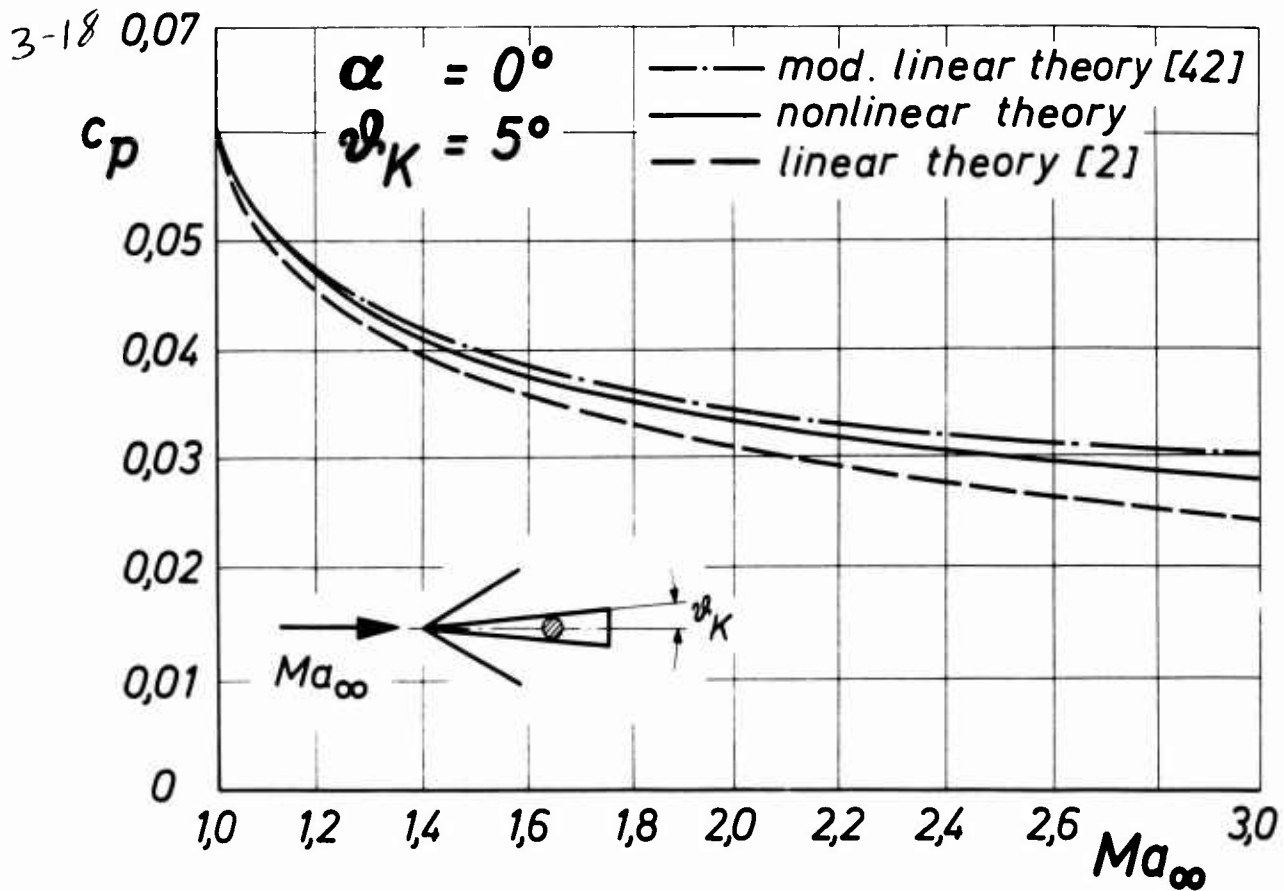


Fig. 3: Pressure coefficient on the surface of a circular cone obtained from linear and non-linear theories of supersonic flow.

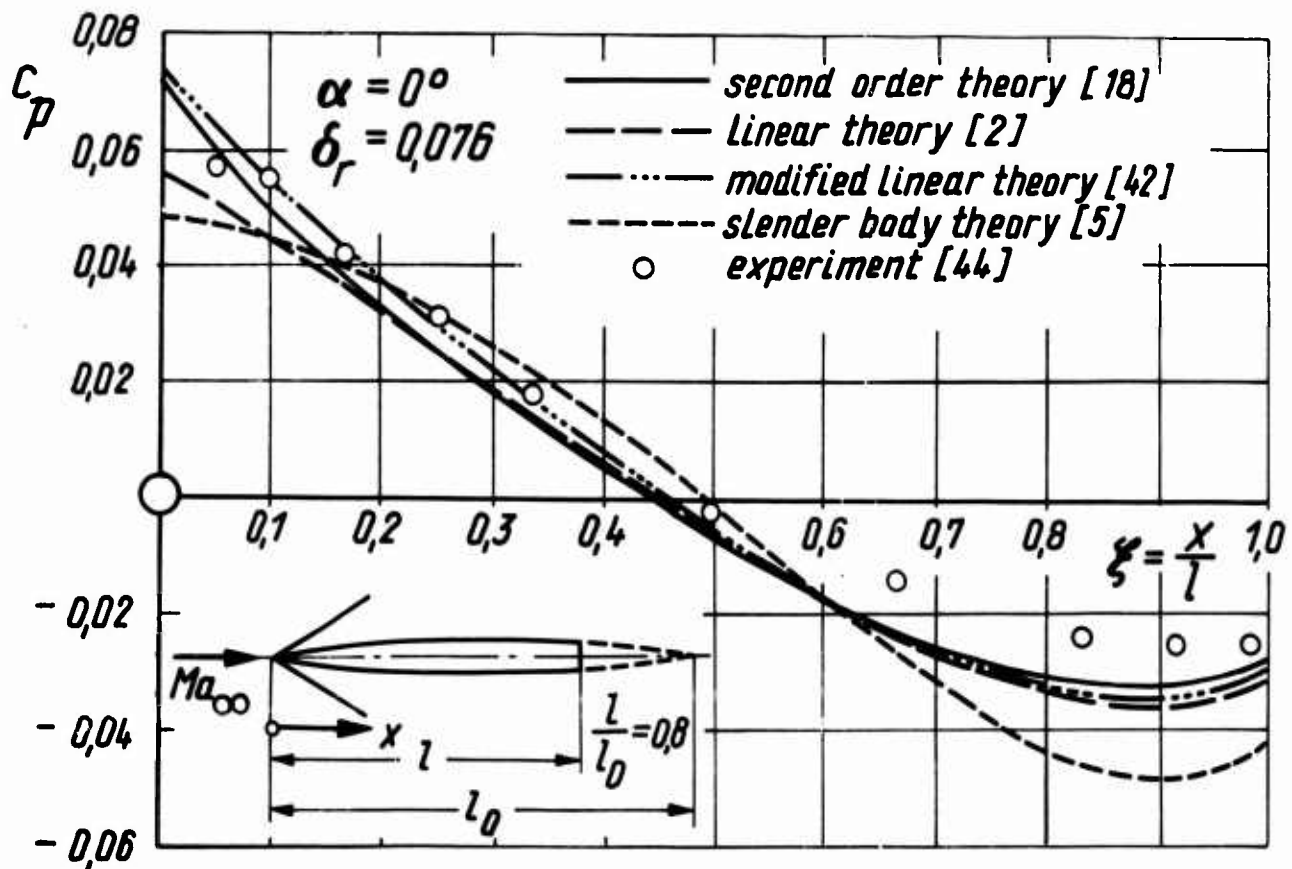


Fig. 4: Pressure distribution at Mach number  $Ma_\infty = 3$  on the surface of an axially symmetric body with parabolic contour according to various theories of supersonic flow.

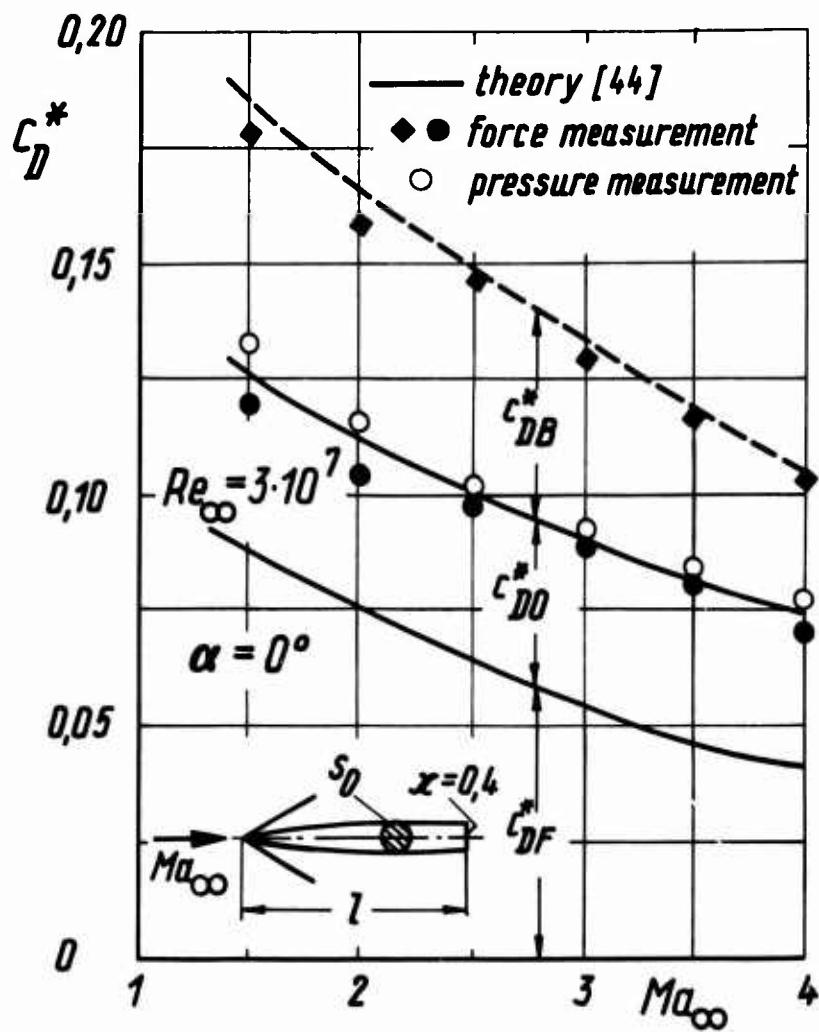


Fig. 5: The drag components of a best-tail axially symmetric body with a given volume, length and base area in dependence of Mach number. ( $d_0/l = 0.086$ )

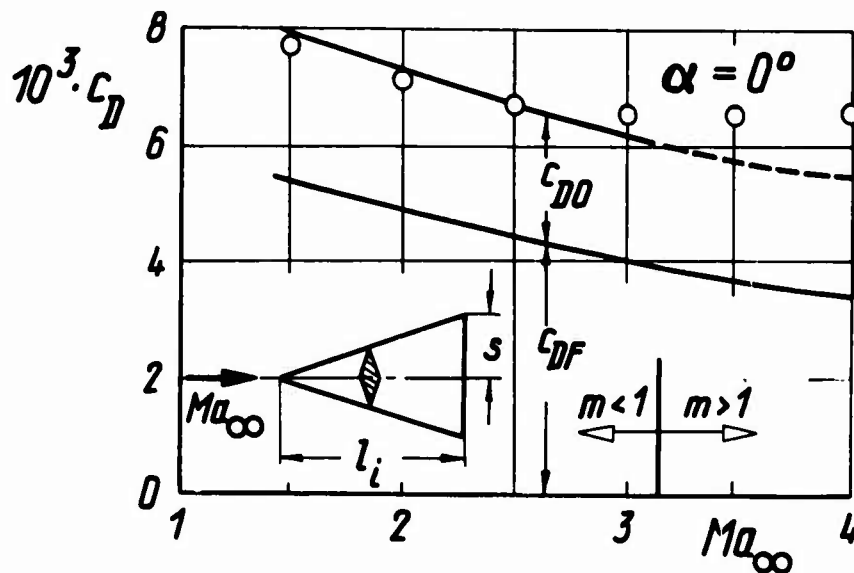


Fig. 6: The drag components of a nonlifting plane delta wing from theory and experiment in dependence of Mach number ( $s/l_i = 1/3$ ;  $\bar{v}_m = 0.02$ ;  $\bar{Re}_m = 1 \cdot 10^7$ ).

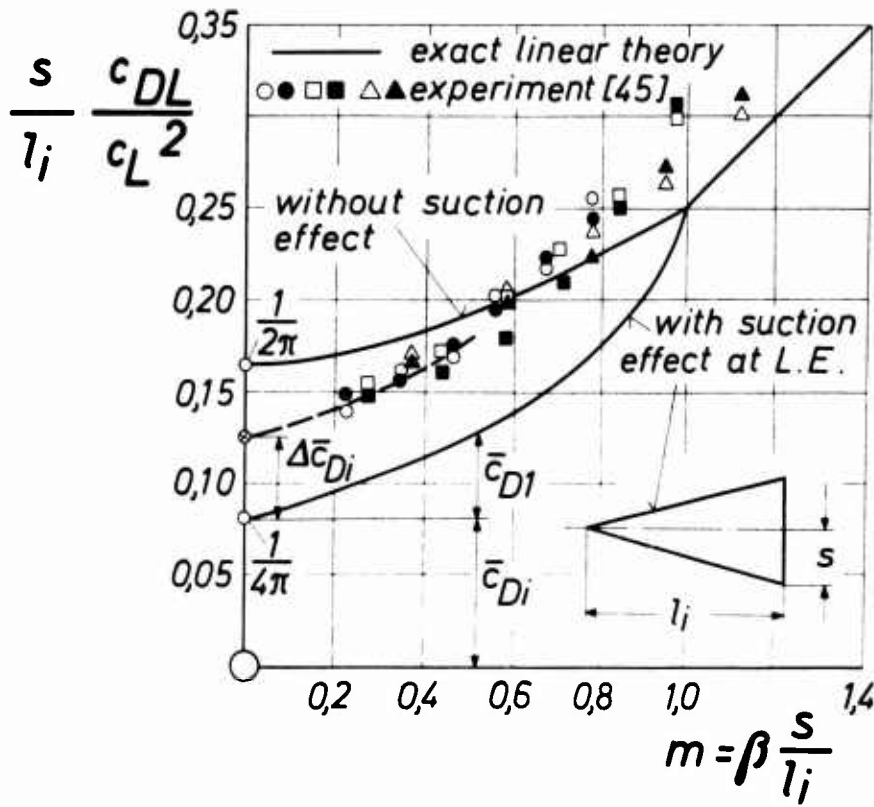


Fig. 7: Drag due to lift of plane delta wings in dependence of the relative slenderness ratio  $m = \beta s/l_i = \sqrt{Ma_\infty^2 - 1} \cdot s/l_i$  (experiment:  $\bar{\tau}_m = 0.02$ ;  $s/l_i = 1/5$  to  $1/3$ ) ( $\bar{c}_D = (s/l_i) \cdot (c_D/c_L^2)$ )

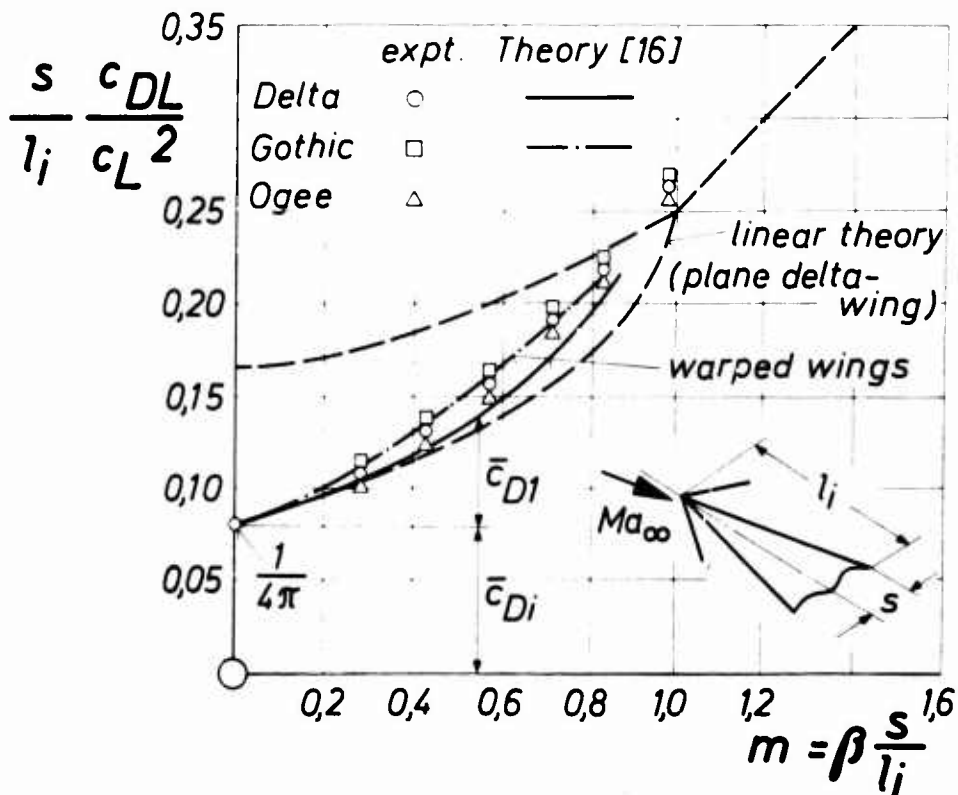


Fig. 8: Drag due to lift of warped wings showing the reduction of vortex drag by suppressing the shedding of rolled up vortices at the leading edges. (experiment:  $\bar{\tau}_m = 0.02$ ;  $s/l_i = 1/4$ )

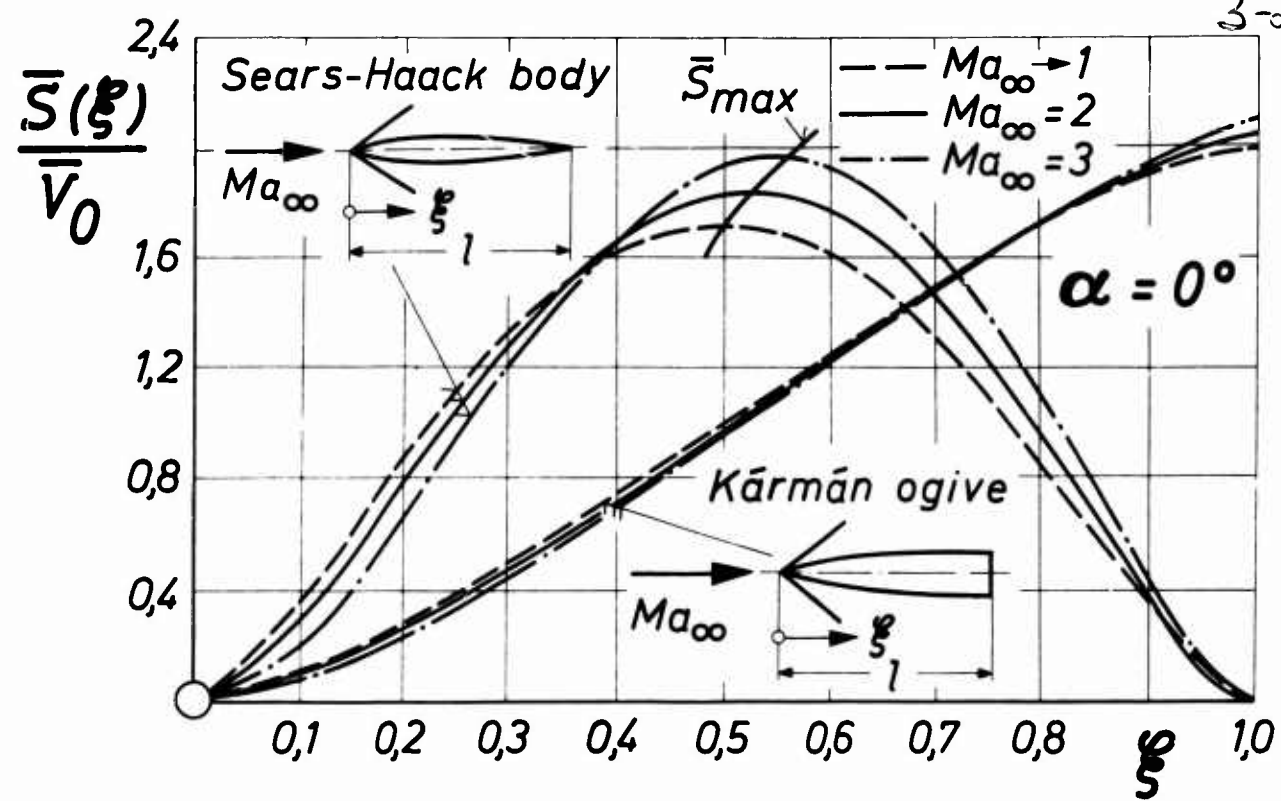


Fig. 9: Deviations in the contour geometry of the Sears-Haack body and of the Kármán ogive of given volume and length determined for minimum wave drag at higher Mach numbers.

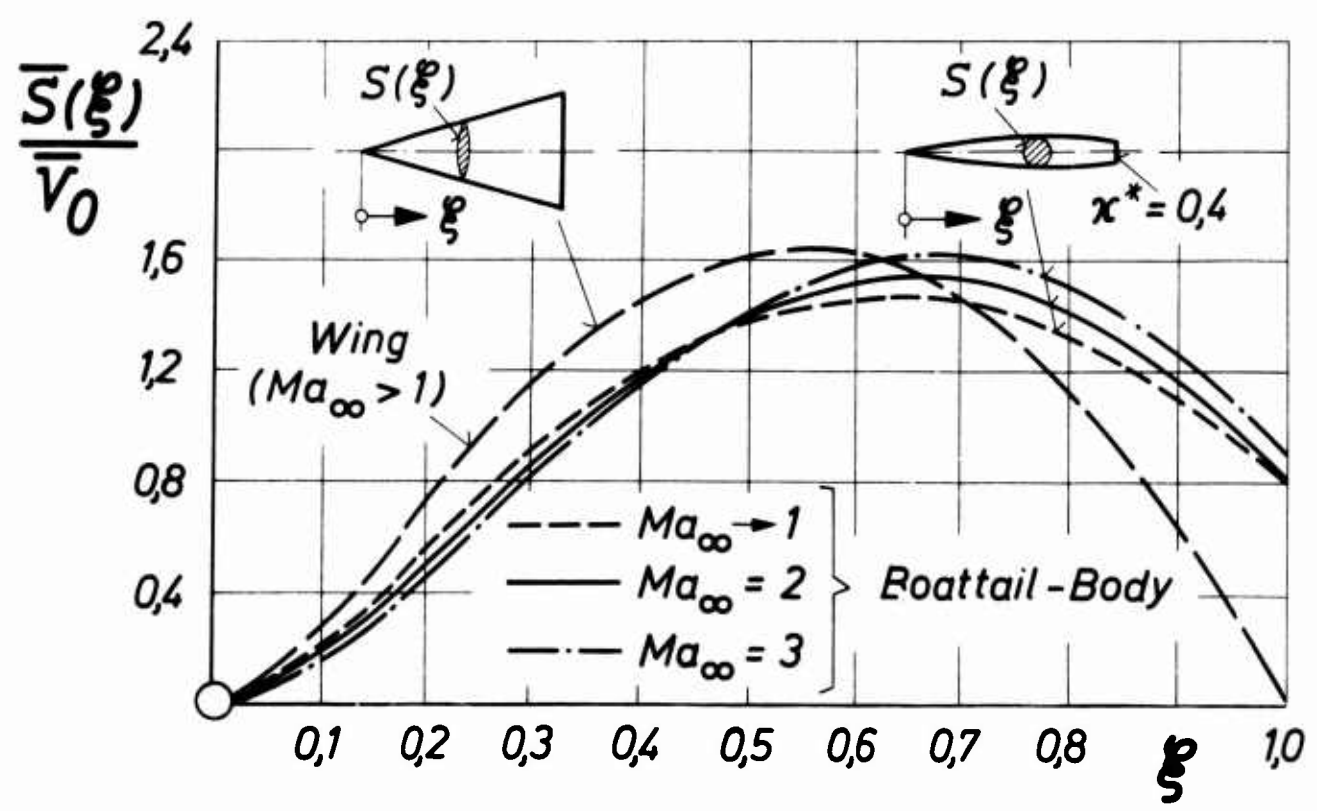


Fig. 10: Optimum volume distribution of a boat-tail body of given volume, length and base area and of a slender wing with unswept trailing edge and given volume and length for minimum wave drag in supersonic flow.

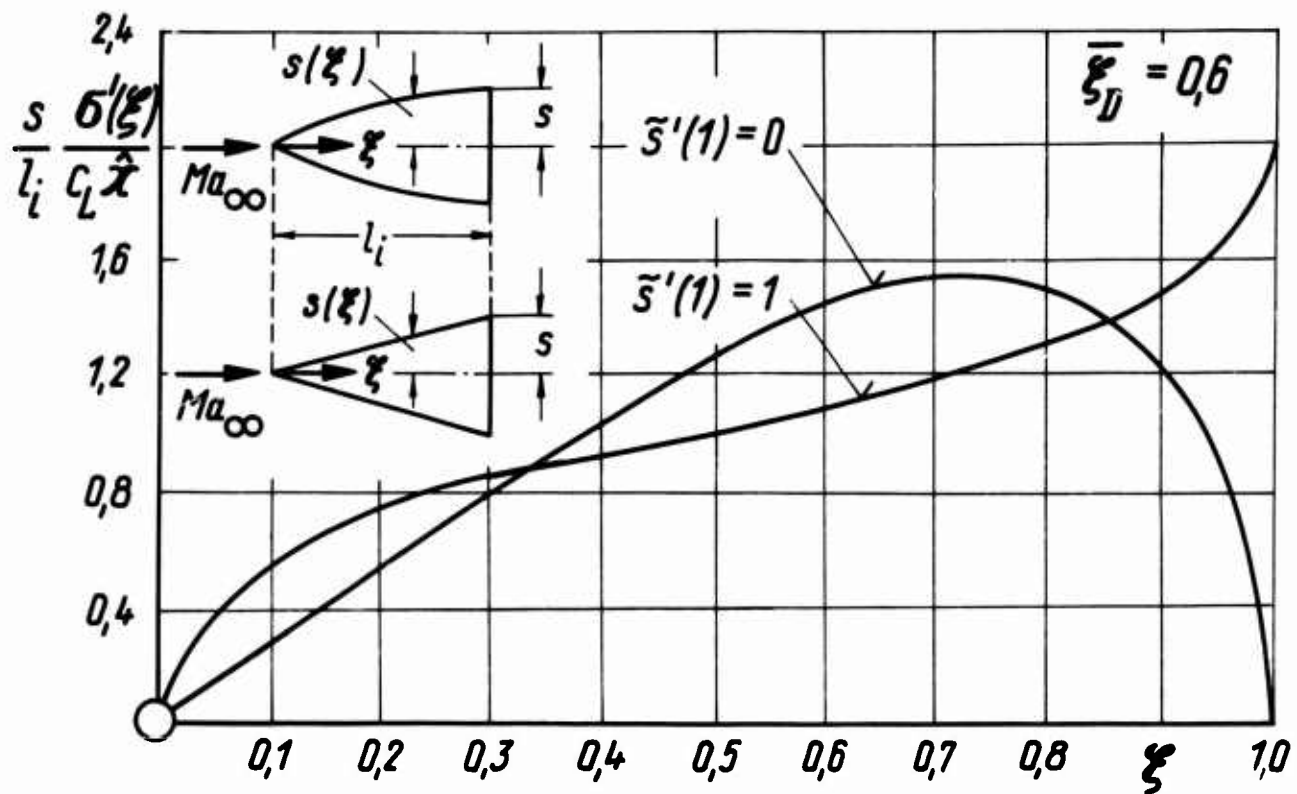


Fig. 11: Optimum lift-load distribution for minimum wave drag of thin slender wings for prescribed total lift and center of pressure in supersonic flow.

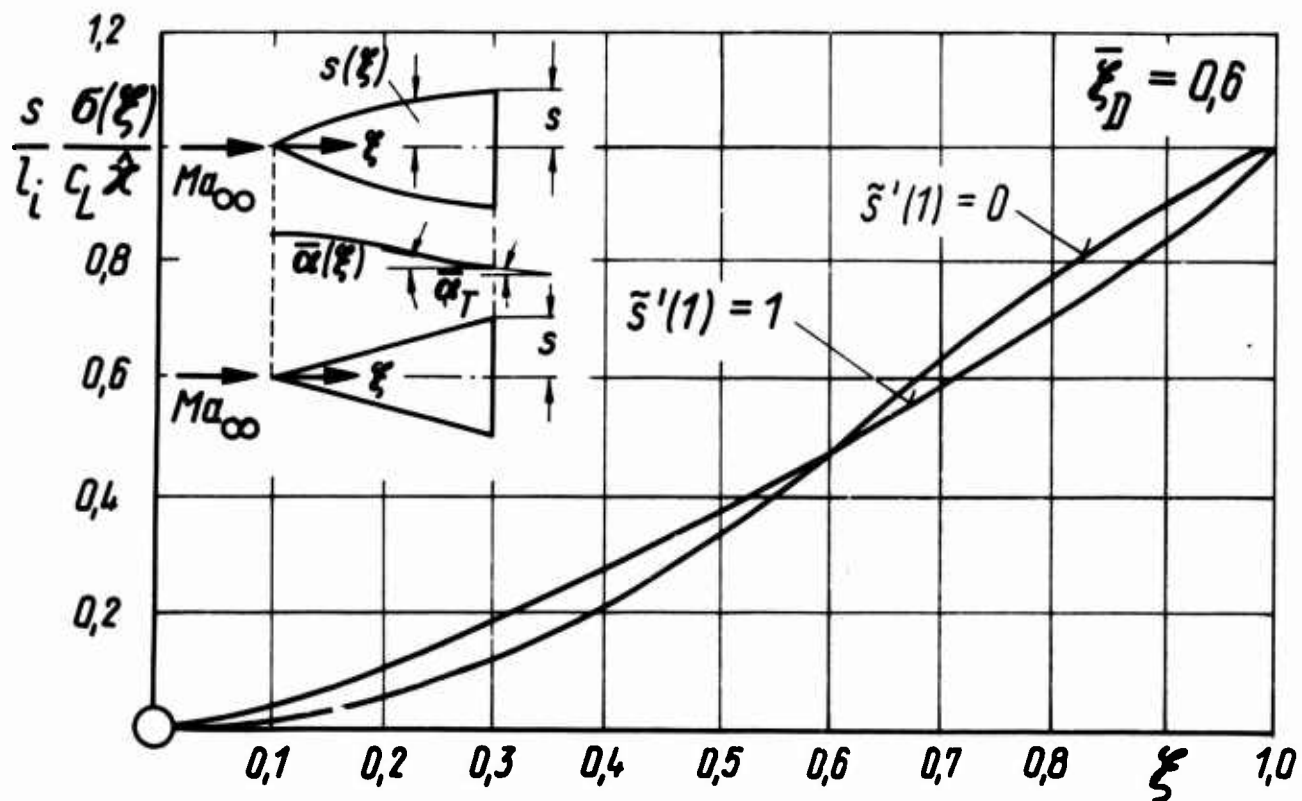


Fig. 12: Optimum distribution of the geometric parameter,  $\sigma(\xi) \sim s^2(\xi) \cdot \bar{\alpha}(\xi)$  of slender wings for prescribed total lift and center of pressure.

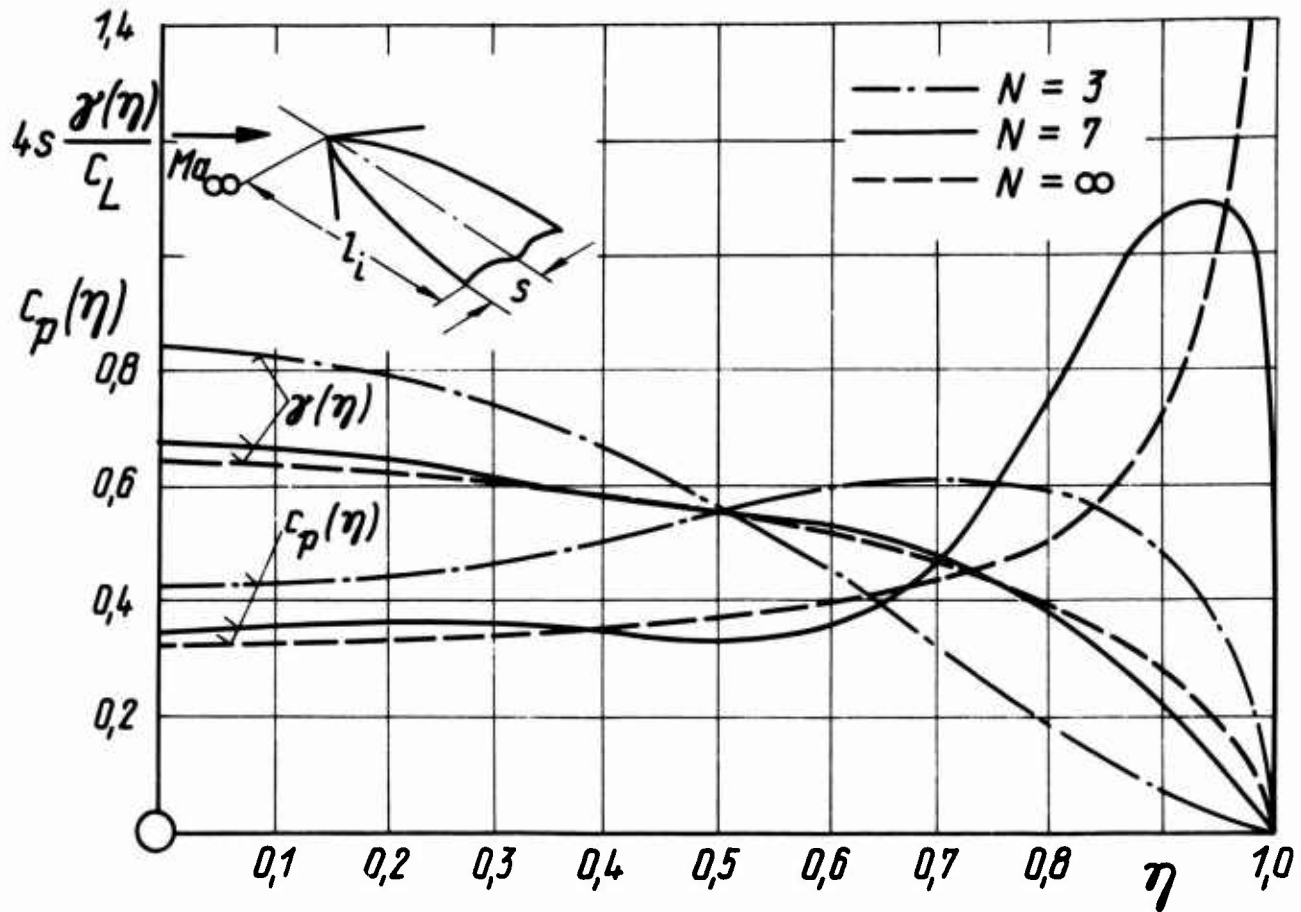


Fig. 13: Spanwise pressure and lift-distribution of wings having different modes of twisting ( $N$ -values) to suppress vortex drag.

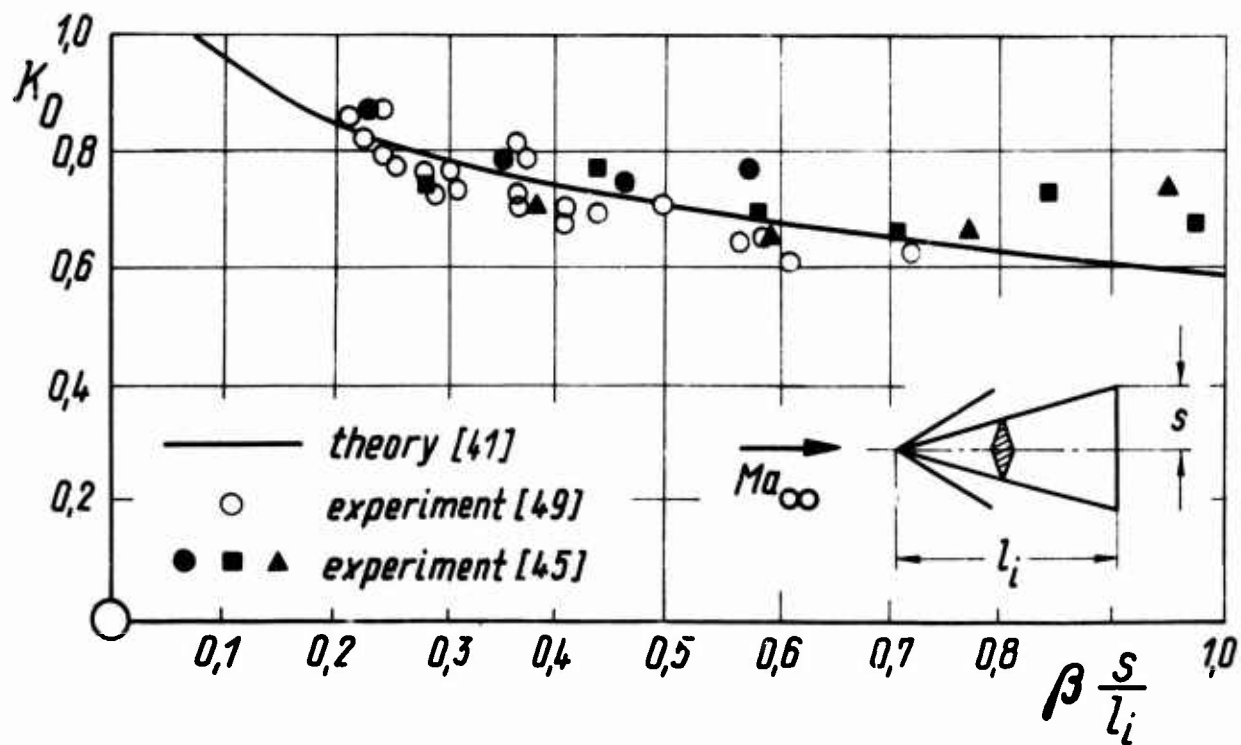


Fig. 14: Minimum wave drag due to volume of slender wings with unswept trailing edge in dependence of the relative slenderness ratio.

3-24

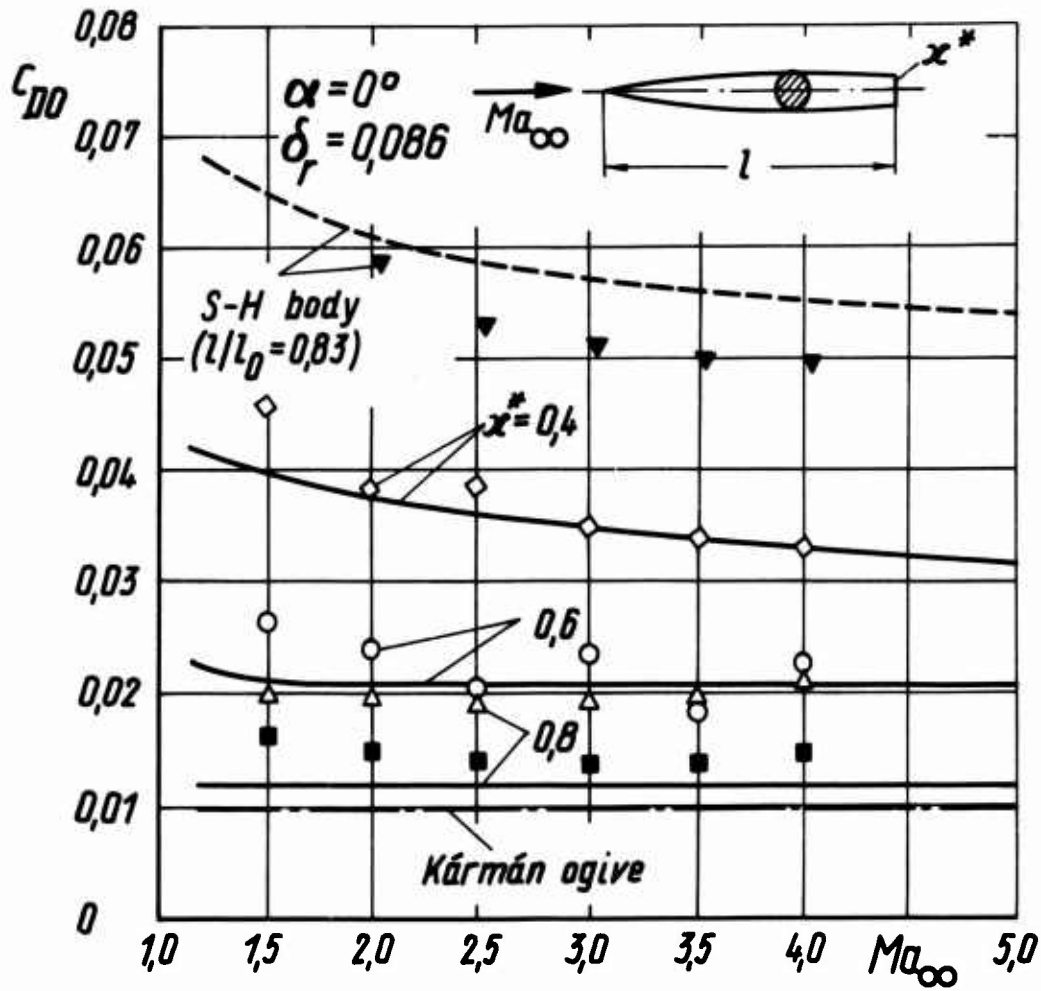


Fig. 15: Minimum wave drag due to volume of axially symmetric bodies with optimum shapes for given volume, length and base area in supersonic flow.

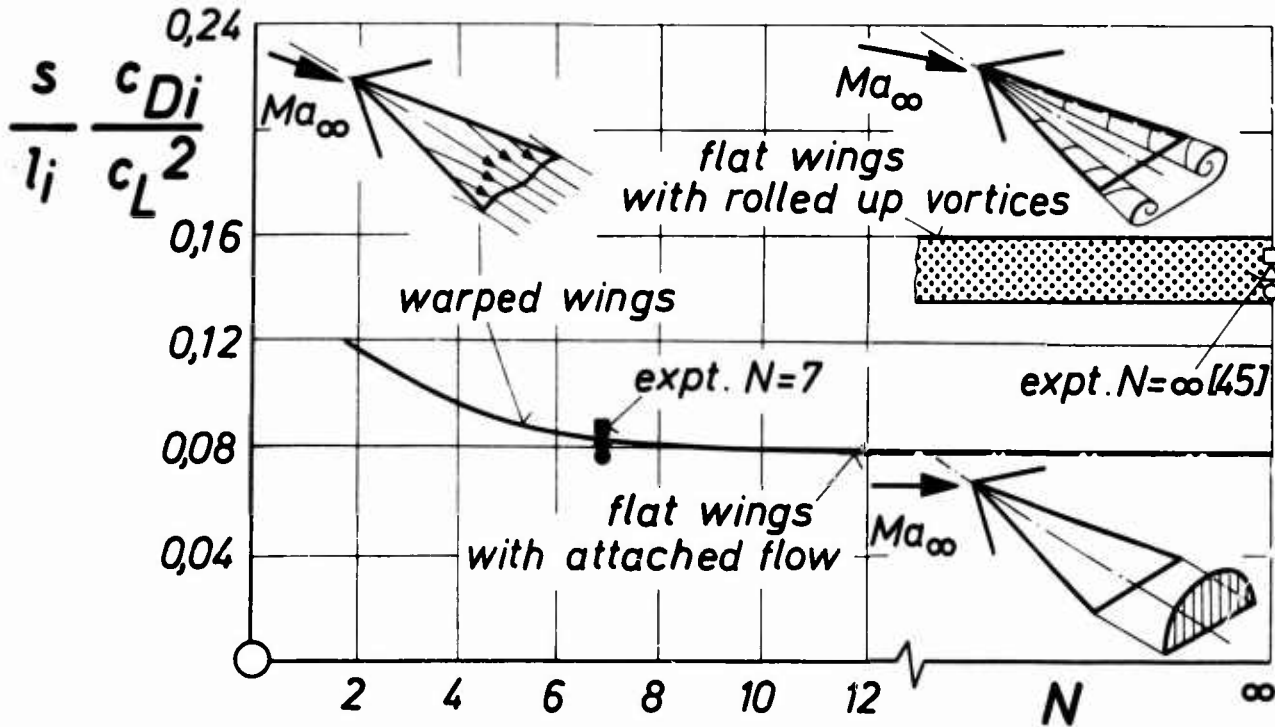


Fig. 16: Comparison of vortex drag coefficients of plane and twisted wings, showing the drag reduction due to suppression of rolled up vortices (Delta  $\bullet$  ; Ogee  $\blacktriangle$  ; Gothic  $\blacksquare$  ).

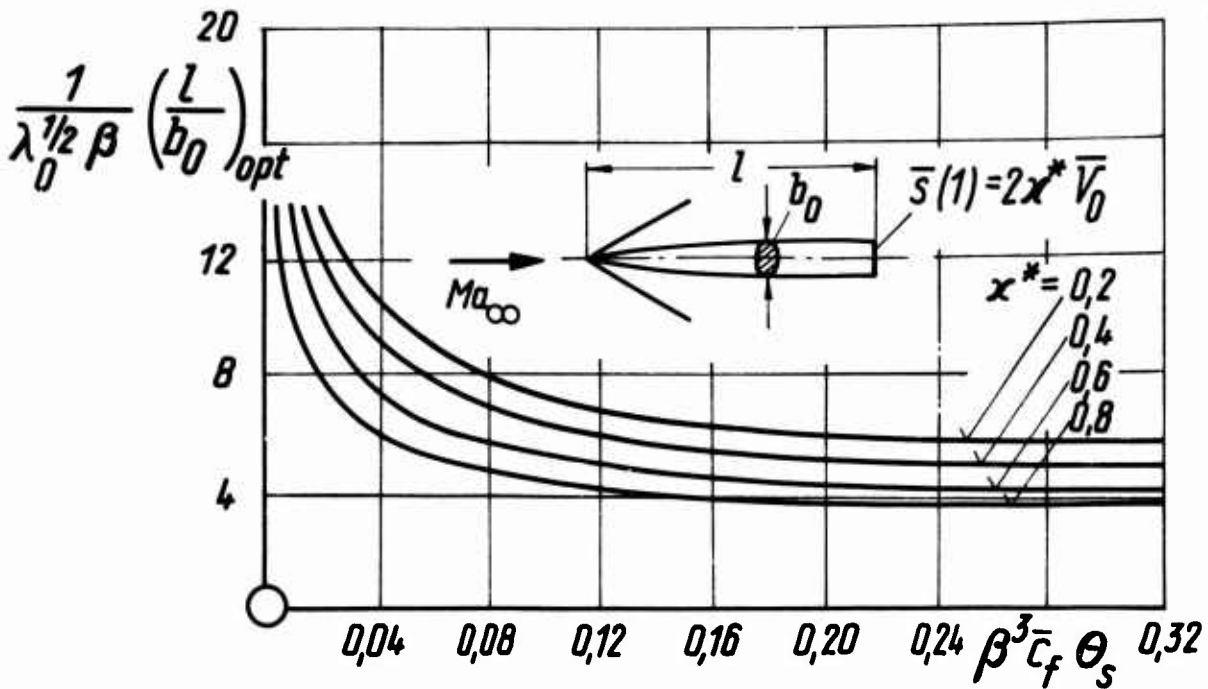


Fig. 17: The optimum slenderness ratio of bodies with given volume, cross-section shape and base area in dependence of skin friction coefficient at given Mach numbers.

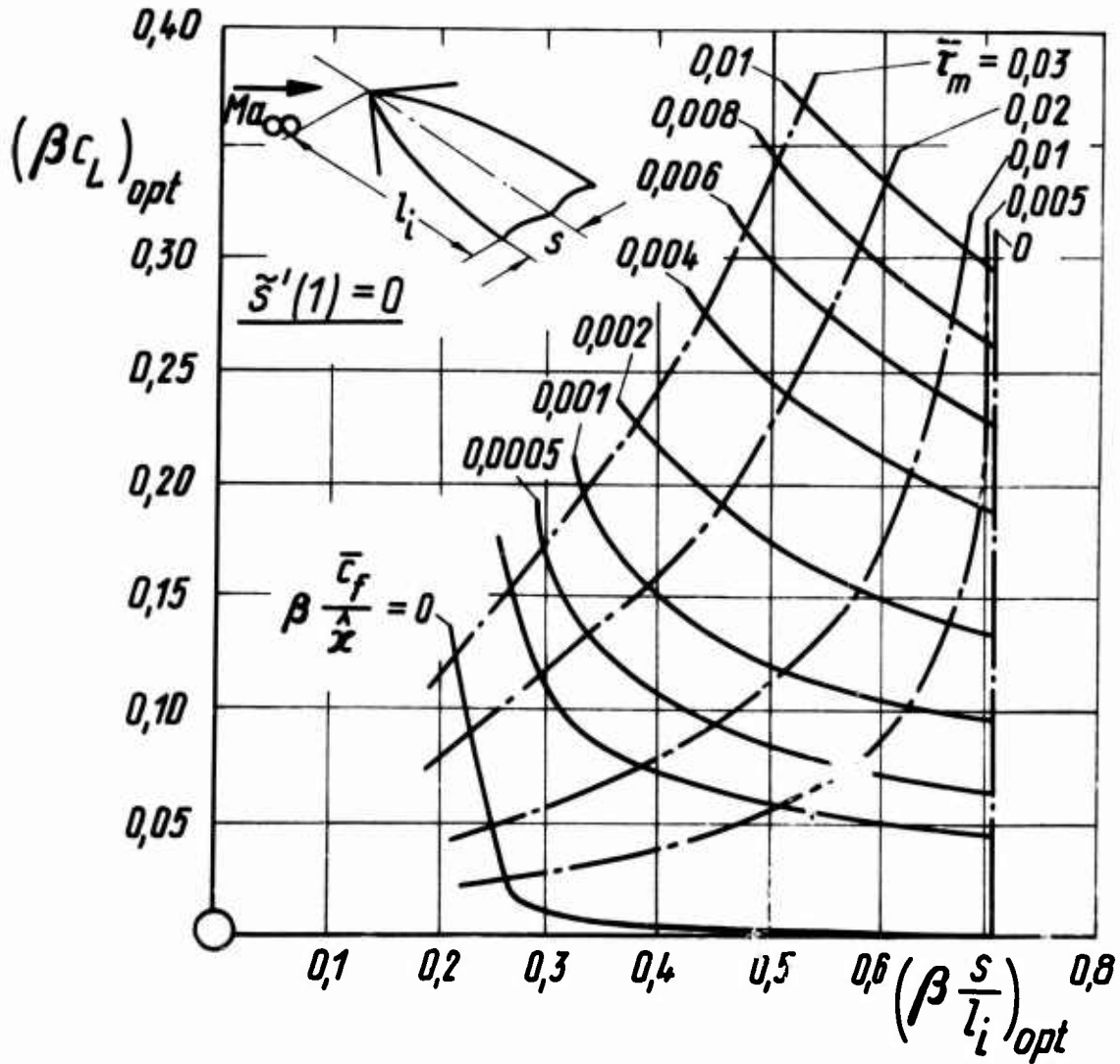


Fig. 18: Optimum matching of lift coefficients and slenderness ratios of wings in dependence of prescribed mean thickness  $\bar{\tau}_m$  and skin friction coefficient  $\bar{c}_f$  for given total lift at supersonic Mach numbers.

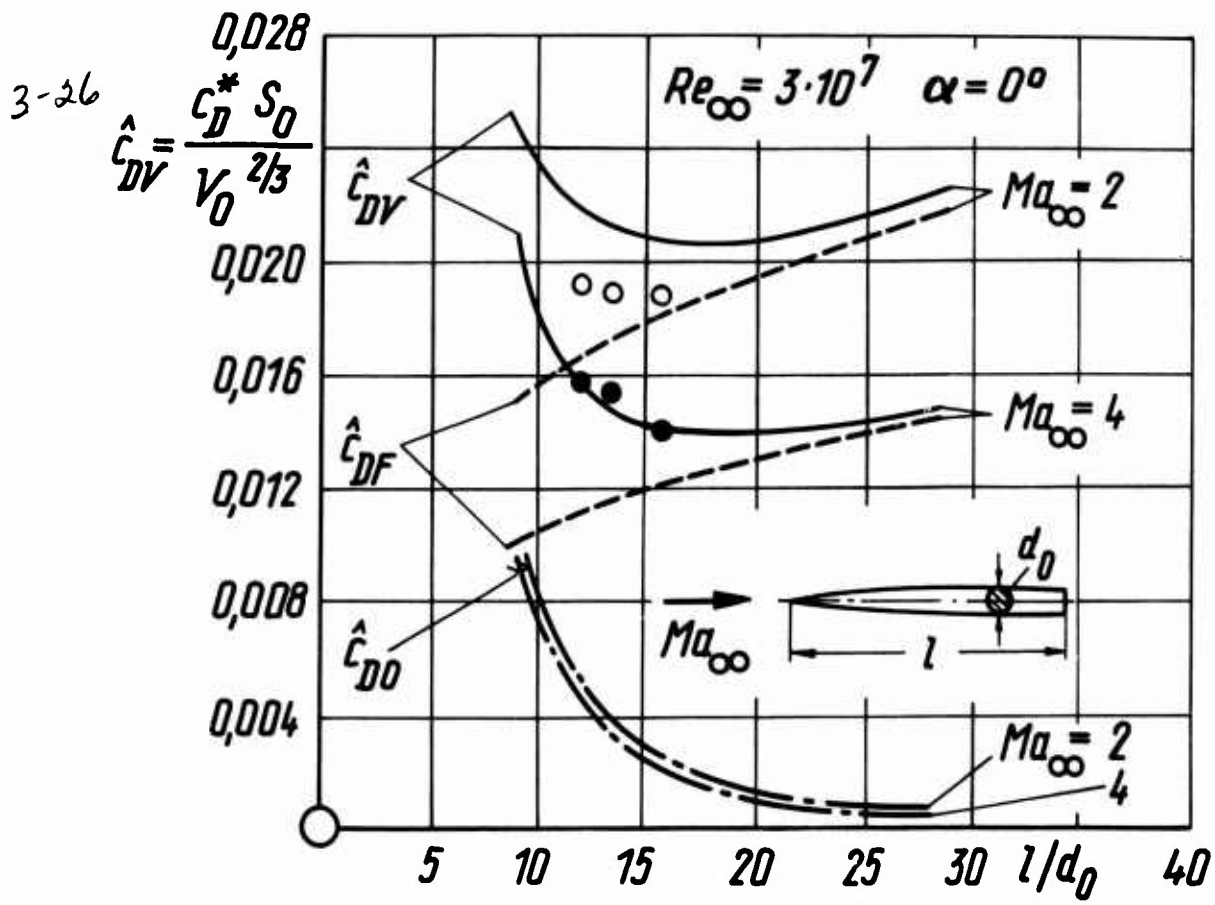


Fig. 19: Calculated and experimental values of drag coefficients for axially symmetric bodies of given volume and dimensionless base area ( $\kappa^* = 0.6$ ) in dependence of the slenderness ratio at different supersonic Mach numbers.

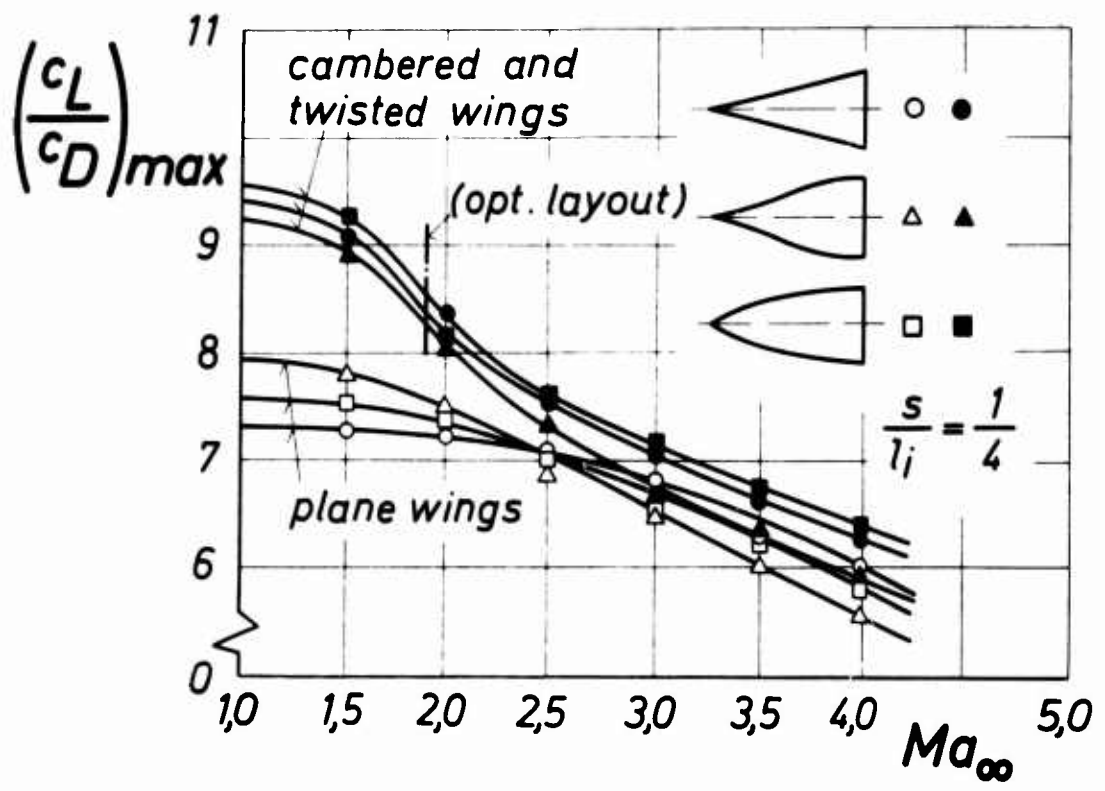


Fig. 20: Comparison of maximum lift/drag ratios of plane wings with those of cambered and twisted wings optimized for the relative slenderness ratio  $\beta s/l_j = 0.4$  ( $Ma_\infty = 1.88$ ) ( $\tau_m = 0.02$ ;  $Re_\infty = 1 \cdot 10^7$ ).

MEASUREMENTS OF THE DRAG OF SOME CHARACTERISTIC AIRCRAFT  
EXCRESCENCES IMMERSED IN TURBULENT BOUNDARY LAYERS

by

L. Gaudet

K.G. Winter

Royal Aircraft Establishment, Bedford

4-1

SUMMARY

Measurements are described of the drag of various forms of excrescence mounted on balances installed in the walls of the working section of the RAE 8ft x 8ft Wind Tunnel. The tests cover a range of Mach numbers between 0.2 and 2.8 (but not transonic) and a range of Reynolds number.

The excrescences tested include two-dimensional steps and ridges, circular cylinders and wings mounted normal to the surface, and holes and fairings. It is shown, for excrescences which are of height small compared with the boundary-layer thickness, that the scale effects on drag are well correlated in terms of the wall variables of the turbulent boundary layer, but that there is a dependence of drag on Mach number. For steps and ridges the effect of chamfering or rounding the upper corners was found to be beneficial at subsonic speeds but far less so at supersonic speeds. For circular holes the drag depends strongly upon the depth to diameter ratio.

The fairings tested were either half-bodies of revolution with pointed or rounded ends or of square or rectangular section with pointed ends. The effects of different amounts of immersion of the bodies into the boundary layer was found in some cases by testing geometrically similar bodies of different sizes.

NOTATION

A } constants in expression for drag of	M	Mach number
B } circular holes. Eqn (4)	r	radius of step or ridge
C } constants in expression for drag of	Re <sub>c</sub>	Reynolds number based on freestream conditions and chord c of stub wing
D } steps and ridges. Eqn (1)	Re <sub>d</sub>	Reynolds number based on freestream conditions and diameter d of circular cylinder
c	s	span of stub wing or circular cylinder
C <sub>D</sub>	w	width of rectangular hole
C <sub>D∞</sub>	δ	loosely, boundary-layer thickness or specifically, thickness to 99% freestream velocity (δ <sub>99</sub> )
C <sub>Dδ</sub>	ν	kinematic viscosity based on wall conditions.
c <sub>f</sub>	ρ	density at wall conditions
d	τ	surface shearing stress
F	τ'	effective shearing stress on a hole
h	u <sub>τ</sub>	friction velocity based on wall conditions = $\left(\frac{\tau}{\rho}\right)^{1/2}$
h <sup>+</sup> = $\frac{u_{\tau} h}{\nu}$		
ℓ		
ℓ		

1 INTRODUCTION

The arrival on the aviation scene of supersonic transport aircraft with a high sensitivity in performance to drag at long-range cruise conditions, and with an enormous development cost, produced a demand for estimates of drag of higher accuracy than hitherto. For one of the ingredients of the drag, that of excrescences, very little information was available. Thus, although it was anticipated that any successful aircraft should be 'clean', it was difficult to assess what allowable tolerance should be placed, for example, on steps at skin joints, or to assess what were the drag penalties of essential excrescences such as aeriels and pitot tubes. At about the same time it was becoming clear<sup>1</sup> that the drag of most current aircraft could have been lower if more attention had been paid to the avoidance of unnecessary excrescences. Even though there existed a considerable body of experimental evidence on the drag of most forms of excrescence at low speeds, mainly from the investigations of Wieghardt<sup>2</sup> and his co-workers and collated by Heerner<sup>3</sup>, there was some doubt as to the application of the results over a wide Reynolds number range. There was thus a clear requirement for an experimental programme to measure the drag of typical forms of excrescences on a surface over which flowed a turbulent boundary layer for wide ranges of both Reynolds number and Mach number. Such a programme required a wind tunnel with variable density (an advantage not enjoyed by most of the previous workers in the field) and capable of operation at subsonic and supersonic speeds. Accordingly tests were made in the RAE 8ft x 8ft Wind Tunnel at Mach numbers between 0.2 and 2.8 with a Reynolds number range of about 10 : 1 at each Mach number. The range of Reynolds number was limited in some cases by the load ranges of the balances used and, for some configurations, the maximum Mach number was restricted to 2 because of unserviceability of the high-pressure section of the tunnel compressor. A shortcoming of the tests is that transonic conditions were not covered. To obtain high Reynolds number the walls of the tunnels were used, taking advantage of the knowledge<sup>4</sup> already gained of the boundary layers there, and of the design of the strain-gauge balance used for measuring skin friction.

The excrescences tested included two-dimensional steps, ridges and grooves representing defects in skin joints, cylinders and stub wings representing aeriels and pitot tubes, circular and rectangular holes, and half-bodies representing fairings over obstructions.

2 TEST ENVIRONMENT

4-2

The drag of the various types of excrescence was measured by supporting them on balances which were mounted at four positions respectively in the sidewalls, roof and floor of the working section of the RAE 8ft x 8ft Wind Tunnel. Since some 50 configurations of excrescence were contemplated, the small interferences, which may have existed between four excrescences tested simultaneously were accepted in the interests of economic operation of the tunnel.

The turbulent boundary layer on the port side-wall of the tunnel has been investigated in great detail and its characteristics are known to be those for a flow with zero pressure gradient. Less complete (and less accurate) investigations have been made of the boundary layers on the other wall and roof and floor. Velocity profiles are not available for all four positions but skin friction measurements - which were made of necessity to define the datum drag measured by the balances - confirm that the flow in the tunnel is symmetrical. Characteristics of the boundary layers relevant to the analysis made of excrescence drag are shown in Figs 1, 2 and 3.

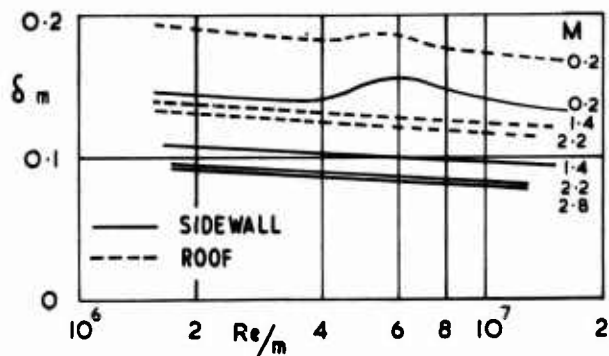


Fig. 1 Boundary-Layer Thickness

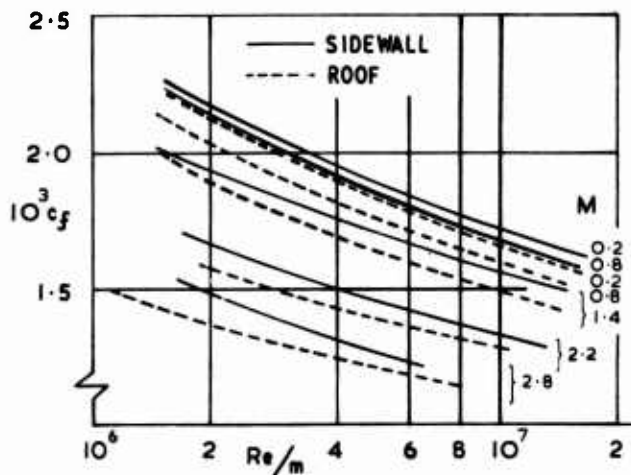


Fig. 2 Skin-friction coefficient

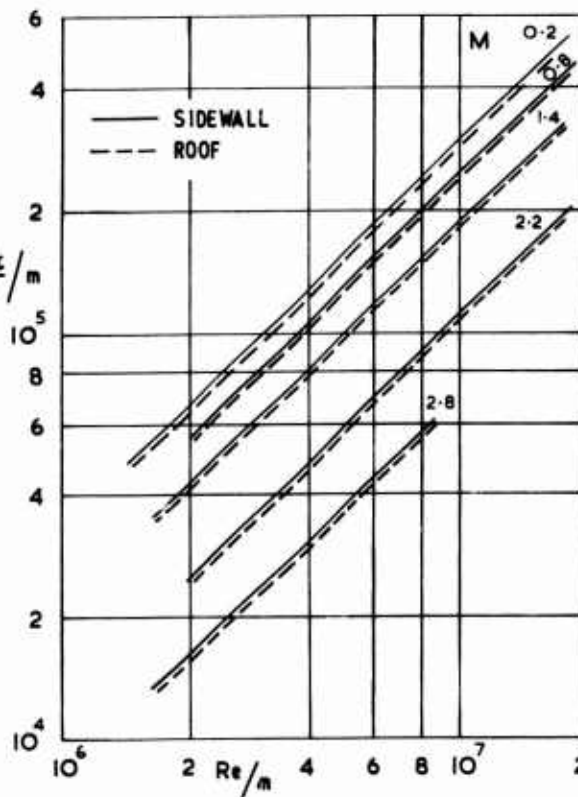


Fig. 3 Friction Reynolds Number

3 EXPERIMENTAL TECHNIQUES

The excrescences were mounted on strain-gauge balances of design similar to that previously used for skin friction measurement<sup>4</sup>. Two of the balances, used for the smaller excrescences, were capable of measuring drag loads up to 1.8 kg and two for larger excrescences, had ranges up to 18 kg. All the balances had front plates of diameter 368 mm (14.5 in).

The primary load calibrations of the balances were made in situ before and after each test by means of weights suspended on a fine cord attached to the centre of the friction plate and passing over a large diameter balanced pulley. The balance readings for zero load (for the balances mounted in the roof and floor) were adjusted to account for gravitational forces arising from the change of slope of the surfaces with change of setting of the nozzle shape with Mach number. A further correction has also been made to the readings to eliminate forces due to the pressure variations round the edge of the friction plate around which twelve pressure tapings were provided, and corrections were made for stresses induced by temperature gradients.

The three-dimensional excrescences were mounted directly on (or in, for the case of holes) the front plate of the balance. For the two-dimensional forms, the excrescence was continued on the sidewall to avoid end

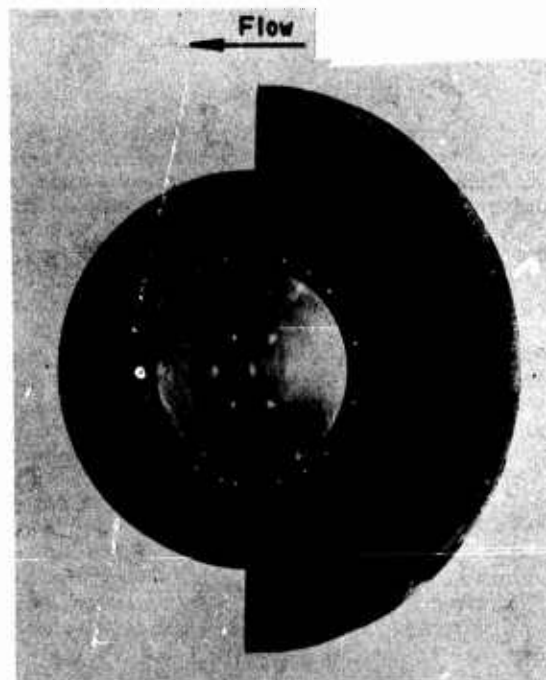


Fig. 4. Fairings for use with steps.

effects. This was straightforward for ridges but for steps necessitated a fairly large fairing attached to the tunnel wall either upstream or downstream of the balance centre-line across which the step was formed. It was checked, by making measurements with both upstream and downstream fairings in position, as shown in Fig. 4, and with a packing piece on the balance plate to maintain a continuous flush surface, that the local skin friction was not affected by the presence of the fairing. 4-3

The drag of an exorescence is given as the difference between the force on the balance with an exorescence present and the force on the clean balance in the same flow conditions. Thus the results presented include the effect of changes in skin friction on the balance but not on the tunnel sidewall.

In a summary paper such as the present one space does not permit a detailed assessment of the potential accuracy of the measurements of drag of many different exorescences at many different conditions. However, as a rough assessment of accuracy a figure of about 5% of the local skin friction on the balance plate may be taken for the small balance at average Reynolds numbers, and ten times this for the large balance.

#### 4. RESULTS

##### 4.1 Steps, ridges and grooves.

The heights of these forms of exorescence were small compared with the boundary-layer thickness being up to approximately 0.03 $\delta$ . The appropriate parameters on which the flow may be expected to depend are therefore those of the inner region of the boundary layer, as employed for example in expressing the calibrations of surface devices used to determine skin friction coefficient. Accordingly a drag parameter,  $C_D/c_f$ , is regarded as a function of a roughness Reynolds number i.e.  $C_D/c_f = f(h^+)$ , with  $h^+ = \frac{u_\tau h}{\nu}$  where  $C_D$  is drag per unit frontal area divided by freestream kinetic pressure,  $c_f$  is local skin-friction coefficient in the absence of the exorescence,  $h$  is height of exorescence and  $u_\tau$  and  $\nu$  are friction velocity and viscosity based on wall conditions. Fig 5 shows that, for a forward-facing step at a given Mach number, there is a unique line (within the scatter due mainly to fluctuations in readings) indicating a linear variation of drag parameter with the logarithm of  $h^+$ . The drag parameter increases, for a given value of  $h^+$ , with increase of Mach number up to  $M = 1.4$  or a little beyond but is apparently independent of Mach number for further increase of Mach number up to the maximum, 2.8, at which the tests were made. The values of  $h^+$  show that in all the conditions of the tests the tops of the steps are within the logarithmic region of the undisturbed turbulent boundary layer. It may be expected that the variation of the drag parameter with  $h^+$  will change for smaller step height in a way analogous to the change in character of the velocity profile in the blending region and sublayer of the boundary layer. In this connection it is worth remarking that the behaviour is different from that for distributed roughness in that there appears not to be a critical height below which no drag increment occurs. Although the present results define a logarithmic variation only for relatively small heights of step, the results of Good and Joubert<sup>5</sup> for the drag of the forward face of a fence at low speeds show that the same variation holds even when the height of the fence exceeds the boundary-layer thickness. This variation implies that neither the 'independent drag coefficient' of Hoerner<sup>3</sup> in which the kinetic pressure used in forming the coefficient is the mean over the height of the step in its absence, nor a drag coefficient based on the velocity at the top of the step is constant over a range of height. In the range of  $h^+$  from 40 to 1000 the former varies at low speed between 0.36 and 0.58 and the latter between 0.17 and 0.41.

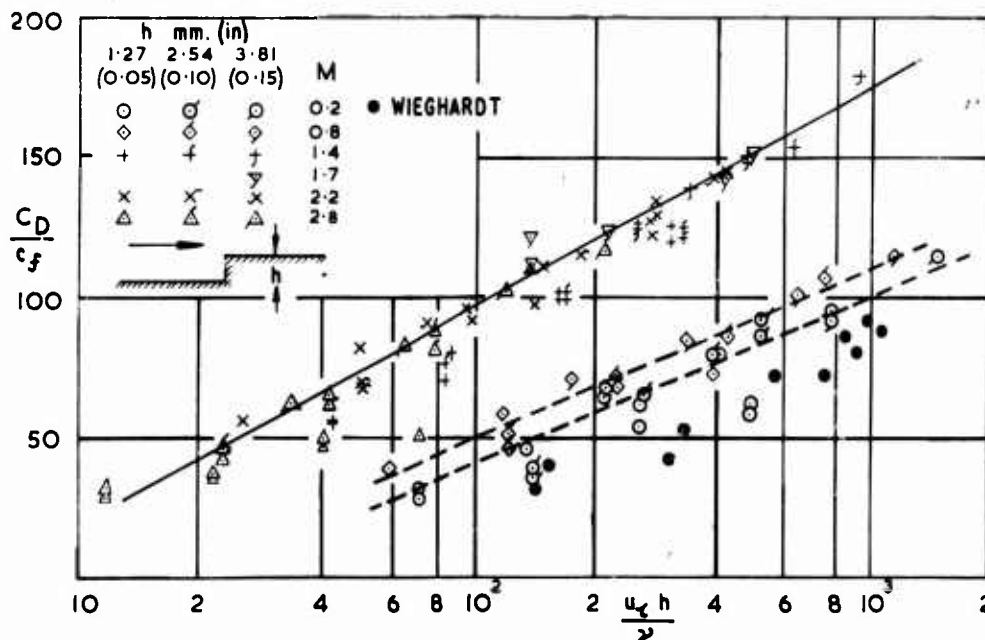


Fig. 5 Forward-facing steps - plain

A detailed survey of previous work has not been made but similar logarithmic variations can be deduced from a selection of measurements from other sources. The results of Wieghardt<sup>2</sup> at low speeds are shown on Fig. 5 and have somewhat lower values of drag. The results of Good and Joubert<sup>5</sup> give values of drag about 50% higher than the present results. They are, of course, for a different configuration and were obtained from pressure measurements thus excluding changes in skin friction on the datum surface.

At supersonic speeds drag deduced for example from the pressure measurements of Kepler and Bogdonoff<sup>6</sup> and Vas and Bogdonoff<sup>7</sup> at Mach numbers of 2.92 and 3.85 is roughly in accord with the present analysis. The calibration of razor-blade surface pitot-tubes expressed in the form of Fig. 5 also is roughly in agreement.

The measurements of Czarnecki et al.<sup>8</sup> of the drag of repeated steps at  $M = 1.61$  on a body of revolution give lower drag, as would be expected qualitatively because of interference between the steps.

The effect of rounding the upper corner of the steps is shown in Fig. 6. The full and broken lines are for values of  $h^+$  of 1000 and 200 respectively. It can be seen that at subsonic speeds a small amount of rounding produces worthwhile reductions in drag. For example the drag is roughly halved for a radius equal to one third of the height. For supersonic speeds the drag reduction is much smaller. A similar difference between the behaviour at subsonic and supersonic speeds occurs for the effect of chamfering as shown in Fig. 7.

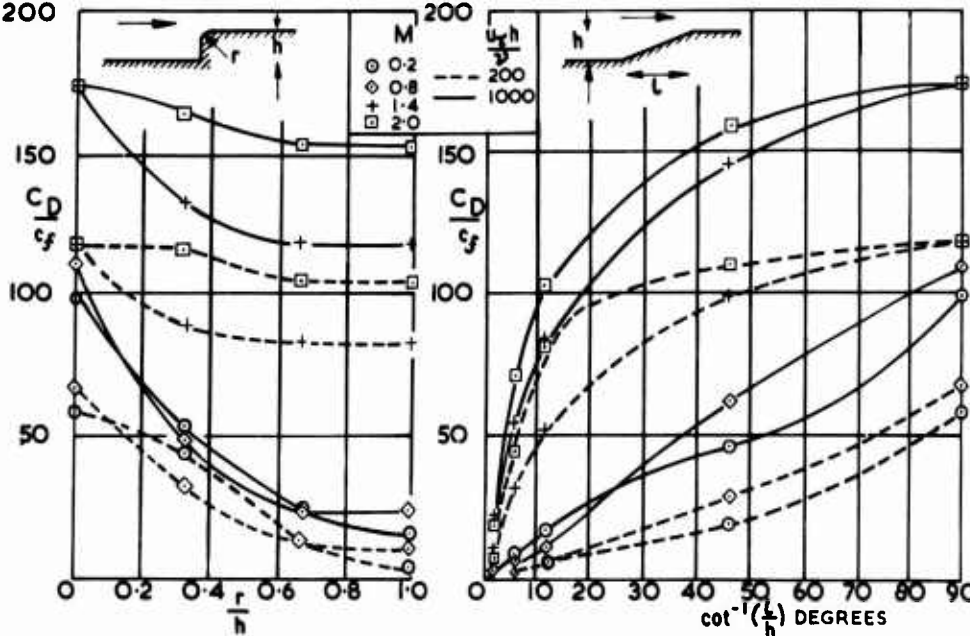


Fig. 6 Forward-facing steps - effect of rounding

Fig. 7 Forward-facing steps - effect of chamfering

This difference in behaviour is perhaps not surprising if the effective wedge angle, which would give the measured drag of a plain step in inviscid flow at supersonic speeds is evaluated. At  $M = 2$  and  $h^+ = 1000$  this angle is only 13 degrees. Thus if the flow attaches on a rounded step at the same angle a radius equal to the step height produces an effective reduction in height of only 3%, and the effect of a chamfer would not be expected to be very great until the angle was reduced to a value of the same order as the effective separation angle.

The drag of rearward-facing steps has been plotted in the same way in Fig. 8. Mean lines only are shown to avoid confusing the figure. The scatter of the experimental points is in fact slightly greater than in Fig. 5. The measurements at  $M = 1.7$  and  $2.0$  which were taken in a different set of tests from the

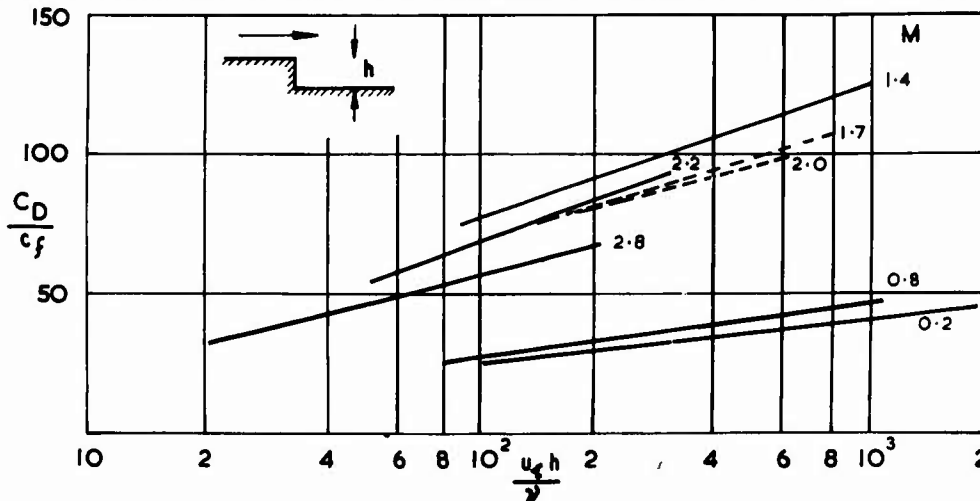


Fig. 8 Rearward-facing steps - plain

body of the results show some inconsistency with the other results. The drag parameter varies linearly with the logarithm of  $h^+$  as for forward-facing steps but the variation with Mach number is different. At a given value of  $h^+$  the drag parameter increases with increase of Mach number from low speeds to reach a maximum at about  $M = 1.4$  and then falls again at higher Mach numbers. This type of behaviour had been noted previously by Hastings<sup>7</sup> in his measurements of base drag. His results at supersonic speeds are in fair agreement with those in Fig. 8. As for forward-facing steps the results of ref 8 give lower drag. At low speeds the results agree well with those of Sieghardt<sup>2</sup> but not of Tani et al.<sup>10</sup>.

The effect of chamfering the rearward-facing step was tested (Fig. 9) but not of rounding. At low speeds, for the lower value of  $h^+$  shown, there appears to be a small penalty for a small amount of chamfer and there is little reduction in drag unless the chamfer angle is reduced to about 20 degrees. This result is confirmed by some measurements of Sieghardt<sup>2</sup>. The drag increase does not occur at supersonic speeds but no substantial benefit is obtained unless the chamfer angle is reduced below 10 degrees.

For the drag of square ridges mean lines only are shown in Fig 10. Also shown as broken lines in the figure are results for rectangular ridges of width  $2h$ , which were taken as a basic section to investigate the effects of rounding since a limiting semi-circular shape was thus obtained with  $r = h$ . The drag of ridges may be compared with the sum of that of forward and rearward-facing steps. For square ridges at low speeds interference between the flows over the two faces leads to a drag parameter about 50% greater than the sum for the separate faces but the interference diminishes at supersonic speeds and is virtually zero at  $M = 2.8$ . Little previous published data has been found with which comparisons can be made. Again, the results at low speeds are in good agreement with Wieghardt<sup>2</sup>, and the drag is slightly less than found by Good and Joubert<sup>5</sup> for a fence. The results for rectangular ridges have lower slope than those for square ridges but have the same characteristic variation with Mach number.

The effects of rounding the top corners of the ridges are shown in Fig. 11. It can be seen that at both subsonic and supersonic speeds there is an optimum in the radius of about  $r = 0.6h$ . The optimum is clearly defined at low speeds but becomes less pronounced at supersonic speeds.

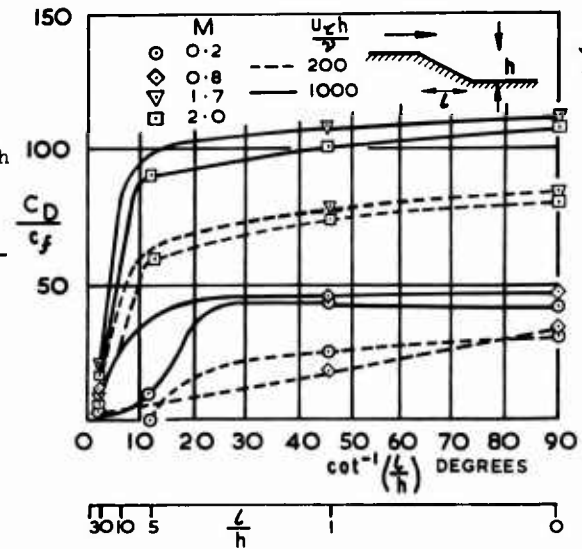


Fig. 9 Rearward-facing steps - effect of chamfering

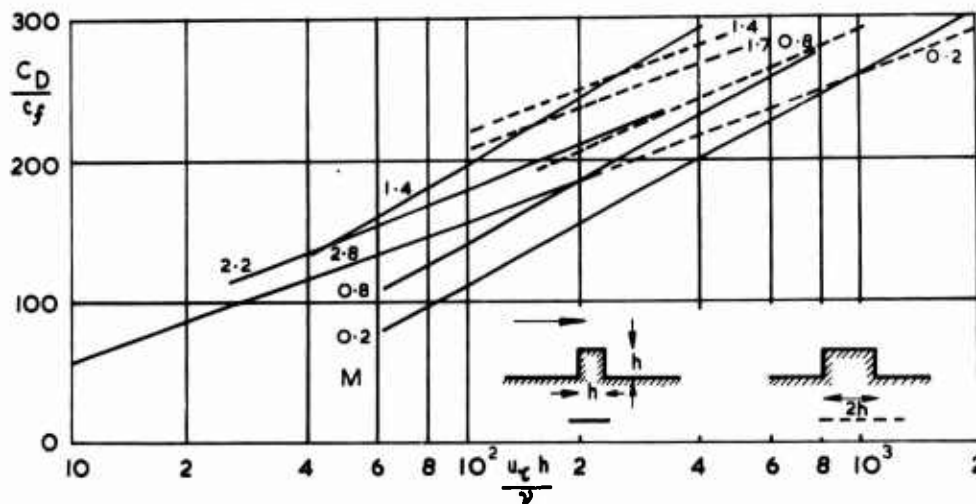


Fig. 10 Plain ridges

No previous information showing this detail has been found but the results for a semi-circular ridge are again in close agreement with those of Wieghardt<sup>2</sup> (even in showing a non-linear variation with  $\log h^+$ , a feature not brought out in the presentation of Fig. 11).

For sharp-edged steps and ridges, the drag may be estimated from the formula

$$\frac{C_D}{C_f} = C \log h^+ + D \quad (1)$$

where C and D have values as given below

	M	0.2	0.8	1.4	2.2	2.8
Forward Step	C	60	60	80	80	80
	D	-80	-70	-65	-65	-65
Rear Step	C	16	20	48	50	35
	D	-6	-13	-18	-30	-12
Square Ridge	C	150	150	160	110	100
	D	-190	-160	-125	-42	-44

For grooves the drag increments were small and the accuracy of the measurements consequently poor. For grooves in the direction of the flow the drag increase measured by the balance was roughly equal to the local skin friction acting on the increased surface area, that is on the sides of the groove. For grooves normal to the flow a drag coefficient has been defined based on the surface area of the groove and a Reynolds number on the width of the groove  $l$ . Approximately the drag is given for all Mach numbers tested (0.2, 0.8, 1.4, 2.2, 2.8) and for three widths of groove ( $l/h = 1, 2, 3$ ) with  $h \geq 0.03\delta$  by the formula  $\frac{C_D}{C_f} = 2 \log \frac{u_* l}{\nu} - 2$  within the range  $10 < \frac{u_* l}{\nu} < 10^5$ . The measurements are not sufficiently accurate to determine the effect of variation in  $l/h$  but the formula above is roughly

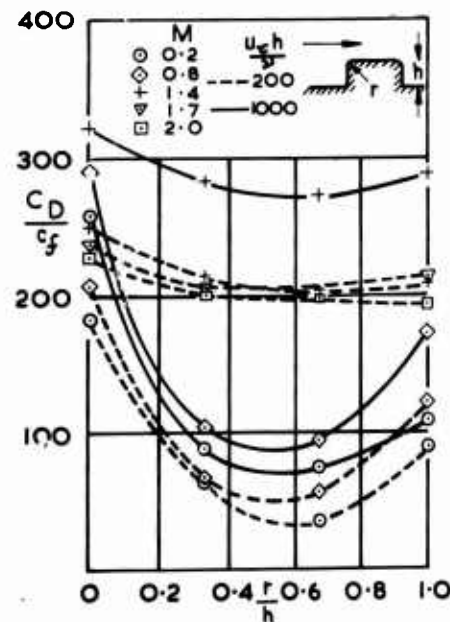


Fig. 11 Ridges - effect of rounding

4-6

consistent with the drag found for rectangular holes and shown in Figs. 14. and 15.

Except at very low Reynolds number the drag of a long groove normal to the flow is thus greater than that of the same groove along the flow. This result differs from that of Wieghardt<sup>2</sup> for screw slots. The difference is attributed to the drag of the ends of the slots being included in Wieghardt's measurements but not in those of the present work.

#### 4.2 Circular Holes

The flow pattern within a hole is of a complex three-dimensional nature and will depend upon the conditions of the flow approaching the hole and the geometry of the hole. It is unlikely that any simple analysis will be capable of describing all the possible flow patterns. For example for very shallow holes, reattachment of the flow leaving the forward edge will occur with subsequent further separation as the downstream edge is approached. In fact it was found that for the shallowest holes tested a fair estimate of the drag could be made by assuming that the pressure variation on the vertical face of the hole was that of forward and rearward facing steps multiplied by the square of the cosine of the local angle of sweep of the edge of the hole. For deeper holes complex vortex patterns will occur within the holes. However, in some way the flow within the hole will be driven by the shear stresses across the face of the hole and these shear stresses will be related to those in the boundary layer approaching the hole. An analysis has therefore been made by considering the drag of the hole as arising from an effective shear stress  $\tau'$ , and this has been non-dimensionalised by the shear stress  $\tau$  in the approaching boundary layer, so that an incremental drag parameter  $\frac{C_D}{c_f} = \frac{\tau'}{\tau} - 1$  has been defined. Here,  $C_D$  is the drag coefficient based on the planform area of the hole and  $c_f$  is the skin-friction coefficient of the approaching boundary layer. The drag parameter will depend upon a Reynolds number of the flow across the hole, (taken as  $\frac{u_\tau d}{\nu}$ , where  $d$  is the hole diameter), the Mach number of the flow and the hole depth. Thus we may take

$$\frac{C_D}{c_f} = F\left(\frac{u_\tau d}{\nu}, \frac{h}{d}, M\right) \quad (3)$$

Inspection of the results for each hole and each Mach number over a range of Reynolds numbers showed that they could be expressed as

$$\frac{C_D}{c_f} = A\left(\frac{u_\tau d}{\nu}\right)^B \quad (4)$$

where  $B$  was found to depend upon Mach number but was sensibly independent of hole depth, whilst  $A$  depends strongly upon both Mach number and hole depth. Values of  $A$  and  $B$  are shown in Fig. 12. There is a practical interest in the drag of holes with depths greater than the maximum of  $\frac{h}{d} = \frac{1}{3}$  of the present tests. The results of previous work at low speeds has therefore been analysed in terms of eqn. (4). In making the analysis it has been necessary to estimate skin-friction coefficients and to assume that the values of  $B$  obtained from the present results could be taken even though the Reynolds numbers were lower. Values of  $A$  derived from the measurements of Wieghardt<sup>2</sup> agree with the present findings in the region of overlap and are shown in Fig. 12. Consistent values (not shown) have also been obtained from the tests of Tillmann<sup>11</sup> and Friesing<sup>12</sup>. These tests covered a wide range of values of  $d/\delta$ , the ratio of hole diameter to boundary layer thickness and the values of  $A$  show no strong dependency upon this parameter. The extension of the results to larger values of  $\frac{h}{d}$  reveals a strong, almost cyclical, variation of  $A$  with  $\frac{h}{d}$ .

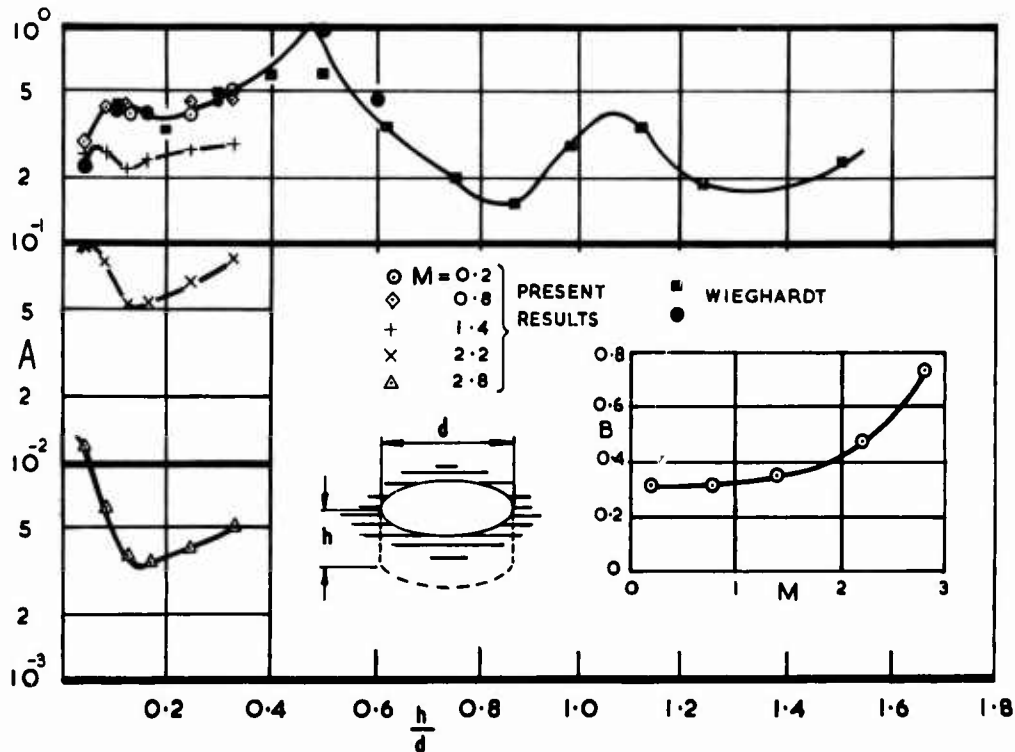
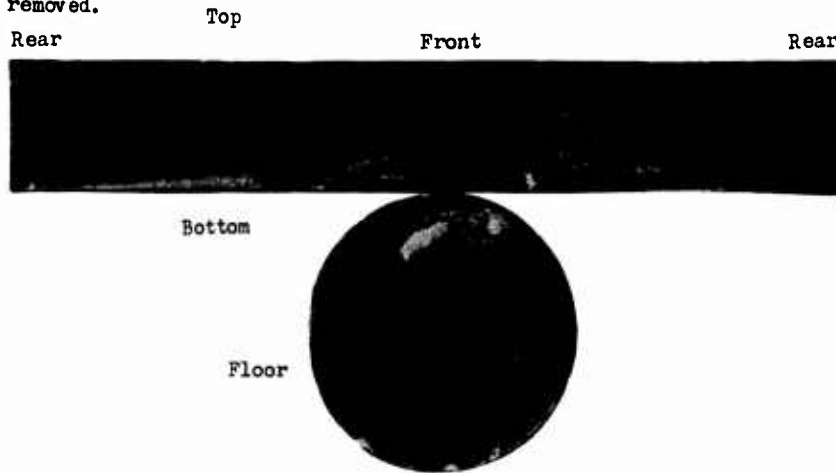


Fig. 12 Circular holes

$$\frac{C_D}{c_f} = A\left(\frac{u_\tau d}{\nu}\right)^B$$

A brief oil-flow study has been made of the flow in holes in an attempt to find the flow patterns associated with this variation. The study was made in a small blower tunnel and it is not known if the drag variations implied by Fig. 12 actually occur in the study. However in view of the apparent generality of Fig. 12 it is assumed that this is likely. The oil-flow pattern for a hole of depth : diameter ratio,  $\frac{h}{d} = 0.47$  was found to have a unique character compared with patterns for other holes in the range tested, ( $0.1 \leq \frac{h}{d} \leq 1.3$ ). A photograph of the pattern is given in Fig. 13 in which a lining to the hole is shown removed.



The photograph implies the existence of two vortex sheets, the upper one rolling up from a spiral point on the starboard wall, and presumably engulfing the lower sheet, emanating from the floor, in the rolling-up process. The coiled sheet appears to lie across the hole at about  $45^\circ$  to the stream direction, and its field to sweep new fluid into the hole roughly normal to its axis, as indicated by the streamlines on the floor. This powerful interchange of fluid presumably could account for the high drag but the reason for the formation of the pattern is not understood. It should be noted that, though the pattern showed a preference for the asymmetry as shown in the photograph, patterns of the opposite hand occasionally occurred.

Fig. 13 Oil-flow pattern in circular hole  $\frac{h}{d} = 0.47$

4.3 Rectangular Holes.

A few measurements have also been made with rectangular holes. Samples of the results are shown in Figs. 14 and 15 at one Reynolds number only,  $\frac{u_\infty \ell}{\nu} = 2 \times 10^4$  where  $\ell$  is the length of the hole in the stream direction. Insufficient combinations of planform aspect ratio and depth to length ratio were tested to make any comprehensive analysis possible. In Fig 14 values of the drag parameter  $C_D/c_f$  are plotted against  $h/\ell$ . The measurements show a trend of decreasing drag with increase of depth ratio. This trend is genuine for the three points with planform aspect ratio of 0.4 but may be coincidental for the points with aspect ratios of 1 and 2.5. As a check on this, results from Friesing<sup>12</sup> for holes with varying depth ratio are shown.

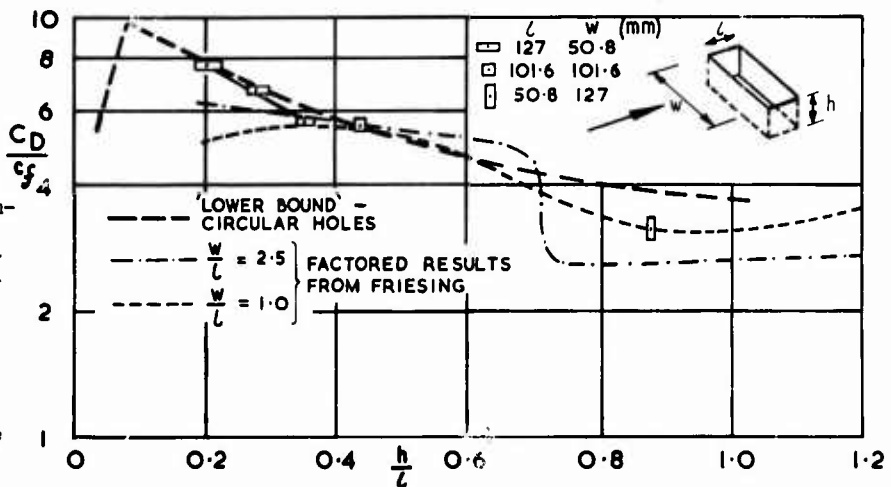


Fig. 14 Rectangular Holes  $M = 0.2$   $\frac{u_\infty \ell}{\nu} = 2 \times 10^4$

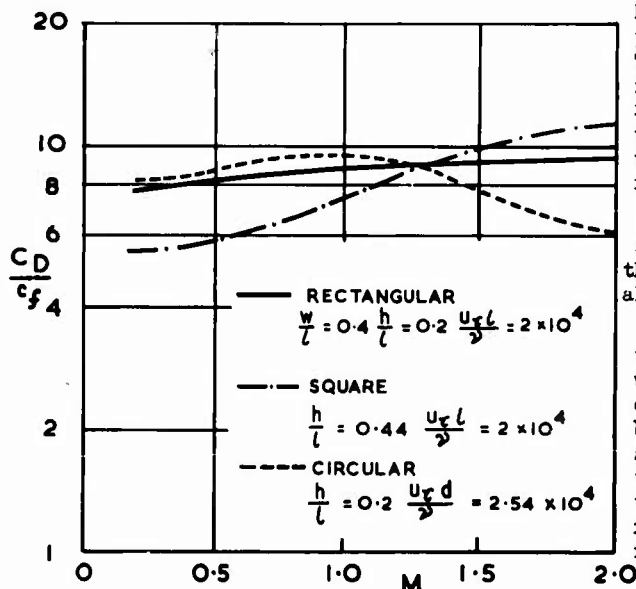


Fig. 15 Rectangular Holes - Variation of drag with Mach number

These results are at different Reynolds numbers and have simply been scaled so that the curves on Fig. 14 pass through the points of the present measurements. The curves imply that the trend, whilst not being unique for different aspect ratios, is followed roughly. It is interesting to note that, if a 'lower bound' is fitted to the oscillatory curve of Fig. 12 and the variation of the drag parameter on the lower bound for circular holes is then estimated at a mean Reynolds number of  $\frac{\pi}{4} \frac{u_\infty d}{\nu} = 2 \times 10^4$ , the general trend of the results for rectangular holes is well matched. This result suggests that at low speeds the drag of a circular hole will generally exceed that of a rectangular hole.

In Fig. 15 the variation of the drag of two particular holes with Mach number is shown and compared with the variation for a circular hole (of depth chosen so that the variation is not unduly influenced by the oscillatory characteristics). At subsonic speeds the drag of the circular hole diminishes whilst the drag for the square and rectangular holes continues to rise. This trend is contrary to that found by McGregor<sup>13</sup>. Further work is needed to resolve the discrepancy and to put the estimation

of the drag of rectangular holes on a firmer basis. McGregor's investigations concentrated on determining the effects of acoustic resonance on drag. The present results may be influenced by such effects but no evidence of their occurrence made itself obvious in the tests.

4.4 Circular cylinders.

The flow past a circular cylinder normal to a wall is also very complex. At the base of the cylinder separation of the approaching flow leads to the formation of one or more horseshoe vortices wrapped round the front of the cylinder, and trailing in the downstream direction. If the flow is supersonic there will also be complicated shock patterns produced by the interaction of the bow shock of the cylinder and the boundary layer. Further out from the wall the variation of the drag along the cylinder will still not be simple since, even with the assumption that the drag may be treated stripwise, the local drag will depend upon the local values of kinetic pressure, Mach number and Reynolds number. An attempt has been made in the analysis to take account of these various factors in an empirical way, ignoring of necessity the development of a proper model of the flow.

For cylinders which are very short with respect to boundary layer thickness, the drag is roughly the same as that of shallow holes, and can be estimated approximately in the same way by using the information on the drag of steps, with a factor for the angle of sweep of the vertical faces. This approach may be considered as a drag analogue to the law of the wall for the velocity profiles of a turbulent boundary layer. The analogy with velocity profiles has been extended for longer cylinders by an attempt to establish a drag defect function as suggested by Good and Joubert<sup>5</sup>.

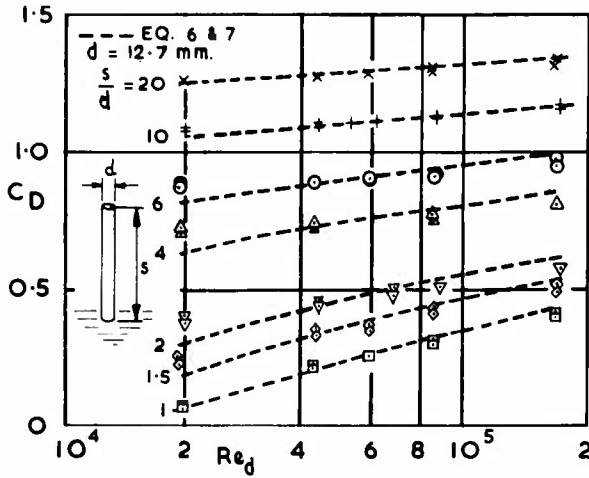


Fig. 16 Circular cylinders - M = 1.4

Measurements were made of the incremental drag created by cylinders of diameter  $d = 12.7$  mm (0.5 in) with length to diameter ratios  $s/d$  ranging from 1 to 20. The boundary layer thickness was of the order of  $10d$ . As a sample of the results the values of drag coefficient (based on frontal area) for a Mach number of 1.4 are shown in Fig. 16 plotted against a Reynolds number  $Re_d$  based on freestream conditions and cylinder diameter. For all lengths of cylinder the drag increases with increase of Reynolds number but the rate of increase diminishes as the length of the cylinder increases.

In order to estimate the drag of cylinders which extend outside the boundary layer knowledge of the drag coefficient under freestream conditions,  $C_{D_{\infty}}$ , is required. It has also been taken as a datum value on which to base other parts of the drag estimate. It has been found by extrapolation from results such as those in Fig. 16 for the five Mach numbers at which

measurements were made, and is shown in Fig. 17, again plotted against  $Re_d$ . At  $M = 0.2$  the range of  $Re_d$  extends just into the critical region, and it is of interest to note that the manner in which  $C_{D_{\infty}}$  decreases falls within the band of previous measurements at low speeds, and that the critical value of  $Re_d$  is not exceptionally low as might have been anticipated from the effects of the proximity of the highly turbulent flow of the boundary layer. At other values of Mach number the flow is dominated by compressibility effects and no drag decrease occurs with increase of  $Re_d$ . A further point to note is that the drag actually

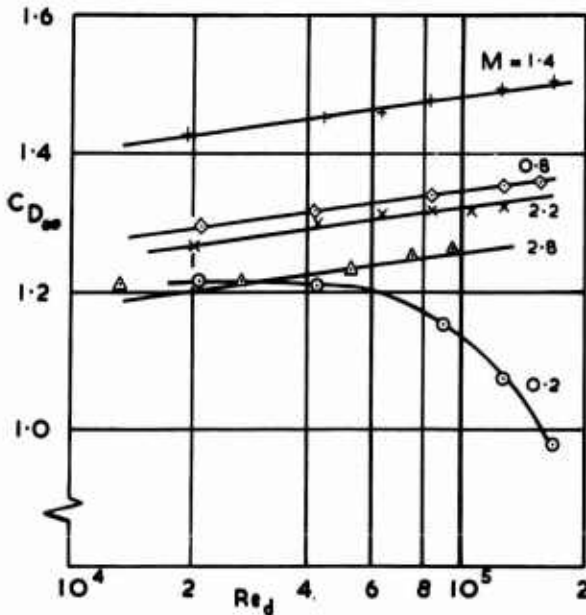


Fig. 17 Drag coefficient of circular cylinders of infinite length

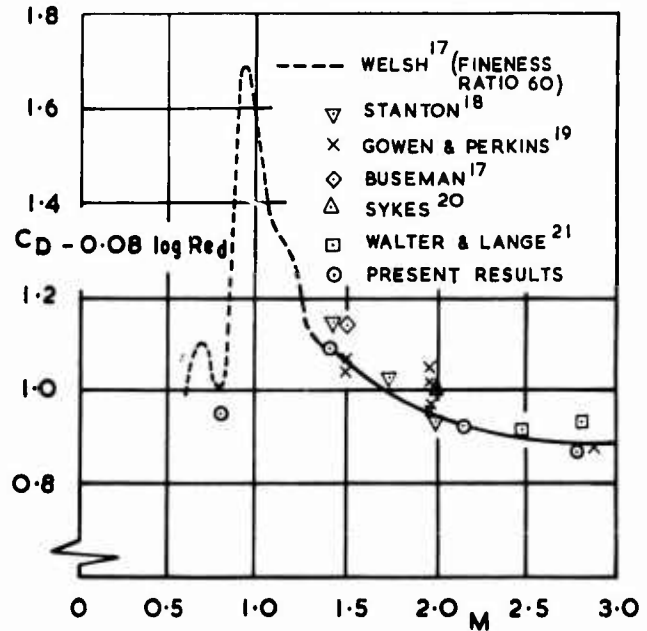


Fig. 13 Comparison of measurements of drag of circular cylinders

increases steadily with increase of  $Re_d$  ( $dC_{D_{99}}/d \log Re_d$  being about 0.08). This increase is slower than that found by Roshko<sup>14</sup> for low speed flow at supercritical Reynolds numbers. The results of Fig. 17 enable corrections for differences in Reynolds number to be made and a comparison with previous measurements to be obtained as shown in Fig. 18.

The analogy with a velocity defect function is taken in the form

$$\frac{C_{D_{\delta}} - C_D}{C_f} = F\left(\frac{s}{\delta}\right) \quad (5)$$

where  $C_{D_{\delta}}$  is the drag coefficient of a cylinder of length  $s = \delta_{99}$ , where  $\delta_{99}$  is boundary-layer thickness to 99% of freestream velocity. Within the range shown by the bars in Fig. 19 it has been found that  $C_{D_{\delta}}$  is proportional to  $C_{D_{99}}$  at a given Mach number and the variation of the ratio is shown plotted against Mach number.

It had been hoped that a drag defect function independent of Mach number could be found, but for the reasons given previously the failure to find this, as shown in Fig. 20 is not surprising.

Figures 18, 19, 20 enable an estimate of drag to be made for cylinders of any length greater than about 0.1 $\delta$ . For cylinders immersed completely in the boundary layer

$$C_D = C_{D_{\delta}} - F C_f \quad (6)$$

and for cylinders which extend into the freestream

$$C_D = \frac{\delta}{s} C_{D_{\delta}} + \left(1 - \frac{\delta}{s}\right) C_{D_{99}} \quad (7)$$

The broken lines on Fig. 16 show estimates derived from equations (6) and (7) with boundary layer characteristics taken from Figs. 1 and 2. The comparison with the measurements shows that the simplifications introduced in the estimation method lead only to small errors for long cylinders and for short cylinders, but that the variation of drag with Reynolds number is overestimated for cylinders of moderate length.

4.5 Stub Wings.

Four different stub wings were tested, of spans 2.5, 1.25, 0.25 and 0.125c, where c is the chord, of length about  $\frac{2}{3}\delta$ . As a sample of the results the drag coefficient (based on frontal area) for a Mach number of 1.4 is shown plotted against Reynolds number based on chord in Fig. 21. The results are similar in character to those for circular cylinders and it was hoped that the analysis made for the cylinders could be carried over to stub wings, or indeed to any other similar sort of object projecting into or through a boundary layer. In particular it was hoped that the drag ratio (Fig. 19) and the drag defect function F (Fig. 20) could be taken as being fairly universal so that given a knowledge of the drag of an object in the freestream its drag in a boundary layer could then be estimated. The drag of the stub wings at subsonic speed is small and has not been resolved with sufficient accuracy. Analysis has been made only of the results at supersonic speed. In the analysis the hopes are only partially realised. The drag defect function was found to have a variation both with Mach number and  $s/\delta$  similar to that for circular cylinders but its values are scaled by a factor of about  $\frac{3}{4}$ . However the drag ratio (Fig 23) whilst having values close to that for a circular cylinder at  $M = 2.2$  and  $2.8$  was about 5% lower at  $M = 1.4$ . The drag of the wing section at freestream conditions at supersonic speeds is shown

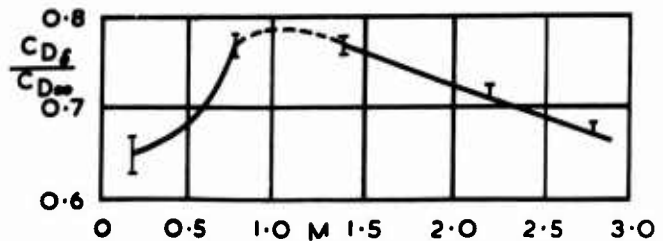


Fig. 19 Circular cylinders - drag ratio for  $s = \delta_{99}$

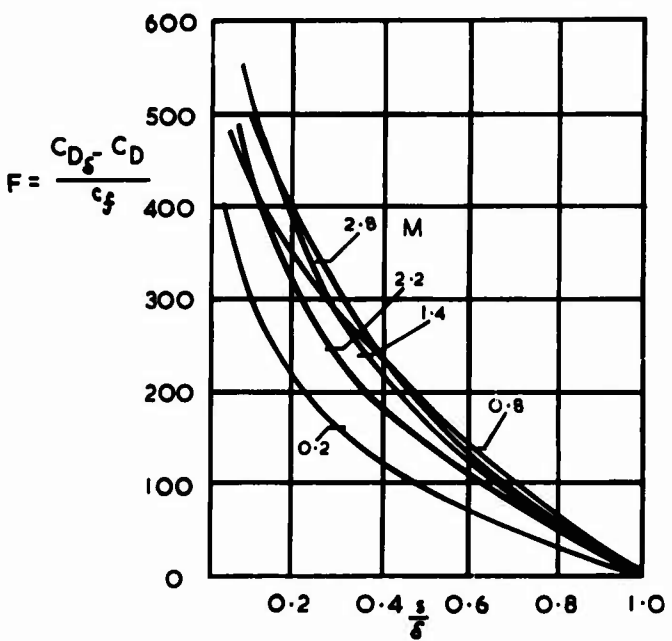


Fig. 20 Circular cylinders - drag defect function

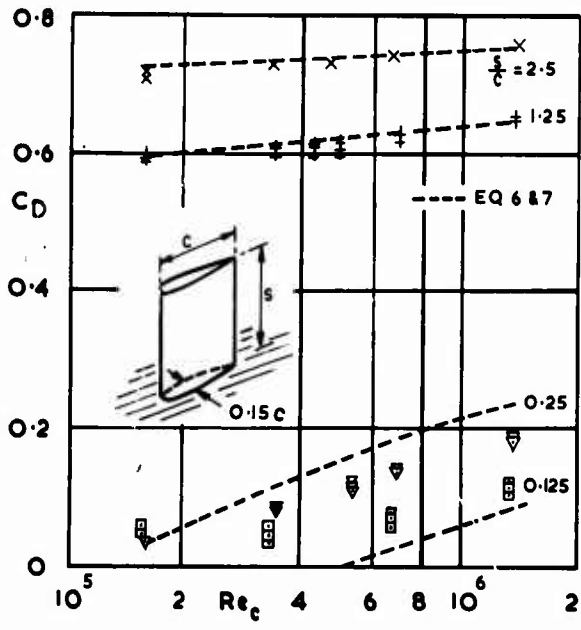


Fig. 21 Stub wings -  $M = 1.4$

in Fig. 22. The streamlining of an aerofoil section compared with a circular cylinder gives a reduction in drag of some 40%. The estimates shown by the broken lines on Fig. 21 are much less satisfactory than for circular cylinders.

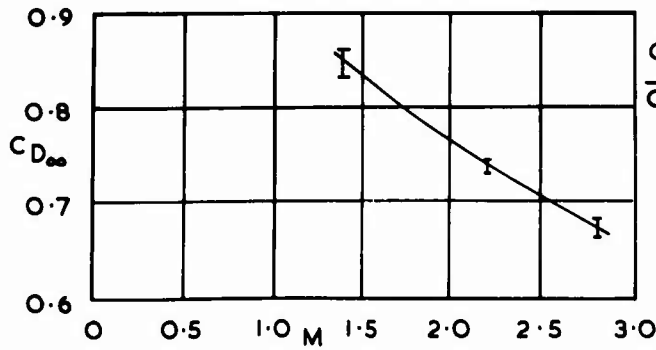


Fig. 22 Drag coefficient of wing of infinite length

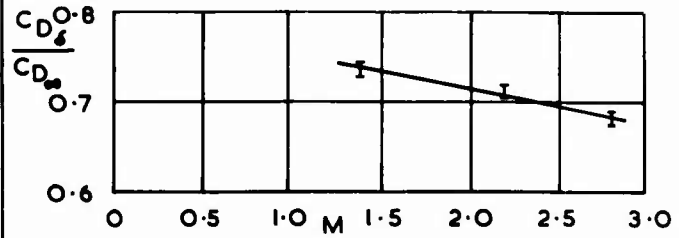


Fig. 23 Stub wings - drag ratio for  $s = \delta_{99}$

4.6 Fairings.

The measurements of the drag of fairings are the least satisfactory part of the investigation, and so far no general understanding of the results has been achieved but some observations can be made about them which give guide lines for design. The results, as drag coefficients based on the frontal area of the fairings, plotted against the ratio of boundary-layer thickness to fairing height are shown in Figs. 24 and 25 for Mach numbers of 0.2 and 1.4 as being typical of the behaviour at subsonic and supersonic speeds respectively. Altogether ten configurations were tested, and the points shown are for the maximum and minimum Reynolds number for each configuration. There is some small inconsistency in the drag as presented because some of the excrescences extended beyond the front plate of the balance so covering parts of the wall, the skin-friction drag of which was not included in the datum drag.

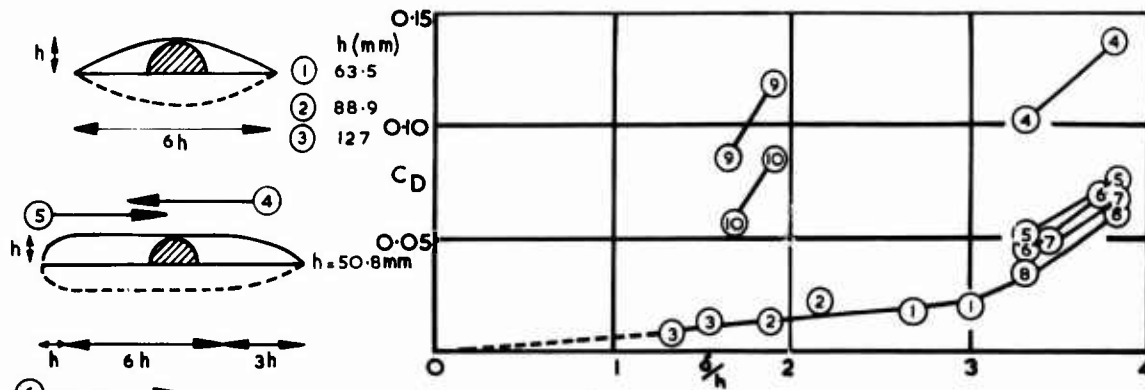


Fig. 24 Fairings  $M = 0.2$

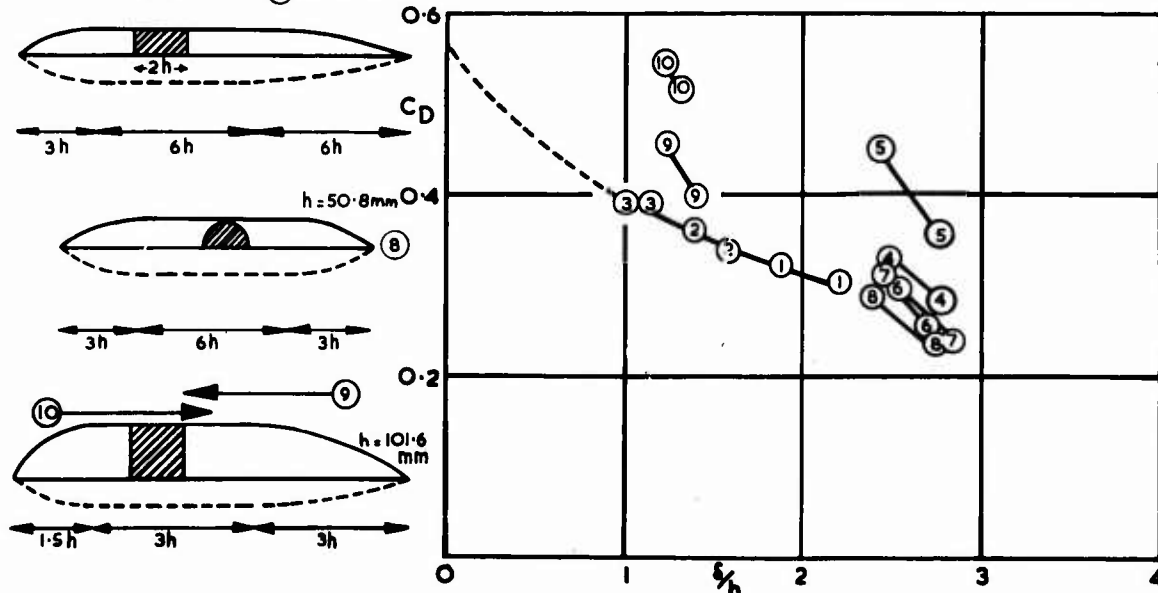


Fig. 25 Fairings  $M = 1.4$

The first observation is that at subsonic speeds  $C_D$  increases with increased immersion of the fairings in the boundary layer and is considerably less than at supersonic speeds where the drag decreases with increased immersion. Apparently at subsonic speed viscous effects are dominant whereas at supersonic speed wave drag is diminished by the damping action of the boundary layer. This is shown most clearly by the results for the parabolic bodies (1), (2), (3) of semi-circular cross section and fineness ratio 3 : 1 for which an extended range of  $\delta/h$  was obtained by testing three sizes of body. At subsonic speed  $C_D$  tends to zero at infinite Reynolds number ( $\delta/h = 0$ ) and at supersonic speed  $C_D$  has been extrapolated to an estimated value for the forebody drag plus a base drag. The estimate has been made in this way because it is known from observation of tufts that there was considerable separation over the rear of the body.

For the remaining bodies, which differ from bodies (1), (2) and (3) in having greater fineness ratio and in having end profiles of circular arcs rather than parabolic arcs, the variation of drag with immersion in the boundary layer is greater. Body (8) which resembles (1), (2) and (3) but with a parallel mid-section has a drag roughly consistent with these bodies, and with them has the lowest drag. Comparison of (8) with (4) and (5) (the arrows on the sketches of the bodies show the wind direction) indicates that a hemispherical forebody (body (5)) has a small penalty compared with a pointed body at subsonic speed and a large penalty at supersonic speed but that the reverse is true for a hemispherical afterbody (body (4)). Bodies (6) and (7) which have a rectangular cross section of 2 : 1 aspect ratio have slightly higher drag than (8) which has a semi-circular cross-section. Their increased length compared with body (8) perhaps compensates for any improvement due to the increased fineness ratio of either the forebody or rearbody. The fact that their drag is roughly the same does not point to any preferential advantage in increasing the forebody or afterbody length above a value of about  $3h$ . Finally the square cross-section bodies (9) and (10) have high drag but the variation with  $\delta/h$  is rapid over the limited range investigated and comparison with other bodies might be different at different values of  $\delta/h$ . The differences in drag between them confirm the penalties of a bluff afterbody at low speed and a bluff forebody at supersonic speed as indicated by the comparison of (4) and (5).

## 6 CONCLUDING REMARKS

It is suggested that the experimental results and the analysis given provide means of estimating the drag of many of the excrescences found on aircraft. There are, however, obvious shortcomings of the work, and considerable scope for extension in various aspects.

A notable omission is the lack of any study of effects which may accumulate downstream because of the effects of disturbances on boundary-layer growth and because of the effects of pressure gradients. Investigation is needed particularly of the downstream effects of three-dimensional forms of excrescence, and of the effects in three-dimensional flow. The work of Nash and Bradshaw<sup>15</sup> has shown that for simple excrescences in two-dimensional flow a 'magnification factor' to account for the effects of pressure gradients is calculable. Cook<sup>16</sup> has given some further confirmation of this for the flow over an aerofoil with a ridge but has drawn attention to the powerful effects which may occur if the flow in the vicinity of the ridge is near critical. Further work is needed both on the drag of excrescences and on their overall effect on the flow over wings and bodies at transonic speeds. The effect of sweepback on steps and ridges could also be studied.

The measurements of the drag of holes need extending to deeper holes, to different forms of holes and to include the exploration of the possible benefits from shaping the edges of holes. Information is also needed on the drag caused by air intakes and exits.

The investigation of the drag of fairings, though providing some guidance for the designer, is far from complete. The superficial assessment made so far, for example, does not cover separately the effects of Reynolds number on the drag of the fairings as distinct from the effects of changes of immersion of the body in the boundary layer with change in overall Reynolds number. Furthermore, since the purpose of fairings is to reduce the drag of some necessary obstacle, a proper approach, from purely aerodynamic considerations, would be to attempt to define a shape with minimum drag surrounding a given obstacle.

There are also other topics not covered in the investigation described here, amongst which are the increments in drag caused by surface distortions and by arrays of excrescences. In the latter aspect it is necessary to establish the way in which interferences between individual excrescences develop as their density increases and the drag changes from that for isolated excrescences to that for distributed roughness.

British Crown Copyright: reproduced by permission of the Controller of Her Britannic Majesty's Stationery Office

## REFERENCES

No	Author(s)	Title, etc
1	A B Haines	Subsonic Aircraft Drag: an Appreciation of Present Standards. Aeronaut. J. Vol 72 No 687 March 1968 pp 253-266
2	K Wieghardt	Increase of the turbulent frictional resistance caused by surface irregularities. MAP R & T No 103. June 1946 (Translation of FB 1563 Z/B 1942)
3	S F Hoerner	Fluid-dynamic drag (1965)
4	K G Winter L Gaudet	Turbulent Boundary-Layer Studies at High Reynolds numbers at Mach numbers between 0.2 and 2.8. R & M 3712. December 1970.

<u>No.</u>	<u>Author(s)</u>	<u>Title, etc</u>
5	M C Good P N Joubert	The form drag of two-dimensional bluff-plates immersed in turbulent boundary layers. J Fluid Mech. Vol 31 Part 3 1968 pp 547-582
6	C E Kepler S M Bogdonoff	Interaction of a turbulent boundary layer with a step at $M = 3$ . Princeton Aero Eng. Rep. 238 September 1953
7	I E Vas S M Bogdonoff	Interaction of a turbulent boundary layer with a step at $M = 3.85$ . Princeton Aero Eng Rep 295 April 1955
8	K R Czarniecki J R Servier M M Carmel	Effect of fabrication-type roughness on turbulent skin friction at supersonic speeds. NACA TN 4299 July 1958
9	R C Hastings	Turbulent flow past two-dimensional bases in supersonic streams. R & M 3401 (1963)
10	I Tani M Inchi H Komoda	Experimental investigation of flow separation associated with a step or groove. Aero Res. Inst. Univ. of Tokyo Rep 364. April 1961.
11	W Tillman	Additional measurements of the drag of surface irregularities in a turbulent boundary layer. NACA TM 1299 January 1951 (Translation of ZWB 6619 1944).
12	H Friesing	Measurement of the drag associated with recessed surfaces: cut-outs of rectangular and elliptic planform. RAE Library Trans. 1614 October 1971 (Translation of ZWB FB 628 1936).
13	O W McGregor	Aerodynamic drag of two-dimensional rectangular notches in transonic and supersonic turbulent flow (with emphasis on the effects of self-induced pressure oscillations). Illinois Univ Ph D Thesis 1969
14	A Roshko	Experiments on the flow past a circular cylinder at very high Reynolds number J Fluid Mech Vol 10 1961 pp 345-356
15	J F Nash P Bradshaw	The magnification of roughness drag by pressure gradients. J R aeronaut Soc. Vol 71. January 1967. pp 44-49
16	T A Cook	The effects of ridge excrescences and trailing-edge control gaps on two-dimensional aerofoil characteristics. R & M No 3698 April 1971
17	C J Welsh	The drag of finite-length cylinders determined from flight tests at high Reynolds numbers for a Mach number range from 0.5 to 1.3. NACA TN 2941 June 1953
18	T E Stanton	On the effect of air compression on drag and pressure distribution of cylinders of infinite aspect ratio. R & M 1210 1929
19	F E Gowen E W Perkins	Drag of circular cylinders for a wide range of Reynolds numbers and Mach numbers. NACA TN 2960 1953
20	D M Sykes	The supersonic and low-speed flows past circular cylinders of finite length supported at one end. Jour. Fl. Mech Vol 12 1962 pp 367-387
21	L W Walter A H Lange	Surface temperature and pressure distributions on a circular cylinder in supersonic cross-flow. NAVORD Rep 2854 June 1953.

SUMMARY

There are several components that make important contributions to the drag of a helicopter, e.g. the drag of the main rotor and of the tail rotor, of the basic fuselage, of the pylon, of the landing gear, of the fairings and the interference drag between these parts. To obtain the total drag of a helicopter one can make flight tests, or measure a large scale, or a full scale model in a wind tunnel, or estimate it by semi-empirical calculations using component tests of a small scale model.

The difficulties and advantages of these three ways of defining the drag of a helicopter are described. Especially the problems associated with tests of small scale helicopter models are discussed since it happens quite often that there is only an incomplete small scale model available. When small scale models are tested there can be parts that make important contributions to the total drag but have to be tested at different critical regions of Reynolds number range whereas at the actual helicopter in normal flight the Reynolds numbers of these parts lie beyond the critical Reynolds number. The problems and methods to estimate the total drag of helicopters using results of model tests are discussed. The results are compared with flight-test results.

NOTATIONS

A	m <sup>2</sup>	rotor disc area, $\pi R^2$	T	kp	rotor thrust
A <sub>f</sub>	m <sup>2</sup>	fuselage frontal area	V	$\frac{m}{sec}$	true airspeed of helicopter along flight path
A <sub>p</sub>	m <sup>2</sup>	projected frontal area	V <sub>C</sub>	$\frac{m}{sec}$	rate of climb of helicopter
b	-	number of blades per rotor	v	$\frac{m}{sec}$	induced velocity at rotor (always positiv)
C	m	blade section chord	W	kp	helicopter gross weight
C <sub>D</sub>	-	drag coefficient, $D/qA_f$ , $D/qA_p$	$\alpha$	deg	rotor angle of attack;
C <sub>L</sub>	-	rotor lift coefficient, $L/qA$	$\gamma$	deg	flight-path angle (positive in climb)
C <sub>P</sub>	-	rotor-shaft power coefficient, $P/\rho A (\Omega R)^3$	$\delta$	-	mean profile drag coefficient of blade
C <sub>T</sub>	-	rotor thrust coefficient, $T/\rho A (\Omega R)^2$	$\lambda$	-	inflow ratio, $(V \sin \alpha - v)/\Omega R$
D	kp	total equivalent drag force of the helicopter	$\mu$	-	tip-speed ratio, $V \cos \alpha / \Omega R$
(D/L) <sub>i</sub>	-	rotor induced drag-lift ratio	$\rho$	$\frac{kp \cdot sec^2}{m^3}$	mass density of air
(D/L) <sub>o</sub>	-	rotor profile drag-lift ratio	$\psi$	deg	blade azimuth angle
(D/L) <sub>R</sub>	-	rotor drag-lift ratio, $(D/L)_o + (D/L)_i$	$\Omega$	$\frac{rad}{sec}$	rotor angular velocity
f	m <sup>2</sup>	parasite-drag area, $D_p/q$			
L	kp	rotor lift			
n	rpm	rotor rotational speed			
P	$\frac{mkp}{sec}$	rotor shaft power			
q	$\frac{kp}{m^2}$	dynamic pressure, $1/2 \rho V^2$			
R	m	blade radius measured from center of rotation			

Subscript:

C	climb
i	induced
o	profile
p	parasite

The studies have been sponsored in part by the Ministry of Defence of the Federal Republic of Germany.

## 1. INTRODUCTION

5-2 In the early days of development of helicopters the engineering effort was mainly concentrated on the mechanics of flight and the development of the rotating and control components. Almost no attention was paid to the aerodynamics of the non-rotating parts (Ref. 1). The designers of the helicopters of today and of the future are noticeably trying to improve the aerodynamic efficiency. It is true, that for some purposes (e.g. agricultural, survey, training, heavy lift, observation) aerodynamic cleanliness is still less important, but for transport, both civil and military, and for attack, speed becomes an important factor. In case of the civil transport helicopter, block speed is the interesting factor. As far as the military transport helicopter is concerned, speed plays the dominant role in possible evasive actions or passive defense. In case of the attack helicopter, the speed factor is evident and needs no further explanation. However, speed is not the only important factor. The customers become more and more interested in economic helicopters which need less power at a given speed. Therefore, reduction of parasite drag will be regarded very carefully in new designs.

To increase the speed of a helicopter or of an airplane there are two possibilities, namely to install more power or to reduce the drag. Ultimately, one has probably to do both, but reduction of drag seems to be more attractive to the designer. As is well known, the total power required of a helicopter in level flight consists of three components (Fig. 1):

- (1) The induced power that is required to produce lift,
- (2) the profile-drag power that is necessary to drag the blades through the air,
- (3) the parasite-drag power that must be supplied to drag the fuselage through the air.

As can be seen from Fig. 1, the induced power decreases with increasing speed. The profile-drag power increases slightly as forward speed is increased, the increase becoming very rapid at high forward speeds. The power required to drag the fuselage through the air, however, increases as the cube of the forward speed and becomes very large at higher speeds. Therefore, when increasing high speed of a helicopter much attention must be paid to its parasite drag.

Reducing the drag of a helicopter means not only a reduction of the propulsive force of the main rotor. It also delays stall and compressibility effects at the main rotor with subsequent less aerodynamic load unsymmetry on the rotor. Thus, the oscillatory loads on the rotor blades and controls as well as the vibration in the cockpit and on the frame are diminished (e.g. Refs. 2 and 3). Therefore, the goal of modern helicopter design is, to come close to the average parasite drag of fixed-wing aircraft as can be seen in Fig. 2 (Ref. 4).

Reduction of drag can, of course, only be achieved by careful aerodynamic consideration of the components. This is necessarily followed by careful testing and analyzing. The possibilities of doing that and the problems associated with estimating the total drag and the drag components of a helicopter are discussed in the following paper.

## 2. BASIC RELATIONSHIPS BETWEEN DRAG FORCES AND POWER REQUIRED OF A HELICOPTER

The power supplied at the rotor shaft of a helicopter is expended in overcoming the profile-drag losses, the induced-drag losses, the parasite-drag losses and in changing the potential energy of the aircraft in climb. The total shaft power is the sum of the various sources and can be written in coefficient form as

$$C_P = C_{P_o} + C_{P_i} + C_{P_p} + C_{P_c} \quad (1)$$

Each individual power loss may be expressed as the energy dissipated per second by an equivalent drag force moving at the translational velocity of the aircraft. Thus, if  $D$  represents the total equivalent drag force and  $D_o$ ,  $D_i$ ,  $D_p$  and  $D_c$  the equivalent drag forces corresponding to each of the sources of power expenditure,

$$D = D_o + D_i + D_p + D_c \quad (2)$$

Dividing equation (2) through by the rotor lift  $L$  yields

$$\frac{D}{L} = \left(\frac{D}{L}\right)_o + \left(\frac{D}{L}\right)_i + \left(\frac{D}{L}\right)_p + \left(\frac{D}{L}\right)_c \quad (3)$$

Since  $(C_P/C_T) = (D/L) \cdot v$ , equation (1) may be written in the usual form (see Ref. 1)

$$\frac{C_P}{C_T} = \frac{C_{P_o}}{C_T} + \frac{C_{P_i}}{C_T} + \frac{C_{P_p}}{C_T} + \frac{C_{P_c}}{C_T} \quad (4)$$

Eq. (4) is the fundamental power relation to solve any problem in helicopter performance. Additional formulas that are necessary for evaluating helicopter performance by means of eq. (4) are taken from Ref. 5:

$$T \cos(\alpha + \gamma) = W + D_p \sin \gamma \quad (5)$$

$$\frac{C_P}{C_T} = \frac{P}{(\Omega R) T} \quad (6)$$

$$\frac{C_{P0}}{C_T} = \frac{P_0}{(\Omega R) T} = \frac{\sigma \delta}{8C_T} (1 + 3\mu^2 + \frac{3}{8}\mu^4) \quad (7)$$

$$\frac{C_{P1}}{C_T} = \frac{C_T}{2\mu [1 + (\lambda/\mu)^2]^{1/2}} \quad (8)$$

$$\frac{C_P}{C_T} = \frac{1}{2C_T} \left[ \frac{f}{A} - \left( \frac{\mu}{\cos \alpha} \right)^3 \right] \quad (9)$$

$$\frac{C_{Pc}}{C_T} = \sin \gamma \left\{ -\sin \gamma \frac{C_{Pp}}{C_T} \frac{\cos \alpha}{\mu} + \left[ 1 - \cos^2 \alpha \cdot \left( \frac{C_{Pp}}{C_T} \right)^2 \frac{\cos^2 \alpha}{\mu^2} \right]^{1/2} \right\} \frac{\mu}{\cos \alpha} = \frac{V_c}{\Omega R} \quad (10)$$

$$\tan \alpha = \frac{\lambda}{\mu} + \frac{C_T}{2\mu^2 [1 + (\lambda/\mu)^2]^{1/2}} \quad (11)$$

These basic equations (4) to (11) can also be used to determine the drag forces of a helicopter if it is possible to measure the different sources of power expenditure. It should be noted that some of these equations are approximations which are only used since they describe the physical background very clearly.

The trends of induced, profile and parasite power with airspeed that are shown in Fig. 1 for a level flight of a utility helicopter indicate that a remarkable portion of power required at high speeds stems from parasite drag, about 50 percent at 240 km/h. While theoretical methods have already been developed to a degree to predict the rotor drag-lift ratio  $(D/L)_R$  with some confidence (Ref. 6) it is still impossible to estimate the parasite drag of a helicopter using theoretical methods. The reason for this fact is that there are several components which make important contributions to the parasite drag of a helicopter but cannot be dealt with analysis because of their shape. Fig. 3 shows a typical drag breakdown of utility helicopters at cruise conditions. The main contribution comes from the basic fuselage. The larger number belongs to a helicopter with great utility. The next important items are the drag contributions of the hub of the main rotor including blade shank drag, of the main rotor pylon and of the landing gear. The remaining parts make smaller contributions to the drag but they add up to a total of 24 to 28 percent.

The drag of a helicopter can be measured in flight tests, large or full scale wind tunnels or in small scale wind tunnels as it is common for fixed-wing aircraft. Only the special problems associated with helicopter testing will be discussed in the following paragraphs since all problems that are valid both for fixed-wing and rotary aircraft will be discussed in many distinguished papers of this meeting. This paper will also not touch the problems of instrumentation and accuracy of measurement (e.g. Refs. 7 and 8).

### 3. FLIGHT MEASUREMENT OF HELICOPTER DRAG

Flight testing allows exactly only measurement of the total drag of a helicopter. The following quantities have to be measured for this purpose:

- helicopter gross weight
- altitude
- temperature
- true air speed
- rotor shaft power
- rotor angular velocity
- flight path angle or rate of climb

Of course, if some parts, e.g. basic fuselage, main rotor hub, landing gear or main rotor pylon, are improved by better aerodynamic shapes, the reduction of drag compared to the original version can readily be determined. Fig. 4 shows a comparison of flight test results between a production BO 105 and an aerodynamically improved BO 105 that has an extended engine cowling and afterbody and advanced geometry blades. The improved fuselage leads to a drag-reduction of 165 kp at a speed of 250 km/h. Adding the improved blades results in an additional drag reduction of 77 kp at the same speed. In an attempt to brake world speed records even more aerodynamic cleanliness is required. E.g. in Ref. 9 the speed gains of the Gazelle as obtained with several streamlinings in flight tests are discussed.

5-4

Another advantage of flight testing is that there do not arise any problems due to scaling effects as it happens when models are tested. Therefore, flight tests are the final judgement of design and of model testing.

The disadvantage of flight tests is the fact that it is not possible to measure exactly the drag forces corresponding to each of the sources of power expenditure. Needless to say that in the design stage no drag data can be achieved by this procedure. In addition, it is too expensive to optimize the drag of components in flight tests by changing the shape. Only the results of the optimization in the wind tunnel are finally checked.

However, there are two possibilities to find the parasite drag of a helicopter in flight testing. As can be seen from Fig. 5 (Ref. 10) the rotor drag  $D_R = D_o + D_i$  can be calculated quite accurately by theory. Thus, the parasite drag or the parasite-drag area can easily be obtained from eqs. (4) to (9) assuming level flight:

$$f = 2A \left(\frac{\cos\alpha}{\mu}\right)^3 \left[ C_P - C_{P_o} - C_{P_i} \right] \quad (12)$$

Another possibility is only valid in the high speed range provided that major portions of the blade are not stalled. But in this case only measured data are used. This idea takes advantage of the fact that the power required to drag the fuselage through the air increases as the cube of the forward speed. Thus, in the high speed range, the changes in total power required stem mainly from the contribution of parasite drag (Fig. 1). In Fig. 6 the rotor-shaft-power coefficient  $C_p$  is plotted versus  $\mu^3$ . The linear dependency between  $C_p$  and  $\mu^3$  proves the assumption stated above. Therefore, when differentiating eq. (4) with respect to  $\mu^3$  several terms can be neglected, and one obtains:

$$\frac{dC_p}{d(\mu^3)} \approx \frac{1}{2} \frac{f}{A \cos\alpha} = \text{Const.} \quad (13)$$

Since in the high-speed range  $(\lambda/\mu) \ll 1$ , eq. (8) yields

$$C_{P_i} \approx \frac{C_T^2}{2\mu} \quad (14)$$

The thrust may be obtained from  $T^2 = W^2 + D^2$ . The constant of eq. (13) can be defined from Fig. 6. Thus, one can calculate  $f$ ,  $C_{P_c}$  and  $C_{P_i}$ . Finally,  $C_{P_o}$  can be computed with the aid of eq. (4):

$$C_{P_o} = C_P - C_{P_i} - C_{P_p} \quad (15)$$

The total power required as obtained from flight tests with the BO 105 shows good agreement with calculations (Fig. 1) which use wind tunnel data for the parasite-drag area. Thus, the small scale wind tunnel data seem to be satisfactory.

Fig. 7 shows a comparison of the drag forces as computed by theory (using the measured parasite drag area) with those obtained by the empirical method mentioned above which uses flight-test data. The agreement is good. The empirical method overestimates a little parasite-drag force, whereas theory underestimates a little total equivalent drag force.

#### 4. FULL-SCALE WIND-TUNNEL TESTING OF HELICOPTER DRAG

Any wind tunnel testing of helicopters that includes the rotor is preferably performed with full-scale helicopters since construction of a rotor model that is aerodynamically and dynamically similar means almost design and development of a new rotor.

The advantages of full-scale wind-tunnel tests are that they usually provide data essentially free of scale effects and permit the evaluation of the actual hardware, such as antennas. The contribution of the landing gear or of various excrescences such as window and door seals, door handles and other protuberances to the parasite drag of a helicopter or the additional drag from leakage and nonflush doors, windows, hatches etc. which not only contribute their own drag but can also cause flow separation on the basic fuselage can only be determined from full-scale tests. This is also true when the drag-lift ratio of the rotor alone or the fuselage forces as influenced by rotor operation are to be measured. Of course, any extreme flight condition that might be dangerous should preferably be measured in a wind tunnel. However, this problem is not so much associated with measurement of drag but more a problem of general flight behavior.

Besides the fact that the number of full-scale wind tunnels is small and the cost of testing is high (but still lower than flight tests) there are several other problems that have to be observed when planning full scale tests. The speed range of wind tunnels is limited, e.g. 200 knots at the NASA Ames 40 x 80 foot wind tunnel. This speed range is usually adequate for testing of pure helicopters. It might some times not be adequate for testing of special high speed rotorcraft at full scale Mach number and advance ratio (e.g. Ref. 11). To simulate the advance ratio tip speed has to be reduced substantially. Thus, the data is obtained at reduced Mach number, and Reynolds number, even though in a full scale wind tunnel.

5-5

There exists another problem when testing V/STOL vehicles in a wind tunnel. There is a minimum speed test limit that results from a breakdown of the flow through the tunnel, see for instance Refs. 12, 13, 14. This flow breakdown is caused by an interaction between the model's high energy wake, the main tunnel flow, and boundaries. In contrast to the free air, the flow in the tunnel at the limiting conditions produces a large region of reversed flow and upwash in front of the wake, see Fig. 8 (Ref. 12). The forward portion of the wake travels forward initially and then upward to roll up into a large and powerful standing vortex in front of the wake as it nears the floor. The rear portion of the wake is subjected to both an acceleration and an upwash so that this portion of the wake assumes a position substantially above its normal free-air position. The flow breakdown is a function of the model's downwash, size, and configuration as well as the tunnel size and configuration, see Fig. 9 (Ref. 13). When data is taken below the flow breakdown point data is not valid.

If these restrictions mentioned before are observed full-scale wind-tunnel tests show usually very good agreement with flight tests (e.g. Refs. 15 and 16) and can therefore be regarded as reliable data. Some important full-scale results which can serve as guidelines for estimating the drag of helicopters or for judging small scale tests are reported in References 16 to 19. Some of them are summarized in the following discussion.

It is shown in Ref. 16 that the rotor-fuselage interference is small when the fuselage with the rotor off has large separated flow areas. It is assumed that this is also true if the fuselage has very small separated flow areas (Ref. 17). A fuselage which has no separated flow but is susceptible to flow separation from relatively small disturbances would be expected to have large interference effects. Fuselage tuft studies during tests of models without a rotor can indicate whether or not interference effects are likely to occur.

In References 16 to 18 several full-scale helicopter fuselages were tested and the influences of different hubs, pylons, landing gears, antennas and several aerodynamic fairings were investigated. Fig. 10 (Ref. 17) shows as an example the parasite drag area of the basic fuselage of a four place, light observation helicopter and the effects of several other parts. The total parasite drag is six times as large as that of the basic fuselage. An aerodynamic cleanup reduces the total drag to 65 percent of the original one. Especially the drag increments of three pylons with three-blade articulated hubs are shown in Fig. 11. Although the curved element pylon has three times the frontal area of the linear element pylon, it is significant that the curved element pylon in combination with the rotor hub has only a slightly higher drag than does the linear element pylon with the same hub. The addition of a ramp to the curved element pylon has no effect on the drag, but might improve the effects of the pylon wake on the tail aerodynamics.

Fig. 12 presents the drag increments of three test hubs the distances of which from the fuselage were varied. As can be seen from results about 50 percent drag reduction are possible. Fig. 12 shows also the drag characteristics of the antennas, door junctures, and door handles. Although none of these items contributed more than 0.023 square meters of parasite-drag area individually, cumulatively they account for about 23 percent of the drag of the complete configuration.

In Ref. 19 the results of parasite-drag measurements of five helicopter rotor hubs are documented. The results of that investigation indicate the following conclusions (Fig. 13):

- (1) In general, angle-of-attack variation do not have large effects on the drag.
- (2) Within the limits of these tests, the drag is not significantly affected by changes in hub rotational speed or forward speed.
- (3) The drag coefficients  $C_D$  of the basic hubs, based on projected hub frontal area, increase gradually with hub area and range from 0.5 to 0.76 for the hubs tested.

Thus, if there are no problems with Reynolds number a nonrotating hub is a fair approximation of the actual behavior in small scale tests.

## 5. OBJECTIVES AND PROBLEMS ASSOCIATED WITH MODEL TESTING

The need for the testing of aircraft was already discussed at the beginning of this paper. The best way of doing it is not a priori obvious, but model testing has in fact certain advantages over full-scale flight testing such as (Ref. 20):

- (1) Cheapness,
- (2) instrumentation may well be easier,
- (3) more controllable experiments are possible,
- (4) ability to test flight regimes which are difficult or dangerous to achieve with, or are outside the range of existing full-scale aircraft,
- (5) ability to test configurations that are in the design stage and not yet in full-scale existence,
- (6) individual components of aircraft, and their mutual interference effects can be relatively easily tested.

Items 2,3, 4 and 6 are of course also valid for full-scale tests compared to flight tests.

The most important problem that has to be solved when conducting model tests is scaling. It is a well-known fact that the forces and moments acting in the fluid and on the body, and the motions of the body and the fluid are completely similar both for model test and actual flight if certain non-dimensional parameters can be arranged to be iden-

tical both for the model and the full-scale aircraft. If no rotors are involved in the tests only the Mach number and Reynolds number are important to achieve similarity. However, since 1/5-scale or 1/4-scale models are usually used it is impossible to fulfill both requirements unless pressurized wind tunnels or those using a gas other than air as a working fluid are considered. Since forward speed of pure helicopters does usually not exceed Mach number of 0.3 testing of fuselages is not aggravated from this point of view. Simulation of Reynolds number is the problem. Fig. 14 (Ref. 18) shows a comparison between full-scale and 1/5-scale data of a light observation helicopter (LOH). The measurements were conducted with the basic fuselage less all antennas and protuberances, landing gear removed, holes and gaps sealed. The fairly good correlation in the drag data may be fortuitous because the differences in lift and pitching moment indicate marked differences in the flow conditions between full-scale and small-scale test. In both tests the drag coefficient was increased about 0.04 when adding the faired landing gear to the fuselage. In the full-scale test, the zero-angle drag coefficient of the LOH was increased by 0.010 by the shortened afterbody, and decreased by 0.012 by the extended afterbody, whereas in the small-scale test the corresponding numbers were, respectively, 0.005 and 0.012.

Fig. 15 presents another comparison of full-scale and 1/5-scale model test results for two slightly different models (labelled C and D) of a LOH (Ref. 21). The drag of model C, both small and full scale, agrees fairly well, as does the lift. However, the drag of model D, 1/5-scale, is nearly twice that of the full-scale model. This difference, according to Ref. 21, results from flow separation on the small-scale model and is related to a low Reynolds number effect. It is also interesting that the slopes of pitching-moment curves for both the full-scale and 1/5-scale models agree reasonably well, but large differences exist between the angles of attack for zero pitching moments. The differences could not be explained in Ref. 21.

These results indicate that there always exist some uncertainty when conducting small-scale tests whether the results are valid or not. The situation gets even worse if parts like tubular landing skids are involved whose parts are slightly supercritical in flight. Needless to say that the influences of various excrescences such as window and door seals, door handles, leakage or nonflush doors cannot be simulated in small-scale tests but have to be estimated.

Several small-scale fuselage models of the BO 105 helicopter were tested in wind tunnels (Refs. 22 to 25). Fig. 16 shows the baseline configuration and several components of a 1/4-scale model. The components of the aft fuselage section (afterbody and engine compartment cowling) include production, extended and blunted aftbody, as well as production, engine exhaust off, extended and blunted engine cowling. In addition, the effects of a main rotor cap, of guide vanes, of vortex generators, of numerous spoilers and of a splitter plate were investigated.

The effect of varying the basic BO 105 model Reynolds number on model drag is also shown in Fig. 16. The model  $D/q$  is constant at  $q$  settings above  $250 \text{ kp/m}^2$ . The other force components were also found to be unaffected by Reynolds number variations above that dynamic pressure. Trip strips of grit were placed on the model nose section, pylon and tails to further increase the effective Reynolds number of the model. The surface of the landing gear extension was roughened with 0.35 mm grid to force transition since even at maximum tunnel  $q$  the model gear Reynolds number is subcritical, whereas the full-scale Reynolds number is supercritical. The trip strip caused a reduction in gear drag. However, since the increase in skin friction drag due to the grit made the results questionable, a final landing-gear Reynolds number correction was conducted by comparing the test results with drag estimates from the Ref. 26 drag analysis. The grid results were used to define the variation of this correction with angle of attack.

As can be seen from curve (4) of Fig. 17 the BO 105 airframe minimum drag occurs at  $+5^\circ$ . This positive minimum drag angle permits the development of a zero drag spoiler at cruise conditions of about  $-7^\circ$  fuselage pitch angle. Fig. 17 also shows that landing gear and hubs produce a drag force of 2/3 of the base (curve 1) at cruise conditions.

The effect of modifying the afterbody contour is demonstrated by curve No. 5. At cruise conditions, the aircraft parasite drag is reduced by about  $0.24 \text{ m}^2$ . It should be mentioned that no attempt was made to optimize the extended afterbody configuration.

Adding a rotor cap caused an increase in the total aircraft drag as illustrated by curve No. 6.

The test also showed that the fuselage produced a relatively high download at cruise conditions (Fig. 18). This is a common problem of helicopters because of the negative pitch angle of the fuselage in forward flight. To prevent this undesirable download a spoiler was proposed at the afterbody the geometry and positioning of which was optimized during these tests. Details of the optimized spoiler-configuration lift and drag characteristics are presented as a function of model pitch angle in Fig. 18. Installation of the spoiler shifted the fuselage zero lift angle of attack from  $+4^\circ$  to  $-4^\circ$ . A corresponding shift in the airframe minimum drag angle of attack is also shown due to a reduction in induced drag at negative attitudes and an increase in drag at positive angles of attack. At cruise conditions, the induced drag reduction is apparently equal to the spoiler parasite drag, resulting in no net spoiler drag penalty.

Thus, the drag breakdown of Fig. 17 at cruise conditions is valid with or without spoiler. In addition to the parasite drag area of Fig. 17 the following items which have been estimated contribute to the total parasite drag at cruise conditions

5-7

Component	$\Delta f, m^2$
Blade Shank Drag	0.047
Protuberances	0.047
Roughness and Leakage	0.055
Momentum Drag	0.046

total 0.195

On the basis of these small-scale tests and these estimates, the total parasite drag polar of the BO 105 was composed and was used in performance calculations. The theoretical results were compared with flight measurements (Fig.1). Since the agreement between both results is good, it is assumed that the parasite drag area of the BO 105 has been estimated fairly accurately.

#### 6. CONCLUDING REMARKS

The discussion of the present paper has summarized the tools that are available to the designer to estimate the drag of a helicopter. It also revealed the problems which are associated with an accurate measurement of the drag of a helicopter. The need for comparative measurement between small-scale and full-scale models became evident. As the aerodynamic cleanliness of helicopters will become more and more important in the future also more wind tunnel tests will be conducted. Thus, the question of building special test facilities for V/STOL models will have to be reconsidered.

#### 7. REFERENCES

1. Gessow, A. and Myers, G.C.Jr. : "Aerodynamics of the Helicopter". Frederick Ungar Publishing Co., New York, 3rd printing, 1967.
2. Van Wyckhouse, J.F. and Cresap, W.L. : "High Performance Helicopter Program - Summary Report, Phase II". Trecom Technical Report 64-61, October 1964.
3. Sonneborn, W.G.C. : "High Mach Number/High Advance Ratio Flight Test Program with the High-Performance UH-1 Compound Helicopter". USAAVLABS Technical Report 71-2, February 1971.
4. Bosco, A. : "Aerodynamics of Helicopter Components other than Rotors". AGARD-CP-111, September 1972.
5. Gessow, A. and Tapscott, R.J. : "Charts for Estimating Performance of High-Performance Helicopters". NACA Report 1266, 1956.
6. Landgrebe, A.J. and Cheney, M.C.Jr. : "Rotor Wakes, Key to Performance Prediction". AGARD-CP-111, September 1972.
7. Sarsted, G.J. and Coles, A.V. : "The Development and Flight Testing of Helicopters". J. of the Royal Aeronaut. Soc., Vol. 64, April 1960, pp. 211-223.
8. Glöckl, H. : "Meßinstrumentierung und Flugmessung am Hubschrauber BO 105". DGLR-Fachausschußsitzung "Drehflügelflugzeuge und Luftschrauben", Stuttgart, 1968.
9. Mouille, R. : "The World Speed Records of the SA. 341 Gazelle". Presented at the 28th Annual National Forum of the American Helicopter Society, Washington D.C., May 1972, Preprint No. 651.
10. Harris, F.D., Tarzanin, F.J. and Fischer, F.K.Jr. : "High Speed Performance, Theory versus Test". Proceedings of the V/STOL Technology and Planning Conference (AFFDL), Las Vegas, Nevada, September 1969.
11. Rabbott, J.P.Jr. : "Model VS. Full Scale Rotor Testing". Proceedings of the Third CAL/AVLABS Symposium, Buffalo, New York, June 1969.
12. Heyson, H.H. : "The Flow Throughout a Wind Tunnel Containing a Rotor with a Sharply Deflected Wake". Proceedings of the Third CAL/AVLABS Symposium, Buffalo, New York, June 1969.
13. Rae, W.H.Jr. and Skindo, S. : "Comments on V/STOL Wind Tunnel Data at Low Forward Speed". Proceedings of the Third CAL/AVLABS Symposium, Buffalo, New York, June 1969.
14. Lazzeroni, Fa.A. and Carr, L.W. : "Problems Associated with Wind Tunnel Tests of High Disk Loading Systems at Low Forward Speeds". Proceedings of the Third CAL/AVLABS Symposium, Buffalo, June 1969.

15. Statler, W.H., Heppe, R.R. and Cruz, E.S. : "Results of the XH-51A Rigid Rotor Research Helicopter Program". Proceedings of the 19th Annual National Forum of the American Helicopter Society, May 1963.
16. McCloud III, J.L., Biggers, J.C. and Maki, R.L. : "Full-Scale Wind-Tunnel Tests of a Medium-Weight Utility Helicopter at Forward Speeds". NASA TN D-1887, May 1963.
17. Jenkins, J.L., Winston, M.W. and Sweet, G.E. : "A Wind-Tunnel Investigation of the Longitudinal Aerodynamic Characteristics of Two Full-Scale Helicopter Fuselage Models with Appendages". NASA TN D-1364, July 1962.
18. Biggers, J.C., McCloud III, J.L. and Patterakis, P. : "Wind-Tunnel Tests of Two Full-Scale Helicopter Fuselages". NASA TN D-1548, October 1962.
19. Churchill, G.B. and Harrington, R.D. : "Parasite-Drag Measurements of Five Helicopter Rotor Hubs". NASA MEMO 1-31-59L, February 1959.
20. Simons, I.A. : "Some Objectives and Problems Associated with Model Testing". The Aeron. J. of the Royal Aeronautical Society, Vol. 74, July 1970, pp. 539-548.
21. Sweet, G.E. and Jenkins, J.L. Jr. : "Wind-Tunnel Investigation of the Drag and Static Stability Characteristics of Four Helicopter Fuselage Models". NASA TN D-1363, July 1962.
22. Lochmann, L. : "Sechskomponenten-Messungen an einem Rumpf für den Hubschrauber BO 105". Bölkow-Entwicklungen KG., Ottobrunn, FM-Windkanalbericht Nr. 31, März 1964.
23. Lochmann, L. : "Druckmessungen an einem Rumpf für den Hubschrauber BO 105". Bölkow-Entwicklungen KG., Ottobrunn, FM-Windkanalbericht Nr. 34, März 1964.
24. Keys, C.N. and Ballauer, W.L. : "Analysis of the BO-105 Drag and Stability Investigation Wind-Tunnel Tests". The Boeing Company, Vertol Division, Philadelphia, Rep.-Number D212-10021-1, November 1970.
25. Polz, G. : "Auswertung von Windkanalversuchen mit modifizierten BO 105-Rümpfen". MBB GmbH, TN-D127-2/72, Dezember 1972.
26. Hoerner, S.F. : "Fluid Dynamic Drag". Published by the Author, Midland Park, New Jersey, 1965.

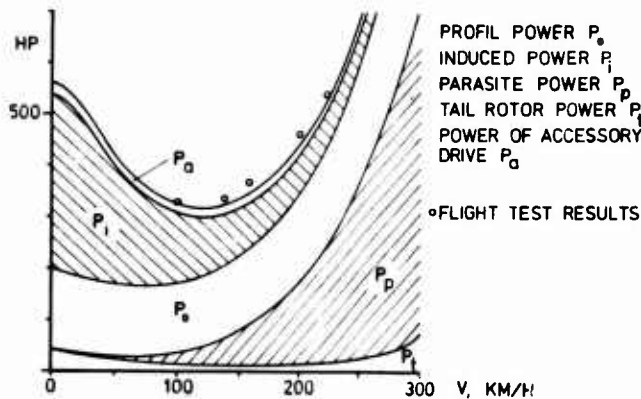


Fig. 1: Breakdown of helicopter power losses

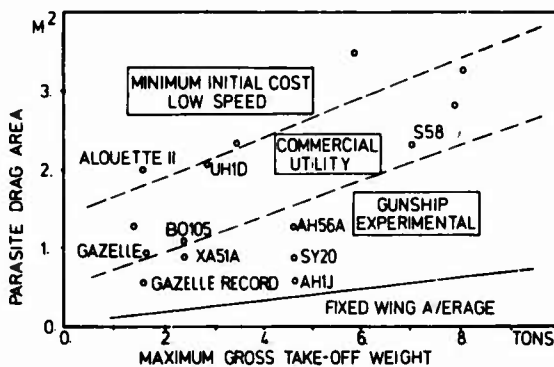
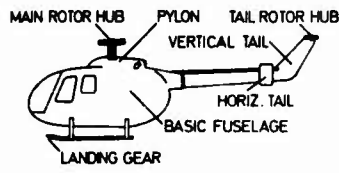


Fig. 2: Parasite drag areas of typical helicopters



COMPONENT	% OF TOTAL PARASITE DRAG AREA
BASIC FUSELAGE	36.5 - 26.5
MAIN ROTOR HUB	21.0 - 24.0
TAIL ROTOR HUB	4.5 - 5.5
MAIN ROTOR PYLON	6.2 - 7.2
LANDING GEAR	12.4 - 14.4
VERTICAL TAIL	2.7 - 3.2
HORIZONTAL TAIL	3.5 - 4.0
PROTUBERANCES	5.5 - 6.4
ROUGHNESS & LEAKAGE	4.2 - 4.8
MOMENTUM LOSSES	3.5 - 4.0
TOTAL	100

Fig. 3: Drag breakdown of typical utility helicopters

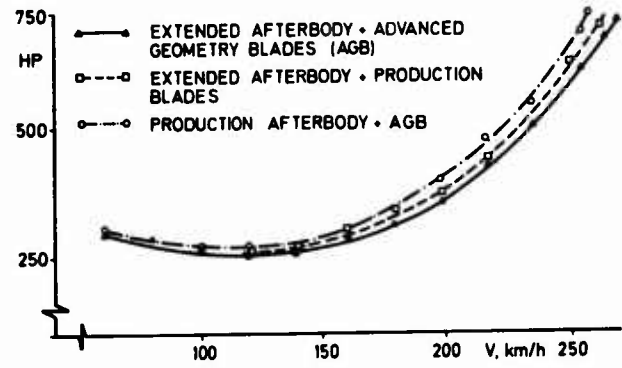


Fig. 4: Flight-test results of the BO 105 with aerodynamically improved parts

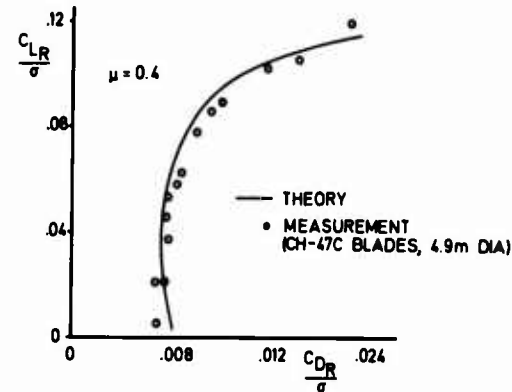


Fig. 5: Comparison of theoretical rotor performance with test results

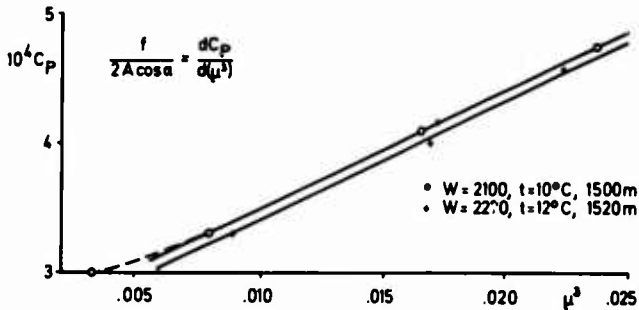


Fig. 6: Approximative method to define parasite drag

5-10

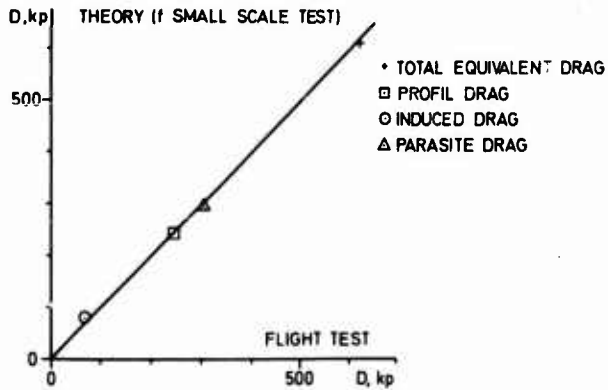


Fig. 7: Comparison of 2 methods to determine the drag breakdown of a helicopter

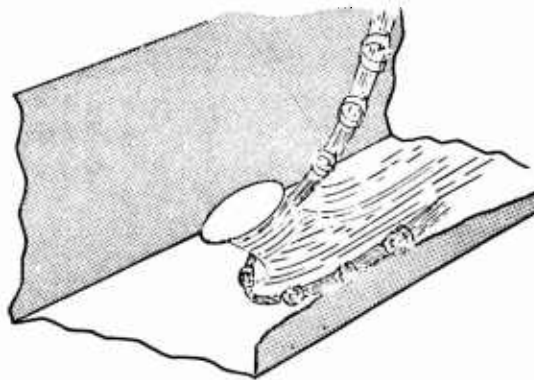


Fig. 8: Sketch of sharply deflected wake in wind tunnel

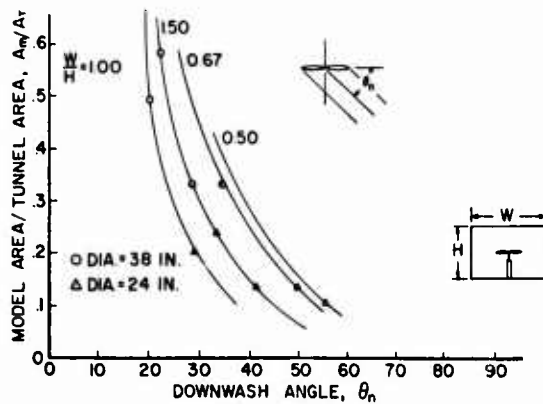


Fig. 9: Estimated limit of rotor downwash angle

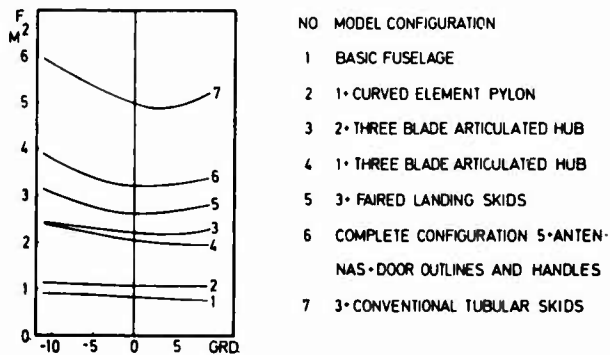


Fig. 10: Drag characteristics of a LOH model

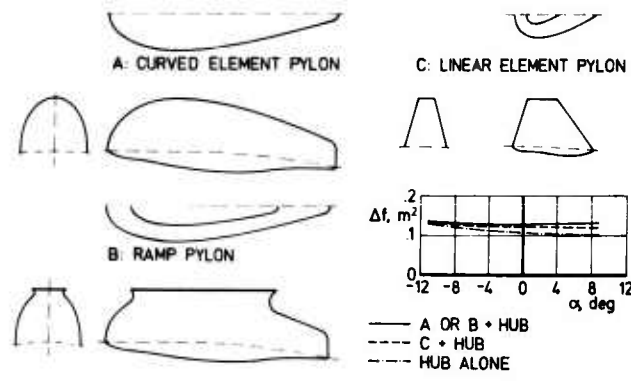


Fig. 11: Incremental drag of pylons with a three-blade articulated hub

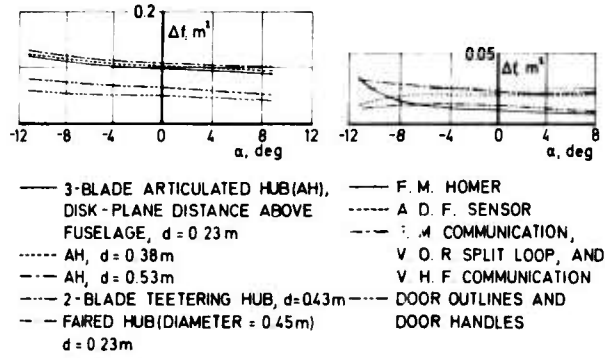


Fig. 12: Incremental drag of test hubs, antennas, door outlines, and door handles

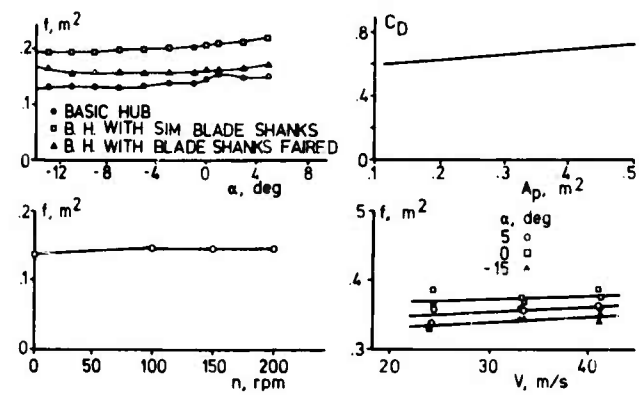


Fig. 13: Effect of angle of attack, projected frontal area, rpm, and speed on hub drag

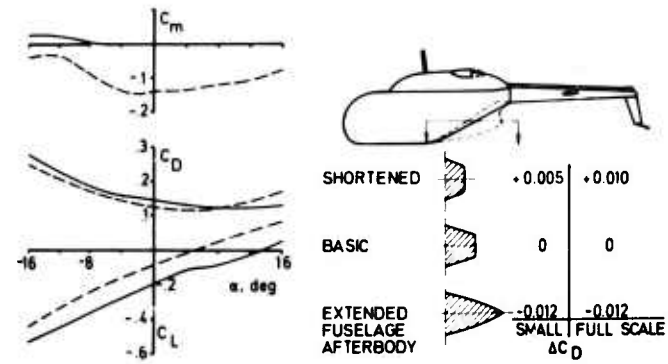


Fig. 14: Comparison of full-scale and small-scale data of a LOH

5-12

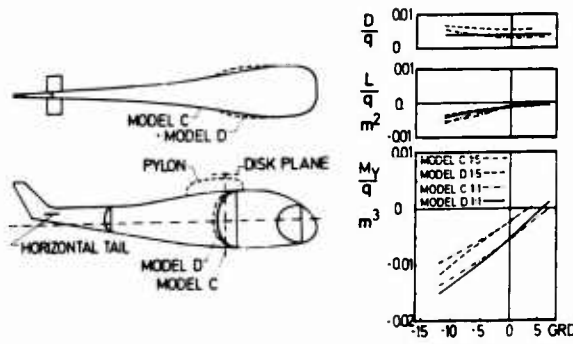


Fig. 15: A comparison 1/5-scale and full-scale results of a LOH

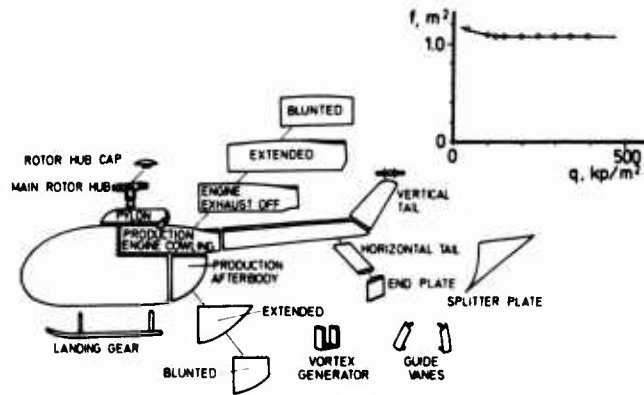


Fig. 16: BO-105 1/4-scale wind-tunnel model and Reynolds number effect on model drag

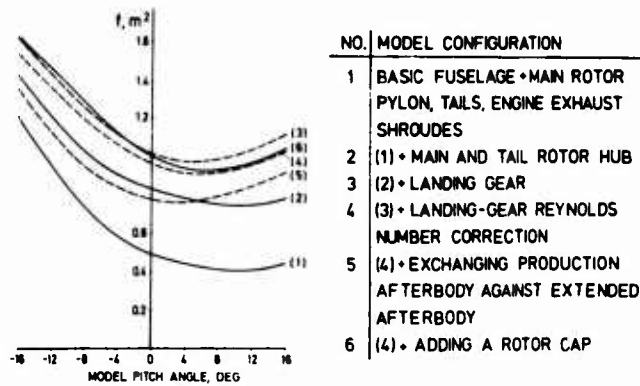


Fig. 17: BO-105 drag breakdown

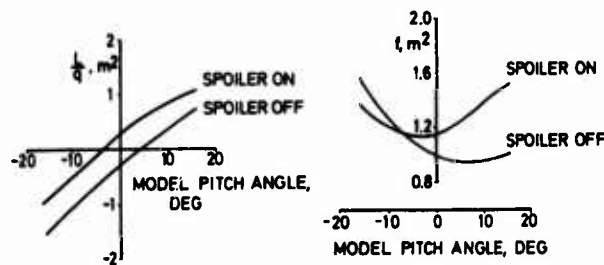


Fig. 18: Effect of spoiler on BO 105

presented by

6-1

S. F. J. Butler, M.Sc.,  
Chairman, UK Ministry - Industry Drag Analysis Panel (MIDAP),  
Royal Aircraft Establishment, Farnborough, Hants., England

## SUMMARY

The principal stages in aircraft feasibility study and design development are considered, leading to the specification of desirable characteristics of aircraft drag prediction models. The contributions to drag modelling to be expected from research are reviewed, together with the impact of computerised design selection and mission analysis methods.

An assessment of the relative importance of different components and sources of drag introduces surveys, based on contributions by UK specialists, which examine the present state of the art of prediction for specific classes of aircraft and for particular aspects of drag. The main problems involved in executing and analysing model and aircraft tests are also discussed in the drag context. An Appendix outlines the role of the Engineering Sciences Data Unit in the collection, analysis and dissemination of data suitable for direct use in practical design methods.

This review is presented on behalf of MIDAP and represents a collective effort by the members of this panel, rather than the official view of SBAC and RAE.

## RESUMÉ

Dans une considération des pas principaux d'une étude de praticabilité et de développement d'un projet, on cherche une spécification des particularités désirées que possèdent des maquettes dont on s'en sert pour les études aériennes de prédiction de traînée. On examine les contributions à la représentation de la traînée qu'on attend des travaux de recherche ainsi que les résultats sur des choix de projets et des méthodes d'analyse de mission en se servant d'un ordinateur.

Une évaluation des importances relatives des composantes différentes de la traînée et des sources de la traînée aux avions comporte des contributions par des spécialistes anglais qui ont examiné la connaissance actuelle de prédiction pour des classes d'avions prescrites ainsi que des aspects particuliers de la traînée. On discute du point de vue de la traînée les problèmes principaux nécessités par l'examination et l'analyse avec des maquettes et avec des avions. On montre dans une annexe le rôle de Engineering Sciences Data Unit pour la collection, pour l'analyse et pour la propagation de données susceptibles d'être utilisées de façon directe pour des méthodes d'étude pratique.

Cette étude vous arrive grâce à une enquête collective poursuivie par des membres du groupe MIDAP. Elle ne comporte pas nécessairement l'avis officiel du SBAC et du RAE.

## CONTENTS

	<u>Page</u>
1 INTRODUCTION	2
2 AIRCRAFT DRAG MODELLING	2
2.1 Three stages in aircraft drag prediction	2
2.2 The figure-of-merit concept	3
2.3 General remarks on drag prediction models	3
2.4 Recommended future procedure for drag prediction models	5
3 SOME SPECIFIC DRAG PREDICTION PROBLEMS	6
3.1 General remarks	6
3.2 Slender-wing aircraft	6
3.3 Military strikefighter aircraft	12
3.4 Powerplant installations for strikefighter aircraft	18
3.5 Powerplant installations for supersonic transport aircraft	23
3.6 Powerplant installations for subsonic transport aircraft	26
3.7 Trim drag	32
3.8 Sweptwing aircraft at high lift	34
3.9 Excrescence drag	42
4 ON THE MEASUREMENT OF DRAG IN WIND-TUNNEL EXPERIMENTS	45
4.1 General requirements and experimental method	45
4.2 Extrapolation	45
4.3 Concluding remarks	46
5 ON THE MEASUREMENT OF DRAG IN FLIGHT	46
5.1 General considerations	46
5.2 Thrust determination	48
5.3 Drag determination	49
5.4 Concluding remarks	49
6 ACKNOWLEDGMENTS	49
Appendix A data item service for aircraft drag estimation	A 1-A 3
References	R 1-R 6

Theoretical and experimental research advances in aeronautical science, and analyses of the extensive R & D undertaken in support of specific projects, can lose much of their effectiveness unless the results are available in a form which encourages direct use in the design and improvement of aircraft. In considering the particular needs of drag prediction models, we note there are three distinct stages (section 2.1) at which such models are required in the aircraft project feasibility and design process, involving quite different levels of sophistication and accuracy. One important direct use of an aircraft drag prediction model is in the implementation of the Figure-of-Merit concept (section 2.2). In a more general consideration of drag prediction models, it is necessary to note the growing influence which will be exerted by computerised design selection and mission analysis methods (section 2.3). Although theoretical design methods, validated by experiment, are expected to play an increasing part in a comprehensive drag synthesis framework, there will be a continuing need for maximum advantage to be taken of the results of model and full-scale R & D in support of specific projects, implying the desirability of elevated standards of test design, execution and analysis (sections 4 and 5).

Aircraft drag breakdowns for selected aircraft (section 3.1) indicate the typical contributions associated with different components and fundamental causes. These are complemented by specialist contributions which assess the present capability for reliable drag prediction for different classes of aircraft (sections 3.2 to 3.6) and for particular aspects of design (sections 3.7 to 3.9). An Appendix considers the part played by the Engineering Sciences Data Unit and by MIDAP in the provision of data of direct use in practical aircraft drag prediction methods.

## 2 AIRCRAFT DRAG MODELLING

### 2.1 Three stages in aircraft drag prediction

Estimates of aircraft drag, as well as of other key functions such as weight, performance, cost, noise etc., are required at three distinct levels<sup>1</sup> of sophistication and reliability. In the preliminary feasibility stage, forecast estimates of the drag are needed, corresponding to aircraft outline schemes generally lacking in design detail. The second stage follows project definition and selection of the main design concepts; the detailed design is determined progressively and information of direct value for drag prediction modelling becomes available from specific project research investigations. At the third stage, following initial prototype performance tests, drag and performance characteristics have to be predicted for production versions of the aircraft.

At the *preliminary feasibility* stage, in response to an apparent market opportunity or an outline staff target for a military aircraft, quick approximate forecast estimates are needed. Nevertheless, the assumed drag and performance characteristics of alternative solutions must be realistic and soundly-based, not only in themselves but also in comparison with current aircraft, their probable derivatives and new aircraft types anticipated from other manufacturers. Such forecasts are usually based on the extrapolation of existing experience, taking due account of desirable R & D advances capable of implementation within the assumed time scale and R & D budget. Elementary statistical analyses, based on existing aircraft of similar layout and guided by theoretical considerations of the main factors on which aircraft drag depends can form the basis for an acceptable forecasting procedure<sup>2</sup>. This approach is essentially conservative, however, and can easily lead to the perpetuation of low design and manufacturing standards. Further, it is of little help when attention is turned to revolutionary concepts, such as Concorde, Harrier or Multi-Role Combat Aircraft. Even in the early feasibility stages, there is considerable merit in the adoption of a more systematic and detailed approach to drag prediction, provided always that the overall results are subjected to careful scrutiny to ensure realism. Such approaches should bear in mind both the procedure which is likely to be adopted in the later stages of the aircraft development process and the possible advantages of computerised design selection and mission appraisal techniques now becoming commonplace.

It is certainly not sufficient merely to estimate the drag and other characteristics of a particular design. One also needs to know what might be possible in the way of drag reduction at the drag-dominated design points. The latter will include not only take-off/climb and cruise but also sustained and transient manoeuvre conditions, particularly for military aircraft. This leads to a need for means of predicting the theoretical lower bounds of drag. Such considerations lead naturally to the concept of a minimum-drag streamlined aircraft, on which can be based a Figure-of-Merit<sup>3</sup> (see section 2.2), relating achieved drag levels to theoretical minima. Whatever the approach adopted in this first stage, the objective must be to arrive at initial estimates which set a demanding, though feasible, target for the design team and reflect an acceptable compromise between technical, operational and economic considerations. Contingency limits should be chosen at this point which allow some room for overall design compromise, without rendering the exercise meaningless; they should be consistent with the assumed technical competence of the manufacturing organisation and project time scale, as well as not being over optimistic.

Let us pass now to the *second stage*, by which time the main design features have been chosen by the aid of detailed engineering studies and preliminary model experiments, and the scope for design modifications has been narrowed considerably. A process of continuous technical validation will commence, involving intensive theoretical and experimental R & D on selected main aspects, using models generally representative of the proposed design. The main factors contributing to aircraft drag, including manufacturing standards and excrescences, should now come under scrutiny and form the subject of studies and calculations. In this stage, it is essential in practice to prepare the drag estimates by a process involving their synthesis, rather than a simple summation, necessitating clear definition of the derivations or assumptions for all the important elements, with care taken to avoid significant omissions and double accounting. It will also be necessary to repeatedly update and review the drag estimates as improved information becomes available, and to take any necessary corrective action. The preparation of detailed drag estimates also facilitates the stipulation and maintenance of design sub-targets for the main aspects, consistent with the main target. In fact, the ability of design organisations to meet the overall target depends essentially on the technical management being able to control and monitor the entire R & D process by means of well-judged subsidiary targets. The estimates should therefore

incorporate the considered view of the design team on its ability to detect and limit drag growth, involving a detached assessment of the general design and manufacturing standards which can be achieved and justified on economic grounds.

63

As the detailed R & D process leads to a determinate aircraft design, which represents a near-optimum practical compromise, the process of validation becomes increasingly more detailed and specialised. There is progressive elimination of areas of doubt, with the replacement of assumptions and estimates by predictions supported by experimental data. Throughout this development period, it is obviously necessary to provide a format for the drag prediction model which can readily accommodate the constantly-changing sources of drag data which become available. The precise composition of the drag (and other) predictive models will need to alter with the accomplishment of the various R & D tasks; the adequacy of the model must therefore be kept under continual review. Before the first flight of the prototype, the spread of the bounds of the drag estimates should have been reduced to that associated with residual uncertainties in the interpretation or extrapolation of test data on specific experimental models, and second-order doubts about the application of prediction methods.

Once reliable prototype flight test data is available, and the necessary, often controversial, interpretations have been undertaken to disentangle thrust from drag, there comes the moment of truth<sup>1</sup> when, as it is to be hoped, the inferred drag lies within the bounds of the final estimates, preferably near to the lower bounds. Such are the problems of flight thrust determination at prototype stage (see section 5) that this is rather an idealised view of what is likely to transpire. In practice, the main emphasis will be on overall comparisons of (thrust - drag) with expectation. Drag analysis may be attempted, but usually only when improvements are found to be necessary, in which case a hurried diagnostic approach under pressure can be expected (see section 5). There may well arise at this point some critical arguments as to whether an apparent deficiency should be debited to engine performance, rather than excess aircraft drag.

From this point onwards, subject to the completion and proving of any unforeseen design modification which are necessary, we enter the *third stage* in which the guaranteed performance for the production aircraft in its main configurations over a full range of flight environments has to be estimated, mainly by analysis and interpretation of the prototype test performance. A new predictive model will be involved, calibrated by reference to the measured prototype performance at selected datum conditions. Some of the more elusive elements of the drag estimates can be checked directly by flight test at this stage (for example, external stores and certain types of excrescences). The tolerances in the estimates will now be dictated by the degree of confidence of the aircraft and engine manufacturers in the engineering quality control standards which can be maintained, by the scale of the differences between the prototype and the production aircraft, and by a critical assessment of the accuracy of the flight test data.

## 2.2 The figure-of-merit concept

One principal use for a good drag estimation method is in the provision of fair and meaningful comparisons of the overall cruising efficiency of different aircraft designs. Haines<sup>4</sup> has argued the merits of using the parameters:-

$$E_{pr} = \frac{C_D - C_{D_i}}{C_{D_{pr}}} \quad \text{and} \quad E_F = \frac{C_D - C_{D_i}}{C_{D_F}} \quad (1)$$

where  $C_{D_i} = C_L^2(1 + \delta)/(\pi A)$  is a theoretical allowance for vortex drag coefficient;  $C_{D_{pr}}$  is the estimated profile drag coefficient (skin friction + form) for a streamlined aircraft with fully-turbulent boundary layers, and  $C_{D_F}$  is the estimated flat-plate skin-friction drag assuming fully-turbulent

boundary layers, both preferably evaluated at the design Mach number and lift coefficient. The choice between  $E_{pr}$  and  $E_F$  is finely balanced, but  $E_{pr}$  represents a more realistic choice since it relates achieved drag with that theoretically possible with a fully-streamlined aircraft (i.e. with minimal aircraft flow separations) of the same general shape. It is emphasised that significant problems attach to the provision of the minimum profile drag estimate for a streamlined sweptwing aircraft at elevated Mach numbers. Also, it should be borne in mind that the datum is nominally associated with fully-turbulent flow, which may be inappropriate for the design under consideration. Nevertheless, this concept is convenient and practical.

In order to avoid superficiality, its use should be accompanied by a critical assessment of the sources of drag. We recall that it was demonstrated<sup>4</sup> that values of  $E_{pr}$  of 1.25 were rarely bettered, whilst values in excess of 1.50 could occur on similar designs. Of course, if a design team is merely prepared to settle for an 'acceptable' value of, say, 1.25, for other than economic reasons, then this could lead to an undesirably-complacent attitude. There is little doubt that there is still considerable scope for improvement in drag standards, but this will only happen if designers challenge all avoidable sources of drag, relative to the fully-streamlined datum, and if low drag levels are stipulated as a major design aim throughout. Further, it is of course possible to achieve significant areas of laminar flow, possibly through boundary-layer control. In addition, there is a need to distinguish between average in-service standard and factory-fresh condition.

## 2.3 General remarks on drag prediction models

An essential tool for each design group is a methodology which accounts for the known drag of existing aircraft designs. This will need to be more sophisticated and detailed than a simple figure-of-merit assessment method for each new design, though such an approach will probably form an important

6-4

element in the early selection process. From consideration of the second stage of aircraft drag prediction, it can be seen that a synthesis approach is to be expected, based jointly on analysis and on research results.

Over a period of years, for established categories of aircraft and engines there will accumulate a considerable body of data from *ad hoc* model and aircraft tests of varying quality. It is common for the flight test data to be analysed by the drag polar method<sup>1</sup>, within limits set mainly by thrust determination considerations (see section 5), the deduced drag being attributed to various causes. A combination of experience and intuition, supported by theory and model-test data, will be used in this interpretative process. Clearly, there is considerable scope for drawing the wrong inferences, and the procedure is necessarily rather subjective. The resulting design charts need to be updated to reflect possible design advances and it is difficult to assign accuracy limits with any degree of confidence. Even with closely-related members of a given aircraft family, significant predictive errors are found to occur<sup>1</sup>, illustrating the inherent dangers of an essentially empirical analysis process which is not accompanied by adequate physical understanding.

A prediction method obviously needs to be anchored by reference to selected flight test data, since only in this way can we be sure that the overall aircraft characteristics have been taken into consideration and also since certain factors, such as roughness and some types of excrescence, cannot be fully represented in model tests. However, it is not possible to achieve a progressive drag breakdown by components, as in model testing, and there will be undesirable restrictions in flight test on the ranges of important parameters (see section 5). Even if the resulting drag model is basically sound, it seems questionable whether prototype flight drag data is ever sufficiently accurate and comprehensive enough to validate the model for wider use. It is therefore argued that aircraft drag prediction methods should not be constructed essentially around empirical analyses of flight data. Of course, appreciable difficulties are involved in the interpretation and extrapolation of model-scale tests to full-scale conditions (see section 4), so that strong objections can also be raised against a method mainly based on empirical analysis of *ad hoc* model tests. Admittedly, by a judicious combination of progressive *ad hoc* model tests and specialist experimental investigations, together with selected flight test data on the same configurations, an improved empirical method can undoubtedly be devised of considerable practical value<sup>5</sup> in the design of evolutionary types of aircraft.

Nevertheless, a clear distinction must be drawn between basically-empirical approaches and those in which model and flight test data are interpreted within a comprehensive and logical synthesis framework, essentially founded on theory and supported by carefully-designed and executed aimed research in key areas. It should be stressed that the R & D work undertaken in support of specific projects could play a much greater part than it does at present in the improvement and validation of theoretical design methods, but only if such tests are designed and executed with this object in mind (see sections 4 and 5). It is also tempting to suggest that such a disciplined and critical approach to project-oriented R & D would lead to a reduction in the duplication and repetition which often seems to occur.

Considering how better predictive methods should be developed, we can first reject as no longer appropriate a simple classification of aircraft drag into components independent of, and dependent on, lift. In view of the considerable advances of aerodynamic theory, one is encouraged to examine the possibility of a more enlightened approach in which the synthesis of drag is achieved by compounding elements arising from different basic causes, associated more directly with the nature of the fluid dynamics. Providing that adequate understanding and quantitative methods are available to allow reliable and consistent modelling of all the significant contributions to an acceptable level of reliability, this would constitute a practical method. Even if, as at present, some elements can only be estimated to a limited accuracy, perhaps in a semi-empirical way, there is much in favour of guiding future research towards this aim and tabling a declaration of future intent to develop a complete drag estimation method, secured within a consistent theoretical framework.

A convenient basic breakdown of drag from the fluid mechanics standpoint is set out in Fig.1. Viscous drag is manifested by a reduction in streamwise momentum in the wake, whereas vortex drag is associated with transverse components of momentum in the wake flow. In principle, then, it is possible to differentiate between these components by means of detailed studies of the wake behind a model. As far as wave drag is concerned, on physical grounds this is most satisfactorily associated with entropy rise through the shock wave, but this is not particularly helpful in practice. Neglecting form drag and assuming small lift forces, wave drag can appropriately be identified with pressure drag, a convenient and common assumption in the analysis of experiments. Linear theory offers a neat discrimination in that wave drag appears as streamwise momentum convected laterally, whereas vortex drag is energy convected downstream.

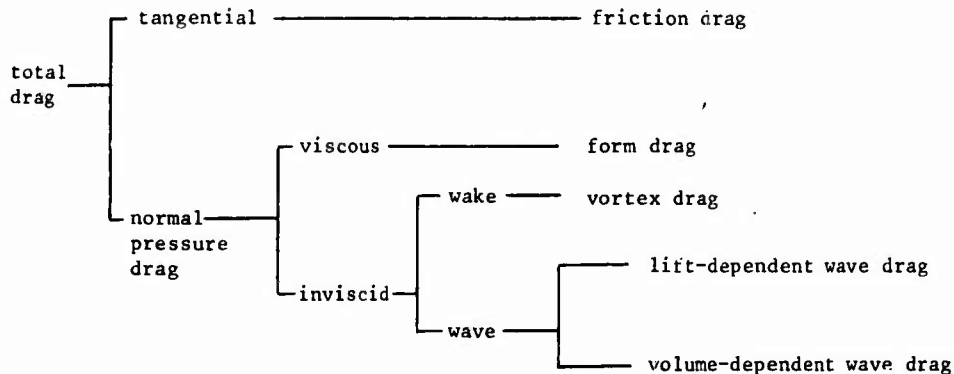


Fig.1 Components of aircraft drag

6-5

For an approach based on fundamental origins of drag to succeed, it is most important to be able to differentiate between the different sources of drag in experimental research. In this connection, we wish to draw the attention of the Conference to current fundamental research at RAE, concerned with study of the composition of the wakes behind selected basic shapes at low freestream speeds, which aims to examine the validity and practicality of identification by wake analysis of viscous and vortex drag. The potential importance of this technique is not thought likely to lie in the routine analysis of specific aircraft model wakes, but rather in the prospect of improved understanding of selected problems (such as the three-dimensional drag of non-planar wings under high-lift conditions).

As regards theoretical methods for aircraft design, the inviscid compressible flow about generalised streamlined wing-body combinations for well-attached flows can already be calculated and allowance made for viscosity effects by boundary-layer growth calculations. There seem to be excellent prospects of extending three-dimensional wing-design methods to cope with the shockfree mixed flows appropriate to super-critical wings. Further, at least to a first approximation, allowance can be made for the presence of engine nacelles and probably the interaction effects, on the assumption of a well-optimised installation avoiding significant flow separations. Therefore, we are certainly close to the position where realistic low targets can be set for profile drag, appropriate to the datum streamlined sweptwing transport aircraft involved in the figure-of-merit approach, even though we cannot expect to be able to deal in similar confidence with adverse engine installation and excrescence effects, two of the main causes<sup>4</sup> of supplementary drag for such aircraft.

Unfortunately, it seems fairly clear (see section 3) that a comprehensive general theoretical drag prediction framework suitable for all the main current classes of military and civil aircraft is certainly not likely to be feasible for some time to come. For example, zero-lift wave drag for non-slender military aircraft, vortex drag for slender-wing aircraft and store installation drag for military aircraft seem likely to prove intransigent. Engine installation effects, when severe, are likely to prove just as difficult to estimate. The prediction of transition position for the full-scale aircraft is a particularly important and difficult problem. For sweptwing subsonic transport aircraft, even, drag prediction in the high-lift configuration is not likely to yield to theoretical attack easily, and there is no immediate prospect of general drag prediction methods for cruise at elevated lift coefficients with substantial flow separations.

#### 2.4 Recommended future procedure for drag prediction models

It seems, then, that an improved framework should anticipate the progressive introduction of theoretical methods. For the foreseeable future, it is reasonable to expect that drag estimates will be built up by a process of synthesis<sup>6</sup>, involving the summation of the estimated contributions of individual elements arising from the different causes of drag. In general, there will be significant interference between the flow fields of the various aircraft components, and the way in which these are accounted for needs careful consideration. In this context, interference drag is defined as the drag which results from modifications in the growth of the boundary layer due to the proximity of the components, together with the drag due to redistribution of the trailing vortex system.

It is therefore recommended<sup>7</sup> that the aircraft is built up in a standard order, aerodynamically speaking, so that, as each component is added, its interference effects on the components already present are included, with the important exception that the wing and fuselage are considered together in the estimation of vortex drag. The following order of build is suggested:-

- (a) Wing drag, including the effect of the presence of the fuselage on vortex drag;
- (b) Fuselage drag, including the effect of the fuselage/wing interference on wing and fuselage profile drag;
- (c) Fin (vertical stabiliser) drag, including fin/fuselage interference;
- (d) Installed drag of the propulsive system;
- (e) Tailplane (horizontal stabiliser) and trim drag, including tailplane-fuselage interference;
- (f) Drag due to surface finish and excrescences, including cavities and leak flows;
- (g) Drag of external store installations;
- (h) Wave drag;
- (i) Contingencies, principally to cover airframe manufacturing tolerances.

Wherever possible, the estimates should be based on validated theory or semi-empirical analyses of systematic experiments. The data items of ESDU form an important element of such a procedure (see Appendix) although important areas of omission are evident as of the present. In practice, it may be convenient to rearrange the items on the lines of the ESDU classification (see Fig.A1). The approach is basically well-suited to the incorporation of theoretical advances. Equally, specific experimental information can be inserted as this becomes available. There is an obvious need to watch for omissions and double accounting. Particularly difficult is proper provision for the complex interactions which can occur, especially in connection with engine and store installations.

It is here appropriate to consider briefly the effect of computers on the form of aircraft drag and other prediction methods. Increasingly, the complete aircraft design process is being computerised<sup>8</sup>. Thus, it can be assumed that theoretical advances and analytical methods will normally be available in this form. The detailed geometry of committed designs will certainly be stored by computer. The introduction of computer design aids including interactive graphic techniques linked directly into the production process is taking place at a fast rate. Methods are already available for the calculation of complex missions, including the optimisation<sup>9,10</sup> of flight path, and for preliminary design appraisals of the whole aircraft<sup>11</sup>. It is to be expected that optimisation methods will quickly become available for subsidiary aspects of the design; for example, the optimisation of engine installations<sup>12</sup>. There are no real problems in preparing computer programs representing existing prediction methods (at least where

6-6  
these are robust and logical enough to survive critical examination). It is attractive and possible to allow a more detailed representation than previously, still with a significant reduction in turn-round time. As regards theoretical design methods, sometimes these can be incorporated directly as sub-routines in the total design procedure. However, particularly where an iterative optimisation is to be effected, it will be preferable to avoid direct use. Instead, the results of systematic application of the design method, if accompanied by adequate understanding, can be used to provide an analytical generalisation of the results in terms of the main design parameters, within prescribed limits: the computer-age equivalent of the classical design data sheet. Thus, the results of the design method may be represented by a matrix of values in terms of the design parameters, with provision for interpolation. The complete design or mission program tends to be built up from a set of linked modules, some theoretical, some analytical, and some representing empirical generalisations or assumptions, with provision for directed sequential use.

One of the main effects is seen to be an increasing need for the early presentation of theoretical, experimental and analytical advances in the form of compact programs, valid within specified limits and specifically written to be suitable for incorporation in existing complex design procedures. Such programs need to be designed to be self-sufficient, with standard interface arrangements, so as to facilitate their integration into existing complex programs and eventual replacement by improved versions. More than ever it will be necessary to subject the outcome of the complete design process to critical judgment. Thus, it will be important to display detailed drag breakdowns and their variation during any optimisation process, to allow the designer to appreciate fully what is happening and to avoid unacceptable design excesses. However, it will not be possible to validate the model in any complete sense, although detailed engineering studies on selected configurations will act as control datums. As computers are not renowned for commonsense, this responsibility will continue to reside in the design team, probably weighing increasingly heavily as more reliance is placed on the use of computerised design selection methods.

### 3 SOME SPECIFIC DRAG PREDICTION PROBLEMS

#### 3.1 General remarks

The set of surveys which follow are intended to highlight the main problems which arise in the prediction of the drag of selected types of aircraft and their engine installations (sections 3.2 to 3.6) and also to consider certain special aspects, namely trim drag (section 3.7), drag at high lift (section 3.8) and excrescence drag (section 3.9). Each section represents the considered view of a UK specialist; although the separate contributions have been subject to editing and some rearrangement, it is hoped that their individual flavours have been retained.

By way of introduction to this section, it seems desirable to discuss briefly the relative magnitude of the drag contributed by the different components of the aircraft and by the different basic causes of drag. Typical drag breakdowns are shown in Fig.2, prepared from studies made at the Cranfield Institute of Technology. Considering first the supersonic civil transport (see section 3.2), at cruise the skin friction, zero-lift wave drag and total lift-dependent drag each typically contribute about 30% of the drag, with the remainder mainly attributable to engine installation drag (see section 3.5) and to excrescence drag (see section 3.9). Much the same applies for a streamlined strategic bomber or a supersonic strikefighter aircraft (see Fig.2). For essentially non-slender supersonic strikefighter aircraft (see section 3.3), the prediction of wave drag is of particular concern. The prediction of the drag of external store installations is of major importance for small military aircraft, as is the prediction of engine installation and rear fuselage drag effects (see section 3.4).

For long-range subsonic transports and for subsonic strikefighters at cruise altitude, reliable estimation of wing profile drag and the lift-dependent drag of the wing-fuselage combination is of great importance; these aspects can together account for half the drag at cruise<sup>6</sup>. For the airbus, or a military strikefighter at high subsonic speeds at low altitude, wing and fuselage viscous drag tends to become predominant. However, engine installation effects are again important (section 3.6), sometimes accounting for 10% or more of the cruise drag. Excrescence drag unfortunately can also reach similar proportions, typically being responsible for half the avoidable drag<sup>4</sup> relative to the fully-streamlined datum aircraft. As regards the effects of external store installations, their presence typically can increase the high subsonic speed drag of a strikefighter by 70%.

Trim drag is significant at cruise and at high lift, particularly in the comparison of different aircraft concepts (see section 3.7); it needs to be calculated carefully.

Under high-lift conditions appropriate to take-off and landing (section 3.8), lift-dependent drag forms the major component of drag and can reach 85% of the whole (see Fig.2).

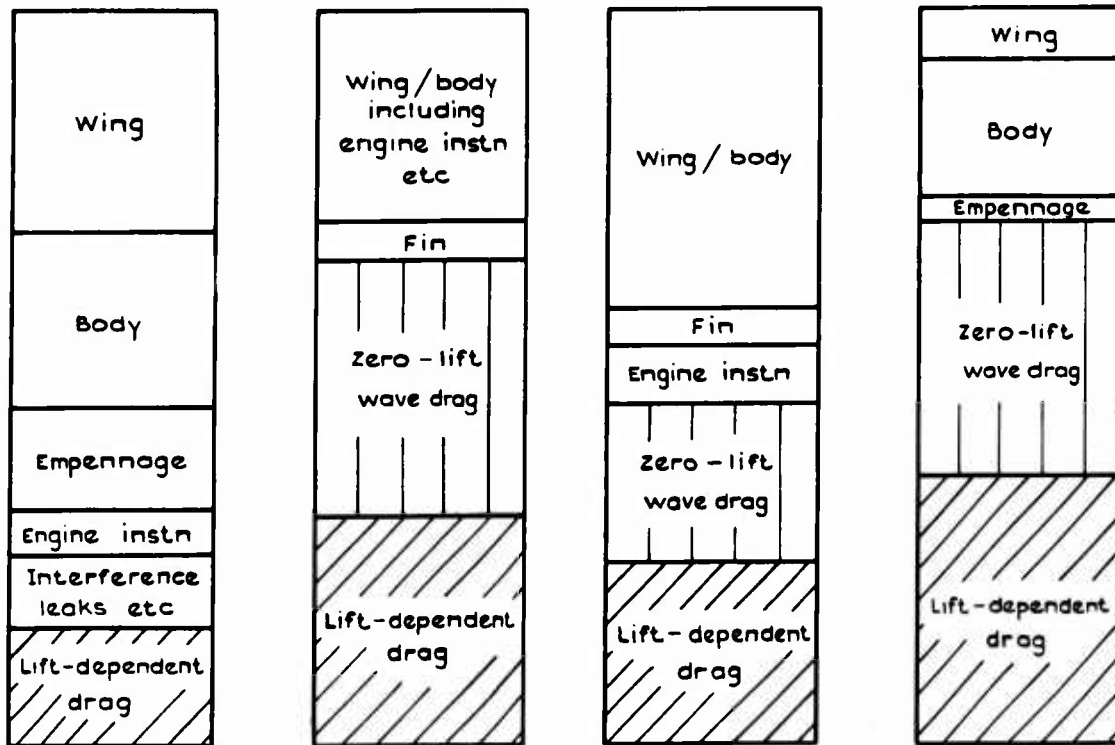
The relative magnitudes of the different drag terms are obviously important in themselves. However, the order of the uncertainty of each significant component of a drag synthesis also needs to be considered, particularly where the contribution can be reduced or avoided altogether by design choice. Such considerations imply a need for a broad, persistent attack on the understanding of aircraft drag and its prediction; there are few aspects of aircraft drag estimation with which we can afford to be satisfied at present.

#### 3.2 Slender-wing aircraft

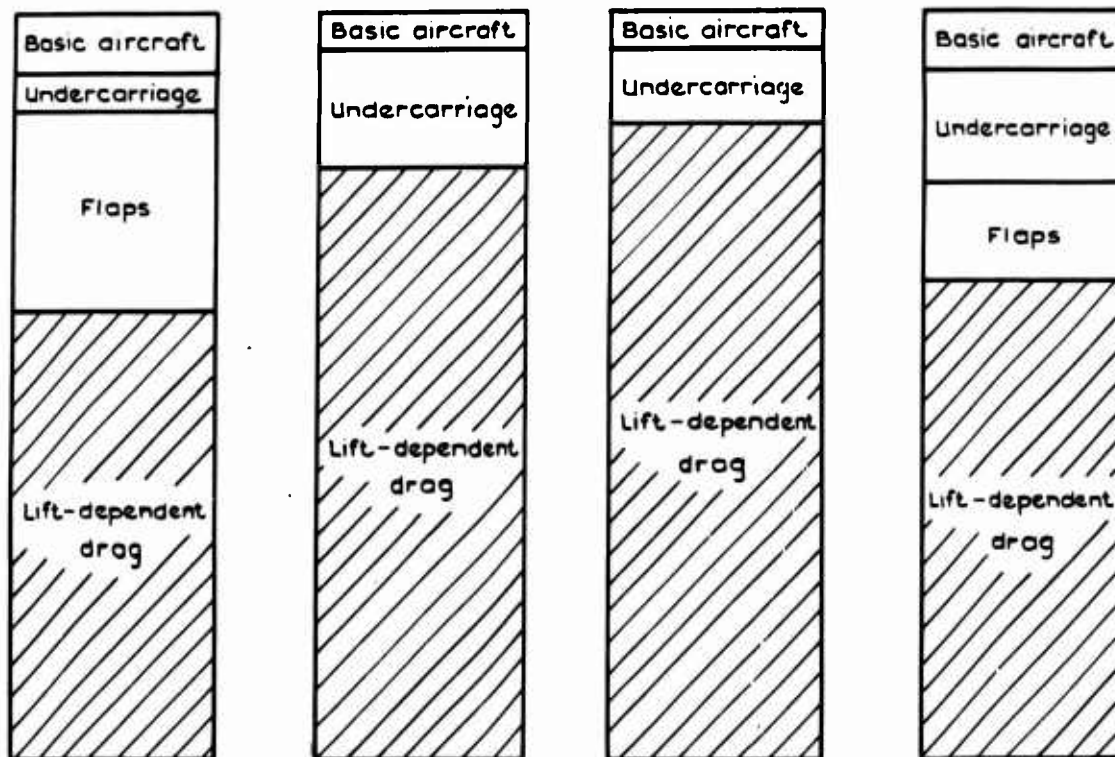
Based on a contribution by J.B.W. Edwards, RAE.

##### 3.2.1 Introduction

In the absence of a precise definition of what is meant by a 'slender' wing, the term is here taken to refer to wings of low aspect ratio, which are designed to operate with the airflow separated from the leading edges forming conical flows over the upper surface. This feature dominates the flow pattern at



a Cruise drag



b Take-off drag

A69 M=0.8  
Airbus

A60 M=2.2  
Integrated slender  
delta airliner

B72 M=2.0  
Slender delta  
strategic bomber

S68 M=2.0  
Variable sweep  
strike fighter

Fig. 2 aab Typical aircraft drag breakdowns (based on studies by Cranfield Institute of Technology)

6-8 low speeds but will also be present at most flight conditions, supersonic and subsonic, provided that the leading edges are restrained to lie largely or entirely within the Mach cone. Such controlled flow separations distinguish slender wings from conventional swept wings and lead to special problems in drag prediction. For uncambered wings with sharp leading edges, this separated flow pattern is formed as soon as the incidence sensibly departs from zero. By cambering the wing (e.g. by drooping the leading edges) the onset of separated flow can be delayed until some significant incidence is achieved, so that the lift coefficient for optimum L/D ratio is correspondingly increased. This design feature is valuable as a drag reduction mechanism, but it complicates the estimation of drag. Accordingly, consideration will be given firstly to uncambered wings, the effects of camber being discussed subsequently. The lack of generalised quantitative methods for calculating flows with leading-edge separations is, perhaps, the major stumbling block at present in slender-wing drag estimation; this, in turn, means that one has to rely largely on correlations of experimental data.

### 3.2.2 Definitions and drag breakdowns

Slender-wing planforms are generally described by the following geometrical parameters:-

$$\begin{aligned} A &= \text{aspect ratio} = \frac{(2s)^2}{S} \\ p &= \text{planform parameter} = \frac{S}{2sl} \\ s/l &= \text{semispan-to-length ratio} \\ S &= \text{planform area} \end{aligned}$$

In addition, the following generic terms are used:-

- Gothic:- planforms with convex leading edges;
- Delta:- planforms with straight leading edges;
- Ogee:- planforms with leading edges having a point of inflexion.

The basic drag breakdown considered here is:-

$$\text{total drag} = \text{skin-friction drag} + \text{zero-lift pressure drag} + \text{lift-dependent drag} \quad (2)$$

For a complete aircraft configuration there would, of course, be additional terms such as trim drag, engine installation drag, excrescence drag etc., which are not considered further. To illustrate the relative magnitude of the three main terms, a typical drag breakdown for a supersonic transport slender-wing design at cruise at  $M = 2$  and in the take-off conditions is as follows:-

(a) For  $M = 2$  cruise, the skin friction, zero-lift pressure and lift-dependent drags each contribute about 30% of the total, the remaining 10% being attributable to engine installation drag and other smaller items;

(b) At take-off, the lift-dependent drag is all important, as much as 85% of the total, whilst skin friction accounts for 7%, zero-lift pressure drag is less than 1%, and engine installation effects and trim drag are largely responsible for the remaining 7%.

### 3.2.3 Drag prediction methods

#### (a) Skin-friction drag

Experimental studies of the surface flow patterns on slender wings show that when the separated flow pattern is established the streamlines on the upper wing surface are far from streamwise under the conical flow regions near the leading edge, while associated measurements show large variations in boundary-layer thickness and, hence, in the local skin-friction coefficient. For estimation purposes, it would be quite impractical to attempt to estimate the local skin-friction coefficients and flow directions in detail, in order that an integration of the forces could be made. It is therefore usual to assume that flat-plate skin-friction formulae can be applied over the whole wetted area. Although this is an approximation, it is not altogether unreasonable. Firstly, the upper wing surface, where the main departure from streamwise flow occurs, is perhaps no more than one-third of the total wetted area of a slender-wing/body combination. Secondly, the pattern<sup>13</sup> of skin-friction coefficient under the vortex flow is one of peaks and troughs which roughly average out to the mean value expected in streamwise flow, when considered in conjunction with the wing lower surface values.

A convenient form of skin-friction coefficient for use in slender-wing estimation, which is valid for  $0.2 < M < 2.8$ , is that given by Winter<sup>14</sup>. The compressible skin-friction coefficient,  $C_{F_c}$ , is given in a simplified form suitable for project estimation, by:-

$$C_{F_c} = \frac{0.49}{F_c} / \log_{10} \left( \frac{F_\delta}{F_c} Re \right)^{2.625} \quad (3)$$

for fully-turbulent flow conditions ,

where  $\bar{r}_c = \sqrt{1 + 0.2M^2}$  and  $F_\delta = 1 + 0.056M^2$ ;  $Re$  is the Reynolds number evaluated using a local mean chord and freestream conditions. Because of the rapidly-varying chord of the wing across the span, it is necessary to consider strips of wing rather narrower than is usual for swept wings in order to assign local mean chords with sufficient accuracy. 6-9

Corrections should be made to the drag evaluated from this formula to allow for likely areas of laminar flow and also (in the case of supersonic speeds) for departures from the zero-heat-transfer condition for which the above expression is valid. As an illustration of this latter correction, for Concorde at  $M = 2$  non-zero heat transfer conditions on areas of the skin which are maintained cool by being in contact with the fuel cause an increase in skin-friction drag of only about 1% and, at lower speeds, this effect is negligible; laminar flow corrections are usually neglected.

(b) Zero-lift pressure drag

At low speeds this term, as we have seen, is very small and can be estimated either by following sweptwing aircraft prediction practice or by suitably factoring the skin-friction drag. At supersonic speeds, this term is identified with the zero-lift wave drag, which now is represented usually by means of a zero-lift wave drag factor,  $K_0$ , defined by the expression:-

$$C_{D_{0W}} = K_0 \frac{128}{\pi} \frac{V^2}{\ell^4 S} \quad (4)$$

where  $V$  = aircraft volume and  $\ell$  = overall length of the wing-body-fin combination. There is a great deal of literature concerned with the calculation of the zero-lift wave drag of slender wings; the basic theory<sup>15,16</sup> has been supplemented by papers on numerical methods for evaluating drags<sup>17,18</sup>.

The calculations involve the first and second derivatives of the longitudinal area distribution, which, for realistic aircraft shapes, cannot easily be obtained sufficiently accurately. For shapes with reasonably-smooth area distributions (which desirably will be the case, since smoothness is a requirement for low drag) the methods are reliable but, for purposes such as generalised project studies, they can prove rather cumbersome. If a value of  $K_0$  is calculated for a representative datum shape, then one can argue it is reasonable to obtain the drag variation for small departures from the datum geometry by assuming  $K_0$  remains constant and applying the volume, length or area changes in the expression above.

Similarly, the effect of changes in Mach number from that of the datum-shape calculations can be adequately estimated. Theoretical studies show that  $K_0$  varies with  $\log \beta s/\ell$ , where  $\beta = \sqrt{M^2 - 1}$ , and experimental evidence confirms this trend. A typical variation of  $K_0$  with Mach number is as follows:-

$$K_0(M) = K_{0M=2} \left\{ 1 - 0.29 \log \frac{\beta}{1.732} \right\}, \quad (5)$$

which was derived by fitting a curve to a collection of theoretical and experimental data for SST-like slender wings and wing-body combinations. The data on which this expression was based suggests that it is valid for  $1.2 < M < 2.5$ .

Such simple formulae for departure from a known datum are useful but do not form an adequate substitute for comprehensive calculations. For project study work, there is a need for simple ways of evaluating zero-lift wave drag; such methods need to be able to deal with realistic aircraft shapes, where the area distribution and its derivatives are not as smooth as one might wish. Current UK research at HSA Brough (see section 3.3) may help in this respect.

(c) Lift-dependent drag at low speeds

In the absence of satisfactory methods for calculating the flow with leading-edge separations, the estimation of lift-dependent drag has inevitably to depend on the analysis of experimental data. In the last few years at RAE, the effects of changes in various geometric parameters of slender wings have been investigated carefully by low-speed wind-tunnel experiments, in which one parameter was varied at a time in a systematic manner. Kirkpatrick and Kirby<sup>19</sup> have analysed the results of these tests and presented data on the induced drag factor,  $K = \pi A(C_D - C_{D_0})/C_L^2$  together with information on the distance,  $h_n$ , of the aerodynamic centre from the centre-of-area. The centre-of-area gives some guide to the centre-of-gravity position, so that  $h_n$  is a measure of the difficulty of balancing the wing, and thus is indicative of the trim drag which is likely to be incurred.

Parameters covered in the study included aspect ratio, planform (ogee, delta or gothic), and thickness-chord ratio. Values for  $K$  and  $h_n$  are given at values of  $C_L$  of 0.5 and 0.2 appropriate to take-off and landing and subsonic cruise respectively. Fig.3 presents some results for  $C_L = 0.5$ .

Analytical expressions can be fitted to the data if required. One geometrical parameter not so far considered is variation of section shape for a given maximum thickness. This can be quite significant, for the leading-edge vortices induce high suction forces locally associated with the non-linear component of lift; if these suction forces can be located on forward-facing surfaces, a component in the thrust direction is obtained giving a drag reduction. Kirkpatrick and Kirby<sup>19</sup> demonstrated this effect, achieving drag reductions of up to 9% at  $C_L = 0.5$ ; they suggest that more refined design methods could lead to

6-10 reductions of, perhaps, double this amount. This is, therefore, an area where further work is justified, both on the design methods and on the prediction of consequent drag changes.

It is stressed that the above analysis applies to uncambered wings in isolation. Some guidance on the effect of adding a body to such wings has been given by Kirby<sup>20</sup>. At low incidences, the body produces linear lift, cancelled out by an equivalent loss of lift on the wing, with no nett effect on the lift-dependent drag coefficient. This situation still holds at incidences of interest for take-off and landing but, at a higher incidence still, body vortices are formed which augment the non-linear lift and lead to a small increase in induced drag.

The majority of experimental evidence on slender wings is for planforms having unswept trailing edges. It was found<sup>21</sup> in the early days of slender wings that trailing-edge sweep had an adverse effect on the zero-lift wave drag at supersonic speeds, so that effort has been concentrated on unswept trailing-edge planforms. These considerations do not preclude the use of such planforms for purely subsonic applications. Kirkpatrick and Hepworth<sup>22</sup> have presented sufficient evidence on the effects of trailing-edge sweepback (at constant span) to enable a reasonable estimate of the effects on drag at low speeds to be made. Positive sweepback reduces the plan area which gives a reduction in skin-friction drag and increases the aspect ratio so that small reductions in lift-dependent drag can result, leading to a favourable effect on the lift-drag ratio. However, more difficult balance problems tend to arise with such planforms.

(d) Lift-dependent drag at supersonic speeds

For uncambered wings at supersonic speeds and at incidences away from zero, there will be flow separations occurring over the upper surface which preclude at present an adequate theoretical method for evaluating the drag. A useful correlation is due to Courtney<sup>23</sup>, who found a linear relationship between the lift-dependent drag factor,  $K$ , as defined previously, and the parameter,  $(1/2p)(\beta s/l)$ , valid for lift coefficients of around 0.1 appropriate to cruising flight at supersonic speeds. The expression,  $K = 0.75 + 2.55((1/2p)(\beta s/l))$ , is a particularly-good fit for wings with streamwise tips. The average value for delta wings is a little higher, as can be seen in Fig.4. The line fits data within the range of  $(1/2p)(\beta s/l)$  from 0.3 to 0.8 or even higher; for typical slender-wing configurations, this implies Mach numbers extending roughly from 1.4 to 3.0. The data was derived from tests on isolated wings without fuselages and restricted to planforms with unswept trailing edges. If shapes with discrete fuselages are considered, the length,  $l$ , in the above expression should be taken as the length of the lifting surface (rather than the overall length, as in the case of the zero-lift wave drag calculations). As at subsonic speeds, the influence of the body is then not appreciable at low incidences.

Now, the usual form for expressing  $K$  is given by supersonic flow similarity considerations as  $K = K_v + 2(\beta s/l)^2 K_w$ , where  $K_v$  and  $K_w$  are the vortex drag and wave drag due to lift respectively. In the absence of changes in  $K_v$  and  $K_w$ , the value of  $K$  would thus be independent of  $p$ . Comparison of the expression with the above correlation implies that  $K_v$  or  $K_w$ , or both, must vary with  $p$ . Qualitatively, this is what one would expect; as  $p$  is reduced to yield cgee wings, both the span and chord loading depart further and further from the elliptical distribution with inefficient load carried near the apex and near the tip which, in turn, would be expected to lead to higher values of  $K_v$  and  $K_w$ .

(e) Drag at transonic speeds

Little effort has been devoted to estimation methods at transonic speeds, partly because of the difficulty in applying theoretical methods close to the speed of sound, but also because available experimental results suggest that slender wings are well-behaved in this speed regime, with a very smooth transition from the values at subsonic speeds to those at low supersonic speeds in the case of the lift-dependent drag. The zero-lift pressure drag also appears to behave reasonably, with almost no drag increase at high subsonic speeds until the onset of the transonic drag rise, which generally begins at Mach numbers in the range 0.95 to 0.98. The wave drag, which peaks at  $M = 1.10$  to  $1.15$ , by  $M = 1.2$  approximates to the values given by conventional supersonic wave drag calculations<sup>24</sup>. This state of affairs may sound rather haphazard as a basis for drag estimation and would certainly be unacceptable for the design of an aircraft to cruise at these speeds. For truly supersonic aircraft, however, it is of reduced importance for, as it is a zone of high drag, supersonic transports need to be designed with an excess of thrust over drag so they can climb and accelerate quickly and economically to their cruising speed; small errors in the transonic drag estimate therefore would be of relatively minor consequence at the project definition stage of a design.

(f) Effect of camber on drag

The estimation of the drag of a generalised cambered slender wing is hardly feasible, since the possible camber shapes are infinite, and cannot even be simply expressed in terms of a few geometrical parameters. Camber shapes are generally designed to give an attachment line along the leading edge, so that flow separations are suppressed except from the trailing edge. This state of affairs can only exist at one incidence for sharp-edged wings, although the lift and drag vary smoothly near this design point. At a given lift coefficient, the minimum-drag member of the family of shapes of given planform is the one cambered such that the leading edge is an attachment line at that condition; thus, there is considerable interest in the design of such wings and their associated drag. Design methods for supersonic speeds are available<sup>25</sup> and the lift-dependent wave drag for attached-flow conditions can be evaluated numerically by means of the theory of Adams and Sears<sup>26</sup>.

The other part of the drag due to lift, the vortex drag, can be obtained by slender-wing theory<sup>25</sup>. For lift coefficients away from that for attachment, there are no adequate theoretical treatments or even experimental correlations. There are, of course, results available for certain specific cambered wings. These suggest that the reduction in  $K$  at attachment due to camber from that for the equivalent plane

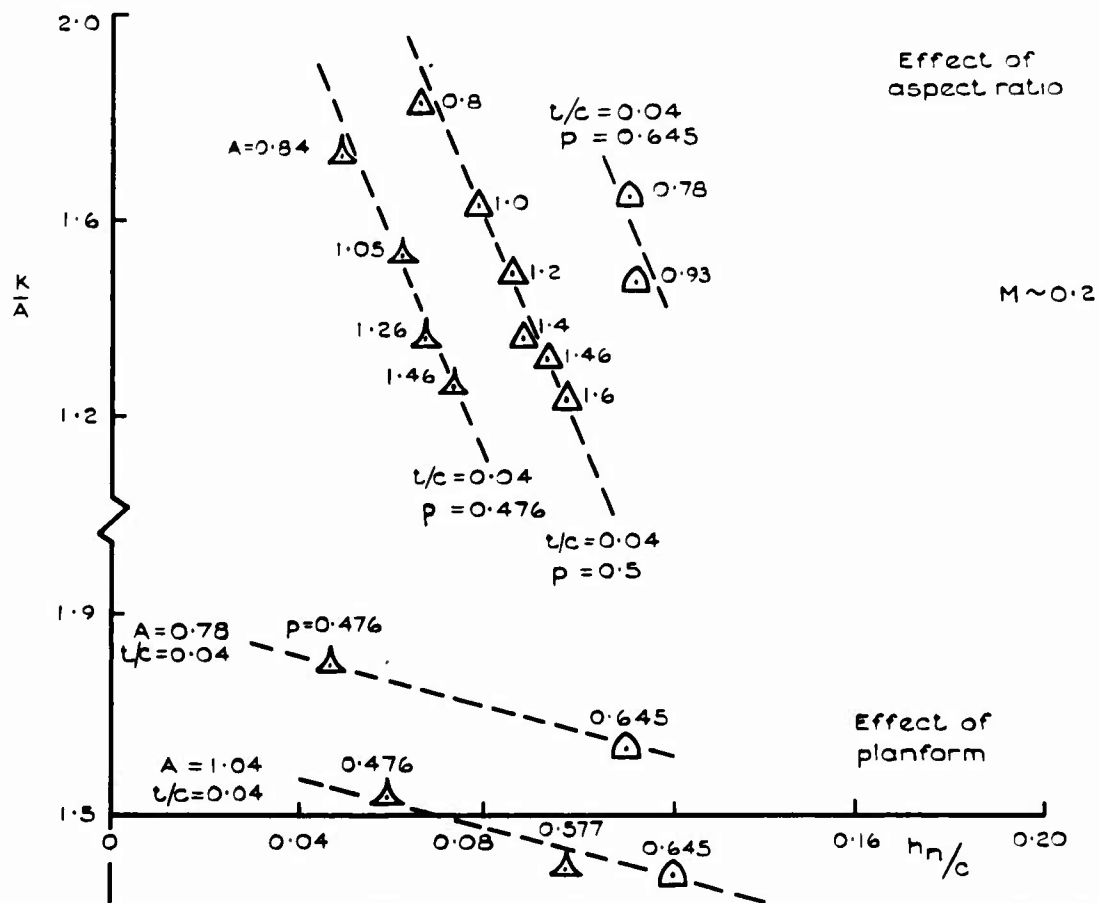


**Fig.3 Drag and stability correlation for slender wings at  $C_L=0.5$  (after Kirkpatrick and Kirby)**

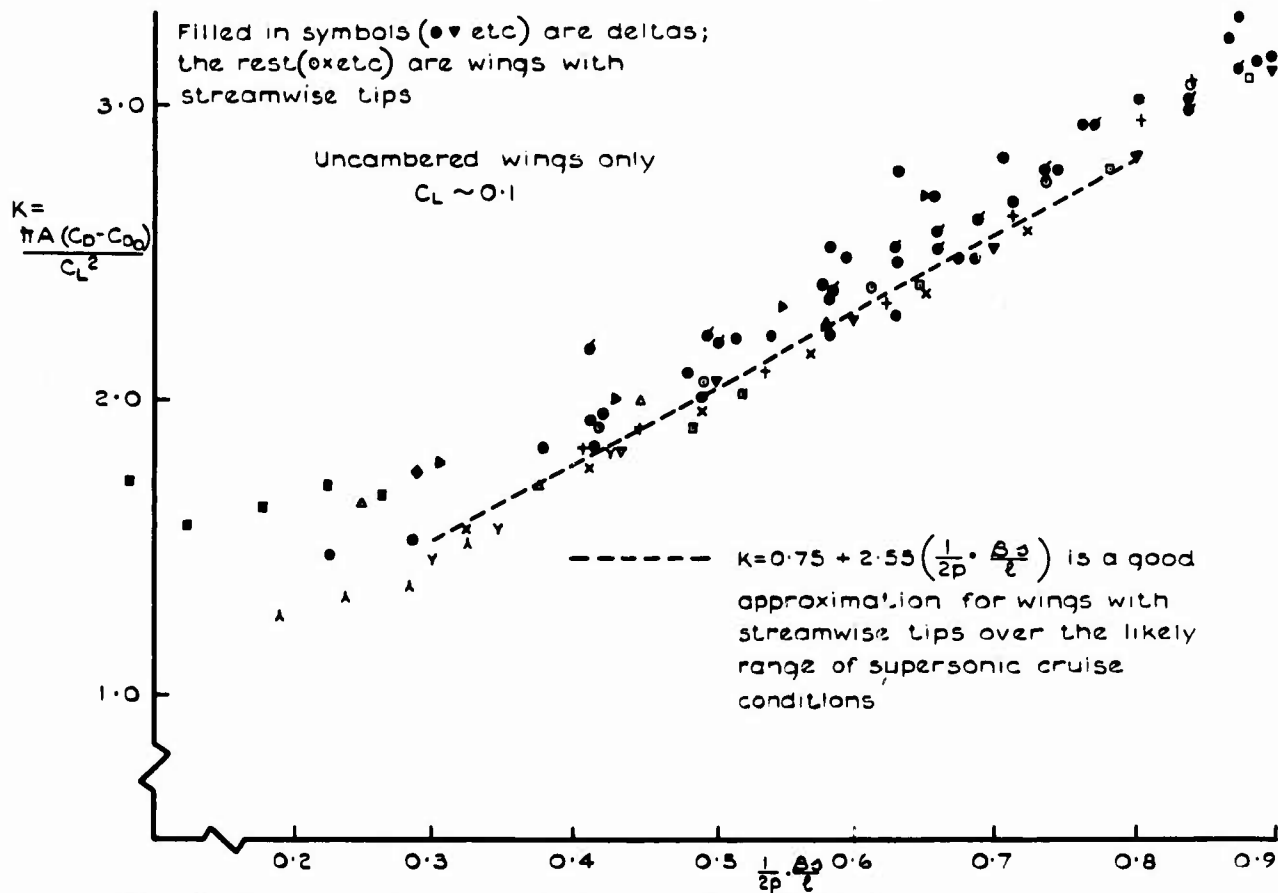


**Fig.4 Overall lift-dependent drag factor, K, for slender wings (after Courtney)**

6-12  
wing is maintained for a limited range of  $C_L$  to either side but that, well away from the design  $C_L$ , the value of  $K$  tends to approach that for the plane wing.

At subsonic speeds the situation is very much the same. Camber designs can be derived which give leading-edge attachment at a specified lift coefficient and, again, a specified load distribution and centre-of-pressure position can be achieved. Surface pressure distributions and drag can be calculated. At supersonic speeds, the cruising lift coefficient could be used as the design lift coefficient for the camber to ensure low lift-dependent drag over all the likely range of cruising conditions. However, at subsonic speeds the operating range of  $C_L$  will be larger, varying from a low value at subsonic cruise speeds to high values for take-off and landing. There is, therefore, considerable interest in drag estimates for cambered wings operating above their design conditions. Unfortunately, the situation regarding estimation techniques for off-design conditions is no better than at supersonic speeds; the same qualitative approach is adopted of assuming that away from the design  $C_L$  the value of  $K$  will smoothly approach that for the plane wing. A good example of the design methods for cambered slender wings at subsonic speeds is given by Davies<sup>27</sup>. Experimental evidence showing that the design aims are achieved, together with useful information about the off-design behaviour of such wings, has been given by Butterworth<sup>28</sup>.

For a slender-wing aircraft with natural stability and a fixed centre-of-gravity position, the centre-of-gravity necessarily will be located close to the furthest forward position of the aerodynamic centre, corresponding to low-speed conditions at high  $C_L$ . In order to avoid major elevator deflection and trim drag penalty at cruise to cope with the rearward movement of aerodynamic centre, longitudinal camber can be incorporated to move forward the centre-of-pressure at cruise<sup>29</sup>.

#### 3.2.4 Concluding remarks

To those who are accustomed to the relatively well-developed and comprehensive drag prediction techniques in use today for conventional sweptwing aircraft, the position for slender-wing aircraft must inevitably seem less satisfactory. Of course it is not at all surprising that this situation prevails, since the slender-wing aircraft is still a relatively new and untried concept (apart from Concorde) so that there is not the large pool of design information available on which project-oriented studies can be based. By differentiating between what can and what cannot be calculated at present, we can hope to draw attention to the aspects where further work could most usefully be commenced. Three areas appear to be of sufficient importance to be singled out:-

(a) Techniques are required for lift-dependent drag estimates for cambered wings at lift coefficients away from the attached-flow value at subsonic, transonic, and supersonic speeds;

(b) Simplified methods are desirable for calculating zero-lift wave drag, suitable for use in parametric studies and multivariate analyses, together with the means for handling the not-so-smooth area distributions typical of realistic aircraft designs;

(c) Further studies are needed of the effects of adding fuselages to slender wings, since so much of the information already available is for isolated wings; an allied aspect requiring further study, which has not been mentioned previously, is the effect of adding engine nacelles and stabilising surfaces.

Clearly, the amount of research effort which should be devoted to refining the drag estimation methods for slender-wing aircraft must be related to considerations of the prospects of new projects employing the slender-wing principle. However, sufficient information is needed at least to permit reliable comparative project assessments for slender-wing aircraft and alternative conventional designs. When such comparisons show the slender-wing aircraft to be a serious competitor for a particular role then it is necessary to refine the design methods. Such a study has recently been made<sup>30</sup>, for which sufficient drag information was available to enable a satisfactory quantitative comparison to be established. One area of deficiency revealed concerned the reduction in lift-dependent drag that might be possible if camber designs for minimum drag at take-off and landing, regardless of the implications on drag at cruise lift coefficients, were to be used.

Although the high level of effort in the UK in the late 1950s and early 1960s (when the foundations of slender-wing knowledge were established on which we still depend today) has now abated, theoretical and experimental work is still proceeding to consolidate the fund of available information and to improve design techniques for future slender-wing aircraft.

### 3.3 Military strikefighter aircraft

Based on a contribution by A.J. Grundy and C.J. Rafe, HSA Brough.

#### 3.3.1 Introduction

This discussion is concerned with drag prediction for small strikefighter aircraft, where the canopy and the fuselage powerplant result in a relatively-stubby non-slender configuration, having somewhat ill-shaped fuselage sections, to which a variety of external store arrangements is added.

The drag of the basic aircraft configuration throughout the subcritical regime can conveniently be considered as the sum of skin-friction drag, zero-lift pressure drag and lift-dependent drag. Naturally, it will be desirable to treat some aspects separately, particularly those connected with the drag of store and engine installations and of excrescences. Once local velocities exceed sonic, supersonic regions terminated in general by shock waves arise in a generally-subsonic flow and pressure drag starts to rise sharply; this increase in pressure drag marks the onset of wave drag. As freestream Mach number is increased, so are the regions of supersonic flow, until supersonic flow is fully established. For the mixed-flow transonic region, although the total drag still can be regarded as the sum of three

terms, the situation is much more complicated and comprehensive mixed-flow theories are not available to form a basis for estimation or analysis. With fully-established supersonic flow, however, the situation is easier since we can express the drag as mainly the sum of skin-friction drag, zero-lift wave drag and lift-dependent drag. For the type of aircraft considered here, the zero-lift wave drag is usually the largest term, and its estimation causes the most concern. 6-13

It is proposed to discuss available methods of drag prediction for both the transonic and supersonic regions. Because zero-lift wave drag is the most important aspect and a theoretical framework does exist, most of the discussion will centre on this subject. As drag is more easy to predict with fully supersonic flow, this aspect will be considered first. Engine installation, trim, and excrescence drag will be excluded from direct consideration here.

The wave drag prediction methods currently used are unsatisfactory. Both the Supersonic Area Rule and the Transfer Rule are employed, but each specialist has evolved a personal method of application, including the introduction of 'Bluffness' correction factors based on correlations with experiment. In the absence of authoritative guidance on the degree of application of theory to real aircraft configurations, it is not surprising that methods have diverged. Confusion has arisen, since now no two workers can produce the same wave drag estimates for a given configuration. Understandably, there is a marked reduction of confidence in ability to estimate the wave drag of specific aircraft configurations.

The accuracy currently being achieved, possibly within 15% on total drag with a mean deviation of 5% over the Mach number range, is surprisingly good in view of the doubts which can be expressed about the validity of some of the assumptions which are made. This encourages the view that a more valid approach, supported by a systematic experimental programme and some theoretical development, could result in acceptable accuracy being achieved for practical design purposes.

An improvement in supersonic drag prediction is most desirable to keep the unit cost of a military project to a minimum and to enable performance guarantees to be given. The incentives are considerable. An uncertainty of  $\pm 12\%$  in drag for a particular case was found to correspond to a variation in the achieved level Mach number from 1.33 to 1.62, whilst an increase in engine thrust by 12% to offset the uncertainty in drag would have resulted in a 9% increase in all-up weight and unit cost of each aircraft, equivalent to an extra total cost of many millions of pounds, quite apart from the additional cost of operating a high-drag aircraft.

### 3.3.2 Skin-friction drag at supersonic speeds

Normal practice is to use one of the accepted references<sup>14,31,32</sup> on compressible flat-plate skin friction at the appropriate Reynolds and Mach numbers and apply the coefficients to the relevant wetted areas. However, the use of flat-plate coefficients for bodies can underestimate skin friction. Fig. 5 shows comparisons of different methods of estimating friction drag on an axisymmetric body at  $M = 1.4$  and  $Re = 1.8 \times 10^7$ . The calculated pressure distribution of the smooth, but wavy, body is indicated. The comparison covers skin-friction estimates for an axisymmetrical body with the calculated pressure distribution and with zero pressure coefficient, as well as flat-plate skin-friction estimates for the same pressure distributions. The flat-plate skin-friction drag in zero pressure gradient, the value which would normally be used, is seen to be 6-7% low, most of this difference being attributable to the threedimensional nature of the flow.

### 3.3.3 Zero-lift wave drag at supersonic speeds

#### (a) Theoretical methods of estimation

The Supersonic Area Rule<sup>33,34</sup>, which reduces at  $M = 1.0$  to the Sonic Area Rule<sup>35</sup>, is the commonly-accepted method of estimating zero-lift wave drag. Another method is the Transfer Rule<sup>36</sup> which can be derived from the Supersonic Area Rule with an assumption regarding the slenderness of the body. Both of these Area Rules are far-field methods, the disturbance from the aircraft being regarded as arising from a family of equivalent bodies of revolution. A near-field approach<sup>37,38</sup> which uses a distribution of finite elements of sources, vortices and doublets for calculating surface pressures, offers improved representation of complex configurations but requires more computer storage capacity and longer run times. The Supersonic Area Rule is:-

$$\frac{D(\theta M)}{q} = \frac{1}{2\pi} \iint_{O(\theta M)}^{L(\theta M)} S''(X_1, \theta M) S''(X_2, \theta M) \log \frac{L(\theta M)}{|X_1 - X_2|} dX_1 dX_2 \quad (6)$$

and

$$\frac{D(M)}{q} = \frac{1}{2\pi} \int_0^{2\pi} \frac{D(\theta M)}{q} d\theta \quad (7)$$

where  $S(\theta M)$  defines an elemental area distribution

$S''(X, \theta M)$  denotes  $d^2S/dX^2$

$O(\theta M)$  and  $L(\theta M)$  define the  $X$  limits of the Mach Diamond enclosing the configuration

$X$  = dimensional distance.

Each elemental distribution representing an equivalent body is determined by cutting through the configuration by a series of parallel tangent planes to the set of cones whose semi-included angle, with reference to the axis of the configuration, is the Mach angle  $\mu$ . The area used for the elemental distribution at each position of the cone apex along the axis is the projection onto a plane normal to the axis of the area intercepted by the cutting plane. By rotating the series of parallel cutting planes around

the cones a family of equivalent bodies can be generated at each Mach number. The wave drag of the configuration is given by the mean of the equivalent body wave drag values.

If the assumption is made that the body of the configuration is so slender that all elemental distributions can be considered the same as the cross-sectional area distribution, i.e. independent of both  $\theta$  and Mach number, then the Supersonic Area Rule equations can be expanded in simple algebraic terms<sup>39</sup> to yield the Transfer Rule<sup>36</sup>:-

$$\frac{D}{q} = \frac{D(B + \bar{A})}{q} + \frac{D(\bar{W})}{q} - \frac{D(\bar{A})}{q} \quad (8)$$

where  $\bar{W}$  denotes the wing system and  $\bar{A}$  denotes the transferred area distribution of the wing system. If further algebraic expansion is performed the equation becomes:-

$$\frac{D}{q} = \frac{D(B + \bar{A})}{q} + \frac{D(W_1)}{q} + \frac{D(W_2)}{q} + \dots - \frac{D(\bar{A})}{q} + \frac{D_i(W_1, W_2, \dots)}{q} \quad (9)$$

where  $W_1, W_2$ , etc. denote each wing-like surface and  $i$  represents interference. This is the form in which the Transfer Rule is commonly applied, except that the interference term is ignored. Since the fuselages of military aircraft are obviously not slender, the use of the Transfer Rule can be argued to represent a greater violation of theory than the use of the Supersonic Area Rule. Bearing in mind the requirement that the wing drags,  $D(W)/q$ , are found from some other source, mainly by analysis of experimental results which are not necessarily free of body interference, use of the Supersonic Area Rule is considered preferable. There is a great need for improved theoretical methods to be developed applicable to realistic aircraft shapes; although efforts are being made in both the USA and USSR, no working method has yet resulted.

#### (b) Application of methods

Practical methods exist for calculating the oblique areas for thin wing-like bodies, which can be performed very accurately by modern computers. Unfortunately this is a formidable task for an arbitrary body, and, although approximate computerised procedures were developed<sup>40</sup> in the USA as long ago as 1963, a simpler procedure was adopted in the UK. Since theory required the body to be slender, it was assumed that there was very little error in accepting the cross-sectional area distribution as being invariant with both  $\theta$  and Mach number. As this approach was being applied to military fuselages which could certainly not be regarded as that slender, this assumption could not be justified, even though it did comply nominally with the Transfer Rule. Fig.6 (from Ref.40) illustrates that for a body of revolution, Slender Body Theory (to which the Transfer Rule reduces for a body) is only applicable for high fineness ratios. From Fig.6, it would seem reasonable to infer that only the Supersonic Area Rule is permissible for configurations which have fuselages of low fineness ratio.

The Supersonic Area Rule can, without exceeding the limitations of theory excepting the definition of 'slender', be applied to a configuration having one or more wing surfaces, symmetrical about both the xz and xy planes and a body with a pointed nose and either a pointed rear or a blunt base. In order to take oblique cuts for a more realistic aircraft geometry, ignoring problems of engine flow simulation for the present, it is first necessary to select a datum axis which, presumably, should be determined by the zero-lift angle of the configuration. Although oblique cuts can conveniently be taken through a body of revolution representing the aircraft cross-sectional area distributions, a more satisfactory method is needed taking better account of the details of the configuration, yet not prohibitive as regards computer time. Practical difficulties arise from local discontinuities and steep slopes in the final area distributions; preferably these are faired after consideration of the smoothing of the airflow around the aircraft which would be expected in practice.

More sweeping assumptions are involved to cater for engine flow effects. Since the introduction of Area Rule concepts, commonly the intake air has been represented by a streamtube extending forwards to infinity, with similar simulation of the exhaust. In calculating the intake streamtube, allowance can be made for the nose and intake shock systems; likewise, secondary air can be included in the exhaust flow and provision made for area increase corresponding to jet expansion. The streamtubes need to be suitably aligned, in a manner consistent with any nacelle treatment.

Although the above process provides a way of extending the Supersonic Area Rule to real configurations lying outside the bounds of theory, and permits a consistent approach to estimation, definitive aimed research is presently lacking to show whether or not a more accurate prediction of wave drag results.

#### (c) Evaluation of the double integral

Although a number of numerical procedures are available for evaluation of the double integral, their accuracy has only been assessed for smooth distributions allowing an analytical solution<sup>18,41-43</sup>. Such assessments can be very misleading since the accuracy for a distribution representing an aircraft is dependent, not only on the shape of the distribution, but also on the frequency and positioning of the points representing that shape. An investigation at HSA (Brough) into the accuracy of the methods of Eminton<sup>18,41</sup> and Cahn and Olstad<sup>42</sup> when applied to analytical bumpy bodies indicated that the former was the more reliable, converging more quickly and consistently with increase in the number of points used (Fig.7). Much depends on the positioning of the points, especially with regard to the rounded noses of wing-like surfaces. Fig.8 shows a plot of approximately 120 calculated values of  $D/q$  plotted against  $\theta$  for a smooth wavy body and symmetrically-mounted wing at  $M = 1.4$ . The value of  $\theta$  at which the Mach plane lies along the leading edge is marked; linear theory would suggest an infinite value of wave drag and the calculation results in a peak value. When the Mach plane cuts through the wing so that the

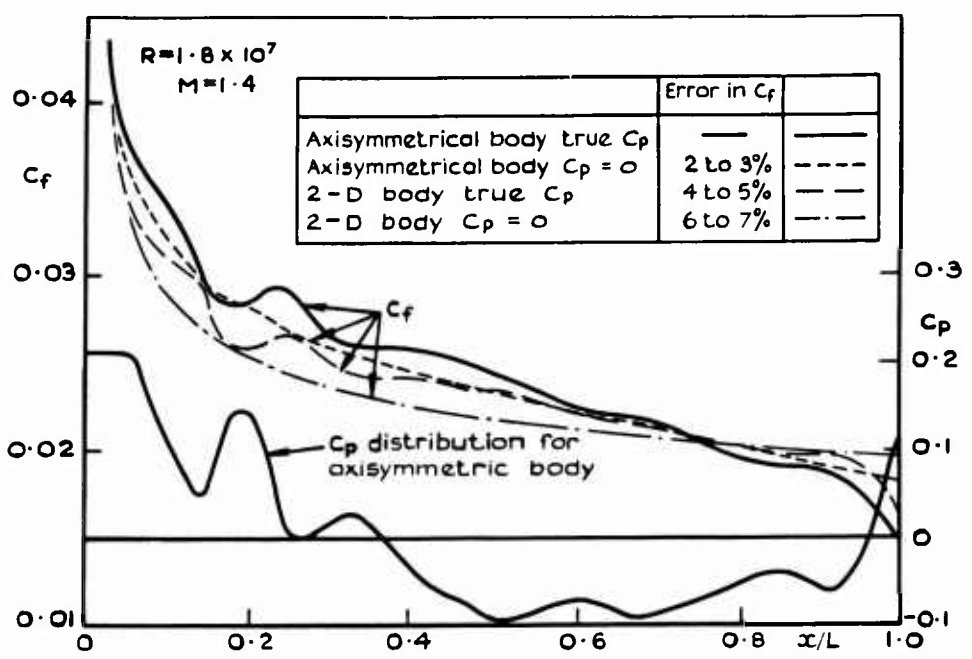


Fig. 5 Sensitivity of estimated skin friction for wavy body to assumptions

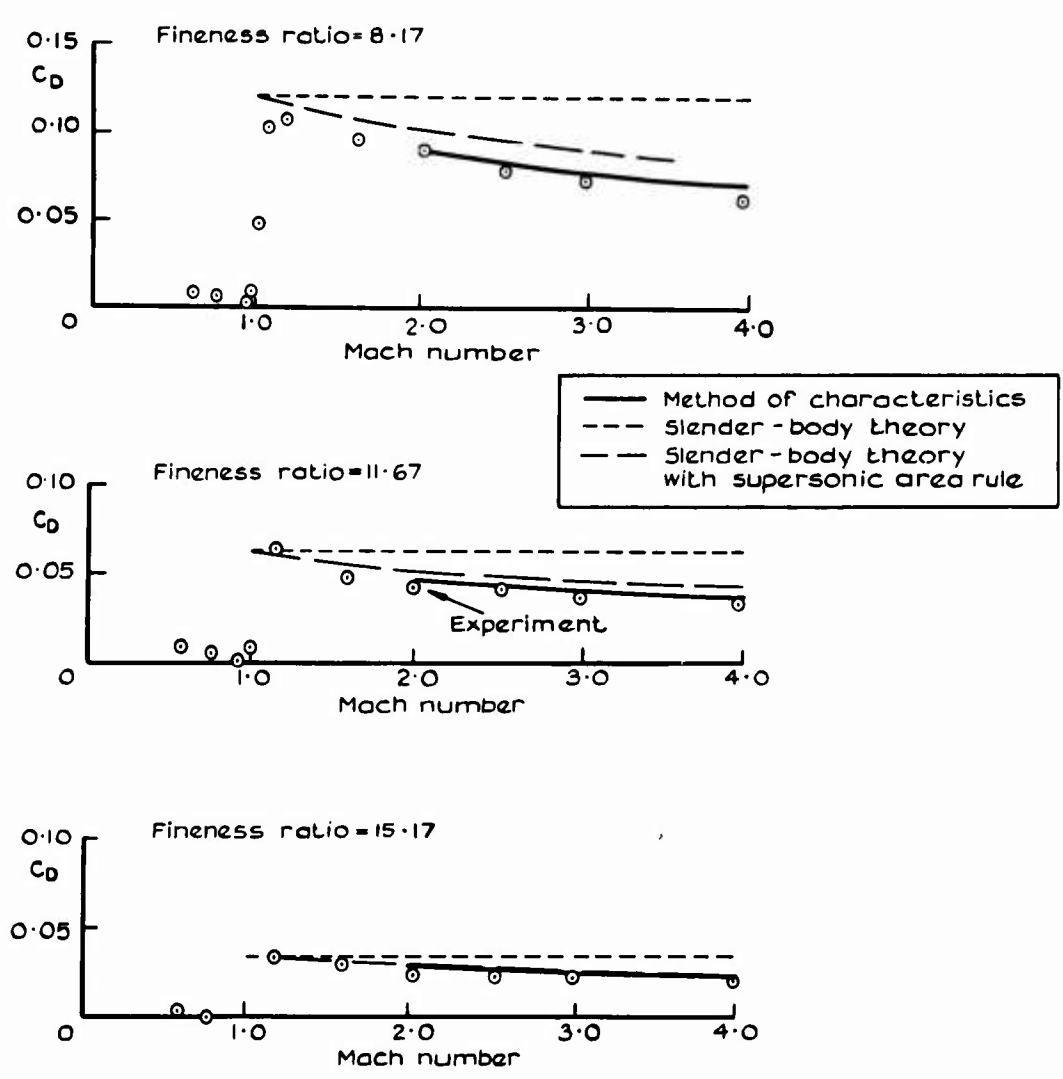


Fig. 6 Comparison between calculated and measured wave drag for optimum axisymmetric bodies (from Ref. 40)

wing cross-sectional area is found ( $\theta = 90^\circ$ ), there is another peak, due to the maximum area reaching its peak value and a deterioration occurring in the shape of the elemental distribution.

The mean  $D/q$  obviously depends on the number of  $\theta$  values at which calculations have been performed. The percentage error, which is also shown in Fig.8 plotted against  $\Delta\theta$ , can be seen to bear little relation to  $\Delta\theta$ . In this particular example,  $\Delta\theta$  must be no greater than  $5^\circ$  to achieve an error of 1% or less. For an aircraft having not so smooth a distribution, the maximum error could be larger and it would be advisable to perform the calculations with a smaller value of  $\Delta\theta$ .

(d) Effect of Reynolds number and boundary-layer displacement thickness

In principle, the effect of the boundary layer on wave drag can be assessed by adding calculated displacement thicknesses to the physical areas of the configuration. In a recent UK investigation<sup>44</sup>, wave drag was calculated for three smooth bodies, of different fineness ratios, and one waisted body, with and without the addition of boundary-layer displacement thickness. Pressure distributions and resulting wave drags were calculated by the method of Warren and Fraenkel<sup>45</sup> and the displacement thickness by an adaptation of the integral method of solution of the turbulent-boundary-layer problem due to Head. The results are presented in Fig.9 for a range of Reynolds numbers, and for Mach numbers between 1.5 to 2.0. The calculated viscous wave drag of a smooth body of fineness ratio of about 8 to 10 (broadly representative of the fuselage of a strikefighter aircraft) at the higher Reynolds number is only about 1% greater than the inviscid value; for the waisted body, the viscous value is only 1% less than the inviscid value. Although the bodies of revolution treated here are very different from the configurations of interest, which include wing-like surfaces, the results imply that an inviscid calculation is acceptable, especially since only a crude calculation of displacement thickness would be possible for the general case.

(e) Experimental research on wave drag

Despite many experiments involving measurement of drag at supersonic speeds, the analysis and understanding of drag has usually been a secondary objective, especially in project-oriented research, whilst much of the results have either been classified and proprietary in nature, or obtained under inadequate and ill-defined test conditions. Further, since skin-friction drag comprises as much as one-third of the zero-lift drag on a strikefighter aircraft configuration, this needs to be determined carefully. Tunnel technique problems also accentuate the difficulties in achieving a meaningful analysis of wave drag from tests on specific aircraft models.

A set of experiments has been arranged, in a specially-calibrated UK wind tunnel, to attempt to provide a basis for improving the methods of wave drag prediction by showing how best to apply Supersonic Area Rule and by demonstrating the degree of empirical adjustment that may be needed. The basic model area distribution is representative of current aircraft. Some 8 bodies, 2 canopies, and 2 wings are to be tested in 12 configurations, 5 of which have the same area distribution at the design Mach number. Selective pressure plotting, flow visualisation and boundary-layer studies will assist the theoretical comparisons. The objects of the tests include:-

- (a) To study canopy effects, including windscreen angle, with and without compensating body waisting;
- (b) To compare the addition of a canopy and of a distributed axisymmetrical bulge;
- (c) To investigate wing effects, with compensating body waisting;
- (d) To assess the validity of linearised theory by testing selected combinations of related bodies and wings which allow, in theory, the identification of the skin friction and wave drag contribution of each element.

3.3.4 Lift-dependent drag

In principle, an equivalent calculation method to that used for the zero-lift wave drag can be used to find lift-dependent drag, but, for the class of aircraft being considered no usable method is known for estimating the required longitudinal distribution of lift. Recent 'near-field' theoretical studies<sup>37,38</sup> offer some hope that practical methods may eventually be developed. At present semi-theoretical methods are used which correlate experimental data by use of supersonic similarity parameters<sup>46,47</sup>. Corrections for trim drag, and for the variation with incidence of the drag of store and engine installations must be made.

3.3.5 Transonic drag

The friction drag may be calculated in transonic mixed flow, assuming the flat-plate approximation. No theoretical methods are available for the estimation of the other drag terms. The interpolation of values between the upper and lower bounds of the transonic region is dependent on the use of *ad hoc* test data which can to a certain extent be generalised by the use of similarity parameters<sup>47</sup>. The Sonic Area Rule<sup>36</sup> may be used to obtain a value at  $M = 1$  consistent with the Supersonic Area Rule, but it is generally accepted that this calculation overestimates the true value.

3.3.6 External store installations

This can truly be regarded as a subject in its own right, of special importance to the designers and users of strikefighter aircraft. For such aircraft, internal carriage of stores cannot usually be justified, as the effects of the extra fuselage drag throughout the mission tend to outweigh the benefits of reduced drag in the outward stage. Other important factors militating against internal carriage include, of course, the effects of flow disturbances in store bays on delivery accuracy, and the increasing variety

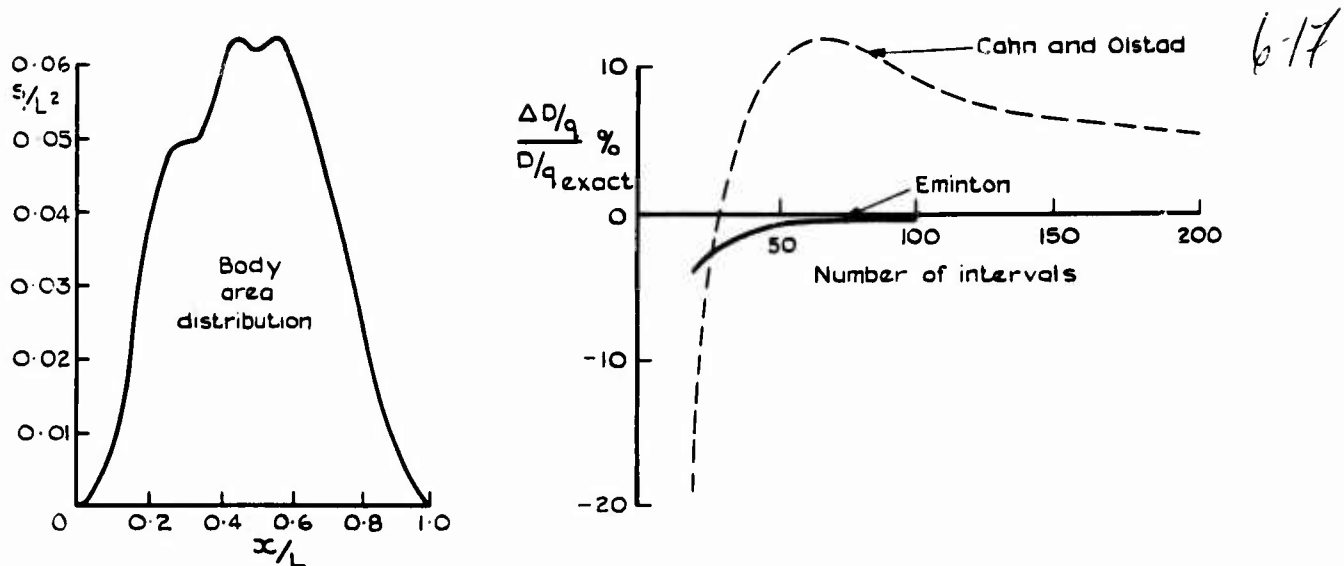


Fig. 7 Comparison of numerical methods for wave drag prediction for a bumpy analytical axisymmetrical body

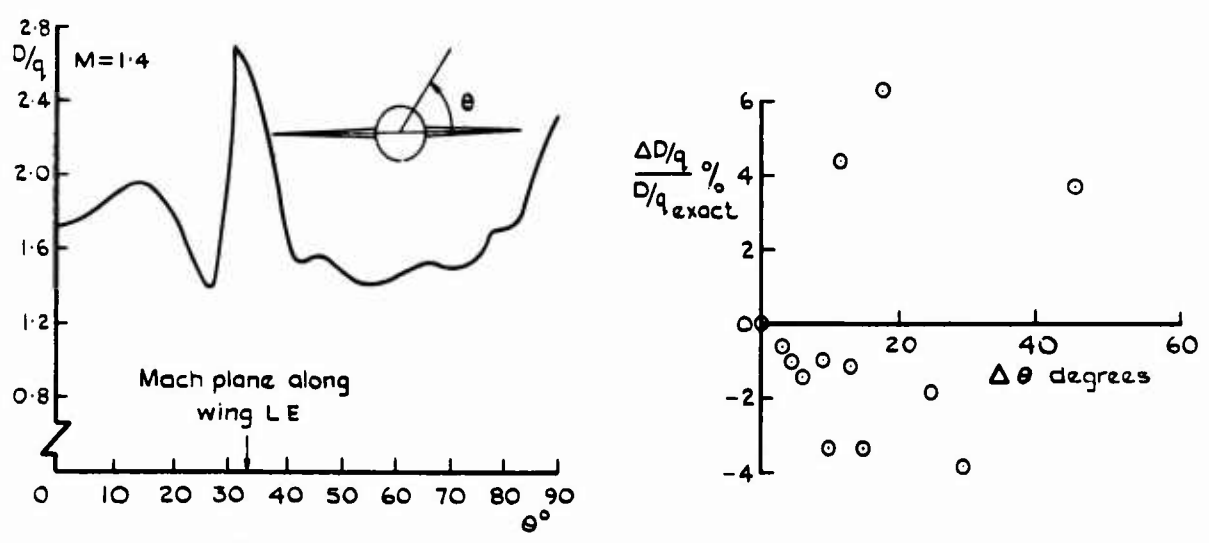


Fig. 8 Sensitivity of numerical integration process to angular interval

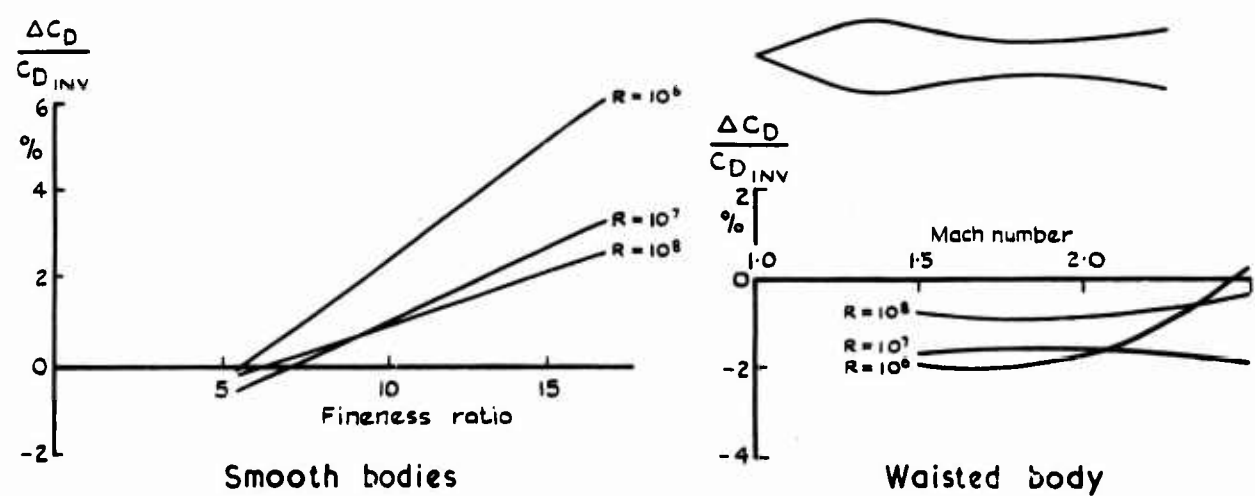


Fig. 9 Calculated effect of boundary layer on wave drag of smooth bodies and a waisted axisymmetrical body

6-18 and constantly-changing combinations of stores which have to be accommodated. A possible compromise, suitable for certain types of stores, could involve the partial use of semi-submerged and conformally-packaged stores.

However, there is a clear continuing need for a prediction method which, preferably, should be sufficiently accurate and reliable to allow the selection of a preferred low-drag installation scheme for a prescribed combination of external stores. Amongst the main considerations are: the basic shapes of the stores and their mountings; the aerodynamic interactions between the stores, their supports and the neighbouring aircraft surfaces; the cleanliness of the stores and of specific support installations; and the possibility of contriving more favourable groupings for the principal store combinations which need to be fitted to a given aircraft.

There exist considerable amounts of *ad hoc* store drag test data, as well as a certain amount of more general research on selected representative cases. Limited progress has therefore been possible towards the derivation of prediction methods based on semi-empirical analyses and basic theoretical considerations, as discussed in a separate paper at this Conference<sup>48</sup>. The recent investigations of store drag by HSA Brough on a Buccaneer aircraft (see Fig.10) taken in conjunction with comparative tunnel research at ARA, seem likely to improve our capacity to interpret model-scale data on store installations and apply it with confidence to full-scale conditions, providing adequate information is available on the basic characteristics of the different components of a particular aircraft installation.



Fig.10 Buccaneer S Mk.2 aircraft for store drag research

Even for conservative aircraft designs, however, there is a need for better understanding of the complex interaction effects involved, if progress is to be made towards the formulation of a more systematic and reliable design procedure. The situation seems likely to become, if anything, more difficult. The scale of the interaction between the store and the aircraft flying surfaces is bound to increase as military aircraft become more compact, particularly in view of the aerodynamic concepts inherent in the advanced design approaches under development, implying a need to consider the complete aircraft system as an integral whole at an early stage in design. A soundly-based method for the prediction of the drag of store installations is basic to the use of modern configuration selection and performance appraisal methods in the design and evaluation of military aircraft.

### 3.3.7 Concluding remarks

The prediction of transonic and supersonic drag for military strikefighter aircraft is not a well-founded art and more needs to be done, both theoretically and experimentally, to improve the capability of designers to predict the performance of future aircraft.

### 3.4 Powerplant installations for strikefighter aircraft

Based on a contribution by D.C. Leyland, BAC Preston.

#### 3.4.1 Introduction

The importance of intake drag has changed with time, as the requirements of aircraft design have altered. In the early days of turbo-jet aircraft, the drag associated with intake flow was often negligible, partly because engines were relatively small and partly because prime design was for subsonic speeds and cowl shaping was such as to give cancellation of pre-entry drag. When aircraft were developed for supersonic speeds, and centre-body intakes were introduced, supersonic pre-entry drag was shown in specific intake tests to be theoretically predictable for the full-flow critical condition and approximations were found possible for subcritical operation. Intake drag has come to be more significant in recent years, both because its relative magnitude has increased and because it has become necessary to make design compromises between the requirements for optimum subsonic and optimum supersonic performance. Generalised data on which to base comparisons and make trade-off studies have, however, been very sparse. Reasonable estimates for supersonic operation have been possible, but it is only within the last five years or so that a selection of information has started to become available on the subsonic drag of intakes suitable for strikefighter aircraft, much of it related to intakes primarily designed for supersonic flight. Little published data is available for intakes which need to be biased towards low drag at subsonic/transonic speeds, yet must be capable of operation at supersonic speeds with adequate performance and acceptable inlet/engine compatibility.

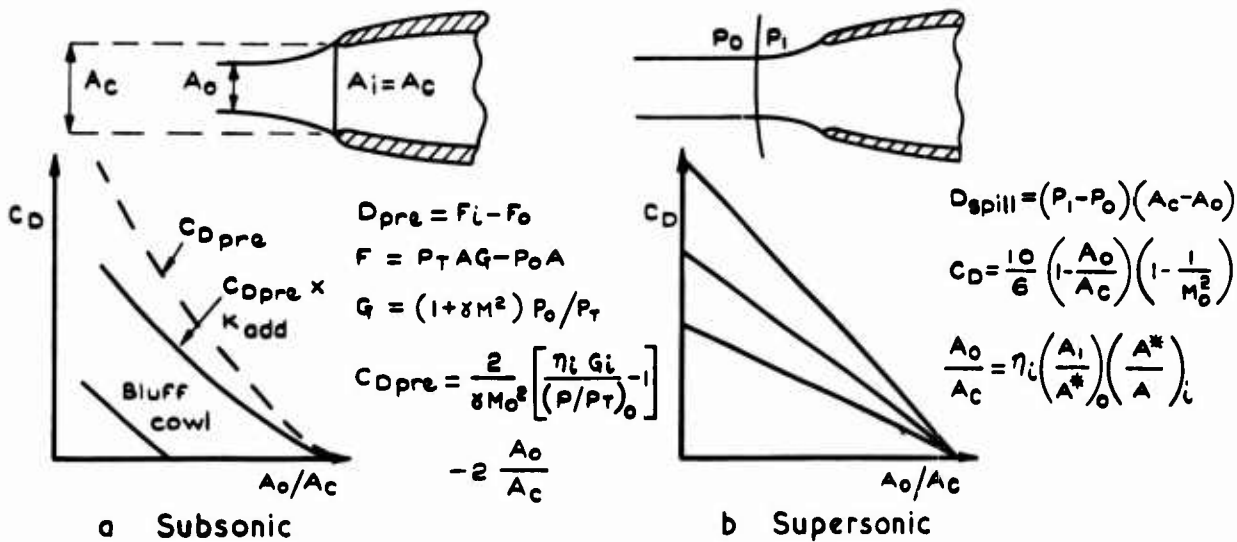


Fig.11 a&b Pitot intake - calculation of spillage drag

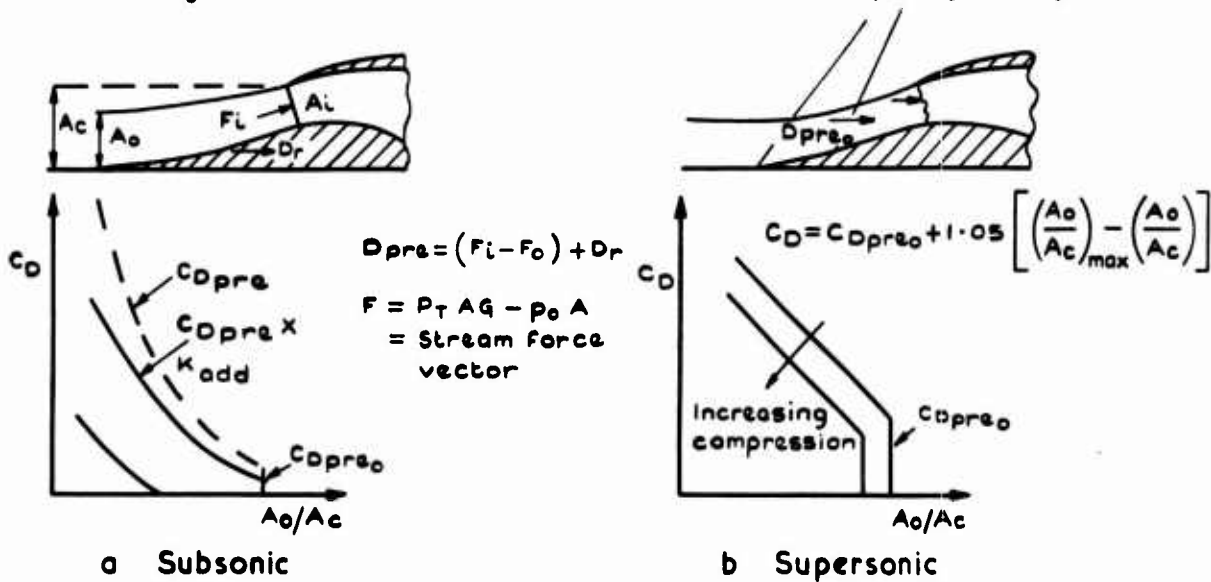


Fig.12 a&b External compression intake - calculation of spillage drag

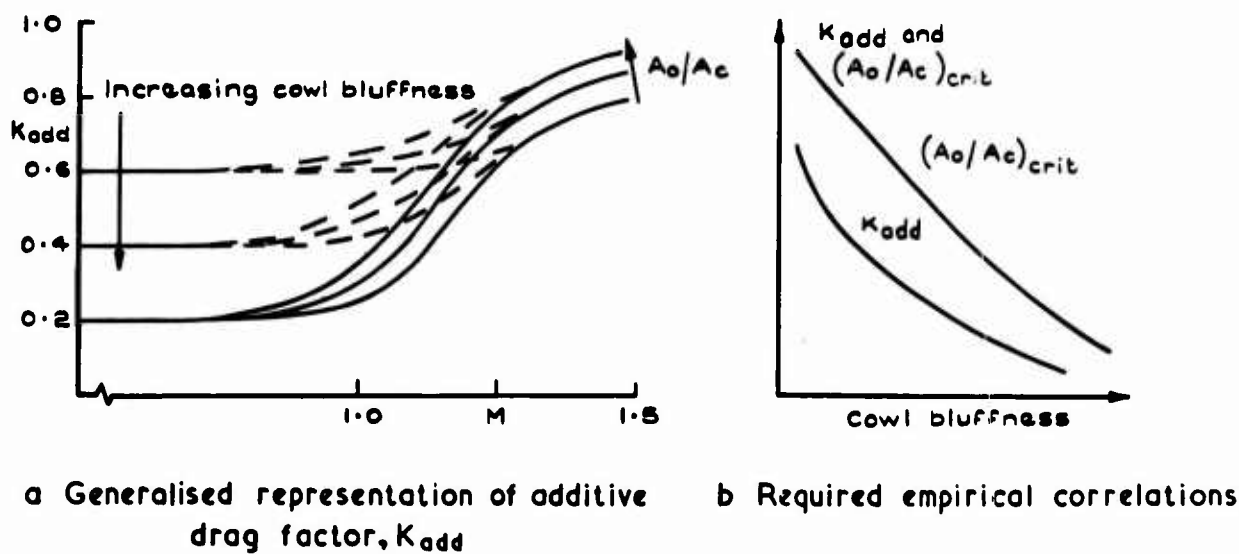


Fig.13a&b Proposed framework for intake drag analysis at transonic speeds

6-20 Certainly, there is nothing resembling a standard data sheet to which the propulsion system designer can refer. At present, it is necessary to make early project estimates from calculated pre-entry drag, possibly guided by available results on similar configurations, and then to await the results of tests on models specific to the project in hand, by which time it may be too late to make radical changes. There is patently a need for a generalised data bank, if design data sheets are not yet feasible, to make intake design more certain and performance estimation more reliable.

Afterbody drag and nozzle design need to be considered together since the major part of afterbody drag arises because of the need for engine nozzles, and, as overall thrust minus drag is being considered, the design of the nozzle must take account of interactive effects with the afterbody and design compromises will usually prove necessary. A simple nozzle design which gives maximum thrust and minimum weight and cost may well introduce unacceptable penalties in drag. As in the case of intake drag, the significance of afterbody drag has increased with time as jet engines have developed. Relative engine size has increased, afterburning requires variable nozzle geometry, and sophisticated nozzle designs are necessary to produce maximum thrust at the high jet pressures associated with supersonic flight. In consequence, the afterbody of an aircraft is necessarily distorted, and many installations are characterised by having large base areas, especially those incorporating twin engines and simple variable nozzles. High drag, therefore, can result, as much as 30% to 40% of the clean aircraft zero-lift drag. In one case, aircraft drag was reduced by some 20% by reductions in base area made during flight development. For a modern jet aircraft, an afterbody drag of 15% is not unusual and special nozzle and afterbody design is necessary to achieve a value below 10%. At these levels, afterbody drag deserves serious study and more attention than it has received in the past.

#### 3.4.2 Intake drag

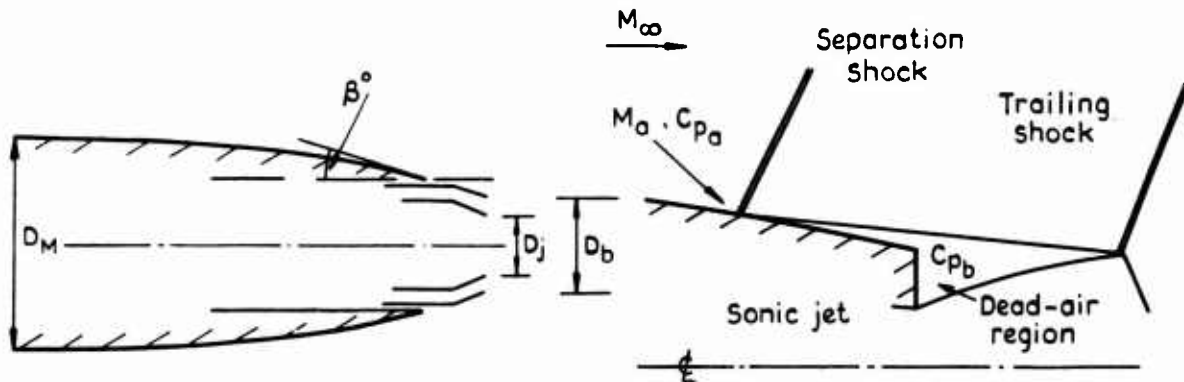
Spillage drag is one of the more descriptive names used in connection with intake drag since the term implies the relationship of drag to a condition where the flow into the intake is less than some datum value. Some differences arise, however, in the definition of the datum: for a centre-body intake, whether it should be the maximum flow that the intake will take at a given flight condition, or the maximum flow that the intake could take were the centre body not present. The latter definition will be taken in the present discussion since this allows full account to be taken of variation in centre-body geometry, and is commonly the datum taken when calculations are made, for example, of the datum supersonic drag of an aircraft. The intake drag is then an additive term associated with the operating condition of the engine and with the geometry of the intake. The fact that there is an additional drag term is sometimes a source of argument; the need arises because it is normal to define net engine thrust with respect to a so-called ram drag calculated at freestream conditions ahead of the intake. There is, then, for all but special conditions, a change in stream force in the streamtube entering the intake between freestream conditions and the intake face, and an appropriate pre-entry drag can be calculated. In inviscid flow, there would be no net increase in overall drag, since changes in the pre-entry streamtube would be reflected by equal and opposite changes over the external surface of the aircraft. In practice, however, pressure changes over the aircraft do not give rise to a reduction in datum aircraft drag sufficient to wholly counterbalance the pre-entry drag, and the estimation of intake drag largely becomes, particularly at subsonic speeds, the craft or art of judging to what extent the nominally-calculable pre-entry drag is offset by cowl thrust.

Current methods of estimation of intake drag are summarised by Figs.11 and 12. Complete definitions are not given but the various concepts will be familiar to specialists and more detail can be obtained by study of the references. Although it must be admitted that there is no such thing as a complete and definitive text on the subject, there is a fairly full discussion in Ref.49 and comments on recent test data are included in the recent AGARD lecture series on airframe/engine integration<sup>50</sup>. Prior to these publications, Sibulkin<sup>51</sup> together with various RAE publications<sup>52-54</sup> constituted the main references for supersonic spillage drag, whilst Mount<sup>55</sup> provided results from a comparative series of tests on pitot intakes at subsonic and transonic speeds. The definition of spillage drag (Fig.11a) introduces the  $K_{add}$  factor used by Mount to give a measure of the degree of cancellation of pre-entry drag. It provides a convenient, if not always precise, way of characterising the intake cowl; a shallow cowl will have a high  $K_{add}$ , a deep cowl a low  $K_{add}$ . Note, however, that it is possible for a bluff cowl to give complete cancellation at high intake flow and there is a need for some means of estimating the value of critical flow where spillage drag begins to build up. The lower curve could then be derived by calculating spillage drag for an intake, scaled down by a factor equal to the critical flow ratio. The method<sup>56</sup> for calculation of spillage drag at low supersonic speeds (Fig.11b) is probably less well-known but has proved to be quite effective.

In the case of an external compression intake (Fig.12a), allowance must be made for the presence of the pre-compression ramp or cone at subsonic, as well as supersonic, speeds. Variation of ramp or cone geometry is naturally used to optimise intake and engine performance at supersonic speeds, but there can also be some trade-off of spillage drag and pressure recovery at subsonic speeds, and certainly, suitable calculations must be made if a choice has to be made between a pitot and a centre-body intake.

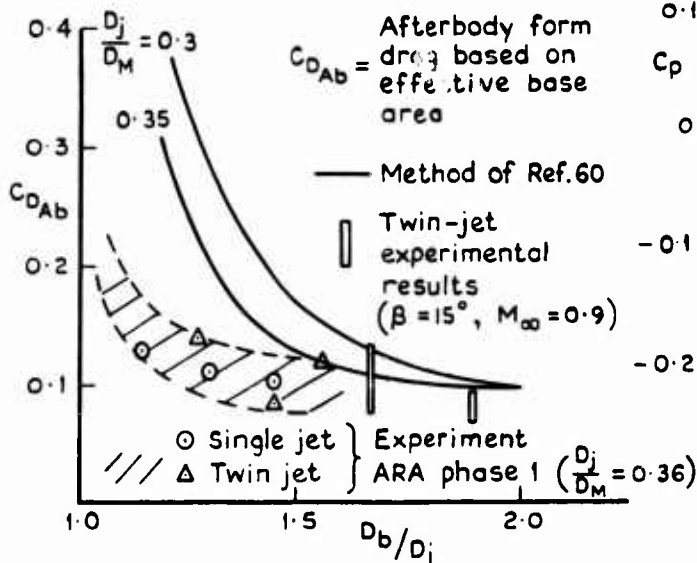
It can readily be shown that pre-entry drag can be calculated either as the drag of the centre body plus the change in stream force or as the force on the approaching streamline. The former is appropriate at subsonic speeds, with ramp drag best obtained from intake pressure measurements or from a correlation of pressures measured on isolated ramps<sup>57</sup>. It is then necessary, as for a pitot intake, to assume an appropriate value of  $K_{add}$  for the intake in question and it is arguable that the same factor applies to the finite drag increment at maximum mass flow, although no evidence is known.

At supersonic speeds the maximum mass flow drag is calculated from shock flow considerations as a pressure integration over the entering streamtube boundary with allowance necessary for sideways spillage. When the intake is operated subcritically further calculations can be made<sup>58,59</sup>, with allowance made for the normal shock position ahead of the intake, but, within an accuracy of about  $\pm 10\%$ , it seems adequate to assume a linear variation (Fig.12b) prior to wind-tunnel tests.



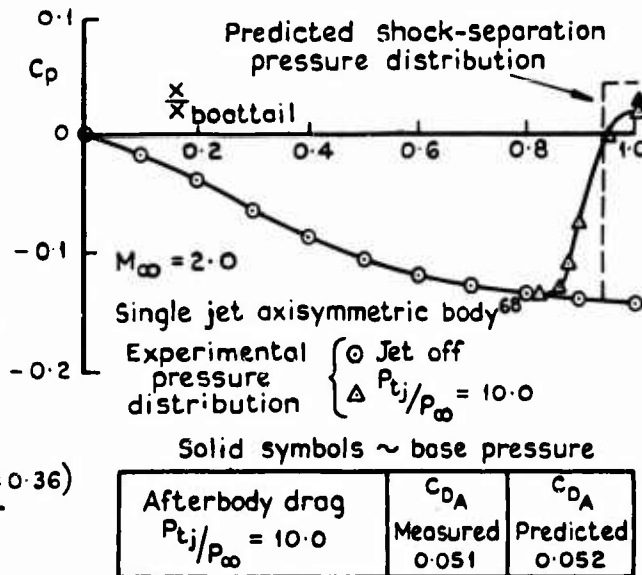
a Afterbody geometry

a Simplified supersonic flow model



b Analysis of experimental data

Fig.14 a & b Variation of afterbody form drag with afterbody geometry



b Comparison with experiment

Fig.15 a & b Effect of jet efflux on supersonic afterbody drag

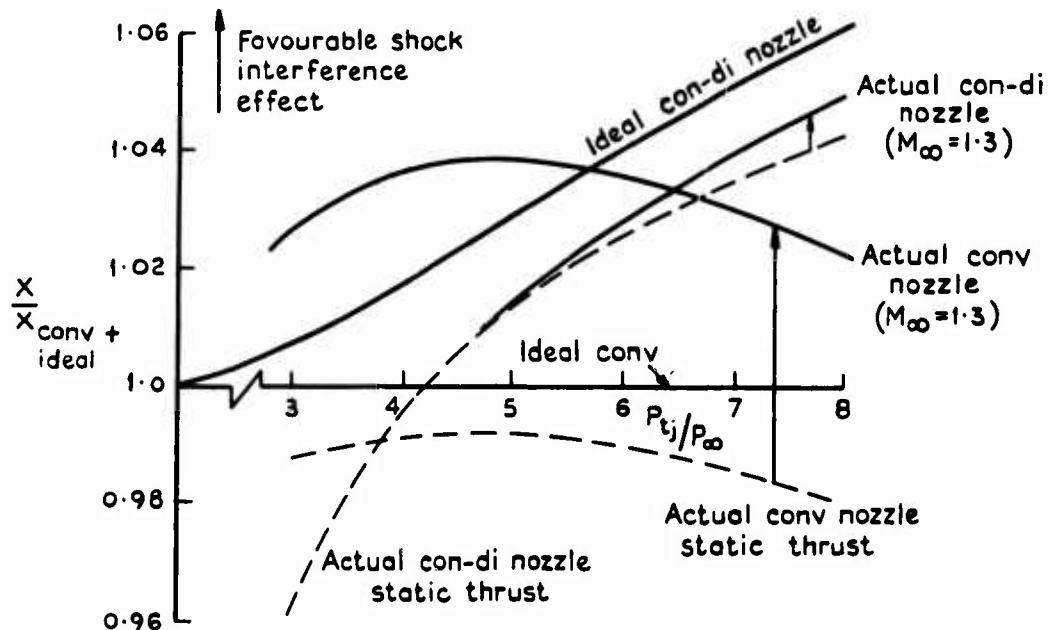


Fig.16 Nozzle-shock interference

6-22 The data which have been used to define existing rules have been obtained on an *ad hoc* basis. Although some relationship to theory would be attractive at this stage, it is difficult to imagine that this would be very successful for realistic intake installations. The intake is commonly located in a region of non-uniform flow, either due to the influence of nearby structure or due to the attitude of the aircraft, and rarely can the flow be considered to be simply two-dimensional or axisymmetric. Possibly, three-dimensional potential flow and characteristics computer programs could become available for use, although the computing effort required may be hard to justify. In the interim, the need seems to be for an attempt to be made to correlate available data on an international basis to define better rules for drag estimation, and to show the way in which installation parameters such as orientation, detailed geometry and the presence of other parts of the aircraft affect intake drag. Hopefully, there will be some progress possible from analysis of results from tests such as those of the American Tailor-Mate programme<sup>58</sup>.

As a suggestion for a framework for a simplified analysis for transonic speeds, Fig.13 shows what appears to be the characteristic variation of  $K_{add}$  with Mach number and, for want of a better name, cowl bluntness. Note that the subsonic values, as quoted by Mount, blend into  $K_{add}$  values derived from the Fraenkel rule. Correlation studies are required to show whether subsonic  $K_{add}$  and critical mass flow (see Fig.12a) can be related to a cowl parameter, and to determine the range of intakes to which such correlations would apply.

#### 3.4.3 Subsonic afterbody drag

Afterbody drag arises because of the incomplete compression of real flow over the rear of a body; for a closed body in viscous flow this is the source of form drag. The drag is significantly increased if the body is truncated, partly because of the low base pressure that results but also because of the modification from the ideal of the flow over the boat-tail; hence, it is preferable to refer to afterbody drag rather than merely to base drag, as has been common practice in the past. The flow is further affected if a jet issues from the base of the body and much model testing has been concerned with determining the effect of the jet. In many cases, this effect is in fact relatively small and the level of drag depends largely upon the geometric design of the afterbody and the jet nozzle. Such testing has also been largely confined to investigations of the characteristics of particular aircraft configurations, though there were tests on families of single-jet afterbodies during the 1950s, when the most comprehensive range was covered<sup>59</sup> by Henry and Cahn. The rules for afterbody design have thus been derived by airframe and engine manufacturers from what are, essentially, *ad hoc* tests.

Estimates of the level of afterbody drag have also been made from the same data, but no general estimating method has been derived. The problem is not amenable to simple theoretical analysis and the number of parameters involved is large. A correlation of data from axisymmetric models was made<sup>60</sup> by McDonald and Hughes which, though nominally limited in its application, does provide a means of broadly estimating the effect of changes in the main parameters<sup>61</sup>. A major difficulty lies in knowing how well the method applies to the twin-jet afterbodies that are more typical of military aircraft.

Some five or six years ago, the only twin-jet data available within the United Kingdom related to afterbody tests on models of specific aircraft. At a meeting of specialists in 1967, it was agreed that a research programme should be initiated at the Aircraft Research Association, Bedford, to provide systematic data for generalised variations of the MRCA, Jaguar, and Harrier configurations. Some results relating to the first class of configuration are shown in Fig.14 in comparison with other experimental data for twin jets and with predictions using the method of Ref.60. When the drag is plotted as a coefficient based on effective base area, there is a broad collapse of the test data to a constant level for a wide range of typical aircraft values of the parameters, for twin-jet as well as single-jet configurations. In fact, a value of 0.13 applied to effective net aircraft base area seems to give as good an estimate of afterbody drag as is possible without specific model tests of the configuration in question or of a configuration of similar geometry. More detailed correlations are desirable for use in design optimisation but it is questionable whether they can produce a better estimate of absolute afterbody drag, especially in view of the known problems which arise in the correction of tunnel test results on afterbody rigs. Afterbody rigs are certainly essential for determining the effect of changes in detailed geometry. A useful collection of data from a general NACA series of tests<sup>62-64</sup> on twin-jet afterbodies with zero base nozzles is now becoming available. An analysis of Pratt-Whitney test data has been given<sup>65</sup> and a general discussion of the subject exists<sup>66</sup>. General trends can be obtained, though much of the data is appropriate to zero-base iris nozzles, rather than to translating-shroud nozzles with associated base area. It should be noted particularly that significant improvements in drag can be obtained by detailed development of a particular configuration. Much care is necessary in interpretation. Thus, it can be shown that increased nozzle spacing reduces the interference drag due to jet and nozzle; however, the overall afterbody drag becomes larger as the jet-off drag increases, especially when there is an accompanying increase in body maximum cross-sectional area.

As regards future studies, the consensus of opinion among UK specialists is that further testing on generalised models representative of practical nozzle/afterbody combinations should be continued. This needs to be accompanied by studies of tunnel technique problems at transonic speeds (see section 4). It would be helpful to reach agreement on a consistent procedure for presentation of the data from afterbody rigs; this could involve adoption of a datum afterbody which would be tested on various rigs and, possibly, on selected complete models. It is also felt that a period of data consolidation is needed, during which an attempt should be made to achieve an acceptable correlation with theory.

#### 3.4.4 Supersonic afterbody drag

Supersonic afterbody drag is primarily the wave drag of the rearward-facing surfaces of the fuselage and as such is included in calculations of supersonic aircraft drag (see section 3.3). However, consideration also has to be given to the effect of the jet flow. With no jet flow and no early flow separation, a terminal compression shock will originate from the rearmost point of a body; in the presence of

an under-expanded jet issuing from a convergent nozzle at supersonic speeds, there is an interaction with the flow over the afterbody. The terminal shock causes separation of the boundary layer on the boat-tail and a balance is reached such that the shock originates forward of the end of the body (Fig.15a) and the base pressure feeds forward onto the afterbody. The jet therefore produces a reduction in afterbody drag which can be appreciable. 6-23

The phenomenon has been discussed by Stoddart<sup>67</sup>, and a simplified method for estimating the drag increment has been suggested. A more detailed method of calculation involving estimation of the point of flow separation can be used, and an example of its effectiveness is given in Fig.15b in comparison with measured data from tests<sup>68</sup> by Reid on a single-jet afterbody. Satisfactory agreement has also been obtained in BAC tests on a realistic twin-jet afterbody. An equivalent axisymmetric body is assumed for the purpose of calculation, and jet effect is taken as the drag change between the aircraft operating pressure ratio and the pressure ratio corresponding to a jet wake equivalent to the terminating cylinder used in the basic aircraft wave drag calculation.

It therefore would seem that reasonable estimates can be made of afterbody drag at supersonic speeds, although no generalised study is known. In consequence, a research programme is to be undertaken in the BAC 4ft wind tunnel in which single-jet and twin-jet bodies of the same geometry as those tested in the first phase of the tests at transonic speeds at ARA Bedford are to be tested at supersonic speeds on an afterbody rig which measures afterbody drag and jet thrust independently. Good discrimination is therefore possible; the effects of changes in geometry and nozzle design can be determined and comparisons made with estimates.

A major variation of interest is the degree of expansion produced by the jet nozzle. If a convergent-divergent nozzle is installed in an aircraft, such that the jet is fully expanded, then the terminal shock remains at the end of the afterbody and there is no reduction in boat-tail drag. Conversely, though the full available expanded thrust is not obtained from a convergent nozzle, a large proportion, as much as 50% of the thrust increment due to full expansion is, in fact, felt on the afterbody so that the apparent benefit of installing a sophisticated nozzle is less than might otherwise be expected. Estimates of typical differences have been given<sup>67</sup> and values taken directly from model tests<sup>69</sup> are shown in Fig.16. Results are shown for a low supersonic Mach number appropriate to the design pressure ratio (5.5) of the con-di nozzle. It is notable that with allowance for installed interference effects (drag reduction) the con-di nozzle shows benefit over a convergent nozzle only above a pressure ratio of 6.5, as against static thrust showing benefit above 3.8, and ideal benefit above 1.9. Similar differences are apparent for other Mach numbers and nozzles but detailed study is required to derive appropriate values.

Since there is a very significant interaction, care must be taken in assessing the performance of nozzles if experimental data have been obtained from models fitted to a cylindrical afterbody, as has commonly been the case. For the future, there is a need for the development of general methods for the prediction of installed thrust and drag for a specific design of afterbody and nozzle. If recourse to experiment is necessary, it is essential that both afterbody and nozzle geometry should be fully represented.

### 3.5 Powerplant installations for supersonic transport aircraft

Based on a contribution by J.W. Britton, RAE.

#### 3.5.1 Introduction

During the last ten years, a considerable international programme of research and development has been mounted to provide direct support for the Concorde project. A large part of this programme, which has involved the major aeronautical test facilities in both England and France, has been devoted to propulsion aerodynamics. This has included not only the development of the engine itself, but also the development of the engine air intake, the engine exhaust nozzle, and the nacelle in which the propulsion system is installed in the airframe.

One of the facets of propulsion aerodynamics for Concorde with which the RAE has been deeply involved is the study of the external forces acting on the engine nacelles in the flow field of the complete aircraft. This programme of work, which began as early as 1962, has extended over the whole period of development of Concorde from the early formative stages, through the definition of the prototypes, to the final phase of refinement and definition of the configuration of the production aircraft.

Even for a configuration such as Concorde, where the nacelles are situated in an orderly and nearly-uniform flow field environment, there is a lack of completely-effective theoretical methods which can be used to predict the best external shapes for the intake and nozzle. Although two-dimensional shock expansion methods and, also, Supersonic Area Rule techniques can be employed in some cases to give a qualitative guide to the effects of variations in external shape, for a quantitative measure of such effects recourse must be had to specialised tests in the wind tunnel.

To illustrate the nature of the R & D support which can be involved, the test and analysis procedures are considered which have been used to provide a basis for the prediction of the drag of the intakes and nozzles of Concorde.

#### 3.5.2 General approach and definitions

The general philosophy relating to the analysis of forces acting on a ducted body, and their relation to engine thrust where appropriate is considered in Refs.70, 71 and 72. For the Concorde configuration, the effects of the internal flow downstream of the exit of the installation are usually small, and the relevant internal forces in most cases are the conventional standard internal forces associated with changes in properties of the internal flow between a station far ahead of the model and the exit of the installation. The particular problems of definition of the aerodynamic forces acting on

6.24 a ducted model with a side intake, which includes bleed or diverter systems for the removal of all or part of the forebody boundary layer, also have been considered<sup>73</sup>, and forms of mutually-compatible internal and external force definitions for such cases proposed. The analysis of the results of the wind-tunnel tests on Concorde models has been based on the proposals and definitions set out in these references.

### 3.5.3 Intake drag

Tests were made on 1/30 scale complete models of Concorde (Fig.17) with different nacelle representations in the 8ft x 8ft supersonic wind tunnel at RAE Bedford over a range of Mach numbers at a Reynolds number of around 1/20 of that for the full-scale aircraft. In all cases, free-flow nacelles were used and there was no attempt to simulate the hot high-pressure exhaust flow from the nozzles.

For tests which were concerned only with the drag of the intake, the external surfaces of the cowl and the sidewalls of the intake up to the engine face station were represented accurately, while the sectional area and shape of the nacelle at all stations aft of the engine face were kept constant. On the simplest of such nacelles, the boundary layer approaching the intake on the lower surface of the wing was allowed to enter the intake itself: with more representative configurations, the wing boundary-layer diverter was represented by a scale model of that on the aircraft and the compression surfaces of the intake were also represented. For measurement of forces acting on the surfaces of the afterbody, or for the measurement of the drag of the complete nacelle, the external shapes of the engine bay and afterbody, as well as the intake, were represented. A fixed model of the appropriate configuration of the variable geometry of the secondary nozzle (Fig.18) was used for these cases. The duct inside the nacelle was designed so that the flow approaching the intake was not affected by conditions inside the nacelle and, also, so that the flow at the exit was choked in order to improve the accuracy of the measurement<sup>74</sup> of standard internal drag.

The installation drag of the nacelle is defined<sup>73,74</sup> as the increment in external pressure drag due to the addition of nacelles to the basic configuration (i.e. wing + body + fin), evaluated at constant lift. The nacelle installation drag can be regarded as an 'absolute' measure of the external drag of the nacelle and is obtained from the following series of tests:-

- (a) Measurement of overall forces acting on basic configuration (i.e. wing + body + fin);
- (b) Measurement of overall forces acting on complete configuration (i.e. wing + body + fin + nacelles);
- (c) Measurement of standard internal forces;
- (d) Measurement of flow approaching intake;
- (e) Measurement of the forces due to the unrepresentative base of the nacelle;
- (f) Measurement or estimation of various skin-friction drags.

The objective of some tests is simply the comparison of a range of external shapes for a nacelle with a given intake, intake environment and internal duct. In such cases, the standard internal forces are constant provided that comparisons are made at constant attitude, and also that the internal flow is not affected by any changes in the external shape of the nacelle. The external forces acting on each of such a range of nacelles can therefore be compared without recourse to separate measurement of the installation drag of each individual nacelle. If it can also be assumed that the external skin-friction drag of each of the range of configurations is the same, then, in order to compare external lift, drag and pitching moment it is necessary only to measure for each configuration:-

- (a) Overall forces acting on the complete configuration;
- (b) Forces due to the unrepresentative base of the nacelle.

The work on the development of the external shape of the intake for Concorde is summarized in Fig.19, where the installation drag of each intake at  $M = 2.2$  is indicated. The programme of work fell into three main phases of activity as indicated, being concerned principally with the choice between all-external and mixed-compression intakes and the choice of the characteristically-steep angle of the cowl for the chosen external-compression intake. Attention was also given to the shape of the fairing from the cowl lip to the engine face and the ratio of nacelle sectional area at engine face to intake area taking account of the possibility of immersing the engine within the wing structure. The ratio of the width to the height of the intake was studied, including consideration of the possibility of interference effects between the cowl and sidewalls of the nacelle and the lower surface of the wing. As can be seen, the measured installation drags for this family of nacelles cover a wide range. However, one of the more striking features of this long series of tests is that, despite the inevitable appearance of problems and consequent design compromises which are inevitable during the development of any aircraft, the penalties in intake performance which can stem from such modifications appear to have been minimised and the drag level for the final intake of each of the three phases is roughly the same.

Because the tests on the complete models were made at low Reynolds number, the relationship between the local wing boundary-layer thickness and the scale model of the intake was incorrect; in particular, the proportion of the wing boundary-layer which was diverted from the intake on the model was lower than that on the full-scale aircraft. The flow processes in the diverter passage and at entry to the intake, were, however, similar in character to those at full scale and an adequate representation of the flow up and into the intake was normally achieved. Separate experiments, of the type described in Ref.75, have been made using a larger-scale model of intake and diverter mounted on a flat plate in order to evaluate changes in diverter lift, drag and pitching moment. These include interference effects between the

6-25

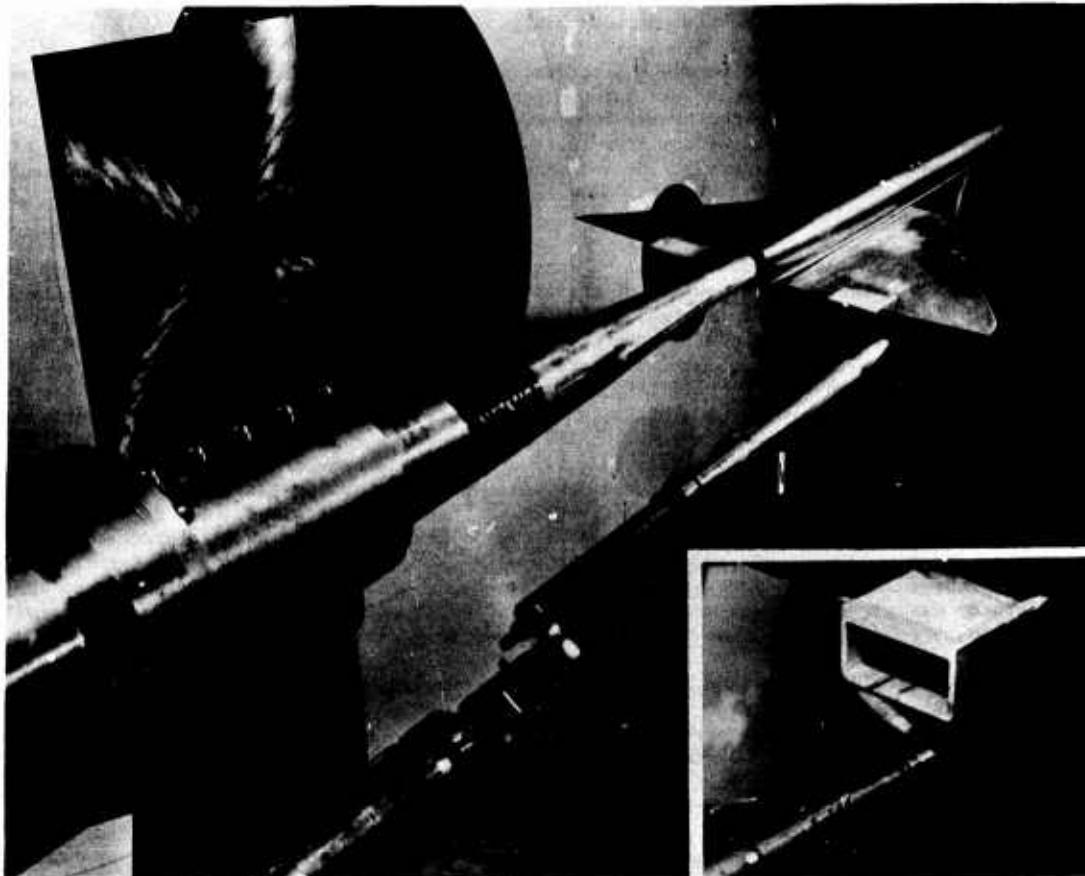


Fig.17 Typical Concorde model in 8ft x 8ft wind tunnel RAE Bedford

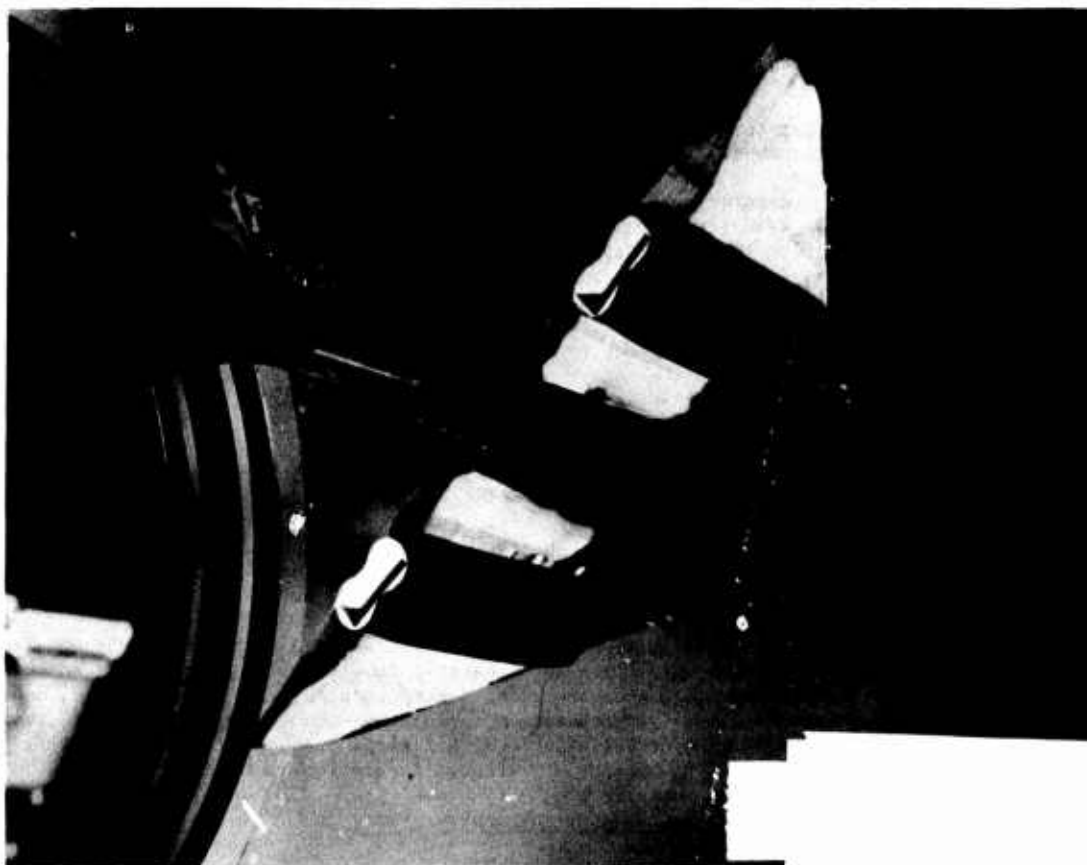


Fig.18 Concorde model for nacelle drag and afterbody load studies

diverter flow and the flow over the lower surface of the wing, due to changes of immersion of the diverter in the local boundary layer and also to detailed changes in the shape of the diverter from the necessarily simplified form of that on the complete model.

On the 1/30 scale models of the complete aircraft, the intake compression surfaces were represented simply by the first fixed wedge of the intake and the intake flow was close to the maximum value for most tests. Additional theoretical and experimental studies, such as those described in Ref.76, were therefore made in order to evaluate the effects of any flow spillage, which is additional to that introduced by the intake on the complete model and which might be necessary to match the intake flow with engine demand.

#### 3.5.4 Afterbody drag

The programme of work for the development of an afterbody for the nozzle for the production aircraft is summarized in Fig.20. The external shapes of the afterbodies are illustrated by showing the section at nozzle exit superimposed on the basically rectangular maximum cross-section of the nacelle. Following measurements on the Type 11 nozzle and afterbody for the pre-production aircraft, an effort was made to design a nozzle arrangement for the production aircraft with reduced drag. Attention was turned to more regular boat-tail shapes which were closely tailored to the rectangular section of the engine bay and which involved more evenly distributed boat-tailing around the periphery. Initially, the effect of nozzle exit area on boat-tail drag was studied systematically. These tests (configurations 2, 3 and 4) showed the expected clear trend of reducing boat-tail drag as nozzle exit area was increased and the rearward-facing area of the boat-tail surfaces was reduced, as well as demonstrating that boat-tail drags which were lower than that for the Type 11 nozzle (configuration 1) could be obtained. Two other afterbodies (5 and 6) were also tested with the width of the afterbody deliberately increased in order to produce some forward-facing surfaces on the sidewalls of the afterbody so as to exploit favourable interference effects. It was confirmed that advantage could be taken of the favourable pressure environment below the wing in which the afterbody was placed. These encouraging results led to specific proposals for the complete nozzle plus afterbody for the production version of Concorde (e.g. configurations 7 and 8).

Since free-flow nacelles were used for most tests, all measurements of the forces acting on the afterbodies were made in the presence of a nozzle exhaust flow which was not representative of the aircraft. Because the natural low-total-pressure jet was in all cases surrounded by a blunt base, and base pressure was usually considerably lower than that on the external surface of the boat-tail immediately upstream of the base, it was assumed that any interference by the flow field of this unrepresentative jet onto the boat-tail ahead was small. In contrast, on the aircraft, interference between nozzle exhaust flow and external flow affects pressures on both base areas and boat-tailed surfaces. It follows, therefore, that the performance of the complete nozzle plus afterbody cannot be defined solely by measurements of external drag obtained from tests on complete aircraft models fitted with free-flow nacelles, together with measurements of the internal thrust obtained from tests on nozzle models where the high-pressure jet is exhausted into low pressure quiescent conditions. Additional tests using models on which both jet and external flow field are represented are necessary to provide measurements of interference effects, and thus to complete the set of data from which the thrust minus drag of the nozzle plus afterbody can be assembled.

For Concorde, the gross thrust minus drag of the complete nozzle plus afterbody was obtained by suitably combining data from the following series of tests:-

- (a) Measurement of the boat-tail drag, on the model of the complete aircraft, fitted with free-flow nacelles and (usually) a somewhat simplified representation of the afterbody;
- (b) Measurement of the external drag of an isolated model of the afterbody in uniform flow using, as nearly as possible, the same standard of representation of both external shape and jet as was used on the complete model of the aircraft. This involves the evaluation and subtraction of the gross thrust of this unrepresentative jet and the drag of the unrepresentative base of this nozzle;
- (c) Measurement of the gross thrust minus drag of the complete nozzle plus afterbody on an isolated model of the nozzle plus afterbody in uniform flow, using the best possible representation of both nozzle and afterbody, as well as of the engine exhaust flow and any other internal flows.

In this way, a gross value of thrust minus drag for the complete nozzle and afterbody was synthesised, such that those terms which were taken to be principally influenced by the airframe flow field were taken from tests on the complete aircraft model and those terms which were taken to be principally influenced by the jet were measured on the isolated afterbody model. Measurements of internal thrust on nozzle models where the high-pressure jet is exhausted into low pressure, quiescent conditions were also made to improve the understanding of the behaviour of the complete nozzle.

#### 3.5.5 Concluding remarks

Because of the lack of comprehensive theoretical methods, it has been necessary to depend almost exclusively on experimental measurements as a basis for prediction of the drag of the intake and nozzle for Concorde. The associated experimental techniques and selected results have been described, and the method of interpretation has been outlined. At present, a large programme of specialised aimed research is involved in the determination of engine installation drag effects for supersonic civil aircraft projects to the required degree of certainty, in the absence of suitable theoretical methods.

#### 3.6 Powerplant installations for subsonic transport aircraft

Based on a contribution by D. Stewart, BAC Weybridge.

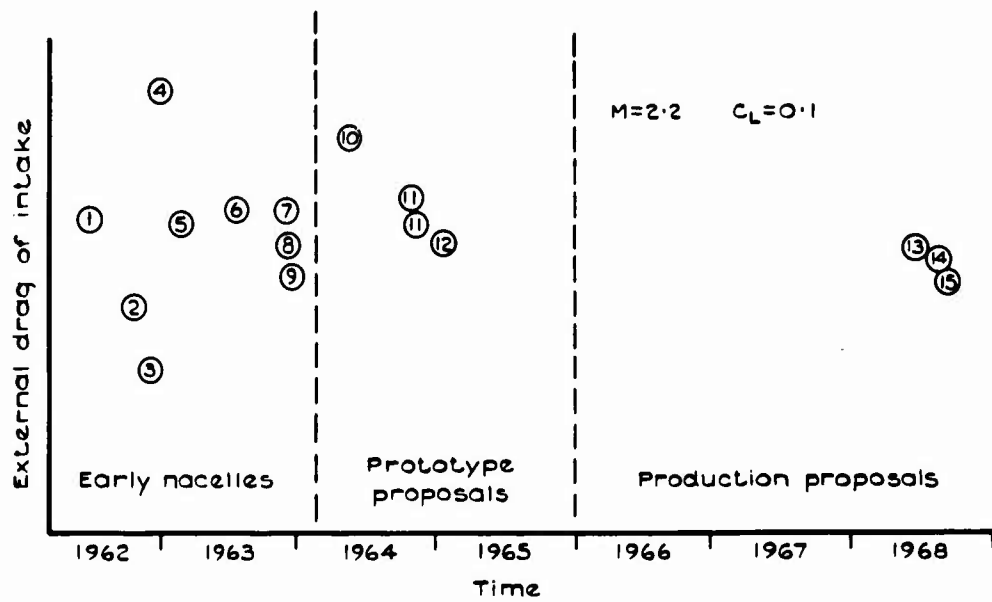


**Fig.19 Development of external intake shape for Concorde**

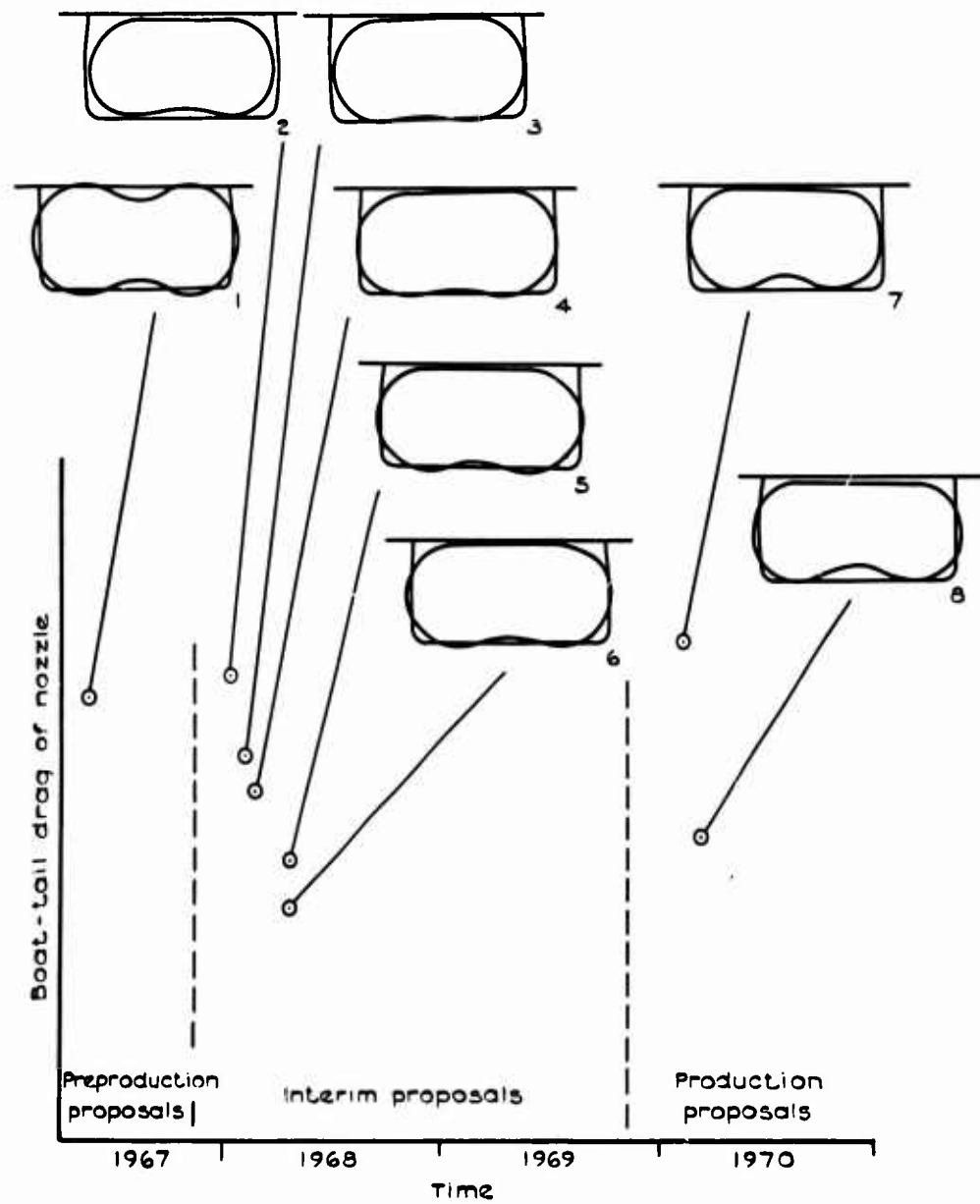


**Fig.20 Development of afterbody and nozzle for Concorde**

### 3.6.1 Introduction

The high-bypass-ratio front fan engine which is now in commercial use on long and medium range subsonic transports, with its short or now more common three-quarter length cowl and two separate coaxial exhaust streams, requires the thrust and drag to be clearly defined to allow correct accounting in the assessment of the aircraft's performance. The problem is complicated by the fact that the flow from the fan exhaust passes over the gas generator afterbody of the nacelle and part of the support pylon or stub. 478

Typically, the total installed 'drag' of a podded engine arrangement effectively amounts to nearly 10% of the total aircraft drag at cruise, when such components are included as the gas generator afterbody drag and the drag of the scrubbed portion of the pylon (which strictly are taken into account in the engine thrust evaluation).

### 3.6.2 Thrust and drag accounting

The definitions of thrust and drag established<sup>70,71</sup> some years ago by an ARC Panel are still valid, with appropriate extensions for real airframe/engine combinations to allow for interactions between the internal and external flows and to overcome difficulties arising in specifying the most appropriate exit conditions. The widely-used standard or 'brochure' net thrust includes an allowance for the pre-entry thrust term but makes no allowance for the post-exit contributions. Accounting for post-exit thrust is important if the overall propulsion equation is to be understood, since the jet effect is felt on the surrounding airframe or engine structure as a change in local pressure distribution or 'jet interference' term. Here, we will follow the ARC Panel in defining nacelle drag as the summation of forces on the outside of the streamtube bounding the flow which passes through the complete engine, and thrust as the summation of forces on the inside of the streamtube. The gas-generator afterbody drag, plug drag and the force on that part of the pylon or stub scrubbed by the fan exhaust therefore will all be considered as parts of the thrust term (see Fig.21). The fan cowl drag, although dependent on the engine operating conditions, will be placed on the drag side of the balance sheet, as will the unscrubbed (external) pylon drag and interference drag.

For a subsonic transport at cruise, with an engine installation drag of about 9% of the total aircraft drag, a typical breakdown might be fan cowl drag 3.2%, fan duct loss 2.2%, gas generator drag 2.1%, strut drag 1.3% and strut scrubbing drag 0.2%.

### 3.6.3 Fan cowl drag

Provided the fan cowl is designed properly for its operating condition, its drag need not exceed the drag of a flat plate of the same wetted area by, say, more than 15%. However, its drag may otherwise increase rapidly with the formation of shock waves and flow separations in the following ways:-

- (a) If the intake is too large for the required engine airflow, considerable spillage results which can lead to flow separation unless the cowl is suitably shaped;
- (b) If the fineness of the cowl forebody is insufficient in relation to the freestream Mach number, expansions aft of the lip will cause a supersonic flow region and shock wave system which, if not well-controlled, can cause significant wave drag and possibly, flow separation;
- (c) If the afterbody curvature is too rapid and the boat-tail angle excessive, separations can spread forwards from the cowl extremity.

Basic NASA work<sup>77</sup> on cowl forebody development has been supplemented by studies undertaken by Rolls Royce and Aircraft Research Association<sup>78</sup> in the ARA transonic tunnel over the past ten years. For subsonic transports, combined increases in cruise Mach number and engine mass flow per unit frontal area have caused a trend towards increased values of the ratio of inlet to maximum diameter, and recent work has therefore concentrated on achieving a high drag-rise Mach number and acceptable spillage drag characteristics for such configurations. Some of the more important geometric variables (see Figs.21 and 25) which affected the drag associated with the NACA Series 1 profile proved to be the highlight diameter to maximum diameter ratio ( $D_1/D_M$ ) and the forebody length to maximum diameter ratio ( $L_F/D_M$ ).

Analysis of this experimental work produces an optimum relationship between these geometric parameters. Of course, not all cowls on the optimum curve have the same characteristics; on the contrary, less sensitive aerodynamic characteristics are produced by moving along the curve in the direction of smaller diameter ratios and larger forebody length ratios, at the expense of increased cowl size and drag. Fig.22 shows the variation of drag with intake mass flow ratio and freestream Mach number for a typical cowl geometry appropriate to current cruise Mach numbers.

Assuming satisfactory geometry has been chosen for the operating conditions, it is possible to base initial drag predictions on a form factor, applied to the turbulent skin-friction drag calculated for the equivalent flat plate. Reliance on a form factor derived from test data on cowls at relatively-low Mach numbers and correlated against an empirical geometrical parameter is, however, generally undesirable, and further research at Rolls Royce<sup>79</sup> has been directed towards the provision of a sounder foundation for forebody drag prediction. From measured cowl pressure distributions, the drag was found by computing boundary-layer momentum thickness at the maximum diameter station and determining the loss of momentum which this represents on displacement to infinity downstream. Simple considerations then led to a satisfactory correlation for freestream Mach numbers up to  $M = 0.85$  between the forebody drag and the main geometrical and engine flow parameters (see Fig.23).

The freestream Mach number at which a rapid rise in drag occurs can be observed to coincide approximately with the passage of a normal shock across the crest of the cowl, affording a simple method for estimating the drag-rise Mach number from calculated pressure distributions. However, for project assessment purposes, it is more convenient to express the drag-rise Mach number as a function of a geometric parameter (see Fig.24) analogous to the thickness-chord ratio of a wing section. The majority

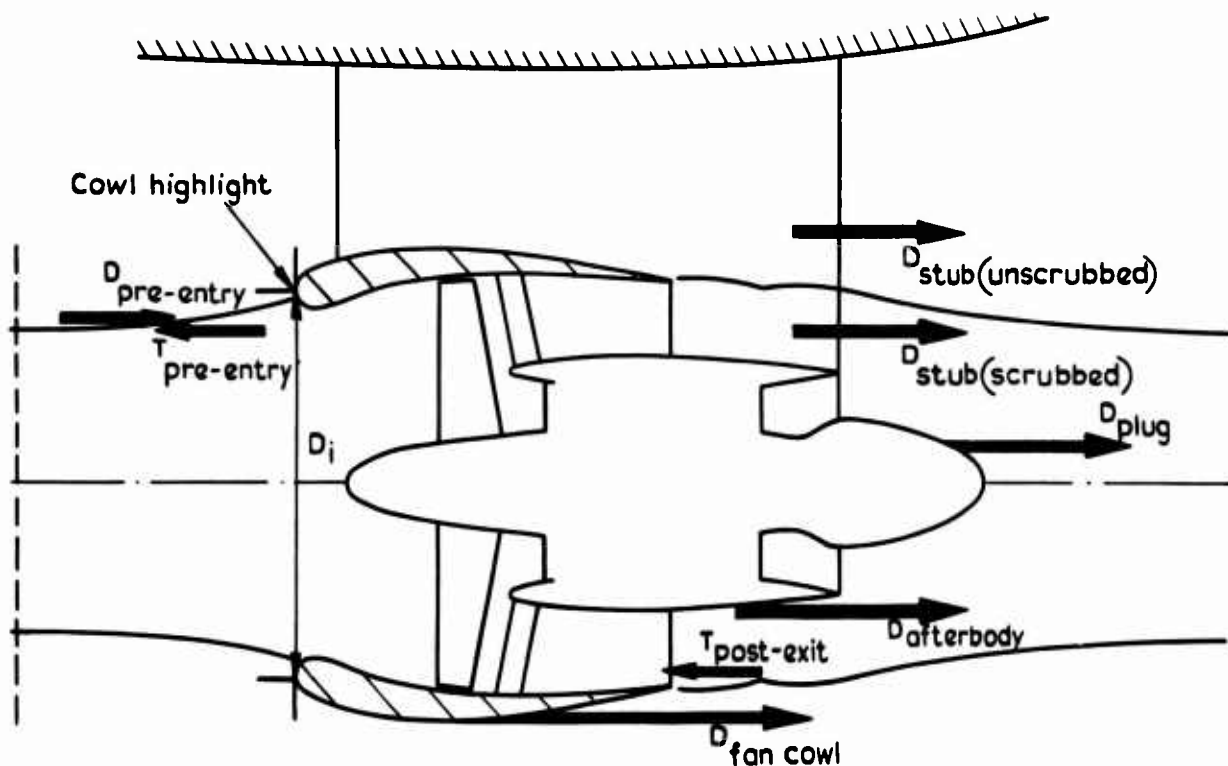


Fig.21 Forces involved in thrust and drag accounting

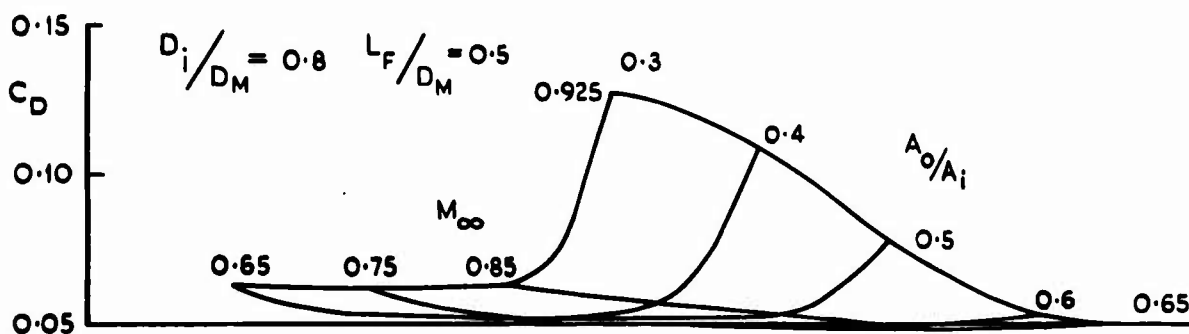


Fig.22 Variation of drag for a typical cowl

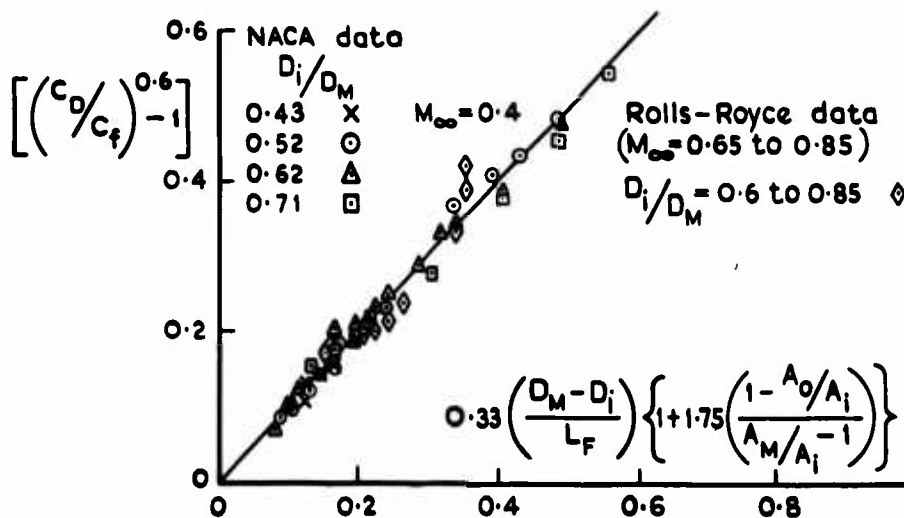


Fig.23 Drag correlation for NACA-I series forebodies

of the data apply to the case of a forebody followed by a relatively-long cylindrical centre body. However, some were also obtained on forebodies followed by a circular-arc afterbody. In these cases, the acceleration of the flow onto the afterbody would be expected to influence the pressure at the crest and hence the drag-rise Mach number. Although few data are available, this effect is seen to be significant for the range of afterbody geometries which are likely to be considered for practical applications.

When the intake operates below the compressibility drag-rise design condition, the drag increases gradually as the mass flow is reduced until the critical mass-flow ratio is reached at which drag rises rapidly as flow separations result from severe pressure gradients or shocks. In large measure, both features are determined by the initial expansion of the flow around the intake lip, which is itself largely governed by the initial curvature of the lip. Thus, it would be expected that the critical mass-flow ratio should correlate with a lip radius parameter (see Fig.25).

Up to now, the discussion has centred around the NACA Series 1 profile, which was primarily designed to produce a high critical Mach number and so tends to exhibit poor spillage characteristics at the low intake-mass-flow ratios and low Mach numbers that exist on the failed engine during a second segment climb or at the engine-out ceiling height. This can result in a significant deterioration in aircraft performance at these flight conditions, especially with a twin-engined aircraft. Recent work on this subject has therefore been concentrated on improving the low intake-mass-flow characteristics of cowl performance, without impairing the cruise Mach number characteristics. For example, the use of a 'peaky' section produces a strong but controlled expansion around the leading edge, followed by isentropic recompression back through the crest, which gives a good pressure recovery on the afterbody. A satisfactory but geometrically-simple 'peaky' section can be provided by a 'circle-conic' forebody. At reduced mass-flow ratios and Mach numbers, the 'circle-conic' forebody is able to retain its required pressure distribution when the suction peak on the NACA Series 1 forebody has collapsed, the corresponding improvement in spillage drag at low mass flow ratios being shown in Fig.26. At higher Mach numbers and mass-flow ratios, the 'circle-conic' forebody exhibits less expansion off the leading edge and recompresses more smoothly than the NACA Series 1 forebody. Some care is needed, however, in the detailed choice of forebody geometry to ensure that the cruise Mach number performance is retained involving, for instance, consideration of the cowl curvature distribution.

#### 3.6.4 Gas generator afterbody drag

Typically the loss of thrust due to the flow passing over the afterbody is about 2%. This results from, basically, two components:-

- (a) increased skin friction due to the higher dynamic head in the fan exhaust; and
- (b) wave drag due to the formation of shock waves.

On current powerplants, such as the RB 211, the fan exhaust pressure ratio (fan total pressure/free-stream static pressure) is about 2.5 at typical cruise conditions so that the fan exhaust flow over the afterbody is supersonic, and the flow is made to expand over a convex surface which serves to accentuate the expansion. Fig.27 shows a simple correlation, based on some Boeing and Rolls-Royce data, of afterbody scrubbing drag (skin friction + wave) as a function of the geometry and the fan pressure ratio. Although this is useful for initial assessments, no simple correlation can be really adequate, since the behaviour of the fan flow and the losses occurring in it are as much determined by the local slope and curvature of the afterbody profile as by its overall aspect ratio or final boat-tail angle.

The method of characteristics can be used for axisymmetric afterbodies to provide a theoretical treatment<sup>80</sup> of the fan flow over the gas generator afterbody. The supersonic flow is assumed to start from a plane normal shock at the fan nozzle exit, with the initial expansion (Prandtl-Meyer) focussed on the nozzle exit lip. The afterbody profile forms one boundary of the flow; the imposed boundary condition is either specified afterbody shape or specified afterbody pressure distribution. For prediction purposes, the outer free boundary of the fan flow is specified by the criterion of constant freestream static pressure along the boundary; a quiescent condition which effectively omits the influence of an external freestream flow, as would exist under cruise flight conditions. However, testing experience on a variety of afterbody profiles suggests that if a profile shows an acceptable performance under quiescent conditions at the fan cruise value of exhaust pressure ratio, then the performance under representative cruise flight conditions is also good. Limited tests of a calculated afterbody profile show little change in afterbody surface pressures between 'quiescent' tests and tests at an external flow Mach number of  $M = 0.85$ . When arbitrary profiles are specified, shocks inevitably occur; currently, these are dealt with on the assumption that they are weak and thus introduce negligible loss in total pressure. This approach can be supported by representative flow-field calculations, which suggest wave drag losses should be small.

The components of the drag of the afterbody can be estimated from pressure distributions by a method under development by Rolls Royce which already gives reasonably good agreement with experiment. As losses in the exhaust system effectively act at the gross (rather than net) thrust level, there is considerable incentive to improve our understanding of the flow over the afterbody and the prediction of its drag.

#### 3.6.5 Interference

For simplicity, nacelle installation drag is considered in terms of the total aircraft drag change due to adding the nacelles and supports, in relation to the estimated drag of the isolated nacelles and support pylons or stubs. For underwing installations, the drag of a nacelle installation is sensitive to the vertical and longitudinal displacement of the nacelle relative to the wing, as well as to the lift coefficient of the wing and the freestream Mach number. The optimum position for an underwing nacelle from an interference drag viewpoint is well ahead of and below the wing leading edge. In practice, this generally means that the nacelle centre line is between three-quarters and one nacelle maximum diameter below the wing leading edge and the nacelle highlight is approximately three-quarters of the nacelle

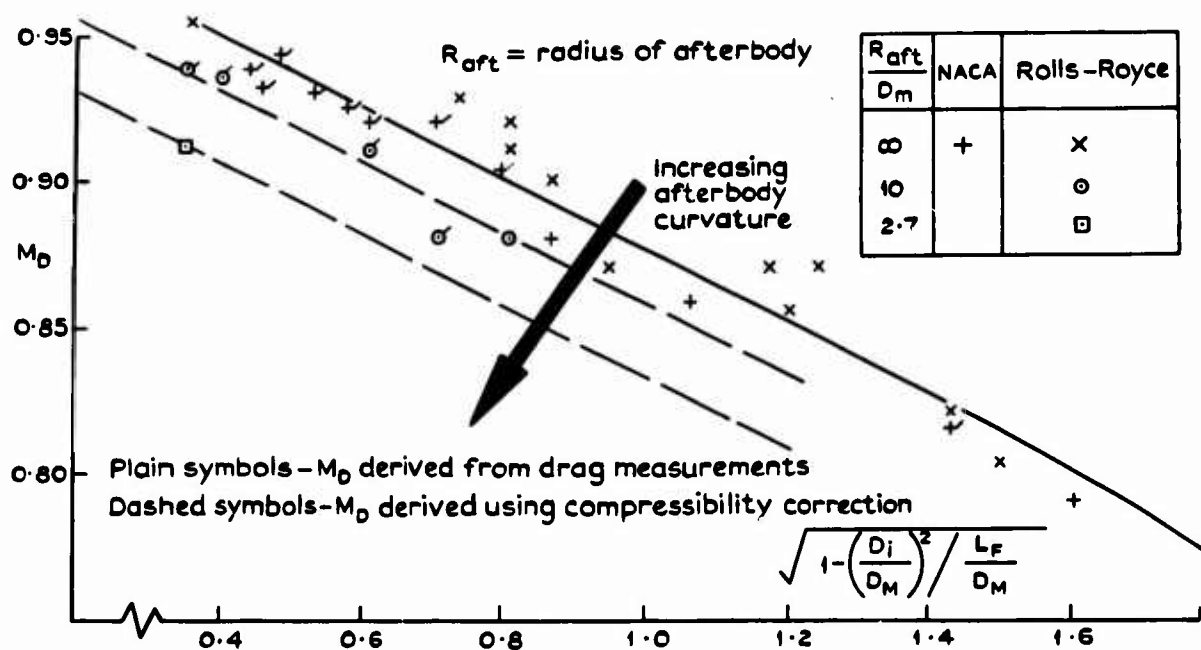


Fig. 24 Drag-rise Mach number correlation for NACA-1 series cowls

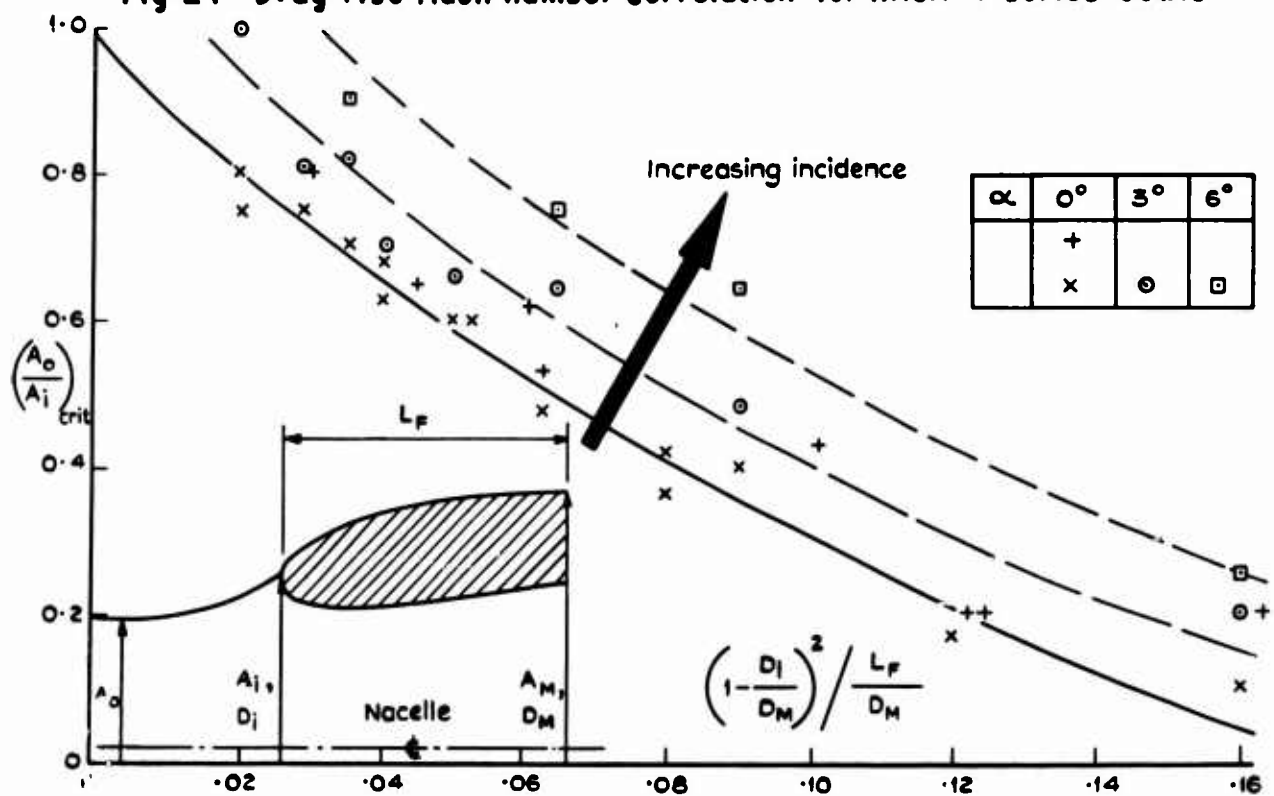


Fig. 25 Critical mass-flow ratio correlation for NACA-1 series cowls

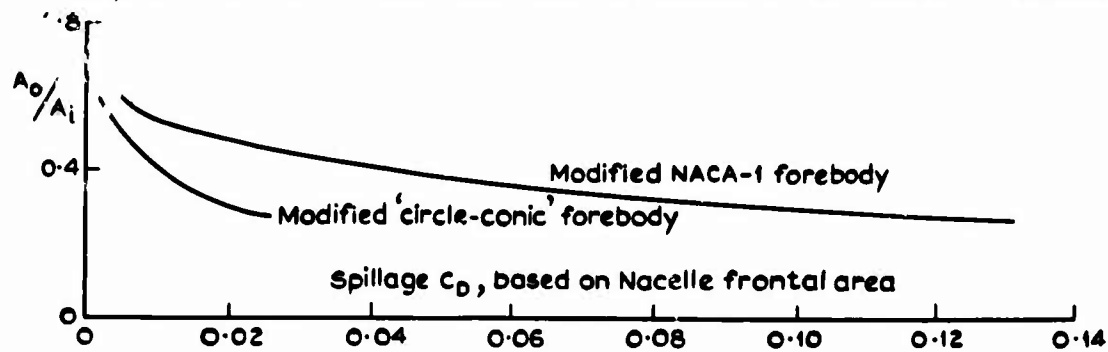


Fig. 26 Comparison of spillage drag characteristics

overall length ahead of the wing leading edge. Zero interference can be achieved effectively up to typical cruise Mach numbers by correct positioning of the nacelle and, in some cases, favourable interference has been claimed<sup>81,82</sup>.

As regards nacelle installations on the rear fuselage, careful optimisation of position is again necessary to achieve satisfactory results. The interference drag falls away rapidly as the nacelles are moved away from the fuselage but the stub drag, of course, increases; minimum drag is usually achieved with a minimum gully width between 0.2 and 0.3 of the nacelle maximum diameter. Nacelle attitude and toe-out must also be optimised. The optimum for a particular design depends to a large extent on the gully shape between the nacelle and fuselage and the nacelle longitudinal position relative to the wing. Fig.28 illustrates the complexity<sup>83</sup> of the problem for specific rear-fuselage nacelle arrangements. It can be seen that although adverse interference takes place with the rear fuselage, this is alleviated by favourable interference with the wing and the rest of the fuselage.

To date, interference drag problems have been resolved mainly by relying upon *ad hoc* wind-tunnel testing. In the more sophisticated tests, engine simulators have been successfully used although even these cannot give a completely satisfactory simulation. Ferri<sup>84</sup> has suggested a new approach is required in dealing with the problem of engine interference whereby analogue and digital simulation is combined. The wind tunnel would furnish the analogue data, with corrections generated by numerical methods applied in order to improve the results obtained, as has been done in other aspects of aerodynamic research. It is considered that consideration should be given to this approach to establish its usefulness in assisting in overall aircraft performance assessment.

Programs for solving the Neumann problem are being developed for the treatment of interference problems in general. Existing programs, with first-order effects of compressibility included, are applicable to axisymmetric and non-axisymmetric cowls. Cowls on either side of a fuselage or below a wing can be treated although, at present, without support stubs or pylons represented. Work currently underway includes extension to underwing pylons and these computing sequences will be applicable automatically to cowl-pylon junctions. The development of the incremental calculation procedures required for local redesign is also underway. Further work is required to include jet effects, but this should not prove too difficult. Some progress has been made in the development of a rapid relaxation technique for the solution of the compressible field equation for subcritical flow, using Neumann influence matrices to restore boundary conditions. The accuracy of the influence matrices will affect the rate of convergence but the accuracy of the converged solution depends only on the field equation errors. If this method is successful, then extension to local regions of supercritical flow can be examined. With further development, such theoretical treatments coupled with boundary-layer calculations should prove to be strong tools for nacelle installation design.

### 3.7 Trim drag

Based on a contribution by D. Howe and R.E. Ward, Cranfield Institute of Technology.

#### 3.7.1 Introduction

The prediction of trim drag has not received much general consideration<sup>85</sup>. No doubt, this is because an accurate estimation of the drag penalty due to trim demands a fairly detailed knowledge of the characteristics of a particular design of aircraft. Nevertheless it is necessary to make an approximate allowance for it during the initial project phase. This is certainly so when it is desired to compare the relative performance of alternative aircraft concepts.

In a complete sense, the drag penalty resulting from longitudinal trim requirements may be defined as the aggregate of the following components:-

- (a) Profile drag of the tailplane (horizontal stabiliser) surface;
- (b) Fuselage-tail interference effect;
- (c) Induced drag due to trim force on tail surface;

(d) Increments in the profile and induced drags of the mainplane and fuselage resulting from the incidence adjustment necessary to compensate for the tail trimming force, and from the interference effects of the tail surface. For purposes of drag prediction it is more convenient to evaluate (a) and (b) above as part of the basic zero-lift drag of the aircraft since, at least to a first approximation, they are independent of trim requirements. The increment in drag due to trim, as given by the sum of (c) and (d) above may then be added to the untrimmed value. The loads on the tailplane can, of course, arise from changes in downwash or from variation in tailplane setting; further complications can arise with sidewash effects if the tailplane has anhedral.

An aircraft of conventional layout and static stability normally requires a down tail load to trim. The magnitude of this load is a function of the zero-lift pitching moment and location of the centre-of-gravity forward of the aerodynamic centre. In general, it can be said that reduction of the tail trim load will result in a reduction of the drag due to trim. Thus, these two major parameters should be kept as low as is possible within the imposed operational limitations, but the interaction between the wing and tail induced velocity fields complicates the issue. It is convenient to describe the variation of trim drag as a function either of centre-of-gravity position or the ratio of tail to total untrimmed lift coefficients which is dependent upon it. The further aft the tailplane location, the smaller is the trim down load and the size of the surface required to generate it. It follows immediately from this that items (a), (b) and (d) above will also be reduced. However, if the fuselage-tail interference penalty is interpreted in its widest sense, it is apparent that this could increase with aft movement of the tailplane due to the additional parasitic drag of a longer fuselage.

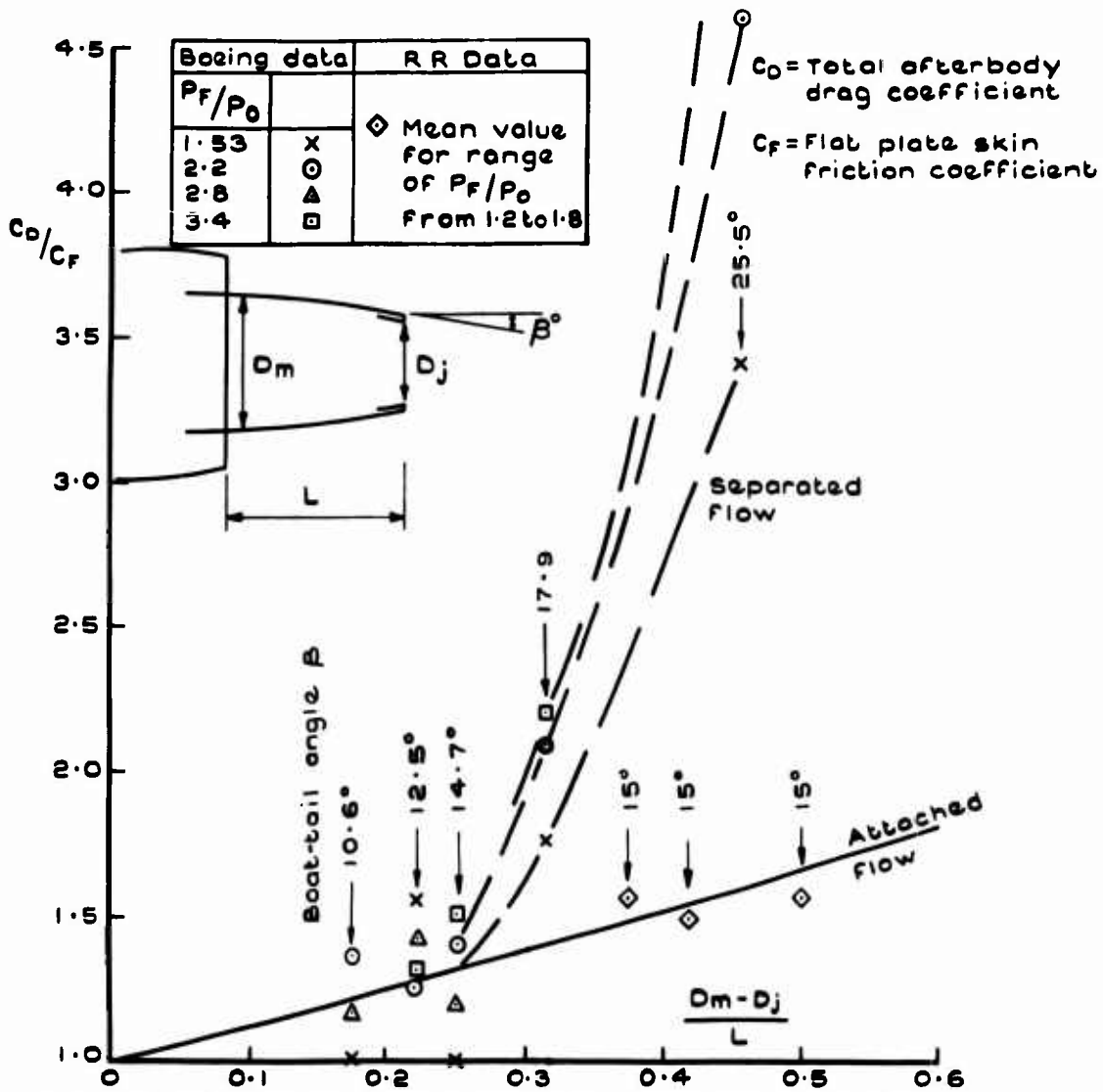


Fig.27 Afterbody drag correlation for gas generator

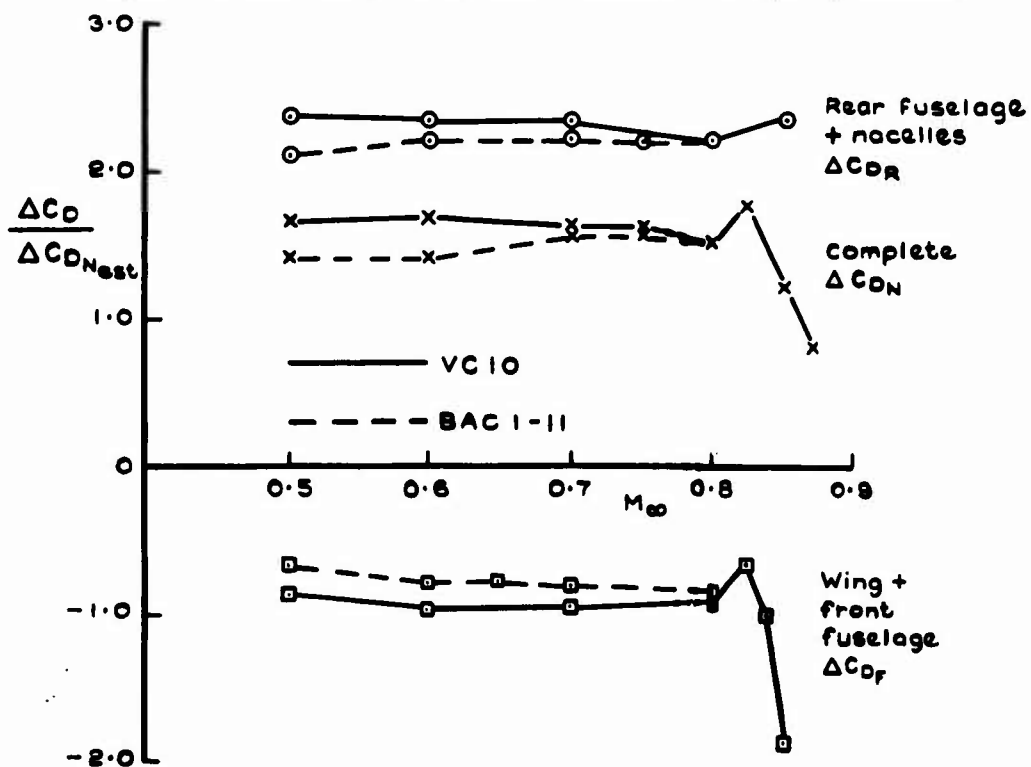


Fig.28 Breakdown of nacelle installation drag for VC10 and BAC 1-11

The case of the canard layout is somewhat different. Here, the foreplane load is normally up so that the trim requirement actually alleviates the wing lift required. This could result in an overall reduction of drag when the aircraft is trimmed but the situation is considerably complicated by the effect of the induced flow of the foreplane, which modifies the wing spanwise load distribution away from the ideal elliptic shape, thus introducing a drag penalty. The analysis can be particularly complex if the foreplane and wing are in close proximity, especially when both exhibit leading-edge vortex flows.

Drag due to trim can be of importance in two flight phases:-

(a) Cruise, where it is desirable to achieve the highest possible lift/drag ratio in a given flight condition for economic and performance reasons. Obviously, the greater the design range the more important is the effect of trim drag;

(b) Take-off and climb out, when it is important to have a high lift/drag ratio consistent with the relatively-high lift coefficient. This requirement is of particular significance when a steep climb associated with reduced engine power is necessitated by noise abatement procedures. Use of wing trailing-edge flaps aggravates the trim drag problem, because of the pitching moments associated with them.

### 3.7.2 Subsonic transport aircraft

An analysis of the trimmed cruise performance of a number of designs for subsonic transport aircraft is illustrated by Fig.29a. This shows the ratio of trim to total untrimmed drag as a function of the ratio of the tail and overall untrimmed lift coefficients. For the various designs, this latter ratio was found to be in the range of -0.1 to -0.5 according to centre-of-gravity position, with a corresponding trim drag of from about 9% to 11% of the untrimmed value. As can be seen from Fig.30a, the tailplane profile drag accounts for the majority so that the increment of drag due to trimming, relative to the untrimmed value, is only between 1 and 3% of the total aircraft drag.

The corresponding curve for the take-off condition is shown in Fig.29b. In the case of CTOL aircraft the range of lift coefficient ratio is typically from -0.1 to -0.3. This suggests that the trim drag penalty varies from about 4% at the aft centre-of-gravity position to 8% at its forward extremity. The contribution of the tailplane profile drag is much smaller than in cruise, as can be seen from Fig.30b. The particular case of an STOL design which employed externally-blown flaps<sup>86</sup> shows that trim drag is of considerable importance for this class of aircraft, due to the large values of tail lift coefficient required to trim out the very high nose-down pitching moment. At the forward centre-of-gravity location, the trim drag amounts to about 30% of the total.

### 3.7.3 Supersonic aircraft

Trim drag is of relatively-great importance in the cruise condition for a supersonic vehicle, not because it is necessarily large in itself but because of the need to develop as high a lift/drag ratio as possible in spite of wave drag. This has led to the suggestion of various different layouts for supersonic aircraft, the choice between them in any particular case<sup>87</sup> being considerably influenced by their trim drag characteristics.

Fig.31 shows the influence of centre-of-gravity position on the cruise trim drag of two tailless delta supersonic transports. One of these was an early design study<sup>88</sup> and the other is Concorde<sup>89</sup>. An interesting point is that, in both cases, there is a small range of centre-of-gravity position where the trim effect is marginally favourable. Advantage is taken of this in the production version of Concorde by using the fuel transfer system to locate the centre-of-gravity at the most favourable position. In the case of the earlier study, the fuel system was only designed to keep the centre-of-gravity within a given range and, in an adverse forward location, a trim drag penalty of some 9% had to be accepted. Some care is needed with the evaluation of take-off trim drag for this class of aircraft. The early design study aircraft was designed for take-off at the forward centre-of-gravity position, with nearly neutral stability and the trim drag close to zero. In general, the absence of wing flaps probably results in take-off trim drag being less critical than for a conventional layout.

The apparent trim drag advantage of the foreplane layout has resulted in the use of this configuration for a number of supersonic cruise vehicles. One example is the Blue Steel stand-off bomb<sup>90</sup>, with a canard surface area some 25% of the wing value. This was found to result in a cruise lift/drag ratio which is some 15% higher than that of a conventional tail layout. In addition there is a considerable reduction in manoeuvre response time. The penalty for this improved performance is that the roll damping characteristics are highly non-linear with incidence, which highlights one of the major difficulties associated with canards. In a design study<sup>88</sup> of a M = 3 airliner, a canard of some 10% of the wing area was used; it was kept small to minimise the foreplane vortex effects on both wing lift and lateral derivatives. The study shows a favourable trim effect of some 2% as the centre-of-gravity location tends towards the neutral point. This is only marginally better than the Concorde value and, in any case, is critically dependent upon the assumed foreplane downwash distribution.

Two specific examples of variable-sweep strike aircraft have been analysed. In the supersonic cruise case, with the wing fully swept, the trim drag penalty varied upwards from a minimum of about 4%, according to the centre-of-gravity location. The take-off trim drag characteristics are similar; there is a tendency for the trim drag to be a somewhat smaller percentage of the total drag.

## 3.8 Sweptwing aircraft at high lift

Based on a contribution by D.N. Foster, RAE.

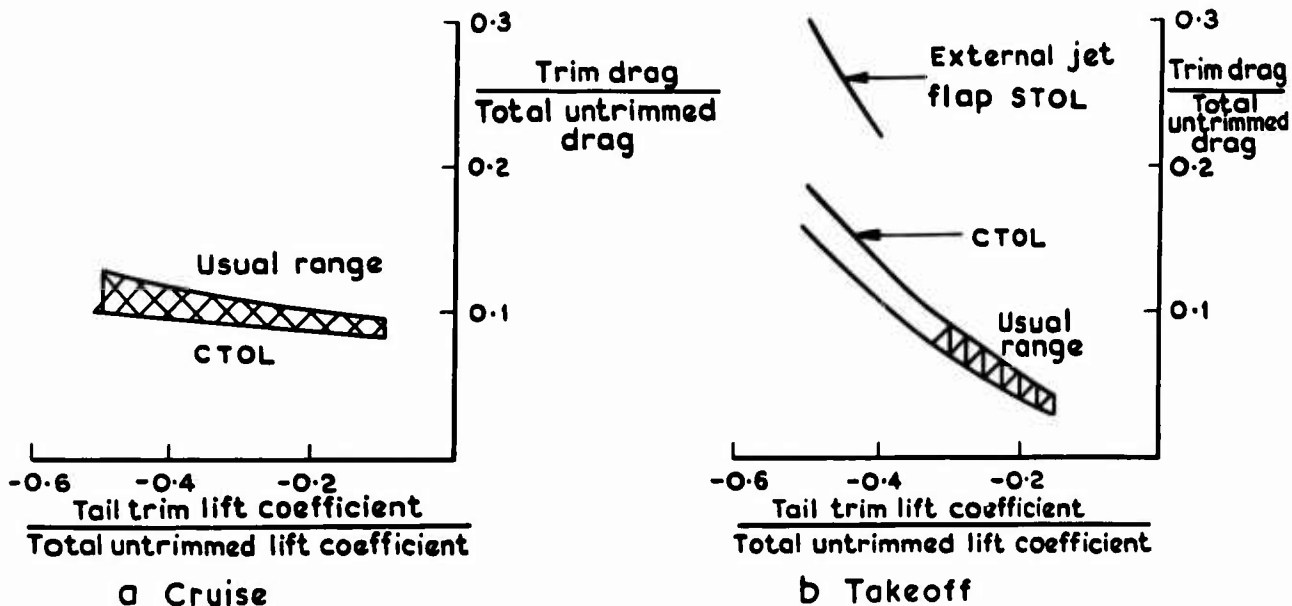


Fig. 29a & b Trim drag penalty for subsonic transports

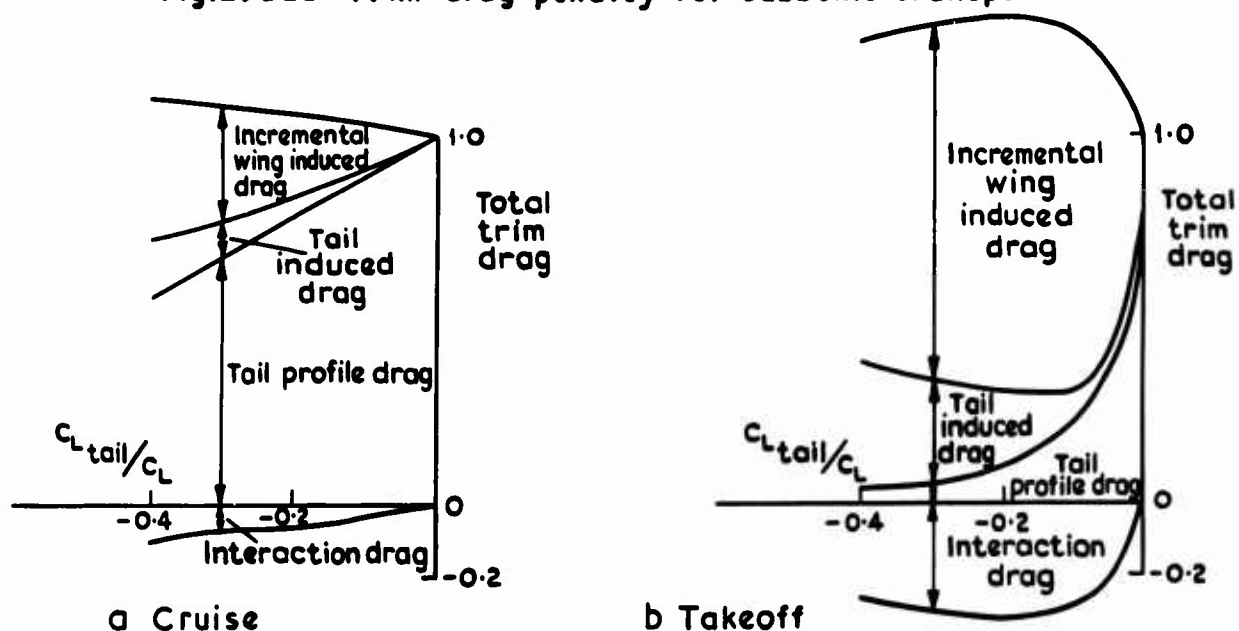


Fig. 30a & b Breakdown of trim drag for subsonic transports

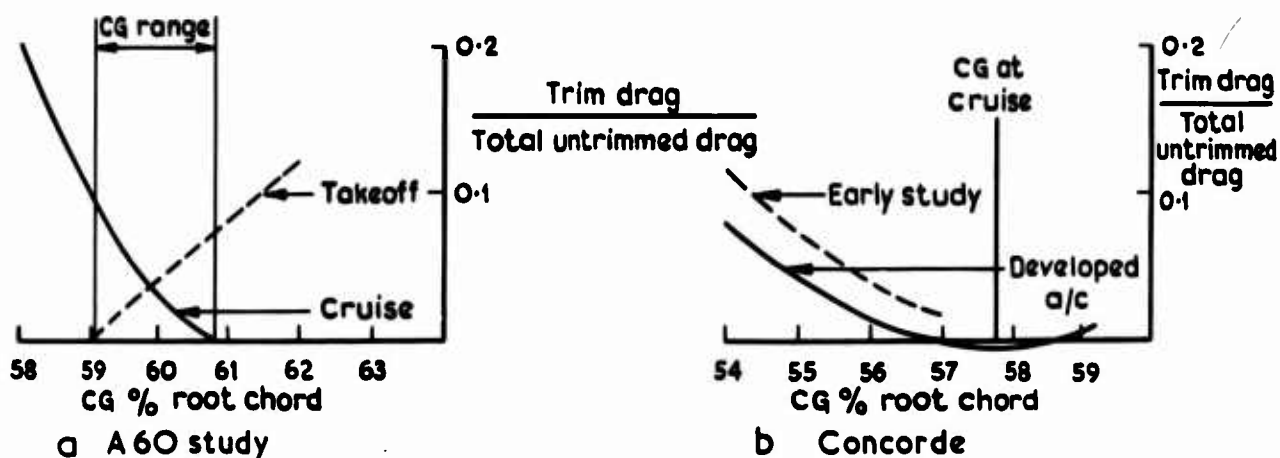


Fig. 31a & b Trim drag penalty for supersonic transports

### 3.8.1 Introduction

In order to achieve acceptable take-off and landing distances, the maximum lift coefficient of a sweptwing aircraft has to be increased substantially from the value which corresponds to the shape of the wing as designed for economical cruise. This increase is achieved by deflecting and, possibly, translating part or whole of the leading edge and trailing edge of the wing section. Whilst it is usually possible to allow changes at the leading edge across the whole of the wing span, often the changes at the trailing edge are restricted to the inner 70% to 80% of the wing span. Thus, under high-lift conditions the wing differs in section from that at cruise, has discontinuities in the position and inclination of the wing trailing edge across the span, and, for high-lift devices which extend the chord, has a different planform with discontinuities in chord. As a result, the drag characteristics of the wing in the high-lift configuration are very different from those which correspond to the cruise configuration.

In order to attempt to analyse and predict the drag under high-lift conditions, it can be assumed that the total drag is composed of three elements:-

$$C_D = C_{D_P} + C_{D_V} + C_{D_A} \quad (10)$$

where  $C_{D_P}$  is the weighted mean across the span of the drag coefficient corresponding to the local wing section shape in two-dimensional flow;  
 $C_{D_V}$  is the vortex drag coefficient of the wing;  
 $C_{D_A}$  is the drag coefficient due to the effect of the three-dimensional nature of the flow on the boundary-layer drag.

The extent to which each of these quantities may be predicted will now be discussed, and indications will be given of ways in which it is expected that the accuracy of these predictions might be increased.

### 3.8.2 Drag in two-dimensional flow

In principle, the drag coefficient of a high-lift wing section in two-dimensional flow could be obtained from a calculation of the development of the viscous layers around the wing section. Although it is now possible to predict theoretically the pressure distribution for highly-cambered and multiple wing sections<sup>91</sup>, the methods currently existing for the prediction of the development of the viscous layers, and in particular those applicable to multiple wing sections<sup>92</sup>, can be used only for certain regions of the flow, and cannot predict the complete development of the viscous layers. Improvements in the methods of predicting these complex flows, involving wake-boundary-layer interactions and regions of separated flow, possibly will entail a change from methods based on an integral approach to more detailed differential methods to allow a complete prediction method to be realised for this element of the total drag coefficient.

Maskell has shown that, if the perturbation velocities due to the deflection of a leading-edge or trailing-edge device are assumed to be linearly dependent on the lift increments due to the deflection of the device, and if the boundary layer is assumed to be turbulent from the leading edge of the wing section, then the drag coefficient may be written as:-

$$C_{D_P} = C_{D_0} \left\{ 1 + J_1 C_L^2 + J_2 C_{L_T}^2 + J_3 C_{L_L}^2 + 2J_{12} C_L C_{L_T} + 2J_{23} C_{L_T} C_{L_L} + 2J_{31} C_{L_L} C_L \right\} \quad (11)$$

where  $C_{D_0}$  is the drag coefficient of the thickness distribution only;  
 $C_{L_L}$  and  $C_{L_T}$  are the lift increments due to deflection of the leading-edge and trailing-edge devices;  
 $J_1, J_2, \dots$  are coefficients virtually independent of the magnitude of the associated lift components.

This expression can be simplified to:-

$$C_{D_P} = C_{D_{P_M}} + J_1 C_{D_0} \left( C_L - C_{L_{P_M}} \right)^2 \quad (12)$$

where  $C_{D_{P_M}}$  is the minimum value of  $C_{D_P}$  occurring at a lift coefficient  $C_{L_{P_M}}$ .

In order to check the validity of these expressions, an analysis was made of measurements, made under as near to two-dimensional conditions as possible, of the drag of a wing section with a slotted flap<sup>93</sup>. The wing section, shown in Fig.32, had no leading-edge device, and the slotted flap was tested at three flap deflections whilst keeping the flap-to-shroud gap and overlap constant. At each flap deflection a range of lift coefficients was defined for which the flow was assumed to be fully attached to the upper surface of the wing flap, with no separation bubble at the leading edge of the wing. The analysis involved the fitting of the experimental data to Eq. (12) and showing that, with  $J_1 C_{D_0}$

invariant with flap angle,  $C_{L_M}$  and  $C_{D_M}$  were linear and quadratic functions of flap lift respectively. The experimental data is compared in Fig.33 with drag polars based on the  $J$  coefficients determined as

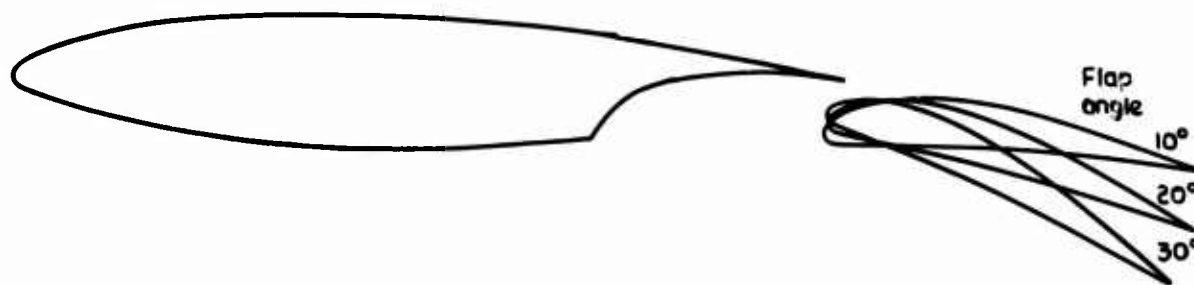


Fig.32 Aerofoil section showing flap positions

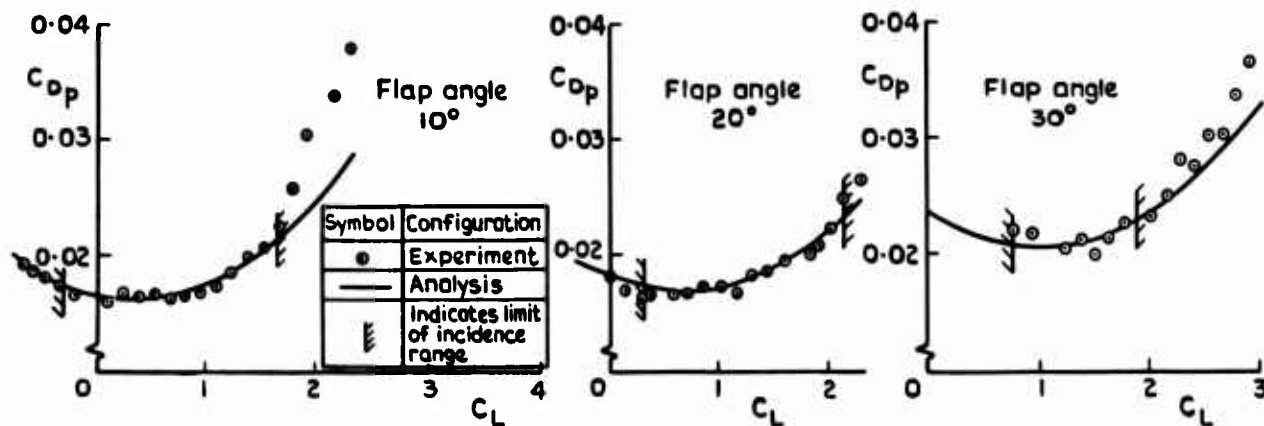


Fig.33 Correlation of drag measurements within Maskell framework

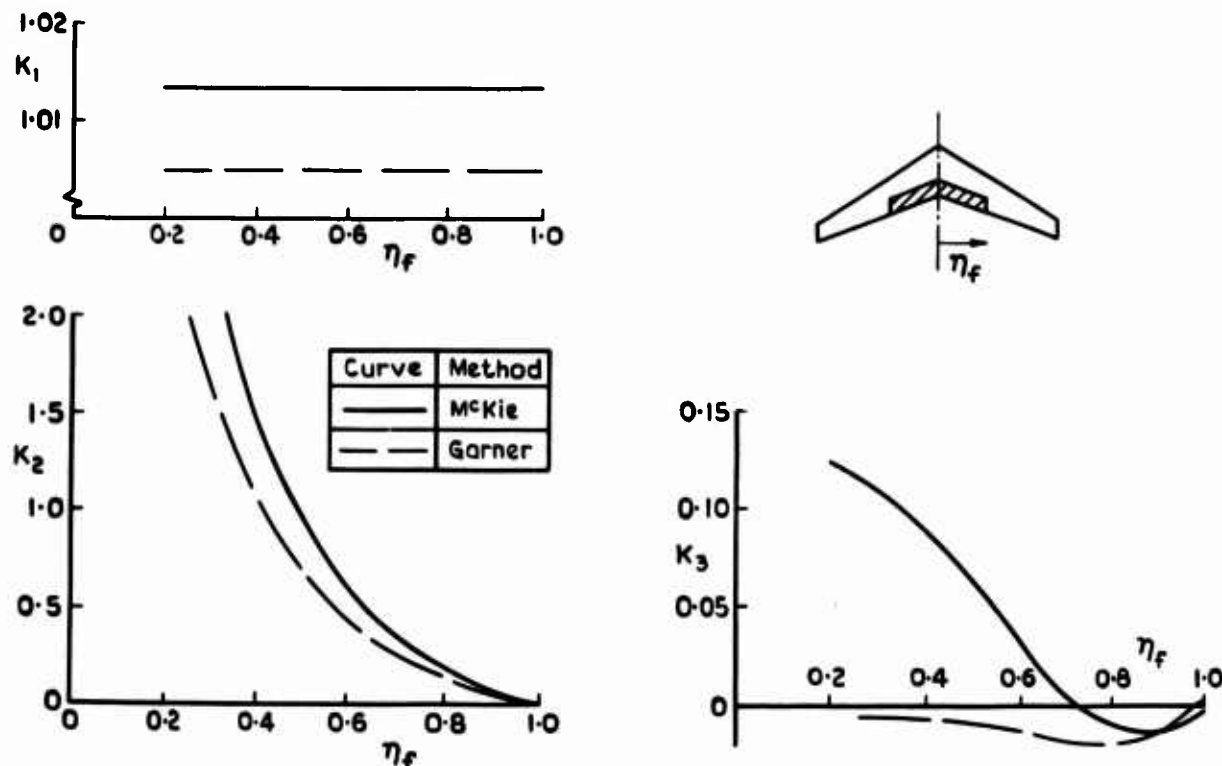


Fig.34 Comparison of coefficients of vortex drag equation predicted by two methods

638

a result of the fitting process. It appears that the experimental data can be adequately represented within the framework given by Maskell's theory.

Two lines of development stem from this conformity of the experimental data to the theory. One is to follow the development of the framework further to Maskell's derivation of the drag from the velocity perturbations, and to carry out the integrations as he has set them down. Holt<sup>94</sup> has done this, using velocity perturbations calculated using Maskew's method. The resulting drag polars underestimate the measured drag consistently, but part of the discrepancy can be attributed to the effect on the growth of the boundary layer of the transition bands which were added to the wing to ensure a turbulent boundary layer from close to the leading edge under all conditions. The second line of development is to repeat the empirical analysis with further good-quality data, and to see if the J coefficients so derived can be related to the model geometry. At present, development along this line must await the provision of the necessary data.

### 3.8.3 Vortex drag

The prediction of the vortex drag of a wing follows from the calculation of the load distribution on the wing. There is currently no well-proven method of calculating the load distribution across a sweptwing with highly deflected leading-edge and trailing-edge devices. As a consequence, the existing data sheets<sup>95</sup> from which vortex drag may be predicted are based on linearised theory<sup>96,97</sup>, with its implications of small deflections of the high-lift device (say, less than 15°) and a trailing-vortex sheet lying within the plane containing the wing chord. These data sheets concentrate on the effect of the deflection of a trailing-edge device. The vortex drag coefficient may then be expressed as:-

$$C_{D_V} = \frac{1}{\pi A} \left[ K_1 C_L^2 + K_2 C_{L_T}^2 + 2K_3 C_L C_{L_T} \right] \quad (13)$$

where A is the wing aspect ratio and K<sub>1</sub>, K<sub>2</sub> and K<sub>3</sub> are constants. However, the linear approximation itself is open to a number of interpretations. Fig.34 compares the values of the K coefficients as predicted by the method of McKie<sup>96,97</sup>, which is an extension of the method of calculating the spanwise load distribution on thin, sweptback wings due to Küchemann, with values predicted by the method of Garner<sup>98</sup>. Although the trends with the ratio of flap span to wing span are similar, the numerical values are appreciably different and this will lead to different values for the vortex drag. It is for this reason that it is recommended that the above data sheets<sup>95</sup> should be used only for the evaluation of limited excursions from reference conditions for which the total drag is known, and not to indicate the absolute magnitude of the vortex drag.

It is possible that an indication of which of the two methods incorporates the more accurate spanwise load distribution might be obtained from an extension of Sells'<sup>99</sup> method for an iterative calculation of the spanloading. Nevertheless, the final result will remain subject to the limitations of linearised theory, and a more general approach to the calculation of the vortex drag must await the development of a theory which will predict the loading on a sweptwing with highly deflected leading- and trailing-edge devices. This may, perhaps, come as an outcome of the work of Hess<sup>100</sup> in extending the well-known Douglas-Neuman method<sup>101</sup> for two-dimensional flows to three-dimensional flows.

### 3.8.4 Three-dimensional boundary-layer drag

One of the basic features of the flow over sweptback wings is that wing sections close to the root and tip carry chordwise loadings which are different from those corresponding to two-dimensional flow. Thus, even in the absence of crossflow in the boundary layer, the development of the boundary layer for these sections, and hence the drag they experience, would be different to that in two-dimensional flow. In addition, the transverse pressure gradients do result in marked crossflow in the boundary layer, and so the development of the viscous flow over a sweptwing is highly three-dimensional in nature. Thus, the total boundary-layer drag differs from the drag of the wing in two-dimensional flow, and the term C<sub>D\_A</sub> is intended to allow for this difference.

A calculation method to predict C<sub>D\_A</sub> would require not only the calculation of the complete load distribution over the wing, as discussed above, but also a method of calculating the three-dimensional development of the type of viscous flow which occurs under high-lift conditions. As was noted in section 3.8.2, the methods available for the calculations of the development of the viscous flow under two-dimensional conditions are not yet sufficiently well developed to allow the complete viscous flow to be calculated, and so extension to three-dimensional flow currently cannot be contemplated. However, when a method is available for two-dimensional flow, extension to three-dimensional conditions may be possible by following the principles used by Myring<sup>102</sup> to extend Head's entrainment method.

An alternative approach to the determination of the three-dimensional boundary-layer drag is to subtract from measurements of the total drag the appropriate values of the section drag and the vortex drag. Whilst it is possible to use values of the section drag measured under as near to two-dimensional flow conditions as possible, as was indicated in section 3.8.3, the values of the vortex drag will be subject to the limitations of linearised theory. As a result, values of the term C<sub>D\_A</sub> derived in this

manner may include a contribution due to the possible difference between the true vortex drag and its linearised approximation. McKie<sup>103</sup> has carried out this procedure for an unswept wing having plain trailing-edge flaps with boundary-layer control by blowing. Fig.35 shows the resulting breakdown of the drag for a part-span flap configuration. In this case the value of C<sub>D\_A</sub> changes sign as the lift

coefficient increases, and it contributes significantly to the total drag only at low values of the lift coefficient. However, the relatively small magnitude of the contribution and the fact that it changes sign may well be attributed to the lack of sweepback on the wing, as intuitive arguments would suggest

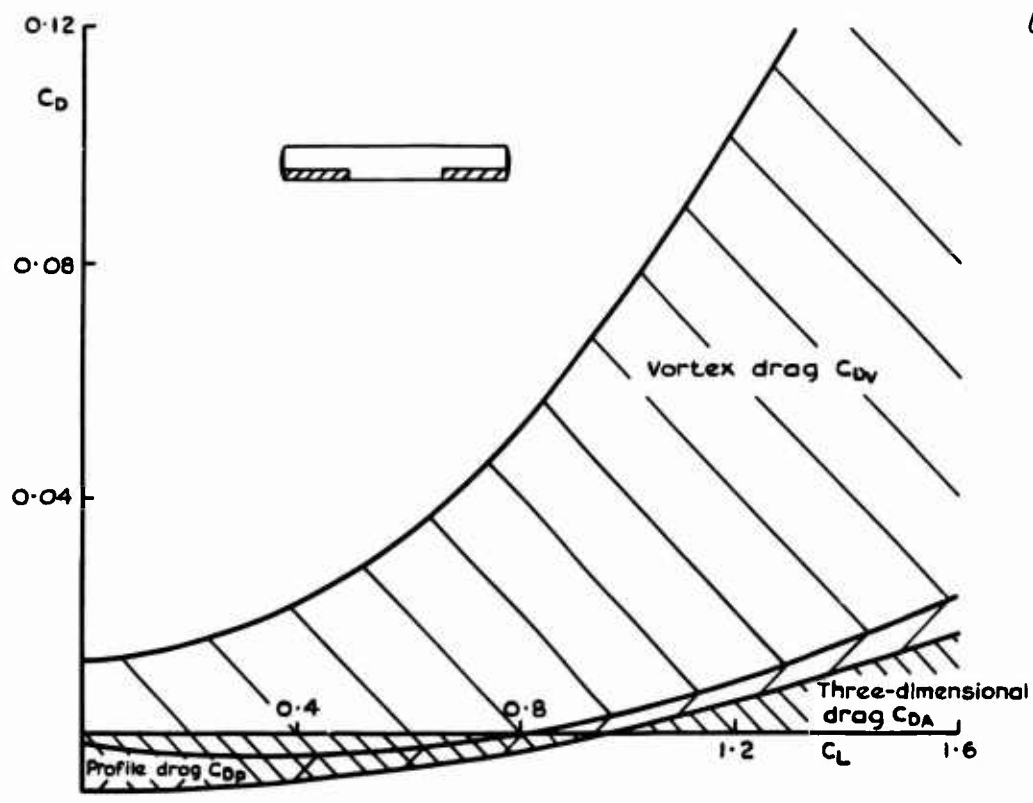


Fig.35 Composition of drag for unswept wing with deflected outboard flaps

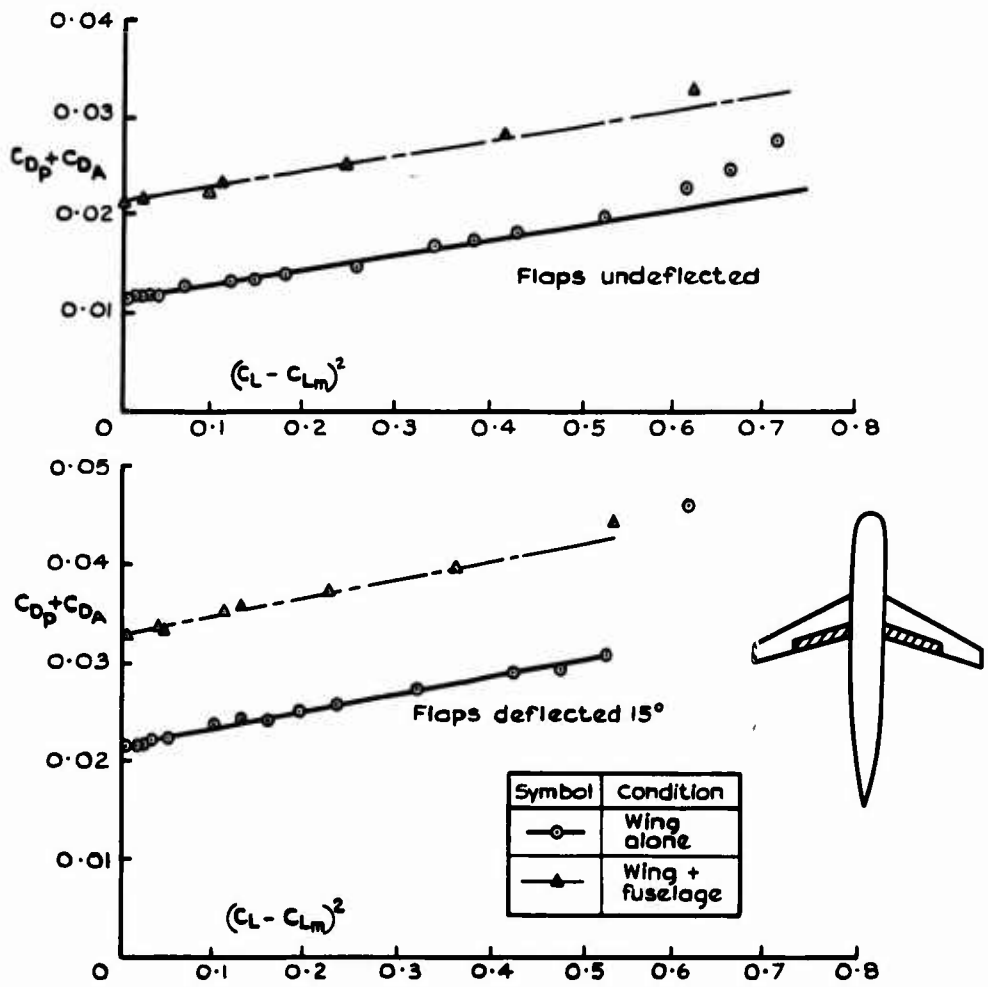


Fig.36 Boundary layer drag for isolated wing and wing-fuselage combination

6-40 that the contribution of the three-dimensional development of the boundary layer to the total drag would be a minimum for an unswept wing. McKie found that the values of the derived three-dimensional boundary-layer drag had a parabolic relationship with lift, as:-

$$C_{D_A} = C_{D_{A_M}} + K_A (C_L - C_{L_{A_M}})^2 \quad (14)$$

and that  $C_{D_{A_M}}$  (in this case negative) could be considered invariant with flap span, with  $C_{L_{A_M}}$  and  $K_A$  increasing linearly with flap span.

Apart from these indications, there is currently little guidance available on the magnitude of the three-dimensional boundary-layer drag, or on the factors which affect it. Further research is needed, perhaps along the lines of McKie's analysis, based on good quality data for sweptback wings with mechanical high-lift devices.

### 3.8.5 Other contributory factors

Whilst the thickness-chord ratio of the wing section has a direct effect on the contribution of the boundary layer to the total drag, calculations for the spanwise load distribution of wings with constant thickness-chord ratio across the span suggest that the  $K$  coefficients of the vortex drag (Eq. (13)) are unaffected by the thickness of the wing.

It has been shown experimentally<sup>104</sup> that the addition of a fuselage to an isolated wing with a flap having a central cut-out in its span results in a reduction of the drag by an amount dependent on the nature of the junction between the inboard end of the flap and the fuselage. The largest reduction was achieved when the flaps ended on the fuselage side, as would occur with a high wing, and the smallest reduction corresponded to a configuration with a physical gap between the inboard ends of the flaps, as would occur with a low wing. In addition to increasing the boundary-layer drag, the presence of the fuselage alters the spanwise load distribution, and thus the vortex drag. Whilst it is possible to calculate the spanwise load distribution on the wing-fuselage combination (again within the limitations of linearised theory) by making assumptions as to the shape of the load distribution across the fuselage, the method whereby the vortex drag of the combination may be found is, in general, not at all clear. Only in the special case of a circular fuselage mounted symmetrically on a thin wing can the vortex drag due to the loading across the wing and centre section of the fuselage be evaluated. Although this estimation ignores the drag due to the loading on the fore- and aft-parts of the fuselage, some comparative calculations were made<sup>105</sup> for a sweptwing configuration. The characteristics of the vortex-drag equation are tabulated.

Configuration	$K_1$	$K_2$	$K_3$
Isolated wing. Flap from centre line to 65% semispan.	1.012	0.486	-0.016
Isolated wing. Flap from 10% to 65% semispan.	1.012	0.796	-0.030
Wing-fuselage combination. Flap from fuselage side (10%) to 65% semispan.	1.038	0.486	+0.003

Values of the vortex drag calculated from these  $K$  coefficients have been subtracted from the measured total drag, and the resultant sum of  $C_{D_P}$  and  $C_{D_A}$  analysed, by a least-squares method, to show the parabolic relationship between this quantity and the lift coefficient (Fig.36). The effect of the addition of the fuselage, both for the unflapped wing and for the wing with a part-span flap deflected  $15^\circ$ , is to increase the boundary-layer contribution to the drag by a constant amount. The value of this increment is slightly different for the two conditions shown on Fig.36, but the mean value is in close agreement with the drag of the fuselage and its accompanying flat-plate fin, as estimated by standard ESDU Data Item methods. Thus, it would appear that the presence of a fuselage probably does not present any additional problems in the analysis of drag at high-lift conditions.

For wings with high-lift devices that extend the chord, the mechanisms which produce the extension usually become exposed in the high-lift configuration. The increase of wetted area results in a direct increase in the drag, but there may be further indirect effects. The wakes which are shed from the extension mechanisms of the leading-edge device pass close to the upper surface of the wing, and have been shown<sup>106</sup> to cause regions of separated flow to appear on the wing upper surface. The drag is then increased both by the separated flow regions and by the changes of vortex drag resulting from the non-uniform spanloading.

### 3.8.6 Concluding remarks

The estimation methods which exist for the prediction of the drag under high-lift conditions are not yet adequate to allow an accurate calculation for a specific aircraft configuration, but will only allow

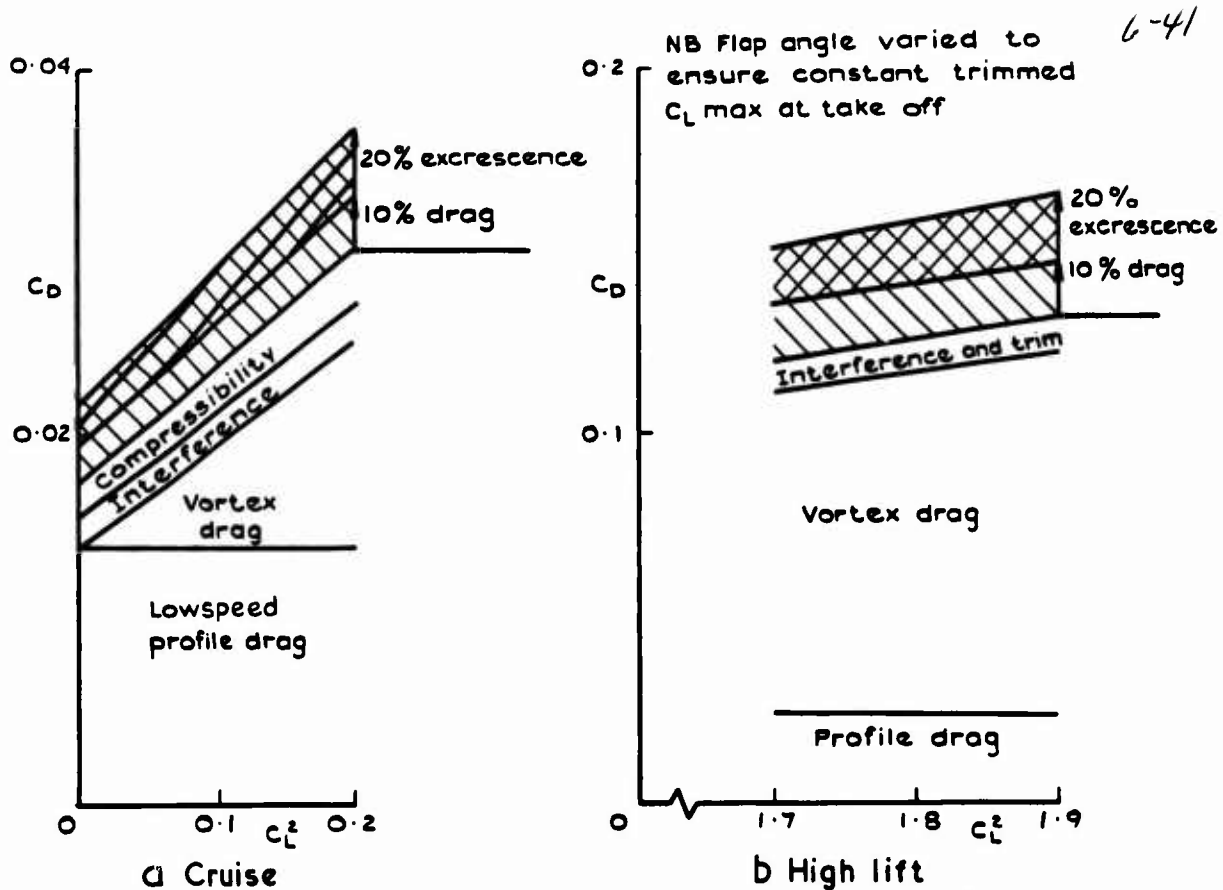


Fig.37 aab Typical contribution of excessances to drag at cruise and at high lift for a subsonic transport

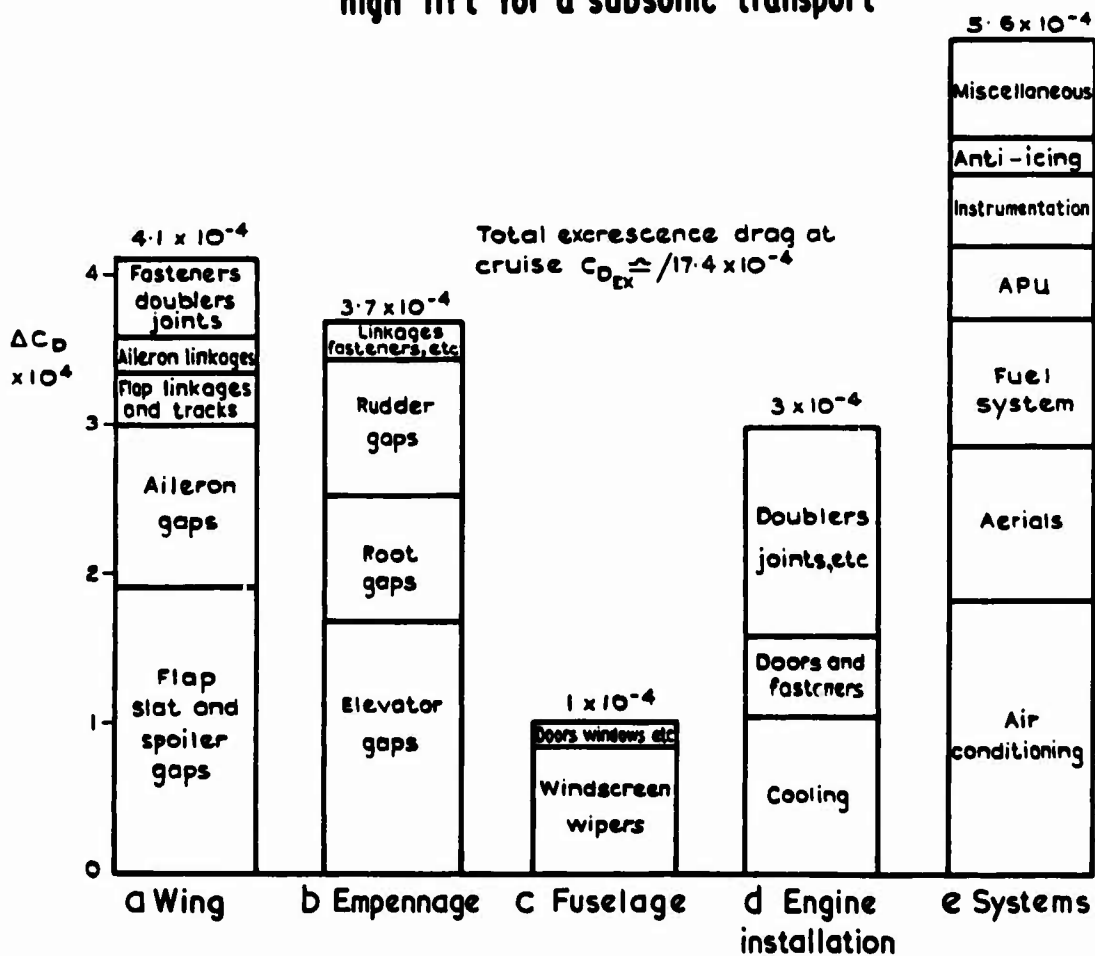


Fig.38 Typical breakdown of excessance drag at cruise

determination of the effect of small perturbations from a reference configuration for which the total drag is known. In order to improve the position, theoretical research will be required into calculation methods to predict the load distributions for wings with highly deflected high-lift devices and to predict the three-dimensional development of the types of viscous layers present under high-lift conditions. Such research will need to be supported by experiments designed to produce good quality data on the drag of sweptwings with high-lift devices and basic two-dimensional data.

### 3.9 Excrescence drag

Based on contributions by D.H. Tipper, HSA Hatfield, and by R.E. Keates and D.I. Husk, HSA Manchester.

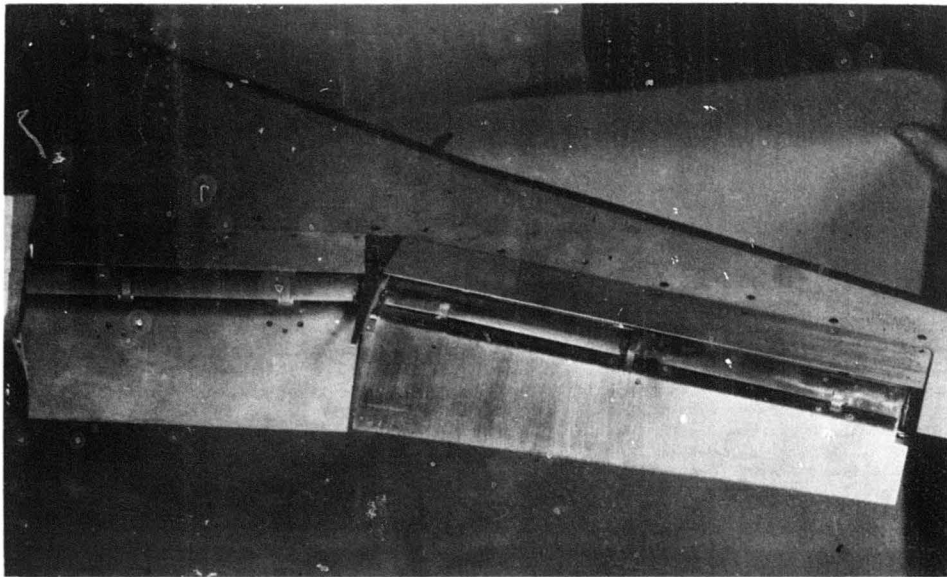
#### 3.9.1 Cruise configuration

Below the drag rise, about 80% of the drag of a modern subsonic jet transport can typically be accounted straightforwardly by estimates of profile and vortex drag, whilst 10% can be attributed to interference drag. The remaining 10% is due to what can be broadly described as 'excrescence' or parasitic drag, covering all drag sources that would not normally be represented on a wind-tunnel model (see Figs.37 and 38). Even if the contribution from excrescences is only 10%, the situation cannot be regarded as satisfactory. A main reason for this conclusion is that aircraft design involves compromises which can only be properly reached with adequate information, which is not yet available for excrescence drag. It should also be emphasised that 10% is a typical contribution and, whilst it will not have been achieved without considerable effort, it is possible to do a lot better if the incentives are strong enough; moreover, in a badly-controlled situation, it is undoubtedly possible to do a great deal worse. Further, what is right for Concorde, where the fuel fraction is high and the payload fraction low, is unlikely to be right for the HS 748, where these fractions are very different and the economic penalties of excrescence drag are relatively small. However, it should not be inferred that excrescence drag is unimportant for any class of aircraft; even a crop-sprayer will be able to carry an increased load and cost less to run if unnecessary drag is avoided. There is another important factor, namely predictability. It is obviously convenient for the aerodynamicist to insist on a minimum of excrescences, since their drag is both difficult and laborious to estimate. Further, he may well be committed to meet an early drag estimate that took inadequate account of the appropriate relationship between low drag on the one hand, and simpler engineering or lightness on the other.

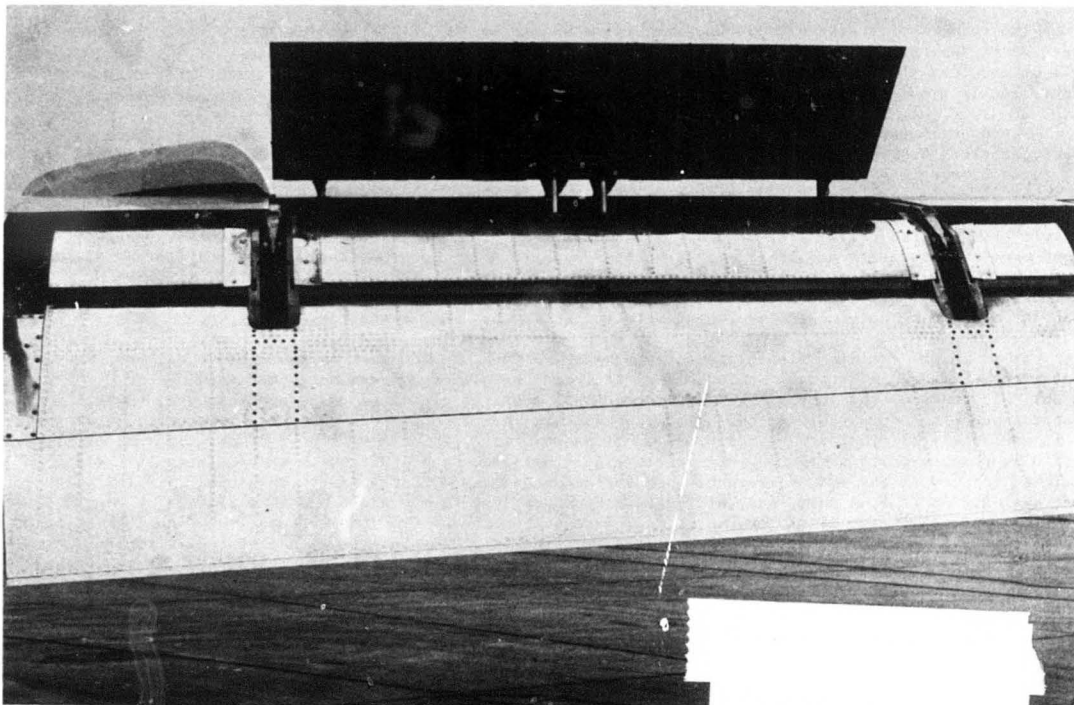
Some of the basic tools required for excrescence drag estimation are to be found in Hoerner<sup>107</sup>. His excellent volume catalogues and summarises the majority of the work done between 1930 and 1945 and, as a starting point, is quite indispensable. Since that date there has been very little attention paid to the subject, with one notable exception - the work carried out in the 8ft x 8ft wind tunnel at RAE, Bedford. This work<sup>108,109</sup> is particularly valuable in two quite different respects. It has provided systematic data on the effect of freestream Mach number (though not in the transonic range) and also introduced new thinking into the analysis of, and hence the application of, test data. However, it is when one comes to the problem of estimating excrescence drag in a real situation that the full deficiencies of the data and methods at our disposal become apparent. The whole range of shapes and situations can never be fully covered and the mutual interference between the excrescence and the flow field in which it finds itself has received little attention. The best that can be done at present is to take the drag of a, hopefully, equivalent object, as measured when mounted on a flat plate rig; to correct this for degree of immersion in the boundary layer; and to allow for the two-dimensional effect of local velocity and velocity gradient just outside the boundary layer, using the method of Nash and Bradshaw. If the excrescence is one of those tested at RAE, a rather more sophisticated evaluation of boundary-layer effects is now possible and the influence of Mach number will be better known than is usually the case. However, any estimates of three-dimensional effects, particularly those involving promotion of early separation or local shocks, and of the drag resulting from the complex internal flows that result from leakages through high-lift systems and flying controls are little more than speculative. Nevertheless, this approach is generally acceptable because, despite all these uncertainties, no one item is large, even in relation to merely the total excrescence drag and thus, as long as systematic errors can be avoided, the aggregate can be viewed with reasonable confidence (see Fig.38). Equally important is the insight gained into sources of drag and their relative importance and the consequent ability to improve drag standards and predictability.

The quality and quantity of the data available needs to be improved. However, it would be uneconomic and take too long to start again from the relatively-small beginnings represented by the recent RAE work. A major aim of future research should be improved understanding of the mechanism of excrescence drag. This ought to lead to a situation in which existing data of acceptable standard can be better applied and in which estimates for untested shapes can be made with reasonable confidence. With regard to the question of correction for different boundary-layer conditions, encouraging test results<sup>110</sup> have been obtained at RAE in confirmation of the Nash-Bradshaw theory<sup>111</sup> of drag magnification and other tests<sup>112</sup> are proceeding at Leicester University. More information is needed on the characteristics of three-dimensional boundary layers and the influence of three-dimensional conditions on excrescence drag. The effect of a very strong favourable pressure gradient, such as exists just downstream of the stagnation point, should be studied. There is also the question of the effect of the depth of immersion in the boundary layer on the drag of an excrescence. The concept of effective dynamic pressure (e.g. Weighardt<sup>113</sup> and Tillman<sup>114</sup>) works reasonably well for excrescence heights greater than about 10% of the boundary-layer thickness, but for smaller excrescences this approach appears to predict drag values which are too low and the RAE analysis using a Reynolds number based on friction velocity seems more satisfactory. Here again, further experimental study should be aimed at obtaining a better physical understanding.

There is a parallel need to establish specific drag data not covered by work already in existence or in hand. The main requirements are seen as being:-



(a) Model representation of aircraft high-lift system



(b) Aircraft high-lift system

Fig.39 Comparison between aircraft and model high-lift systems

(a) Rivets. The drag of rivets is probably the most important example of the analysis problems discussed earlier and thus, although there is a fair amount of data available, it is desirable to do a direct assessment of the types of rivet and other fasteners that are currently in use;

(b) Fairings. Over the years fairings have developed away from the part-bodies-of-revolution usually tested towards much more two-dimensional forms. There is, therefore, a need to explore the effects of aspect ratio and fineness ratio on drag;

(c) Inlets and outlets. Although there is a considerable body of data<sup>115</sup> on the drag of inlets and outlets it relates, in general, to poor designs and there is need for drag measurements on auxiliary inlets and outlets that are representative of good modern design practice. These tests should include internal performance assessment and be followed, if necessary, by development work;

(d) Gaps in flying surfaces. A limited body of data on the drag of control gaps exists including some recent work<sup>110</sup> by RAE. However, there appears to be little published data on the drag due to leading-edge slats in the closed position, or that resulting from the complex flow paths that exist around the flaps of a modern aircraft. Data on the effect of gap sealing and on different methods of sealing are also required.

### 3.9.2 High-lift configuration

Most of the foregoing comments on fluid dynamic aspects of excrescence effects in cruise conditions are equally applicable to the high-lift case. However, the division of drag between profile, vortex, interference and excrescence contributions is nowhere near as simple as in cruise. Moreover, the relative importance of various types of excrescences is different, particularly in view of the need to meet flap and slat engineering requirements. In order to define the importance of excrescence drag at high lift as a research topic, it is vital that contributions should be apportioned in roughly the right ratios. Allowing for the drag arising indirectly from the need to increase the flap deflection to maintain flap lift, direct and indirect excrescence drag typically can account for 10% of the aircraft drag for a modern developed high-lift system (see Fig.37b). This could well be doubled with an inferior system. The proportion of drag attributable to excrescences is thus similar to that at cruise. The effect can be striking because of the direct link through climb performance with take-off weight. Thus, a 10% reduction in  $D/W$  can allow the take-off climb-gradient limited weight to be increased by 8% for a typical case. In view of its importance, it is surprising that drag at high lift and excrescence drag have not attracted more general research effort. To be fair, this subject has received considerable attention in recent years in the design and development of specific projects. Further worthwhile improvements are certainly feasible and, as in the case of excrescence drag at cruise, there is a need to be able to choose with more certainty an optimised compromise between performance, weight, cost, and complexity.

The results of cruise excrescence drag tests should be applicable to high-lift flight, provided these cover appropriate ranges of Reynolds number, Mach number and pressure gradient. Lower Mach numbers will be involved than for cruise flight, Reynolds numbers are rather less, but pressure gradients significantly greater. Mach number effects are usually, but not always, small at subsonic speeds.

There are a few available tests at high lift of small excrescences of such sizes that their characteristics are considerably affected by the boundary-layer conditions. The data are mostly old and the types of roughness elements used were not representative of modern practice, so that the results are of doubtful applicability. However, they do show that, at least in some cases, there can be significant differences between excrescence effects at high and low lift. The fact that one has to refer back forty years<sup>116</sup> for limited evidence of such differences serves to illustrate the need for further research. Since pressure gradients are likely to be greater at high lift, Nash-Bradshaw type magnification factors should be larger than for low lift. However, it should still be possible to apply the existing procedures under high-lift conditions; recent developments in boundary-layer theory and computational procedures could be helpful in developing use of the Nash-Bradshaw technique.

It is in the field of flap-slat engineering that there are the most marked differences from the cruise case. There is virtually no published information, although there have been a number of unpublished tests to show the effects of flap tracks, linkages, fairings, slat brackets etc. Such features are often comparable in height to the boundary layer. Scale effects are, therefore, large, and it is inherently difficult to represent these items realistically on models of ordinary size and still obtain reasonably-valid results. This problem is illustrated by Fig.39, which shows a high-lift model designed for use in the RAE Bedford 8ft pressurised tunnel in comparison with the actual aircraft high-lift system. Apart from this, many of the specific test results may not be made available for general use. Further, there are likely to be too many inconsistencies between the various investigations to make a general analysis practicable. Since the drag increments of all such items on a typical aircraft are far from negligible in total, there is a case for a further series of self-consistent systematic investigations. In this case, tunnel-wall tests do not seem to form the best approach. It would seem better to test such items on two-dimensional aerofoil sections, which could be swept if required. It should be possible to achieve sufficiently-high values of the Reynolds number in a low-speed tunnel of moderate size. Pilot tests could be made for representative cases to determine the minimum Reynolds number at which tests should be run. There is the possibility of substantial compressibility effects occurring in flows through slots, making simulation of the correct flight Mach number important, and the models needs to be large enough to allow accurate reproduction of detail as well as to provide a minimum Reynolds number. Flow field tests would also be useful, particularly as regards the assessment of wake effects due to the supports for leading-edge devices.

### 3.9.3 Concluding remarks

Excrescence drag is a topic that has received scant attention in the past twenty-five years. Renewed interest, at least in the UK, is leading to a better situation, based on the fundamental work of Winter,

et al. at RAE. However, a great deal remains to be done both on the application of two-dimensional data to real situations and on the establishment of drag data and design principles for those excrescences which repeatedly occur.

6-45

#### 4 ON THE MEASUREMENT OF DRAG IN WIND-TUNNEL EXPERIMENTS

Based on a contribution by C R. Taylor, RAE.

##### 4.1 General requirements and experimental method

Exact standards are required, either for validation of theoretical methods of drag prediction or in the support of specific projects. Model drag measurements generally should be made at the correct Mach number in an experiment performed to standards which allow the basic accuracy to remain adequate after extrapolation to full-scale conditions. The accuracy which is desirable<sup>17</sup> is roughly 1 drag count ( $C_D = 0.0001$ ) for subsonic cruise conditions or  $\frac{1}{2}$  drag count ( $C_D = 0.00005$ ) for supersonic cruise conditions, although higher resolution may be needed to interpret variations with Reynolds number, to understand the effects of small changes of configuration, and to establish sting interference. The achievement of such accuracies implies balance resolutions and repeatability of better than 0.001 to 0.002 in normal force coefficient, 0.00005 to 0.0001 in axial force, and 0.01 deg in incidence. The special problems of tunnel testing at high-lift conditions are not considered in this paper.

There are several designs of internal balance which offer adequate sensitivities but temperature effects seriously degrade the repeatability and thus the accuracy of the measurements. It is very difficult to simulate in the laboratory the changes in balance environment which may occur during model tests. Further, the current methods for temperature compensation are, at best, unsophisticated. At present, the inaccuracies due to temperature effects should be minimised by a combination of careful balance design (to ensure good heat flow from one section of the balance to another) and by suitable control of the balance environment (for example, by control of tunnel total temperature). Variations of humidity of the air surrounding the balance can also prove a serious source of error. Suitable remedies entail control of the tunnel humidity, maintenance of the power supply to the strain-gauge bridges when not in use, and storage of the balance under conditions equivalent to those prevailing in the tunnel. In addition, the gauges may be waterproofed, using proprietary dopes.

The incidence requirement is also exacting; there are wind tunnels having quadrants with excessive backlash or insufficient angular resolution, mounted on support systems lacking in rigidity. In such cases, recourse is made to high-resolution accelerometers; depending on the steadiness of the tunnel flow and the design of the quadrant, three or perhaps more pitch readings are taken at each datum in the hope that the mean value will reach the desired accuracy. In the USA, tuned dampers have been installed in tunnel models to reduce the vibrations due to flow unsteadiness. In some transonic tunnels, where the model is mounted from a long sting, the amplitude of model oscillation may be sufficient to cause longitudinal (centrifugal) acceleration forces equivalent to several drag counts. High-resolution accelerometers are also prone to most of the problems associated with strain-gauge balances.

Measured angles of pitch must be corrected for flow angularity, which is best done by testing the model erect and inverted over the full incidence range; provided the flow angularity is small enough, the mean of the erect and inverted readings can be regarded as corrected data<sup>18</sup>. However, for large models, the measurements will also be affected by the streamwise curvature of the flow (fairly common in supersonic tunnels) and by spanwise variations in the flow angularity. In such circumstances, the mean drag will not be the value appropriate to a uniform flow. Flow angularity and swirl effects seriously limit the accuracy which can be achieved in many tunnels.

The flow in supersonic tunnels is usually very steady and the main problems usually are connected with temperature and flow angularity effects. In subsonic and transonic tunnels, model oscillations are an additional problem, although matters can be significantly improved if the tunnel flow is choked in the diffuser and a good incidence quadrant is provided.

##### 4.2 Extrapolation

It is necessary to allow for:-

- (a) changes of Reynolds number, transition position, surface condition and heat transfer;
- (b) the effects of tunnel constraint, non-uniformity of tunnel flow, aeroelastic distortion of the model, and the actual shape of the aircraft under flight conditions;
- (c) excrescences not represented on the model, internal flows, changes of intake flow and effects of the jet.

In respect of the first group of effects, extrapolation to full-scale requires a detailed knowledge of the boundary layer on the tunnel model and the aircraft. Model tests at low Reynolds number should include careful assessment of test Reynolds number transition-trip effects. Trip drag is deduced from measurements with different trip heights or by variation of bandwidth, necessitating good accuracy and repeatability of drag measurement and (for tests with variable trip height) careful control of trip size and particle density. The larger trips may well affect the boundary-layer development downstream of the trip, leading to changes in lift at constant incidence and, possibly, non-linear variations in drag with trip height. Even if full-scale Reynolds numbers can be achieved, allowance may be necessary for surface condition and heat transfer, each of which can affect the boundary-layer development; consideration may also need to be given to the freestream turbulence level.

The second group of corrections all interact on model design. For example, it is obviously better to test a model which fully represents the aircraft shape at a selected condition where drag is important,

6-45

6-46  
than test a model faithfully representing the aircraft jig-shape. Careful consideration must be given to model manufacturing accuracy standards, which often are demanding. In certain cases, it is possible to arrange that the effects of aeroelastic distortion and tunnel constraint on the effective shape are allowed for at one test condition, thus reducing the size of the corrections which are involved. The model support system also limits the extent to which the model represents the aircraft, so that correction is needed for the change in geometry and the forward effect of the sting. Such corrections are usually determined by supplementary experiments for which various techniques have been devised<sup>19</sup>. Longitudinal pressure gradients in the tunnel-empty flow have a powerful effect on drag measurements; special calibration techniques are necessary to ensure corrections of adequate accuracy.

Tunnel interference poses a range of problems for the user of ventilated-wall tunnels, principally because one does not know for sure the effective porosity of the tunnel walls. A common method for deducing the effective overall blockage is to compare data for open and closed wall tests in the same tunnel, using a reference model. The solid-wall results, suitably corrected, are taken as correct and an effective porosity, based on the classical corrections<sup>19</sup> for vanishingly-small models, is deduced. These corrections, and the inferred effective porosity, have then to be assumed to apply for higher Mach numbers at which the model could not be tested with solid tunnel walls. It is very doubtful whether the desired accuracy of 0.0001 is attainable in the transonic speed range at present. It can be argued that the attainment of the required accuracy for subsonic conditions necessitates a closed-wall tunnel with a choked diffuser and a stiff sting support, as provided by the RAE Bedford 8ft tunnel. In such a tunnel, the maximum Mach number will be limited by the non-uniformity of the blockage corrections. Supposing the latter are limited to ensure that the variation of Mach number does not exceed 0.003 over the model, then the probable errors are less than would apply with a ventilated-wall tunnel of the same size.

Turning now to the third group of corrections, we note that very few aircraft excrescences can be represented on the model (see section 3.9). Those that are expected to affect the general flow should, of course, be fitted; these include wing fences, flap-track fairings, and large control gaps. It is advisable to be able to remove such excrescences so as to measure their drag. Internal flows provide another big problem. Since the intake is invariably upstream of the exit, and intake spillage effects can interact on surfaces downstream of the intake, it is generally better to allow some distortion of the exit geometry to achieve more representative intake flows, rather than the reverse. Subsonic testing presents more difficulties than supersonic. For instance, in tests of the Super VC 10, a 50% increase in exit area of the free-flow nacelles was barely enough to increase the intake flow to the point where spillage drag is largely independent of the intake flow, the aircraft design aim. There appears to be no really effective way of getting the correct intake flow for nacelles of high-bypass-ratio fans, other than by distorting the gas-generator cowl, or omitting it altogether. The accuracies involved tend to preclude the use of blown or powered nacelles, although it must be admitted that there are some who have convinced themselves that such devices can be used to obtain accurate measurements of nacelle interference drag, given sufficient attention to flow calibration problems.

The measurement of internal drag deserves careful thought, commencing at the stage of model design. For short ducts in subsonic tests, it is worthwhile designing a smoothly-contracting duct that will maintain a laminar boundary layer through the exit and ensure a fairly-uniform core to the flow there. The core Mach number can then be measured by static pressure tappings at the exit and one-dimensional flow equations used to estimate the velocity distribution along the duct sufficiently accurately to estimate the boundary layer at the exit. The isentropic and friction components of the internal drag can then be calculated. Comparable accuracy can be attained at supersonic speeds<sup>20</sup> if the intake shock is suitably located. Otherwise, recourse to comprehensive surveys of the exit flow is necessary, but these seem unlikely to provide estimates of internal drag which are accurate enough to justify detailed drag analyses. Supplementary experiments are needed to measure the effects of intake spillage and of jet effects on the afterbody. It is essential that the configurations tested include one which represents closely the wind-tunnel model configuration used for the overall drag measurements.

#### 4.3 Concluding remarks

Accurate and meaningful measurements of model drag and extrapolations to full-scale are certainly difficult and require careful planning with attention to detail. Often, a special model and balance will be necessary, together with a set of subsidiary experiments. Elevated standards of measurement and technique are essential. Many, if not most, existing tunnels are unsuitable, merely because the quality of flow is inadequate. In particular, the present generation of transonic tunnels tend to suffer from unsteady flows, and the knowledge of tunnel interference is not yet such as to allow calculation of the effects on drag of non-uniform interference. Such problems are exacerbated by the current tendency to use models which are rather too big for the tunnel. The biggest single problem is that of representing the engine flows in a way that allows the drag to be analysed and synthesised from a related series of model tests.

Unfortunately, there exists a degree of complacency about the general accuracy achieved in model drag measurements. Possibly, this arises partly from the difficulties involved in effecting convincing correlations between tunnel and flight data. This situation may well be aggravated by the fact that aircraft drag measurements are seldom aimed at resolving the main problems inherent in the extrapolation of model results to full-scale conditions. Elevated standards of test design, execution and analysis are certainly essential if model test data are to be of maximum value in drag modelling.

### 5 ON THE MEASUREMENT OF DRAG IN FLIGHT

Based on a contribution by Dr. C.S. Barnes, RAE.

#### 5.1 General considerations

The present conference is a tacit admission that much remains to be done to ensure that drag prediction methods achieve sufficient accuracy in major areas. To obtain adequate validation of such methods, including those used to extrapolate model-scale results, it is essential to have a body of

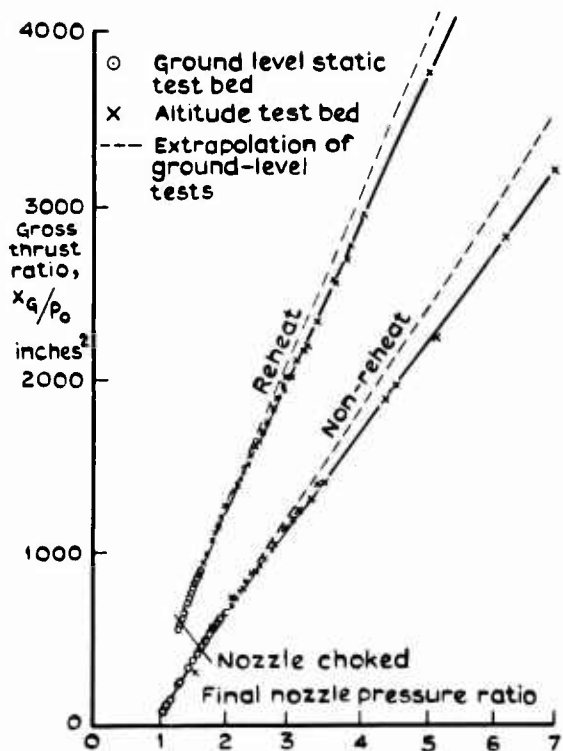


Fig.40 Comparison between extrapolated ground-level static test bed results and altitude test cell data

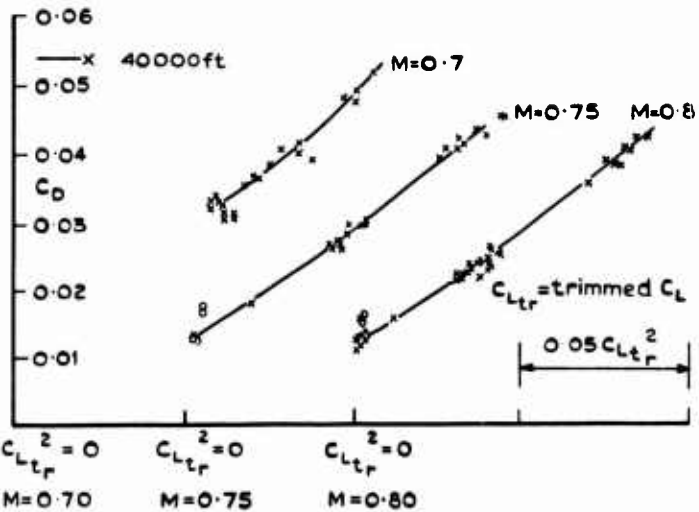


Fig.42 Typical trimmed drag data from quasi-steady flight tests on Fairey Delta 2

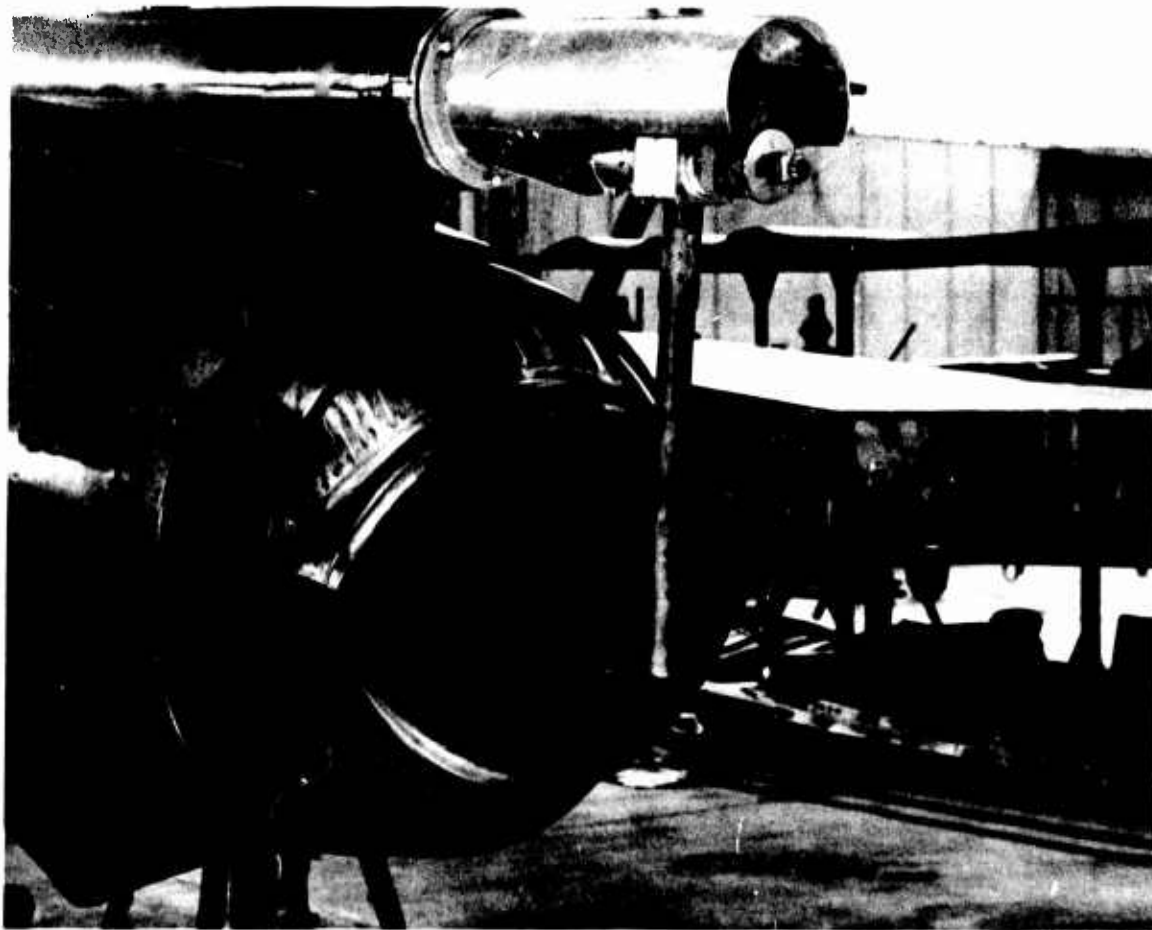


Fig.41 Swinging probe installed in the Fairey Delta 2

high-quality data on aircraft drag, both accurate and reliable. The overall systematic error in derived drag needs to be limited to about 1%. The aircraft engine and atmospheric ambient conditions must be well-defined; the physical condition of the aircraft at the time of test is of particular importance and should be determined in some detail.

Most flight measurements of drag are made by the airframe manufacturers during performance tests on prototype and development aircraft. Such tests are made at a time when commercial pressures dictate the need for rapid results. Furthermore, the accurate measurement of drag will not be the main aim of such flight testing. This is particularly so for transport aircraft, where the need to demonstrate overall engine/airframe performance as it affects, for example, field length, climb gradient, or specific range at cruise is of paramount importance. Drag measurement is commonly regarded as a diagnostic tool, necessary in an imperfect aeronautical world because the prototype aircraft will rarely reach its predicted performance without some modification. Moreover, the measurement of drag is necessarily linked to the measurement of engine thrust; this is inherently difficult, but even more so in the situation likely to pertain during tests of a new aircraft, where the engine is often itself at the development stage.

It follows that manufacturers' development tests are unlikely to yield drag data of sufficient quality to enable a confident assessment of prediction methods and of the usefulness of wind-tunnel tests. A notable exception, however, has been the Concorde flight test programme, which has yielded data of the highest quality. The operating economics which follow from the inevitably-smaller payload fraction of a supersonic transport placed a particular premium upon accurate drag measurements in this case, especially as the prototype aircraft differ in significant respect from the production model. However, even here the measurements were necessarily concentrated on those areas of particular commercial importance, such as supersonic cruise, so that, for instance, the range of lift coefficient over which drag has been measured is small.

Thus, if high quality and comprehensive aircraft drag data are to be measured in flight, it would appear essential that the exercise must involve a research programme on a well-developed airframe/engine combination, directly under the control of a research establishment or by an aircraft company under contract. In general, it cannot be expected that drag measurements alone will suffice. Indeed, it will normally be necessary to measure other parameters to achieve adequate understanding of the sources and reasons for the measured drag. Typically, this may involve extensive pressure plotting of the wing and of boat-tail and base zones. Also, structural distortion in flight may need to be determined so that wind-tunnel results can be extrapolated to the correct in-flight shape.

The scale of such an exercise should be recognised from the outset, and adequate support arranged both in respect of manpower and facilities. Not least amongst the needs is accurate assignation of thrust, which will be briefly considered.

## 5.2 Thrust determination

The accurate measurement of thrust in flight remains the most difficult part of any drag measurement exercise, and is a problem which has not yet been properly solved. The best-documented and most extensive British work in this field<sup>121</sup> is that on the Avon engine fitted to the Fairey Delta 2 supersonic research aircraft. Following extensive engine calibrations in both sea-level and altitude test-beds at NGTE, several methods of thrust determination were evaluated in flight. The results from this exercise demonstrated that altitude test-cell calibrations are needed to avoid possibly misleading extrapolations of sea-level test-bed data to representative flight jet pressure ratios (Fig.40). The need for altitude-cell calibrations is now generally accepted if high quality thrust measurements are to be made. Preferably, flight instrumentation should be included in the test-cell rig.

Even with the use of the altitude cell, uncertainties remain. The flow distribution associated with the aircraft intake is not represented normally; this may affect thrust calibrations in, or even downstream of, the engine. Further research on this aspect is needed. Again, the external flow at the nozzle is absent, and its effect on nozzle performance must be allowed for by use of model-scale tests. The increasing complexity of modern engine installations makes calculation of thrust based on internal measurements of pressure and temperature etc., so-called gas-generator methods, increasingly difficult<sup>122</sup>. Experience on Concorde confirms, however, that high-quality thrust measurements on complex installations can be made providing a sufficiently detailed attack is made on the problem. Considerable effort is being expended by the UK aero-engine and airframe companies in collaboration with the research establishments in a joint appraisal by the MIDAP Study Group on Thrust and Drag Measurement in Flight. General guide-lines covering the major aspects involved in thrust measurement in flight are now in preparation.

As a further attack on the problem, RAE and NGTE are beginning a joint programme to design, manufacture and test a rake which will traverse across the propulsive jet immediately downstream of the nozzle exit. In principle, net thrust can be deduced from temperature and pressure distributions in the jet, with only minor corrections for engine bleeds. If this ideal can be realised in practice, the traversing rake offers a considerable simplification in the measurement of thrust, particularly under reheat conditions on aircraft with variable nozzles where the measurement of nozzle area is extremely difficult. However, numerous technical difficulties result from the hostile environment in the jet. Construction of a rake capable of remaining within the jet long enough to minimise the effect of the time constants of the sensors, particularly the thermocouples, is difficult. The traversing rake is not a new concept. An early design was tried in the tests<sup>121</sup> on the Fairey Delta 2 (Fig.41) with a measure of success. Considerable work<sup>123</sup> has been done in the USA, including detailed traverses behind turbo-jet and bypass engines, although difficulties were experienced in the latter case. NGTE have made extensive studies on a rake similar to that used in the American research and identified areas where improvement is feasible by use of a stiffer rake, improved sensors and more detailed traverses. The joint NGTE and RAE programme has been started as a result of these studies, with a view to testing the new rake design behind an engine in the coming year.

6-49  
It is not to be expected that the MIDAP deliberations and the planned research on the rake will solve the problem of thrust measurement in flight. However, it is felt that identification of the particular approach most likely to succeed for a particular powerplant installation should be assisted materially by such an approach.

### 5.3 Drag determination

In order to measure drag in flight, having overcome the major problem of thrust measurement, one is left with determining the thrust minus drag term. The classical technique, that of steady, stabilised levels, aims to reduce this term to as near zero as possible. Normally, only minimal corrections for altitude and airspeed changes are required to time-averaged data obtained during intervals of the order of a minute. This technique is extremely demanding on flight test time and is in the main limited to the range of conditions attainable in straight-and-level flight. Not only is it expensive in terms of time and money, but also it is restrictive in that the range of lift coefficients at which drag can be measured is relatively small at a given Mach number. Limitation to a level flight condition is most undesirable in a research exercise aimed at the production of data for validation purposes. In particular, measurements close to zero-lift conditions are needed to define the minimum drag with adequate accuracy.

It is now more generally accepted that quasi-steady techniques, where the aircraft acceleration is recorded continuously during relatively-slow changes of aircraft speed, can yield sufficiently high quality drag measurements. Such techniques allow at least an order of magnitude increase in the amount of data that can be obtained in a given time, compared with the stabilised-levels method. A disadvantage could be that drag measurements based on a series of readings at single instants of time might be expected to show rather more scatter than the same number of measurements, each obtained by averaging over a period of time, as in stabilised levels. However, the great increase in number of data points obtained with the quasi-steady techniques allows a mean line to be drawn with great confidence. Sufficient computing capacity must be provided to process the necessarily large body of data in a time-scale consistent with the need for corrected results to guide the flight programme.

A small sample of the data obtained in the RAE tests on the Fairey Delta 2 aircraft is shown in Fig.42; more extensive results can be found in the full report<sup>124</sup>. The data at high  $C_L$  were obtained during turns in which quite high values of normal acceleration were present. The scatter of the data, most of which was obtained under quasi-steady conditions, is seen to be small; no significant differences were found relative to data obtained during steady levels. The Fairey Delta 2 tests were made at a time when instrumentation and recording techniques were less well-developed than now, and much improved accuracy is now possible.

Further evidence justifying the use of quasi-steady techniques has recently been forthcoming from tests on a Buccaneer aircraft, with a variety of external stores, which have been made by Hawker-Siddeley Aviation Ltd. (see Fig.10). These tests form part of an extensive research programme to derive prediction methods for the drag of store installations. Preliminary analysis shows no significant difference between results obtained using the two techniques.

Two possible criticisms of the quasi-steady technique should be mentioned. Firstly, part of the scatter on drag measurements is related to the difficulty of measuring incidence precisely; incidence is needed to resolve the components of aircraft acceleration, as measured by aircraft-mounted accelerometers, along directions along and normal to the flight path. However, for the purposes of comparison with predictions and tunnel results, there is no fundamental reason why accelerometer axes should not be used.

The second objection is that since quasi-steady techniques involve continuous, albeit slow, changes in flight conditions, the engine conditions are not sufficiently stable to justify the use of thrust calibrations derived in an altitude test-cell under stable conditions. Experience with the Fairey Delta 2 and the Buccaneer does not suggest that this is a problem, although further comparative tests with different rates of change of flight conditions would be helpful, possibly using the rake traverse technique if the jet can be spanned in a time sufficiently short that the change of flight conditions involved can be ignored.

### 5.4 Concluding remarks

Accurate measurement of drag in flight and, by implication, thrust is a task of very considerable magnitude. To be of real value in validation of prediction methods, systematic errors greater than about 1% in drag cannot be tolerated. In order to approach this target, the expenditure in manpower, time and money must be substantial and a concerted programme of flight, powerplant and model tests, supported by computing facilities, will be required. The short-term expense needs to be set against the potential gains in aircraft operating economics and possible reductions in R & D expenditure for future aircraft designs.

## 6 ACKNOWLEDGMENTS

In the preparation of this review, the author has been grateful for advice and help from colleagues at RAE (Messrs. J.E. Rossiter, J.B. Edwards and D.A. Treadgold) and ARA (Mr. P.G. Hutton). Specific sections have been based on contributions prepared by members of MIDAP, whose help is gratefully acknowledged, as follows:-

### Section 3.2 (Slender-wing aircraft)

- Mr. J.B.W. Edwards, Royal Aircraft Establishment.

### Section 3.3 (Military strikefighter aircraft)

- Mr. A.J. Grundy and Mr. C.J. Rafe, Hawker Siddeley Aviation Ltd., Brough.

- Section 3.4 (Powerplant installations for strikefighter aircraft)  
- Mr. D.C. Leyland, British Aircraft Corporation, Preston.
- Section 3.5 (Powerplant installations for supersonic transport aircraft)  
- Mr. J.W. Britton, Royal Aircraft Establishment
- Section 3.6 (Powerplant installations for subsonic transport aircraft)  
- Mr. D. Stewart, British Aircraft Corporation, Weybridge, assisted by  
Mr. F.W. Stanhope, Rolls-Royce (1971) Ltd., and Mr. A. Seed, NGTE.
- Section 3.7 (Trim drag)  
- Mr. D. Howe and Mr. R.E. Ward, Cranfield Institute of Technology.
- Section 3.8 (Sweptwing aircraft at high lift)  
- Mr. D.N. Foster, Royal Aircraft Establishment.
- Section 3.9 (Excrescence drag)  
- Mr. D.H. Tipper, Hawker Siddeley Aviation Ltd., Hatfield;  
Mr. R.E. Keates and Mr. D.I. Husk, Hawker Siddeley Aviation Ltd., Manchester.
- Section 4 (On the measurement of drag in wind-tunnel experiments)  
- Mr. C.R. Taylor, Royal Aircraft Establishment.
- Section 5 (On the measurement of drag in flight)  
- Dr. C.S. Barnes, Royal Aircraft Establishment.
- Appendix (A data item service for aircraft drag estimation)  
- Mr. M.D. Hodges, *et al.*, Engineering Sciences Data Unit.

Based on a contribution by M.D. Hodges, *et al.*, ESDU

### A.1 The ESDU concept

In 1940, at the request of the UK Government and Industry, the Royal Aeronautical Society established a small Staff (the Technical Department) to work with Technical Committees in the provision of authoritative data for use in aircraft design; from this developed what is now known as the Engineering Sciences Data Unit (ESDU). The original form of what is now called an ESDU Data Item was the well-known R.Ae.S Data Sheet, first produced for Stressed Skin Structures and shortly afterwards introduced for the subject of Aerodynamics. The subjects now covered have expanded to include in addition to many still specifically of aerospace interest others more directly related to the needs of chemical, mechanical and general structural engineering; a number of other professional institutions now collaborate with ESDU, in addition to the Royal Aeronautical Society.

The principles behind ESDU's work may be briefly described as follows. In each subject area, an expert committee defines a programme of work based on its own particular needs for Data Items, paying special attention to the views of members invited from Industry, which represents the main eventual user of the Data Items; other Committee members are drawn from research laboratories and academic institutions. Qualified permanent staff members at ESDU collect on a world-wide basis from the literature and many unpublished sources a mass of basic data relevant to these established needs. They then attempt to correlate the valid data filtered from this mass, resolving apparent conflicts, constructing new mathematical models to generalise collections of experimental data, comparing established theories with available experimental data and so on, as appropriate to each case. The results are drafted into a form which reflects the needs of the eventual user, is straightforward to apply, states the ranges of applicability, illustrates calculation procedures with flow charts or numerical examples and, above all, represents as authoritative a statement of the known facts and numerical data as can be made at the time. After exposure to rigorous examination by the appropriate Technical Committee and additional specially-invited experts and after any necessary redraftings and re-examinations, a Data Item is issued. It should be understood that the most appropriate form is sought for a Data Item; this could include production as a computer design program package.

It is interesting to reflect here that AGARD and ESDU have certain features in common and have collaborated usefully<sup>A.1,A.2</sup> in several subject areas. Both have permanent Staffs that are small relative to the community involved and both are international in character. Increasingly, the work of ESDU is being carried on as an international cooperative venture. World-wide sources of data have always been used and a rapidly increasing number of new recipients of the service are sited in some 40 countries apart from the United Kingdom. Over recent years, the direction of ESDU's work by the Technical Committees has been widened to include membership from companies and establishments overseas and this trend is being encouraged.

The outcome of what is, undoubtedly, a time-consuming and expensive process is the replacement of a mass of often-conflicting information, widely scattered through the literature and partly unpublished, by a straightforward statement of authoritative data produced to very high standards, backed not by the view of one individual but by a consensus of opinion amongst those best able to judge. Further, the existence of permanent staff enables any user of this service to obtain immediate assistance on the application of the data and to draw the attention of involved professionals to his data requirements.

### A.2 Origins of MIDAP

It is a feature of the technological world that there is a revival of interest in a particular subject area from time to time, often brought about by a new advance. Just such an advance occurred about the time that Nash, Moulden and Osborne<sup>A.3</sup> questioned the once-classical assumption that the drag coefficient of an aerofoil section at constant incidence was insensitive to compressibility effects below the critical Mach number. Their paper quickly led not only to a greater understanding of the development of profile drag on a two-dimensional aerofoil but also to a realisation<sup>A.4</sup> that confidence in the methods of profile drag prediction would depend on the derivation of a reliable method for estimating the effects of compressibility and viscosity for Mach numbers up to the critical value.

During the subsequent decade, there have been significant advances in just this direction. Principal among these has been the achievement of Powell<sup>A.5</sup> in developing a method for calculating the subcritical pressure distribution on an aerofoil in compressible viscous flow. Powell's original concept has now been further developed<sup>A.6,A.7</sup>, incorporating the more-recent description of compressibility effects due to Lock and Wilby. Coupled with advances in predicting the growth of the turbulent boundary layer<sup>A.8-A.10</sup>, much more reliable estimates of profile drag can now be provided than by the concept of form factors, which was sometimes wrongly applied in compressible flow. The concept of form factors, of course, still remains of value in early project work, prior to the full definition of the section shape. Thus there is a need for a spectrum of methods of drag estimation that can provide more elaborate and reliable results as the design develops and the project begins to take shape.

However, the facility for greater accuracy in drag prediction in one area throws into relief the inadequacies that exist in other areas and demonstrates forcibly that drag design standards could and should be improved<sup>4</sup>. This growing realisation prompted discussions<sup>2,A.11,A.12</sup> in the UK over the adequacy of the, then, current methods for aircraft drag prediction. Such considerations led ESDU to form in 1964 a working group, drawn from the R.Ae.S. Aerodynamics, Performance and Transonic Aerodynamics Committees, to consider, primarily in the context of subcritical flight speeds, the adequacy of Data Items concerned with drag estimation.

A general review by the UK Government and Industry of the situation regarding the analysis and prediction of aircraft drag led in 1967 to the decision to set up the UK Ministry/Industry Drag Analysis Panel (MIDAP). Upon the formation of MIDAP, the ESDU group was allowed to fall into abeyance, whilst ESDU accepted participation in the activities of MIDAP through the appointment of M.D. Hodges as a permanent member of the Panel. From 1967 until the beginning of 1971, MIDAP was led by J.E. Rossiter as RAE Coordinator; since then the review author has performed this role. Originally, permanent membership of the panel was confined to the UK airframe industry, but it was broadened in 1971 to include representatives of the aero-engine industry. A sub-panel led by P.F. Ashwood of NGTE is presently considering the difficult problems connected with in-flight assignment of thrust and derivation of aircraft drag (see section 5).

The current terms of reference of MIDAP are:-

- (a) To collect and disseminate to the UK aircraft design teams selected information on drag prediction for sweptwing aircraft;
- (b) To arrange for the correlation and analysis of relevant data, in a way compatible with accepted drag prediction methods;
- (c) To formulate a comprehensive framework for the analysis and synthesis of aircraft drag;
- (d) To encourage the introduction and adoption of improved drag prediction methods by UK aircraft design teams;
- (e) To scrutinise existing drag research programmes and to recommend new work.

#### A.3 ESDA data items for aircraft drag estimation

Since 1964, ESDU has issued 29 Data Items relevant to drag estimation. These provide data on:-

- (a) Particular types of drag, e.g. wave drag<sup>A.14,A.15,A.30,A.40</sup>, base pressure<sup>A.16,A.17</sup>, lift-dependent drag<sup>A.18,A.19</sup>, profile drag<sup>A.22</sup>, skin friction<sup>A.24,A.25</sup>;
- (b) The drag of various aircraft components, e.g. flat plates<sup>A.14,A.24,A.25,A.33</sup>, bodies of revolution<sup>A.17</sup>, slender wings<sup>A.37</sup>, wings<sup>A.18,A.19</sup>, aerofoils<sup>A.15,A.22,A.30</sup>, canopies<sup>A.23</sup>, cones<sup>A.26</sup>, cylinders<sup>A.31,A.32</sup>, rectangular blocks<sup>A.39</sup>, and fairings<sup>A.40</sup>;
- (c) The changes in drag associated with ground effect<sup>A.41</sup>;
- (d) The interrelations between thrust and drag<sup>A.27-A.29,A.34-A.36</sup>;
- (e) The boundary (in terms of a lift coefficient/Mach number locus) beyond which wave drag is to be anticipated<sup>A.13</sup> and on the exchange rates along such a boundary<sup>A.20-A.22</sup>.

Such a listing of Data Items, of course, implies that the drag of an aircraft can be broken down into component parts and, conversely, that in the estimation process the drag of a complete aircraft can be synthesised from such a breakdown. Such an approach has been the subject of an unpublished paper by the Royal Aeronautical Society Performance Committee, on which the following comments have been based. Fig.A1 illustrates a breakdown of airframe subcritical drag in shock-free flow in unconstrained flight (no ground effect) which can be used for the purpose of estimation. It shows, in a readily assimilable form, all the contributions which normally need consideration in the completely general case (not all the contributions shown would necessarily be present on a particular configuration). Fig.A1 omits, however, wave drag. The full list of Data Items available on this, or any other topic, may be obtained from the booklets INDEX 1972 and TITLES 1972 issued by ESDU. The form adopted for Fig.A1 implies a particular approach to drag estimation and its description as being 'conventional' is debatable. Just as new data are continually being obtained, and new theoretical advances occur regularly, so the process of drag estimation should be continually under review. What is 'conventional' in one decade might reasonably be regarded as decidedly antiquated in the next.

#### A.4 Recommended procedure for synthesis of subcritical aircraft drag

The traditional approach to drag estimation was once to estimate and to sum the zero-lift profile drag of each major physical component of the aircraft; to make allowance in some way for interference effects and for sundry individually-minor contributions; and to add drag due to lift. In more recent years, there has been a move away from this process because it is intrinsically inaccurate. One reason for this is because the various major physical components considered are usually mounted at relative incidence to each other (e.g. engine nacelles relative to the wings, wings relative to the fuselage, etc.), so that, at a given aircraft attitude, each component will be at a different incidence; indeed, some components may be at negative incidence. Thus, the summation of zero-lift profile drags and the addition of a drag due to lift must involve significant errors. Secondly, interaction effects can be important, so consideration is needed of the characteristics of the flow field in which each major component is situated. A final, and perhaps most important, reason has been the advent of wings of appreciable camber and twist which may well have a significant component of vortex drag present at zero lift.

It is the intention that the drag of each physical aircraft component listed in Fig.A1 should be estimated at the incidence and flow conditions appropriate to flight at some (non-zero) datum or design lift coefficient. Separate drag predictions in principle have to be made for each flight condition considered (i.e. at the incidence appropriate to the weight, speed and load distribution of the aircraft) including, when appropriate, flight in the constrained flow appropriate to ground effect; for small departures from the datum conditions, overall factors to account for changes in Mach number, lift coefficient and trim might be considered adequate.

6-A2

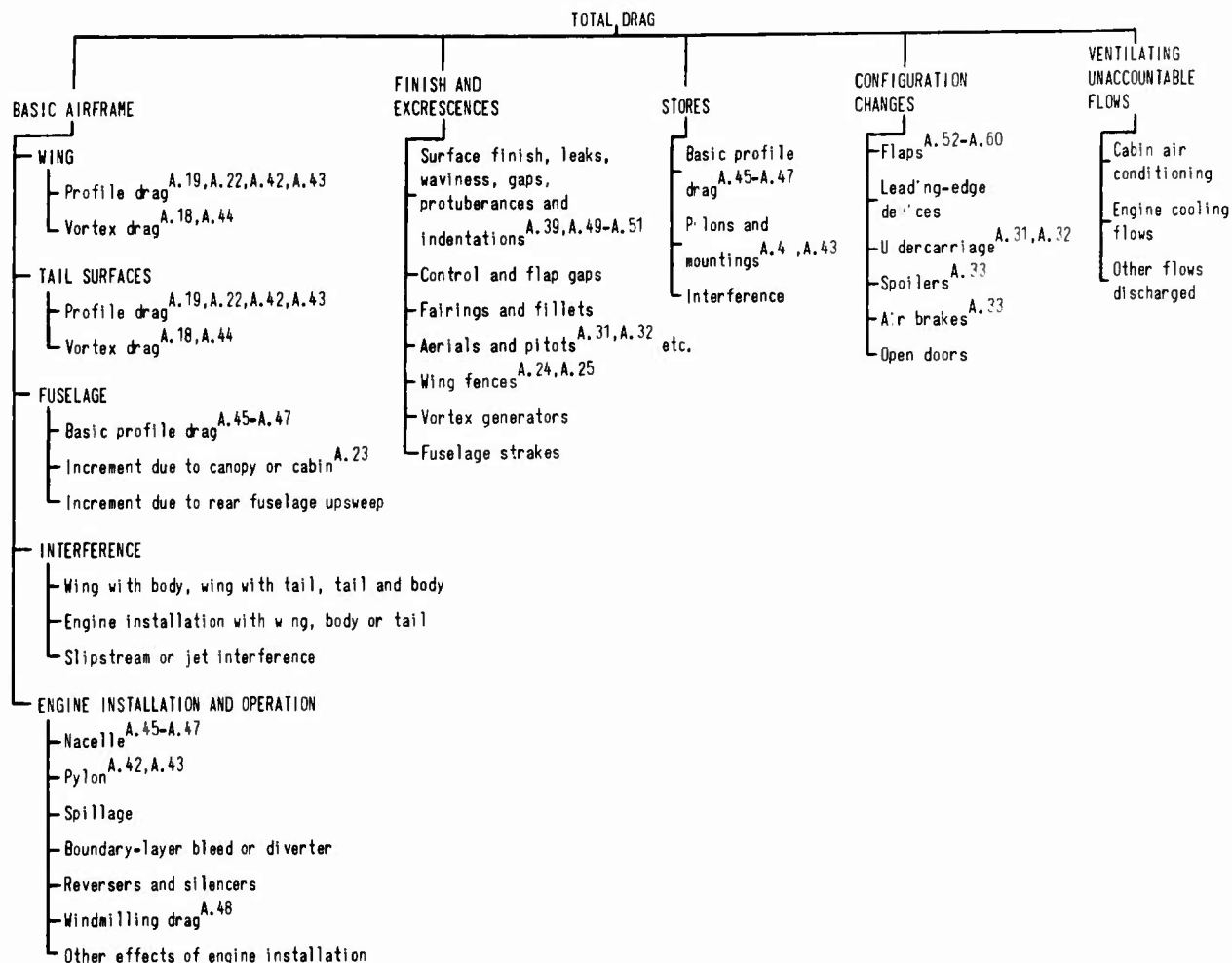


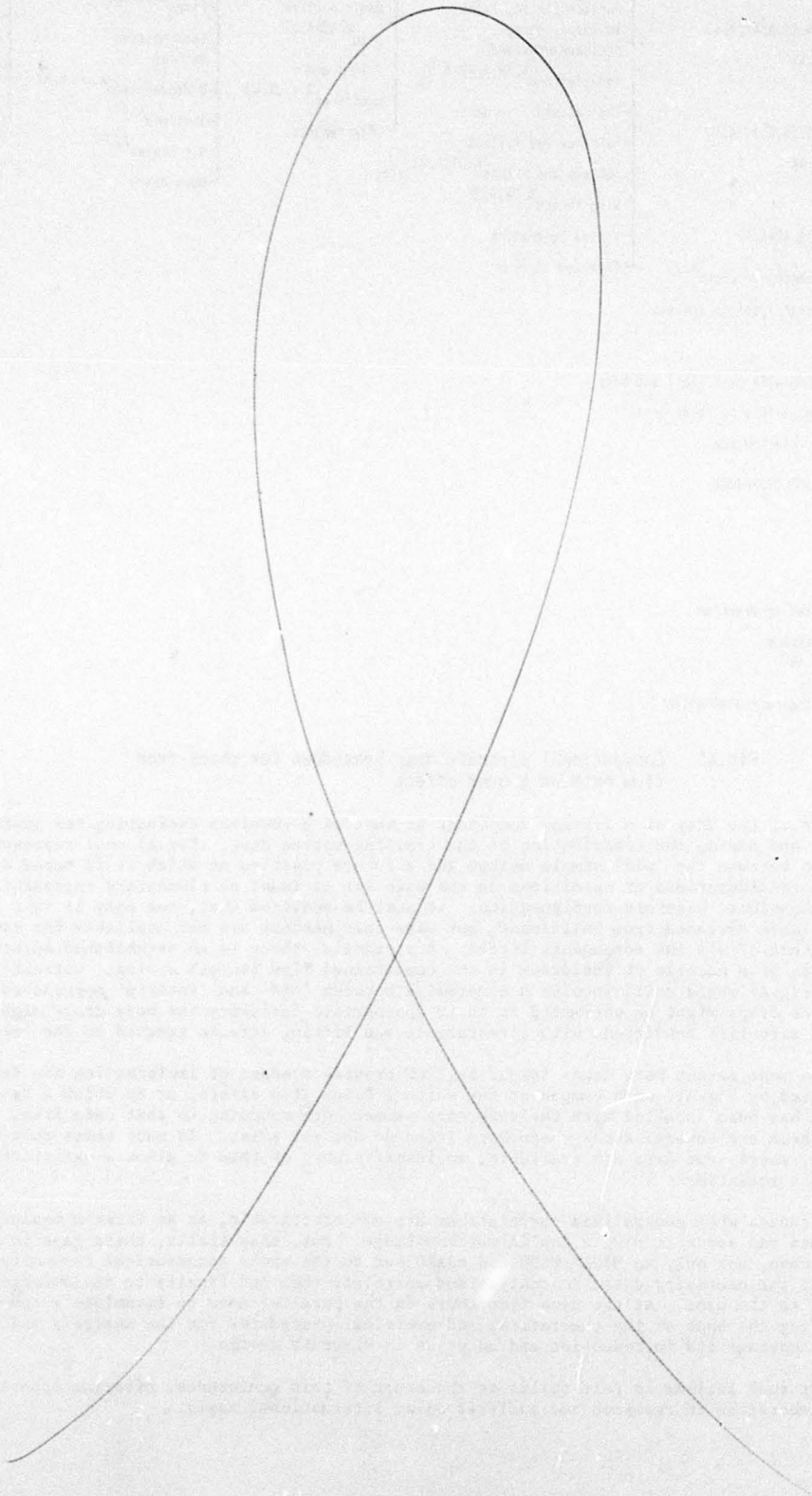
Fig.A1 Conventional aircraft drag breakdown for shock-free flow outside ground effect

The estimate of the drag of a lifting component at incidence involves estimating the profile drag at that incidence and adding the contribution of the trailing vortex drag. Fig.A1 thus represents an 'interim' position between the 'old' simple method and a future position at which it is hoped drag could be estimated from considerations of conditions in the wake for at least an elementary representation of the true three-dimensional aircraft configuration. It must be admitted that, not only is this future state some appreciable distance from fulfilment, but also that methods are not available for estimating the drag at incidence of all the components listed. For example, there is no established method of estimating the drag of a nacelle at incidence in the constrained flow beneath a wing. Currently, the practical use of Fig.A1 would still involve a compromise between 'old' and 'interim' approaches. Thus, the lifting-surface drags might be estimated at their appropriate incidence but body drags might still be estimated at some zero-lift condition, with interference and lifting effects treated in the 'old' way.

To assess to what extent Data Items issued by ESDU provide a means of implementing the drag estimation process implied by Fig.A1, each component for which a Datum Item exists, or to which a Data Item might be adapted, has been labelled with the reference number corresponding to that Data Item. It is at once clear that there are several areas where Data Items do not yet exist. In many cases this highlights a lack of data or, where some data are available, an insufficiency of them to allow a satisfactory basis for a generalised correlation.

In some instances when generalised correlations are not practicable, as an interim measure simple collections of data can serve to plug a gap in our knowledge. But, essentially, these gaps in knowledge represent a challenge, not only to MIDAP, ESDU and AGARD but to the whole aeronautical community, to provide or collect the necessary data, to analyse and correlate them and finally to disseminate them in a form convenient to the user. At the same time there is the parallel need to formulate a comprehensive framework, involving the best of the theoretical and empirical procedures for the analysis and synthesis of drag, and to encourage its introduction and adoption in aircraft design.

The need for such actions is felt to lie at the heart of this conference, offering opportunities for constructive collaboration in research and analysis on an international basis.



REFERENCES

- 1 Norton, D.A., Aircraft drag prediction. *N.Y. Acad. Sc. Annals*, 154, pp.306-328, 1968
- 2 Somerville, T.V., Drag analysis of twenty-four turbo-jet aircraft. RAE unpublished work
- 3 Jones, B.M., The streamline aeroplane. *J.R.Ae.S.*, 1929
- 4 Haines, A.B., Subsonic aircraft drag: an appreciation of present standards. *Aero J.*, 72, 687, pp.253-266, 1968
- 5 Simper, J.I. and Hutton, P.G., Results of a series of wind-tunnel model breakdown tests on the Trident 1 aircraft and a comparison with drag estimates and full-scale flight data. ARA Report 14 (ARC CP 1170), 1970
- 6 Rossiter, J.E., An appraisal of cruise drag prediction problems at subsonic speeds. RAE unpublished work, 1967
- 7 Rossiter, J.E., *et al.*, A method for estimating subsonic cruise drag at the early stages of an aircraft design. MOD(PE) unpublished work
- 8 Hitch, H.P.Y., The application of modern computer techniques to aeronautical design problems. ICAS 70-27, 1970
- 9 Landgraf, S.K., Some practical applications of performance optimisation techniques to high-performance aircraft. AIAA 64-288, 1964
- 10 Schmitz, F.H., Optimal take-off trajectories of a heavily-loaded helicopter. AIAA 70-931, 1970
- 11 Kirkpatrick, D.L.I. and Peckham, D.H., Multivariate analysis applied to aircraft optimisation. Some effects of research advances on the design of future subsonic transport aircraft. RAE Technical Memorandum Aero 1448 (DGLR 72-093), 1972
- 12 Goldsmith, E.L., Brown, C.S. and McGregor, I., RAE unpublished work, 1970
- 13 Wyatt, L.A. and East, L.F., Low speed measurements of skin friction on a slender wing. RAE Technical Report 66027, 1966
- 14 Winter, K.G. and Gaudet, L., Turbulent boundary-layer studies at high Reynolds numbers at Mach numbers between 0.2 and 2.8. RAE Technical Report 70251, 1970
- 15 Ward, G.N., Supersonic flow past slender pointed bodies. *Q. J. Mech. and Appl. Maths.*, 1949
- 16 Lighthill, M.J., The wave drag at zero lift of slender delta wings and similar configurations. *J. FL. Mech.*, 1, 1956
- 17 Weber, J., Numerical methods for calculating the zero-lift wave drag and the lift-dependent wave drag of slender wings. RAE Report Aero 2629, 1959
- 18 Einton, E., On the minimisation and numerical evaluation of wave drag. RAE Report Aero 2564, 1955
- 19 Kirkpatrick, D.L.I. and Kirby, D.A., An experimental investigation of the subsonic longitudinal characteristics of five slender-wing models with gothic planforms. RAE Technical Report 71137, 1971
- 20 Kirby, D.A., An experimental investigation of the effect of planform shape on the subsonic longitudinal characteristics of slender wings. RAE Technical Report 67142 (ARC R & M 3568), 1967
- 21 Cooke, J.C. and Beasley, J.A., Zero-lift wave drag of slender wings with swept trailing edges. RAE Technical Note Aero 2699, 1960
- 22 Kirkpatrick, D.L.I. and Hepworth, A.G., Experimental investigation of the effect of trailing-edge sweepback on the subsonic longitudinal characteristics of slender wings. RAE Technical Report 70039, 1970
- 23 Courtney, A.L., A collection of data on the lift-dependent drag of uncambered slender wings at supersonic speeds. RAE unpublished work
- 24 Bateman, T.E.B. and Haines, A.B., A comparison of results in the ARA transonic tunnel on a small and a large model of a slender wing. ARA Wind Tunnel Note 42 (ARC R & M 3287), 1961
- 25 Weber, J., Design of warped slender wings with the attachment line along the leading edge. RAE Technical Note Aero 2530, 1957
- 26 Adams, Mac C. and Sears, W.R., Slender body theory - review and extension. *J.Ae.Sc.*, 20, 1953
- 27 Davies, P.J., RAE unpublished work, 1971
- 28 Butterworth, P.J., Low-speed wind-tunnel tests on a family of cambered wings of mild gothic planform of aspect ratio 1.4. RAE Technical Report 70185, 1970
- 29 Spence, A. and Smith, J.H.B., Some aspects of the low speed and supersonic aerodynamics of lifting slender wings. Proc. Third ICAS, Stockholm, 1962

6-R-1

## REFERENCES (continued)

- 30 Kirkpatrick, D.L.I. and Peckham, D.H., Project studies of subsonic transport aircraft with low-aspect-ratio wings. RAE unpublished work
- 31 Clutter, D.W., Charts for determining skin friction coefficients on smooth and on rough plates at Mach numbers up to 5.0 with and without heat transfer. Douglas Report, 1959
- 32 Spalding, D.B. and Chi, S.W., The drag of a compressible turbulent boundary layer on a smooth flat plate with and without heat transfer. *J. Fl. Mech.*, 18, 1964
- 33 Jones, R.T., Theory of wing-body drag at supersonic speeds. NACA Report 1284, 1964
- 34 Whitcomb, R.T. and Fischetti, T.L., Development of a Supersonic Area Rule and an application to the design of a wing body combination having high lift-to-drag ratios. NACA unpublished work
- 35 Whitcomb, R.T., A study of the zero lift drag rise characteristics of wing body combinations near the speed of sound. NACA Report 1273, 1956
- 36 Ward, G.N., The drag of source distributions in linearised supersonic flow. Cranfield College of Aeronautics Report, 1955
- 37 Woodward, F.A., Tinoco, E.N. and Larsen, J.W., Analysis and design of supersonic wing-body combinations, including flow properties in the near field. Part 1 - Theory and application. NASA CR 73106, 1967
- 38 Carmichael, R.L., A critical evaluation of methods for computing wing-body interference at supersonic speeds. ICAS 68-08, 1968
- 39 Rafe, C.J., On the relation between the Supersonic Area Rule and the Area Transfer Rule. HSA (Brough) unpublished work
- 40 Harris, R.V., Jnr., An analysis and correlation of aircraft wave drag. NASA unpublished work
- 41 Emlinton, E., On the numerical evaluation of the drag integral. ARC R & M 3341, 1963
- 42 Cahn, M.S. and Olstad, W.B., A numerical method for evaluating wave drag. NACA TN 4258, 1958
- 43 Holdaway, G.H. and Mersman, W.A., Application of Tchebichef form of harmonic analysis to the calculation of zero-lift wave drag of wing-body-tail combinations. NACA unpublished work
- 44 Farmer, P.J., Stoddart, J.A.P. and Roberts, W.J., A computer study of wave drag calculations. BAC unpublished work
- 45 Warren and Fraenkel, A combination of quasi-cylinder and slenderbody theories. *J.R.Ae.S.*, 1955
- 46 Callan, M.M. and Templin, R.J., NAE unpublished work
- 47 Ellison, D.E., *et al.*, USAF unpublished work
- 48 Pugh, P.G. and Hutton, P., The drag of externally-carried stores - its prediction and alleviation. Conference Paper for AGARD Meeting on Aerodynamic Drag, Izmir, 1973
- 49 Little, F.K., *et al.*, Internal aerodynamics manual. North American Rockwell Corporation, NR68H-434, 1970
- 50 Antonatos, P.P., Surber, L.E. and Stava, D.J., Inlet/airplane interference and integration. AGARD Lecture Series 53, 1972
- 51 Sibulkin, M., Theoretical and experimental investigations of additive drag. NACA Report 1187, 1954
- 52 Fraenkel, L.E., Some curves for use in calculations of the performance of conical centrebody intakes at supersonic speed and at full mass flow. RAE Technical Note Aero 2135, 1951
- 53 Goldsmith, E.L. and Griggs, C.F., The estimation of shock pressure recovery and external drag of conical centre body intakes at supersonic speeds. RAE Technical Report Aero 2463 (ARC R & M 3035), 1952
- 54 Dutton, R.A. and Goldsmith, E.L., The drag of some wedge centre-body intakes at Mach numbers of 1.56, 1.86, and 2.14. RAE Technical Report 66208 (ARC CP 968), 1966
- 55 Mount, J.S., Effect of inlet additive drag on aircraft performance. AGARDograph 103, 1965
- 56 Fraenkel, L.E., The external drag of some pitot type intakes at supersonic speeds. RAE Technical Notes Aero 2380 and 2422, 1950/1951
- 57 Bryson, A.E., An experimental investigation of transonic flow past two-dimensional wedge and circular arc sections using a Mach-Zehnder interferometer. NACA Report 1094, 1951
- 58 Hill, P.W., Airframe-inlet integration. AIAA 70-933, 1970

## REFERENCES (continued)

- 59 Henry, B.Z. and Cahn, M.S., Results of an investigation at transonic speeds to determine the effects of a heated propulsive jet on the drag characteristics of a related series of afterbodies. NACA unpublished work
- 60 McDonald, H. and Hughes, D.F., A correlation of high subsonic afterbody drag in the presence of a propulsive jet or support sting. *J. Aircraft*, 2, 1965
- 61 Weir, J., Aircraft performance problems associated with engine and intake installation. AGARDograph 103, 1965
- 62 Mercer, C.E. and Berrier, B.L., Effect of afterbody shape, nozzle type and engine lateral spacing on the installed performance. NACA TM-X-1855, 1969
- 63 Maiden, D.L. and Runckel, J.F., Effect of lateral spacing on afterbody drag and performance of twin jet afterbody models with convergent nozzles at Mach numbers up to 2.2. NASA TM-X-2099, 1970
- 64 Pendergraft, O.C. and Schmeer, J.W., Effect of nozzle lateral spacing on afterbody drag and performance of twin jet afterbody models with convergent-divergent nozzles at Mach numbers up to 2.2. NASA TM-X-2601, 1972
- 65 Swavelly, C.E., US unpublished work
- 66 Aulehla, F. and Lotter, K., Nozzle/airframe interference and integration. AGARD Lecture Series 53, 1972
- 67 Stoddart, J.A.P., Jet effects on boat-tail pressure drag at supersonic speeds. AGARD CP-91-71, 1971
- 68 Reid, J., The effect of a sonic jet on the drag of boattail afterbodies at  $M = 0.9$  and  $2.0$ . RAE Technical Report 71124, 1971
- 69 Lee, E.E. and Runckel, J.F., Performance of closely spaced twin jet afterbodies with different inboard-outboard fairing and nozzle shapes. NASA TM-X-2329, 1971
- 70 Report of the definitions panel on the definitions of the thrust of a jet engine and the drag of a ducted body. ARC CP 190, 1955
- 71 Report of the definitions panel on definitions to be used in the description and analysis on drag. ARC CP 369, 1957
- 72 Britton, J.W. and Dobson, M.D., Notes on the internal drag, lift and pitching moment of a ducted body. RAE unpublished work
- 73 Britton, J.W., Some notes on the analysis of the forces on bodies or wings with side intakes. RAE unpublished work
- 74 Britton, J.W., Measurements of the internal drag of air breathing installations on slender wing body combinations at supersonic speeds. RAE Technical Report 65275 (ARC CP 914), 1965
- 75 Piercy, T.G. and Johnson, H.W., Experimental investigation at Mach numbers 1.88, 3.16, 3.83 of pressure drag of wedge diverters simulating boundary layer removal systems for side inlets. NACA RM E53L14b, 1954
- 76 Bryce, J.D. and Cocking, B.J., NGTE unpublished work
- 77 Baals, D.D., Smith, N.F. and Wright, J.B., The development and application of high-critical-speed nose inlets. NACA Report 920, 1948
- 78 Carter, E.C., Experimental determination of inlet characteristics and inlet and airframe interference. AGARD Lecture Series 53, 1972
- 79 Hetherington, R., Engine component design problems associated with large subsonic transports. Lecture given at Von Karman Institute, 1969
- 80 Street, P.G., Calculation of the flow field downstream of the fan nozzle of a turbofan aero engine. *Aero. J.*, 1970
- 81 Patterson, J.C., A wind-tunnel investigation of jet-wake effect of a high bypass engine on wing-nacelle interference drag of a subsonic transport. NASA TN D-4693, 1968
- 82 Patterson, J.C. and Flechner, S.G., Jet-wake effect of a high bypass engine on wing-nacelle interference drag of a subsonic transport airplane. NASA TN D-6067, 1970
- 83 Williams, P.R.G., and Stewart, D.J., The complex aerodynamic interference pattern due to rear fuselage mounted power plants. AGARD CP-71, 1971
- 84 Ferri, A., Engine airplane interference definition of the problem and related basic fluid dynamic phenomena. AGARD Lecture Series 53, 1972
- 85 Marshall, V.L., Aircraft trim drag. Cranfield Thesis, 1970

## REFERENCES (continued)

- 86 Howe, D. and Ward, R.E., Aeroplane design study STOL airliner (A71). Cranfield Report
- 87 Brown, R.B., Trim drag helps mold supersonic transport's shape. *J.S.Ae.E.*, 69, 1961
- 88 Howe, D., Aeroplane design studies. Mach 2.2 and Mach 3 supersonic airliners. College of Aeronautics Report
- 89 Wilde, M.G. and Cormery, G., The aerodynamic derivation of the Concorde wing. Eleventh Anglo-American Aeronautical Conference, 1969
- 90 Francis, R.H., The development of Blue Steel. *J.R.Ae.S.*, 68, 1964
- 91 Foster, D.N., Note on methods of calculating the pressure distribution over the surface of two-dimensional cambered wings. RAE Technical Report 67095, 1967
- 92 Irwin, H.P.A.H., A calculation method for the two-dimensional turbulent flow over a slotted flap. RAE Technical Report 72124, 1967
- 93 Moir, I.R.M., Foster, D.N. and Holt, D.R. (HSA), The measurement and analysis of the profile drag of a wing with a slotted flap. RAE Technical Report 71158, 1971
- 94 Holt, D.R., Progress Report on some calculations of the lift-dependent profile drag of a slotted flapped aerofoil. HSA unpublished work
- 95 Rutt, D.E., Analysis of the linear theory vortex drag of plane swept wings with part-span non-extending chord flaps in incompressible flow. HSA unpublished work
- 96 McKie, J., The estimation of the loading on swept wings with extending chord flaps at subsonic speeds. RAE Technical Report 69034 (ARC CP 1110), 1969
- 97 McKie, J., Some modifications to the calculation method for wings with part-span extending chord flaps given in RAE Technical Report 69034. RAE Technical Report 71201 (ARC CP 1213), 1971
- 98 Garner, H.C., The vortex drag of a swept wing with part-span flaps. NPL Aero Report 1324 (R & M 3695), 1970
- 99 Sells, C.C.L., An iterative method for calculation of the loading on a thin unswept wing. RAE Technical Report 72009, 1972
- 100 Hess, J.L., Calculation of potential flow about arbitrary three dimensional lifting bodies. US unpublished work
- 101 Hess, J.L. and Smith, A.M.O., Calculation of potential flow about arbitrary bodies. *Progress in Aeronautical Sciences*, 8, 1, 1967
- 102 Myring, D.F., An integral prediction method for three-dimensional turbulent boundary layers in incompressible flow. RAE Technical Report 70147, 1970
- 103 McKie, J., Low-speed wind tunnel tests on an unswept wing of aspect ratio 7 with plain part-span trailing-edge flaps. RAE unpublished work
- 104 Foster, D.N., Exploratory low-speed tunnel tests of part-span flaps and fuselage effects on a high-lift wing. RAE Technical Report 65288, 1965
- 105 Foster, D.N., Some aspects of the RAE high-lift programme. Part II of the Aerodynamics of High-Lift Devices on Conventional Aircraft. *J.R.Ae.S.*, 73, 1969
- 106 Foster, D.N., The low-speed stalling of wings with high-lift devices. Paper No.11 of Fluid Dynamics of Aircraft Stalling. AGARD CP 102, 1972
- 107 Hoerner, S.F., Fluid dynamic drag, 1965
- 108 Gaudet, L. and Johnson, P., Measurement of the drag of various two-dimensional excrescences immersed in turbulent boundary layers at Mach numbers between 0.2 and 2.8. RAE Technical Report 70190, 1970
- 109 Gaudet, L. and Johnson, P., Measurement of the drag of excrescences immersed in turbulent boundary layers at Mach numbers between 0.2 and 2.8-circular holes. RAE Technical Report 71181, 1971
- 110 Cook, T.A., The effect of ridge excrescences and trailing edge control gaps on two-dimensional aerofoil characteristics. RAE Technical Report 71080, 1971
- 111 Nash, J. and Bradshaw, P., The magnification of roughness drag by pressure gradients. *J.R.Ae.S.*, 1967
- 112 Lacey, J., A boundary-layer wind tunnel. University of Leicester R 72-9, 1972
- 113 Weighardt, K., Increase of the turbulent frictional resistance caused by surface irregularities. UK unpublished report (translation)

REFERENCES (continued)

- 114 Tillman, W., Additional measurements of the drag of surface irregularities in turbulent boundary layers. NACA unpublished report (translation)
- 115 Dennard, J.S., The total pressure and drag characteristics of several auxiliary inlets at transonic speeds. NASA unpublished work.
- 116 Jacobs, E.N., Airfoil section characteristics as affected by protuberances. NACA Report 446, 1933
- 117 Treon, S.L., *et al.*, Data correlation from investigations of a high-subsonic speed transport aircraft model in three major transonic wind tunnels. AIAA 69-794, 1969
- 118 Treon, S.L., *et al.*, Further correlation of data from investigations of a high-subsonic speed transport aircraft model in three major transonic wind tunnels. AIAA 71-291, 1971
- 119 Taylor, C.R., Hall, J.R. and Hayward, R.W., Super VC 10 cruise drag - a wind-tunnel investigation. Part 1 - Experimental techniques. RAE Technical Report 69180 (ARC CP 1125), 1969
- 120 Goldsmith, E.L. and Carter, E.C. (ARA), A review of methods used for the representation of engine flows in high speed wind tunnel testing. RAE Technical Report 72012, 1972
- 121 Woodfield, A.A., Cronin, Ann and Vorley, Glynis, Measurement of the performance of a turbo-jet engine with reheat (RR RA28R Avon) in high-speed flight and under simulated conditions in test beds. RAE Technical Report 66060 (ARC R & M 3538), 1966
- 122 Woodfield, A.A., Thrust measurement in flight; the requirements, current situation and future possibilities. *J.R.Ae.S.*, 74, pp.314-321, 1970
- 123 Davidson, T.W., Method of net thrust measurement in supersonic flight. Aerodynamics of power plant installations. AGARDograph 103, Part 1, 1965
- 124 Rose, R., Barnes, C.S. and Woodfield, A.A., Flight measurements of the lift, longitudinal trim and drag of the Fairey Delta 2 at Mach numbers up to 1.65 and comparisons with wind-tunnel results. RAE Technical Report 67036 (ARC R & M 3577), 1967
- A.1 Material Properties Handbook (Vols.1-4). Structure and Materials Panel of AGARD
- A.2 Thomson, A.G.R., Acoustic figure design data, Part I. AGARDograph 162, 1972
- A.3 Nash, J.F., Moulden, T.H. and Osborne, J., On the variation of profile drag coefficient below the critical Mach number. NPL Aero Report 1084 (ARC CP 758), 1963
- A.4 Osborne, J., The variation of profile drag with Mach number up to the critical value; a comparison of recent predictions with early flight and wind-tunnel measurements, and a comment on an earlier prediction. NPL Aero Report 1197, 1966
- A.5 Powell, B.J., The calculation of the pressure distribution on a thick cambered aerofoil at subsonic speeds including the effect of the boundary layer. NPL Aero Report 1238, 1967
- A.6 Lock, R.C., Wilby, P.G. and Powell, B.J., The prediction of aerofoil pressure distributions for sub-critical viscous flows. *Aero Q.*, XXI, pp.291-302, 1970
- A.7 Firmin, M.C.P., A computer program for the calculation of the pressure distribution, lift and drag of a single aerofoil at subcritical speeds where an allowance is made for the effect of the boundary layer and wake. RAE unpublished work
- A.8 Nash, J.F., Osborne, J. and MacDonald, A.G.J., A note on the prediction of aerofoil profile drag at subsonic speeds. NPL Aero Report 1997, 1966
- A.9 Bradshaw, P., Ferriss, D.H. and Atwell, N.P., Calculation of boundary-layer development using the turbulent energy equation. *J. Fl. Mech.*, 28, pp.593-616, 1967
- A.10 Green, J.E., Application of Head's entrainment method to the prediction of turbulent boundary layers and wakes in compressible flow. RAE Technical Report 72079, 1972
- A.11 Scott-Wilson, J.B., A brief review of subsonic drag estimation. UK unpublished work
- A.12 Salisbury, M.W., Some thoughts on the estimation of profile drag at subsonic speeds. UK unpublished work
- A.13 R.Ae.S. Transonic Data Memo 6407, 1964
- A.14 R.Ae.S. Data Item Aero WS 02.03.10, 1964
- A.15 R.Ae.S. Data Item Aero WS 02.03.09, 1965
- A.16 R.Ae.S. Data Item Aero WS 02.03.07, 1965
- A.17 R.Ae.S. Data Item Aero BS 02.03.12, 1965

6-R5

REFERENCES (concluded)

- A.18 ESDU Data Item 66031, 1966  
A.19 ESDU Data Item 66032, 1966  
A.20 ESDU Data Item 67009, 1967  
A.21 ESDU Data Item 67010, 1967  
A.22 ESDU Data Item 67011, 1967  
A.23 ESDU Data Item 67041, 1967  
A.24 ESDU Data Item 68019, 1968 (Amendment A, 1970)  
A.25 ESDU Data Item 68020, 1968 (Amendment A, 1970)  
A.26 ESDU Data Item 68021, 1968  
A.27 ESDU Data Item 69006, 1969  
A.28 ESDU Data Item 69007, 1969  
A.29 ESDU Data Item 69008, 1969  
A.30 ESDU Data Item 69013, 1969  
A.31 ESDU Data Item 70013, 1970 (Amendment A, 1971)  
A.32 ESDU Data Item 70014, 1970 (Amendment A, 1971)  
A.33 ESDU Data Item 70015, 1970 (Amendment A, 1971)  
A.34 ESDU Data Item 70019, 1970  
A.35 ESDU Data Item 70020, 1970  
A.36 ESDU Data Item 70021, 1970  
A.37 ESDU Data Item 71006, 1971  
A.38 ESDU Data Item 71012, 1971  
A.39 ESDU Data Item 71016, 1971  
A.40 ESDU Data Item 71018, 1971  
A.41 ESDU Data Item 72023, 1972  
A.42 R.Ae.S. Data Item W.02.04.02, 1947  
A.43 R.Ae.S. Data Item W.02.04.03, 1953  
A.44 R.Ae.S. Data Item W.02.01.02, 1965  
A.45 R.Ae.S. Data Item B.02.04.01, 1947  
A.46 R.Ae.S. Data Item B.02.04.02, 1947  
A.47 R.Ae.S. Data Item B.02.04.03, 1947  
A.48 R.Ae.S. Data Item Perf. ED1/1, 1962  
A.49 R.Ae.S. Data Item Aero W.02.04.08, 1948  
A.50 R.Ae.S. Data Item Aero W.02.04.10, 1948  
A.51 R.Ae.S. Data Item Aero W.02.04.11, 1943  
A.52 R.Ae.S. Data Item Aero F.02.01.01, 1944  
A.53 R.Ae.S. Data Item Aero F.02.01.02, 1944  
A.54 R.Ae.S. Data Item Aero F.02.01.03, 1944  
A.55 R.Ae.S. Data Item Aero F.02.01.04, 1944  
A.56 R.Ae.S. Data Item Aero F.02.01.05, 1944  
A.57 R.Ae.S. Data Item Aero F.02.01.06, 1944  
A.58 R.Ae.S. Data Item Aero F.02.01.07, 1944  
A.59 R.Ae.S. Data Item Aero F.02.01.08, 1945  
A.60 R.Ae.S. Data Item Aero F.02.01.09, 1945

by

A. M. O. Smith\* and Tuncer Cebeci\*\*  
Douglas Aircraft Company  
Long Beach, California

7-1

## SUMMARY

While predictions of low speed profile drag are accurate for monoelement airfoils at low angle of attack, the methods are not very accurate at higher angles of attack, or for multielement airfoils or for fatter bodies of revolution. Two courses that might lead to possible improvement in accuracy have been investigated. One was an attempt to perform direct shear and pressure stress calculations on an airfoil or body. The other was an attempt to improve the Squire-Young momentum defect method by actually solving the wake for a short distance. The first method was not successful but the second method shows promise. Hence, it is tentatively concluded that refinement of the momentum defect method is the most promising path towards improved accuracy.

## PRINCIPAL NOTATION

$c$	chord, as of an airfoil	$R$	maximum radius of a body of revolution
$c_f$	local skin friction coefficient $2\tau_w/\rho u_e^2$	$R_c$	Reynolds number based on chord
$\bar{c}_f$	mean friction drag coefficient, based on chord	$R_L$	Reynolds number of a body of revolution based on length
$\bar{c}_{f\pi}$	mean friction coefficient for a body of revolution, based on frontal area	$s$	distance, measured along surface of a body
$C_{Dp}$	profile drag coefficient based on chord	$T$	tangential velocity ratio on surface of a body $T = u_e/u_\infty$
$C_{Dpress.}$	pressure drag coefficient, based on chord	$T_0$	tangential velocity ratio according to inviscid theory, i.e., on "naked" body
$C_{D\pi}$	drag coefficient of a body of revolution, based on frontal area	$T_1$	perturbation tangential velocity ratio due to effect of boundary layer
$C_{D\pi press.}$	pressure drag coefficient of a body of revolution, based on frontal area	$u$	velocity
$C_p$	pressure coefficient $(p - p_\infty)/\frac{1}{2}\rho u_\infty^2$	$u_c$	velocity at center of a wake
$H$	shape factor, $\delta^*/\theta$	$u_e$	inviscid edge velocity
$H_{TE}$	shape factor at trailing edge, or end of body	$u_{TE}$	edge velocity at the trailing edge
$H_\infty$	shape factor of wake far downstream	$u_\infty$	ambient velocity
$j$	index in summation. See (19) for example.	$v$	velocity perpendicular to a wall
$L$	length of a body of revolution	$x, y$	coordinates
$p$	pressure	$\alpha$	angle of attack, or local slope of a surface
$q$	exponent in generalized Squire-Young formula. See (7). Also velocity magnitude	$\delta^*$	displacement thickness of a boundary layer
$r$	local radius of a body of revolution	$\epsilon_m$	eddy viscosity
		$\theta$	momentum thickness of a boundary layer
		$\rho$	mass density
		$\tau_w$	shear stress at the wall

## 1. INTRODUCTION

For a limited set of problems the existing methods of drag calculation are reasonably satisfactory but for problems of a more general nature the methods are definitely unsatisfactory. The one area in which accuracy is about as good as can reasonably be expected is the low-speed drag of airfoils at the lower angles of attack. Figure 1, taken from reference [1] summarizes the state of the art. The root-mean-square error for the points shown is 2.9%. In a separate study, Nark [2] generally reaches the same conclusion.

But there are many more problems of importance than this one. A few are: the drag of bodies of revolution, the drag of multielement airfoils, the losses in cascades, and the effects of Mach number. Effects of heating and cooling are still others. We do not even mention three-dimensional effects. None of the problems just mentioned can now be solved with an accuracy comparable to that of simple airfoils as indicated in figure 1.

The primary tools needed for any calculation of drag are a good general boundary-layer method and a good general potential flow method. Both are now available, whereas a few years back they were not.

\*Chief Aerodynamics Engineer, Research

\*\*Senior Engineer/Scientist

1.2

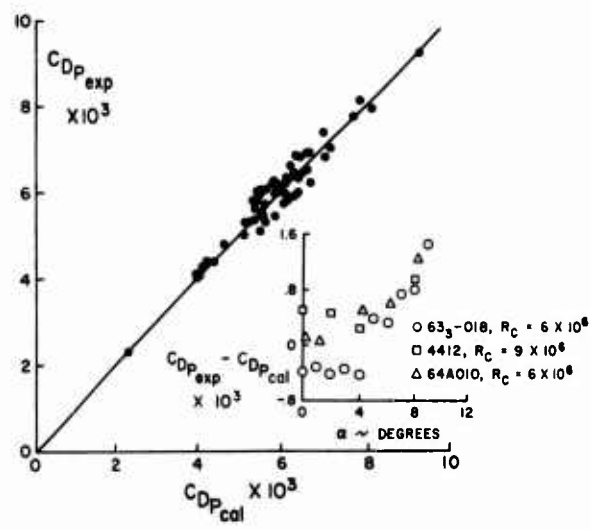


Figure 1. Comparison of calculated and experimental results for two-dimensional bodies. 57 drag values are shown for angles of attack,  $\alpha$ , less than  $6^\circ$ . Insert shows error growth with angle of attack for three of the airfoils studied.

Therefore, it was decided to apply these methods in more than one way in an endeavor to make progress on the more difficult problems just mentioned. But before describing the particular methods that were investigated it is useful to review the leading current method, that used to establish figure 1.

## 2. CURRENT MOMENTUM DEFECT METHODS

Current methods all compute profile drag by attempting to calculate the defect in momentum in the flow at some distance downstream of the body, at a point outside the pressure field induced by the body. The boundary-layer development is calculated over the body from nose to trailing edge. This, of course, requires knowledge of the pressure distribution, which might come from experiment or might come from theory. The boundary-layer calculations stop at the trailing edge or tail of the body, but because of local pressure effects the momentum defect cannot be examined at this point. Rather, in some way the defect must be corrected to conditions far downstream so that Newton's second law can be applied to establish the force on the body.

Squire and Young [3] made use of von Karman's momentum integral equation to derive a relation. In its simplest, two-dimensional incompressible form the momentum integral equation is

$$\frac{d\theta}{dx} = \frac{\tau_w}{\rho u_e^2} - (2 + H) \frac{\theta}{u_e} \frac{du_e}{dx} \quad (1)$$

The equation is exact. In the wake there is no wall, so that  $\tau_w$  equals zero and (1) can then be written

$$\frac{1}{\theta} \frac{d\theta}{dx} = - (2 + H) \frac{d}{dx} \left( \ln \frac{u_e}{u_\infty} \right) \quad (2)$$

The constant velocity  $u_\infty$  has been introduced for normalization purposes. This equation can be formally integrated by parts between the trailing edge and far downstream to yield, since  $H(\infty) = 1$ .

$$\theta_\infty = \theta_{TE} \left( \frac{u_{TE}}{u_\infty} \right)^{H_{TE}+2} \exp \left( \int_1^{H_{TE}} \ln \frac{u_\infty}{u_e} dH \right) \quad (3)$$

This equation is an exact relation between the momentum thickness at the trailing edge and that far downstream. In order to evaluate the integral a functional relation between  $H$  and  $u_e/u_\infty$  must be given. Squire and Young had one set of experimental data and that justified a linear relation. Hence they proposed the following expression

$$\ln \frac{u_\infty}{u_e} = \frac{H-1}{H_{TE}-1} \quad (4)$$

When used in (3) we obtain the very simple relation

$$\theta_\infty = \theta_{TE} \left( \frac{u_{TE}}{u_\infty} \right)^{\frac{H_{TE}+5}{2}} \quad (5)$$

Then it can be shown that the drag coefficient for the airfoil is

$$C_D = 2 \left[ \frac{\theta_{TE}}{c} \left( \frac{u_{TE}}{u_\infty} \right)^{\frac{H_{TE}+5}{2}} \right]_U + 2 \left[ \frac{\theta_{TE}}{c} \left( \frac{u_{TE}}{u_\infty} \right)^{\frac{H_{TE}+5}{2}} \right]_L \quad (6)$$

where the equation has been written out at length to explicitly indicate the contribution from both the upper and lower surfaces. When the relation (5) is used, people commonly say they are using the Squire-Young method, even though their method of boundary-layer calculation may be entirely different from Squire's and Young's.

Relation (4) is critical to this method. Just how good is it? A few more tests have been made since the work of Squire and Young, but the information is still scanty. The main data known to the authors is included in the normalized H-velocity plot shown in figure 2. The chart covers both compressible flow and axially symmetric flow. The same kind of linear relation as (4) was assumed by Young [4] in his work on bodies of revolution. The Firmin-Cook data [5] are for low-lift coefficients. No systematic relations or variations are discernible in this chart. The Squire-Young relation is just the diagonal line in the figure.

- × SQUIRE - YOUNG [3]
- △ RAE 101 AIRFOIL M=0.74 [5]
- ▽ RAE 101 AIRFOIL M=0.4 [5]
- RAE 2815 AIRFOIL M=0.72 [5]
- + 12% SYM JOUKOWSKI [6]
- BODY OF REV [7]
- ◇ RAE 2814 M=.72 C<sub>L</sub>=.42 [8]
- △ RAE 2815 M=.664 C<sub>L</sub>=.70 [8]
- △ RAE 2815 M=.661 C<sub>L</sub>=.51 [8]

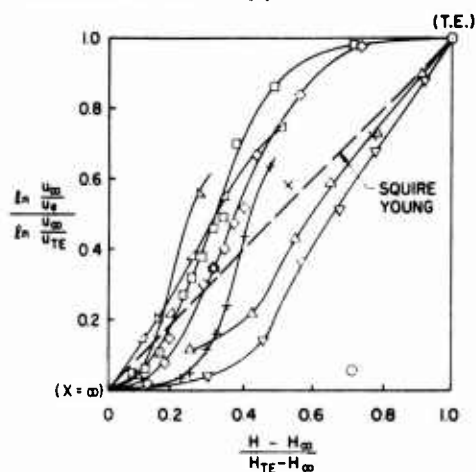


Figure 2. Summary of measured  $H - u_e$  relations in the wake.

Since  $u_{TE}/u_\infty$  does not differ greatly from unity,  $\theta_{A_\infty}$  is not very sensitive to values of  $q$ . For instance, if we let  $q_1 = 1$ , corresponding to the Squire-Young and Young assumption, and  $q_2 = 7$ , corresponding to Granville's assumption, and if we let  $u_{TE}/u_\infty = 0.9$  we obtain from (9)

$$\frac{\theta_{A_\infty 2}}{\theta_{A_\infty 1}} = 0.9 \frac{3(H_{TE}-1)}{8} \quad (10)$$

Then with a typical value for  $H_{TE}$  of 1.6, we obtain

$$\frac{\theta_{A_\infty 2}}{\theta_{A_\infty 1}} = 0.9^{0.225} = 0.977 \quad (11)$$

or about 2% difference. Hence, provided  $u_{TE}/u_\infty$  is not greatly different from unity, the results are not very sensitive to the form of the functional relation, or more exactly, to the value of  $q$ . It is interesting to note that the effect of a function antisymmetric about the midpoint of the diagonal in figure 2 has been examined. Its contribution is self-canceling.

Although sensitivity of  $\theta_\infty$  to the functional relation does not seem great, we have been considering only the simple case of airfoils at low angle of attack. When one considers highly unsymmetrical wakes from airfoils at higher angles of attack, wakes from slats that flow along over the main airfoil and that leave with  $u_{TE}/u_\infty$  of 1.5 or greater, or wakes from bodies of revolution, it appears obvious that a Squire-Young type of approximation is not the final answer. This fact is indeed confirmed by actual calculations for bodies of revolution and multielement airfoils. Calculations and experiment are not in satisfactory agreement.

### 3. PRETSCH'S METHOD

A quite different approach to the problem was made by Pretsch [9] at about the same time as Squire and Young were developing their method. Instead of using the momentum defect in the wake as a base for calculation, Pretsch attempted to calculate the shear and pressure forces that acted on the airfoil. The unique part of his analysis was the method for computing pressure drag. It is well known that the boundary layer displaces inviscid streamlines outward from the body by an amount  $\delta^*$ . Even in the wake this displacement streamline never closes, so that a half body is formed.

It is well known from classical hydrodynamic theory that the drag of a half body is zero. Hence, the drag of the part forward of the trailing edge must equal the negative of the part behind the trailing edge. Therefore, to find the pressure drag that acts on the airfoil, Pretsch studied the flow in the wake. The pressure force exerted on the wake is

$$D_w = \left[ \int_{\delta^*_{TE}}^{\delta^*_{\infty}} p(\delta^*) d\delta^* \right]_{upper} + \left[ \int_{\delta^*_{TE}}^{\delta^*_{\infty}} p(\delta^*) d\delta^* \right]_{lower} \quad (12)$$

In this equation  $\delta^*$  in each of the two terms represents the final value from each of the two boundary layers. The two upper limits are not the same except when a flow is symmetrical. How are the integrals

In view of the large scatter of data, the Squire-Young approximation would appear as reasonable as any other curve. 7-3

Granville [7] proposed replacing the relation (4) by one of more general type

$$\frac{\ln u_\infty/u_e}{\ln u_\infty/u_{TE}} = \left( \frac{H-1}{H_{TE}-1} \right)^q \quad (7)$$

For a body of revolution this leads to the result, with  $\theta_A$  being the momentum area

$$\theta_{A_\infty} = \theta_{A_{TE}} \left( \frac{u_{TE}}{u_\infty} \right)^{\frac{(H_{TE}+2)q+3}{q+1}} \quad (8)$$

For two different values of  $q$ ,  $q_1$  and  $q_2$  the ratio of values of  $\theta_{A_\infty}$  is

$$\frac{\theta_{A_\infty 2}}{\theta_{A_\infty 1}} = \left( \frac{u_{TE}}{u_\infty} \right)^{\frac{(H_{TE}-1)(q_2-q_1)}{(q_1+1)(q_2+1)}} \quad (9)$$

1-4 evaluated? Pretsch's basic method is to assume that each filament in the wake flow retains the same total head that it had as it left the trailing edge. Then as pressures change the velocity changes follow from Bernoulli's law. Often this is a very reasonable assumption.

For purposes of working out pressure correction curves, Pretsch assumed the boundary-layer profiles could be approximated by profiles of the standard form

$$\frac{u}{u_e} = \left(\frac{y}{\delta}\right)^{1/n} \quad (13)$$

The exponent  $n$  has a well known relation to the shape factor  $H$ . Once a particular profile at the trailing edge is assumed, then with the aid of Bernoulli's equation it is a straightforward matter to compute  $\delta^*$  for  $p$ , and hence evaluate the integrands of (12). The pressure  $p$  as a function of  $x$  is not needed, only initial and final values are of importance. Intermediate values of  $p$  must be assumed for purposes of constructing the integrand but it is not necessary to know the  $x$ -position at which a value of  $p$  occurs. Furthermore, it is not necessary to assume power-law profiles as in (13). The actual boundary layers could very easily be used, subject to the Bernoulli assumption if computing were done on an automatic computer.

To delineate clearly the differences between Pretsch's and the Squire-Young momentum defect approaches, we present the following table. Pretsch's method has never been applied to a body of revolution as far as the writers know but the extension should not be difficult.

#### Crucial Features of the Pretsch and Squire-Young Methods

<u>Squire-Young</u>	<u>Pretsch</u>
1. Computes on the principle that total section drag is equal to the momentum defect at $x = \infty$ , i.e., $C_{Dp} = 2\theta_\infty/c$ .	Computes on the principle that total section drag is the sum of the shear stress drag and the pressure drag.
2. Computes the development of $\theta$ over the airfoil.	Computes $c_f$ and boundary-layer profiles over the entire airfoil.
3. Uses a strictly empirical relation to correct $\theta$ at the trailing edge to $\theta_\infty$ , which occurs at $x = \infty$ .	Obtains pressure drag by computations on the wake, which are semi-empirical and assumes that Bernoulli's equation applies to every streamline in the wake.

The first question is which can be calculated best along the airfoil  $\theta$  or  $c_f$ . In older methods  $c_f$  was quite empirical, and  $\theta$  was clearly the more accurate quantity. In newer methods the differences in accuracy are so small that considerable study would be necessary to establish the best.

The second question is whether or not the  $\theta$  correction of Squire and Young can be done more accurately than the pressure drag correction of Pretsch. The answer is not now known. It would be useful to examine the question carefully. Pretsch's method could prove better than Young's for bodies of revolution. B. M. Jones' wake drag formulas make the same assumption about Bernoulli's equation as Pretsch, and Jones' method has proven to give good accuracy in airfoil drag measurements. It is interesting to note that P. S. Granville states he has proven that the Squire-Young correction and Pretsch's pressure drag correction are equivalent, independent of the exponent  $q$  in (7). The writers have seen no details of the proof nor the conditions.

If Bernoulli's equation holds along streamlines as Pretsch assumes, the final velocity of the one in contact with the surface will be

$$u_{w\infty} = \sqrt{2/\rho (p_{TE} - p_\infty)} \quad (14)$$

Now if  $p_{TE} > p_\infty$ ,  $u_{w\infty} > 0$ . Pressures at the tails of airfoils and bodies of revolution are positive, so no problem arises with respect to this point for Pretsch's method. But there are cases when the concept breaks down. The trailing edge of a slat is in a negative pressure region. Then  $u_{w\infty}$  becomes imaginary according to (14), and a physically more realistic correction method is indicated.

#### 4. A SHEAR AND PRESSURE METHOD

##### 4.1 Description

Because of inadequacies of the methods just described, a search was made for improvements. It was questioned whether it was really necessary to continue calculations on into the wake. Forces on the airfoil or body are ultimately applied through shear or pressure stresses. Could not these be calculated directly? This, of course, is not a new thought. The problem is that drag is about two orders of magnitude less than lift. Hence, insufficient accuracy can be obtained in calculating pressure drag. But much better tools for analysis have become available and a method involving only the perturbation pressure effects was conceived. Therefore, an investigation was made. The Douglas Neumann potential-flow program and the Cebeci-Smith turbulent-boundary-layer program were available and ideally suited for the study. The method will now be described.

A boundary layer displaces the inviscid flow outward from the surface by an amount  $\delta^*$ , creating effectively a semi-infinite half-body as sketched in figure 3. A first approximation for the effect on pressures of this displacement of streamlines is to solve an inviscid problem that has a streamline that matches the  $\delta^*$  locus. One way is just to treat the  $\delta^*$  locus as a new solid body and calculate the flow about it, stopping calculations at the trailing edge. That means treating an open-ended body. That

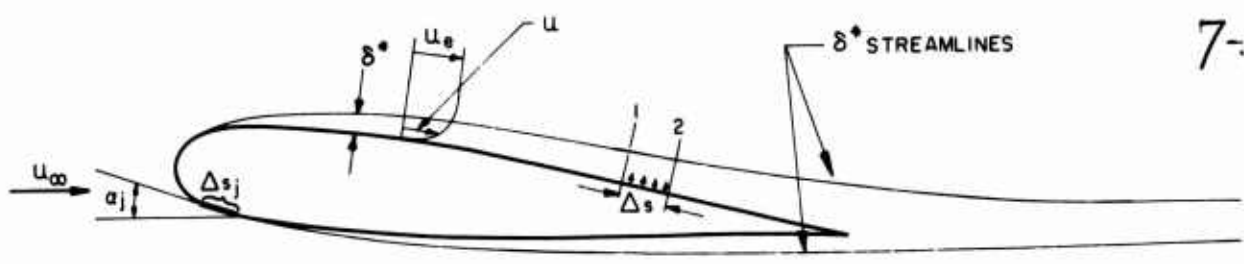


Figure 3. Schematic of viscous flow over an airfoil.

method is currently in use at Douglas and has given hundreds of satisfactory results[18]. It should be noted that accuracy is not satisfactory without any boundary-layer correction. One drawback of this method is that a new matrix of influence coefficients must be calculated for each new boundary layer because for each, the geometric shape of the boundary is different.

A method that is equivalent to first order is to solve the problem with conditions along the original boundary - the airfoil - to account for the growth of  $\delta^*$ . This is legitimate because boundary layers are thin. Consider flow relations at stations 1 and 2 in figure 3. At station 1, an inviscid approximating flow will be moving with a velocity  $u_{e1}$  and the flux will be  $u_{e1}\delta^*_1$ . At station 2 the flux will be

$$u_{e1}\delta^*_1 + \frac{\partial}{\partial s} (u_{e1}\delta^*_1)\Delta s$$

The difference at the two stations is just

$$\frac{\partial}{\partial s} (u_{e1}\delta^*_1)\Delta s$$

This difference in flux can be supplied by blowing from the wall as sketched, with a velocity  $v_w$ . Then

$$v_w\Delta s = \frac{\partial}{\partial s} (u_e\delta^*)\Delta s \tag{14}$$

If we normalize by dividing through by  $u_\infty$  we obtain

$$\frac{v_w}{u_\infty} = \frac{\partial}{\partial s} (T_0\delta^*) \tag{15}$$

Here  $T_0$  is the tangential velocity ratio  $u_e/u_\infty$  and it is obtained from the inviscid solution for the naked airfoil. Equation (15) then is the boundary condition to be applied along the wall to account for the growth of  $\delta^*$ . Prætor [10] obtained this relation in 1945 by slightly different reasoning.

Potential flows, being solutions of a linear equation, can be superimposed. Then it is axiomatic that for an airfoil at angle of attack with lift, and with boundary layer, a steady flow solution meeting the boundary conditions is a linear combination of the following elementary solutions.

1. A simple potential flow about the airfoil moving in steady rectilinear motion at  $\alpha = 0^\circ$ .
2. A simple potential flow about the airfoil moving in steady rectilinear motion at  $\alpha = 90^\circ$ .
3. A pure circulatory flow with no translation.
4. A flow with wall blowing in accord with (15) and with no translation.

For basic theory see Hess and Smith [11]. The four elementary solutions are shown in figure 4. Unless the blowing solution is symmetrical there will be flow around the trailing edge. This will affect the amount of the circulation solution that is required to satisfy the Kutta condition, and hence the lift.

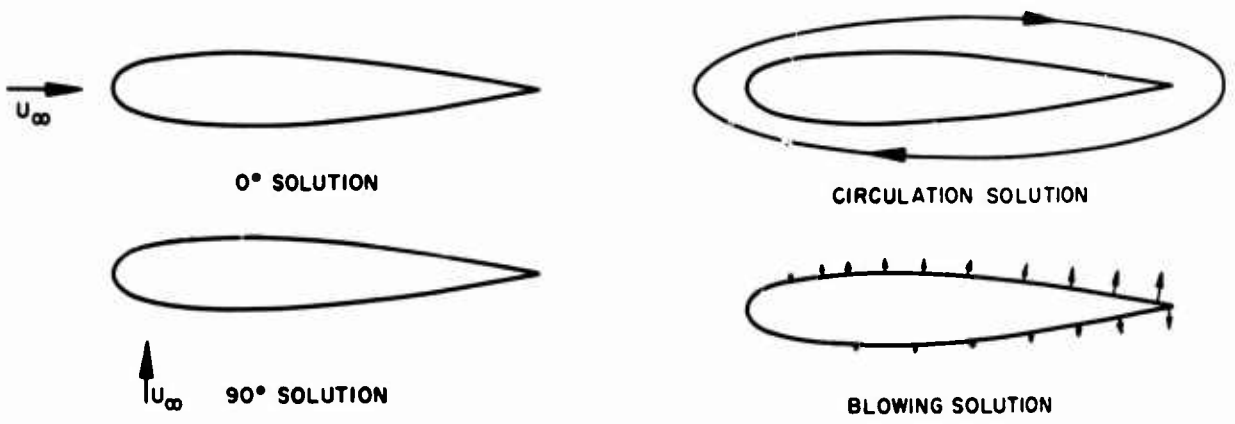


Figure 4. The four fundamental solutions used for approximating the viscous flow about a lifting airfoil at angle of attack.

7-6  
 Due to blowing there is a slight normal velocity at the surface. Then the final solution that satisfies all the boundary conditions including the blowing will be identified as  $q(s)$  where  $s$  is peripheral distance around the airfoil measured in a clockwise direction, beginning at the trailing edge. Then

$$C_p(s) = 1 - (q/u_\infty)^2(s) = 1 - T^2(s) - (v_w/u_\infty)^2(s) \quad (16)$$

where  $v_w/u_\infty$  is given by (15). Let the velocity perturbation due to the blowing solution be  $T_1$ , and the basic or naked airfoil solution be  $T_0$  as already noted. Then  $T = T_0 + T_1$  and

$$C_p = 1 - (T_0 + T_1)^2 - (v_w/u_\infty)^2 = (1 - T_0^2) - [2T_0T_1 + T_1^2 + (v_w/u_\infty)^2] \quad (17)$$

But  $1 - T_0^2$  is just  $C_{p0}$ , the pressure distribution for the naked airfoil. Hence,

$$C_p = C_{p0} - [2T_0T_1 + T_1^2 + (v_w/u_\infty)^2] \quad (18)$$

But we know theoretically that the inviscid pressure forces on a body sum to zero in the drag direction. Hence, the large quantity  $C_{p0}$  can be dropped. The  $T_1^2$  and  $(v_w/u_\infty)^2$  terms in (18) are quite small and can be neglected, but it is not necessary to in this problem. Then if  $\alpha_j$  is the angle of some element of length  $\Delta s_j$  (see figure 3), the total pressure force on the airfoil will be, if the airfoil is subdivided into elements,

$$C_{D_{\text{press.}}} = \sum_{j=1}^n - [2T_0T_1 + T_1^2 + (v_w/u_\infty)^2]_j (\Delta s_j/c) \sin \alpha_j \quad (19)$$

But  $\Delta s_j \sin \alpha_j$  is just  $\Delta y_j$ , and so finally, assuming  $T_1^2$  and  $(v_w/u_\infty)^2$  are small

$$C_{D_{\text{press.}}} = \sum_{j=1}^n - 2(T_0T_1)_j (\Delta y_j/c) \quad (20)$$

If  $\tau_w$  is the shear stress due to viscous effects, we have similarly

$$F_{x_{\text{shear}}} = \sum_{j=1}^n \tau_{wj} \Delta s_j \cos \alpha_j \quad (21)$$

By definition

$$\bar{c}_f = \frac{F_{x_{\text{shear}}}}{1/2 \rho u_\infty^2 c}, \quad c_f = \frac{\tau_w}{1/2 \rho u_e^2} \quad (22)$$

Then if we note that  $\Delta s_j \cos \alpha_j = \Delta x_j$ , we have

$$\bar{c}_f = \sum_{j=1}^n c_{fj} T_{0j}^2 \left( \frac{\Delta x_j}{c} \right) \quad (23)$$

Equation (20) plus (23) together define the drag for a two-dimensional shape. The extended formulas for a body of revolution should be obvious.

#### 4.2 Some Results

About 20 two-dimensional calculations have been made by the method just described. The Douglas Neumann program solves the problem in terms of a surface source-sink distribution so that it is well suited for finding the blowing solution, figure 4. After some preliminary runs for a lifting airfoil were found to lead to considerable confusion, it was decided to study a systematic family of symmetrical Joukowski airfoils at  $\alpha = 0^\circ$ . Calculations were made for shapes, 10%, 15%, 20%, 25% and 30% thick. Joukowski sections were chosen because they have no rear stagnation point and none have separation, even with potential flow used as the edge flow in the boundary-layer analysis. The family of pressure distributions is shown in figure 5. In the interests of brevity  $\delta^*$  as computed by the Cebeci-Smith boundary-layer program is not shown, but the product  $T\delta^*$  is shown in figure 6. The break in the curves occurs at the transition point. Figure 7 is the numerically computed set of derivatives of  $T_0\delta^*$  used as boundary conditions for (15) and the blowing solution.

Figure 8 is the set of perturbation solutions. Stagnation points for these flows occur at  $T_1 = 0$ . For the 10% Joukowski, the stagnation point is at about 60% chord and the point moves back with thickness until it is almost at 95% for the 30% airfoil. These solutions show that the perturbation velocity subtracts from the inviscid solution in the forward parts of the airfoil and adds in the regions aft of the side stagnation point. Figure 9 shows the perturbation values of  $C_p$ , neglecting the quadratic terms, see (18). These curves resemble the  $T_1$  family because  $T_0$  is not greatly different from unity over most of the airfoil.

When  $\Delta C_p$  is plotted against  $y/c$ , the peculiar loops of figure 10 are obtained. The area inside the loops is the pressure force, that is, the pressure drag. Because it is hard to understand these curves, the curve for the 30%-thick Joukowski is plotted alone in figure 11. Here the airfoil shape is shown too, and numbers are spotted along both the airfoil and pressure distribution to show to what point on the airfoil each point on the pressure distribution corresponds. Both thrust and drag forces occur on the airfoil.

Figure 12 shows the plots of local friction coefficient. Values are low forward of 10% chord because the flow is laminar. It is interesting to observe that increased thickness increases skin friction in the

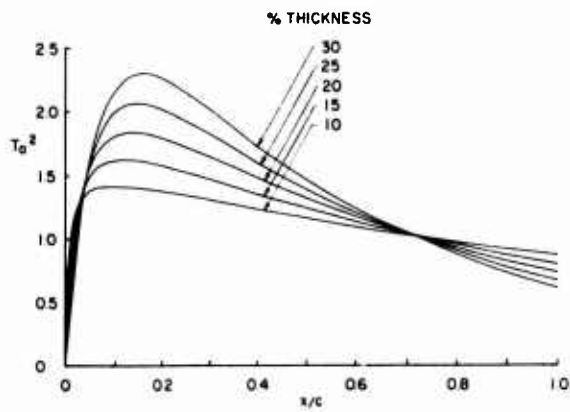


Figure 5. The set of Joukowski airfoils that were studied. Transition was assumed to be at 10% chord for all thicknesses.

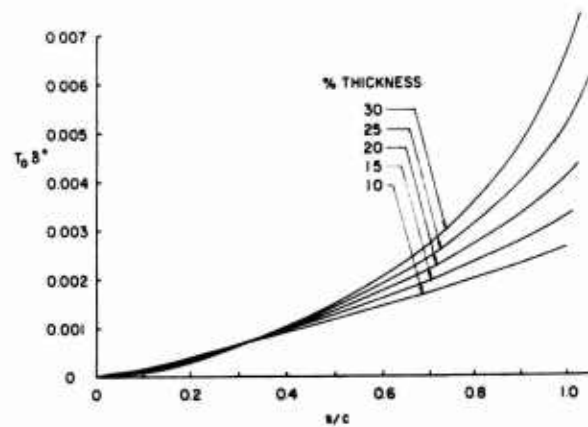


Figure 6. Values of  $T_0 \delta^*$  for the five Joukowski airfoils. Note that  $s/c$  is used instead of  $x/c$ .  $R_c = 10^7$  all cases.

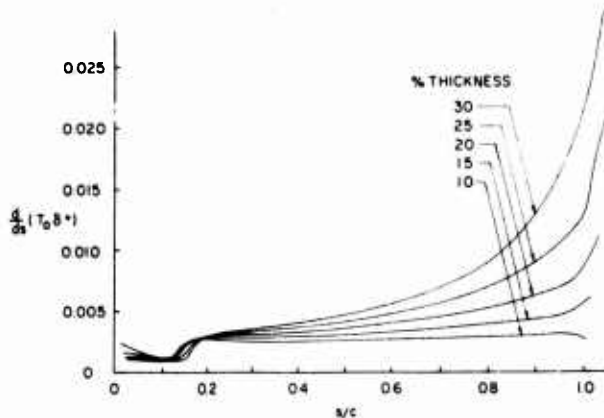


Figure 7. Derivatives of  $T_0 \delta^*$  for the five Joukowski airfoils. These are the boundary values that are used in the blowing suction.

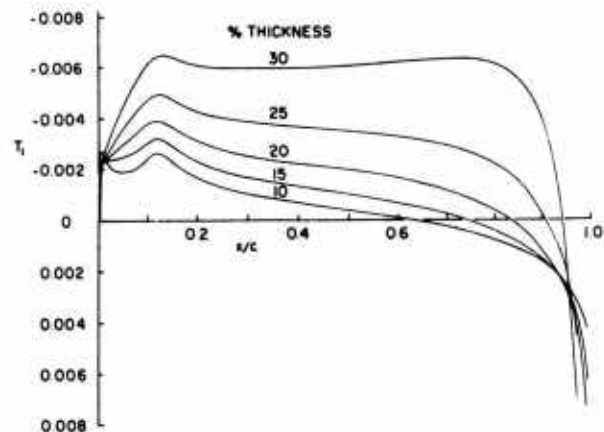


Figure 8. Blowing solutions for the five Joukowski airfoils. These are tangential velocity perturbations caused by the boundary layer. Because of symmetry, solutions only for the top side are shown.

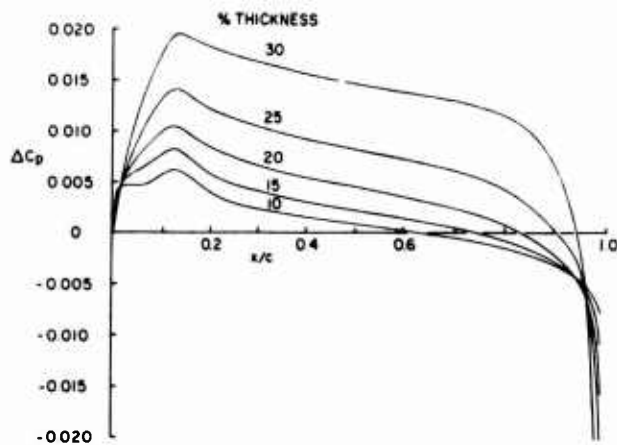


Figure 9. Perturbation pressures for the five Joukowski airfoils, due to the boundary layer.

forward regions but reduces it in the rear parts. The area under these curves is half the mean friction coefficient of the complete airfoil, see (23). Table 1 summarizes results of the calculations. The last column contains results from the Squire-Young momentum defect method which should be quite accurate for this problem. It, too, used the Cebeci-Smith boundary-layer method. Observe that the pressure drag goes negative. More will be said about this in the discussion.

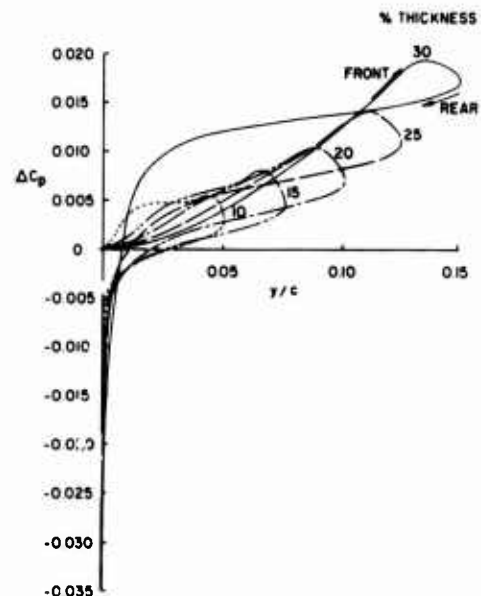


Figure 10. Perturbation pressures for the five Joukowski airfoils.  $y/c$  plots. Because of symmetry only top half shown.

Similar studies were made on the NACA 0010, 0015, 0020, and 0025 airfoils which have finite trailing edge angles. Results were generally similar to and consistent with the Joukowski set. They, too, showed negative pressure drag for the thickest airfoil. One calculation was done at  $\alpha = 6^\circ$ . The blowing

7-8

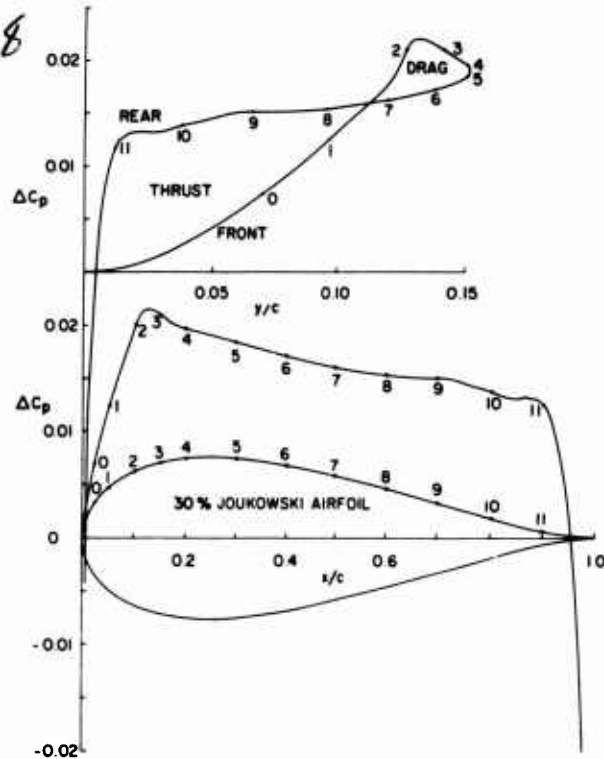


Figure 11. Illustration to increase understanding of drag loop. Numbered points are corresponding points on the three plots.

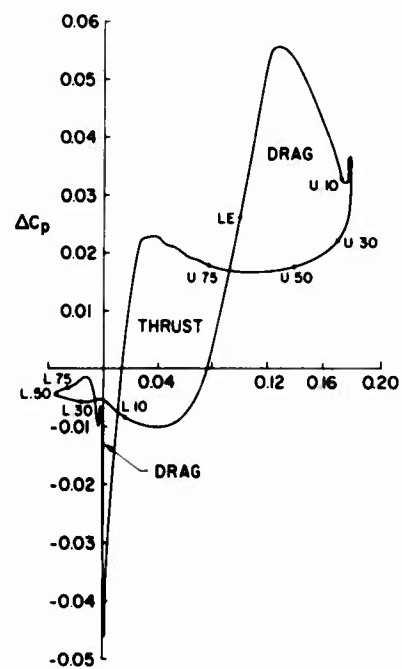


Figure 13. Pressure drag loop for NACA 0020 airfoil. Points on airfoil are noted along pressure distribution. Note that  $y$  is perpendicular to wind vector.

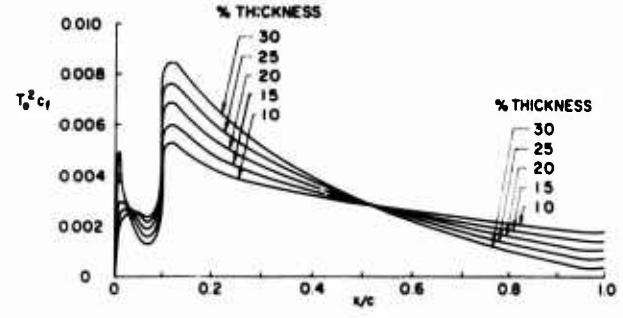


Figure 12. Skin friction distribution for the five Joukowski airfoils.

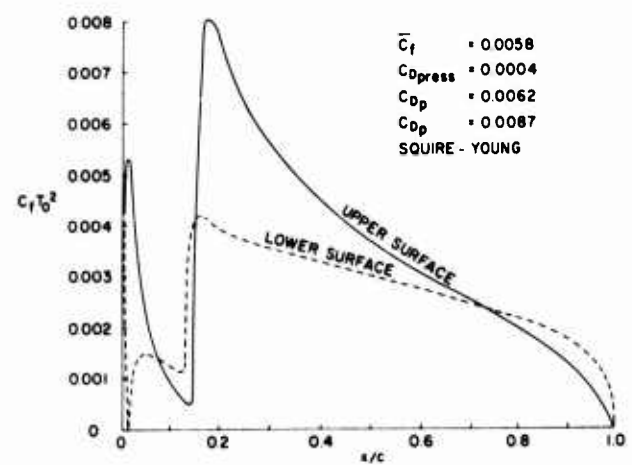


Figure 14. Skin friction distribution for NACA 0020 airfoil at  $\alpha = 6^\circ$ . Drag results are noted.

treatment accounted very well for the changes in pressure distribution due to viscous effects. Figure 13 shows the perturbation pressure loops and figure 14 the  $c_f$  distribution as well as final drag values. The pressure drag is barely positive and again the drag is considerably below the Squire-Young prediction, which is approximately correct.

By obvious modifications considering ring elements the method was adopted to bodies of revolution. Because they are the more critical two rather plump

Table 1. Final Results for the Five Joukowski Airfoils

Percent Thickness	$\bar{c}_f$	$C_{Dpress.}$	$C_{Dp}$	$C_{Dp}$ (Squire-Young)
10	0.0057	0.0005	0.0062	0.0065
15	0.0058	0.0007	0.0065	0.0072
20	0.0060	0.0007	0.0067	0.0080
25	0.0061	0.0004	0.0065	0.0090
30	0.0062	-0.0008	0.0054	0.0102

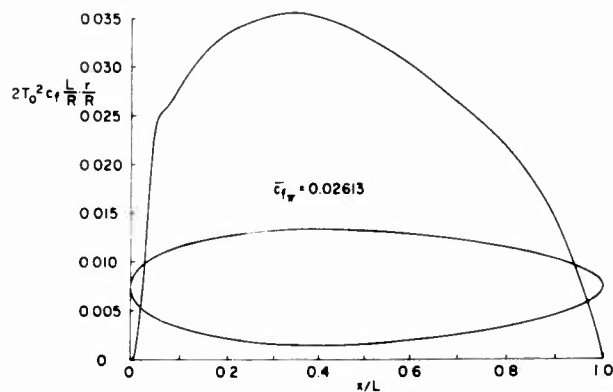


Figure 15. Shape and axial shearing stress distribution for XZS2G-1 airship.  
 $R_L = 188 \times 10^6$ .

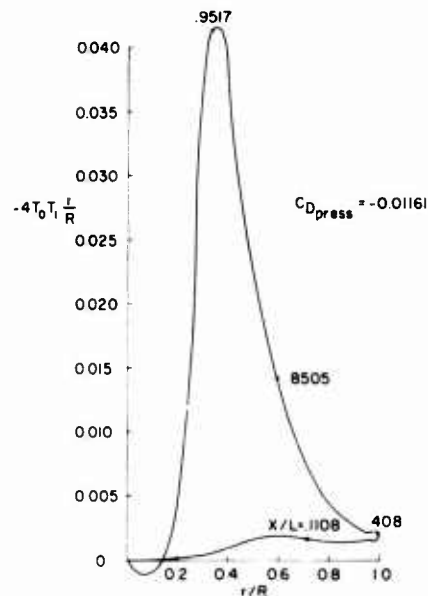


Figure 16. Pressure loop for the XZS2G-1 airship.

bodies were examined. Because results were rather similar we report only one, an airship that had extensive boundary-layer measurements in flight. Its shape and axial shearing stress distribution are shown in figure 15. Figure 16 shows the pressure force distribution. Again we find that the pressure drag is negative. The total drag coefficient based on frontal area  $C_{D_T}$  is 0.0145, a value ridiculously low.

#### 4.3 Discussion

After presentation of the past several results it hardly seems necessary to say that the method is quite unsatisfactory. The shear stress calculation appears quite satisfactory as far as we can tell without much further study. But the pressure drag calculation is all wrong. Exactly why is not really clear. The Douglas Neumann program appears to be giving correct answers for the boundary conditions that are given to it. It checks out with one known analytic solution.

The difficulties arise partly from improper boundary conditions over the last five percent or so of the body. The boundary condition is the derivative of  $T_0 \delta^*$  or its axially symmetric counterpart. Except for flow past cusps  $T_0$  goes to zero. Boundary-layer calculations would always indicate separation because boundary layers cannot decelerate to zero velocity in any finite distance. Then there is a strong interaction at the tail and the shape is so modified that  $T$  does not more go to zero. Furthermore, we know that  $\delta^*$  at the trailing edge is finite. Hence, so is the product  $T_0 \delta^*$ . But that is about all we know and it roughly amounts to saying that the product  $T_0 \delta^*$  is  $O(x^\infty)$  to give a finite number. But the only available way of estimating its value is to extrapolate. Because the slope near the tail is steep, extrapolation is most uncertain. It could be concave upward or concave downward. Slight differences could make large changes in the derivative of  $T_0 \delta^*$  which serves as the boundary condition. Hence, it seems that this method is very sensitive to values in the very region where our ability to calculate them is poorest.

Let us amplify these statements by considering figure 11 in some detail, where shape,  $\Delta C_p$  vs  $x/c$  and  $\Delta C_p$  vs  $y/c$  are shown. In the  $x/c$  plot the side stagnation point is very far back — at about 0.95c. Hence, forward of this point pressures are increased. Physically, it means that forward of 0.95c the blowing solution produces a tangential velocity in the upstream direction that reduces velocities, hence the positive values of  $\Delta C_p$ . The negative values of  $\Delta C_p$  that occur aft of 0.95c may be very large, but they occur in such a short distance that calculation accuracy will be poor, in addition to uncertainties in the boundary condition. On the  $y/c$  plot, while pressures over most of the airfoil are positive it is interesting to note that they are more positive at given  $y/c$  locations on the rear than on the front. Hence, much of the airfoil is undergoing a thrust force. If the net pressure force is to be a drag then the area inside the spike near  $y/c = 0$  must be much larger than the greatly spread-out area noted as thrust in the figure.

If there is a finite rate of blowing at the trailing edge of a cusped airfoil, the velocity at the trailing edge will be logarithmically infinite. There is probably the same kind of singularity for a finite wedge angle. This infinity and its effects are missed in a Douglas Neumann program because calculations are made at midpoints of elements. The significance of this fact is not known, but the effect amounts to a drag.

For approximating the effects of boundary layer by blowing, where should the pressures be calculated? Right on the surface or along the  $\delta^*$  streamline? We might assume these values are then impressed on the surface. Differences in values are considerable at the trailing edge. Some comparisons were made, but again changes in pressure drag answers were small.

### 5. AN IMPROVED MOMENTUM DEFECT METHOD

#### 5.1 Description

The second approach is to stick to the basic momentum defect method but try to improve the calculations in the wake, which means replacing the Squire-Young type of treatment by something better. A logical step is to try to solve the wake flow by continuing the boundary-layer calculations on past the tail or trailing edge of the body. That can be done in an approximate fashion by a simple modification of the C.S. boundary

7-9

1.10

layer program. Such is the second method. In actuality we attempt to solve the wake for only a short distance, about 1/4 to 1/2 chord length, and then apply Squire and Young's formula. By this procedure we get through the regions of very rapid change more accurately, and then apply Squire and Young's formula to conditions where it applies rather well. This combination procedure avoids lengthy calculations through a long run of wake flow.

Because the basic C.S. method has been described elsewhere [12], only a bare outline will be given here. The governing equations applicable to both two-dimensional and axisymmetric flow with transverse curvature effects are

$$\frac{\partial}{\partial x} (ru) + \frac{\partial}{\partial y} (rv) = 0 \tag{24}$$

$$\frac{u\partial u}{\partial x} + \frac{v\partial u}{\partial y} = -\frac{1}{\rho} \frac{dp}{dx} + \frac{1}{\rho r} \frac{\partial}{\partial y} \left( r \frac{\partial \tau}{\partial y} \right) \tag{25}$$

where for turbulent flow

$$\tau = \tau_l + \tau_t = \mu \frac{\partial u}{\partial y} - \rho \overline{u'v'} \tag{26}$$

and  $\rho \overline{u'v'}$  is the Reynolds stress due to the turbulence. Equations (24) and (25) are solved by an efficient numerical method described in [13]. The method uses the eddy-viscosity concept, where the eddy viscosity  $\epsilon_m$  is defined by

$$-\rho \overline{u'v'} = \rho \epsilon_m \frac{\partial u}{\partial y} \tag{27}$$

However, in the wake we find it more convenient to use the mixing length concept, that is

$$-\rho \overline{u'v'} = \rho l^2 \left( \frac{\partial u}{\partial y} \right)^2 = \rho (c_1 b)^2 \left( \frac{\partial u}{\partial y} \right)^2 \tag{28}$$

Here  $b$  is assumed to be a characteristic width of the wake flow. It is defined as follows:

$$b = y_2 - y_1 \tag{29}$$

where  $y_1$  is the value at which

$$\frac{u - u_c}{u_e - u_c} = 0.1 \tag{30a}$$

and  $y_2$  is the value at which

$$\frac{u - u_c}{u_e - u_c} = 0.9 \tag{30b}$$

For two-dimensional flows  $c_1$  is taken to be 0.125 and for axisymmetric it is 0.11. These values are arbitrary and quite empirical. Accurate wake calculations would demand much more sophisticated calculations of the Reynold's stress.

### 5.2 Results

Some of the basic character of the solutions is shown by figures 17, 18 and 19. Figure 17 is the simplest case, the wake downstream of a flat plate. What this figure shows is the calculated evolution of the wake, starting with test data at the first station,  $x = 0$ . At  $x = 0$  the initial profile was still a boundary layer, but in order to get started it was arbitrarily refaired near the center line as shown. Then with this initial profile the succeeding ones were calculated: Diffusion appears to be more rapid than calculated, see Sta. 240.

Figure 18 is the wake downstream of an airfoil. Initial calculations were begun by modifying the experimental data as shown. Then calculations were carried on downstream, subject to the local pressures that occurred at each station. The evolution of  $\theta$ ,  $H$  and the wake profiles are shown. Again the experimental rate of diffusion is greater than calculated.

Figure 19 presents results for a body of revolution. Again calculations were started with the slightly modified profile that was given at  $x = 0$ . This case appears to have about the same accuracy as the two-dimensional solution. Again calculated diffusion rates are low.

Figure 20 is an example of a true drag calculation. Here the boundary-layer growth was calculated from the very leading edge, including transition. The wake was calculated starting with the theoretical boundary-layer profiles at the trailing edge. Calculations were made at several angles of attack and the scatter band of the measured values is shown. The solid symbols are the classic Squire-Young result, based on the C.S. method of boundary-layer calculation. The open symbols denote wake calculations to the point where the symbol is located, at which point  $\theta$  is corrected to  $\theta_e$  by the Squire-Young formula (5). The resulting answers show improved accuracy. Very conveniently most of the improvement is picked up after only a short wake calculation. Wake calculations of length 1/4 to 1/2 chord are all that seem to do any good. In fact, several of the results drift away from correct values rather badly when calculations are continued more than one or two chord lengths downstream. One of the most encouraging results from figure 20 is that for  $\alpha = 8^\circ$ . In figure 1 it was pointed out that theoretical drag predictions are low at higher values of  $\alpha$ . That is just the case here for  $\alpha = 8^\circ$ , but the wake solution brings the theory right in line with test.

Figure 21 shows two more airfoils. The reason why predicted drag is high for the RAE 2815 is not known. It may be that the airfoil had more laminar flow than assumed. Nothing is said about this point in the references. Results for the RAE 2814 again show improvement over standard Squire-Young. Note that these two tests are at high subsonic Mach numbers. In these two cases trailing-edge profiles were known from experiment. Therefore, calculations began with this information.

### 5.3 Discussion

Attempts were made to calculate the drag of a plump streamline body, one of fineness ratio 4, but the deadline for this paper prevented completion. This particular body was studied because results are very good right now on ones of higher fineness ratio [17]. With fatter bodies the tail fairing is often so blunt that a slight bit of separation develops. That happened on the body studied. It makes the problem of

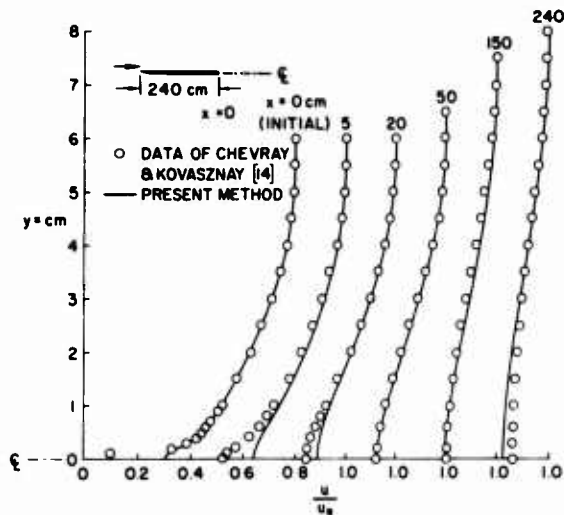


Figure 17. Evolution of the wake downstream of a flat plate. Comparison of calculations and experiment. Calculations began with the solid line at  $x = 0$ .  $R_c = 0.65 \times 10^6$ .

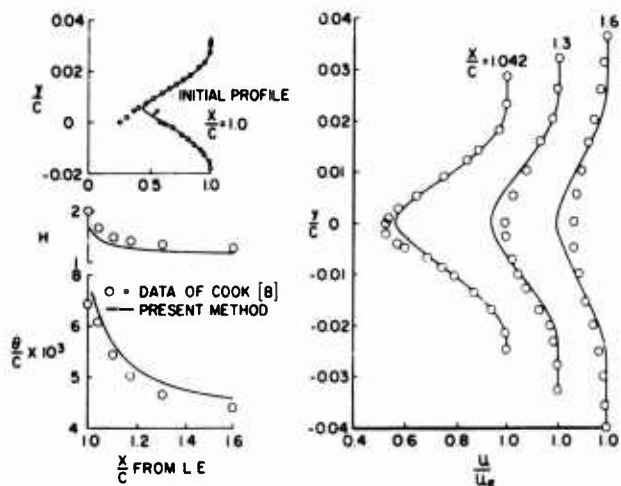


Figure 18. Evolution of the wake downstream of RAE 2815 airfoil at  $C_L = 0.51$ ,  $M = 0.661$  and  $R_c = 15 \times 10^6$ . Comparison of calculations and experiment. Calculations began with solid line shown at  $x/c = 1.0$ .

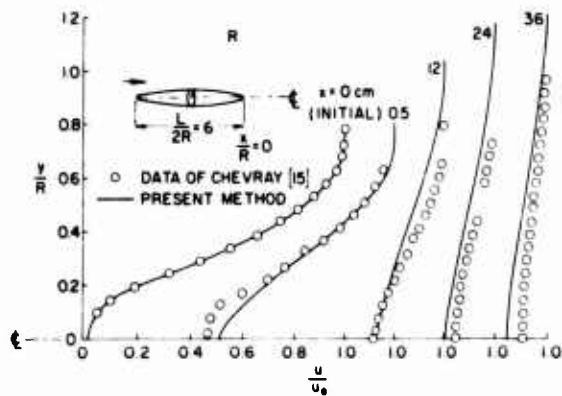


Figure 19. Evolution of the wake downstream of a prolate spheroid of fineness ratio 6. Comparison of calculations and experiment. Calculations began with solid line shown at  $x/R = 0$ .  $R_L = 2.75 \times 10^6$ .

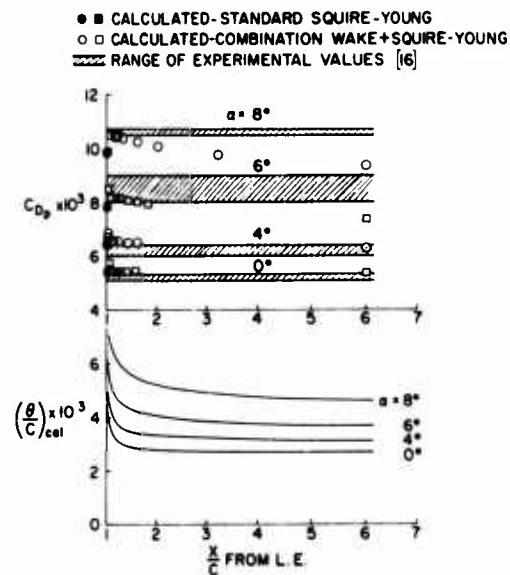


Figure 20. Drag predictions for the NACA 63018 airfoil made by partial calculation of the wake. Calculations in this case are absolute. The only data given was Reynolds number and coordinates of the airfoil.  $R_c = 5.8 \times 10^6$ . Solid symbols are standard Squire-Young results. Open symbols denote solution of wake to their location and then application of Squire-Young formula.

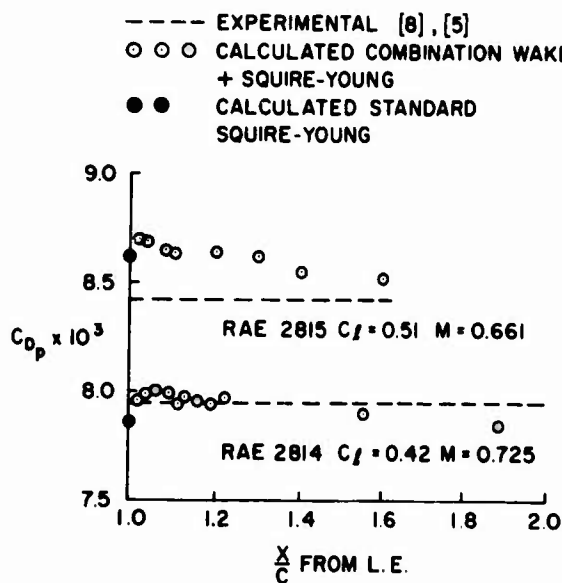


Figure 21. Drag predictions for the RAE 2814 and 2815 airfoils.  $R_c = 15 \times 10^6$ . Here calculations began with experimental profiles at the trailing edge.

improved prediction far more difficult, for now we must not only make an improved accounting for evolution of the wake, but also, in some manner must produce calculations across the separated region.

Nevertheless, the results are encouraging. Both axisymmetric and two-dimensional wakes have been calculated with accuracy acceptable for the present needs. (Almost any wake solution should be more accurate than the bold Squire-Young approximation.) For the airfoil cases where drag was actually calculated a definite improvement in accuracy was noted. This fact should lend encouragement to work along similar lines on the more difficult problem of drag of multielement surfaces.

Values of  $\theta$  at the trailing edge must not only be corrected accurately to conditions at infinity but they must be accurate in the first place. Often very near the trailing edge, especially at higher angles of attack, calculated values of  $\theta$  are low compared with experiment. Hence, in any attempt to improve

the accuracy of drag calculation both sources of error should be considered. We have not mentioned this defect in the boundary-layer calculations until this point mainly because that subject was not the basic purpose of the paper. But it should not be assumed that the boundary-layer calculations are exact.

## 6. CONCLUSIONS

The shear and pressure method seems to hold no promise, at least in the form presented in this paper. Drag results are very sensitive to the boundary values near the tail and require highly accurate calculations in that region. The momentum defect method does not show this same high sensitivity. Therefore, the correct course for improvement is to stick with the momentum defect method and improve it. A promising method for improving it is to perform direct numerical solutions of the wake through the initial regions of rapid change just beyond the trailing edge. After the region of large change has been traversed, then the Squire-Young relation is used to correct values to  $x = \infty$ . This course amounts to adding an intermediate step in the classical Squire-Young procedure.

## 7. REFERENCES

1. Cebeci, T., Mosinskis, G.J., and Smith, A.M.O.: Calculation of Viscous Drag in Incompressible Flows. *J. Aircraft*, Vol. 9, No. 10, Oct. 1972, pp. 691-692.
2. Nark, T.C., Jr.: Theoretical Prediction of Airfoil Drag Polars. SAE Paper No. 680200, April 1968.
3. Squire, H.B., and Young, A.D.: The Calculation of the Profile Drag of Airfoils. *British R&M* 1838, 1938.
4. Young, A.D.: The Calculation of the Total and Skin Friction Drags of Bodies of Revolution at Zero Incidence. *British R&M* 1874, 1939.
5. Firmin, M.C.P., and Cook, T.A.: Detailed Exploration of the Compressible Viscous Flow Over Two-Dimensional Aerofoils at High Reynolds Numbers. RAE Tech. Memo. Aero 1076, July 1968.
6. Lieblein, S., and Roudebush, W.H.: Low-Speed Wake Characteristics of Two-Dimensional Cascade and Isolated Airfoil Sections. NACA TN 3771, 1956.
7. Granville, P.S.: The Calculation of the Viscous Drag of Bodies of Revolution. D.W. Taylor Model Basin Report 849, 1953.
8. Cook, T.A.: Measurements of the Boundary Layer and Wake of Two Aerofoil Sections at High Reynolds Numbers and High-Subsonic Mach Numbers. RAE Tech. Rept. TR 71127, June 1971.
9. Pretsch, J.: Theoretical Solution of Profile Drag. NACA TM 1009, 1942.
10. Preston, J.H.: The Effect of the Boundary Layer and Wake on the Flow Past a Symmetrical Aerofoil at Zero Incidence. *British R&M* 2107, 1945.
11. Hess, J.L., and Smith, A.M.O.: Calculation of Potential Flow about Arbitrary Bodies. *In Progress of Aeronautical Science*, Vol. 8, Pergamon Press, 1966.
12. Cebeci, T., and Smith, A.M.O.: A Finite Difference Method for Calculating Compressible Laminar and Turbulent Boundary Layers. *ASME J. of Basic Engineering*, Sept 1970, pp. 523-535.
13. Keller, H.B., and Cebeci, T.: Accurate Numerical Methods for Boundary-Layer Flows. II. Two-Dimensional Turbulent Flows. *AIAA J.*, Vol. 10, No. 9, Sept. 1972, pp. 1193-1199.
14. Chevray, R., and Kovaszny, L.S.G.: Turbulence Measurements in the Wake of a Thin Flat Plate. *AIAA J.*, Vol. 7, No. 8, Aug. 1969, pp. 1641-1642.
15. Chevray, R.: The Turbulent Wake of a Body of Revolution. *J. Basic Engineering*, Vol. 90, Series D, No. 2, June 1968, pp. 275-284.
16. McCullough, G.B., and Gault, D.E.: Examples of Three Representative Types of Airfoil-Section Stall at Low Speed. NACA TN 2502, 1951.
17. Cebeci, T., Mosinskis, G.J., and Smith, A.M.O.: Calculation of Viscous Drag and Turbulent Boundary-Layer Separation on Two-Dimensional and Axisymmetric Bodies in Incompressible Flows. Douglas Aircraft Co. Rept. MDC J0973-01, 1970.
18. Callaghan, J.G., and Beatty, T.D.: A Theoretical Method for the Analysis and Design of Multi-element Airfoils. *J. Aircraft*, Vol. 9, No. 12, Dec. 1972, pp. 844-848.

BY

J.J. KACPRZYNSKI

National Research Council of Canada  
National Aeronautical Establishment  
Ottawa, Canada

8-1

SUMMARY

Analytical methods of evaluation of drag coefficients of contemporary supercritical airfoils are discussed. Some results of experimental values of drag coefficient for supercritical airfoils are compared against results of theoretical evaluations. Some results of drag coefficients of conventional airfoils are included for comparison. Difficulties of accurate experimental recording of drag coefficients are indicated.

1.0 INTRODUCTION

The advantage of application of contemporary airfoils have been already proven by flight tests. In an excellent way they were demonstrated by Polhamus (Ref. 1) and his two figures are repeated here (Fig. 1). They show that the replacement of conventional airfoils by contemporary ones gives the possibility either to increase, in the transonic regime, the flight Mach number by about 15%, or at the same speed to increase by over 40% the thickness of the wing. These improvements are possible due to higher drag rise Mach number of supercritical airfoils.

Designing new supercritical airfoils has become very popular and several methods are actually used, starting from empirical experimental, through empirical numerical (2) to highly sophisticated methods of Nieuwland (3) and Garabedian et al, (4). In the empirical methods a shape of the airfoil is assumed and the pressure distribution is verified by numerical calculations or by experiment. Usually many modifications of the airfoil shape are necessary in order to obtain an acceptable pressure distribution. In the design method of Garabedian the equation of motion are integrated in the hodograph plane for a certain flow field specified by about seventy parameters. Values of these parameters have to be guessed. It requires usually several hundred computer trials to obtain a closed contour, having acceptable shape and aerodynamic characteristics in shockless supercritical flow.

Although the purpose of designing new airfoils is drag reduction, actually in none of the design methods the value of the drag or drag rise Mach numbers are used in the process of designing except of course in the wind tunnel verification. Only in the Garabedian's method the drag coefficient appears as a parameter in shockless flow but it represents rather the thickness of the trailing edge than the drag itself.

Besides the drag at design conditions, the aerodynamic properties of an airfoil in off-design conditions are equally important and those cannot be determined in the design methods. Hence the performance of the airfoil has to be established either by direct calculations or by wind tunnel experiments.

Of existing methods of transonic flow calculations the numerical ones appear to be most useful. The actually used methods, in order to save computer time, assume that the flow is isentropic. Two basically different numerical approaches are used. In the first approach the problem is treated as unsteady and the steady solution is obtained by integrating in time using time dependent difference scheme. An example of this approach is Yoshihara-Magnus method (5), with integration in the physical plane. The second approach is based on the steady relaxation method, with solution of the linearised problem in the physical plane (e.g. Murman & Cole (6), Krupp (7), Steger and Lomax (8)), or of the nonlinear problem with integration in the Sells plane after mapping the exterior of the airfoil into the interior of the circle (Garabedian et al (4), Jameson (9), author (10)).

It has been shown that in some cases of supercritical flow both the time dependent difference method, and the steady relaxation methods give very good agreement with experiment and with inverse design calculations. As an example results for a Boerstoele's (11) shockless symmetrical airfoil 0.11-0.75-1.35 are shown in Fig. 2. Three cases of experimental pressure distributions (12, 13) are compared against the design pressure distribution and direct off-design calculations. The agreement is very good, and both the experiment and the calculations show large sensitivity to the change of flow parameters. The second example is also for a shockless airfoil but a lifting one (Fig. 3 and Ref. 15). This airfoil was designed by Garabedian and Korn for shockless inviscid flow at  $M = .75$ . In experiment due to the viscous effects the shockless flow appeared at

Mach number  $\approx .768$ . The blockage correction is of order .006 in this case, so the viscous corrections to the Mach number is of order .012. Additional comparisons for a conventional airfoil NACA 64A410 are shown in Fig. 4(16).

A comparison of calculated pressure distributions obtained by steady relaxation methods (9, 10) and by the time dependent method (17) for airfoil NACA 64A410 is shown in Fig. 5. It is a rather extreme case of very high local Mach number at which the isentropic solution becomes inaccurate. Nevertheless the general agreement is very good apart from the location and strength of the shock wave. It is known that steady relaxation methods do not satisfy the Rankine - Hugoniot condition at the shock wave. This can easily be corrected if the exact strength of the shock wave is essential.

An important question that arises whether the isentropic supercritical calculation can be used for the evaluation of drag. It is obvious that in the case of a mathematically correct solution of isentropic flow the wave drag should be zero by definition. It is actually zero (except truncation error) if one uses the isentropic equation in conservative form and the proper differencing scheme. On the other hand it is known (e.g. 18, 19, 20) that the weak discontinuous solution to the isentropic problem does not conserve the momentum in the direction normal to the shock, and this feature can eventually be used as a mechanism for the representation of drag.

Because the mathematically correct solution of the nonisentropic problem is economically prohibitive, attempts to evaluate the drag from isentropic flow have been made by many authors. Recently Steger and Baldwin (20) tried to give a physical interpretation of the "shock losses" in isentropic flow, using Oswatitsch theorem (21) that drag of the body in steady flow is related to the entropy change and can be approximated by the expression

$$D \approx \frac{T_{\infty}}{V_{\infty}} \int_F \rho V_n (S - S_0) dF$$

where  $T_{\infty}$ ,  $V_{\infty}$  are the temperature and velocity in free stream,  $\rho$  density,  $V_n$  normal component of velocity and  $F$  is a surface extended over all sources of entropy changes.

Applying the Oswatitsch formula along a closed contour indicated by the dotted line in Fig. 6 all the conservative equations are satisfied and hence drag in isentropic flow is zero. Steger and Baldwin (20) explain that non satisfied x momentum through the shock has the physical meaning of a thrust, which must be equal but opposite to the drag obtained from integration of the pressure distribution along the airfoil. They further develop the method of numerical calculations of the drag by integration along the shock, which in the case of the linearised relaxation method gives better accuracy than integration along the contour of the airfoil. In the case of the nonlinear solution with integration in the Sells plane, the integration along the surface of the airfoil can be done very accurately. All the data presented in this paper have been obtained using integration along the contour of the airfoil.

## 2.0 CALCULATIONS OF DRAG IN INVISCID FLOW

The integration of the pressure distribution on the surface of the airfoil is used to calculate the drag. The pressure distribution is calculated using steady relaxation method for isentropic flow (10). Some results are presented here. In Fig. 7 inviscid drag results are compared with experimental wake drag data from high Reynolds number tests (12, 13), and low Reynolds number NLR results (22). The agreement in the drag rise Mach number is very good. Results of calculations of drag for NACA 0012 airfoil (23) compared with experimental data obtained at NAE by Dixon (24) are shown in Fig. 8.

A comparison of calculated drag with experimental data for the shockless lifting airfoil No. 1 (14, 15) is shown in Fig. 9 and for airfoil NACA 64A410 in Fig. 10. One can see that for the same lift coefficient and Mach number the drag of airfoil NACA 64A410 is much higher than the drag of shockless airfoil No. 1, although this latter airfoil is about 11.6% thick.

From the above comparisons it appears that isentropic supercritical flow drag calculations predict quite well the drag rise Mach number, although the actual values of drag coefficients are not correct.

### 3.0 APPROXIMATE VISCOUS FLOW CALCULATIONS

In many cases results of inviscid flow calculations do not agree with results of test due to the viscous effects. In some cases the differences are small so that inviscid calculations for the same lift coefficient do not differ very much from test results, in the other cases the differences are very large.

Many ways of including viscous effects have been tested numerically. Some of the conclusions and results of performed numerical experimentations are collected here.

The most elementary way of including viscous effects is by adding to the airfoil the displacement thickness of the boundary layer, recalculate the pressure distribution for a modified airfoil, repeat the boundary calculations and so on until the process converges. Unfortunately it has not been possible to obtain a convergent solution. Just stopping the iterations at a certain point may show some improvement compared to the completely inviscid flow, but it does not represent the actual flow, because the boundary layer thickness is incorrect and in some cases even small differences in the boundary layer thickness have very large effects.

The viscosity of the flow changes the flow past the airfoils by

1. Changing the thickness of the airfoil
2. Changing the camber
3. Influence of wake

These three effects were tested in a simplified way in numerical experimentation. The calculations were performed in the Sells plane. The supercritical inviscid calculations are performed by marching along the surface of the airfoil from leading edge to trailing edge on the upper surface and on the lower surface independently. At each point of the surface a potential solution is solved in the column extending from the surface of the airfoil to the origin of the circle representing infinity. The boundary layer calculations in most methods are performed in the same way by marching with the integration from the leading edge towards the trailing edge. In the case of very thin boundary layer the boundary condition can be satisfied not at the edge of the boundary layer but on the surface of the airfoil itself. For relatively low lift coefficients, so that the camber of the airfoil is not changed, the change of the mapping function of the airfoil into the circle may be neglected. In this case the boundary layer changes only one boundary condition in the Sells plane from

$$\frac{\partial \phi}{\partial r} = 0 \quad \text{in inviscid flow}$$

to

$$\frac{\partial \phi}{\partial r} = - \frac{\partial \bar{\delta}^*}{\partial \theta} \frac{\partial \phi}{\partial \theta} \quad \text{for } r = 1$$

where  $\bar{\delta}^*$  is the non-dimensional displacement thickness transformed into Sells plane.

Modifying in this way the boundary condition for the supercritical calculations and at each point of the surface of the airfoil evaluating the boundary conditions from a solution of the boundary layer, it is possible to obtain a convergent solution, if the thickness of the boundary layer is under-relaxed. The process of iteration is nearly twice slower than for inviscid flow calculation. Additional time is necessary for boundary layer calculation, so the total calculating time is up to three times longer than for the inviscid flow. In the above process the boundary layer was calculated using the Nash - MacDonald method (24). Some of the results of viscous flow calculations performed for airfoil NACA 65<sub>1</sub>-213 are shown in Figs. 11 - 12 with comparison against NACA flight results (26) and wind tunnel tests performed at NAE by Brown (27). The results of viscous flow calculations show better agreement with flight test and wind tunnel test than the inviscid calculations. The drag versus Mach number is shown in Fig. 13. This airfoil at these flow conditions represents a case where camber changes due to viscosity are small; airfoil itself has low camber, lift coefficient is low, so the boundary layer develops nearly symmetrically on both sides of the airfoil.

The same method has been applied for the shockless lifting airfoil No. 1 and the results are shown in Fig. 14. In this case the viscous drag calculations agree with wake drag results but it is an exception.

It is important to underline that both cases represent one group for which the inviscid flow results calculated for experimental lift coefficients give good agreement with experiments. The viscous effects are mainly accounted for by a change of incidence of the airfoil and thickness effects have rather secondary influence.

As previously mentioned, calculated inviscid results do not agree with tests in many cases and small changes of incidence or Mach number in the calculations do not produce better agreement. In the process of including viscous corrections it was discovered that the disagreements are caused by changes of the camber of the airfoil by boundary layer development, namely by decreasing it. Hence in such cases it is necessary to introduce modifications of the mapping function correcting the shape of the airfoil by slightly modified boundary layer. It is a very difficult and computer time-consuming process and it follows that the viscous corrections cannot be treated as a small perturbation of inviscid flow any more. An example of experimental calculations for airfoil "x" is shown in Fig. 15 in comparison with wind tunnel tests performed by Bowker (28) at Reynolds number  $14.6 \times 10^6$ . The viscous calculations were stopped after 1000 iterations with residue .00031, so the iterations had not fully converged. The viscous calculations were performed at Reynolds number  $Re = 21.10^6$  and  $M = .74$  and  $\alpha = 0^\circ$ . The lift coefficient is .448 against .89 in inviscid flow. The experimental data with similar lift coefficient happens to be at lower Reynolds number. This comparison shows that the influence of the viscous effects is very significant and the viscous calculations show the right trend. It appears that in this case the boundary layer is separated on the lower surface in the region  $.675 < x/c < .92$ . On the upper surface the boundary layer separates at  $x/c = .98$ . The calculated drag coefficient is .006, while the experimental value is .0084.

This example illustrates tremendous viscous effects for some airfoils. Unfortunately, modifications of the mapping function (in calculated case about 100 times) is very computer time-consuming.

A modification of the mapping function in an empirical way as it was done nearly forty years ago for incompressible flow by Pinkerton (29) is rather impossible because too many parameters have an influence, namely Mach number, Reynolds number, lift coefficient and geometry of airfoil. Therefore, it may be more economical to perform the viscous flow calculations in the physical plane, where calculations of the mapping functions are not necessary.

Some numerical studies of the effects of the wake on the shockless lifting airfoil No. 2 were performed by adding a wake in an artificial way. No conclusive results were obtained, but it seems that the wake has rather secondary effect on pressure distribution in transonic flow. A correct way of evaluating the wake effect would be by solving the near-wake problem, which is a problem by itself.

From the numerical experimentation it can be concluded that the viscosity has the largest influence through modification of the camber of the airfoil.

#### 4.0 FLOW PAST SHOCKLESS LIFTING AIRFOIL NO.2

The discussed above shockless airfoils, symmetrical one and lifting No. 1 were designed for inviscid flow, and no changes to the shape of models were introduced with an exception of replacement of the cusped trailing edges by edges with finite thickness. In the case of the lifting airfoil No. 1 the experimental Mach number for the shockless flow had to be increased from design one  $M = .75$  to .765 and .768 for 6 and 20% porosity of the wall of the wind tunnel respectively. The actual "blockage" corrections were much smaller ( $\nu.003 \div .006$ ). Hence the experimental higher Mach number was necessary to compensate the viscous effects. It was thought that by modifying the shape of the airfoil by subtracting the boundary layer thickness calculated for a certain Reynolds number, this discrepancy in the Mach number value could be eliminated and a better condition for a shockless flow could be created, which will lead to a lower drag.

This airfoil section was designed by Frances Bauer and P.R.Garabedian. It is a 15.1% thick airfoil and its design Mach number is  $M = .75$  for shockless flow with a lift coefficient  $C_L = .667$ . The design drag coefficient, which actually represents the thickness of the trailing edge and not the drag itself, is .0334. The design shape of the airfoil with characteristics in the supersonic region is shown on the left side of Fig. 16. The boundary layer thickness was calculated at Reynolds number  $20.10^6$  using the Nash-MacDonald method. After subtracting the displacement thickness, the airfoil shape indicated by a dotted line B was used for manufacturing a wind tunnel model and for further calculations. It was expected that if the boundary layer calculations were correct, then in the flow at  $Re = 20.10^6$  the design pressure distribution indicated on the left side of Fig. 16 should be obtained in the wind tunnel tests. The inviscid pressure distribution calculated by the author for the thinner airfoil B are shown on the right side of the Fig. 16. It has completely different character than the design pressure distribution, with supersonic region terminated by a very strong shock wave. The maximum local Mach number was  $M_{10c} = 1.68$ , so the isentropic approximation is not

8-4

valid any more. Supercritical airfoils with such strong shock waves are usually rejected. The calculated inviscid flow lift coefficient  $C_L = 1.183$  is nearly twice higher than the design one at the same angle of attack  $\alpha = 0$ . The comparison of these two pressure distributions illustrates how important in some cases the viscous effects can be. Differences of this magnitude have been observed for many airfoils in supercritical flow. In many cases the inviscid flow calculations show very strong shock wave while in the experiments the shocks are weaker and the lift coefficients are much smaller.

In recently performed wind tunnel tests (30) the design pressure distribution was not obtained, which is not surprising, because it was known a priori that the Nash-MacDonald method used for the boundary layer calculations is not very accurate. Unfortunately none of the existing boundary layer methods is accurate in the transonic regime. For the theoretical design case it was not possible to obtain shockless flow, and the experimental lift coefficient was much lower than expected. After very careful experimentation it was possible to find two regions of shockless or nearly shockless flow at much higher Mach numbers, one nearly shockless flow at  $M = .767$  with  $C_N = .585$  and the second one with much smoother termination of the supersonic region at  $M = .778$  and with  $C_N = .494$ . The discovered nearly shockless pressure distributions are shown in Figs. 17 and 18. To illustrate how sensitive the shockless flow is to small perturbations of the flow parameters, some pressure distributions are presented in Fig. 19. For the same Mach number  $M = .778$  pressure distributions at the end of the supersonic region are shown at three incidences different from one another by  $.03^\circ$ . The middle one corresponds to near shockless conditions, changing the angle of attack by only  $.03^\circ$  in one or the other direction causes the appearance of shock waves. The strength of the shock wave increases rapidly with change of the angle attack. It is important to underline that the obtained drag coefficient for this 15% thick airfoil is really very low at shockless flow -  $C_{d_w} = .0115$  for  $C_N = .494$  and  $M = .778$ . Comparison of the drag coefficient with shockless lifting airfoil No. 1 (11.6% thick) shows that both airfoils have identical drags at  $M = .778$ ,  $C_N = .494$ , although the airfoil No. 2 is 15% thick.

On the other nearly shockless flow condition slightly poorer pressure distribution was obtained (Fig. 17). The lift coefficient was  $.585$  and at  $M = .767$   $C_{d_w} = .0125$ . Hence from the drag point of view this airfoil is very good at shockless condition. Unfortunately preliminary analysis of the experimental data indicate that the general characteristics of this airfoil are not very good. For example, for the same angle of attack in the wind tunnel as for shockless flow at  $M = .76$ , but at a Mach number  $M = .85$  and  $Re = 20.10^6$ , the velocities on the lower surface increase so much that the pressure distribution is nearly symmetrical on the upper and lower surface. Strong shock waves develop on both surfaces and lift drops to zero. By increasing angle of attack it is possible to obtain lift at this Mach number but with very high drag and with the shock on the upper surface at the trailing edge. The angle of zero lift of this airfoil at low speeds is  $-4.426^\circ$  and changes significantly with Mach number. The maximum lift coefficient is rather low at high  $M$ .

## 5.0 EXPERIMENTAL EVALUATION OF DRAG

The experiments were performed in the NAE 5x5 ft blowdown wind tunnel with two-dimensional insert with dimension 15 x 60 inches (Fig. 20). In order to eliminate interactions between shock waves and boundary layers on the side walls of the tunnel in the vicinity of the model sidewall suction is applied (Fig. 21). The amount of suction is selected during the test in such a way that the best possible two-dimensional flow is obtained. Oil drops flow visualisation is used to check two dimensionality of the flow. Sidewall body-axis balances are used to measure total forces. Surface pressure is recorded at eighty points using scanivalves. Wake pressure profiles are measured at four cross-sections normal to the trailing edge.

The experimental measurements of drag in transonic flow have the usual difficulties connected with drag measurements, namely due to the low values of drag, good accuracy is difficult to obtain. In transonic drag testing one additional difficulty appears, namely, however carefully the sidewall suction is selected, it is not possible to have completely two-dimensional flow on the model. The recorded values of the wake drag are not uniform along the span of the model, with differences of order up to 30%. Some examples selected at random are shown in the table below.

Airfoil	Shockless Symmetrical	Shockless Lift.1	Shockless Lift.2
$C_N$	0.130	.464	.351
M	.792	.801	.758
$Re.10^{-6}$	25.1	20.1	20.3
Central probe	.0096	.01768	.01141**
$C_{d_w}$	Probe II	.00891	.00966
	Probe III	.00876	.01299
	Near wall probe	.0522*	.11434*

\* affected by sidewall boundary layer

\*\* the location of the probes for airfoil S.L.II was different than for the other airfoil.

In the tests no tripping of the boundary layer was used. In all results presented by the author only the data obtained from the central probe have been used to represent the experimental drag. From the above table it is obvious that it is rather difficult to determine what the actual wake drag is. The balance drag indicates a certain average value for the model.

In order to determine the repeatability of the experiment, four scans were performed during one wind tunnel run on shockless lifting airfoil No. 2 at a fixed angle of attack higher than for shockless conditions. Fig. 22 shows signals from the pressure transducers for the four scans as printed on an XY-plotter. The outputs, printed one on the other, show only some scatter near the shock wave. This data after data reductions are shown in Fig. 23. The repeatability of results is excellent. The corresponding aerodynamic data are as follows:

Scan	1	2	3	4
M	.770	.770	.771	.771
$Re.10^{-6}$	24.78	24.80	24.80	24.68
$\alpha_g^*$	1.983	1.981	1.981	1.981
$C_N$ pressure	.530	.534	.531	.538
$C_N$ balance	.551	.510	.509	.509
$C_C$ balance	.00865	.00872	.00875	.00886
Wake 1 (central)	.01310	.01260	.01134	.01235
Wake 2	.01108	.01106	.01038	.01059
Wake 3	.01193	.01505	.01336	.01397
Wake 4 (near wall)	.00859	.01078	.01368	.01076

The small oscillation of the shock wave causes oscillations of the wake, which may account for the rather large variations in wake drag.

## 6.0 CONCLUSIONS

1. It has been shown that the application of contemporary airfoils gives possibility of increasing flight Mach number in transonic speeds or allows for application of thicker wings.
2. In all existing design methods of contemporary airfoils the drag coefficient is not taken into account.
3. The accurate analytical determination of the drag coefficient requires solution of the non-isentropic problem and is not possible because of costs.
4. The estimation of the drag coefficients from isentropic supercritical pressure calculations gives inaccurate values of drag, but indicates quite accurate drag rise Mach number.
5. Supercritical viscous flow calculation is possible.
6. Shockless lifting airfoils have drag coefficients much lower than conventional airfoils.
7. On the basis of the experience with only one airfoil (shockless lifting II) it is difficult to generalize on the usefulness of subtracting the boundary layer thickness in order to obtain a better airfoil. The expected low drag was obtained, but the general off-design characteristics

of this airfoil was worse than for the shockless lifting airfoil No.1.

8-7

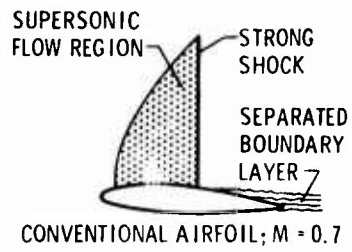
8. Inviscid supercritical flow calculations are very useful in evaluating the general characteristics of the airfoil and allow to guess when the viscous effects are important by indicating regions of large pressure gradients and shock waves, although their strength is not indicated correctly. If in the inviscid flow the shock waves are weak, then they are much weaker in viscous flow.
9. In the two-dimensional transonic testing at NAE it has not been possible to obtain a fully two-dimensional flow even by using sidewall suction and the drag varies significantly along the span making it difficult to establish an accurate drag value.

#### REFERENCES

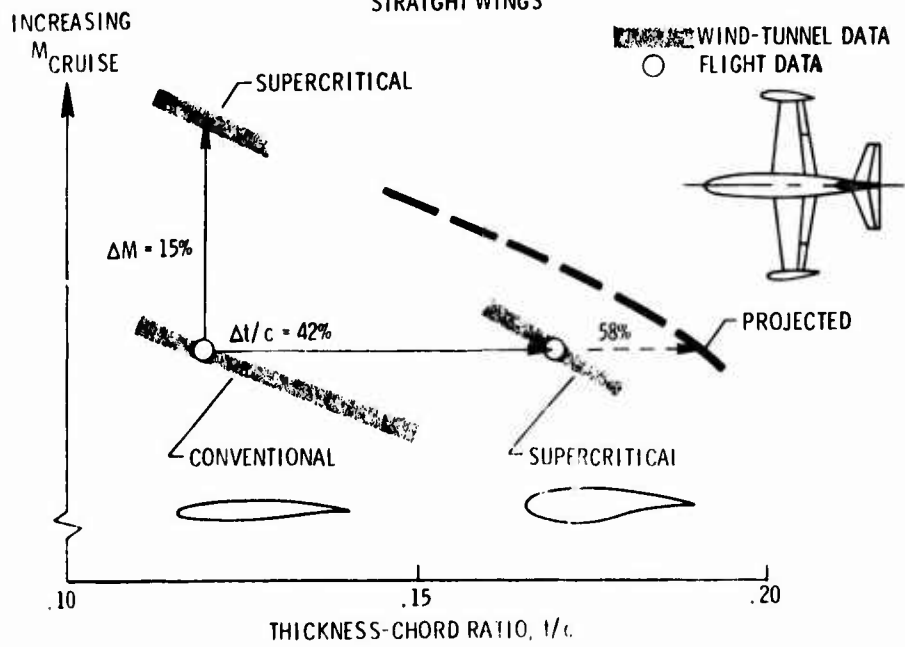
1. Polhamus, E.C., Subsonic and transonic aerodynamic research, NASA SP-292.
2. Kacprzynski, J.J., Study of feasibility of designing supercritical airfoils through direct supercritical flow calculations. NRC/NAE LTR-HA-12, 1973 (Confidential).
3. Nieuwland, G.Y., Transonic potential flow around a family of quasi-elliptical airfoil sections. NLR Report T.R. T.172 (1967).
4. Bauer, F., Garabedian, P., Korn, D., Supercritical wing sections, Springer Verlag, 1972.
5. Magnus, R, and Yoshihara, H., Steady inviscid transonic flows over planar airfoils, NASA CR No.2186, 1972.
6. Murman, E.M., and Cole, J.D., Calculations of plane steady transonic flows. AIAA Journal, Vol.9, pp.114-121 (1971)
7. Krupp, J.A., The numerical calculation of plane steady transonic flows past thin lifting airfoils. Boeing Sci. Res. Lab. Rep. D180-12958-1, Seattle, 1971.
8. Steger, J.L., and Lomax, H., Numerical calculation of transonic flow about two-dimensional airfoils by relaxation procedures. AIAA 4th Fluid and Plasma Dynamics Conference, Palo Alto, Calif. June 1971.
9. Jameson, A., Transonic flow calculations for airfoils and bodies of revolution. Grumman report 390-71, 1971.
10. Kacprzynski, J.J., Extension of the Sells method to supercritical flow calculations (not published)
11. Boerstael, J.W., A survey of symmetrical transonic potential flow around quasi-elliptical airfoil sections. NLR-TR T.136, Jan 1967.
12. Kacprzynski, J.J., Wind tunnel investigation of a Boerstael shockless symmetrical airfoil 0.11-0.75-1.375. NRC/NAE Project Report 5x5/0061(1972)
13. Kacprzynski, J.J., Analysis of the flow past the Boerstael shockless symmetrical airfoil 0.11-0.75-1.375. NRC/NAE LTR-HA-10 (1973).
14. Kacprzynski, J.J., Ohman, L.H., Garabedian, P.R., Korn, D.G., Analysis of the flow past a shockless lifting airfoil in design and off-design conditions. NRC/NAE LR-554(1971)
15. Kacprzynski, J.J., A second series of wind tunnel tests of the shockless lifting airfoil No. 1, NRC/NAE Project Report 5x5/0062 (1972)
16. Ohman, L.H., Kacprzynski, J.J., Brown, D., Some results from tests in the NAE high Reynolds number two-dimensional test facility on "shockless" and other airfoils. ICAS Paper No.72-33, 1972.
17. Yoshihara, H., A survey of computational method for 2D and 3D transonic flows with shocks. Lecture notes for AGARD-VKI Lecture Series No.64, 1972.
18. Lax, P., Weak solution of nonlinear hyperbolic equations and their numerical calculation. Comm. on P. and Appl. Math., Vol. VII, 1959.
19. Lomax, H., Kutler, P., Fuller, F.B. The numerical solution of partial differential equations governing convention. AGARDograph 146-70, 1970.
20. Steger, J.L., Baldwin, B.S., Shock waves and drag in the numerical calculation of isentropic transonic flow. NASA TN D-6997, 1972.
21. Oswatitch, K. Gas Dynamics, Academic Press Inc., 1956.

22. Spee, B.M., Uijlenhoet, R., Experimental verification of shock-free transonic flow around quasi-elliptical aerofoil sections. NLR-MP 68003U, 1968.
23. Kacprzyński, J.J., Theoretical studies of the inviscid transonic flow past airfoil NACA 0012. NRC/NAE LTR-HA-9, 1973.
24. Dixon, R.C. Private Communication.
25. Nash, J.F., MacDonald, A.G.J., The calculation of momentum thickness in a turbulent boundary layer at Mach number up to unity. ARC - CP No.963, 1967.
26. Brown, H.H., Clousing, L.A., Wing pressure measurements up to 0.866 Mach number in flight on jet-propelled airplane. NACA TN 1181, 1947.
27. Brown, D. Private Communication.
28. Bowker, A.J. Private Communication.
29. Pinkerton, R.M., Calculated and measured pressure distributions over the midspan section of the NACA 4412 airfoil, NACA report 563, 1936.
30. Kacprzyński, J.J., Wind tunnel test of the supercritical flow past shockless lifting airfoil No. 2 (in preparation).
31. Ohman, L.H., Brown, D., Private Communication.

### SUPERCRITICAL AERODYNAMICS TWO-DIMENSIONAL



### APPLICATIONS OF SUPERCRITICAL AIRFOIL STRAIGHT WINGS



POLHAMUS, NASA SP-292

Fig.1 Advantages of application of supercritical airfoil

### NLR SHOCKLESS SYMMETRICAL 0.11-0.75-1.35

8-10

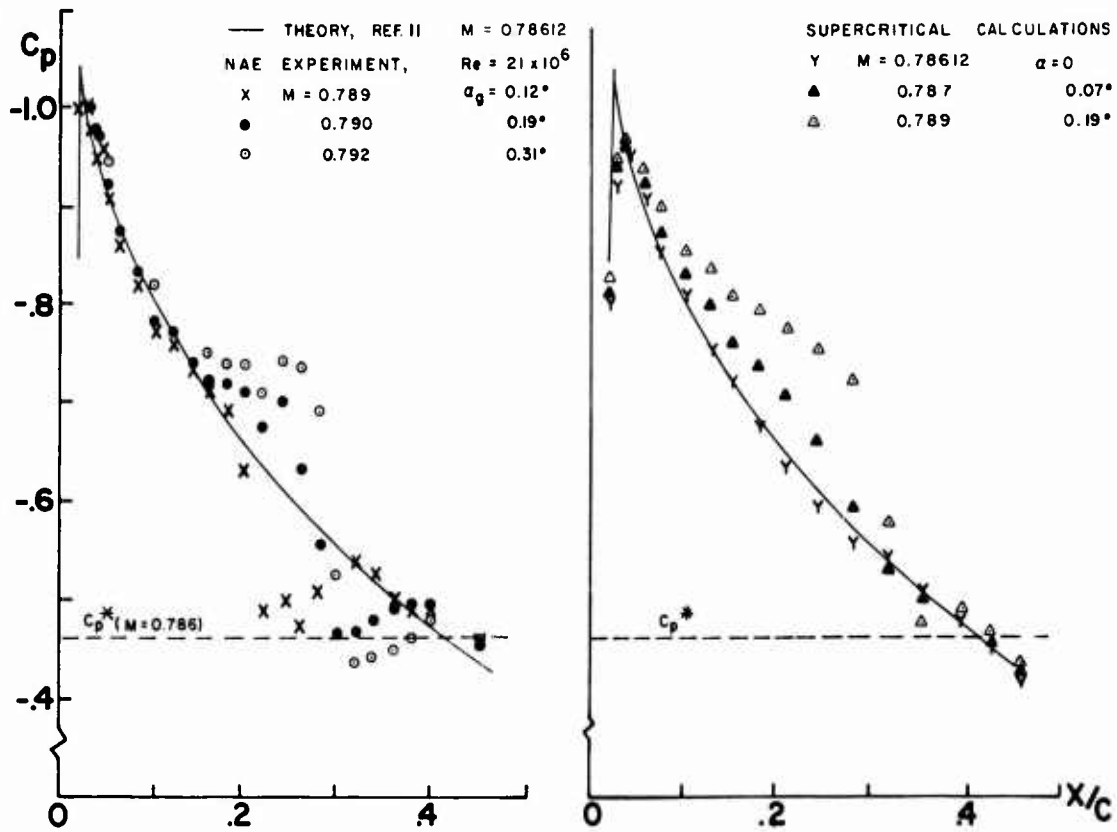


Fig.2 Pressure distribution on Boerstool shockless symmetrical airfoil 0.11-0.75-1.35 at near design flow conditions

### SHOCKLESS LIFTING I

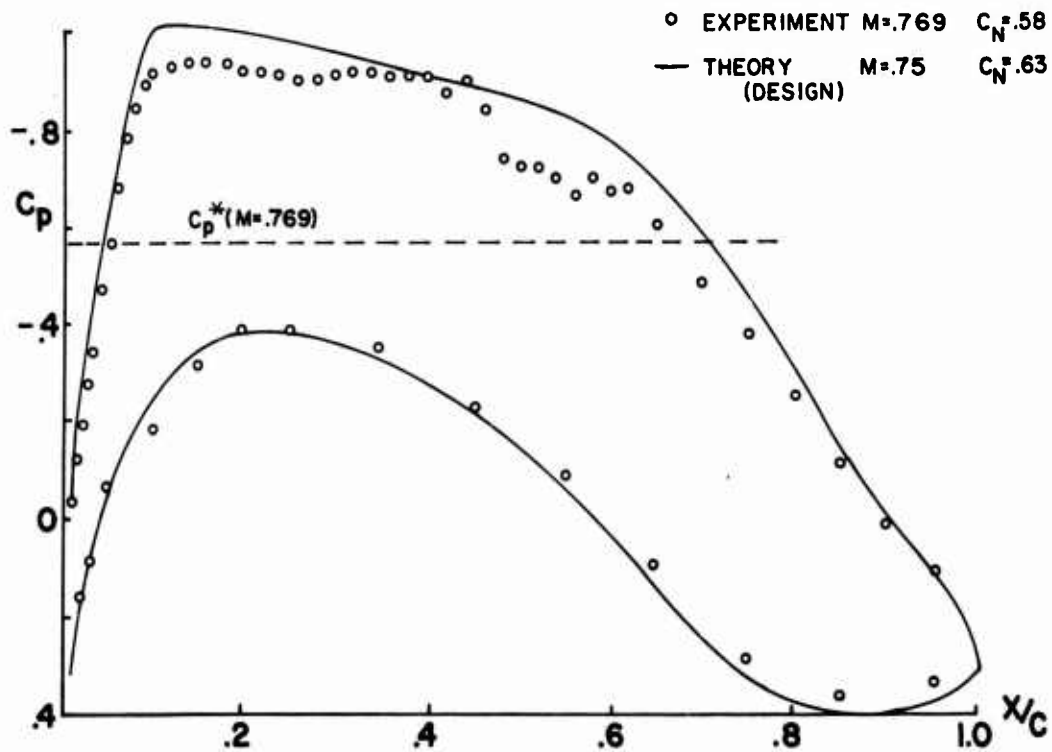


Fig.3 Pressure distributions on Garabedian-Korn shockless lifting airfoil No.1 at design flow conditions

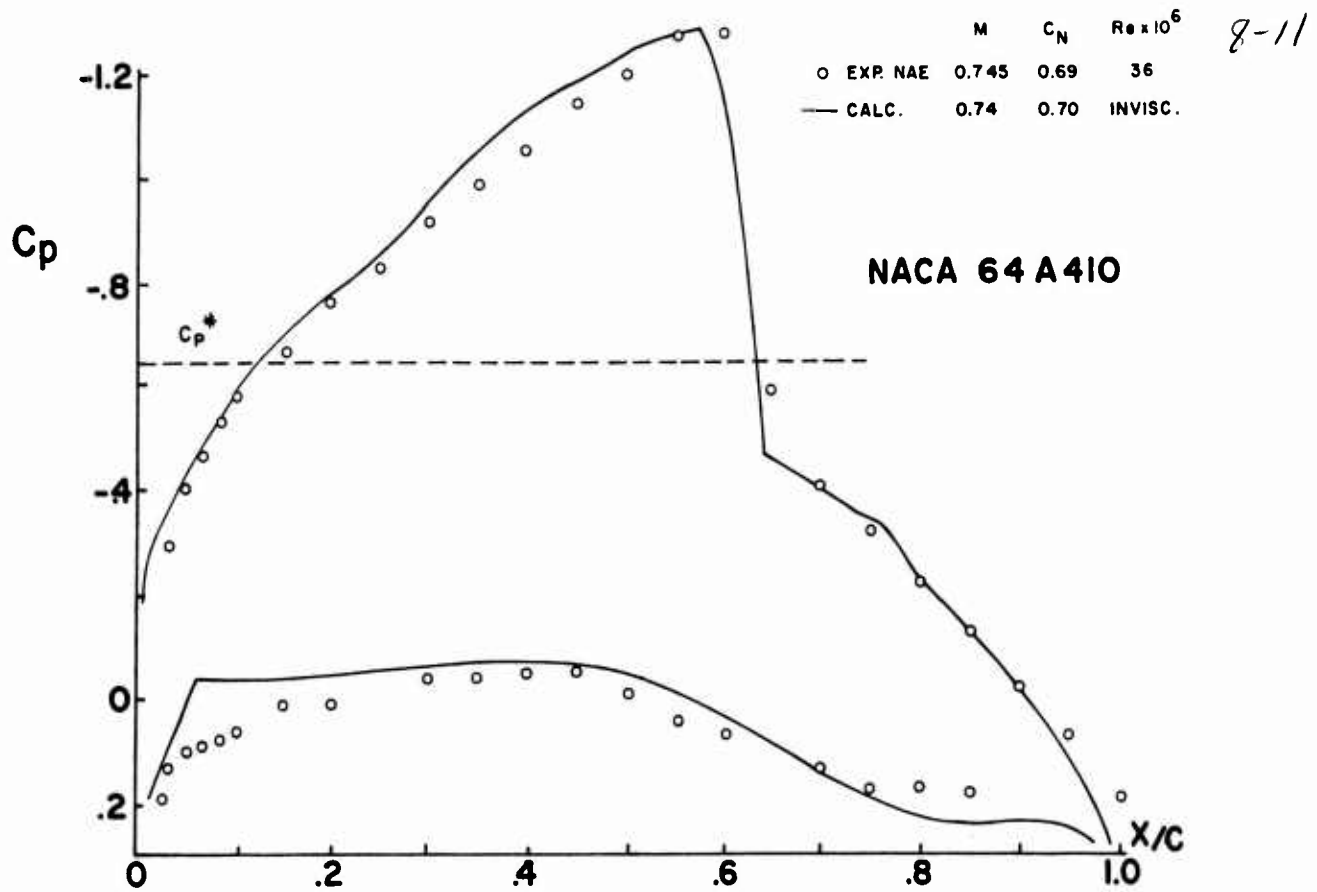


Fig.4 Comparison of pressure distribution on airfoil NACA 64A410

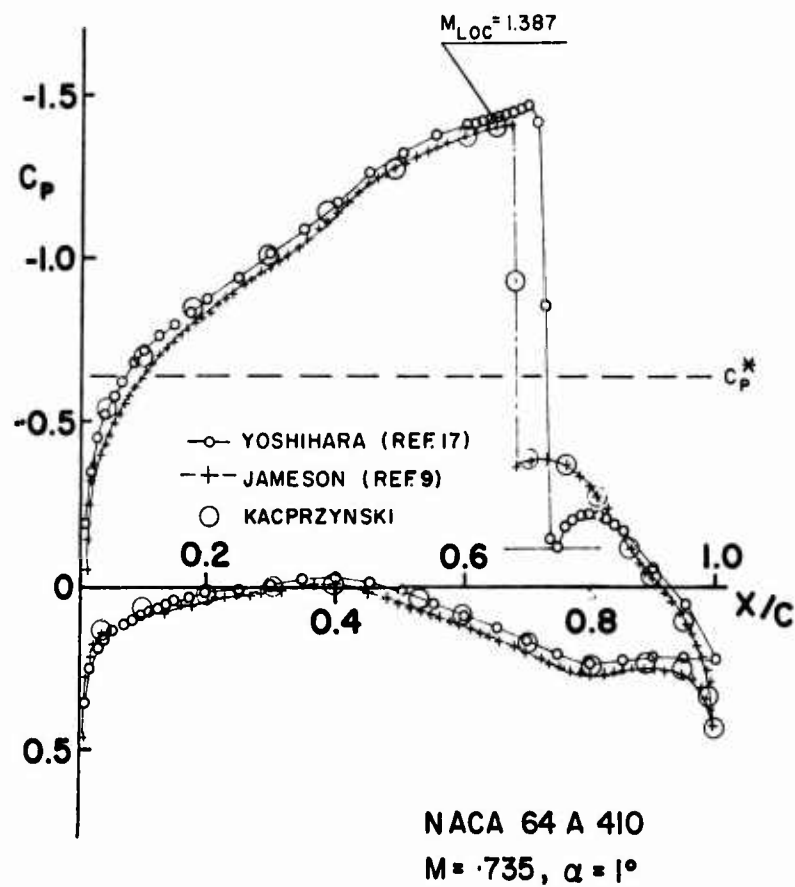


Fig.5 Comparison of pressure distributions calculated by time dependent method (Yoshihara) and steady relaxation methods

8-12

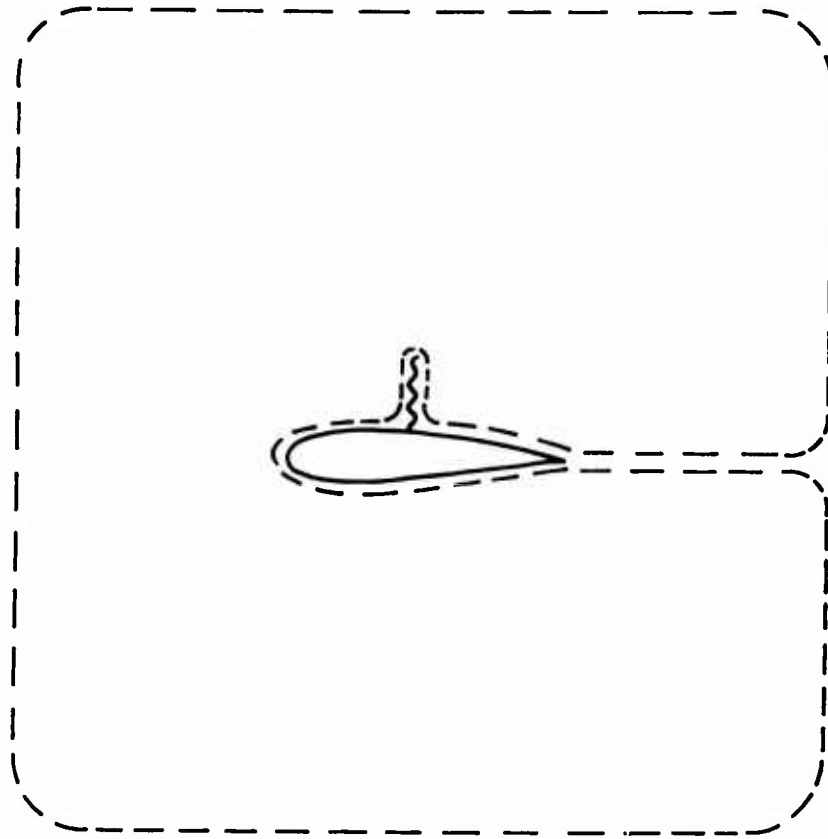


Figure 6

### NLR SHOCKLESS SYMMETRICAL 0.11-0.75-1.375

× INVISCID CALCULATIONS  
○ NAE  $Re = 21 \times 10^6$   
TEST  $D_w$  { --- NLR FREE TRANSITION }  $Re \approx 2 \times 10^6$   
          { ——— NLR FIXED TRANSITION }

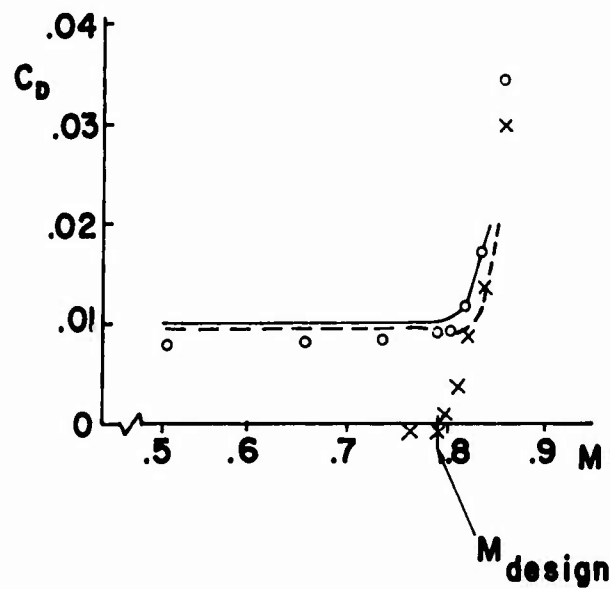


Fig.7 Drag of shockless symmetrical airfoil

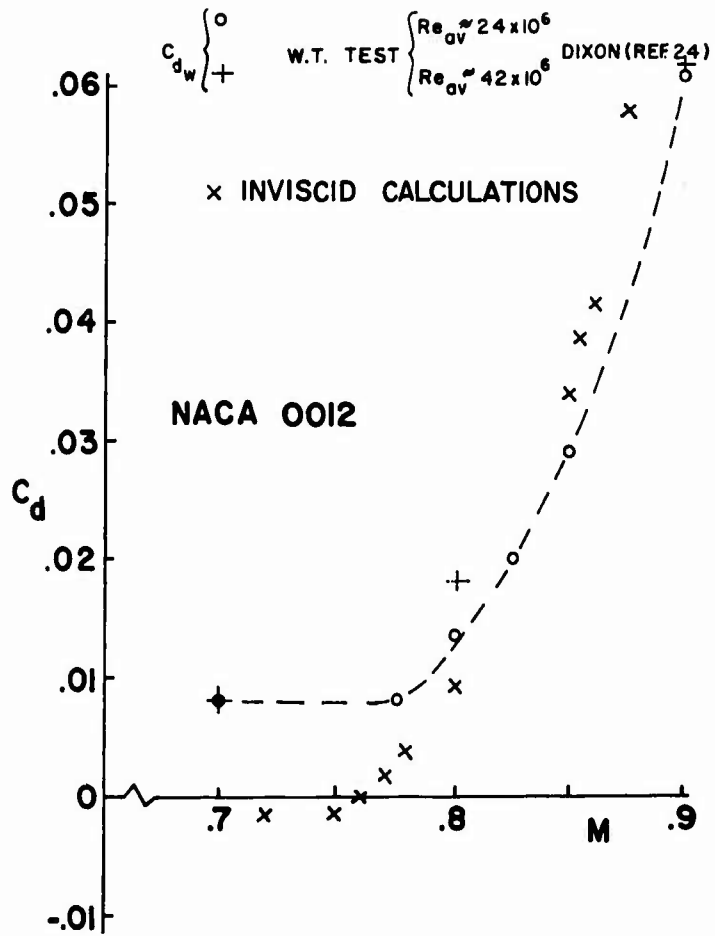


Fig.8 Drag of airfoil NACA 0012

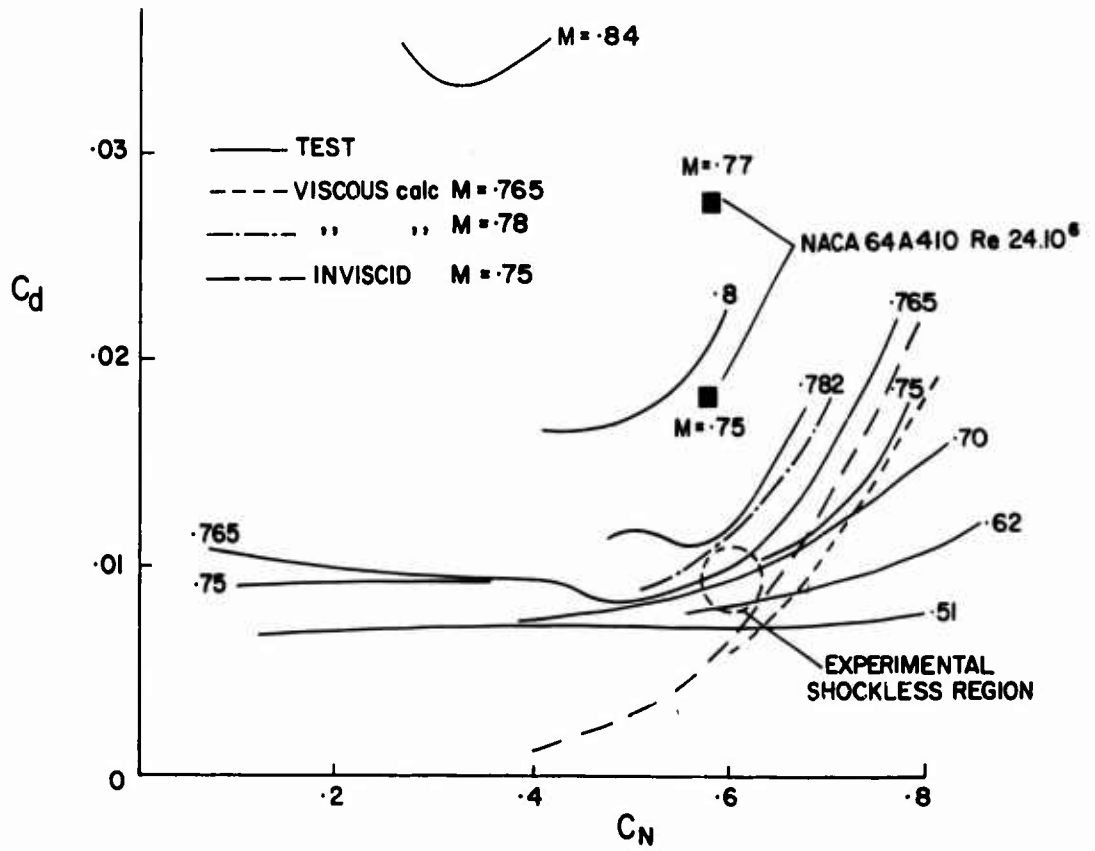


Fig.9 Drag of shockless lifting airfoil No.1

8-14

NACA 64 A 410

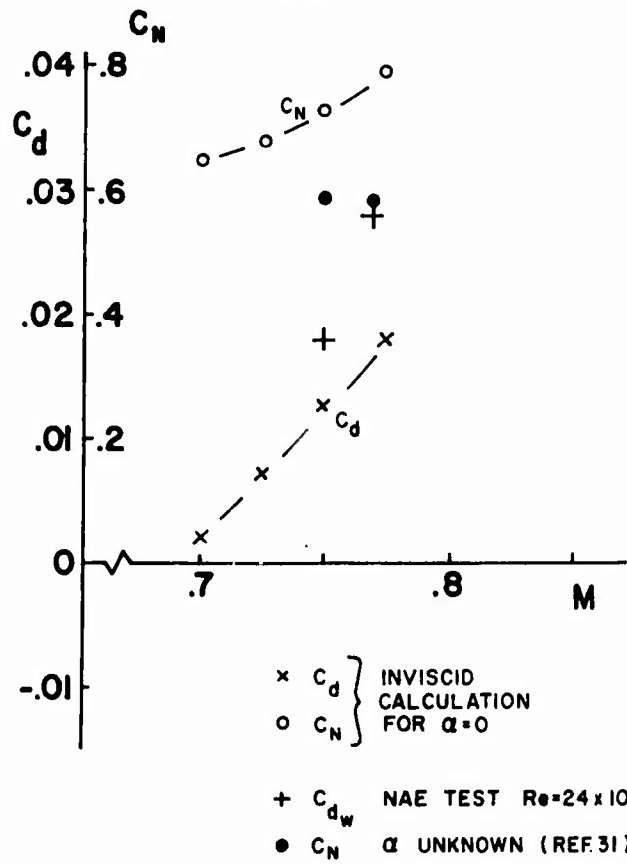


Fig.10 Drag of airfoil NACA 64A410

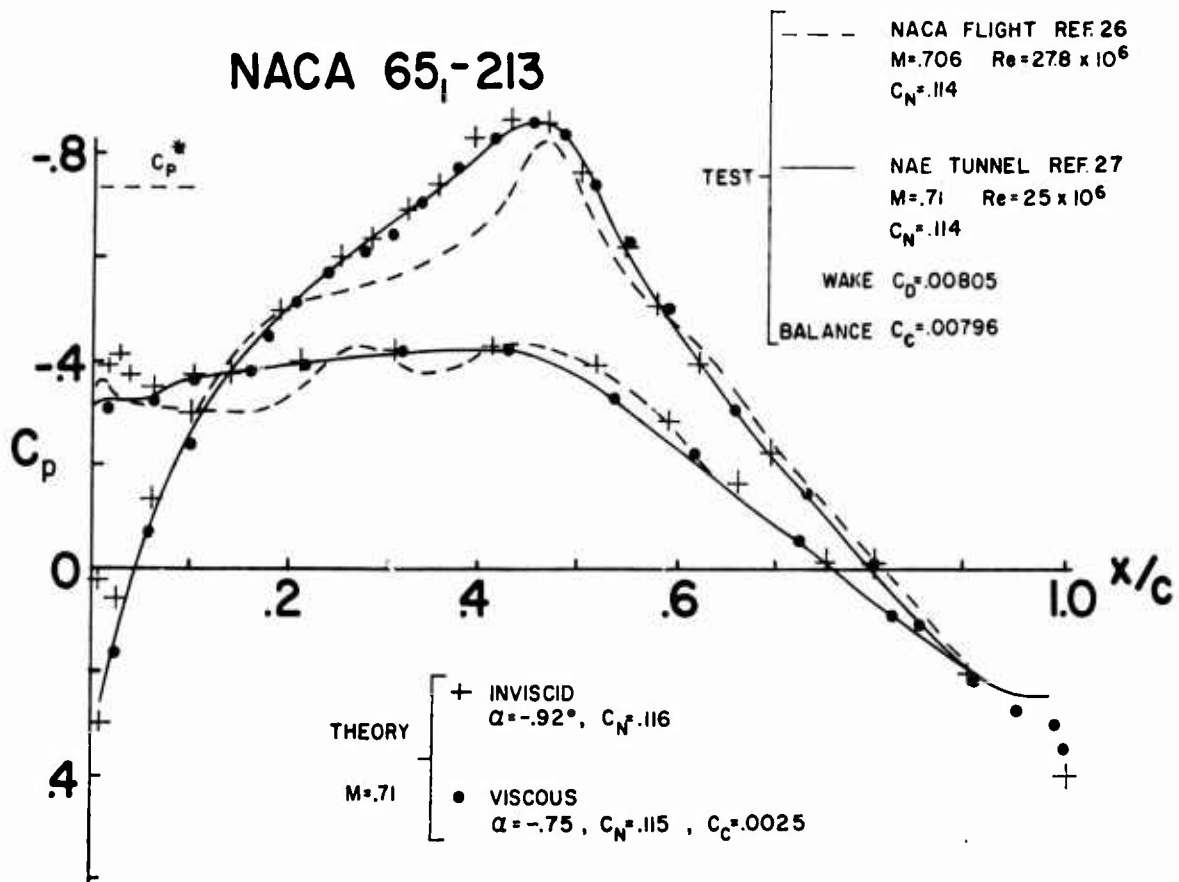


Fig.11 Pressure distributions on airfoil NACA 65, - 213

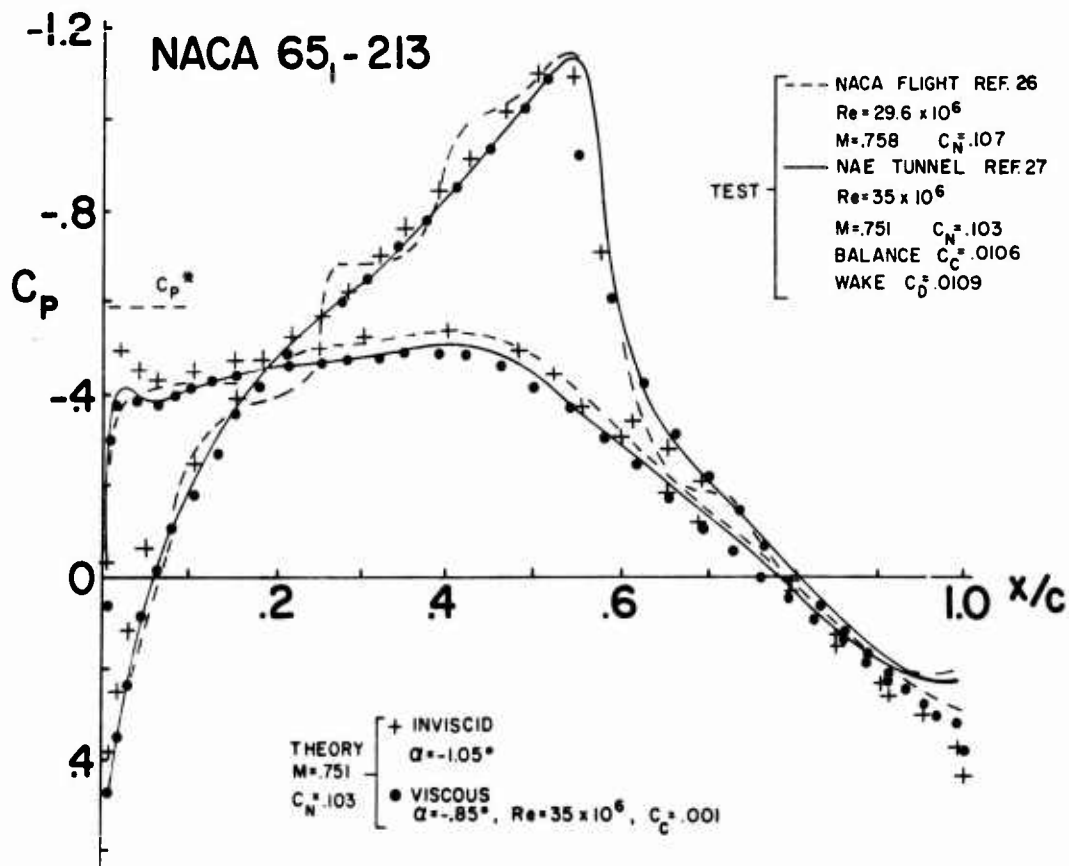


Fig.12 Pressure distributions on airfoil NACA 65<sub>1</sub> - 213

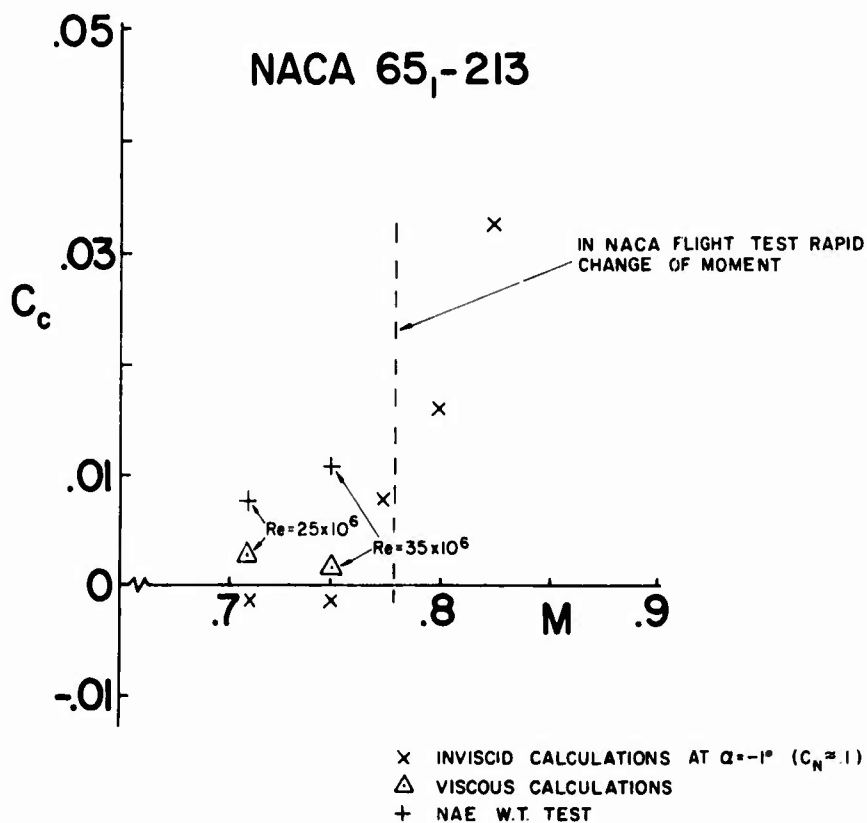


Fig.13 Drag of airfoil NACA 65<sub>1</sub> - 213

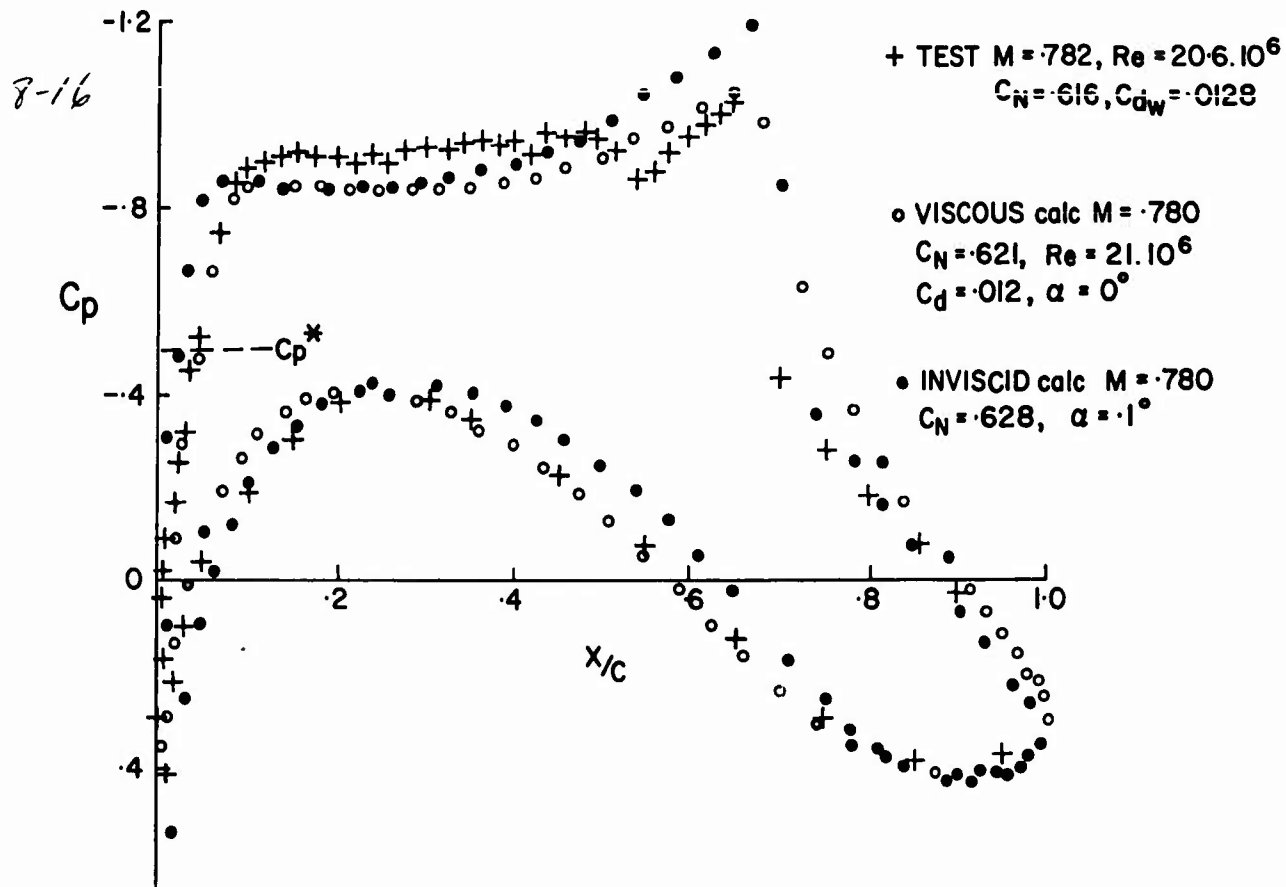


Fig.14 Pressure distribution on shockless lifting airfoil No.1

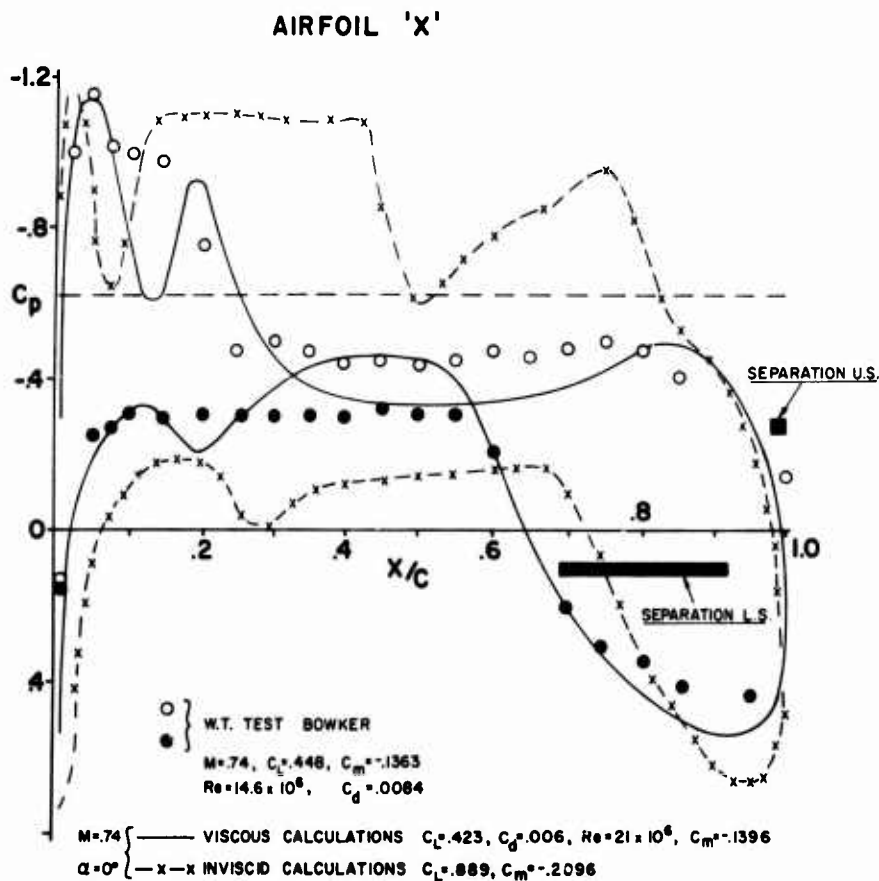
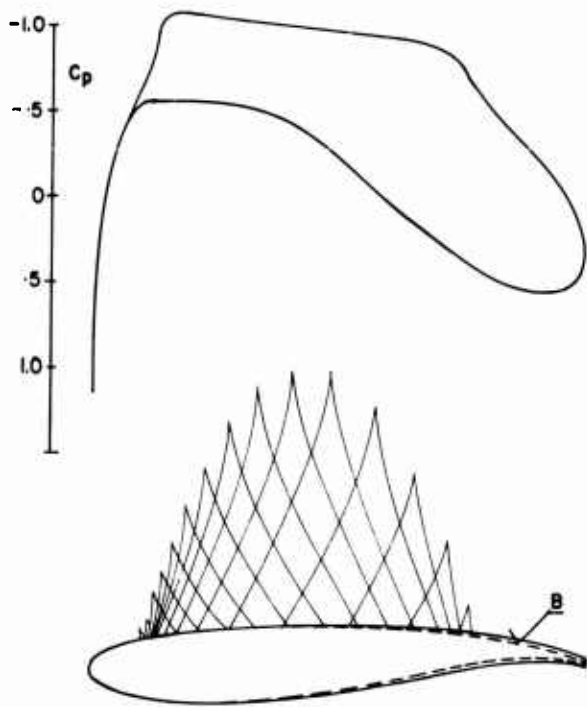
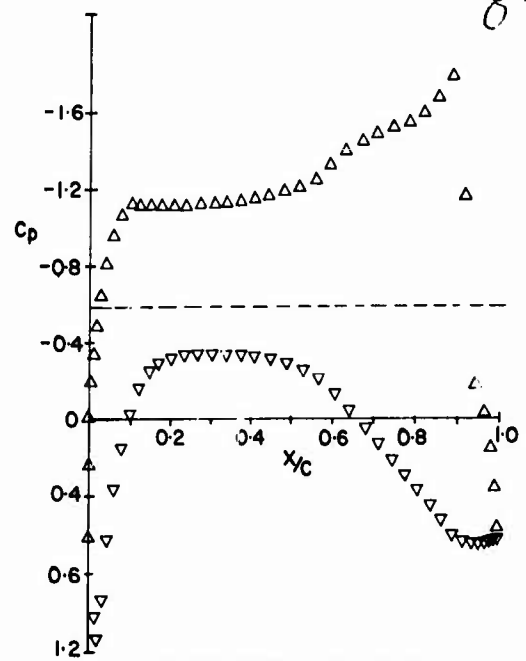


Fig.15 Pressure distribution on supercritical airfoil "X"



$M = .75$     $C_L = .687$     $C_d = .0334$     $T/C = .151$



INVISCID FLOW PAST AIRFOIL B  
OF  $M = .75$ ,  $\alpha = 0^\circ$ ,  $C_L = 1.1834$

Fig.16 Shockless lifting airfoil No.2

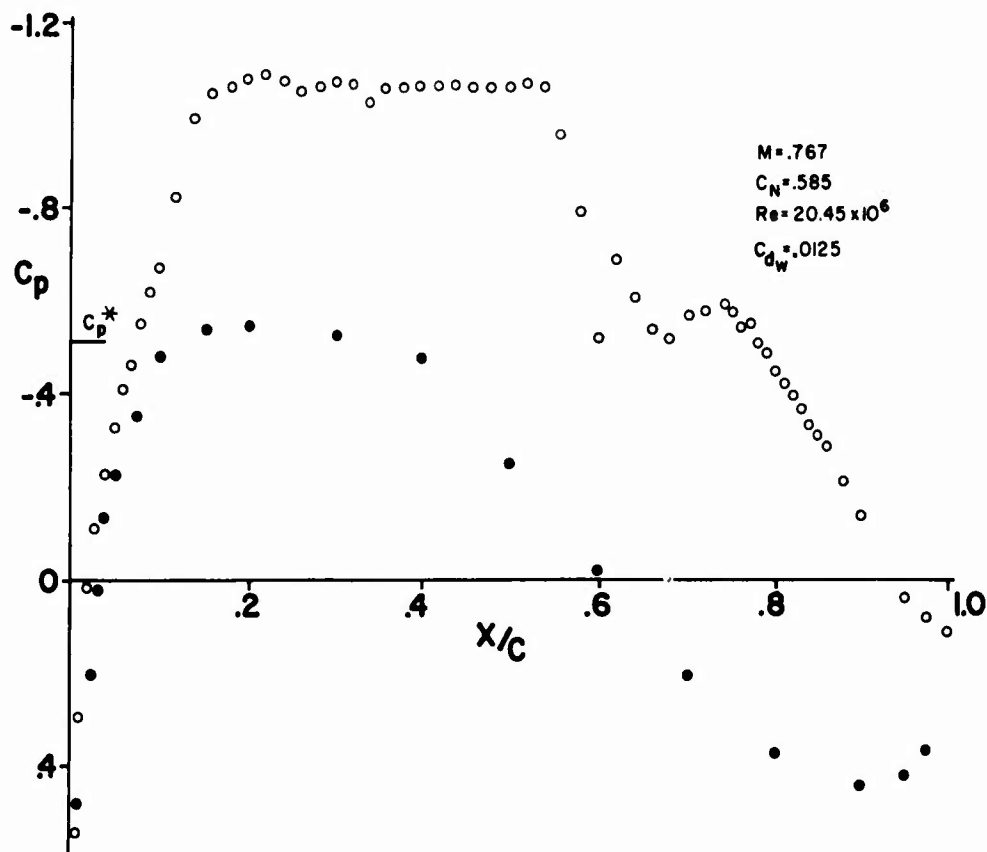


Fig.17 Pressure distribution on shockless lifting airfoil No.2 at near shockless flow at  $M = .767$

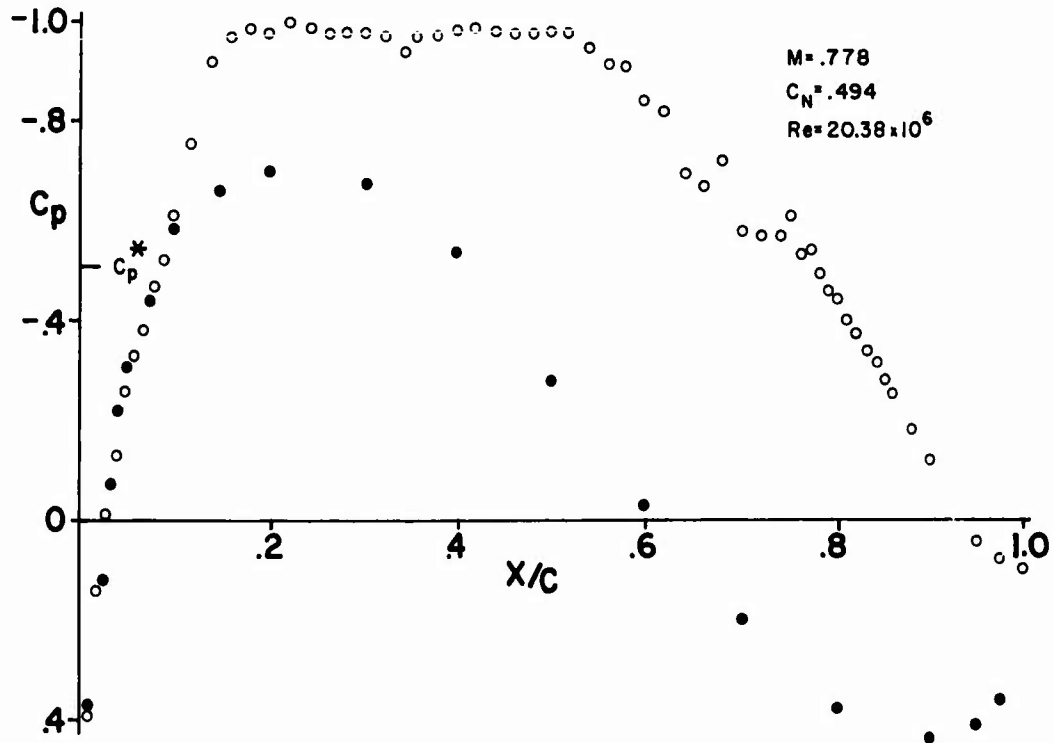


Fig.18 Pressure distribution on shockless lifting airfoil No.2 at shockless flow at  $M = .778$

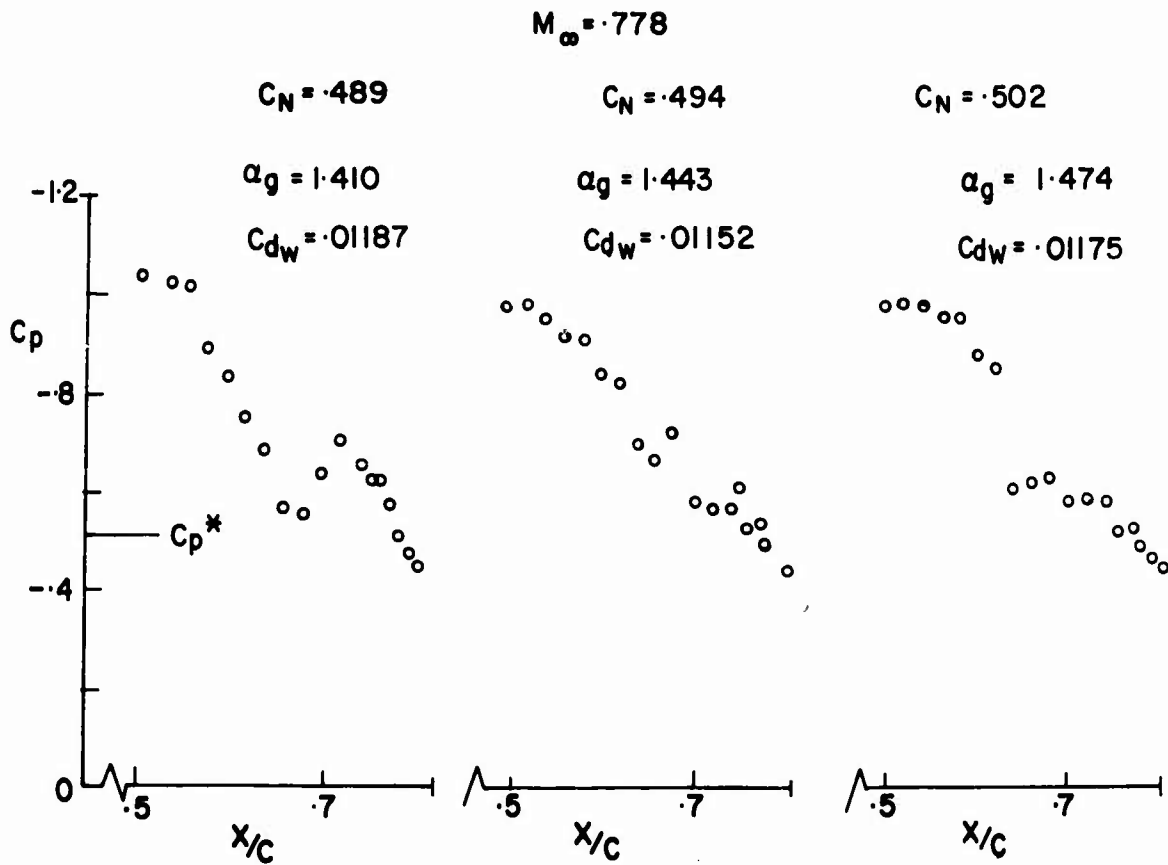
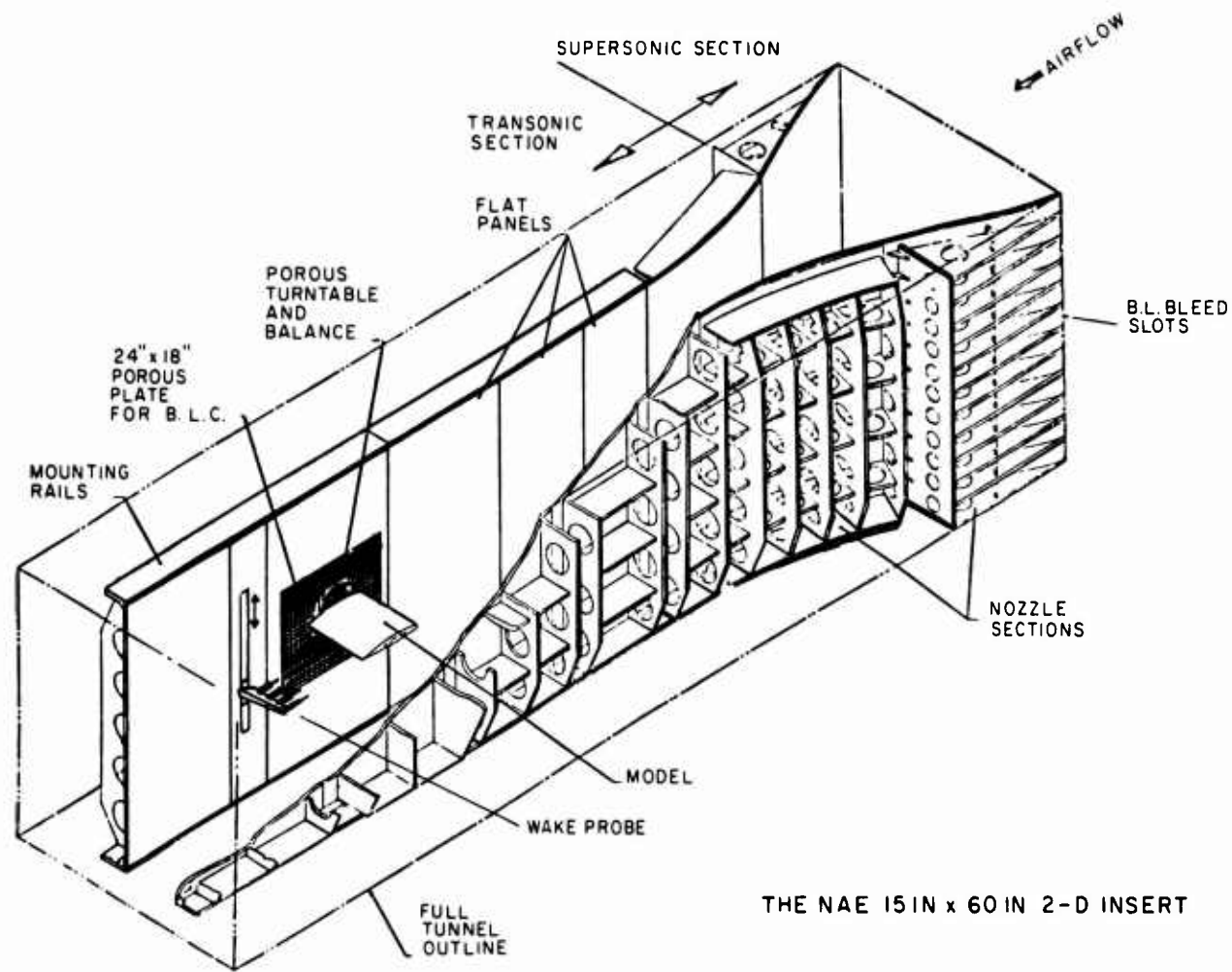


Fig.19 Variations of pressure distributions on shockless lifting airfoil No.2 at  $M = .778$  for changes of  $\alpha$  by  $.03^\circ$



THE NAE 15 IN x 60 IN 2-D INSERT

Fig.20 NAE two-dimensional high Reynolds number test facility

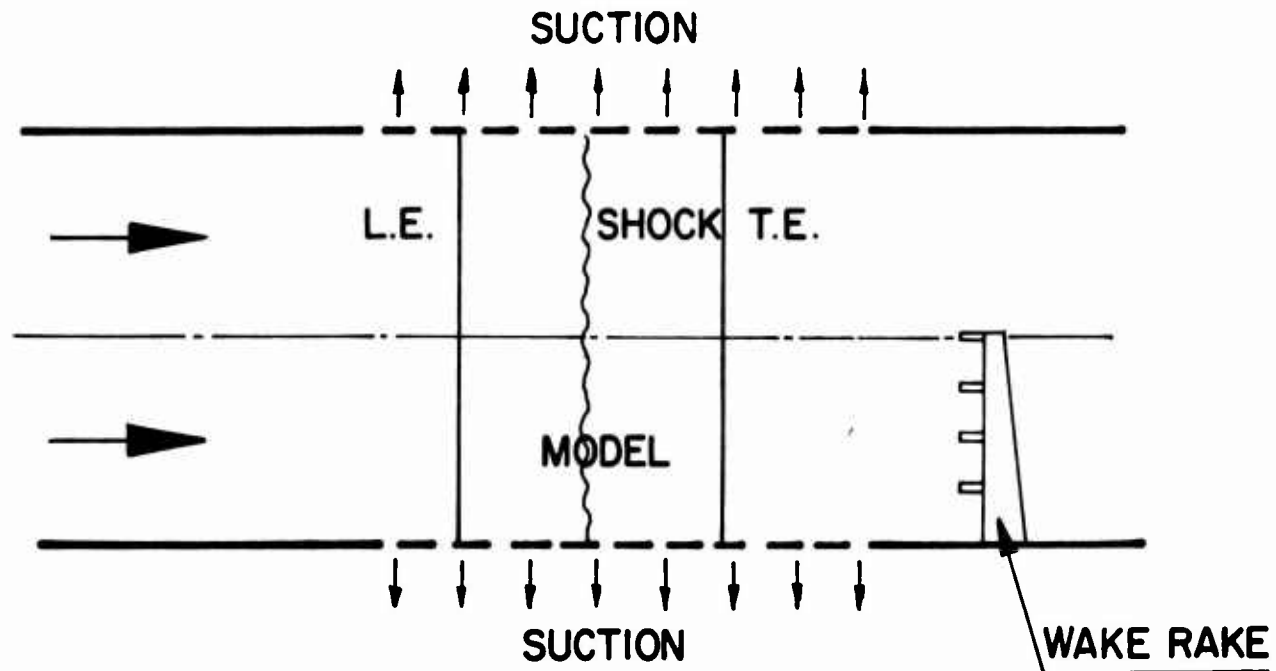


Figure 21

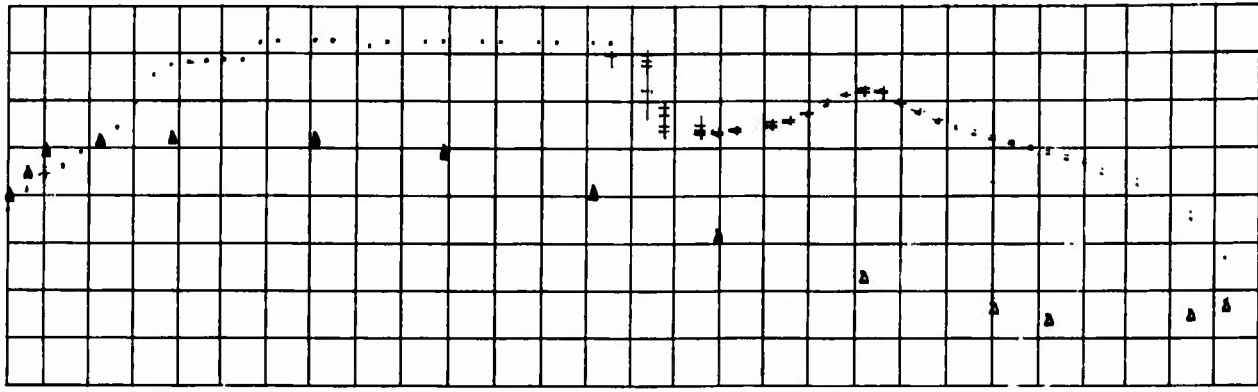


Fig.22 Outputs of pressure transducers from four pressure scans on shockless airfoil No.2 in supercritical flow at  $M = .77$ ,  $\alpha_g = 1.98^\circ$ ,  $Re = 24.10^6$

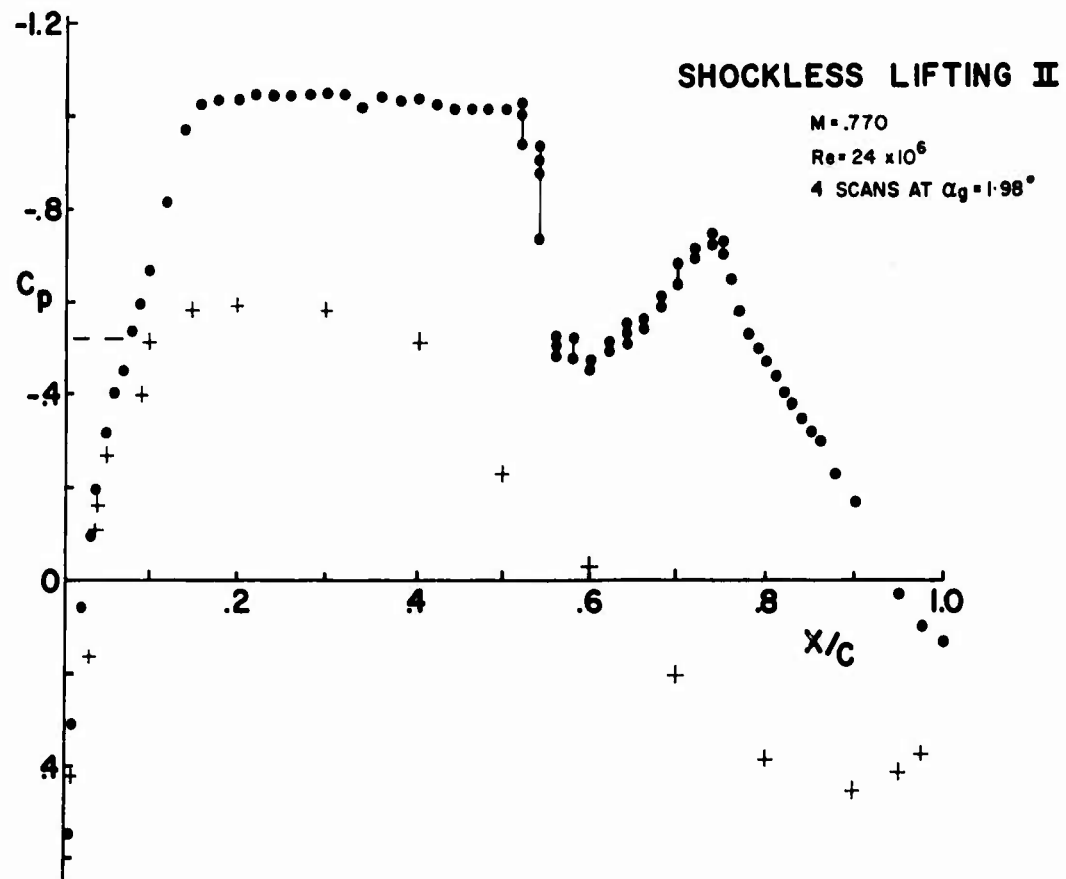


Fig.23 Pressure distribution on shockless lifting airfoil No.2 at four scans at  $M = .77$ ,  $\alpha_g = 1.981^\circ$ ,  $Re = 24.10^6$

# TRANSONIC DRAG DUE TO LIFT OF PLANAR JET-FLAPPED AIRFOILS

H. Yoshihara and R. Magnus  
Engineering Staff Specialists  
General Dynamics Convair Aerospace Division  
Mail Zone 642-2, P. O. Box 80847  
San Diego, California 92138 USA

and

D. Zonars  
Chief Scientist  
USAF Flight Dynamics Laboratory  
Dayton, Ohio 45433 USA

9.1

## SUMMARY

In contrast to the low speed case test results indicate that lift augmentation by the jet flap in the transonic regime is accompanied, not by a large thrust recovery, but by a significant increase in drag. However to achieve moderate to high lifts the use of jet flaps rather than incidence has led to a significant reduction in the drag due to lift. To calculate the transonic jet flap flow a modified Spence jet flap condition is postulated and incorporated into the (unsteady) finite difference procedure. An example is then calculated and compared with experimental results.

## 1. INTRODUCTION

The jet flap at low speeds is an effective lift augmenting device, and this augmentation is not only achieved without a drag penalty, but a significant recovery of the jet momentum as thrust is obtained largely independent of the jet inclination. Here the thrust beyond the streamwise component of the jet momentum is produced by the thrusting pressures induced on the airfoil by the jet flap. These effects of the jet flap are reasonably well predicted by the use of the thin jet model of the jet flap used by Spence (Ref. 1), which is based upon the condition that a pressure jump arises across the jet which just balances the centrifugal force of the curving constant "momentum" jet.

As the free stream Mach number is increased into the transonic regime, significant modifications of the flap effect can be expected primarily due to the appearance of a supersonic subdomain and its accompanying terminating shock wave on the airfoil upper surface. To determine these modifications a series of tests were undertaken in the 2D high Reynolds number transonic wind tunnel at the National Aeronautical Establishment (NAE) in Ottawa on a series of jet flapped aft-cambered profiles of 10% thickness ratio. The results were reported in part earlier in Ref. 2, and they showed that a significant lift augmentation can be obtained in much the same manner as in the low speed case, and that a considerable reduction of drag due to lift arises by the use of the jet flap. In the first phase of the present paper we shall examine in more detail the effect of the jet flap on the drag due to lift to determine in particular the changes in the "thrust recovery" due to the increase of the Mach number.

As mentioned earlier the effect of the jet flap was found to be reasonably modeled by the thin jet approximation used by Spence. At transonic speeds, however, the greatly magnified effect of the flow curvature on the flow will now require a modification of the Spence model, particularly in the treatment of the jet upper surface region just downstream of the trailing edge. In the second phase such a modification will be proposed in which a postulated wake flow is superimposed above the jet. The resulting jet-wake model is then incorporated as a boundary condition in the finite difference procedure of Ref. 3. The resulting procedure is then used to calculate the flow at  $M_\infty = 0.85$  over a jet-flapped aft-cambered airfoil tested earlier at NAE.

## 2. EFFECT OF THE JET FLAP ON THE TRANSONIC DRAG DUE TO LIFT

The data which we shall utilize in the present section has been obtained in the NAE 15 x 60 inch 2D tunnel. The upper and lower walls are perforated with a porosity of 20%, so that an open type wall interference effect on the incidence will be present in the results as presented. The models are described in detail in Ref. 2, and they are aft cambered airfoils of 10% thickness ratio with the simple jet flap (sonic) nozzle located on the lower surface near the trailing edge. The chord of the airfoils was 15 inches, and based upon this length the Reynolds number of the test was  $30 \times 10^6$ .

In Fig. 1 we first show the chordwise and "axial" pressure distributions at  $M_\infty = 0.8$  and at a given geometric incidence of  $2^\circ$  for jet momentum coefficients of 0 and 0.02. Consider first the more familiar chordwise distributions shown on the right side of the figure. As reported earlier the lift augmentation by the jet flap (shaded area) is produced primarily by a near uniform overpressure induced over the lower surface, by increased suction over the aft portion of the upper surface resulting from the relaxation of the Kutta condition, and by the chordwise

9-2 extension of the upper surface suction effected by the rearward displacement of the shock wave. It is of interest here to note that the shock has been weakened by its downstream displacement.

On the left side of Fig. 1 is shown the less familiar "axial" distributions where the pressures are plotted as a function of the airfoil ordinate at  $\alpha = 0$ . (The correspondence between these plots and the earlier plots of Fig. 1 is indicated by the lower case letters). The area enclosed by the curves here would then yield the axial pressure drag ( $C_a$ ). It is seen here that at a fixed incidence the lift augmentation is obtained at a considerable cost in drag, in stark contrast to the low speed case where one obtained a full thrust recovery. Here the additional drag arising is not only due to the increase of  $C_a$ , but due to the increased drag component of the normal force  $C_n$ . The primary contributor to this increased drag is the large suction (de of Fig. 1) induced by the relaxation of the Kutta condition on the inclined aft upper surface portion of the airfoil. These increased suctions have not only decreased the area of the suction loop but also increased the pressure loop.

The results of Fig. 1 as mentioned earlier have not been corrected for wall interference effects. In the jet flapped case with the higher  $C_n$  the effective incidence should be somewhat less than for  $C_\mu = 0$ , so that the actual drag penalty here should be less than that resulting from the use of the geometric incidence.

In Fig. 2 we next show the "axial" pressure distributions for a geometric incidence of  $2^\circ$  but at  $M_\infty = 0.7$  and  $0.9$ . At both Mach numbers the impact of the relaxation of the Kutta condition on  $C_a$  persists. Note for  $M_\infty = 0.9$  the near collapse of the suction loop and the expected overall reduced effect of the jet flap.

Finally in Fig. 3 we compare the pressure distributions for Airfoil A at  $M_\infty = 0.85$  with and without the jet flap at comparable lift coefficients. Here the geometric incidence in the  $C_\mu = 0$  case has been increased to  $4.34^\circ$  to match approximately the lift obtained in the jet flapped case for  $C_\mu = 0.02$  and  $\alpha = 2.12^\circ$ . Airfoil A differs from the Basic Airfoil in that a "peaky" nose has been incorporated leading to the second suction loop on the lower surface. Except for the latter suction loop the "axial" pressure distributions here exhibit the same general difference as found previously, but now due to the greater drag contribution from the  $C_n$  due to the higher incidence for the  $C_\mu = 0$  case, the latter will have a substantially greater drag, in fact an increase  $\Delta C_D \sim 0.027$ . (Here we have again not corrected the incidences for wall interference).

Here the rapid increase of drag with incidence can be simply explained by the fact that suctions predominate over the upper surface, while overpressures predominate over the lower surface, and that an increase of incidence simply increases the dragwise projections of both surfaces on which these pressures act to produce the added drag.

In the general considerations of the drag due to lift at transonic Mach numbers it is amply clear that lift should be produced without extensively increasing the "dragwise" projections of the airfoil surface. Thus for example the use of aft camber instead of incidence to produce lift is to be preferred. The use of aft camber should however be restricted to moderate  $C_{Ls}$  ( $\sim 0.5$ ) since the aft camber must not be excessive to keep the "projected area" tolerable, and of course to avoid trailing edge separation over the upper surface. Jet flaps are simply an extension of the aft camber to greater angles, and their use should be considered for large  $C_{Ls}$  ( $\sim 1$ ) on the largest tolerable aft camber. It has the advantage that the adverse forces acting on the jet flap are not directly transmitted onto the airfoil.

In contrast to the aft camber case the Kutta condition is not fulfilled in the case of the jet flap. This leads to a significant contribution to the lift, but when the jet flap is used in conjunction with an aft camber, the added suctions here as seen earlier will lead to increases of drag that will clearly more than offset the benefits of the increased lift. Finally so far as lift augmentation is concerned, the "effective  $C_\mu$ " of the "solid" aft camber cannot be matched by reasonable  $C_\mu$ s in the case of the jet flap alone, so that for moderate lift coefficients the jet flap is clearly not a satisfactory substitute for aft camber.

### 3. JET FLAP BOUNDARY CONDITION

As mentioned earlier at low speeds the jet flap effect was reasonably modeled by the thin jet approximation used by Spence. In this approximation a limiting process is carried out in which the thickness of the jet is reduced to zero, while the absolute value of the jet momentum is kept invariant. Mixing of the jet with the surrounding ambient fluid is neglected, so that the jet momentum is constant along the jet. After the jet exits into the external stream, aerodynamic forces will rapidly turn the jet in the direction of the free stream, the jet assuming a shape such that the centrifugal force of the curving jet is just counterbalanced by the jump in the pressures induced across the jet. Thus if  $y = y_j(x)$  is the shape of the jet, then at a given point on the jet a pressure jump  $P_l(x) - P_u(x)$  arises which is given in terms of the constant momentum flux of the jet  $\dot{M}_j$  and  $y_j(x)$  by the relation

$$P_l(x) - P_u(x) = \dot{M}_j y_j'' [1 + y_j'^2(x)]^{-3/2} \quad (1)$$

where the subscripts l and u denote the lower and upper sides of the jet, and the primes denote derivatives. Further the flow on either side of the jet must be tangent to the jet surface, so that

$$v_u(x, y_j)/u_u(x, y_j) = v_l(x, y_j)/u_l(x, y_j) = y_j'(x) \quad (2)$$

where  $u$  and  $v$  are the velocity components. Eqs. (1) and (2) then constitute the thin jet boundary condition.

9.3

In the treatment of the jet flap Spence linearized the above conditions consistently with the thin airfoil theory prescribing them in a planar fashion. He then solved the resulting mixed boundary value problem by distributing vortices of appropriate strength along the airfoil and jet.

In the transonic case the inviscid model of the jet flap as given above by Eqs. (1) and (2) does not adequately model the flow over the upper surface of the jet, particularly just downstream of the trailing edge. The extreme sensitivity of the flow to its curvature in the transonic regime will necessitate the inclusion of a wake above the jet to modulate the convexity of the flow to a realistic value over the upper surface trailing edge. In the absence of such a wake (inviscid flow) depending upon the free stream Mach number  $M_\infty$ , the airfoil shape, and its incidence either of two unrealistic flows will be obtained. First if a terminating shock forms on the airfoil (lower  $M_\infty$  and  $\alpha$ ) a second supersonic region will be formed above the jet by the expansion arising at the trailing edge that will then be terminated by further shocks that must now impinge on the jet. The second possibility (higher  $M_\infty$  and  $\alpha$ ) is that the terminating shock is simply sucked downstream past the trailing edge forming a supersonic region that extends downstream of the trailing edge.

To avoid the occurrence of the above severe unrealistic trailing edge expansions, in the modified model of the jet flap we shall simply place a postulated wake above the jet as shown in Fig. 4. To define the wake we shall first assume an a priori knowledge of the trailing edge pressure at the upper surface. In most cases (below buffet conditions) this pressure is subsonic, and it would then be reasonably close to the base pressure. In the NAE tests it was found that for a given Reynolds number and  $M_\infty$  the above trailing edge pressure was closely invariant to  $C_{L,u}$ . Along the upper surface of the wake the pressures are assumed to vary in a simple prescribed fashion from the above trailing edge value to the free stream value far downstream. Across the wake the pressure is then assumed to be invariant. For the jet the thin jet condition in the nonlinear form given in Eqs. (1) and (2) is retained, but now  $P_u(x)$  will assume the prescribed values along the upper surface of the wake. The thin jet here forms the lower surface of the wake.

To be sure the above model will be but a first order description of the jet-wake as a whole, but it should satisfactorily describe the flow upstream of the trailing edge, in particular the surface pressures, provided the trailing edge pressure on the upper surface can be reasonably assigned. Since the initial jet flap angle that is prescribed is known, the lower surface trailing edge pressure should be reasonably well predicted by the inviscid theory since the separated region that generally forms upstream of such a blunt "step" is constantly being entrained away by the jet.

Lastly, at the high subsonic  $M_\infty$  of interest here it should be noted that there will be negligible upstream propagation of the possible errors due to the inadequate portrayal of the jet-wake further downstream.

#### 4. FINITE DIFFERENCE PROCEDURE

The jet-wake condition as postulated above has been incorporated into the finite difference procedure of Ref. 3. Here the exact inviscid equations have been used in an unsteady form to avoid the mixed elliptic-hyperbolic character of the steady equations. In this form the equations are of hyperbolic type permitting the use of a marching process. With the prescription of suitable conditions at the airfoil and in the free stream, the desired steady flow is then obtained as the asymptotic flow for large times. As initial conditions a known neighboring flow is used, and the initial flow is then driven towards the desired steady flow by abruptly imposing the airfoil condition. When the equations are used in the proper conservation form, the embedded shocks are properly captured by the marching process. To an adequate approximation the flow can be assumed as an isentropic flow, since the entropy production by the expected shocks is negligible.

For the class of blunt-nosed airfoils of interest, planar boundary conditions are inadequate. The exact airfoil boundary conditions must be used, and it must be fulfilled on the exact boundary in the nose region. (Ref. 3). Downstream of the nose the exact conditions may be imposed however in a planar fashion. Thus in Ref. 3 the airfoil and the trailing stagnation streamline were replaced by a semi-infinite slab with the parallel sides aligned with the free stream direction and with the semi-circular nose, forming the upstream extremity of the slab, overlaying the airfoil leading edge circle. In the case of the jet flap the prescribed pressures on the upper surface of the wake are imposed along the upper side of the slab downstream of the trailing edge point, while the thin jet condition is prescribed along the lower surface.

For the finite difference analogue a cartesian mesh is used in most of the flow domain with a variable mesh spacing employed to match the expected flow gradients. Thus in the vicinity of the airfoil, and in particular about the expected location of the shock, a finer mesh is used. In a semicircular concentric sector about the nose of the slab and in the far field, the equations in polar coordinates are used to facilitate the fulfillment of the boundary condition at the surface and at infinity. Suitable overlap of the various mesh regions must be provided to maintain the necessary flow continuity. The Lax-Wendroff second order difference scheme is used to derive the difference equations.

To illustrate the above procedure we have calculated the flow over Airfoil A at  $M_\infty = 0.85$  for a jet flap

angle  $\theta_j = 80^\circ$  and  $C_{\mu} = 0.02$ . As an artifice to locate the shock and to incorporate the change of the effective aft camber due to the boundary layer displacement effects, we have prescribed the measured pressures aft of the shock as the boundary condition rather than the geometric slopes. The results of the calculation would then yield the "boundary layer displacement ramp" where the experimental pressures were prescribed. Since the effective incidence in the experiments was unknown due to wall interference effects, we have further adjusted the incidence in the calculations to obtain a match of the plateau pressures.

The resulting calculated pressure distribution is shown in Fig. 5 where also the measured pressures are given. The undulations in the latter pressures along the upper surface plateau region, are most probably the consequence of a small confined leading edge separation that has propagated downstream along a reflecting sequence of Mach waves. These undulations have decreased the surface Mach number just upstream of the shock, resulting in a weaker shock.

The "boundary layer displacement ramp" is also shown in Fig. 5. The actual ramp with the weaker experimental shock would be thinner than that calculated. The use of such calculated displacement ramps has been suggested as an empirical input for the determination of semi-empirical turbulent boundary layer equations applicable for cases with shock-induced separations. (Ref. 3).

## 5. CONCLUDING REMARKS

An examination of the experimental pressure distributions showed that a significant decrease in the drag due to lift results if a given (large) lift is obtained by the use of jet flaps rather than by airfoil incidence alone. On the other hand at transonic speeds the jet flap lift augmentation was obtained at a severe cost in added drag, in contrast to the low speed case where the lift augmentation was accompanied by a near full recovery of the jet momentum as thrust. The above results should not be surprising, since they are merely the reflections of the fact that the production of lift in the transonic regime is "costly", no matter the mode utilized; and that the use of incidence is more "expensive" than the use of jet flaps. In the planar case, lifts with the jet flap can of course be achieved that are unattainable by incidence alone.

The suggested finite difference method to treat the jet flap at transonic speeds is by no means complete. Completeness must await the determination of a reliable empirical formulae for the trailing edge pressures and the development of a procedure to treat the boundary layer.

## 6. REFERENCES

1. Spence, D., A Treatment of the Jet Flap by Thin Aerofoil Theory, R. A. E. Report Aero-2568, 1955.
2. Peake, D. J., Yoshihara, H., Carter, W., Zonars, D., The Transonic Performance of Two-Dimensional Jet-Flapped Aerofoils at High Reynolds Numbers, AGARD-CP-83-71, April 1971.
3. Magnus, R., and Yoshihara, H., Steady Inviscid Transonic Flows Over Planar Airfoils - A Search for a Simplified Procedure, NASA CR NO. 2186, 1972.

BASIC AIRFOIL :  $M_\infty = 0.8$  ;  $\alpha = 2^\circ$

$C_{\mu} = 0$  (Run No. 8058)  $C_n = 0.704$  ;  $C_a = 0.0013$      
  $C_{\mu} = 0.02$  (Run No. 8055)  $C_n = 1.085$  ;  $C_a = 0.0146$

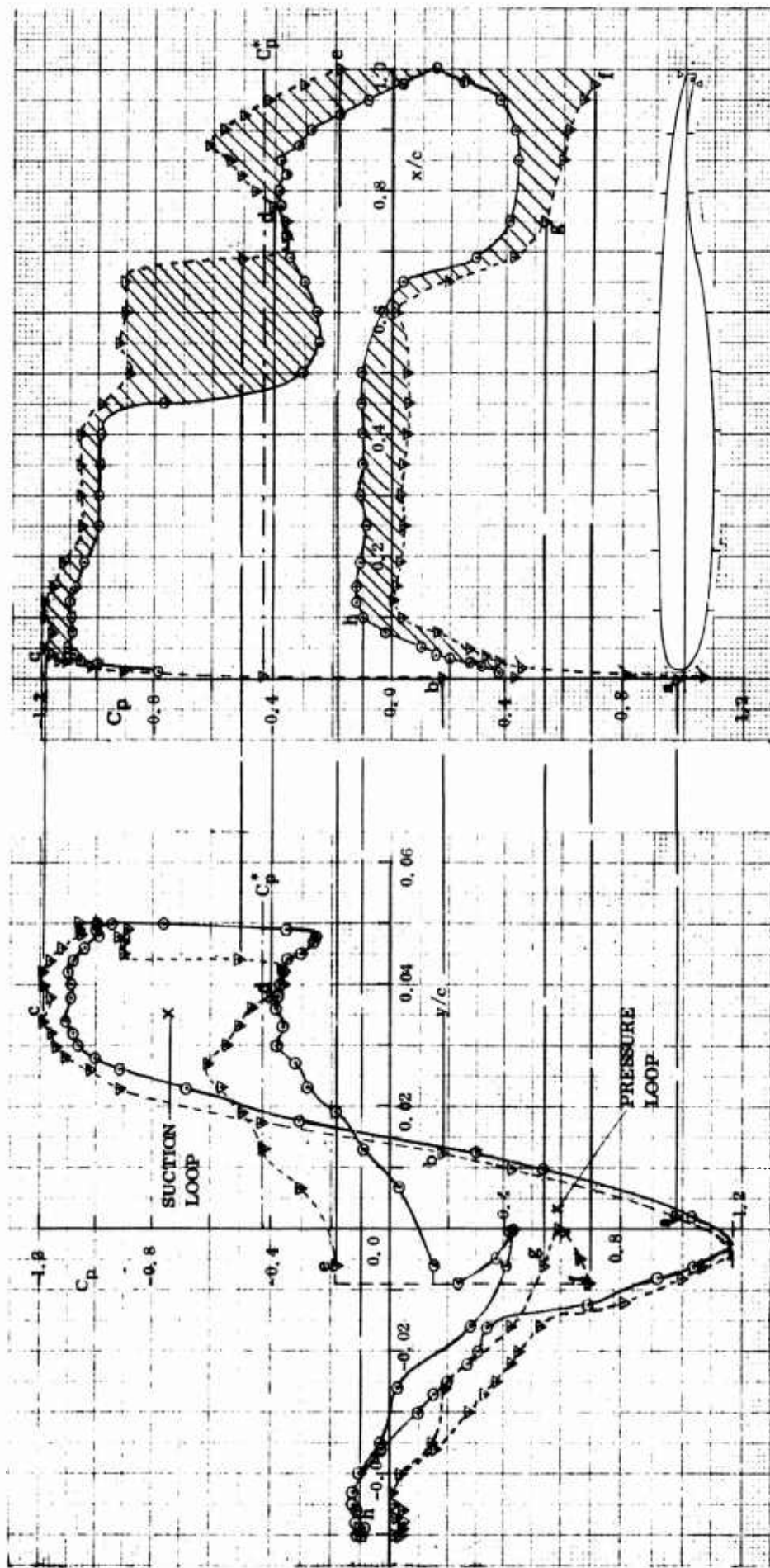


Figure 1. Effect of the Jet Flap on the Pressure Distributions for a Given Incidence.

9.6

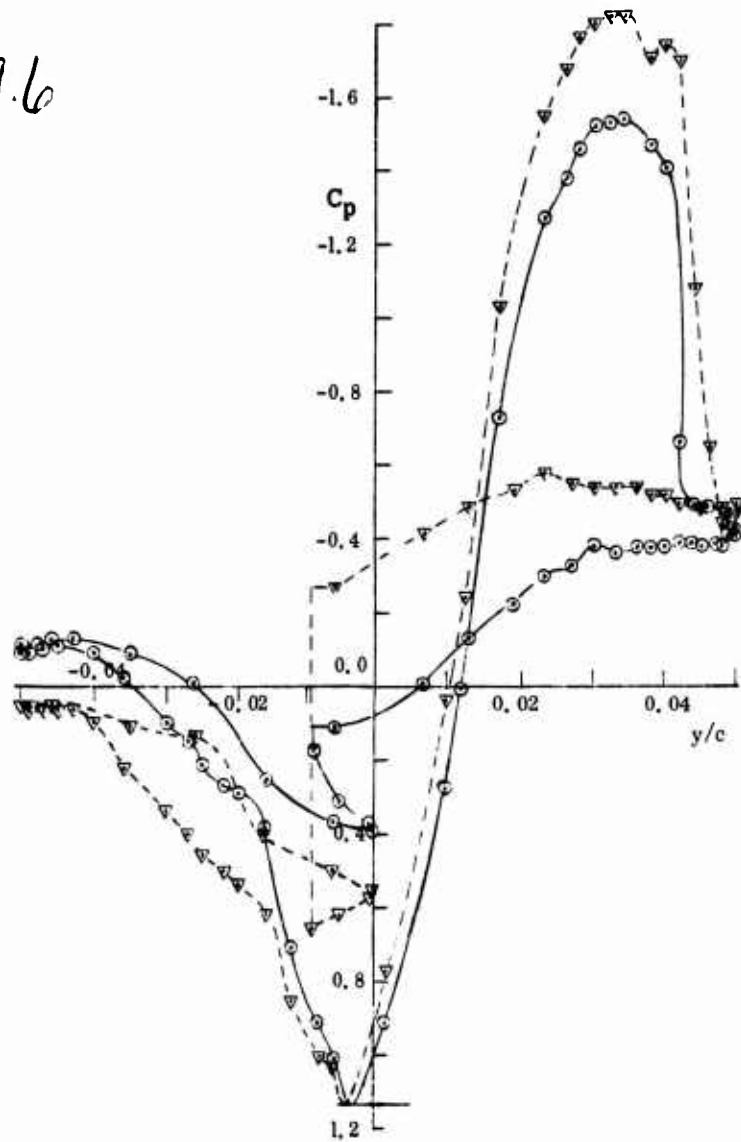
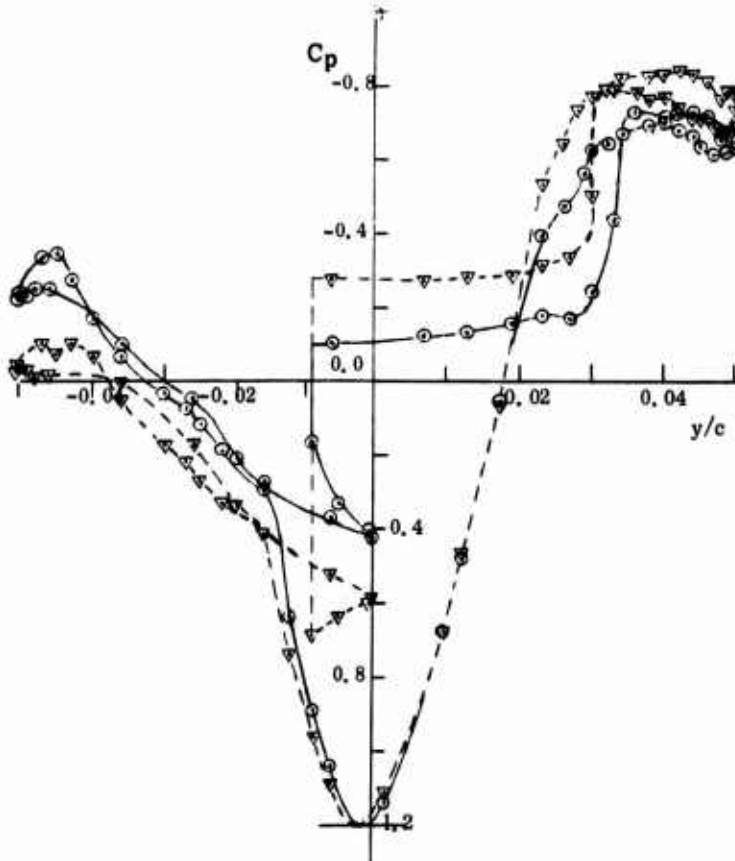


Figure 2  
Effect of  $C_{\mu}$  on the "Axial" Pressure  
Distributions for  $M_{\infty} = 0.7$  and  $0.9$ .

BASIC AIRFOIL :  $\alpha = 2^{\circ}$

$M_{\infty} = 0.7$

- $C_{\mu} = 0$  (Run No. 8064)  
 $C_n = 0.564$  ;  $C_a = -0.0135$ .
- ▽---  $C_{\mu} = 0.02$  (Run No. 8042)  
 $C_n = 0.921$  ;  $C_a = -0.0091$ .



$M_{\infty} = 0.9$

- $C_{\mu} = 0$  (Run No. 8066)  
 $C_n = 0.562$  ;  $C_a = 0.0125$ .
- ▽---  $C_{\mu} = 0.02$  (Run No. 8050)  
 $C_n = 0.871$  ;  $C_a = 0.0164$ .

AIRFOIL A :  $M_\infty = 0.85$

-----  $\nabla$  ---  $C_\mu = 0$  (Run No. 9792)  $\alpha = 4.34^\circ$ ;  $C_{\mu 1} = 0.872$ ;  $C_a = 0.0053$  ---  $\circ$  ---  $C = 0.02$  (Run No. 9823)  $\alpha = 2.12^\circ$ ;  $C_{\mu 1} = 0.942$ ;  $C_a = 0.0130$

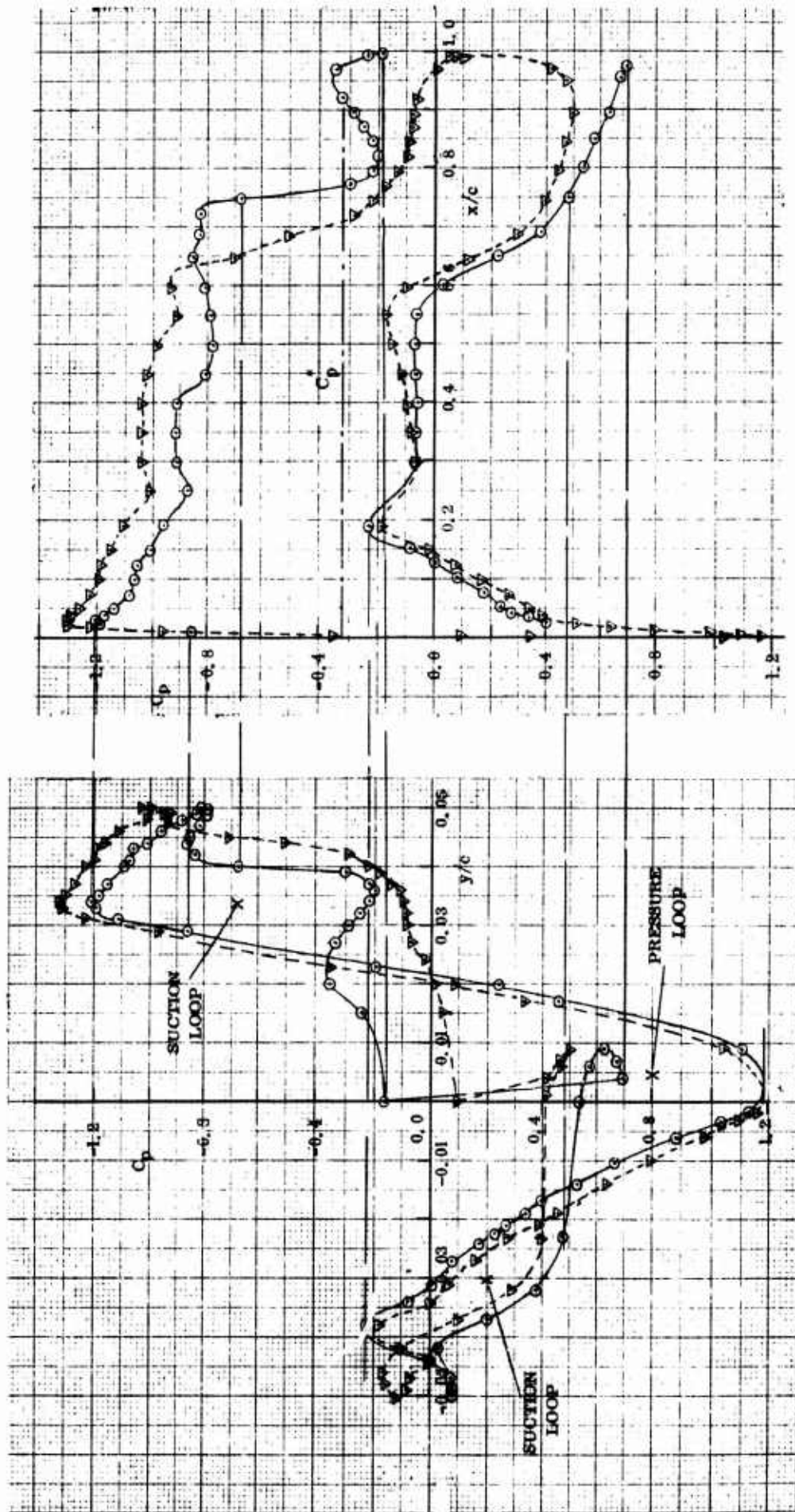


Figure 3. Effect of the Jet Flap on the Pressure Distributions for a Given  $C_L$ .

9.8

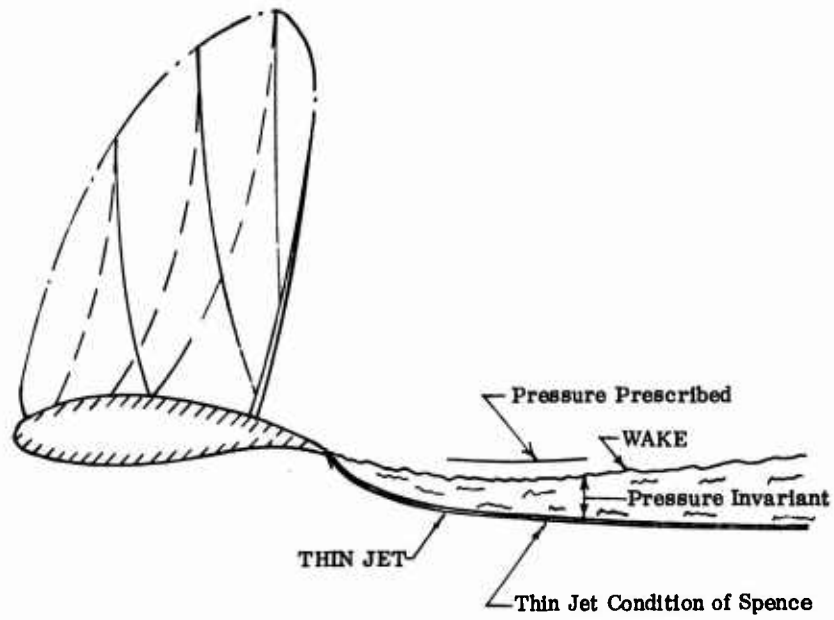


Figure 4. Modified Jet Flap Model - The Jet-Wake Model.

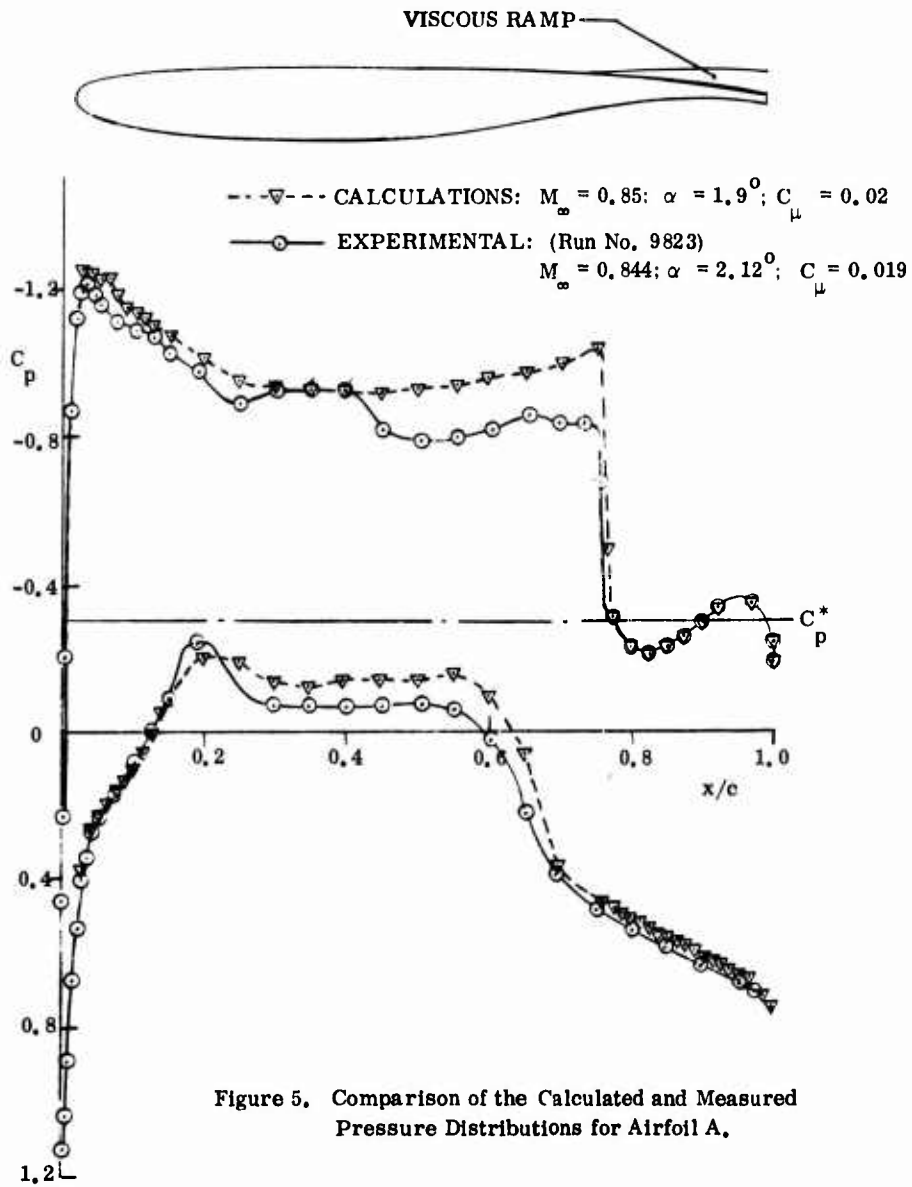


Figure 5. Comparison of the Calculated and Measured Pressure Distributions for Airfoil A.

COMPARISON OF VARIOUS METHODS FOR CALCULATING PROFILE DRAG FROM  
PRESSURE MEASUREMENTS IN THE NEAR WAKE AT SUBCRITICAL SPEEDS

by

J. Zwaaneveld

National Aerospace Laboratory NLR, Amsterdam

SUMMARY

Three methods for calculating the profile drag from total and static pressure measurements in the wake have been compared. An analytical model of a compressible two-dimensional wake is used to obtain numerical results.

Both the oldest method of Betz and the widely used method of Jones allow the static pressure variation across the wake to be taken into account. These methods are therefore suitable to treat the flow in the very near wake. The third method developed by Squire and Young is in principle only valid when the static pressure variation across the wake is negligible. To extend this method to the more general case, two modifications are considered, the first as proposed by Squire and Young, the second as presented by the author. The latter modification makes use of the momentum integral equation with modified parameters. The numerical results show this new approach to be in far better agreement with the method of Jones than the first mentioned modified version.

SOMMAIRE

Trois méthodes pour calculer la traînée de profil à partir des mesures de pression totale et statique dans le sillage ont été comparées. Un modèle analytique d'un écoulement compressible et bidimensionnel, dans le sillage est utilisé pour obtenir des résultats numériques.

La méthode la plus ancienne de Betz aussi bien que la méthode de Jones qui est appliquée fréquemment permettent de tenir compte d'une variation de la pression statique à travers le sillage et ces méthodes peuvent donc être appliquées à l'écoulement dans le sillage près du bord de fuite. La troisième méthode, celle de Squire et Young, est en principe seulement valable dans le cas où la variation de pression statique à travers le sillage est négligeable. Pour élargir le domaine d'application de cette méthode deux variantes ont été considérées, l'une déjà proposée par Squire et Young, l'autre par l'auteur. La dernière variante utilise l'équation intégrale de quantité de mouvement avec des paramètres modifiés. Les résultats obtenus avec cette nouvelle approche sont en meilleur accord avec la méthode de Jones que ceux de l'autre variante mentionnée.

NOTATION

$c$	airfoil chord	$\gamma$	ratio of specific heats
$c_d$	drag coefficient	$\delta$	boundary layer or wake thickness
$\bar{c}_{d_{SY}}$	drag coefficient, equation (20)	$\delta^*, \bar{\delta}^*$	displacement thicknesses [respectively Eq.(A.7) and Eq.(A.21)]
$\bar{c}_{d_{SY}}$	drag coefficient, equation (22)	$\theta, \bar{\theta}, \bar{\theta}$	momentum thicknesses [respectively Eq.(A.6), Eq.(18) and Eq.(A.20)]
$c_p$	static pressure coefficient, $2(p-p_\infty) / \rho_\infty U_\infty^2$	$\rho$	density
$\Delta c_p$	$c_{p_w} - c_{p_e}$	$\tau$	shear stress
$c_{p_t}$	total pressure coefficient, $2(p_{t_\infty} - p_t) / \rho_\infty U_\infty^2$	<u>Subscripts</u>	
$D$	drag of unit span	$e$	edge
$F$	force on source distribution	$i$	inviscid flow
$G$	strength of source distribution	$j$	value calculated from $p_t$ and $p$
$H, \bar{H}, \bar{H}$	shape factors	$w$	wall, centre line
$M$	Mach number	$\infty$	free stream, infinity downstream
$p$	static pressure	$B$	Betz
$p_t$	total pressure	$J$	Jones
$U, V$	velocity components in X and Y directions	$SY$	Squire and Young
$u, v$	velocity components in x and y directions		
$X, Y$	co-ordinate system, see figure 1		
$x, y$	co-ordinate system, see figure 1		

## 1 INTRODUCTION

In view of current experimental investigations and theoretical studies of the compressible flow near the trailing edge of an airfoil, where the static pressure differs considerably from the free stream pressure and in general varies across the boundary layer and the wake, a comparison of existing methods for determining the drag of two-dimensional airfoils from wake surveys under these circumstances is of general interest.

The origin of the underlying methods stems from Froude almost a century ago (Ref. 1). He showed how the skin friction resistance of a ship must be entirely accounted for by the momentum it gives to the water through which it passes. Taylor (Ref. 2) introduces this method in aerodynamic research and derives a relation between the drag of a flat plate and a wake integral representing the defect of flow momentum per unit time. This solution is limited to conditions where the static pressure in the wake equals the free stream pressure. It appears in the more general case, if the static pressure in the wake differs from the free stream pressure, that the exact expression of the drag from the momentum theorem contains static pressure terms to be measured outside the viscous wake flow. Several approximate methods have been published to eliminate this unpractical feature. The first method is that of Betz, published in 1925 (Ref. 3). The effect of the wake flow on the outer field is taken into account by the introduction of a source at the model location. A second method is given by Jones (Ref. 4). He introduces an imaginary inviscid flow from the survey plane to a plane far downstream where the static pressure equals the free stream pressure. The third method is due to Squire and Young (Ref. 5). They calculate the profile drag from the momentum thickness at the trailing edge, applying the integral momentum equation of the wake and an empirical relation between the shape factor and the velocity at the edge of the wake.

The three mentioned methods give the same results for survey planes located sufficiently far downstream where the difference between the static pressure in the wake and the free stream pressure is negligible. However, close to the trailing edge of an airfoil the static pressure in the wake differs from the free stream pressure and in the very near wake there exists in general a static pressure variation across the wake. In these cases the methods produce differences in the calculated drag coefficients. Because of present interest in the details of trailing edge flow it was found to be useful to compare the various methods closely.

The methods of Betz and Jones allow a static pressure variation across the wake to be taken into account. The method of Squire and Young, however, is based on standard boundary layer approximations and a modification is necessary to account for such a static pressure variation. Two modifications will be considered. In the first place, as suggested by Squire and Young, by a correction to the momentum thickness but leaving the displacement thickness unchanged. The correction term is found from the static pressure distribution across the wake. In the second place another solution is derived in the present report which is based on a momentum integral equation with modified wake integral parameters. The used modified definitions of the momentum thickness and the displacement thickness were first suggested, in principle, for a boundary layer with a normal pressure gradient by Myring (Ref. 6). To show the differences between the various methods some numerical examples will be presented using a simple analytical model of a compressible two-dimensional wake flow with and without a normal pressure gradient.

## 2 DISCUSSION OF BASIC METHODS FOR DETERMINING PROFILE DRAG

## 2.1 Method of Betz

In reference 3 Betz derived for an incompressible flow an expression to determine the profile drag from the static and total pressure distribution in the wake cross section. As far as known a solution for compressible flow has not been published. Such a solution will be presented here. The approach differs typically from the original one, but the same features of Betz's method have been used.

Consider a two-dimensional steady compressible subsonic flow around an airfoil (Fig. 1). Far upstream the flow is uniform with density  $\rho_\infty$  and velocity  $U_\infty$  parallel to the X-axis. The drag D is defined as the resulting force in the X-direction on the airfoil of unit span. Application of the momentum theorem to the control surface S results in

$$D = - \int_S p \, dY - \int_S \rho U (U \, dY - V \, dX) \quad (1)$$

According to Betz an inviscid flow is introduced which satisfies the boundary conditions of the actual flow along S outside the viscous wake flow. In the wake region the assumption is made that the static pressure of the inviscid flow equals the actual static pressure. Therefore in this region the velocity of the inviscid flow will be larger than the actual velocity due to the total pressure loss in the wake of the actual flow. Because this latter flow satisfies the continuity equation, the inviscid flow contains within the control volume a source distribution of total strength

$$G = \int_A^B (\rho_i U_i - \rho U) \, dY = \int_\delta (\rho_i U_i - \rho U) \, dY \quad (2)$$

where the integration across the wake is taken normal to the X-axis. If the interaction between the source distribution downstream of the survey plane and G is neglected, then the force on the source distribution of total strength G in the X-direction amounts to

$$F = - U_\infty \int_\delta (\rho_i U_i - \rho U) \, dY \quad (3)$$

Application of the momentum theorem to the inviscid flow gives

$$F = - \int_S p_i dY - \int_S \rho_i U_i (U_i dY - V_i dX) \quad (4)$$

Subtracting equation (4) from equation (1) it follows

$$D - F = \int_S \rho_i U_i^2 dY - \int_S \rho U^2 dY \quad (5)$$

Substitution of equation (3) into equation (5) results in the profile drag

$$D = \int_S \rho U (U_\infty - U) dY - \int_S \rho_i U_i (U_\infty - U_i) dY \quad (6)$$

It can be shown that for an incompressible flow this last expression agrees with the expression of Betz from reference 3.

The profile drag coefficient is defined as

$$c_d = \frac{2D}{\rho_\infty U_\infty^2 c} \quad (7)$$

and it follows from equation (6)

$$c_{d_B} = \frac{2}{c} \int_S \frac{\rho U}{\rho_\infty U_\infty} \left(1 - \frac{U}{U_\infty}\right) dY - \frac{2}{c} \int_S \frac{\rho_i U_i}{\rho_\infty U_\infty} \left(1 - \frac{U_i}{U_\infty}\right) dY \quad (8)$$

## 2.2 Method of Jones

A simple method is due to Jones (Ref. 4). He introduced an imaginary inviscid wake flow between the survey plane and a plane far downstream where the static pressure equals the free stream pressure. The compressible case has been considered by Young (Ref. 7). Along the streamlines of the imaginary isentropic flow assumed now the total pressure and the total temperature remain constant. The mass flow in the wake does not change and the velocity  $U_j$  on the imaginary streamlines far downstream is known

from the total pressure and total temperature at the survey station and the static pressure of the free stream. Application of the momentum theorem to the far field results in the following expression for the drag per unit span (Ref. 7)

$$D = \int_0 \rho U (U_\infty - U_j) dY \quad (9)$$

The profile drag coefficient using the method of Jones in compressible flow is thus

$$c_{d_J} = \frac{2}{c} \int_0 \frac{\rho U}{\rho_\infty U_\infty} \left(1 - \frac{U_j}{U_\infty}\right) dY \quad (10)$$

## 2.3 Method of Squire and Young

This method was originally derived to calculate the profile drag from theoretical boundary layer calculations up to the trailing edge (Ref. 5). A compressible solution is given in reference 8, and it appears that this method is in use to determine the profile drag from wake surveys (Ref. 9). The method is primarily based on the solution of the boundary layer momentum integral equation with zero normal pressure gradient. If applied to the wake flow, where the wall shear stress vanishes, the governing equation for the compressible case (Ref. 8 and of Eq. (A.9) of the Appendix)

$$\frac{d\theta}{dx} + \frac{\theta}{\rho_e} \frac{d\rho_e}{dx} + \frac{\theta}{u_e} \frac{du_e}{dx} (2 + H) = 0 \quad (11)$$

can be written in the form

$$\frac{1}{\theta} \frac{d\theta}{dx} + \frac{1}{\rho_e} \frac{d\rho_e}{dx} + (2 + H) \frac{d}{dx} \left( \ln \frac{u_e}{U_\infty} \right) = 0 \quad (12)$$

Integration over  $x$  from the survey plane to a plane far downstream where  $u_e = U_\infty$  and  $p = p_\infty$  gives

$$\ln \left( \frac{\rho_e \theta}{\rho_\infty \theta_\infty} \right) + (2 + H) \ln \frac{u_e}{U_\infty} = \int_{H_\infty}^H \ln \frac{u_e}{U_\infty} dH \quad (13)$$

According to reference 10 the shape factor at infinity is given by  $H_\infty = 1 + (\gamma - 1)M_\infty^2$ . Assuming a linear relation between  $\ln(u_e/U_\infty)$  and  $(H - H_\infty)$  (see Refs. 5 and 8) it follows

$$\theta_\infty = \theta \frac{\rho_e}{\rho_\infty} \left( \frac{u_e}{U_\infty} \right)^{\frac{H + H_\infty + 4}{2}} \quad (14)$$

From the momentum theorem applied to the far field the profile drag coefficient is given by

$$c_d = \frac{2D}{\rho_\infty U_\infty^2 c} = \frac{2\theta_\infty}{c} \quad (15)$$

Hence the profile drag coefficient, using the method of Squire and Young, for the case of a compressible flow with constant static pressure across the wake is

$$c_{dSY} = 2 \frac{\theta}{c} \frac{\rho_e}{\rho_\infty} \left( \frac{u_e}{U_\infty} \right)^{\frac{H+H_\infty+4}{2}} \quad (16)$$

### 3 MODIFICATION OF THE BASIC METHOD OF SQUIRE AND YOUNG FOR A WAKE WITH A NORMAL STATIC PRESSURE GRADIENT

#### 3.1 General

If the static pressure varies across the wake the method of Squire and Young has to be modified. In the appendix it is shown that, for a boundary layer with a normal pressure gradient, the momentum integral equation can be derived in two different ways. In the first approach the conventional definitions of the boundary layer parameters are used, and an additional pressure term appears in the momentum integral equation. Squire and Young suggested in an appendix to reference 5 to correct the momentum thickness with this pressure term and they derived a drag coefficient in the usual way. This will be discussed in section 3.2.

In a second approach modified definitions of the boundary layer parameters are used. It appears that along these lines a momentum integral equation is obtained of the conventional form. This second approach will be presented in section 3.3.

#### 3.2 Modification as proposed by Squire and Young

As discussed in the previous section, Squire and Young suggested to make allowance for the static pressure variation across the wake by adding to the momentum thickness a term which depends on the static pressure distribution across the wake. They consider only an incompressible flow. For the compressible case the governing equation (A.8) applied to the wake flow with zero wall shear stress results in

$$\frac{d}{dx} (\rho_e u_e^2 \theta) + \rho_e u_e \delta^* \frac{du_e}{dx} - \frac{d}{dx} \int (p - p_e) dy = 0 \quad (17)$$

With the introduction of the corrected momentum thickness as proposed by Squire and Young

$$\bar{\theta} = \theta - \int \frac{p - p_e}{\rho_e u_e^2} dy \quad (18)$$

the following equation can be derived

$$\frac{1}{\bar{\theta}} \frac{d\bar{\theta}}{dx} + \frac{1}{\rho_e} \frac{d\rho_e}{dx} + (2 + \bar{H}) \frac{d}{dx} \left( \ln \frac{u_e}{U_\infty} \right) = 0 \quad (19)$$

where  $\bar{H} = \delta^*/\bar{\theta}$

Integration over  $x$  from the survey plane to a plane far downstream where  $u_e = U_\infty$  and  $p = p_\infty$ , and assuming a linear relation between  $\ln(U_\infty/u_e)$  and  $(\bar{H} - H_\infty)$ , a drag coefficient can be derived in a similar way as discussed in section 2.3

$$\bar{c}_{dSY} = 2 \frac{\bar{\theta}}{c} \frac{\rho_e}{\rho_\infty} \left( \frac{u_e}{U_\infty} \right)^{\frac{\bar{H}+H_\infty+4}{2}} \quad (20)$$

#### 3.3 Present modification

If the boundary layer momentum thickness and displacement thickness are calculated using the modified definition (as discussed in the appendix) the governing momentum equation (A.18) applied to the wake, results in

$$\frac{d}{dx} (\rho_{iw} u_{iw}^2 \bar{\theta}) + \rho_{iw} u_{iw} \bar{\delta}^* \frac{du_{iw}}{dx} = 0 \quad (21)$$

Again, in a similar way as in the previous section, a drag coefficient can be derived

$$\bar{c}_{dSY} = 2 \frac{\bar{\theta}}{c} \frac{\rho_{iw}}{\rho_\infty} \left( \frac{u_{iw}}{U_\infty} \right)^{\frac{\bar{H}+H_\infty+4}{2}} \quad (22)$$

where  $\bar{H} = \bar{\delta}^*/\bar{\theta}$

4.1 General

To be able to compare in a systematic way the various methods for determining the drag from wake surveys, a two-dimensional compressible wake-flow model is introduced. For simplicity the symmetrical case is considered only. From experiments it is found that, for a symmetrical airfoil at zero incidence the total pressure loss distribution in the wake can be approximately expressed by

$$c_{p_t} = c_{p_{tw}} \cos^2 \left( \frac{y}{\delta} \right) \pi \quad (23)$$

where  $c_{p_{tw}}$  is the pressure coefficient on the centre line of the wake (Fig. 2) and  $\delta$  equals the width of the symmetrical wake.

In order to study the effect of a static pressure variation across the wake a somewhat arbitrary but simple pressure distribution is chosen

$$c_p = c_{p_w} - \Delta c_p \sin^2 \left( \frac{y}{\delta} \right) \pi \quad (24)$$

Here  $c_{p_w}$  is the static pressure coefficient on the centre line of the wake and  $\Delta c_p$  the difference between the pressure coefficient on the centre line and the edge of the wake.

A comparison of assumed and measured velocity distributions for incompressible flow is given in figure 3. For the assumed velocity distributions representative combinations of  $c_{p_{tw}}$  and  $c_{p_w}$  values are chosen. A possible static pressure variation across the wake is neglected. It appears that the agreement with the experimental data is reasonable. However, it should be noted that the assumed shape factor at the trailing edge is somewhat too high. It can be pointed out that this has a very slight effect on the ratios of the drag coefficients to be calculated. Bearing in mind the objective of the present study, it seems acceptable to apply the assumed pressure distributions for compressible flow too. To illustrate the effect of Mach number on the velocity distribution, the shape factor  $H$  is given in figure 4 as a function of  $c_{p_{tw}}$  for a wake with free stream static pressure. It may be noted that going downstream the total pressure loss on the centre line of the wake decreases and the shape factor goes to  $H_\infty = 1 + (\gamma - 1) M_\infty^2$  as applied in section 2.3.

From experiments it appears that at the trailing edge of an airfoil with attached flow a static pressure coefficient of  $c_{p_w} = 0.2$  to  $0.3$  is mostly found. Experimental data with regard to the static pressure variation across the wake are scarce. Jones (Ref. 4) found for a 20% thick airfoil at low lift at about 4% of the chord downstream from the trailing edge, a pressure difference across the wake of  $\Delta c_p = 0.07$ . For the numerical examples given in the present report the value  $\Delta c_p = 0.1$  is used.

To calculate the drag coefficients it is assumed that the normal velocity component may be neglected. If the total temperature is assumed to be constant everywhere in the flow, the velocity and density ratios can be calculated from the isentropic flow relations (for arbitrarily chosen conditions 1 and 2)

$$\frac{U_1}{U_2} = \frac{\left[ \left( \frac{p_{t1}}{p_1} \right)^{\frac{\gamma-1}{\gamma}} - 1 \right]^{\frac{1}{2}}}{\left[ \left( \frac{p_{t2}}{p_2} \right)^{\frac{\gamma-1}{\gamma}} - 1 \right]^{\frac{1}{2}}} \left[ \frac{p_1}{p_{t1}} \frac{p_{t2}}{p_2} \right]^{\frac{\gamma-1}{2\gamma}} \quad (25)$$

$$\frac{\rho_1}{\rho_2} = \left( \frac{p_1}{p_2} \right)^{\frac{1}{\gamma}} \left( \frac{p_{t1}}{p_{t2}} \right)^{\frac{\gamma-1}{\gamma}} \quad (26)$$

The drag coefficients are obtained by numerical integration using 512 points resulting in an accuracy of better than  $10^{-4}$ .

For the particular case that the static pressure in the wake equals the free stream pressure, it can be easily shown that the various methods produce the same results. This means that differences between the various methods exist only if the static pressure in the wake differs from the free stream pressure.

4.2 Wake with constant static pressure

Computed values of  $c_d$   $c/\delta$  for the various methods are presented in figure 5 as a function of the maximum total pressure loss for  $M_\infty = 0$ ;  $c_{p_w} = -0.2, 0$  and  $0.2$  and  $\Delta c_p = 0$ . It appears that in the case of positive static pressure coefficients the methods of Jones, and Squire and Young differ only slightly. The method of Betz results in a drag coefficient which is too low as compared with the other ones. In figure 6 the ratios of the drag coefficients are presented for some positive static pressure coefficients. The maximum difference between  $c_{dSY}$  and  $c_{dJ}$  exists just before the maximum possible total pressure

106  
 loss at the trailing edge occurs. The maximum difference between the two methods appears to be surprisingly small. The effect of Mach number is seen from figure 7. It appears that the maximum differences between  $c_{dSY}$  and  $c_{dJ}$  are nearly independent of Mach number.

#### 4.3 Wake with a normal static pressure gradient

It turns out that the ratio  $c_{dB}/c_{dJ}$  is nearly independent on the variation of the static pressure across the wake. Therefore the results of  $c_{dB}/c_{dJ}$  presented in figures 6 and 7 hold approximately for the case of  $\Delta c_p$  unequal zero.

Published experimental data (Ref. 4) show that the deduced values of  $c_{dB}$  decrease when approaching the trailing edge of an airfoil. This indicates that the method of Betz does not predict under these conditions the drag coefficient very well. However, the results obtained with the method of Jones appear to be good.

Using as a basis the method of Squire and Young to calculate the drag coefficient for the case of a static pressure variation across the wake two modifications have been derived in section 3. When the modified versions are compared with the method of Jones (for an assumed static pressure coefficient  $c_{pw} = 0.2$  and a variation  $\Delta c_p = 0.1$ ) there appears to be a noticeable difference between the two modifications (Fig. 8).

In the case of the modification based on the corrected momentum thickness  $\bar{\theta}$ , the differences with Jones are largest. This suggests that the  $\bar{\theta}$ -method is less correct, which is probably due to the fact that the derived integral equation (19) has lost its physical meaning. In this approach the static pressure variation is known to be completely accounted for in the momentum thickness, leaving the displacement thickness unchanged. As a result the displacement thickness  $\bar{\delta}^*$  does not satisfy the continuity concept. The foregoing conclusion is further supported by a comparison of the calculated shape factors (Fig. 9). With decreasing total pressure loss the shape factor has to approach the value  $H_{\infty} = 1$  in the incompressible case. However,  $\bar{H}$  increases with a decrease of total pressure loss below  $c_{ptw} = 0.4$  approximately. On the contrary  $\bar{H}$  shows the correct trend. On the other hand it appears that the differences between the drag coefficient  $\bar{c}_{dSY}$ , calculated with modified definitions of the wake parameters, and  $c_{dJ}$  are comparatively small (Fig. 8) and are of the same order as found in the case of a constant static pressure across the wake (Fig. 6).

The favourable results obtained indicate that the expression (A.15) of the modified momentum integral equation, as derived by Myring (Ref. 6), has a real meaning and that the von Kármán's integral equation (A.19) with modified integral parameters, derived in the present report, can be used for practical purposes. Therefore it is to be expected that this modified momentum equation is suitable to treat boundary layer flows, where a static pressure variation across the viscous layer exists, as for example close to a separation point or close to the trailing edge of an airfoil, or in the case that a shock wave interacts with a boundary layer, etc.

#### 5 ERRORS INTRODUCED BY STATIC PRESSURE APPROXIMATIONS

The determination of a total pressure distribution across the wake with a total pressure tube is a relatively simple matter as compared with static pressure measurements. It seems therefore of some interest to determine the errors in the calculation of the drag coefficient if simplified assumptions are made concerning the wake static pressure. The errors will be calculated for the discussed example of section 4.3. Thus for the assumed actual case the static pressure coefficient in the wake decreases from  $c_{pw} = 0.2$  on the centre line to  $c_{pe} = 0.1$  at the wake boundary with a distribution given by equation (24). This pressure distribution will now be approximated by a constant static pressure at the following levels:

- the centre line pressure  $p_w$
- the edge pressure  $p_e$
- the free stream pressure  $p_{\infty}$

It is obvious, that the resulting errors depend on the assumed values of  $c_{pw}$ ,  $c_{pe}$  and the total pressure loss in the wake. The maximum error is found at the trailing edge, where a maximum in the total pressure loss appears. The calculated errors in per cent of the correct values are presented in the table. Only the errors in the drag coefficient  $\bar{c}_{dSY}$  are given, because it appears that the other drag methods of Betz and Jones give nearly the same results.

$M_{\infty}$	case	approximated conditions			error in %			
		$\Delta c_p$	$c_{pw}$	$p$	$\bar{c}_{dSY}$	$\bar{\delta}^*$	$\bar{\theta}$	$\bar{H}$
0	a	0	0.20	$p_w$	-6.6	2.3	-5.6	8.3
	b	0	0.10	$p_e$	34.0	-18.1	6.1	-22.8
	c	0	0	$p_{\infty}$	57.3	-29.7	3.8	-32.3
1.0	a	0	0.20	$p_w$	-3.8	2.5	-3.0	5.7
	b	0	0.10	$p_e$	28.6	-14.7	6.0	-19.5
	c	0	0	$p_{\infty}$	43.5	-25.2	1.8	-26.6

For the actual case considered, the velocity on the centre line of the wake  $u_w = 0$ . This condition on the trailing edge can also be conceived as a turbulent boundary layer flow. The errors in the boundary layer (wake) parameters as compared with the values found from the modified definitions as given in the appendix, are presented in the table too. The results show that the errors in the drag coefficient and the displacement thickness are smallest if the actual pressure distribution in the wake is approximated by a constant static pressure equal to the wall or centre line pressure.

From the calculation given before and from the results presented in figure 5 it can be concluded that at a given total pressure distribution in the wake the calculated drag coefficient at high total pressure loss depends strongly on the static pressure in the wake. That means that small errors in the experimentally determined static pressure level cause large errors in the drag coefficients. As an example it is found for  $c_{pw} = 0.2$  at the trailing edge that an error of 0.01 in the static pressure coefficient results in an error of 4 to 6 % in the drag coefficient depending on the method used. The error decreases slightly with increasing Mach number.

The scatter in the experimental drag data near the trailing edge of an airfoil, as found by Firmin and Cook (Ref. 9), may probably be attributed to the discussed effect of errors in the static pressure readings.

## 6 CONCLUSIONS

The main results of the comparative numerical study on methods for calculating the profile drag from total and static pressure measurements in the near wake can be summarized as follows.

- For a wake with a positive static pressure coefficient, constant across the survey plane, the drag coefficients obtained by the method of Squire and Young show negligible differences with those obtained by the method of Jones. Betz's method, in the present report extended to compressible flows, results for this case in lower drag coefficients.
- If in the very near wake a static pressure variation exists across the survey plane, the basic method of Squire and Young has to be modified. Two modifications of this method have been considered. It is shown that the results obtained with the modification derived in the present report, using the momentum integral equation with modified definitions of the momentum thickness and displacement thickness, agree far better with the results from the method of Jones than those obtained with the modification as originally proposed by Squire and Young. Because the method of Jones appears to be an adequate approach for the experimental determination of the drag coefficient, it can be concluded from the foregoing result that the von Kármán's integral equation with modified integral parameters has undoubtedly a practical meaning.
- An appreciable error may appear in the calculated drag coefficient if the static pressure variation across the near wake is neglected.
- At survey planes close to the trailing edge, where the maximum total pressure losses are high, the resulting drag coefficients are highly sensitive to errors in the static pressure readings.

## 7 REFERENCES

1. Froude, W. Report of the British Association, 1874, page 249.
2. Taylor, G.I. Skin friction on a flat surface. ARC R and M 604, 1918-1919.
3. Betz, A. Ein Verfahren zur direkten Ermittlung des Profilwiderstandes. ZFM, 3 Heft, 16 Jahrgang, 1925, S 42-44.
4. Jones, B.M. The measurement of profile drag by the pitot traverse method. ARC R and M 1688, 1936.
5. Squire, M.B.  
Young, A.D. The calculation of the profile drag of aerofoils. ARC R and M 1838, 1937.
6. Myring, D.F. The effects of normal pressure gradients on the boundary layer momentum integral equation. RAE TR 68214, 1968.
7. Young, A.D. Note on the effect of compressibility on Jones' momentum method of measuring profile drag. ARC R and M 1881, 1939.
8. Young, A.D. Note on momentum methods of measuring profile drags at high speeds. ARC R and M 1963, 1940.
9. Firmin, M.C.P.  
Cook, T.A. Detailed exploration of the compressible, viscous flow over two-dimensional aerofoils at high Reynolds numbers. ICAS Paper No. 68-09, 1968.
10. Groth, E.E. Boundary layer suction experiments at supersonic speeds. Boundary layer and flow control. Edited by G.V. Lachman, Vol.2, 1961, pp. 1049-1076.
11. Schlichting, H. Boundary-layer theory. McGraw-Hill, New York, sixth edition, 1968.

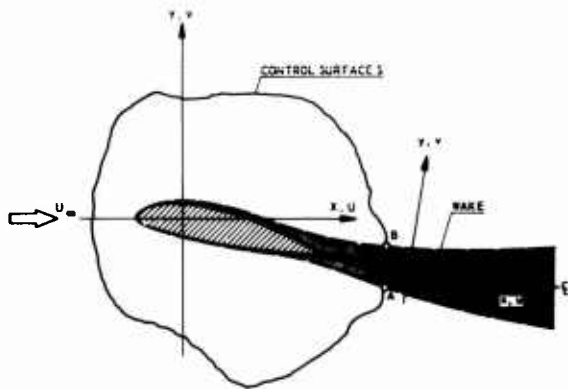


FIG. 1 SCHEMATIC REPRESENTATION OF THE VISCOUS FLOW AROUND AN AIRFOIL AND THE COORDINATE SYSTEMS.

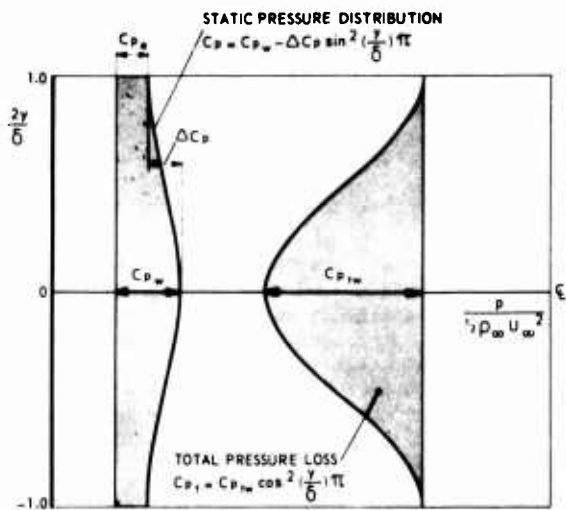


FIG. 2 ASSUMED TOTAL AND STATIC PRESSURE DISTRIBUTIONS ACROSS THE WAKE.

$\Delta C_p = 0$		$C_{p_{tw}}$	$C_{p_w}$	H
ASSUMED ( $M_\infty = 0$ )	①	.80	.20	2.699
	②	.60	.10	1.447
	③	.20	0	1.086
EXPERIMENT ( $M_\infty = 0.3$ )	○	.807	.216	2.35
	△	.567	.111	1.42

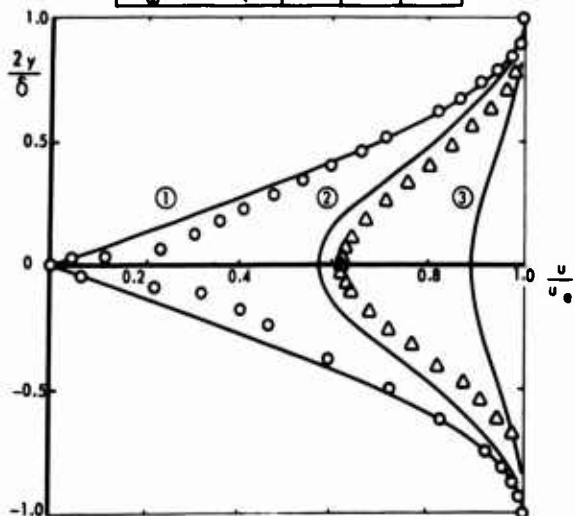


FIG. 3 COMPARISON OF ASSUMED AND EXPERIMENTAL VELOCITY DISTRIBUTIONS.

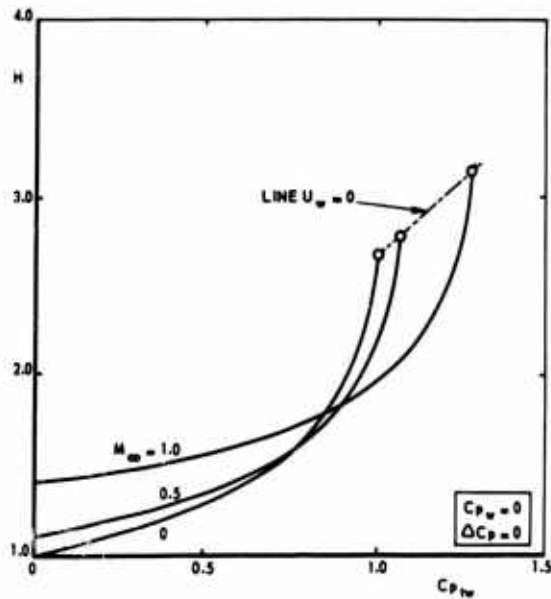


FIG. 4 CALCULATED SHAPE FACTOR FOR THE ASSUMED TOTAL PRESSURE DISTRIBUTION IN THE WAKE.

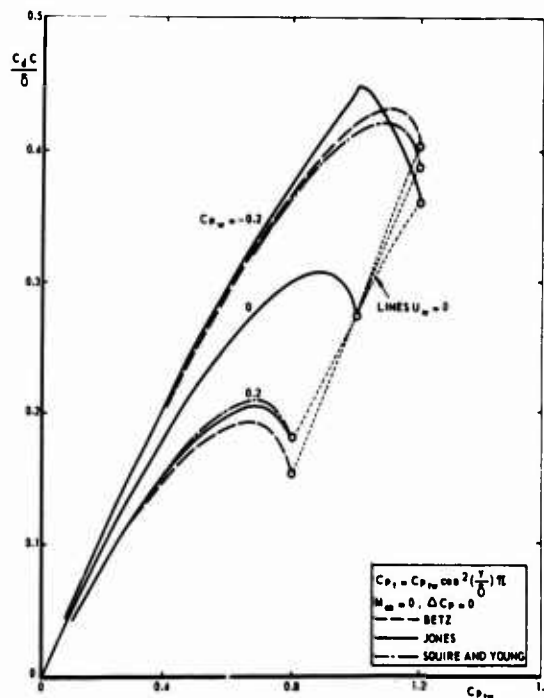


FIG. 5 DRAG COEFFICIENTS ACCORDING TO DIFFERENT METHODS FOR A WAKE WITH CONSTANT STATIC PRESSURE.

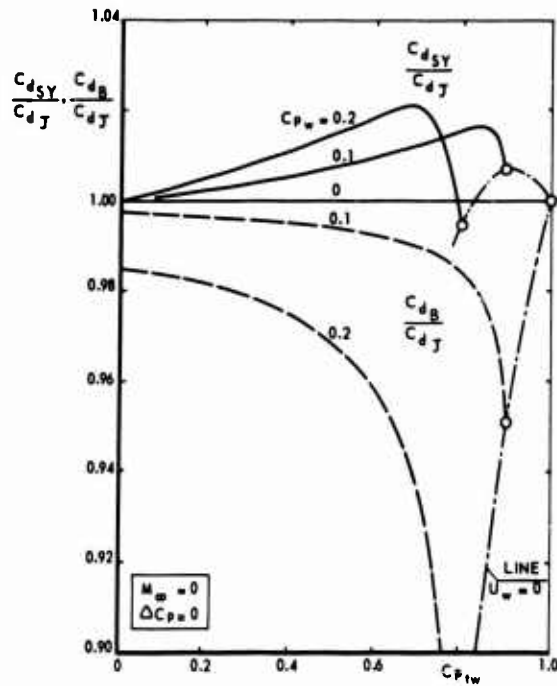


FIG. 6 RATIOS OF DRAG COEFFICIENTS FOR A WAKE WITH CONSTANT STATIC PRESSURE.

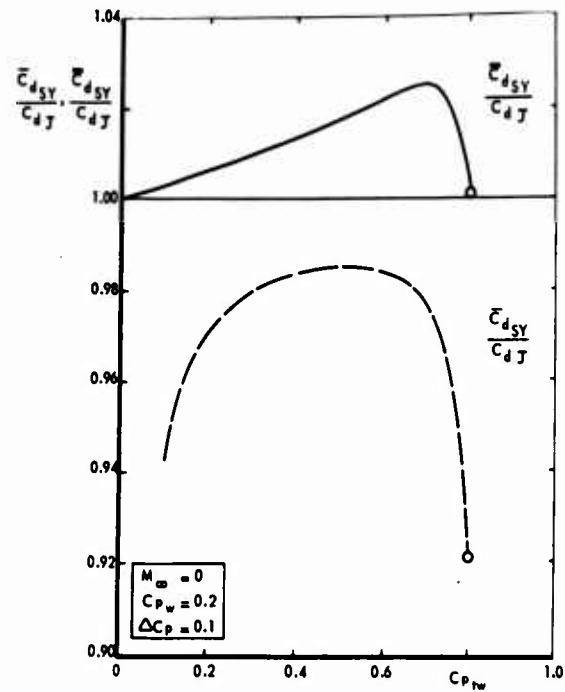


FIG. 8 COMPARISON OF THE TWO MODIFIED VERSIONS OF THE METHOD OF SQUIRE AND YOUNG FOR A WAKE WITH A NORMAL STATIC PRESSURE GRADIENT.

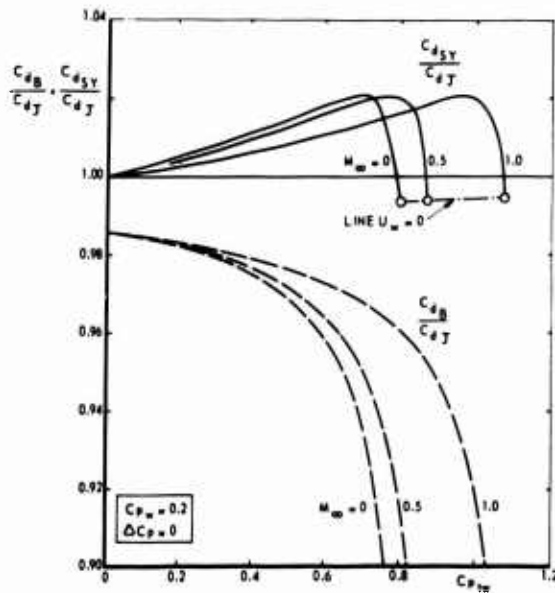


FIG. 7 EFFECT OF MACH NUMBER ON RATIOS OF DRAG COEFFICIENTS FOR A WAKE WITH CONSTANT STATIC PRESSURE.

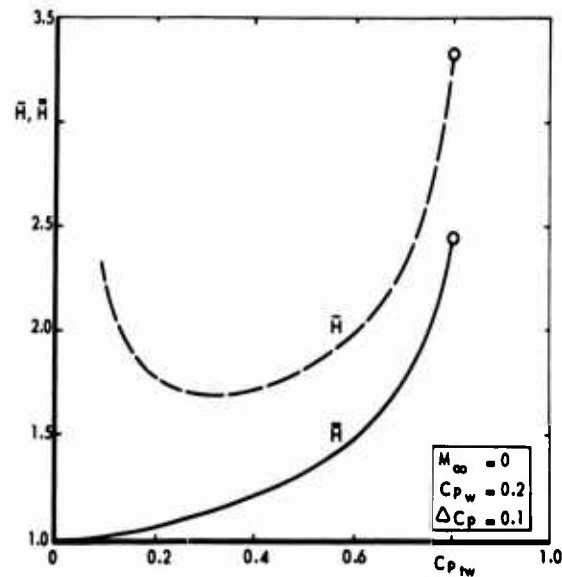


FIG. 9 SHAPE FACTORS AS CALCULATED FROM DIFFERENT DEFINITIONS FOR A WAKE WITH A NORMAL STATIC PRESSURE GRADIENT.

## APPENDIX

## THE MOMENTUM INTEGRAL EQUATION FOR A BOUNDARY LAYER WITH A NORMAL PRESSURE GRADIENT

To derive the drag coefficient according to the method of Squire and Young for a wake with a static pressure variation across the survey plane, the momentum integral equation of the boundary layer (and the wake) has to be modified. In this appendix two modifications will be briefly described. The results are applied respectively in the sections 2.2 and 2.3.

FIRST APPROACH: using conventional definitions of the boundary layer parameters.

The viscous flow close to the trailing edge of an airfoil is relatively highly curved. As a result, the static pressure normal to the airfoil surface varies across the boundary layer. It is assumed that in this case the NAVIER-STOKES equation for a compressible turbulent flow may be simplified to

$$\rho u \frac{\partial u}{\partial x} + \rho v \frac{\partial u}{\partial y} = - \frac{\partial p}{\partial x} + \frac{\partial \tau}{\partial y} \quad (A.1)$$

where the normal Reynolds stresses and the wall curvature are neglected as usual, but not the pressure variation across the viscous layer. The x-axis and the y-axis are taken along and normal to the wall (or wake centre line, see figure 1). Equation (A.1) may be integrated with respect to y from 0 to  $\delta$  for the boundary layer flow to give

$$\int_0^{\delta} \rho u \frac{\partial u}{\partial x} dy + \int_0^{\delta} \rho v \frac{\partial u}{\partial y} dy = - \int_0^{\delta} \frac{\partial p}{\partial x} dy + \int_0^{\delta} d\tau \quad (A.2)$$

Using the continuity equation

$$\frac{\partial}{\partial x} (\rho u) + \frac{\partial}{\partial y} (\rho v) = 0 \quad (A.3)$$

and the boundary conditions  $u = 0$  for  $y = 0$  and  $\tau = 0$  for  $y = \delta$  it can be shown (Ref. 11) that equation (A.2) can be written as

$$\frac{d}{dx} \int_0^{\delta} \rho u^2 dy - u_e \frac{d}{dx} \int_0^{\delta} \rho u dy = - \int_0^{\delta} \frac{\partial p}{\partial x} dy - \tau_w \quad (A.4)$$

where  $\tau_w$  is the shear stress at the wall. If the normal velocity component is neglected then the pressure term becomes approximately

$$\int_0^{\delta} \frac{\partial p}{\partial x} dy = \frac{dp_e}{dx} \delta + \frac{d}{dx} \int_0^{\delta} (p - p_e) dy = - \rho_e u_e \frac{du_e}{dx} \delta + \frac{d}{dx} \int_0^{\delta} (p - p_e) dy \quad (A.5)$$

Substitution of equation (A.5) into equation (A.4) and defining the momentum thickness

$$\theta = \int_0^{\delta} \frac{\rho u}{\rho_e u_e} \left(1 - \frac{u}{u_e}\right) dy \quad (A.6)$$

and the displacement thickness

$$\delta^* = \int_0^{\delta} \left(1 - \frac{\rho u}{\rho_e u_e}\right) dy \quad (A.7)$$

in the usual way, the result is

$$\frac{d}{dx} (\rho_e u_e^2 \theta) + \rho_e u_e \delta^* \frac{du_e}{dx} - \frac{d}{dx} \int_0^{\delta} (p - p_e) dy = \tau_w \quad (A.8)$$

Differentiating equation (A.8) with subsequent substitution of equation (A.7) gives

$$\frac{d\theta}{dx} + \frac{\theta}{\rho_e} \frac{d\rho_e}{dx} + \frac{\theta}{u_e} \frac{du_e}{dx} (2+H) - \frac{d}{dx} \int_0^{\delta} \frac{p - p_e}{\rho_e u_e^2} dy = \frac{\tau_w}{\rho_e u_e^2} \quad (A.9)$$

where  $H = \delta^* / \theta$ .

From the isentropic flow relations it follows that at the outer edge of the boundary layer (neglecting the normal velocity component as before)

$$\frac{d\rho_e}{\rho_e} = -M_e^2 \frac{du_e}{u_e}$$

and equation (A.9) can be reduced to a more usual form

$$\frac{d\theta}{dx} + \frac{\theta}{u_e} \frac{du_e}{dx} (2+H-M_e^2) - \frac{d}{dx} \int_0^{\delta} \frac{p-p_e}{\rho_e u_e^2} dy = \frac{\tau_w}{\rho_e u_e^2} \quad (\text{A.10}) \quad 10-A1-2$$

SECOND APPROACH: using modified definitions of the boundary layer parameters.

Myring (Ref. 6) has compared the actual flow with a hypothetical inviscid flow over a surface displaced over a distance  $\delta^{**}$  from the wall. It is assumed that the static pressure in the hypothetical flow equals the static pressure of the actual flow. Equation (A.4) then reduces for the hypothetical flow to

$$\frac{d}{dx} \int_{\delta^{**}}^{\delta} \rho_i u_i^2 dy - u_e \frac{d}{dx} \int_{\delta^{**}}^{\delta} \rho_i u_i dy = - \int_{\delta^{**}}^{\delta} \frac{\partial p}{\partial x} dy \quad (\text{A.11})$$

If the mass flows in the two comparative flow fields are made equal, then

$$\int_{\delta^{**}}^{\delta} \rho_i u_i dy = \int_0^{\delta} \rho u dy \quad (\text{A.12})$$

and the modified displacement thickness  $\delta^{**}$  should satisfy this equation.

Equation (A.4) may now be subtracted from equation (A.11) to give

$$\frac{d}{dx} \left[ \int_{\delta^{**}}^{\delta} \rho_i u_i^2 dy - \int_0^{\delta} \rho u^2 dy \right] = \int_0^{\delta^{**}} \frac{\partial p}{\partial x} dy + \tau_w \quad (\text{A.13})$$

If a modified momentum thickness is introduced

$$\bar{\theta} = \frac{1}{\rho_{iw} u_{iw}^2} \left[ \int_{\delta^{**}}^{\delta} \rho_i u_i^2 dy - \int_0^{\delta} \rho u^2 dy \right] \quad (\text{A.14})$$

where  $\rho_{iw} u_{iw}^2$  is the value of  $\rho u^2$  calculated from the local wall static pressure  $p_w$  and the free stream total pressure  $p_{t\infty}$ . Equation (A.13) can then be written as

$$\frac{d}{dx} (\rho_{iw} u_{iw}^2 \bar{\theta}) - \int_0^{\delta^{**}} \frac{\partial p}{\partial x} dy = \tau_w \quad (\text{A.15})$$

Equation (A.12) which defines  $\delta^{**}$  cannot be immediately integrated. To yield an explicit expression for the modified displacement thickness  $\delta^{**}$ , Myring assumes a constant static pressure equal to the wall pressure for  $0 \leq y \leq \delta^{**}$ . This means for the considered region that  $\rho_i = \rho_{iw}$  and  $u_i = u_{iw}$ . The modified displacement thickness  $\delta^{**}$  can now be simply derived from equation (A.12) and becomes

$$\delta^{**} = \frac{1}{\rho_{iw} u_{iw}} \int_0^{\delta} (\rho_i u_i - \rho u) dy \quad (\text{A.16})$$

For unknown reasons Myring does not apply the introduced simplified assumption concerning the static pressure for  $0 \leq y \leq \delta^{**}$  to equations (A.14) and (A.15). However, there seems to be no doubt that this is correct as a first approximation. Equation (A.15) can then be written as

$$\frac{d}{dx} (\rho_{iw} u_{iw}^2 \bar{\theta}) - \delta^{**} \frac{dp_w}{dx} = \tau_w \quad (\text{A.17})$$

or

$$\frac{d}{dx} (\rho_{iw} u_{iw}^2 \bar{\theta}) + \rho_{iw} u_{iw} \delta^{**} \frac{du_{iw}}{dx} = \tau_w \quad (\text{A.18})$$

A reduction similar to that in the first approach results in

$$\frac{d\bar{\theta}}{dx} + \frac{\bar{\theta}}{u_{iw}} \frac{du_{iw}}{dx} (2 + \bar{H} - M_{iw}^2) = \frac{\tau_w}{\rho_{iw} u_{iw}^2} \quad (\text{A.19})$$

where  $\bar{H} = \delta^{**} / \bar{\theta}$

If equations (A.19) and (A.10) are compared it can be concluded that the pressure term in the last equation has disappeared and that equation (A.19) represents the expression of the von Kármán's integral equation in conventional form, however, with modified boundary layer parameters. For a boundary layer with a constant static pressure across the layer it can easily be proven that the equations (A.10) and (A.19) are identical and in agreement with the well known conventional equations (Ref. 11).

The expression (A.14) for the modified momentum thickness can be reduced using the introduced assumption of a constant static pressure between  $0 \leq y \leq \delta^*$ . If use is made of equation (A.16) it follows that

$$\bar{\delta} = \int_0^{\delta} \frac{\rho u}{\rho_{iw} u_{iw}} \left(1 - \frac{u}{u_{iw}}\right) dy - \int_0^{\delta} \frac{\rho_i u_i}{\rho_{iw} u_{iw}} \left(1 - \frac{u_i}{u_{iw}}\right) dy \quad (\text{A.20})$$

For convenience, the modified displacement thickness equation (A.16) is written as

$$\bar{\delta}^* = \int_0^{\delta} \left(1 - \frac{\rho u}{\rho_{iw} u_{iw}}\right) dy - \int_0^{\delta} \left(1 - \frac{\rho_i u_i}{\rho_{iw} u_{iw}}\right) dy \quad (\text{A.21})$$

The second term of the righthand sides of equations (A.20) and (A.21) become zero if the static pressure is constant across the boundary layer. Because in this case  $\rho_{iw} = \rho_e$  and  $u_{iw} = u_e$  it follows  $\bar{\delta} = \delta$  and  $\bar{\delta}^* = \delta^*$ .

## TRAINÉE ET DÉCOLLEMENT

par Maurice SIRIEIX \*

OFFICE NATIONAL D'ÉTUDES ET DE RECHERCHES AÉROSPATIALES (ONERA)

92320 - CHATILLON - FRANCE

RESUME

Après avoir décrit le caractère instationnaire de certains décollements et les effets qui en résultent, on définit différents types d'écoulement séparés turbulents, localisés, de caractère permanent en moyenne, qui sont usuellement rencontrés.

Les effets attendus de ces décollements sur la traînée sont examinés et les moyens de calcul disponibles brièvement exposés. Des exemples très divers où ces décollements apparaissent sont ensuite analysés.

SUMMARYDRAG AND SEPARATION

After describing the unsteady character of some separated flows and their resulting effects we define different sorts of turbulent separated flows of a limited extend and quasi-steady character which are to be found usually.

The expected effects of these separated flows on the drag are studied and the available theoretical methods of prediction are briefly described. Miscellaneous examples in which these separated flows appear are then analysed.

## NOTATIONS

- $C_x$  : coefficient de traînée =  $\frac{\text{Traînée}}{(\text{pression dynamique} \times \text{Surface})_{\text{référence}}}$
- $C_z$  : coefficient de portance
- $C_{x_c}$  : coefficient de traînée de culot ; en général pour un écoulement bidimensionnel
- $C_{x_R}$  : coefficient de traînée de pression d'un arrière-corps rapporté à la section au maître couple
- $i$  : quantité de mouvement injectée au culot
- $h$  : hauteur de décrochement
- $h_i$  : enthalpie d'arrêt
- $L$  : longueur
- $M$  : nombre de Mach
- $p$  : pression statique
- $p_i$  : pression d'arrêt de l'écoulement externe
- $p_{ij}$  : pression d'arrêt de l'écoulement interne
- $q$  : pression dynamique
- $q_m$  : débit injecté au culot
- $q_{ma}$  : débit maximum entraîné par voie de mélange
- $Re$  : nombre de Reynolds
- $S$  : entropie
- $S$  : nombre de Strouhal  $\frac{\text{fréquence} \times \text{Longueur de référence}}{\text{Vitesse de référence}}$

\* Directeur Adjoint de l'Aérodynamique

$T$  : température  
 $V$  : module de la vitesse  
 $\vec{V}$  : vecteur vitesse  
 $\vec{X}$  : force de traînée  
 $\delta$  : épaisseur de la couche limite  
 $\delta_1$  : épaisseur de déplacement  
 $\delta_2$  : épaisseur de quantité de mouvement  
 $\eta$  : efficacité d'une prise d'air =  $\frac{\rho_i \text{ entrée moteur}}{\rho_{i\infty}}$   
 $\theta$  : angle  
 $\lambda$  : allongement  
 $\rho$  : masse spécifique  
 $R$  : constante des gaz  $\frac{p}{\rho} = RT$

#### INDICES

$\infty$  : conditions de référence écoulement uniforme amont  
 $j$  : conditions relatives au jet  
 $c$  : conditions relatives au culot  
 $i$  : conditions d'arrêt

### 1. INTRODUCTION

La nécessité d'optimiser dans un large domaine de fonctionnement, des ensembles aérodynamiques complexes dans lesquels intervient notamment l'intégration du système propulsif, entraîne la recherche de configurations utilisées souvent au voisinage de leurs performances maximales et pour lesquelles l'existence de zones décollées est un phénomène usuel.

Par ailleurs et sous certaines conditions, le décollement, loin d'être une source de troubles plus ou moins graves, peut constituer lorsqu'il est quasi stationnaire et n'intéresse que des domaines localisés dont on est en mesure de contrôler l'étendue, une sorte d'autoadaptation des formes à des conditions d'utilisation variées. Accepter la présence de zones décollées impose en contrepartie une connaissance aussi précise que possible de leurs effets.

Nous nous proposons d'examiner l'incidence du décollement sur le bilan de traînée, dans un nombre limité de cas qui nous paraissent significatifs. L'intérêt de cette démarche peut être illustré de façon caricaturale par la figure 1 empruntée à Batchelor, où sont présentés côte à côte et à la même échelle deux obstacles cylindriques bidimensionnels de même traînée par unité d'envergure dans un écoulement uniforme donné ( $\mathcal{R}_L = 2.10^5$ ).

Le coefficient de traînée du profil d'aile rapporté à la surface projetée sur la direction de la vitesse est  $C_x \approx 0,005$ .

Celui du cylindre circulaire est de l'ordre de l'unité ; le décollement étendu qui apparaît dans ce cas est la cause essentielle d'une résistance de forme aussi élevée. La disproportion évidente des tailles montre à quel point l'incidence du décollement sur le bilan de traînée peut être forte.

L'analyse de ce problème comportera tout d'abord l'examen des effets liés à la nature de la couche limite et plus spécialement à l'échappement plus ou moins périodique de structures tourbillonnaires.

Se limitant aux configurations de décollement à caractère quasi-permanent et à nombre de Reynolds élevé, on décrira ensuite les différents types de décollement usuellement rencontrés, les différences fondamentales existant entre zones décollées bidimensionnelles et tridimensionnelles, et l'on examinera brièvement les conséquences attendues sur le bilan de traînée.

Après avoir succinctement passé en revue les modèles de calcul utilisés pour prédire les effets du décollement, un certain nombre d'exemples seront analysés. Ils ont été choisis de façon à couvrir une grande variété de problèmes d'application.

### 2. CARACTERES GENERAUX DES ZONES DECOLLEES ; DIFFERENTS TYPES DE DECOLLEMENTS

#### 2.1 - Exemples du cylindre circulaire

Farmi les configurations qui associent étroitement traînée et décollement, celle du cylindre circulaire placé dans un écoulement uniforme incompressible a fait l'objet d'un nombre considérable de travaux théoriques et expérimentaux. [2 - 3]. A ce titre, elle se révèle extrêmement riche d'enseignements. L'analyse des résultats obtenus, faite notamment par Morkovin [3] et Roshko [4] permet de distinguer lorsque le nombre de Reynolds de l'écoulement varie, les régimes suivants (figure 2) :

A très faible nombre de Reynolds ( $\mathcal{R}_L < 1$ ), on observe un écoulement parfaitement attaché (a).

Lorsque le nombre de Reynolds augmente ( $1 < Re < 30$ ) un décollement laminaire organisé sous forme de deux tourbillons symétriques se produit ; il est suivi d'un sillage stable à proximité du cylindre (b). 11-3

L'apparition d'instabilités du type laminaire dans ce proche sillage (c ;  $30 < Re < 90$ ), annonce la formation lorsque  $90 < Re < 200$  du régime bien connu des tourbillons alternés de Bénard-Karman (d).

La désorganisation de ces tourbillons se produit en aval du cylindre lorsque  $Re < 200$  et entraîne la formation d'un sillage turbulent instable à structure fortement tridimensionnelle.

Le décollement est toujours laminaire. Il se fixe au voisinage d'une position repérée par un angle  $\theta$  compris entre 80 et 85°. Ce régime est appelé régime subcritique (e) ;  $200 < Re < 10^5$

Le nombre de Reynolds continuant à croître ( $10^5 < Re < 3,5 \cdot 10^6$ ), la transition laminaire-turbulent progresse vers l'amont, dans le proche sillage d'abord, dans la zone de décollement ensuite, pour se situer enfin en amont du point de décollement D. Ce dernier se déplace alors brutalement et se localise au voisinage du point  $\theta = 110^\circ$  à l'aval du maître couple. Le déplacement de D entraîne une réduction de l'épaisseur du sillage. L'établissement d'un décollement entièrement turbulent définit le régime critique - post critique, caractérisé par des effets d'instabilités marqués en aval du décollement et par la disparition d'une fréquence prédominante d'échappement tourbillonnaire (f). Lorsque  $Re$  augmente au-delà de  $3,5 \cdot 10^6$ , les informations expérimentales deviennent plus rares ; il semble toutefois qu'une périodicité assez marquée dans la formation de structures tourbillonnaires évacuées par le sillage réapparaît à grand Reynolds (régime transcritique).

Cette transformation de l'écoulement autour du cylindre se reflète dans l'évolution du  $C_x$  moyen et de l'inverse du nombre de Strouhal  $\frac{1}{S}$  en fonction du nombre de Reynolds extraite de [3] (figure 3).

La courbe ( $C_x$ ) présente pour des nombres de Reynolds inférieurs à  $10^3$  une forte décroissance qui découle de la prédominance des effets visqueux. L'extension progressive des zones décollées entraîne toutefois une augmentation de la traînée de forme qui prend une part de plus en plus grande dans le bilan global de résistance.

Dans la plage  $10^3 < Re < 10^5$ , correspondant au régime subcritique, le  $C_x$  reste à peu près constant.

Le décollement laminaire est alors fixé en un point situé en amont du maître couple ; la pression de culot réduite est peu évolutive et la traînée de forme prépondérante, ce qui explique le stationnement observé.

La chute rapide du  $C_x$  qui se produit aux environs de  $Re \approx 5 \cdot 10^5$  marque l'apparition du régime critique. Elle résulte d'une forte décroissance de la traînée de pression due au passage brutal d'un point de séparation laminaire ( $\theta = 80-85^\circ$ ) à un décollement turbulent situé à  $\theta \approx 110^\circ$ .

L'augmentation  $C_x(Re)$  qui se manifeste ensuite se retrouve dans toutes les configurations de décollement turbulent au culot d'un obstacle.

La courbe ( $\frac{1}{S}$ ) reproduit très fidèlement les variations du  $C_x$ , mettant en évidence une étroite corrélation entre ces deux grandeurs.

Du point de vue théorique, la prévision de ces différents phénomènes est très loin d'être acquise. Si des solutions ont été obtenues dans le cas des écoulements à faible Reynolds [5], et si d'autre part des tentatives ont été consacrées à la prévision du champ de pression induit par l'échappement périodique de tourbillons [6 - 7], il n'en demeure pas moins que la plupart des phénomènes extrêmement complexes liés à la formation de structures turbulentes plus ou moins organisées sont actuellement très mal connus et pratiquement incalculables. Pourtant, l'échappement à tendance périodique de tourbillons dans les sillages joue un rôle décisif sur le niveau de la traînée moyenne. Afin de réduire sinon supprimer cet effet, il est usuel de matérialiser, tout ou partie du plan de symétrie à l'aval d'un obstacle bidimensionnel obtus par une plaque plane, de façon à minimiser les interférences entre bords opposés du sillage. On constate que lorsque la longueur de la plaque est suffisante, la zone décollée turbulente, présente un caractère quasi permanent. Dans ces conditions, les pressions moyennes de décollement étant beaucoup plus élevées qu'en l'absence de plaque, le gain sur la résistance de forme peut être très sensible, comme le montre (figure 4) l'évolution de la résistance du culot en écoulement subsonique [8].

De ces divers exemples, nous retiendrons essentiellement deux aspects concernant l'action du décollement sur la traînée :

- d'une part l'influence déterminante de la nature laminaire ou turbulente de la couche limite et de la transition de l'un à l'autre état. Ces effets ne se font sentir qu'à des nombres de Reynolds faibles ou modérés, c'est pourquoi nous n'examinerons leurs conséquences que dans un nombre très limité de cas (décollements de bord d'attaque) ;
- d'autre part, les effets fortement pulsatoires et instationnaires attachés à certains types de décollement, qui doivent être distingués des effets propres à la turbulence et qui dans l'état actuel de nos connaissances ne peuvent être correctement prévus.

Nous n'aborderons pas l'examen de ces décollements, généralement étendus, provoquant la formation de remous turbulents qui se propagent par bouffées dans le sillage.

Les configurations décollées que nous analyserons maintenant, correspondent à un état stationnaire de l'écoulement extérieur et comportent une structure interne généralement turbulente dont l'organisation présente un caractère permanent en moyenne.

## 2.2 - Décollements turbulents stationnaires sur des configurations de caractère bidimensionnel

### 2.2.1 - Propriétés communes

De tels décollements se rencontrent aussi bien en écoulement subsonique qu'en supersonique. Ils sont essentiellement caractérisés par la présence d'une structure tourbillonnaire complexe qui se comporte en moyenne comme s'il existait un tourbillon principal assurant la recirculation de l'écoulement décollé dans un domaine fermé. Cette schématisation ne tient pas compte d'effets secondaires liés à la turbulence tels que: transferts de masse de part et d'autre de lignes de courant moyennes, structure tridimensionnelle de la turbulence, petits déplacements des points de séparation et de recollement. L'existence de ces effets tridimensionnels a été mise en évidence notamment par Ginoux [9] et Roshko [10] dans des études de zones décollées supersoniques et sur des configurations dont on pouvait difficilement suspecter a priori la nature non bidimensionnelle. C'est ainsi (figure 5) que dans le cas d'un corps axisymétrique pseudo plan (distance à l'axe très grande devant l'échelle du décollement) où les effets de limitation transversale sont absents, l'on observe à l'aide de visualisations pariétales de l'écoulement de culot, une série de compartiments régulièrement espacés au voisinage du recollement. Un phénomène analogue a été remarqué par J. Mirande [11] lors de l'étude du recollement turbulent incompressible en aval d'une marche descendante de grand allongement

$$\lambda \left( \lambda = \frac{\text{Dimension transversale}}{\text{hauteur de marche}} > 20 \right).$$

Sans négliger l'importance de ces phénomènes, il n'en demeure pas moins que lorsque  $\lambda$  est assez grand, la présence de telles singularités n'affecte pas sensiblement l'uniformité transversale des pressions dans tout le domaine voisin de cette pseudo ligne de recollement.

Les différences existant entre zones décollées subsoniques et supersoniques bidimensionnelles interviennent davantage au niveau de l'écoulement extérieur que dans l'organisation même du domaine de recirculation. Toutefois, la contrainte directionnelle plus sévère imposée par l'écoulement extérieur dans le cas supersonique peut contribuer à assurer une plus grande stabilité des configurations obtenues, spécialement au niveau des zones décollées susceptibles de se former près du bord de fuite d'un obstacle.

Dans les exemples que nous allons commenter, nous ne distinguerons le cas supersonique du cas subsonique que lorsque les circonstances l'exigeront.

### 2.2.2 - Différents types de zones décollées turbulentes stationnaires

Les exemples les plus courants sont présentés figure 6. Ils appartiennent grosso modo à trois catégories de configurations :

- a) celles pour lesquelles les points de décollement D et de recollement R sont pratiquement fixés par une condition géométrique de paroi (discontinuité de pente) ; c'est le cas de la cavité rectangulaire étroite ;
- b) celles où l'un des points D ou R étant imposé, le second est "libre" ; c'est le cas des marches ou du culot ;
- c) enfin, le troisième type est celui où les points D et R sont "libres". Il en est ainsi pour des configurations telles que décollement de bord d'attaque, décollement dans un coin, décollement provoqué par la réflexion d'un choc.

Dans le cas de l'écoulement de culot supersonique symétrique où deux zones décollées stables I et II sont obtenues (figure 7 a), les deux zones sont séparées par une frontière fluide M R. La structure de I ou II est très voisine de celle qui s'établirait si une plaque matérielle très mince remplaçait la frontière M R et la prolongeait.

Lorsque les écoulements de part et d'autre du culot sont différents, la configuration réalisée, également stable peut être schématisée de la manière indiquée figure 7 b [12]. Deux zones tourbillonnaires de recirculation apparaissent alors, elles contribuent à l'établissement d'un processus permanent d'échange turbulent entre les deux écoulements. Une ventilation naturelle de l'écoulement du culot existe alors.

Un autre cas important dans la pratique, spécialement en ce qui concerne l'étude du profil d'aile placé en incidence dans un écoulement incompressible est celui où la transition laminaire turbulente se produit au sein du décollement. La figure 8 présente la visualisation d'une telle configuration obtenue au tunnel hydrodynamique par Werlé. Cette expérience, effectuée selon la technique du bord d'attaque agrandi [13] montre de façon frappante la naissance au coeur du courant de recirculation laminaire d'instabilités qui s'amplifient et s'étendent transversalement de façon très brutale pour créer la turbulence de la couche limite extérieure et du domaine de recirculation voisin du recollement. A l'inverse, une forte atténuation de la turbulence au voisinage de la paroi apparaît dans le courant de retour si bien que la zone décollée laminaire au voisinage du point de séparation demeure préservée.

Dans presque tous les cas examinés, l'établissement d'un domaine de recirculation fermé au niveau des lignes de courant moyennes est une propriété spécifique des décollements turbulents stables du type bidimensionnel.

Lorsque l'écoulement est tridimensionnel, les zones décollées stables ne sont plus assujetties à cette condition de fermeture.

### 2.3 - Décollements tridimensionnels stationnaires

Depuis 1950, (M. Roy, R. Legendre, Maskell)[14 - 15 - 16], la caractérisation des écoulements décollés tridimensionnels a fait l'objet de nombreuses recherches; la visualisation au tunnel hydrodynamique de l'ONERA a joué un rôle essentiel, dans la compréhension de ces phénomènes [17 - 18].

Des nombreux cas traités (ailes en flèche, ailes de faible allongement, corps élancés etc ...) pour lesquels les structures des zones décollées sont extrêmement complexes, on peut toutefois dégager un certain nombre de remarques générales.

Tout d'abord, on observe l'existence de nappes de séparation tourbillonnaires organisées qui se détachent de l'obstacle et s'enroulent autour de leur noyau.

On note ensuite que la zone décollée est souvent alimentée de façon permanente par le fluide extérieur, ce qui est contraire au processus de recirculation fermé et implique nécessairement l'échappement du fluide ainsi introduit.

En dernier lieu, il apparaît que certaines de ces structures tourbillonnaires ont un caractère potentiel.

Un exemple typique est celui de l'aile  $\Delta$  mince et élancée placée en incidence dans un écoulement uniforme (figure 9).

Une étude détaillée de l'écoulement effectuée conjointement au tunnel hydrodynamique et en soufflerie a permis d'obtenir une description précise de l'organisation du décollement; celle-ci est pratiquement la même en incompressible et en écoulement supersonique [16] :

- la nappe de courant issue de l'intrados décolle au bord d'attaque puis s'enroule en cornet pour constituer l'ossature du tourbillon principal (1) ;
- une seconde nappe aboutit sur l'aile suivant la ligne de recollement M et constitue la frontière extérieure du domaine tourbillonnaire ;
- les lignes de courant qui forment cette seconde nappe longent la paroi en (4) suivant des trajectoires très déviées par rapport à la direction de référence OX et décollent en (5) pour former un tourbillon secondaire (2), moins intense que le premier et de sens opposé.

Le fluide circulant entre ces deux nappes alimente les deux tourbillons qui constituent les éléments essentiels de la zone décollée ; le partage des débits relatifs à chacun d'entre eux s'effectue le long de N.

Dans une telle organisation, les effets liés à la turbulence et la viscosité tiennent une place plus réduite qu'en écoulement bidimensionnel. Toutefois, lorsque ces structures tourbillonnaires sont mises en présence de forts gradients de pression positifs, comme c'est le cas par exemple lorsque l'aile  $\Delta$  est placée à très forte incidence, elles peuvent éclater (figure 10), leur noyau qui est formé d'un écoulement à plus faible énergie cinétique ne pouvant surmonter la recompression à laquelle il est soumis.

Il est bien évident qu'un décollement tridimensionnel ne présente pas dans tous les cas une organisation aussi parfaite que celle de l'exemple précédent. Cependant, il est le plus souvent caractérisé par la présence de structures tourbillonnaires et d'écoulements transversaux. Le cas de la marche d'envergure limitée est typique. Le dessin perspectif de la figure 11 représente les résultats de visualisations faites par Werlé. Il met en évidence la complexité de l'écoulement, et montre l'échappement transversal tourbillonnaire du fluide provenant de la couche limite, qui distingue cette configuration du cas bidimensionnel pur.

### 3. EXAMEN DES ELEMENTS INTERVENANT DANS LE BILAN DE RESISTANCE ; INFLUENCE DU DECOLLEMENT

- 3.1 - La décomposition de la résistance d'un obstacle portant selon les trois modes classiques :
- résistance de forme ou de pression,
  - résistance de frottement,
  - résistance induite (spécifique des corps tridimensionnels),

permet de distinguer les facteurs de production de la traînée. Dans le cas d'un écoulement permanent, uniforme à l'infini amont, l'application du théorème des quantités de mouvement à travers la surface de contrôle représentée figure 12, lorsque l'on fait tendre  $S$ ,  $C_0$ ,  $C$ , vers l'infini, conduit à la relation classique qui détermine la traînée  $\bar{X}$  :

$$(1) \quad \bar{V}_\infty \cdot \bar{X} = \int_{C_1} \bar{V}_\infty (\bar{V}_\infty - \bar{V}_1) dq$$

Si l'on admet qu'en tout point de  $C_1$  la condition  $\left| \frac{V_\infty - V_1}{V_\infty} \right| \ll 1$  est réalisée et que l'écoulement est isoénergétique ( $h_1 = cte$ ), le second membre de la relation (1) peut s'exprimer en fonction de la variation d'entropie  $\Delta$  par :  $\bar{V}_\infty \cdot \bar{X} = \int_{C_1} T_\infty \cdot \delta \Delta \cdot dq$

Cette expression montre que la traînée d'un obstacle est définie par les irréversibilités de toute nature au sein de l'écoulement, qui se traduisent par une production d'entropie. En écoulement subsonique, ces irréversibilités proviennent de l'évolution des couches limites le long des parois, ainsi que de la dissipation d'énergie dans les zones décollées et dans les sillages. Lorsque des ondes de choc se forment au sein de l'écoulement, l'accroissement d'entropie correspondant, est à l'origine de la traînée d'onde. Quand un décollement se produit en supersonique, la déviation qu'il impose à l'écoulement extérieur engendre un système d'ondes de choc obliques dont les effets sur la traînée s'ajoutent à ceux qui proviennent de la viscosité et de la turbulence. Pourtant un décollement ne conduit pas nécessairement à une augmentation de la traînée comme va le montrer l'analyse de deux exemples typiques.

Considérons tout d'abord un profil d'aile placé à une incidence positive telle que le choc qui s'établit à la pointe arrière de l'obstacle fasse décoller la couche limite d'extrados (figure 13).

La configuration de fluide parfait (figure 13 a) est remplacée par une structure plus complexe (figure 13 b) correspondant à un dédoublement du choc de recompression aval. Le décollement induit donc sur la partie arrière à l'extrados une augmentation sensible des pressions et entraîne de ce fait une diminution de la traînée de forme et de frottement. L'augmentation totale d'entropie résultant des deux chocs est en effet plus faible que celle qui est produite pour une même déviation totale par un choc unique plus intense.

De la même manière, une réduction sensible de la traînée d'un corps obtus peut être obtenue en écoulement supersonique ( $M > 1,5$ ) par la création d'un décollement de bord d'attaque, au moyen d'une pointe émergente (figure 14) [20]. En l'absence de pointe, l'écoulement comporte une onde de choc détachée qui provoque une augmentation d'entropie importante (figure 14 a). La mise en place d'une sonde dont la pointe est convenablement située en amont de l'obstacle (figure 14 b) modifie la structure de l'écoulement.

Un décollement approximativement conique et quasi isobare se produit au voisinage de la pointe, entraînant la formation d'une nappe de choc également conique. Une réduction très sensible des pertes par choc et par suite de la traînée de l'avant-corps est alors obtenue.

### 3.2 - Cas des écoulements tridimensionnels ; traînée induite

L'apparition de décollements dans un écoulement tridimensionnel entraîne non seulement un effet de déplacement résultant de l'épaississement des couches dissipatives, mais encore la formation de structures tourbillonnaires organisées qui interviennent notamment en subsonique dans le schéma théorique d'évaluation de la traînée induite. En particulier, la connaissance des lignes d'échappement de ces tourbillons est un élément essentiel de l'application de ce schéma [21] dans lequel la nappe décollée est considérée comme une surface de discontinuité s'étendant jusqu'à l'infini au sein de l'écoulement isentropique.

## 4. MODELISATION DES ECOULEMENTS DECOLLES TURBULENTS

Examinons brièvement sur quels fondements les calculs de décollement s'appuient et quelles en sont les limites.

### 4.1 - Problèmes bidimensionnels

#### 4.1.1 - Méthodes basées sur le concept de ligne limite

Les principes essentiels de ces méthodes de calcul appliquées aux écoulements turbulents supersoniques ont été définis par l'analyse de H.H. Korst [22]. Celle-ci a été reprise par de nombreux auteurs [ ] dans le but de rechercher une meilleure représentation des facteurs d'influence agissant sur le recollement. Le modèle qui a servi de base à l'établissement de ces diverses théories est celui de la marche descendante placée dans un écoulement supersonique uniforme (figure 15).

Dans la formulation initiale, l'hypothèse de base était que sur la ligne de courant ( $\ell$ ) aboutissant au point de recollement R, l'évolution dans la zone de recompression II était isentropique.

La théorie du mélange turbulent (domaine I) permet de définir ( $\ell$ ) et de connaître l'état de l'écoulement sur cette ligne au début de II ; en identifiant la pression d'arrêt isentropique  $p_i(\ell)$  avec la pression aval  $p_1$  après recollement (III), H.H. Korst a établi un critère de recollement sous la forme :  $\frac{p_2}{p_1} = f(M_1)$

Les tentatives successives faites pour améliorer la théorie initiale, concernant essentiellement :

- la prise en compte de façon simple de l'effet de la couche limite en A [23],
- l'amélioration à partir de données expérimentales des hypothèses concernant le processus de recompression (Domaines II et III) [24,27]
- l'extension au cas des écoulements axisymétriques [28-30]

En particulier, les recherches poursuivies à l'ONERA dans cette voie ont permis d'établir une loi de recollement turbulent, basée sur le concept de critère angulaire de recollement et applicable aux écoulements plans et de révolution [30].

Dans le cadre de ces méthodes, la solution d'un problème de décollement consiste à chercher par tâtonnement, un écoulement de fluide parfait isobare sur la frontière de la zone décollée, qui satisfait aux lois de recollement turbulent retenues (saut de pression au recollement ou déviation angulaire).

Cette technique se généralise au cas où le point de décollement est a priori indéterminé ; elle nécessite alors l'utilisation d'un critère de décollement turbulent.

11-7

L'intérêt de ces méthodes réside dans leur simplicité alliée à une extrême souplesse. Elles conduisent à une bonne prise en compte de divers facteurs d'influence agissant sur le recollement et s'appliquent sans difficulté au cas des écoulements dissymétriques confluants de part et d'autre d'un culot [22]

Lorsque l'écoulement est subsonique à la frontière du décollement, un modèle de calcul basé sur l'analyse des échanges turbulents à la frontière du domaine de recirculation a été proposé par Tanner pour des obstacles en forme de coin [32].

Une représentation très schématique du sillage à l'infini du corps permet d'établir à l'aide d'un calcul de fluide parfait défini lorsque la pression de culot est connue, une relation entre la traînée du culot et le débit maximal entraîné par voie de mélange :  $C_{q_{m\alpha}} = f_1(C_{x_c})$

Une seconde relation  $C_{q_{m\alpha}} = f_2(C_{x_c})$  est obtenue à partir de l'étude du mélange ; elle fait intervenir des coefficients empiriques ajustés sur l'expérience.

Ces deux relations déterminent la pression de culot.

#### 4.1.2 - Méthodes du type couche limite

Après les travaux de Crocco et Lees en 1952 [33] et les améliorations de la méthode originale résultant surtout de l'introduction de données empiriques mieux adaptées [34], des solutions nouvelles aux problèmes de décollement et recollement supersonique turbulent n'ont été proposées qu'assez récemment [36]. Les applications actuellement connues concernent le calcul de la pression de culot et celui du décollement devant une rampe en écoulement bidimensionnel plan [37]. Les résultats obtenus donnent une description qualitativement correcte de l'évolution des pressions, soit dans le plan de symétrie du culot, soit à la paroi de la rampe. Parmi les améliorations proposées, on retiendra essentiellement la prise en compte des effets des gradients de pression normaux [38-39]. Les voies de recherche récentes sont orientées vers une description plus précise de la structure de l'écoulement dissipatif [40].

En écoulement subsonique de par la nature elliptique des équations régissant l'écoulement extérieur non visqueux, les méthodes de calcul du type couche limite sont nécessairement plus lourdes qu'en supersonique et se prêtent de surcroît aux mêmes objections.

Malgré quelques difficultés numériques, les résultats obtenus notamment par Green [41] sont en assez bon accord avec l'expérience.

Signalons également les travaux de Nash [42] concernant le profil d'aile tronqué à incidence nulle, basés sur une analyse du développement du sillage jusqu'à l'infini et ceux de N'Guyen Van Noi et Mirande relatifs au décrochements de paroi qui font intervenir notamment une loi empirique d'évolution du paramètre de forme dans la région de recollement [43].

#### 4.1.3 - Méthodes de résolution complète

Des tentatives en vue d'obtenir par différences finies des solutions des équations aux valeurs moyennes dérivées de celles de Navier-Stokes ont été effectuées dans quelques cas simples tels que décrochements de paroi, par Spalding et ses collaborateurs notamment [44].

Ces méthodes se heurtent encore à des difficultés numériques (stabilité, convergence des schémas, durée). De plus, les modèles de turbulence utilisés sont généralement trop simplistes.

Les progrès qui peuvent être enregistrés dans ce domaine dépendent dans une large mesure d'une connaissance plus approfondie des phénomènes de transfert turbulent dans les zones décollées et à leur voisinage. Les recherches expérimentales entreprises par Bradshaw dans le cas du recollement subsonique constituent un premier pas dans cette voie [45].

#### 4.2 - Décollements tridimensionnels

Etant donné la complexité de tels écoulements, la recherche d'un "modèle" n'a été entreprise que dans un nombre très limité de cas pour lesquels le décollement comporte une structure bien organisée où les effets de la viscosité peuvent être négligés en première approximation.

Il en est ainsi pour l'aile  $\Delta$  mince et très effilée (figure 10). Un certain nombre de travaux théoriques initiés par M. Roy et R. Legendre ont été consacrés à ce problème [46].

Le modèle le plus élaboré est celui qui a été proposé par J.H.B. Smith [46]. La nappe est schématisée (figure 16) par une couche tourbillonnaire mince pour sa partie extérieure, et par un tourbillon isolé pour la partie représentative du noyau.

Cette nappe qui est confondue avec une surface de courart, part du bord d'attaque où la vitesse doit être nécessairement finie.

La distribution des intensités tourbillonnaires dans la couche mince est déterminée par la condition de continuité des pressions à sa traversée ; la position du tourbillon isolé est obtenue en assurant l'équilibre du système tourbillonnaire (somme des forces agissantes nulle).

11-8

Les résultats fournis par ce modèle sont assez bien vérifiés par l'expérience, aussi bien du point de vue des efforts globaux qu'en ce qui concerne la position du noyau.

La généralisation de cette méthode au cas du contournement d'un bord arrondi est un problème très complexe même dans l'hypothèse où la structure de la zone décollée présente un caractère non visqueux prépondérant [21]. Le choix de la ligne de séparation, définie à partir d'un calcul de couche limite tridimensionnelle (figure 17) s'impose comme ligne de départ d'une nappe tourbillonnaire enroulée. En principe, la solution complète d'un tel problème ne peut être obtenue que par un calcul couplé de la couche limite et de l'écoulement extérieur.

Des cas de figures beaucoup plus compliqués se présentent : ils sont hors de portée des méthodes de calcul actuelles

Dans le cas où l'aile étudiée est de plus grand allongement, les méthodes appliquées dans la pratique [47] ne représentent les effets d'un décollement tridimensionnel que d'une manière assez grossière. En particulier, l'influence des nappes de tourbillon qui délimitent les zones décollées n'est pas traitée, ce qui de l'aveu même des utilisateurs constitue une lacune importante.

## 5. EXEMPLES PRATIQUES D'INFLUENCE DU DECOLLEMENT SUR LE BILAN DE TRAINEE

### 5.1 - Décollements de bord d'attaque

Pour caractériser les effets de ce type de décollement, nous retiendrons trois exemples.

#### 1er exemple : Décollements localisés de bord d'attaque sur le profil d'aile en écoulement incompressible

Au cours de la recompression qui suit le pic de survitesse apparaissant sur les profils d'ailes en incidence, la couche limite laminaire décolle en général conformément aux prévisions théoriques, et, suivant le nombre de Reynolds et l'incidence, il se forme soit une zone décollée très étendue, soit un bulbe de décollement limité dont la structure varie selon les circonstances. Dans la plupart des cas, cette structure comporte comme le montre la figure 8, une partie laminaire voisine du décollement, suivie d'une zone de transition, le recollement s'effectuant en régime turbulent. On distingue cependant deux catégories de bulbe [48.49] : les bulbes longs pour lesquels la recompression qui se produit hors du recollement est lente et progressive, les bulbes courts qui conduisent à des recompressions très brutales. En ce qui concerne l'incidence de ce type de décollement sur la traînée du profil d'aile, on peut faire les remarques suivantes :

Dans le cas du bulbe court, la présence d'un décollement n'altère que très localement la distribution des pressions sur le profil (figure 18). Par suite, son action sur la traînée de forme est négligeable.

Par contre, la prévision de la résistance de frottement qui comporte un calcul aussi exact que possible de la couche limite, doit nécessairement faire intervenir une estimation précise des effets du bulbe sur l'évolution des épaisseurs caractéristiques de déplacement et de quantité de mouvement.

A titre d'exemple, la figure 19 montre deux cas de calcul.

Le premier (a) est effectué en fixant arbitrairement la transition au point de séparation laminaire ; le second (b) tient compte de la présence du bulbe selon une méthode récente développée en [50].

On voit que le calcul b représente bien l'expérience et que des écarts significatifs peuvent être introduits par l'hypothèse arbitraire de la transition en S, qui conduit à sous-estimer la traînée de frottement.

Dans le cas du bulbe long, la répartition expérimentale des pressions sur le profil est sensiblement différente de celle que fournit un calcul de fluide parfait (figure 20). L'existence d'une telle zone décollée induit donc une résistance de forme qui peut être appréciable (figure 21). De la même manière que dans le cas du bulbe court, mais avec une importance accrue liée à l'extension longitudinale du bulbe, le calcul de la couche limite impose une caractérisation précise de la structure de la zone décollée, notamment de la transition et de l'évolution des épaisseurs caractéristiques dans ce domaine. Ce sont actuellement des problèmes ouverts.

#### 2ème exemple : Décollements de bord d'attaque dans une prise d'air

Le fonctionnement d'une prise d'air aux divers régimes qui lui sont imposés (décollage, croisière, montée, attente etc...) met en jeu des variations notables de débit et par suite des conditions d'écoulement au voisinage des lèvres d'entrée extrêmement différentes selon les circonstances.

Lorsque pour une vitesse de vol subsonique, une réduction du régime moteur (figure 22 a) intervient, elle conduit à une diminution du débit capté ; des survitesses apparaissent à l'extrados de la carène et un décollement se produit à la recompression qui suit, de sorte que, du point de vue de la traînée externe, ce cas s'apparente à celui du profil, dans l'exemple précédent.

Au décollage, où le débit prélevé est important, figure 22 b, un phénomène analogue se produit dans l'écoulement interne et provoque une perte d'efficacité du moteur et (figure 23) une réduction de la poussée. Cette situation peut être aggravée s'il existe un vent latéral notable. Dans le cas de la prise d'air d'un avion supersonique dont les lèvres sont obligatoirement très minces, l'introduction de dispositifs auxiliaires de prélèvement permet de réduire ces effets défavorables.

Un décollement de bord d'attaque peut également se produire en supersonique lors de la mise en dérapage d'une prise d'air de type bidimensionnel, sur la paroi latérale de la prise attaquée suivant une incidence positive. Pour illustrer ces considérations, nous donnerons deux exemples :

Le premier concerne le fonctionnement à débit réduit d'une prise d'air axisymétrique adaptée à un régime de vol subsonique. La figure 23 donne la réduction d'efficacité de la prise d'air au point fixe, en fonction du nombre de Mach moyen  $M_2$  de l'écoulement à l'entrée du moteur, due à la présence d'un décollement de bord d'attaque. Une amélioration de la forme des lèvres permet d'éliminer le décollement et ses effets [51].

Le second exemple extrait de [52] est relatif à une prise d'air placée en dérapage dans un écoulement supersonique (figure 24).

Dans le cas examiné, le flanc mis en incidence positive se comporte à la manière d'une aile  $\Delta$  à bord d'attaque subsonique, ce qui conduit à la formation d'un tourbillon en cornet (figure 9) et provoque une perturbation sensible de l'écoulement interne entraînant de la distorsion et une perte d'efficacité de l'ordre de 4%.

Pour éviter la formation de ce vortex, une échancrure a été pratiquée dans le flanc, il en résulte une réduction de l'incidence locale du bord d'attaque par déviation vers l'extérieur d'une partie très faible de l'écoulement capté (de l'ordre de 0,2% du débit total). La perte d'efficacité résiduelle est alors de 1%, pour le même angle de dérapage.

### 3ème exemple : Décollement créé par une pointe émergente

Comme nous l'avons déjà signalé (§ 3.2.2.), l'organisation d'un décollement au voisinage du bord d'attaque d'un corps obtus provoque en supersonique une réduction de la traînée qui peut être appréciable lorsque l'incidence est modérée [20]. La longueur d'émergence  $L$  de la pointe est un paramètre essentiel qui agit sur le gain de résistance et sur la stabilité des décollements obtenus.

En régime stable, la courbe  $C_x(L)$  évolue de la manière suivante (figure 25) : le  $C_x$  est pratiquement inchangé lorsque  $L$  est inférieur à la distance de détachement du choc. Il décroît progressivement lorsque  $L$  augmente, passe par un minimum pour une longueur critique  $L_c$ , puis croît brutalement pour plafonner ensuite à une valeur sensiblement constante. Cette remontée rapide correspond à un déplacement du point de séparation depuis la pointe ou son voisinage jusqu'à une position située sur le corps de la sonde où le décollement devient rapidement turbulent. A partir de cette observation, Rom et alii ont établis une méthode de calcul de  $L_c$  bien recoupée par l'expérience [53].

Lorsque l'incidence du corps augmente (figure 26), l'expérience montre que la réduction du  $C_x$  s'amenuise et disparaît aux incidences élevées ( $\alpha \approx 15^\circ$ ).

Les régimes d'instabilités qui sont observés correspondent le plus souvent à des longueurs d'émergence relativement faibles pour lesquelles des conditions de recollement stationnaires en régime supersonique ne peuvent être réalisées.

La prévision complète de ces phénomènes est actuellement hors de portée des méthodes de calcul existantes.

## 5.2 - Décollements turbulents de bord de fuite : pression de culot

5.2.1 - La détermination précise de la traînée de culot est un problème d'intérêt pratique évident qui intervient spécialement dans les recherches d'optimisation.

La traînée de culot représente en effet dans certains cas un élément important de la traînée totale qui peut atteindre 40% pour un corps de révolution. Nous nous limiterons à l'exposé de quelques indications générales concernant les paramètres d'influence qui agissent sur la traînée de culot et la précision avec laquelle on peut en prédire les effets. La maîtrise de ces problèmes est très différente selon que l'écoulement est subsonique ou supersonique, c'est pourquoi nous distinguerons ces deux cas.

### 5.2.2 - Pression de culot en écoulement supersonique

L'étude théorique et expérimentale de l'écoulement bidimensionnel en aval d'une marche descendante a permis de dégager les principaux facteurs agissant sur la traînée de culot [23].

L'influence du nombre de Mach est très importante comme le montre la figure 27, le  $C_x$  culot décroissant fortement lorsque  $M_\infty$  augmente. Toutefois, la dispersion des points figurant sur ce diagramme qui n'est pas seulement le fait d'imperfections d'origine expérimentale illustre parfaitement la nécessité de tenir compte d'autres effets tels que :

- l'état de la couche limite au point de décollement, caractérisé par l'épaisseur de quantité de mouvement  $\delta_2$  ;
- le débit masse  $q_m$  et de quantité de mouvement  $i$  échangé avec la zone décollée par soufflage ou aspiration à faible vitesse ;
- éventuellement la non uniformité de l'écoulement à l'extérieur de la zone décollée.

Des exemples destinés à illustrer l'action de ces divers paramètres sont présentés figures 28 à 31.

Un accroissement progressif de l'épaisseur  $\delta_2$  de la couche limite initiale pour une hauteur  $R$  de culot donnée se traduit, quel que soit le nombre de Mach, par une décroissance d'abord rapide de la traînée de culot, s'atténuant très vite lorsque  $\delta_2$  augmente pour tendre vers une valeur quasi constante dans une large plage de variations de  $\frac{\delta_2}{R}$ .

L'injection de masse dans la zone décollée, conduit à une évolution analogue de la traînée de culot, la pente  $\frac{dC_x}{dC_h}$  étant particulièrement importante aux faibles taux de soufflage  $C_h$ .

L'identité de ces deux effets pour de faibles valeurs de  $\delta_2$ ,  $q_m$ ,  $i$  a été démontrée par P. Carrière [23].

Sur ces mêmes figures ont été portés les résultats de différentes méthodes de calcul basées soit sur le concept de ligne limite (I), soit sur une technique intégrale du type couche limite (II). On constate que ces prévisions sont en général proches de l'expérience et il est normal que les premières (I), faisant plus largement appel à des données empiriques, conduisent à un meilleur résultat d'ensemble.

Lorsque les écoulements de part et d'autre du culot sont fortement dissymétriques, il s'établit comme nous l'avons vu précédemment (§ 2.2.2) une ventilation naturelle du domaine de confluence (figure 7b), le niveau des échanges étant fixé par les conditions de conservation de la masse et de l'énergie dans ce domaine.

Une telle situation se rencontre en particulier dans les problèmes de propulsion, lorsque l'on étudie la confluence d'écoulements internes et externes. [54]

La variation de la pression de culot pour différents régimes de fonctionnement d'un éjecteur bidimensionnel est représentée figure 32. Cette évolution est très caractéristique et se retrouve dans de nombreux problèmes de confluence.

La résistance du culot décroît d'abord dans le domaine des très faibles débits (I), puis augmente rapidement pendant la phase d'amorçage de la tuyère (II). On assiste ensuite à une décroissance régulière de la traînée de culot, lorsque la confluence des écoulements étant supersonique, le taux de détente du flux interne augmente. Le passage du domaine II au domaine III peut être discontinu et instable.

Le calcul basé sur la notion de ligne limite demeure dans l'état actuel des choses le moyen le plus commode et vraisemblablement le plus sûr pour traiter cette catégorie de problèmes. Sur cet exemple, il permet d'obtenir une bonne prévision des différents régimes d'écoulement et fournit des valeurs numériques proches de l'expérience.

Les difficultés de calcul les plus grands se situent au niveau de la représentation du domaine II (phase d'amorçage).

Dans le cas des écoulements axisymétriques, la résistance de culot est soumise aux mêmes facteurs d'influence qu'en écoulement plan. Toutefois, la non uniformité de l'écoulement à l'extérieur de la zone décollée qui est une propriété spécifique de ce type d'écoulement joue dans ce cas un rôle prépondérant, de même que les modifications apportées à l'évolution des couches de mélange par l'effet de révolution.

Ces effets sont spécialement importants dans le cas d'un corps tronqué ; à égalité de nombre de Mach, la traînée de culot est alors plus faible que celle d'une configuration plane équivalente comme le montre la figure 33.

L'extension aux écoulements axisymétriques des méthodes de calcul bidimensionnelles basées sur le concept de ligne limite a été proposée par divers auteurs [29, 30].

Les résultats obtenus conduisent à un recoupement assez satisfaisant avec l'expérience, aussi bien dans le cas du culot sans jet (figure 34) que dans le cas de la confluence supersonique (figure 35). En particulier, les effets favorables sur la traînée de culot d'un rétreint (figure 34b) ou d'un soufflage à faible vitesse sont correctement prévus (figure 35).

Les principales limitations auxquelles se heurtent les méthodes de calcul que nous venons d'évoquer concernent des configurations pour lesquelles :

- l'épaisseur de la couche limite initiale est très grande devant la longueur de la zone décollée ;
- des effets d'incidence ou de géométrie de l'obstacle entraînent une organisation tridimensionnelle du décollement ;
- une perturbation importante et localisée (onde de choc notamment) se produit en aval du recollement et à son voisinage [55].

### 5.2.3 - Pression de culot en écoulement subsonique et transsonique

Nous avons vu (§ 1) que la traînée de culot d'un corps tronqué en écoulement subsonique dépend fortement de la stabilité du proche sillage comme le montrent les exemples bidimensionnels des figures 4 et 36.

Selon que l'écoulement dans ce domaine est quasi permanent (recollement sur paroi) ou fortement instationnaire (confluence), le  $C_{x_c}$  varie du simple au double. Cet écart s'amenuise dans le domaine transsonique (figure 4 b) et disparaît pratiquement lorsque le recollement est supersonique ce qui correspond à un nombre de Mach et l'infini légèrement supérieur à l'unité ; l'écoulement dans la zone décollée est alors stable et exempt d'oscillations à fréquence faible ou modérée quelle que soit la configuration.

La figure 4 b fournit également une illustration de l'influence du nombre de Mach sur la résistance de culot. Cet effet est peu important tant que le nombre de Mach critique n'est pas atteint. Par contre, en régime transsonique, une augmentation sensible de  $C_{x_c}$  apparaît, spécialement dans le cas du recollement sur paroi, une valeur maximale étant atteinte pour  $M_\infty$  voisin de un.

Pour un nombre de Mach fixé, la résistance de culot est par ailleurs soumise aux mêmes facteurs d'influence qu'en supersonique.

La figure 37 fournit un exemple de l'effet de la couche limite initiale, qui, comme prévu, provoque une diminution de la résistance de culot, particulièrement significative lorsque la hauteur  $h$  du décrochement est petite devant l'épaisseur de cette couche limite.

La non uniformité de l'écoulement à l'extérieur de la zone décollée, créée notamment par la forme de l'obstacle joue un rôle très important sur le niveau de la pression de culot, d'une manière différente de celle qui est observée en supersonique, de par la nature des équations qui régissent l'écoulement non visqueux.

Le cas traité figure 38 est à ce propos instructif. Il concerne la traînée de culot d'une marche bidimensionnelle de hauteur variable, disposée dans un canal à section constante en amont du décrochement de paroi. La couche limite initiale est la même pour toutes les configurations étudiées. La décroissance de la traînée de culot enregistrée, lorsque  $\frac{h}{D}$  augmente, résulte de la modification du champ provoquée par l'élargissement du canal en aval de la marche. Cette décroissance est plus faible que celle qui serait obtenue si la couche limite initiale était d'épaisseur négligeable. Une même configuration abordée par un écoulement supersonique uniforme de nombre de Mach suffisamment élevé ferait apparaître une résistance de culot sensiblement constante dans le domaine des valeurs  $\frac{h}{D}$  expérimentées, l'écoulement restant alors uniforme à la frontière du décollement.

Les effets dus à la non uniformité du champ sont très accusés pour des formes d'obstacle peu élancées.

C'est la cas par exemple de profils en forme de coin (36) pour lesquels une forte croissance de la résistance de culot est enregistrée lorsque l'angle d'ouverture  $\varphi$  du dièdre de bord d'attaque augmente.

Les méthodes de calcul de la pression de culot en subsonique (§ 4) n'ont été établies que pour un décollement bidimensionnel, quasi permanent et incompressible ou faiblement compressible. Elles s'appliquent soit à des profils tronqués symétriques [41-42], soit à des obstacles en forme de dièdre ou de marche [32]. Les recoupements avec l'expérience sont satisfaisants comme le montrent les figures 36 - 37 - 38. Dans le domaine transsonique, il n'existe pas encore, à notre connaissance, de méthode fiable, en raison des difficultés qui apparaissent aussi bien dans le calcul de l'écoulement extérieur non visqueux, que dans la prise en compte des effets d'interactions entre ondes de choc et zones décollées.

Dans le cas des écoulements axisymétriques, l'évolution des phénomènes est qualitativement la même que celle qui est enregistrée en écoulement plan, par contre la résistance de culot est en général plus faible. Les méthodes de calcul sont pratiquement inexistantes à l'heure actuelle ; on ne dispose donc que de corrélation du type de celles qui ont été proposées par Hoerner [2].

### 5.3 - Décollements provoqués par l'interaction couche limite turbulente - onde de choc

5.3.1 - Quelques exemples typiques où le phénomène d'interaction entre une onde de choc intense et une couche limite turbulente provoque un décollement sont présentés figure 39. Ils concernent les applications suivantes :

- braquage d'une gouverne au-delà de l'angle critique de décollement naissant (39 a) ,
- réflexion d'un choc sur la paroi d'une prise d'air (39 b) ,
- tuyère surdétendue (39 c) ,
- confluence des écoulements interne et externe au bord de fuite d'un arrière-corps (39 d) ,
- profil d'aile en écoulement transsonique (39 e).

Nous nous bornerons à examiner les deux derniers exemples qui nous paraissent les plus significatifs, du point de vue de l'incidence du décollement sur le bilan de traînée.

#### 5.3.2 - Confluence de deux écoulements au bord de fuite d'un arrière-corps de propulseur

Dans le cas d'un arrière-corps à bord de fuite mince B, lorsque la pression en sortie de tuyère est nettement plus élevée que celle de l'écoulement extérieur, l'écoulement interne se détend fortement. Si l'onde de choc créée par cette déviation brusque du jet en B est suffisamment intense, un décollement de l'écoulement externe se produit dont l'origine se situe sur l'arrière-corps en amont de B. La présence de compressions importantes sur le rétreint de l'arrière-corps en aval du point de séparation est extrêmement favorable du point de vue de la traînée externe, le gain ainsi obtenu pouvant compenser une partie des pertes qu'entraîne la non adaptation de la tuyère. L'exemple présenté figure 40 concerne un arrière-corps de révolution à méridienne circulaire comportant une tuyère axiale sonique. Les essais ont été effectués à  $M = 1,83$ .

11-12

Lorsque le taux de détente  $\frac{P_{ij}}{P_{\infty}}$  du jet augmente, les répartitions de pression mesurées sur l'arrière-corps (figure 40 a) indiquent clairement le déplacement vers l'amont d'un décollement qui provoque une recompression importante. Les répercussions de ce décollement sur l'évolution du coefficient de traînée de pression  $C_{xA}$  de l'arrière-corps sont données figure 40 b ; le  $C_x$  décroît continûment lorsque  $\frac{P_{ij}}{P_{\infty}}$  augmente et s'annule pour  $\frac{P_{ij}}{P_{\infty}} \approx 35$

Le calcul de telles configurations peut être effectué en utilisant notamment la méthode décrite réf. [57].

### 5.3.3 - Décollements provoqués par l'interaction couche limite turbulente - onde de choc en transsonique

Ces phénomènes ont été étudiés d'une façon systématique par Pearcey qui en a dégagé les caractères essentiels [58]. Son analyse met en évidence deux types d'interaction représentés schématiquement figure 41.

Dans ce cas (B) le couplage qui s'établit entre les deux zones décollées entraîne des modifications significatives, lorsque l'incidence ou le nombre de Mach varie légèrement, intéressant l'étendue du décollement, de la pression au bord de fuite et par suite de la position de l'onde de choc.

Généralement la présence d'un décollement important se manifeste d'abord par une réduction de la recompression en aval du choc, d'autant plus sensible que le décollement est plus étendu, ensuite par une position de choc moins reculée (figure 42).

La traînée de forme du profil est donc liée à l'importance relative de ces deux effets.

L'influence du décollement sera en particulier plus grande dans le type (B) que dans le type (A), du fait du couplage. Le calcul de ces phénomènes est actuellement à peine abordé [62]. Il met en jeu la solution simultanée de problèmes dont la maîtrise commence seulement à être acquise pour l'écoulement transsonique non visqueux. Il n'en est pas de même de l'interaction couche limite onde de choc, ni des couches limites turbulentes avec bulbe de recirculation, en présence de gradients de pression longitudinaux et transversaux importants, ni de la formation du proche sillage, etc....

### 5.4 - Contrôle du décollement

Les moyens mis en oeuvre pour éviter ou réduire les effets du décollement (aspiration, soufflage à grande vitesse, utilisation de générateurs de tourbillons) ont fait l'objet de nombreuses publications détaillées [59-61]. Ils sont généralement inspirés du souci de créer des effets hypersustentateurs ou encore, dans le cas du vol transsonique d'atténuer des troubles de portance ou de stabilité. L'effet de ces dispositifs sur la traînée est souvent considéré comme secondaire. Dans le cas toutefois des générateurs de tourbillon leur résistance parasite pénalise la traînée de l'aile dans tout le domaine de vol, c'est pourquoi ce procédé ne peut être considéré que comme un remède.

Parmi les applications moins classiques intéressant directement le bilan propulsif, signalons le contrôle des couches limites par aspiration dans les prises d'air qui constitue un moyen extrêmement efficace d'obtenir une efficacité optimale du moteur. Toutefois, l'éjection malencontreuse de ce débit dans l'écoulement extérieur peut provoquer un accroissement de traînée.

Un moyen, moins connu mais très efficace de réduction de la traînée par contrôle du décollement, consiste dans le cas des écoulements de culot, à utiliser l'effet favorable de l'injection de masse à faible vitesse. Ce contrôle, comme les précédents, doit s'intégrer dans une recherche d'optimisation de systèmes propulsifs. Un exemple suivant extrait d'une étude de Addy (figure 43) en montre l'intérêt. Il concerne un arrière-corps cylindrique placé dans un écoulement supersonique de nombre de Mach  $M_{\infty}$  égal à 2. La réduction de la traînée externe est obtenue en associant les effets d'un rétreint tronconique d'ouverture  $\theta$  à ceux de l'injection au culot d'un débit  $q_m$  prélevé sur l'alimentation de la tuyère propulsive dont le nombre de Mach de sortie est égal à 2,5 et le taux de détente  $\frac{P_i}{P_{\infty}}$  à 3.

L'écart sur le coefficient de poussée nette de l'arrière-corps par rapport à la configuration de référence ( $\theta = 0$ ,  $q_m = 0$ ) est porté figure 43 en fonction de l'angle  $\theta$  du rétreint pour différents taux de ventilation du culot. Dans ce calcul, il a été tenu compte de la perte de poussée consécutive au prélèvement du débit de soufflage. Un gain important (6% de la poussée globale) est obtenu pour un angle de rétreint de l'ordre de  $6^\circ$  et un taux de soufflage rapporté au débit de la tuyère  $\frac{q_m}{Q} = 0,005$ .

Cet exemple montre le bénéfice que l'on peut tirer d'un moyen de contrôle simple et met également en évidence les services que peut rendre l'utilisation de méthode de calcul du décollement dans les problèmes d'optimisation.

## 6 - CONCLUSION

Cette revue des problèmes où le décollement peut jouer un rôle important dans le bilan de traînée, même si elle est très incomplète, a toutefois permis de montrer la limite actuelle de nos connaissances de base ainsi que des moyens de prévision du décollement et de ses effets sur la traînée.

Dans les problèmes d'écoulements bidimensionnels (plans ou de révolution), des méthodes pratiquement assez satisfaisantes sont disponibles en supersonique, il n'en est pas de même en subsonique et transsonique.

D'une manière générale, la prédiction des zones décollées tridimensionnelles n'est possible que

11-13  
dans un nombre très réduit de cas simples, lorsque le phénomène se traduit par la formation d'une nappe tourbillonnaire organisée issue d'une ligne de décollement connue a priori ; sinon un calcul couplé de l'écoulement extérieur non visqueux ① et de la couche limite ② est nécessaire, le décollement ainsi prévu par ②, fixant l'origine de la nappe dont l'enroulement doit être nécessairement introduit dans ① mais il est actuellement hors de portée.

En définitive, les problèmes les plus importants à résoudre pour marquer un progrès dans ce domaine sont les suivants :

- Prévion des effets de l'interaction couche limite turbulente - onde de choc et traitement de la confluence en écoulement transsonique bidimensionnel;
- Caractérisation et calcul des décollements tridimensionnels ;
- Prise en compte des effets instationnaires dans des écoulements décollés.

#### R E F E R E N C E S

- [1] Batchelor G.K. An introduction to Fluid Dynamics  
Cambridge University Press.
- [2] Chang P. Separation of flow  
Pergamon Press.
- [3] Morkovin H.V. Flow around circular cylinder - A kaleidoscope of challenging fluid phenomena  
Symposium on fully separated flows - ASME 1964
- [4] Roshko A. Experiments on the flow past a circular cylinder at very high Reynolds number  
Journal of Fluid Mechanics - 1961 - 345-356
- [5] Tritton D.J. The flow past a circular cylinder at low Reynolds numbers  
Journal of Fluid Mechanics - 1959 - Vol. 6, p. 547
- [6] Ujihara B.H. An analytical study of separated flow about a circular cylinder  
NASA CR-72253 - 1966
- [7] Harlow F.H.  
Fromin J.E. Computer experiments in fluid dynamics  
Scientific American - Vol. 212, p. 104 - 1965
- [8] Nash J.F.  
Quincey V.G.  
Callinan J. Experiments on two-dimensional base flow at subsonic and transonic speeds  
NPL Aero Report 1070
- [9] Ginoux J.J. On the existence of cross flows in separated supersonic streams  
TCEA TN 6 - 1962
- [10] Roshko A.  
Thomke G.J. Flow separation and reattachment behind a downstream-facing step  
Douglas Report SM-43056-1 - 1964
- [11] Mirande J. Travail non publié
- [12] Carrière P. Interaction de l'écoulement externe et de l'écoulement interne à la sortie d'un réacteur aux vitesses transsoniques et supersoniques  
Journées internationales de Sciences Aéronautiques - PARIS - 1957
- [13] Erlich E. Exemples de recherches sur les profils dans la soufflerie du CEAT à TOULOUSE  
Colloque AFITaE (1969) - TP ONERA 766
- [14] Roy M. Caractères de l'écoulement autour d'une aile en flèche accentuée  
C.R. Ac. Sc. t. 234, pp. 2501, 2503 - 1952
- [15] Legendre R. Ecoulement au voisinage de la pointe avant d'une aile à forte flèche aux incidences moyennes  
Rech. Aér. n° 30 (1952) - n° 3 (1953)
- [16] Maskell E.C. Flow separation in three dimensions  
RAE Report Aero n° 2565 - 1955

11-14

- [17] Werlé H. Sur l'éclatement de tourbillons  
N.T. ONERA 175 (1971)
- [18] Werlé H. Hydrodynamic flow visualization  
Annual review of Fluid Mechanics, vol. 5 (1973)
- [19] Monnerie B.  
Werlé H. Etude de l'écoulement supersonique et hypersonique autour d'une aile élancée  
en incidence  
Hypersonic boundary layers and flow field  
AGARD Specialists' Meeting - LONDRES (1968)
- [20] Mair W.A. Experiments on separation of boundary layers on probes in front of blunt  
nosed bodies in a supersonic air stream  
Phil. Mag., vol 43 (1952)
- [21] Legendre R. La condition de Joukowski en écoulement tridimensionnel  
Communication présentée au 13ème Congrès de l'IUTAM - MOSCOU 1972 - TP ONERA  
1156
- [22] Korst H.H.  
Page R.H.  
Childs M.E. A theory for base pressure in transonic and supersonic flow  
University of Illinois ME TN. 392.2 (1955)
- [23] Carrière P.  
Sirieix M. Facteurs d'influence du recollement d'un écoulement supersonique  
10è Congrès de Mécanique Appliquée - STRESA 1960
- [24] Nash J.F. An analysis of two dimensional turbulent base flow including the effect of  
the approaching boundary layer  
A.R.C. R et M 3344 (1962)
- [25] Mac Donald H. Turbulent shear layer re-attachment with special emphasis on the base pressure  
problem  
Aero. Quant. vol 15 (1964)
- [26] Page R.H.  
Kessler I.J.  
Hill W.G. Reattachment of two-dimensional supersonic turbulent flows  
Paper 67 FE 20 (1967) ASME
- [27] Carpenter P.W.  
et al. Survey and evaluation of supersonic base flow theories  
NASA CR. 97129 (1969)
- [28] Mueller I.J. Determination of the turbulent base pressure in supersonic axisymmetric flow  
AIAA Paper n° 67446 (1967)
- [29] Sirieix M.  
Delery J.  
Mirande J. Recherches expérimentales fondamentales sur les écoulements séparés et  
applications  
TP ONERA n° 520 (1967)
- [30] Solignac J.L.  
Delery J. Contribution à l'étude aérodynamique des systèmes propulsifs à double flux  
Israël Journal of Technology Vol. 10 (1972)
- [31] Tanner M. The wake pressure behind wedge as influenced by splitter plates and section  
AGARD Specialist Meeting on separated flows (1966)
- [32] Tanner M. Der Begriff der Ausströmung aus dem Totwasser und seine Anwendung auf Totwasser-  
untersuchungen  
Z.F.W. S 7473 E (1970)
- [33] Crocco L.  
Lees L. A mixing theory for the interaction between dissipative flows and nearly  
isentropic streams  
J.A.S. Vol 19, n° 10 (1952)
- [34] Glick H.S. Modified Crocco Lees mixing theory for supersonic separated and reattaching  
flows  
CALTEC Memo n° 53 (1960)
- [35] Rom J. Near wake flow studies in supersonic flow  
Technion TAE Report 38 (1965)
- [36] Alber I.E.  
Lees L. Integral theory for supersonic turbulent base flows  
AIAA Paper n° 68101 (1968)

- [37] Hunter L.G.  
Reeves B.L. Results of a strong interaction wake like model of supersonic separated and reattaching turbulent flow  
AIAA Journal , vol. 9, n° 4 (1971)
- [38] Shamroth S.J.  
Mac Donald A new solution of the turbulent near wake recompression problem  
AIAA Paper n° 70228 (1970)
- [39] Chow W.L. Recompression of a two dimensional supersonic turbulent free shear layer  
University of Illinois (1971)
- [40] Delery J.  
Le Balleur J.C.  
Sirieix M. Etude expérimentale de l'interaction couche limite onde de choc en écoulement supersonique  
Communication au 13<sup>e</sup> Congrès IUTAM MOSCOU 1972
- [41] Green J.E. Two dimensional turbulent reattachment as a boundary layer problem  
AGARD Specialists' Meeting on separated flows (1966)
- [42] Nash J.F. An approximate method for the prediction of the zero lift pressure distribution and drag of symmetrical blunt-trailing edge aerofoil sections at subsonic speeds in the absence of a vortex street  
NPL Aero report 1112 (1964)
- [43] Nguyen Van Noi Etude théorique et expérimentale du recollement subsonique incompressible d'un écoulement plan turbulent à sa frontière  
Thèse Faculté des Sciences PARIS (1971)
- [44] Gosman A.D.  
Fun W.M.  
Runchal A.K.  
Spalding D.B.  
Wolfstein M. Heat and mass transfer on recirculating flows  
Academic Press (1969)
- [45] Bradshaw P.  
Wong F.Y.F. The reattachment and relaxation of a turbulent shear layer  
Journal of Fluid Mechanics, vol 52, part 1 (1972)
- [46] Smith J.H.B. Improved calculations of leading edge separation from slender, thin, delta wings  
Proc. Roy. Soc. A 306 (1968)
- [47] Perrier P. Calculs tridimensionnels d'hypersustentation  
9<sup>e</sup> Colloque d'Aérodynamique Appliquée A.A.A.F. (1972)
- [48] Young A.D.  
Worton W.P. Some results of investigations of separation bubbles  
AGARD Specialists' Meeting on separated flows (1966)
- [49] Gaster M. The structure and behaviour of laminar separation bubbles  
AGARD Specialists' Meeting on separated flows (1966)
- [50] Vincent de Paul M. Prévission du décrochage d'un profil d'aile en écoulement incompressible  
AGARD Meeting LISBONNE (1972)
- [51] Leynaert J.  
Meauzé G. Situation de l'étude d'une prise d'air pour avion subsonique rapide  
Document ONERA non publié
- [52] Carrière P. Aperçu de quelques problèmes aérodynamiques actuels posés par les prises d'air supersoniques  
T.P. ONERA n° 1102 (1972)
- [53] Zorea C.  
Rom J. Effect of a spike on the drag and on the aerodynamic stability of blunt bodies in supersonic flow  
J.S.R., vol. 7, n° 8 (1970)
- [54] Korst H.H.  
Chow W.L. Non isoenergetic turbulent jet mixing between two compressible streams at constant pressure  
Université de l'Illinois ME TN 393-2 (1959)
- [55] Carrière P. Aperçu de quelques résultats nouveaux obtenus à l'ONERA sur les phénomènes de décollement et de recollement  
T.P. ONERA n° 1072 (1972)

- [56] Compton W.B. Jet effects on the drag of conical afterbodies at supersonic speeds  
NASA T.N. D. 6789 (1972)
- [57] Carrière P. Confluence of two supersonic jets at the trailing edge of a turbine blade  
Cours au V.K.I. (1971)
- [58] Pearcey H.H.  
Haines A.B.  
Osborne J. The interaction between local effects at the shock and rear separation  
AGARD Conf. Proc. n° 35 (1968)
- [59] von der Decken J. Aerodynamics of pneumatic high-lift devices  
AGARD L.S. 4371 (1970)
- [60] Lachmann G.V. Boundary layer and flow control  
Pergamon Press (1962)
- [61] Addy A.L. Thrust minus drag optimization by base bleed and/or boattailing  
J.S., vol 7, n° 11 (1970)
- [62] Klineberg J.M.  
Steger J.L. Calculation of separated flows at subsonic and transonic speeds  
Third International Conference on Numerical methods in fluid Mechanics  
PARIS (1972)

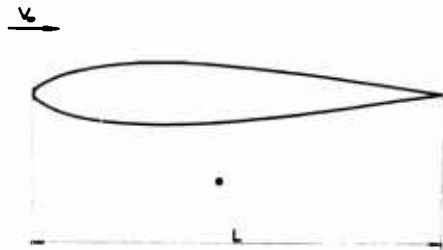


Fig. 1 - Corps de même traînée totale à même vitesse ( $\frac{V_{\infty} L}{\nu} \approx 2 \cdot 10^5$ ) (Batchelor [1])

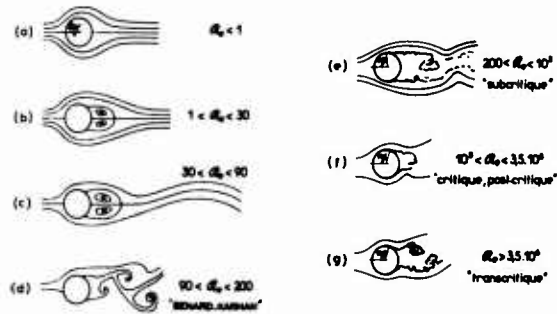


Fig. 2 - Régimes d'écoulements incompressibles autour du cylindre circulaire (Morkovin [3])

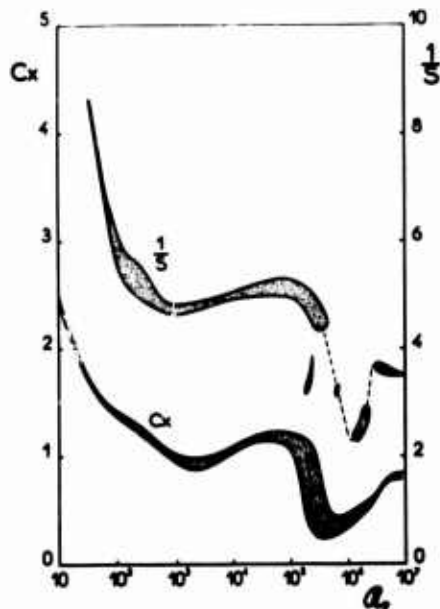


Fig. 3 - Evolution du coefficient de traînée et du nombre de Strouhal en fonction du nombre de Reynolds (Morkovin [3])

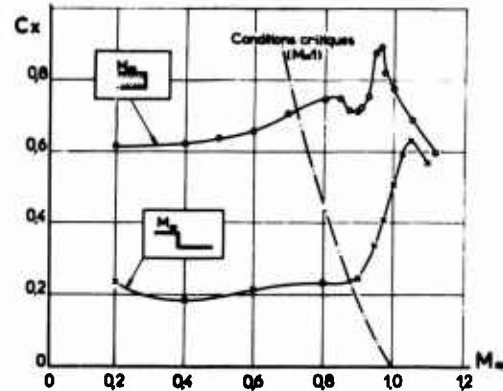


Fig. 4 - Traînée de culot en subsonique. Influence des conditions de recollement

11-16

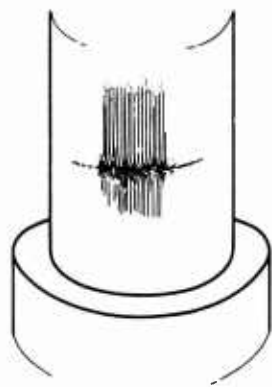
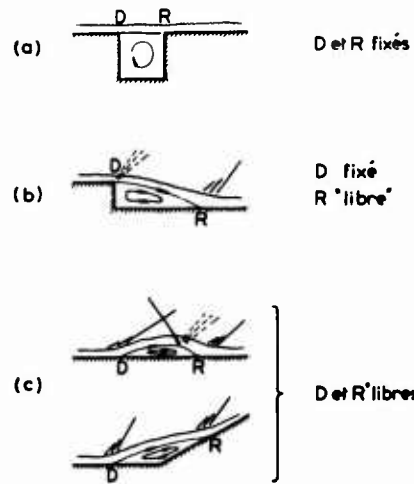


Fig. 5 - Visualisation pariétale du recollement en aval d'une marche (Roshko [10])



11-17

Fig. 6 - Différents types de décollement turbulent

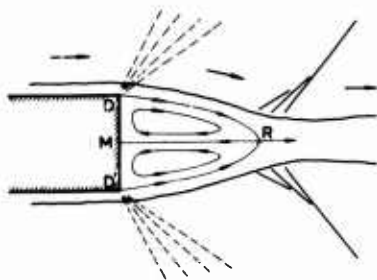


Fig. 7 a - Ecoulement de culot stable (cas bidimensionnel symétrique)

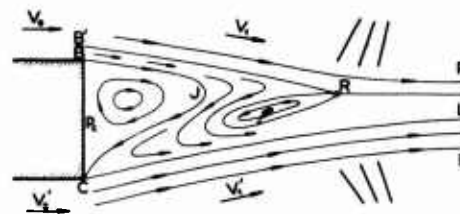


Fig. 7 b - Ecoulement de culot stable (cas bidimensionnel dissymétrique)



Fig. 8 - Bulbe de décollement avec transition dans la zone décollée

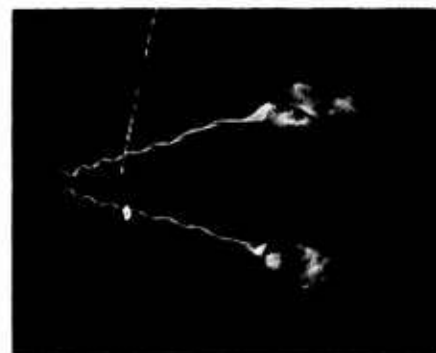


Fig. 10 - Eclatement de tourbillon sur une aile  $\Delta$  à forte incidence

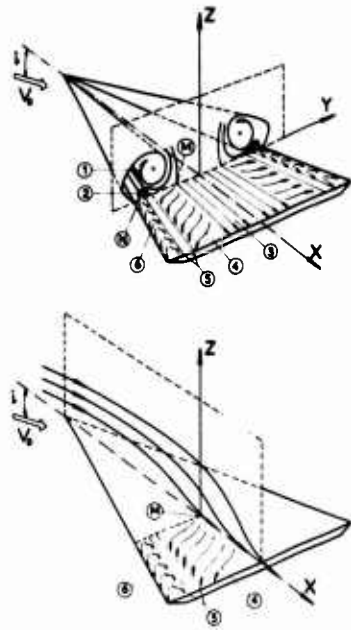


Fig. 9 - Ecoulement autour d'une aile  $\Delta$  mince et élancée en incidence

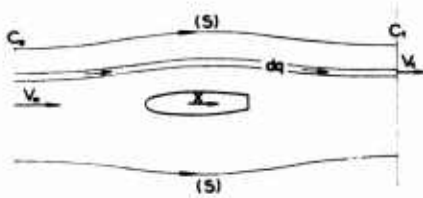


Fig. 12 - Traînée d'un obstacle : surface de contrôle

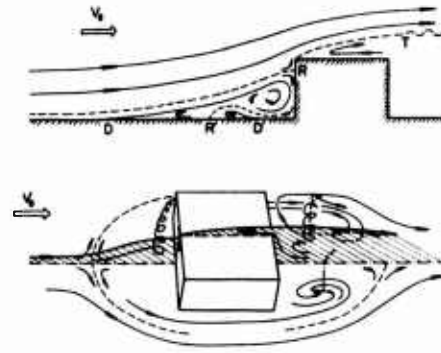
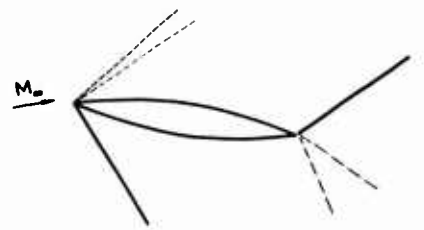
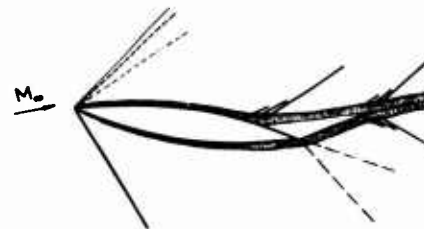


Fig. 11 - Ecoulement incompressible autour d'une marche d'envergure limitée



A. Fluide parfait



B. Fluide visqueux (couche limite turbulente)

Fig. 13 - Ecoulement supersonique autour d'un profil en incidence

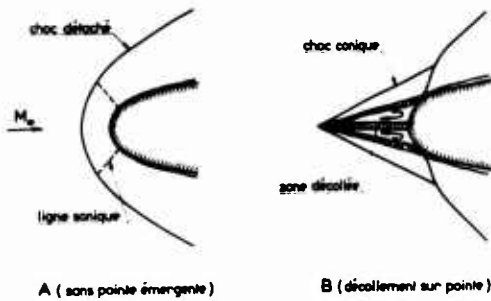


Fig. 14 - Décollement sur pointe émergente

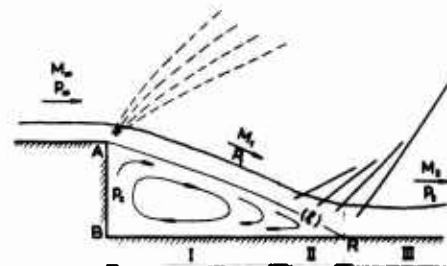


Fig. 15 - Ecoulement supersonique en aval d'une marche descendante

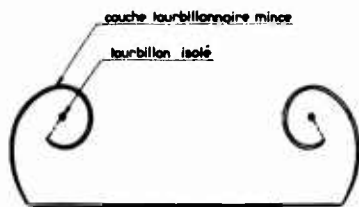


Fig. 16 - Tourbillon en cornet. Schématisation de J.H.B. Smith

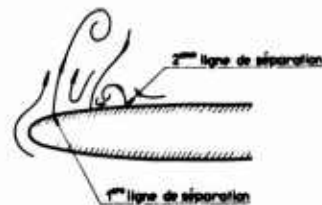


Fig. 17 - Contournement d'un bord arrondi. Coupe transversale de l'écoulement

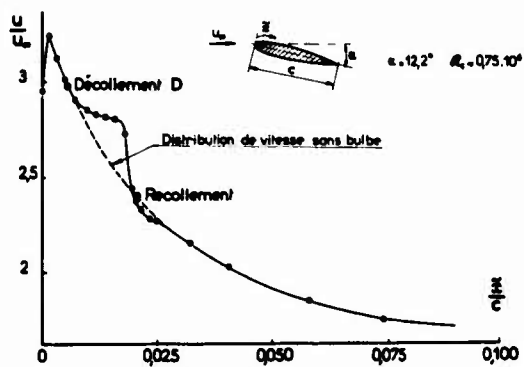


Fig. 18 - Distribution des vitesses au bord d'attaque d'un profil en incidence. Effet d'un bulbe court

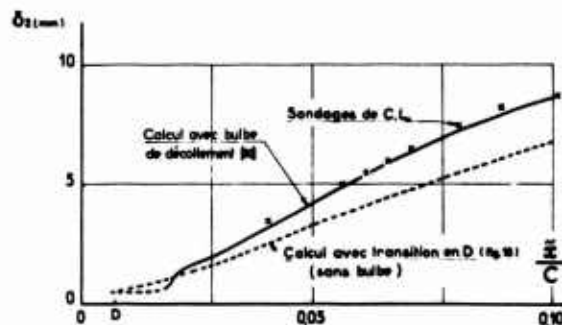


Fig. 19 - Influence d'un bulbe court sur l'évolution de la couche limite aval

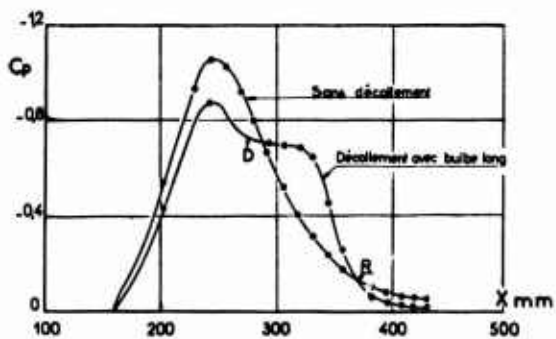


Fig. 20 - Distribution des pressions sur un obstacle. Effet d'un bulbe long

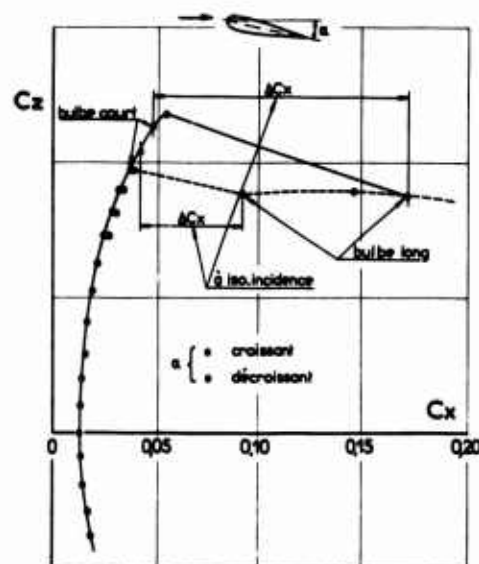


Fig. 21 - Effet d'un bulbe long sur la traînée d'un profil

11-20

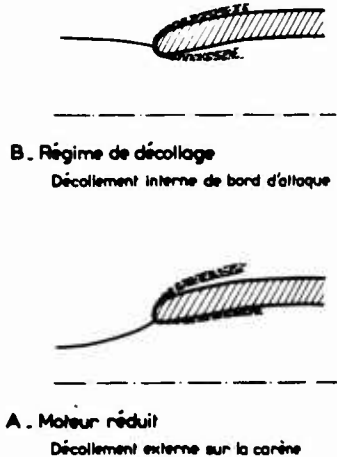


Fig. 22 - Prise d'air subsonique. Différents régimes de fonctionnement

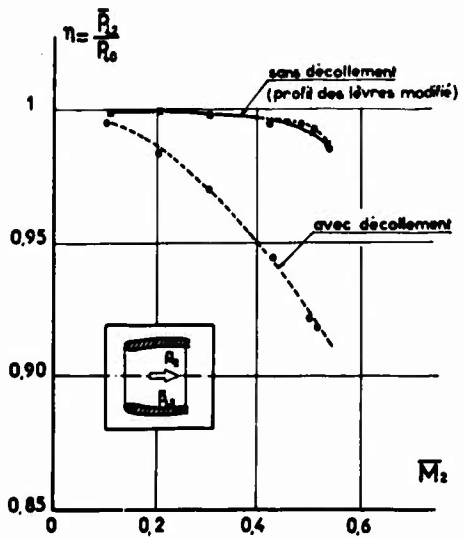


Fig. 23 - Influence d'un décollement de bord d'attaque sur l'efficacité d'une prise d'air au point fixe

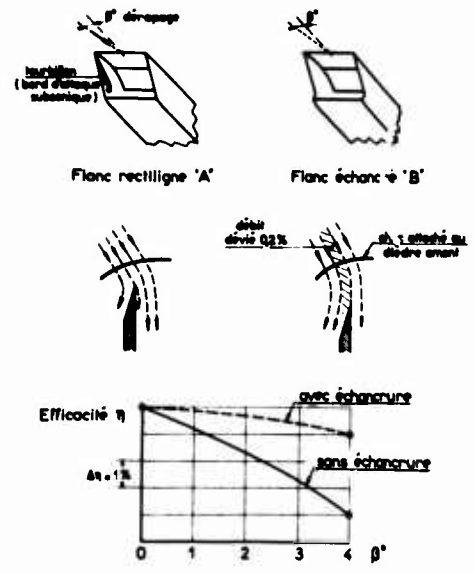


Fig. 24 - Effet d'un décollement de bord d'attaque sur l'efficacité d'une prise d'air supersonique à  $M = 2$

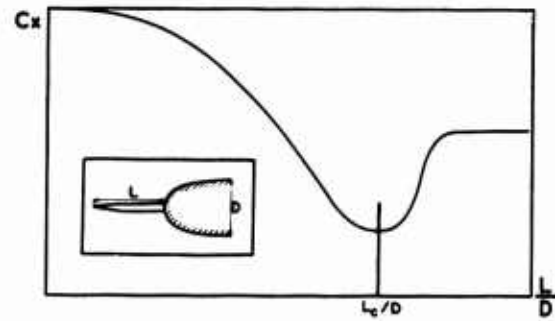


Fig. 25 - Evolution schématique de la traînée d'un corps arrondi en fonction de la longueur d'émergence de la pointe

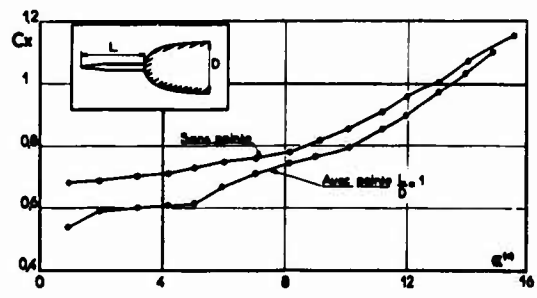


Fig. 26 - Evolution avec l'incidence de la traînée d'un corps ogive-cylindrique à  $M = 2,25$  [53]

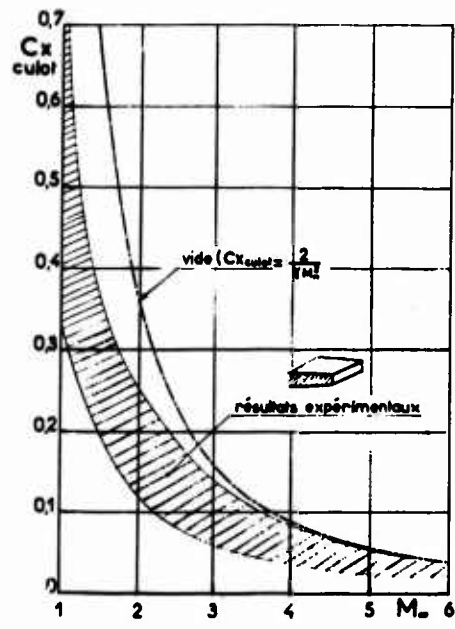


Fig. 27 - Traînée de culots bidimensionnels. Evolution avec le nombre de Mach

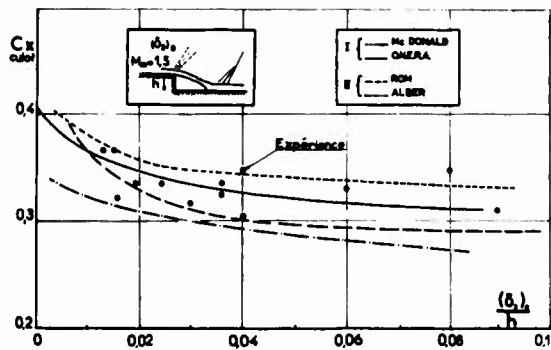


Fig. 28 - Effet de la couche limite initiale sur la traînée de culot à  $M = 1,5$ . Comparaison théorie-expérience en écoulement plan

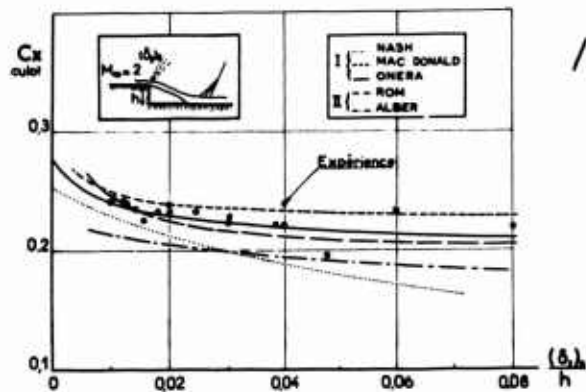


Fig. 29 - Effet de la couche limite initiale sur la traînée de culot à  $M = 2$ . Comparaison théorie-expérience en écoulement plan

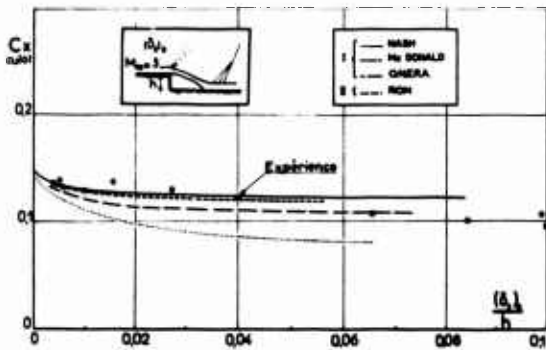


Fig. 30 - Effet de la couche limite initiale sur la traînée de culot à  $M = 3$ . Comparaison théorie-expérience en écoulement plan

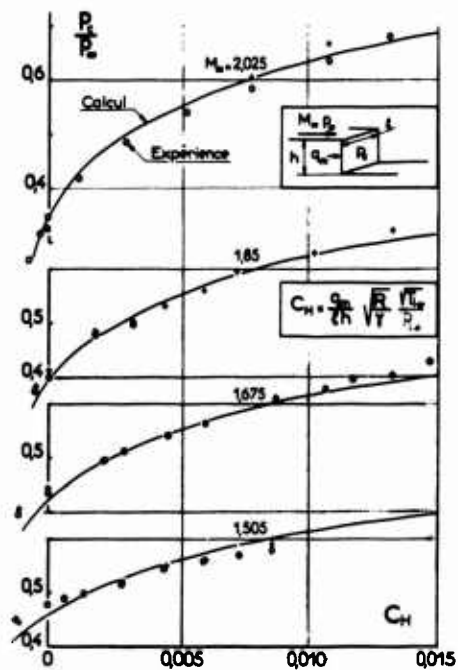


Fig. 31 - Effet du soufflage sur la traînée de culot en écoulement plan à différents nombres de Mach

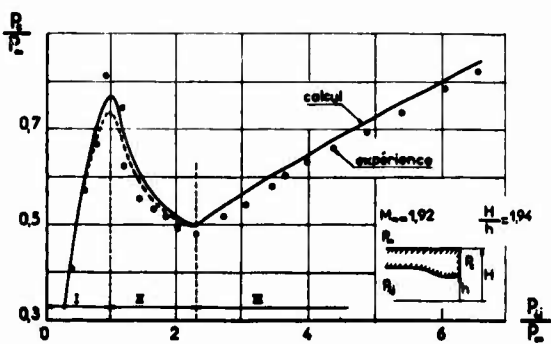


Fig. 32 - Confluence d'écoulement de part et d'autre d'un culet bidimensionnel. Influence du taux de soufflage interne d'après Korst [54]

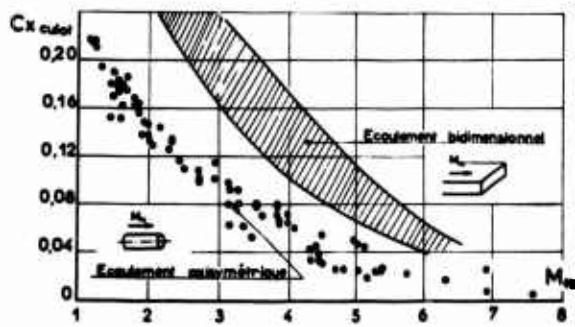


Fig. 33 - Traînée de culot de corps de révolution. Influence du nombre de Mach. Comparaison avec le cas bidimensionnel

11-22

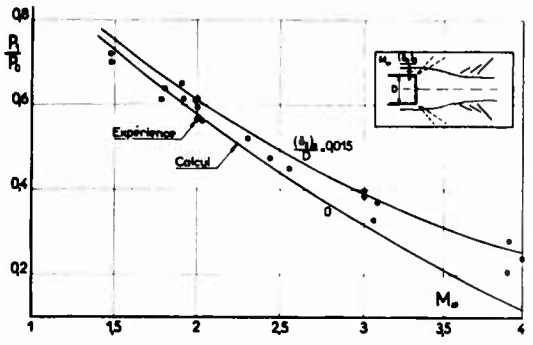


Fig. 34 a - Traînée de culot d'arrière-corps cylindriques. Comparaison théorie-expérience

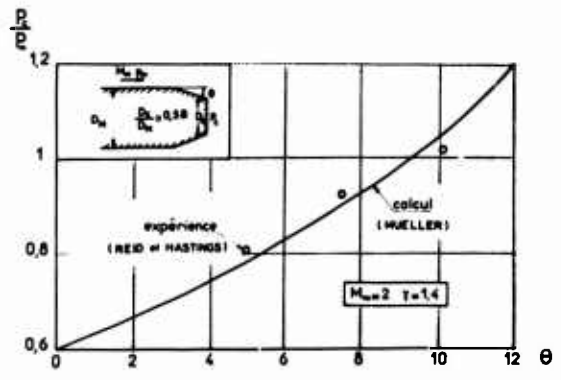


Fig. 34 b - Effet d'un rétreint sur la traînée de culot d'un arrière-corps de révolution en supersonique

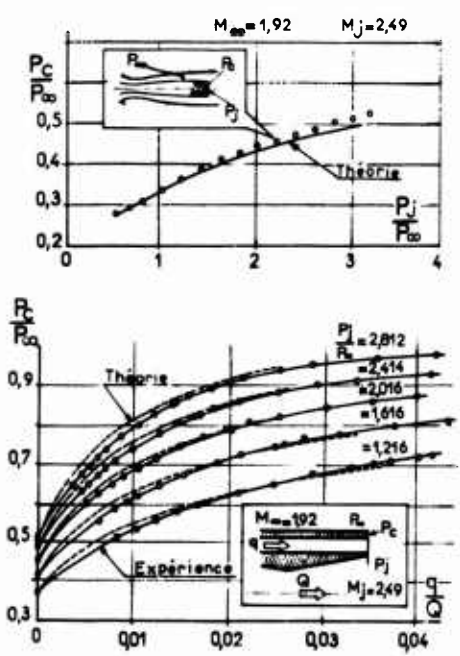


Fig. 35 - Confluence d'écoulements internes et externes en écoulement de révolution supersonique

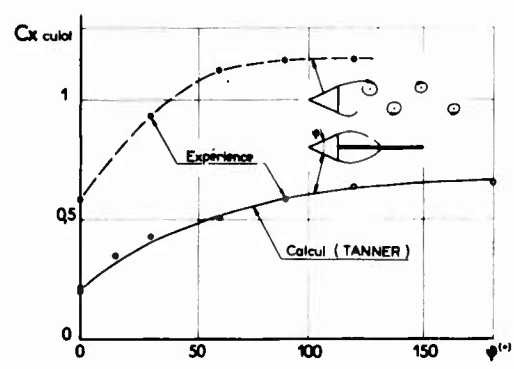


Fig. 36 - Traînée de culot d'obstacles en forme de coin en incompressible

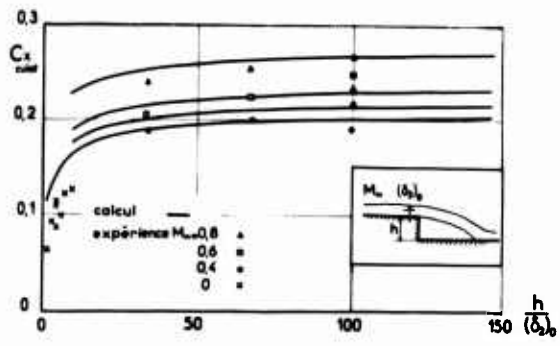


Fig. 37 - Effet de la couche limite sur la traînée de culot subsonique

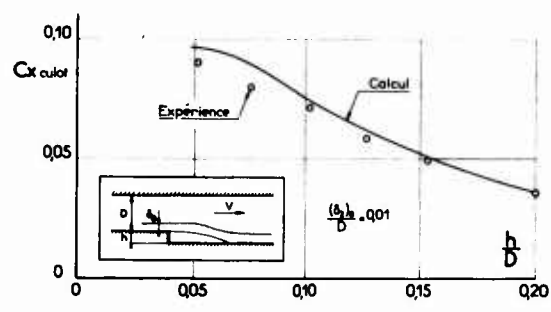


Fig. 38 - Influence sur champ extérieur sur la traînée de culot en écoulement incompressible

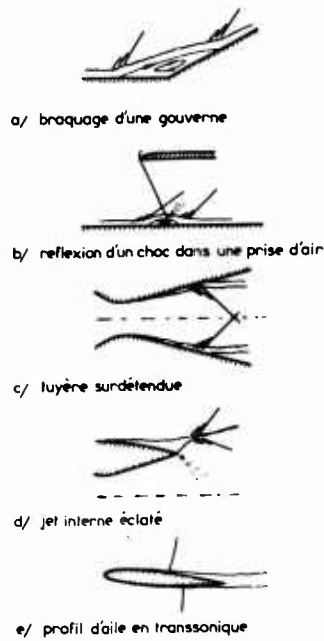


Fig. 39 - Exemples de décollement provoqués par l'interaction couche limite turbulente - onde de choc

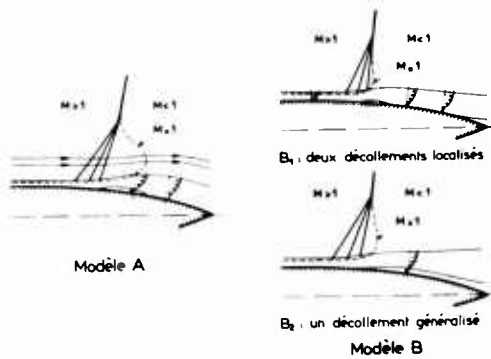
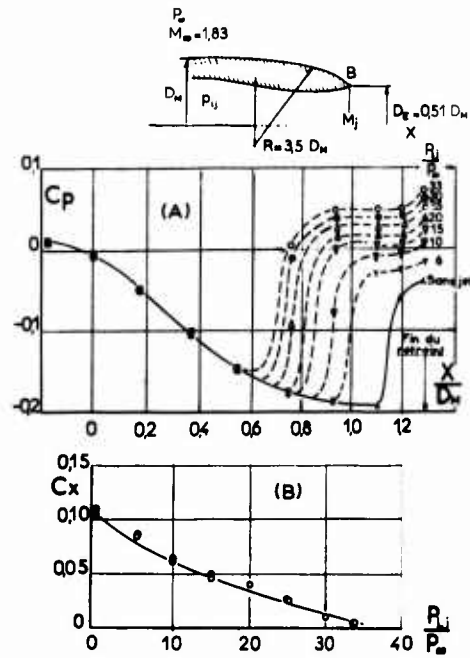


Fig. 41 - Interaction couche limite turbulente - onde de choc avec décollement en transsonique d'après Pearcy [58]

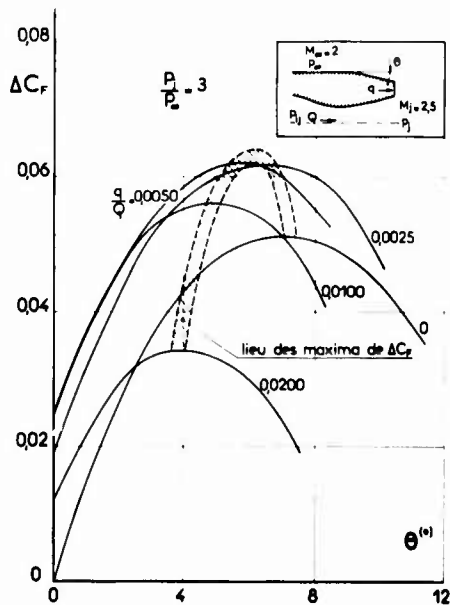
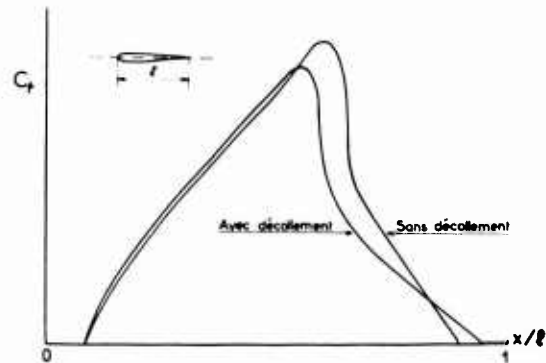


Fig. 43 - Contrôle du décollement de culot par soufflage. Exemple d'optimisation [61]

NEW INVESTIGATIONS FOR REDUCING THE BASE DRAG  
OF WINGS WITH A BLUNT TRAILING EDGE

12-1

Dr. Mauri Tanner

Deutsche Forschungs- und Versuchsanstalt  
für Luft- und Raumfahrt E. V.  
Aerodynamische Versuchsanstalt Göttingen

SUMMARY

In order to improve existing methods for reducing base drag of wings with a blunt trailing edge, such as e. g. the broken trailing edge introduced by the present author some years ago, measurements were performed on a rectangular wing in the Low Speed Wind Tunnel of the DFVLR-AVA in Göttingen. For these investigations the wing was fitted with broken trailing edges, splitter plates and splitter wedges. The Mach number was  $M_\infty = 0.15$  and the Reynolds number  $R_\infty = 2 \cdot 10^6$ .

The results from tests using broken trailing edges show that the base drag could still be decreased by 13 per cent, as compared with the best broken trailing edge used in previous measurements. For the improved broken trailing edge the base pressure coefficient has a value of  $c_{pB} = -0.16$ , as compared with the value  $c_{pB} = -0.44$ , for a straight blunt edge.

A still smaller base drag could be obtained by a straight blunt trailing edge, to which a long thick splitter plate was attached. For the best splitter plate the base pressure coefficient had a value of  $c_{pB} = -0.11$ .

The smallest drag, however, was obtained by fitting a splitter wedge on the trailing edge. For the most advantageous splitter wedge the base drag was nearly zero. In this case the maximum lift to drag ratio for the wing with a blunt trailing edge was as great as that for the corresponding wing with a conventional sharp trailing edge.

NOTATION

b	wing span	L	lift
s	half-span of the wing	D	drag
c	wing chord	$c_D$	drag coefficient
d	maximum profile thickness	$c_{DB}$	base drag coefficient
h	trailing edge thickness	$c_{Do}$	drag coefficient at zero lift
F	wing area	$c_{Dp}$	coefficient of profile drag at zero lift
$F_B$	base area	$c_{pB}$	base pressure coefficient
l	length of splitter plate or splitter wedge	$(c_{pB})_{eff}$	effective base pressure coefficient (Eq. (1))
$h_1$	thickness of splitter plate; maximum thickness of splitter wedge	$c_{pE}$	pressure coefficient acting on the end of the splitter plate
$\beta$	boat tail angle (Fig. 4)	$M_\infty$	free stream Mach number
$b_1, b_2, a, \gamma$	dimensions of the broken trailing edge (Fig. 7)	$R_\infty$	Reynolds number based on wing chord and free stream conditions
$\alpha$	angle of incidence		

1. INTRODUCTION

As has been pointed out by various authors [1], [2], [3], wing profiles with a blunt trailing edge may have many advantages in high speed flow in comparison with conventional profiles with a sharp trailing edge. The high base drag of such profiles is a great penalty, however, and therefore methods for reducing base drag have been the object of numerous investigations (see e. g. [4], [5], [6]).

Fig. 1 shows the effectiveness of various devices for reducing the base drag in subsonic two-dimensional flow. With a short splitter plate of a length equal to the base thickness, approximately, a base drag reduction of the order of 50 per cent of that for a straight blunt trailing edge can be achieved. Trailing edge slots are still more effective, especially at high subsonic speeds, where the base drag can be reduced by 60 per cent as shown by the measurements of J. F. Nash et al and J. Osborne and H. H. Pearcey [6]. The greatest base drag reduction - about 64 per cent - obviously is obtained by using a "broken" trailing edge as introduced by the present author [7], [8]. It may be remarked that the results of M. Tanner [7], [8] have been obtained by measurements on a wing with finite span, i. e. in three-dimensional flow, whereas the measurements of the other authors, as previously stated, have been performed at two-dimensional test conditions.

12-2



	$M_\infty$	Splitter Plate	Ventilated Cavity (Slots)	Broken Trailing Edge
Bearman [4]	0.1	50%		
Tanner [8]	0.1			64%
Nash et al [6]	0.4	52%	52%	
	0.8	44%	60%	
Osborne and Pearcey [6]	0.4		54%	
	0.8		60%	
Nash et al [6]	0.4	51%		
	0.8	48%		

Fig. 1 Comparison of effectiveness of various devices for decreasing base drag at subsonic speeds

In order to investigate the characteristics of airfoils with blunt broken trailing edges at transonic and supersonic Mach numbers, measurements in 1969 were performed in the Transonic Wind Tunnel of the Aerodynamische Versuchsanstalt in Göttingen. In the next section a short summary of the results from these measurements [9], [10] is presented.

## 2. RESULTS FROM PREVIOUS INVESTIGATIONS AT TRANSONIC AND SUPERSONIC MACH NUMBERS

The measurements were carried out on two wings which are shown in Fig. 2 and 3. One of the wings (Fig. 2) had a conventional sharp trailing edge, whereas the other had a blunt trailing edge, either straight or broken (Fig. 3). The profiles of both wings had the same moment of inertia about the chord line, i. e. they had the same strength, approximately [9], [10].

In Fig. 4 one can see the drag coefficient at zero lift in dependence of the Mach number for three different

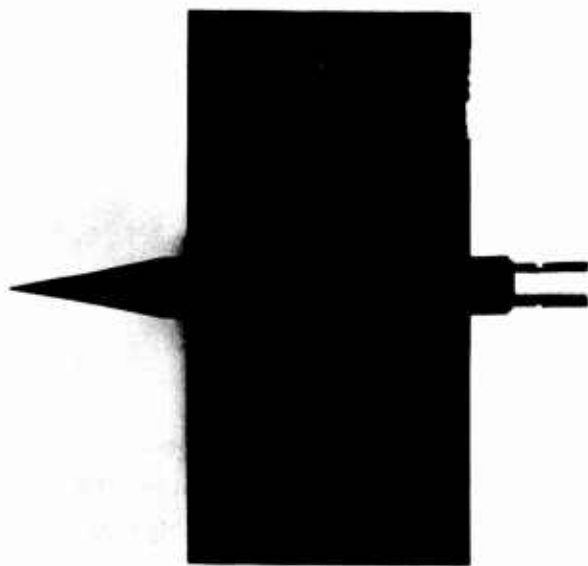


Fig. 2 Wing I with a sharp trailing edge

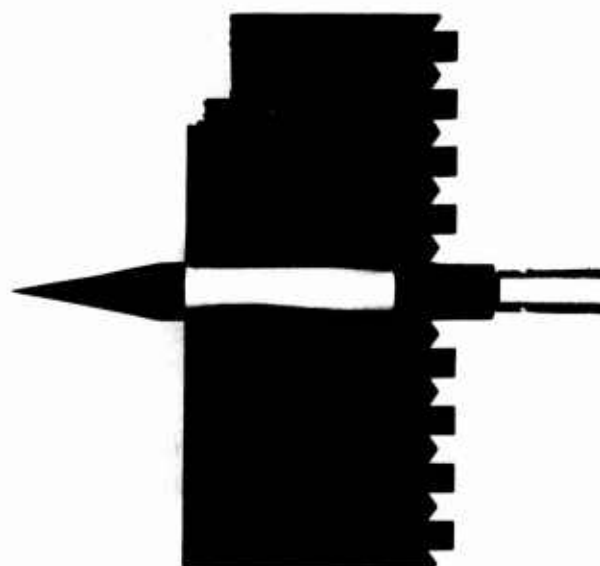


Fig. 3 Wing II with a blunt broken trailing edge

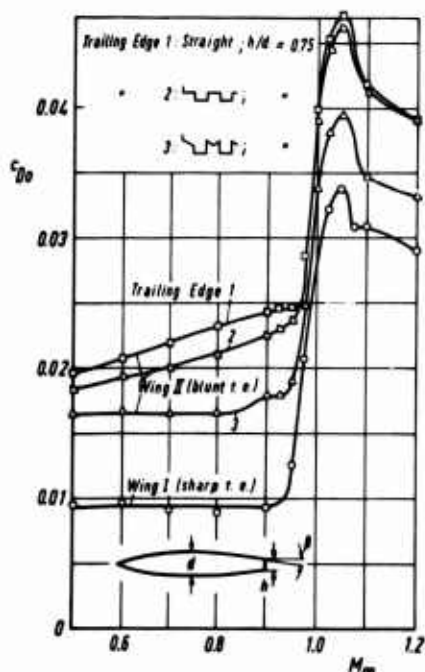


Fig. 4 Drag coefficient at zero lift as function of the Mach number

blunt trailing edges of equal thickness ( $h/d = 0.75$ ). For comparison the drag coefficient of the wing with a sharp trailing edge is also shown in the Figure. The drag reduction attained with the best broken trailing edge, compared with the drag of the straight blunt trailing edge of equal thickness, is quite remarkable. At transonic Mach numbers the drag with the best blunt trailing edge is only about 14 per cent higher than that for the wing with a conventional sharp trailing edge.

Further measurements have shown that the drag of the wing with the straight blunt trailing edge can be reduced by reducing the trailing edge thickness. For supersonic Mach numbers,  $M_\infty \leq 2$ , the optimum trailing edge thickness of straight blunt trailing edges then has a value of  $h/d = 0.30$ , approximately\*). This value probably should also be valid at transonic Mach numbers. By using a broken trailing edge with an optimum thickness, the total drag of the wing with a blunt trailing edge could, of course, be reduced and made smaller than that shown in Fig. 4.

Furthermore, the measurements have shown that at subsonic Mach numbers the lift curve slope for the wing with a blunt trailing edge for all trailing edges is greater than for the wing with a sharp trailing edge. This also is true for Mach numbers above  $M_\infty = 1$  if the boat tail angle  $\beta$  (see Fig. 4) is small, i. e.

\*) The optimum thickness of the trailing edge increases, of course, with increasing base pressure.

$\beta \leq 2^\circ$ , approximately. Therefore, the maximum lift to drag ratio for the wing with a blunt trailing edge can be relatively large, as shown in Fig. 5. For Mach numbers  $M_\infty \approx 0.95$  the maximum lift to drag ratio of the wing with a sharp trailing edge is only a few per cent greater than that of the wing with a blunt broken trailing edge of thickness  $h/d = 0.75$  and with a boat tail angle of  $\beta = 1.7^\circ$ .

Thus, it can be supposed that by using a blunt broken trailing edge of the thickness  $h/d = 0.3$  having a small boat tail angle the maximum lift to drag ratio would be somewhat higher than for a corresponding wing with a sharp trailing edge. A further conclusion, however, is that the devices for reducing base drag should still be improved, because the base drag is too large, even if a blunt broken trailing edge is used. In the next section new measurements carried out in order to improve the devices for reducing base drag will be discussed.

### 3. NEW MEASUREMENTS FOR REDUCING BASE DRAG

#### 3.1 Experimental Set-up

The measurements were performed in 1972 in the Low Speed Wind Tunnel of the Aerodynamische Versuchsanstalt in Göttingen. This wind tunnel has an open test section and the dimensions of the test section are  $3 \times 3 \text{ m}^2$ .

The rectangular wing had a span of  $b = 1.50 \text{ m}$  and a chord of  $c = 0.60 \text{ m}$ . Thus, the aspect ratio was equal to  $A = 2.5$ . The profile of the wing is shown in Fig. 6. The foremost part of the profile was identical with NACA 65 A 006. After the first joint the upper and lower profile contours were straight lines. The maximum thickness of the profile was  $d = 36 \text{ mm}$  and the thickness of the trailing edge  $h = 21 \text{ mm}$ . Therefore, the relative trailing edge thickness had a value of  $h/d = 0.58$ .

During the investigations the wing was fitted with broken trailing edges, splitter plates and splitter wedges. The Mach number of the undisturbed flow was equal to  $M_\infty = 0.15$  and the Reynolds number, based on the wing chord, had a value of  $R_\infty = 2 \cdot 10^6$ , approximately.

#### 3.2 Measurements on Broken Trailing Edges

For the broken trailing edge the following parameters are important, Fig. 7: the relative "span" of the trailing edge element  $b_1/h$ , the ratio  $b_1/b_2$ , the ratio  $a/h$  and the angle  $\gamma$  ( $h$  means the trailing edge thickness). From previous investigations we know that a value of  $a/h = 1.9$  is nearly optimal and for  $\text{tg } \gamma = 0.5$  the base drag is far less than for  $\text{tg } \gamma = 0$ . Measurements therefore were performed on trailing edges with  $b_1/b_2 = 1$ ,  $a/h = 1.9$  and  $\text{tg } \gamma = 0.5$  but with different values of the parameter  $b_1/h$ . The results, for the angle of incidence  $\alpha = 0^\circ$ , are shown in Fig. 8. The optimum value for  $b_1/h$  seems to be about  $b_1/h = 5.5$ ; then the base pressure coefficient is  $c_{pB} = -0.165$ , compared with the value  $c_{pB} = -0.179$  valid for the dimensions of the best trailing edge of the previous investigations [7], [8] i. e. for  $b_1/h = 3.8$ .

Subsequent measurements have shown that for  $\text{tg } \gamma = 0.66$  and  $b_1/h = 5.0$  the base pressure is somewhat higher than for  $\text{tg } \gamma = 0.50$  and  $b_1/h = 5.0$ , giving  $c_{pB} = -0.156$ . Compared with the value  $c_{pB} = -0.179$  valid for the best trailing edge of the previous measurements [7], [8], the base drag thus has been reduced by 13 per cent, approximately. It is possible that the base drag can still be reduced by some per cent, if the optimum value of the parameter  $\gamma$  is found.

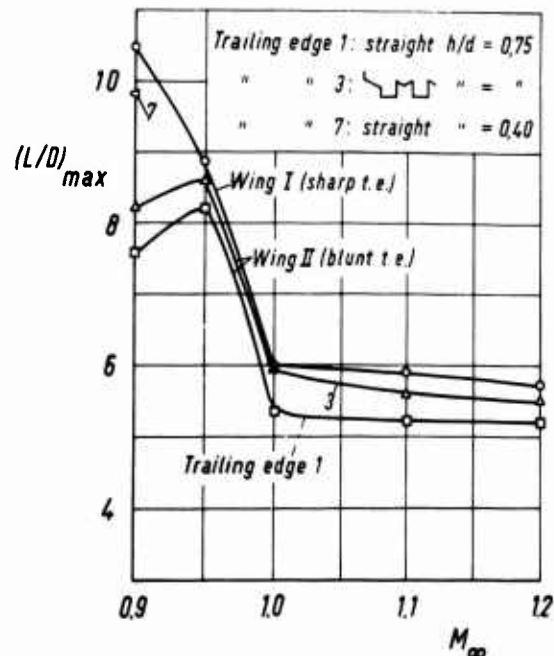


Fig. 5 Maximum lift to drag ratio versus Mach number

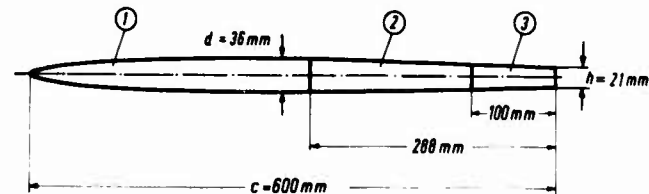


Fig. 6 The wing profile

- ① Front part, NACA 65 A 006
  - ② Second part
  - ③ Trailing edge
- } straight line contour

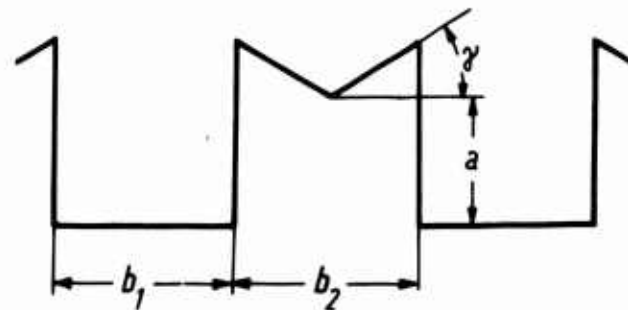


Fig. 7 Important parameters for the broken trailing edge

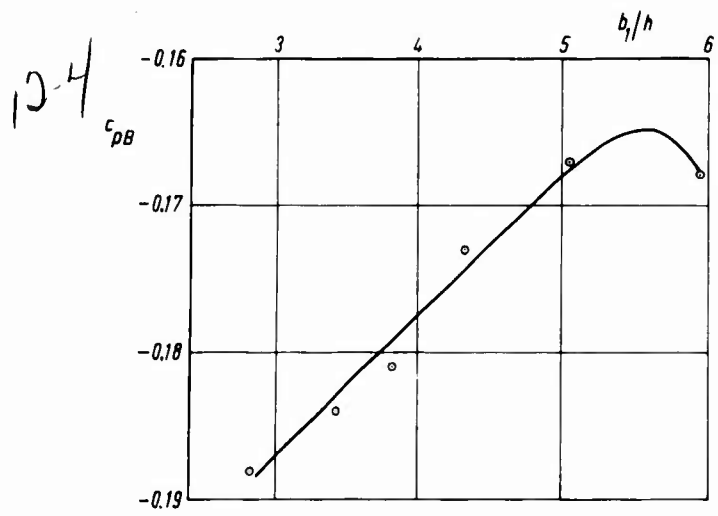


Fig. 8 Mean base pressure coefficient for broken trailing edges  $b_1/b_2=1$ ,  $a/h=1.9$ ,  $\text{tg}\gamma=0.5$

### 3.3 Measurements with Splitter Plates in the Wake

During these measurements the wing had a straight blunt trailing edge on which various splitter plates were fitted. The full details of these measurements are given in [13].

Figure 9 shows the splitter plates used in this experiment. For all these trailing edge configurations the distribution of the base pressure over the span and the lift and drag of the wing were measured during this investigation.

In Fig. 10 the distribution of the base pressure coefficient over the half-span is shown for the blunt straight trailing edge without splitter plate in the wake for an angle of incidence of  $\alpha = 0^\circ$ . The pressure distribution is of pronounced three-dimensional character.

In Fig. 11 the quite different pressure distribution

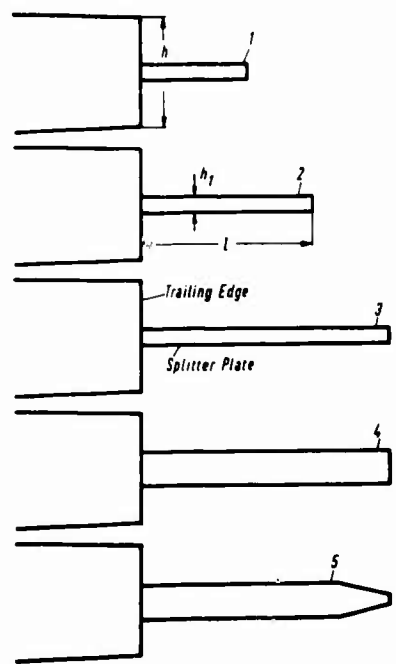


Fig. 9 Splitter plates used in this investigation

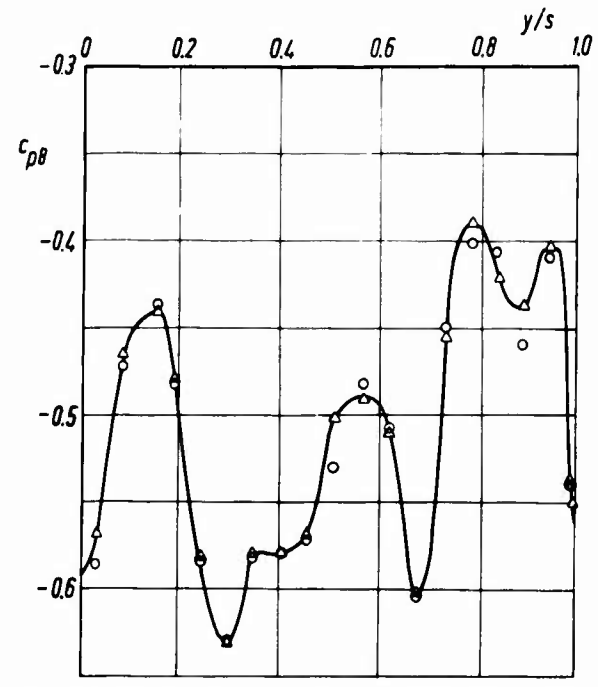


Fig. 10 Distribution of the base pressure coefficient over the half-span for a straight blunt trailing edge without splitter plate

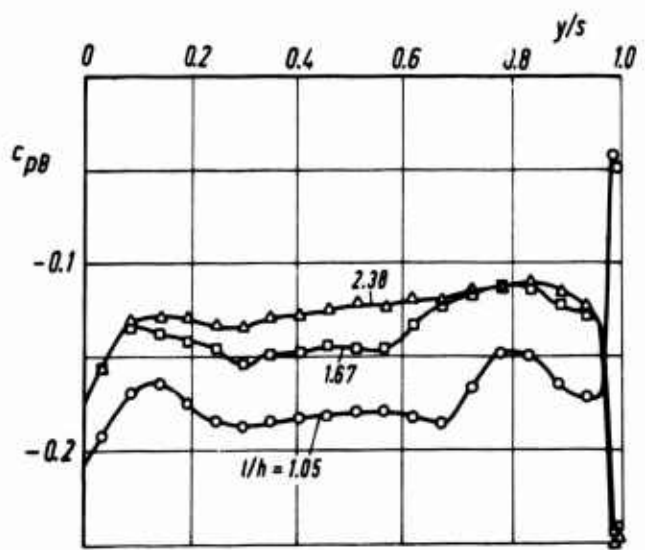


Fig. 11 Distribution of the base pressure coefficient over the half-span for a straight blunt trailing edge fitted with the thin splitter plates No. 1, 2 and 3

for the wing fitted with the thin splitter plates 1, 2 and 3 is plotted. In these cases the base pressure coefficients are nearly constant over the span, especially for the longest splitter plate.

The results show that the mean base pressure increases with increasing length of the splitter plate. But the splitter plate also has another influence on the base drag. To explain this, we refer to Fig. 12, which shows pressure distributions downstream of the separation point at the Mach number  $M_\infty = 0.4$ , as measured by J. F. Nash et al [11]. Such pressure distributions are typical for subsonic base flows.

The curve ① refers to the flow past a back step, i. e. to the flow past a thin section with blunt trailing edge at the incidence  $\alpha = 0^\circ$  having a very long splitter plate in the wake. The curve denoted by ② refers to the flow past the same section without splitter plate. For short splitter plates the pressure distribution lies somewhere between both curves. Therefore, the

pressure acting on the end of the splitter plate probably depends on the length of the splitter plate. Since the splitter plate has a finite thickness, the effective base pressure, defined as the pressure corresponding to the base drag, differs from the pressure acting on the airfoil base. The coefficient of the effective base pressure, defined by

$$(c_{pB})_{\text{eff}} = -\frac{F}{F_B} c_{DB} = -\frac{c}{h} c_{DB} \quad (1)$$

with  $F_B$  as base area and  $F$  as wing area, is related to the base pressure coefficient  $c_{pB}$  by the equation

$$(c_{pB})_{\text{eff}} = \frac{h_1}{h} c_{pE} + c_{pB} \left(1 - \frac{h_1}{h}\right) \quad (2)$$

where  $h_1$  is the splitter plate thickness and  $c_{pE}$  the pressure coefficient acting on the end of the splitter plate. If

$$\left. \begin{array}{l} c_{pE} > c_{pB} \\ h_1 > 0 \end{array} \right\} \quad (3)$$

the effective base pressure is higher than the base pressure, i. e. higher than the pressure acting on the airfoil base at  $x = 0$ . Referring to Fig. 12 it is plausible that for long splitter plates  $(c_{pB})_{\text{eff}} > c_{pB}$ . For short splitter plates the contrary may be true.

It can be seen from Eq. (2) that the base drag can be reduced by increasing the splitter plate thickness, provided that the base pressure is not affected. The curve ① in Fig. 13 shows the distribution of the base pressure coefficient over the half-span for the case that the wing is fitted with the splitter plate No. 4 with a blunt end having a length of  $l/h = 2.38$  and a thickness of  $h_1/h = 0.31$ . By comparison with Fig. 11 one can see that for this thick splitter plate the base pressure coefficient is remarkably lower than for the thin splitter plate No. 3 of equal length. This effect can be explained by the additional influence of the thick blunt end of the splitter plate on the back flow in the near wake (see e. g. experimental results by I. Tani [12]). Therefore, if the end of the splitter plate is made sharper, the base pressure should increase. This seems actually to be the case, because the base pressure coefficient is evidently higher for the splitter plate No. 5 with a "sharp" end than for No. 4 with a blunt end, as shown by the curve ② in Fig. 13.

For the prediction of the base drag the profile drag has to be subtracted from the total drag. By using carefully measured values of base pressure and total drag for the wing with a blunt broken trailing edge, the value

$$c_{Dp} = 0.0060 \quad , \quad (\alpha = 0^\circ) \quad (4)$$

was estimated for the coefficient of profile drag (without base drag). The base drag coefficient, therefore, was predicted from the equation

$$c_{DB} = c_D - 0.0060 \quad , \quad (\alpha = 0^\circ) \quad (5)$$

By using the base drag and base pressure values, the pressure acting on the end of the splitter plate could be calculated from Eq. (2). The results are given in Table 1.

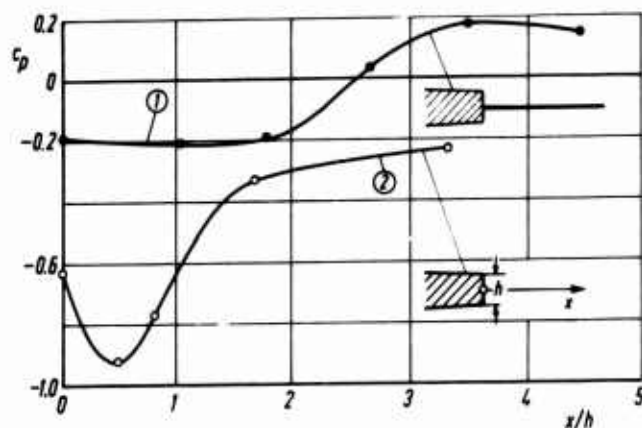


Fig. 12 The pressure distribution in the plane of symmetry of the near wake. After J. F. Nash et al [11]

curve ① : with a long splitter plate  
curve ② : without splitter plate

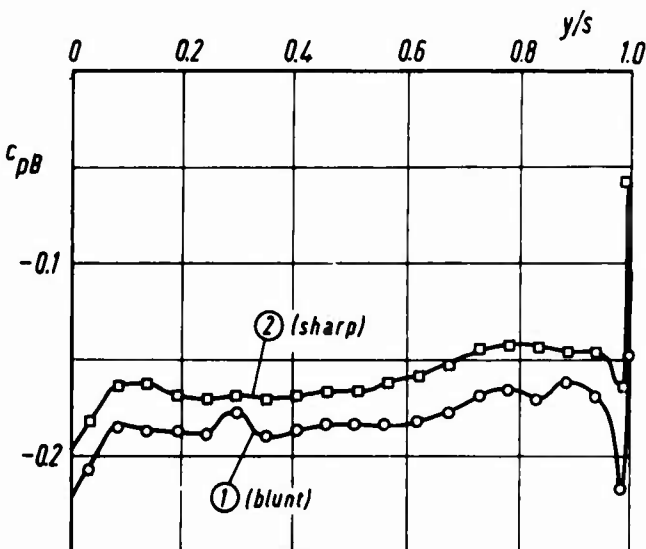


Fig. 13 Distribution of the base pressure coefficient over the half-span for a straight blunt trailing edge fitted with the thick splitter plates No. 4 and 5

curve ① : Splitter plate No. 4 with a blunt end  
curve ② : Splitter plate No. 5 with a "sharp" end

12-6

Trailing edge configuration		$c_{pB}$	$c_{pE}$	$(c_{pB})_{eff}$
without splitter plate	$l/h = 0$	- 0.440		- 0.440
with splitter plate No. 1	$l/h = 1.05$ $h_1/h = 0.14$	- 0.171	- 0.27	- 0.186
" " " No. 2	$l/h = 1.67$ $h_1/h = 0.14$	- 0.139	- 0.30	- 0.163
" " " No. 3	$l/h = 2.38$ $h_1/h = 0.14$	- 0.130	- 0.02	- 0.114
" " " No. 4	$l/h = 2.38$ $h_1/h = 0.31$ "blunt"	- 0.181	+ 0.04	- 0.114
" " " No. 5	$l/h = 2.38$ $h_1/h = 0.31$ "sharp"	- 0.159	+ 0.01	- 0.106
broken trailing edge		- 0.166		- 0.166

**Table 1** Coefficients of base pressure, of effective base pressure and of pressure acting on the end of the splitter plate for various trailing edge configurations

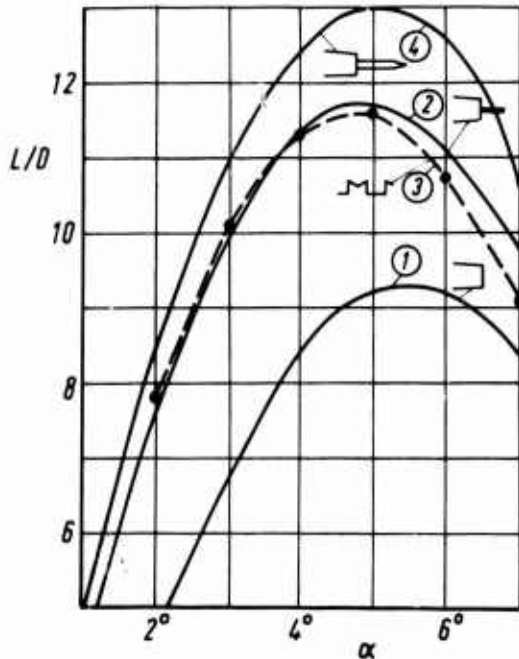


**Fig. 14** Lift to drag ratio versus angle of incidence for various trailing edge configurations

- curve ① : straight blunt trailing edge without splitter plate
- curve ② : with splitter plate No. 1
- curve ③ : broken trailing edge  
 $b_1/h = 5.0$ ,  $a/h = 1.9$ ,  
 $\text{tg } \gamma = 0.50$
- curve ④ : with splitter plate No. 5

For the shorter thin splitter plates No. 1 and 2 with  $l/h = 1.05$  and  $l/h = 1.67$  the effective base pressure is lower than the base pressure, depending on the relatively low pressure acting on the end of the splitter plate. For the longest thin splitter plate No. 3 with  $l/h = 2.38$  the effective base pressure is, however, higher than the base pressure, because in this case the pressure at the end of the splitter plate is relatively high, with  $c_{pE} = - 0.02$ . For the thick splitter plate No. 4 with a blunt end the effective base pressure has the same magnitude as for the long thin splitter plate No. 3 although the base pressure for the thick splitter plate is far lower. If the end of the thick splitter plate is made "sharp" (splitter plate No. 5), the base pressure increases and then the effective base pressure has the highest value obtained in this test on splitter plates, with  $(c_{pB})_{eff} = - 0.106$ . The base drag is then only about 24 per cent of that for a straight blunt trailing edge without splitter plate. With the best splitter plate of this investigation, therefore, a base drag reduction of 76 per cent is achieved, a value much greater than those previously reported (see Fig. 1).

By using this most advantageous splitter plate the base drag is about 32 per cent smaller than for the best broken trailing edge. It seems, therefore, that in three-dimensional flow the splitter plate is a more efficient device for reducing base drag than a broken trailing edge, provided that the dimensions of the splitter plate are chosen in a reasonable way. It may be remarked that the optimum dimensions of the splitter plate are still to be found.

**Fig. 14** shows the lift to drag ratio as function of the angle of incidence for some trailing edges. For the straight blunt trailing edge the maximum value of the lift to drag ratio is  $(L/D)_{max} = 9.3$ , approximately. If the trailing edge is fitted with the short thin splitter

plate No. 1, with  $l/h = 1.05$ , the maximum lift to drag ratio is much higher with  $(L/D)_{\max} = 11.7$ . It can also be seen that the best broken trailing edge is equally advantageous, approximately, as the short splitter plate No. 1. The highest  $L/D$ -values, however, are achieved by using the long thick splitter plate No. 5 with a "sharp" end. In this case the maximum lift to drag ratio has a value of  $(L/D)_{\max} = 13.0$ . The corresponding drag coefficient is about 19 per cent smaller than that for the short thin splitter plate No. 1. 12-7

### 3.4 Measurements with Splitter Wedges in the Wake

In the measurements on the wing fitted with splitter plates it was observed that by using such a long splitter plate that its end lies in the region of relatively high pressure near the reattachment point, the effective base pressure could be increased remarkably over the value of the base pressure. By this means the base drag could be decreased appreciably. However, one can do still a further step: by fitting the blunt trailing edge with a body having inclined walls, e. g. with a wedge as shown in Fig. 15, it is possible to take advantage of the pressure rise in the reattachment region. The full details of these measurements are given in [14]\*).

For such a configuration the effective base pressure coefficient - defined by Eq. (1) - is given by \*\*)

$$(c_{pB})_{\text{eff}} = (1 - m)c_{pB} + m \frac{1}{l} \int_0^l c_p dx \quad (6)$$

where  $c_{pB}$  means the base pressure coefficient,  $c_p$  the local pressure coefficient on the wedge,  $l$  the length of the wedge and

$$m = h_1/h \quad (7)$$

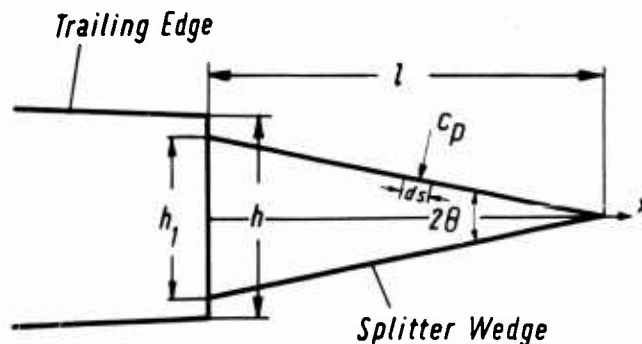


Fig. 15 Trailing edge with splitter wedge

the ratio of wedge thickness to trailing edge thickness. If the pressure distribution on the wedge surface is not affected by the value of the parameter  $m$ , the highest effective base pressure coefficient will be achieved for  $m = 1$ , since then the negative part  $(1 - m)c_{pB}$  in Eq. (6) vanishes. Equation (6) then reduces to

$$(c_{pB})_{\text{eff}} = \frac{1}{l} \int_0^l c_p dx \quad (8)$$

The values for the measured drag coefficient at zero lift  $c_{D0}$  and its components are given in Table 2

Wedge No.	$h_1/h$	$l/h$	$c_{D0}$	$c_{Dp}$	$c_{DB}$	$(c_{pB})_{\text{eff}}$
1	0.75	2.42	0.0090	0.0060	0.0030	- 0.086
2	0.65	2.37	0.0098	0.0060	0.0038	- 0.109
3	0.75	2.82	0.0085	0.0060	0.0025	- 0.071
4	0.72	2.14	0.0097	0.0060	0.0037	- 0.106
5	0.72	3.51	0.0081	0.0060	0.0021	- 0.060
6	0.92	3.06	0.0066	0.0060	0.0006	- 0.017
7	0.94	3.50	0.0065	0.0060	0.0005	- 0.014
8	0.93	3.97	0.0061	0.0060	0.0001	- 0.003
9	0.93	4.67	0.0065	0.0060	0.0005	- 0.014
10	0.89	3.50	0.0068	0.0060	0.0008	- 0.023

Table 2 Drag coefficients and coefficients of effective base pressure for the wing with a blunt trailing edge fitted with various splitter wedges

\*) Results from measurements with "triangular fillets" behind a back step are in 1957 reported by I. Tani [12].

\*\*\*) By deriving this equation, one can use the expressions  $ds = dx/\cos \theta$  and  $\text{tg } \theta = h_1/l$  (see Fig.15).

12-8

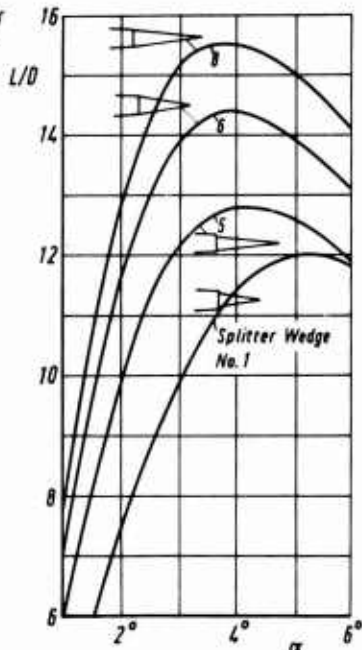
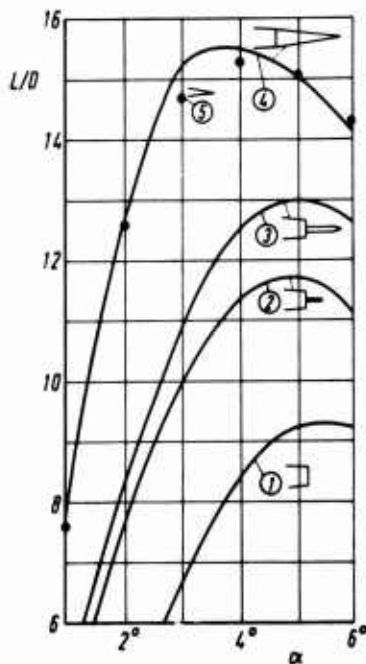


Fig. 16 Lift to drag ratio versus angle of incidence for various splitter wedges



for all 10 splitter wedges measured during this investigation. It can be seen that the drag in general decreases with increasing value of  $h_1/h$  - i. e. with increasing splitter wedge thickness - whereas a splitter wedge length of about  $l/h = 4$  seems to be the most favourable.

For the wedges 6, 7 and 9 the effective base pressure coefficient is  $(c_{pB})_{\text{eff}} > -0.02$  and for the wedge No. 8  $(c_{pB})_{\text{eff}}$  is almost equal to zero. Fitted with this wedge the wing with a blunt trailing edge thus practically has no base drag. It seems, therefore, that a splitter wedge is the most efficient device for reducing base drag, provided that its dimensions are properly chosen.

The lift curve slope  $dc_L/d\alpha$  for the wing with a blunt trailing edge fitted with the wedges 6 to 10 is equal to or somewhat greater than that for the corresponding wing with a sharp trailing edge. For the smaller splitter wedges, however, the lift curve slope is smaller than for the wing with a sharp trailing edge. By using the splitter wedge No. 2 the lift coefficient at the incidence  $\alpha = 6^\circ$  is about 11 per cent smaller than for the wing with a conventional sharp trailing edge.

In Fig. 16 the lift to drag ratio is plotted as function of the angle of incidence for some splitter wedges. For the wedge No. 1 the maximum lift to drag ratio has a value of about  $(L/D)_{\text{max}} = 12.0$ , i. e. a value somewhat higher than that, which was achieved by using the short thin splitter plate No. 1 (see Fig. 14). For the wedges 5 and 6 the corresponding values are  $(L/D)_{\text{max}} = 12.8$  and  $(L/D)_{\text{max}} = 14.4$ . The latter ratio is already very good. The highest lift to drag ratio, however, is obtained for the wedge No. 8, for which  $(L/D)_{\text{max}} = 15.5$ .

In Fig. 17 lift to drag ratios of the wing with a blunt trailing edge using different devices for reducing base drag are shown together with values for the corresponding wing with a sharp trailing edge from [7]. It can be seen that the most favourable splitter wedge No. 8 gives the best results. The maximum lift to drag ratio of the wing with a straight blunt trailing edge fitted with this splitter wedge is about 67 per cent greater than that for the same wing with a straight blunt trailing edge without splitter plate. The corresponding total drag in the first case is about 55 per cent smaller than in the second one. The figure also shows that the wing with blunt trailing edge fitted with the most efficient splitter wedge has the same maximum lift to drag ratio, approximately, as the corresponding wing with a conventional sharp trailing edge. Then also the total drag is of equal magnitude in both cases.

Thus, at present the splitter wedge seems to be the best device for reducing the base drag. Therefore, measurements on profiles with blunt trailing edges and splitter plates at high subsonic, transonic, and supersonic Mach numbers would be of interest.

Fig. 17 Lift to drag ratio versus angle of incidence

- curve ① : straight blunt trailing edge without splitter plate
- curve ② : with splitter plate No. 1
- curve ③ : with splitter plate No. 5
- curve ④ : with splitter wedge No. 8
- ⑤ : wing with a sharp trailing edge

#### 4. CONCLUDING REMARKS

In order to reduce the base drag of airfoils with a blunt trailing edge, measurements in the Low Speed Wind Tunnel were performed on a wing with finite span having various trailing edge configurations. The Mach number had a value of  $M_\infty = 0.15$  and the Reynolds number a value of  $R_\infty = 2 \cdot 10^6$ , approximately.

The results show that by variation of some geometrical parameters of the broken trailing edge, its drag could be reduced by an amount of 13 per cent, approximately, giving a base pressure coefficient of  $c_{pB} = -0.156$ , compared with  $c_{pB} = -0.440$  valid for a straight blunt trailing edge.

By using relatively long and thick splitter plates the base drag could be reduced even stronger giving  $(c_{pB})_{\text{eff}} = -0.106$  for the best splitter plate. Then the maximum lift to drag ratio has a value of  $(L/D)_{\text{max}} = 13.0$ , compared with  $(L/D)_{\text{max}} = 9.3$  valid for the straight blunt trailing edge.

The greatest reduction of base drag was attained by fitting splitter wedges on the trailing edge. For the best splitter wedge the base drag is practically zero. Then the wing with a blunt trailing edge has a maximum lift to drag ratio of  $(L/D)_{\text{max}} = 15.6$ , a value which is equally good as that for a corresponding

wing with a sharp trailing edge. Then the total drag also is equal in both cases.

In incompressible flow the best broken trailing edge - which has been used in previous measurements at high speed - has a base pressure coefficient of  $c_{pB} = -0.180$ , approximately. At transonic Mach numbers the maximum lift to drag ratio for a wing fitted with this trailing edge was only some per cent smaller than that for a corresponding wing with a sharp trailing edge (Fig. 5). It is therefore possible that a wing with a blunt trailing edge fitted with an optimum splitter wedge has more favourable characteristics at transonic Mach numbers than a corresponding wing with a sharp trailing edge.

## 5. REFERENCES

- [1] Holder, D. W. The transonic flow past two-dimensional aerofoils  
J. Roy. Aero. Soc. 68 (1964), pp. 501-516
- [2] Chapman, D. R. Airfoil profiles for minimum pressure drag at supersonic velocities  
- General analysis with application to linearized supersonic flow  
NACA TR 1063 (1952)
- [3] Pearcey, H. H. The aerodynamic design of section shapes for swept wings  
Advances in Aeronautical Sciences, Vol. 3, Proc. 2nd Int. Congr. Aero.  
Sci. Zürich 1960. Pergamon Press 1962
- [4] Bearman, P. W. Investigation of the flow behind a two-dimensional model with blunt trailing edge and fitted with splitter plates  
J. Fluid Mech., Vol. 21 (1965), pp. 241-255
- [5] Bearman, P. W. Investigation into the effect of base bleed on the flow behind a two-dimensional model with a blunt trailing edge  
AGARD Conference Proceedings No. 4, Separated Flows, Part 2 (1966), pp. 479-507
- [6] Nash, J. F. A discussion of two-dimensional turbulent base flows  
ARC R & M No. 3468 (1967)
- [7] Tanner, M. Dreikomponenten- und Basisdruckmessungen an Flügeln mit dicker Hinterkante  
AVA-Bericht 68 A 30 (1968)
- [8] Tanner, M. A method for reducing the base drag of wings with blunt trailing edge  
The Aero. Quart., Vol. 23 (1972), pp. 15-23
- [9] Tanner, M. Der Einfluß der Hinterkantenform auf den Widerstand eines Rechteckflügels im Machzahlbereich von  $Ma_{\infty} = 0,5$  bis 2,2  
DLR FB 71-85 (1971)
- [10] Tanner, M. Experimental investigation of the drag of wings with a blunt trailing edge at transonic speeds  
AGARD CP-83-71 (1971), pp. 8-1 to 8-6
- [11] Nash, J. F. Experiments on two-dimensional base flow at subsonic and transonic speeds  
Quincey, V. G. NPL Aero. Rep. 1070 (1963)  
Callinan, J.
- [12] Tani, I. Experimental investigation of flow separation over a step  
Grenzschichtforschung IUTAM-Symposium, Freiburg/Br. 1957.  
Hrsg. H. Görtler, Springer-Verl. 1958, S. 377-386
- [13] Tanner, M. Dreikomponenten- und Basisdruckmessungen an einem Rechteckflügel mit stumpfer Hinterkante mit verschiedenen Trennplatten im Totwasser  
DFVLR-AVA-Bericht 187-72 A 19 (1972)
- [14] Tanner, M. Einfluß von Trennkeilen auf den Auftrieb und Widerstand eines Rechteckflügels mit stumpfer Hinterkante  
DFVLR-AVA-Bericht 187-72 A 20 (1972)

A STUDY OF FLOW SEPARATION IN THE BASE REGION AND ITS EFFECTS DURING POWERED FLIGHT

13-1

A. L. Addy\*  
H. H. Korst\*\*  
R. A. White\*\*\*

Department of Mechanical and Industrial Engineering  
University of Illinois at Urbana-Champaign  
Urbana, Illinois 61801 U.S.A.

and

B. J. Walker†  
Directorate for Research, Development, and Engineering  
U.S. Army Missile Command, AMSMI-YDK  
Redstone Arsenal, Alabama 35809 U.S.A.

SUMMARY

It is well established that aircraft and missile performance during powered flight is significantly affected by the separated-flow region resulting from the interaction between the propulsive-jet and the free-stream flows. The Chapman-Korst component flow model allows, due to its generality and flexibility, the qualitative and quantitative discussion of the effects on the afterbody-base problem of all pertinent design and performance parameters. The usefulness of the component approach has been enhanced by semi-empirical modifications, improvements of individual components, and the development of comprehensive computer programs. Parametric studies of the base pressure, base temperature, plume-induced separation, and combined afterbody-base drag are presented. Modifications of the afterbody drag, thermal and chemical environment in the base region, and possible loss of stability and control can result if plume-induced separation occurs on the afterbody. It is shown that the onset and location of plume-induced separation of the external flow can be predicted given a suitable boundary-layer separation criterion. It is found that prediction of the system behavior depends strongly on the proper formulation of the boundary-layer separation criterion and experimental evidence is introduced to illustrate the need for further improvements in flow-component analyses. For conducting experiments, correct plume simulation is essential; a new and effective method of modeling is demonstrated.

NOMENCLATURE

Symbols

A	= area	P	= absolute pressure
C	= Crocco number	r	= recompression coefficient
$C_p$	= specific heat at constant pressure	R	= radius
$C_D$	= afterbody-base drag coefficient	s	= mixing length
		T	= absolute temperature
$\Delta C_f$	= incremental thrust-minus-drag coefficient	$\sigma$	= empirical mixing parameter
$\beta$	= geometric flow angle	$\rho$	= density
$\gamma$	= ratio of specific heats	$\Lambda$	= stagnation temperature ratio
$\eta$	= dimensionless mixing coordinate, $\sigma y/x$	$\phi$	= velocity ratio

Barred Symbols

$\bar{E}_o$	= bleed-to-nozzle mass flow ratio	$\bar{X}, \bar{R}$	= coordinate ratios: $X/R_{2E}, R/R_{2E}$
$\bar{E}_e$	= base-to-nozzle energy transfer ratio	$\bar{X}_{SE}$	= plume-induced separation location, $X_{SE}/R_{2E}$
$\frac{\bar{P}_{BS}}{\bar{T}_{BS}}$	= solution ratios: $P_{BS}/P_E, T_{BS}/T_{o1}$		

Subscripts

a	= adjacent inviscid flow	o	= stagnation conditions
B	= base region	s	= slipline, oblique shock
BS	= base-flow solution	SE	= plume-induced separation location
d	= discriminating streamline	SEP	= separation
E, I	= external, internal streams	1E, 1I	= terminus of afterbody, nozzle
j	= jet-boundary streamline	2E	= initial afterbody point

\*Associate Professor; \*\*Professor and Head; \*\*\*Professor; and †Aerospace Research Engineer.

Numbers appearing in brackets throughout this paper refer to entries in REFERENCES.

## 1. INTRODUCTION

Aircraft and missile performance during powered supersonic flight can be significantly affected by the separated flow region formed by the interaction between the free-stream and propulsive-nozzle flows. As a consequence, important design considerations are:

- i. The base and afterbody drag contributions and the significant factors influencing these contributions.
- ii. The potential gains from optimization techniques for the afterbody base-flow region.
- iii. The onset and effects of plume-induced separation on the afterbody and the modification of the flowfield in the vicinity of control surfaces.
- iv. The thermal and chemical environments maintained in the base and near-wake regions.

A tenable and practical way to study these complex problems is by means of a generalization of the Chapman-Korst baseflow model which includes axisymmetric flow with various afterbody and propulsive-nozzle geometries, plume-induced separation, and empirical correlations. This generalization of the Chapman-Korst component model is based on a highly idealized but physically perceptible flow model which distinguishes between and ultimately synthesizes individual components. From its original conception until the comprehensive model and methods available today, numerous improvements have been made in individual components. Of particular significance are the contributions of Nash in England, Carriere, et al., in France, and Page, et al., in the United States who have pointed to the importance of modifying the recompression process and of considering the effectiveness of mixing along and between various portions of the bounding mixing layers. More recently, the development of comprehensive high-speed computer programs by Addy that provide a means for rapidly and easily investigating the effects of parameter and model component variations has been a major step forward.

The purpose of this paper is to demonstrate the capabilities of these computational programs based on the generalization of the Chapman-Korst baseflow model. This is done by presenting case studies of parametric variations in the variables governing the base-pressure and -temperature problem, of the combined afterbody-base drag and potential optimization procedures, of plume-induced separation, and of plume-simulation techniques.

## 2. THEORETICAL FLOW MODEL

The Chapman-Korst flow model [1-4] for analyzing two-dimensional supersonic flow over a simple backstep and its subsequent application by Korst, Chow, and Zumwalt [5] to axisymmetric flows provides the basis for the analysis of the two-stream axisymmetric base-pressure problem. Although details of the development and application of this flow model are given in [5-7] a summary of the concepts, assumptions, and relevant equations is included here.

The basic configuration and associated notation for the two-stream axisymmetric base-pressure problem are shown in Fig. 1. Application of the Chapman-Korst flow model consists of four parts.

- i. The separated flow region is approximated by a constant-pressure region formed by the base geometry and the "corresponding" inviscid boundaries. The "corresponding" inviscid boundaries are determined by their respective initial flow conditions and the requirement that the flows expand to a common base pressure. As a consequence of this assumption, there is no local interaction between the streams until their mutual impingement point is reached. Flow properties immediately downstream of the impingement point are determined by the requirements of common pressure and flow direction downstream of the impingement point.
- ii. The two-dimensional constant-pressure turbulent mixing region is locally superimposed on each of the "corresponding" inviscid boundaries at their mutual impingement point. The mixing profiles are located with respect to each of the boundaries by satisfying the integral momentum balance for the respective streams on a local two-dimensional basis.
- iii. The pressure level that the entrained fluid must recompress to is determined by the oblique shock system which occurs at the impingement point of the "corresponding" inviscid boundaries. The recompression criterion defines the "discriminating" streamline within the mixing region as the streamline which possesses just sufficient mechanical energy to recompress by stagnating from the base pressure to the pressure level sustained by the oblique shock system at the impingement point.
- iv. Solution values of base pressure and base temperature, for given geometry and flow conditions, are determined by satisfying the continuity and energy equations for the overall separated flow region.

### 2.1 "Corresponding" Inviscid Flow Fields

The supersonic flow fields are determined by the *method of characteristics* for irrotational axisymmetric flow. The external (free-stream) flow is assumed to be initially a uniform supersonic stream; downstream of this uniform external flow station, the flow can either immediately separate, as for a cylindrical afterbody, or continue over a prescribed afterbody before separating. The internal (propulsive-nozzle) flow is assumed to be from an ideal full-flowing supersonic conical-flow or uniform-flow nozzle. After the separation of the internal and external flows, the flow fields are calculated for a constant-pressure boundary condition and a trial value of the base-to-freestream pressure ratio. At the impingement point of the inviscid stream, if it exists, the oblique-shock recompression system is determined.

The general case of a uniform external (free-stream) flow upstream of an afterbody is shown in Figs. 1 and 2. The afterbody flow-field calculations are made from the known uniform-flow characteristic through the initial point (2E) on the afterbody. The flow-field calculations proceed from these known data on the II-characteristic along I-characteristics to the boundary points on the afterbody surface where the boundary condition of flow tangency is satisfied; these calculations are illustrated in Fig. 2. An iteration sequence is used to find the I-characteristic which passes through the terminus of the afterbody. This calculation sequence completely determines the flow field over the afterbody; to link the afterbody and constant-pressure boundary flow fields, the II-characteristic through the afterbody terminus is determined as shown in Fig. 2. The free-stream flow conditions, the afterbody flow-field calculations, and the constant-pressure boundary flow-field calculations are linked, respectively, along characteristic curves which are specified or determined through points (2E) and (1E) of Fig. 1. The afterbody geometries considered herein are: the ogive, parabola, and cone.

For the internal (propulsive-nozzle) flow, the ideal uniform-flow propulsive-nozzle reduces to the specification of the uniform Mach number and flow direction along the straight characteristic through the terminus of the nozzle. The ideal conical-flow nozzle is specified by the constant nozzle Mach number and the variable conical flow direction along the known non-characteristic curve through the nozzle terminus. Thus, the flow field between the non-characteristic curve and the initial characteristic is constructed. The propulsive-nozzle flow conditions are linked with the constant-pressure boundary flow-field calculations along a characteristic curve specified or determined through point (1I) of Fig. 1.

The "corresponding" inviscid flow fields are shown in Fig. 3; the recompression shock system is determined by the requirements that a common pressure and flow direction exist immediately downstream of the impingement point. The oblique shock pressure rise can be expressed functionally for both the internal and external streams at the impingement point by

$$P_S/P_B = f[M_{BI}^*, (\theta_{BI} - \theta_S)] = f[M_{BE}^*, -(\theta_{BE} - \theta_S)] \quad (1)$$

The values of  $M_{BI}^*$  and  $M_{BE}^*$  are determined by the isentropic expansion of the respective streams from  $P_{1I}$  and  $P_{1E}$  to  $P_B$ ;  $\theta_{BI}$  and  $\theta_{BE}$  are determined at the impingement point of the streams from the "corresponding" inviscid flow-field calculations. Thus, the unknown slip-line angle  $\theta_S$  is determined from Eq. (1) along with the value of the pressure rise  $P_S/P_B$  across the oblique shock system.

Oblique shock waves can occur in the external flow field prior to or at onset of plume-induced separation of the external flow, or for nozzle geometries with large exit flow angles and/or highly overexpanded nozzle flows. Imbedded shock waves occurring in the internal or external flow fields are considered approximately as reversible compressions in the flow-field analysis. In the afterbody calculations, the oblique shock wave for conical-flare configurations is approximated by a single-line reversible compression.

## 2.2 Turbulent-Mixing Component

For a two-dimensional constant-pressure mixing region with a "thin" approach boundary layer, the velocity profile within the mixing region can be represented by

$$\phi \equiv U/U_a = \frac{1}{2} [1 + \operatorname{erf}(\eta)] \quad (2)$$

The stagnation temperature profile in the mixing zone for nonisoenergetic flow with a unit turbulent Prandtl number is given by Crocco's relationship as

$$\Lambda \equiv T_o/T_{oa} = \Lambda_b + (1 - \Lambda_b) \phi \quad (3)$$

where  $\Lambda_b \equiv T_b/T_{oa}$ . For nonisoenergetic mixing at constant pressure, the local-to-freestream density ratio is

$$(\rho/\rho_a) = (1 - C_a^2)/(\Lambda - C_a^2 \phi^2) \quad (4)$$

The use of similarity solutions other than the error function [8], combinations of locally similar profiles with rotational flow regions [9,10], and even numerically integrated developing mixing profiles have been suggested to improve the accuracy of the mixing component.

The intrinsic coordinate system (x,y) and, consequently, the velocity profile are localized with respect to the "corresponding" inviscid boundary by satisfying the integral momentum equation. The j-streamline is defined as that streamline which separates the fluid originally in the jet and the fluid entrained by the mixing process. The j-streamline within the mixing region is located by applying the integral continuity equation. The resulting integral equation to be solved for  $\eta_j$  is

$$\int_{\eta_j}^{\eta_{Ra}} \left( \frac{\rho}{\rho_a} \right) \phi \, d\eta = \int_{\eta_{Rb}}^{\eta_{Ra}} \left( \frac{\rho}{\rho_a} \right) \phi^2 \, d\eta \quad (5)$$

Thus, for given values of  $C_a^2$  and  $\Lambda_b$ , the velocity ratio along the j-streamline is found from Eqs. (2) to (5) and has the functional form  $\phi_j = \phi_j(C_a^2, \Lambda_b)$ .

The mass and energy transport per unit width associated with the mixing process are determined in relation to the j-streamline. The mass flow rate between the j-streamline and any d-streamline is

$$\frac{\sigma_g}{s \rho_a U_a} = \int_{\eta_j}^{\eta_d} \left( \frac{\rho}{\rho_a} \right) \phi \, d\eta \quad (6)$$

The energy, referenced to a zero temperature, convected along with the mass flowing between the j- and d-streamlines and energy transfer rate across the j-streamline due to shear work and conduction define the combined energy transfer rate

$$\frac{\sigma_e}{s \rho_a U_a C_p T_{oa}} = \int_{\eta_{Rb}}^{\eta_d} \left( \frac{\rho}{\rho_a} \right) \Lambda \phi \, d\eta - \Lambda_B \int_{\eta_{Rb}}^{\eta_j} \left( \frac{\rho}{\rho_a} \right) \phi \, d\eta \quad (7)$$

The important results of the two-dimensional constant-pressure mixing analysis used in the analysis of the two-stream axisymmetric base pressure problem, Fig. 4, are summarized by Eqs. (5), (6), and (7). These equations, however, form an incomplete set. As a consequence, they must be augmented with a recompression criterion and with the requirement of conservation of mass and energy for the overall separated flow region.

### 2.3 Conservation of Mass and Energy for the Wake Region

Referring to Fig. 4, the conservation of mass and of energy for the overall separated flow region requires that

$$G_o + G_E + G_I = 0 \quad \text{and} \quad E_o + E_E + E_I = 0 \quad (8)$$

The mass and energy transport rates ( $G_E, E_E$ ) and ( $G_I, E_I$ ), due to mixing along the external and internal streams' boundaries, are approximated by using the two-dimensional mixing analysis. The two-dimensional mixing profiles are superimposed on the "corresponding" inviscid flow boundaries at their impingement point. Thus, the mixing terms in Eqs. (8) can be expressed approximately as

$$(G_E + G_I) \approx 2\pi R_{imp} (g_I + g_E) \quad \text{and} \quad (E_E + E_I) \approx 2\pi R_{imp} (e_I + e_E) \quad (9)$$

Values of the two-dimensional mixing functions ( $g, e$ ) are determined from Eqs. (6) and (7) for the flow conditions and mixing lengths determined from the "corresponding" inviscid flow-field analysis.

For convenience, the following dimensionless mass and energy ratios are defined as

$$\bar{B}_o \equiv G_o/G_{NI}, \quad \bar{B} \equiv -[2\pi R_{imp} (g_I + g_E)]/G_{NI}, \quad \bar{E}_o \equiv E_o/E_{NI}, \quad \text{and} \quad \bar{E} \equiv -[2\pi R_{imp} (e_I + e_E)]/E_{NI} \quad (10)$$

where the propulsive-nozzle mass-flow rate  $G_{NI}$  and the total enthalpy rate  $E_{NI} = C_p T_{oI} G_{NI}$  serve as reference values.

In terms of mass and energy ratios, conservative requirements obtained by combining Eqs. (8) and (10) become

$$\Delta \bar{B}(\bar{P}_{BS}, \bar{T}_{BS}) \equiv \bar{B}_o - \bar{B} = 0 \quad \text{and} \quad \Delta \bar{E}(\bar{P}_{BS}, \bar{T}_{BS}) \equiv \bar{E}_o - \bar{E} = 0 \quad (11)$$

For given values of geometry and flow conditions, solution values of the base-pressure ratio  $\bar{P}_{BS}$  and base-temperature ratio  $\bar{T}_{BS}$  must result in Eqs. (11) being satisfied simultaneously.

### 2.4 Recompression Criterion

The recompression criterion links the flow-field and mixing analyses by identifying the d-streamline as the streamline possessing just sufficient mechanical energy to recompress by stagnating from the base pressure  $P_B$  to the high-pressure  $P_S$  downstream of the shock system. Thus, this pressure rise distinguishes between the fluid energized by the mixing which has sufficient mechanical energy to recompress to this pressure level from that which has insufficient mechanical energy and, as a consequence, must recirculate into the base region. The recompression process, although irreversible, is assumed to be equivalent to an isentropic compression. Thus, for recompression from  $P_B$  to  $P_S$ , the d-streamline Crocco number  $C_d$  is found by solving the isentropic pressure-ratio function

$$P_{od}/P_d [C_d, \gamma] = (1 - C_d^2)^{-[\gamma/(\gamma-1)]} = (P_S/P_B) \quad (12)$$

The d-streamline velocity ratio is then determined from

$$\phi_d = C_{nr} \left\{ \frac{1}{2} C_{nr} (1 - \Lambda_B) + \left[ \frac{1}{4} C_{nr}^2 (1 - \Lambda_B)^2 + \Lambda_B \right]^{1/2} \right\} \quad (13)$$

where  $C_{nr} \equiv C_d/C_a$ .

13-14

Experience has shown that general trends and the functional dependence of base-pressure and base-temperature ratios on the governing variables can be predicted with this flow model. There are, however, geometrical and flow conditions wherein significant discrepancies exist between the level of predicted and experimental values of the base-pressure ratio; these discrepancies are most pronounced for those cases wherein the nozzle is relatively small in comparison with the base.

The recompression process is central in determining the base-flow solution since it links the viscous and inviscid components of the flow model. Since the recompression process is not well understood and does strongly influence the solution to the base-flow problem, the need to improve agreement between predicted and experimental values has resulted in several empirical modifications to this part of the flow model.

Nash [11] proposed and determined an empirical "reattachment condition" for the supersonic single-stream two-dimensional case. An approach was adopted by Carriere and Sirieix [12] in which they proposed and determined an empirical law of reattachment, for a negligible initial boundary layer, based on an "angular criterion of turbulent reattachment." Page, Kessler, and Hill [13] offered an alternative empirical reattachment for two-dimensional supersonic flows based on the "discriminating-streamline" velocity ratio.

For the axisymmetric two-stream base-flow problem under consideration herein, the recompression resulting from the interaction of separated supersonic freestream-nozzle flows apparently cannot be analyzed by a direct carry-over of the empirical reattachment criteria determined in the aforementioned investigations. Sirieix, Delery, and Mirande [14] have presented a more generalized "criterion of turbulent reattachment" which involves geometric, as well as flow variables. Dixon, Richardson, and Page [15] considered this problem under the experimentally supported assumption that the external inviscid flow boundary remains straight after initially turning to adjust to the base pressure.

With this background and the availability of a computer program based on the flow model of Chapman-Korst, a simple empirical flow-model modification was proposed [16,17]. The recompression criterion is modified by assuming that the discriminating streamlines or the jet-boundary streamlines are capable of recompressing to only a fraction of the pressure rise from the base region to the downstream shock region as determined for the "corresponding" inviscid flowfields. If the pressure rise immediately downstream of the oblique shock system, Fig. 5, is given relative to the base pressure as  $(P_B/P_S)$ , then the pressure level to which the discriminating streamline must recompress by stagnating is given by

$$\frac{P_{od}}{P_d} (C_d, \gamma) = r(P_S/P_B) > 1 \quad (14)$$

Equation (14) defines the empirical recompression coefficient  $r$ . Detailed comparison with approximately 150 sets of experimental data have shown that the recompression coefficient for cylindrical afterbodies is principally a function of one dimensionless geometrical variable: the nozzle-to-base radius ratio. Although data used in these comparisons represented a wide range of geometrical and flow variables, they were obtained principally in cold flow air-to-air experiments. With a single value of this empirical coefficient which corresponds to a particular geometrical configuration good agreement can be achieved throughout the range of variation in the internal-to-external streams pressure ratio. Values of the recompression coefficient determined for cylindrical afterbodies are presented in Fig. 6 as a function of the nozzle-to-base radius ratio,  $R_{11}$  [16,17]. When adequate experimental data were available, the maximum variations in  $r$  were determined and are indicated in Fig. 6.

A similar empirical correlation for boattailed afterbodies is in progress.

## 2.5 Plume-Induced Separation

The occurrence of turbulent boundary-layer separation on the afterbody due to the interaction between the free-stream and the propulsive-nozzle flows is well known. In this case, the base pressure is determined by the boundary-layer separation pressure while the separation location and base temperature are to be determined, Fig. 7. As a consequence, the boundary-layer separation component must be defined and introduced into the base-flow model. The free-interaction concept [18] was adopted by Korst, et al., [5] for their early analyses of the two-stream base-pressure problem; a similar approach has been adopted by Fong [19] and herein.

Based on the free-interaction concept, correlations for the pressure rise across the separation region have been determined for shock and step induced separation on flat plates. Zukoski [20] analyzed separation data for the Mach number range of 1 to 6 and developed simple correlations for the pressure rise at and across the separation region as a function of the local Mach number at separation. These correlations have the form  $P_{SEP}/P_{SE} = (1 + a M_{SE})$  where  $a = 0.36$  or  $0.5$ , respectively, for the separation or plateau pressure ratios. However, preliminary experimental data indicate that the boundary layer history on the boattail due to streamline curvature and the expansion at the boattail-cylinder junction tends to result in lower pressure ratios across the separation region than are given by Zukoski's correlation [21].

When plume-induced separation occurs, Eqs. (11) have the more general form

$$\Delta \bar{B}(\bar{P}_{BS}, \bar{T}_{BS}, \bar{X}_{SE}) = 0 \quad \text{and} \quad \Delta \bar{E}(\bar{P}_{BS}, \bar{T}_{BS}, \bar{X}_{SE}) = 0 \quad (15)$$

where  $\bar{P}_{BS} = \bar{P}_{SEP}(M_{SE}, \dots)$  is imposed by the separation component. Equations (15) must be solved for  $(\bar{T}_{BS}, \bar{X}_{SE})$ .

## 2.6 "Effective" Mixing Lengths

The mixing lengths of the internal and external streams are determined in the unmodified base-flow model, Fig. 4, from the "corresponding" inviscid flowfields. These mixing lengths are the rectified lengths of the constant-pressure boundaries between the separation points and the impingement point. Since the mixing layers merge upstream of the impingement point as shown in Fig. 8, the actual mixing lengths can be significantly less than the values determined from the inviscid analysis; Hong [22] observed that the "effective" mixing lengths can be approximately one-half of their inviscid values.

A simplified model to study the effects of back-flow in the recompression region on the "effective" mixing lengths, base pressure, and base temperature has been developed. With this model, the "effective" widths of the two-dimensional mixing layers are estimated and then superimposed on the inviscid boundaries to determine the approximate location of the merge point of the mixing layers in the recompression region, Fig. 8. The "effective" mixing lengths are taken to be the lengths between the separation points and the merge point.

From Fig. 8, the non-dimensional decrease in mixing length is given for either stream by

$$(\Delta S/S)_i = [1 + 2\sigma_i \tan \theta_{ME} \sqrt{\pi} (Y_{dR}/\delta)_i]^{-1} \quad (16)$$

where  $i = I, E$  and the values of  $(\theta_{ME}, \theta_{MI})$  must satisfy  $(Y_{dRI}/Y_{dRE}) \sin \theta_{ME} = \sin \theta_{MI}$ .

The "effective" width  $Y_{dR}$  of the mixing layer is found with the simplified velocity profile shown in Fig. 9 to be

$$Y_{dR}/\delta = 1 + 2\phi_d + y_m/\delta \quad (17)$$

where  $y_m/\delta = 1 - (1 - C_a^2) C_a^{-2} (C_a^{-1} \ln((1 + C_a)/(1 - C_a)) - 2)$ .

The boundary layers at the separation points of the streams can also affect the "effective" mixing lengths. This effect can be treated by inclusion of a virtual-origin shift for each of the mixing layers. Origin shifts (positive [13] or negative [10]), as well as, transition criteria [4] applied to the dissipative mixing zone surely have to be applied to account properly for significant initial disturbances [10].

It is expected and has been our experience that the base-pressure and -temperature solutions are not strongly influenced by mixing length modifications for configurations and operating conditions wherein the mixing lengths are approximately equal. However, mixing length modification can have a significant influence for those situations (plume-induced separation, nozzle extension, etc.) wherein the mixing lengths are significantly different.

## 3. COMPUTER PROGRAM

Based on the theoretical flow model described in Section 2, a computer program, TSABPP-3†, has been developed for analyzing the two-stream axisymmetric base-pressure problem [23-25]. The program subdivision, solution procedures, and organization closely parallels that of the theoretical flow model. A simplified flowchart, Fig. 10, illustrates the main program organization and iteration-solution procedures employed. Referring to Fig. 10, the program consists of the following principal sub-programs:

- i. INØUT controls the input of data to the main program and the computational options to be used.
- ii. ABTS performs the afterbody and final afterbody II-characteristic calculations.
- iii. ACPBS performs the internal and external constant-pressure boundary calculations.
- iv. CRØSS determines the impingement point, the recompression shock system, and the inviscid mixing lengths.
- v. TJMIX performs all the mixing calculations: mixing integrals, modified mixing lengths, and mass energy rate ratios.
- vi. ITER controls iteration sequences for the various solution procedures to find  $(\bar{P}_{BS}, \bar{T}_{BS})$  or  $(\bar{P}_{BS} = \bar{P}_{SEP}, \bar{X}_{SE}, \bar{T}_{BS})$  without or with plume-induced separation, respectively.

The input variables required for specifying the system configuration, Fig. 1, are  $[X_{11}, R_{11}, \beta_{11}, R_1, Y_1, M_{11}, NSHAPE, X_{2E}, R_{2E}, \beta_{2E}, X_{1E}, R_{1E}, R_E, Y_E, M_E, T_{0E}/T_{0I}, r, P_{0I}/P_E \text{ or } P_{1I}/P_E, E_0, E_0]$  along with a suitable boundary-layer separation criterion, e.g.,  $\bar{P}_{SEP} = f(M_{SE}, \dots)$ . From these data, the program will determine, if possible, solution values of  $(\bar{P}_{BS}, \bar{T}_{BS})$  without plume-induced separation or  $(\bar{P}_{BS} = \bar{P}_{SEP}, \bar{X}_{SE}, \bar{T}_{BS})$  with plume-induced separation.

For the IBM 360/75 system, typical computational times are:

- i. 5 to 15 seconds for isoenergetic ( $T_{0E}/T_{0I} = 1$ ) cases without plume-induced separation.
- ii. 10 to 30 seconds for isoenergetic ( $T_{0E}/T_{0I} = 1$ ) cases with plume-induced separation.
- iii. 45 to 75 seconds for non-isoenergetic ( $T_{0E}/T_{0I} < 1$ ) cases without or with plume-induced separation.

#### 4. CASE STUDIES

13-7

Representative parametric afterbody and base-flow solution data are presented herein to demonstrate the qualitative behavior of the theoretical solutions over a range of geometric and flow variables and to demonstrate the capabilities of the component-model based computer program.

##### 4.1 Parametric Variations in Selected Geometric and Flow Variables [23,24]

For the parametric study of the base-pressure and base-temperature problem, a typical cylindrical afterbody configuration was selected. The detailed specification of this reference configuration is given in TABLE 1. Successive parametric variations were made in the following variables:  $[M_{1E}, \gamma_1, M_{1I}, \beta_{1I}, \bar{B}_o, \bar{T}_{oE}]$ .

The functional behavior of theoretical solutions resulting from the above parametric variations is evident in Figs. 11-16. Trends observed from these data are that the base-pressure ratio is *increased*: by *decreasing* the freestream (Fig. 11) or nozzle (Fig. 12) supersonic Mach numbers; by *decreasing* the specific heat ratio of the propulsive-nozzle flow (Fig. 13); by *increasing* the propulsive-nozzle exit flow angle (Fig. 14); by *bleed* into the base region (Fig. 15); and by *decreasing* the freestream-to-nozzle stagnation temperature ratio (Fig. 16).

The extent and desirability of using any one or combinations of these effects to increase the base-pressure must be based on a thorough analysis of the trade-offs and interactions involved.

For the parametric study of the afterbody-base problem, several of the variables were restricted to mid-range values used in the parametric study of the base-flow problem with a cylindrical afterbody; in addition, the afterbodies considered were limited to a one-caliber length. The afterbody geometries considered herein are: conical boattails and conical flares. The configuration and flow data are summarized in TABLE 2 for this parametric study. It is apparent from Fig. 17 that boattailing can significantly *decrease* the base drag coefficient; the opposite behavior is seen from Fig. 18 to be the case for the conical-flare afterbody. Figure 17 shows that the overall afterbody-base drag coefficient can be *minimized* by proper selection of the boattail; in all cases considered, boattailing tended to *reduce* significantly the overall afterbody-base drag. For the conical-flare afterbody, the afterbody significantly *increases* the overall afterbody-base drag, Fig. 18.

The effects of base "bleed" on the overall boattail-base drag coefficient are shown in Fig. 17 for conical boattails at two fixed operating pressure ratios and parametric values of the base-bleed ratio. The overall drag coefficient is significantly *reduced* by base "bleed"; however, the effectiveness of base "bleed" *decreases* with *increasing* base-bleed ratios. The possibility of *minimizing*  $C_D$  by the proper selection of the base-bleed ratio and boattail angle is evident from Fig. 17.

##### 4.2 Afterbody-Base Optimization [24,26]

Figure 17 demonstrates the dependence of the over-all afterbody-base drag coefficient  $C_D$  on the conical-boattail angle  $\beta_{1E}$  for several operating pressure ratios and base-bleed flow. For a given operating pressure ratio,  $C_D$  can be minimized by the proper selection of  $\beta$ ; the locus of these minimum values of  $C_D$  is indicated in Fig. 17. The influence of base-bleed flow for this configuration can be demonstrated best for fixed operating pressure ratios; the functional behavior and the possible minimization of  $C_D$  are shown in Fig. 17 for operating pressure ratio of  $P_{1I}/P_E = 3$  and parametric values of the base-bleed flow ratio. Thus, the possibility of reducing and minimizing the base drag coefficient by proper selection of a conical-boattail angle and base-bleed flow-rate ratio is demonstrated.

For diversion of the base-bleed flow of Fig. 17 from the propulsive-nozzle stagnation chamber, Fig. 19 demonstrates the potential gains in incremental thrust-minus-drag force,  $\Delta C_F$ , that could be achieved with both boattailing and base-bleed flow. For this operating condition,  $\Delta C_F$  can be maximized by proper selection of the conical-boattail angle and base-bleed flow-rate ratio.

##### 4.3 Plume-Induced Separation [21,25]

Combined afterbody-base drag can be minimized by proper boattail-propulsive nozzle combinations and base bleed; this fact was demonstrated for a representative configuration in Figs. 17, 19, and 20. However, optimized configurations tend to produce flow separation on the boattail due to the increased base pressure which accompanies the decrease in drag; also, increased engine-to-freestream pressure ratios tend to increase the base pressure and promote flow separation. For vehicles which operate over a wide range of altitudes, it may not be possible to avoid engine-to-freestream pressure ratios which could cause separation.

The prediction of plume-induced separation and its effects requires the specification of a separation criterion. For the examples given herein, Zukoski's separation criterion was used:  $P_{SEP}/P_{AE} = (1 + 0.36 M_{1E})$ . The combined drag coefficient curves, Fig. 20, for an optimized system (described in TABLE 2 with  $\beta_{1I} = 20^\circ$ ) show the onset and effects of separation; separation is seen to occur near the minimum values of  $C_D$ .

Figure 21 is a Schlieren photograph of a system operating with the plume-induced separation of the flow on the boattail; superimposed on this photograph are the details of the flowfields as calculated with TSABPP-3. The agreement of the near-wake flow-field details is good; however, this agreement is somewhat fortuitous since only this particular operating condition happens to be in good agreement with the separation criterion used. This fact is demonstrated by Fig. 22 wherein the experimentally and theoretically determined separation locations are presented for a range of operating pressure ratios. Experimentally, the onset of separation occurs at a much lower operating pressure ratio and the rate of change of the separation location with increasing operating pressure ratio is less than predicted by the theoretical analysis using Zukoski's criterion.

It can indeed be questioned whether Zukoski's criterion should be applied to the present situation. The sensitivity of separation criteria to different dynamic conditions imposed on the boundary layers on boattails with considerable adverse pressure gradients has not been sufficiently clarified.

#### 4.4 Plume Simulation

In the design and development of afterbody-base-nozzle configurations, it is desirable but often not possible to investigate experimentally prototype systems with the actual or a simulated propulsive-nozzle flow having the proper value of the ratio of specific heats. To simulate the effects of the plume on the afterbody-base flow, model studies are often conducted with cold air flow and a model of the prototype system, with solid-body plume simulators, with radial jet simulators, etc.; the principal disadvantage of these techniques is that the correspondence and relationship between the behavior of the model and the prototype systems are not always obvious or well understood.

An analytical method to determine geometrically and dynamically similar plumes for the purpose of experimental simulations has recently been developed by Korst [27]. The computer program, TSAEPP-3, has been utilized to conduct numerical computational experiments for evaluating the merits of different simulation techniques.

Figure 23 compares the base pressure characteristics for prototype configurations ( $M_{II} = 2.5$ ,  $\gamma_{II} = 1.2$ ,  $\beta_{II} = 0, 7.5, 15^\circ$ ), for the prototype configurations operated with air ( $\gamma_{II} = 1.4$ ), and for the simulated configurations ( $\gamma_{II} = 1.4$ ,  $M_{II}$  and  $\beta_{II}$  varied). The simulated configurations were based on a model law simulating the plume surface Mach number; TABLE 3 contains the simulated configurations used in this study.

#### 5. CONCLUSIONS

A computer program has been developed for the quantitative analysis of a large variety of propulsion problems involving jet-slipstream interactions.

Based on the Chapman-Korst flow model for base flows, this program has considerable flexibility inasmuch as it can synthesize both simple, and if needed, more complicated flow components.

Aside from its utilization for preliminary design and the prediction of performance characteristics it can also serve as a tool for carrying out numerical computational experiments. When compared to wind-tunnel and free-flight tests, much insight can be gained into the physical nature of the flow processes and the adequacy of simplifying assumptions included in the components of the model. In addition, the computer program can also be used to explore the merits of proposed component refinements and identify areas in which additional critical experimentation is still needed.

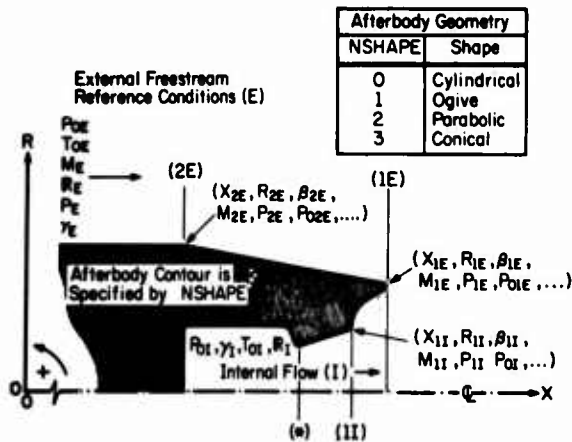


Fig. 1 Two-stream axisymmetric base-flow configuration with an afterbody

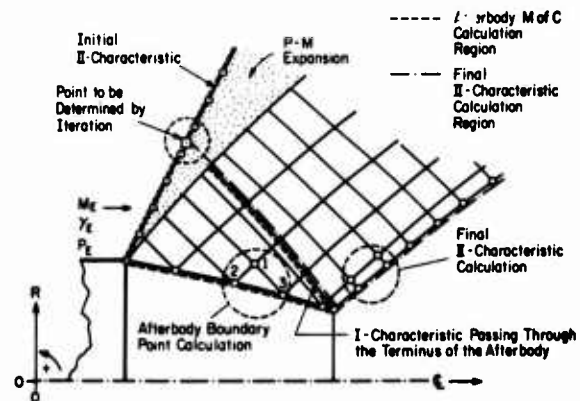


Fig. 2 Inviscid-afterbody-flowfield analysis

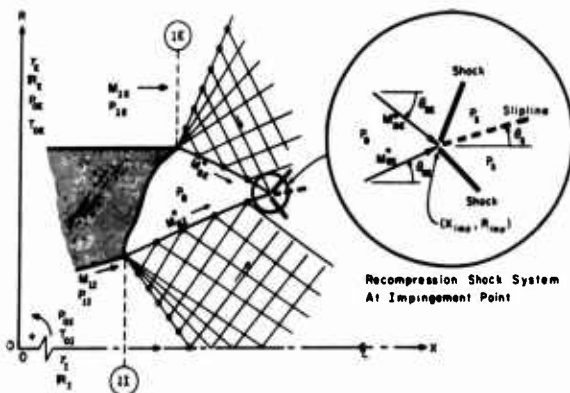


Fig. 3 "Corresponding" inviscid flowfield

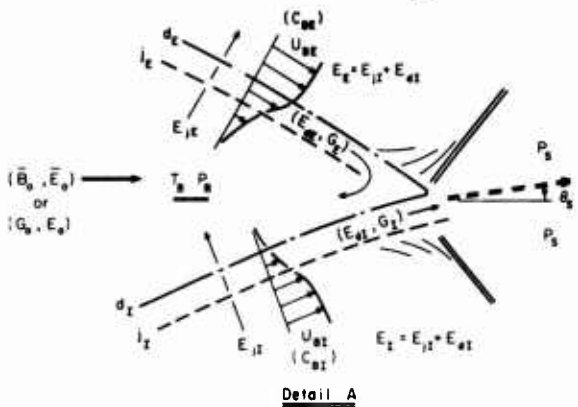
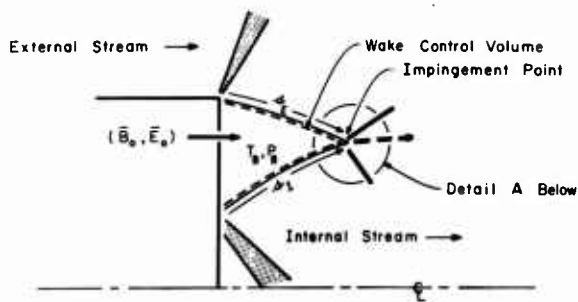


Fig. 4 Base-flow mixing model

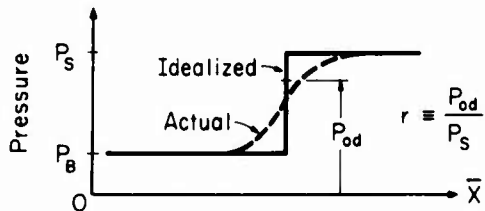
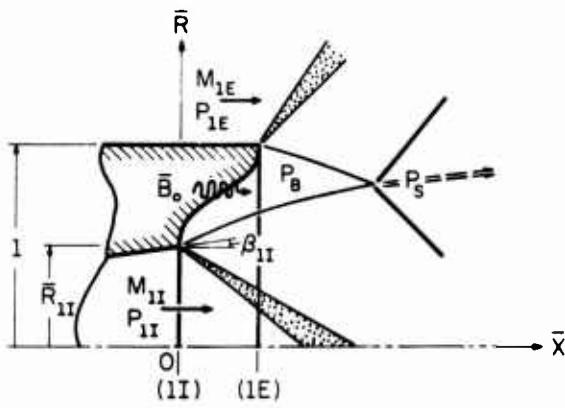


Fig. 5 Definition of the empirical recompression coefficient

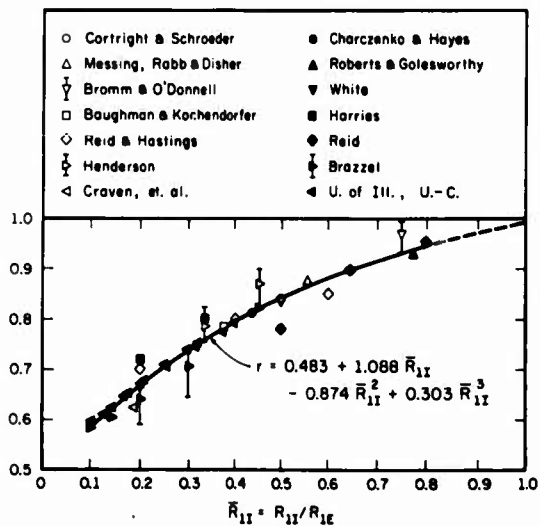


Fig. 6 Recompression coefficient [17]

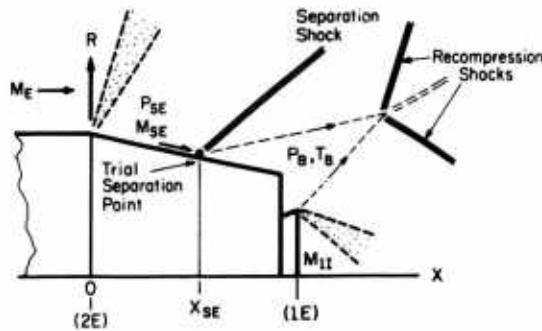


Fig. 7 Plume-induced separation on the afterbody

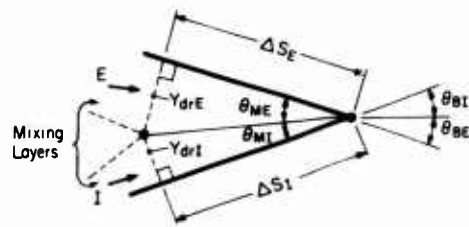
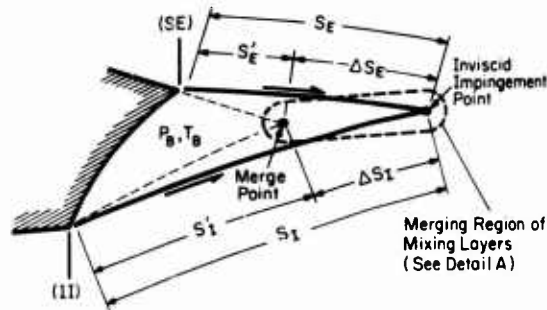


Fig. 8 "Effective" mixing length determination

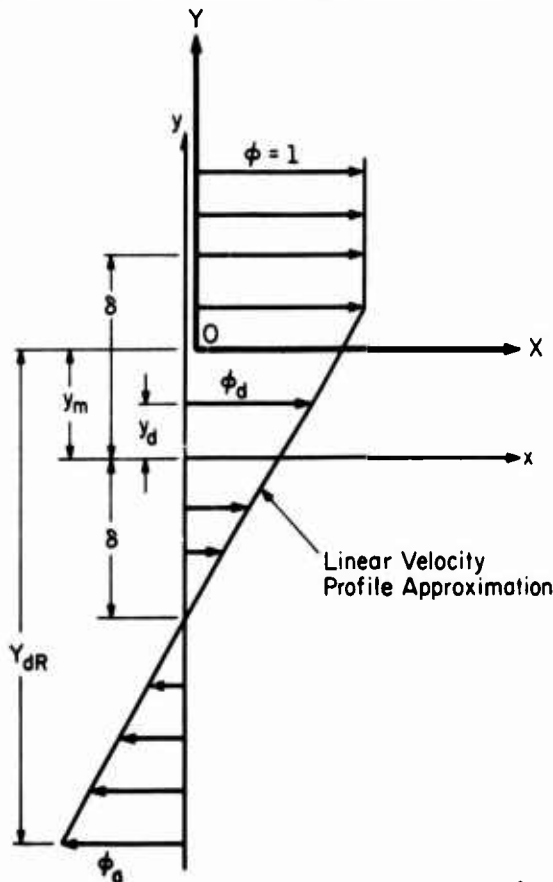


Fig. 9 Simplified velocity profile with backflow

13-10

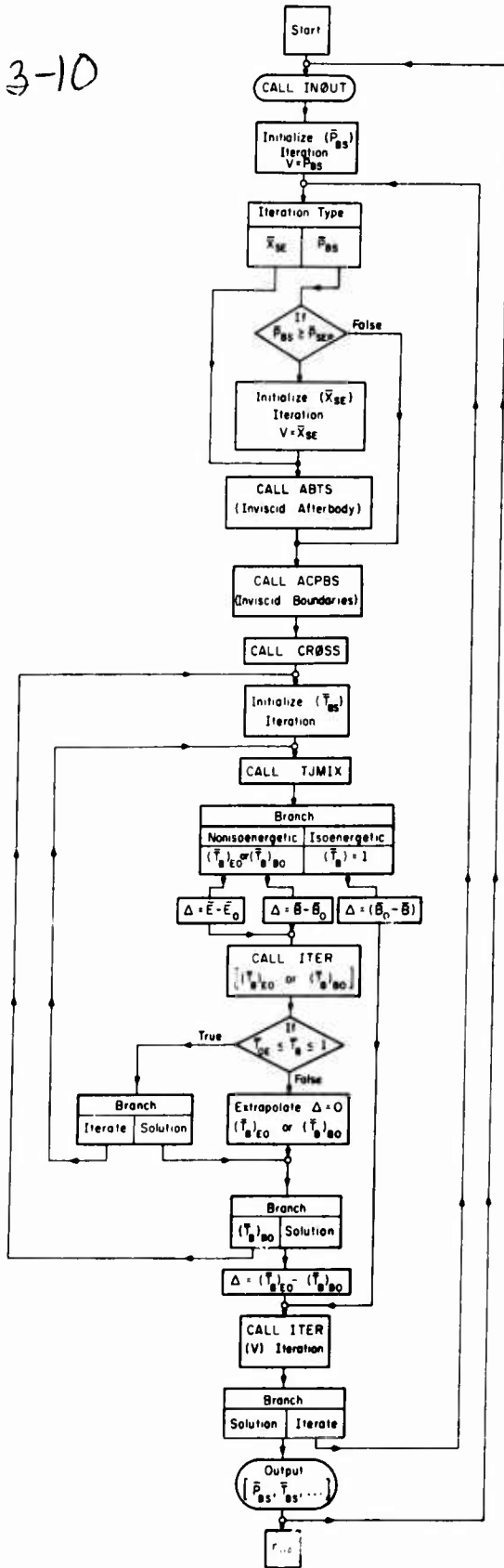


Fig. 10 Simplified flowchart of the main program for TSABPP-3 [25]

Table 1 Parametric Study of the Base-Pressure Problem with a Cylindrical Afterbody [23]

Fig.	$M_{1E}$	$\gamma_1$	$M_{1I}$	$\beta_{1I}$	$\bar{B}_0$	$T_{0E}/T_{0I}$
11	1.25 to 3.0	1.4	2.5	$0^\circ$	0.0	1.0
12	2.0	1.1 to 1.4	2.196 to 2.5*	$0^\circ$	0.0	1.0
13	2.0	1.4	1.0 to 3.0	$0^\circ$	0.0	1.0
14	2.0	1.4	2.5	$0^\circ$ to $20^\circ$	0.0	1.0
15	2.0	1.4	2.5	$0^\circ$	0.0 to 0.08	1.0
16	2.0	1.4	2.5	$0^\circ$	0.0	0.05 to 1.0
Ref.	2.0	1.4	2.5	$0^\circ$	0.0	1.0

\* $\gamma_E = 1.4$ ,  $\beta_{1E} = 0^\circ$ ,  $X_{1E}/R_{1E} = 0$ ,  $R_1 = 53.35$ ,  $r = 1.0$ ,  $X_{1I}/R_{1E} = 0$ .

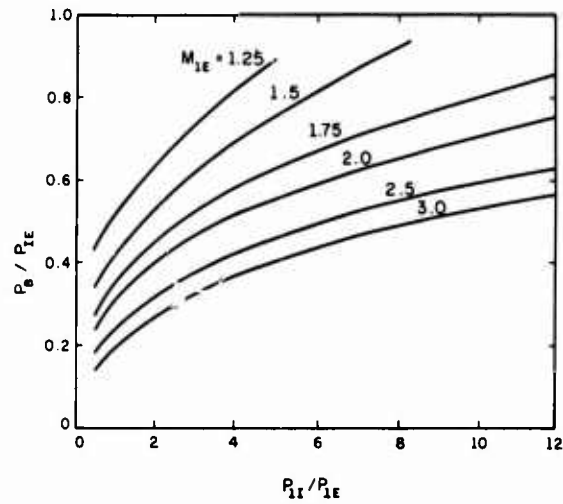


Fig. 11 Parametric variation in  $M_{1E}$

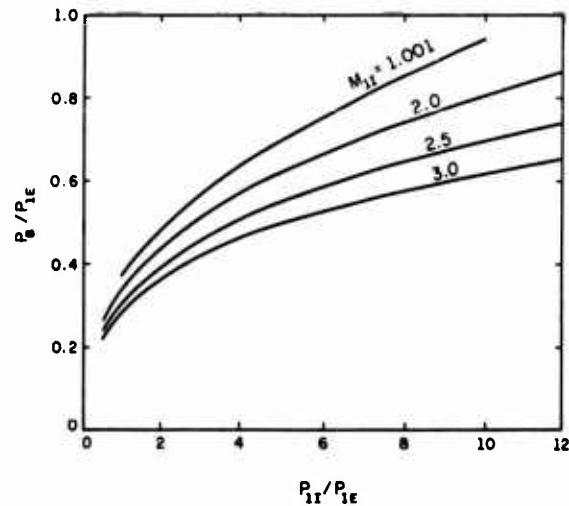


Fig. 12 Parametric variation in  $M_{1I}$

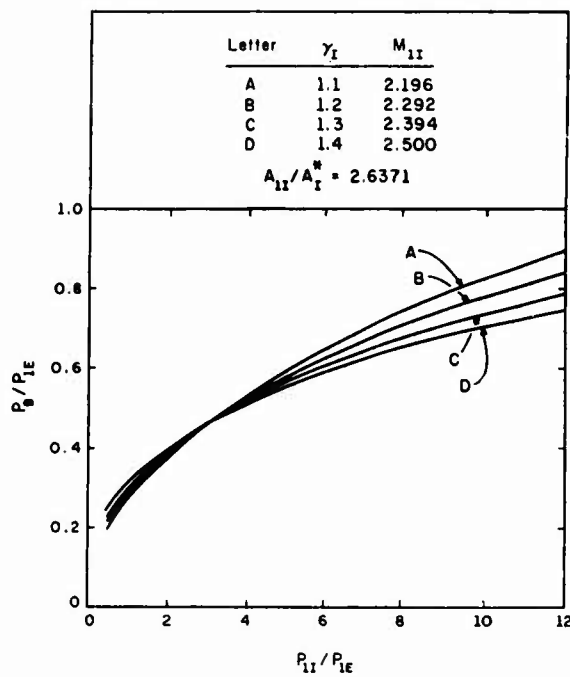


Fig. 13 Parametric variation in  $\gamma_I$

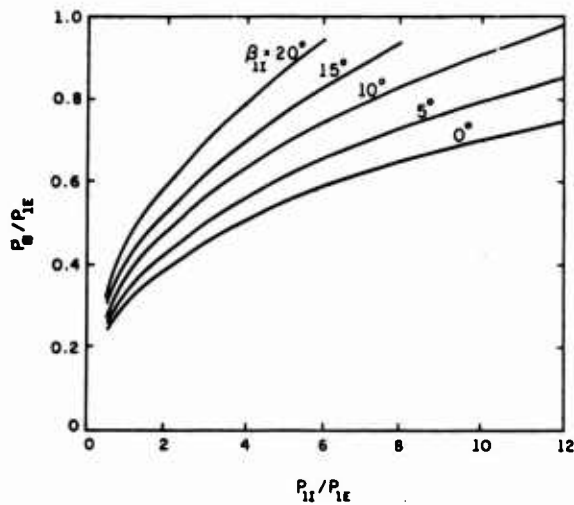


Fig. 14 Parametric variation in  $\beta_{1I}$

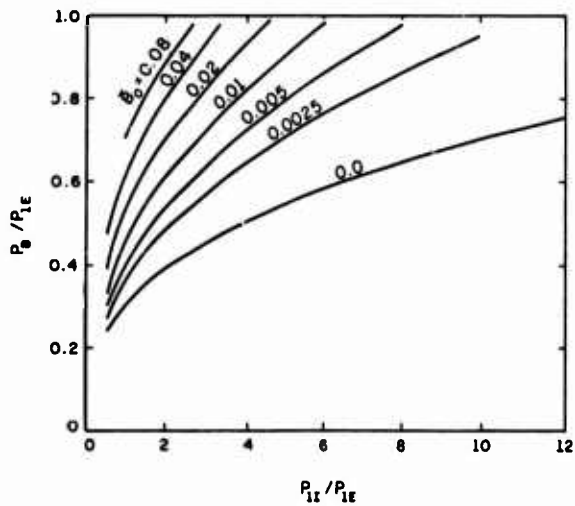


Fig. 15 Parametric variation in the base-bleed ratio,  $\bar{B}_0$

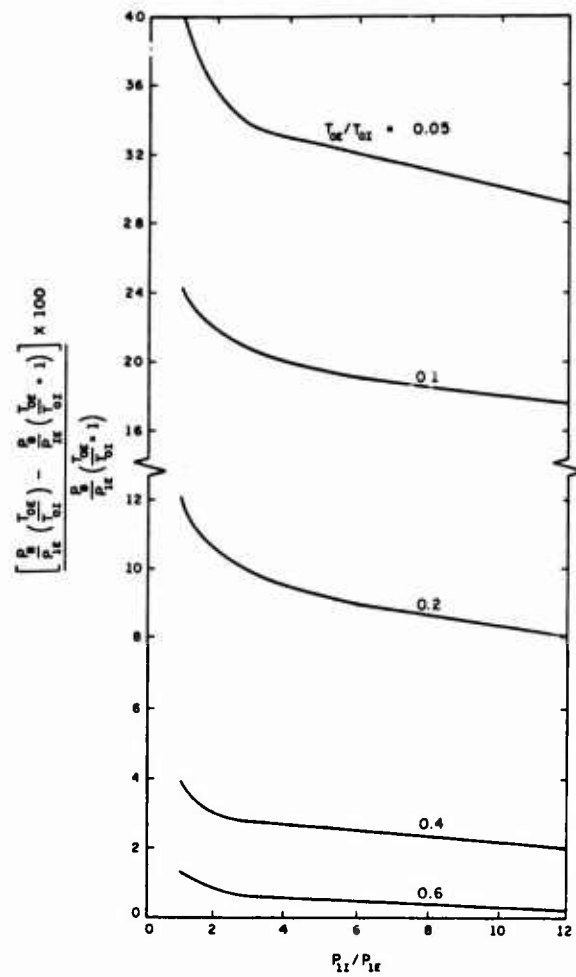


Fig. 16 Parametric variations in the external-to-internal stagnation temperature ratio

Table 2 Parametric Study of the Base-Pressure Problem with a Conical Afterbody [24]

Variable	External Flow (E)		Internal Flow (I), (II)
	(2E)	(1E)	
$\gamma$	1.4		1.4
$R[\text{lb}_f - \text{ft}/\text{lb}_m - ^\circ R]$	53.35		53.35
$M$	2.0		2.5
$\bar{X}$	0.0	2.0	2.0
$\bar{R}$	1.0	$\bar{R}_{1E}$	0.6
$\beta$ (degrees)	$\beta_{2E}$	$\beta_{1E}$	0.0

$T_{0E} = 1, E_0 = 0, r = 1.0, \bar{B}_0 = 0$  or as noted.

Conical Boattail NSHAPE = 3	$-11.309^\circ \leq \beta_{2E} \leq 0^\circ$	Fig. 17
Conical Flare NSHAPE = 3	$0^\circ \leq \beta_{2E} \leq 10^\circ$	Fig. 18

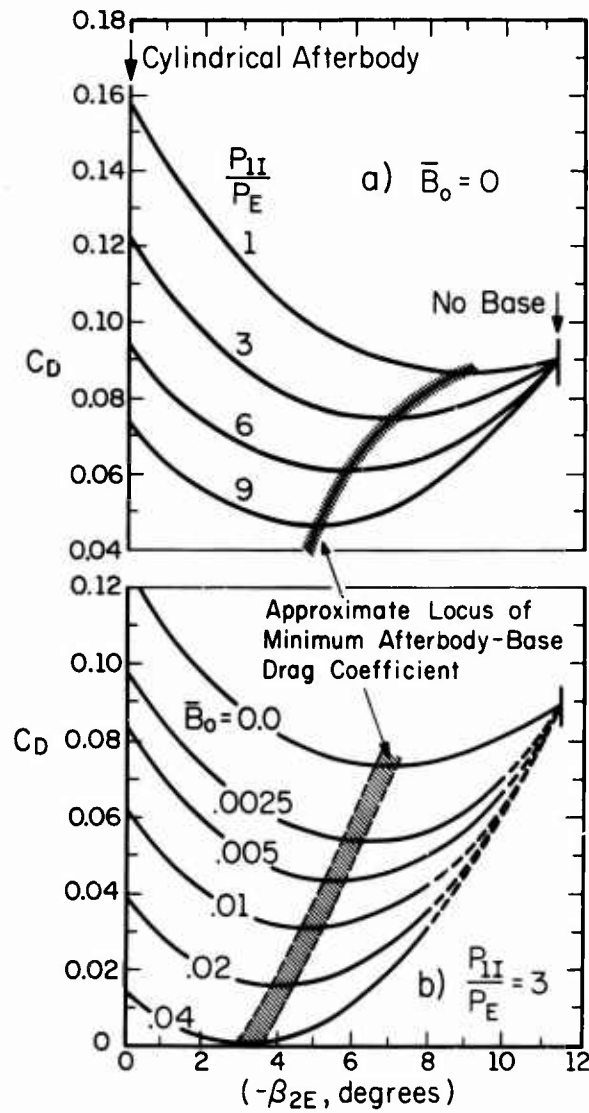


Fig. 17 Variations in the combined conical boat-tail-base drag coefficient for several base-bleed ratios at fixed operating pressure ratios

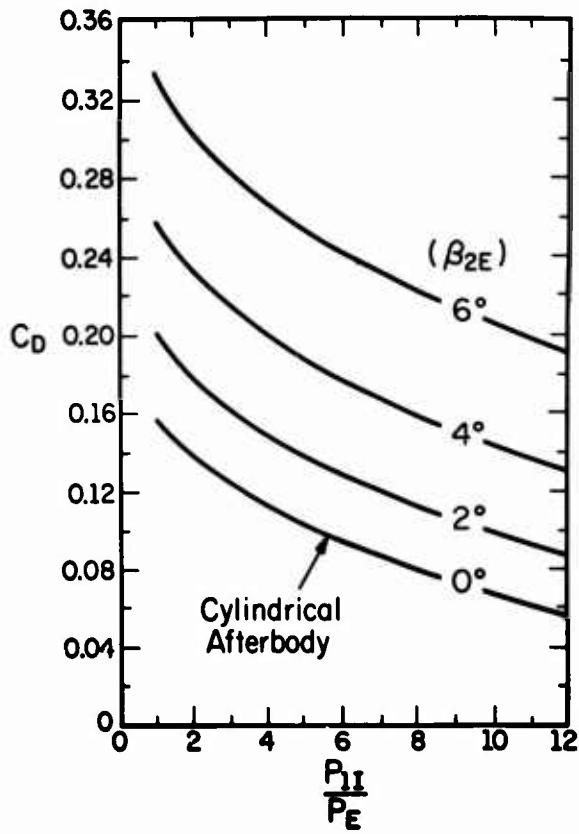


Fig. 18 Variation of the combined conical flare-base drag coefficient for several conical-flare angles

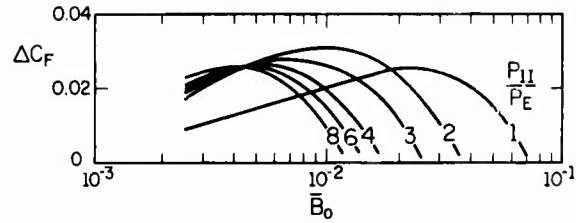


Fig. 19 Variation in the incremental thrust-minus-drag force coefficient due to base-bleed flow diverted from the propulsive-nozzle stagnation chamber (cylindrical afterbody)

Table 3 Nozzle Configurations for Prototype and Plume-Simulation Model for Identical Operating Pressure Ratio  $P_{11}/P_E$

Prototype $M_{11} = 2.5, \gamma_1 = 1.2$		Simulated Model $M_{s1} = M_{su}, \gamma_1 = 1.4$	
$\beta_{11}$	$P_{11}/P_E$	$M_{11}$	$\beta_{11}$
0°	2	2.2	~ 0°
	6	2.1	~ 0
	10	1.9	~ 0
7.5°	2	2.1	5.5°
	6	1.98	5.4
	10	1.96	4.9
15°	2	2.13	12.5°
	6	2.02	11.8
	10	1.85	9.1

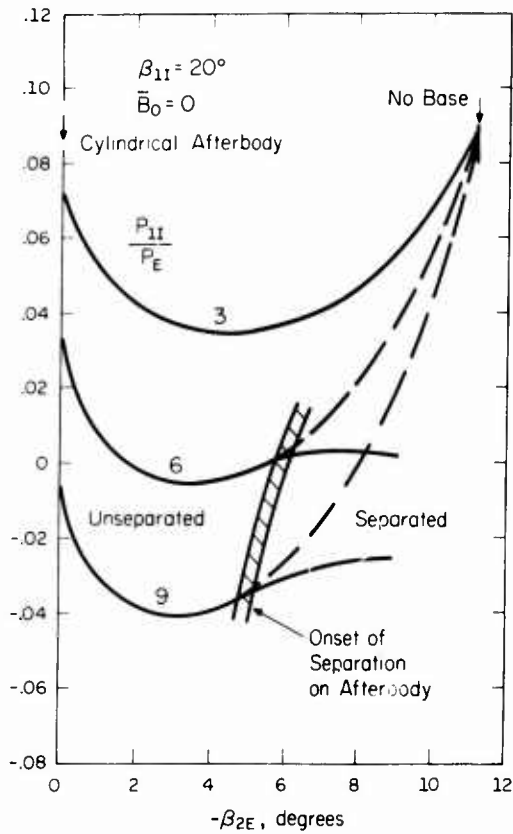


Fig. 20 Total afterbody drag versus boattail angle for several operating pressure ratios



Fig. 21 Schlieren photograph and superimposed theoretical solution for plume-induced separation

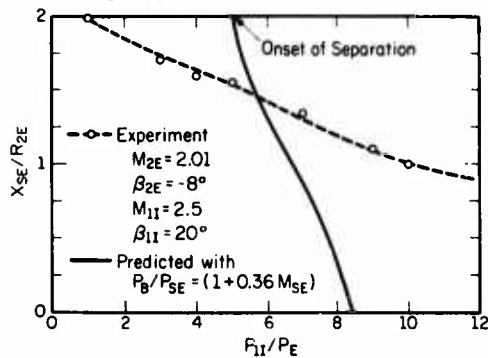


Fig. 22 Afterbody separation location for plume-induced separation

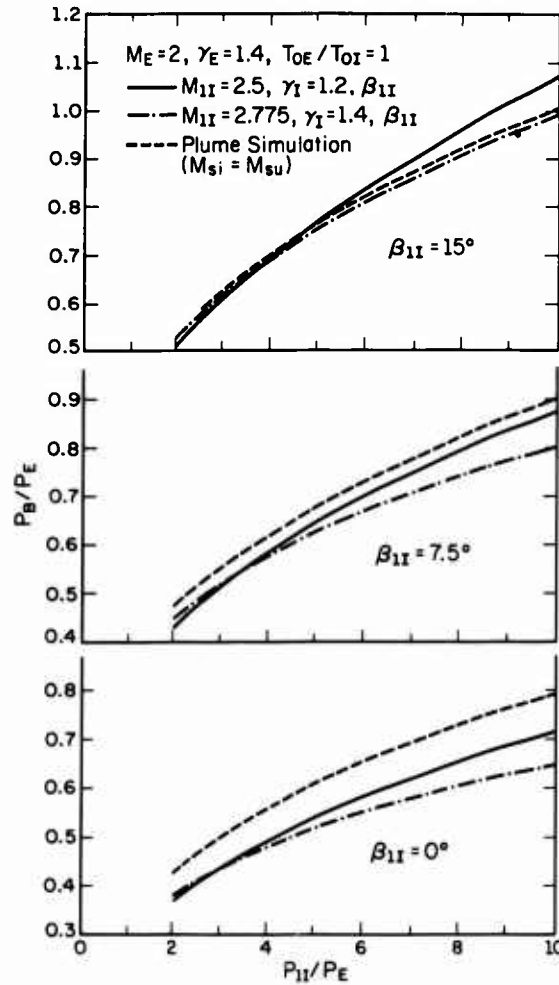


Fig. 23 Comparison of base-pressure solutions for two methods of propulsive-nozzle flow simulation

## REFERENCES

1. Korst, H. H., Page, R. H., and Childs, M. E., "Compressible Two-Dimensional Jet Mixing at Constant Pressure." University of Illinois, Urbana, Ill., ME-TN-392-1 (also OSR-TN-54-82), April 1954.
2. Korst, H. H., Page, R. H., and Childs, M. E., "A Theory for Base Pressure in Transonic and Supersonic Flow," University of Illinois, Urbana, Ill., ME-TN-392-2 (also OSR-TN-55-89), March 1955.
3. Korst, H. H., "A Theory for Base Pressure in Transonic and Supersonic Flow," J. of Applied Mechanics, Vol. 23, pp. 593-600, 1956.
4. Chapman, D. R., Juehn, D. M., and Larson, H. K., "Preliminary Report on a Study of Separated Flows in Supersonic and Subsonic Streams," NACA RM A55Lk4, 1956.
5. Korst, H. H., Chow, W. L., and Zumwalt, G. W., "Research on Transonic and Supersonic Flow of a Real Fluid at Abrupt Increases in Cross Section (with Special Consideration of Base Drag Problems) --Final Report," University of Illinois, ME-TR-392-5, December 1959, Contract No. AF 18(600)-392.
6. Addy, A. L., "Detailed Analyses for Base-Pressure Programs [TSABPP-1,2]," Report No. RD-TN-69-7, U.S. Army Missile Command, Redstone Arsenal, Ala. (August 1969).
7. Greenwood, T. F., "An Analytical Study of the Base Flow Problem Including the Theories of Korst, Zumwalt, and Nash," Technical Memorandum AA-3-65-8, Brown Engineering Co., Inc., Aero-Astroynamics Support Group, Contract No. NAS8-5285, March 1965.
8. Korst, H. H., and Chow, W. L., "On the Correlation of Analytical and Experimental Free Shear Layer Similarity Profiles by Spread Rate Parameters," Trans. ASME, J. of Basic Engineering, Series D, Vol. 93, pp. 377-382 (1971).
9. Carriere, Pierre, "Apercu de Quelques Resultats Nouveaux Obtenus a L'O.N.E.R.A. sur les Phenomenes de Decollement et de Recollement," ONERA, T.P. No. 1072, 1972.
10. Gerhart, P. M., "A Study of the Reattachment of a Turbulent Supersonic Shear Layer with the Closure Condition Provided by a Control Volume Analysis," Ph.D. Thesis, Department of Mechanical and Industrial Engineering, University of Illinois at Urbana-Champaign, Urbana, Ill., 1971.
11. Nash, J. F., "An Analysis of Two-Dimensional Turbulent Base Flow, Including the Effect of the Approaching Boundary Layer," Reports and Memoranda No. 3344, 1963, Aeronautical Research Council, Ministry of Aviation, London, U. K.
12. Carrière, P., and Sirieix, M., "Résultats Récents dans l'Étude des Problèmes de Mélange et de Recollement," T.P. No. 165, 1964, Office National d'Études et de Recherches Aérospatiales (ONERA), 29, Avenue de la Division Leclerc, Chatillon-sous-Bagneux (Seine), France, (also available as: Library Translation No. 1113, May 1965, Royal Aircraft Establishment, Ministry of Aviation, Farnborough, Hants, U.K.).
13. Page, R. H., Kessler, T. J., and Hill, W. G., Jr., "Reattachment of Two-Dimensional Supersonic Turbulent Flows," ASME Paper No. 67-FE-20, presented at ASME Fluids Engineering Conference, 1967, Chicago, Ill.
14. Sirieix, M., Détery, J., et Mirande, J., "Recherches Expérimentales Fondamentales sur les Écoulements Séparés et Applications," T.P. No. 520, 1967, Office National de'Études et de Recherches Aérospatiales (ONERA), 29, Avenue de la Division Leclerc-92, Chatillon, France.
15. Dixon, R. J., Richardson, J. M., and Page, R. H., "Turbulent Base Flow on an Axisymmetric Body with a Single Exhaust Jet," AIAA Paper No. 69-650, presented at AIAA Fluid and Plasma Dynamics Conference, 16-18 June 1969, San Francisco, California.
16. Addy, A. L., "Analysis of the Axisymmetric Base-Pressure and Base-Temperature Problem with Supersonic Interacting Freestream-Nozzle Flows Based on the Flow Model of Korst, et al., Part II: A Comparison and Correlation with Experiment for Cylindrical Afterbodies," Report No. RD-TR-69-13, U.S. Army Missile Command, Redstone Arsenal, Ala. (December 1969).
17. Addy, A. L., "Experimental-Theoretical Correlation of Supersonic Jet-on Base Pressure for Cylindrical Afterbodies," AIAA J. of Aircraft, Vol. 7, No. 5, pp. 474-477 (September-October 1970).
18. Mager, A., "On the Model of the Free, Shock-Separated Turbulent Boundary Layer," J. of Aero. Sci., Vol. 23, 1956, pp. 181-184.
19. Fong, M. C., "An Analysis of Plume-Induced Boundary-Layer Separation," J. of Spacecraft and Rockets, Vol. 8, No. 11, pp. 1107-1113 (November 1971).
20. Zukoski, E. E., "Turbulent Boundary-Layer Separation in Front of a Forward-Facing Step," AIAA J., Vol. 5, No. 10, pp. 1746-1753 (October 1967).
21. Addy, A. L., and White, R. A., "Optimization of Drag Minimums Including Effects of Flow Separation," ASME Trans., J. of Engineering for Industry, (also ASME Paper No. 72-WA/Aero-1), (February 1973).

22. Hong, Y. S., "Base Flow Environment Analysis of a Single Engine Booster," AIAA Paper No. 71-643, also published as a Synoptic in J. of Spacecraft and Rockets, Vol. 9, No. 7, pp. 481-482 (July 1972).
23. Addy, A. L., "Analysis of the Axisymmetric Base-Pressure and Base-Temperature Problem with Supersonic Interacting Freestream-Nozzle Flows Based on the Flow Model of Korst, et al., Part I: A Computer Program and Representative Results for Cylindrical Afterbodies," Report No. RD-TR-69-12, U.S. Army Missile Command, Redstone Arsenal, Ala. (July 1969).
24. Addy, A. L., "Analysis of the Axisymmetric Base-Pressure and Base-Temperature Problem with Supersonic Interacting Freestream-Nozzle Flows Based on the Flow Model of Korst, et al., Part III: A Computer Program and Representative Results for Cylindrical, Boattailed, or Flared Afterbodies," RD-TR-69-14, U.S. Army Missile Command, Redstone Arsenal, Ala., February 1970.
25. Addy, A. L., "Plume-Induced Free-Stream Separation During Powered Supersonic Flight: A Computer Program and Representative Results," Report RD-72-20, December 1972, U.S. Army Missile Command, Redstone Arsenal, Ala.
26. Addy, A. L., "Thrust-Minus-Drag Optimization by Base Bleed and/or Boattailing," AIAA Journal of Spacecraft and Rockets, Vol. 7, No. 11, November 1970, pp. 1360-1362.
27. Korst, H. H., "Approximate Determination of Jet Contours Near the Exit of Axially Symmetric Nozzles as a Basis for Plume Modeling," Report No. RD-72-14, U.S. Army Missile Command, Redstone Arsenal, Ala. (August 1972).

PREDICTION OF BUFFET ON-SET FOR AIRCRAFT -  
RECENT PROGRESS IN WIND TUNNEL - FLIGHT TEST DATA CORRELATION

by

R. C. McWherter\*  
LTV Aerospace Corporation  
Dallas, Texas USA

14-1

SUMMARY

A review was conducted of significant problems and progress with buffet prediction and experiences since the Wright Brothers airplane. Interestingly enough, probably the earliest pilot remarks concerning buffet were made by Wilbur Wright in 1903 when he reported a "tapping" from the structure prior to a "stall", a word which he coined.

Presented and analyzed are results reported from USAF-sponsored studies on the F-4 airplane and an LTV program on the F-8 airplane plus some unpublished LTV data on the A-7 airplane. It is noteworthy that the successful prediction of buffet from wind tunnel testing almost requires a knowledge of the answer in order to determine which of 3 main wind tunnel techniques is most successful. Recent work from Great Britain is examined to help determine the capability of the LTV 4-foot transonic wind tunnel to predict buffet on-set.

Diagnostic data on wind tunnel flow is examined to single-out what property or properties are necessary to obtain repeatable, sensible buffet on-set predictions from model testing. An obvious deduction from this examination is that 2 flow properties emerge which distinguish "good" tunnels from "bad" tunnels insofar as buffet measurement is concerned - (1) the static pressure fluctuation level in the test section must be relatively low (relative to tunnels known as "acceptable") and (2) the frequency at which pressure fluctuations are highest should not be close to test model natural frequencies.

About 2 years ago a modification to the LTV 4-foot wind tunnel was commenced and the program was completed early in 1972. This modification resulted in a reduction in stilling chamber pressure fluctuation level by a factor of almost 10. Test model results "before and after" are presented. Probably for the first time, wing root bending buffet measurements are obtained from a blowdown wind tunnel which are satisfactory to be analyzed. Comparisons with flight test data also are made. One further modification is described which will complete the program.

NOTATION

WRB	- Wing root bending moment, inch-pounds	HZ	- Cycles per second
q	- Dynamic pressure, foot-pounds	M	- Mach number
C <sub>L</sub>	- Lift Coefficient	R/L	- Reynold's number per foot
H	- Altitude, feet	alpha	- Angle of attack

1. INTRODUCTION

Since the early days of manned flight, the condition of flying in the presence of unpleasant shaking, known as buffet, has been regarded with apprehension. For many years, buffet served as a distinct warning to the pilot of approaching stall. Most safe airplanes gave this clear warning with increasing amplitude as stalled flight was approached. A "wicked" airplane would fly right up to the stalled angle of attack and often flip rapidly to inverted flight.

Of interest is a quotation from a report by Wilbur Wright on manned glider experiments presented to a Chicago meeting of the Western Society of Engineers in June, 1903:

"On two occasions we observed a phenomenon whose nature we were not able to determine with certainty. One day my brother noticed in several glides a peculiar tapping as if some part of the machine were loose and flapping. Careful examination failed to disclose anything about the machine that could possibly cause it. Some weeks later, while I was making a glide, the same peculiar tapping began in the midst of a wind gust. It felt like little waves striking the bottom of a flat-bottomed row-boat. While I was wondering what the cause could be, the machine suddenly, but without any noticeable change in its inclination to the horizon, dropped a distance of nearly ten feet, and in the twinkling of an eye was flat on the ground."

From our vantage point of many years, we would say that Wilbur had simply "stalled" his aircraft, a word depicting lack of aerodynamic lift coined in 1903 by Wilbur himself. The unusual "tapping" or "waves striking" words probably describe for the first time the phenomenon we know as buffet.

"Buf-fet - vt 1: to strike with or as if with the hand 2a: to strike repeatedly: BATTER b: to contend against vi 1: STRIVE, CONTEND 2: to make one's way especially under difficult conditions." (Webster's Seventh New Collegiate Dictionary, 1965).

Examining the definition of the word "buffet" above, one wonders which particular description the person had in mind who first named the phenomenon. Modern high performance aircraft exhibit several forms of buffet unknown in the early days; such as gear and flap deployment, shock induced separation and reattachment, control system resonant response, etc. Recently, considerable attention has been given to transonic maneuvering buffet which tends to reduce combat efficiency of attack and fighter aircraft. In this brief report, we are addressing in particular an improvement in wind tunnel buffet data measurement capability due to modifications to the LTV 4-foot blowdown transonic-supersonic wind tunnel.

2. CURRENT CAPABILITY

14-2

In the late 1960's the United States Air Force awarded several R & D contracts to major aircraft companies with the objectives of (1) procuring good quality flight test buffet data at transonic speeds on current aircraft and (2) comparing these data with results from wind tunnel tests, where available, to evaluate the degree of data correlation (or lack thereof). These results are published for the F-4 (reference 1), F-105 (reference 2) and F-106 (reference 3) airplanes. Many other reports have been published both in the USA and Europe on analytical and experimental studies.

A gross summary of the results of examining reports plus conversation with experts in the field indicates that we can generally screen a new configuration in certain select wind tunnels and predict with fair confidence that our configuration should be free from serious buffet problems up to some angle of attack. As the configuration departs from those for which wind tunnel and flight test data exist, the ability to prognosticate with confidence deteriorates rapidly. What is needed is wind tunnel buffet data on a quality similar to that available for routine lift, drag, and pitching moment for "static" tests at fixed angle of attack.

3. ANALYSIS

Suppose that we examine some of the published flight test data on the F-4 airplane from reference 1. Notice in figure 3.1 that we have a fairly clean break point based on measured wing bending moment at Mach 0.81 and 35,000 feet. Actually the pilot reported buffet on-set about 1 degree alpha before the wing bending moment break. Oddly enough a subsequent test on the same aircraft-type to evaluate the effect of maneuvering slats showed measured buffet on-set about 3 degrees before the pilot report.

Figure 3.2 from reference 1 shows the results from 3 different means of flight measurement on buffet on-set. Wing bending moment (WBM), as noted before, usually gives a buffet on-set prediction after separation has taken place and reached a level sufficient to change the normal background level of the airframe. Since the pilot's sensitive "seat" has already alerted him to buffet, the signal from the wing bending moment measurements must be either submerged in the background level or absorbed in structural damping. Wing tip accelerometer (WTA) measurements give probably the best indication of initial separation - about 2 degrees in angle of attack before pilot response. Lastly, the outer wing panel (OWP) static pressure tap gave a good indication of initial wing flow separation similar to that from wing tip accelerometer. We see that the 3 techniques bracket the pilot response, at least for the F-4 airplane used in these tests.

A comparison of the flight test results and wind tunnel tests with Mach number again from reference 1 shows that adequate prediction of airflow separation is available from measurements of outer wing static pressure coefficient data (figure 3.3) and from wing tip accelerometer measurements

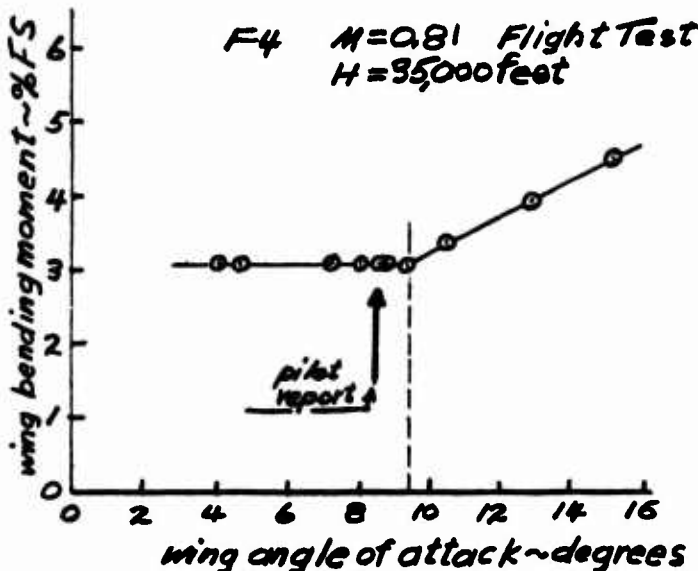


FIGURE 3.1

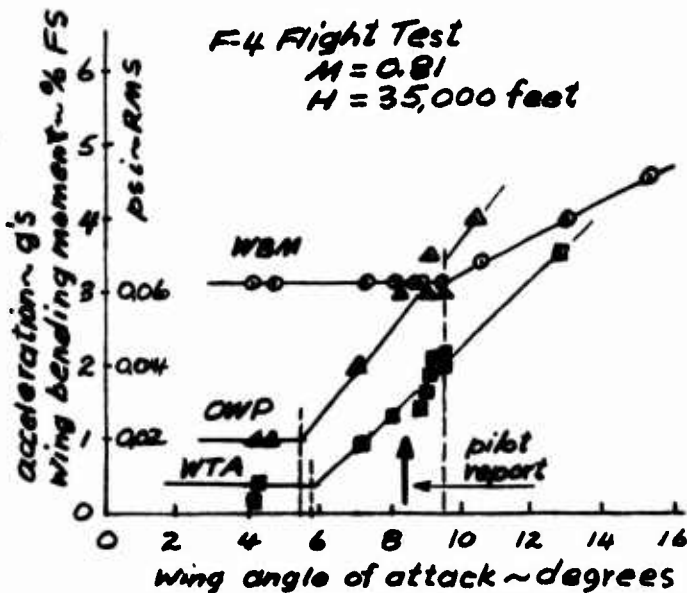


FIGURE 3.2

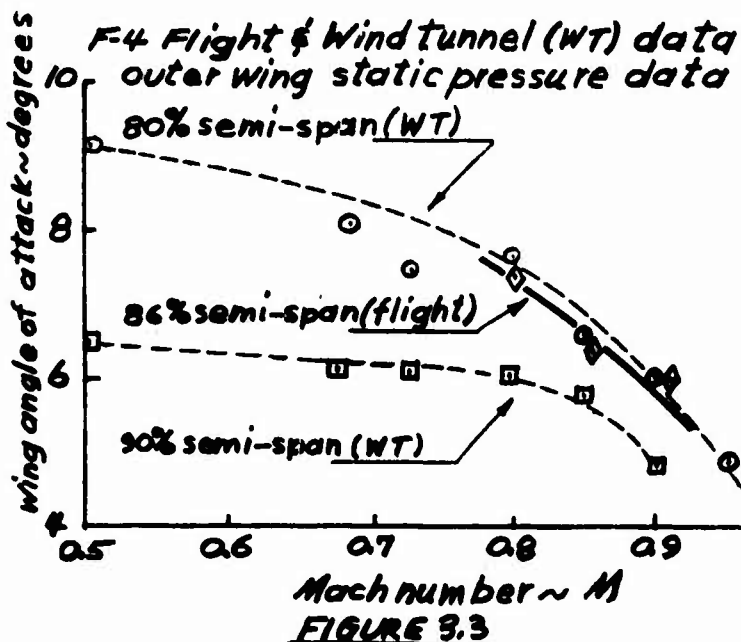


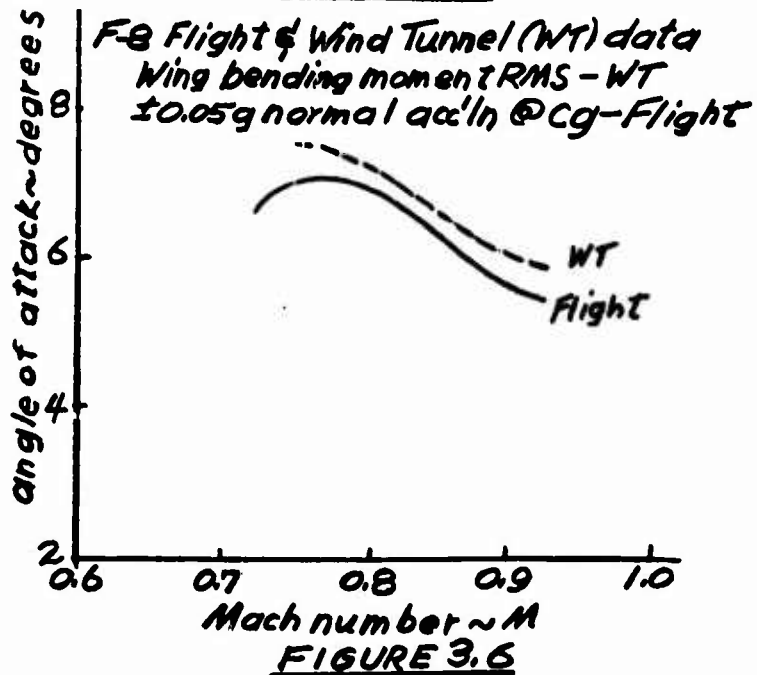
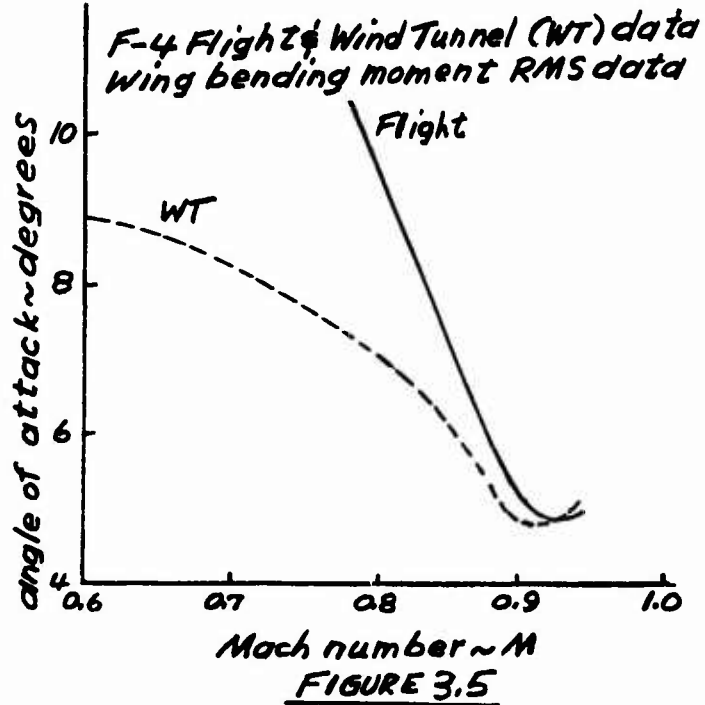
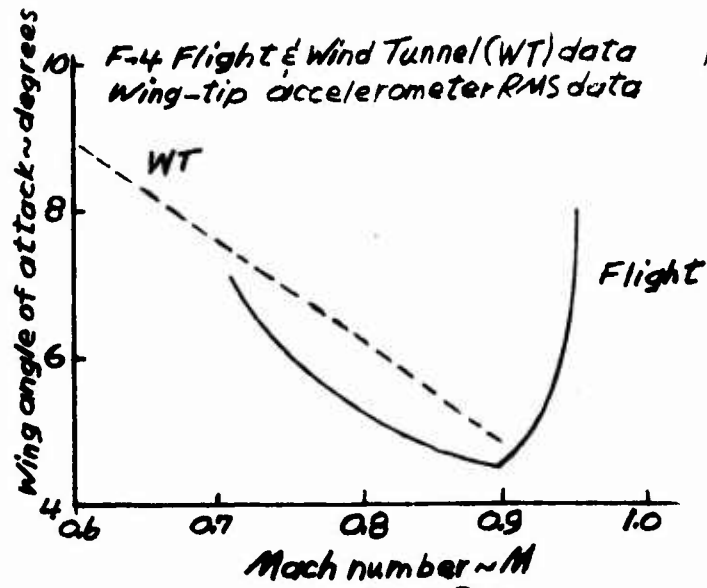
FIGURE 3.3

(figure 3.4) on the model. Measurement of wing root bending moment variation (figure 3.5) showed poorer comparison particularly at lower Mach numbers. Interestingly, from figure 3.3 the wind tunnel measurement of the outer wing static pressure coefficient behavior at the 80% spanwise position correlated almost exactly with flight measurements at the 86% spanwise location. Note in figure 3.3 that the pressure data from the 90% b/2 spanwise model tap, however, was not so good.

For the F-4 flight test and wind tunnel data comparisons of reference 1, no comparison was made of pilot's report of buffet on-set with Mach number with data from the various wind tunnel methods. Since both initial on-set and allowable penetration are important parameters, some combination of these measurement techniques is needed to predict aircraft performance from wind tunnel testing.

Presented in figure 3.6 is a comparison of Flight Test Buffet data on the F-8 airplane with wind tunnel data from NASA-Langley (reference 4). Notice that wing bending moment RMS buffet prediction data from the NASA-Langley facility showed good agreement with flight data based on  $\pm 0.05g$  normal acceleration measured at the airplane center of gravity (cg). Instrumentation at the pilot's seat for the F-8 airplane generally gave a buffet on-set prediction, based on  $\pm 0.05g$  instrumentation reading, about  $1\frac{1}{4}$  degrees alpha above the data read at the center of gravity. This probably represents structural damping between the center of gravity and the pilot station which is several feet forward of the c.g.

In summary, then, correlation between flight and wind tunnel data is fair at best. Measurements of wing static pressure distribution is needed to provide forcing functions to the structure. Also not only is the location of initial separation needed but also the manner in which it spreads. At the present time one almost needs to know the performance of the actual aircraft before he can pick the proper wind tunnel tests for best correlation. For new configurations we are heavily dependent upon results from wind tunnel tests to provide us with some knowledge of buffet on-set. Most investigators agree that at least 2 of the several types of wind tunnel data available should be used to guide buffet prediction. Generally these are wing root bending combined with either trailing edge pressures or wing tip accelerometers. From the wind tunnel standpoint, flow quality must be adequate to produce repeatable measurements without "contamination" from wind tunnel flow disturbances.



14-4 4. WIND TUNNEL FLOW DIAGNOSIS

Most wind tunnel buffet data measurements are made using a Root Mean Square (RMS) signal converter which produces a DC-type signal representative of the oscillatory energy content. Since the measurement produced by the RMS converter represents a standard deviation-type operation, the contribution of a discrete signal somewhat above the noise level will be considerably enhanced. Conversely, a low-level signal can be obscured if the noise level is high.

In modern blowdown wind tunnels, the noise level due to turbulence, acoustics, vorticity, and vibration is quite high. Consequently most "acceptable" buffet wind tunnel data has been obtained from large, continuous flow transonic facilities, such as at NASA-Langley and the Cornell Aero Lab where the background noise level has been regarded as low in comparison to blowdown wind tunnels.

In our case at LTV, we made a serious effort to procure good quality buffet data from our 4-foot blowdown wind tunnel in 1968 with poor to modest success. The same models were tested at NASA-Langley and Cornell to get data that would be accepted by the technical community. Careful examination of these data revealed some significant information which led us to a course of action designed to enhance our buffet measurement ability in the LTV 4-foot transonic wind tunnel.

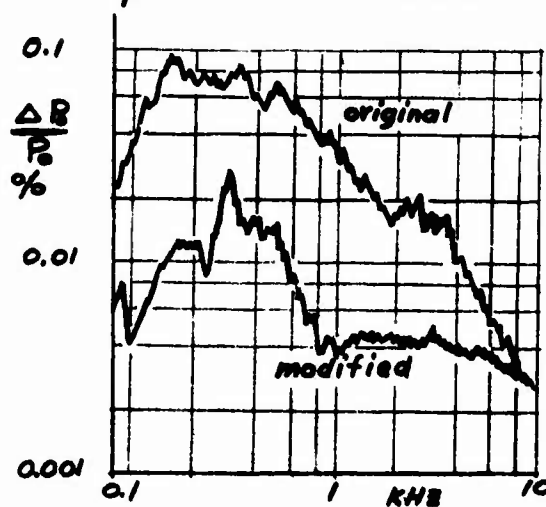
First we examined the stilling chamber pressure unsteadiness as a function of frequency. Note in figure 4.1 from reference 5 that the pressure fluctuations in the range of frequencies from 0.1 to 1.0 KHZ (1,000 cycles per second) are as much as 10 times as high as those in the range 1.0 to 10 KHZ. For models of a size and strength to be tested in the LTV 4-foot wind tunnel, the wing first mode natural frequency in bending generally is from 0.1 to 0.4 KHZ. Since the wing will also respond to buffet in this frequency range, we needed a modification to the facility to reduce the fluctuating pressure magnitude in general and in this frequency band in particular. Shown in figure 4.1 is the pressure fluctuation trace from the modified tunnel which will be explained in the next section.

Presented in figure 4.2 from reference 5 is the ITV tunnel variation of test section static pressure fluctuation with Mach number compared with data from other facilities. Again these measurements illustrate the problem that we needed to solve in order to get background excitation suitably low to produce acceptable buffet data.

5. TUNNEL IMPROVEMENT

Figure 5.1 shows the LTV 4-foot tunnel pressure regulation system after modification. A discussion of the modification may be found in reference 5. Essentially the flow from the high pressure reservoir formerly was reduced from 600 psig to

Spectra of stilling chamber pressure fluctuation



ref. to 1 HZ bandwidth

FIGURE 4.1

Variation of test section static pressure fluctuation

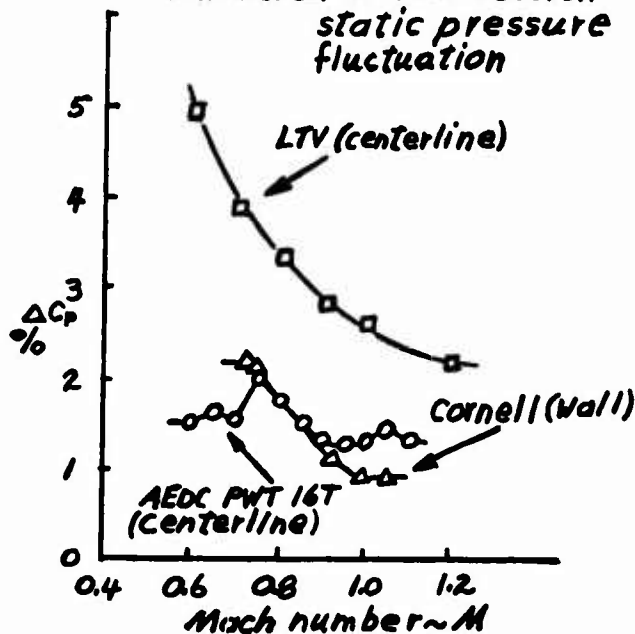


FIGURE 4.2

Diffuser Modification

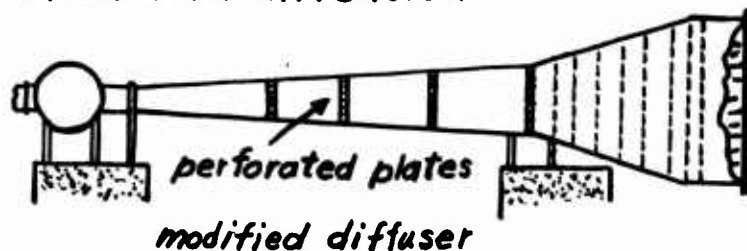
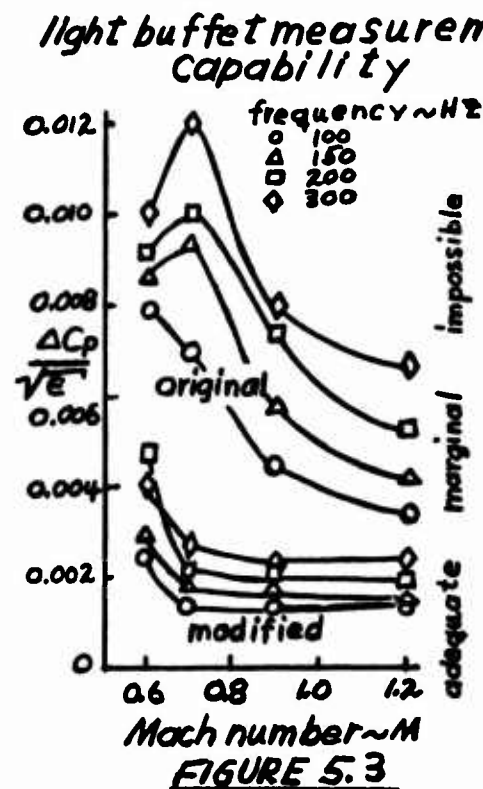


FIGURE 5.1

25 psig by means of a regulator valve, several flow stabilizers and a series of wire grids. The modification consisted of inserting 4 perforated plates in place of the stabilizers which produced the required pressure drop by means of choked orifices so that the radiating intense shock system is eliminated. The dramatic reduction in the stilling chamber fluctuating pressure level may be seen in figure 4.1. Presented in figure 5.2 is a comparison of test section pressure fluctuation variation with Mach number before and after modification.

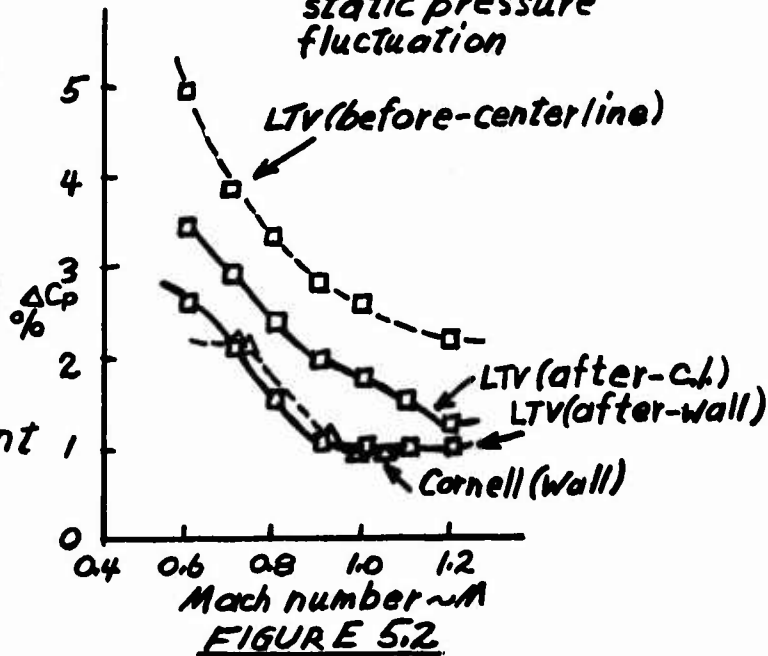
Mabey of England in reference 6 propounded a means of data presentation which established in a general way the ability of specified tunnel to produce meaningful buffet data. Figure 5.3 presents the "before and after"



Aero Lab and NASA-Langley. LTV data prior to modification was meaningless and is not presented. Data from the revised LTV tunnel shows that the background level is twice that of NASA-Langley and nearly 3 times that of Cornell. The same model and instrumentation was used for all tests.

Analysis of the 3 sets of data indicates that buffet on set should be at 7.2 degrees alpha (NASA-Langley), 7.5 degrees alpha (Cornell) and 10.6 degrees alpha (LTV. Indicated by an arrow on the plot is a buffet on-set angle of 6.7 degrees alpha from flight test (reference 4). The rather linearly increasing pressure fluctuation trend with angle of attack from the LTV test as compared with the other 2 data sets coupled with a strange little "hook" just before obvious buffet was verified by repeated measurements. It seems fairly obvious that initial buffet on-set data from the LTV tunnel is still submerged in the tunnel background level, at least for the F-8 model and at this Mach number. Thus our capability

**Variation of test section static pressure fluctuation**

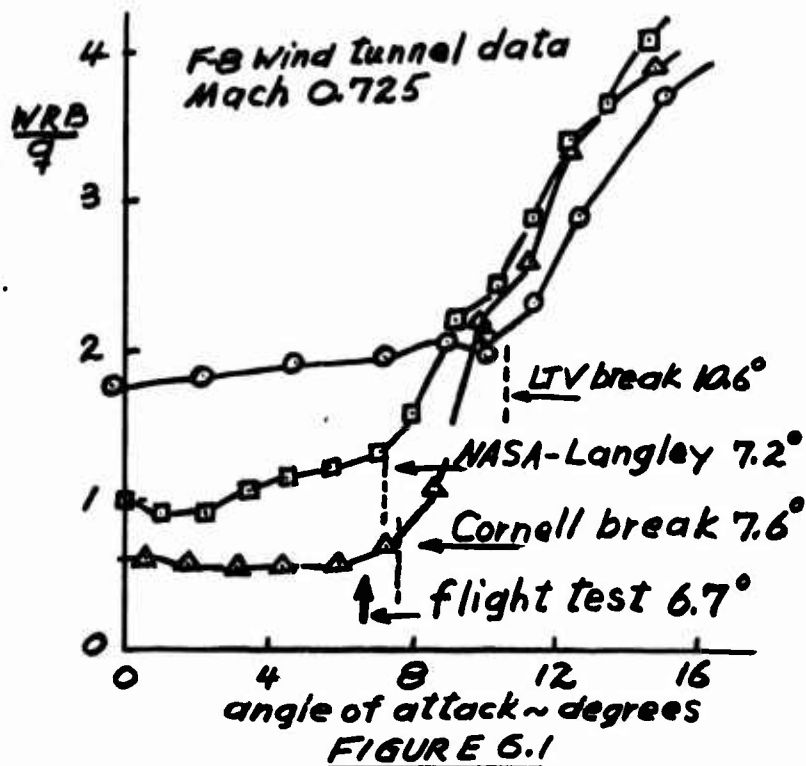


for the LTV facility. The symbol  $\epsilon$  used in the expression  $\frac{\Delta C_p}{\sqrt{\epsilon}}$  is derived from characteristics of wind tunnel instrumentation. For further information, see reference 6.

6. ANALYSIS OF RESULTS FROM TUNNEL IMPROVEMENT

Again with reference to figure 5.3, Mabey's Light Buffet Criteria would indicate that we should be able to make meaningful buffet measurements in the VAC 4-foot tunnel at all Mach numbers from 0.6 up to 1.2. At Mach 0.6, our capability would be "marginal" and at Mach 0.7 and above "adequate". Prior to tunnel modification, of course, the tunnel capability was "marginal", at best, and generally "impossible."

Notice the data in figure 6.1 from reference 4 on the 5% scale F-8 Crusader model at Mach 0.725 tested at Cornell



14-6

at Mach 0.725, although much improved, still remains "marginal", rather than "adequate" as predicted by Mabey. Effects of model support and balance flexibility may influence the data as much or more than pressure unsteadiness in defense of Mabey's criteria. From figure 6.2 we can see a comparison at Mach 0.927 similar to that just studied at Mach 0.725. All 3 sets of data display similar trends with the LTV data again showing a higher initial level. Noted are the deduced buffet on-set "break" points along with a point from flight test.

More recent tests again using the wing root bending moment measurement variation were conducted on a 5% scale A-7 airplane model both in the Cornell tunnel and the LTV wind tunnel. Initial results are presented in Figure 6.3 at Mach 0.60 and in Figure 6.4 at Mach 0.90. Shown in Figure 6.3 at Mach 0.60 are filled-in points to demonstrate data results before tunnel modifications. Note the interesting "bump" in the "before modification" data around 6-degrees alpha and the relatively high background level combined with a general curved increase trend making discrete "break" point determination difficult to assess.

Also in Figure 6.3, data taken at Cornell on the same model using the same brand name and

**FB Wind tunnel data  
Mach 0.927**

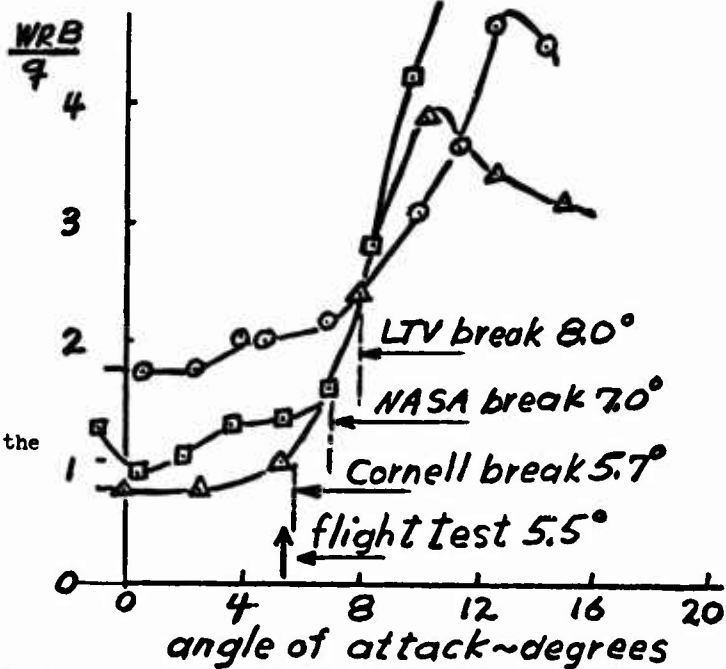


**FIGURE 6.2**

**A-7 Wind tunnel data  
Mach 0.60**

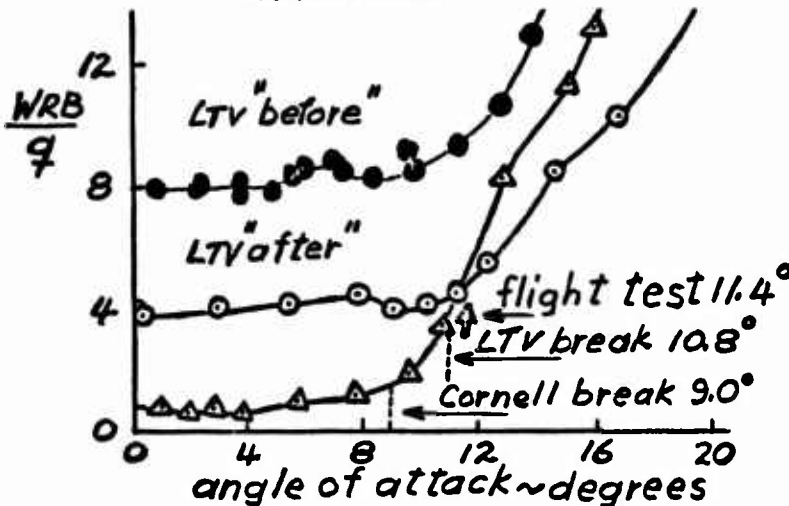


**FIGURE 6.3**

Since Mabey's light buffet criteria had been shown on earlier programs to predict tunnel buffet prediction capability quite well, we instituted a search of model, sting, test techniques and instrumentation to see what might yield an explanation. The instrument that was used at both facilities to produce a signal equivalent to the RMS perturbation level depended on heating a wire with the unknown AC signal (thus performing an integration function) and sensing the integrated temperature of that wire and heating a similar wire segment to the same temperature with a DC power supply. Thus with suitable calibration, one can produce a reading equivalent to the RMS signal fluctuation.

Now to make meaningful comparisons from tunnels that operate at different dynamic pressure levels the wing root bending moment RMS signal was normalized by dividing by the tunnel dynamic pressure. This approach had been shown to be satisfactory by previous experience. Hence a low level signal from the Cornell tunnel where the dynamic pressure

and type of instrumentation showed low background level followed by a reasonably distinct break which would yield a buffet on-set point of about 9-degrees alpha, depending somewhat on the "independence" of the evaluator.

To our disappointment a repeat of the A-7 test at Mach 0.60 shown in Figure 6.3 in our modified wind tunnel showed marked improvement, but not to the degree anticipated from tunnel flow analysis. Remember that figure 5.2 had shown that the tunnel pressure fluctuation levels on the wall at Cornell and at LTV matched quite well at all Mach numbers from 0.6 to 1.2. Also we were using the same model and the same brand-name instrumentation.

**A-7 wind tunnel data  
Mach 0.90**

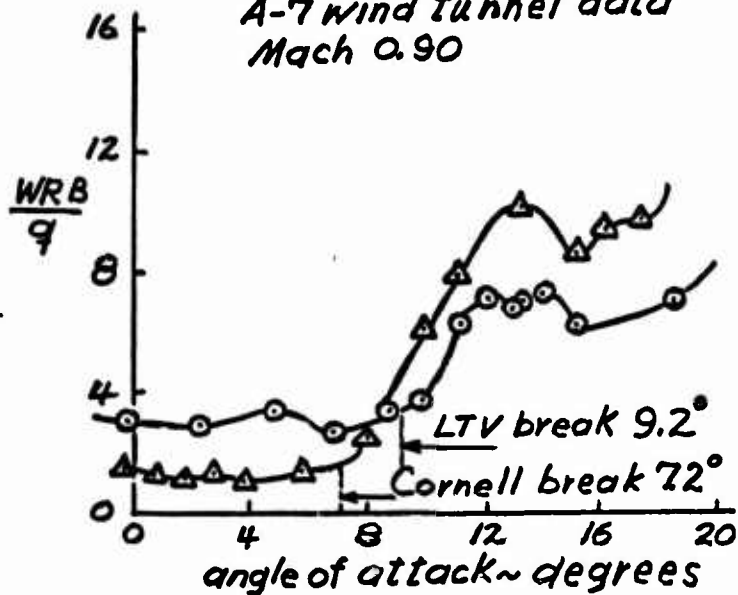


**FIGURE 6.4**

was about 700 PSF would compare with a signal of higher level from the LTV tunnel where the dynamic pressure was about 1200 PSF. Since these instruments must cover a large range to measure from a low background level up to a heavy response at high angles of attack, often it is necessary to change sensitivity range during the test, not generally a desirable condition.

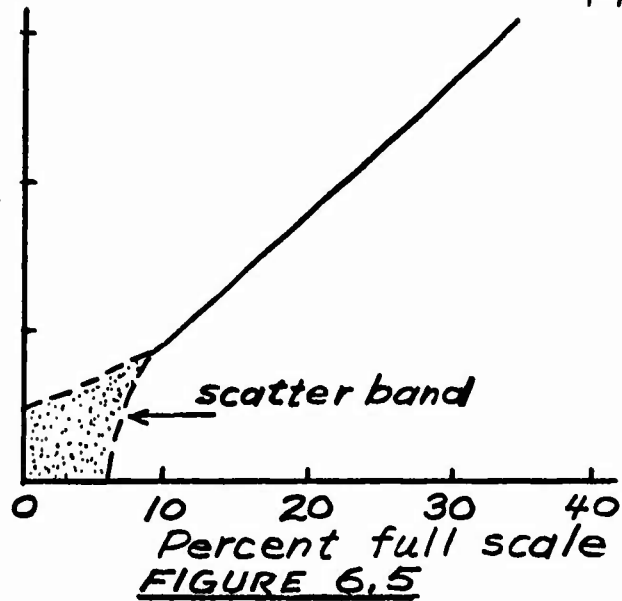
In the calibration laboratory an interesting phenomenon was observed (predicted by the manufacturer). The instrument calibration produced data as indicated in Figure 6.5.

When the instrument was operated below 10% full scale output, the output reading in volts RMS would often vary considerably even though the higher level calibration remained good. Hence our postulate - due to lower level excitation below the buffet level at Cornell, "could we be operating in a possible lower-than-normal reading mode even though the instrument calibrated o.k. at higher levels?" Fortunately we had an opportunity to check the postulation in a subsequent A-7 entry in the Cornell tunnel. With their full cooperation we were able for sure this time to test the same model, same balance, and same instrumentation to determine if we obtained the same buffet data from both the modified LTV tunnel and the Cornell wind tunnel. All measurements covered the frequency band from 1 to 1,000 Hertz.

### RMS Meter Calibration

14-7

RMS output



### A-7 Wind Tunnel data Mach 0.60

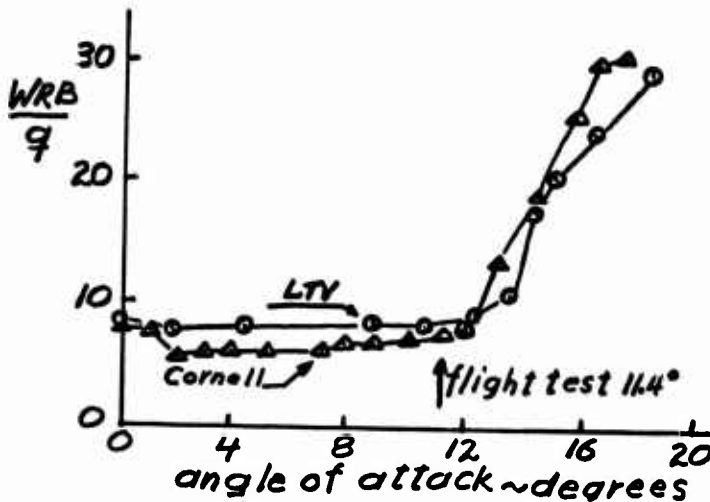


FIGURE 6.6

that all of our treatment to reduce turbulence and acoustic effects have produced little reduction in free stream vorticity. If this is the case, the effect of timewise vorticity variation on the model would appear as a variation in angle of attack and the effect would be more pronounced than a variation in dynamic pressure.

Accordingly we have ordered aluminum honeycomb material with cell dimensions of  $\frac{1}{2}$ -inch square and 6-inches in depth. This honeycomb has been installed in the tunnel chamber (14-feet in diameter) and should have the effect of drastically reducing any free stream vorticity.

The results are presented in figure 6.6 for Mach 0.6 in both tunnels. Time did not permit the desired point density in the LTV tunnel, but the agreement between the 2 facilities was regarded as excellent considering the general character of all buffet wind tunnel data. Figure 6.7 demonstrates the same testing for Mach 0.9

### 7. ANOTHER MODIFICATION

We have conjectured that our treatment to the LTV wind tunnel has reduced the background noise level due to normal pressure fluctuations about as low as practical. And yet we still show a measured background level on the model higher than might be expected. If the model excitation is produced by pressure fluctuations only, it must be generated by timewise variations in dynamic pressure. Suppose, however,

### A-7 wind tunnel data Mach 0.90

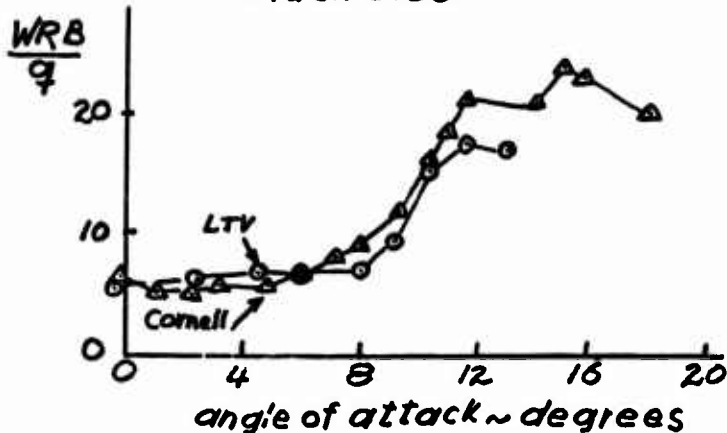


FIGURE 6.7

## 8. CONCLUSIONS

- (1) The LTV 4-foot blowdown wind tunnel can produce satisfactory buffet-on-set data with the tunnel modified to reduce the background pressure fluctuations.
- (2) For the F-8 airplane at Mach 0.725 and Mach 0.90, buffet on-set predictions from 3 different wind tunnels was less than that predicted from flight test although the Cornell and NASA-Langley data is reasonable.
- (3) For the case of the A-7 airplane at Mach 0.60, the buffet on-set predictions from both the Cornell and LTV tunnels is satisfactory. Agreement of data from the 2 tunnels in the buffet penetration area also is regarded as good.
- (4) Extreme care must be exercised in modeling, testing and interpretation of instrumentation results to yield satisfactory buffet-on-set wind tunnel data.
- (5) In this instance the technique propounded by Mabey in reference 6 was of great value in guiding our tunnel flow improvement program.

## 9. REFERENCES

1. Determination of F-4 Aircraft Transonic Buffet Characteristics, E. G. Hollingsworth and M. Cohen - McDonnell Aircraft Company, St. Louis, Mo. AIAA Journal of Aircraft Vol. 8, No. 10, Oct. 1971
2. F-105F Transonic Buffet Study and Effect of Maneuvering Flaps, Milton Margolin and Jung G. Chung, Technical Report AFFDL-TR-69-37 dated July 1969
3. F-106A Transonic Buffet Flight Test, E. R. Emerson, Technical Report AFFDL-TR-70-87 June 1970
4. Transonic Flight and Wind-Tunnel Buffet Onset Investigation of the F-8D Aircraft, E. K. Damstrom and J. F. Mayes., AIAA Journal of Aircraft, Vol. 8, No. 4, April 1971, pp. 263-270
5. Flow Quality Improvements in a Blowdown Wind Tunnel Using a Multiple Shock Entrance Diffuser, J. W. Arnold and J. M. Cooksey, AIAA 7th Aerodynamics Testing Conference, Palo Alto, California, September 1972
6. Mabey, D. G., Flow Unsteadiness and Model Vibration in Wind Tunnels at Subsonic and Transonic Speeds, C. P. No. 1155, Aeronautical Research Council, Ministry of Aviation Supply

ASSESSMENT OF THE INFLUENCE OF INLET AND AFTBODY/NOZZLE PERFORMANCE  
ON TOTAL AIRCRAFT DRAG

by

Philip P. Antonatos  
Director, Flight Mechanics Division

Lewis E. Surber  
Aerospace Engineer

James A. Laughrey  
Aerospace Engineer

Donald J. Stava  
Aerospace Engineer

Air Force Flight Dynamics Laboratory  
Wright Patterson Air Force Base, Ohio

USA

SUMMARY

Airframe-propulsion system integration plays an important part in the determination of aircraft performance. Considering range as the key measure of aircraft performance, there are several parameters which may be influenced significantly by the design and operation of the inlet/exhaust system, namely thrust, weight, lift, and drag. The primary consideration of this paper is the influence of propulsion system installation on aircraft drag. Using information from several recent investigations, different aspects of airframe propulsion integration are explored, each of which affects the assessment of aircraft drag. A great deal of apparently conflicting data has been generated on airframe-propulsion integration simply because the investigators concerned with different aspects of a system development have not properly integrated their own efforts to assure that theoretical analysis methods are consistent with wind tunnel test methods, that the test models are consistent with each other, and that adequate corrections for the effect of model mounting systems can be made. Even rather small inconsistencies in just a few of these considerations may result in errors of sufficient magnitude to affect aircraft design decisions adversely. A major part of the difficulty of making an accurate assessment of inlet/aftbody nozzle effect on aircraft drag is the prediction of flight performance from wind tunnel test data. Early system development should be studied carefully to assure that the program of airframe-propulsion integration and the demands on propulsion related drag assessment are consistent with drag estimate accuracy for the airframe.

ACKNOWLEDGEMENT

This paper makes use of source material from a number of USAF contracts which have not, as yet, resulted in documentation which is suitable for referencing. Consequently, the authors gratefully acknowledge the work of engineering personnel from Lockheed, McDonnell Douglas, Boeing, General Dynamics Convair, North American Rockwell, General Electric, and Pratt & Whitney whose efforts have made this paper possible.

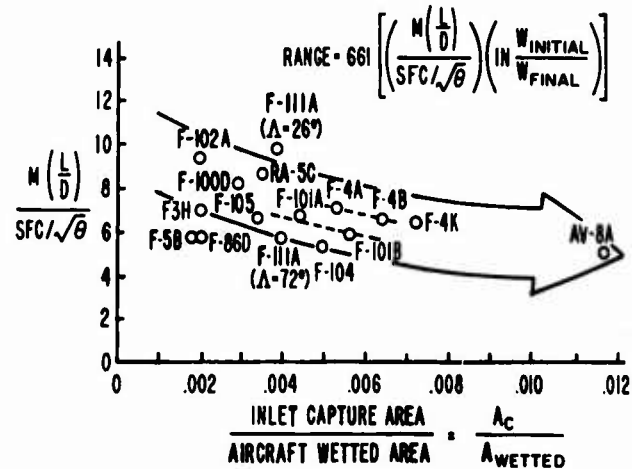
## List of Symbols

A	Area		
$A_{MAX}$	Aftbody or nozzle maximum projected area		
$A_o/A_c$	Inlet mass flow ratio		
A/B	Afterburning or reheat condition		
c	Chord length		
$C_L$	Lift coefficient $L/q_o S_w$		
$C_D$	as Airplane drag coefficient $D/q_o S_w$		
	as Inlet drag coefficient $D/q_o A_c$		
	as Nozzle drag coefficient $D/q_o A_{MAX}$		
$C_{D_{AFT}}$	Aftbody/nozzle (afterbody) drag coefficient $D/q_o A_{MAX}$		
$C_{D_N}$	Nozzle drag coefficient $D/q_o S_w$		
$C_{D_P}$	Nozzle integrated pressure drag coefficient $D/q_o A_{MAX}$		
$C_{D_T}$	Total aftbody/nozzle (afterbody) drag coefficient $D/q_o S_w$		
$C_P$	Pressure coefficient $(p-p_o)/q_o$		
d	Diameter		
D	Drag		
D	Nozzle diameter		
F	Force		
$f_1(C_c)$	Cowl Suction parameter		
	$= \frac{\Delta C_c (t/c)_{ramp}^{.34} (A_c/A_{MAX})^{.805}}{(t/c)_{cowl}^{.531}}$		
$f_2(A_o/A_c)$	Mass flow parameter	$\theta$	Temperature ratio ( $T_t/518.7^\circ R$ )
	$= A_o/A_c M_t (A_c/A_t)/(A/A_*)$	$\delta$	Ramp angle
F.S.	Fuselage station		Subscript:
IN	Inches	A	aftbody
L	Lift	aero.	Denotes Aerodynamic Force and Moment Model flow-through conditions
L, l	Length	bal.	Force balance measurement
M	Mach No.	c	Capture
NPR	Nozzle Pressure ratio, $P_{T_J}/P_o = P_{t_j}/P_o$	e	Exit
P	Static pressure	E	Engine
$P_{T_J}$	Exhaust jet total pressure	F.C.	Fixed Capture
q	Dynamic pressure	MAX	Maximum value
Re	Reynolds No.	MIN	Minimum value
S	Nozzle spacing (centerline to centerline)	N	Nozzle
SFC	Specific fuel consumption	o	Freestream conditions
$S_w$	Wing area	RMS	Root mean square
t	Thickness	t	Throat
W	Weight	T	Total
X	Length	TOT	Total of ramp plus cowl
$\alpha$	Airplane angle-of-attack	V.C.	Variable capture
$\Delta$	Incremental value or difference	*	Sonic conditions
$\sigma$	Standard deviation	2	Compressor face station

## 1.0 Introduction

In recent years, the development of advanced aircraft has forced the consideration of airframe-propulsion system integration into a position of increased prominence. Earlier development programs worked around these problems with reasonable effectiveness, developing an airframe without giving a great deal of thought to the engine installation. The response to the need for high thrust supersonic aircraft and the development of fan engines have, however, resulted in much larger engines which process relatively larger stream tubes of air, thus impacting the total aircraft flow field and total aircraft performance with much greater significance.

As suggested in Reference 1, (see Figure 1-1) an increase in the ratio of inlet capture area to airplane surface area ( $A_c/A_{\text{wetted}}$ ) has typically been associated with decreased performance in terms of the range factor,  $M(L/D)/(SFC/\theta)$ . In spite of the fact that the uninstalled specific fuel consumption (SFC) of engines tends to decrease in the more recently developed high-flowing engines, the range factor does not improve. This trend - especially in the case of successive models of the same basic aircraft - can be ascribed to increased propulsion installation losses.



### SUBSONIC CRUISE PERFORMANCE TRENDS

Figure 1-1

Unfortunately, there has not been a great deal of refinement of the techniques for accomplishing efficient engine/airframe integration in the design of high performance aircraft. Aircraft designers and developers have been slow to respond to the full potential of the increasing impact of propulsion integration on performance because of its complexity. Yet this total design capability is becoming increasingly more important to the types of aircraft being conceived. Better understanding of these effects and their susceptibility to improved design is essential to facilitate the proper allocation of resources during design development. Furthermore, it is necessary to have some means of tracing the progress of all of the different elements of an aircraft design during development to assure satisfactory conclusion of the total program.

It is generally agreed that airframe-propulsion integration plays a significant role in the total performance of an aircraft. On the other hand, much confusion exists concerning its magnitude. At times it seems to serve as a type of "catch-all" for unresolved performance problems. This tendency is understandable because the development of an aircraft system virtually always includes a number of experimental tests to determine aircraft drag polars and engine thrust over a wide range of operating conditions. If an aircraft then fails to meet estimated levels of performance, it is quite natural for the interface between the aerodynamics and propulsion disciplines to emerge as the "accepted" problem area. In actuality, the performance decrement is most likely distributed over a rather wide range of problems which embraces several aspects of both aerodynamics and propulsion. These contributions also probably vary widely among different aircraft designs.

The objective of this paper is more to provide direction than to quantify the assessment of inlet and nozzle performance on total aircraft drag. It intends to provide observations about force accounting systems, experimental techniques, theoretical analysis methods, recent test results and wind tunnel/flight data comparisons which should be of use in making such an assessment. When working on the airframe-propulsion integration problem, it must be kept in mind that the ultimate objective of development effort must be to improve overall aircraft performance - not just reduce its drag. If, for instance, range is selected as the basic figure of merit for an aircraft, several other parameters come into play due to their direct effect on range (R):

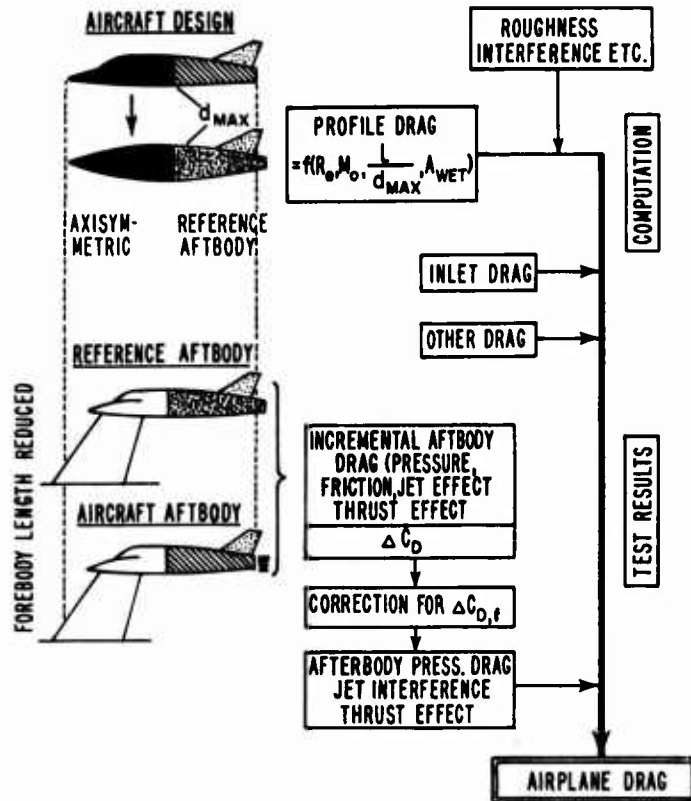
$$R = f(\text{weight, thrust, SFC, Lift, Drag}).$$

The design of inlet and nozzle systems is involved to some degree in each of the above parameters; therefore, the improvement of an inlet or nozzle design in one area may work to the detriment of the total system performance due to its adverse impact on other important performance parameters. For the purpose of this paper, the primary concern is aircraft drag, but some other parameters of particular interest (such as lift) will also be mentioned and it should further be kept in mind that perturbations in inlet and/or aftbody/nozzle design may have a significant effect on one or more other parameters at the same time.

## 2.0 Force Accounting System

The combined objective of all aircraft research and development effort is to produce a system which couples high performance with low cost. In order to realize this objective, it is highly desirable to have the ability from the early stages of development to predict the system performance accurately and identify the contributions of each subelement to that level of performance. A type of bookkeeping system is therefore required which facilitates this type of system and subsystem growth "visibility" throughout the development process. It is necessary to pay particularly close attention to the propulsion interference forces to be certain that they are all properly included in the performance "stack-up".

Performance estimates must be accomplished for all of the various pieces of a mission scenario, but usually the most critical parts as far as range is concerned are the cruise conditions. Early performance calculations are generated from a mixture of theoretical analysis and experimental data adaptations which result in estimates which are crude, but which establish the foundation for later development. Reference 2 (Figure 2-1) points out a typical technique employed early in aircraft development. In this method, the profile drag of a particular aircraft design is determined by performing the drag calculation for an axisymmetric fuselage of equivalent cross section distribution with friction drag calculated for the proper amount of wetted area surface. This equivalent body may be extended in length to assure absence of large areas of separation ahead of the base region. Special afterbody tests using both the reference afterbody and the real afterbody shape with jet effects generate the only experimental data taken specifically for this phase of the development. In this particular case, inlet operation corrections to the drag are presumably made by means of simple theoretical analysis or semi-empirical techniques utilizing existing data.



## PRELIMINARY PERFORMANCE ESTIMATE PROCEDURE

Figure 2-1

Later development and its associated performance estimates rely much more heavily on sophisticated wind tunnel test data; consequently, additional constraints must be placed on the force accounting system in order for it to be adequate to integrate both types of performance subelements. The force accounting system should, of course, be consistent from the early to the later performance estimates in order to provide a rational basis of comparison between the two levels of development. Many times, however, the degree of foresight during the time of concept formulation and early development is not sufficient to provide for such consistency. When this happens, the bookkeeping system is almost always revised as necessary to make it consistent with the sophisticated wind tunnel test techniques to be employed and to facilitate the extrapolation of that data to a flight performance condition as efficiently as possible. The basic problem is illustrated in Figure 2-2 where it is seen that the task is to generate a  $C_D$  versus  $C_L$  curve for an aerodynamic force and moment model and apply the corrections shown in the figure in order to generate the correct drag polar for an aircraft at flight conditions. Using the simplified condition where the engine thrust is parallel to the line of flight, the forces acting on an aircraft in straight and level flight (arbitrary thrust setting) can be expressed by the simple equation:

$$F_{total} = F_N + D_{aero} + \Delta D_{inlet} + \Delta D_{exhaust} + \Delta D_{Re} + \Delta D_{protub.}$$

Where:

$F_N$  = Installed engine thrust including effects of inlet pressure recovery and distortion, internal nozzle performance, and power extraction.

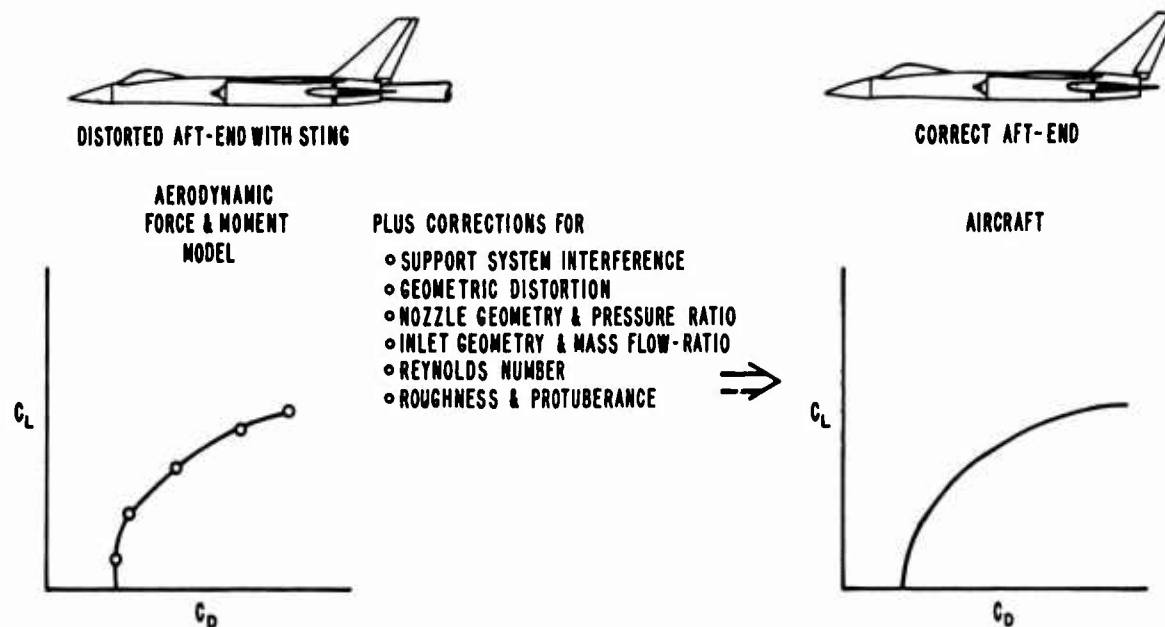
$D_{aero.}$  = Airplane exterior friction and pressure drag plus additive drag of the air entering the inlet.

$\Delta D_{inlet}$  = All drag increments between the  $D_{aero.}$  configuration and a model which reproduces the range of inlet mass flow ratios and all other inlet-related flows (bleed and by-pass).

$\Delta D_{exhaust}$  = All drag increments between the  $D_{aero.}$  configuration and a model which reproduces the real aftbody/nozzle geometry, flowfields, and critical operating parameters.

$\Delta D_{Re}$  = Drag correction due to Reynolds Number effect

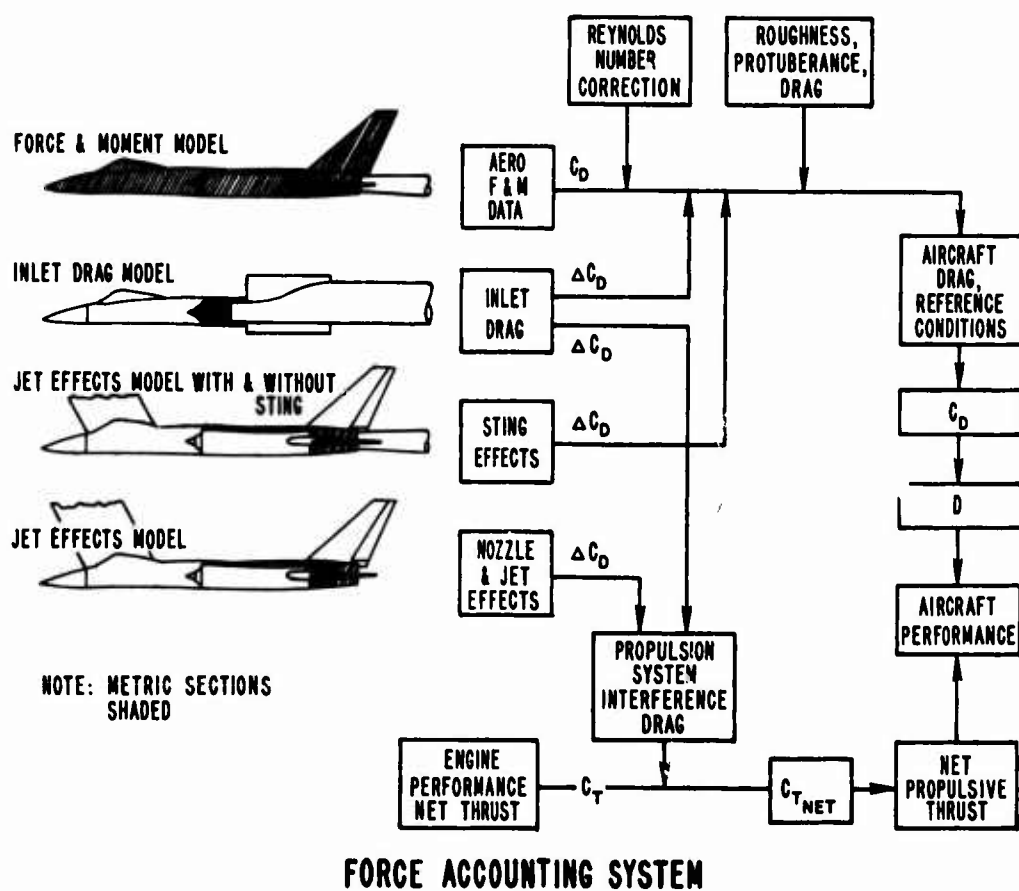
$\Delta D_{protub.}$  = Drag correction due to excrescence, i.e., roughness, protuberance, leakage, etc.



WIND TUNNEL DRAG POLAR CORRECTIONS

Figure 2-2

The above equation shows the basic types of increments involved in the determination of aircraft performance and Figure 2-3 shows the types of models and corrections made in a typical force accounting system. Division of the forces may vary somewhat from that illustrated according to particular system or development requirements. In the Figure shown, three basic models are employed to generate  $D_{aero}$ ,  $\Delta D_{inlet}$ , and  $\Delta D_{exhaust}$ .



FORCE ACCOUNTING SYSTEM

Figure 2-3

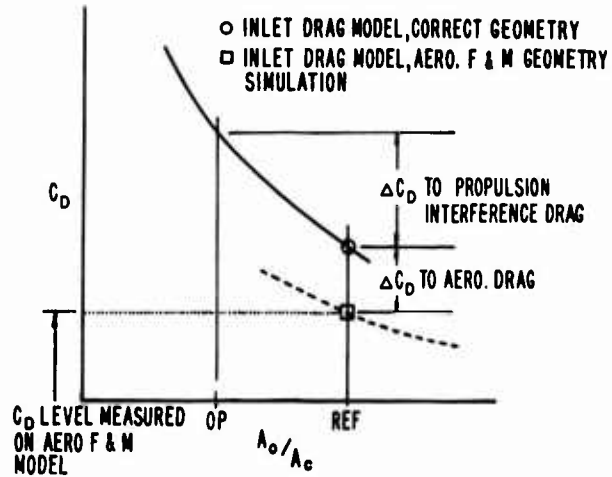
15-6

The first model shown is the Aerodynamic Force and Moment model. It is from this model that the left-hand drag polar in Figure 2-2 is formed. Using this model,  $D_{aero}$  in the equation above is calculated by subtracting the sting mount effect and the engine stream tube momentum loss from the force balance measurement:

$$D_{aero} = F_{bal} + [(P_{e,aero} - P_o) A_{e,aero} + P_{e,aero} V_{e^2,aero} A_{e,aero} - P_o V_o^2 A_{o,aero}] - \Delta D_{sting}$$

In the accounting system of Figure 2-3, the correction for sting mount effects ( $\Delta D_{sting}$ ) is taken from a Jet Effects model (described later), but it is possible (as indicated in Reference 2) to obtain this correction from the Aerodynamic Force and Moment (F & M) model.

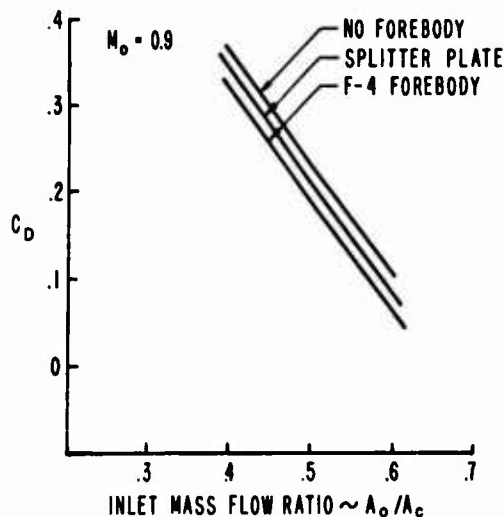
Next, an inlet drag model is usually employed. It is the purpose of the inlet drag model to determine the change in inlet drag from the Aerodynamic F & M model to the desired reference and/or aircraft operating condition. The increment thus measured is  $\Delta D_{inlet}$  in the  $F_{total}$  equation. Inlet drag models can be built in larger scale than the Aerodynamic F & M model since (as illustrated) they normally involve duplication of only the forebody portion of the airframe. This larger scale is usually required to obtain better duplication of important inlet flow phenomena such as boundary layer bleed flow and as a consequence, generate a more accurate measure of the drag with variations in inlet mass flow ratio (Figure 2-4). Note that the point in the Figure identified as "INLET DRAG MODEL, CORRECT GEOMETRY" includes a correction due to addition of bleed, bypass, and/or other model sophistication. (The  $\Delta C_D$  correction from a simulation of the Aerodynamic



INLET DRAG CORRECTIONS

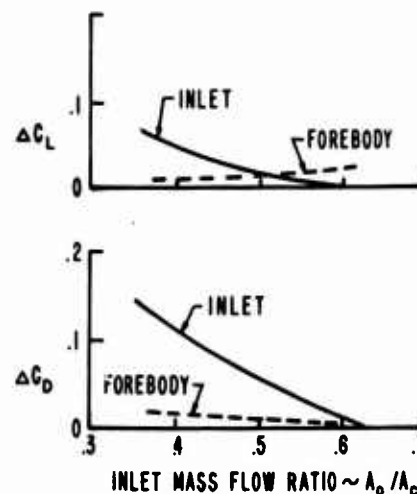
Figure 2-4

F & M to the Inlet Drag model at the reference mass flow ratio is applied as a correction to the aerodynamic drag polar. Additional changes due to mass flow variations are included as a part of the Propulsion System Interference drag.) It is assumed in some inlet drag tests that the only effect of great importance is the effect of mass flow ratio on the inlet drag level. The result of such an assumption leads to isolated drag tests of the inlet. Actually, the forebody affects the inlet flow field and, as illustrated in Figure 2-5, the level of inlet drag can be affected measurably by the degree of simulation of its presence. Furthermore, Figure 2-6 shows that there may be an effect of the inlet mass flow variation on forebody drag and lift as well. The side-mounted, vertical ramp inlets used in the illustrated test should inherently exhibit little of the sensitivity shown. Other designs incorporating horizontal ramp inlets and/or shielded inlets should show a greater sensitivity. Therefore, the accuracy required of inlet drag test data may make it necessary to provide multi-component force measurements on both the inlet and forebody over a wide range of inlet mass flows. (Additional note should be taken at this point that the inlet and its operation is becoming more important not only to aircraft drag, but also to its lift. Space does not permit a separate examination of inlet lift, but suffice it to say that its magnitude in many designs is sufficient that it should be included as a design consideration and accounted for in the calculation of system performance.)



EFFECT OF FOREBODY SIMULATION ON INLET DRAG

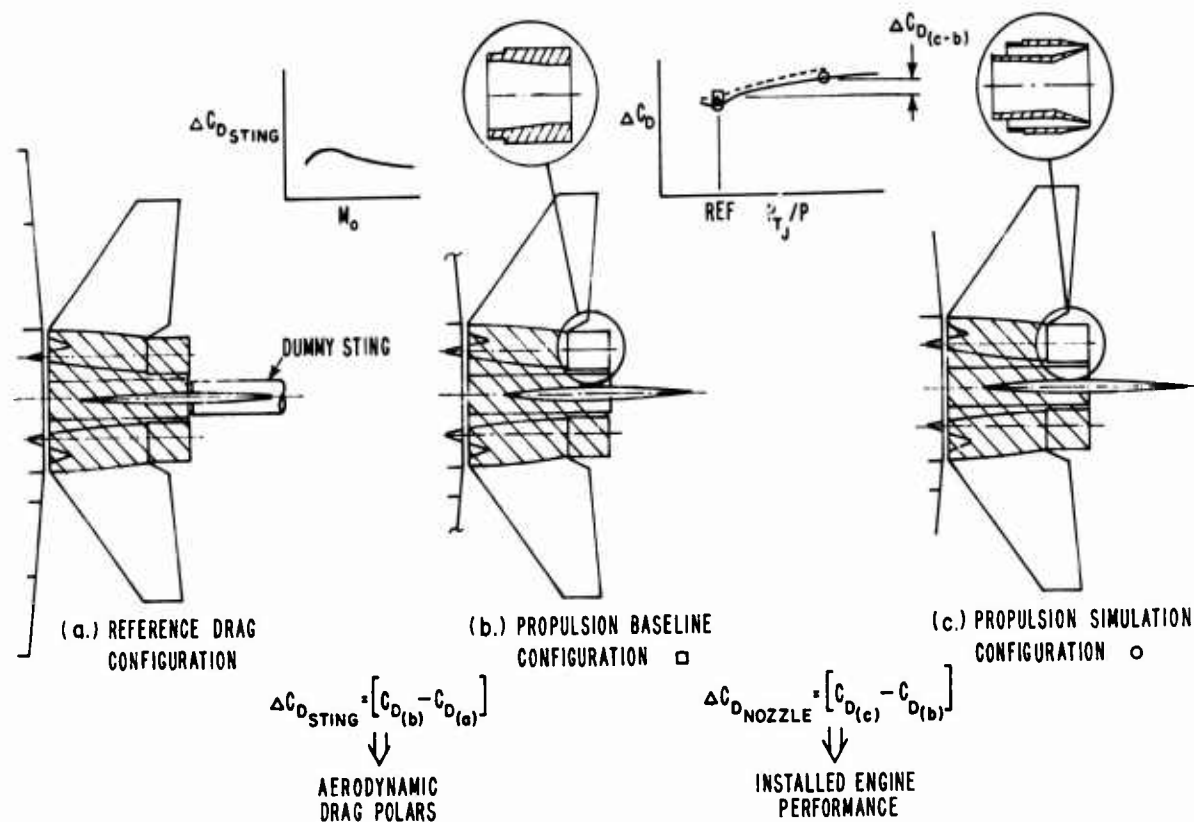
Figure 2-5



EFFECT OF INLET MASS FLOW ON INLET AND FOREBODY LIFT AND DRAG

Figure 2-6

The third model required for an accurate performance assessment may be referred to as the Jet Effects model. One of the corrections made with this model (as previously noted) is the change in the Aerodynamic F & M model drag due to the presence of the sting and the distortion in the aircraft lines to accommodate the sting. This incremental drag is usually determined experimentally by using models as shown in Figure 2-7. 15-7



### AFTBODY-STING, NOZZLE GEOMETRY, AND JET EFFECTS CORRECTIONS

Figure 2-7

The entire model is mounted on a strut with the afterbody forces measured by a force balance. The inlets are faired over and the exhaust nozzle flow is supplied by pressurized gas which enters the model through the strut mount. This gas is driven at a pressure determined by the level of  $P_{T1}/P$  desired. The horizontal and vertical tail need not be attached to the balance, but should be on the model. In this way, the balance can be given additional sensitivity without losing empennage effects. In Figure 2-7a the model is tested in an Aftbody/Nozzle Reference Drag Configuration to determine the drag of the distorted afterbody in the presence of the dummy sting with the nozzle flow simulating that of the Aerodynamic F & M model. Another drag value is determined using the Aftbody/Nozzle Propulsion Baseline Configuration (Figure 2-7b) which has the correct afterbody lines except for the nozzles, which are the same as or similar to the reference drag model, being cylindrical in shape to prevent local flow separation. The drag increment determined from these tests ( $\Delta D_{sting}$  in the  $D_{aero}$  equation) is normally applied to the aerodynamic drag polar. Assuming that the preceding drag increment is applied to the drag polar, then the influence of aftbody/nozzle performance on installed thrust remains to be determined. Another aftbody/nozzle configuration (Propulsion Simulation) shown in Figure 2-7c is then used to determine the thrust and aftbody/nozzle drag for the actual aircraft lines with the nozzle flow simulating flight conditions. If there is no influence on the internal nozzle flow by the external flow, then the change in drag on the aftbody/nozzle is the total incremental force ( $\Delta D_{exhaust}$  in the  $F_{total}$  equation) that is needed to correct the installed engine performance. If, however, the external flow does affect the internal nozzle flow, then a change in thrust must be determined. This is normally accomplished by measuring the thrust of the nozzle at static conditions (no external flow) and at flight conditions, for the same nozzle pressure ratio (NPR). The total incremental force then consists of a change in aftbody/nozzle drag plus a change in thrust.

In summary, there are basically two incremental force values that normally have to be determined when assessing the influence of aftbody/nozzle flow fields on total aircraft performance. One increment gives a correction to the basic aerodynamic force data to account for model mounting differences. The other corrects engine thrust from an uninstalled to an installed value and accounts for a drag change due to model geometrical variations plus a change in engine operating conditions.

Again note from Figure 2-3 that all effects have been accounted for, with some being included in the basic aircraft drag polar at the Aerodynamic F & M model mass flow ratio and others accounted for as propulsion system interference corrections. If desired, an aircraft operating condition could be chosen as a reference condition. In this case, as depicted in Figure 2-8, corrections to the aircraft drag polar would include all of the inlet and aftbody/nozzle drag corrections necessary to make it reflect flight conditions at this new reference or "baseline" condition. Operating conditions away from the baseline inlet mass flow and exhaust nozzle configuration and pressure ratio would be reflected in the propulsion system interference drag. It has been argued that an accounting system of this type affords better "visibility" of the total aircraft development progression. Also, arguments in favor of various Aerodynamic F & M model flow-through conditions may be made, but the importance of such considerations tends to vary with the specific aircraft type and design undergoing development.

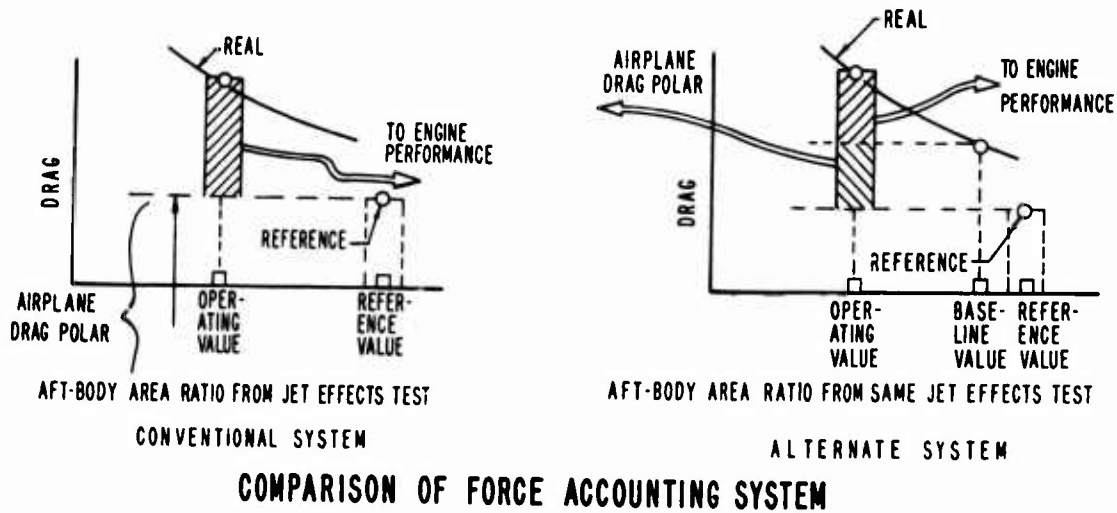


Figure 2-8

### 3.0 Experimental Performance

The accuracy of any aircraft performance calculation procedure depends upon proper accounting of all drag and lift effects, but it also depends upon the accuracy of the corrections made. This section will be devoted to two aspects of experimental development, namely the effects of experimental test techniques employed, and effects of design and test variables.

#### 3.1 Model Mounting Techniques

It is the goal of any test technique to reproduce the physical flow phenomena of interest and provide for a measurement of that phenomena. The method of test associated with the Section 2.0 force accounting systems is currently the most widely used system for the development of supersonic aircraft (particularly twin-engine types), but is by no means the only one. The method illustrated in Figure 2-3 has several problems of varying importance. It assumes in the use of an abbreviated Inlet Drag model and faired over inlets in the Jet Effects model, that the effect of inlet mass flow variations are not felt on the aftbody/nozzle region. It further assumes that there is no interaction of the strut and dummy sting when the sting effect is determined on the jet effects model and that the strut effect on aftbody forces does not vary from the increment determined at reference conditions.

One technique employed to eliminate the strut effect on jet effects models has been to use a nose mounting system where the nose boom reaches far upstream, sometimes to the wind tunnel plenum, Figure 3-1. A variation of this technique would extend the nose somewhat and mount this extension on a strut far enough upstream to avoid creating major cross section area variations in the region of the maximum model cross section area, Figure 3-2. Both of these methods, however, create anomalies in fuselage flow fields and boundary layer development which have not been shown to be an improvement over the effects of typical strut mounts. Another test option for the jet effects model is the wing tip mount, Figure 3-3. While a system of this type does eliminate the strut mount, the question of the effect of wing distortion (required for passage of nozzle high pressure air) and mounting pylons has not yet been determined. Another model mounting system which can be employed makes use of a type of sting mount in the Aerodynamic F & M model (Figure 3-4). The dual sting mounts entering the exhaust nozzles require no aft end geometrical distortion of the model and can be used to meter air flow- ing through the model inlets. Thus, an Aero. F & M model is created which directly measures the effect

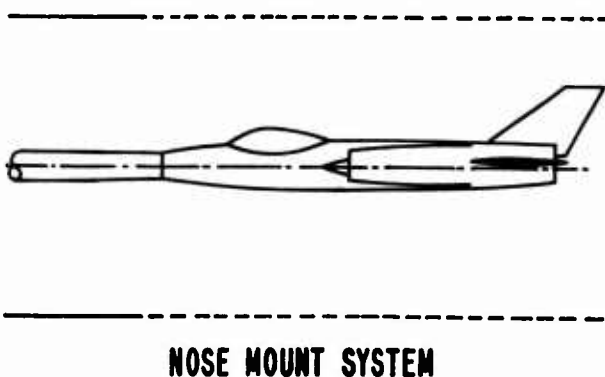


Figure 3-1

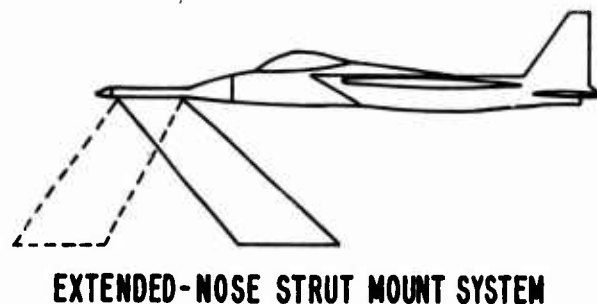


Figure 3-2

of a wide range of inlet mass flow ratios on total aircraft drag and lift. Such a model can also incorporate a separate inlet balance. It has been suggested further that the stings of such a model could even be used to simulate jet effects with solid plume boundaries, but this will be discussed in the next subsection. The primary problem with a model of the type described here (in terms of its use as a combination Aero. F & M model and Inlet Drag model) would be the reduced inlet scale size for the inlet drag data. In order to have a satisfactory trade in this area (compared to the conventional technique) it would be necessary to build a model large enough to reproduce all of the inlet drag effects with reasonable accuracy.

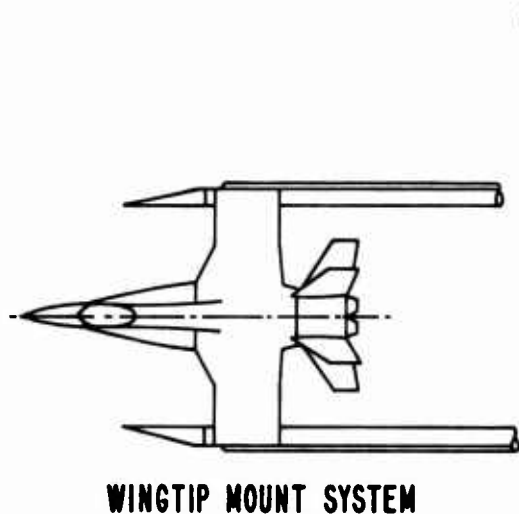


Figure 3-3

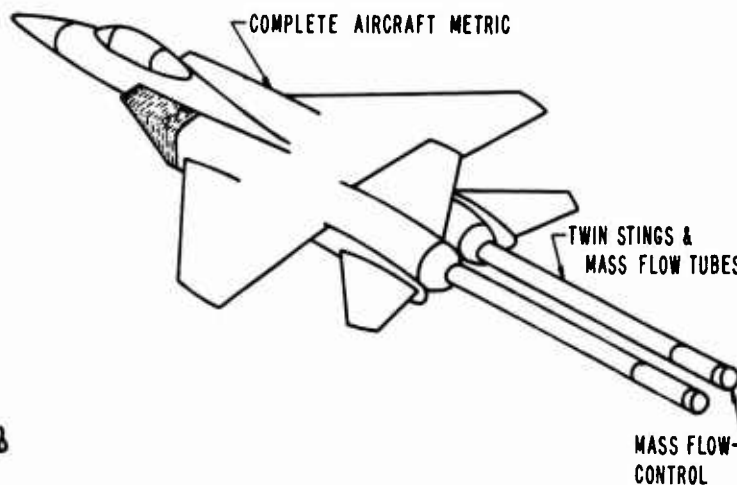
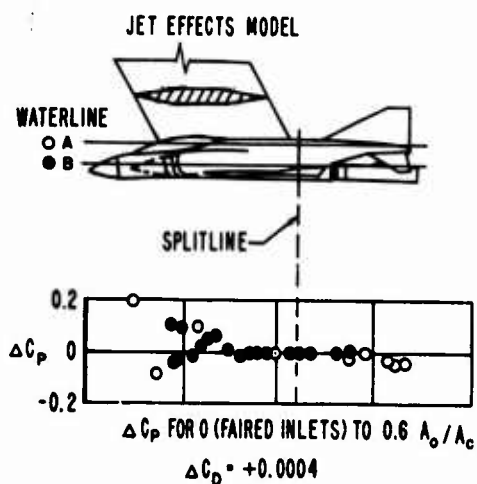


Figure 3-4

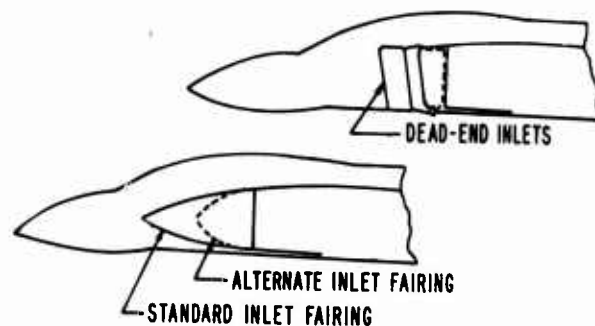
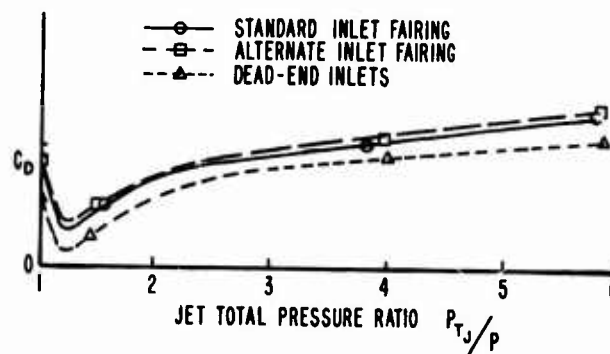
3.2 Corrections for Mounting Systems and Test Methods

In the conventional test method discussed in Section 2.0, use was made of a faired-over inlet on the jet effects model, with the attendant assumption that there would be no significant difference in aftbody/nozzle drag between the flow-through inlet and the faired inlet. The accuracy of this assumption tends to be verified at transonic Mach numbers on some aircraft models where, as illustrated in Figure 3-5, the difference in body pressure coefficients ( $\Delta C_p$ ) between faired inlets and inlets flowing at a mass flow ratio of  $A_0/A_c = 0.6$  (measured at two different water lines) does not appear to extend more than a short distance downstream of the inlet. Figure 3-6, indicates that reasonably careful fairing is advisable; the dead-ended inlet/aftbody drag coefficient varies somewhat from the values obtained



EFFECTS OF INLET FAIRING,  $M = 0.9$

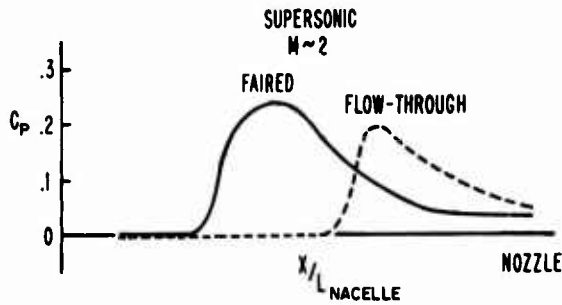
Figure 3-5



EFFECT OF INLET FAIRING ON AFTBODY/NOZZLE PRESSURE DRAG COEFFICIENT,  $M_0 = 0.9$

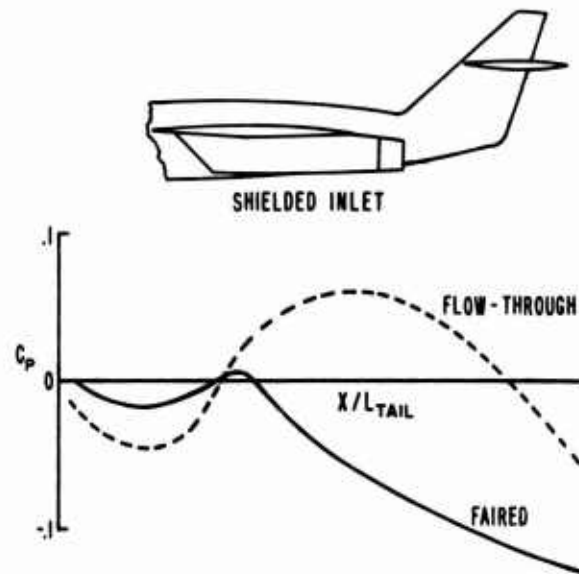
Figure 3-6

15-10



EFFECT OF INLET FAIRING ON NACELLE PRESSURE DISTRIBUTION

Figure 3-7



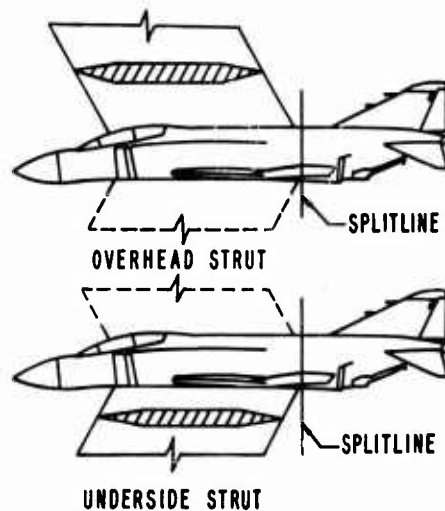
EFFECT OF INLET FAIRING ON HORIZONTAL TAIL PRESSURE DISTRIBUTION

Figure 3-8

with faired inlets. Supersonically, a different trend is indicated in Figure 3-7, where the nacelle pressure differences are quite significant. For this particular installation, perhaps a more significant aspect of the problem is illustrated in Figure 3-8 where the pressure distribution on the horizontal tail is appreciably altered by inlet flow in supersonic flight, giving rise to entirely different trim drag characteristics. Effects such as these could give rise to projected flight discrepancies. Wind tunnel data would be projected on the basis of one aircraft trim condition while flight could require an entirely different tail setting. All of these effects are very configuration oriented and the exact magnitudes and sensitivities associated with any high performance aircraft design must be determined from carefully conceived model tests of that particular configuration. The supersonic test results presented here have been obtained from models with limited pressure instrumentation, i. e., insufficient to determine pressure integrated drag levels; consequently, they only serve to identify certain problem areas requiring further study.

Another item of concern in the conventional test technique and force accounting system is the previously mentioned assumption that strut and sting effects can be "corrected out" of the data. In the system previously described, there is no actual attempt to remove the strut effect on drag, but rather it is assumed that the strut effect is very nearly the same for all of the jet effects model configurations and jet pressure ratios. Since the accounting system requires only drag coefficient changes,  $\Delta C_D$ , the actual strut effect

need not be determined. If, on the other hand, actual aftbody/nozzle drag coefficients are required (as in a comparison with theoretical analysis) some means of removing the strut effect must be employed. One manner of doing this, shown in Figure 3-9, is to provide a test of the Jet Effects model supported by an alternate strut (dashed lines) on the side opposite the primary test support position. Then, a dummy strut mount (solid lines - primary test support position) is also tested simultaneously with the alternate strut mount. The difference between these two is a measure of the primary strut support effect. Figure 3-9 gives the results of such tests and shows that in this particular case the correction at  $M_o = 1.2$  is rather large.



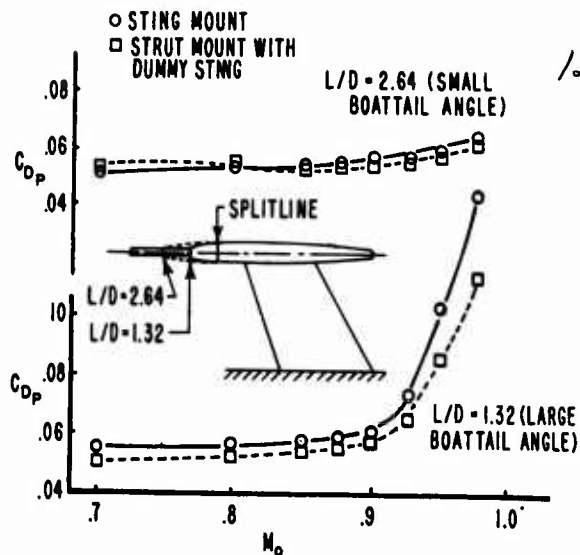
EFFECT OF STRUT MOUNT ON AFTBODY/NOZZLE DRAG

Figure 3-9

$M_o = 0.7$	$M_o = 1.2$
AFT-END DRAG, $C_{DAFT}$	
0.0841	0.1190
DRAG CORRECTIONS $\Delta C_{DAFT}$	
0.0013	0.0320
0.0013	0.0450

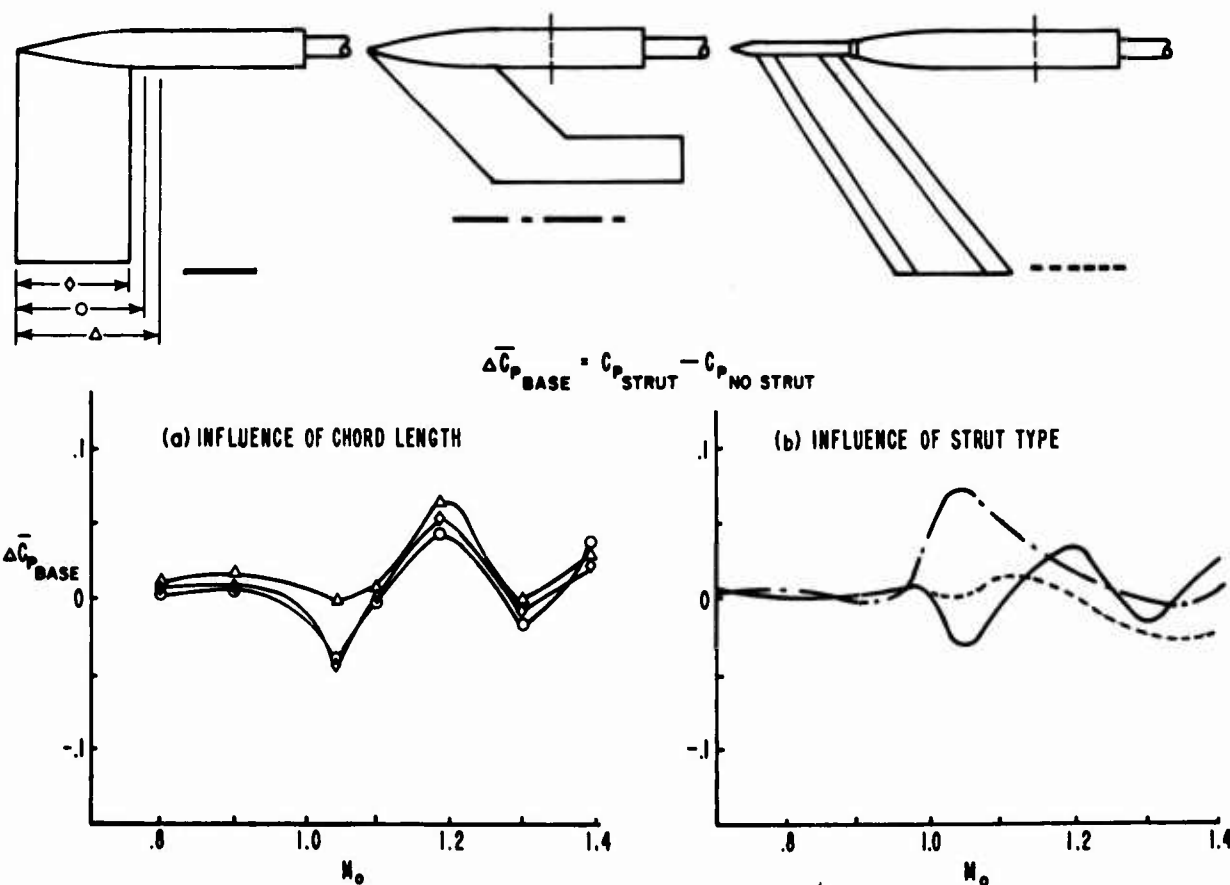
$$C_{DAFT} = C_{DMEASURED} - \Delta C_{DAFT}$$

Other experimental investigations have explored various aspects of the strut interference. Figure 3-10 indicates that the level of strut interference is, in part, dependent upon the aftbody rate of closure while Figure 3-11 suggests effects due to strut type and relative strut chord length. The biggest problem, however, is one of the interaction of the real mounting system with the dummy mounting system in making corrections.



EFFECT OF NOZZLE BOATTAIL ANGLE ON STRUT INTERFERENCE

Figure 3-10



BASE PRESSURE EFFECTS OF SUPPORT STRUT DESIGN

Figure 3-11

An example is taken from a recent test program involving drag tests of a large-scale supersonic twin engine fighter model (Figure 3-12). This model incorporates separate force and pressure measurements of both fuselage aftbody and nozzle boattail. Most of the tests have been run with a strut mounting system, but in order to isolate the strut effects, a special sting mounting system has been devised in a manner similar to that mentioned previously. In this latter case, the model is supported by twin stings which simulate the nozzle plume shape, but do not distort the nozzle or aftbody geometry. In fact, three different sting mounts representative of different plume shapes, were tested and the drag difference due to strut interference measured in each case with the result shown in Figure 3-13 and Figure 3-14. This data is still considered preliminary, but the trend illustrated is considered to be valid. It appears that the strut correction changes depending upon the sting being used. This sting/strut interaction indication suggests that the complete removal of strut effects may be extremely difficult, if not impossible. It also

15-12 brings into question the assumption that strut effects on aftbody/nozzle drag remain constant over a wide range of jet pressure ratios.

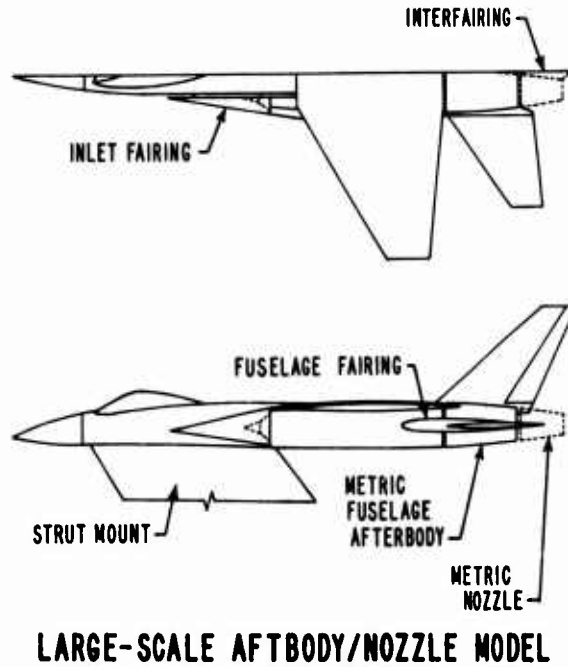
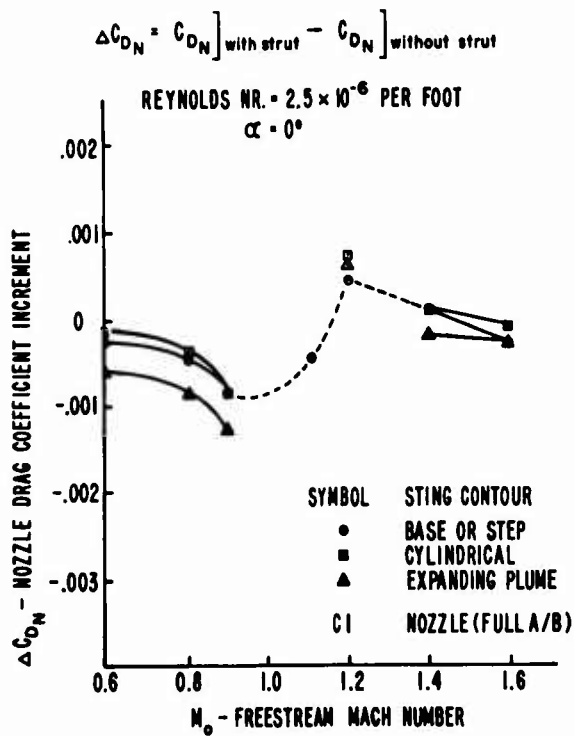
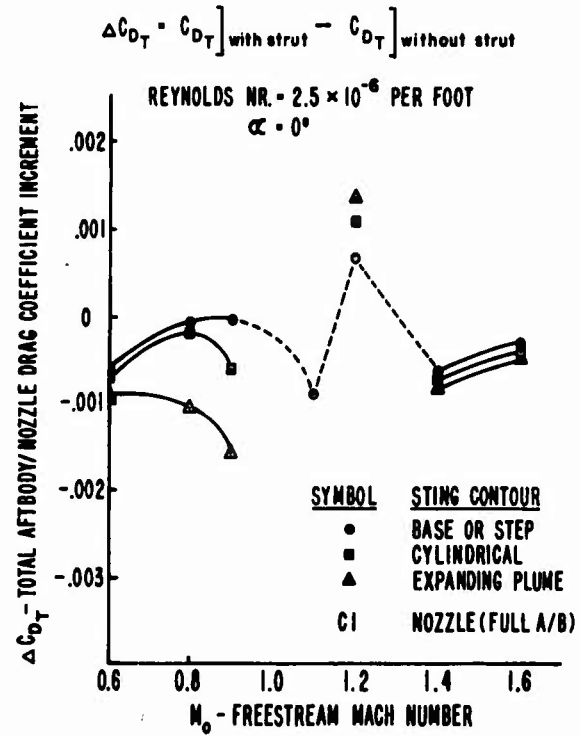


Figure 3-12



EFFECT OF STRUT INTERFERENCE ON NOZZLE DRAG

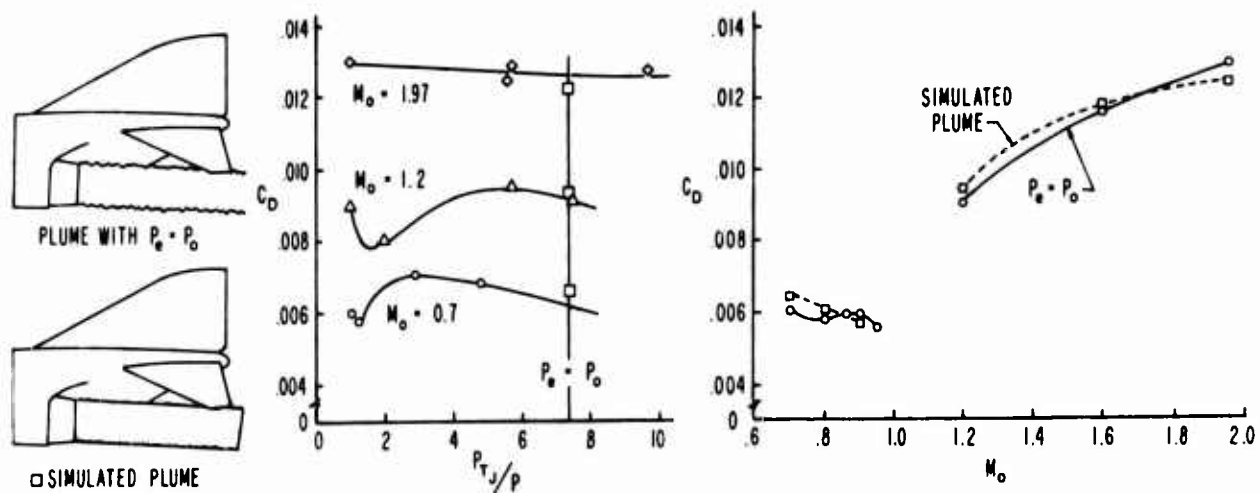
Figure 3-13



EFFECT OF STRUT INTERFERENCE ON AFTBODY/NOZZLE DRAG

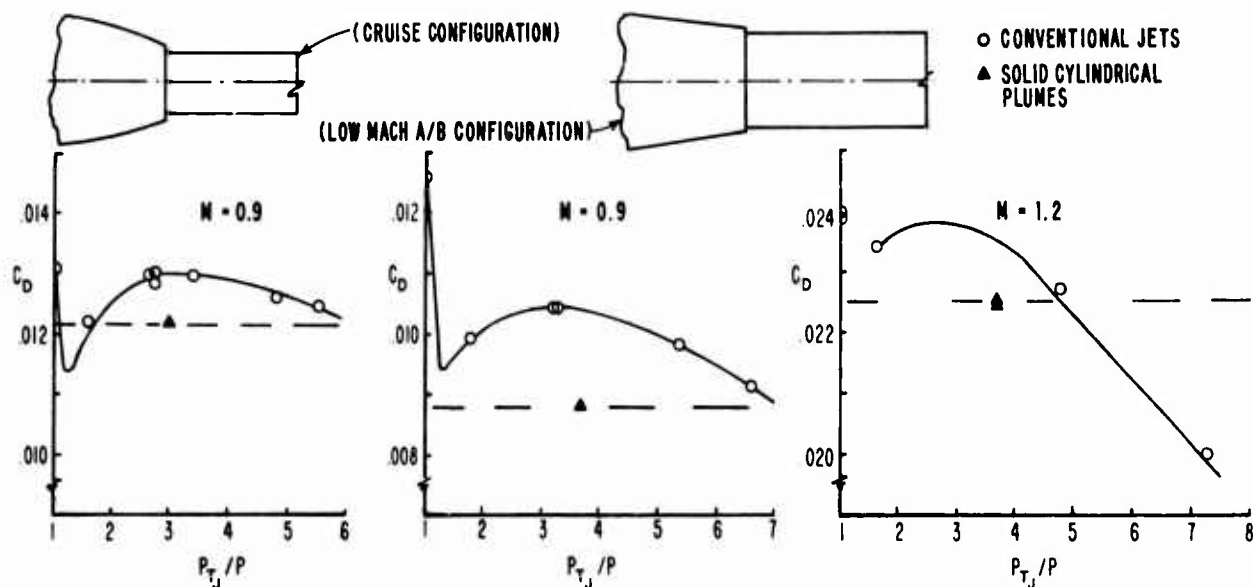
Figure 3-14

Before leaving the subject of the nozzle sting mounting system it is considered worthwhile to consider some data gathered on other models using this sting mounting technique. Some of the early work on the F-4 (Figure 3-15) indicated that it might be a useful technique for determining aftbody drag - at least at the condition where  $P_e = P_o$ . However, in another case (Figure 3-16) where conventional jets were compared with solid cylindrical plumes, the results showed a rather poor correlation either in a cruise configuration or low Mach afterburner configuration. An attempt was made to improve this basic technique by adding annular jets at the exits (Figure 3-17). The results thus far obtained indicate much better agreement with the conventional jet data.



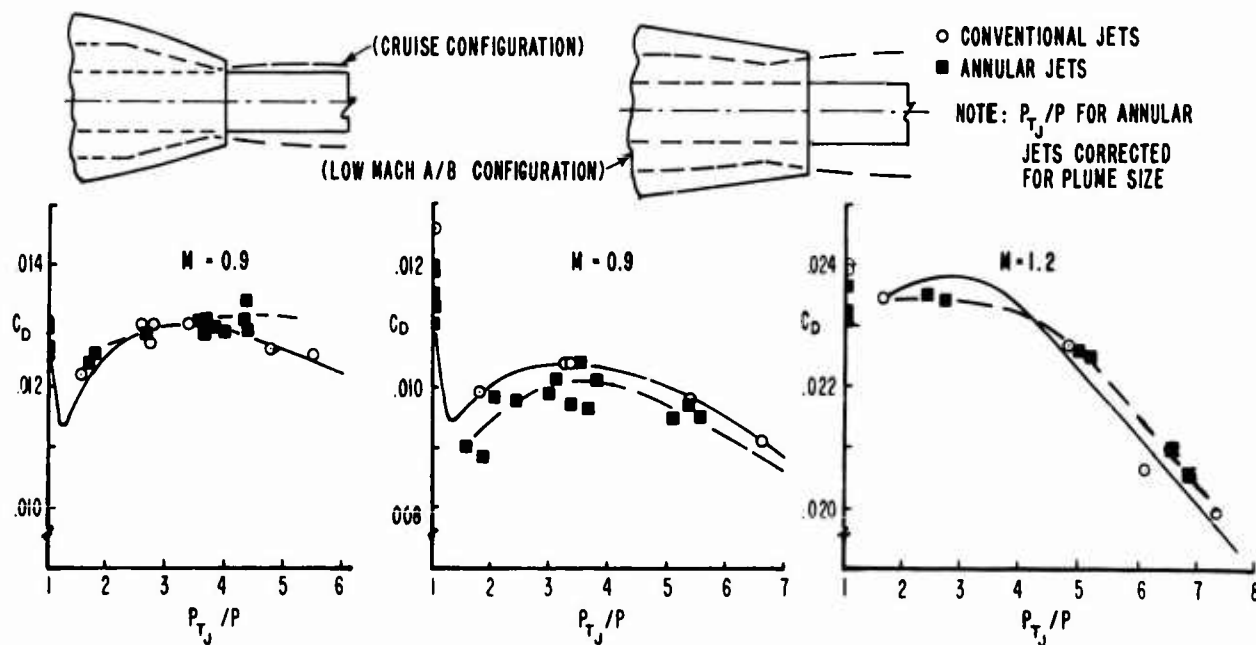
EXHAUST PLUME SIMULATION

Figure 3-15



AFTBODY/NOZZLE DRAG COMPARISON - SOLID CYLINDRICAL PLUMES VS. CONVENTIONAL JETS

Figure 3-16



AFTBODY/NOZZLE DRAG COMPARISON - ANNULAR VS. CONVENTIONAL JETS

Figure 3-17

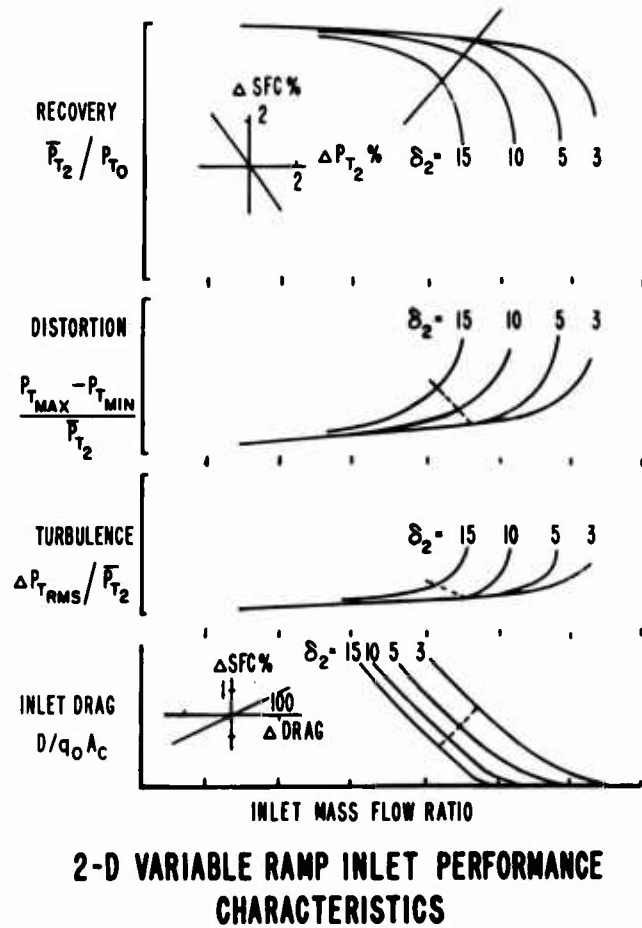
### 3.3 Effects of Design Variables on Performance

#### 3.3.1 Inlet Design Variables

15-14

With the selection of the force accounting procedure to be used during system development, a systematic program can be set up to evaluate inlet component design variations. These design evaluations are necessary to develop trade off data required for vehicle design optimization. This process requires a large matrix of drag data as well as other information concerning cost, reliability, and weight. The discussions here will concentrate on the installed inlet drag aspects of the vehicle design, but the trade off criteria actually includes installed thrust minus drag, which requires the consideration of inlet total pressure recovery as well as the drag characteristics. Any selection process must consider these two parameters together.

Many test results have shown that appreciable flow spillage can be accommodated transonically with little drag penalty when the inlet throat Mach number is kept high. This can be accomplished by means of increasing the compression surface angles to reduce throat area. Figure 3-18 presents typical data obtained from a two dimensional variable ramp inlet. As can be seen, increasing the ramp angle can result in an appreciable reduction in inlet drag at a constant engine demand. However, the reduction in throat area results in increases in both steady state and time variant diffuser exit flow distortion as well as a decrease in total pressure recovery due to the higher throat Mach numbers. Assuming that the distortion generated is within engine tolerances, inlet operation at the highest ramp angle and lowest drag would be desired. However, for the data presented here, operation at the high ramp angle incurs a 3% loss in pressure recovery and a 50% reduction in inlet drag. Employing the sensitivity factors shown in the figure for a typical flight condition, it is readily apparent that the loss in pressure recovery results in a much larger increase in SFC than the benefits reduced drag level can offset. At a typical high altitude cruise condition, operation at a second ramp angle of  $\delta_2 = 15^\circ$  would result in a 4% loss in SFC, while at sea level this would be decreased to approximately 1% SFC loss. Operation at some intermediate condition however, such as  $\delta_2 = 5^\circ$  would be of benefit because there is a substantial drag reduction with essentially no loss in pressure recovery.

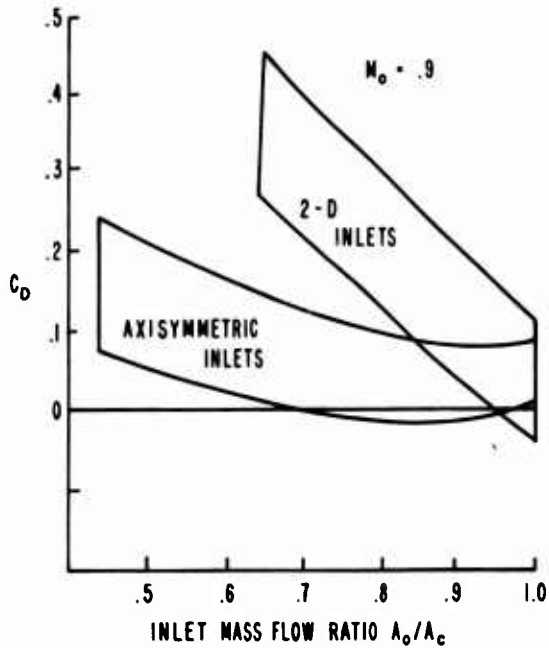


2-D VARIABLE RAMP INLET PERFORMANCE CHARACTERISTICS

Figure 3-18

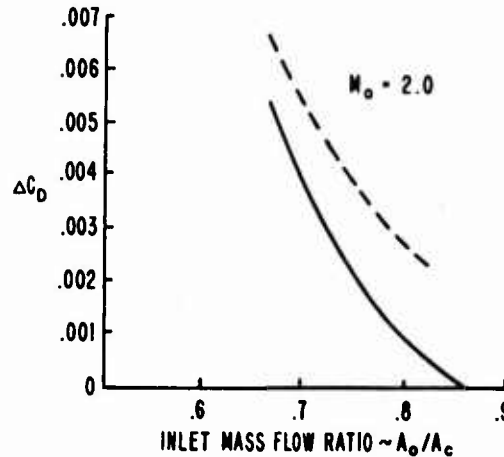
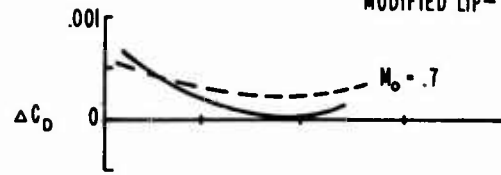
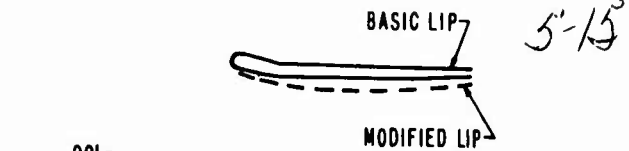
Reference 2 attempted to identify inlet design features that might be investigated from the inlet drag standpoint. Considerations of inlet geometry, inlet engine matching, and inlet installation all impact the drag levels experienced. Some of this data is incorporated here to illustrate the significance of the force accounting system used. Generally, the first design parameter selected during a system development will be the basic inlet geometry to be used, e.g., two dimensional or axisymmetric. Several investigations have shown that axisymmetric conical inlets have less drag than two dimensional ramp inlets with equal throat/capture area ratios and equivalent ramp or cone angles. Typical data are shown in Figure 3-19. This characteristic can be explained by the relief provided by the three dimensional spillage of the cone resulting in lower flow spillage angles, i.e., the cone flow deflection is less than the two dimensional flow deflection, resulting in lower drag. As the system development and force accounting methodology progress, most programs then concentrate on the inlet component effects such as lip, sideplate, and cowl shapes, bleed system design and ramp schedule variations. At this point, the force accounting methodology must be sufficiently refined to identify the small variations in drag that these components can produce. Figure 3-20 indicates the level of aircraft drag sensitivity to slight modifications of the external cowl lip geometry. However, the external cowl lip geometry (as well as the internal cowl lip geometry) that results in the minimum drag is dependent on the local flow angularity approaching the lip. This flow angularity is, of course, highly dependent upon both the compression surface geometry and flight condition.

The minimum drag configuration parameters are of primary concern because they govern the inlet drag at cruise conditions. Nevertheless, the performance assessment methodology employed should permit evaluation of off-design conditions. While off-design operation may be transitory and of short duration it should not be neglected. A small error in the transonic acceleration drag can seriously degrade the supersonic capability of a system. The typical airflow mismatch during this condition usually requires consideration of bypass systems. When one considers the drag of the bypass system, a drag trade off occurs between the spillage and bypass drag such that the minimum inlet drag may occur at an airflow



EFFECT OF INLET SHAPE ON INLET DRAG

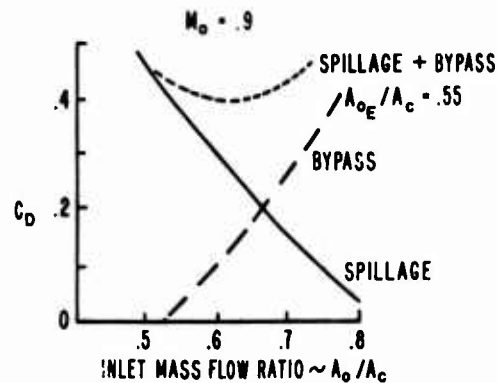
Figure 3-19



EFFECT OF LIP SHAPE ON INLET DRAG

Figure 3-20

condition less than that for minimum spillage drag. A typical trade study is shown in Figure 3-21 where the increments of spillage and bypass drags are shown along with the airflow associated with minimum drag for constant engine demand. This is an ideal situation and does not consider the interference of bypass air on aircraft drag and stability characteristics. In operational use, the bypass air must be dumped and this usually occurs in an unfavorable location such as above the wing. Any drag impact here should be assessed and accounted for in the bookkeeping system employed. Another possibility to reduce this bypass drag penalty is to incorporate variable inlet capture.



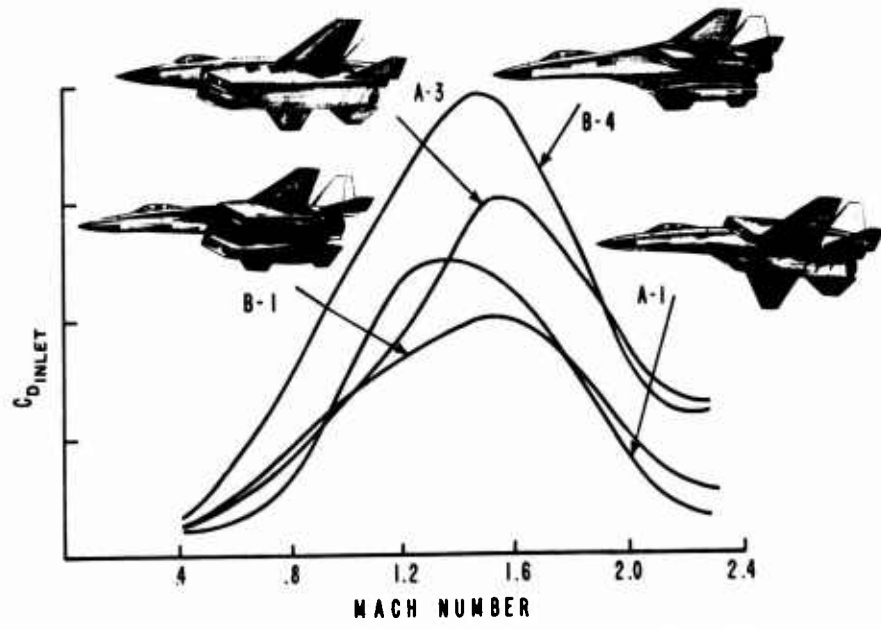
TRADEOFF OF SPILLAGE AND BYPASS DRAG

Figure 3-21

Illustrated in Figure 3-22 are the predicted drag characteristics for four two dimensional inlets designed for typical fighter aircraft. In this case, consideration of the local inlet flow field as well as other vehicle design constraints led to the selection of different inlet design features for each installation. Configurations A-1 and B-1 employ a variable capture feature to reduce transonic spillage drag at the expense of some weight and complexity. Figure 3-23 further illustrates some of the drag and design characteristics for the fixed and variable capture inlet designs shown in the previous figure. At transonic conditions, operation at part power usually results in high spillage drag levels, but inclusion of the variable geometry feature permits inlet operation at higher mass flow ratios (lower  $A_0$ ) and, thus, reduced drag. While this feature reduces spillage drag, care must be taken to insure that this is not nullified by increased external drag on the variable component. The other point illustrated in Figure 3-23 is the benefit of the variable geometry in reducing inlet drag during maneuvering conditions. Although the inlet drag reduction can be appreciable, it is of course a smaller portion of the vehicle drag at high angle-of-attack conditions.

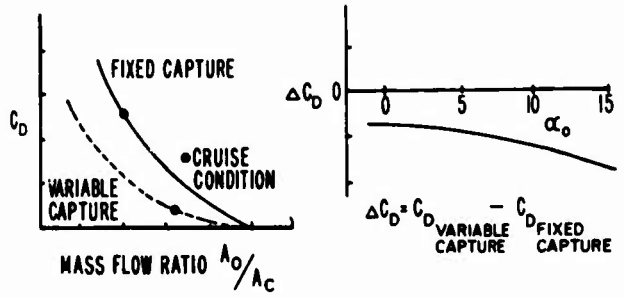
The existing parametric data on ramp geometries, lip shape, cowl shapes, sideplate shapes, bleed patterns, etc., are primarily useful for indicating trends when a new system is being developed. For any new system the absolute inlet drag and performance level determination requires parametric tests for that particular installation design. Figure 3-24 shows that a broad range of data has been taken in

15-16



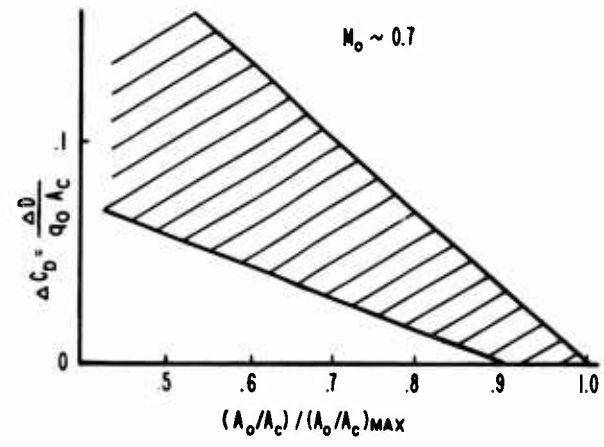
COMPARISON OF PREDICTED INLET DRAG VALUES

Figure 3-22



EFFECT OF VARIABLE INLET CAPTURE AREA ON INLET DRAG

Figure 3-23



RANGE OF DRAG CORRECTIONS DUE TO INLET MASS FLOW VARIATIONS

Figure 3-24

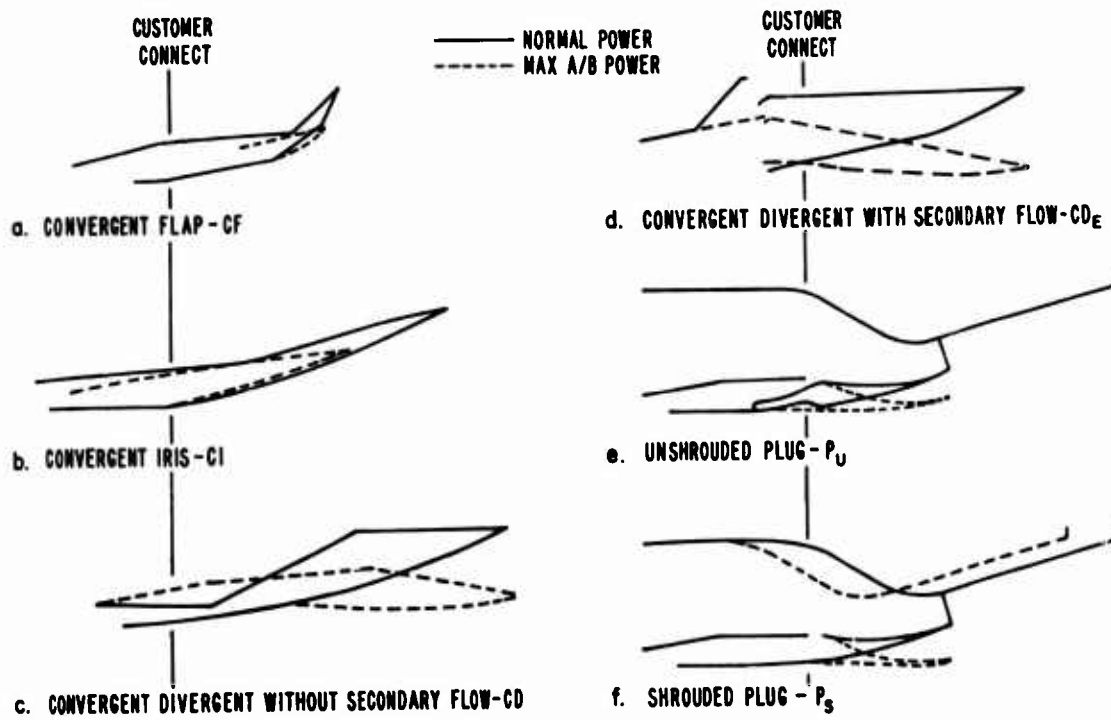
some of the various drag tests of two dimensional inlets for specific transonic or supersonic aircraft designs. These tests have incorporated many different aspects of inlet design. It is not considered possible to extract accurate drag data for a new inlet design from such a variety of results. Thus, an improved (but not optimum) inlet design must be developed in the wind tunnel for a given system application. Then, projected flight performance can be predicted from that wind tunnel data. If data acquisition is to be consistent throughout system development, the force accounting system should allow for isolation and verification of all component performance. With this in mind, it appears highly desirable, if not mandatory, to rely not only on inlet force balance data but to also extensively pressure instrument all inlet test configurations.

3.3.2 Exhaust Nozzle Design Variables

The exhaust nozzles of a particular airframe/engine combination must be designed to satisfy the specific performance, structural, and operational requirements involved. A variable throat area and a variable exit area are needed to maximize the gross thrust throughout the flight range. Maximum gross thrust is achieved when the nozzle exit pressure is matched to the ambient pressure. Providing too large an area ratio results in a much larger penalty at low Mach numbers than the gain provided at high Mach numbers.

The external flow field over an airplane affects the design and mission performance of the airplane in several ways. The flow interacts with the nozzle exhaust so that the installed nozzle performance, in terms of thrust and drag, may be lower than for an isolated nozzle; and the flow can cause internal nozzle flow separation. External flow interaction with the flow from the exhaust nozzle can result in large aftbody drags, especially for twin-engine installations where factors such as inlet, tail surfaces, and stores location restrict optimum airplane/nozzle integration. Different types of nozzles can better satisfy specific requirements such as lightweight design (convergent) or secondary flow handling capability (convergent-divergent ejector).

The convergent nozzle excels in lightweight aircraft whose supersonic mission requirements are only dash periods, since it has low performance at high pressure ratios. The short flap convergent nozzle (Figure 3-25a) is short and light but has relatively high boattail drags. The iris convergent nozzle (Figure 3-25b) is longer and heavier to achieve the same required nozzle throat area change between the afterburning and non-afterburning engine operating conditions due to the long translating, cantilevered flaps involved. However, this yields a shallower boattail angle and consequently a lower boattail drag than the short flap convergent nozzle. This is true, in general, for either the boattail of an isolated nozzle or the more complex aftbody-nozzle fairing employed in an aircraft installation. Convergent-divergent (C-D) nozzles are used when the nozzle pressure ratios required are significantly greater than the critical value. They are heavier than the convergent nozzle but give large improvements in supersonic performance for airplanes having missions requiring long periods of supersonic operation. The C-D nozzle (Figure 3-25c) eliminates the detrimental steep boattail of the short flap convergent nozzle and lends itself to an optimum area ratio scheduling. If the engine requires secondary air for engine cooling purposes, or if the aircraft mission justifies the weight and complexity of a secondary flow system when using an engine which does not require external cooling, a version of a C-D nozzle known as a convergent-divergent ejector becomes desirable. This nozzle system (Figure 3-25d) allows the required inlet bleed flows to be utilized for nacelle purging, engine cooling, and the relief of pressure differentials across the engine case. The secondary flow also provides cooling for the nozzle and helps eliminate overexpansion of the primary nozzle gases. Plug nozzles (Figure 3-25e-f) present interesting possibilities for airbreathing propulsion. The exhaust area of plug nozzles can be varied by expanding and collapsing the plug, by translating the plug and by actuating cowl mounted flaps. The plug allows lower boattail angles during non-afterburning operation than an equivalent convergent nozzle, and wider area ratio variations can be accommodated within a given flap size limitation than for conventional C-D nozzles.

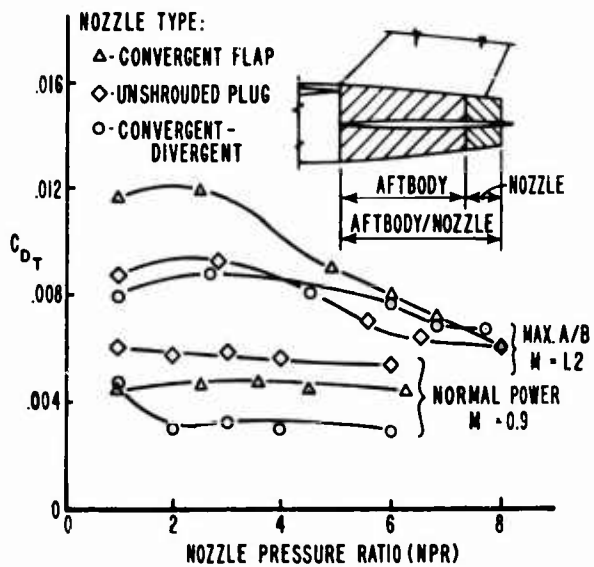


### BASIC AXISYMMETRIC NOZZLE DESIGNS

Figure 3-25

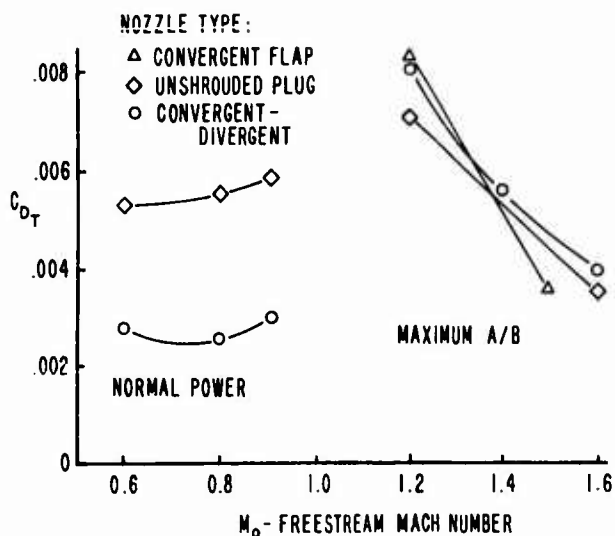
Some of the aftbody/nozzle configuration variables to examine during development tests are nozzle type, interfairing type and length, vertical stabilizer type and lateral spacing. Data applicable to such changes are presented in Figures 3-26 through 3-32 for a typical twin-jet fighter aircraft. The data presented includes the external drag of the aftbody/nozzle combination as shown on Figure 3-26. The value of the drag coefficients plotted exclude the drag of the tails but not their influence on the aftbody and nozzle.

The geometrical differences in nozzle types can influence the external flow field sufficiently to greatly alter the drag coefficients of the nozzle boattail and aftbody. The effect of nozzle geometry on total aftbody/nozzle drag as a function of nozzle pressure ratio is shown in Figure 3-26. In general, the long, smooth contours of the C-D type nozzles are needed to obtain the lower drags. Typical aftbody/nozzle drag coefficients for nozzles operating at their design pressure ratios are given in Figure 3-27. Since the differences in drag are highly dependent on Mach number, the choice of nozzle type must be made with mission requirements in mind.



EFFECT OF NOZZLE TYPE ON TOTAL AFTBODY/NOZZLE DRAG

Figure 3-26



TOTAL AFTBODY/NOZZLE DRAG - TYPICAL MISSION APPLICATIONS

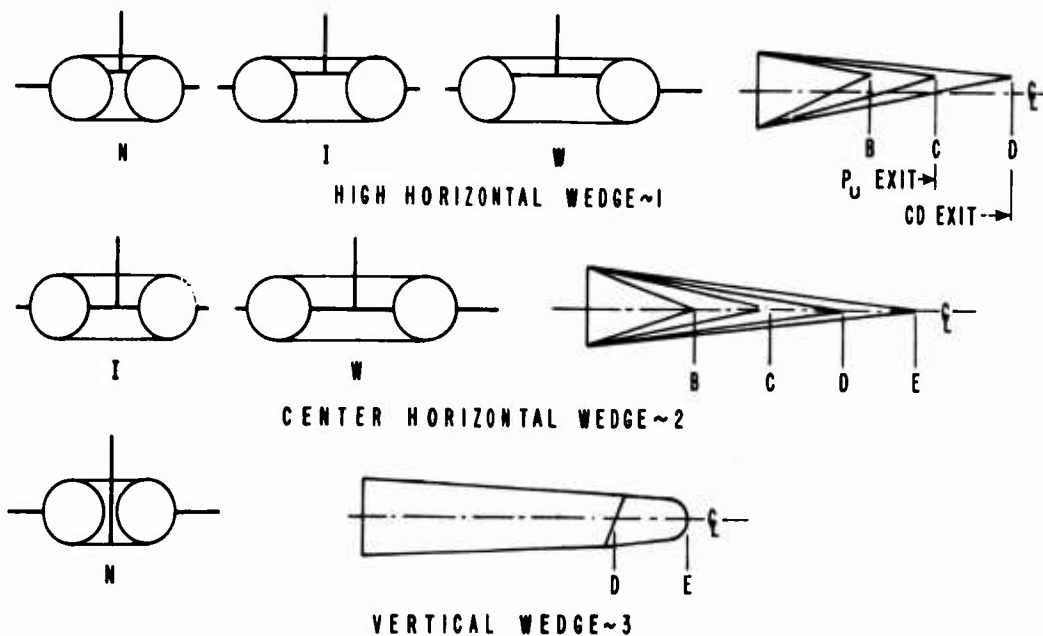
Figure 3-27

Twin engine fighter aircraft with conventional axisymmetric nozzles will have an interfering between the nozzles. As the interfering type or length is changed, the nozzle boattail, aftbody boattail, and total aftbody/nozzle drag coefficients vary. Shown in Figure 3-28 are some variations in interfering type and length that were made on the twin jet fighter model. Some of the changes in the aftbody/nozzle drag coefficients due to these variations are given in Figures 3-29 and 3-30. At the subsonic Mach number, the drag is significantly lower for a horizontal wedge interfering than for a vertical wedge (Figure 3-29), and the aftbody/nozzle drag generally decreases with increasing interfering length (Figure 3-30). Figure 3-31 presents the effect of changing the vertical stabilizer type and position on the total aftbody/nozzle drag coefficient. At all Mach numbers, a change from a single to twin vertical stabilizers increases the total aftbody/nozzle drag coefficient on a C-D nozzle installation. (Note that stabilizer drag is not in the measurement.)

AFTBODY/NOZZLE CONFIGURATION KEY

EXAMPLE: N I B  
 NOZZLE SPACING RATIO "N"  
 INTERFERING TYPE "I"  
 INTERFERING LENGTH "B"

SPACING RATIO  
 N - NARROW  
 I - INTERMEDIATE  
 W - WIDE



INTERFERING NOMENCLATURE

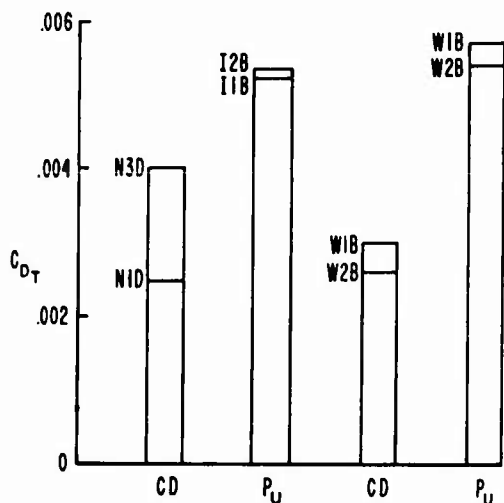
Figure 3-28

NOZZLE TYPE:  
 CD - CONVERGENT-DIVERGENT  
 P<sub>U</sub> - UNSHROUDED PLUG

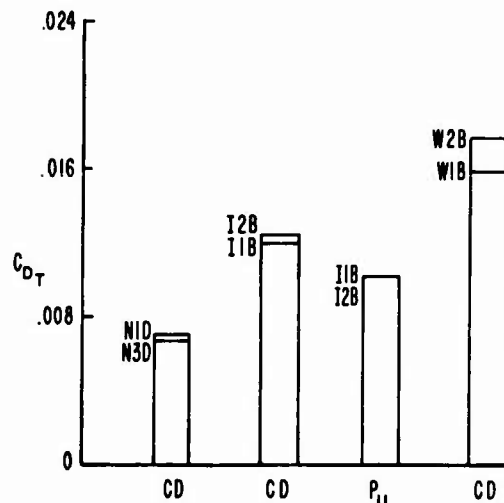
SPACING RATIO:  
 N - NARROW  
 I - INTERMEDIATE  
 W - WIDE

INTERFAIRING TYPE:  
 1 - HIGH WEDGE  
 2 - CENTER WEDGE  
 3 - VERTICAL WEDGE

INTERFAIRING LENGTH:  
 B - SHORTEST  
 C - P<sub>U</sub> EXIT  
 D - CD EXIT  
 E - LONGEST



a. NORMAL POWER NOZZLES  
 M<sub>0</sub> = 0.9 NPR = 4.0



b. MAXIMUM A/B NOZZLES  
 M<sub>0</sub> = 1.2 NPR = 6.0

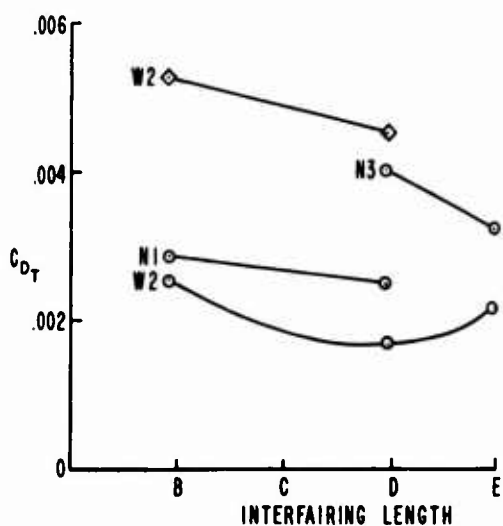
EFFECT OF INTERFAIRING TYPE ON TOTAL AFTBODY/NOZZLE DRAG

Figure 3-29

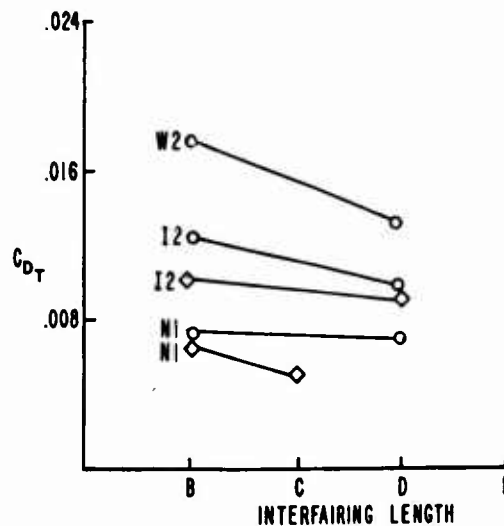
NOZZLE TYPE:  
 ◇ ~ UNSHROUDED PLUG  
 ○ ~ CONVERGENT-DIVERGENT

SPACING RATIO:  
 N ~ NARROW  
 I ~ INTERMEDIATE  
 W ~ WIDE

INTERFAIRING TYPE:  
 1 ~ HIGH WEDGE  
 2 ~ CENTER WEDGE  
 3 ~ VERTICAL WEDGE



a. NORMAL POWER NOZZLES  
 M<sub>0</sub> = 0.9 NPR = 4.0

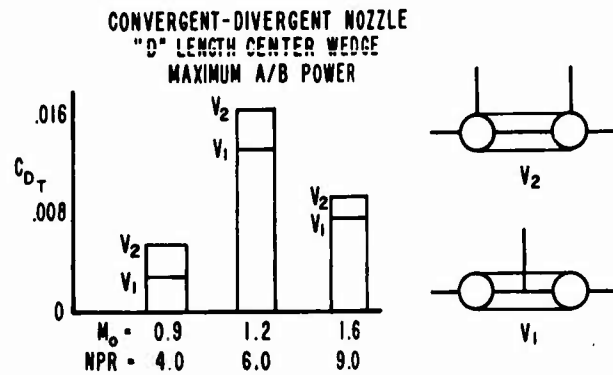


b. MAXIMUM A/B NOZZLES  
 M<sub>0</sub> = 1.2 NPR = 6.0

EFFECT OF INTERFAIRING LENGTH ON TOTAL AFTBODY/NOZZLE DRAG

Figure 3-30

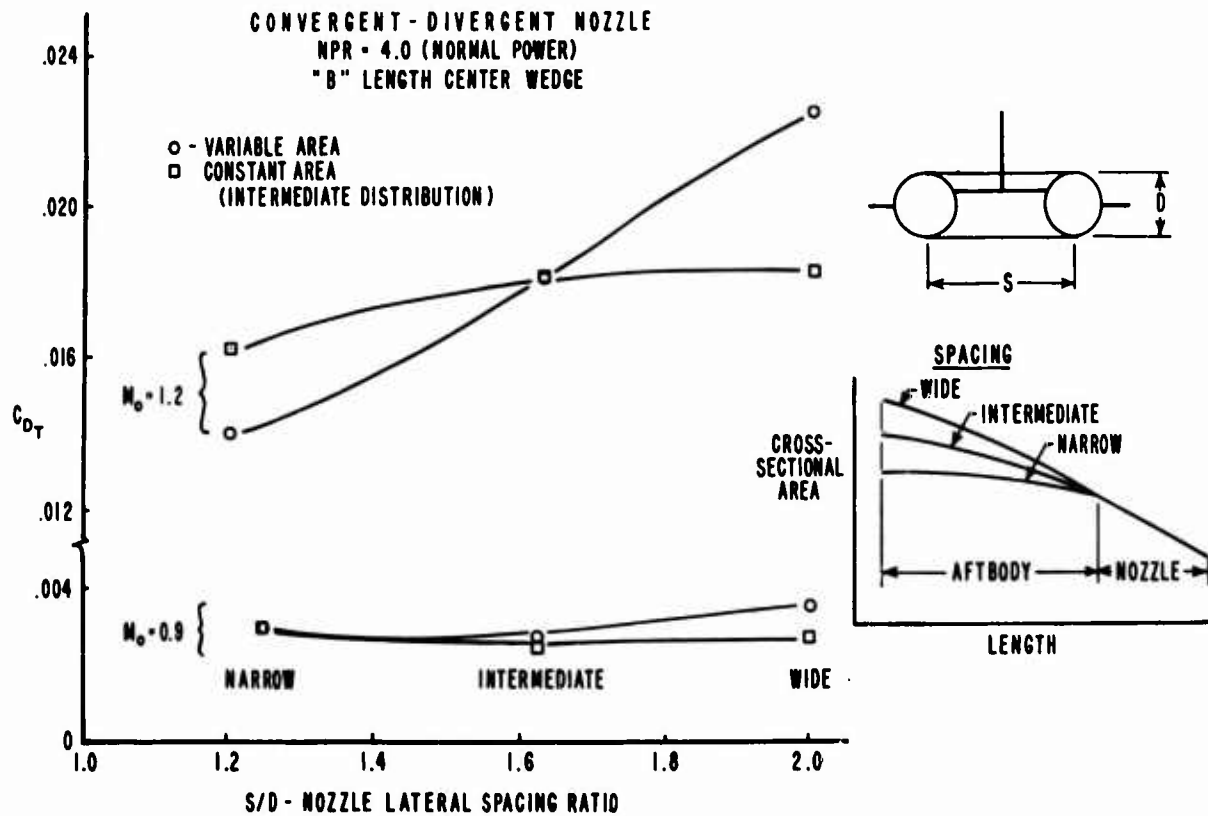
15-20



**EFFECT OF VERTICAL STABILIZER ON TOTAL AFTBODY/NOZZLE DRAG**

Figure 3-31

Keeping a constant interfering type and varying the nozzle spacing ratio changes the aftbody component drag. Figure 3-32 shows the effect of nozzle lateral spacing on total aftbody/nozzle drag coefficient for variable and constant aftbody area distribution. For the total aftbody/nozzle drag coefficient, the nozzle lateral spacing ratio effect is negligible up to a Mach number of 0.9 but the effect becomes significant above a Mach number of 1.0 where wave drag effects become predominant when the aftbody area distribution is allowed to increase with spacing ratio.

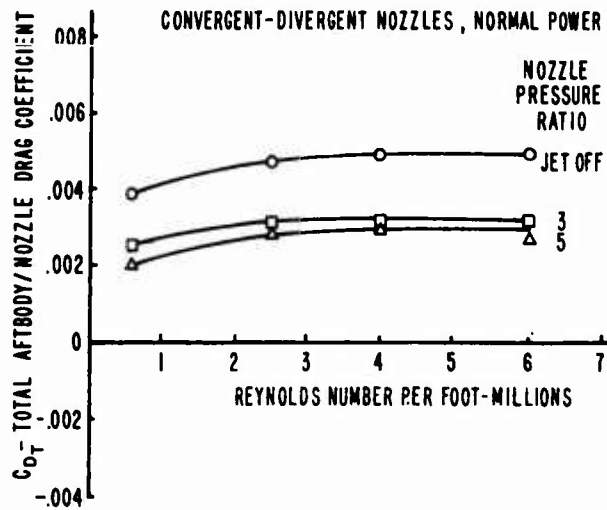


**EFFECT OF NOZZLE LATERAL SPACING ON TOTAL AFTBODY/NOZZLE DRAG**

Figure 3-32

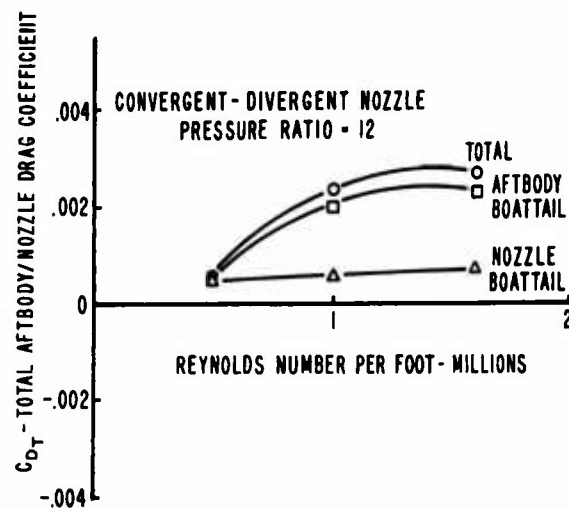
### 3.4 Effect of Reynolds Number on Performance

Further results from the twin-jet aircraft model tests indicated that the total aftbody/nozzle drag coefficient increased with increasing Reynolds Number both subsonically and supersonically. Typical results of these tests at subsonic and supersonic Mach numbers are shown in Figures 3-33 and 3-34 respectively. The total aftbody/nozzle drag coefficient for the subsonic Mach number reached a plateau for a Reynolds Number between 4 to 6 x 10<sup>8</sup>/ft, whereas the drag coefficient at a freestream Mach number of 2.0 appears to approach a plateau at a Reynolds Number of 1.6 x 10<sup>8</sup>/ft. Static and total pressure data obtained during these tests substantiated the external drag trends with Reynolds Number. Boundary layer rake data indicated a decrease in boundary layer displacement and momentum thicknesses with increasing Reynolds Number.



EFFECT OF REYNOLDS NUMBER ON TOTAL AFTBODY/NOZZLE DRAG,  $M_0 = 0.9$

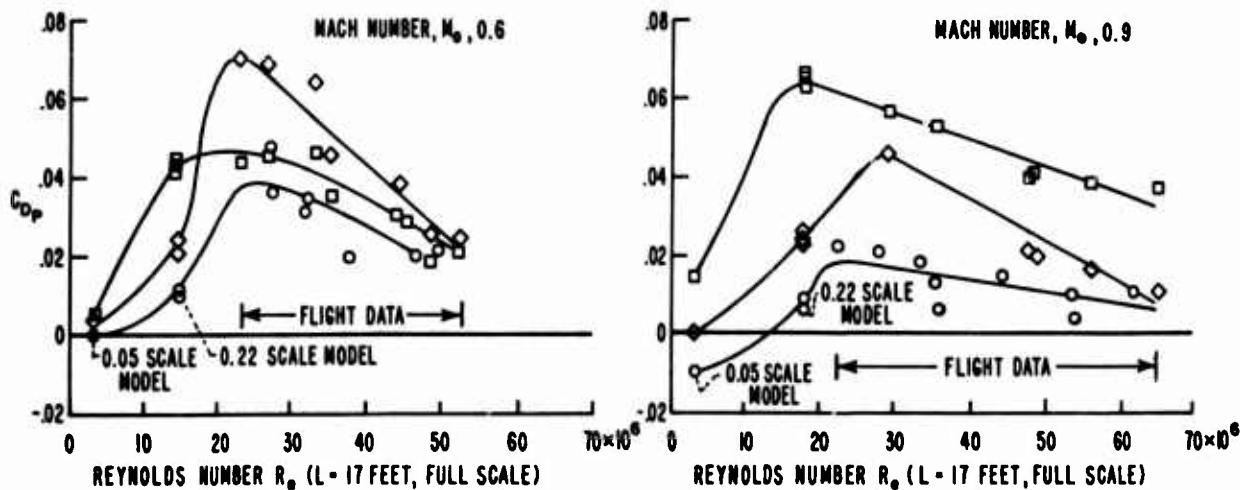
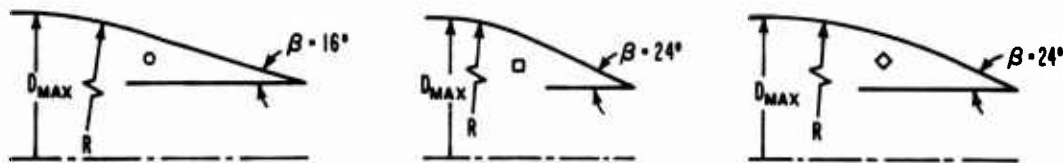
Figure 3-33



EFFECT OF REYNOLDS NUMBER ON TOTAL AFTBODY/NOZZLE DRAG,  $M_0 = 2.0$

Figure 3-34

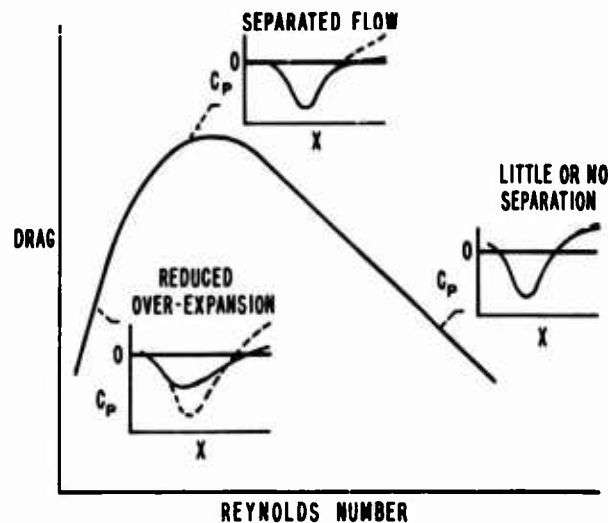
Similar data was obtained from another investigation (Reference 3) in which the Reynolds Number was varied in the wind tunnel by testing different scale models and in flight by varying altitude. Tests were run on an underwing nacelle installed on a modified F-106 aircraft and two different scale wind tunnel models. The highest installed aft nacelle nozzle boattail drag coefficient was obtained at intermediate Reynolds Numbers corresponding to the lower flight values and those of the 22% scale model. As shown in Figure 3-35, significantly lower drag was obtained at both higher and lower Reynolds Numbers. The trend of the drag coefficient at the lower Reynolds Number is similar to that observed in the wind tunnel data for the twin-jet fighter investigation.



EFFECT OF REYNOLDS NUMBER ON NOZZLE BOATTAIL DRAG COEFFICIENT

Figure 3-35

Two different flow phenomena appear to occur which change the aftbody/nozzle external static pressure distributions and drag. These changes are shown schematically in Figure 3-36. At the very low Reynolds Number, the degree of overexpansion on the aftbody/nozzle is small. In this case, the effective boattail angle has been reduced due to the presence of a relatively thick boundary layer and only a very small recompression is needed to minimize the drag. At the intermediate Reynolds Numbers, a reduced boundary layer thickness increases the effective boattail angle leading to greater overexpansion and insufficient recompression to maintain low drag. According to the data, flow separation can be extensive at these intermediate Reynolds Numbers, thus preventing any significant recompression. The separation point is closest to the boattail shoulder at the intermediate Reynolds Number and moves farther aft as the Reynolds Number increases. The overexpansion remains essentially the same at the higher Reynolds Numbers, but the separation is reduced and the flow recompresses significantly above the freestream static pressure to again reduce the drag.



SUMMARY OF REYNOLDS NUMBER EFFECTS

Figure 3-36

The results of these investigations show a significant change in aftbody/nozzle drag coefficients due to changes in flow conditions which appear to be attributable to variations in Reynolds Number. However, other factors such as changes in scale and nonsymmetrical flow separation may have a significant effect on the results. These data indicate that it can be very difficult to predict absolute full scale aftbody/nozzle drag coefficients with limited wind tunnel data. Additional data (from both flight and wind tunnel tests) are required to define the primary sensitivity variables and describe aftbody/nozzle drag sensitivity to those variables.

#### 4.0 Theoretical Analysis

##### 4.1 Inlet Drag Analysis Techniques

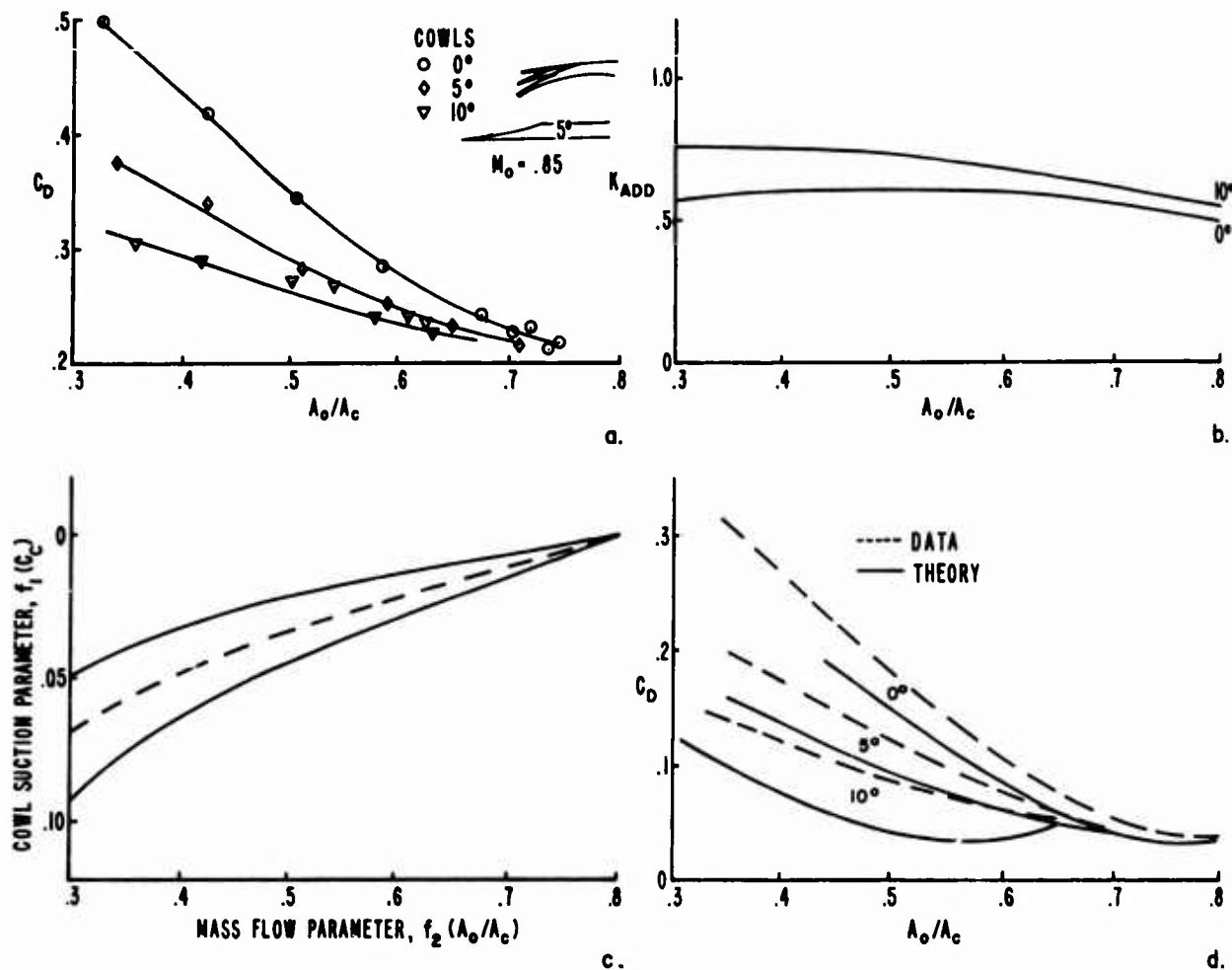
Inlet drag analysis procedures are required (consistent with current force counting procedures) to predict that portion of inlet drag chargeable to the propulsion system. Many analytical techniques have been documented previously, and some are widely used either in their basic format or together with some special modification resulting from other data comparisons or predictions. The success of most of these procedures seems, however, to be directly related to the degree of similarity between the configuration analyzed and the configuration for which the analysis procedure was developed. Generally, system developments have initially used parametric data from similar configurations in a preliminary assessment of inlet performance. Later, when a basic configuration has been identified for development, more "sophisticated" procedures have been employed.

Typical of the preliminary analysis procedures employed is one for which the  $K_{ADD}$  factor was developed some time ago. Inlet spillage drag coefficient ( $C_{D_{SPILL}}$ ) data were obtained on a series of isolated models with variations in cowl geometry (Figure 4-1a). This experimental inlet drag was then compared with a simplified theoretical assessment on the same configuration to arrive at  $K_{ADD}$  factors of additive drag ( $C_{D_{ADD}}$ ) which were used to calculate the spillage drag ( $C_{D_{SPILL}} = K_{ADD} C_{D_{ADD}}$ ) shown in Figure 4-1b. While these parameters have been developed on simplified inlets, they are many times applied to very complex configurations. The data obtained during these tests have been reviewed by other sources in order to develop another correlation parameter,  $\Delta C_{LIP\ SUCTION}$  (Figure 4-1c). This empirical relation has been developed to give greater confidence in estimating the cowl suction effects for varying geometry. The relationship employed,

$$C_{D_{SPILL}} = C_{D_{ADD}} - \Delta C_{LIP\ SUCTION}$$

still requires a theoretical assessment of  $C_{D_{ADD}}$ , and is based on the same isolated data. This is still basically an example of a curve fit of experimental data even though it is based on some of the geometric inlet characteristics.

Both of these correlations are based on a simple one-dimensional analytical solution for the additive drag utilizing the momentum equation. Others have attempted more in-depth analytical procedures based on evaluation of the flow field surrounding the inlet. One such technique is illustrated in Figure 4-1d. In this case, a compressible, two dimensional, potential flow solution has been developed using finite difference techniques and applied to the data of Figure 4-1a. The data however, has been shifted to agree with the theoretical calculation at the maximum mass flow. It appears that this purely theoretical technique does provide reasonable estimates of the drag slope, but its ability to reproduce experimental drag levels at a given mass flow ratio may still be questioned.

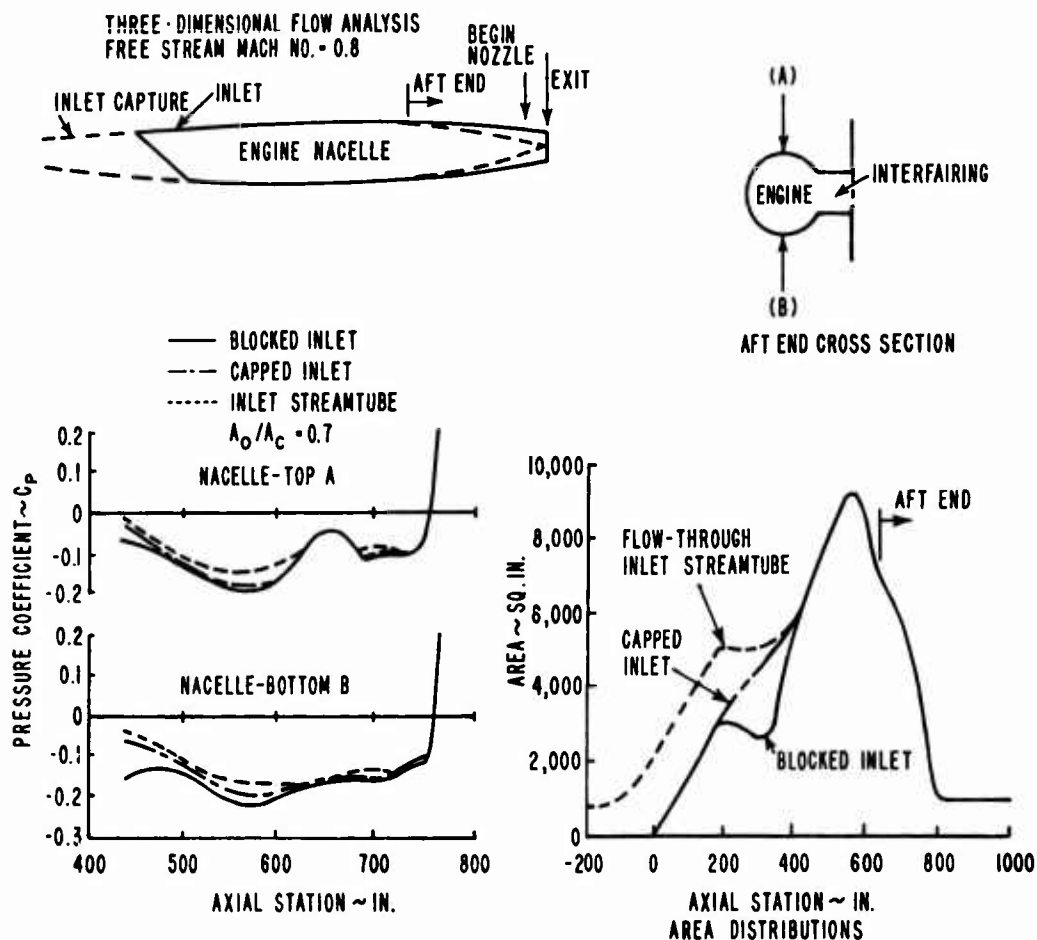


### INLET DRAG CORRELATIONS

Figure 4-1

A basic shortcoming of these and most other inlet drag analysis procedures is the fact that they treat the inlet as an isolated subsystem. It is considered necessary that the inlet analysis be performed consistent with the total aircraft performance analysis. Forebody flow analysis procedures should be used to define the inlet flow field for input into inlet performance calculations. Similarly, as part of the inlet analysis, an effort should be made to assess the impact of the inlet flow condition or geometry on the rest of the aircraft. Experimental assessments of these effects have been made and it seems reasonable that part of the preliminary design efforts should include theoretical analysis to predict them. While no single analysis procedure has been developed as yet that gives completely reliable and accurate results, recent advances do offer the possibility of at least qualitatively assessing some of the more complex flow interactions. Illustrated in Figure 4-2 are the results of a three dimensional transonic potential flow solution applied to a twin engine aircraft configuration. In this illustration the effect of inlet flow condition on nacelle pressure distribution does indicate some effects considerably downstream of the inlet station. This theory is basically inviscid; hence, some of the effects would be altered if the boundary layer was included, especially for cases where flow separation could be predicted. Theory such as this should be applied to test configurations in order to help identify the extent of model simulation required during component drag tests to properly account for all forces. It also appears quite reasonable to employ procedures of this sort during early development to augment the evaluation of all inlet design trades to be considered.

Extensive development of analytical procedures, both simplified and rigorous, are still required in the inlet/airframe area. The techniques used today still leave many unresolved questions. Unfortunately, many times the analysis procedures are dropped when experimental test data begins to be obtained. As a system program continues, less and less detailed data is taken. Finally, when flight tests take place, there is so little data taken that it is impossible to determine component drag levels from the overall measure of aircraft performance. It would appear that an in-depth program is required which combines unified analysis with heavily instrumented wind tunnel models and flight test aircraft to develop a sound analytical tool and define such things as scale and Reynolds number effects.



### PREDICTED TWIN-JET NACELLE PRESSURE DISTRIBUTIONS

Figure 4-2

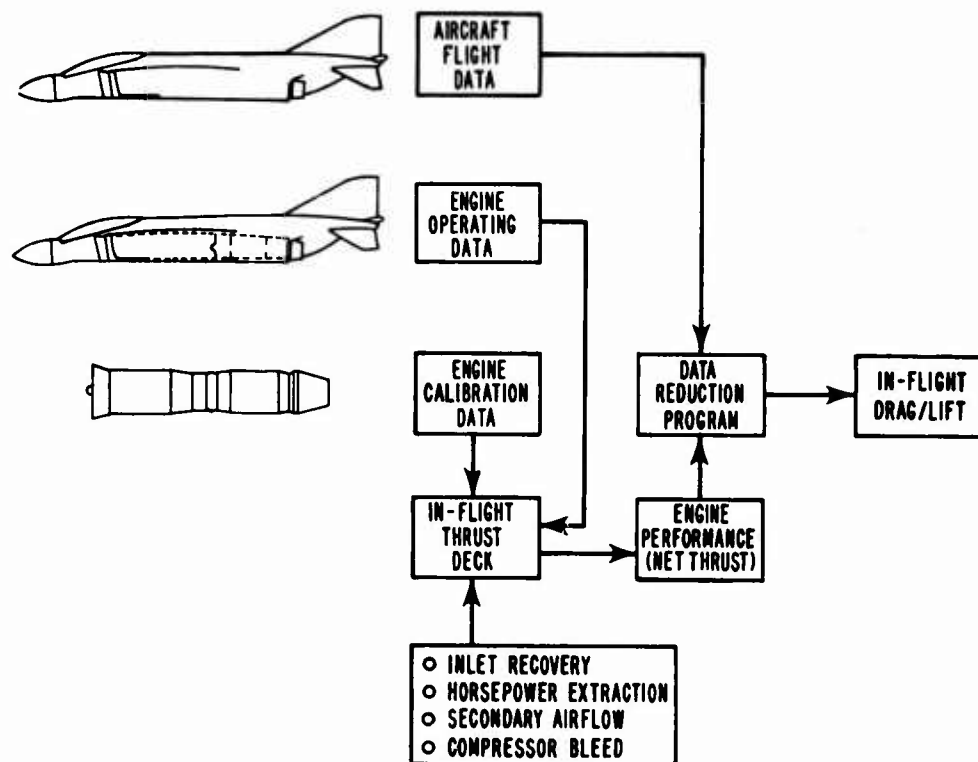
#### 4.2 Aftbody/Nozzle Drag Analytical Techniques

Recent extensive investigations of analytical and empirical techniques for predicting the drag associated with the nozzle and aftbody have concluded that available analytical methods are not capable of accurately predicting the absolute drag levels but are useful in predicting the trends of aftbody pressure distributions. Some data correlation procedures using empirical techniques have been partially successful in predicting the drag of particular configurations. The most critical flow situation is in the transonic flight regime where the discrepancy between theory and experiment is still considerable.

Flow phenomena that require a deeper analytical investigation include the jet effects on the base and boattail pressures and the extent of mixing between the plume and freestream. An assumption of constant pressure mixing in the wake and the fact that shear stress normal gradients are normally neglected in the base pressure analyses has led to inaccurate results. The separation criteria used to date have not been completely reliable, since they usually do not consider viscous effects. The boundary layer and Reynolds number effects on the boattail and nozzle plug pressures cannot be neglected and the superposition principle presently used to couple the viscous and inviscid solutions to account for boundary layer displacement is inadequate to account for the relatively thick boundary layer over the aftbody and nozzle. It appears that 3-D analyses, both viscous and inviscid should be considered to obtain better results even though they present major mathematical complexities. Some of the analytical methods that could be used are time dependent techniques which can account for the presence of embedded shocks on the afterbody.

#### 5.0 Flight Performance Prediction

The usefulness of theoretical and experimental estimates of aircraft performance may be measured by the accuracy with which they predict actual in-flight performance. Although this statement appears to be self-evident, the actual accomplishment of wind tunnel flight test correlation is extremely difficult. One example of some of the difficulties encountered has involved the comparison of flight performance projections based on a variation of the conventional test and accounting procedures described in Section 2.0 with in-flight drag and lift calculated in the manner shown in Figure 5-1.



### IN-FLIGHT DRAG/LIFT CALCULATION

Figure 5-1

In this calculation procedure, the engines used in the flight test were calibrated in an engine test facility. Such data, however, must be corrected (most likely in the IN-FLIGHT THRUST DECK) by means of wind tunnel data in order to reflect internal nozzle thrust levels which are more nearly correct. The figure also shows additional corrections leading to a net thrust term, but the actual calculation employed to determine drag and lift are given in the following equation:

$$\text{DRAG: } C_D = \frac{1}{q_s} (F_G \cos(\alpha + \epsilon) - D_R - W \sin \gamma - \frac{W}{g} \frac{dV}{dt} - \frac{V}{g} \frac{dW}{dt})$$

$$\text{LIFT: } C_L = \frac{1}{q_s} (W \cos \gamma - F_G \sin(\alpha + \epsilon) + \frac{W}{g} V \frac{d\gamma}{dt})$$

Where

- $D_R$  = Ram Drag
- $F_G$  = Gross Thrust
- $*g$  = Acceleration Due to Gravity
- $q$  = Dynamic Pressure
- $*s$  = Wing Reference Area
- $V$  = Airplane Velocity

$\frac{dV}{dt}$  = Acceleration Rate

$W$  = Weight

$\frac{dW}{dt}$  = Time Rate of Change of Weight

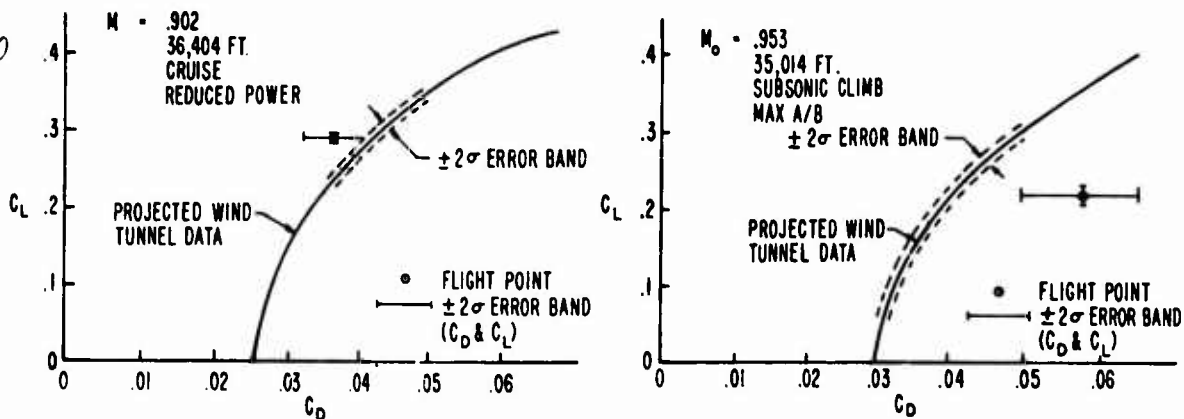
$\alpha$  = Angle of Attack

$\gamma$  = Flight Path Angle

$*\epsilon$  = Angle Between Thrust Vector and Wing Chord Plane

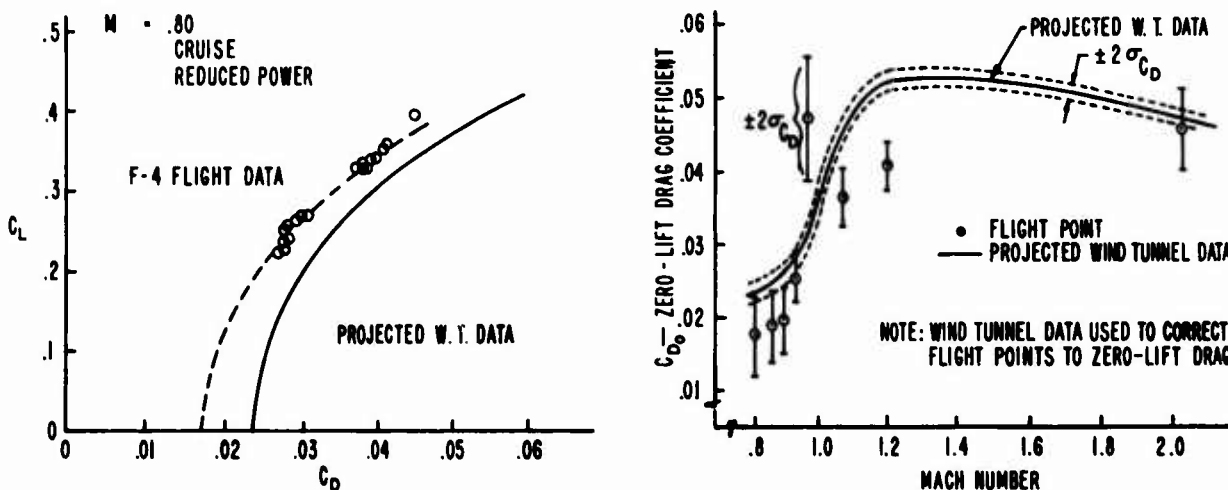
The asterisked elements are the only ones which are not sources of error. Figure 5-2 shows two sample calculations of in-flight drag and lift at transonic Mach numbers compared to projected wind tunnel data. In the case of both flight and projected wind tunnel estimates, attempts have been made to define  $\pm 2\sigma$  error bands based, apparently, on the data scatter associated with each element of the calculation. Over 90% of the variance ( $\sigma_{C_D}^2$ ) associated with the flight data drag estimates stems from uncertainty in gross thrust measurements. The wind tunnel data has been used as illustrated in Figure 5-3 to correct flight data points to a zero-lift drag condition. Eight of the flight drag points thus generated are compared with a curve of the projected wind tunnel data in Figure 5-4. In order to facilitate this data comparison, a variation of the conventional force accounting system has been employed in which all variations in Inlet Drag model forces and Jet Effects model forces between the Aerodynamic F & M model reference conditions and aircraft operating conditions have been assigned to the aircraft drag and included in the drag polar.

15-26



COMPARISON OF IN-FLIGHT PERFORMANCE WITH PROJECTED WIND TUNNEL DRAG POLARS F-4

Figure 5-2



FLIGHT DATA EXTENSION TO ZERO LIFT CONDITION

Figure 5-3

COMPARISON OF FLIGHT DATA WITH PROJECTED WIND TUNNEL DATA AT ZERO LIFT

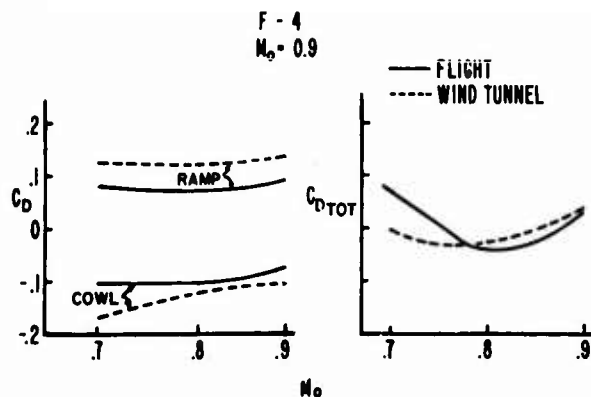
Figure 5-4

No detailed explanation has been offered for the large differences between flight test and projected wind tunnel drag levels; however, several possible sources for the discrepancy have been suggested. They include:

- a. Inadequate corrections for Roughness and Protuberances
- b. Wind Tunnel Blockage, Shock Reflection Effects
- c. Test Techniques
  - Failure to eliminate strut interference
  - Failure to duplicate Inlet/Aftbody Flowfield Interactions
  - Failure to simulate hot gas effects
- d. Scale and Reynolds number effects
- e. Incorrect assessment of In-Flight Inlet/Engine operating characteristics

One of the more important aspects of this comparison is that when the discrepancy occurs, it is impossible to isolate the sources of the differences. The design development by means of test models and the method of flight test were not compatible with a requirement for wind tunnel flight test correlation. Recognition of this problem emphasizes the need for extensive model pressure instrumentation in addition to provision for force measurements. Then, by careful distribution of pressure instrumentation on the aircraft, flow field development in critical regions can be examined in order to obtain at least a qualitative comparison of drags on specific elements.

One attempt to arrive at a flight test level of inlet drag produced the results shown in Figure 5-5. Although the agreement in total inlet drag for some conditions is quite good, the projected cowl and ramp drags show substantial disagreements. The data in this case was obtained from pressure integration of a limited number of taps. This problem coupled with the inaccuracy of the various measurements of flight condition and engine airflow is felt to make the flight data highly questionable.



**INLET DRAG ~ COMPARISON OF FLIGHT  
AND WIND TUNNEL DATA**

Figure 5-5

## 6.0 Conclusions

From the foregoing discussions, the following conclusions are made:

1. Modern aircraft require extremely careful design development in the area of airframe/propulsion integration in order to take maximum advantage of improvements in aerodynamic design and propulsion system efficiency. This work must, however, be done as an integral part of the total aircraft development.
2. A force accounting system which effectively integrates both aerodynamic and propulsion forces and moments acting on an aircraft must be generated during the period of early design development. This accounting system must, throughout the aircraft development cycle, provide for consistent comparison of vehicle and component performance assessments by theoretical analysis, wind tunnel test data, and/or flight test data.
3. Aircraft development wind tunnel test programs must be carefully devised and the model designs coordinated in order to assure delineation of inputs to the force accounting system without introducing large extraneous influences. Otherwise, the combination of several wind tunnel test models to generate aircraft performance estimate can result in drag and lift errors due to model mounting system interference effects or failure to adequately simulate model geometry and the associated flow fields.
4. Available inlet drag data from simple models may be used in the establishment of basic preliminary trends, but the actual development and assessment of the performance of a particular design must be accomplished by means of wind tunnel tests designed to measure the total effect of inlet design and operation on aircraft performance.
5. Several aftbody/nozzle design parameters are important to the determination of total aircraft performance. Influences of nozzle type, interfairing geometry and length, stabilizer geometry, and spacing ratio must be carefully examined in conjunction with aircraft mission requirements in order to assure maximum performance.
6. Recent test programs have indicated an aftbody/nozzle drag sensitivity to Reynolds Number which results in a drag peak at intermediate Reynolds Numbers. Close examination of these results, however, suggests that the drag depends heavily on afterbody boundary layer development and separation which are, in turn, probably dependent upon a combination of model scale and Reynolds Number variations.
7. Theoretical analysis techniques for the prediction of inlet and aftbody/nozzle forces and moments have not, in the past, proved to be highly successful. Some of the three-dimensional compressible computations being developed presently, however, offer hope of better qualitative flow phenomena description in the future. Such a capability is especially important during early aircraft design development.
8. Improvements are required in the coordination of data measurement techniques between wind tunnel and flight tests. Detailed force and pressure measurements should be employed on wind tunnel models to provide accurate performance predictions, but it is also considered highly advisable to provide for selected pressure measurements on the aircraft in order to establish data correlations in critical flow regions.

1. Schumacher, H.E., and Trent, W.C.; "Significant Considerations in the Development of Engine/Airframe Systems for High Performance Aircraft", JANNAF/AIAA/SAE Propulsion Meeting, New Orleans, Louisiana, 27-29 November 1972; MCAIR 72-042.
2. Airframe/Engine Integration, AGARD Lecture Series No. 53, May 1972, AGARD-LS-53.
3. Chamberlin, R. and Blaha, B.J.; "Flight and Wind-Tunnel Investigation of the Effects of Reynolds Number on Installed Boattail Drag at Subsonic Speeds", AIAA Paper 73-139.
4. Engine-Airplane Interference and Wall Corrections in Transonic Wind Tunnel Tests, AGARD Advisory Report No. 36, August 1971, AGARD-AR-36-71.
5. Inlets and Nozzles for Aerospace Engines, AGARD Conference Proceedings No. 91, December 1971, AGARD CP-91-71.
6. Osmon, R.V.; "Improved Methods of Spillage Drag Prediction for Two-Dimensional Supersonic Inlets", Northrop Corporation, Norair Division, Hawthorne, California, AIAA Paper 67-449.

THE PROBLEM OF INSTALLING A MODERN HIGH BYPASS  
ENGINE ON A TWIN JET TRANSPORT AIRCRAFT\*

17-1

by

Walter C. Swan and Armand Sigalla  
The Boeing Commercial Airplane Company  
Renton, Washington, U.S.A.

ABSTRACT

An examination of the engine placement on a modern jet transport presents new drag and stability problems. Large high bypass ratio engines create large annular and wetted area drag and blockage surfaces which can cause difficult configuration problems as well as large interference drag and stability effects. The option is open to conventional underwing and aftbody mounted installations as well as renewed opportunity for over-the-wing installations. In this paper the drag and stability consequences for each class of configuration is examined for a typical intermediate range transport. The results are equally valid for short haul and certain STOL missions. In some instances, it is shown, proper pod shape and positioning may result in favorable drag increments, especially on modern swept wings with supercritical airfoil sections. Side effects such as pod influences on wing flutter, deep stall, and general sizing of the empennage are discussed.

SUMMARY

Factors affecting the location of the modern high bypass ratio engine and propulsion system on an airplane are reviewed using the jet transport as an example. The configuration options that are examined include conventional underwing and aftbody mounted engine installations, and it is shown that a renewed opportunity exists for over-the-wing engine installations. The influence of each class of installation upon the airplane is examined, with results derived basically for a typical intermediate range transport and for airplanes designed for short haul and certain STOL missions.

Finding the best place for the engines is an activity involving virtually all the disciplines of aeronautical engineering. The engine location influences the cruise drag decisively, and very high performance and speed losses will result from an installation that is less than very good. The structural weight of the airplane is affected in many ways by engine location. Putting the engines on the wing will influence strongly, as one might expect, the weight of the wing; and it is shown that relief of airloads, flutter, and impact upon stalling speed are all factors to be considered in the design of the installation.

The placement of the engines will influence the location and size of the vertical and horizontal tail and control surfaces. The weight of the propulsion system is an important factor that determines the location of the center of gravity of the airplane, thus affecting directly longitudinal stability and control requirements. Also, large yawing moments can be produced in some engine-out conditions affecting similarly directional control requirements, and attention has to be given to the effects of jet flow on the control surfaces to prevent unfavorable interactions in certain flight conditions.

The field performance of an aircraft is particularly sensitive to engine location. It is shown that engine location and size does influence the maximum lift-coefficient of an airplane as well as its lift-drag ratio in the high-lift mode. It is also shown that engine location affects the engine noise heard on the ground below an airplane. This can happen when the source of noise is shielded by an airframe component.

It is found that engine size variations, such as those that occur when turbofan engines of different bypass ratios are considered, affect the choice of engine location. The high bypass engine with its large annular and wetted area poses a more difficult airframe-engine integration problem. The flutter problem is complicated by the lift on the nacelles, and it is more difficult to achieve low drag. In some instances, however, proper pod shape, pod location, as well as the application of area-rule and streamline contour principles may result in favorable drag increments. Experimental results are shown illustrating these effects.

Airplanes with wing-mounted engines and airplanes with fuselage-mounted engines each have their good points and their problems, and very careful analysis and laboratory work are necessary to determine which of the two is better for a given mission, type of airplane, and type of engine. It is shown in this paper that after such a general choice is made that additional investigations are necessary to find detailed specific engine locations. It is further indicated that overwing engine installations offer certain attractive options and these are reviewed.

ACKNOWLEDGEMENT

The authors wish to acknowledge in particular the help of Emmett Omar, Lowell Richmond, and Henry Showber of The Boeing Commercial Airplane Company in assembling the data presented in this paper.

\* Some of the data shown in this paper have been obtained in cooperation with Aeritalia SPA of Naples as part of a joint Boeing/Aeritalia project. The authors wish to thank Aeritalia for permission to present such data.

## INTRODUCTION

Designing engine nacelle installations for low drag is one of the more challenging problems of aerodynamics. Analysis of the flow is complex, involving the interaction of the flow from different airplane components. In addition, as is often the case, it is not possible to design for low drag alone, and one is constrained by many other considerations which make the problem more difficult; and the selection of a good nacelle installation is the result of compromise with aerodynamic drag, one of many factors albeit a dominant one.

The introduction of the efficient high bypass ratio turbofan engine has brought about renewed interest in the problems of engine placement. The current family of high bypass ratio engines was designed specifically for the so-called "jumbo" airplanes, like the military C-5A transport or the wide-bodied commercial jets. These engines are very efficient but also of large size for given installed cruise thrust. Designing smaller airplanes around such engines poses, therefore, new problems of engine-airframe integration.

The primary object of this paper is to review the problems of installation of high bypass ratio turbofan engines and to examine possible solutions. This will be done considering a medium range, twin-engined subsonic transport aircraft on which there are essentially two options for the location of the engines. The engines can be either wing-mounted or fuselage-mounted but many different versions of these two basic locations may be considered. That there is no obviously clear choice is apparent from the fact that almost every conceivable variation has been tried at least once. Indeed, many airplanes with quite different engine installations have met equal success apparently without obviously different characteristics that could be related directly to the engine installation. Yet, where the engines go on the airplane does matter a great deal, and the best location must follow from the type of mission that one is after, the size of one's airplane, the relative size of the engines, and the specific performance objectives.

Problems that are basically independent of the size and type of the engine will be reviewed at first for airplanes with conventional underwing engines and for airplanes with the engines on the aft-fuselage, respectively. It will be seen that structural and configuration aspects have a strongly constraining influence on the decision that determines engine location with aerodynamic expertise necessary for the detail design to avoid large drag penalties. As the relative size of the nacelle gets larger, because of bypass ratio increase, increasing penalties become associated with the installation and these subtract from the inherent benefits of the high bypass ratio engine. Although the constraining influences are qualitatively the same as for smaller bypass ratio engines, the penalties due to poor design can be much greater and aerodynamic design skill becomes of increasing importance. It is necessary to design low drag installations within tighter constraints and there is need to search for new installation concepts that will eliminate some of these constraints. For instance, putting the engines on top of the wing rather than under the wing virtually eliminates constraints associated with landing gear length, assuming that the former installation is aerodynamically possible.

In the next section of this paper, following this introduction, the advantages and disadvantages of conventional underwing engines are discussed. This is then followed by a review of the factors affecting airplanes with fuselage-mounted engines. Following that the specific influence of relative engine size upon engine placement is discussed and then the less orthodox airplane with overwing-mounted engines is considered.

## UNDERWING ENGINE INSTALLATIONS

Let us consider a subsonic airplane with a reasonably high aspect ratio wing. It is desired to investigate a configuration with underwing engines and to consider the factors that determine spanwise location, chordwise location, as well as distance between the nacelle centerline and the plane of the wing.

A factor that favors nacelle locations outboard on the span of the wing is relief of wing bending moments. The weight of the engines is put where the majority of the lift is carried. The magnitude of the bending moment at the root of the wing is reduced, and a reduction in the weight of the wing can be realized. This is illustrated in Figure 1 for a typical subsonic swept-wing jet aircraft, and it is seen that large benefits in wing weight are potentially available as the engine position is moved outboard toward the 70 percent semispan location.

Moving the engines outboard on the wing has, however, other less favorable consequences. The size and hence drag and weight of the vertical tail surfaces increase in magnitude steadily for spanwise positions greater than about 35 percent as shown in Figure 2. The reason for this is the unfavorable yawing moment that results from an outboard engine failure. Another adverse effect of an underwing outboard engine location is the need for a longer landing gear when the engine is located too far outboard, as illustrated in Figure 3. The length of the landing gear has to increase to allow for minimum engine clearance at extreme airplane attitudes at touchdown. This is a constraint that becomes increasingly more severe with increasing relative engine size.

The drag of the airplane is sensitive to spanwise engine location. The results of theoretical calculations illustrating this are shown in Figure 4. The data are for a typical subsonic transport airplane with moderately swept-back wings. Owing to the effect that the engine nacelle has on the spanwise load distribution, the induced drag of the wing is increased as the nacelle position is moved outboard.

In Figure 5 are shown experimental results of the spanwise distribution of wing lift on a wind tunnel model with and without engine nacelles. The accelerated flow field around the nacelle interferes more with the wing lower surface than with the upper surface, and it is seen that a local loss of lift and thus more drag results. There are many factors that affect this problem. These include the size of the nacelle relative to the local wing chords, the distance between the nacelle and the wing, the fineness ratio and shape of the cowl, the planform of the wing and its airfoils. Given the large number of factors it is difficult to generalize, but broadly speaking, the drag problem is harder to solve when the size of the nacelle increases relative to the size of the wing. The data shown in Figure 5 are for a wing with conventional airfoils; the solution of the problem by local airfoil changes would be more complex on a wing with supercritical airfoils because of the need for more complicated theoretical methods and also because these airfoils tend to be more critically loaded near the leading edge. 173

Wind tunnel results are shown in Figure 6 for two different nacelle locations spanwise on a swept wing. The extreme sensitivity of the transonic drag to the position of the nacelles is apparent. The sensitivity of the drag to chordwise and vertical movement at a given spanwise position is shown in Figures 7 and 8 where experimental results from transonic wind tunnel testing are shown. It is suggested in these figures that attention to the local axial area distribution of the nacelle, pylon, and part of the wing will result in lower transonic drag.

Considerably more wind tunnel testing and analysis have had to be carried out on the Boeing 747 and 737 airplanes than on the Boeing 707 to solve the wing nacelle integration problem. This was due mostly to the larger relative nacelle size on the former two airplanes. The higher bypass ratio engine on the 747 offered an additional independent variable in the design, namely the length of the fan-cowl relative to the length of the nacelle. It was found desirable to maintain the exit plane of the fan ahead of the leading edge of the wing to minimize interference on that part of the wing.

Design for flutter prevention is another factor that has to be considered when defining nacelle positions on the wing. The effects of spanwise engine location upon flutter speed are shown in Figure 9. It is seen that flutter speed is very sensitive to engine location. Evidently, some spanwise positions will require an increase in wing torsional stiffness and the attendant increase in weight to provide adequate flutter speeds. As the relative size of the nacelles increases, the aerodynamics of the nacelles themselves complicate the analysis and the solution of flutter problems, as will be shown later. It is again not possible to draw generalized conclusions on the effect that wing-mounted nacelles have on wing flutter because the solution of the problem is subject to many variables in addition to nacelle position. An important variable is the elastic stiffness of the pylon or strut attaching the nacelle to the wing. Further additional variables include wing geometry, engine weight, and flight profile. The complexity of the flutter problem is illustrated in Figure 10. The results of calculations are shown that indicate that moving the nacelle forward makes the airplane more flutter prone, contrary to simple ideas about flutter and divergence. The calculations are, however, for a specific situation and cannot be generalized; the point is that the problem is not at all simple and that detailed flutter analyses and testing are necessary to investigate nacelle placement.

Another factor that has to be considered in nacelle placement choice is shown in Figure 11. It has to do with the distance the nacelle is below the wing. As the nacelle is brought near the wing, there is a condition where the jet impinges strongly upon the flaps when these are extended. To avoid this, it is necessary to provide spanwise relief in the flaps. This, in turn, affects the lift distribution as shown in Figure 11. Whether this is important or not depends on the mission of the airplane and its design requirements. A solution that does not affect the lift distribution is to extend the nacelle pylon so that the jet efflux passes underneath the flaps, but this leads to other penalties such as longer landing gear length and greater pylon weight as shown in Figure 12.

It is seen that there is no specific location for a wing-mounted nacelle that is obviously good and that detailed studies are necessary to weigh quantitatively the pros and cons of different spanwise and chordwise locations. Wind tunnel testing is necessary to understand the influence upon drag and flutter, and care is required in the detailed design of the wind tunnel models to prevent adverse interference drag, particularly at transonic Mach numbers. Different mission requirements will put more emphasis on some factors than others.

#### FUSELAGE-MOUNTED NACELLE INSTALLATIONS

A primary advantage that airplanes with fuselage-mounted nacelles have over airplanes with conventional underwing engines is the fact that the aerodynamics of the wing remain practically unaffected by adverse effects from the nacelles. An example of this is the effect upon the maximum lift coefficient of the airplane. This is one of the more important aerodynamic parameters affecting the general efficiency of an airplane. It may dictate increases in the size of the airplane's wing area beyond the size necessary for efficient cruise performance. In particular, the parameter is of decisive importance for an airplane whose mission requires short takeoff or landing performance. The effect of engine location upon airplane maximum lift coefficient is illustrated in Figure 13 with results from wind tunnel experiments. The advantage of the fuselage engine installation in providing maximum lift capability is clearly apparent.

A problem with the fuselage-engine installation is the effect the installation may have on the airplane post-stall characteristics. With such an arrangement it is often desirable to locate the horizontal tail surfaces atop the vertical tail surfaces to avoid jet-flow interference, and unless particular care is taken in the overall arrangement of the aircraft configuration, the turbulent slow moving wake from the nacelles at high angles of attack will affect adversely the flow in the vicinity of the horizontal tail. This is illustrated with wind tunnel results in Figure 14. The unfavorable effect of the engine nacelles upon stall recovery is clearly apparent. A solution can be found with additional horizontal tail area, but this is more drag and a large weight penalty unless

17-4 the added area is needed also for another design requirement, e.g., lower landing speeds.

Special care is needed to achieve low drag at high subsonic Mach numbers with airplanes with aft-fuselage mounted nacelle installations. Engine nacelles designed for high-subsonic or transonic Mach numbers have exit areas that are smaller than their intake areas. Proximity of these nacelles near a tapering aft-fuselage leads locally to high flow velocities which give rise to premature compressibility problems. Attention to aerodynamic design, as shown in Figure 15 and 16, will result, however, in satisfactory solutions. Experimental results show, in Figure 15, that transonic drag increase is delayed to higher Mach numbers when the fuselage is modified to compensate for nacelle interference. The application of theoretical aerodynamics is particularly rewarding in this area of aircraft design. The theoretical representation of the nacelle-fuselage combination for which the test data shown in Figure 15 were obtained is shown in Figure 16. To construct the wind tunnel model, the fuselage was designed in the flow field of the nacelle, while constraining the theoretical velocities to values smaller than those that had been observed to lead to flow breakdown in practice. The success of this design approach is clearly apparent.

An interesting feature of airplanes with their engines on the fuselage behind the wing is the effect the overall configuration has on some components of the noise heard on the ground below the airplane. This is particularly important for modern commercial transport aircraft where noise is a primary design constraint. In figure 17 are shown noise data recorded by Boeing underneath Boeing 727 and 737 aircraft, respectively. The data have been adjusted to similar aircraft and engine conditions so that the effect of configuration differences could be isolated. The data were recorded with the aircraft in the approach condition prior to landing. At that condition noise radiating forward from the inlets is dominant so that the 727 airplane tends to appear somewhat quieter to an observer in front of the aircraft than the 737. This is because for that observer noise from the engines is shielded by the wing.

Airplane balance is the relationship of the center of gravity of the airplane to the aerodynamic stability limits for different loading conditions. This is more difficult to achieve for an airplane when the engines are on the aft-fuselage. This is because of the large difference in the positions of the center of gravity of the payload and the center of gravity of the propulsion system. Large shifts in center of gravity, therefore, occur from one operating condition to the next. It is obvious that the problem would be worse with increasing payload and engine weight.

The aft-engined configuration has many attractive features, however, particularly for an aircraft whose mission demands good airport performance in terms of high-lift and noise; but extreme care is needed in the aerodynamic design to ensure good post-stall characteristics and satisfactory transonic drag characteristics. It will be shown in the next section that some of the less attractive features of the aft-engined airplane become increasingly more severe with increasing airplane and engine size.

#### EFFECTS ON INCREASING ENGINE SIZE

The decisive effect that increasing bypass ratio has on the propulsive efficiency of turbofan engines is illustrated in Figure 18. It can be seen that an increase in bypass ratio from zero to six on a subsonic turbofan engine leads to an improvement of about 50 percent in the uninstalled specific fuel consumption of the engine. Accordingly, it is no surprise that the high bypass ratio engine is finding increasing application on military and commercial subsonic transport aircraft where good fuel consumption is a primary design goal.

High bypass ratio turbofan engines are bulkier and heavier per unit of cruise thrust. Their size makes the problems of nacelle-airframe integration much more difficult to solve. Not only are the direct aerodynamic problems more difficult, the configuration problems resulting from the size of the engine constrain the aerodynamic design more severely than is the case for the smaller turbojet engines.

In Figure 19 is shown how the size of a typical subsonic turbofan engine would have to change with increasing bypass ratio. It has been assumed that bypass ratio is varied while maintaining constant uninstalled thrust at cruise altitude and speed, that is at constant airplane cruise drag. It is seen that engine dimensions almost double when bypass ratio is increased from bypass one to bypass eight. Obviously, then it is not likely that an airplane designed with the higher bypass ratio engine will have the same drag as the airplane with the lower bypass ratio so that the propulsion efficiency benefits of high bypass ratio engines cannot be directly translated into performance benefits. The need to design for low drag is then also obvious, particularly when mission goals include an engine sizing requirement for cruise thrust and/or climbing thrust.

The aerodynamic design problem to achieve low cruise drag and one method of solution are illustrated in Figure 20. On the left hand side of the figure is shown a side view of the nacelle of the Boeing 707 airplane relative to its local airfoil. Around the nacelle an estimated contour is shown inside of which the flow is at a Mach number equal to or greater than Mach 0.9 when the airplane is at Mach 0.87. It is seen that the distance between the nacelle centerline and the wing is such as just to avoid serious interference problems. On the right-hand side of Figure 20 is shown a similar sketch for the Boeing 747. The 747 features an engine with a much greater bypass ratio than the 707 engine. The potentially more serious problem was solved by shortening the fan cowl so that the field of high Mach number flow around the nacelle was kept well away from the airfoil. A short fan cowl has other losses, however, so that this method of solution is not always the best.

The large engine cowls have extensive and strong flow fields. Not only are the cruise drag and high-lift capability of the airplane affected, but so are the flutter characteristics of the wing, as shown in Figure 21. In this figure relative flutter speed is shown plotted versus outboard nacelle side bending frequency as measured in two wind tunnel experiments with flutter models. In one case, the

175  
model was tested with small heavy bodies which retained the mass and inertia effects of the engines, but which had essentially no aerodynamic effect because of their small size. In the second case flow through nacelles of high bypass ratio engines were added to the model. The unfavorable effect of nacelle aerodynamics can be seen clearly.

An additional serious problem resulting from the integration of higher bypass ratio engines is the impact these have on the design of the landing gear for airplanes with conventional underwing mounted engines. The effect is illustrated in Figure 22. It can be seen that substantial increases in landing gear weight are associated with increasing bypass ratio. The plot is for constant engine cruise thrust. In practice, the penalty would be greater owing to the increase of airplane drag with increasing bypass ratio so that engine size would have to increase somewhat more to allow for needed additional cruise thrust. Additional engine airframe integration problems can result directly from the large engine airflow associated with the high bypass ratio engine. Shown in Figure 23 is the adverse effect such flow can have on rudder effectiveness when the engine is in a thrust reversing mode. The configuration examined here is one with engines mounted aft on the fuselage in the vicinity of the vertical tail. Complicated and expensive wind tunnel testing is necessary to develop such installations and eliminate serious potential design problems.

As engines get bulkier and heavier, configuration problems become more difficult. This is particularly true for configurations where the engines are located long distances from the airplane's center of gravity. The point is illustrated in Figure 24. Two airplane configurations with different engine arrangements are compared. One configuration has the center of gravity of the engines at the center of gravity of the airplane; the other has the engines on the aft-fuselage. Payload is then increased for both configurations while maintaining mission and performance capability. To allow this increase in payload, it is necessary to increase fuselage size; and to maintain mission and performance goals, it is necessary to increase, correspondingly, takeoff gross weight and engine size. It is seen that the efficiency of the airplane with aft-mounted engines deteriorates with increasing airplane size. This is due to the consequences of increasing weight of the engines at the back of the airplane. The airplane gets heavier not only because the engine gets heavier, but also because more area is needed at the back of the airplane to provide additional stabilizing surface for the aft-moving center of gravity and lengthening forebody. The forebody must be lengthened relative to the aft-body to balance the added weight at the back of the airplane, and as a consequence, the spread between the center of gravity of the airplane at full payload and the center of gravity of the empty airplane increases rapidly. When the weight of the engines becomes increasingly large, the efficiency of the airplane with aft-mounted engines diminishes rapidly.

It was shown that increasing engine size has adverse effects on both conventional underwing engine arrangements as well as aft-body mounted engine arrangements. In the next section, overwing engine installations are considered.

#### OVERWING ENGINE INSTALLATIONS

It is interesting to consider overwing engine installations with high bypass ratio engines for many reasons. One might expect that many of the engine-airframe integration problems that are due to the bulkier engine might be easier to solve. The center of gravity problems of the aft-fuselage installation are avoided, and so is the installation problem associated primarily with the length of the landing gear for underwing engine installation. In Figure 25 are shown typical airplane configurations with overwing engines. Some additional obvious advantages are reviewed below.

The overwing engine installation is less susceptible to suffering from ingestion of stones and slush into the engine inlets during ground operations, particularly at takeoff; see Figure 26. This configuration would be of special value to military transport aircraft operating from unprepared runways, and this type of mission would therefore benefit from such an engine arrangement.

With the jets blowing over the upper surface of the wing, Figure 27, advantage can be taken of the Coanda effect to achieve lift augmentation. This is a particularly effective method of producing high lift at the lower aircraft velocities associated with takeoff and landing operations. Such an engine arrangement should be attractive, therefore, for airplanes designed for short or intermediate airfield operations.

Of special value to the design of modern commercial transport aircraft is the good community noise characteristics of the overwing engine installation. Relative to an observer on the ground, the airplane's wings act as a shielding surface protecting the observer from the important high frequency component of the aft-radiated engine noise. Experimental results are shown in Figure 28. It is seen that when the engine nozzle is positioned suitably above the wing, considerable shielding of the noise emanating from the back of the engine takes place. It can be shown that, to achieve comparable noise suppression by other means, with a more conventional engine installation would result in significant performance penalties in terms of weight and internal propulsion system losses.

One of the more serious questions on overwing engine installations has been aerodynamic cruise drag. At the high-speed cruise condition the flow on the upper surface of a swept-wing jet transport generally determines the airplane's "critical" Mach number. At a Mach number only slightly greater than the critical Mach number, the airplane has much more drag, and it is not profitable to operate an airplane at Mach numbers greater than the critical Mach number. The increase in drag can be associated with many causes, but in general it occurs when a shock wave on the upper surface of the wing (where they often first occur) becomes strong enough to provoke large-scale boundary-layer separation. One might assume, at first sight, that locating engine nacelles in the critical flow on the upper surface of a wing would cause early flow breakdown. This would be due to increased local velocities as the flow goes around the nacelle. It has been shown, however, that early flow

breakdown can be avoided if attention is given to this effect in the design of the wing-nacelle combination, as will now be discussed.

It is well over ten years since digital computing machines have been introduced in aeronautical design offices. The use of these machines has made possible the extension of proven aerodynamic theory from simple shapes such as airfoils and bodies of revolution to more complicated geometries. In Figure 29 is shown the theoretical representation of a swept-wing airplane with overwing nacelles. The irrotational subcritical flow around the airplane, and in particular over the wing upper surface, can be calculated with great accuracy and the shape of the nacelle and wing readjusted in each other's presence to achieve a desirable flow field. To design a low drag configuration it is necessary, however, to augment the theoretical calculations with wind tunnel experiments. This is because the real flow contains many features that are beyond the bounds of validity of theory and the theoretical flow has to be related to the actual flow. Now the application of the digital computer also to wind tunnel data processing has increased the capability of the latter by several orders of magnitude so it is expedient as well as useful to apply such data to theoretical calculations. In Figure 30 are shown estimated surface flow streamlines over a swept wing with supercritical airfoils at lifting transonic conditions. These were determined on the basis of experimental pressure distributions, surface flow visualization studies, and theoretical calculations. Using these data and with other calculations a wind tunnel model was designed and tested. The results, Figure 31, showed that it is practical to consider upper-wing nacelles in conjunction with a high-speed wing. The goal of the wind tunnel model was to demonstrate a cruise Mach number of 0.8 with a wing of 25 degrees sweep, along the quarter chord line, using thick supercritical airfoils. As is the case with these airfoils, the wing operates at cruise with a shock wave of moderate strength on the upper surface. The location and strength of the shock wave is critical to the success of the wing. Two sets of overwing nacelles were tested; one aligned in the average local flow field, the other contoured in detail for favorable interference at the cruise condition. It can be seen that the design procedure was successful and that contouring the nacelle produced a shock wave movement and weakening with favorable effects. The actual measured wing-body-nacelle drag, at lift, is very close to what is calculated when the estimated profile drag of the nacelles is added to the measured drag of the wing-body. The achievement of low drag with overwing nacelles, although a problem, is thus amenable to satisfactory solution.

The successful design of airplanes with overwing nacelles will require examination of many other problems as well. As an example, the design of the internal contours of the nacelle, in particular the nozzle, must take place taking account of the external flow field. This is another area where the solution will depend on the successful combination of modern experimental and theoretical techniques. Complicated wind tunnel models will be necessary to sort out drag and thrust and indeed lift, moments, and thrust. Different detail design may be necessary if the specific performance goals are aimed at high-speed cruise performance, or very low takeoff and landing speeds, or particular engine noise shielding with the wing. These will have to be well understood to achieve the correct compromise. Careful simulation will be necessary to investigate airplane flying characteristics and to relate these to different engine operating modes. Fortunately, the "state of the art" has reached the stage where all this is possible.

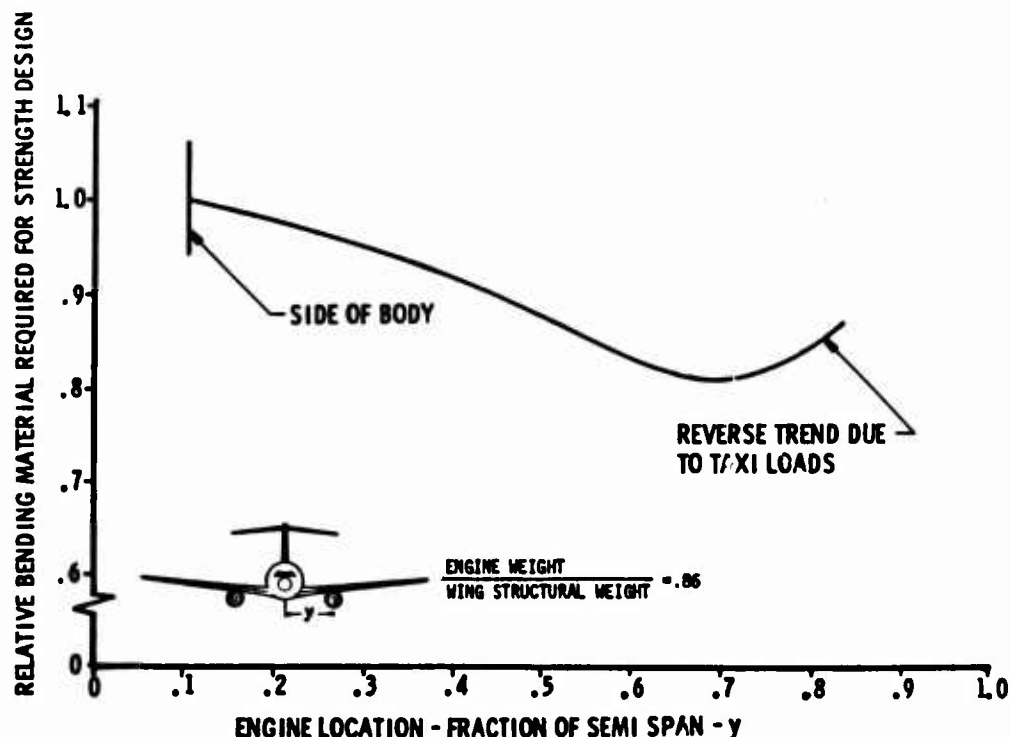


Figure 1. Effect of engine spanwise location on wing bending loads

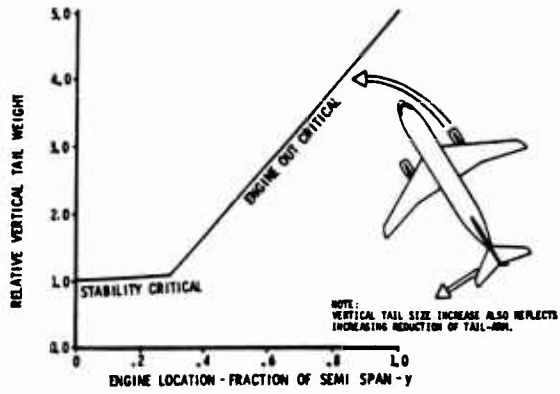


Figure 2. Effect of engine spanwise location on vertical tail weight

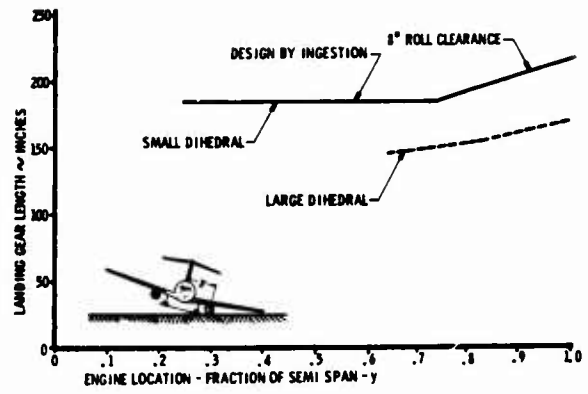


Figure 3. Variation of landing gear length versus spanwise location of under wing nacelle

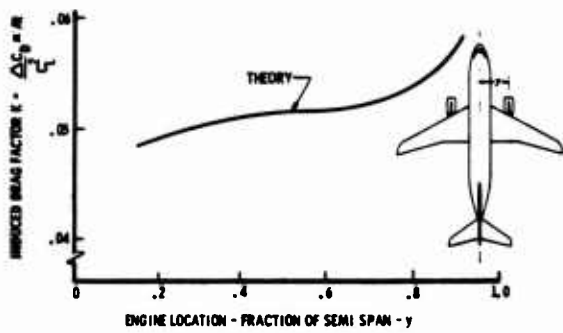


Figure 4. Effect of engine spanwise location on induced drag

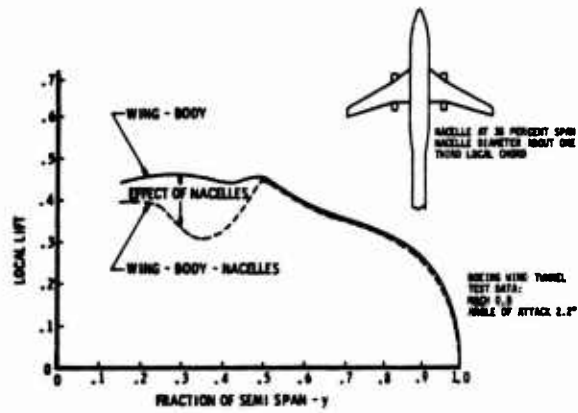


Figure 5. Effect of nacelles on spanwise landing

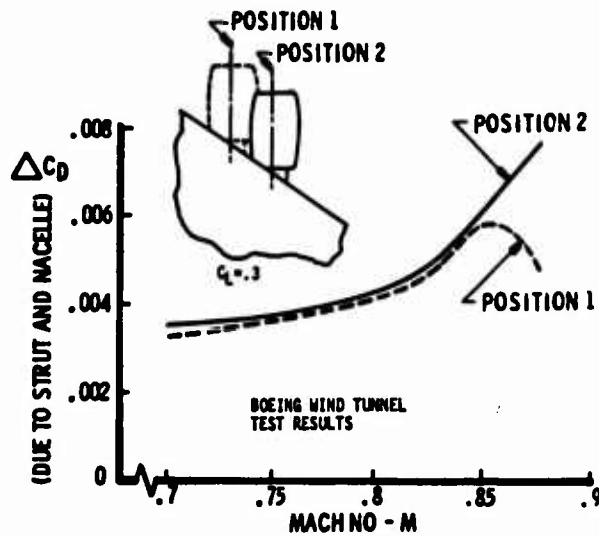


Figure 6. Effect of engine spanwise location on transonic drag

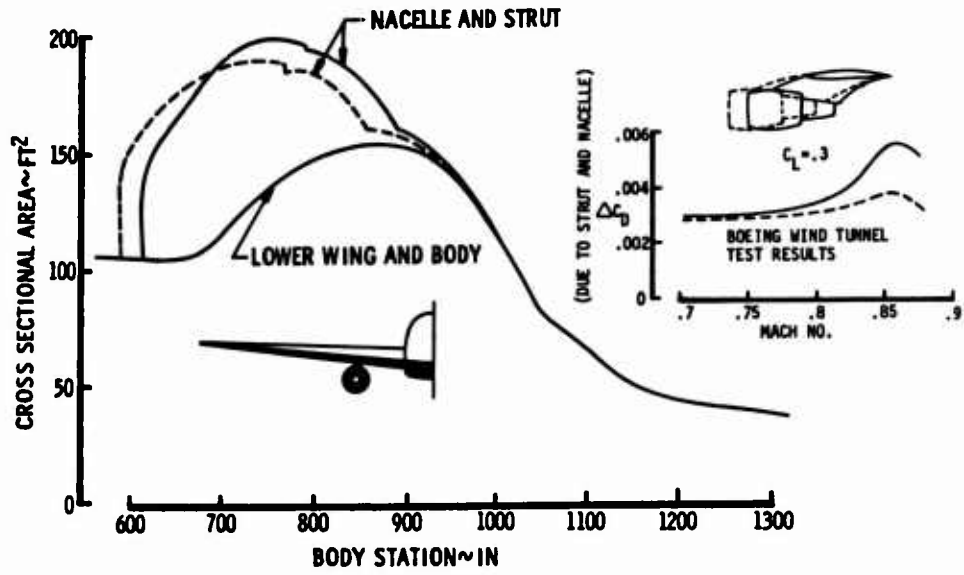


Figure 7. Effect of chordwise position of nacelle on drag

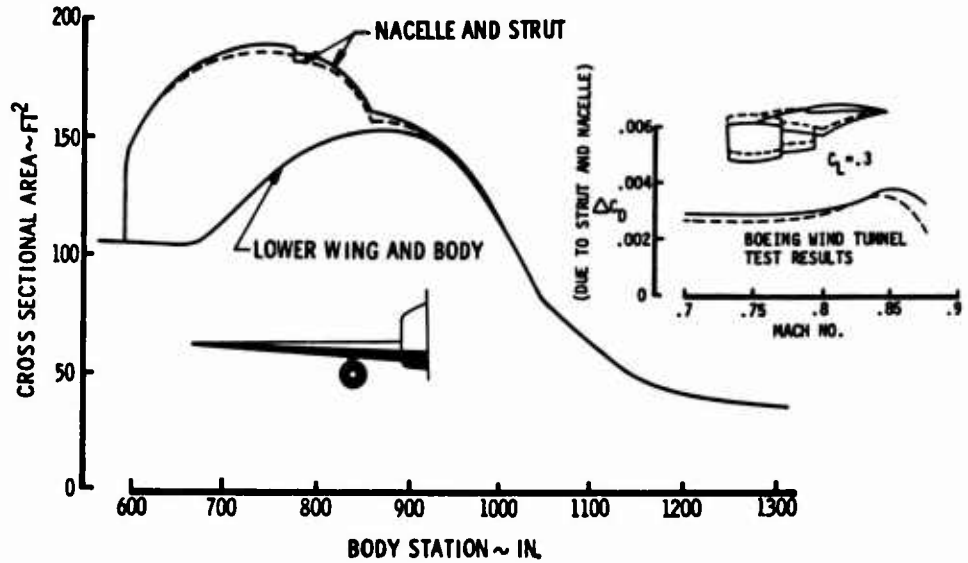


Figure 8. Effect of vertical position of nacelle on drag

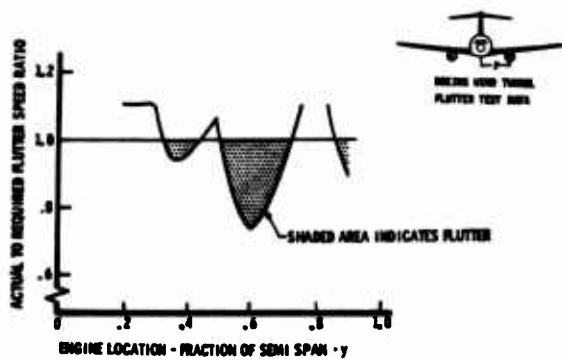


Figure 9. Effect of nacelle spanwise location on wing flutter speed

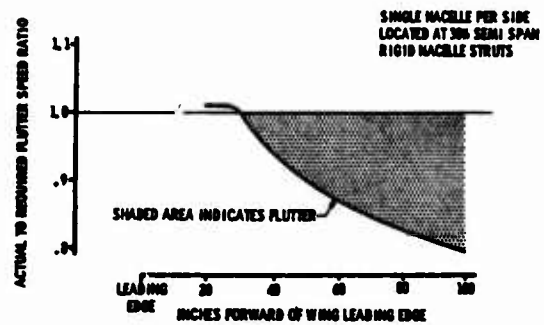


Figure 10. Effect of chordwise position of nacelle center of gravity on wing flutter speed

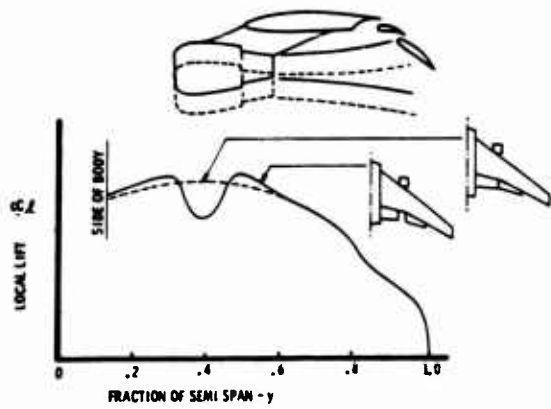


Figure 11. Effect of nacelle height on the spanwise lift distribution at high lift

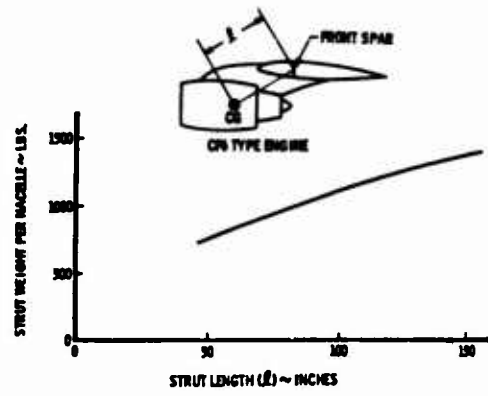


Figure 12. Effect of nacelle height on strut weight

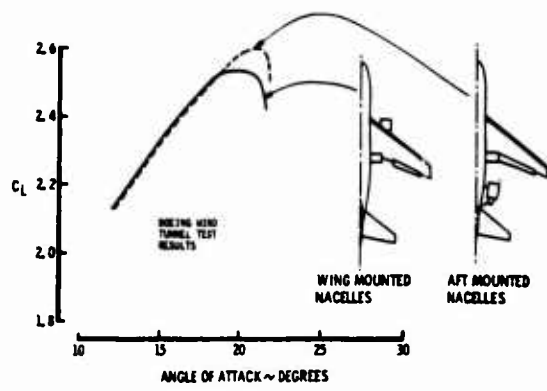


Figure 13. Effect of nacelle location on maximum lift

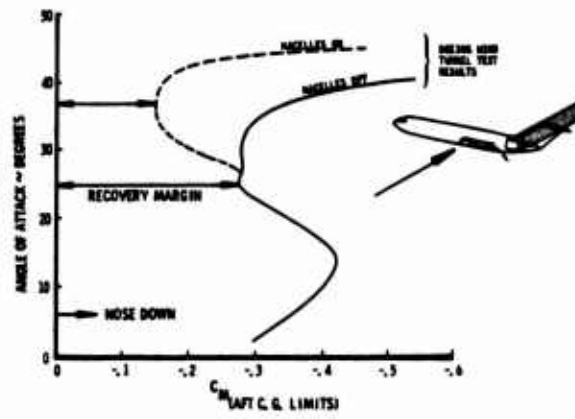


Figure 14. Effect of nacelles on stall characteristics

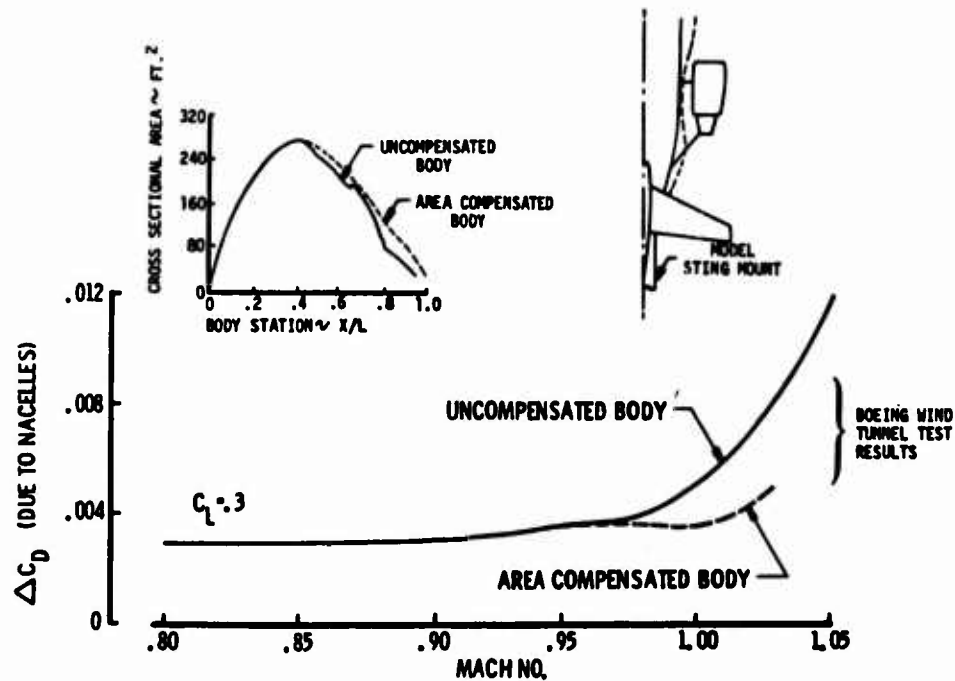


Figure 15. Drag of a body mounted engine installation

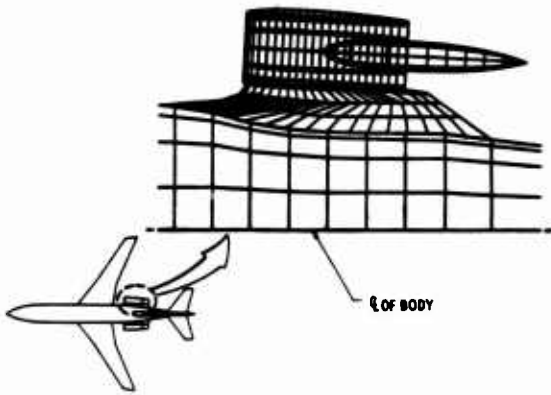


Figure 16. Area-ruled aft nacelle installation

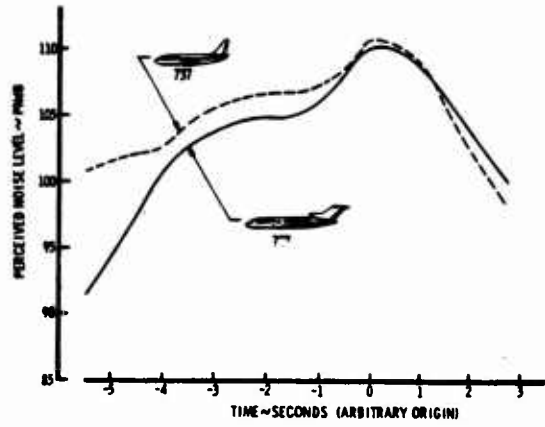


Figure 17. Effect of engine location on flyover noise

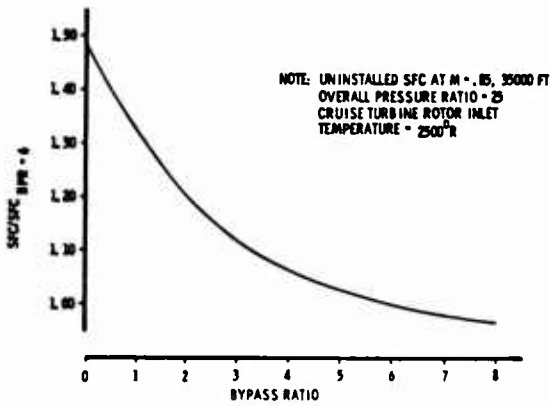


Figure 18. The effect of engine bypass ratio on specific fuel consumption

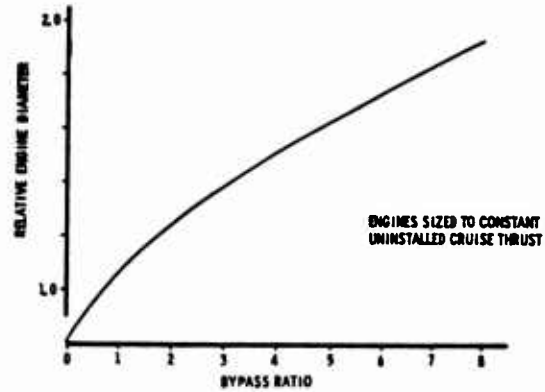


Figure 19. The effect of bypass ratio on engine size

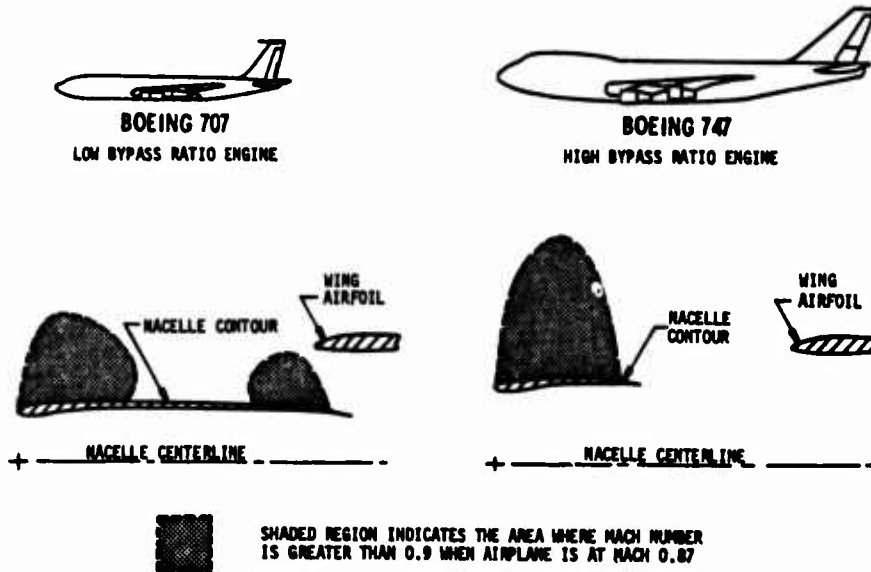


Figure 20. Nacelle installation on Boeing 707 and 747 airplanes

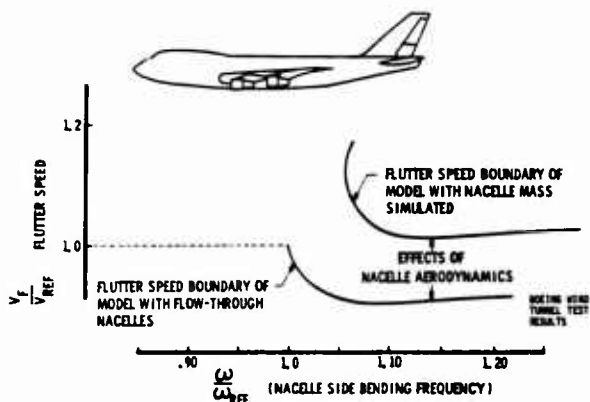


Figure 21. Effect of nacelle aerodynamics on wing flutter for Boeing 747

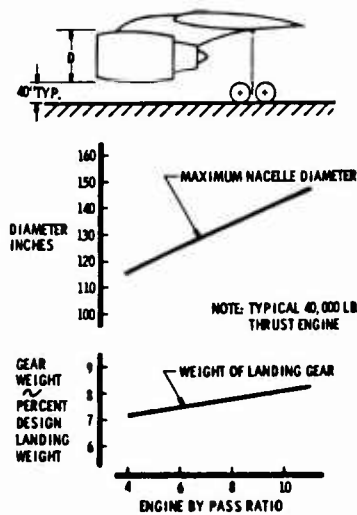


Figure 22. Effect of by pass ratio on landing gear weight

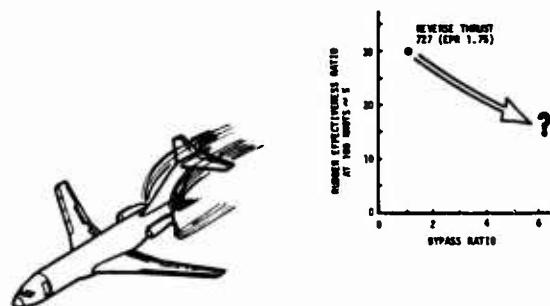


Figure 23. Blanketing of rudder during ground reverse thrust operation

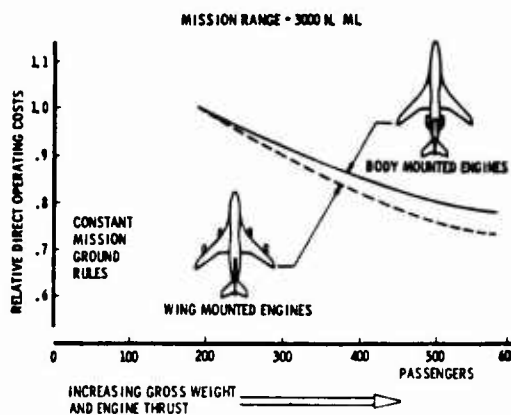


Figure 24. The influence of increasing airplane size on mission weight effect of engine configuration



Figure 25. Typical medium range jet transports with overwing engines



Figure 26. Overwing engines - effect on inlet ingestion

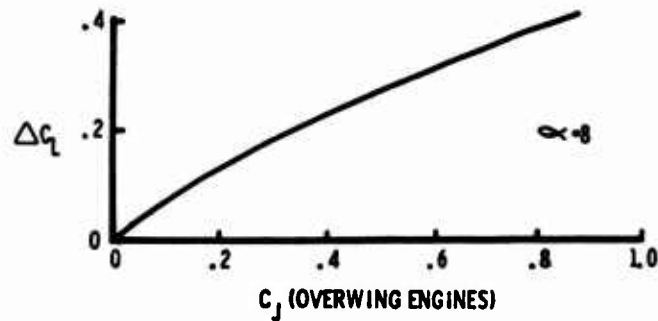


Figure 27. Overwing engine - effect on lift augmentation

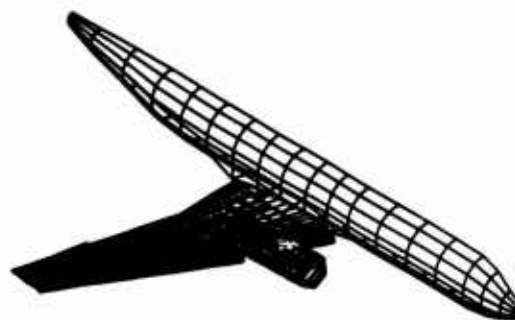
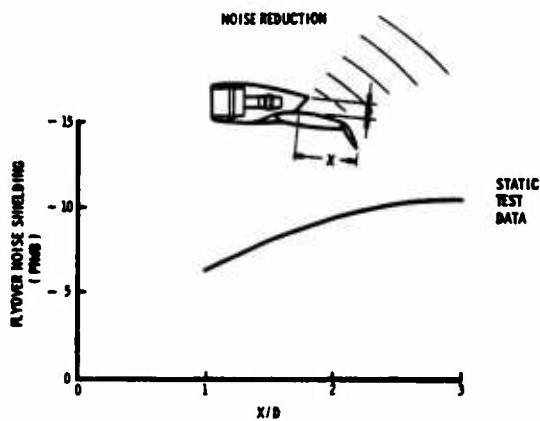


Figure 29. Theoretical model of wing fuselage combination with overwing nacelles

Figure 28. Overwing engine - effect on noise



Figure 30. Streamline pattern on high speed wing

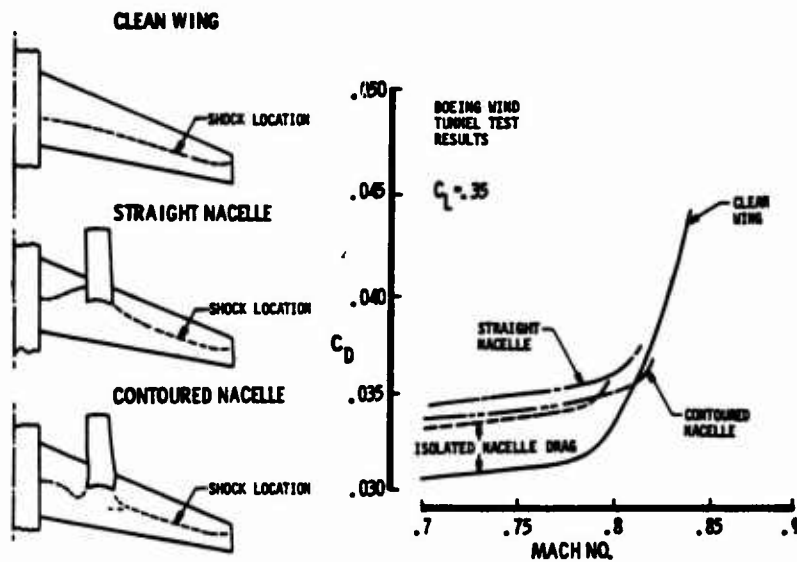


Figure 31. Installation of overwing engine on high speed wing

THE DRAG RESULTING FROM THREE-DIMENSIONAL SEPARATIONS CAUSED  
BY BOUNDARY-LAYER DIVERTERS AND NACELLES IN SUBSONIC AND  
SUPERSONIC FLOW

18-1

DAVID J. PEAKE  
National Aeronautical Establishment  
National Research Council of Canada  
Ottawa, Canada

WILLIAM J. RAINBIRD  
Faculty of Engineering, Carleton University  
Ottawa, Canada

SUMMARY

Three-dimensional viscous flow separations and their effect on configuration drag are examined in high Reynolds number tests conducted in the NAE 5-ft x 5-ft blowdown wind tunnel in both subsonic and supersonic flow. In particular, emphasis is placed on the geometry of the system to divert the oncoming boundary layer about propulsion nacelles.

To avoid significant three-dimensional separations, it is clear that one must avoid imposing large adverse streamwise pressure gradients upon an oncoming boundary layer, such as those produced near stagnation point regions of bluff diverters, or adjacent to intakes operating below design mass flow. The avoidance of these strong streamwise pressure gradients is seen to be readily achieved by increasing the diverter slenderness ratio and by keeping intakes operating at design conditions by means of auxiliary by-pass arrangements.

LIST OF SYMBOLS

$\alpha$	angle of incidence
BWN#	body/wing/nacelle configuration on drone model
$C_D$	drag coefficient; for drone, based on body cross-sectional area (except where noted); for delta wing, based on wing area
$C_L$	lift coefficient of delta wing, based on wing area
$C_N$	normal force coefficient of delta wing, based on wing area
$\delta$	boundary layer thickness
$h$	height of boundary layer diverter
$L$	length of drone model; also length of simulated propulsion nacelle
$L/D$	slenderness ratio of simulated propulsion nacelle on drone model
$M_\infty$	mainstream Mach number
$R_{C_0}$	Reynolds number based on undisturbed stream conditions and maximum chord length of delta wing
$R_L$	Reynolds number based on undisturbed stream conditions and length of drone
$S$	planform area of delta wing
$V$	"thickness" volume of delta wing

1. INTRODUCTION

In comparing wind tunnel and flight measurements of configuration drag, the aircraft or missile project engineer often finds significant differences between these and between the estimates that gave rise to the configuration under study. Such differences are usually attributed to a host of uncertainties, among which are: differences in Reynolds number, incorrect simulation of engine and exhaust flows, and support interference; while on the flight vehicle, leakage, local protuberances and cavities, poor fitting between butt-joints of the skin panels, and paint roughness, provide contributions to drag that are not found on the wind tunnel model, nor are they often included in the estimates with any degree of certainty. Where local protuberances and cavities exist, or where there are externally imposed pressure fields from neighbouring nacelles, three-dimensional separations of the configuration boundary layers ensue. Unfortunately, these are not generally accounted for, either because there is no suitable calculation procedure available, or because there is a lack of appreciation of the fluid mechanics. Indeed, two aspects of aerodynamic design that receive less than due attention, are flows about boundary layer diverters, and about cavities. In this paper, we should like to concentrate on discussing the merits of various boundary-layer diverter shapes in subsonic and supersonic flow that were introduced in Reference 1. All measurements were made in the NAE 5-ft x 5-ft blowdown wind-tunnel under conditions of high dynamic pressure where Reynolds numbers were about 25 million based on typical vehicle lengths of 3-feet.

As many of the results to be discussed will involve the observation of surface shear stress trajectories from oil flow visualisation tests, we should perhaps recapitulate on how we identify lines or regions of three-dimensional separation and attachment. We identify a separation line as being where the surface

shear stress trajectories converge and coalesce, and an attachment line as where they originate and diverge rapidly. When the lines of separation are at an oblique angle with respect to the direction of the external (inviscid) mainstream, the resulting shear layers roll-up to form comparatively steady vortex motions. It would appear that the alternative long bubble type flows (see Maskell(2)) where the shear stress trajectories within the bubble originate far downstream, are not generally found under high Reynolds number test conditions.

## 2. DIVERTERS IN SUBSONIC FLOW

### 2.1 The model

In subsonic flow, emphasis was placed upon evolving a boundary-layer diverter (of cylindrical form) that was situated between a fuselage and an adjacent propulsion nacelle, and which produced the least extent of separation of the fuselage boundary layer. It was considered that such a design would be tantamount to providing a nacelle/boundary-layer diverter configuration that yielded the least component drag. A suitable carrier for the nacelles was a one-third scale model of a pilotless drone, which was mounted on a sting support in the blowdown wind tunnel. Surface shear stress patterns in the regions of separation and under the interacting flows over the vehicle afterbody were visualised using surface oil flow techniques, to provide a skeleton structure on which to synthesise the flow.

Most of the measurements were made at zero angle of attack and at Mach numbers between 0.5 and 0.8 with a mainstream dynamic pressure of about 1100 psf. This high dynamic pressure along with a sensitive drag balance made it possible to determine small changes in component drag coefficient to an accuracy of  $\pm 5$  drag counts (that is,  $\pm 0.0005$ ). In addition, static pressure measurements on the boat-tail surface provided the means of obtaining afterbody pressure drags and correlating the effects of the upstream nacelles with the observed surface flow patterns. We should mention that since the base area plus the boat-tail thickness was together 26.5 percent of the body cross-sectional area, the strain gauge drag balance recorded the external drag minus the thrust given by the positive base pressure coefficient. In fact, the base "thrust" was almost 70 percent of the balance drag measurement, so that the balance readings were corrected to an effective base pressure equal to that of the mainstream.

The model, of length 33.75-inches, consisted of a 4.33-inch diameter cylindrical fuselage, to which was attached a tangent-ogive nose and a circular arc boat-tail whose radius in the longitudinal section was 2.5 times the body diameter. Unswept cruciform wings of 4-inches span, 2.67-inches chord, and thickness/chord ratio of 9 percent, were mounted at the rear of the vehicle, just ahead of the boat-tail. Two diametrically-opposed "D-shaped" propulsion nacelles shown on Figure 1, were situated along lines midway between the wings and upstream of the wing leading-edge. Before conducting the tests, we noted that there was scanty information available in the literature, either of an analytical or an empirical kind, on the pressure distributions and interference drags of body/wing/nacelle combinations of this type. Consequently to widen the investigation, a series of interchangeable propulsion nacelles was designed, possessing three slenderness ratios, L/D, of 5, 6.67 and 10. The centre-line depth of the boundary layer diverter was kept constant at  $h = 0.2$ -inch, this being equal to about 70 percent of the calculated local fuselage boundary layer thickness, and representative of a flight vehicle installation. In addition, the nacelle length was maintained constant for each nacelle slenderness ratio. Hence, we note that the L/D ratio was varied by scaling the radial dimension in the cross-sectional plane of the nacelle. Figure 1, in fact, lists the scaling factors. Since the propulsion nacelles were solid and did not possess a "through-flow" capability, the nacelle length included an extension forward of the capture plane to "fair-in" the intake and thus to attempt simulation of the boundary between the internal and external flow.

Figures 2 and 3 show that four interchangeable boundary layer diverters were available for each nacelle slenderness ratio. These were a bluff elliptical section; a blunt bi-convex section of the same length; plus slender bi-convex and bi-cusped sections of almost double the length of the bluff planforms.

### 2.2 Flow visualisation

The progressive improvement in diverter flow obtainable by increasing the slenderness of the diverter itself, whilst maintaining a constant maximum diverter frontal width, is demonstrated on Figures 4A to 4F, for a nacelle slenderness ratio of 5. These tests were run at mainstream Mach numbers of about 0.7 (and 0.8) at a Reynolds number of 23 million based on the length of the drone. On the photographic illustrations, the upper pictures display the nacelles in situ on the drone body, while the nacelles have been removed on the lower photographs to reveal the diverter shapes and the oil flow visualisation. The four shapes of boundary-layer diverter are seen, ranging from the bluff, elliptical diverter that causes a large separation region about and downstream of the obstacle, to the slender bi-cusped diverter that does not generate any appreciable separation. Interspersing the photographs are Figures 4C and 4F, which are tracings of the three-dimensional separation lines plotted upon an unrolled fuselage wall, to provide additional views of the lateral extent of each separation region in proximity to the diverter. The results for the other nacelle slenderness ratios of 6.67 and 10 were qualitatively the same.

While concentrating on the flow visualisation photographs of Figure 4, we should remark on the region of high scour (and consequently high shear stress) downstream of the nacelle, which is present irrespective of the diverter used. It is not clear from Figure 4 how this region develops. Turning to Figure 12 however, where incidence exacerbates the severity of the three-dimensional separations about another nacelle/wing configuration, the clue is provided for resolving the commencement of the afterbody high shear region. We see on this figure, where streaks from oil dots provide a clearer indication of surface shear direction, that coalescence of the surface shear stress trajectories occurs on the back surface of the nacelle, to herald two lines of three-dimensional separation which proceed rearwards along the afterbody. The rolled-up free shear layers from these separations would appear to induce an attachment region along the extension of the nacelle centre-line along the afterbody, where we view the divergence of the oil streaks. It is hoped that our schematic interpretation on Figure 12 of a given cross-section of the flow at the rear of the nacelle, where wing root separations are also substantial, will assist in the above description.

One further point: the accumulation of surface oil in what are apparently low shear areas on the boat-tail, does not indicate separation, for a substantial recovery in surface pressure all the way to the base was given by the boat-tail static pressure measurements. In the event of a poor boat-tail boundary-layer flow, on the other hand, the rolled-up shear layers might well provide a vortex generator effect to fill out the velocity distribution in the remaining boundary layer, and perhaps reduce a high form drag.

### 2.3 Drag measurements

Substantial support for the interpretation of the flow visualisation results was provided by the model balance and boat-tail pressure drags, which demonstrated that the total configuration drag could be reduced significantly by changing the boundary-layer diverter design. Except where noted, drag coefficients were based on the body cross-sectional area of the drone. Component drags for the nacelles (including the diverters) and wings, were determined from tests with and without the appropriate component added to a given configuration. The results showed that within the accuracy of measurement, the incremental component drags were independent of the configuration to which they were added; with the exception of adding nacelles to the body without wings at  $M_\infty = 0.7$ . In this latter case, two different diverters, N1 and N7, were attached to the "body only", and both showed a doubling of the nacelle (plus diverter) drags when compared with attachment to the wing body configuration. At  $M_\infty = 0.5$ , however, no such difference was found. Thus it appears that when compressibility effects become important, the addition of the wings in the vicinity of the nacelles reduces the pressure drag to provide a favourable interference effect.

Figure 5 illustrates that the nacelle incremental drag appears substantially independent of Mach number in the range  $0.5 < M_\infty < 0.7$ . In contrast, the same figure shows that the total drag of the body/wing nacelle configurations increases with Mach number, while the same trend is noted for the boat-tail pressure drags displayed on Figure 6. A closer examination of Figures 5 and 6, however, indicates that the increase in total drag may be attributed to the increase in boat-tail pressure drag alone. We observe, moreover, that increasing both the diverter slenderness and the nacelle slenderness produces a progressive reduction in boat-tail pressure drag.

We should emphasise that in none of the tests was there any evidence of a two-dimensional separation on the boat-tail (apart from the anomaly of the surface oil accumulation previously mentioned). The static pressures along each longitudinal generator of the boat-tail (Figure 7) increased smoothly to a base pressure coefficient of about 0.2. Unfortunately, it would appear that the circumferential spacing between the static pressure orifices, Figure 8, was probably too large to permit identification of local suction peaks caused by the rolled-up shear layers from the vicinity of each nacelle.

The nacelle (plus diverter) incremental drag is displayed on Figure 9 as a function of nacelle slenderness ratio,  $L/D$ . Because the  $L/D$  ratio was achieved by varying the nacelle diameter, whilst maintaining a constant nacelle length, the drag increments attributable to mounting a nacelle-plus-diverter on the drone are here based on the frontal area of the nacelle (including the diverter). As we expressed before, no significant change of drag increment with Mach number was evident throughout the Mach range,  $0.5 < M_\infty < 0.7$ .

Nevertheless, we note that changing the nacelle slenderness ratio from 5 to 10, causes the drag to rise to a maximum; and in the case of the bi-convex and bi-cusped diverters, to reduce again. The replacement of the elliptical diverter by either the slender bi-convex or the bi-cusped diverter yields a significant reduction in the total drag of the nacelle. Correspondingly, at  $L/D = 5$ , the slender bi-convex diverter itself possesses about 2/3 of the drag of the elliptical diverter; whereas, at  $L/D = 10$ , the fraction improves to almost 1/2.

## 2.4 Influence of intake "through-flow" and angle of attack

We determine from the foregoing, therefore, that not only is nacelle shape important, but that when designing boundary layer diverters, we must avoid the imposing of large adverse streamwise pressure gradients, such as those produced near stagnation point regions of bluff cylinders. Provided the slenderness ratio of the diverter itself is such that it presents a bluff-body pressure field to the oncoming boundary layer—and this would be for diverter slenderness ratios near unity it is clearly immaterial whether the shape of the diverter is rounded or wedge-shaped, for strong separations will always be generated(3).

Some questions will be raised concerning the procedure of testing with the "blocked" propulsion nacelles that have been discussed thus far. As a qualitative answer, Figure 10 provides a comparison between the patterns of surface shear stress trajectories around a nacelle with an elliptical diverter operating with and without "through-flow", and at the same Reynolds number as before. The details of the configuration geometry have been changed from those investigated previously, but we note that operating with a mass flow ratio of about 0.6 provides only small changes to the streak patterns about the diverter. Moreover, we see on Figures 11 and 12, that with the drone at angle of attack, the close proximity of the wings to the propulsion nacelle provides a constraint to reduce the incidence at the intake capture plane; but does not alter the fact that a three-dimensional separation exists about the bluff diverter.

## 2.5 Post-script

In flight trials with a drone three times the scale of the wind tunnel model discussed herein, and where much of the relevant configuration geometry was duplicated between model and full-scale, the replacement of elliptical boundary-layer diverters by the bi-cusped design on "through-flow" nacelles, produced a 6 to 7 percent reduction in total drag at  $M_\infty \approx 0.7$ (4). Surprisingly, this welcome decrease was significantly larger than that measured in the wind tunnel. A tentative reason for the discrepancy was thought to be related to the differences between the wind tunnel and full-scale boat-tail flows. Because, in flight, there were protuberances and cavities on the boat-tail, its flow would be more disturbed than that on the wind tunnel model. This, coupled with the hot jet efflux in flight controlling the base pressure level at a more-or-less constant setting at a given Mach number, would probably require the improvement in diverter flows to be indicated directly as a reduction in nacelle drag - rather than as a diverter drag/base drag trade-off that was established in the tunnel tests.

## 3. DIVERTERS IN SUPERSONIC FLOW

### 3.1 The model

A viscous problem somewhat related to diverter flows occurs when attempts are made to take advantage of so-called "favourable interference" effects, particularly on supersonic aircraft layouts. Such favourable interference is always accompanied by local adverse pressure gradients that are superimposed upon the wing and fuselage boundary layers and which usually promote three-dimensional separations. The interaction between the shock system from an unstarted inlet and an adjacent wing boundary layer, for instance, would be one extreme case where large scale separation with free vortices would be formed.

A 70°-delta wing with four axisymmetric intake nacelles (plus supporting pylons) that were positioned and scaled to be typical of a supersonic transport layout, was tested at Reynolds numbers of about 25 million based on the maximum wing chord of 30-inches. The cropped wing span at the trailing-edge was 21.07-inches, while the wing volume coefficient  $V/S^{1.5}$  was chosen to be 0.04. The uncambered wing had a thickness distribution chosen from the RAE Lord V series\*, but modified near the centre-line to accommodate a six-component strain-gauge balance and model support sting. Off-design Mach numbers of 0.71 and 1.59, and the design case of  $M_\infty = 2.75$ , were used to investigate the increase in drag due to adding diverters (the pylons) and simple "through-flow" engine nacelles. The nacelles contained a fixed axisymmetric centre-body cone of 11.5° semi-apex angle with little internal supersonic compression. The included angle of the cowl lip was 2.75° to provide a low cowl drag while the capture diameter was 1.125-inches.

\*

$$\frac{t}{t_{\max}} = \left(1 - \frac{x}{c}\right) \left[1 - \left(\frac{1 - \frac{x}{c}}{1 - \frac{y}{b}}\right)^3\right]$$

where  $c = 30.0"$ ,  $b = 21.9"$ ,  $t_{\max} = 1.810"$ .

The diverters with included angle of  $11^\circ$ , were machined to a height of 0.5-inch, which was about two-and-a-half times the oncoming boundary layer thickness mid-way between the two nacelles situated on one semi-span. Some additional diverters of the same height and slenderness ratio as the wedge diverters, but with an elliptical planform, were formed by moulding modelling clay around a pair of the original pylons (see Figure 16C).

### 3.2 Lift, drag and flow visualisation results

Figure 13 presents the lifting performance of the delta wing to illustrate the "favourable interference" accruing when the underwing nacelles are mounted on the diverters. The design cruise lift coefficient of 0.08 occurred at about  $\alpha = 3^\circ$  and we notice that with the intakes throttled to 70 percent of design mass flow, a change in lift was recorded of about 30 percent. Notwithstanding the substantial lift increment produced by the pods and diverters, we observe on Figure 14A that a large drag penalty results at design incidence, with the wedge diverters providing about 25 percent of the nacelle plus diverter drag at full throttle.

As the Mach number increases, we note on Figures 14B and 14A the gradual reduction in incremental nacelle-plus-diverter drag. At  $M_\infty = 2.75$ , the shock wave from the centre-body spike is situated on or just inside the cowl lip so that no intake flow is spilled. For  $M_\infty < 1.75$ , however, the cowl shock is detached and large spillage occurs.

Figure 15A, for example, illustrates the limiting streamline pattern on the undersurface of the lifting  $70^\circ$ -delta wing, at  $M_\infty = 1.6$  and  $\alpha = 2^\circ$  ( $C_L = 0.08$ ). The two intakes in the lower half of Figure 15A are operating with the throttle wide-open, but the detached cowl normal shock causes a large-scale interaction. With the throttles half-closed within the upper two intakes, there is even more spillage with a well-defined three-dimensional separation line extending virtually across the wing semi-span. With the intakes removed on Figure 15B, one may infer local regions of subsonic flow downstream of the interaction.

Figure 16A shows the delta wing with the two lower intakes operating at design mass flow with centre-body cone shock on lip. We note from Figure 16B the relatively small regions of three-dimensional separation caused by the wedge-shaped diverters and cowl pressure field. The upper pair of intakes was throttled internally to about 70 percent design mass flow, forcing the throat normal shock again outside of the cowl lip. The result of this subcritical operation is to once more cause a massive three-dimensional separation of the starboard underwing boundary layer, a substantial induced rolling moment, and high local heat transfer rates in the reattachment regions downstream of the separation. The corresponding large increase in drag with all intakes unstated is shown on Figure 14A.

Finally, Figure 16C depicts the differences in surface flow patterns about the streamlined and bluff diverters. The bluff elliptical leading-edges promote regions of separation that are clearly many times more extensive than the interaction regions about the  $11^\circ$  (included angle) wedge diverters.

## 4. CONCLUSIONS

- (1) In subsonic flow, a substantial reduction in diverter drag was measured by increasing the slenderness of the diverter to reduce the extent of the three-dimensional separation region. The replacement of an elliptical bluff diverter by a slender bi-cusped section reduced the component drag of a nacelle plus diverter of slenderness ratio 5 by as much as 30 percent.
- (2) In supersonic flow, diversion of a boundary layer on a  $70^\circ$ -delta wing in proximity to a propulsion nacelle was shown to be accommodated without significant separation at design cruise incidence and Mach number of 2.75 using a  $5.5^\circ$  wedge semi-angle. The throttling of the intake flow, to cause large spillage and intake shock/wing boundary layer interaction, produced a massive three-dimensional separation region with a corresponding increase in drag of 40 percent.
- (3) It is clear that the aircraft or missile designer must recognise the existence of three-dimensional boundary layers on a given configuration, and be aware of the components that promote diverse kinds of three-dimensional separations.

## 5. REFERENCES

1. Peake, D.J.                    Three-Dimensional Flow Separations on Aircraft and  
   Rainbird, W.J.                Missiles.  
   Atraghji, E.                    AIAA Journal, Vol.10, No.5, May 1972, pp.567-580.
2. Maskell, E.                    Flow Separation in Three Dimensions.  
                                      RAE Report 2565, November 1955.
3. Davenport, C.                 A Further Investigation of the Drag at Subsonic Speeds  
                                      of Side Intake Boundary Layer Diverters, S & T Memo 7/68,  
                                      British Ministry of Technology, September 1968.
4. Woolley, D.                    Private communication between Canadair Ltd., and NAE,  
                                      August 1966.

## ACKNOWLEDGEMENTS

The authors wish to express their appreciation to R.de B. Edwardes and L. Pon of Canadair Ltd., Montreal, and to J.R.Digney and D.B. Thomason of NAE for their help in the preparation of the paper.

CAPTURE PLANE OF INTAKE WOULD BE BETWEEN STATIONS ③ & ④

18-7

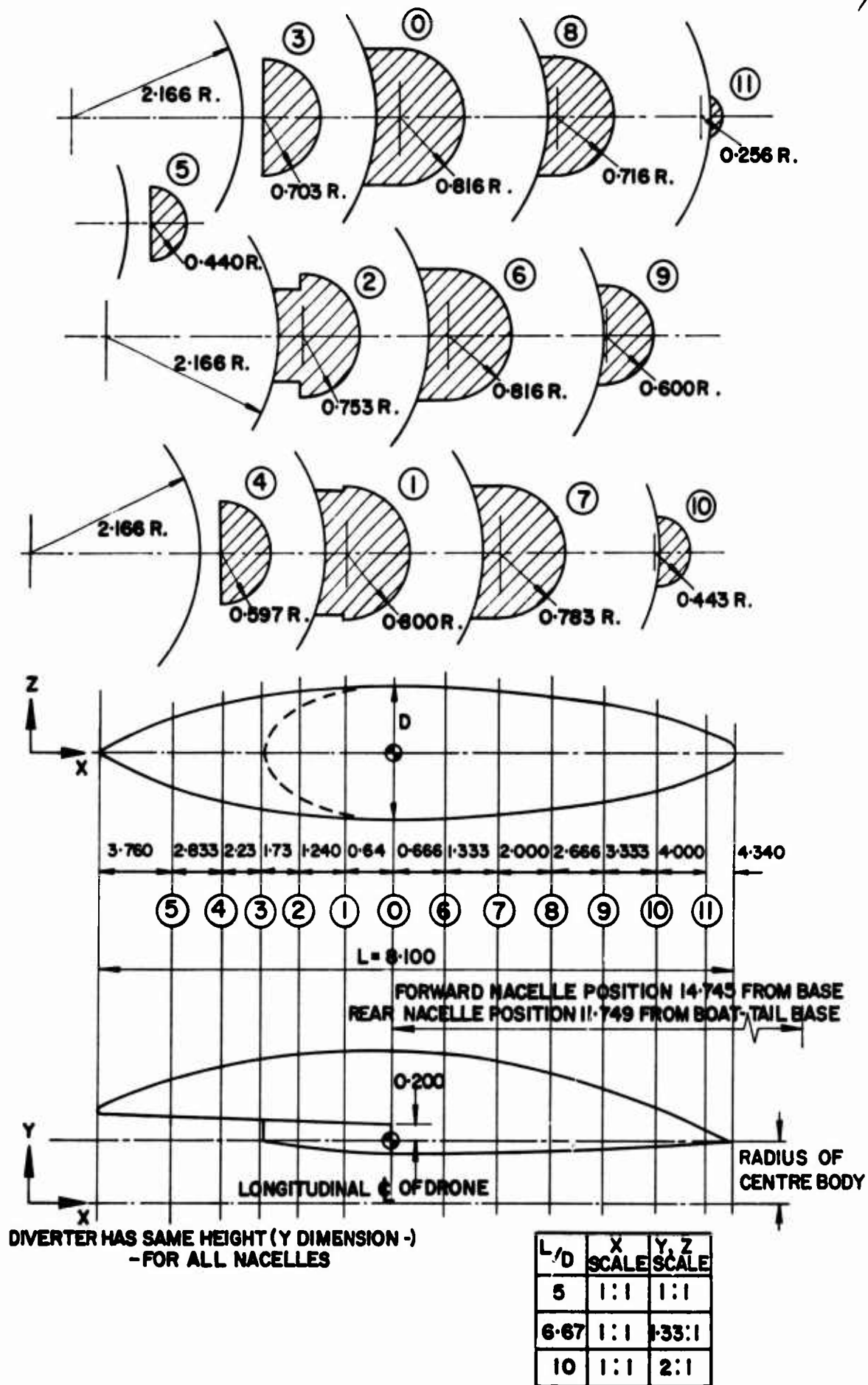


Fig.1 Simulated intake nacelle with elliptical B/L diverter

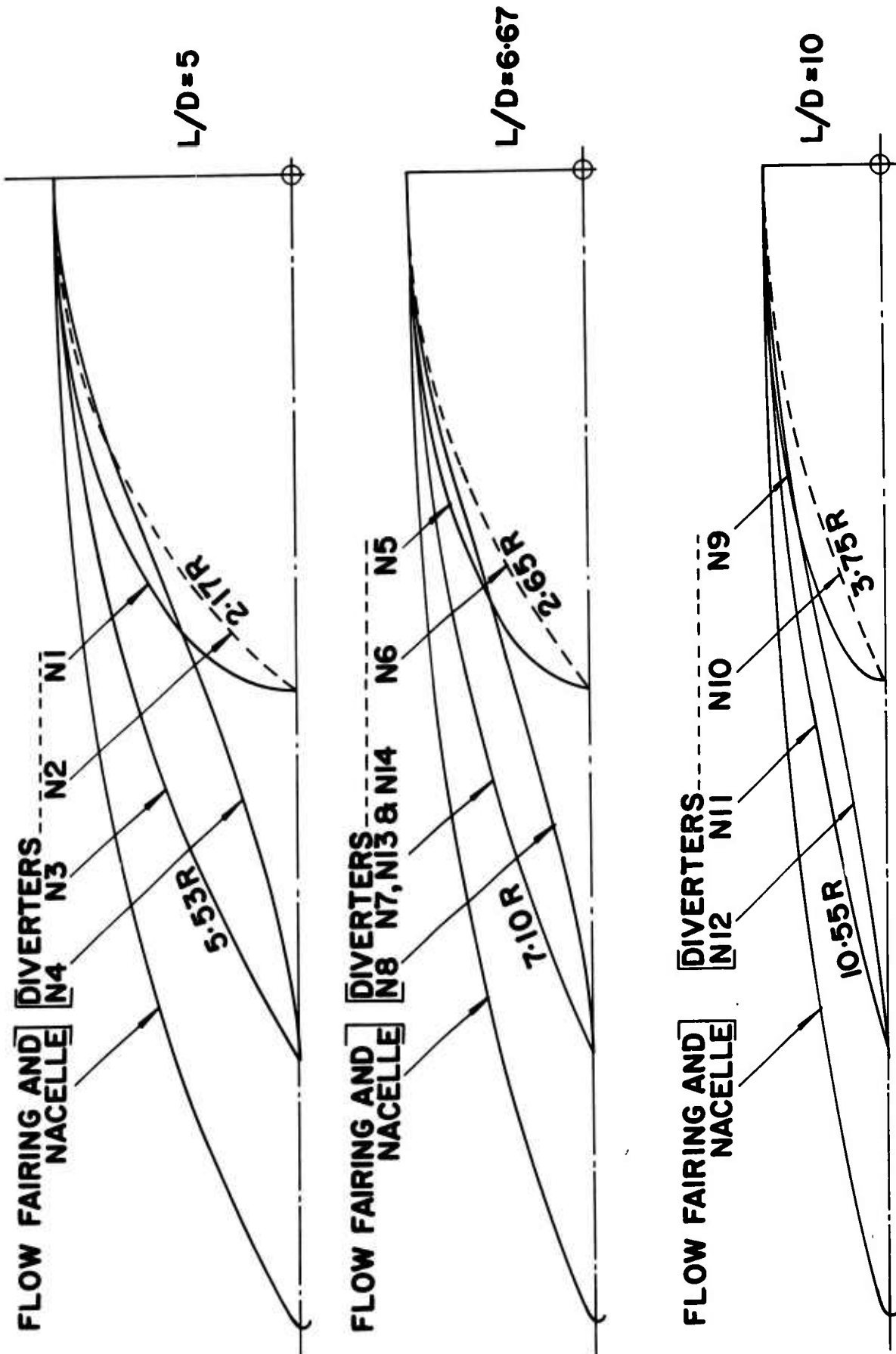
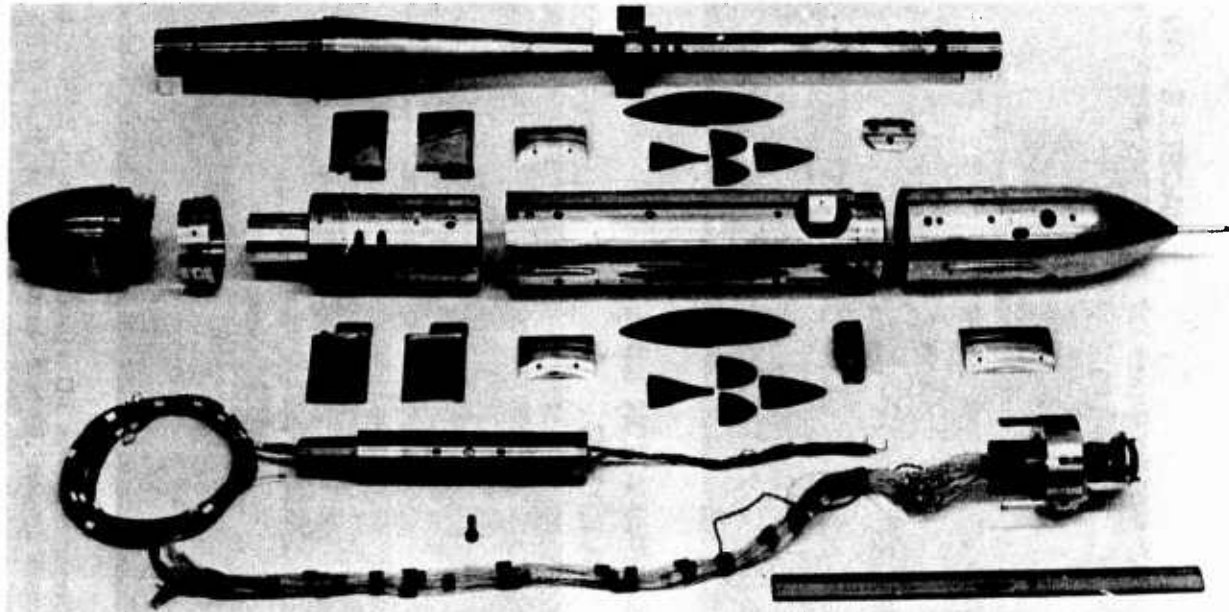
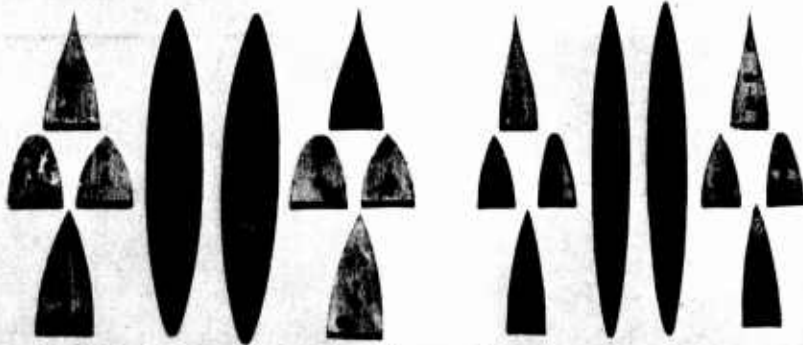
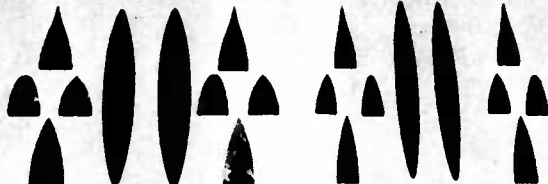


Fig.2 Diverter profiles on drone in subsonic flow



**EXPLODED  
VIEW  
OF MODEL**



**NACELLES  
AND  
DIVERTERS**

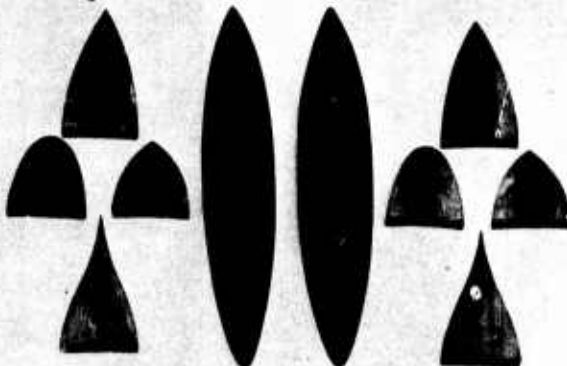


Fig.3 Breakdown of model drone

18-10

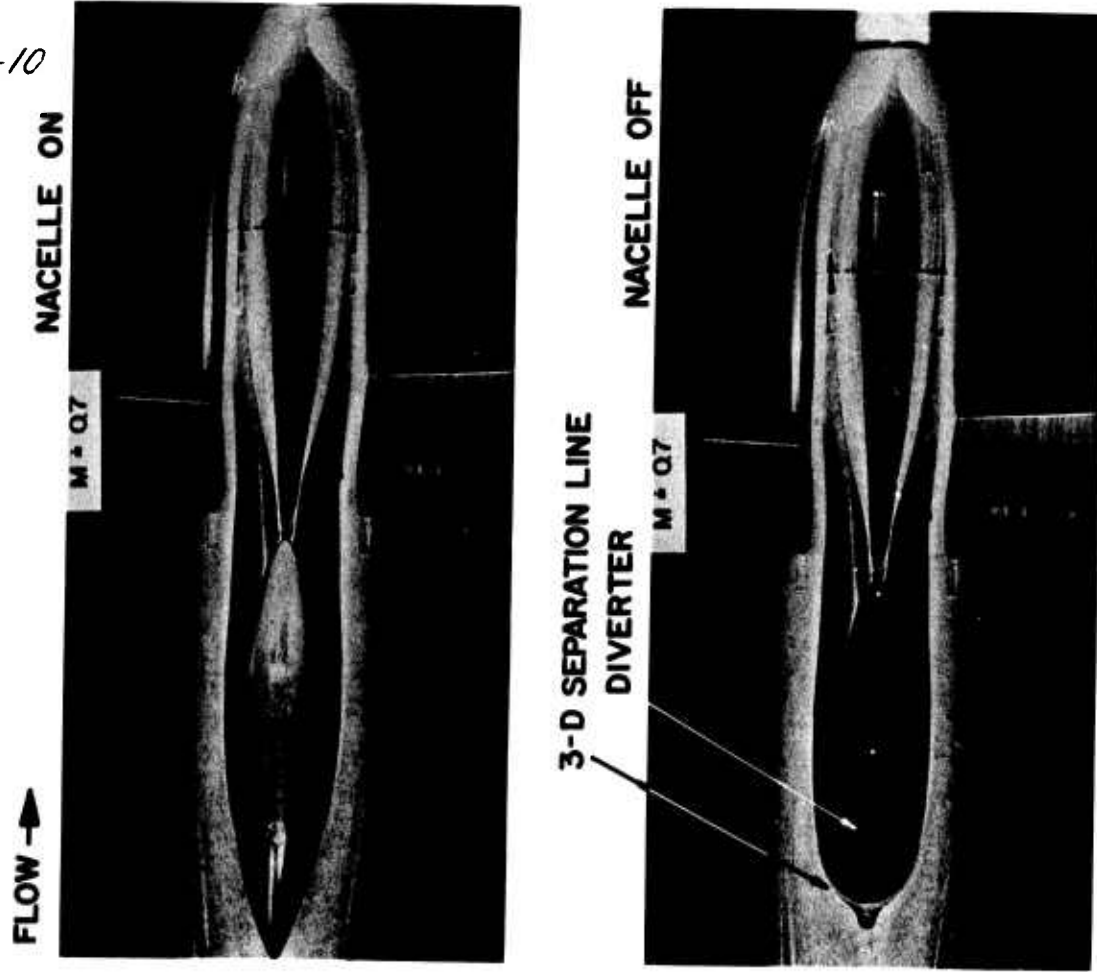


Fig.4(b) Effect of diverter shapes on 3-D separations at  $R_L = 23.10^6$ ,  $L/D = 5$ , blunt bi-convex diverter BWN 2 configuration at  $M_\infty = 0.7$

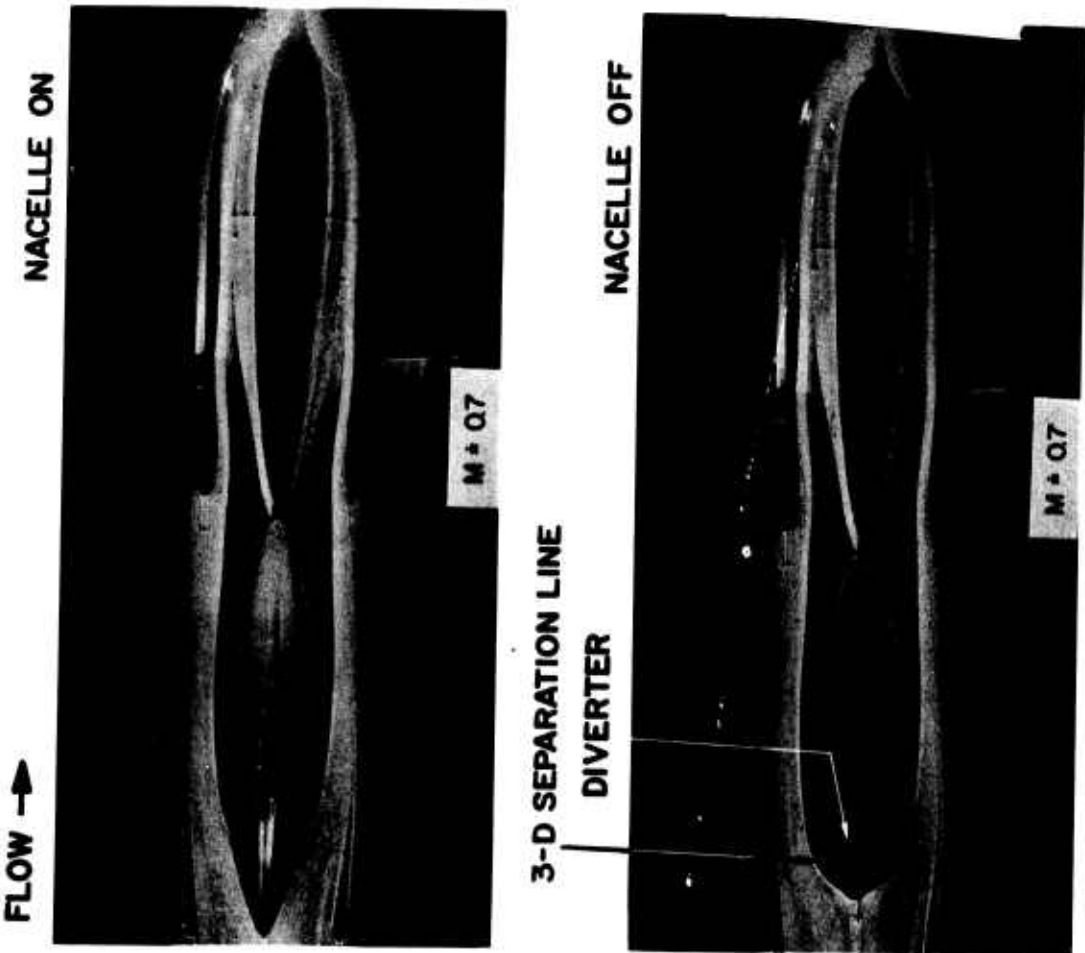


Fig.4(a) Effect of diverter shapes on 3-D separations at  $R_L = 23.10^6$ ,  $L/D = 5$ . Elliptical diverter BWN 1 at  $M_\infty = 0.7$

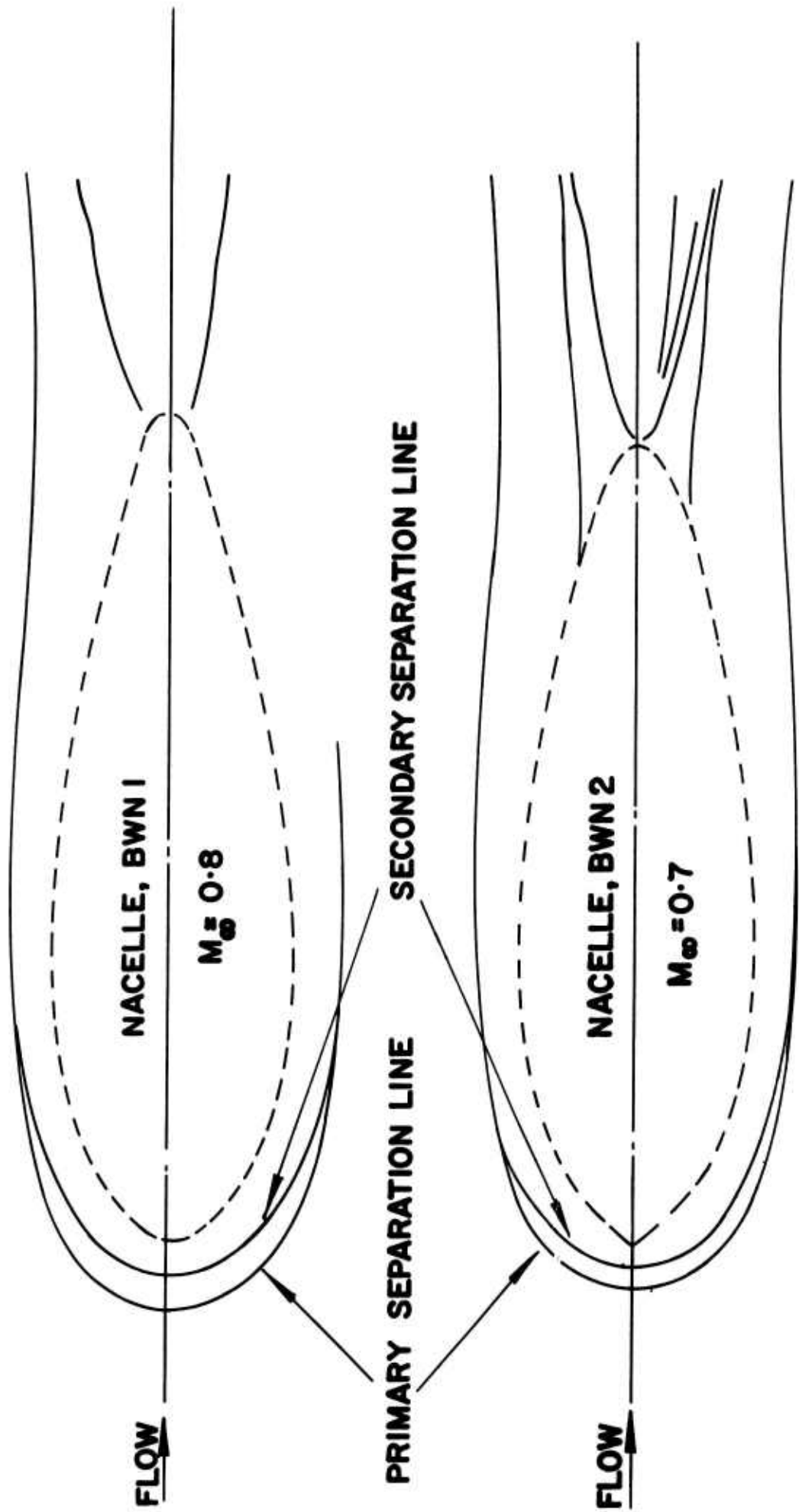


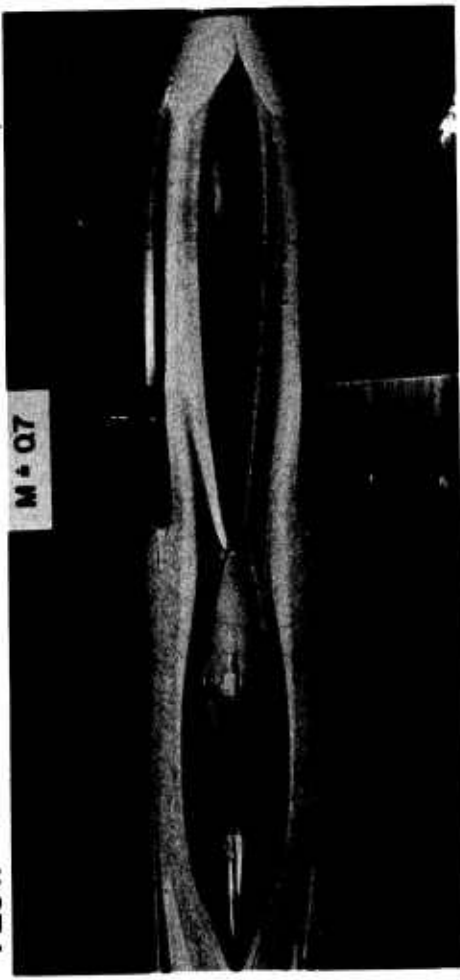
Fig.4(c) Tracings of separation lines about BWN 1, BWN 2 at  $M_\infty = 0.8$  and  $0.7$

18-11

18-12

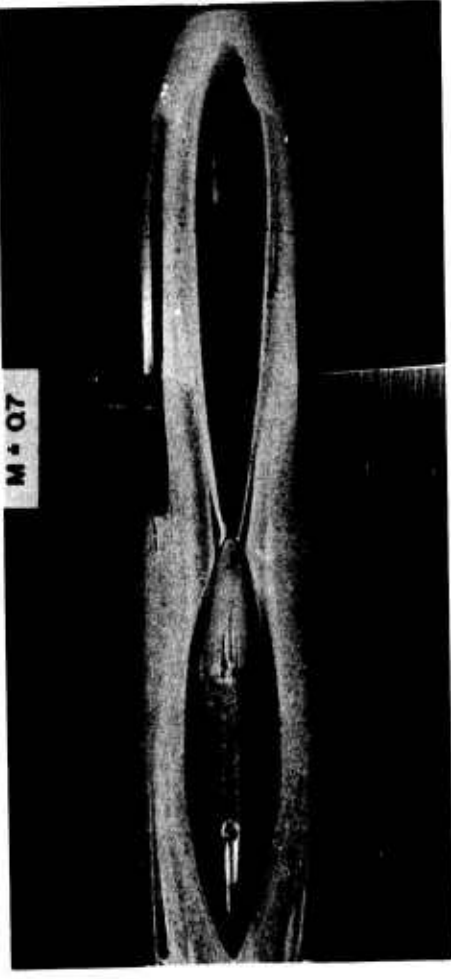
FLOW →

NACELLE ON



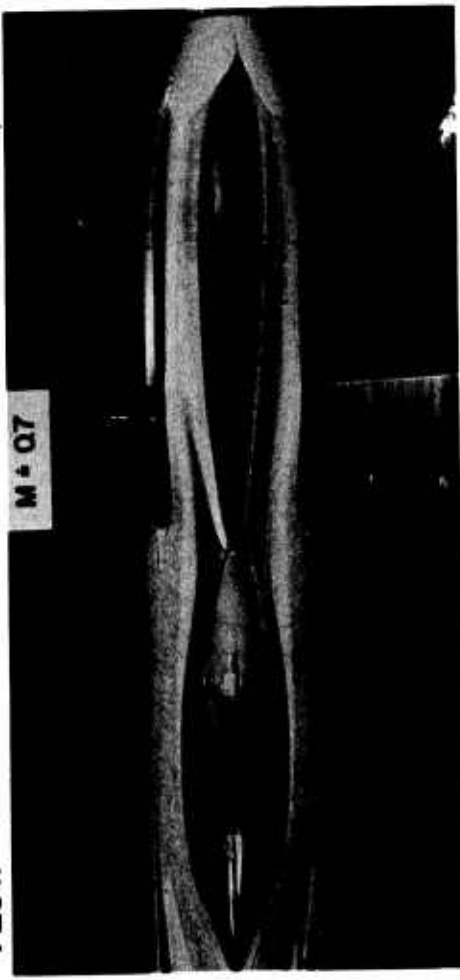
NACELLE ON

M = 0.7



FLOW →

M = 0.7



3-D SEPARATION LINE  
DIVERTER

M = 0.7

NACELLE OFF

3-D SEPARATION LINE  
DIVERTER

M = 0.7

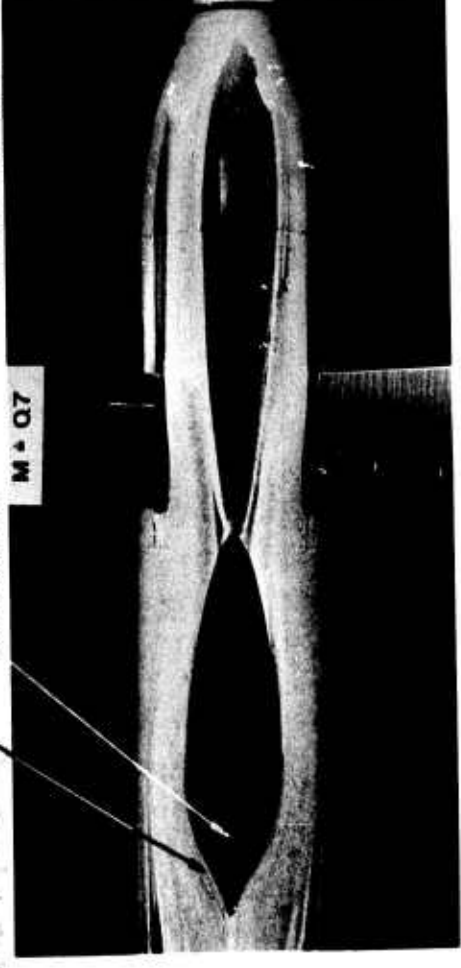


Fig. 4(d) Effect of diverter shapes on 3-D separations at  $R_L = 23.10^6$ ,  $L/D = 5$ , slender bi-convex diverter BWN 3 configuration at  $M_\infty = 0.7$

Fig. 4(e) Effect of diverter shapes on 3-D separations at  $R_L = 23.10^6$ ,  $L/D = 5$ , slender bi-cusped diverter BWN 4 configuration at  $M_\infty = 0.7$

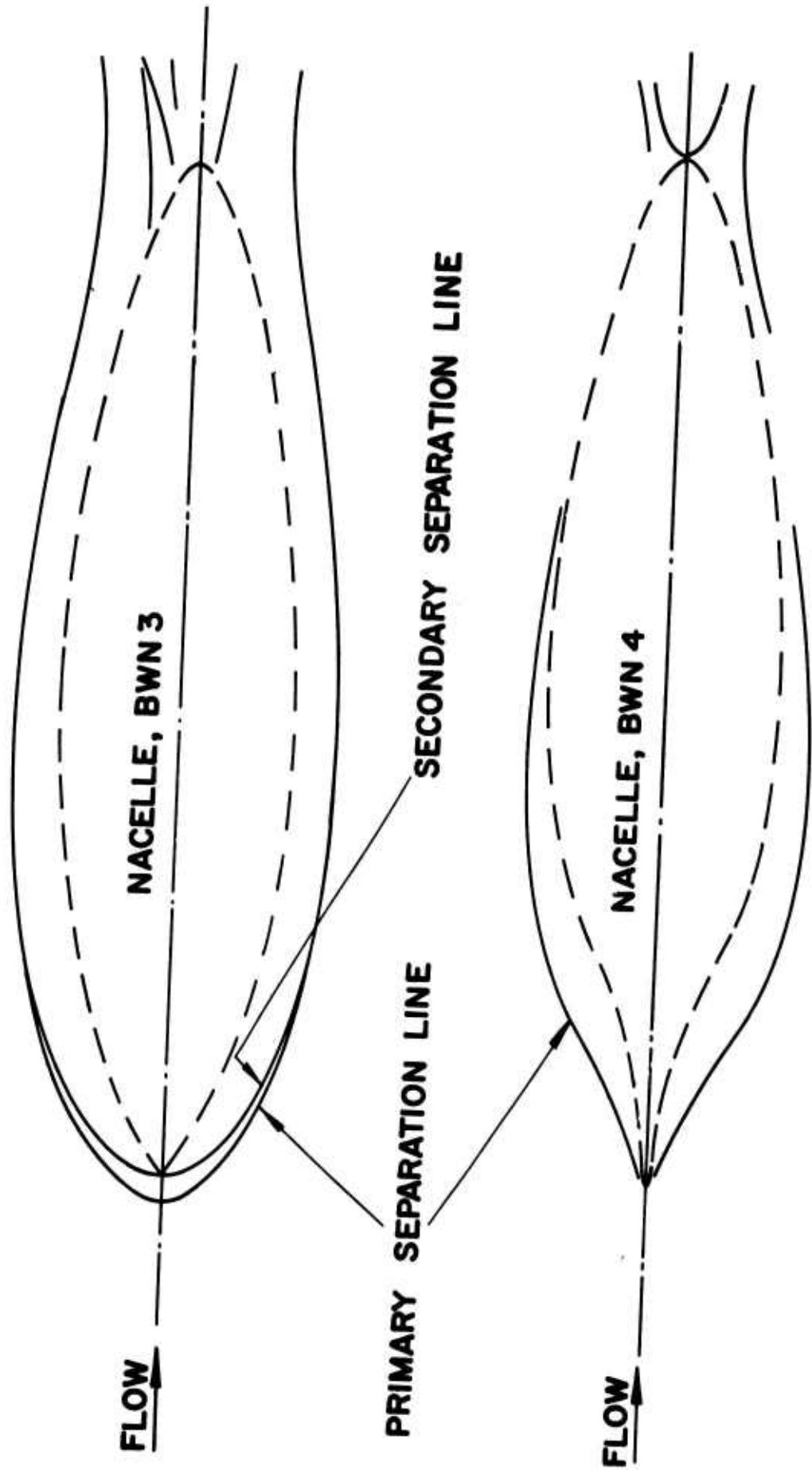


Fig.4(f) Tracings of separation lines about BWN 3, BWN 4 at  $M_\infty = 0.7$

(i) NOTE : MAJORITY OF INDIVIDUAL EXPERIMENTAL POINTS ARE OMITTED FOR PURPOSES OF CLARITY

(ii)  $C_D$ : TOTAL DRAG OF CONFIGURATION AT  $\alpha = 0^\circ$  BASED ON FRONTAL C/S AREA OF DRONE

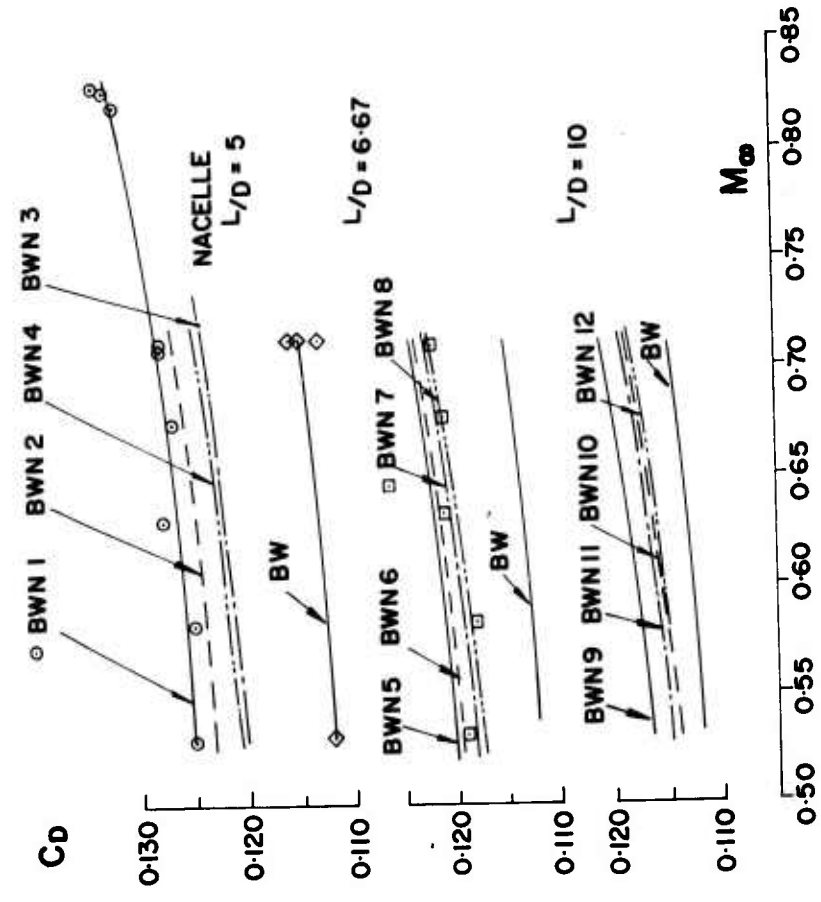


Fig.5 Variation of body/wing/nacelle drag with Mach number

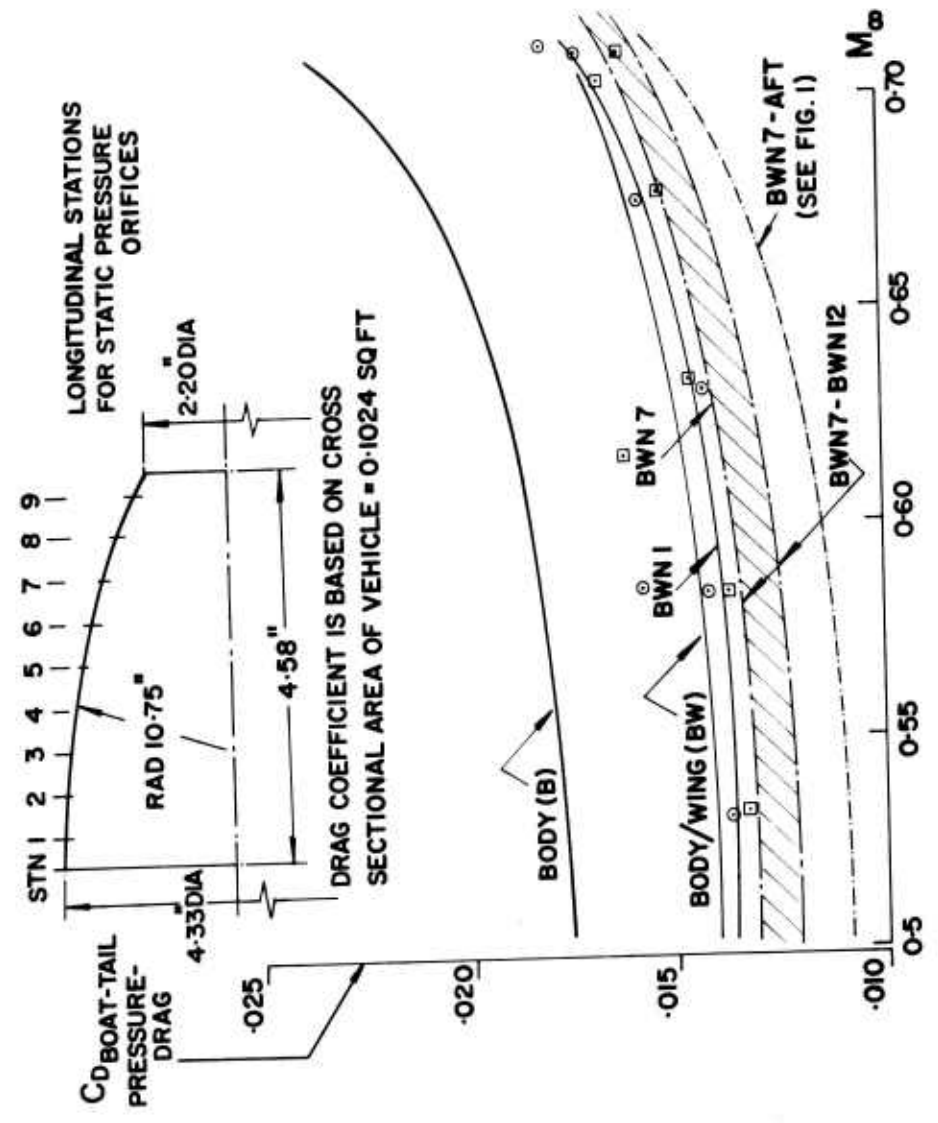


Fig.6 Variation of boat-tail pressure drag with Mach number

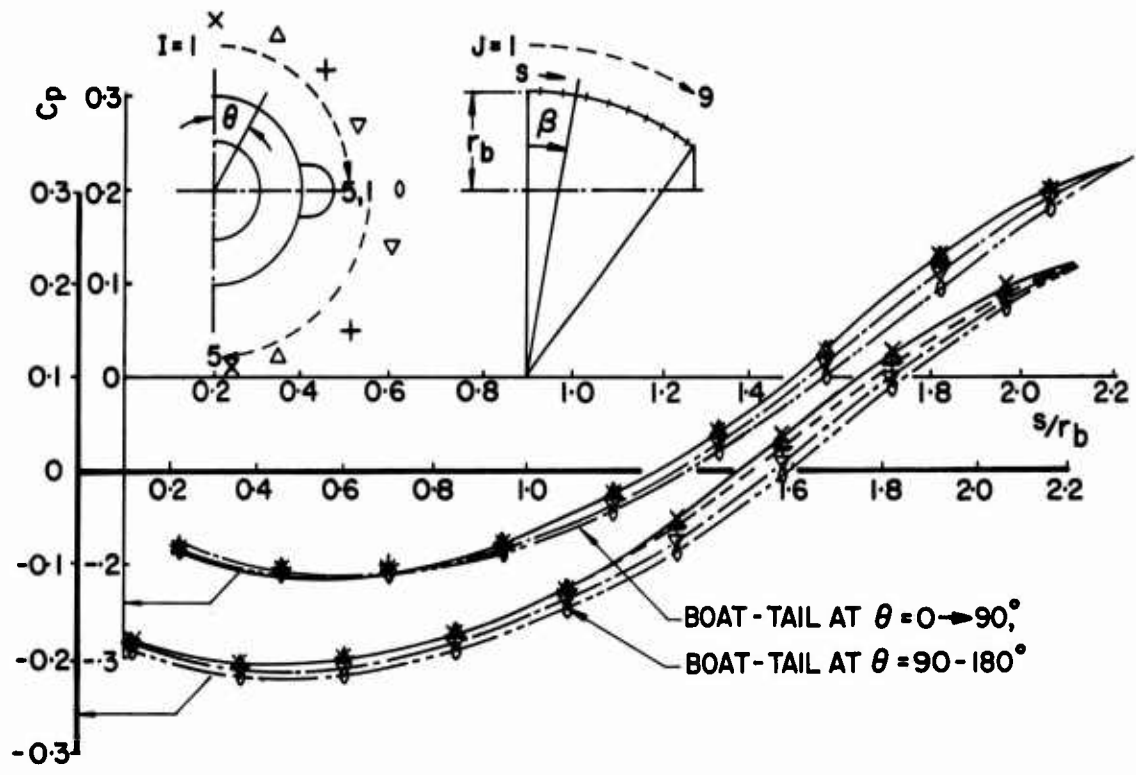


Fig.7 Effect of nacelle N1 on boat-tail pressure distribution at  $M_\infty = 0.5$ ; configuration BWN 1

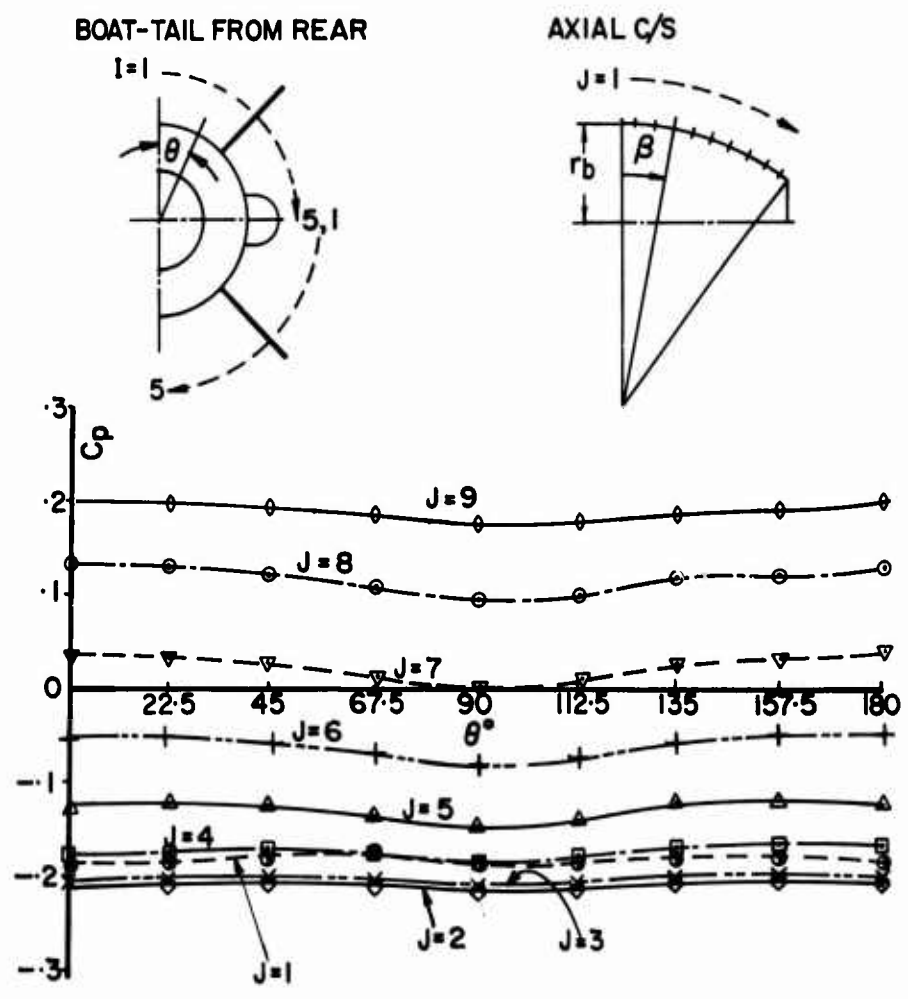


Fig.8 Effect of nacelle N1 on boat-tail circumferential pressures; configuration BWN 1 at  $M_\infty = 0.5$

18-16

WITH 'THROUGH FLOW'



← FLOW

WITH NO 'THROUGH FLOW'



→ FLOW

Fig.10 Effect of intake "through flow" on 3-D separations about elliptical diverter at  $R_L \approx 23.10^6$ ,  $L/D \approx 3.3$  at  $M_\infty = 0.55$ , and  $\alpha = 14^\circ$

DRAG COEFFICIENT IS BASED ON NACELLE PLUS DIVERTER  
FRONTAL AREA

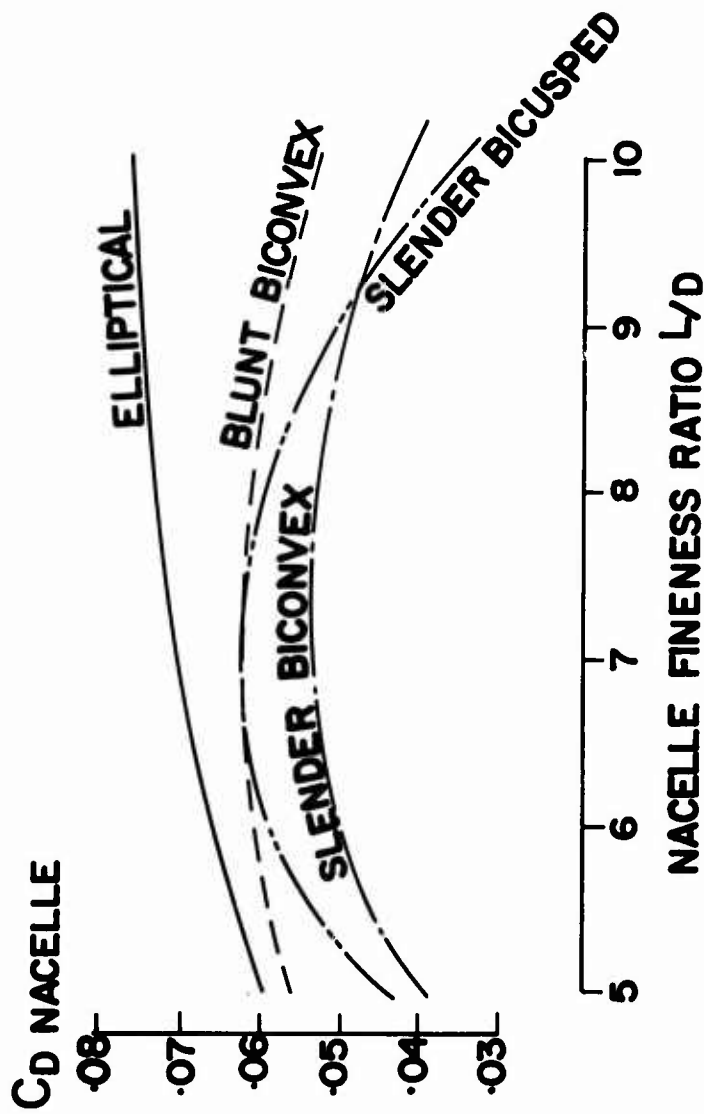


Fig.9 Dependence of incremental nacelle-plus-diverter drag on nacelle fineness ratio at  $M_\infty = 0.71$  and  $R_L = 23.10^6$

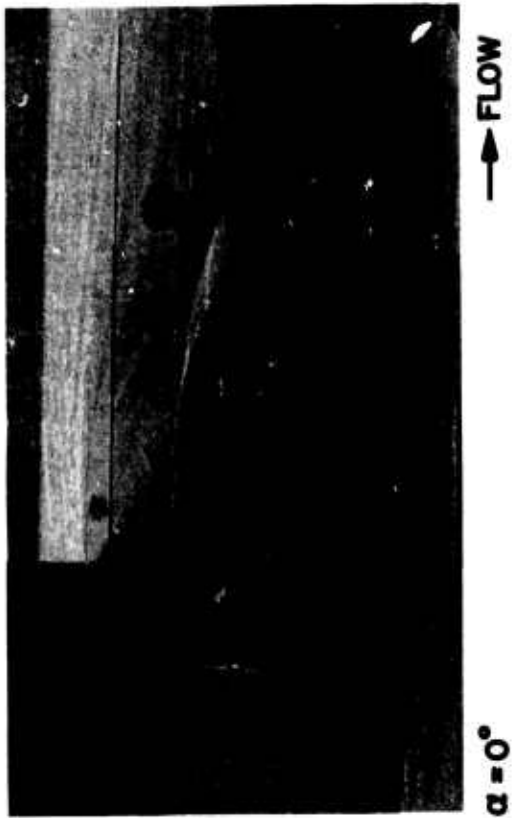
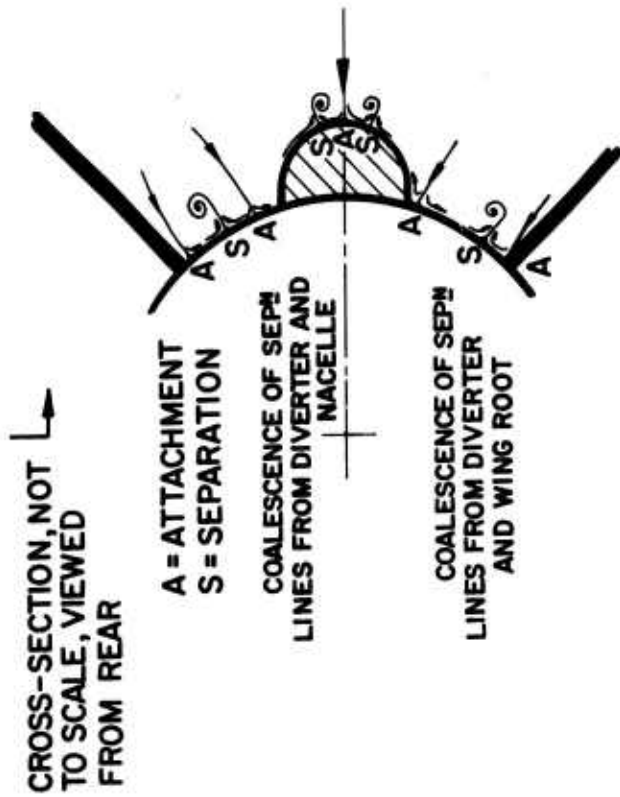


Fig.11 Effect of angle of attack on 3-D separations about elliptical diverter at  $R_L = 23.10^6$ ,  $L/D = 3.3$  at  $M_\infty = 0.55$



CROSS-SECTION, NOT TO SCALE, VIEWED FROM REAR

Fig.12 Interpretation of flow downstream of wing trailing-edge at  $M_\infty = 0.55$ ,  $R_L = 23.10^6$ ,  $L/D = 3.3$  and  $\alpha = 14^\circ$

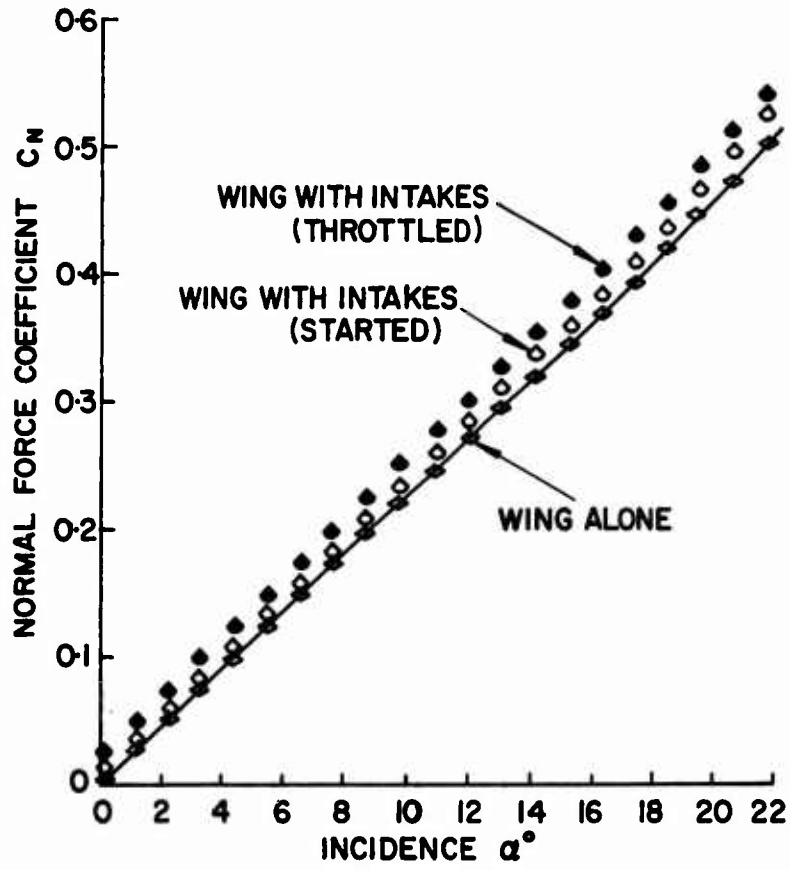


Fig. 13 "Favourable interference" effect on lift of  $70^\circ$  delta wing at  $M_\infty = 2.75$ ,  $R_{C_0} = 24.10^6$

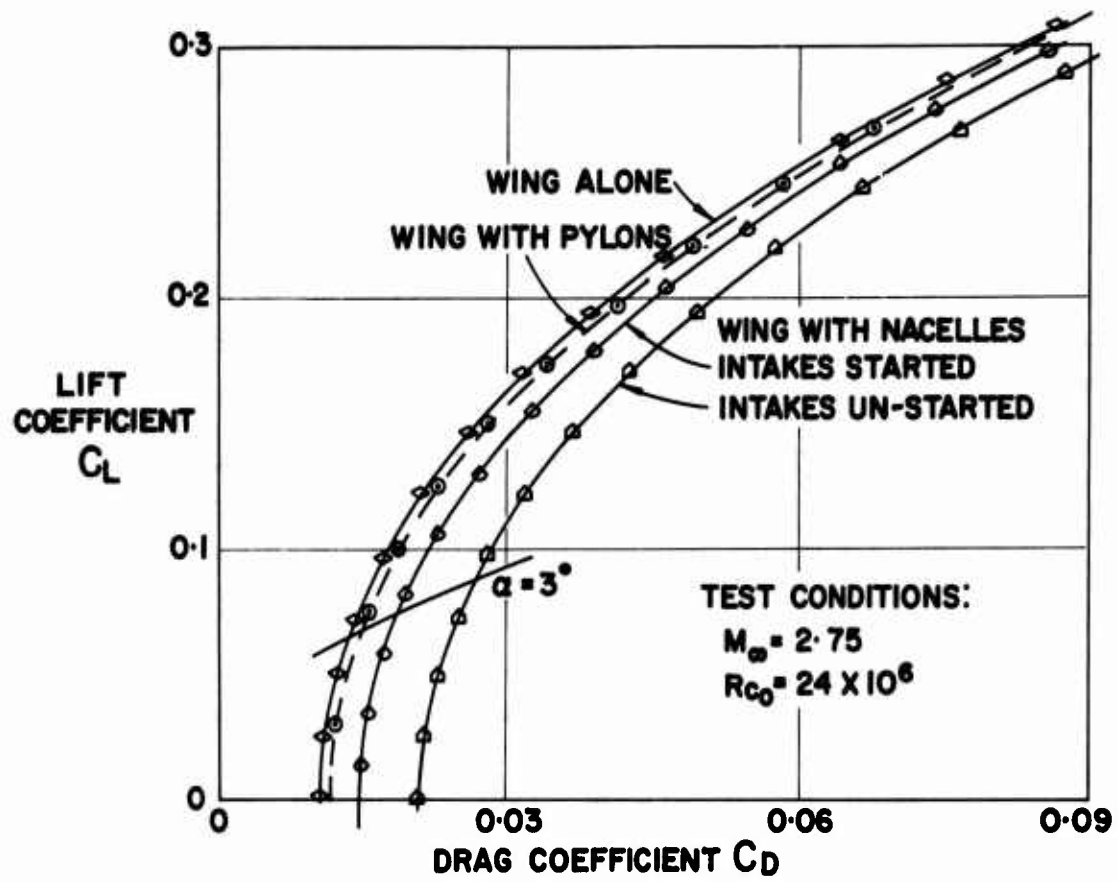


Fig.14(a) Lift/drag polars: 70° delta wing with 4 nacelles supported on pylons at design Mach number

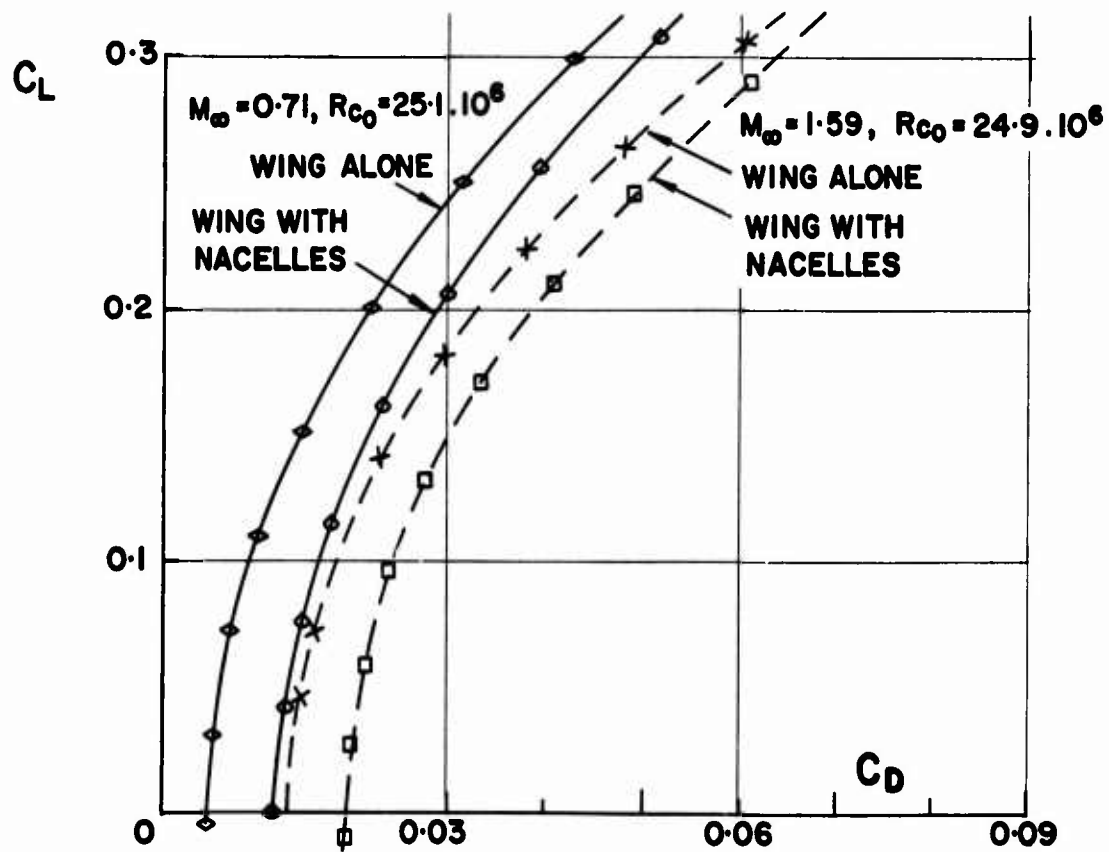


Fig.14(b) Lift/drag polars: 70° delta wing with 4 nacelles supported on pylons at off design Mach numbers

18-26

**WITH TOP NACELLES HALF-THROTTLED AND LOWER  
NACELLES WITH THROTTLES WIDE OPEN**

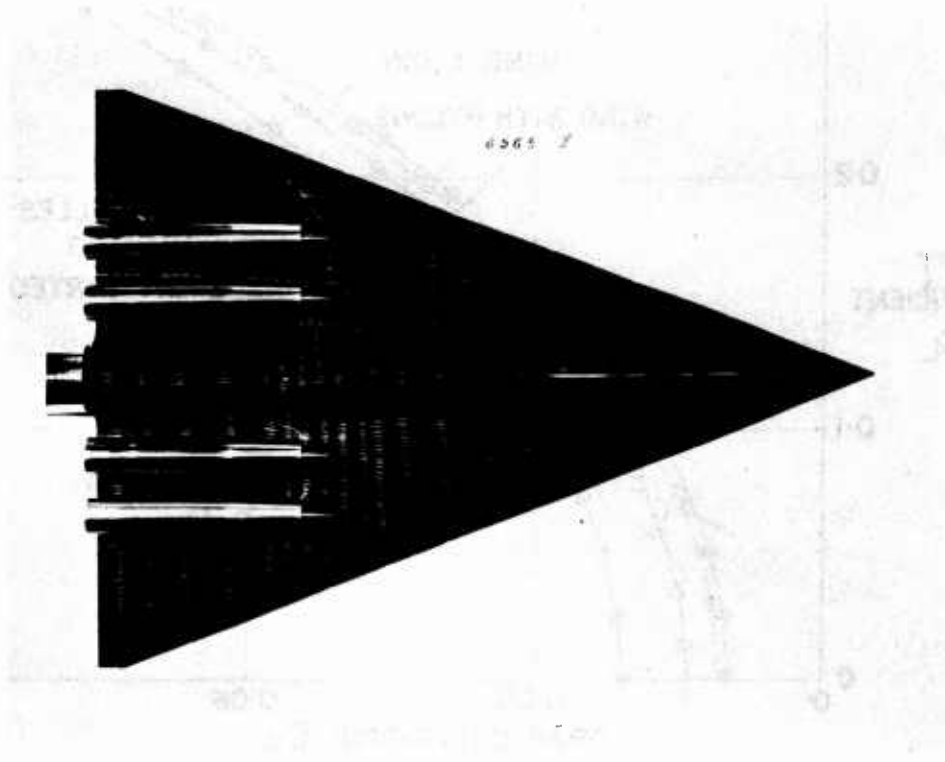


Fig.15(a) Lower surface oil flow visualisation on 70° delta wing at off-design Mach number  
 $M_\infty = 1.59$ ,  $\alpha = 2^\circ$ ,  $R_{c_0} = 15.10^6$

**WITH NACELLES REMOVED TO SHOW PYLONS  
( BOUNDARY LAYER DIVERTERS )**

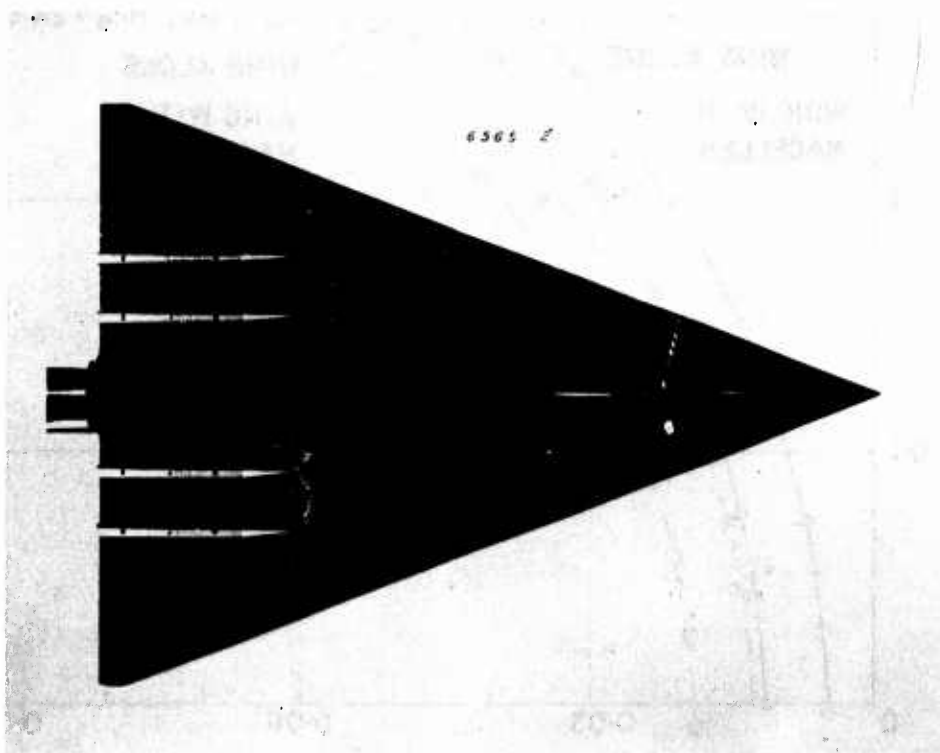


Fig.15(b) Lower surface oil flow visualisation on 70° delta wing at off-design Mach number  
 $M_\infty = 1.59$ ,  $\alpha = 2^\circ$ ,  $R_{c_0} = 25.10^6$

WITH PYLONS REMOVED

18-21

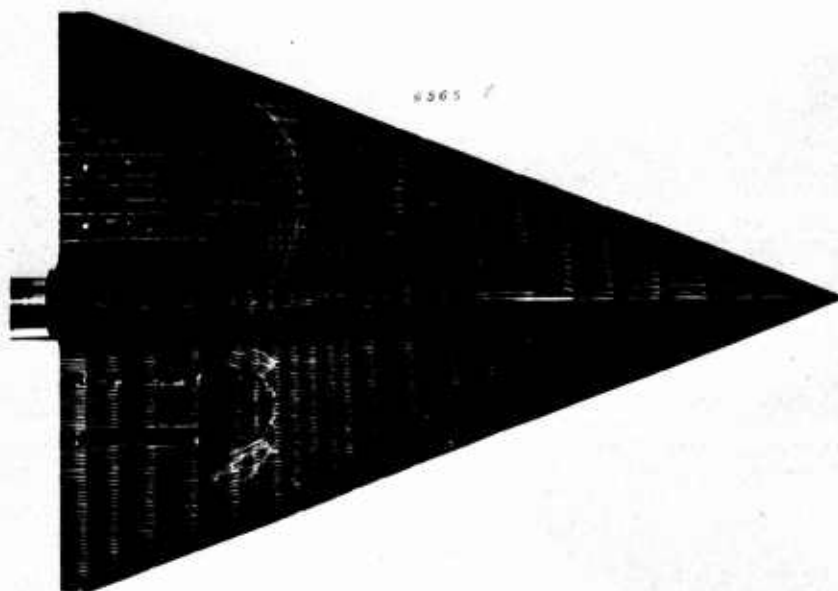


Fig.15(c) Lower surface oil flow visualisation on 70° delta wing at off-design Mach number  
 $M_\infty = 1.59$ ,  $\alpha = 2^\circ$ ,  $R_{c_0} = 25.10^6$

WITH TOP NACELLES THROTTLED TO 70% OF  
DESIGN MASS FLOW AND LOWER NACELLES WITH  
THROTTLE WIDE OPEN, OPERATING AT DESIGN CONDITION

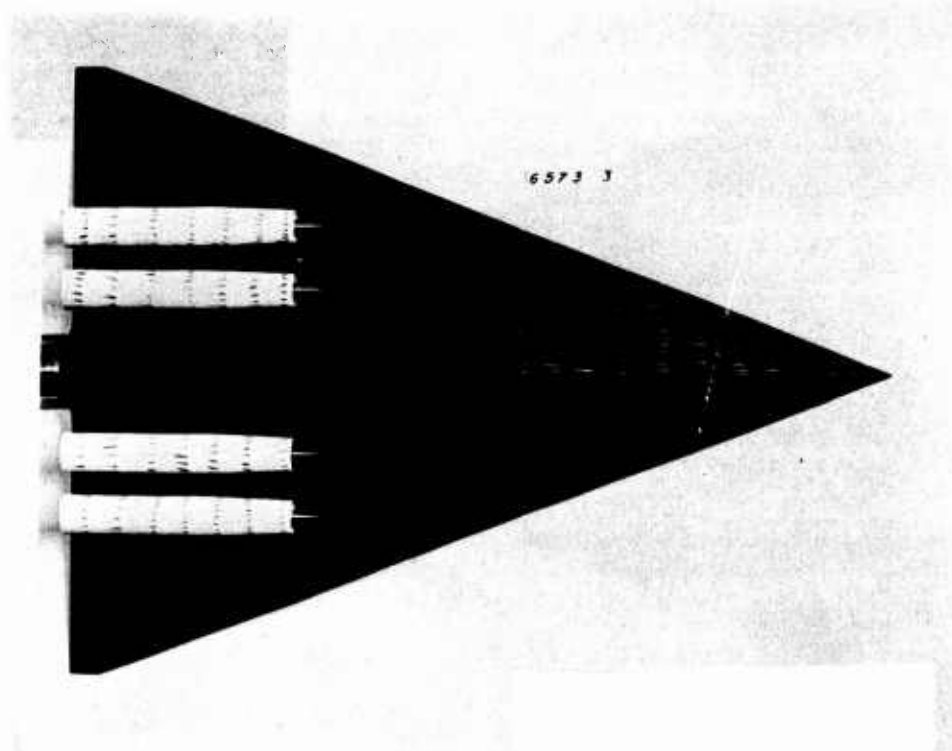


Fig.16(a) Lower surface oil flow visualisation on 70° delta wing at design Mach number  
 $M_\infty = 2.75$ ,  $\alpha = 3^\circ$ ,  $R_{c_0} = 24.10^6$

18-22

## COMPARISON BETWEEN LIMITING STREAMLINES ABOUT WEDGE AND BLUFF ELLIPTICAL DIVERTERS

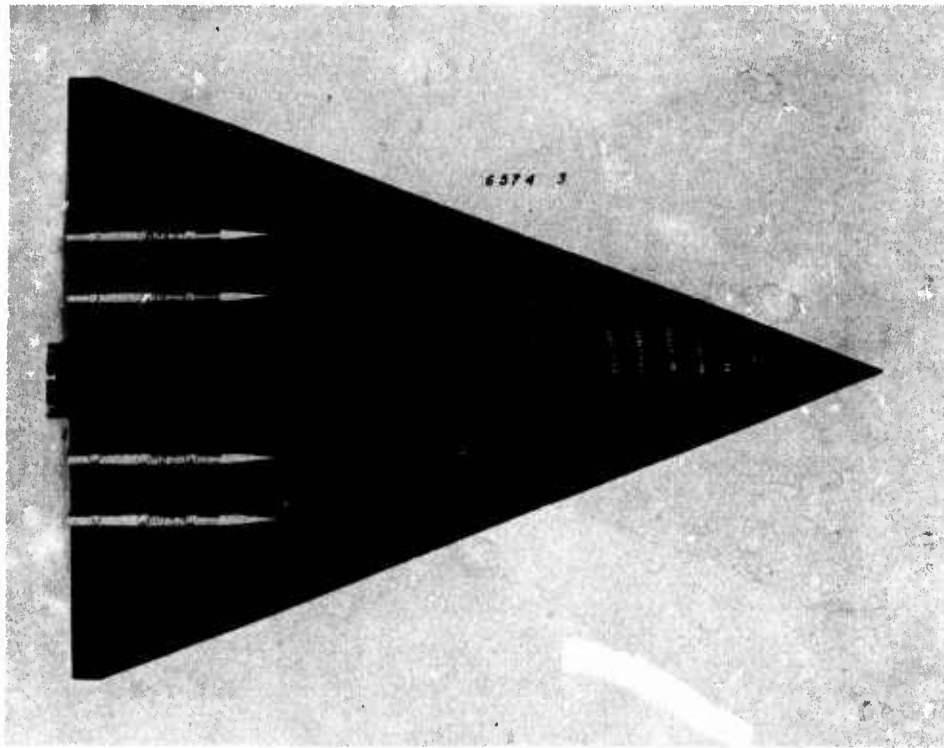


Fig.16(c) Lower surface oil flow visualisation on 70° delta wing at design Mach number  
 $M_\infty = 2.75$ ,  $\alpha = 3^\circ$ ,  $R_{Co} = 24.10^6$

## WITH NACELLES REMOVED TO SHOW PYLONS (BOUNDARY LAYER DIVERTERS)

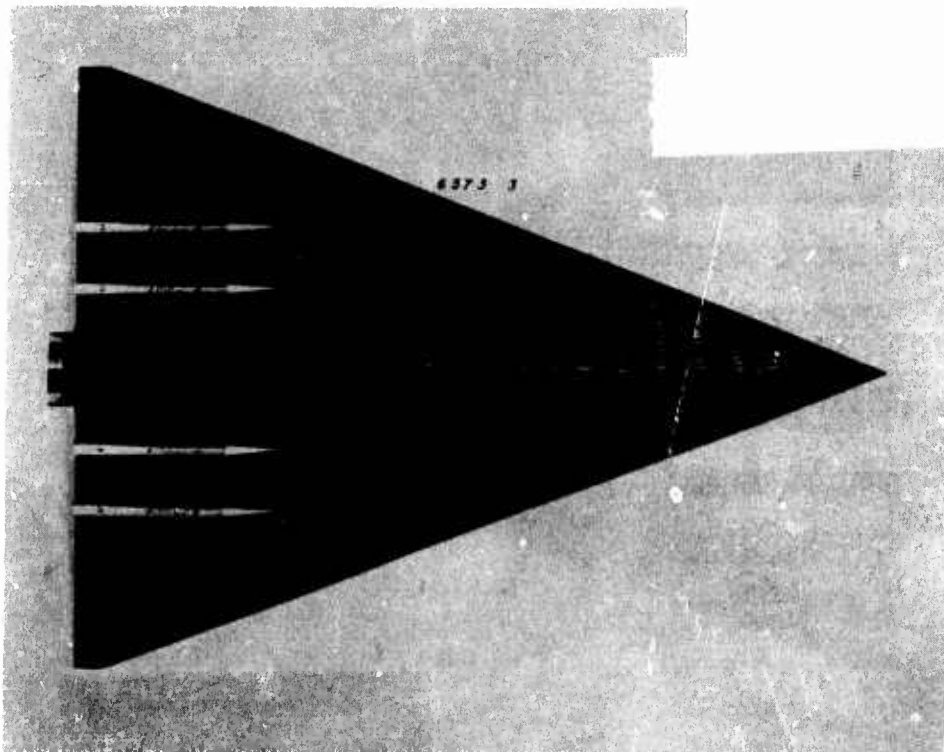


Fig.16(b) Lower surface oil flow visualisation on 70° delta wing at design Mach number  
 $M_\infty = 2.75$ ,  $\alpha = 3^\circ$ ,  $R_{Co} = 24.10^6$

by

P.G.Pugh and P.G.Hutton

Royal Aircraft Establishment, Bedford, England  
Aircraft Research Association Ltd, Bedford, England

19-1

## SUMMARY

The installed drag of stores makes a major contribution to the total drag of combat aircraft. It can be several times the sum of the free-air drags of the individual stores and its prediction and reduction are essential to the design of high-performance aircraft. Interference effects involved range from simple buoyancy to complex interactions involving viscous and wave drag phenomena.

For the simpler cases there are good prospects that the installed drag can be accurately predicted either by current methods or by relatively straightforward extensions of these. However, empirical methods will continue to be needed for the prediction of the drag of complicated cases eg multiple store arrays at transonic speeds.

Finally, some examples are given to show the opportunities for reducing the installed drag either by redesigns to take advantage of improved mechanical systems or through the development of radically new installations.

## NOTATION

$C_A$	axial force coefficient
$C_D$	Drag coefficient
$\Delta C_D$	Increment in $C_D$
$\Delta C_{DA}, \Delta C_{DC}$	$\Delta C_D$ at $M_A$ and $M_C$ respectively
$\Delta C_{DA \text{ SWET}}$	low speed increment in drag coefficient based on wetted area of store assembly
$\sum C_{D \text{ COMP}}$	Sum of free-stream drag coefficients of components of store assembly
$C_{Dsi}$	$C_D$ of a single isolated store
$C_p$	Pressure coefficient
$C_L$	Lift coefficient
$D$	Maximum diameter of store
$f_{si}$	Fineness ratio of a single isolated store
$K_A$	Factor defined in section 2
$K_I$	Factor defined in section 2
$K_S$	Installation factor (defined in section 1)
$M$	Free-stream Mach number
$M_A$	Initial drag rise Mach number
$M_C$	The Mach number at the start of the steep drag rise
$x_s$	Axial stagger of stores
$\lambda_{SI}$	Parameter defined in section 3

## 1 THE IMPORTANCE OF THE PROBLEM

The majority of military stores are carried externally. This practice has much to commend it. External carriage facilitates the interchangeability of a wide range of stores and is often associated with lower release disturbances than internal carriage. Also, as opposed to an aircraft of sufficient size to permit internal carriage of sufficient stores, an aircraft designed for external store carriage can be smaller, lighter, and have a higher performance when flown "clean", for example, on the return part of a strike mission. Nevertheless, a considerable price may have to be paid for these gains. In particular, externally carried stores may make a large contribution to the total drag of a fully-loaded combat aircraft. This penalty arises for two reasons. Firstly, the design of the stores themselves and their mountings is strongly influenced by many considerations other than their free-air, zero-lift, drag. They are not always low-drag devices. Secondly, the way in which they are installed may give rise to large interference effects which can further increase the installed drag of the stores. The magnitude of the problem is well illustrated by the example, by no means an extreme one, in Fig (1). This shows the variation with Mach number, at a fixed lift coefficient ( $C_L = 0.2$ ), of both the drag of a typical strike

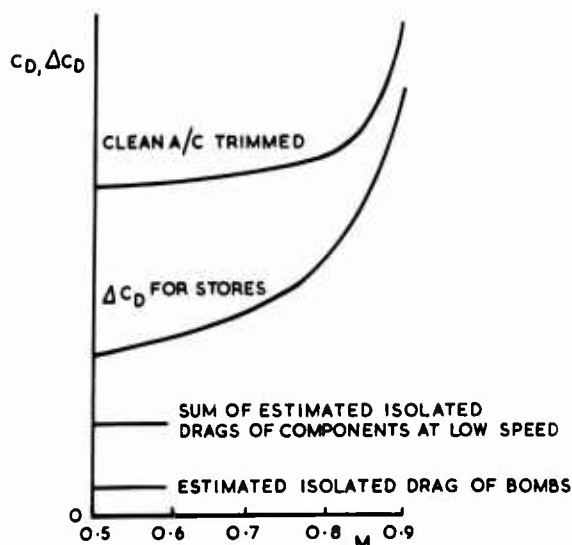


FIG. 1 EXAMPLE OF INSTALLED DRAG INCREMENT

aircraft in the clean condition and the increment in drag due to the addition of a typical bomb-load (and associated carriers, pylons etc). Comparison of these two curves highlights the severity of the problem and suggests the extent of the loss in the performance of an aircraft that can be caused by the external carriage of stores. Another modern strike aircraft has a maximum level speed of 1007 km/hr at sea level when flown with a 5016 kg bomb load but, at the same altitude, the maximum speed is increased to 1101 km/hr after the bombs have been dropped.

Other examples are legion, and confirm that the drag penalties of current external store loads can be very severe. Nor is the problem likely to get easier in the future. For example, one profitable way of exploiting advances in wing design would be to design smaller (and, hopefully, cheaper) combat aircraft capable of carrying similar, or greater, loads than at present. Thus, the size of stores relative to the parent aircraft may tend to increase, and this will, in turn, increase the relative importance of the installed drag of the stores. Also, stores may need to be carried at greater speeds. This will lend further importance to the installed drag of the stores at transonic speeds - where especially severe interference effects have been encountered.

Conversely, any means of reducing the installed drag of stores will have a large beneficial effect on the performance of the loaded aircraft.

The importance of the installed drag gives rise to two demands upon aerodynamicists. Firstly, there is a need for methods of predicting the installed drag of a multitude of stores in a wide variety of combinations, mountings, and locations on different aircraft. This is a formidable problem but one which it is essential to solve because the total utility of a projected combat aircraft cannot be properly assessed unless such an important contribution to its drag can be accurately estimated. Secondly, there must be a continuing quest for means of reducing the installed drag of stores. Such reductions can considerably improve the performance of a combat aircraft. Indeed, it may well be far more difficult to obtain as large reductions in the total drag from any other source.

The first steps towards meeting either of these requirements is to examine the way in which the installed drag arises and to set up some framework for analysis. Returning to Fig (1), the installed drag increment can be compared with the free-air drag of the bombs alone and with the summation of the estimated free-air drags of the bombs, pylons, carriers and their excrescences. It is clear that the free-air drag of the bombs is small compared to their installed drag increment. The additional drag comes partly from the mounting system (pylons, and carriers) and partly from interference effects. The latter is exemplified by the considerable difference between the estimated summation of the various free-air drags and the actual installed drag increment.

In studying such effects it is convenient to work in terms of an installation factor,  $K_S$ . Definitions of installation factors are not universally consistent but the one used here is believed to be the most common. This is the ratio of the measured increment,  $\Delta C_D$ , in the drag of the aircraft (due to the addition of a store assembly) to the sum,  $\sum C_{D,COMP}$ , of the free-stream drags of the components of the store assembly at low speed and zero lift. Estimates must be used for some or all of these component drags because experimental data are not available. Thus the incremental installed drag is the product of  $K_S$  and  $\sum C_{D,COMP}$ ;  $K_S$  is a measure of the interference effects. Since free-stream drags of most stores and associated components in isolation are either known or can be estimated to reasonable accuracy, the major problem in predicting the installed drag is in estimating  $K_S$ .

While the prospects of reducing the drag of the individual stores themselves are outside the scope of this paper, this by no means exhausts the possibilities of reducing the free-stream drag of parts of the store assembly. Conventional pylons, carriers and other components of the assembly often have drag producing features which can be ameliorated. Reducing the installation factors involves modifications of the flow interactions between aircraft and store components and/or of the interactions between components of the store assembly e.g. between individual stores mounted on multiple racks. This is more difficult for multi-role aircraft carrying a wide variety of stores than for specialised aircraft. Nevertheless, it should be possible to achieve important gains in this way.

## 2 THE NATURE OF THE PROBLEM

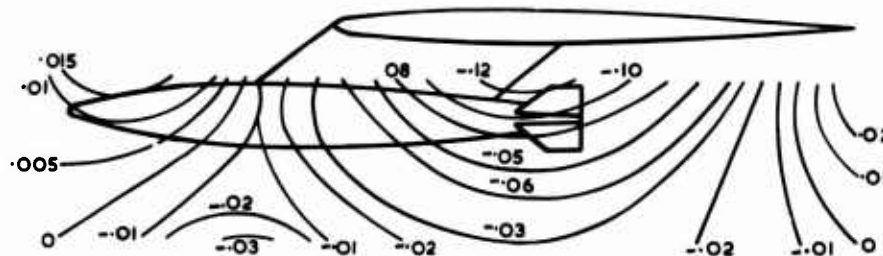
As indicated in the preceding section the flow about externally carried stores is compounded of the flow about the aircraft, about the store assemblies, and mutual interference effects. The store assemblies may present aerodynamic problems because they are not always aerodynamically clean and comprise several components in close proximity. The flow about the aircraft, especially the wing, usually represents the fruits of much subtle and detailed research. Judging the way in which this will respond to

the influence of the flow about the stores is often difficult.

To provide a comprehensive description and/or prediction of the general case of flows about externally carried stores demands a knowledge of aerodynamics well beyond the present state of the art. It is necessary to consider many aspects and to study simplified, more specific, cases if some progress is to be made. As in other branches of aerodynamics, one important distinction that can be drawn is that between those flows which closely resemble potential (i.e. inviscid, and irrotational) flows and those involving wavedrag or viscous phenomena other than thin boundary layers. The flow about aerodynamically clean installations at subsonic speeds is generally of the former type. For such installations, the interference effects<sup>6</sup> arise because of:-

- a) changes in the pressure distribution over the store, pylon and wing due to the interaction of the wing, pylon and store pressure fields i.e. buoyancy effects
- b) local changes in the skin friction drag due to changes in dynamic pressure arising from interactions between the various flow fields
- c) changes in flow direction due to the interference causing induced drag on the store or changes in the induced drag of the wing.

Experimental data suggest that in many cases the second and third of these are generally small. Thus, in such cases the only large effects remaining are those due to buoyancy, which in potential flow would cancel. Their magnitude is illustrated in Fig (2). Using the measured pressure field due to a very similar model, the buoyancy forces on two stores have been estimated<sup>2</sup> for different chordwise locations of



STREAMLINED STORE LOCATED IN WING PRESSURE FIELD  
(FROM REF. 13)

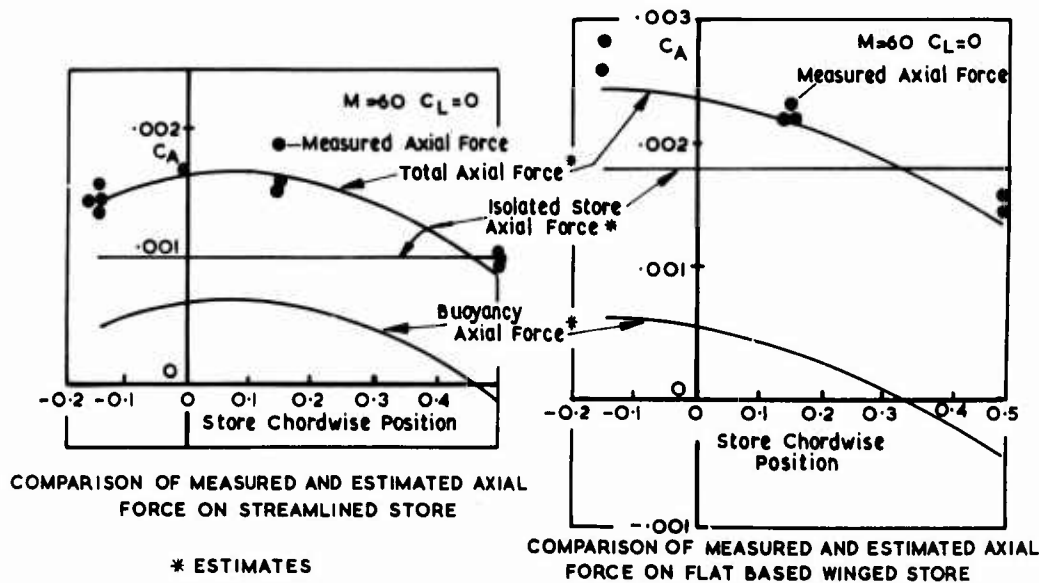


FIG. 2 BUOYANCY EFFECT ON UNDER WING STORES

the store with respect to the wing upon which they were mounted. When the estimated buoyancy forces were added to an estimate of the free-stream drag of the isolated store, to obtain estimated values of the axial forces on the installed store, the resulting curves agree extremely well with the measured axial force data points. This suggests that, for similar cases, the axial force on an installed store can be accurately calculated from a knowledge of the underlying flow field. (Some of these results are described

19.4  
in more detail in Ref. 12).

For most practical store locations, the buoyancy forces increase the drag force on the store and reduce that on the wing. In potential flow these effects balance. Thus, at low incidence and Mach number, it is found that the large interference drag forces acting on single stores, when pylon-mounted not too close to a wing lower surface, are effectively cancelled giving installation factors close to 1.0.

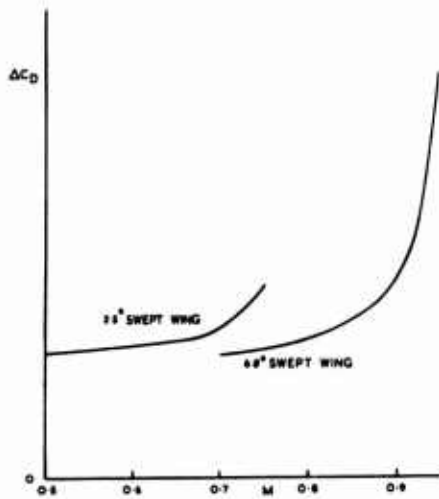


FIG. 3 DRAG INCREMENTS FOR STORES ON WINGS OF DIFFERENT SHAPE

This simple result becomes invalid as viscous or wavedrag phenomena become important, for example, as Mach number is increased. Figure 3 shows the variation of the installed drag increment of a store when carried under wings of two different wing-sweep angles. It will be seen that higher drag increments are found at the higher Mach numbers. Increased wing-sweep tends to delay the occurrence of these unfavourable effects.

Interference effects also occur between the components of a store assembly. For this reason it is sometimes convenient to treat the installation factor,  $K_S$ , as composed of two factors,  $K_A$  and  $K_I$ , where  $K_A$  is the ratio of the free stream drag of the store assembly to the sum,  $\sum C_{D,COMP}$ , of the free stream drags of its component parts and  $K_I$  is the ratio of the measured increment in the drag of the aircraft (due to the addition of the store assembly) to the free stream drag of the store assembly. A simple case of interference between components of an assembly occurs between a single store and the pylon upon which it is mounted. An example is given in Fig (4). In this the measured drag of the combination of a store and a pylon is compared with the measured free-stream drags of these components when tested in isolation<sup>3</sup>. The sum of the free-stream drags of the pylon and the store is reasonably close

to the drag of the combined store and pylon. In this case, the interference effects are relatively small ( $K_A \approx 1.2$ ).

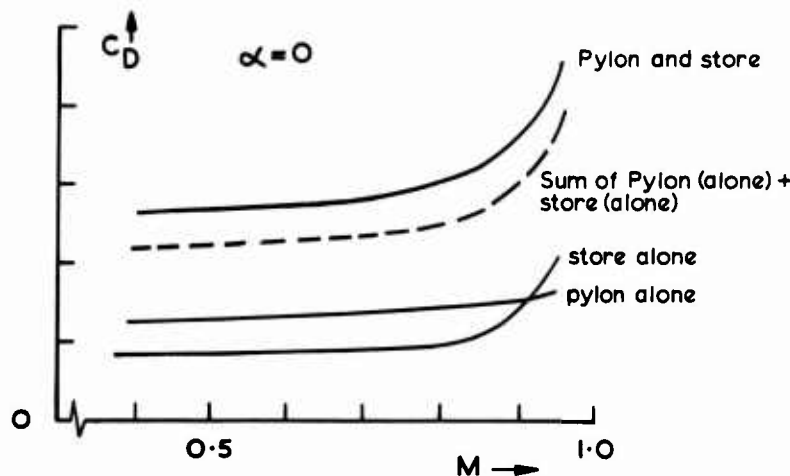


FIG. 4 INTERFERENCE BETWEEN STORE & PYLON

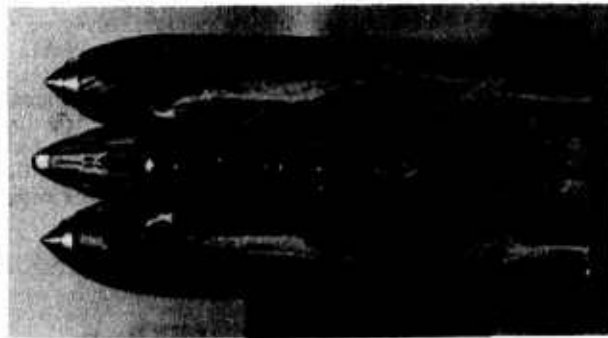
A much larger contribution to the drag of the store assembly arises from interference between the stores themselves and between the stores and the carrier when several stores are hung from the same pylon. This will be discussed in more detail later, but the complexity of the resulting flows is well illustrated by Fig (5). These are photographs of oil flow patterns obtained from models of two triple carriers each carrying three bombs<sup>3</sup>. In order to show the flow between the bombs, one of these was removed after the test and the photographs show the flow patterns

on the underside of two bombs and the carrier and the upper surfaces of the remaining bomb. Of particular interest are the areas of separated and reverse flow above and between the bomb afterbodies, and the out-flow between the bombs from the central "channel". Also, it will be seen that these undesirable features are considerably modified by modest changes to the geometry of the carrier.

Although far from comprehensive, the examples quoted above demonstrate the wide variety of problems that are encountered when attempting to predict drag increments or to design a low draw installation. The problems of prediction are now considered in more detail.

### 3 THE PROSPECTS FOR THE PREDICTION OF INSTALLED DRAG INCREMENTS

The simplest case is provided by a single streamlined store at low incidence and low Mach number. As discussed earlier, the interference effects are then predominantly of a potential flow type. The buoyancy effects generally cancel and the result is a drag increment close to the total free-stream drag of the components of the store assembly. In addition, if the aircraft flow-field is known for the vicinity of the store location, the drag force on the store can be calculated. A drag increment further



standard



"cleaned up"

### FIG.5 OIL FLOW: TRIPLE CARRIER

removed from  $\sum C_{D,COMP}$  can be expected if the store is placed in a region where the mean local velocity is very different from free stream. Such installations are fairly readily identified and those with high velocities should be avoided. Low velocity regions can sometimes be exploited e.g. small diameter stores can be wholly or partly submerged in the fuselage boundary layer. Again, if the aircraft flow-field is known (including viscous effects in some cases) it should be possible to estimate first order corrections for such effects.

Similar considerations apply to groups of stores, but some caution is necessary. As long as mutual interference effects within the groups of stores and between them and the aircraft are of the potential flow type, the buoyancy effects will cancel and  $K_S$  will be near unity. A factor,  $K_S$ , of near unity has also been found to apply to assemblies containing some individual components over which the flow must be very different from potential flow, provided that such differences are local. For example, the increments due to bluff excrescences on single, otherwise streamlined, stores are near the free stream drag of the excrescences provided they are not placed in high velocity regions and the flow separations due to the excrescences remain local.

However, many groups of stores comprise bodies, often relatively bluff, either in contact or in close proximity to each other. Under such circumstances, significant areas of separated flow may be present or some stores may carry sufficient lift for their induced drag to be important. Such effects have not been found to be serious for streamlined stores well spaced apart or even for bombs separated by distances as small as 1 calibre. Nevertheless, these effects can be important for bluff stores or stores in very close proximity.

As indicated above, a knowledge of the flow field about the aircraft can be valuable both for calculating buoyancy forces and in identifying suitable store locations. Such information is usually obtained experimentally. This requires detailed explorations of flow fields which are time-consuming and difficult. However, in recent years notable advances have been made in the development of numerical methods for the calculation of such flow fields. Also, the prediction of the development of three-dimensional boundary-layers has become practicable - at least for some cases. The time is not far off when it will be possible to calculate the complete flow field about an aircraft and externally carried stores provided that large-scale separated flows are not present. In fact, a simple example is reported in Ref. 10 and the similar problem of nacelles in Ref. 14. When this can be done, it should be possible to obtain reasonable predictions not only for essentially potential flows, but also to estimate the conditions for the onset of flow separation or of local supersonic flow. This would at least provide a design tool comparable to current methods of wing design. However, the magnitude of this task should not be underestimated. Moreover, there is the insidious danger, inherent in all elaborate calculation methods, that the resulting program would be so complex as to demand long running times on large, expensive, computers. It is likely that such methods would be too expensive to use in order to calculate all of the multiplicity of cases that are required during project studies. Simple, semi-empirical methods of prediction will continue to have an important role throughout the foreseeable future.

Certainly, semi-empirical methods provide the only reasonable basis upon which to tackle the most difficult cases, for example, an aircraft at high Mach number and high lift carrying a store arrangement

19-6

with many component parts. The flows about the components of the store assembly will all interfere with each other and with the parent aircraft so that the resulting flow contains shockwaves, separation bubbles, vortices and wakes. In this case there is no immediate hope of devising accurate estimation methods and recourse must be had to virtually unadulterated empiricism. This is particularly unfortunate since the interference effects can be very large and variable <sup>3</sup>. For example, of the installations shown in Fig (5) the one having the highest drag had an installation factor  $K_S = 2.19$  at  $C_L = 0$  and  $K_S = 1.68$  for  $C_L = 0.3$ , even at Mach numbers as low as 0.5. At a Mach number of 0.8 (a little below the drag-rise Mach number of one of the stores in isolation), the increment in installed drag coefficient had risen to about 1.6 times its value at  $M = 0.5$  at both  $C_L = 0$  and  $C_L = 0.3$ . Thus, the interference effects both within the store assembly and between this and the aircraft at  $M = 0.8$  amount to a multiplication of the sum of the low-speed free-stream drag of the components of the store assembly by factors of between 2.7 and 3.7.

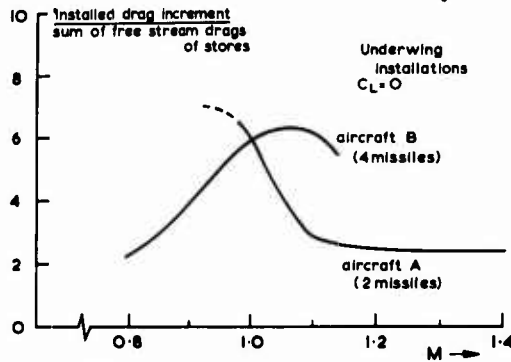


FIG. 6 INSTALLATION EFFECTS FOR TWO AIRCRAFT

Large installed drags occur at transonic speeds even for simple installations as shown in Fig (6). This shows results, derived from free-flight trials for missiles pylon-mounted from the wings of two delta wing/body combinations at zero lift <sup>7</sup>. The ratio of the incremental installed drag to the free-stream drag of the missiles at the same Mach number rises to a high peak in the transonic speed range.

Fortunately, many practical installations lie between the extremes of difficulty quoted above and, for these, it is or could eventually be possible to devise prediction methods to various standards and to varying degrees of empiricism. An example is provided by the prediction of the drag increments due to a range of underfuselage stores at both low and high subsonic speeds <sup>2</sup>. This is considerably simpler, in principle, than a method for underwing stores because the fuselage flow field is less complicated than that under a wing and the effects of

the store assembly on the fuselage are, in general, less significant than on a wing.

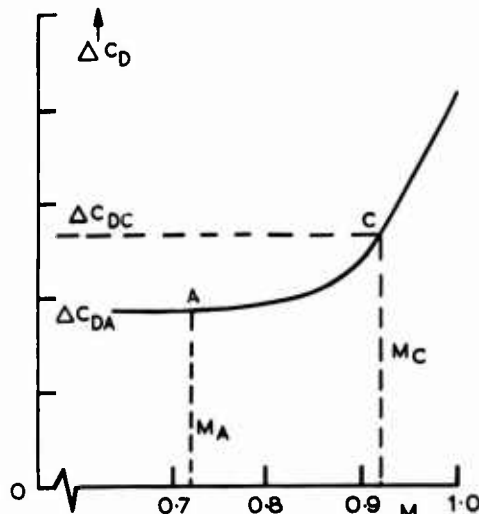


FIG. 7 FRAMEWORK FOR ANALYSIS OF INSTALLED DRAG (UNDERFUSELAGE STORES)

In developing this method it was assumed that the drag increment due to the installation of underfuselage stores would vary with Mach number in the manner shown in Fig (7). Thus it was necessary to devise methods to predict the following quantities:

- 1  $\Delta C_{DA}$  for  $M \leq M_A$  is the low-speed incremental drag.
- 2  $M_A$  i.e. the initial drag-rise Mach number for the drag increment.
- 3  $M_C$ , the Mach number at the start of the steep drag rise.
- 4  $\Delta C_{DC}$  for  $M = M_C$ .
- 5 A fairing between point A and point C i.e. for  $M_A \leq M \leq M_C$ .
- 6  $\Delta C_D$  at  $M = 1$ .

Taking each of these in turn,  $\Delta C_{DA}$  may, as has been seen previously, be written as  $K_S \sum C_{D,COMP}$ . The earlier discussion points to  $K_S$  being about 1.0 for single streamlined stores and in practice this value has been found to apply to most single, pylon mounted underfuselage stores. However, for closely spaced side-by-side stores on a single pylon or carrier the interference is typically sufficient to give  $K_S \approx 1.7$ . Favourable interference,

i.e.  $K_S < 1$ , often arises with stores in tandem, particularly with bluff noses and large bases. This will be discussed later.

The correlation of the initial drag-rise Mach number,  $M_A$ , is complicated by the difficulty of obtaining it from experimental results to an acceptable degree of accuracy. This is for two reasons, firstly the rise in  $\Delta C_D$  is often so gradual that it is difficult to define  $M_A$  and, secondly, many tests generate data at rather large increments in Mach number. Approximate correlations Fig (8) have been achieved for single and side-by-side stores using an aerodynamic fineness parameter,  $\lambda_{SI}$ , of the store assembly defined by  $\lambda_{SI} = \frac{\text{Estimated low speed profile drag, excluding base \& bluff nose drag}}{\text{Estimated flat plate skin friction}}$

$M_C$ , the Mach number for the start of the steep drag rise, has been found to be  $M = 0.92 \pm 0.02$  for a wide range of configurations with no obvious correlation of the variations. For prediction purposes, therefore, we take  $M_C = 0.92$ .

The drag increment,  $\Delta C_{DC}$ , at the start of the steep drag rise divided by  $\Delta C_{DA}$  correlates moderately well in terms of  $M_A$  and the low speed drag increment coefficient based on the wetted area of the store assembly  $(\Delta C_{DA})_{SWET}$ . This coefficient may be considered as combining a "dirtiness parameter" with the low-speed installation factor. The resultant family of curves is shown in Fig (9). The trends may appear surprising at first sight, but since  $\Delta C_{DC}$  cannot increase without limit  $\Delta C_{DC}/\Delta C_{DA}$  must approach unity at very high values of  $(\Delta C_{DA})_{SWET}$ .

A mean curve, Fig (10), for the fairing of the data for  $M_A \leq M \leq M_C$  in normalised form fits the data well enough for practical purposes.

There are very few data available for  $\Delta C_D$  at  $M = 1$ , the "aiming point" for the drag curve for  $M \geq M_C$ , but some evidence from other types of store installation suggests that wave drag calculations by the Emlinton method, <sup>11</sup> with some fairing of discontinuities in the area distribution, should give a good guide.

Fig (11) compares estimates of store drag increments by this method for a typical installation with measured values. The maximum error is about +6.0%. Other examples checked show errors up to about 10% under some conditions. This is typical of the performance of current prediction methods. While these are very useful for project studies, there is still room for improvement, but this will certainly require more fundamental investigations aimed at providing a better understanding of the flow processes involved.

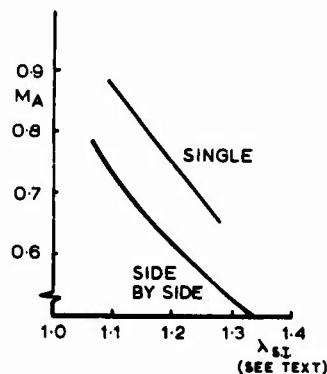


FIG. 8 CORRELATION OF  $M_A$

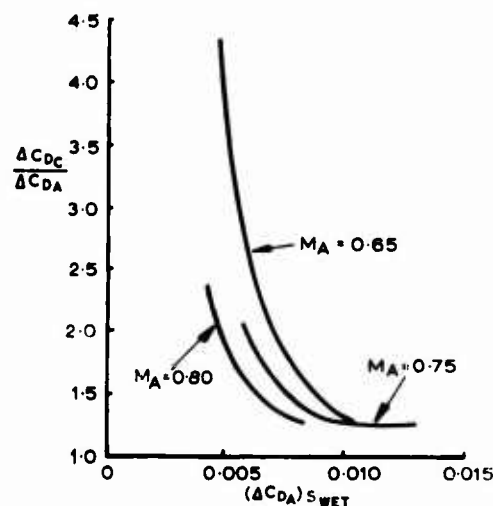


FIG. 9 CORRELATION OF  $\Delta C_{DC}$

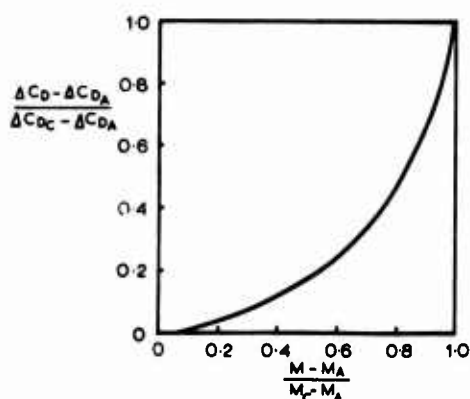


FIG. 10 INITIAL DRAG RISE FAIRING FOR  $M_A$  TO  $M_C$

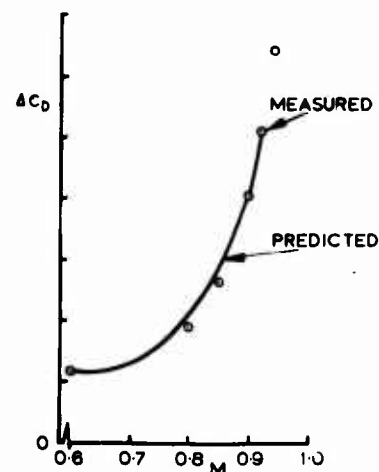


FIG. 11 ACCURACY OF PREDICTION METHOD

As has been shown, comprehensive prediction methods are not available. Nevertheless, basic aerodynamic principles can be used as a guide to the design of either improved or radically new installations. The aerodynamic principles involved range from little more than common sense to the application of the simplest aerodynamic theories. Sophisticated or complex theoretical methods have not been necessary in order to produce significant reductions in installed drag. This is not to say that current installations have wilfully been made to have high drags; in many cases there may be good reasons, often operational in nature, for the configurations chosen but in other cases one suspects that insufficient attention has been paid to drag considerations. In view of the great influence that store drag can have on the performance of modern aircraft, the aerodynamicist should be entitled to enquire as to whether the proper balance has been established between aerodynamic and other factors. Certainly, provided that totally impractical configurations are excluded, the aerodynamicist should not be inhibited from investigating new types of installation. At least, his work can enable the worst pitfalls to be avoided and also establish targets towards which the mechanical design should strive.

Recent work has not been directly concerned with reducing interference between the store assembly and the aircraft. Rather, it has concentrated upon reducing the drag of the store assembly itself. This has involved studies both of the possibilities of reducing the free-stream drags of the components of the store assembly and of reducing unfavourable mutual interference effects between the latter i.e. reducing  $K_A$  (see Section 2). There is a direct benefit in reducing the free-stream drag of the components or the assembly. In addition, at high subsonic speeds, the appropriate factor  $K_S$  or  $K_I$  by which these have to be multiplied may well be lower. For example, a reduction in  $\lambda_{SI}$  increases  $M_A$ .

It is convenient to distinguish between improvements to existing installations and entirely new installations. The former category includes redesigns to take advantage of improved mechanical systems. For example, it has long been known that crutch arms (sway braces) contribute a substantial part of the total free-stream drag of a store assembly. Recently, a new system (MAGE) has been developed in the UK. From the aerodynamicist's viewpoint, its outstanding feature is the elimination of crutch arms. The pylon/store combination for which data was shown in Fig (4) was also used in an investigation of the benefits to be obtained from the deletion of the crutch arms<sup>4</sup>. The results are shown in Fig (12). From this it will be seen that the crutch arms make a very large contribution indeed, which in this simple case is approximately equal to the estimated free-stream drag of the arms themselves.

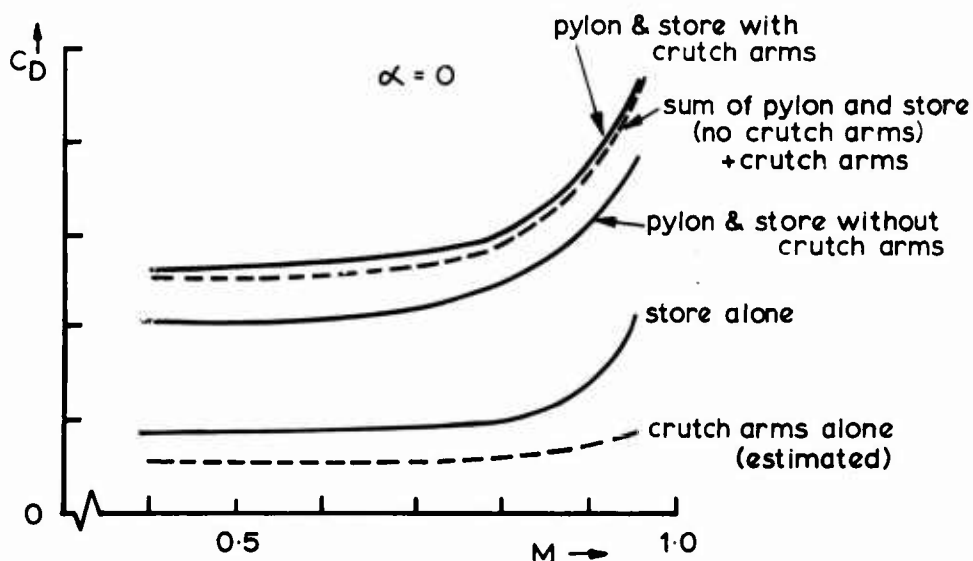


FIG.12 DRAG REDUCTION - SINGLE STORE ON PYLON

While these data demonstrate the benefits to be gained by eliminating even relatively small "dirty" excrescences, they do not give a complete picture. It will be recalled that this pylon/single store combination exhibited little aerodynamic interference between the pylon and the store. Additional information is required to determine whether the additional drag forces due to excrescences such as crutching arms are subject to similar installation factors as the stores themselves. This information was provided by tests on the assembly illustrated in Fig (5). In these tests the installed drag of a model of a conventional loaded triple carrier was compared to the same installation but with the carrier "cleaned up" i.e. with the crutching arms removed and various other excrescences deleted or faired in<sup>5</sup>. Figure (13) compares the measured drag reductions with the sum of the estimated free-stream drags of the deleted excrescences and also with these estimates multiplied by the installation factor (at  $M = 0.5$ ) of the original installation. The latter estimates correspond much better to the measured drag reductions than do the former. At least for low and subsonic speeds, the free-stream drag contributions of any crutch arms or other excrescences must be multiplied by much the same installation factors as for the complete

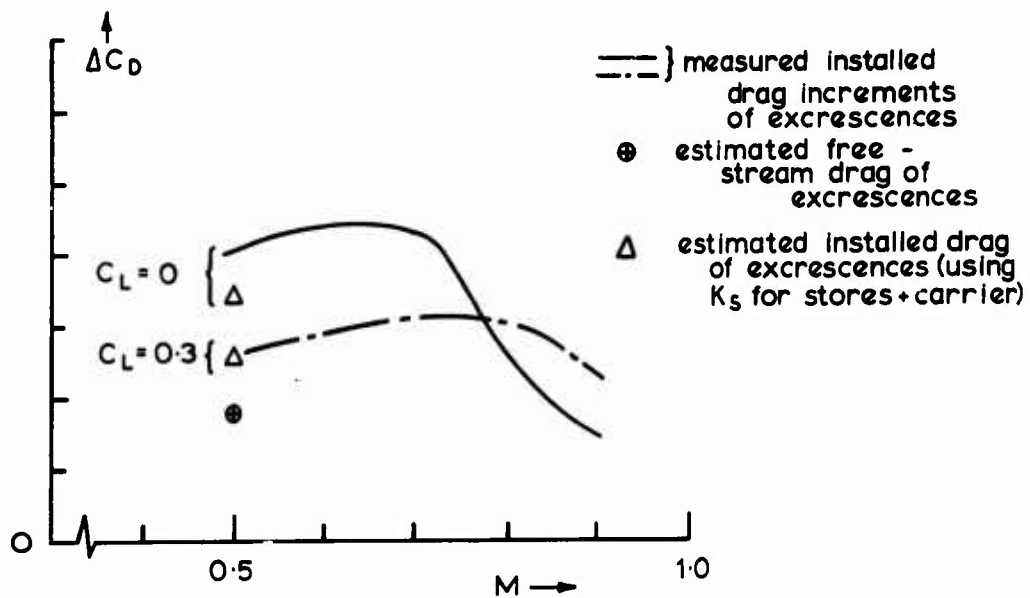


FIG. 13 DRAG REDUCTION - LOADED TRIPLE CARRIER

store assembly when estimating their contribution to the total installed drag. The drag saving due to cleaning up the installation is seen to be less at high Mach number. The most probable reason for this is that then, much of the high drag pattern of separated flows, etc is present with or without the excrescences and is caused by inter-store interference instead of excrescence-store interference as at low Mach number.

Turning to radically new installations, the main mechanism that has been exploited is the mutual interference between stores. This can involve both phenomena that are present in inviscid flows as well as phenomena that are essentially due to viscous effects. An example of the former is the influence of mutual interference on wave drag. Considerable insight into the wavedrag of store assemblies can be gained by use of the area rule.

In its simplest and most approximate form the area rule states that the wave-drag of a body at near-sonic speeds depends only on the streamwise distribution of its cross-sectional area. This principle may equally well be applied to several bodies in proximity to each other. For example, the drag of two identical slender bodies each of fineness ratio  $f_{si}$  (the ratio of body length to diameter) situated close together and with their noses in the same lateral plane is equal to the drag of a single body whose lateral dimensions are 2 times those of one of the pair of bodies but which is of the same length (i.e. its fineness ratio is  $f_{si}/2$ ).

Such considerations may be applied to a pair of stores. The principle is readily illustrated by considering stores which are well streamlined. In particular, consider stores which are of the form of a body of revolution with a parabolic arc generator. For such bodies at transonic speeds the wavedrag coefficient, based on maximum cross-sectional area, is roughly proportional to the inverse square of the fineness ratio. Thus, two identical stores having the same axial position and close together in the lateral direction have a total wavedrag equal to four times the drag of one of the bodies in isolation or, in other words, the total drag is twice that for the two bodies at infinite distance from each other. If one of these bodies is moved half a body length forward or backward, the equivalent body of revolution is then very close in shape to a body having a nose of the same shape as one of the bodies followed by a nearly cylindrical part of half a body length and finally terminated by an afterbody of the same shape as that of one of the single bodies. This equivalent body is expected to have a wavedrag roughly the same as one of the single bodies. Thus, a reduction in wavedrag at transonic speeds by a factor of about 4 might be obtained simply by moving one of the bodies by half a body length.

This prospect has been examined experimentally<sup>1</sup> for a pair of such "parabolic" bodies each of which had a fineness ratio of 8.48. Some relevant results are shown in Fig (14) which shows the ratio of the drag of a pair of bodies to the drag of a single body at the same M. The sensitivity of total drag to axial position is clearly large at  $M = 1$  but diminishes as the magnitude of the difference between the free-stream Mach number and  $M=1$  increases<sup>8</sup>. This is primarily due to the changing relative magnitudes of skin-friction and wavedrags. At  $M = 0.9$  the flow is entirely subsonic. Interference is then primarily due to buoyancy effects and has little influence on the total drag. The appearance of interference effects on the total drag and the drag rise Mach number are closely correlated for each configuration. The magnitude of the mutual interference effects, and, hence, the benefits of axial stagger, vary with Mach number in a way that reflects the growth and subsequent decay of the wave-drag coefficient as M increases.

Current stores are often less streamlined than the bodies for which data are shown in Fig (14). They commonly feature a cylindrical centre-section which, in combination with their somewhat lower fineness ratios, places the fineness ratio of the forebodies within the range 1.0 to 2.0 as compared to a fineness ratio of 4.2 for the forebody of the models discussed above. Their drag-rise Mach numbers are thus much

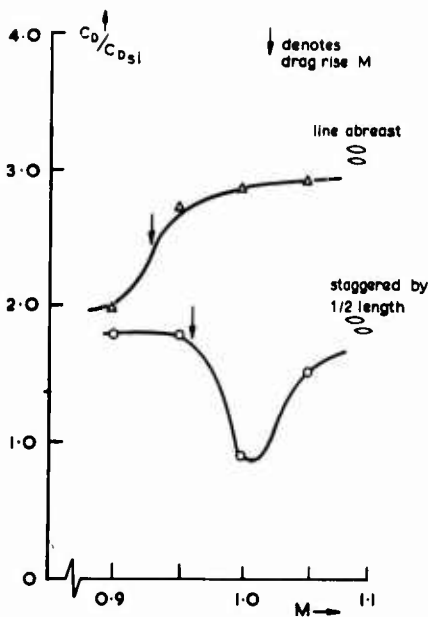


FIG.14 MUTUAL INTERFERENCE - STREAMLINED STORES

lower than 0.9, being typically about 0.83. The range of Mach numbers within which wavedrag makes an important contribution to the total is correspondingly extended also.

The presence of the cylindrical centre section makes it impossible to achieve as good an equivalent body as for stores of "parabolic" form. The equivalent body for a pair of such stores is unlikely to have a drag as small as that of only one of the stores in isolation<sup>8</sup>. However, there is no reason to doubt that extremely unfavourable interference effects will still be associated with line-abreast arrangements. Equally, axial stagger can be used to generate equivalent bodies of lower drag, albeit not as low as that of a single store. An interesting and useful result of studies of such configurations is that the minimum drag is achieved with only small amounts of stagger<sup>9</sup>. As an example Fig (15) shows results from tests in which the drag of a single isolated bomb was compared to its drag when in line abreast with another identical bomb ( $x_s = 0$ ) or else staggered fore and aft of the second bomb by 0.75 calibre ( $x_s = \pm 0.75D$ ). By combining the last two sets of data, the total drag of a staggered pair can be derived. In this figure the average of the two drags when at  $x_s \pm 0.75D$  are plotted. Thus, when the interference effects are predominantly of the buoyancy type, as at low Mach number, all the curves for the different cases coincide. The large difference between the curves for the isolated bomb and for  $x_s = 0$  demonstrate the large unfavourable interference effects that are then present. The average of the drag coefficients for  $x_s = \pm 0.75D$  is much closer to that for the isolated store, showing that these interference effects have been substantially reduced by this small amount of axial stagger. The benefits of axial stagger are reduced for  $M > 0.95$ . This is associated with the development of a shockwave/boundary-layer interaction in the diverging passage formed by the boattails of the two bombs<sup>9</sup>. This is present both for the unstaggered and staggered stores and has a major influence on the drag at these speeds. Different relative dispositions of the bombs may be optimum for different Mach numbers. Nevertheless, these results show that modest axial spacings can effect substantial reductions in wavedrag, and, hence, in total drag at Mach numbers above about 0.8.

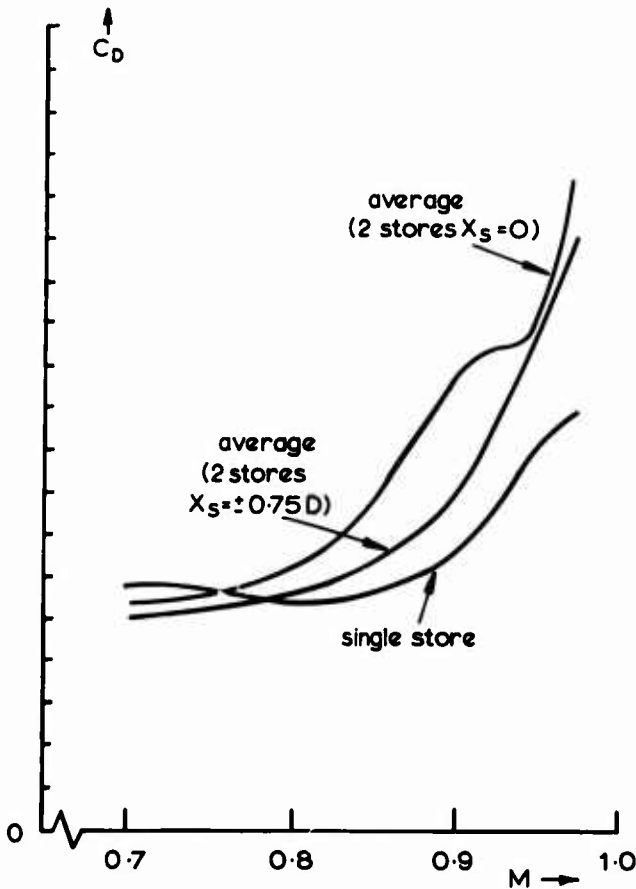


FIG.15 MUTUAL INTERFERENCE - STORES WITH CYLINDRICAL MIDBODY

In contrast to the above example in which viscous effects tend to be disadvantageous, benefit can be derived from viscous effects in the case of under fuselage stores<sup>2</sup>. In particular, the drag characteristics of arrays of underfuselage stores greatly depend upon the shape of the stores carried. At low Mach numbers the installation factors of both streamlined and flat based stores decrease considerably as transverse rows of stores are added to an array. Two well separated flat-based stores adjacent to the fuselage have an installation factor well below unity. This is attributed to either immersion in the fuselage boundary layer and/or an increase in base pressure due to the proximity of the fuselage. When a single transverse row of stores is added to a fuselage there is a basic unfavourable "side by side" interference effect. This causes a transverse row of streamlined stores to have a high installation factor;

but it is offset by the favourable effect noted earlier for bluff-based stores so that these have installation factors near unity. When, further aft, rows of stores are added there is a large, favourable, fore and aft interference. This reduces the installation factors for both types of store. In the case of flat-based stores this probably results from increases in the base pressures of the forward stores due to the proximity of the noses of the aft stores. The envelopment of the aft stores in the wake of the forward stores is probably not significant, at least for streamlined stores, because tandem pairs of streamlined stores have installation factors near 1.0. However, it is possible that the "side by side" interference within the aft row is reduced by wake effects in the passages between them.

The advantageous, fore-and-aft interference is especially great for arrays of flat-based stores at transonic speeds<sup>2</sup>. This is shown in Fig (16) in which the incremental installed drag of a single row of 5 identical stores is compared with the corresponding drag of 4 such rows (i.e. 20 stores in all). The drag of 20 stores is actually less than that of 5 stores for  $0.92 \leq M \leq 1.08$ . For streamlined stores, the effects are less dramatic but while the incremental drag of 20 stores is about twice that of 10 stores at  $M = 0.7$ , the corresponding ratio falls to only 1.5 at  $M = 0.95$ .

## 5 CONCLUSIONS

It has been shown that the installed drags of externally carried stores have a serious effect on the performance of combat aircraft. This is important in the design of such aircraft not only because of the magnitude of the installed drags but also because of uncertainties in their prediction. Fortunately, improvements are being made in their prediction and there is considerable promise that new or revised designs of installations will effect marked reductions in the drag penalties attributable to external carriage. However, much work remains to be done, and a sustained effort in this field could well reduce the drag of combat aircraft to an extent which would be difficult to obtain from any other source.

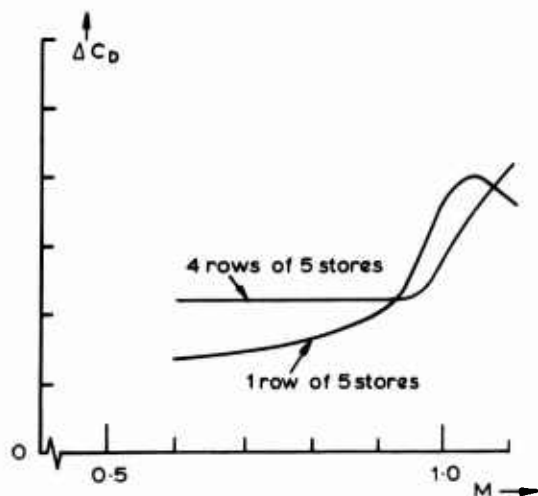


FIG.16 FAVOURABLE INTERFERENCE - UNDERFUSelage  
FLAT BASED STORES

## REFERENCES

1. Drougge, G., "An experimental investigation of the interference between two bodies of revolution at transonic speeds with special reference to the sonic and supersonic area rules". FFA(Sweden) Report 83, (1959).
2. Pallister, K.C., and Miss M.J. Evans, "Unpublished ARA paper".
3. Pallister, K.C. and P.G. Hutton, "Unpublished ARA paper".
4. Pugh, P.G., L.C. Ward and J.W. Peto, "Unpublished RAE work".
5. Capps, D.S., "Unpublished RAE paper".
6. Berry, J.B., P.G. Hutton and A.B. Haines, "Unpublished ARA paper".
7. Hunt, G.K. and G.H. Greenwood, "Some experiments in the zero-lift-drag of missiles carried externally on aircraft", RAE Tech Note Aero 2476, (1958).
8. Pugh, P.G., "Unpublished RAE paper".
9. Pugh, P.G., L.C. Ward and J.W. Peto, "Unpublished RAE work".
10. Loeve W., Sloof J.W., "On the use of 'panel methods' for predicting subsonic flow about aerofoils and aircraft configurations" NLR MD F1018U (October 1971).
11. Einton, E. "On the minimisation and numerical evaluation of wave drag" RAE Report Aero 2564 (1955).
12. Berry, J., "Examples of airframe-store interference" AGARD CP 71 (September 1970).
13. Alford, W.J. Jnr., "Theoretical and experimental investigation of the subsonic flow fields beneath swept and unswept wings with tables of vortex induced velocities" NACA Report 1327 (1957).
14. Hess, J.L. and Faulkner S.M., "Determination of low-speed interference effects by superposition", AGARD CP 71 (September 1970).

## ACKNOWLEDGEMENTS

The authors wish to acknowledge the assistance that they have received, during their studies of this problem, from their colleagues upon whose work they have drawn.

Summary

The drag force in hypersonic flow may be divided into cold pressure drag (incident molecules), temperature depending pressure drag (diffusively reflected molecules) and friction drag. The pressure drag dominates on blunt bodies which show a slighter drag variation with rarefaction whereas on slender bodies friction drag dominates and the total drag is strongly influenced by rarefaction. Relaxation and radiation do not appreciably alter the pressure drag but influence the flow field, stand-off distance of shock wave, and heat transfer.

Résumé

La résistance en écoulement hypersonique à basse densité peut être divisée dans la résistance de pression indépendante et dépendante de la température de surface et la résistance de frottement. La résistance de pression domine à des corps émoussés qui montrent une variation inférieure de la résistance avec la raréfaction pendant qu'à des corps élancés la résistance de frottement est plus importante et la résistance totale est fortement influencée par le degré de raréfaction. La relaxation et la radiation ne changent pas sensiblement la résistance de pression mais ils influencent le champ d'écoulement, la distance de détachement de l'onde de choc et le transfert de chaleur.

Notations

$c_D$	drag coefficient, $c_D = \frac{D}{\frac{1}{2} \rho V_\infty^2}$	$\alpha$	incidence angle
$c_L$	lift coefficient, $c_L = \frac{L}{\frac{1}{2} \rho V_\infty^2}$	$\gamma$	ratio of specific heats
$c_{ps}$	pressure coefficient behind normal shock	$\delta$	angle between wind velocity and normal to surface
$\vec{n}$	normal vector to the surface	$\lambda$	mean free path
$l_R$	reaction path	$\rho$	density
$p$	pressure	$\sigma$	accommodation coefficient for tangential momentum
$r(x)$	radius of axisymmetric body	$\sigma'$	accommodation coefficient for normal momentum
$\vec{v}$	wind direction vector	$\tau$	shear stress
$t$	thickness	$\bar{\tau}$	relaxation time
$A$	area	$\chi$	hypersonic similarity parameter, $\chi = Ma_\infty^3 \sqrt{C/Re_x}$
$A_P$	projected body area (in the direction of wind velocity)		
$A_R$	reference area		
$C$	Chapman-Rubesin function, $C = \frac{\mu}{\mu_\infty} \frac{T_\infty}{T}$	Indices	
$Kn$	Knudsen number, $Kn = \frac{\lambda}{l} = 1.26 \sqrt{\gamma} Ma/Re$	$\infty$	free stream condition
$K_r$	reaction constant	$w$	wall
$Ma$	Mach number	$o$	stagnation condition
$Re$	Reynolds number	$s$	behind normal shock
$Re_x$	Reynolds number, $Re_x = Vx/\nu$		
$T$	temperature		
$V$	flow velocity		

<sup>1)</sup> Prof. Dr. rer. nat.

20-2 1. INTRODUCTION

Hypersonic flow conditions are not only encountered in the flight of hypothetical aircraft of the future but also in the orbital flight and in the first steps of the reentry of a space vehicle and in the flight of long-range missiles. The hypersonic flow conditions are usually connected with high stagnation enthalpy and high altitudes or low densities. Therefore the forces acting upon a hypersonic vehicle are influenced by low density, high temperature, surface conditions, and real gas effects. Hypersonic flow may be simulated rather satisfactorily in a hypersonic low density wind tunnel. The necessary high gas velocities may be produced by expanding a heated gas in a nozzle. A rather large range of available stagnation pressures should be provided to cover if possible the whole range from hypersonic continuum flow to free molecular flow. In order that wind tunnel measurements are of practical use an adequate interpretation of experimental results is necessary. The flight conditions of a hypersonic vehicle may not be adequately defined by altitude and velocity but rather by the corresponding Reynolds- and Mach numbers. Typical flight conditions of various hypersonic vehicles are shown in an altitude-velocity chart in fig. 1 and in the corresponding Reynolds- and Mach number chart in fig. 2. Rarefaction effects are characterized by the well-known similarity parameter  $Ma_\infty \sqrt{Re_\infty}$  for hypersonic low density flow, which is essentially the ratio of the mean free path and the boundary layer thickness.

The criterion

$$Ma_\infty \sqrt{Re_\infty} \approx 0.01$$

characterizes the high altitude regime and it is seen from fig. 2, that this criterion corresponds in terms of decreasing altitude to the occurrence of transition from laminar to turbulent boundary layer.

Indicated in fig. 2 are also the continuum flow regime ( $Ma_\infty \sqrt{Re_\infty} < 0.1$ ) and the transitional rarefied regime, in which the number of the collisions between the molecules decreases considerably, and finally the free molecular regime, in which no collisions occur in the flow field and which may be characterized by the criterion  $Ma_\infty / Re_\infty > 3$ .

2. HYPERSONIC CONTINUUM FLOW

A characteristic feature of hypersonic frictionless continuum flow is the Mach number independence. In the limiting case of  $\gamma \rightarrow 1$  one is led to the Newtonian theory, which is discussed in the next section. A possible extension would be a development using the deviation  $(\gamma - 1)/(\gamma + 1)$  as parameter. The slow convergence of this procedure, however, makes it not very successful. Another limitation is given by the hypersonic friction drag originating mainly in the boundary layer. The shock wave - boundary layer interaction is a characteristic feature of this part of the drag.

2.1 Newtonian theory

The name of Sir Isaac Newton is attached to one branch of hypersonic flow theory. Following Newton's hypothetical model the component of the impulse contributing to the resistance is proportional to the square of the cosine of the angle between the wind velocity and the normal to the surface

$$c_p = \frac{p - p_\infty}{\frac{1}{2} \rho V^2} = 2 (\vec{n} \cdot \vec{v})^2 = 2 \cos^2 \delta \quad (1)$$

In the case of  $\delta = 90^\circ$  this formula should be identical with the pressure relation behind a normal shock

$$c_{ps} = \frac{2}{\gamma Ma_\infty^2} \left[ \left( \frac{\gamma+1}{2} Ma_\infty^2 \right)^{\frac{\gamma}{\gamma-1}} \left( \frac{\gamma+1}{2\gamma Ma_\infty^2 - \gamma + 1} \right)^{\frac{1}{\gamma-1}} - 1 \right] \quad (2)$$

However  $c_{ps} = 2$  only in the limiting case  $Ma_\infty \rightarrow \infty$  and  $\gamma \rightarrow 1$ . LEES (Ref. 1) has proposed on a purely empirical basis to use in the case  $\gamma \neq 1$  the formula

$$c_p = c_{ps} \cos^2 \delta \quad (3)$$

where for blunt bodies  $c_{ps}$  is given by formula (2) (modified Newtonian theory).

The total force coefficient is then given by integration over the surface of the body

$$\vec{c}_F = \frac{1}{A_R} \int_A c_p \vec{n} dA = \frac{c_{ps}}{A_R} \int_A (\vec{v} \cdot \vec{n})^2 \vec{n} dA \quad (4)$$

and the drag coefficient is

$$c_D = (\vec{c}_F \cdot \vec{v}) = \frac{c_{ps}}{A_R} \int_A (\vec{v} \cdot \vec{n})^3 dA \quad (5)$$

Recently the problem of finding the aerodynamic forces of a nonslender body using Newtonian theory has been reduced to finding the solution to a set of differential equations (Ref. 2). For axisymmetric bodies these equations can be written

203

$$c_{D\alpha\alpha} + c_{D\alpha} \cot \alpha + 12 c_D = 6 c_{ps} A_p/A_R \quad (6)$$

$$c_{D\alpha} = 3 c_L \quad (7)$$

where subscript  $\alpha$  denotes differentiation to the incidence angle  $\alpha$ ,  $A_p$  is the projected area of the body in the free stream direction and  $A_R$  is a reference area. If the variation in the forward projected area with incidence can be expressed in the form  $A_p = \sum_{n=0}^{\infty} A_n \sin^n \alpha$ , a solution has been obtained by PIKE (Ref. 3) and applied to blunt-nosed cylinder bodies in hypersonic flow. Fig. 3 illustrates the drag coefficient difference  $c_D - c_{D \text{ SPHERE}}$  or  $c_D - 1$  for a pointed cone with spherical base. For spherically-nosed bodies the values must be multiplied by  $(1 - (r/R)^2)$  and the cylindrical body is accommodated by adding  $8 \frac{l}{R} \sin^3 \alpha / 3\pi$ .

The Newtonian formula may also be used to determine shapes of minimum drag. If the shape of a symmetric two-dimensional or axisymmetric body is given by  $r(x)$ , the solution is given by

$$\frac{r^j r'^3}{1 + r'^2} = \text{const} \quad (8)$$

with  $j = 0$  in the two-dimensional and  $j = 1$  in the axisymmetric case. In the first case the body of minimum hypersonic drag is given by a wedge, in the second case, the solution is very near to the power law  $r \sim x^{3/4}$  (Ref. 5).

## 2.2 Limits of Newtonian theory

The Newtonian theory does not take into account viscous effects and therefore may only be compared with nonviscous theories e. g. with the method of characteristics in supersonic flow fields. It has been observed, that for values of  $\gamma$  near 1 (e. g.  $\gamma = 1.05$ ) the Newton-Busemann formula, which considers also the curvature effect, is in best agreement with the method of characteristics, but for larger values of  $\gamma$  (say  $\gamma = 1.4$ ) the simple Newtonian theory gives better results than the Newton-Busemann formula. If however viscous effects predominate, large deviations from the Newtonian pressure distribution are to be expected. Pressure distribution measurements (fig. 4) on a half-elliptical cone ( $11^\circ$  semi-angle) in hypersonic flow show a satisfactory agreement if the angle between flow direction and surface is more than  $15^\circ$ .

## 2.3 Viscous interactions

The high temperatures encountered at hypersonic speeds behind the shock or in the boundary layer result in an increase of boundary layer thickness. This increase contributes to two types of interaction of the boundary layer with the inviscid flow field. The boundary layer itself generates an inviscid hypersonic shock layer from the leading edge. In general this phenomenon is only important for slender bodies, since on blunt bodies the bow shock is detachment and the flow velocities are subsonic or only moderately supersonic. The second type of interaction associated with large boundary layer thickness becomes important when the vorticity in the inviscid layer due to the curved shock wave becomes of the same order as the average vorticity in the boundary layer due to the shear stress.

### 2.3.1 Slender bodies with sharp leading edge

According to fig. 5 the interaction regions for a slender body may be divided into the leading edge zone, the strong interaction region and the weak interaction region. Solutions are especially known for the sharp-nosed flat plate, where the pressure distribution is given in the weak interaction case by

$$\frac{p}{p_\infty} = 1 + (0.0775 + 0.202 \frac{T_w}{T_o}) \chi \quad (9)$$

with

$$\chi = \frac{Ma_\infty^3 \sqrt{C}}{\sqrt{Re_x}} \quad (C = \frac{\mu}{\mu_\infty} \cdot \frac{T_\infty}{T}, \quad Re_x = \frac{V_\infty x}{\nu_\infty})$$

and for strong interaction by

$$\frac{p}{p_\infty} = (0.1520 + 0.397 \frac{T_w}{T_o}) \chi \quad (10)$$

assuming  $\gamma = 1.4$ . The formulas show the strong influence of wall temperature. For an intermediate value

$$\chi = \chi^* = \frac{1}{0.0745 + 0.195 T_w/T_o}$$

both formulas lead to the same result. Formula (9) should be applied for  $\chi \ll \chi^*$  and (10) for  $\chi \gg \chi^*$ .

### 2.3.2 Slender bodies with blunt leading edge

A finite thickness of the leading edge causes a strong inviscid effect and according to HAMMIT and BOGDONOFF (Ref. 6), the pressure distribution may be given by

$$\frac{\Delta p}{P_1} = 0.016 Ma_\infty^3 \sqrt{\frac{C}{Re_x}} (1 + 40 \sqrt{\frac{C}{Re_t}}) \quad (11)$$

where  $t$  is the plate thickness.

The average skin friction coefficient tends towards and nearly matches the zero pressure gradient value downstream, but increases to approximately twice that value as the leading edge is approached (Ref. 7).

## 3. FREE MOLECULAR FLOW

Free molecular flow is characterized by such a degree of rarefaction that intermolecular collisions are negligible. Thus in the flow field only undisturbed molecules, coming from infinity, and molecules reflected from the wall are present. The reflection of the molecules may be specular or diffuse and the accommodation coefficient  $\sigma'$  ( $0 < \sigma' < 1$ ) indicates that part of the molecules which is reflected diffusely. If the wall has convex curvature only single reflexions are possible in this free molecular approximation, but for walls with concave curvature multiple reflexions must be considered.

### 3.1 Bodies with single reflexion at the wall (convex curvature)

In this case simple formulas are obtained for the normal and tangential momentum which in the hypersonic limit take the form (8)

$$p = \rho V^2 \left[ (2 - \sigma') \cos^2 \delta + \frac{\sigma'}{2} \sqrt{\frac{2\pi T_w}{\gamma T}} \frac{\cos \delta}{Ma_\infty} \right] \quad (12)$$

$$\tau = \sigma \rho V^2 \sin \delta \cos \delta, \quad (13)$$

where  $\sigma$  is the accommodation coefficient for tangential momentum. The drag force, which is received by integrating pressure and shear stress is composed by three parts

- a) temperature independent pressure drag
- b) temperature dependent pressure drag
- c) friction drag.

It is seen from equ. (12), that the temperature independent pressure drag (i. e. the pressure drag for  $T_w/T \rightarrow 0$ ) is identical with the Newtonian drag for diffuse reflexion ( $\sigma' = 1$ ).

An example is given in fig. 6 for the different parts of cylinder drag in dependance from wall to free stream temperature ratio.

### 3.2 Bodies with multiple reflexion at the wall (concave curvature)

The theory of free molecular flow on bodies with multiple reflexion at the wall (e. g. bodies with concave curvature, wing-body configurations or interaction of separate bodies) requires the solution of an integral equation. In the case of the free molecular flow through circular tubes one obtains the well-known Clausing-Integral-Equation (Ref. 9), which has also been extended to the flow in conical tubes (Ref. 10) and to corresponding two-dimensional problems. Also the interaction of a wall with a cone has been studied in view of skimmer interaction at the generation of molecular jets (Ref. 11).

#### 4. TRANSITIONAL DRAG

The transitional flow region between continuum flow and free molecular flow is characterized by a Knudsen number  $Kn = \lambda/l$  where  $\lambda$  is the free mean path and  $l$  a characteristic length. The Knudsen number is connected to the Mach- and Reynolds number by the relation

$$Kn = 1.26 \sqrt{\gamma} Ma/Re .$$

The approximate limits of the transition region are  $0.01 < Kn < 10$ , thus covering three decades of Knudsen number.

No exact theory is available for this flow regime. Approximate theories use first collision methods in the vicinity of free molecular flow or integral methods or numerical Monte-Carlo techniques. Experimental data are available especially for simple shapes but also for lifting bodies of different kind.

##### 4.1 Calculation methods using the Monte-Carlo technique

The gasdynamics of transitional flow is described by the Boltzmann equation, which unfortunately cannot be solved by analytical methods. Among the different approximative methods the "direct simulation Monte-Carlo method" seems to be most promising. In this method proposed by BIRD (Ref. 12) the flow field is divided into a large number of cells. A multitude of molecules is supposed to be in each cell and the motion and collision data of the molecules are calculated and stored in an efficient computer. Results have been obtained for plates (Ref. 13, 14) wedges and cylinders in transverse flow and for spheres (Ref. 15) and cones (Ref. 13). Large Knudsen number ranges from 0.025 till 100 were reached by improving the calculation procedure. In fig. 7 the calculated drag coefficient of a strip in transverse flow is compared with measurements. Fig. 8 shows a comparison of Monte-Carlo data with measurements by KOPPENWALLNER (Ref. 16).

##### 4.2 Experiments on transitional drag of simple shapes

Experimental results on transitional drag of simple shapes such as cylinders, spheres, cones or flat have been obtained in different hypersonic low density wind tunnels. Of special interest are the cylinder measurements by KOPPENWALLNER (Ref. 16), because they cover the whole range from continuum flow to free molecular flow, including also similar measurements on cooled cylinders. The results of fig. 9 show a remarkable difference between the data of the uncooled and the cooled cylinder. Whereas in the first case the free molecular limit is reached monotonically, in the latter case the drag coefficient has a maximum near  $Kn = 3$ . As the pressure drag of uncooled cylinders could be determined separately by pressure distribution measurements it was possible to get the friction drag by subtraction of the pressure drag from the total drag. The results plotted in fig. 10 show that the rise of total drag with increasing Knudsen number is essentially caused by the increasing friction drag and that the friction drag has a maximum value at a Knudsen number of about  $Kn = 0.5$ . This behaviour may be compared with the flow of a rarefied gas through a tube, where KNUDSEN (Ref. 17) has found a minimum of flow rate (known as "Knudsen minimum") which corresponds to a maximum of friction. This minimum of tube flow rate is found at a Knudsen number  $Kn = \lambda/d = 0.4$ . Also for very slender cones an overshoot of drag coefficient is predicted in the theory of WILLIS (Ref. 18). Due to this theory for cooled cones this overshoot may be expected for cone half angles below  $8.4^\circ$ . In the cone data of fig. 11 the cone angle is too large to show an overshoot (Ref. 19). In the near continuum region the cone data show a very strong dependence on cone angle and wall to stagnation temperature ratio. As shown by KIENAPPEL (Ref. 20) all these data may be correlated by the following semi-empirical formula

$$c_D^{(0)} = c_{D\text{Newton}}^{(0)} \left( 1 + \frac{2}{3} \frac{Ma_\infty}{(\sin \theta)^{5/2} \sqrt{Re_{\infty l}}} \frac{T_w}{T_o} \right) .$$

With  $Re_{\infty l}$  referred to the length of the cone as is shown in fig. 12. The drag data of cones at angle of attack (fig. 13) show a large dependence on Mach- and Reynolds number, whereas the normal force is quite independent of Mach- and Reynolds number. Nevertheless the drag variation with angle of attack is represented fairly well by Newtonian theory (Ref. 21).

Strong viscous interactions have also been found on caret wings, where the induced pressure may be fairly well computed from the viscous interaction theory for wedges (Ref. 22). It is evident that the viscous effects influence the zero lift drag coefficient very seriously as is shown in fig. 14, where the deviation from wedge theory becomes stronger with decreasing Reynolds number.

##### 4.3 Drag measurements on lifting bodies in rarefied flow

Force measurements have been undertaken on a number of different lifting bodies for reentry vehicles. Some of these measurements were carried out in different hypersonic wind tunnels with an extended range of Reynolds numbers. The drag coefficient versus angle of attack is strongly influenced by Reynolds number as is shown in the plot of fig. 15. The correlation of zero incidence angle drag coefficient with the rarefaction parameter  $\frac{Ma_\infty}{\sqrt{Re_\infty}}$  is seen in fig. 16 different shapes. It is obvious

that blunt bodies have a large pressure drag which is only slightly dependent on Reynolds or Knudsen number, whereas on slender bodies the friction drag dominates with a strong dependence from Reynolds number. This behaviour is clearly shown by the comparison of the drag data for a blunt semielliptical cone ( $\llcorner$  Integral body  $\gg$ ) and a sharp edged delta wing with  $10^\circ$  wedge angle (fig. 17). The latter shows a much stronger influence of Reynolds number.

#### 4.4 General conclusions from drag measurements in transitional regime

The drag measurements, available in the transitional regime, give an insight into the general behaviour for different stages of rarefaction. They may not be sufficient to establish semiempirical theories and further systematic work is needed. The following conclusions may be drawn from existing data:

- 1) The total drag force is composed of
  - a) temperature independent pressure drag corresponding to Newtonian drag. This part is only slightly dependent on Reynolds- or Knudsen number.
  - b) temperature dependent pressure drag. This part of the pressure depends on the temperature ratio  $T_w/T_o$  and on rarefaction. It is negligible at the continuum flow limit.
  - c) friction drag rises with the rarefaction parameter  $Ma_\infty \sqrt{Re_\infty}$  from nearly zero at  $Ma_\infty \sqrt{Re_\infty} = 10^{-2}$  to a maximum value at a Knudsen number  $Ma_\infty / Re_\infty \sim 0.5$  and remains constant at a value below the maximum for higher Knudsen numbers.
- 2) The variation of total drag with angle of attack is essentially determined by the temperature independent pressure drag and follows therefore closely the difference in Newtonian drag.
- 3) The variation of total drag coefficient with increasing rarefaction is different for blunt and slender bodies, because of the different behaviour of pressure drag and friction drag. The decrease of the drag coefficient in the free molecular limit starts for the more slender bodies at larger Reynolds numbers than for blunt bodies.
- 4) Configuration with combined blunt and slender bodies (wing-body-configurations) will show an intermediate behaviour for the integral drag.

#### 5. RELAXATION EFFECTS

Rather numerous theoretical investigations are concerned with the question of relaxation effects on fundamental flow phenomena e.g. shock formation in relaxing gases or nonequilibrium boundary layers. Unfortunately there seems to be no theoretical work on how relaxation affects the total flow about hypersonic vehicles or models of parts of them, placed into the nonequilibrium flow of test facilities.

##### 5.1 Chemical relaxation

At high flight velocities and subsequently high total enthalpy internal degrees of freedom of the molecules are excited. These "chemical effects" (because of the occurrence of dissociation and ionisation) are only found in certain flow regimes. At velocities below 3 km/s no chemical reactions are possible, because the total enthalpy is not high enough. The characteristic reaction time  $\bar{\tau}$  is inversely proportional to the density ( $\bar{\tau} = (\rho \cdot K_r)^{-1}$  where  $K_r$  is a reaction constant). If therefore the reaction path  $l_R = V \cdot \bar{\tau}$  is much longer than a characteristic dimension  $l$  of the body (say  $l_R/l > 100$ ), the reaction may be considered as frozen. On the other hand, the reaction may be considered to be in equilibrium, if  $l_R/l < 0.01$ . With these limits the regime of nonequilibrium reaction kinetics is given by

$$0.01 < \frac{l_R}{l} < 100.$$

These limits are plotted in fig. 18 for a sphere of 0.3 m diameter in hypersonic low density flow.

It is generally accepted that chemical relaxation affects the stand-off distance of the shock but does not essentially influence the pressure distribution and pressure drag. The temperature dependent drag and the heat transfer should be influenced in a stronger way.

##### 5.2 Translational and rotational relaxation

At extremely low density even the translational degrees of freedom of the molecules are in nonequilibrium. This is especially observed when a gas is expanded into a high vacuum. For the limiting case of free molecular flow the effect of translational nonequilibrium on the forces acting upon a body in hypersonic rarefied flow have been calculated (Ref. 24).

## 6. RADIATION EFFECTS

A very high velocities the hot gas in the "shock layer" between the bow shock wave and the body surface is losing energy by radiation. A certain amount of the radiative energy reaches the body surface where part of it is absorbed. Another part of the radiative energy may be absorbed by the cool gas in front of the shock wave. This so called precursor effect entails a preheating zone which already signalizes the body yet to come even before the bow shock wave arrives.

As in the case of relaxation effects the pressure distribution around a blunt body remains unaltered by radiation effects because these quantities are governed mainly by the momentum flux which is independent of radiation. The temperature in the shock layer is reduced due to radiative energy losses, and, as a consequence, the density is increased. A further consequence is that the shock detachment distance is reduced (Ref. 25).

## 7. CONCLUSIONS

The drag in hypersonic rarefied flow is a function of Mach- and Reynolds number. It may be divided into temperature independent pressure drag, the temperature dependent pressure drag and the friction drag. The first part is only slightly dependent on rarefaction and dominates on blunt bodies. The friction drag seems to show a characteristic behaviour in dependence of rarefaction with a maximum near  $Kn \sim 0.5$ . On slender bodies the friction drag influences strongly the total drag, so that the dependance of total drag from rarefaction is different for blunt and slender bodies. Relaxation and radiation does not appreciably alter the pressure drag but influences the flow field, stand-off distance of shock and heat-transfer.

## REFERENCES

1. Lees, L. Hypersonic Flow. Proc. 5th Internat. Aero. Conf., Los Angeles, Inst. Aero. Sci. New York, 241-276, 1955.
2. Jaslow, H. Aerodynamic Relationships Inherent in Newtonian Impact Theory. AIAA J., Vol. 6, 4, 1968.
3. Pike, J. The Lift and Drag of Axisymmetric Bodies in Newtonian Flow. AIAA J., Vol. 7, 1, 1969.
4. Pike, J. The Lift and Drag of Blunt-Nosed Cone-Cylinder Bodies in Newtonian Flow. Roy. Aircraft Establ. Techn. Rep. 71086, 1971.
5. Chernyi, G. G. Introduction to Hypersonic Flow. Academic Press, New York 1961.
6. Hammitt, A. G. Bogdonoff, S. M. Hypersonic Studies of the Leading Edge Effect on the Flow over a Flat Plate. Jet Propulsion 26, 1956, 241-246.
7. Kendall, J. M. An Experimental Investigation of Leading-Edge Shock-Wave-Boundary-Layer Interaction at Mach 5.8. J. Aero. Sci. 24, 1957, 47-56.
8. Schaaf, S. A. Mechanics of Rarefied Gases. Handb. Physik, Vol. 8/2, Fluid Mechanics II, Springer 1963.
9. Clausing, P. Über die Strömung sehr verdünnter Gase durch Röhren von beliebiger Länge. Ann. Physik 12, 951-989, 1932.
10. Townsend, S. J. Free Molecule Flow through Axisymmetric Tubes. UTIAS Rep. No. 106, USA FOSR-6 S. 0749.
11. Raghuraman, P. Kinetic Theory Study of Free Jet. Expansions in Pre-Skimmer Chambers. Deutsche Luft- u. Raumfahrt, Forsch. Ber. 1973. Interner AVA-Bericht 063-72 H 13, 1972, AVA Göttingen.
12. Bird, G. A. Aerodynamic Properties of Some Simple Bodies in the Hypersonic Transition Regime. AIAA J., Vol. 4 (1966) No. 1.

13. Vogenitz, F. W., et al. Rarefied Hypersonic Flow about Cones and Flat Plates by Monte Carlo Simulation.  
AIAA Fluid and Plasma Dynamics Conf. San Francisco 1969, AIAA-Paper 69-651.
14. Boettcher, R. -D. Monte-Carlo-Simulation der hypersonischen verdünnten Strömung um einen querangeströmten Streifen.  
DFVLR-Aerodynamische Versuchsanstalt Göttingen, Ber. 71 A 20, 1971.
15. Bird, G. A. The Structure of Rarefied Gas Flows Past Simple Aerodynamic Shapes.  
J. Fluid Mech., Vol. 36, 1969, No. 3.
16. Koppenwallner, G. Experimentelle Untersuchung der Druckverteilung und des Widerstandes von querangeströmten Kreiszylindern bei hypersonischen Machzahlen.  
Z. Flugwiss. 17 (1969) p. 321-332.
17. Knudsen, M. Die Gesetze der Molekularströmung und der inneren Reibungsströmung der Gase durch Rohre.  
Ann. d. Physik 28, 1909, p. 75-130.
18. Keel, A. G., Jr. Critique of Near-Free-Molecule Theories for Flow over Cones.  
Rep. No. AS-71-5, College Eng. Univ. Calif., Berkeley, 1971.
19. Legge, H. Drag Measurements of Cones at Zero Angle of Attack in Near Free Molecular Flow.  
Deutsche Luft- u. Raumfahrt, Forsch. Ber. 72-64, 1972.
20. Kienappel, K. Experimentelle Untersuchungen an schlanken Kegeln bei verdünnter Hyperschallströmung.  
Bundesminst. Bildung u. Wissenschaft, Forsch. Ber. W 71-30, 1971.
21. Koppenwallner, G. Wind Tunnel Testing on Real Configurations in Hypersonic Flow.  
Deutsche Luft- u. Raumfahrt, Forsch. Ber. 71-49, 1971.
22. Hefer, G. Untersuchung eines Wellenreiters bei kleinen Reynoldszahlen.  
Astronaut. Congr. Konstanz 1970, Deutsche Luft- u. Raumfahrt, Forsch. Ber. 70-46, 1970.
23. Harney, M. D. Chemical Kinetic Regimes of Hypersonic Flight Simulation.  
AEDC TDR 63-3, 1963.
24. Legge, H. Kraft- und Wärmeübergang in freier Molekülströmung mit verschiedenen Verteilungsfunktionen von Expansionsströmungen.  
Deutsche Luft- u. Raumfahrt, Forsch. Ber. 70-65, 1970.
25. Schneider, W. Radiation Gasdynamics of Planetary Entry Concepts and Recent Advances.  
Invited pap. 23rd Internat. Astronaut. Congress Vienna, Oct. 8-15, 1972.

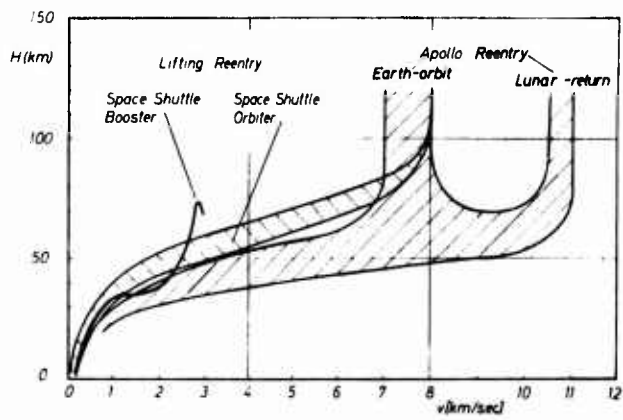


**Fig. 1.** Flight trajectories of typical reentry vehicles (Altitude  $H$  versus velocity).

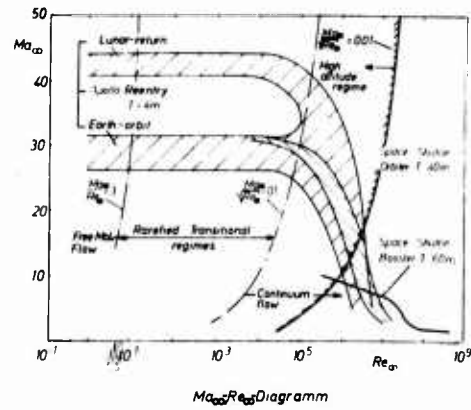


**Fig. 2.** Flight trajectories of typical reentry vehicles (Mach-Reynolds diagram).

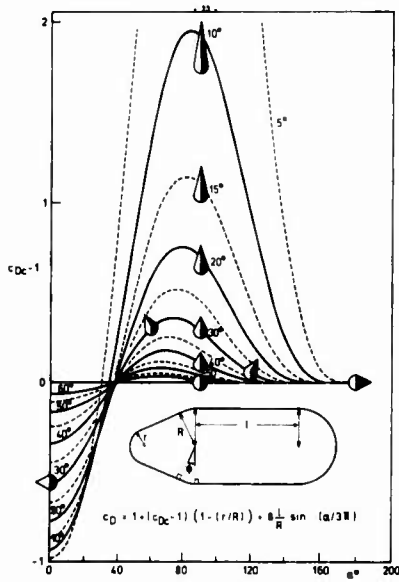


**Fig. 3.** The drag coefficient of cones with spherical bases.

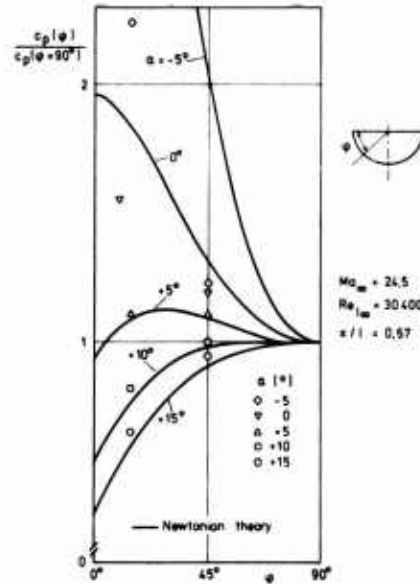


**Fig. 4.** Comparison of measured pressure distribution on half-elliptical cone with incidence angle with Newtonian theory.

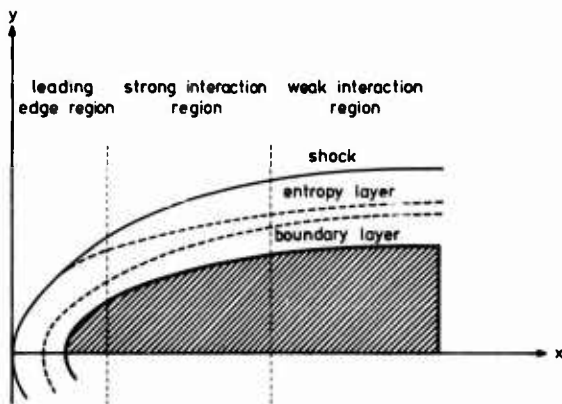


**Fig. 5.** Interaction regions on blunt nosed slender bodies.

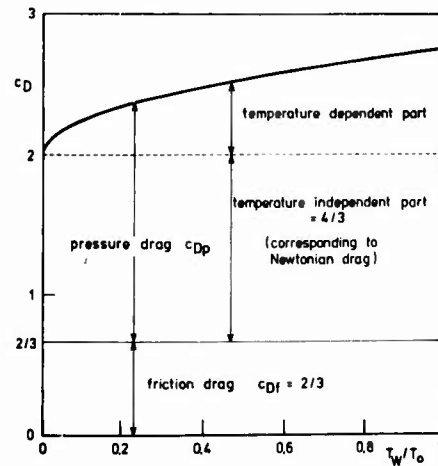


**Fig. 6.** Different parts of cylinder drag in free molecular flow.

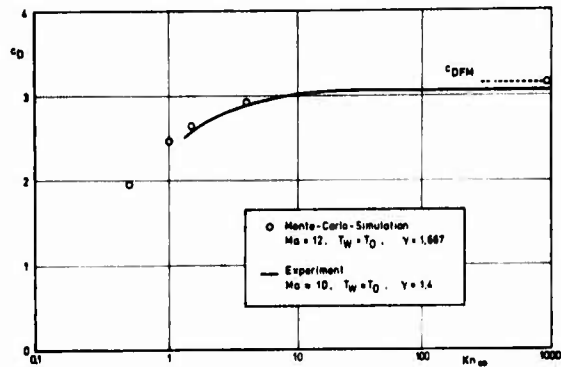


Fig. 7. Comparison of drag data for a strip calculated by Monte-Carlo-technique with measured values.

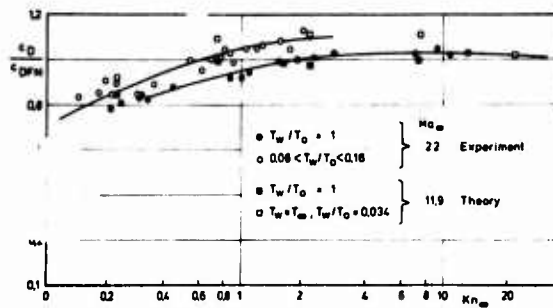


Fig. 8. Comparison of drag data for cooled and uncooled cylinders calculated by Monte Carlo technique with measured values.

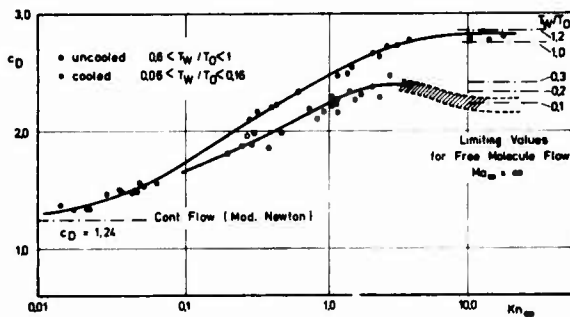


Fig. 9. Measured drag coefficient for uncooled and cooled cylinders in transitional flow.

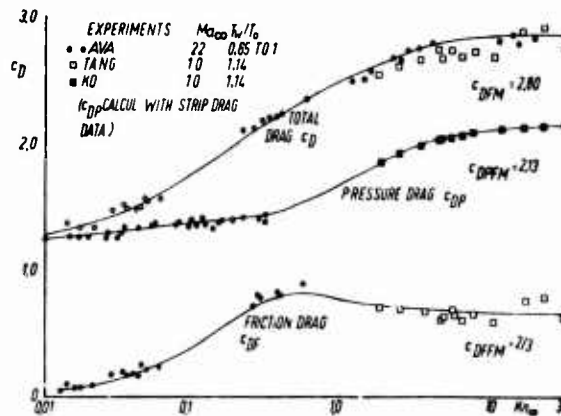


Fig. 10. Partition of total drag of uncooled cylinders in transitional flow regime into pressure drag and friction drag.

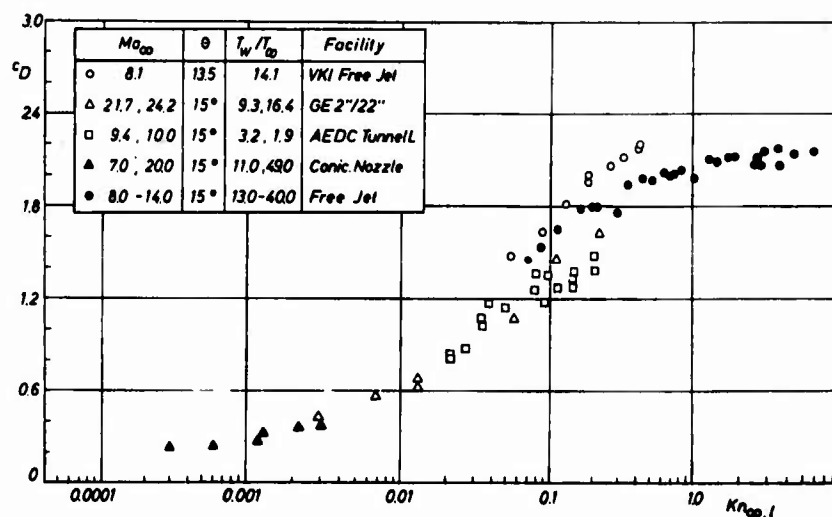


Fig. 11. Comparison of experimental cone data.

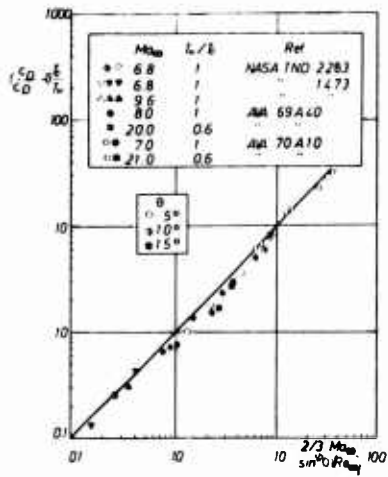


Fig. 12. Correlation of zero angle of attack cone drag data in slip flow regime.

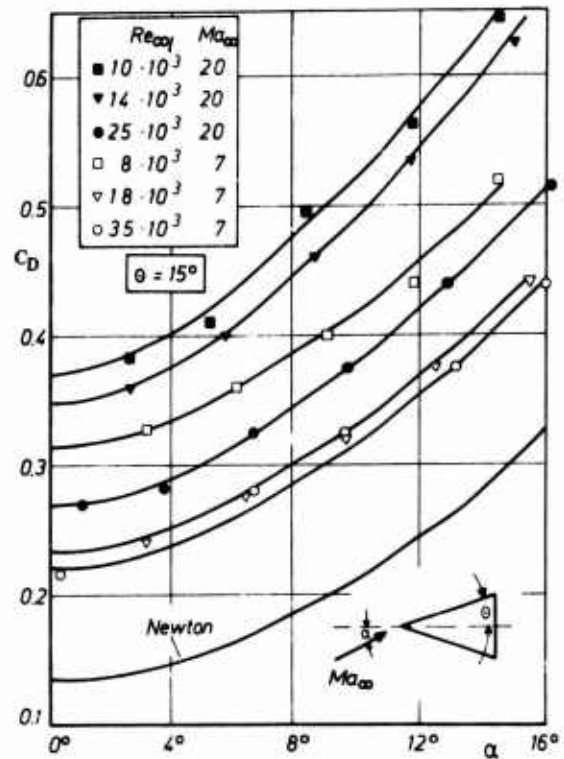


Fig. 13. Cone drag coefficient versus angle of attack.

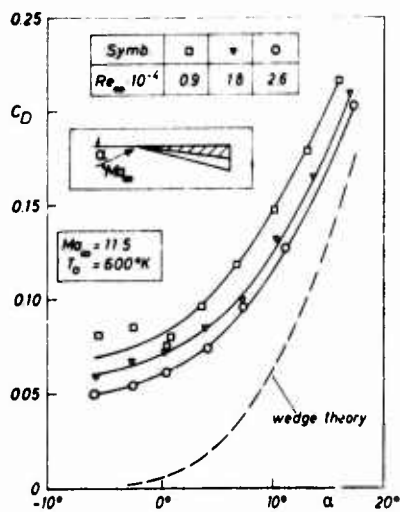


Fig. 14. Caret wing drag coefficient versus angle of attack.

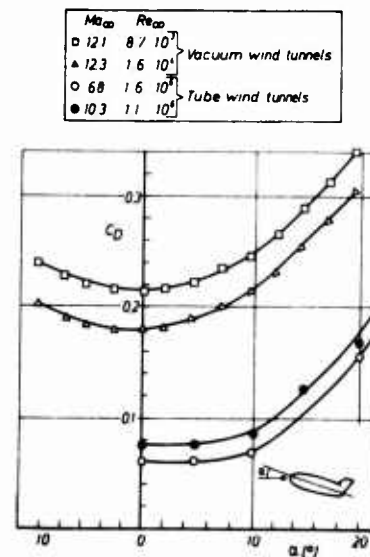


Fig. 15. Drag coefficient versus angle of attack for a lifting body with lateral fins.

20-12

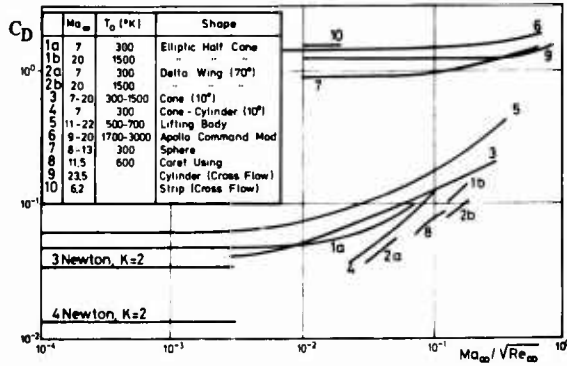


Fig. 16. Drag coefficient versus angle of attack for a lifting body with lateral fins.

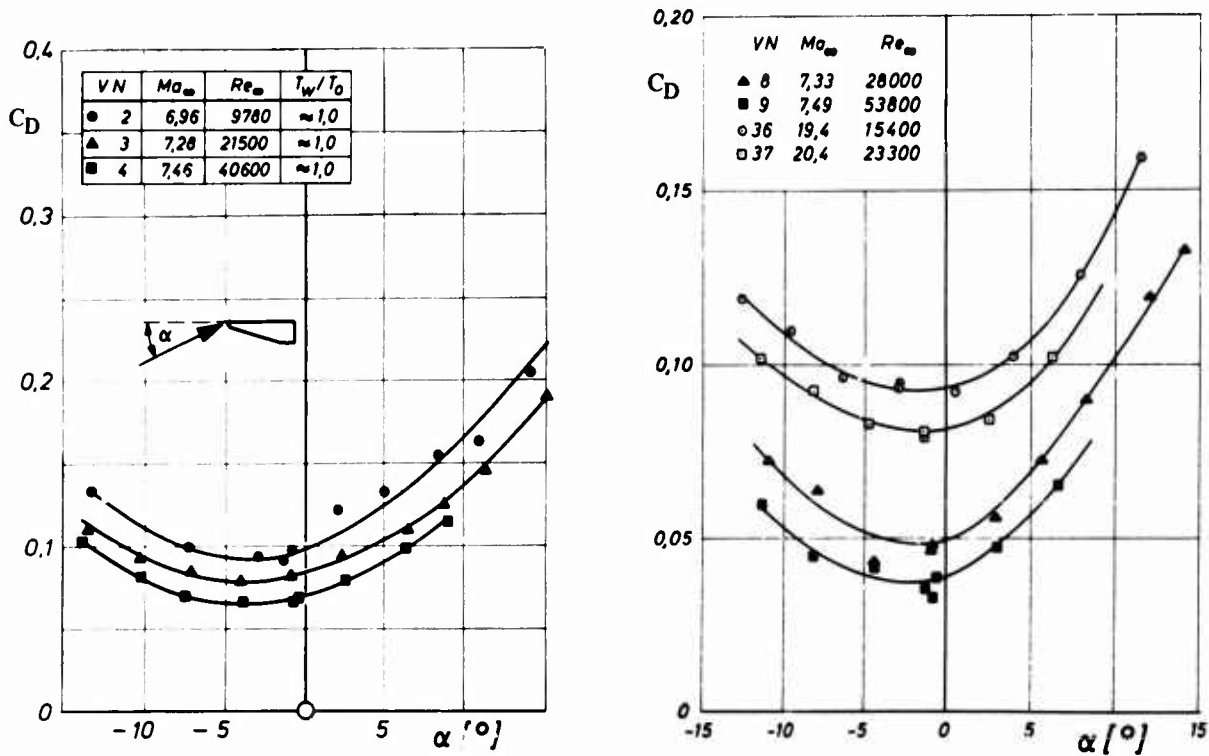


Fig. 17. Comparison of drag coefficient versus angle of attack for a blunt half-elliptical cone (left) and a sharp-edged delta wing (right).

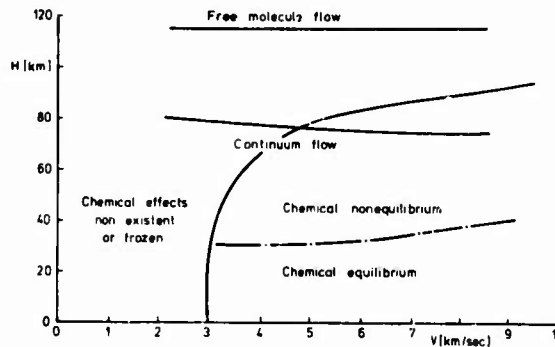


Fig. 18. Hypersonic flow regimes with chemical effects for a sphere with 0.3 m diameter.

## TRAINÉE DE CORPS PORTANTS PILOTES A HAUTE ALTITUDE

par  
J. Allègre, C. Matrand, M.F. Scibilia  
Laboratoire d'Aérodynamique du C.N.R.S., 92190-Meudon (France)

## RESUME

Les corps portants choisis sont des ailes delta planes, de 60° de flèche, munies de dispositifs aérodynamiques et mécaniques de guidage. Ces dispositifs sont disposés au voisinage du bord de fuite des ailes.

L'étude expérimentale du comportement aérodynamique de l'aile est réalisée dans le cadre d'un vol hypersonique pour une altitude voisine de 70 km. Les essais sont effectués dans une soufflerie à veine libre et à fonctionnement continu ; l'écoulement d'air y est caractérisé par un nombre de Mach de 8,1 et un nombre de Reynolds de 2200 par cm.

Pour un tel régime de transition où prédominent les effets de viscosité et les effets de déplacement de couche limite, les valeurs des coefficients de traînée sont supérieures à celles qui correspondent au régime d'écoulement continu. De plus, les résultats montrent dans quelle mesure les dispositifs de guidage directionnel de l'engin par spoilers restent efficaces et peuvent être utilisés pour contrôler la trajectoire en atmosphère raréfiée. Les grandeurs des coefficients aérodynamiques sont données pour une plage de variation de l'incidence de l'aile s'échelonnant de - 20° à + 20°. La comparaison entre les efficacités respectives des spoilers solides et des spoilers fluides de bord de fuite a permis de mettre en évidence quelques avantages des spoilers fluides. Ces derniers permettent en particulier d'assurer le contrôle directionnel de la plate-forme sans entraîner corrélativement une sensible augmentation de sa traînée.

## SUMMARY

The considered lifting bodies are 60° swept delta wings fitted out with control devices, located near the trailing edge of the wings.

The present experimental study of the aerodynamic behaviour of the wing is realized in a rarefied flow simulating a flight altitude of about 70 km. Experiments are performed in an open jet and continuously operating wind tunnel. The air flow is characterized by a Mach number of 8.1 and a free stream Reynolds number of 2200 per cm. Results show how much aerodynamic devices associated with the delta wing, like spoilers, remain efficient and can be used in order to control the trajectory at high altitude. Drag coefficient data are given in the range of incidences between - 20° and 20°. A comparison between efficiencies of trailing edge solid spoilers and trailing edge fluid spoilers allows to point out some advantages of the fluid spoilers. In particular, this jet control mechanism can create a sufficient side thrust without entailing a large increase of the drag.

## NOTATIONS

$C_A$	coefficient de force axiale
$C_N$	coefficient de force normale à l'aile
$C_X$	coefficient de traînée
$C_{Xp}$	composante de $C_X$ due aux seules forces de pression
$C_{Xf}$	composante de $C_X$ due aux forces de frottement
$C_Z$	coefficient de portance
$e$	épaisseur du bord d'attaque
$E$	écartement entre les spoilers fluides
$h$	hauteur du spoiler solide
$i$	incidence
$M$	nombre de Mach
$p$	pression locale, pression pariétale
$p_\infty$	pression de l'écoulement à l'infini amont
$Re$	nombre de Reynolds
$Re_L$	nombre de Reynolds fondé sur la longueur de l'aile
$T_p$	température pariétale
$T_o$	température génératrice de l'écoulement
$x$	abscisse mesurée à partir de l'apex
$y$	ordonnée dirigée suivant le bord de fuite de l'aile
$\gamma$	rapport des chaleurs spécifiques
$e = \frac{\gamma-1}{\gamma+1}$	
$\bar{\chi}$	paramètre hypersonique d'interaction visqueuse
$\chi_e = c [0,664 + 1,73 T_p/T_o] \bar{\chi}$	

## 1. INTRODUCTION

De nombreuses recherches ont déjà porté sur les ailes delta mais elles sont pour la plupart relatives à un régime d'écoulement continu. L'intérêt lié au vol à haute altitude et à des vitesses hypersoniques, et notamment le développement du programme de la navette spatiale, nous a amené à étendre les précédents travaux à de plus faibles valeurs du nombre de Reynolds. Il est en effet utile de connaître les principales caractéristiques de l'écoulement autour de corps portants dans des régimes d'écoulement de transition pour lesquels les effets combinés de viscosité et de déplacement de couche limite deviennent très importants.

Les plate-formes pilotées doivent être pourvues de moyens de guidage ; les spoilers de bord de fuite ont été choisis ici en raison de la simplicité de leur utilisation. Il est nécessaire d'étudier leur efficacité en fonction de l'angle d'incidence du véhicule et des conditions de raréfaction de l'écoulement pour lesquelles les zones de décollement de couche limite laminaire sont très étendues.

En régime de forte interaction visqueuse, la présente communication donne quelques résultats de pression pariétale et de coefficients de forces aérodynamiques lesquels rentrent en ligne de compte pour la détermination de la traînée de l'aile. Après avoir indiqué les performances d'une aile delta plane dépourvue de dispositif de guidage, on montrera l'effet dû à l'adjonction d'un spoiler solide de bord de fuite sur les caractéristiques aérodynamiques de l'aile. Enfin, on précisera le comportement de cette dernière en présence de spoilers fluides qui semblent particulièrement bien adaptés au vol à haute altitude.

## 2. MOYENS D'ESSAIS

Les expériences sont réalisées dans la soufflerie SR 2 du Laboratoire d'Aérodynamique. Cette soufflerie à gaz raréfié est à fonctionnement continu et à veine libre. La température génératrice et la pression génératrice ont respectivement pour valeur 700 K et 1 bar. L'écoulement d'air est caractérisé par un nombre de Mach de 8,1, une pression à l'infini de 70 microns de mercure, une température de 50 K et un nombre de Reynolds de 2200 par cm. Une tuyère évolutive rend négligeable le gradient du nombre de Mach au sein de la zone explorée de la veine d'essai.

Les pressions pariétales sont mesurées à l'aide d'un capteur différentiel de pression ou au moyen de thermistances selon le niveau de pression appliqué. Les forces aérodynamiques sont enregistrées au moyen d'une balance à trois composantes. Les éléments sensibles de cette balance à dard sont constitués de lames de flexion munies de ponts de jauges extensométriques de 350 ohms à trame pelliculaire.

## 3. AILE DELTA PLANE

Aux nombres de Reynolds élevés, l'étude de l'aile delta plane en écoulement hypersonique a fait l'objet de multiples travaux. Les références 1 à 5 apportent des informations concernant les effets de bord d'attaque, de flèche et de déplacement de couche limite sur les caractéristiques de l'écoulement au voisinage de l'aile.

Pour de faibles valeurs du nombre de Reynolds et des écoulements hypersoniques caractérisés par d'importants effets d'interaction visqueuse, les recherches théoriques et expérimentales relatives aux ailes delta sont au contraire peu nombreuses (références 6 à 8). Les présents résultats sont afférents à des ailes de 60° de flèche dont on a fait varier l'épaisseur du bord d'attaque entre 0,04 mm et 2 mm. Les longueurs de cordes prises égales à 40, 50 et 60 mm fixent respectivement à 8800, 11000 et 13200 les valeurs du nombre de Reynolds rapporté à la longueur de l'aile.

Aux faibles incidences (6), on s'est attaché à mettre en évidence les effets de l'éroussissement du bord d'attaque et de l'incidence des maquettes, effets qui s'ajoutent à celui de la viscosité de l'écoulement. Les efforts aérodynamiques s'exerçant sur les maquettes résultent à la fois des forces de pression pariétales et des forces de frottement. Ces diverses composantes peuvent être mises en évidence grâce à des mesures combinées d'efforts aérodynamiques et de pressions pariétales et il a été possible de comparer les forces déduites de l'intégration des pressions pariétales avec les forces globales mesurées à l'aile de la balance aérodynamique.

Pour un Reynolds de 13200 rapporté à la longueur de l'aile, la figure 1 donne l'évolution du coefficient de traînée en fonction de l'incidence. En trait continu, les valeurs correspondent aux coefficients de traînée globaux déduits des forces mesurées à l'aide de la balance. Les courbes en trait discontinu représentent la part due aux seules forces de pressions pariétales dans ces coefficients.

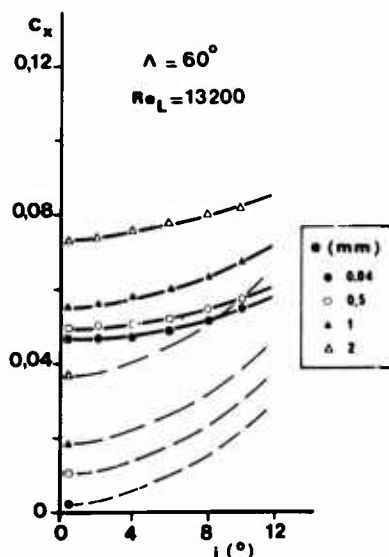


Fig.1 - Répartition du coefficient de traînée

Les forces de frottement représentent en fait la différence qui existe entre les forces globales et les forces de pression. La figure 2 montre le pourcentage de la traînée de frottement sur la traînée totale en fonction de l'épaisseur et pour plusieurs angles d'incidence des ailes. A titre indicatif, à l'incidence nulle et pour une aile effilée, 90 % de l'effort de traînée résulte de la force de frottement; ce pourcentage diminue bien sûr considérablement lors d'une augmentation d'épaisseur ou d'incidence. 21-3

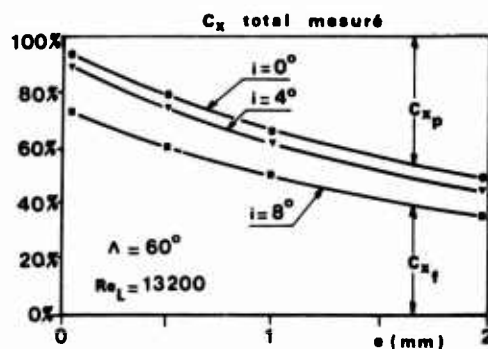


Fig. 2 - Décomposition de la force de traînée

Les niveaux de pressions pariétales mesurées le long de l'axe d'une aile de  $60^\circ$  de flèche, 50 mm de longueur et 1 mm d'épaisseur de bord d'attaque sont portés sur la figure 3 en fonction de l'incidence. Ils sont comparés, d'une part, à de précédentes données relatives à des valeurs supérieures du nombre de Reynolds (9) mais correspondant approximativement au même nombre de Mach de l'écoulement et, d'autre part, avec les valeurs théoriques résultant de l'application des théories du cône tangent et du dièdre tangent.

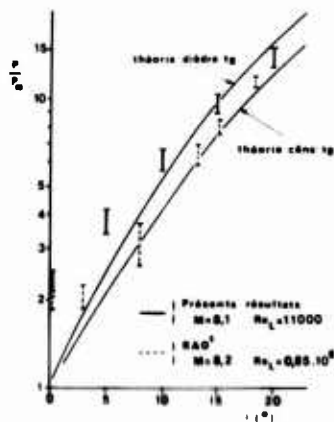


Fig. 3 - Niveau de pression pariétale le long de l'aile

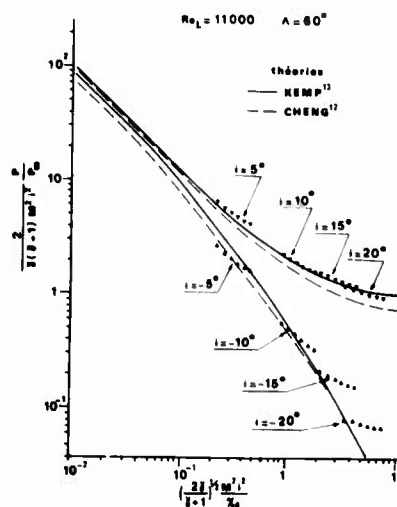


Fig. 4 - Corrélation de pression longitudinale

Des études antérieures mesurées à de plus fortes valeurs du nombre de Reynolds, en particulier celles de Rao (9) et Barber (5) ont montré que le niveau de pression sur l'axe de l'aile est peu différent de la valeur théorique du cône tangent lorsque l'incidence de l'aile est supérieure à  $15^\circ$ . Dans nos conditions d'expérience, caractérisées par un nombre de Reynolds de 11000, le niveau de pression sur l'axe est comparativement plus élevé et dépasse même la valeur théorique du dièdre tangent pour les faibles incidences allant jusqu'à  $10^\circ$  environ. Cette élévation de pression peut s'expliquer ici par la prédominance des effets d'interaction visqueuse.

Dans le cadre de cette représentation de pression pariétale, une seule épaisseur de bord d'attaque fixée à 1 mm a été retenue. En effet, si l'on ne considère que la région avoisinant l'axe de l'aile et dans le cas d'angles de flèche voisins ou supérieurs à  $60^\circ$ , des études antérieures (5, 10) ont montré qu'une variation même sensible de l'épaisseur du bord d'attaque n'influençait que très localement et faiblement les valeurs des pressions pariétales axiales mesurées. Il en serait tout autrement pour un corps bidimensionnel, par exemple dans le cas d'une plaque plane, où l'effet d'émoussement est très marqué et affecte grandement la répartition longitudinale de pression pariétale (11).

Les valeurs des pressions pariétales mesurées le long de l'axe de l'aile entre l'apex et le bord de fuite sont également comparées sur la figure 4 avec l'évolution théorique définie par Cheng (12) et Kemp (13). Ces théories de forte interaction visqueuse s'appliquent en fait à des écoulements bidimensionnels ; on remarquera toutefois que, même pour l'aile delta, l'accord entre les valeurs expérimentales et théoriques est relativement satisfaisant, exception faite des incidences négatives les plus élevées -  $15^\circ$  et -  $20^\circ$  pour lesquelles l'écart est d'autant plus marqué que les orifices de prises de pression correspondants sont plus éloignés de l'apex.

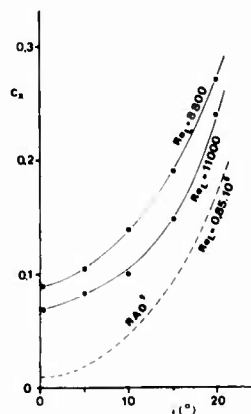


Fig. 5 - Influence du nombre de Reynolds sur le coefficient de traînée

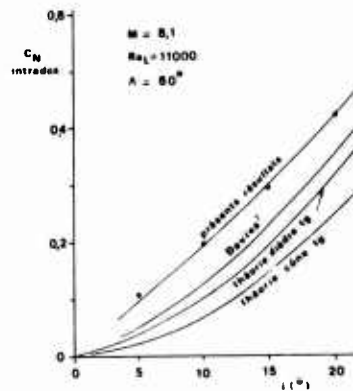


Fig. 6 - Coefficient de force normale appliquée sur l'intrados

Les efforts aérodynamiques ont été mesurés pour les nombres de Reynolds de 8800 et 11000 et une incidence d'aile pouvant atteindre  $40^\circ$ . Les résultats indiquent qu'un changement d'épaisseur du bord d'attaque n'affecte pratiquement que la traînée, aucune variation corrélative n'étant perceptible dans la répartition de portance. On a pu comparer les valeurs des coefficients de forces  $C_N$  et  $C_A$  avec des précédentes données relatives à des nombres de Reynolds plus élevés (9). Le niveau de raréfaction n'a que peu d'influence sur les valeurs du coefficient de force normale mais par ailleurs il affecte considérablement le coefficient de force axiale. En ce qui concerne la traînée, figure 5, un écart considérable apparaît entre les valeurs correspondant aux faibles nombres de Reynolds et celles calculées d'après les résultats de Rao (9) à des densités nettement supérieures pour lesquelles les forces de frottement deviennent négligeables.

A titre d'information, la répartition du coefficient d'effort normal s'appliquant sur l'intrados de l'aile est représentée sur la figure 6. Les valeurs expérimentales sont calculées à partir des forces normales globales mesurées, lesquelles sont décomposées sur chaque face latérale de l'aile en tenant compte des valeurs moyennes de pressions pariétales enregistrées. Les courbes représentatives de la théorie du cône tangent et du dièdre tangent sont tracées sur la même figure ainsi que les valeurs théoriques définies par Davies (7) dont le modèle analytique s'applique au cas de l'aile delta dans les régimes combinés de faible et forte interaction visqueuse.

#### 4. AILE DELTA MUNIE D'UN SPOILER SOLIDE

21-5

Le guidage de l'aile peut être assuré par l'adjonction de gouvernes ; on se limitera dans le présent paragraphe au seul cas d'un spoiler solide s'étendant sur toute l'envergure du bord de fuite. Monté sur un véhicule spatial, un tel dispositif peut être actionné par un mécanisme très simple qui n'aurait pas à supporter des variations de moment de charnière comme pour d'autres types de volets à braquage variable et pour lesquels il est nécessaire de communiquer un couple dont l'intensité est liée au processus du décollement et du recollement sur la gouverne.

Le spoiler associé à l'aile delta donne naissance à un décollement tridimensionnel. A des vitesses hypersoniques et pour de fortes valeurs du nombre de Reynolds, quelques auteurs (14, 17) ont analysé les effets associés à de tels écoulements. Le travail de Rao (9) montre la complexité des phénomènes de décollement ; ces derniers varient simultanément en fonction de l'incidence de l'aile, de la géométrie du volet et suivant la viscosité de l'écoulement.

Les mesures présentées sont limitées au cas d'une aile delta de 0,5 mm d'épaisseur et de 50 mm de long. En présence d'un spoiler solide de 7,5 mm de hauteur et en incidence nulle, les isobares de pression d'arrêt et les traces des chocs dans le plan de symétrie de l'aile sont portées sur la figure 7. Une visualisation de l'écoulement de surface par film d'huile a également permis de montrer la complexité de l'interaction. Sur la figure 8, les régions ombrées correspondent aux zones d'accumulation d'huile ; la limite amont du décollement tridimensionnel y est clairement indiquée.

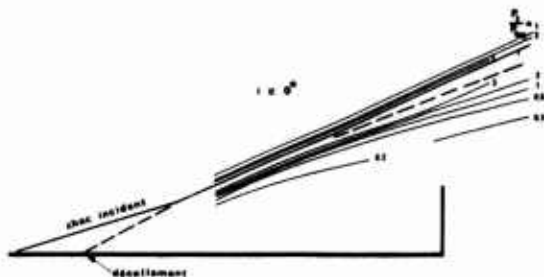


Fig. 7 - Configuration de l'écoulement dans le plan de symétrie de l'aile

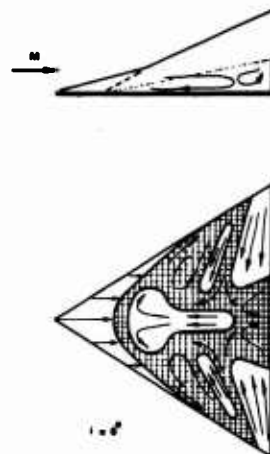


Fig. 8 - Visualisation de l'écoulement à la surface de l'aile

La distribution longitudinale de pression est donnée sur la figure 9 depuis l'apex défini par une abscisse nulle jusqu'au pied de l'élevon. L'effet du décollement apparaît à partir de 10 mm à l'aval de l'apex, la pression s'élevant progressivement pour atteindre un niveau quasi-uniforme dans la région décollée. Le léger maximum observé à 10 mm en amont de l'élevon pourrait s'expliquer par un phénomène d'écoulement tridimensionnel.

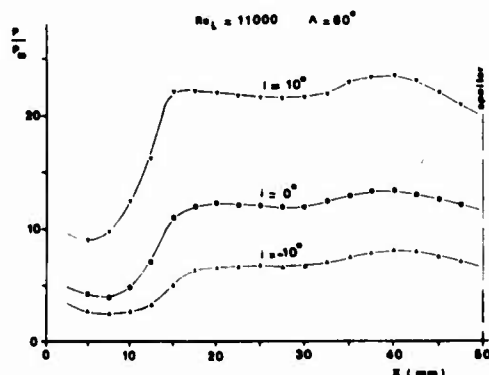


Fig. 9 - Répartition de pression pariétale sur l'axe de l'aile avec spoiler solide

En considérant la même configuration d'aile, la répartition transversale de pression mesurée à mi-hauteur de spoiler est indiquée sur la figure 10. Le niveau de pression sensiblement constant dans la région centrale du spoiler s'accroît très rapidement au fur et à mesure que l'on se rapproche de ses extrémités. Ceci résulte vraisemblablement d'une très intense interaction entre les parties latérales du spoiler, d'une part, et les chocs incident et de recollement, d'autre part. A  $10^\circ$  d'incidence l'interaction est d'autant plus accentuée que le choc tridimensionnel induit par les bords d'attaque de l'aile frappe une surface plus importante du spoiler. L'examen de la figure montre, pour quelques incidences, que les parties latérales du spoiler provoquent l'effet le plus important en entraînant de sensibles modifications des caractéristiques aérodynamiques de l'aile. Ceci est également mis en évidence dans les mesures de forces.

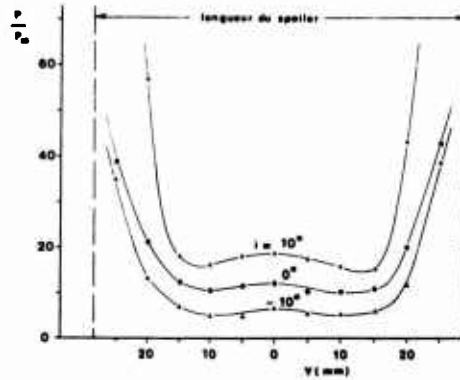


Fig. 10 - Répartition de pression pariétale à mi-hauteur le long du spoiler solide

Pour plusieurs hauteurs de spoiler, la figure 11 présente la variation du coefficient de traînée de l'aile en fonction de l'incidence. L'incidence est considérée comme positive pour un écoulement en compression sur la face de l'aile delta qui porte le spoiler. Les régions décollées sont très étendues et les interactions entre les chocs incidents et les portions latérales du spoiler conduisent à un important effet de la hauteur de spoiler. A une incidence inférieure à  $-20^\circ$ , le spoiler est presque entièrement situé dans le sillage de l'aile et devient inefficace.

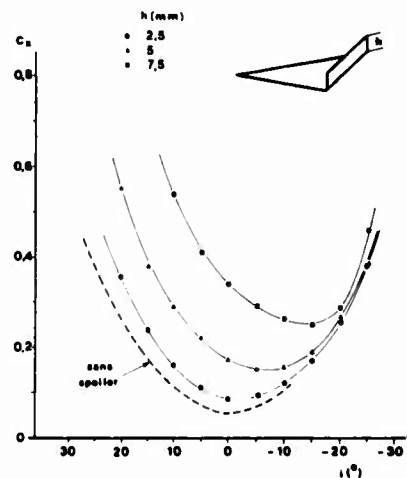


Fig. 11 - Effet de la hauteur de l'élevon sur la répartition du coefficient de traînée

### 5. AILE DELTA MUNIE DE SPOILERS FLUIDES

Le contrôle directionnel d'un corps portant peut également s'effectuer à l'aide de spoilers fluides, essentiellement à haute altitude où l'intensité des efforts aérodynamiques est relativement faible. Dans ces conditions, la force d'impulsion des jets secondaires, affectée d'un facteur multiplicateur lié au mode d'interaction qui s'établit entre l'écoulement extérieur principal et les jets secondaires, est suffisante pour communiquer un mouvement de guidage au véhicule. Une précédente étude (18) montre que, dans le cas d'une aile delta placée dans un écoulement à Mach 4 caractérisé par de grands nombres de Reynolds, la variation de force normale due à une injection fluide représente en incidence nulle et selon les conditions d'injection 2,5 à 3,6 fois la force d'impulsion propre du jet.

Les maquettes utilisées dans le cadre de notre recherche sont représentées sur la figure 12. L'aile delta de  $60^\circ$  de flèche et 50 mm de longueur est munie de deux orifices circulaires d'injection de 2 mm de diamètre localisés à 3 mm à l'amont du bord de fuite. Ces spoilers sont disposés symétriquement de part et d'autre de l'axe longitudinal de l'aile. Une telle disposition a été retenue compte tenu du fait que

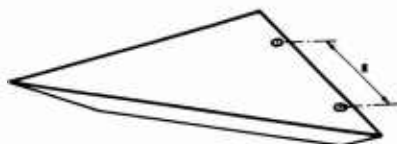


Fig. 12 - Disposition des spoilers fluides

sur le plan pratique un soufflage simultané des deux jets ou un soufflage d'un seul des deux jets permet de communiquer au modèle soit un mouvement de tangage, soit un mouvement de roulis et de lacet. On se bornera ici à la configuration d'un soufflage simultané des deux spoilers.

Les répartitions de pression pariétale mesurées le long de l'axe de l'aile sont portées sur les figures 13, 14 et 15 pour les incidences respectives de  $-20^\circ$ ,  $0^\circ$  et  $+20^\circ$ . Pour un même débit d'air injecté fixé à  $10^{-4}$  kg/s., deux écartements de 10 mm et 40 mm entre spoilers ont été choisis. A titre de comparaison, on a indiqué sur les mêmes figures les répartitions de pressions pariétales en présence d'un spoiler solide de 5 mm de hauteur et couvrant toute l'envergure du bord de fuite.

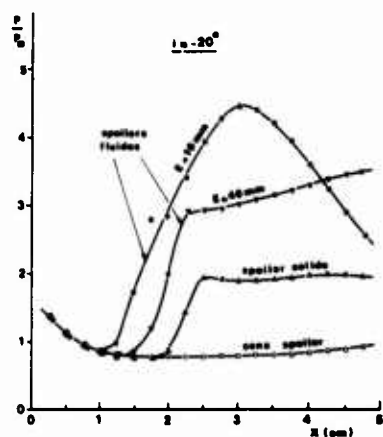


Fig. 13 - Répartition longitudinale de pression pariétale  $i = -20^\circ$

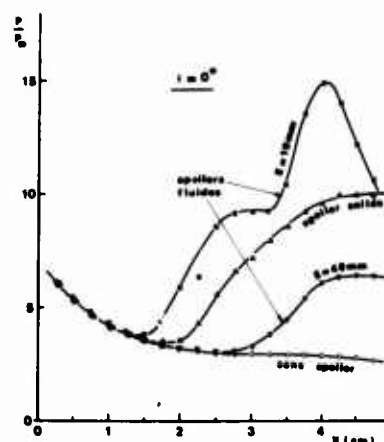


Fig. 14 - Répartition longitudinale de pression pariétale  $i = 0^\circ$

218

A l'incidence de  $-20^\circ$ , figure 13, les décollements induits par les injections fluides sont nettement plus importants que le décollement associé à l'élevon solide ; le plus faible écartement entre les orifices d'injection, figure 12, entraîne le niveau de pression le plus élevé au sein de la zone décollée. A l'incidence nulle, figure 14, l'effet résultant de l'injection fluide caractérisée par le plus faible écartement demeure prédominant. Des visualisations d'écoulements par film d'huile ont montré que plus l'écartement entre les orifices d'injection augmentait, moins l'interaction entre les deux zones décollées situées en amont des orifices devenait importante. A la limite, les deux zones décollées n'interfèrent pratiquement plus entre elles comme c'est le cas à l'incidence de  $20^\circ$  pour l'écartement de 40 mm. A cette dernière incidence, figure 15, l'élevon solide entraîne un décollement plus accentué que celui résultant des injections fluides.

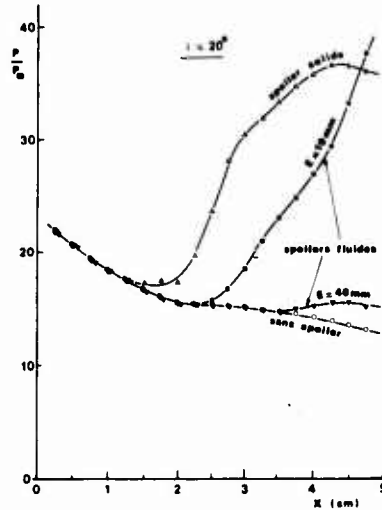


Fig. 15 - Répartition longitudinale de pression pariétale  $i = 20^\circ$

Les mesures de forces aérodynamiques confirment l'évolution constatée de ces résultats partiels de pressions pariétales. Au plus faible écartement des spoilers fluides correspond une région décollée plus importante, et en conséquence la force d'interaction engendrée est plus intense ; cette force d'interaction, normale à la surface de l'aile, s'ajoute à la force de réaction du jet de spoiler.

Les valeurs du coefficient de traînée en fonction de l'incidence de l'aile sont portées sur la figure 16 pour les trois configurations sans spoiler, avec spoiler solide de 5 mm de hauteur et avec spoilers fluides distants de 10 mm. Le bord d'attaque de l'aile étant dissymétrique, figure 12, si l'on considère l'aile sans spoiler l'incidence nulle ne correspond donc plus exactement au minimum de traînée. Les spoilers fluides étant orientés perpendiculairement à la surface de l'aile, la variation de traînée qu'ils entraînent représente seulement la somme des composantes de traînée de la force de réaction des jets, d'une part, et de la force de pression induite par la présence des décollements à l'amont des injections, d'autre part. Par contre, l'utilisation d'un spoiler solide donne lieu à un très net accroissement de la traînée sauf aux incidences inférieures à  $-20^\circ$  pour lesquelles le spoiler est situé pratiquement dans le sillage de l'aile.

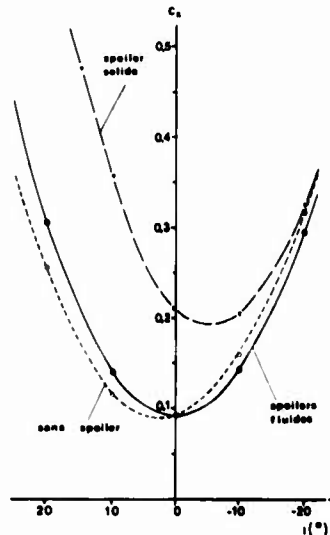


Fig. 16 - Effets de spoilers sur la répartition du coefficient de traînée

Si l'on s'intéresse au contrôle directionnel de la plate-forme, les valeurs enregistrées des forces aérodynamiques normales à la surface de l'aile montrent que les spoilers fluides restent efficaces quelle que soit l'incidence. Aux présentes conditions de raréfaction d'écoulement caractérisées par un nombre de Reynolds de 11000 fondé sur la longueur de l'aile et dans le cas d'une incidence positive de l'aile, la variation de force normale communiquée par le soufflage secondaire représente plus du double de la valeur d'impulsion propre des spoilers. Même aux très fortes incidences négatives pour lesquelles le spoiler solide situé dans le sillage de l'aile devient totalement inefficace, l'utilisation des spoilers fluides permet de récupérer au moins la force de réaction des jets. 21-9

Pour les trois configurations d'ailes, on a porté à titre indicatif sur la figure 17 les valeurs de la finesse en fonction de l'incidence. Aux incidences positives, le spoiler solide affecte très sensiblement la valeur de la traînée de l'aile, et en conséquence la finesse correspondante est nettement plus faible que celle qui résulte de l'utilisation de spoilers fluides.

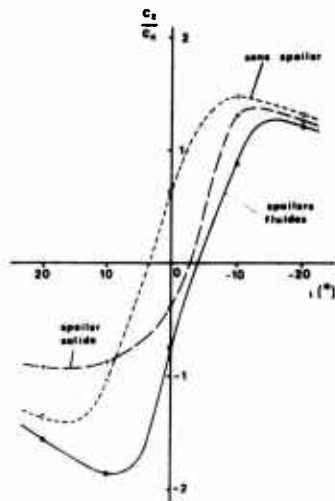


Fig. 17 - Evolution de la finesse

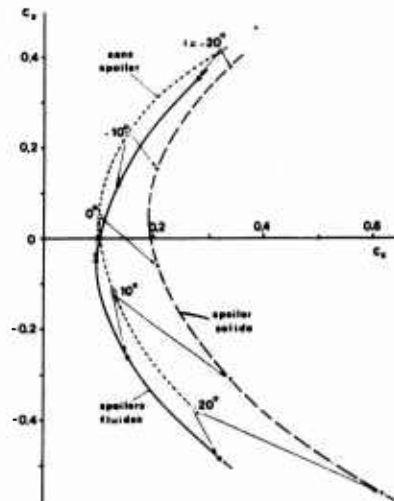


Fig. 18 - Efficacité comparée des spoilers solides et fluides

## 6. CONCLUSIONS

L'étude expérimentale du comportement aérodynamique d'une aile delta a été réalisée dans un écoulement d'air hypersonique à Mach 8 caractérisé par un nombre de Reynolds de 2200 par cm. Pour un tel régime de forte interaction visqueuse les résultats de pressions pariétales et de traînée aérodynamique montrent à quel point les effets de viscosité et de déplacement de couche limite affectent les grandeurs aérodynamiques.

Dans le cas de l'aile delta plane et notamment à faible incidence, une part très importante de la traînée résulte des seules forces de frottement ; de plus, les résultats expérimentaux font apparaître un net accroissement du coefficient de traînée avec la diminution du nombre de Reynolds. A de fortes densités d'écoulement et pour une incidence de l'aile supérieure à 15°, certains auteurs ont montré que le niveau de pression pariétale enregistré sur l'axe de l'aile était peu différent des valeurs calculées d'après la théorie du cône tangent. Aux présentes conditions de raréfaction, les pressions mesurées sont plus élevées et suivent valablement les lois de forte interaction de Cheng et de Kemp.

Les résultats apportent également des renseignements et des données quantitatives sur l'efficacité de dispositifs de guidage directionnel de l'aile à haute altitude par spoilers solides ou par spoilers fluides. Dans le cadre de l'utilisation d'un spoiler solide de bord de fuite, il a été possible de caractériser l'effet du spoiler sur les valeurs des coefficients aérodynamiques. Des visualisations ont également permis de définir le mode d'interaction entre la gouverne et l'écoulement extérieur et de préciser l'étendue de la zone décollée, siège de phénomènes tridimensionnels très complexes. Pour une large plage d'incidences, les parties latérales du spoiler solide interfèrent directement avec l'onde de choc émanant des bords d'attaque de l'aile ; elles jouent de ce fait un rôle prépondérant dans l'accroissement mesuré de la traînée.

Il était intéressant d'étudier parallèlement l'efficacité du guidage directionnel de l'aile par spoilers fluides dans le même cadre de leur utilisation à faible nombre de Reynolds. L'analyse du mécanisme de l'injection montre en particulier que l'effet des spoilers fluides est d'autant plus marqué que ces derniers sont plus rapprochés de l'axe de symétrie de l'aile ; ils engendrent alors un décollement plus accentué s'accompagnant d'une forte élévation de pression induite pariétale. Pour la quasi-totalité des incidences considérées et surtout aux incidences positives, l'utilisation des spoilers fluides entraîne une variation de traînée très inférieure à l'augmentation enregistrée avec le spoiler solide.

A titre de comparaison, la figure 18 présente les variations corrélatives de traînée et de portance communiquées par la présence de spoilers solides ou de spoilers fluides. L'aile delta de 60° de flèche et de 50 mm de longueur est munie dans ce cas, soit d'un spoiler solide de bord de fuite de 5 mm de hauteur, soit de deux spoilers fluides de bord de fuite distants de 10 mm.

Pour une même incidence, on constate que le passage de la configuration de l'aile plane à celle de l'aile avec spoiler solide s'accompagne d'une variation de portance mais surtout d'une très nette augmentation de traînée ; cette augmentation est prédominante aux incidences positives. Comparativement, le

passage de l'aile plane à l'aile munie de spoilers fluides donne lieu à une variation de portance souvent équivalente sans entraîner corrélativement un accroissement démesuré de la traînée préjudiciable pour certaines configurations de vols.

## REFERENCES

- 1 BERTRAM M.H. et EVERHART P.E., "An experimental study of the pressure and heat transfer distribution on a 70° swept slab delta wing in hypersonic flow", NASA TR-153 (1963)
- 2 WETCOFSKI R. et MARCUM D., "Effect of thickness and sweep angle on the longitudinal aerodynamic characteristics of slab delta planforms at a Mach number of 20", NASA TN-D 3459 (juin 1966)
- 3 CROSS E.J. et HANKEY W.L., "Investigation of the leeward side of a delta wing at hypersonic speeds", J. Spacecraft Rockets, 6, 2, (février 1969) pp. 185-190
- 4 MURRAY W. et STALLINGS R., "Heat transfer and pressure distributions on 60° and 70° swept delta wings having turbulent boundary layers", NASA TN-D 3644 (octobre 1966)
- 5 BARBER E.A., "Some experiments on delta wings in hypersonic flow", AIAA J., 4, 1 (janvier 1966) pp. 72-83
- 6 ALLEGRE J., FESTINGER J-C. et HERPE G., "Etude expérimentale de corps portants en écoulement hypersonique à basse densité", l'Aéronautique et l'Astronautique, 1969-8, 15 (août 1969)
- 7 DAVIES L., "On the effects of viscous interaction for a flat delta wing at incidence", Aero. Report 1315, 1970, N.P.L., Teddington
- 8 ALLEGRE J., LARTIGUE D. et SCIBILIA M-F., "Rarefied hypersonic flow characteristics of delta wings and trailing edge spoilers", AIAA J., 10, 7 (juillet 1972) pp. 900-905
- 9 RAO D.M., "Hypersonic control effectiveness studies on delta wings with trailing edge flaps", thèse 1970, Imperial College, Londres
- 10 ALLEGRE J. et FESTINGER J-C., "Etude d'un écoulement hypersonique à basse densité autour d'ailes delta", Rapport 70-9 du Laboratoire d'Aérothermique du CNRS (septembre 1970)
- 11 ALLEGRE J. et HERPE G., "Effets d'incidence et d'émoussement sur les caractéristiques aérodynamiques d'une plaque plane en régime de forte interaction", Rapport 70-4 du Laboratoire d'Aérothermique du CNRS (mai 1970)
- 12 CHENG H.K., HALL J.G., GOLIAN T.C. et HERTZBERG A., "Boundary layer displacement and leading edge bluntness effects in high temperature hypersonic flow", J. Aerospace Sciences, 28, 5 (mai 1961) pp. 353-381
- 13 KEMP J.H., "Hypersonic viscous interaction on sharp and blunt inclined plates", AIAA J., 7, 7 (juillet 1969) pp. 1280-1289
- 14 FETTERMAN D.E. et NEAL L., "An analysis of the delta wing hypersonic stability and control behavior at angles of attack between 30° and 90°", NASA TN-D 1602 (1963)
- 15 KEYES J.W. et ASHBY G.C., "Calculated and experimental hinge moments on a trailing edge flap of a 75° swept wing at Mach 6", NASA TN-D 4268 (1967)
- 16 WHITEHEAD A.H. et KEYES J.W., "Flow phenomenon and separation over highly swept delta wings with trailing edge flaps at Mach 6", AIAA J., 6, 12 (décembre 1968) pp. 2380-2387
- 17 SRINIVASAN R., LEBLANC R. et ALZIARY DE ROQUEFORT T., "Décollement tridimensionnel sur une aile delta en écoulement supersonique", 9ème Colloque d'Aérodynamique Appliquée, Paris (novembre 1972)
- 18 AMICK J.L. et CARVALHO G.F., "Interaction effects of a jet flap on a 60° delta wing at Mach number 4 and comparison with two dimensional theory", Report CM-1031, University of Michigan (février 1963)

22-1

A REVIEW OF SUPERSONIC SPHERE DRAG  
FROM THE CONTINUUM TO THE FREE MOLECULAR FLOW REGIME

Prof. E. VALLERANI  
AERITALIA - Uffici di Torino (Italy) - Servizio Studi Speciali

## SUMMARY

The evaluation of the sphere drag coefficient has been the object of extensive theoretical investigations for a long time; a large amount of experimental data has been collected to substantiate those studies and to provide the needed information for the flow regimes for which the theoretical approaches are still missing.

The scope of the present review is to attempt the establishment of a more complete panorama of the supersonic sphere drag predictions over the entire range of flow regimes ranging from the continuum flow to the free molecular flow, in order to provide in a consistent form the design engineer of the information required for the aerodynamic design of space vehicles.

The theoretical methods developed to cover the various flow regimes such as: continuum low density-free molecular - near free molecular - intermediate - have been reviewed and discussed in the light of the comparison with the pertinent experimental data available.

New semiempirical formulas for the correlation of the experimental data are derived for the low density continuum flow and for the near free molecule flow regimes.

For the intermediate flow regimes, ranging between the continuum flow and the free molecular flow, the results of a semiempirical method recently developed by the author are presented and discussed.

## 1. INTRODUCTION

The interest in methods for correctly evaluating the drag coefficient for a sphere, over all the range of the Knudsen number from the continuum limit up to the free molecular limit, dictated, apart from the pure theoretical speculation, by the increasing needs supported by space applications, has stimulated several theoretical approaches and has promoted in recent years extensive experiments.

The concern in supersonic flow drag predictions previously confined, due to the aircraft applications, to the continuum flow regime, has been extended in recent years to cover the entire spectrum of flow regimes because in atmospheric entry flights a vehicle initially flies through a free molecule atmosphere, successively passes through the transitional regimes and completes its flight in the continuum regime.

Among the different flow regimes into which fluid mechanics has been subdivided, only ordinary continuum gasdynamic, for which the density is sufficiently high so that intermolecular collisions dominate ( $Kn \ll 1$ ), and free molecule flow for which the gas is sufficiently rarefied that collisions with the boundaries dominate over collisions between molecules ( $Kn \gg 1$ ), are well defined; the physical situation for the intermediate flow regimes is very involved so that only sophisticated and complex mathematical models have been developed, which are generally impractical for engineering purposes.

In the present note five distinct regimes are separately analyzed: the continuum flow, the low density continuum flow, the free molecular flow, the near free molecule flow and the intermediate or transitional flow; for each of them the theoretical prediction available has been discussed and compared, the pertinent experimental results have been reviewed and new correlation formulas have been developed.

### 1.1. Drag force definition

The aerodynamic forces rising from the interaction of a body moving through a fluid at rest are the resultant of the local actions exerted by the fluid on the body surface elements.

The unit force acting on each surface element can formally be subdivided into a normal component "pressure" and a tangential one "friction or shear"; "pressure drag" is the component in the direction of motion of the resultant of these "pressure unit forces" and "friction or shear drag" the one of the "friction unit forces".

What is usually called "Drag of Resistance" is the total force acting in the direction opposite to that of motion, sum of the "pressure and friction drag components".

Even when the geometry of the body is as simple as the sphere the evaluation of the drag force is not easily accomplishable; in fact a complete theoretical formulation does not yet exist to predict with sufficient accuracy, of the level required for engineering applications, the value of drag over all the flow regimes ranging from the continuum to the free molecular flow.

As well known, the first resistance law was derived by Newton on the basis of the momentum theorem adopting an hypothetical medium consisting of particles not exerting any influence whatsoever on each other, the drag relation:  $D = f \rho V^2 A$  was obtained, by simple summation of the actions exerted on the unit surface elements of the body surface, being  $\rho$  the fluid density,  $V$  the velocity,  $A$  the projected area of the body in the flow direction (reference area),  $f$  a proportionality factor.

The newtonian model, as discovered many years later, fails to predict the drag when the fluid, as air at low altitudes, needs to be considered as a continuum medium, with fluid particles influencing each other; in such conditions shock and boundary layers are formed around the body and more complex approaches are required to evaluate the drag force.

Following the form proposed by Newton it has become usual practice to express the drag force through a non dimensional proportionality factor called the drag coefficient:  $C_D = D / \frac{1}{2} \rho V^2 A$

Such a drag coefficient can accordingly be expressed as the sum of a pressure and a shear drag coefficient; in the case of a sphere here considered, geometrical considerations allow the establishment of the basic relationship:

$$C_D = C_{Dp} + C_{Ds} = 1 / \frac{1}{2} \rho_0 V_0^2 \left[ 2 \int_0^\pi p \sin \alpha \cos \alpha d\alpha + 2 \int_0^\pi \tau \sin^2 \alpha d\alpha \right] \quad \text{eq. 1}$$

on the basis of which the drag coefficient is obtainable by means of simple integrations provided the distribution of the pressure  $p$  and the shear stress  $\tau$  along the body is known.

Unfortunately only for the two extreme cases of continuum and free molecular flow regimes the knowledge of the flow field is such as to allow a theoretical evaluation of the drag force; so that the experimental drag data are of great importance in substantiating the theoretical predictions when available and in supplying the information needed for some flow regimes for which such predictions are lacking.

## 2. CONTINUUM AND LOW DENSITY CONTINUUM FLOW REGIMES

### 2.1. General remarks

Dimensional analysis leads to the conclusion that in continuum flow, for a given body shape, the drag coefficient turns out to depend on the Reynolds and Mach numbers, in the more general case in which as in compressible fluids elastic forces are of the same importance as inertia and friction forces

For the hypersonic flow regimes, realized for a sphere for  $M > 6$ , the drag coefficient turns out to be dependent only on the Reynolds number.

The Reynolds number that has been used in the classical analysis, as well as in the early correlations of the experimental results, is the infinity Reynolds number based on free stream conditions:  $Re_\infty = \rho V D / \mu_\infty$ . Subsequently it has been found that different forms of the Reynolds number could be more profitably adopted as scaling parameters for presenting drag data, especially when low density effects have to be investigated:

- The wall Reynolds number  $Re_w = \rho_w V_w D / \mu_w$  based on free stream mass flow and fluid viscosity evaluated at the wall temperature.
- The stagnation Reynolds number  $Re_0 = \rho_0 V_0 D / \mu_0$  with fluid viscosity evaluated at the stagnation point temperature.
- The shock Reynolds number  $Re_s = \rho_s V_s D / \mu_s$  with flow properties behind the normal part of the bow shock wave evaluated according to conventional Rankine-Hugoniot shock wave relations.

The evaluation of the drag coefficient involves as said (eq. 1) the knowledge of the pressure and shear distribution along the body surface, that can be expressed in principle on the basis of the Van Dyke (56) perturbation procedure of the Navier-Stokes equations in term of the parameter

$$\epsilon = \sqrt{2} \left\{ \frac{(\gamma-1)(\gamma+1)^2 M^4 / [2\gamma M^2 - (\gamma-1)] [(1-\gamma)M^2 - 2]}{1} \right\}^{1/4} \frac{1}{\sqrt{Re_s}}$$

$$\text{as: } p = p_1 + \epsilon p_2 + \epsilon^2 p_3 \quad \text{and} \quad \tau = \epsilon \tau_1 + \epsilon^2 \tau_2$$

The pressure distribution  $p_1$  is resulting from the inviscid flow field analysis; theoretical methods in the form of numerical solutions are available but are applicable only to the front part of the sphere, (fortunately the contribution of the rear part of the sphere is not too high, especially for supersonic flow conditions, so that it can be neglected without invalidating the solution).

The first order shear force distribution  $\tau_1$ , is resulting from the classical boundary layer analysis based on the inviscid pressure distribution  $p_1$ ; the solution is extended downstream up to the point of separation, (the contribution due to shear in the region beyond separation is usually neglected being generally small); boundary layer analysis provides in addition the information on the displacement thickness, that in turn allow the evaluation of the modified pressure distribution on a corrected body shape.

The second order pressure and shear stress distribution can be evaluated on the basis of the perturbation type procedures and account for the vorticity, longitudinal and transverse curvature, displacement, slip and temperature effects.

A good approximation to the sphere drag can therefore be obtained using only boundary layer theories by integrating the pressure and shear distribution up to the point of separation; the drag coefficient results:

$$C_D = \left( \frac{1}{2} \rho_0 V_0^2 \right)^{-1} 2 \left\{ \int_0^\pi p_1 \sin \alpha \cos \alpha d\alpha + \epsilon \int_0^\pi p_2 \sin \alpha \cos \alpha d\alpha + \epsilon^2 \int_0^\pi p_3 \sin \alpha \cos \alpha d\alpha + \right. \\ \left. \epsilon \int_0^\pi \tau_1 \sin^2 \alpha d\alpha + \epsilon^2 \int_0^\pi \tau_2 \sin^2 \alpha d\alpha \right\} = C_{Dc} + \epsilon (C_{Dp_2} + C_{Ds_1}) + \epsilon^2 (C_{Dp_3} + C_{Ds_2}) \quad \text{eq. 2}$$

sum of the near inviscid, essentially infinite Reynolds number, pressure drag coefficient  $C_{Dc}$ , plus a first order boundary layer term, accounting for skin friction and induced pressure effects, plus a third term representing all the second order boundary layer effects.

Introducing the shock Reynolds number  $Re_s$  we obtain the relation:  $C_D = C_{Dc} + K_1 / \sqrt{Re_s} + K_2 / Re_s$  eq. 3 expressing the drag coefficient in the same form as the one proposed by Aroesty (1) and later adopted by Kinslow and Potter (27) to correlate experimental results.

## 2.2 Continuum flow

For the evaluation of the near inviscid continuum flow drag coefficient  $C_{DC}$ , being questionable the theoretical predictions of the pressure distribution, experimental data have often been used; several direct evaluations of the sphere drag coefficient have been accomplished using supersonic wind tunnels and aeroballistic ranges, we recall Charters and Thomas (12), Clark and Harris (14), May and Witt (32), Hodges (23), Halperson, Boltz and Hall (20), Hallsmaier (19), Kinslow and Potter (27), Bailey (5) results, that indicate as for  $Re_s > 10^4$  the sphere has to be considered in the realm of continuum flow.

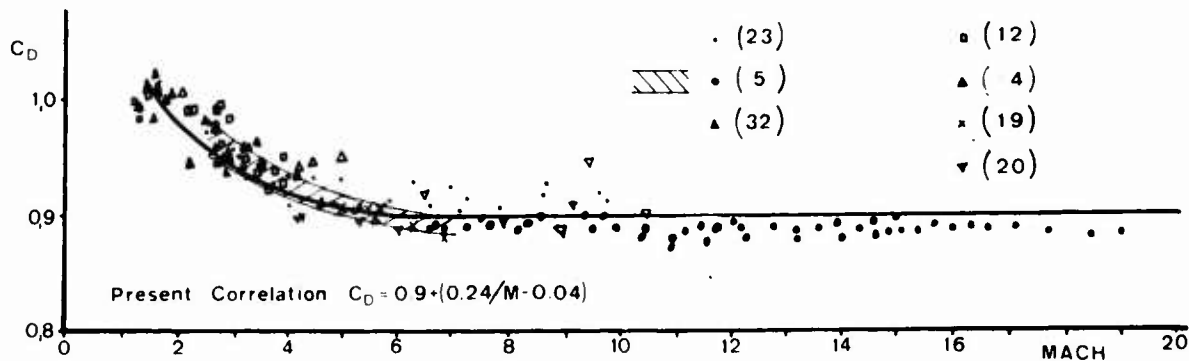


Fig 1 CONTINUUM FLOW DRAG DEPENDENCE ON MACH

A progressive reduction of the drag coefficient, the higher the Mach number, is noticeable for all the sets of data, with an asymptotic limit for  $M > 6$  (fig. 1). Old wind tunnel data, especially the ones by Hodges (23), seem to fix this hypersonic limit value to 0.92 while more recent results obtained by Bailey (5) with an aeroballistic range consistently give, with 1.5% accuracy a limiting value of 0.88. The wall temperature effect can be of some relevance to account for such differences; Bailey results are indeed for a cold wall model ( $T_w/T_0 \sim 0.2$ ) while Kinslow and Potter results, that agree with the Hodges ones, are for the same Mach number and for higher wall temperatures ( $T_w/T_0 \sim 0.7$ ); the latter giving higher drag values, in agreement qualitatively with the established influence exerted by wall temperature on drag, as brought to evidence by the investigations of Ashkenas (2).

Correlating the above experimental results, an empirical expression for the mean drag coefficient is derived for the supersonic flow conditions  $1.5 < M < 6$ :  $C_{DC} = 0.9 + (0.24/M - 0.04)$  eq. 4 the value of  $C_{DC} = 0.9$  being retained for the hypersonic flow conditions.

## 2.3. Low density continuum flow

For flow conditions extending in the low density regimes  $Re_s < 10^4$  it is necessary to account for boundary layer first and second order effects. The evaluation of the first order skin friction term poses the still formidable problem of resolution of the non similar boundary layer viscous flow; approximate solutions have confirmed that the skin friction drag has a dependence on the rarefaction parameter of the type  $1/\sqrt{Re_s}$ .

Another first order effect induced by the reduced density is the one introduced on the pressure distribution by the boundary layer displacement; Potter and Bailey (40) have predicted on the basis of the Navier-Stokes equations and the Rankine-Hugoniot shock relations, an increase of the stagnation point pressure, over the continuum flow value, given by the relation  $p_0/p_{0\infty} = 1 + 2\sqrt{2} (p_0/p_s)^{1/2} / \sqrt{Re_s}$ ; such effect has been confirmed experimentally by Potter and Bailey (40), while the form of the pressure distribution along the sphere surface has been found by Potter and Bailey (40), Bailey and Sims (6) to be almost unaffected by the rarefaction effects, at least for  $Re_s$  as low as 20.

The pressure component of drag therefore can be scaled directly as the increase of the stagnation point pressure and the form  $1/\sqrt{Re_s}$ , found for the first order friction term, applies as well for the pressure induced effects, as obtained formally by the perturbation type analysis previously recalled.

The extension of boundary layer analysis to more rarefied flow regimes has brought in evidence the importance of higher order boundary layer effects not present in the classical analysis. Perturbation procedures with an expansion of the complete Navier-Stokes equations in inverse power of the square root of a Reynolds number have been adopted by Van Dyke (56), to investigate the stagnation point region and extended by Davis and Flugge-Lotz (15) to derive second order boundary layer solutions on blunt bodies, such as the sphere, up to locations several radii downstream of the stagnation point.

Such complex analyses do not provide closed form solutions, but allow only to deal with specific cases; for the sphere it has been obtained:  $C_D = 0.89 + 2.8/\sqrt{Re_s}$  ( $M=10, T_w/T_0=0.1$ )  $C_D = 0.89 + 3.8/\sqrt{Re_s}$  ( $M=10, T_w/T_0=0.6$ )

The drag coefficient has been computed through numerical integration of the pressure and shear distribution, including only terms order  $1/\sqrt{Re_s}$  because even if the shear distribution was known up to order  $1/Re_s$  the pressure was not, due to the fact that, to obtain a second order perturbation pressure distribution, it is necessary to solve the outer flow region including third order terms, thus requiring a coupling of the inviscid and viscous solutions. By examining Davis and Flugge-Lotz second order shear terms results, it can be inferred that, at least for the front part of the sphere, these effects are expected to bring in a negative contribution to the drag coefficient, being negative the coefficient of the shear term order  $1/Re_s$ .

In the recent years a large amount of experiments have been performed to investigate the behaviour of supersonic sphere drag under low density continuum flow conditions, that is to say for approximately  $10 < Re_s < 10^4$ , we recall among others the results of the experiments conducted by Srekanth (54), Wege

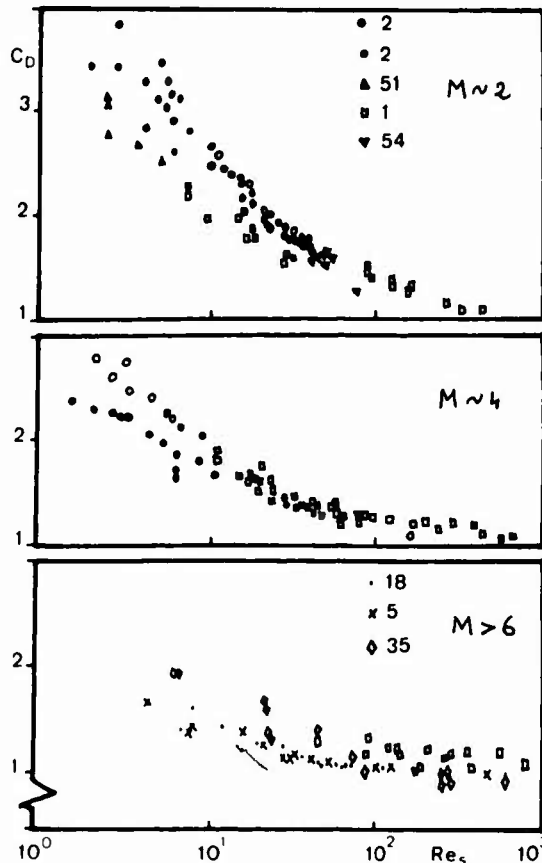


Fig. 2 LOW DENSITY DRAG

ner and Ashkenas (59) Aroesty (1), Ashkenas (2), Geiger (18), Kinslow and Potter (27), Bailey (5), Phillips and Kuhlthau (39), Smolderen Wendt Naveau and Brailette (53), Koppenwallner (28), Kussoy and Horvath (29) some of which are collected in fig. 2 to provide a general picture of the available results.

The above investigations have been performed for different wall temperature conditions and cover a wide range of Mach numbers ( $1.5 < M < 15$ ); the scatter among the results is rather high and turns out to be lower for aerobalistic range experiments than for the wind tunnel ones.

Following Aroesty (1) it has become in use to correlate the results in the form previously discussed:

$$C_D = C_{Dc} + K_1 / \sqrt{Re_s} + K_2 / Re_s \quad \text{eq. 5}$$

with  $K_1 = K_1(M, T_0, T_w)$  and  $K_2 = K_2(M, T_0, T_w)$

The function  $K_1$  has been found to be positive and to decrease for increasing Mach, up to the hypersonic conditions for which it depends only on the surface wall temperature.

The dependence from the stagnation temperature and on the wall temperature levels, has been put in evidence by Kinslow and Potter (27) through the parameter  $H_w = T_w/T_0 - 1$ ; a reduction of the skin friction drag coefficient, and in general of the first order terms, has been found to be associated with a reduction in wall temperature, as it has been demonstrated theoretically, for the flat plate case, and is ascribable to the fluid viscosity variations with temperature within the boundary layer.

The function  $K_2$  has been found to be negative, with a similar dependence on Mach number and temperature parameter, this confirms the observation previously done on the basis of the Davis and Flugge-Lotz theoretical results. We remind that an analysis, similar to the one of Kinslow and Potter (27), has been successively conducted by Bailey (5) for cold wall conditions, that has lead to different conclusions on the value of  $K_2$ , that has been found to be positive.

Apart from the still existing uncertainties on the values of  $K_1$  and  $K_2$  and on their dependence from the basic parameters, that is due to the unavailability of closed form solutions able to predict the shear stress distribution and the corrected pressure distribution along the sphere surface, the conclusion generally reached is that the two terms formulation is sufficient to deal with the extension in the low density regimes of the continuum flow drag formula up to about  $Re_s = 10$ ; further extensions to more rarefied flow conditions have to be accomplished applying a non continuum flow analysis.

The available results have been reexamined and a new correlation formula, that seems to correlate reasonably well a wide body of results, has been obtained.

It has been assumed that in the flow regimes  $10 < Re_s < 10^4$  the supersonic sphere drag coefficient is expressed by the relation:

$$C_D = C_{Dc} + (C_1 + f) / \sqrt{Re_s} - (C_2 + f) / Re_s \quad \text{eq. 6}$$

the constants  $C_1$  and  $C_2$  have been determined on the basis of the cold wall hypersonic conditions results obtaining

$$C_1 = 1.78 \text{ and } C_2 = 0.5.$$

The function  $f(M, X)$  has been assumed to be dependent on the Mach number and on the parameter  $X = \sqrt{T_w/T_\infty}$  ratio of the wall to free stream temperature. Several correlations of the experimental results have been attempted, the best one has been found (see fig. 3) to be versus parameter  $\Phi = X^2/M^3$

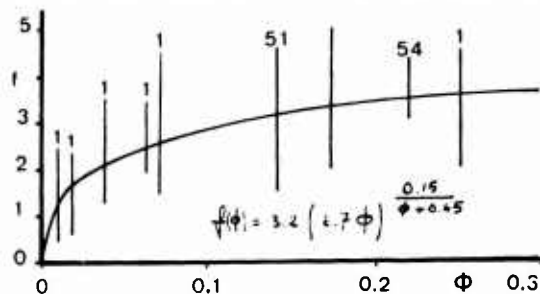


Fig. 3 PRESENT CORRELATION FORMULA

### 3. FREE MOLECULE FLOW REGIME

For highly rarefied gas flows, denominated free molecule flows, occurring when the appropriate mean free path of the incoming molecules  $\lambda$  is much greater than the characteristic body dimension, diameter  $D$  for the sphere, the aerodynamic forces acting on a body are determined only by the collisions between gas molecules and solid surface, being ignorable the intercollisions between gas molecules.

In the free molecule flow regime, due to absence of intermolecular momentum transfer, the incoming and the reflected flows are not interacting and the aerodynamic forces  $dF$  acting on a surface element  $dA$  can be evaluated as sum of impact momentum of free stream molecules and reactive momentum of reflected molecules; it is convenient, as done in continuum flow, to resolve the momentum flux per unit area to the surface element into a normal component  $p$  (pressure) and a tangential component  $\tau$  (shear stress).

### 3.1. Incident molecules momentum transfer

For a comprehensive treatment of the free molecule flow transfer theory, reference is made to Tsien (55) Ashley (3) and to the classical textbooks by Schaaf and Chambre (49) and Hayes and Probstein (21); we recall only hereafter some conclusions relative to the incoming molecules momentum transfer. For unit surface element, at an angle of attack  $\theta_i$  with respect to the flow direction, the contribution to the normal pressure turns out to be:

$$p_i = \frac{\rho_\infty V_\infty^2}{2\sqrt{\pi} S_i} \left\{ \bar{v}_i \exp(-\sigma_i^2) + \sqrt{\pi} \left( \frac{1}{2} + \sigma_i^2 \right) (1 + \epsilon_f \sigma_i) \right\} \quad \text{eq 7}$$

and the one the shear tangential stress:

$$\tau_i = \frac{\rho_\infty V_\infty^2}{2\sqrt{\pi} S_i} \left\{ \exp(-\sigma_i^2) + \sqrt{\pi} \sigma_i (1 + \epsilon_f \sigma_i) \right\} \cos \theta_i \quad \text{eq 8}$$

being  $\bar{v}_i = S_i \sin \theta_i$  with  $S_i = V_\infty / \sqrt{2R T_\infty} = \sqrt{\gamma/2} M$  the incident molecules "speed ratio", that is to say the ratio of the free stream mass velocity  $V_\infty$  to the most probable random speed of the molecules in the free stream.

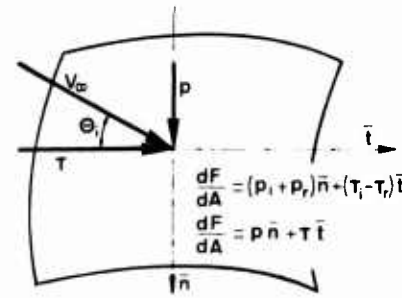


Fig.4 FORCE COMPONENTS

### 3.2. Reflected molecules momentum transfer

To calculate the contribution of the reflected molecules to momentum transfer it is necessary to possess an insight of the mechanism of interaction phenomena occurring at the surface after collision of the free stream molecules; several models have been developed to treat the interaction process, all introduce a set of parameters whose value has to be determined to better match the experimental results, that offer a very complex panorama due to the intrinsic difficulty in assessing the effect of the very many parameters entering the problem.

Maxwell in the original treatment of free molecule flow postulated two simple types of reflection processes:

- the "specular or elastic reflector" according which incident molecules are assumed to hit the surface and to rebound perfectly elastically with the normal velocity component reversed and the tangential component unchanged:  $p_{sr} = p_i$  and  $\tau_{sr} = \tau_i$

- the "diffuse reflection" according which incident molecules are assumed to be trapped by the surface and successively reemitted with a Maxwellian velocity distribution having zero mean velocity, corresponding to thermal equilibrium at the surface temperature; the direction of reemission being independent of the one of incidence:  $p_{dr} = p_w$  and  $\tau_{dr} = 0$ .

The normal momentum (pressure) for the diffuse reflection case is calculated assuming the reflected molecules as issuing from a hypothetical gas at rest at a temperature  $T_w$  resulting from the balance of energy influx and efflux to and from the surface.

$$p_w = \frac{\rho_w V_w^2}{2 S_i} \left\{ \frac{1}{2} \sqrt{T_w/T_i} \exp(-\sigma_i^2) + \frac{\sqrt{\pi}}{2} \sqrt{T_w/T_i} \sigma_i (1 + \epsilon_f \sigma_i) \right\} \quad \text{eq 9}$$

These two types of reflection processes can be considered as extremes between which the actual process lies; in the Maxwell reflection model it was assumed that  $(1-f)$  of the impinging molecules are reflected specularly and the remainder  $(f)$  diffusively.

The reflected momentum turns out to be a linear combination of the quantities relative to specular and diffuse reflection  $p_r = (1-f) p_{sr} + f p_{dr}$  and  $\tau_r = (1-f) \tau_{sr} + f \tau_{dr}$  and the total values, sum of the incident and reflected molecules contribution, result to be:

$$p = p_i + p_r = (2-f) p_i + f p_w \quad \text{eq 11} \quad \tau = \tau_i - \tau_r = f \tau_i \quad \text{eq 12}$$

Schaaf (48) and Hurlburt (24) have suggested to introduce two different coefficients for the transport of momentum to and from the body surface, respectively in directions normal and parallel to the surface:  $f_n = (p_i - p_r) / (p_i - p_w)$  normal accommodation coefficient and  $f_t = (\tau_i - \tau_r) / \tau_i$  tangential accommodation coefficient, in order to ameliorate the maxwellian model that the experiments by Hurlbut (24) have shown not to be sufficient to describe the reflection process of momentum adequately.

According to what is known as the Schaaf Chambre (49) model the total pressure results to be therefore:  $p = (2-f_n) p_i + f_n p_w$  eq 13 and the total shear:  $\tau = f_t \tau_i$  eq 14

Shamberg (50) has developed a somewhat more elaborate and realistic gas surface interaction model in the attempt to improve the description of the surface reemission momentum exchange.

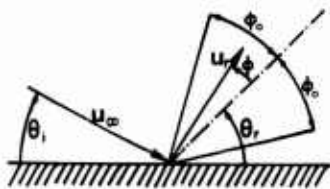


Fig.5 SCHAMBERG REFLECTION

The random motion of the incident molecules is neglected, being the flow assumed hyperthermal so that the incident particles are assumed to approach the surface with a uniform velocity  $V_i$  and angle of incidence  $\theta_i$ ; after interaction with the surface the molecules are reemitted in the form of a beam having half angular width  $\phi_0$ , centered around the most probable angle of reflection  $\theta_r$ , that accounting for the general trend towards diffuse reflection is assumed:  $\pi/2 < \theta_r < \theta_i$

A simple relation between incident direction and reemitted direction has been postulated by Shamberg:  $\cos \theta_r = (\cos \theta_i)^{1/\nu}$  that satisfies the limiting cases of specular reflection  $\nu=1$  ( $\theta_r = \theta_i$ ) and diffuse reflection  $\nu \rightarrow \infty$  ( $\theta_r = \pi/2$  whatever  $\theta_i$ ).

The distribution of the reemitted molecules has been assumed symmetric

226

about the axis of the beam with a cosine distribution, as suggested by surface interaction experiments by Hurlbut (24), and the reemission speed has been postulated independent of the angle of emission and related to the incident velocity  $V_i$  and surface temperature  $T_w$ , in the conventional way by means of the energy accommodation coefficient  $\alpha$ :  $V_r/V_i = [1 + \alpha(T_w/T_w - 1)]^{1/2}$  being  $T_i, T_r$  the kinetic temperatures of incoming and reflected molecules.  $V_r/V_i = \sqrt{T_r/T_i} = \sqrt{1-\alpha}$

Such a model involves three interaction process parameters  $\phi_0, \nu, \alpha$  the definitive choice of the numerical values to be given to them is not possible in absence of consistent experimental data; Shamburg discusses the evaluation of the accommodation coefficient  $\alpha$ , on the basis of an highly simplified model of surface interaction due to Baule (7) leaving open the problem of defining  $\phi_0, \nu$ .

Nocilla in a series of relevant papers (37) (38) has proposed a model for the description of the reemitted molecules that possesses, without losing in simplicity, a large capability of matching with suitable adjustments of its parameters a wide variety of experimental results relative to different gas-surface conditions.

The basic idea introduced in the model (37) is that the reemitted molecules behave as a gas in Maxwellian equilibrium subject to a reemission temperature  $T_r$ , not necessarily equal to the wall temperature  $T_w$ , but resulting from the energy balance equation, and to a mass velocity  $V_r$  (drift velocity). The reemitted molecules therefore are assumed to exert on the body actions that can be determined in a way completely similar to the one adopted to derive the actions of the incident molecules.

If the speed ratio of the reemitted molecules  $S_r = V_r/(2RT_r)^{1/2}$  is introduced in the analysis, the outgoing flow of reemitted molecules can be expressed in terms of three parameters  $S_r, V_r, \theta_r$ .

A remarkable agreement has been put into evidence by Nocilla (37) between the intensity distribution of the reemitted molecules obtained with the model and the experimental data collected by Hurlbut (24).

The Nocilla model has been successively adopted, by Hurlbut and Sherman (25) to derive the drag coefficients of simple bodies. By analogy with the formulas previously obtained for the incoming molecules, the normal pressure and the shear tangential stress resulting on a surface element from the reemitted molecule flux can be easily derived:

$$P_r = \frac{(n_r m) V_r^2}{2\sqrt{\pi} S_r^2} \left\{ \sigma_r \exp(-\sigma_r^2) + \sqrt{\pi} (1/2 + \sigma_r^2) (1 + \epsilon_f \sigma_r) \right\} \quad \text{eq 15}$$

$$\tau_r = \frac{(n_r m) V_r^2}{2\sqrt{\pi} S_r} \cos \theta_r \left\{ \exp(-\sigma_r^2) + \sqrt{\pi} \sigma_r (1 + \epsilon_f \sigma_r) \right\} \quad \text{eq 16}$$

The number density  $n_r$  appearing in the distribution of the reemitted molecules is obtained by matching the outgoing molecule flux with the incoming one, so that:

$$(n_r m) = (n_i m) (T_i/T_r)^{1/2} \chi(\sigma_i) / \chi(\sigma_r) \quad \text{eq 17} \quad \chi(\sigma) = \exp(-\sigma^2) + \sqrt{\pi} \sigma (1 + \epsilon_f \sigma)$$

These authors have removed the dependence on the effective temperature of reemission  $T_r$  present implicitly in a way that satisfies the energy conservation by introducing the partial energy accommodation coefficient  $\alpha_2$  defined as:  $\alpha_2 = (E_i - E_r) / (E_i - E_w)$ .

Substituting into  $\alpha_2$  the expressions for the corresponding energy fluxes, the following relation has been found for the temperature  $T_r$ :

$$(2RT_r)^{1/2} = V_w \left\{ \frac{(1-\alpha_2) \left\{ 1 + \frac{\gamma+1}{2(\gamma-1)S_i} + \frac{\sqrt{\pi} \sigma_i (1 + \epsilon_f \sigma_i)}{2 \chi(\sigma_i) S_i^2} \right\} + \alpha_2 \frac{2RT_w}{V_w^2} \left( \frac{\gamma+1}{\gamma-1} \right)}{S_r + \frac{\gamma+1}{2(\gamma-1)} + \frac{\sqrt{\pi} \sigma_r (1 + \epsilon_f \sigma_r)}{2 \chi(\sigma_r)}} \right\}^{1/2} = V_w B^{1/2} \quad \text{eq 18}$$

The pressure and the shear stress relative to the reemitted molecules are defined therefore in terms of parameters defining the incident stream  $V_w, S_i, \theta_i$ , the interaction process parameters  $S_r, \theta_r, \alpha_2$  and the wall temperature  $T_w$ , according to the relations:

$$P_r = \frac{\chi(\sigma_r)}{\sqrt{\pi} S_i} \frac{\rho_w V_w^2}{2} \left\{ B^{1/2} (\sigma_r + \sqrt{\pi}/2 (1 + \epsilon_f \sigma_r) / \chi(\sigma_r)) \right\} \quad \text{eq 19}$$

$$\tau_r = \frac{\chi(\sigma_r)}{\sqrt{\pi} S_i} \frac{\rho_w V_w^2}{2} \left\{ B^{1/2} S_r \cos \theta_r \right\} \quad \text{eq 20}$$

The proposed model by appropriate restriction of the reemission parameters includes the classical results; in particular for  $S_r = 0$  we have the diffuse scattering, for  $S_r = 0, \alpha_2 = 1$  the Maxwellian reemission with  $T_r = T_w$  and for  $S_i = S_i, \theta_r = 0, \alpha_2 = 0$  we have the specular reflection.

The model provides in addition a large degree of freedom in the choice of the interaction parameters  $S_r, \theta_r, \alpha_2$ ; from the examination of the trend of molecular beam results it is possible to find simple empirical representations of their behaviour; Hurlbut and Sherman (25) introduced the following assumptions:

- the reemitted momentum is concentrated in a single lobe, the macroscopic drift velocity  $V_r$  is directed at an angle  $\theta_r$  numerically equal to  $\theta_i$ ;
- the value of  $\alpha_2$  is linearly dependent on  $\theta_i$  being maximum at normal incidence and minimum at glancing incidence:  $\alpha_2 = (\alpha_2)_0 + 2/\pi [(\alpha_2)_{90} - (\alpha_2)_0] \theta_i$ .
- the value of  $S_r$ , never greater than  $S_i$  is linearly dependent on  $\theta_i$  being minimum at normal incidence and maximum at glancing incidence:  $S_r = (S_r)_0 + 2/\pi [(S_r)_{90} - (S_r)_0] \theta_i$ .

Epstein (17) has presented a new approach to the problem of surface reemission treating it from a stochastic point of view; the reflected molecules velocity distribution is determined assuming that a frac-

22-7

tion  $P(v_r)$  of the molecules is scattered diffusely and the remaining  $1 - P(v_r)$  specularly:  $f_r = f_o P + f_i (1 - P)$   
 The form of the probability function  $P = \exp(-c^2/2 R \theta_1) + B [1 - \exp(-c^2/2 R \theta_2)]$  has been derived from the observations that the low energy particles are almost accommodated while for the higher energy particles the degree of accommodation decreases because they have sufficient energy to overcome the trapping effect produced by the interaction potential; the quantities  $\theta_1, \theta_2, B$  can be determined to match the prediction of some macroscopic quantity. The Epstein model represents a generalization of the Maxwell scattering model to which it reduces for  $P = \text{const}$ .

Chiado-Piat and Riganti (13) have recently proposed a spatial impulsive interaction model for a monogenergetic beam impinging on a surface that brings in evidence two parameters:  $\eta$  a reduction factor to account for dissipative effects occurring in the interaction process and  $\epsilon$  a surface roughness parameter, according to which the normal and tangential stresses due to the reemitted molecules turns out to be:

$$P_r = \eta f_o V_o^2 [(\cos^2 \theta_i + \lambda^2) H_2 - H_0 \sin \theta_i \cos \theta_i + \lambda^2] \quad \text{eq. 21}$$

$$\tau_r = \eta f_o V_o^2 [(\cos^2 \theta_i + \lambda^2) H_2 + 1/2 (1 - H_1 - H_2) \sin \theta_i \cos \theta_i] \quad \text{eq. 22}$$

with  $\lambda^2 = KT_w/m_o V_o^2$  and  $H_0, H_1, H_2$  complex double integrals function of the angle of incidence and of the roughness parameter  $\epsilon$ , connected to the number flux of molecules reemitted according to the model of reemission developed.

### 3.3. Drag evaluation

The aerodynamic total actions such as "drag" are evaluated by integrating along the body surface the streamwise components of the pressure and shear unit forces previously discussed, resultant from the actions of the incident and reemitted molecules.

For the sphere, keeping separate the contribution of the incident and reemitted pressure and shear terms the drag coefficient turns out to be:  $C_D = (C_{DP})_i + (C_{D\tau})_i + (C_{DP})_r + (C_{D\tau})_r$  eq. 23

$$C_{DP} = 2 \int_0^\pi (P/1/2 f_o V_o^2) \sin \alpha \cos \alpha d\alpha \quad C_{D\tau} = 2 \int_0^\pi (\tau/1/2 f_o V_o^2) \sin^2 \alpha d\alpha$$

The integration for the free stream incident molecules contribution has been performed since long time (3) (49) and the results have entered the classical text books.

$$(C_{DP})_i = (C_{D\tau})_i = \left(1 + \frac{1}{S^2} - \frac{1}{4S^4}\right) \epsilon f S + \left(\frac{1}{3} + \frac{1}{2S^2}\right) \frac{1}{\sqrt{\pi}} \exp(-S^2/2) \quad \text{eq. 24}$$

The contribution due to the reemitted molecules changes according to the model of reemission adopted. Specular or elastic reflection:

$$(C_{DP})_r = (C_{DP})_i \quad \text{and} \quad (C_{D\tau})_r = -(C_{D\tau})_i \quad \text{eq. 25}$$

Diffuse reflection

$$(C_{DP})_r = 2/3 \sqrt{\pi}/S \cdot \sqrt{T_w/T_i} = 2\sqrt{\pi}/3 S_w \quad \text{eq. 26}$$

$$(C_{D\tau})_r = 0 \quad \text{eq. 27}$$

The total drag coefficient results for such extreme cases are reported as a function of the speed ratio  $S$  in fig. 6.

For hypersonic flow regimes ( $S \gg 4$ ) a constant asymptotic value of  $C_D = 2$  is attained for both the reemission models, due to the fact that of hypersonic speeds the reemitted molecules contribution is indeed negligible compared with the incoming molecules momentum flux especially for cold wall conditions.

Considering the Schaaf-Chambre model with total pressure and shear forces given by equation (11) and (12) respectively the pressure and shear drag coefficient result to be:

$$C_{DP} = (2 - f_n) \left[ \left(1 + \frac{1}{S^2} - \frac{1}{4S^4}\right) \epsilon f S + \left(\frac{1}{3} + \frac{1}{2S^2}\right) \frac{\exp(-S^2/2)}{\sqrt{\pi}} \right] + f_n \frac{2\sqrt{\pi}}{3 S_w} \quad \text{eq. 28}$$

$$C_{D\tau} = f_t \left[ \left(1 + \frac{1}{S^2} - \frac{1}{4S^4}\right) \epsilon f S + \left(\frac{1}{3} + \frac{1}{2S^2}\right) \frac{\exp(-S^2/2)}{\sqrt{\pi}} \right] \quad \text{eq. 29}$$

Such a model turns out to be rather insensitive to values of  $f_n$  and  $f_t$  when  $f_n = f_t$ , case in which the model reduces to the classical Maxwellian one, as shown in fig. 7 in which the least square fit of the experimental free flight aeroballistic range results by Hersh, Friichtenicht and Slattery (22) are compared. A value of  $f_n = f_t = 1/2$  seems the best approximation over the entire range of speed ratios; for  $S > 4$  all the curves fall within the range of accuracy of the experimental results.

At hypersonic flow conditions, expected as said to occur for  $S > 4$  the equations (28) (29) reduce to

$$C_{DP} = (2 - f_n) + 2/3 \sqrt{\pi} \cdot (\gamma - 1/\gamma)^{1/2} (T_w/T_o)^{1/2} \quad \text{eq. 30} \quad C_{D\tau} = f_t \quad \text{eq. 31}$$

so that the total drag coefficient is simply expressed by the relation:

$$C_D = (2 - f_n) + f_t + 2\sqrt{\pi}/3 \cdot (\gamma - 1/\gamma)^{1/2} \sqrt{T_w/T_o} \quad \text{eq. 32}$$

The term of pressure drag temperature dependent reduces to zero for cold wall conditions, in such con-

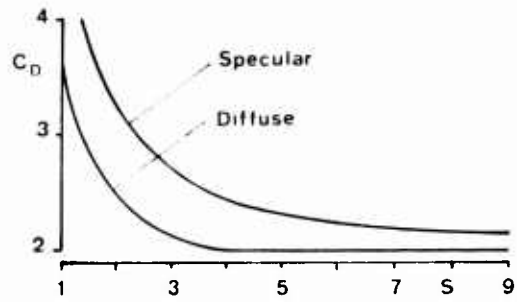


Fig. 6 SPECULAR AND DIFFUSE REFLECTION

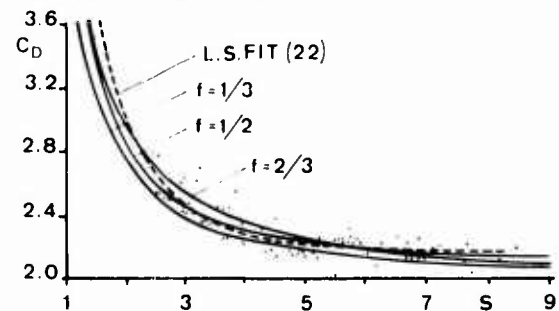


Fig. 7 SCHAAF-CHAMBRE MODEL RESULTS

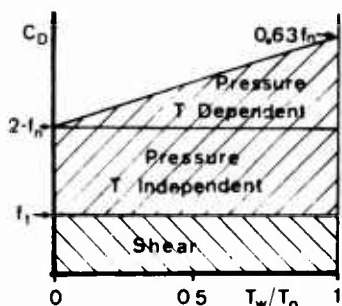


Fig. 8 DRAG COMPONENTS

the first term inside the bracket represents the contribution that the incident molecules would produce if all of them stuck on the body ( $V_r=0$ ), the second term represents the contribution to the drag of the momentum of the molecules reemitted from the surface, this term can be in general positive or negative depending on whether the molecules are predominately reemitted in the direction of flight or in the opposite direction respectively.

The factor  $\phi$  is a function of the beam width of the reemitted molecules representing the ratio of the axial momentum effectively transferred, to the momentum that could be carried away if all the molecules were aligned with the beam axis; in virtue of the postulated cosine distribution law within the beam the magnitude of  $\phi$  is almost insensitive to the magnitude of the beam width ( $1 < \phi < 2/3$  for  $0 < \varphi < \pi/2$ ). The molecular speed ratio is given in terms of the accommodation coefficient  $V_r/V_i = (1-\alpha)^{1/2}$  and the shape factor  $g(\nu)$  accounts for the combined effect of the reflection law and shape of the body; for a sphere (fig. 10) is always positive; for specular reflection ( $\nu=1$ )  $g=0$  and for diffuse reflection ( $\nu=\infty$ )  $g=2/3$ . The results obtained with the Schamberg model are reported in fig. 11.

An extension of the model to non hyperthermal speeds has been worked out by Schamberg himself on the basis of the Joule simplest kinetic model, by considering the incident molecules stream as sum of six uniform beams corresponding to the six possible directions of motion of the Joule gas; it has been obtained through appropriate transformation of the original formula for a sphere:

$$C_D/C_{D_{hyp}} = \frac{1}{3} \left( 2 + \sqrt{1 + \gamma/2S^2} \right) \sqrt{1 + \gamma/2S^2} \quad \text{eq 34}$$

that confirms as for  $S \gg 4$  the hypersonic condition is reached for the sphere. A comparison of the results obtainable with the Schamberg model and the more classical Schaaf-Chambre model has shown that the agreement between the two models is quite good for the two extreme cases analyzed, also at low speeds. The experimental data of Hersh, Friichtenicht and Slattery have been compared with the results for  $\alpha=0.98$ ,  $\phi=\pi/2$ ,  $\nu=\infty$  relative to diffuse reflection and for  $\alpha=0.68$ ,  $\phi=67^\circ$ ,  $\nu=1.7$ ; for speed higher than 5 the agreement is quite good. To better match the experimental data, therefore the choice of the reemission parameters turns out to be not unique.

The Nocilla (37) model has been applied by Hurlbut and Sherman (25) to derive drag coefficient for the

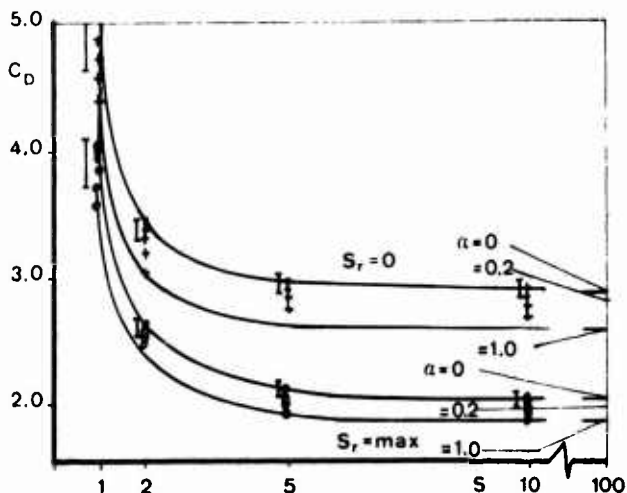


Fig. 12 HURBUT SHERMAN ANGLE DEPENDENT CASE

front surface of spheres without establishing analytical formulas. For  $S \gg 2$  the front surface drag coefficients are essentially equal to the full drag coefficients, the back surfaces making an insignificant contribution. A set of results have been obtained for  $S_r$  and  $\alpha_s$  constant, independent of local angle of attack for classical specular (warm and cold wall) and diffuse scattering (warm and cold wall) obtaining standard values.

More interesting is the behaviour exhibited by the angle dependent results for which  $S_r$  and  $\alpha_s$  have been permitted to vary with angle of attack in accord with the relations established.

Two families (see fig. 12) are plotted for cold wall conditions,  $S_r=0$  and  $S_r=\max$  and two families for warm wall  $RT_w/V_0^2 = 0.25$  conditions.

The thermal accommodation coefficient assumes six values on the range  $0 < \alpha_s < 1$ . For the cold wall  $S_r=0$  case the hypersonic drag coefficient is

Considering the hypertherm Shamberg (50) model the drag coefficient can be expressed as:

$$C_D = 2 \left\{ 1 + \phi \frac{V_r}{V_i} g(\nu) \right\} \quad \text{eq 33}$$

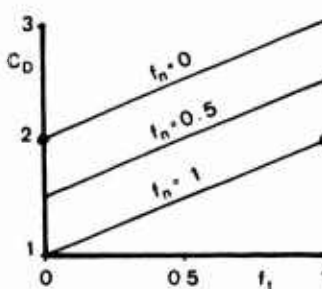


Fig. 9 HYPERSONIC COLD WALL

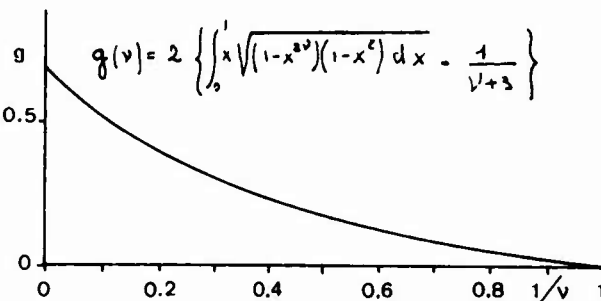


Fig. 10 SCHAMBERG FUNCTION  $g(\nu)$

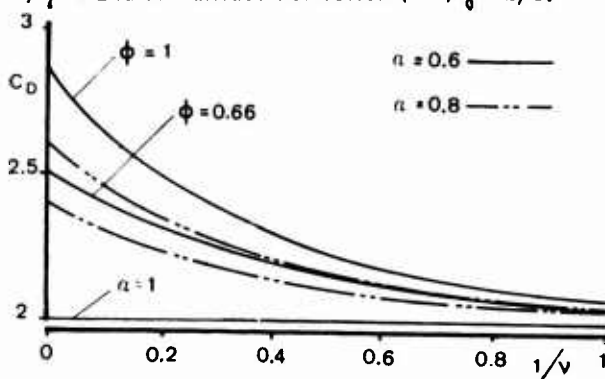


Fig. 11 DRAG ACCORDING TO SCHAMBERG MODEL

22-8

$2.55 < C_D < 2.8$  while for the cold wall  $S_r = \max$  the hypersonic drag coefficient is  $1.8 < C_D < 2$ ; impressive is the occurrence of  $C_D < 2$  due to the large area of sphere elements in regions hit tangentially where  $C_D$  can be smaller than two.

The effect of  $T_w$  is not relevant as can be noticed from fig. 12 where the results are reported with a bar.

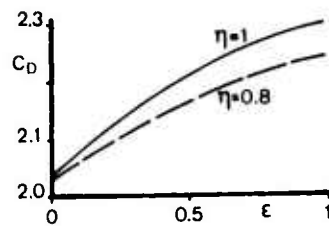


Fig.13 ROUGHNESS EFFECT

Riganti and Chado-Piat (44) have applied the spatial impulsive interaction model they have developed to the evaluation of the front surface sphere drag coefficient obtaining:

$$C_D = 2 + 4\eta [D_1 - \frac{1}{2}D_3 - 2D_5 + \frac{1}{2}D_4 + \lambda^*(D_6 - D_7 + \frac{1}{2}D_8) - \frac{1}{18}] \quad \text{eq 35}$$

with  $D_1, D_2, D_3, D_4, D_5, D_6, D_7, D_8$  integrals involving the functions  $H_0, H_1, H_2$ . The influence of the two basic parameters  $\eta$  and  $\epsilon$  has been investigated (fig. 13) bringing into evidence a strong dependence of  $C_D$  on the roughness parameter; in addition it has been found that the drag has a small dependence on the parameter  $\lambda^*$ , combining the mass of the solid surface atoms and the wall temperature effects.

Unfortunately no closed form solution of the Nocilla model, that has been proved to be more complete and more adequate to predict the reemission process, is yet available; we retain therefore for the free molecule flow drag prediction a simple formula based on the combined Schaaf-Chambre and Shamborg models that have been found to match reasonably well the experimental data:

$$C_{DPM} = [(2-f_n) + f_t + \frac{2}{3} \sqrt{\frac{2\pi}{\gamma}} \cdot \sqrt{T_w/T_\infty} \cdot 1/M] \left[ \frac{1}{3} (2 + \sqrt{1+1/M^2}) \sqrt{1+1/M^2} \right] \quad \text{eq 36}$$

The momentum accommodation coefficients, noticeably different from each other and from the usually adopted value of one, have to be determined to match the experiments.

#### 4. NEAR FREE MOLECULAR FLOW REGIME

Significant deviations from the free molecule flow regime occur when, due to a reduction of the gas rarefaction, the incoming molecules mean free path becomes comparable with the body dimension; the incoming molecules interact with the reemitted ones modifying the transfer of momentum to the body surface with respect to the free molecule flow condition.

Analytical techniques have been developed to cover this regime called "near free molecular flow" and experimental data have been obtained to allow comparisons; only a brief description of the models and a limited discussion of the results are hereafter reported.

Baker and Charwat (4) have developed a "first collision model" that takes into account the first intermolecular collision between free stream molecules and molecules reemitted from the body surface.

Three classes of molecules are foreseen in the model: (i) the incoming free stream molecules assumed to be perfectly elastic spheres, (e) the emitted molecules assumed diffusively reemitted from the surface with velocity  $V_e$ , (s) the scattered molecules resulting from the collisions of incoming and emitted molecules.

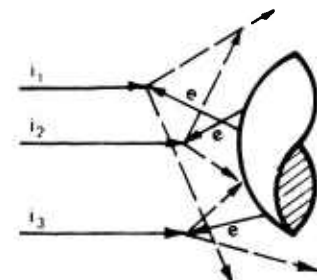


Fig.14 FIRST COLLISION MODEL

The free stream molecules (i) suffer collisions with the reemitted ones (e) and a change in the momentum transfer at the surface occurs with respect to the free molecular flow condition; some incoming molecules ( $i_1$ ) are entirely deflected by the collision and do not contribute to momentum transfer, some others ( $i_2$ ) after collision hit the body and transfer only part of the original momentum, having lost part in the collision, and finally others ( $i_3$ ) are deviated by the collision to the body whereas otherwise they would have bypassed the body.

As an overall action the body is expected to undergo a decrement of momentum with respect to the free molecule condition if the "shielding" effect prevails over the "scattering" effect otherwise an increment has to be expected.

After having evaluated the distribution of the emitted molecules and analyzed the scattering collision process the transfer of momentum to a sphere has been determined through a series of reasonable approximation; the drag coefficient has been obtained in terms of two interaction parameters:  $V_e/V_i$  ratio of emitted and incident velocity and  $B = D/\lambda$  inverse of local Knudsen number based on emitted molecules mean free path relative to the incoming free streams:

$$C_D = 2 \left\{ 1 + 0.44 \frac{V_e}{V_i} - 0.23 B - 0.65 B \frac{V_e}{V_i} \right\}$$

The first term is the free stream incoming molecules contribution in free molecular flow conditions, the second term is the reemitted molecules contribution in free molecular flow conditions and the third and fourth terms are the contribution due to the interaction process; for a sphere this contribution has been found to be negative prevailing the shielding effect over the scattering effect. The two interaction parameters can be interpreted in terms of free stream Reynolds number and surface to free stream temperature ratio, therefore the drag coefficient referred to the free molecular flow condition is expressed by the relation:

$$C_D/C_{DPM} = 1 - 0.15 Re (T_\infty/T_w)^{1/2} / C_{DPM} = 1 - 0.22 M / Kn (T_\infty/T_w)^{1/2} / C_{DPM}$$

Willis (60) has utilized, in connection to the classical Knudsen interaction procedure outlined by Jaffe (26), that consists in expanding the molecular distribution in inverse powers of the mean free path starting from the free molecular flow solution, a modified form of the model of collisions proposed by Bhatnager Gross and Krook (8) that extends the understanding of the transfer process from the free mole

52-10 cular into the transition regime where, both interparticles and wall collisions, are significant.

Rose (46) has adopted a linearized form of the Krook model for the collision term performing the iteration through a Fourier transform of the kinetic equation, accounting for all the collisions and not merely the first collisions, thus obtaining a complete first order perturbation model.

The drag coefficient, found by integration along the sphere surface of the impinging and reflected molecules momentum contribution has resulted to be:  $C_D - C_{DPM} = -1/Kn \left( 0.33(T_w/T_\infty)^{1/2} + 0.17/\sqrt{M} \right)$  eq. 37

The results of iterative methods can be expressed as  $C_D - C_{DPM} = \alpha M_2$ , in terms of a natural small parameter  $\alpha = \delta^2 n_\infty D/2 (1/2 RT_w)^{1/2}$  with  $H_2$  order one and being  $\delta$  a collision parameter related according to the Krook model to viscosity by the relation  $\delta = \kappa T/\mu$ . An appropriate reference temperature  $T^*$  has to be introduced to relate the parameter  $\alpha$  to the classical free stream conditions parameters; Sherman, Willis, Maslach (51) have developed the relation:  $\alpha = \sqrt{\pi}/4 (S_w/S_\infty) C_2 / Kn_\infty$  with:  $S_w^2 = V_w^2/2 RT_w$ ,  $S_\infty^2 = V_\infty^2/2 RT_\infty$ ,  $Kn_\infty = \lambda_\infty/D$ ,  $C_2 = T^*/T_\infty \cdot \mu_\infty/\mu^*$

In the case when the stagnation temperature is assumed as reference  $T^* = T_0$ , adequate to describe the hypersonic flow testing conditions, the following relation holds:  $\alpha_0 = Re_0/4 S_0 (T_0/T_\infty)^{1/2}$  with  $Re_0 = \rho_\infty V_\infty D/\mu_0$  and  $S_0^2 = V_\infty^2/2 RT_0$ . The adequacy of the parameter  $\alpha_0$  to correlate the experimental results is demonstrated by the comparison with the Kinslow and Potter results (fig. 13), that are predicted to  $\pm 2\%$  by the simple correlation formula:  $C_D - C_{DPM} = -0.5\alpha + 0.09\alpha^2$ , no systematic dependence upon  $S_w$  being noticeable. Theoretical formulas restricted to the case  $S_\infty$  have been recast in terms of  $\alpha_0$  assuming that the dependence on  $S_w$  can be represented in terms of power series in  $S_w$  obtaining:

$$\begin{aligned} C_D - C_{DPM} &= -\alpha_0 (1 + 4.36/S_w) && \text{Baker Charwat} && \text{eq. 38} \\ &= -\alpha_0 (0.37 + 3.32/S_w - 2.57/S_w^2) && \text{Willis} && \text{eq. 39} \\ &= -\alpha_0 (0.75 - 0.26/S_w) && \text{Rose} && \text{eq. 40} \end{aligned}$$

Another comparison of the above methods has been attempted by Maslach, Willis, Tang, Ko (34) by rearranging the formulas for the sphere drag coefficient prediction, in terms of  $Kn_\infty$ ,  $S_\infty$ ,  $S_w$ :

$$\begin{aligned} C_D - C_{DPM} &= - (0.24 S_w + 1.06) / Kn_\infty && \text{Baker Charwat} && \text{eq. 41} \\ &= - (0.165 S_w + 1.44 - 1.13/S_w) / S_\infty Kn_\infty && \text{Willis} && \text{eq. 42} \\ &= - (0.33 S_w - 0.12) / S_\infty Kn_\infty && \text{Rose} && \text{eq. 43} \end{aligned}$$

The comparison with Kinslow and Potter (27) results  $S_\infty = 8.8$ ,  $S_w = 6.25$  shows fig. 16 a good agreement of the Willis model, also the Rose model is in reasonable agreement while Baker and Charwat has a slope too high. The comparison with Davis and Sims (16) results  $S_\infty = 3.15$ ,  $S_w = 1.60$  confirms the good agreement obtainable with the Willis model while the Rose model is too low and the Baker Charwat too high in predicting the slope. The same situation exist for the comparison with Phillips and Kuhltau (39) results  $S_\infty = 1.87$ ,  $S_w = 1.87$

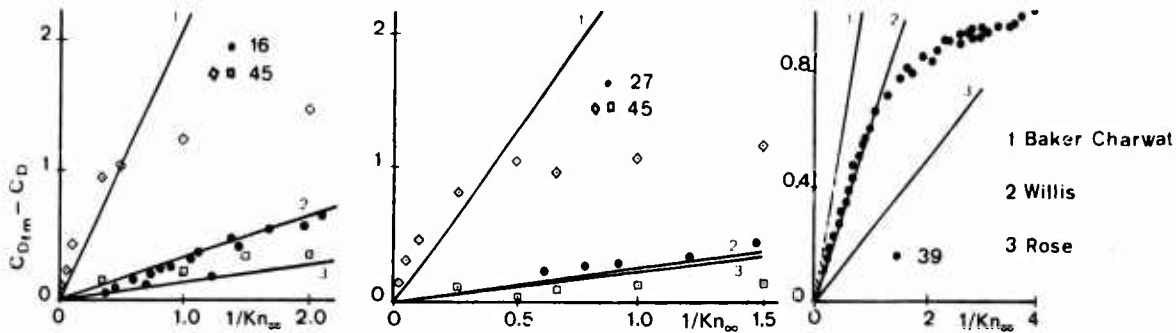


Fig. 16 NEAR FREE MOLECULE FLOW RESULTS COMPARISON

More recently Monte Carlo statistical simulation techniques have been introduced to treat the near free molecular flow regimes; trajectories and interactions of a large number of molecules are mathematically simulated to derive the actions on bodies having simple geometry. Bird (9) and Vogenits, Bird, Broadwell and Ringaldier (58) have developed a powerful time dependent approach assuming hard sphere molecules and complete momentum and energy accommodation of the molecules for their collisions with the surface.

The ratio of the sphere drag coefficient in near free molecular flow value has been evaluated by Bird as a function of the Knudsen number  $Kn = \lambda/D$ .

For the cold wall ( $T_w = T_\infty$ ) results (see fig. 17) have been found to rise above the free molecule limiting value (overshoot) due to

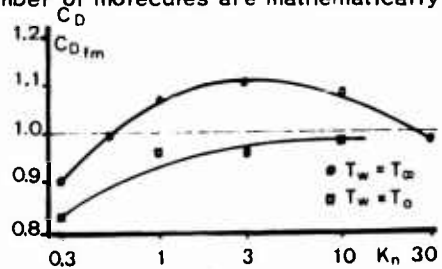


Fig. 17 BIRD (MONTE CARLO RESULTS)

the fact that for  $5 < Kn < 30$  the fall in streamwise momentum of the molecules striking the surface is over-compensated by the increase of the flux of these molecules; for the hot wall condition ( $T_w = T_0$ ) this effect has not been found to occur.

A steady state first collision Monte Carlo approach, having the merit of relative simplicity, has been developed by Robertson (45) the method is applicable to elastic hard spheres and to Maxwell molecules (inverse fifth power law repulsion).

Sphere drag coefficients have been evaluated for several speed ratio  $S$ , Knudsen numbers  $Kn$  and surface temperatures  $T_w/T_0$  and compared with experimental measurements by Davis and Sims (16) and Kinslow and Potter (27) as well as with the previously discussed analytical techniques by Baker-Charwat, Willis and Rose (see fig. ).

The results obtained adopting the Maxwellian molecules are in both cases in close agreement with the experiments while the hard sphere ones deviate considerably.

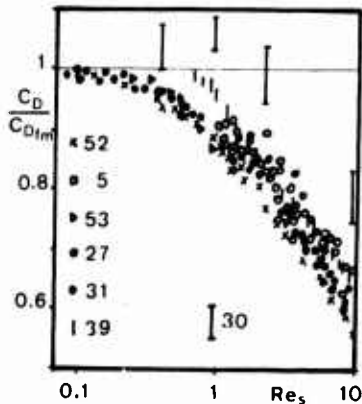


Fig.18 EXPERIMENTAL RESULTS

Due to the inherent complexity in treating the near free molecule flow regime semianalytical methods have been attempted we quote the Rott and Whittenbury (47) and the Kinslow and Potter (27) ones having a free parameter to obtain the best agreement with experiments. The experimental results by Phillips Kuhltau (39) Kinslow and Potter (27) Davis and Sims (16) previously recalled and the ones by Smolderen (53) Sims (52) Legge and Koppenwallner (31) Hersh Frichtenicht Slattery (22) Potter and Miller (41) (see fig. 18) who have focused attention on the near free molecules flow limit indicate no tendency to overshoot the free molecule limit; only the recent results by Kussoy and Horstman (29) and Kussoy Stewart Horstman (30) report, for cold wall conditions, the occurrence of an overshoot of the drag coefficient over the free molecule value computed for test condition, assuming diffuse reflection and an accommodation coefficient of one.

As seen discussing the free molecule flow regime higher drag coefficients can be evaluated according to the reflection model adopted;

nevertheless the accuracy of such high experimental values confirming the overshoots predicted by Bird poses the problem of accurately evaluating the drag coefficient in near free molecular flow conditions through a series of test extending far in the free molecule flow regime so that the appropriate limit can be experimentally determined.

A new correlation formula, of the form  $C_D - C_{Dfm} = \alpha_0 H_2 + \alpha_1 H_2^2$  with  $H_2 = a + b/S_w$ , has been derived to cover the near free molecule flow regimes, down to  $Re_s = 10$ .

The shock Reynolds number used in the low density data correlation has been related to  $\alpha_0$ .

$$\alpha_0 \propto 0.25 \sqrt{(1-\gamma)/\gamma} (T_0/T_w)^{1/2} Re_s \quad \text{and accounting for the wall temperature effect, it has been obtained:}$$

$$C_D - C_{Dfm} = -0.284 q Re_s + 0.0185 q^2 Re_s^2 \quad \text{eq 44}$$

with  $q = 0.037 (T_0/T_w)^{1/2} Re_s$  that correlates reasonably well the above quoted results, reducing the scattering that in part can be ascribable to different wall temperature conditions.

### 5. INTERMEDIATE FLOW REGIMES

The existence of a large variety of flow regimes ranging between the continuum and the free molecular flows, different according to the degree of rarefaction has been evidenced; following Probst and Kemp (12) the transition is accomplished through a vorticity interaction, a viscous layer, an incipient merged layer, a fully merged layer, a transitional and a first collision sub-regime.

Complex mathematical models, impractical for engineering purposes, have been developed to solve time by time specific problems in one of the above recalled subregimes; except for the Monte Carlo numerical technique the other approaches have a limited validity, no general analytical method has yet been found to correctly derive the aerodynamic actions in all the above sub-regimes that can be called in one word "intermediate or transitional flow regimes".

Engineering applications in the field of space activities have stimulated therefore approximate approaches based mainly on the well established flow conditions existing at the two extreme flow regimes; those methods are based on several assumptions and bring in several simplifications and a certain degree of empiricism so that their validity can be confirmed only by careful comparison with the available experimental results.

Martino (33) probably has been the first to derive a semiempirical correlation formula that has been successively applied with success by Blick (10) for predicting aerodynamic coefficients.

In the Martino model it is assumed that, depending on the degree of rarefaction of the medium part of the molecules reaches the body surface without having previously experienced any collision with molecules of the gas layer adjacent to the body, exerting therefore on the body an influence proportional to the free molecule value, while the other part of incoming molecules collides first with the molecules standing in the gas layer and exert therefore an influence on the body proportional to the continuum flow value.

The sphere drag coefficient is therefore expressed by the relation:  $C_D = C_{Dfm} \cdot P + C_{Dc} \cdot (1-P)$  The function  $P$  representing the probability that a given molecule has to collide directly with the body surface is a function of the degree of rarefaction of the gas, that Martino and Blick have simply postulated to be:  $P = Kn / (1+Kn)$  being the Knudsen number  $Kn$  a suitably defined one.

22-12

The ability of this model to provide satisfactory correlations of the experimental results lies in the appropriate definition of the Knudsen number; considering that in the intermediate regimes the Knudsen number that seems more appropriate is the one obtained assuming as characteristic length the shock detachment distance  $\Delta$  and as mean free path the one evaluated behind the normal shock  $\lambda_s$ :  $K_n = \lambda_s / D$ . Blick has proposed being  $\Delta/D = \kappa \rho_\infty / \rho_s$  and  $\lambda \rho$  almost independent on temperature, to adopt a particular Knudsen  $K_n = \kappa \rho_\infty / \rho_s \lambda_s / D = \beta \lambda_\infty / D$  that introduces the Martino number  $\beta$ , a numerical factor that

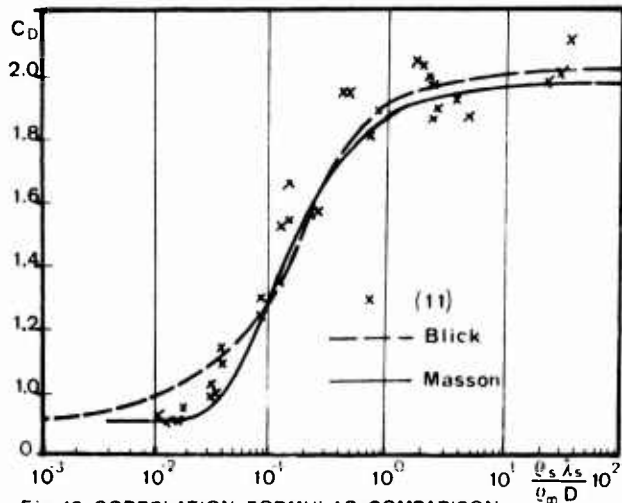


Fig.19 CORRELATION FORMULAS COMPARISON

fits the Martino equation as closely as possible to the experiments.

For the sphere drag coefficient Blick found that  $\beta = 4$  gives good agreement with Bloxson and Rhodes (11) experimental results (see fig. 19).

Masson, Morris and Bloxom (35) have developed a simple model for the hypersonic flow of rarefied gas over a blunt body by considering a collimated molecular beam passing through a region containing a scattering gas.

The presence of a flow discontinuity shock wave, noticed even for regimes having very low Reynolds values, delimits the region of gas having a scattering effect with respect to the free stream molecules that are likely to be comparable to a collimated beam.

According to the classical kinetic theory of gases the fraction of beam molecules passing through the gas cloud having thickness  $\Delta$  and directly impinging the body surface without experiencing collisions, is  $N/N_\infty = \exp(-\Delta/\lambda_s)$  being  $\lambda_s$  the mean free path of the free stream molecules in the gas cap. The gas cap thickness assumed equal to the shock detachment thickness, can be expressed approximately for a sphere as  $\Delta = \kappa D \rho_\infty / \rho_s$ .

The value of the constant K is usually evaluated of the order 1/3 but to better match the experimental results a value 1/10 has been introduced obtaining a good agreement with their experiments (35).

The drag coefficient according to the exposed model is assumed to be made up therefore by the contribution of two parts: one relative to continuum flow conditions and one to free molecule flow conditions.

$$C_D = C_{Dc} (1 - N/N_\infty) + C_{DPM} (N/N_\infty) = C_{Dc} + (C_{DPM} - C_{Dc}) \exp(-1/10 \rho_\infty D / \rho_s \lambda_s) \quad \text{eq.45}$$

It is worthwhile to notice that the parameter  $\rho_\infty D / \lambda_s \rho_s$  can be interpreted as the inverse of a Knudsen number that is the significant parameter in rarefied gas regimes under investigations.

Matting (36) has developed engineering methods of calculation called "bridging relations" for evaluating aerothermodynamic actions in the transitional regime.

A simple first collision model, similar to the one of Masson, Morris and Bloxom (35) is used; molecules having a mean free path larger than the effective collision layer thickness are assumed to make their first effective collision with the body surface and therefore contribute to free molecule drag, while the other molecules for which  $\lambda < \Delta$  make collisions with each other becoming part of the continuum boundary layer and only finally strike the surface thus contributing to continuum drag.

The model considers a two phase flow, the total actions exerted on the body being the sum of the actions exerted by each phase; the final form of the drag coefficient accordingly turns out to be:

$$C_D = C_{Dc} (1 - \exp(-\Delta/\lambda)) + C_{DPM} \exp(-\Delta/\lambda) = C_{Dc} + (C_{DPM} - C_{Dc}) \exp(-\Delta/\lambda) \quad \text{eq.46}$$

that correctly limits is the continuum and free molecule flow conditions at the asymptotes. We notice that the same equation was obtained by Masson, Morris and Bloxom (35) but through a somewhat different derivation.

The values of the effective collision layer thickness  $\Delta$  and of the mean free path of the molecules  $\lambda$  ought to be functions of the position on the body but average value are retained in the analysis. Matting has derived from dimensional considerations  $\Delta/\lambda = G R \rho_\infty$  with the constant  $G = 1.5 \cdot 10^8$  selected to match the drag value calculated according to the above bridging relation with the experimental data of Wegener and Ashkenas (2).

Whitfield (61) has proposed a collision surface model that allows closed form analytical evaluations of the sphere drag in the intermediate flow regimes, yielding the free molecule drag value in the limit  $K_n \rightarrow \infty$  and the newtonian continuum value in the limit  $K_n \rightarrow 0$ .

Four basic assumptions are introduced in the model:

- a) The free stream is hyperthermal so that the number flux of molecules having a chance to collide with the surface of a sphere is  $N_\infty = n_\infty V_\infty \pi R^2$
- b) all the molecules are reemitted normal to the surface
- c) each reemitted molecule experiences only one collision with a free stream molecule
- d) all the collisions occur on a "collision surface" located at a distance  $\lambda_w$  from the body surface.

This implies that the sphere surface behaves, with respect to the molecules surviving the collision surface, as in the case of free molecule flow regime, therefore the drag in the intermediate regime can be determined as:  $C_D / C_{DPM} = N_s / N_\infty = n_s / n_\infty$  being  $n_\infty$  the free stream number density and  $n_s$  the number density behind the collision surface.

The free stream molecules, per unit time, involved in the process are  $N_\infty = n_\infty V_\infty \pi R^2$ , while the number of molecules per unit time emitted from the sphere surface in the normal direction turns out to be

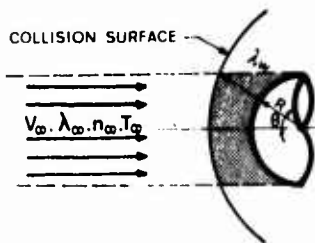


Fig. 20 WHITFIELD MODEL

The angle  $\theta$  depends on  $\lambda_w$ , the distance of the collision surface from the sphere surface, geometrical consideration allow to determine  $\sin \theta = (1 + \lambda_w/R)^{-1/2}$  so that substituting into the above equation gives the drag coefficient as:

$$C_D / C_{DPM} = n_s / n_{\infty} = (1 + \sin^2 \theta)^{-1} = [1 + (1 + \lambda_w/R)^{-2}]^{-1} \quad \text{eq 47}$$

The ratio  $\lambda_w/R$  has once more the meaning of a Knudsen number and indeed using the relationship derived by Whitfield and Stephenson (62), simplified to accomplish

for the fact that  $\lambda_w$  turns out to be a weak function of  $\theta$ , it can be expressed by:  $\lambda_w/R = 2\sqrt{2} K_{n\infty} / (1 + 4Sw/3\sqrt{\pi})$  accounting for which it is possible to express the intermediate regime drag coefficient in terms of a free stream Knudsen number:

$$C_D / C_{DPM} = [1 + (1 + 2\sqrt{2} K_{n\infty} / (1 + 4Sw/3\sqrt{\pi}))^{-2}]^{-1} \quad \text{eq 48}$$

At the limit  $Kn \rightarrow 0$  appropriate for the continuum flow regime the collision surface collapses over the body surface  $\lambda_w = 0$ , only one half of the molecules having a chance to collide with the body surface can actually collide with it because each molecule at the surface prevents another molecule from colliding with the surface and the drag coefficient assumes the value  $C_{Dc} = 1/2 C_{DPM}$  that is the same value obtainable from Newtonian theory.

The correct limiting to the free molecule flow is embodied in the derivation of the formula itself. Good agreement has been obtained by Whitfield with the recent drag measurements by Phillips and Kuhlthau (39) (see fig. 21).

Vallerani (57) has recently developed a semiempirical method for the evaluation of aerothermodynamic properties in the intermediate flow regimes, based essentially on the Martino correlation formula; the evaluation of the Knudsen number and of the probability function has been accomplished in a different way.

As pointed by Tsien (55) the characteristic flow field dimension appearing in the definition of the Knudsen number is for the continuum flow the boundary layer thickness while for the free molecule flow is the body dimension itself  $R$ :  $(K_n)_{PM} = \lambda_w/R = 1.25\sqrt{2} M/R_0 = C_{PM}/\xi$  and  $(K_n)_c = \lambda_w/\delta = 1.25\sqrt{2} M/R_0 R/\delta = C_c/\xi$  being  $\xi = R_0/M$  the ratio of free stream Reynolds-Mach numbers.

To properly account for the effective boundaries between the continuum flow and the lower region of the intermediate flow regimes and between the free molecule flow and the upper region of intermediate flow regimes two modified Knudsen number have been introduced:  $(\bar{K}_n)_c = K_{nc} - K_2$   $(\bar{K}_n)_{PM} = [K_{nPM} - K_1]^{-1}$  being  $K_1 = 10$  the value proposed by Tsien to limit the free molecule flow regime and  $K_2 = 0.05$  the value proposed by Reeves (43) for the delimitation of the upper boundary of the continuum flow regime.

The leading idea of the new method, that circumvents the difficulty of appropriately defining a Knudsen number is the consideration that the Knudsen number itself, as whatever other quantity, has to be determined in the intermediate flow regime by applying the Martino formula:  $K_n = P K_{nPM} + (1-P) K_{nc}$  eq 49. The structure of the function  $P$  representing as said the probability that an incoming molecule collides directly with the body surface before colliding with any other molecule of the gas layer has been determined starting from the "collision surface model" of Whitfield (61) previously discussed.

The probability  $P$  assumed to be the fraction of molecules passing through the gas layer without collision, is given by the relation:  $P = N_s/N_{\infty} = (c + K_n)^2 / c^2 + (c + K_n)^2$  with  $c = \sqrt{2} (4Sw/3\sqrt{\pi} + 1)^{-1}$  eq 50 evaluated on the bases of the Whitfield model, it has the structure:  $P = K_n^2 / (\alpha + K_n^2)$  that not only satisfies as the original Martino relation  $P = K_n / (1 + K_n)$  the two limiting conditions but also enables the fulfillment of the smooth limiting condition of the derivative at the two limits. The presence of a parameter directly introduced into the probability function allows an improved capability of the correlation formula to generate results in better agreement with the experimental data whenever available.

By combining the equation (50) defining the new probability function  $P$  with the one (49) defining the modified intermediate flow regime Knudsen number a cubic equation is obtained:

$$a P^3 + b P^2 + (c + \alpha) P + d = 0 \quad \text{eq 51}$$

$$\begin{aligned} a &= [(\bar{K}_n)_{PM} - (\bar{K}_n)_c]^2 \\ b &= 2(\bar{K}_n)_c [(\bar{K}_n)_{PM} - (\bar{K}_n)_c] - [(\bar{K}_n)_{PM} - (\bar{K}_n)_c]^2 \\ c &= [(\bar{K}_n)_c]^2 - 2(\bar{K}_n)_c [(\bar{K}_n)_{PM} - (\bar{K}_n)_c] \\ d &= -[(\bar{K}_n)_c]^2 \end{aligned}$$

The value of the modified probability function  $P$  turns out to be a complex but algebraic function of the modified Knudsen  $(\bar{K}_n)_c$  and  $(\bar{K}_n)_{PM}$  that is to say the probability function depends on the quantity  $\xi$

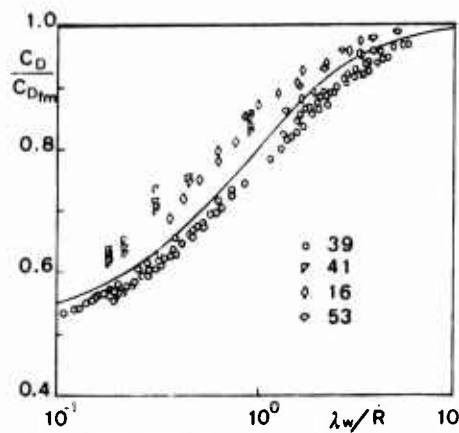


Fig. 21 WHITFIELD CORRELATION

52-13

22-14

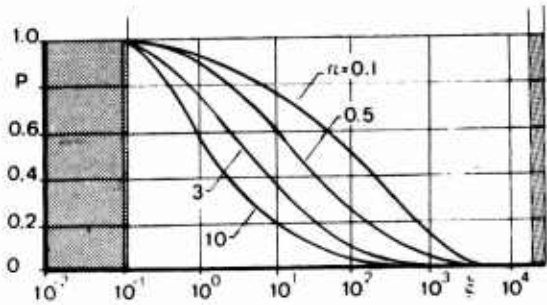


Fig. 22 PROBABILITY FUNCTION  $P=P(z)$

ratio of the Reynolds to the Mach number, the parameters  $K_1$  and  $K_2$  defining the limits of the two extreme flow regimes and the free parameter  $\alpha$ . (fig. 22). By normalizing the intermediate flow values with respect to the free molecule flow regime, the form  $\Gamma = C_D / C_{DPM} = P + (1-P)C_{0c} / C_{DPM}$  is obtained. Such a bridging formula predicts close to the free molecule boundary a value higher than the one predictable according to the free molecule formula and close to the continuum flow boundary a value higher than the one predictable according to the continuum theory formula.

The occurrence of those "overshoots" not predictable by any other correlation formula bridging the intermediate flows regimes, is sustained by some of the more recent theoretical predictions as discussed in the near free molecular flow regime and is supported by some experimental data.

In the analysis performed by Vallerani (57) the continuum flow drag coefficient has been evaluated according to the theoretical formula of Davis and Flugge-Lotz (15), retaining first order boundary layer effects. Some of the experimental data spanning over the entire intermediate flow regime range have been compared (fig. 23) with the results of the available theories of Baker-Charwat (4) Rose (46) Willis (60) Bird (9) relative to the near free molecular flow regime and Davis on Flugge-Lotz (15) for low densities continuum flow regimes and with the correlation formulas by Blick and Whitfield, (10) (61).

A value of  $\alpha=10$  has been selected to better correlate the experimental results; from the panorama reported it was concluded that if the occurrence of overshoots is admitted the proposed correlation formula is the only one able to predict reasonably well the drag coefficient over the entire intermediate flow regime range; at the same time it was pointed out in the analysis that the scatter of the experimental results is quite high and that proper account has to be taken of the Mach and wall temperature effects.

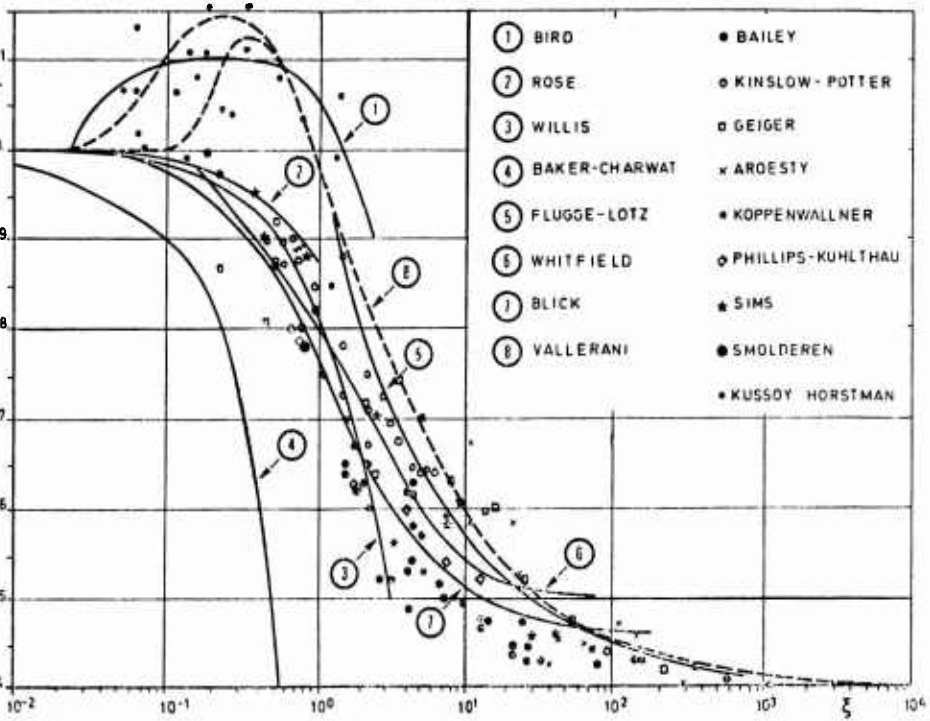


Fig. 23 Intermediate Regime Drag Coefficient Theories and Experiments

## 6. CONCLUSIONS

The review of the theoretical methods and of the available experimental data concerning the supersonic flow sphere drag determination, has brought into evidence that, even if a complete solution leading to closed form formulas has not yet been found, a large number of possibilities exists to predict with sufficient accuracy the behaviour of this relevant quantity over the entire range of flow regimes from the continuum to the free molecule flow.

Different possibilities have been found to exist for selecting the set of basic parameters suitable to represent the flow conditions and to correlate the experimental results. The more widely adopted choice is the one that introduces the Mach number  $M = V_{\infty} / a_{\infty}$ , the shock Reynolds number  $Re_s = \rho_{\infty} V_{\infty} D / \mu_s$  and the wall to free stream temperature ratio  $\chi = \sqrt{T_w / T_{\infty}}$ .

The Reynolds number, in our opinion, exhibit the disadvantage of combining in one parameter a dependence on the body speed and on the fluid properties; we consider useful to propose therefore the adoption of the Knudsen number  $Kn_{\infty} = \lambda_{\infty} / D$  to account for the rarefaction effects dependent for a given body, only on the medium properties; a simple relation exists between those two parameters:  $Re_s = 3.3 / Kn_{\infty}$ .

As a result of the analysis performed we have attempted to establish correlation formulas to cover the entire range of flow regimes; the main difficulties stay in the extension of the available data from the very conditions to which they refer up to cover the entire range of free stream velocity and wall temperature variations of interest.

Theoretical methods that have supplied predictions confirmed by the experiments can be used as milestones to derive the correlation formulas whose structure is the one dictated by the theoretical analysis and whose free coefficients have to be fixed by matching at the best the experimental results.

We recall the correlation formulas that have been derived:

- Continuum flow regime  $C_D = C_D(M)$   $Re_S \gg 10^4$   $Kn_\infty < 3.3 \cdot 10^{-4}$

$$C_{Dc} = 0.9 + (0.24/M - 0.04) \quad 1.5 < M < 6$$

$$C_{Dc} = 0.9 \quad M > 6$$

- Continuum flow low density regime  $C_D = C_D(M, Kn, \chi)$   $10^2 < Re_S < 10^4$   $3.3 \cdot 10^1 > Kn_\infty > 3.3 \cdot 10^{-4}$

$$C_D = C_{Dc} + \frac{1.78 + f}{\sqrt{Re_S}} - \frac{0.5 + f}{Re_S}$$

$$= C_{Dc} + (0.99 + 0.55f) \sqrt{Kn_\infty} - (0.152 + 0.3f) Kn_\infty$$

$$\text{with } f = 3.2 (6.7 \phi)^{0.15/0.45 + \phi} \quad \text{and } \phi = \chi^2/M^2$$

- Near free molecule flow regime  $C_D = C_D(M, Kn, \chi)$   $10^1 < Re_S < 10^4$   $3.3 > Kn_\infty > 3.3 \cdot 10^{-1}$

$$C_D = C_{DFM} - 0.284 q Re_S + 0.0185 q^2 Re_S^2$$

$$= C_{DFM} - 0.93 q / Kn_\infty + 0.06 q^2 / Kn_\infty^2$$

$$\text{with } q = 0.96 + 0.0165 M / \chi$$

- Free molecule flow regime  $C_D = C_D(M, \chi)$   $Re_S < 10^1$   $Kn_\infty > 3.3$

$$C_{DFM} = \left[ (2-f_n) + f_t + \frac{2\sqrt{\pi}}{3} \sqrt{\frac{2}{8}} \chi/M \right] \frac{1}{3} \left[ 2 + \sqrt{1+1/M^2} \right] \sqrt{1+1/M^2}$$

## 7. REFERENCES

- 1) Aroesty (62) III RGD 261
- 2) Ashkenas (62) III RGD 276
- 3) Ashley (49) JAS 95
- 4) Baker-Charwat (58) Phys. Fluids 73
- 5) Bailey (66) V RGD
- 6) Bailey-Sims (64) AIAA J. 2867
- 7) Baule (14) Annalen der Physik 145
- 8) Bhatnagar-Gross-Krook (54) Phys. Rev. 511
- 9) Bird (66) AIAA J. 55
- 10) Blick (63) AIAA 2657
- 11) Bloxson-Rhodes (62) JAS 1429
- 12) Charters-Thomas (45) JAS 268
- 13) Chiado-Piat-Riganti (71) IMA TN 77
- 14) Clark-Harris (52) JAS
- 15) Davis-Flugge-Lotz (64) Fluid Mech. 593
- 16) Davis-Sims (67) Lockheed MSC/TM 54/20
- 17) Epstein (67) AIAA J 1797
- 18) Gelger (63) General Electric R 635023
- 19) Hallsmaier (61) NOL-TR-61-58
- 20) Halpherson-Boltz-Hall (60)APGC-TR-60-39
- 21) Hayes-Probstein "Hypersonic Flow Theory"
- 22) Hersh-Friichtenicht-Slatery (68) VI RGD 757
- 23) Hodges(57)JAS 758
- 24) Hurlbut (59)RAND Rept. 339
- 25) Hurlbut-Sherman (68) Phys. Fluids 486
- 26) Jaffe (30) Ann. Physik 398
- 27) Kinslow-Potter (63) AIAA J. 2467
- 28) Koppenwalner (68) VI RGD 739
- 29) Kussoy-Horstman (68) VI RGD
- 30) Kussoy-Stewart-Horstman(68)VI RGD
- 31) Legge-Koppenwallner (70) VII RGD
- 32) May-Witt (53)JAS 635
- 33) Martino (55)UTIA Rept. 35
- 34) Maslach-Willis-Tang-Ko (64) IV RGD 433
- 35) Masson-Morris-Bloxon (60) II RGD 643
- 36) Matting (71) AIAA J. 35
- 37) Nocilla (64) IV RGD 315
- 38) Nocilla (65) IMA TN 27 and 36
- 39) Phillips-Kuhlthau (68) VI RGD 711
- 40) Potter-Bailey (64) AIAA J. 743
- 41) Potter-Miller (68) VI RGD 723
- 42) Probstein-Kemp (60) JAS
- 44) Riganti-Chiado-Piat IMA TN 78
- 43) Reeves(59)Mc Donnell Rept. 6859
- 45) Robertson (68) VI RGD
- 46) Rose (64) Phis Fluids 1262
- 47) Rott-Whittenbury (61) Douglas Rept SM 38524
- 48) Schaaf (53) Heat Transfer Symp. Univ. Michigan
- 49) Schaaf-Chambre (58) "Flow of Rarefied Gases"
- 50) Scamberg (59) Aerodynamics of the upper Atm. "
- 51) Sherman-Willis-Marshlach (64) Univ. Calif. Rep. A6-16
- 52) Sims (68) VI RGD
- 53) Smolderen-Wendt-Naueau-Bramlette (68) VI RGD 903
- 54) Sreekanth (61) UTIA Rept. 74
- 55) Tsien (46) JAS 653
- 56) Van-Dyke "Hypersonic Flow Research
- 57) Vallerani (72) VIII ICAS Congress Paper 72-O3
- 58) Vogenitz-Bird-Broadwell Rungaldier (68)AIAA
- 59) Wegener-Ashkenas (61) Fluid Mech. 550
- 60) Willis Princeton Rept 440 and 442
- 61) Whitfield (70) VII RGD
- 62) Whitfield-Stephenson (70) AEDC-TR 70-32

RGD - Rarefied Gas Dynamics - International Symposium

JAS - Journal Aero-Space Sciences

AIAA - American Institut Aeronautics and Astronautics

IMA - Istituto Meccanica Applicata - Politecnico di Torino

THE INFLUENCE OF WAVE DRAG ON HYPERSONIC  
ENTROPY WAKE OBSERVATIONS

23-1

by

Wolfgang Merzkirch<sup>+</sup>

Ruhr-Universität, Bochum, Germany

and

Alois Stilp<sup>++</sup>

Ernst-Mach-Institut, Freiburg i.Br., Germany

SUMMARY

In the wake of a blunt hypersonic body one can distinguish between two different flow regimes: the viscous wake and the inviscid or entropy wake. The latter can be associated to the wave drag of the body. By means of a schlieren system the entropy wake of various blunt hypersonic bodies is visualized in a great distance behind the bodies. The observed schlieren pattern is analyzed with the aid of optical schlieren theory and can be related to the flight Mach number and the drag coefficient of the body. These observations are in good agreement with a theoretical approach of WEBB.

1. INTRODUCTION

In the wake of a blunt hypersonic body one can distinguish between two different regimes: the viscous wake which originates from the separated boundary layer, and the inviscid or entropy wake formed by the streamlines which have traversed the curved part of the bow shock. While the viscous wake can be regarded as the trace of the viscous drag of the flight body, the entropy wake is associated to the entropy production at the strong bow shock wave and therefore represents the trace of the wave drag of the body. As will be shown later, this entropy wake is a long cylinder which is filled with hot gases and extends far downstream behind the body, provided that the flow remains laminar; the cylinder axis coincides with the flight axis.

It has been observed by WILSON (ref. 1) that in a great distance behind the body, where the pressure has already returned to the ambient value, the entropy wake can be visualized by means of a schlieren system and displays on the photograph in form of two parallel horizontal bands, dark and bright, on either side of the flight axis (Fig. 1). Further experimental investigations (refs. 2 to 4) showed, that the distance between the bands in the schlieren photograph increases with the flight Mach number for a given body shape. Most of these experiments had been performed in ballistic ranges with spheres as the flying models. From some preliminary results (ref. 4) it can be seen that the mentioned distance also depends on the body shape, thus indicating an influence of the drag coefficient.

The observed schlieren pattern can be calculated with the aid of optical schlieren theory. Such a procedure, however, requires the knowledge of the flow or of the density distribution in the far wake. Following an earlier proposal made by NUYTS (ref. 5), the schlieren pattern is here calculated by using a wake flow model which can be derived from the known or measured bow shock geometry. An alternate analysis of the schlieren pattern produced by the entropy wake has been described by WEBB (ref. 6); he assumes a Gaussian distribution of the density in the far wake and develops a formula which explicitly contains the drag coefficient of the body. This dependence on the drag coefficient is examined in the present paper by means of further ballistic range experiments.

2. SCHLIEREN VISUALIZATION OF THE ENTROPY WAKE

If the schlieren knife edge is parallel to the flight axis, the far entropy wake becomes visible on the schlieren picture in form of a band on each side of the flight axis, one band being bright, the other dark (Fig. 1). It is required for this visualization that the respective Reynolds numbers are low enough in order to prevent an early laminar-to-turbulent transition of the wake flow. The two bands in Fig. 1 designate a maximum and a minimum of the light deflection angle  $\epsilon$  in the schlieren system. When assuming an axisymmetric distribution of the refractive index in the test object, i.e.

<sup>+</sup> Professor of Fluid Mechanics

<sup>++</sup> Group Leader, Hypersonics Division

in the entropy wake,  $n = n(r)$ , the deflection angle  $\epsilon$  is given by

$$\epsilon = 2Y \int_Y^R \frac{1}{n} \frac{dn}{dr} \frac{dr}{(r^2 - Y^2)^{1/2}}, \quad (1)$$

where  $Y$  is the distance from the flight axis of an incident light ray, and  $R$  is the outer radius of the object. The aim of the calculations is to determine the extreme values of  $\epsilon$  as a function of  $Y$ .

One has to introduce a certain assumption for the distribution of the refractive index  $n$ , or, of the density  $\rho = \rho(r)$  in the far wake. One therefore assumes an isentropic expansion of all streamlines from their position immediately behind the bow shock to the far wake regime which is represented by the constant pressure assumption  $p = p_\infty$ . Although the pressure is constant, the far wake field still exhibits certain profiles of entropy, temperature, and density, which cause the observed schlieren pattern. While the temperature and the entropy have a maximum on the flight axis, the density there has a minimum, and the streamlines throughout the wake are parallel, due to the uniform pressure. The calculation which is described in detail in refs. 3 and 4 allows to map the system of streamlines in the far wake from the streamline geometry at the bow shock without a knowledge of the flow pattern in the intermediate regime. The entropy profile behind the bow shock,  $s(y)$ , is thereby associated to the entropy profile in the far wake,  $s(r)$  (see Fig. 2), and a streamline is described by  $y = f(r) = \text{const}$ .

$s(y)$  can be derived from the bow shock shape, which may be given either as the result of an experiment or in the form of an analytic curve. The latter is only available for the case of a sphere, due to an empirical formula reported by KORKAN (ref. 7). For all other body shapes the shock profile must be determined from an experiment, e.g. from an appropriate shadowgraph. With this information available, density profiles in the far wake and the extreme values of  $\epsilon$  according to equation (1) have been calculated with the inclusion of considering real gas effects for the change of state variables at the bow shock front (Figs. 3 and 4). The profiles thus obtained do not include the entropy production in the intermediate regime between the bow shock and the far wake. At high Mach numbers, these additional dissipative effects, e.g. due to secondary shocks, can be regarded to be small in comparison to the entropy jump at the bow shock.

### 3. INFLUENCE OF THE DRAG COEFFICIENT

The above calculations with which one determines the distance between the two bands in the schlieren picture do not explicitly include the influence of the body drag. This influence can only be derived from the shape of the applied bow shock profile. In some cases, the drag coefficient of the investigated bodies can be found from available data of forebody pressure drag as estimated from measured bow shock shapes (ref. 8). It can be assumed, that the total drag of blunt bodies flying at hypersonic Mach numbers is well described by the forebody pressure drag.

A quite different approach of analyzing the schlieren measurements of the hypersonic entropy wake has been described by WEBB (ref. 6). In this analysis the enthalpy profile in the far wake is taken as a measure of the body drag, and this enthalpy distribution is approximated by a Gaussian profile. The problem is to determine the appropriate constants of the Gaussian distribution. After inserting this approximation into the schlieren formula for axisymmetric density fields (eq. (1)), one obtains an expression for the schlieren deflection angle  $\epsilon$ , from which one derives, after some rearrangements, for the position  $y_{\max}$  of the extreme values of  $\epsilon$ :

$$y_{\max} = \pm \text{const. } M_\infty \sqrt{C_D} \quad (2)$$

Hence, this results shows explicitly, that the distance between the observed schlieren bands increases linearly with the flight Mach number  $M_\infty$  and with the square root of the drag coefficient. The constant on the right side of eq. (2) contains several flow parameters, e.g. the ratio of the free stream enthalpy and the enthalpy on the wake axis, and the ratio of specific heats,  $\gamma$ , of the gas in the wake flow.

### 4. EXPERIMENTAL INVESTIGATIONS

Ballistic range experiments have been performed in order to photograph the entropy wake by means of a schlieren system. Blunt models of various shapes have been launched with a light gas gun in a Mach number range of  $8 < M_\infty < 16$ . The model shapes which have been investigated are: spheres, cylinders flying in the direction of their axes, cylinders with a spherical forebody, cylinders with elliptical forebodies, and cones with a spherical nose. The respective  $C_D$ -values are known or extrapolated from different sources and tables (refs. 8 to 10). Additional but very reliable information on the  $C_D$ -values was obtained by measuring flight times between several light-screen systems in the ballistic range.

The wake was visualized in a double-path schlieren system and photographed by means of a high speed drum camera. This allowed to survey the wake over several hundred diameters behind the body and to omit those experiments in which the wake had become turbulent too early, or in which the model had flown unstable or with an angle of attack. The laminar wake flow was established by lowering the pressure in the range to a value below

20 Torr. The very low density level associated with this pressure required to use an extremely sensitive optical system. The recorded schlieren pictures were evaluated by utilizing a densitometer. This allowed to determine the position of the extreme values of  $\epsilon$  (see section 2) with a much better precision than from a visual inspection of the schlieren photographs (Fig. 1).

## 5. DISCUSSION

For a given body shape, e.g. for the sphere ( $C_D = 0.96$ ) or the cylinder flying in the direction of its axis ( $C_D = 1.69$ ), the measured values show the expected dependence on the flight Mach number  $M_\infty$  (Figs. 3 and 4). The experimental errors which arise in positioning the extreme values of the schlieren deflection angle decrease with increasing Mach number. In some cases, the bow shock shapes of the respective bodies have been photographed and used to evaluate the presented schlieren theory. These results agree well with the experimental values within the error limits of the measurements. Agreement is also found between the experimental results and an evaluation of WEBB's theoretical approach which predicts a linear dependence of the position of the extreme values of  $\epsilon$  (here designated as  $r_{\max}$ ) and the flight Mach number. WEBB's formula, however, should not be evaluated with a value of  $\gamma = 1.4$  (for air), but rather with  $\gamma$  smaller than 1.4, according to the temperatures behind the strong bow shock wave. The measurements are well matched by using a value of  $\gamma = 1.2$ , while there appears a tendency of the experimental points to approach the curve obtained with  $\gamma = 1.3$  at the lower Mach numbers.

Results obtained for different body shapes or  $C_D$ -values but with the same (or nearly the same) Mach number are shown in Fig. 5 for  $M_\infty = 12$  and in Fig. 6 for  $M_\infty = 14$ . Also included is an experimental point derived from ref. 11. Within the error limits, these results confirm the prediction that the distance between the observed schlieren bands increases with the square root of the drag coefficient. Thus, such a representation could be used to determine  $C_D$ -values of blunt bodies launched in a ballistic range, provided that the flight Mach number is known. The practical application of such a procedure might be limited, since it appears necessary to control in any case the stability of flight and the existence of a laminar wake flow.

## 6. REFERENCES

1. Wilson, L. N. Far Wake Behavior of Hypersonic Spheres, AIAA Journal, Vol. 5, 1967, pp. 1238-1244
2. Albe, R. Quantitative Schlierography of Hypersonic Wakes at Low Pressure Using a Double Traversing Polarized Light Beam. Proceed. 9th Int. Congress on High-Speed Photography, SMPTE, New York, N.Y., 1970, pp. 414-417
3. Giesbrecht, H. Berechnung und Visualisierung des Entropie-Nachlaufs stumpfer Hyperschall-Flugkörper. Ernst-Mach-Institut, Freiburg i.Br., Bericht 8/71, 1971
4. Giesbrecht, H. Schlieren Visualization of the Hypersonic Entropy Wake. AIAA Journal (in print)
5. Nuyts, J. Sur le sillage d'entropie derrière une sphère en vol hypersonic. ISL N 29/67, 1967
6. Webb, W.H. Comments on Schlieren Measurements of the Inviscid Hypersonic Wake of a Sphere. AIAA Journal, Vol. 6, 1968, pp. 2239-2240
7. Korkan, K.D. Comments on "Bow Shock about a Spherical Nose". AIAA Journal, Vol. 4, 1966, pp. 380-381
8. Philpott, D.R. An Investigation into the Flow around a Family of Elliptically Nosed Cylinders at Zero Incidence at  $M_\infty = 2.5$  and  $M_\infty = 4$ . Aeron. Quart., Vol. 23, 1972, pp. 315-326
9. Pugh, P.G. The Estimation of Zero Incidence Forebody Pressure Drag Coefficients of Axisymmetric Bodies from Measured Bow Shock Shapes. NPL Aero Report 1245, 1967
10. Hoerner, S.F. Résistance à l'avancement dans les fluides. Gauthier-Villars, Paris, 1965
11. Albe, F. Visualisation des sillages de cônes émoussés en vol hypersonique par strioscopie. Fagot, H. Sutterlin, P. ISL RT 4/71, 1971

23-4

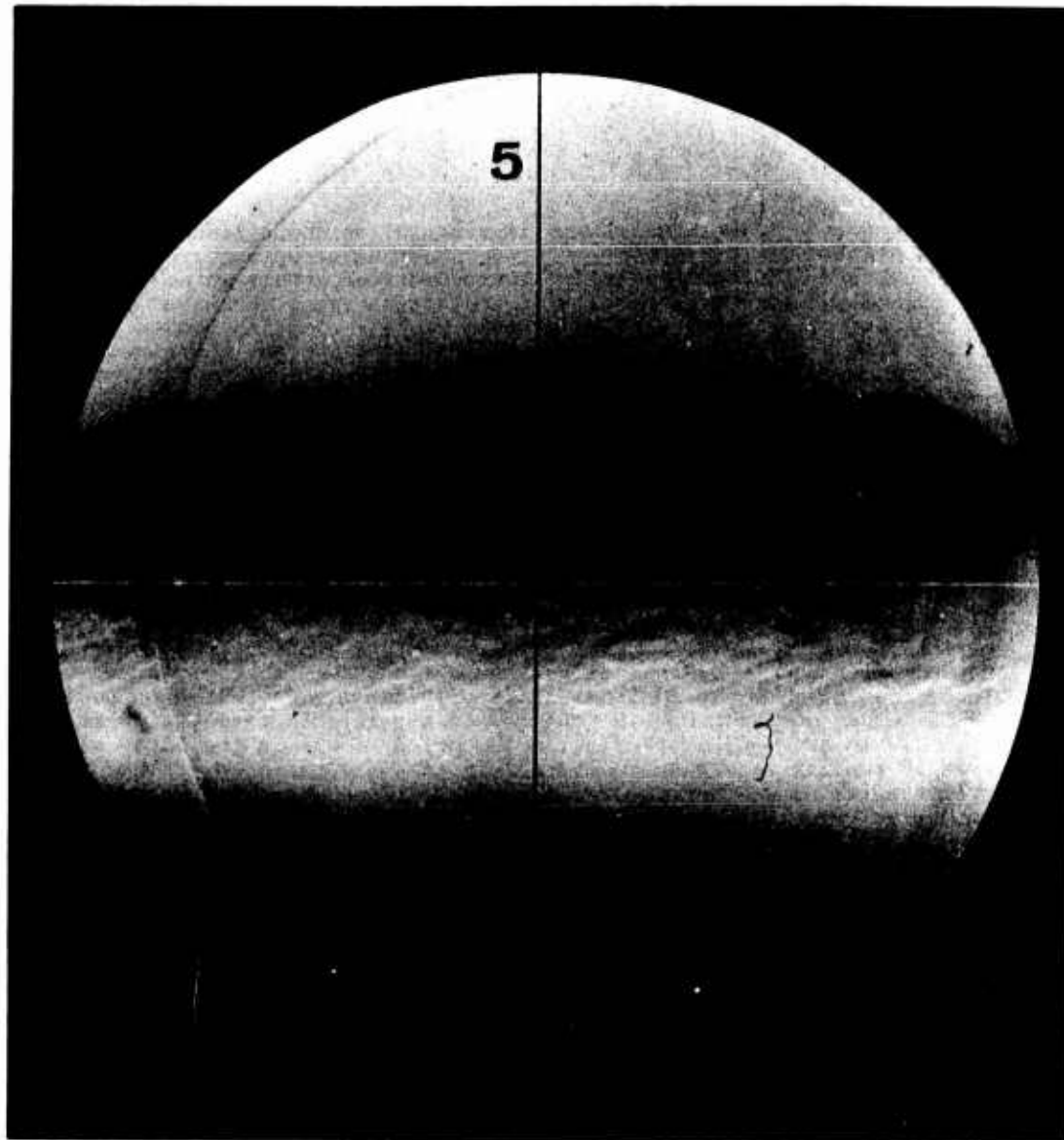


Fig. 1 Schlieren photograph of the laminar for wake (entropy wake) behind a sphere flying with a Mach number of  $M_\infty = 12$ ; flight direction is horizontal.

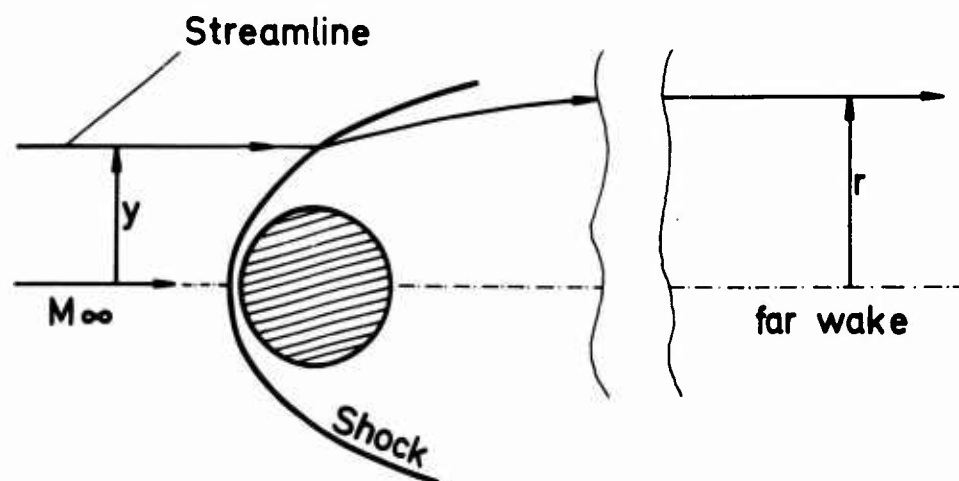


Fig. 2 Coordinate system of the flow model used to evaluate schlieren observations (section 2).

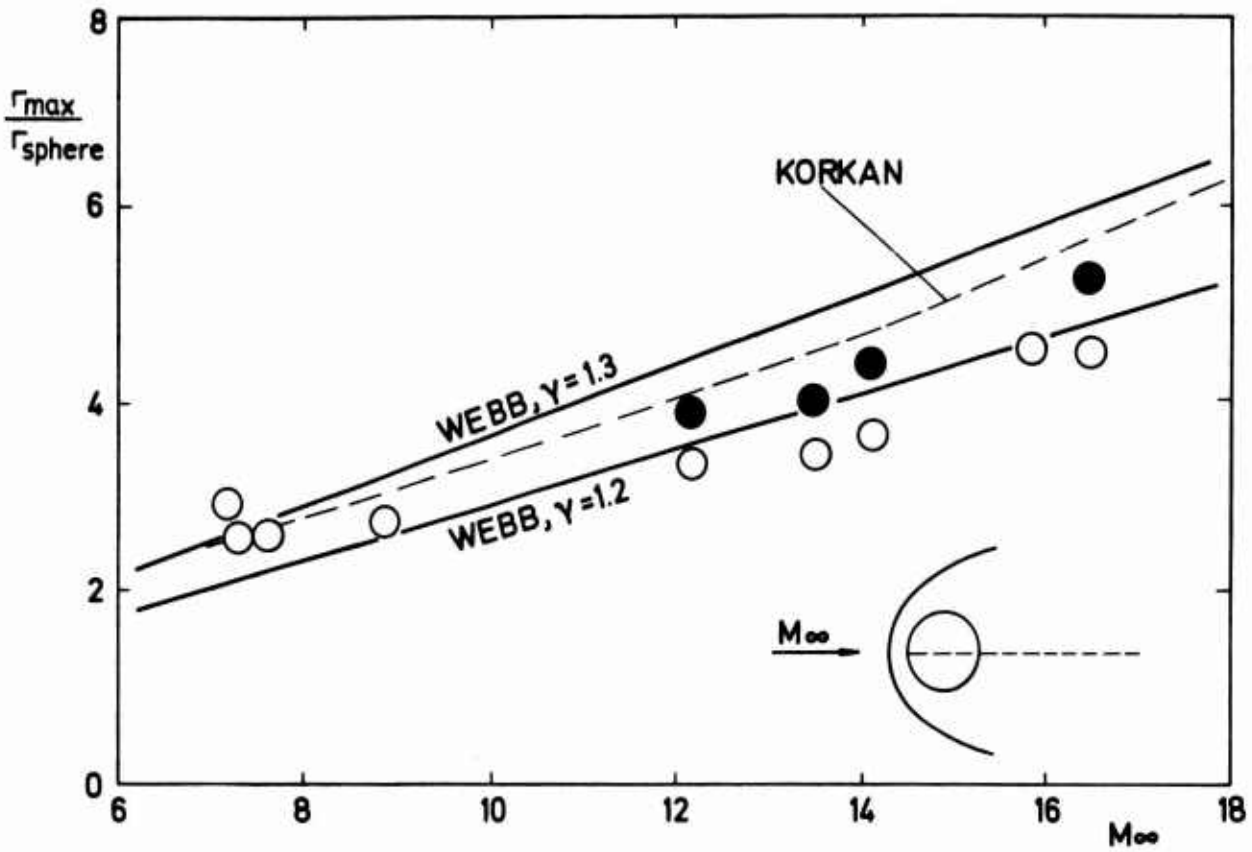


Fig. 3 Position  $r_{max}$  of the extreme values of the schlieren deflection angle in the wake behind a sphere. Open symbols: Free flight range experiments. Full symbols: Evaluation of schlieren theory with measured bow shock shapes. Curves designate WEBB's theory, and schlieren theory evaluated with KORKAN's shock profile.

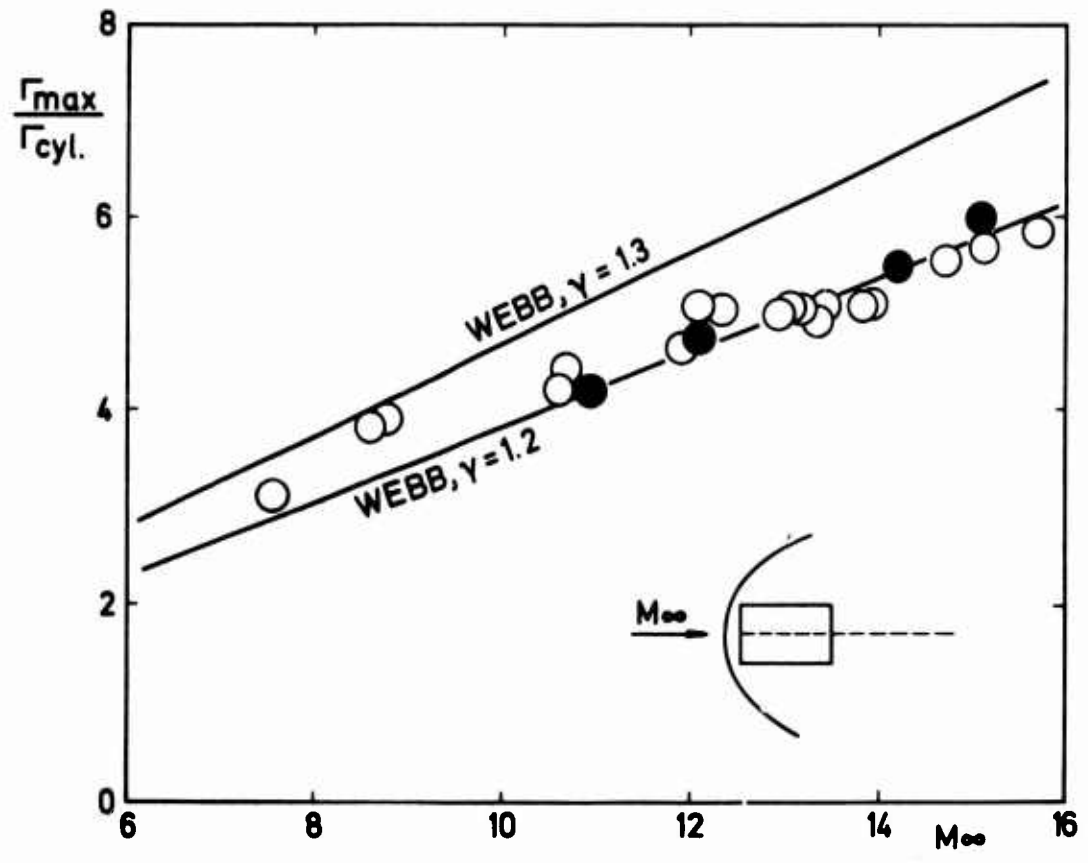


Fig. 4 Results for cylinder flying in the direction of its axis. Notation see Fig. 3.

23-6

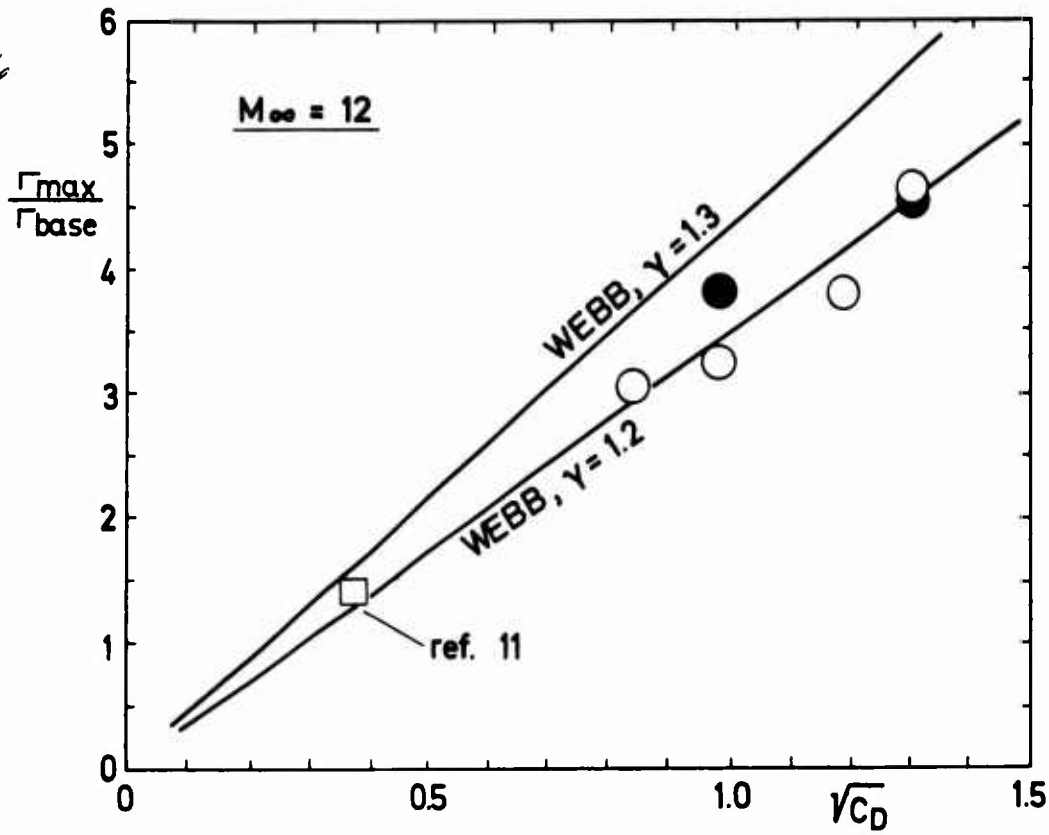


Fig. 5 Position  $r_{\max}$  of the extreme values of the schlieren deflection angle in the wake of various blunt bodies flying at a Mach number of  $M_{\infty} = 12$ . Open symbols: Free flight range experiments. Full symbols: Evaluation of schlieren theory with measured bow shock shapes. Curves designate WEBB's theoretical prediction.

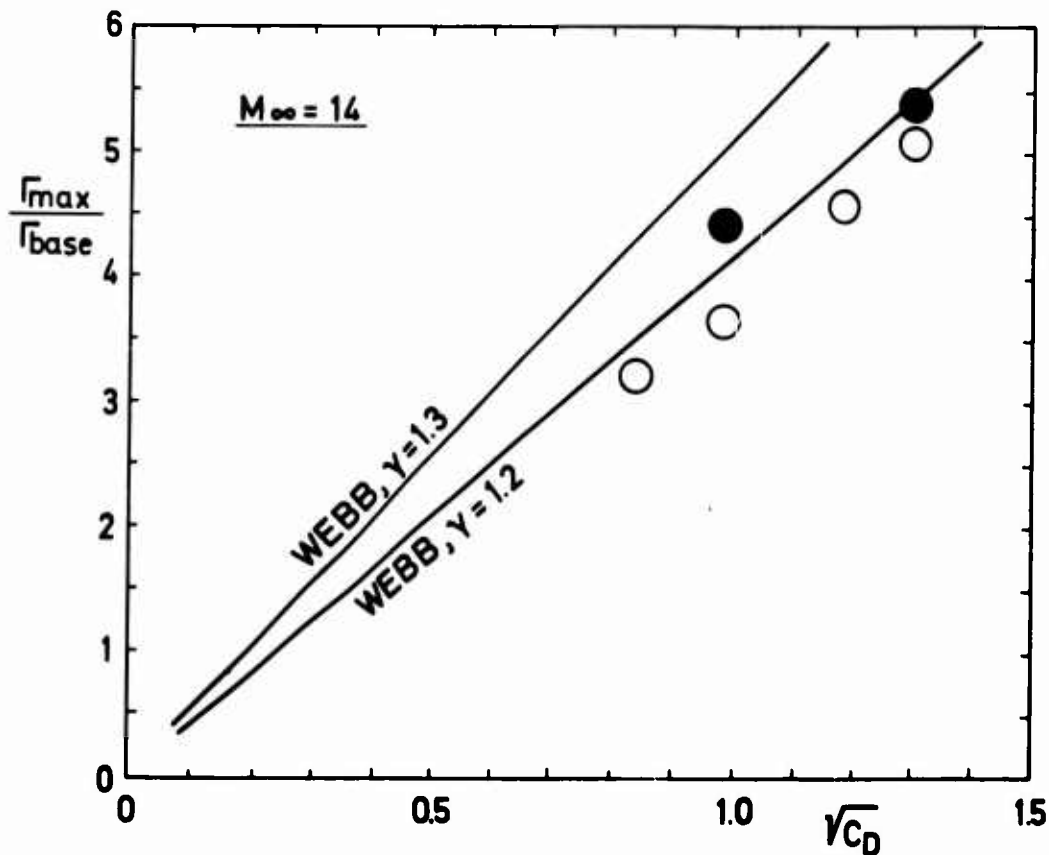


Fig. 6 Results for  $M_{\infty} = 14$ . Notation see Fig. 5.

DEVELOPMENT OF TECHNIQUES TO MEASURE IN-FLIGHT DRAG OF  
A U. S. NAVY FIGHTER AIRPLANE AND CORRELATION OF  
FLIGHT MEASURED DRAG WITH WIND TUNNEL DATA

24-1

by

E. C. Rooney\*  
Naval Air Systems Command  
Washington, D. C. 20360  
United States of America

SUMMARY

This paper discusses wind tunnel and flight drag measurement techniques and correlation of wind tunnel and flight drag data for a U. S. Navy fighter airplane.

Wind tunnel drag data were obtained with aerodynamic, induction system and powered nozzle/afterbody models. A common reference afterbody configuration between aerodynamic and propulsion models was utilized to assure compatibility of thrust and drag measurements.

Flight drag data were obtained from steady-state, quasi steady-state and dynamic (wind-up/down turn) maneuvers utilizing sensitive three-axis accelerometers to determine excess thrust and the internal pressure method for measuring engine thrust. Compressor airflow, afterburner pressure drop and nozzle coefficients used for computing engine net thrust were obtained from isolated engine tests at simulated flight conditions throughout the flight envelope. Wind tunnel data were used to account for propulsion system drag caused by subcritical inlet spillage and nozzle interference drag.

Utilization of dynamic test maneuvers has resulted in a significant reduction in the amount of flight time required to obtain lift/drag/angle of attack relationships and has allowed assessment of induced drag characteristics to angles of attack not attainable by conventional methods. These techniques have produced flight data quantity, accuracy and repeatability not heretofore achievable. Data scatter is  $\pm 1\%$  for steady-state maneuvers and  $\pm 2\%$  to  $\pm 4\%$  for quasi steady-state and dynamic maneuvers depending on Mach number. General conclusions reached relative to wind tunnel drag estimates include: (1) good to excellent agreement in subsonic minimum drag, drag rise Mach number and slope, external store drag increment, high-lift configuration drag and drag increment due to nozzle configuration changes; (2) unexplained differences exist in minimum supersonic drag; (3) slightly greater airplane induced drag exists throughout most of the Mach envelope; and (4) Reynolds number effect on subsonic skin friction drag is verified.

LIST OF SYMBOLS

A	Geometric area	MAX	Maximum
a	Acceleration	Min	Minutes, minimum
AB	Afterburner	N	Newton (0.224 lb)
ABPD	Afterburner pressure drop	N <sub>1</sub>	Low pressure compressor rotor speed
ATF	Altitude Test Facility	N <sub>2</sub>	High pressure compressor rotor speed
C	Centigrade	NPR	Nozzle pressure ratio, P <sub>T10</sub> /P <sub>a</sub>
C <sub>D</sub>	Drag coefficient, D/qS	P	Pressure
C <sub>Dmin</sub>	Minimum drag coefficient	p	Longitudinal body axis accel. misalignment
C <sub>Fe</sub>	Equivalent skin friction drag coefficient	PCM	Pulse code modulation
CG	Center of gravity	psi	Pounds per square inch
C <sub>g</sub>	Nozzle coefficient	psia	Pounds per square inch absolute
CL	Lift coefficient, L/qS	psid	Pounds per square inch differential
CL <sub>po</sub>	Power off lift coefficient, $L/qS - F_g \sin(\alpha + \tau)/qS$	q	Dynamic pressure, normal body axis accel. misalignment
D	Drag	R	rudder vane displacement from airplane CG
Deg	Degrees	r	Accel. displacement from airplane CG
EPR	Engine pressure ratio, P <sub>T7M</sub> /P <sub>T2</sub>	Re	Reynolds number
F	Fahrenheit	RPM	Revolutions per minute
F <sub>g</sub>	Gross thrust	S	Wing area
F <sub>m</sub>	Meter measured thrust	sec	Seconds
F <sub>r</sub>	Ram drag	SL	Sea Level
ft	Feet	T	Temperature, thrust
FRL	Fuselage reference line	TRS	Traversing rake system
g	Gravitational constant	V	Velocity
hr	Hour	W <sub>a</sub>	Airflow
HZ	Hertz	W <sub>f</sub>	Fuel flow
IRT	Intermediate rated thrust	W <sub>g</sub>	Total gas flow (W <sub>a</sub> + W <sub>f</sub> - bleed airflow)
k	Times 1000	W <sub>T</sub>	Airplane weight
kg	Kilograms	$\alpha$	Angle of attack
kN	Kilonewtons	$\beta$	Angle of sideslip
km	Kilometers	$\gamma$	Ratio of specific heats
kt	Knots	$\Delta$	Incremental quantity change
L	Lift	$\delta$	Ratio of ambient to standard SL static pressure
lb	Pounds	$\theta$	Ratio of ambient to standard SL static temperature
M	Mach number	$\Theta$	Pitch angle
m	Meters		
MAC	Mean aerodynamic chord		

\* Senior Performance Engineer - Fixed Wing Aircraft

$\Lambda$	Wing sweep angle
$\tau$	Longitudinal thrust line inclination
$\phi$	Roll or bank angle
$\psi$	Yaw angle
$(\ )^\circ$	Degrees
$(\dot{\ })$	First time derivative
$(\ddot{\ })$	Second time derivative

#### Subscripts

a	Ambient, actual
FP	Flight path

FUSB	Fuselage bending
i	Ideal, indicated
MISAL	Misalignment
M	Mixed
NBB	Nose boom bending
REF	Reference
T	Total, true
x	Longitudinal axis
y	Lateral axis
z	Vertical axis

Numerals: Engine and ATF measurement planes

24-2

## 1.0 INTRODUCTION

### 1.1 Importance of In-Flight Drag Measurement

Aircraft performance estimates are dependent on an accurate knowledge of aircraft drag.

The process of aircraft drag estimation, during the design and development stages, involves calculation from theory and empirical relations followed by measurement of the drag of scale models in wind tunnels. Model test results must be extrapolated to full scale flight Reynolds number and adjustments made for details not represented on the model. The validity and accuracy of this process can only be substantiated if full scale flight measurements of drag are available for comparison with the design estimates and wind tunnel derived drag.

Actual aircraft performance can be accurately determined in flight without a knowledge of engine thrust or aircraft drag; for example, aircraft specific range through measurement of fuel flow and airspeed; maximum airspeed by determining the point at which excess thrust is equal to zero. However, responsibility between airframe and engine(s) for any variance between actual and estimated aircraft performance cannot be made because any differences could be caused by either a change in propulsive efficiency or in aircraft drag. Separation of these items must be accomplished to account for any difference between actual and estimated aircraft performance.

One approach to defining production aircraft final performance capabilities is separate evaluation of the many aspects of aircraft performance (cruise, climb, acceleration, maximum airspeed, etc.) in the various external store loadings representative of the mission capabilities of the airplane. Another approach is a flight program designed to provide a thorough understanding of the components of aircraft drag (minimum or zero lift drag, induced drag, drag divergence, external stores drag, etc.) and engine performance throughout the flight envelope. The latter approach is more efficient, timely and economical and provides data from which aircraft performance can be confidently calculated throughout the aircraft's airspeed, altitude and normal acceleration envelope.

Measurement of drag in flight is often necessary to evaluate the effects of aerodynamic changes to improve drag, to optimize aircraft performance (especially for variable geometry aircraft), and to provide a baseline from which aircraft performance may be predicted for changes in aerodynamic configuration to perform alternate missions or for the installation of different engines.

### 1.2 Inadequacies of Conventional Drag Measurement Techniques

In the past, attempts to measure in-flight drag have not proven entirely satisfactory because of insufficient data of dubious accuracy. The industry standard for drag measurement ( $\pm 3\%$  accuracy) is seldom achieved, even under carefully controlled conditions. As a result, attempts to correlate flight and wind tunnel drag data have been viewed with scepticism and obvious anomalies left unresolved. Drag determination from conventional performance testing techniques involves evaluation of aircraft and engine data obtained from steady-state and quasi steady-state maneuvers (energy method). Quasi steady-state maneuvers are defined as those either flown near 1 g and/or excess thrust near zero (climbs, descents, accelerations, decelerations and sustained g turns). These techniques have proved inadequate from the following standpoints:

a. Data scatter and unknown systematic errors are such that absolute drag levels are uncertain and drag increments for external stores and aircraft changes are not readily discernible. The data scatter, or random errors, is caused by inaccuracies in flight instrumentation and inability or failure to properly account for, either wholly or in part, many items that directly effect drag measurement. Some of the items that cause data scatter include aircraft acceleration (non steady-state), Reynolds number effects and aircraft flexibility and trim effects. Items that not only contribute to data scatter but could also cause systematic errors are engine airflow (to determine ram drag), engine gross thrust in the flight nozzle operating environments and airframe/engine interaction effects.

b. Evaluation of induced drag characteristics (drag due to lift) is incomplete and time consuming because drag over only a limited lift coefficient range can be obtained by varying altitude, aircraft mass and normal acceleration at a single Mach number. Drag under instantaneous g conditions cannot be evaluated.

c. The large amount of flight time required to fully evaluate aircraft drag, especially for aircraft with large altitude/Mach envelopes is either costly or not available because of limited program resources and restrictive development schedules.

### 1.3 In-Flight Thrust Measurement Techniques

The fundamental parameter in the determination of aircraft drag is accurate measurement of in-flight engine thrust. The most satisfactory method of measuring thrust in-flight would be by a direct measurement of the axial force produced by the engine. This method requires that the engine be free from

243  
longitudinal constraints. This is difficult to achieve in practice because of engine-to-airframe seals, connections and support requirements for the engine nozzle. Reference (1) reports that attempts to measure engine trunnion thrust in a Fairey Delta 2 research aircraft was found to be wholly unsatisfactory, probably because of significant engine constraints produced by the jet pipe supports. In addition to accurate measurement of the engine axial force, a correction must be applied to account for the pressure forces acting on the inside of the inlet. This correction is also difficult to determine.

The more useable methods are indirect approaches which deduce engine net thrust from the difference between engine gross thrust and ram drag. Gross thrust is defined as the sum of the momentum and pressure forces at the nozzle exit and ram drag is defined as the free stream momentum of the air mass flow entering the engine compressor. In these internal or gas generator methods, the ideal gross thrust is calculated from engine pressure and temperature measurements based on perfect gas laws assuming one dimensional, adiabatic continuous flow with isentropic expansion to free stream pressure at the nozzle. In reality none of these assumptions are completely valid and calibration factors must be applied to the ideal theoretical calculations to obtain actual gross thrust. Early in jet aircraft development, the gross thrust calibration factor was based on actual measurement of thrust on a static sea level thrust stand and extrapolated to altitude and airspeed flight conditions. With the establishment of engine test facilities to simulate flight conditions at the engine compressor and exhaust, it was found that this extrapolation produced considerable errors in gross thrust measurement. Reference (1) reports a systematic error on the order of 5%. The advent of the engine ATF (altitude test facility), coupled with wind tunnel calibrations of inlet and exhaust nozzles have resulted in considerable refinement in this in-flight measurement technique. However, considerable errors in thrust measurement in-flight still exist. Reference (1) tests with a Fairey Delta 2 research airplane indicate random errors of + 4% with the possibility of systematic errors on the order of 2%. Reference (2) static tests with an F-111A airplane and an influence coefficient study for important thrust measurement parameters, indicate in-flight random errors at military thrust levels of + 3% for one method based on nozzle pressure and area and + 5% for a second method based on nozzle total temperature and air mass flow. Systematic errors and considerably greater random errors could exist at lower thrust levels.

A third method that, in principle, measures gross thrust and mass flow without the need for an engine ATF calibration is by utilization of a "Swinging Rake" or TRS (Traversing Rake System). This concept was initially developed by the Grumman Corporation under contract to the U. S. Navy and provides a simple means of surveying the total and static pressures and total temperature at the jet exit immediately aft of the nozzle plane. TRS installations have been installed on F-11, A-5A and A-7A airplanes. A typical installation is shown in Figure 1. TRS installations have provided in-flight data with random errors of + 3% and no known systematic errors for turbojet engine airplanes. Reference (3) discusses the results of in-flight tests of a dual TRS installation on the twin turbojet engine A-5A airplane. However, thrust data obtained with the TF30-P-6 turbofan engine installation in the A-7A airplane generated doubt as to the validity of TRS measurements because of asymmetric pressure profiles and disagreement with thrust stand measurements. Although data scatter was only + 2%, systematic errors as high as 7% existed when compared to thrust stand and engine ATF data. The tests of reference (4) subsequently showed that the method is also unsatisfactory for afterburning turbofan engines because of large gradients in pressure and temperature at the nozzle exit. Other difficulties of the TRS as related to measurement of airplane drag are: (1) aircraft operation is limited to steady-state conditions, (2) the drag of the TRS installation must be isolated from the drag of the airplane and (3) the effect of the installation on nozzle/airframe interference drag is unknown.

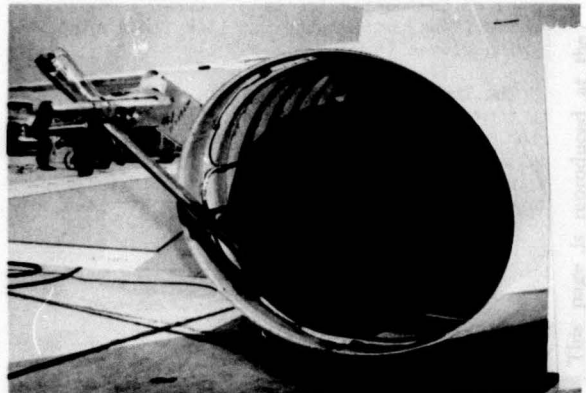


Figure 1 TRS Installation on A-7 Airplane

It is important to note that these thrust calculation methods concern only the derivation of engine net thrust. Because the airframe and engine must function as a unit, engine and airframe characteristics cannot completely be divorced from each other. Calculation of aircraft net propulsive effort, in addition to engine net thrust, requires inclusion of propulsion system drag items. Failure to account for these items may result in failure to obtain generalized drag data from in-flight thrust measurements. Some of these interactions for jet type aircraft are as follows:

- a. Additive drag caused by spillage of inlet air for off design inlet mass flow conditions.
- b. Interference drag caused by the effects of externally induced flow produced by nozzle exit flow conditions.
- c. Flow distortion at the engine compressor face produced by inlet design and resulting effect on engine performance.

#### 1.4 New In-Flight Drag Measurement Techniques

The need for timely, efficient and accurate evaluation of the performance capabilities of a Navy fighter airplane over a large Mach, altitude, normal acceleration envelope, with variable geometry (wing sweep, inlet ramps, exhaust nozzle and maneuvering devices) and multi-mission stores carriage capability, dictated exploitation of new flight test techniques and engineering procedures for determination of aircraft drag. Instrumentation accuracies were improved and a sensitive three-axis accelerometer package was utilized to accurately define excess thrust for quasi steady-state and dynamic test maneuvers. Dynamic test techniques were developed and refined, in order to define in a single maneuver, airplane

induced drag characteristics at a single Mach number over a large portion of the useable lift coefficient range. Dynamic maneuvers are defined as those performed at g levels significantly greater or less than 1 g and consist mainly of push-over/pull-up (roller coaster) and wind-up/down turn maneuvers. Accurate determination of in-flight engine performance was accomplished through use of the engine internal pressure method in conjunction with calibration of engine compressor airflow characteristics, gross thrust nozzle coefficient and afterburner pressure drop throughout the airplane flight envelope from isolated engine tests in altitude test facilities. Airframe/engine interaction effects were evaluated on wind tunnel propulsion models (induction model and powered propulsion model) and the flight measured thrust data adjusted for those propulsion system drag items that are functions of inlet mass flow and nozzle pressure ratio.

This paper discusses the development and flight results of these new techniques and procedures. Also discussed are wind tunnel thrust/drag measurement and accounting procedures and correlation of flight and wind tunnel drag data based on available flight test data.

## 2.0 DESCRIPTION OF TEST EQUIPMENT

### 2.1 Test Vehicle

The test airplane is an F-14A supersonic, tandem seat, twin engine air superiority fighter designed and manufactured by the Grumman Aerospace Corporation. A three-view drawing of the airplane is shown in Figure 2. The design is characterized by its high wing, variable wing sweep, twin vertical tails and podded engine nacelle configuration. The wing panels rotate through leading edge wing angles of  $20^\circ$  to  $68^\circ$  about outboard wing pivots housed in highly swept wing gloves. Wing sweep can be automatically or manually controlled in flight. Vanes in the glove leading edges extend to compensate for changes in the wing aerodynamic center. Lift augmentation for take-off, landing and maneuvering in flight is provided by conventional full span leading edge slats and single-slotted trailing edge flaps. Speed brake surfaces are located on the upper and lower aft fuselage. Missiles and external stores are carried from eight hardpoint stations located on the center fuselage between the engine nacelles (four), under the nacelles (two) and on the wing gloves (two).

The induction system consists of two horizontal, two-dimensional, all external compression, variable geometry air inlets with three hydraulically actuated ramps and a fixed capture area. The inlets are separated from the fuselage for boundary layer control. An inlet throat bleed door is located on top of each inlet for inlet ramp boundary layer control and for inlet air bypass. The variable exit area is programmed as a function of inlet ramp position.

The airplane is powered by two Pratt and Whitney Aircraft TF30-P-412A, twin spool, turbofan engines equipped with afterburners for thrust augmentation. It is a low bypass ratio engine (.878:1.0) with afterburner thrust augmentation of 65%. Figure 3 shows a cutaway view of the engine. A three-stage fan and a six-stage low-pressure compressor are driven at  $N_1$  speed by a three-stage low pressure turbine. A seven-stage high-pressure compressor is driven by a separate shaft at  $N_2$  speed by a single stage high pressure turbine. Combustion is accomplished in an eight-chamber combustor. Fan air is directed rearward through a full annular fan duct and discharged into the forward section of the afterburner duct where it is combined with the basic engine turbine discharge exhaust gases. A fully modulating five zone afterburner arranged in annular rings is located downstream of the turbine at a point where the core and fan streams merge.

The exhaust nozzles are self cooled variable area C-D (convergent-divergent) iris nozzles with 18 flaps translated by four actuators. The throat varies from a minimum of  $3.53 \text{ ft}^2$  in partial and intermediate thrust to  $7.5 \text{ ft}^2$  at maximum afterburning thrust. Fan discharge air, taken from between the afterburner liner and shell, cools the internal nozzle surfaces.

Two loadings were utilized for the tests reported herein. The Baseline Loading consisted of the basic airplane plus four Sparrow missiles semi-submerged in cavities at the center fuselage store stations. The Phoenix Missile Loading consisted of: (a) four dual tandem mounted Phoenix missiles installed on pallets at the center fuselage stations, and (b) two pylon mounted Phoenix missiles attached to the wing gloves. Fairings to minimize installation drag were installed ahead of the forward fuselage Phoenix missiles.

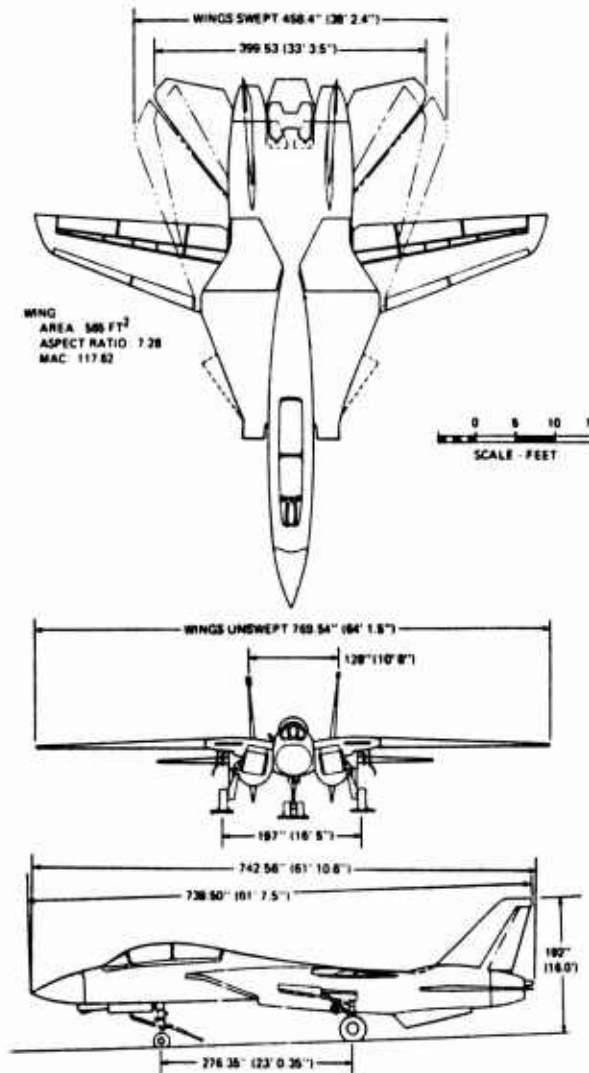


Figure 2 Three-View Drawing of Test Vehicle

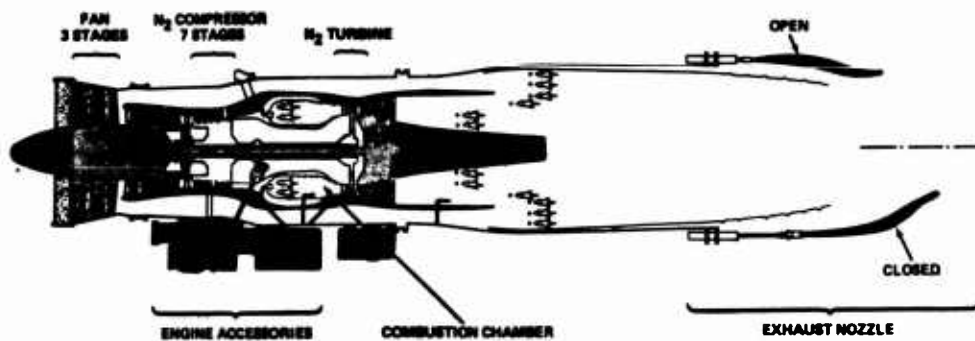


Figure 3 Engine Schematic Diagram

## 2.2 Test Vehicle Instrumentation

The instrumentation consisted of a digital PCM (Pulse-Code Modulation) system with signal conditioning, timing, magnetic tape recording and telemetry subsystems. The system has the capacity to record all PCM data on magnetic tape and to telemeter it to the ground data reduction complex for real-time analysis. Instrumentation assemblies and transducers installed in the test aircraft included the following:

a. A nose boom assembly (Figure 4) containing a Rosemont heated pitot/static head, and angle of attack and angle of sideslip vanes.

b. A forty (40) probe inlet compressor face rake consisting of eight (8) radial arms with five (5) total pressure pick-ups on each arm (on one aircraft only).

c. A body axes accelerometer package containing thermally controlled sensitive Systron Donner longitudinal, lateral and normal accelerometers. The accelerometer temperature was maintained at approximately 35°C (95°F). A photograph of the body axes accelerometer package is shown in Figure 5.

d. The test airplanes contained instrumentation parameters for performance, stability and control and propulsion system flight testing. The instrumentation pertinent to the results discussed in this paper are tabulated in Table I. The instrumentation parameter accuracies of Table I are for a (1) sigma standard deviation (except where noted) based on a Gaussian distribution function of data. In addition to the parameters listed in Table I, the following inlet/engine parameters were monitored for diagnostic purposes: inlet ramps and bleed door positions; compressor hub total pressure ( $P_{T2}$ ); fan, low pressure and high pressure compressor discharge static pressures ( $P_{2.5}$ ) ( $P_3$  and  $P_4$ ); turbine inlet temperature ( $T_{T5}$ ); engine nozzle control parameters; and compressor bleed flow temperature and pressure.

## 2.3 Engine Altitude Test Facility

Calibration data for engine airflow, ABPD (Afterburner Pressure Drop) and gross thrust nozzle coefficient, used in conjunction with in-flight measured parameters for the calculation of in-flight engine net thrust, were obtained at simulated altitude conditions in an engine ATF. These tests were conducted at the engine manufacturer's facility and at the NAPTC (Naval Air Propulsion Test Center), Trenton, New Jersey. A diagram of engine test cell installation and instrumentation at the NAPTC is presented in Figure 6. Conditioned air, provided through compressors and heaters (or refrigerators), is supplied to the compressor face at total temperature and pressure conditions to simulate flight altitude, Mach number and inlet pressure recovery. The engine external surfaces and nozzle are maintained at ambient pressure for the altitude being simulated through the use of exhausters. Typical of the engine test cells utilized was NAPTC altitude chamber 1E which has a test section 4.42 m (14.5 ft) in diameter and 5.5 m (18 ft) long. This chamber will handle a maximum airflow of 159 kg/sec (350 lb/sec) from

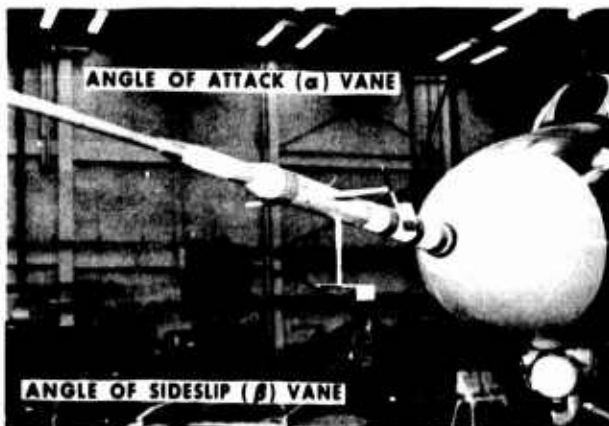


Figure 4 Nose Boom Assembly with  $\alpha$  and  $\beta$  Vanes

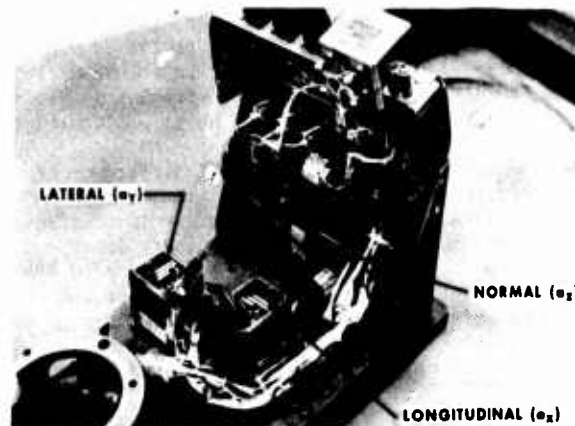


Figure 5 Body Axes Accelerometer Package

24-6

TABLE I

## Aircraft Test Instrumentation

Parameter	Measurement Range	Freq.	Estimated Accuracy
<b>AIRFRAME:</b>			
Airspeed (Nose Boom)	93-1853 km/hr (50-1000 kts)	5 HZ	+1.86 km/hr (+1 Kt)
Altitude (Nose Boom)	- 305 to 19,750m (-1000 to 65,000 ft)	5 HZ	+13.4 m (44 ft) at SL +25.9 m (85 ft) at 65K
Time IRIG "B" Time Code)	hr, min, sec and millisec	-	-
Free Air Temperature	- 48°C to +232°C (-55°F to +450°F)	5 HZ	+ .56°C (+1.0°F)
Pitch Attitude	+35°	6.5 HZ	**+0.24°
Roll Attitude	+20°	6.5 HZ	**+0.24°
Angle of Attack (Nose Boom)	-5° to +35°	10 HZ	**+0.17°
Angle of Sideslip (Nose Boom)	+15°	10 HZ	**+0.17°
Rate of Pitch	+10°/sec	10 HZ	+0.15°/sec
Rate of Roll	+5°/sec	10 HZ	+0.10°/sec
Rate of Yaw	+5°/sec	10 HZ	+0.10°/sec
FRL Longitudinal Acceleration	+0.6g	10 HZ	+ .001g
FRL Normal Acceleration	-1g to +3g	10 HZ	+ .004g
FRL Lateral Acceleration	+0.6g	10 HZ	+ .001g
Correction Temp for FRL Accelerometers	-46°C to +93°C (-50°F to 200°F)	0.2 HZ	+1.7°C (3°F)
CG Normal Acceleration	-3g to +8g	10 HZ	+0.027g
Wing Sweep Position	20° to 68°	10 HZ	+0.2°
Control Surfaces	+Full Surface Deflection	20 HZ	+1°
Fuel Quantity (8 Tanks)	0 to Tank Capacity	5 HZ	+0.45 kN (+ 100 lb)
<b>INLET:</b>			
Left Engine Compressor Face $\Delta P$ 40 Probe Rake (Rake $P_T$ - PREF)	+35 kN/m <sup>2</sup> (+ psid)	10 HZ	+1.4 kN/m <sup>2</sup> (+0.2 psi)
Left Engine Reference Pressure - $P_{T2}$ (for inlet Rake)	14 to 336 kN/m <sup>2</sup> (2 to 48 psia)	10 HZ	+0.62 kN/m <sup>2</sup> (+0.09 psi)
<b>ENGINE (left and Right):</b>			
Low Pressure Compressor Rotor Speed ( $N_1$ )	0 to 10,000 RPM	5 HZ	+18 RPM
High Pressure Compressor Rotor Speed ( $N_2$ )	0 to 14,500 RPM	5 HZ	+27 RPM
Basic Engine Fuel Flow (Mass)	0 to 4,500 kg/hr (0 to 10,000 lb/hr)	5 HZ	+1% of Indication
Afterburner Fuel Flow (Mass)	0 to 37,000 kg/hr (0 to 80,000 lb/hr)	5 HZ	+1% of Indication
Basic Engine Fuel Used	0 to 89 kN (0 to 20,000 lb)	5 HZ	+1.25% of Indication
Afterburner Fuel Used	0 to 89 kN (0 to 20,000 lb)	5 HZ	+1.25% of Indication
Mixed Turbine Discharge Pressure ( $P_{T7M}$ )	35 to 420 kN/m <sup>2</sup> (5 to 60 psia)	5 HZ	+1.0 kN/m <sup>2</sup> (+0.15 psi)
Nozzle Area ( $A_{10}$ )	0.325 to 0.7m <sup>2</sup> (3.5 to 7.5ft <sup>2</sup> )	10 HZ	+0.0028m <sup>2</sup> (+0.03 ft <sup>2</sup> )
Power Lever Position	0. to 120°	5 HZ	+1°

\* Accuracies based on a 2.33 sigma deviation.

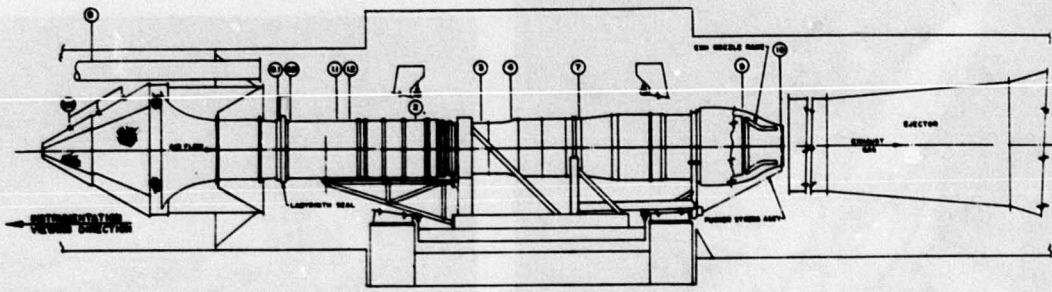
204 kN/m<sup>2</sup> (4250 lb/ft<sup>2</sup> to 5.76 kN/m<sup>2</sup> (120 lb/ft<sup>2</sup>) absolute pressure with temperatures which vary from -54°C (-65°F) to +160°C (+320°F). Maximum continuous design exhaust temperature is 1927°C (3500°F) and exhaust pressures range from 101 kN/m<sup>2</sup> (2116 lb/ft<sup>2</sup>) to 2.71 kN/m<sup>2</sup> (56.6 lb/ft<sup>2</sup>) absolute. The ATF test cell instrumentation and instrumentation accuracies are tabulated in Table II.

The engine airflow characteristics were measured utilizing a bellmouth inlet and circular duct containing temperature and pressure instrumentation calibrated independently by the choked nozzle measurement technique. As shown in Figure 6, Station 1.1, airflow measurement instrumentation consisted of: (a) four wall mounted static pressure sources, (b) two wall mounted 5 probe total temperature rakes and (c) two total pressure rakes arranged with probes to evaluate total pressure across the duct in ten concentric equal areas. A six probe wall mounted boundary layer rake sampled the 10% of the cross sectional area closest to the duct walls. A nine probe integrating type rake spanned the diameter of the duct and sampled the remaining 90% of the cross sectional area.

The ABPD was determined as the difference between the engine turbine discharge pressure, measured with production engine instrumentation, and the nozzle discharge pressure, measured with a water cooled total pressure rake. The pressure drop measuring station, as shown in Figure 6, Station 9; was located just downstream of the afterburner inner liner and upstream of the variable position exhaust nozzle throat. Eighteen total pressure fingers equally spaced spanned the nozzle to determine the pressure profile across the main gas stream. To more completely define the profile across the entire gas stream, wall static pressures were taken at the afterburner liner in addition to total and static readings in the cooling stream passage. All pressure readings were area weighted to obtain a representative pressure level at the measuring station. The nozzle area was increased to account for the blockage of the pressure rake.

The gross thrust nozzle coefficient,  $C_g$ , was computed as the ratio between actual measurement of engine gross thrust at the simulated flight condition, using load cells and a tension flexure thrust stand installed in the test cell, and the calculated ideal gross thrust for the simulated conditions as discussed in Section 4.2.

24-6



24-7

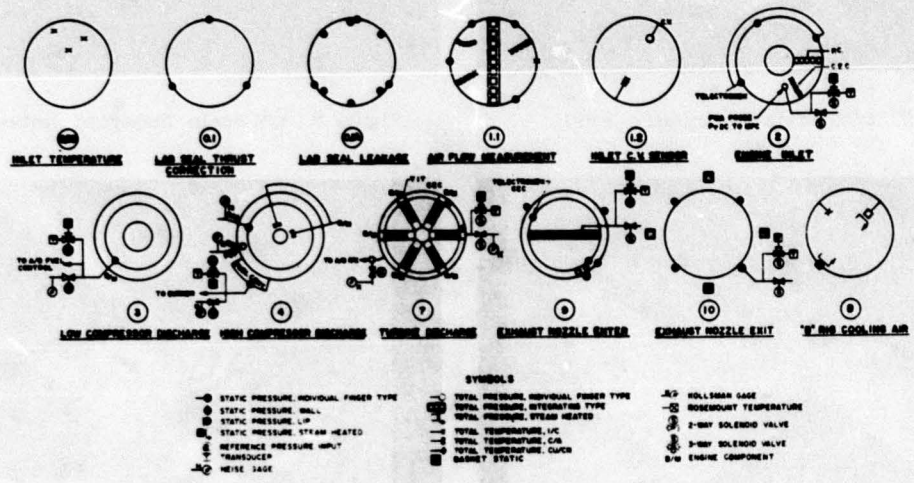


Figure 6 ATF Engine Installation and Instrumentation Diagram

TABLE II

ATF Test Instrumentation

Parameter	Measurement Range	Estimated Accuracy
Pressures Pt2.1, Pt7M, Pt9 & P10	3.5 to 210 kN/m <sup>2</sup> (0.5 to 30 psia)	+ 0.175 kN/m <sup>2</sup> (0.025 psi)
Pressures Pt7M & Pt9	35 to 2100 kN/m <sup>2</sup> (5 to 300 psia)	+ 1.0 kN/m <sup>2</sup> (0.15 psi)
Pressures Pt1.1 & P1.1	3.5 to 31.5 kN/m <sup>2</sup> (0.5 to 4.5 psia)	+ 0.042 kN/m <sup>2</sup> (0.006 psi)
Total Temperatures TTo, Tt1.1 & Tt2	I/C (Iron-Constantan) Thermocouples	+ 1.7°C (3°F)
Engine Component Total Temperatures (see Fig. 6)	C/A (Chromel-Alumel) Thermocouples	+ 3.3°C (6°F)
Fuel Flowmeters:		
3/4 inch diameter	0 to 4,400 kg/hr (0 to 10,000 lb/hr)	+ 0.3% of value
1 1/4 inch diameter	0 to 16,000 kg/hr (0 to 35,000 lb/hr)	+ 0.3% of value
2 inch diameter	0 to 32,000 kg/hr (0 to 70,000 lb/hr)	+ 0.3% of value
Rotation Speeds	0 to 16,000 RPM	+ 0.01% of value
Nozzle Area	0.325 to 0.7m <sup>2</sup> (3.5 to 7.5 ft <sup>2</sup> )	+ 0.2% of value
Thrustmeters	22.3 kN (5,000 lb) Range	+ 0.067 kN (15 lb)
	44.6 kN (10,000 lb) Range	+ 0.134 kN (30 lb)
	89.2 kN (20,000 lb) Range	+ 0.267 kN (60 lb)

2.4 Wind Tunnel Models

Aerodynamic force and moment, induction system, propulsion nozzle/afterbody and reference backend wind tunnel models were used to establish model drag through state-of-art wind tunnel test techniques and procedures.

Subsonic and transonic aerodynamic force and moment data were obtained with a 1/16 scale model (shown in Figure 7). Supersonic aerodynamic force and moment data were obtained with a 1/22 scale model. Internal drag and mass flow were determined on these models through separate calibration of a single inlet probe against a 48 probe nozzle exit rake. Cylindrical reference nozzles were incorporated on these models for a portion of the wind tunnel tests to provide a common reference drag configuration between the aerodynamic and propulsion model tests. High-lift configuration force and moment data were obtained with a 1/10 scale model.

The induction system model, Figure 8, is an accurate 1/7 scale representation of the inlet, inlet variable geometry, internal ducting and adjacent external lines. The induction system model was instrumented to provide data on inlet drag variation with mass flow, inlet pressure recovery and distortion and turbulence.

The propulsion nozzle/afterbody model is a 1/12 scale duplication of the aircraft backend mounted behind a nose-supported forebody/wing combination as shown in Figure 9. The model had provisions for

24-8

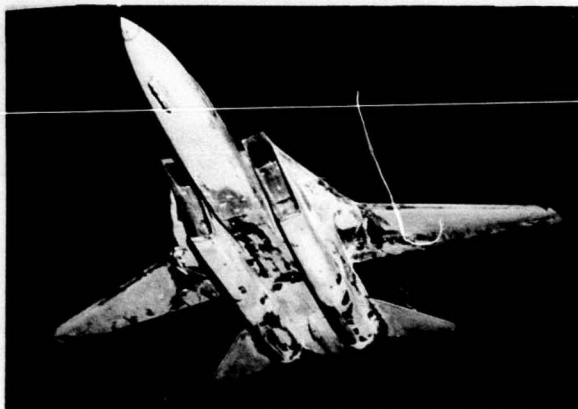


Figure 7 1/16 Scale Aerodynamic Model

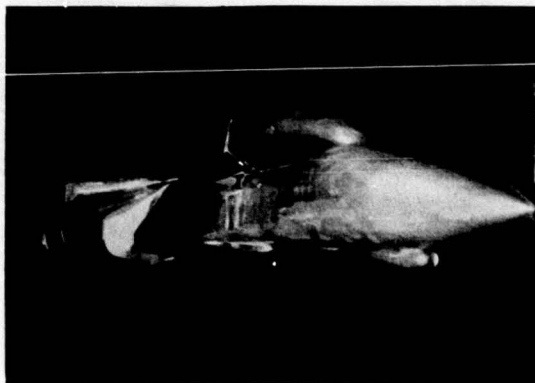


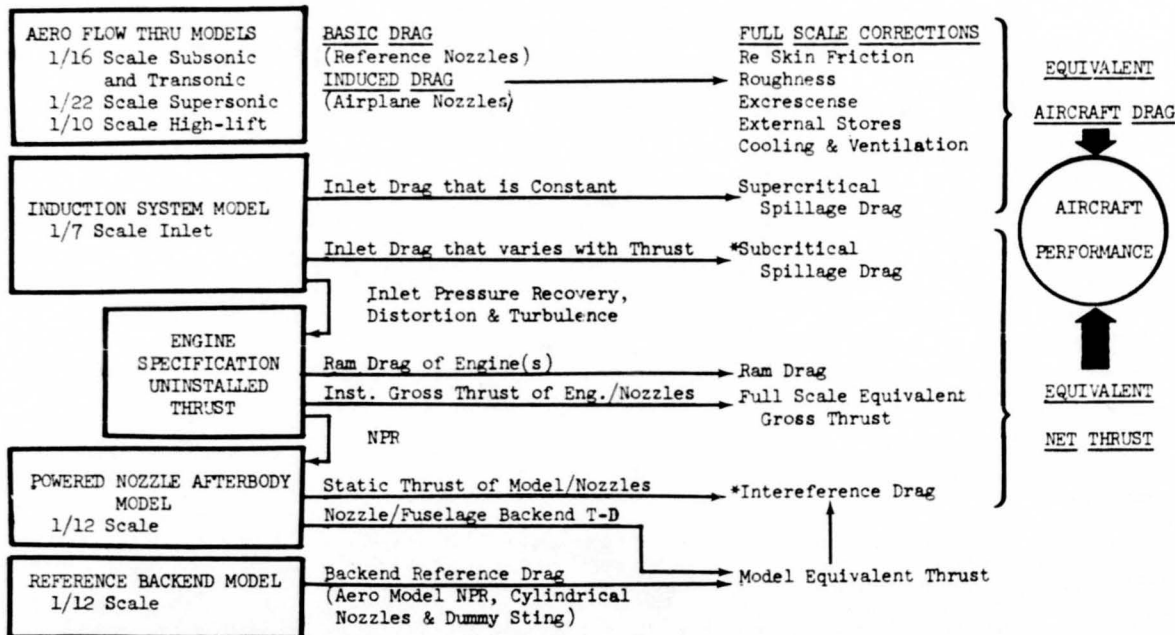
Figure 8 1/7 Scale Induction System Model



Fig. 9 1/12 Scale Propulsion Nozzle/Afterbody Model



Figure 10 1/12 Scale Reference Backend Model



\*Wind Tunnel Data Utilized in In-Flight Thrust Calculation Procedure.

Figure 11 Thrust/Drag Bookkeeping Procedures

duplicating flight exhaust nozzle and exhaust nozzle flow conditions to determine nozzle thrust losses, nozzle pressure drag and interference, and the influence of exhaust flow on the nozzle and fuselage afterbody.

The reference backend model, Figure 10, is the propulsion nozzle/afterbody model with the nozzle/afterbody replaced by a duplication of the aerodynamic force model afterbody, including cylindrical nozzles,

aero model exhaust conditions and dummy sting support arrangement.

24-9

Wind tunnel facilities utilized during the conduct of wind tunnel test program included the NASA Langley Research Center 16 ft Transonic and 4 ft Unitary Plan supersonic wind tunnels, the NASA Ames Research Center 12 ft Pressure Tunnel, and the Cornell Aeronautical Laboratory 8 ft Transonic Tunnel.

### 3.0 WIND TUNNEL THRUST AND DRAG ACCOUNTING

The basis used for thrust and drag bookkeeping in estimating full scale aircraft performance is outlined in Figure 11 and is composed of three major elements: (1) Equivalent Aircraft Drag, (2) Equivalent Net Thrust, and (3) a Reference Configuration.

#### 3.1 Equivalent Aircraft Drag

All force components independent of power setting are accounted for in equivalent aircraft drag. The aerodynamic model testing provided data on aircraft form drag, external store drag and friction drag at model scale Reynolds number and boundary layer transition conditions. These data were obtained from the aerodynamic force and moment models and induction system models discussed in Section 2.4. The remainder of the equivalent aircraft drag components are determined by accepted theoretical or empirical methods. These adjustments include: (1) correction between model and full scale skin friction drag, (2) roughness drag, (3) excrescence drag not duplicated on the model, and (4) cooling and ventilation drag. In addition, all drag values below 0.9M were adjusted for a beneficial effect on drag due to lift observed from wind tunnel tests as the tunnel Reynolds number was increased.

#### 3.2 Equivalent Net Thrust

All drag components which are functions of thrust level are accounted for in equivalent net thrust. Equivalent net thrust is defined as engine net thrust adjusted for propulsion system drag items. Operation of the propulsion system in an airplane produces mutual interactions between internal and external flow near the inlets and exhaust nozzles. Because these interactions vary with engine operation, it is convenient to include their effects in the installed thrust determination and avoid changes in aerodynamics, especially induced drag, due to changes in power setting. These items include subcritical inlet spillage drag and nozzle interference drag and were determined during wind tunnel testing with the induction system model and propulsion nozzle/afterbody models described in Section 2.4. Since it is currently not possible to measure inlet subcritical spillage drag and nozzle interference drag in flight, these wind tunnel determined results were also incorporated in the in-flight thrust calculation procedure outlined in Section 4.2 to determine full scale drag.

#### 3.3 Reference Configuration

Conventional aerodynamic wind tunnel tests do not accurately simulate the flow conditions that exist on the airplane in the presence of the operating engine nozzle. To address this situation a reference configuration was established to provide an interface between aerodynamic and propulsion wind tunnel model investigations. This method recognizes and accounts for a number of complex flow interactions associated with airframe/engine integration. The reference configuration consisted of a twin sting supported model (dummy stings were installed for the propulsion model reference condition) incorporating cylindrical nozzles in place of the actual airplane nozzles, as shown in Figure 10. The utilization of the reference nozzles during both aerodynamic force testing and propulsion installed nozzle tests established a base from which the effects of operating nozzle pressure ratio could be determined.

### 4.0 FLIGHT TEST DRAG MEASUREMENT

#### 4.1 General

Three-dimensional equations for in-flight lift and drag determination of aircraft without lateral thrust inclination angles are as follows:

$$\text{Lift } L = -F_g \sin(\alpha + \tau) + W T a_{zFP} \quad (1)$$

$$\text{Drag } D = F_g \cos(\alpha + \tau) \cos \beta + F_g \sin \beta - F_r \cos \beta - W T a_{xFP} \quad (2)$$

In equations (1) and (2) the longitudinal thrust inclination angle ( $\tau$ ) is constant, the aircraft weight (WT) can be readily accounted for, and test procedures ensure that the sideslip angle ( $\beta$ ) be zero or held to a minimum. It can be seen, therefore, that the calculation of lift and drag are dependent on accurate determination of gross thrust and ram drag ( $F_g$  and  $F_r$ ), the longitudinal and normal acceleration along the flight path ( $a_{xFP}$  and  $a_{zFP}$ ), and angle of attack ( $\alpha$ ). The approach to measurement of these items, as discussed in this paper, involved laboratory calibrations and accurate in-flight measurement of the required instrumentation parameters, integration of theoretical computations with calibration data from isolated engine tests and the use of wind tunnel data to adjust in-flight measured thrust for the effects of propulsion system drag items. Analytical methods, ground check procedures and flight test data were employed to obtain the effects of nose boom bending and upwash characteristics on angle of attack measurement.

Paragraphs 4.2, 4.3 and 4.4 discuss the primary techniques and methods for measurement of thrust, acceleration and angle of attack. However, additional approaches were employed to assure consistency and continuity of results and for crosscheck purposes.

Paragraphs 4.5 and 4.6 and 4.7 present and discuss the results of drag data obtained by steady-state, quasi steady-state, and dynamic test techniques; and correlation between these techniques.

The flight lift/drag data presented in this Section and in Section 5 has evolved through continual refinement and iteration as updated isolated engine information, wind tunnel data and flight data pertinent

to thrust, acceleration and angle of attack measurement became available.

24-10  
 Primary test techniques employed were quasi steady-state and dynamic maneuvers because of the large quantity of data that can be obtained by these methods. Steady-state data were also obtained to verify the validity of data obtained from quasi steady-state and dynamic maneuvers.

The drag data presented in this Section and in Section 5 are adjusted to a common set of conditions to enhance data generalization and for comparison with wind tunnel data. These conditions include:  
 (1) trim for zero pitching moment at a common center of gravity position consistent with wing sweep position,  
 (2) common Reynolds number based on 10,668 m (35,000 ft) altitude for skin friction drag and (3) the removal of the increment of lift contributed by the component of engine thrust in calculating aircraft lift. Thrust/drag scales are not included on graphs because of security considerations.

#### 4.2 Thrust Measurement

The engine gross thrust,  $F_g$ , and ram drag,  $F_r$ , terms of equations (1) and (2) were determined from in-flight measurements and isolated engine ATF test data using the following relationships:

$$F_g = F_{gi} C_g \quad (3) \quad F_r = (W_a V_T)/g \quad (4)$$

where  $F_{gi}$  is defined as the ideal gross thrust obtained when the nozzle flow is isentropically expanded to free stream pressure. The ideal gross thrust for unchoked and choked nozzle flow conditions, as derived in references (2) and (5) in various forms, are defined by the following:

$$\text{Unchoked } F_{gi} = P_a A_{10} \left[ \frac{2\gamma}{\gamma-1} \right] \left[ \left( \frac{P_{T10}}{P_a} \right)^{(\gamma-1)/\gamma} - 1 \right] \quad (5)$$

$$\text{Choked } F_{gi} = P_{T10} A_{10} \gamma \left[ \frac{2}{\gamma+1} \right]^{\gamma/(\gamma-1)} \left[ \frac{\gamma+1}{\gamma-1} \right]^{1/2} \left[ 1 - \left( \frac{1}{P_{T10}/P_a} \right)^{(\gamma-1)/\gamma} \right]^{1/2} \quad (6)$$

In equations (3), (4), (5) and (6);  $\gamma$  and  $g$  are constants;  $V_T$ ,  $A_{10}$  and  $P_a$  are obtained by direct in-flight measurements; and  $W_a$ ,  $P_{T10}$  and  $C_g$  are obtained indirectly by in-flight measurements in conjunction with engine ATF calibration data. ATF calibration data for these items were obtained on TF30-P-412 engines during engine development testing.

The engine airflow,  $W_a$ , as a function of corrected low pressure compressor RPM,  $N_1/\sqrt{\theta_{T2}}$ , was measured using a calibrated bellmouth and circular inlet duct as discussed in Section 2.3. This method was used in lieu of in-flight data obtained from the 40 probe inlet compressor face rake discussed in Section 2.2 for reasons of accuracy. Airflow accuracy obtained by the ATF calibration method is estimated to be  $\pm 0.8\%$  based on a theoretical error analysis and is independent of inlet distortion. The accuracy of obtaining airflow measurements with the 40 probe inlet rake, assuming no distortion or temperature gradients in the inlet, is estimated to be  $\pm 2$  to  $4\%$  depending on inlet airflow velocity. The inlet rake data were used to obtain inlet pressure recovery and inlet pressure distortion at the compressor face. The variation of corrected airflow with corrected low pressure compressor RPM and engine pressure ratio is represented in Figure 12.

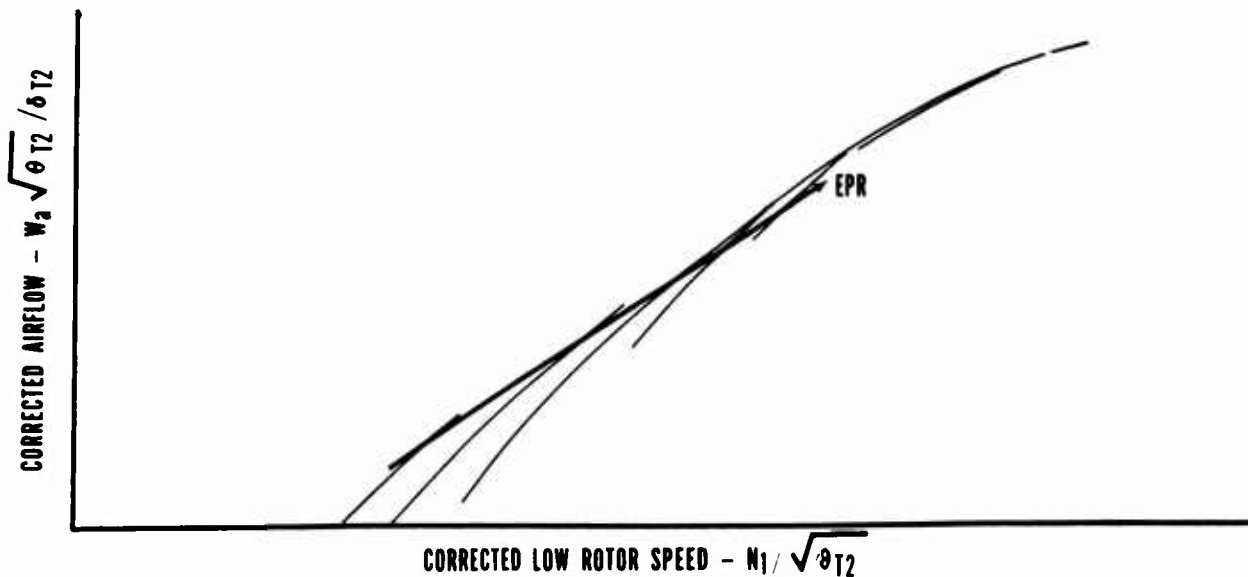


Figure 12 ATF Engine Airflow Calibration

The nozzle discharge pressure,  $P_{T10}$ , was obtained at engine operating conditions by measuring the turbine discharge pressure and applying a correction factor for the pressure drop to the nozzle exit plane. The turbine discharge pressure,  $P_{T7M}$ , was measured using production engine instrumentation consisting of six probes spanning both the fan discharge and turbine discharge passages. The probes are manifolded together externally to provide a single source of average pressure,  $P_{T7M}$ , ( $P_{T7}$  mixed). The pressure loss in the afterburner was established from engine ATF tests as discussed in Section 2.3 using a water cooled pressure rake to measure the nozzle discharge pressure at the nozzle throat. The pressure drop in the afterburner represents the summation of the effects of aerodynamic drag of the internal hardware plus the momentum pressure change resulting from the addition of heat. The aerodynamic drag is a function of afterburner inlet Mach number, whereas the momentum change is a function of both the afterburner inlet Mach number and the afterburner temperature ratio. The ABPD correction is represented in Figure 13 for AB and

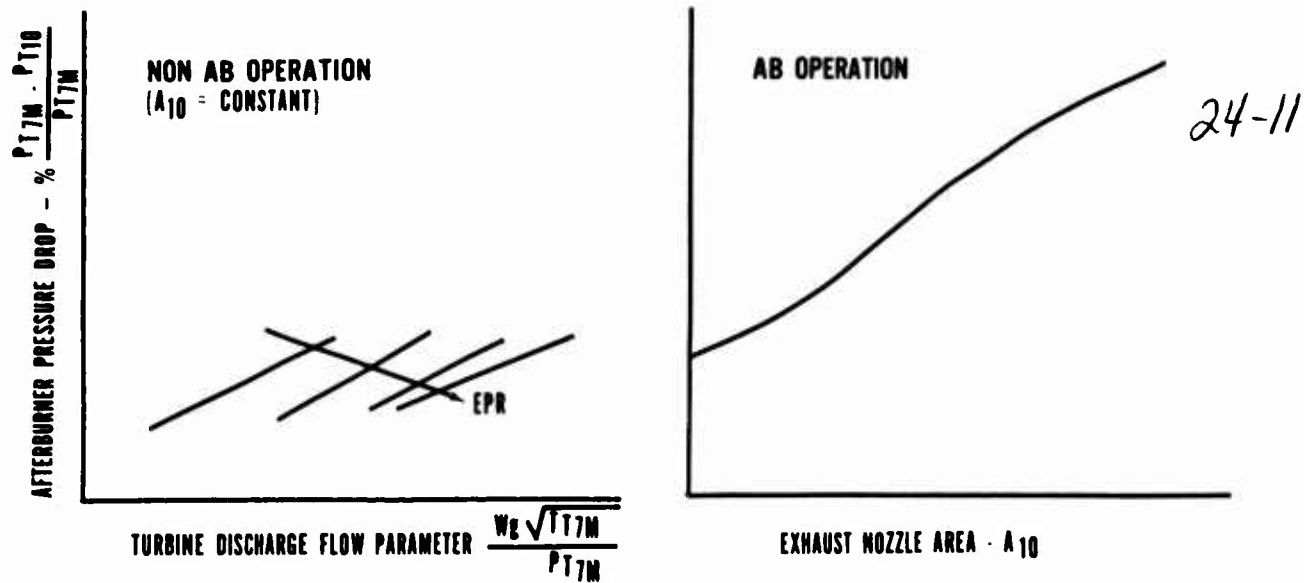


Figure 13 ATF Afterburner Pressure Drop Calibration

non AB engine operation. The ABPD is correlated with nozzle area,  $A_{10}$ , for AB operation and with engine pressure ratio,  $P_{T7M}/P_{T2}$ , and the turbine discharge flow parameter,  $W_g \sqrt{T_{T7M}}/P_{T7M}$ , for non AB operation. The mixed turbine discharge total temperature,  $T_{T7M}$ , used to compute the turbine discharge flow parameter is derived empirically from compressor inlet total temperature and engine fuel/air ratio.

The gross thrust coefficients used for in-flight thrust calculations were computed as the ratio between actual measurement of engine gross thrust at the ATF simulated flight condition and the calculated ideal gross thrust for the simulated conditions using equations (5) and (6). The actual gross thrust,  $F_{ga}$ , is the summation of the thrust stand meter measurement and the momentum and pressure forces acting on the engine in the test cell:

$$F_{ga} = F_m + W_a/g (V_{1.1}) + A_{1.1} (P_{1.1} - P_{10}) \quad (7)$$

(see Figure 6 for measurement planes) where the thrust meter force,  $F_m$  was obtained by load cell measurement of the engine axial force from a tension flexure thrust stand installed in the test cell.

The basic  $C_g$  curves for AB and non AB engine operation are functions of nozzle pressure ratio and exhaust nozzle area are shown in Figure 14. The basic  $C_g$  is modified by a delta  $C_g$  to account for the decrease in engine thrust caused by degradation in the  $P_{T7}$  station mixing characteristics with increases in engine air bypass ratio. This adjustment is represented in Figure 15 in which delta  $C_g$  is presented as functions of both nozzle pressure ratio and engine pressure ratio.

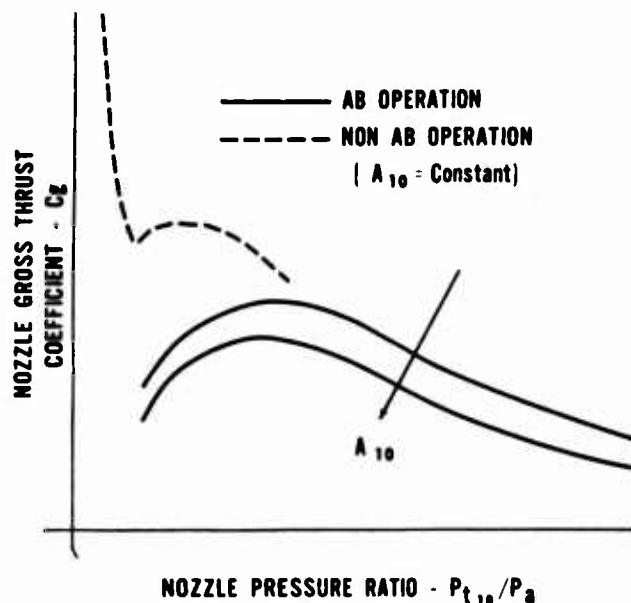


Figure 14 ATF Nozzle Calibration

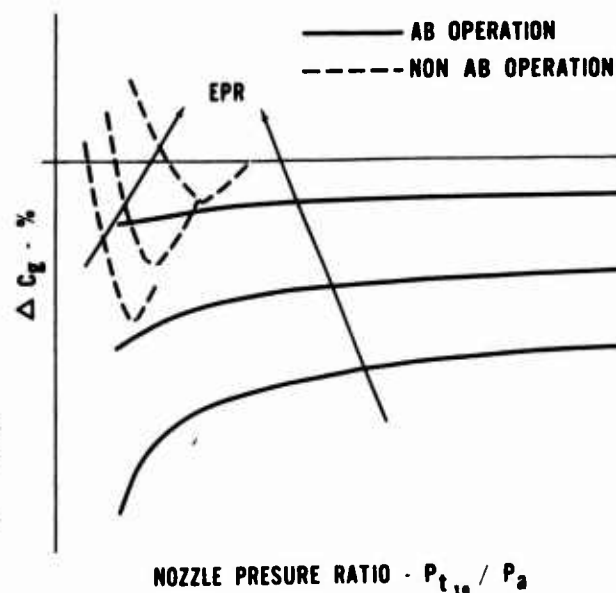


Figure 15 EPR Incremental Effect on Nozzle Calibration

Finally, the in-flight engine thrust resulting from the above procedures was adjusted to include the effects of propulsion system drag items resulting from mutual interaction between internal and external flow near the inlets and exhaust nozzles as discussed in Section 3.2. Since these items cannot be measured in-flight, the results of wind tunnel tests for subcritical inlet spillage drag and nozzle interference drag were used to make this adjustment. It is recognized that this latter procedure could cause problems in drag

24-12 generalization if subcritical inlet spillage drag and nozzle interference drag are influenced by Reynolds number.

#### 4.3 Excess Thrust Measurement

Resolution of excess thrust by the energy method requires evaluation of the "time dependent" variables, airspeed and altitude, through differentiation. Any error in the measurements is amplified by the differentiation and the magnitude of the time interval used for the differentiation may significantly effect the results. This process results in excessive scatter for drag data determined by that procedure. The accelerometer method, however, is "time independent" or instantaneous in that a measurement of acceleration along with flight path is a direct measure of excess thrust.

Significant improvement in the accuracy of the accelerometer ( $\pm 0.001g$  for longitudinal acceleration) in controlled temperature environments has been achieved making it an extremely useful device in determining aircraft excess thrust. Two applications of the accelerometer consider the location of (a) a three-axis accelerometer package oriented parallel to the Body Axes of the vehicle and (b) a nose boom mounted angle of attack vane accelerometer package oriented along the flight path of the vehicle. The equations developed for either of these applications are independent of flight path or vehicle attitude restrictions. The flight path accelerometer is less sensitive to errors in measurement of angle of attack but may present environmental control problems for supersonic aircraft because of aerodynamic heating. The body axes accelerometers, on the other hand, are less sensitive to errors in pitch rate measurement due to their proximity to the aircraft center of gravity and environmental control problems are also less severe.

A temperature controlled body axes accelerometer package was chosen for installation in the test aircraft because its supersonic flight envelope made the survivability and accuracy of a flight path accelerometer questionable without expensive and complicated cooling provisions. Laboratory calibration of the body axes accelerometers included checks for cross-axis sensitivity and for temperature sensitivity.

The acceleration along the flight path for calculating lift and drag in equations (1) and (2) are represented by the following relationships as derived in reference (6):

$$a_{xPP} = a_{xNet} \cos(\alpha + p) \cos \beta + a_{yNet} \sin \beta - a_{zNet} \sin(\alpha + q) \cos \beta \quad (8)$$

$$a_{zPP} = a_{xNet} \sin(\alpha + p) + a_{zNet} \cos(\alpha + q) \quad (9)$$

where  $p$  and  $q$  are misalignment corrections.

Since the body axes accelerometers are displaced from the center of gravity of the vehicle by values by  $r_x$ ,  $r_y$  and  $r_z$  measured along the body axes the accelerometers also experience accelerations due to rotation of the body axis and their output must be corrected for those effects:

$$a_{xNet} = a_x + 1/g [r_x (\dot{\theta}^2 + \dot{\psi}^2) + r_y (\ddot{\psi} - \dot{\psi} \dot{\theta}) + r_z (\ddot{\theta} + \dot{\theta} \dot{\psi})] \quad (10)$$

$$a_{yNet} = a_y + 1/g [-r_x (\ddot{\psi} + \dot{\psi} \dot{\theta}) + r_y (\dot{\theta}^2 + \dot{\psi}^2) - r_z (\dot{\theta} - \dot{\psi} \dot{\theta})] \quad (11)$$

$$a_{zNet} = a_z + 1/g [-r_x (\ddot{\theta} - \dot{\theta} \dot{\psi}) + r_y (\ddot{\psi} + \dot{\psi} \dot{\theta}) + r_z (\dot{\theta}^2 + \dot{\psi}^2)] \quad (12)$$

These acceleration equations, corrected for cross axis sensitivity, are utilized in equations (1) and (2) to determine in-flight lift and drag from quasi steady-state maneuvers.

The airplane drag during dynamic maneuvers is obtained by applying increments in drag starting from the trim condition. While the lift equation (equation (1)) is used to calculate instantaneous lift at the trim (stabilized) condition and then at  $L_1, L_2 \dots L_n$  during the maneuver, the drag equation (equation (2)) is used to obtain only the airplane drag at the trim condition. The equations for computing drag incrementally; i.e. adding drag increments from point to point during the maneuver, are derived in reference (6) and involve resolution of the incremental angle of attack and acceleration changes during the maneuver.

#### 4.4 Angle of Attack Measurement

In-flight angle of attack was obtained from the nose boom mounted angle of attack vane system, shown in Figure 4, adjusted for the effects of nose boom misalignment and bending, fuselage bending, vane position pitch rate and nose boom upwash by the equation:

$$\alpha_T = \alpha_i + \Delta \alpha_{MISAL} + \Delta \alpha_{NBB} + \Delta \alpha_{FUSB} + \Delta \alpha_{PITCH} - \Delta \alpha_{UPWASH} \quad (13)$$

where  $\alpha_i$  is the indicated nose boom angle of attack.  $\alpha_i$  was calibrated through the signal conditioning and recording system using a calibrated boom mounted throw-board before and after each flight.

Nose boom misalignment,  $\Delta \alpha_{MISAL}$ , was determined through optical measurement. The nose boom bending,  $\Delta \alpha_{NBB}$ , due to inertia loads was determined by statically loading the boom with weights and the deflection at the angle of attack vane location measured optically. Nose boom bending due to aerodynamic loads was considered as part of the boom upwash calibration. Fuselage bending,  $\Delta \alpha_{FUSB}$ , was determined from static structural testing in the same manner.

The correction due to pitching velocity,  $\Delta \alpha_{PITCH}$  was computed from the equation:

$$\Delta \alpha_{PITCH} = R \theta / V_T \quad (14)$$

where R is the distance from the aircraft center of gravity to the nose boom vane location.

The nose boom upwash,  $\Delta \alpha$  UPWASH, was determined from in-flight calibration in which the indicated vane angle of attack, corrected for all of the above items, was compared with the airplane sensitive pitch attitude gyro during steady-state maneuvers.

24-13

The nose boom angle of sideslip,  $\beta$ , vane system was calibrated in the same manner as the angle of attack system.

#### 4.5 Steady-State Test Technique

The steady-state test technique is based on the premise that engine thrust equals aircraft drag for stabilized flight conditions (no acceleration along the flight path). The test technique consists of stabilizing the airplane in altitude and airspeed at the desired trim conditions and recording any aircraft motions over a time interval of approximately three minutes. The airplane drag is determined through evaluation of engine performance as outlined in Section 4.2 with adjustment for any residual excess thrust using the energy method. The residual excess thrust is determined from time-histories of altitude and airspeed.

Figure 16 presents the baseline drag polar obtained by this technique for two airplanes with three different sets of engines. The data were obtained over the entire Mach/altitude cruise flight regime at a constant wing sweep angle ( $22^\circ$ ), constant nozzle area ( $3.53\text{ft}^2$ ) and over a nozzle pressure ratio range of 1.4 to 2.6. The data are presented for only those test points at lift coefficients and airspeeds below drag divergence.

The aerodynamic configuration utilized for earlier flights of airplane number 8 was duplicated, after a six month period in which the effect many aerodynamic changes were investigated, to evaluate any change in the baseline configuration.

The generalized data of Figure 16 show a remarkable independence of altitude, engine installation, nozzle pressure ratio and airplane (for the two aircraft investigated). All data fall with a scatter band of  $\pm 1.0\%$ . The mean deviation for the 48 data points of Figure 16 is  $\pm 3$  drag counts. Assuming no errors in drag adjustment for residual excess thrust, the data scatter is attributable to the ability to determine in-flight gross thrust and ram drag using the procedures discussed in Section 4.2.

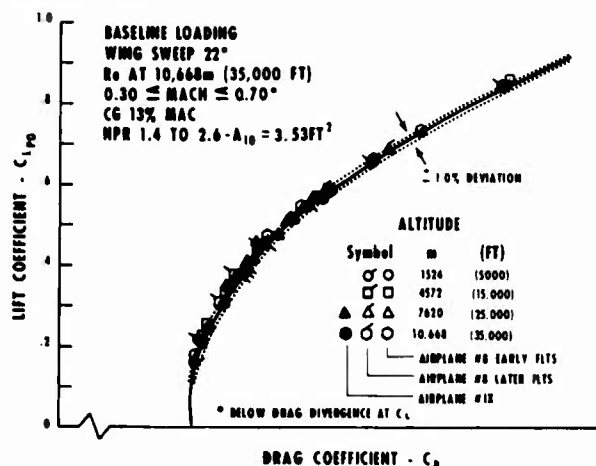


Figure 16 Steady-State Test Technique

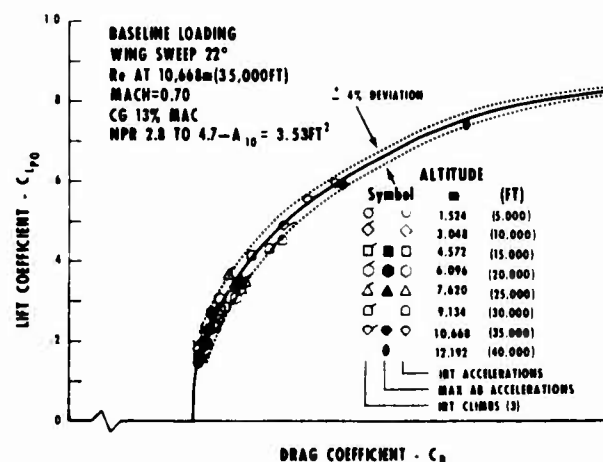


Figure 17 Quasi Steady-State Test Technique

#### 4.6 Quasi Steady-State Test Technique

The quasi steady-state test technique is based on evaluation of aircraft drag from equations (1) and (2) as the difference between measured engine net thrust and airplane excess thrust from acceleration along the flight path. The primary test maneuvers employed in evaluation of aircraft drag by this method were constant altitude accelerations and decelerations and constant Mach climbs. In-flight engine thrust is determined by the procedures outlined in Section 4.2 and airplane excess thrust from the body axes accelerometers as discussed in Section 4.3.

Figure 17 presents a  $0.7M$ ,  $22^\circ$  wing sweep drag polar derived from an accumulation of quasi steady-state drag data obtained during constant Mach climbs and intermediate and maximum afterburner thrust constant altitude accelerations. These data were obtained over the altitude range 1,524 m (5,000 ft) to 12,192 m (40,000 ft) with nozzle pressure ratios varying from 2.8 to 4.7. The fairing through the data is identical to the fairing through the steady-state data of Figure 16 except that  $0.7M$  drag divergence is included at lift coefficients greater than 0.60. The results show excellent drag level correlation between steady-state and quasi steady-state drag measurement techniques.

Figure 18 presents airplane minimum drag variation with Mach number obtained from sixteen (16) maximum afterburner constant altitude accelerations over various Mach increments covering the Mach range  $0.8M$  to near  $2.0M$  and altitude range 4,752 m (15,000 ft) to 13,720 m (45,000 ft). The nozzle pressure ratio during these maneuvers varied from 4 to 8. Wing sweep was varied as a function of Mach number as shown in Figure 18. Minimum drag at a given Mach number was obtained from faired Mach versus  $C_L$  and  $C_D$  curves by subtracting induced drag from measured airplane drag at the test lift coefficient. The airplane induced drag characteristics were determined independently using primarily the dynamic test

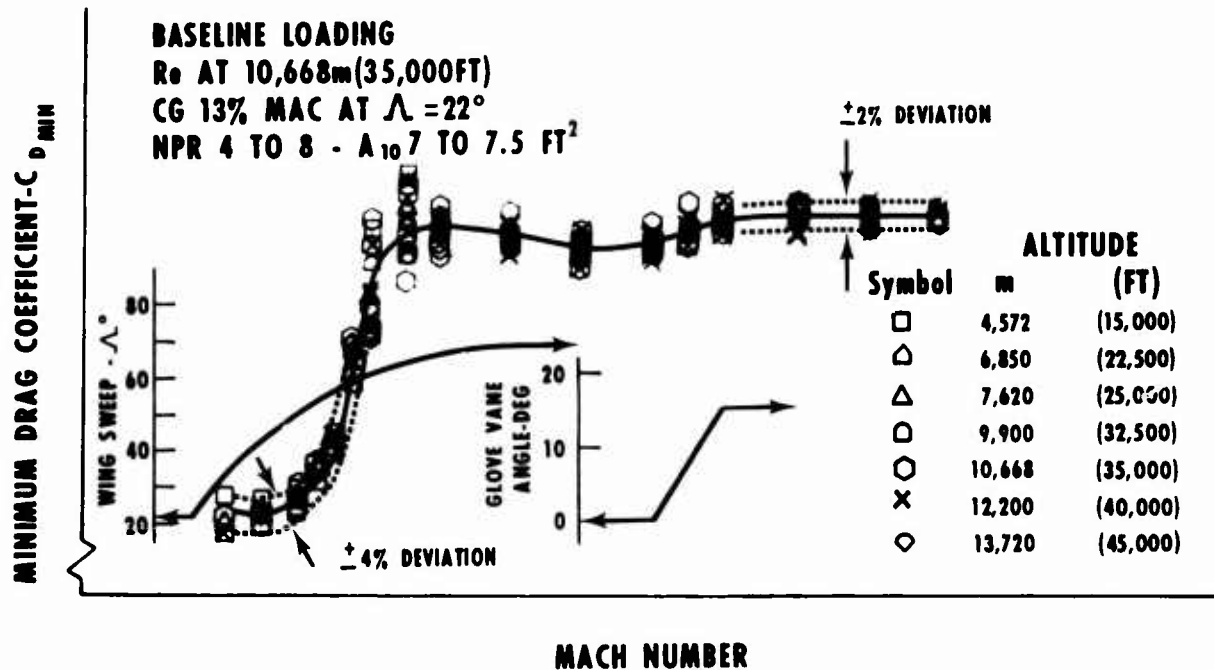


Figure 18 Maximum Afterburner Accelerations

technique discussed in Section 4.7.

No trends are discernible from the drag data of Figures 17 and 18 for altitude or nozzle pressure ratio. Excluding the 0.95 to 1.05 Mach regime of Figure 18, where airspeed and angle-of-attack measurements are uncertain because of the effect of the airplane normal shock on the sensors for these parameters, the random data scatter for the quasi steady-state maneuvers varies between + 4% subsonic to + 2% near 2.0M. The items that may contribute to these random errors are: (1) basic thrust measurement accuracy (+ 1% from paragraph 4.5), (2) transient nature of thrust measurement during these maneuvers, (3) accelerometer accuracy (approximately + 1%), (4) shifts in accelerometer bias during flight and from flight to flight, and (5) errors in angle of attack measurement. The significance of this data scatter over that obtained by the steady-state technique is somewhat diminished because of the large quantity of data that can be obtained using quasi steady-state test techniques. Note that, despite the data scatter, the drag increase produced by extension of the glove vane in the mid supersonic Mach range is readily discernible.

#### 4.7 Dynamic Test Technique

Induced drag definition by the steady-state technique requires a substantial amount of flight time because only one data point can be obtained for every 2 - 3 minute stabilized flight period. The dynamic test technique, using highly accurate accelerometers to measure aircraft acceleration in wind-up/down turns and push-over/pull-up (roller coaster) maneuvers, allow collection of a large number of data points in 20 - 30 seconds covering a wide range of lift coefficients at a given Mach number. Dynamic test maneuvers differ from quasi steady-state maneuvers in that they are performed at acceleration levels significantly greater or less than 1 g. These maneuvers reduce the flight time required to obtain lift/drag/angle of attack relationships by approximately 70%.

Unlike the steady-state and quasi steady-state maneuvers, accuracy and repeatability are highly dependent on pilot technique. Dynamic test maneuvers must be performed slowly, smoothly and uniformly and be flown at low pitch rates (not more than 1.5 degrees/sec) and at pitch rate variations as small and gradual as possible. Wind-up turn and push-over/pull-up maneuvers are performed after a 2 - 3 minute stabilization at Mach and altitude to obtain a trim base drag level from which drag variation with lift coefficient is obtained from resolution of incremental angle of attack and acceleration changes during the maneuver. In the wind-up turn maneuver, bank angle and normal acceleration are gradually increased to a maximum of 3.0 g holding thrust and Mach constant. In the push-over/pull up maneuver, a slow 0 to 2.0 g (maximum) push-over/pull-up is performed while holding thrust constant.

Figure 19 presents representative subsonic, transonic and supersonic drag polars obtained by dynamic test techniques at 0.7M, 22° wing sweep; 0.95M, at a mid wing sweep position; and 1.2M and 2.0M at 68° wing sweep. These data were obtained over the altitude range 1524 m (5,000 ft) to 16,450 m (54,000 ft). Adjustment of trim drag to steady-state and/or quasi steady-state trim drag levels was required for some maneuvers because of disagreement probably caused by an insufficient stabilization period to establish the exact trim drag level. Figure 19 shows excellent drag polar definition to lift coefficients not obtainable by the steady-state or quasi steady-state techniques and with results independent of altitude. Data scatter is about equivalent to the quasi steady-state technique and, again, decreases with increasing Mach number. As for the quasi steady-state test technique, the significance of data scatter using the dynamic technique is diminished because of the large number of data points obtainable.

Subsonic 22° wing sweep dynamic maneuvers performed in .05M increments from 0.5M to 0.85M have allowed easy definition of drag divergence variation with Mach number and lift coefficient.

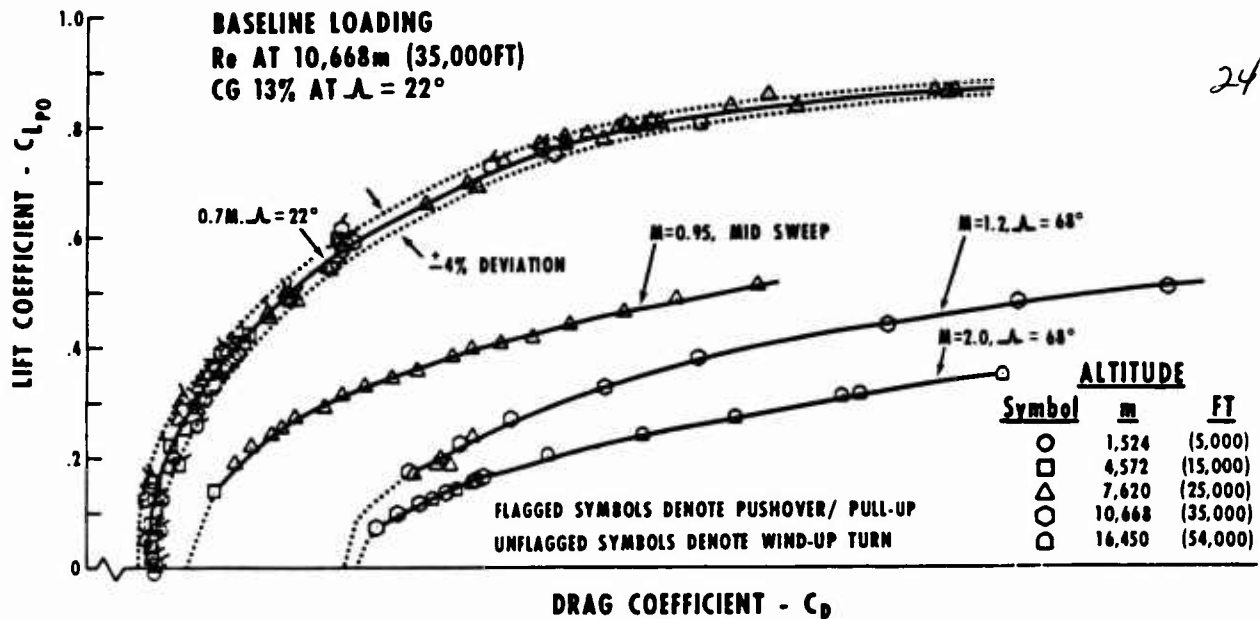


Figure 19 Dynamic Test Technique

## 5.0 FLIGHT - WIND TUNNEL DRAG COMPARISONS

### 5.1 General

The evaluation of the test vehicle drag characteristics and drag components are currently under investigation utilizing the drag measurement techniques and procedures outlined in this paper. Although this program is not yet complete, sufficient data have been accrued to commence appraisal of the results against wind tunnel based estimates for full scale drag. The wind tunnel results used for this comparison are reported in reference (7) except for adjustments to: (1) account for differences between wind tunnel model and test aircraft aerodynamic configuration and (2) correct isolated areas of wind tunnel analyses resulting from attempts to rationalize differences between flight and wind tunnel data. The procedures and methods for adjustment of wind tunnel data from model test conditions to full scale estimated drag are discussed in reference (7). The flight data are adjusted to a common set of conditions consistent with the wind tunnel analysis (Reynolds number, CG, thrust effects, etc.) as discussed in Section 4.1. Selected items for flight/wind tunnel drag comparison are presented and discussed in the following paragraphs.

### 5.2 Minimum Drag

Figure 20 shows the variation of minimum drag with Mach number from flight and tunnel drag measurements over a portion of the subsonic and supersonic Mach envelope. The comparison of Figure 20 shows excellent agreement between flight and wind tunnel in the subsonic flight regime and identical Mach number for commencement of drag rise. The shallower drag rise slope for the tunnel data is based on evaluation of early wind tunnel data, with an insufficient number of wing sweep angles, up to 0.95M. The drag rise fairing between 0.95M and 1.1M was estimated since no wind tunnel data were obtained over this Mach range. Analysis of later wind tunnel data, covering the full range of wing sweep angles, indicate good correlation with flight measured drag at 0.95M (within ten drag counts - 3%) as shown in Figure 20. The supersonic comparison shows slightly lower airplane drag compared to wind tunnel estimates in the low supersonic Mach range and greater airplane drag in the mid to high supersonic Mach range. The flight data do not collaborate the wind tunnel supersonic decrease in minimum drag with increasing Mach number. Although the characteristic wind tunnel decrease in supersonic minimum drag with Mach number has not been substantiated on most U. S. Navy supersonic airplane (F-4, A-5, F-111B), the quality and quantity of flight data from these aircraft has not been sufficient to conclusively establish this difference. The reasons for the divergence between flight and wind tunnel minimum supersonic drag is currently unknown and requires detail investigation by the aerodynamicist.

### 5.3 Induced Drag Characteristics

Figure 21 shows the flight/wind tunnel comparison for those drag polars presented in Figure 19. The wind tunnel polar minimum drag levels are adjusted to be coincident with the flight polars at minimum drag for the 0.95M, 1.2M and 2.0M polars because of the difference between flight and wind tunnel minimum drag discussed in Section 5.2. The flight induced drag characteristics are slightly degraded over the wind tunnel at all wing sweep angles and Mach numbers except at 1.2M. A contributing factor in this difference is an increase in the amount of airplane trim stabilizer required for zero pitching moment over the wind tunnel model. Retrimming of the model data based on flight trimmed stabilizer settings result in close agreement between flight and wind tunnel model induced drag characteristics. This process, however, compromises the good agreement between flight and wind tunnel trimmed lift versus angle of attack. Resolution of this item is awaiting measurement of flight stabilizer loads in an attempt to isolate any differences between airplane and model wing-body lift and stability or stabilizer effectiveness.

### 5.4 External Store Drag

Figures 22 and 23 present the flight/wind tunnel external store drag comparison for the Phoenix

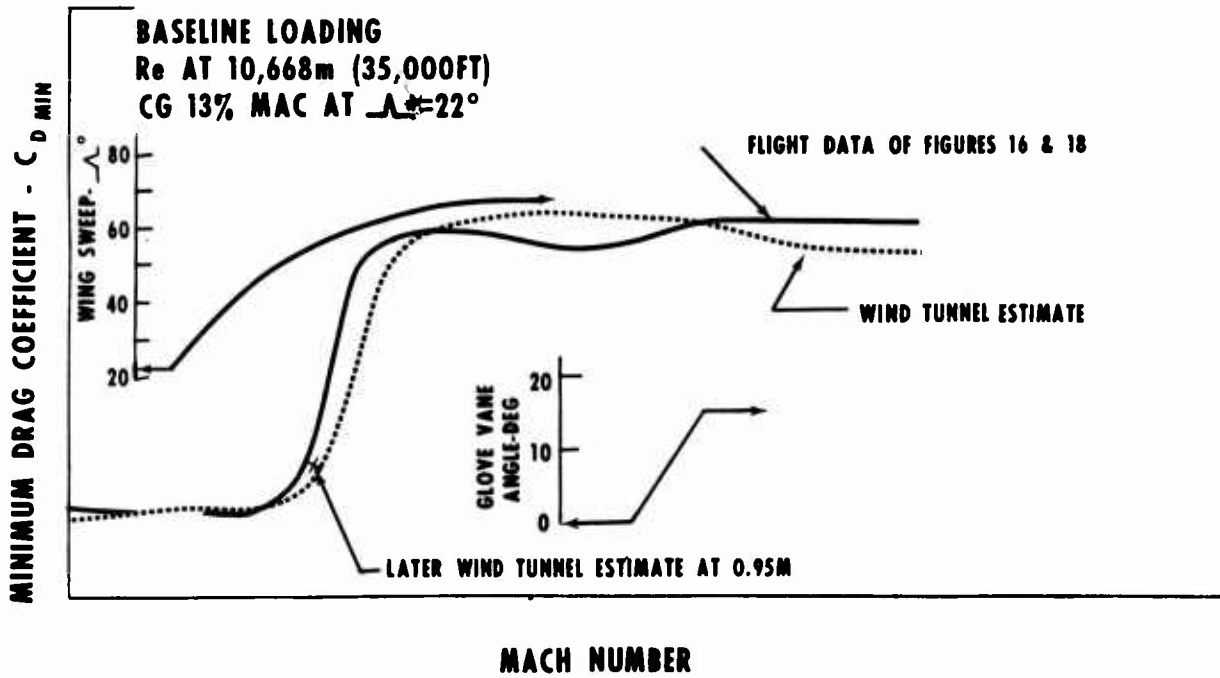


Figure 20 Minimum Drag Variation with Mach Number

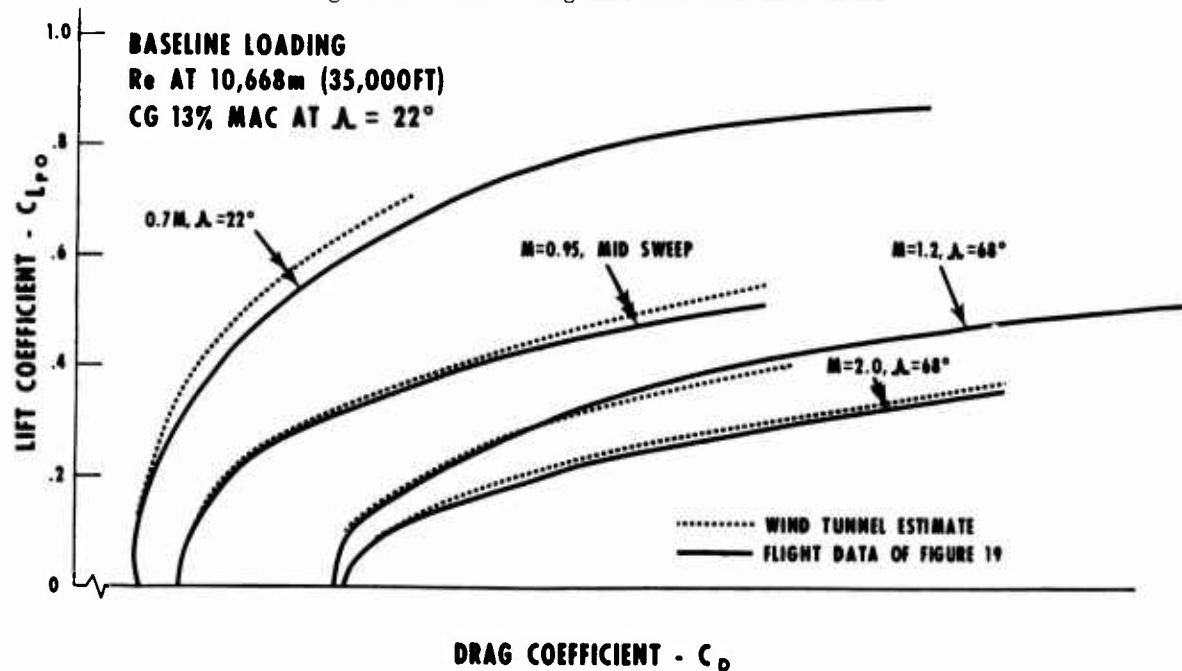


Figure 21 Induced Drag Variation with Mach Number

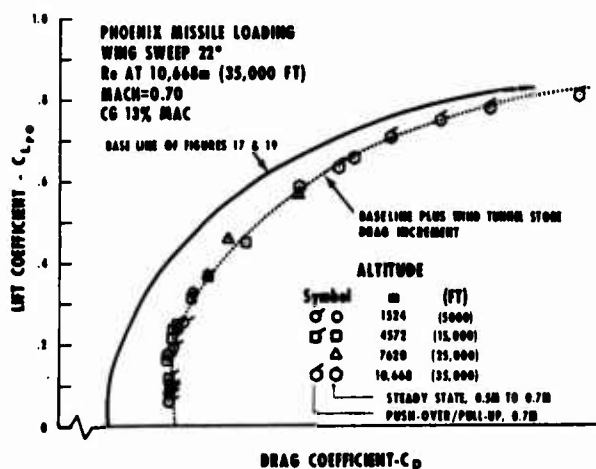


Figure 22 Subsonic External Store Drag

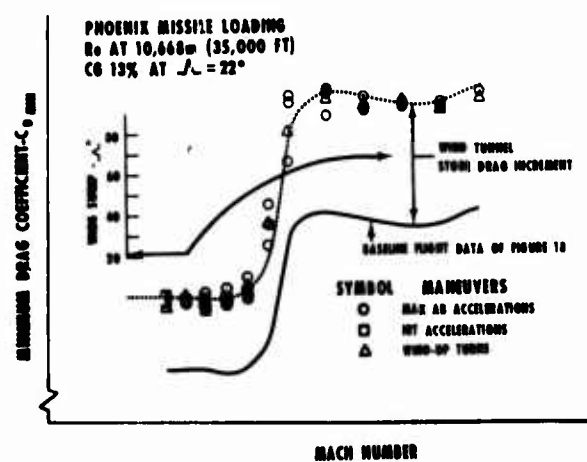


Figure 23 External Store Loading Minimum Drag Variation with Mach

missile loading described in Section 2.1. The wind tunnel procedure for determining the drag of external stores is to measure the incremental drag increase over the baseline or reference model configuration at a single stabilizer incidence angle (usually  $0^\circ$ ). This increment, uncorrected for scale effects, is then applied directly to the final adjusted, trimmed wind tunnel model drag level to determine the combined airplane/store drag level. In the store drag comparison of Figures 22 and 23, this same procedure is followed in that the wind tunnel store drag increment is applied directly to the baseline configuration to predict total airplane/store drag.

24-17

Figure 22 shows the flight measured total airplane/store drag at 0.7M as compared to the baseline drag level of Figures 17 and 19 and baseline plus wind tunnel store drag increment. This comparison is made at a common CG position for both loadings to eliminate any differences caused by trim effects. The comparison of Figure 22 shows exact agreement between wind tunnel and flight store drag increment between the lift coefficient range 0 to 0.6. Above 0.6  $C_L$  the flight data show a slightly higher store drag increment than that predicted by the wind tunnel.

Figure 23 makes the same comparison in airplane minimum drag over the Mach range from subsonic to mid supersonic based on the flight baseline drag data of Figure 18. Again the subsonic and supersonic Phoenix store drag increment is in excellent agreement with the wind tunnel increment.

### 5.5 High-Lift Configuration Drag

Figure 24 presents the flight/wind tunnel drag comparison for the landing approach configuration with wing flaps and slats deflected and with landing gear and speed brakes extended. The flight data show excellent agreement with the wind tunnel estimate (within 1%) over the lift coefficient range tested.

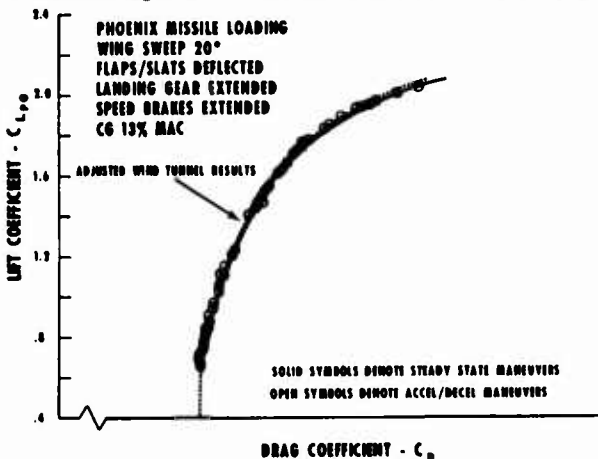


Figure 24 High-Lift Configuration Drag

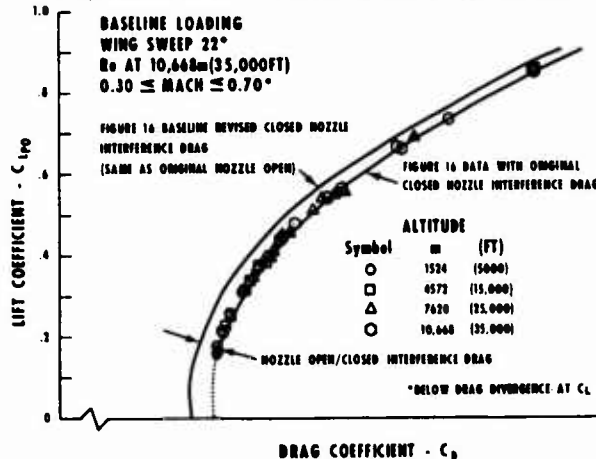


Figure 25 Nozzle Configuration Drag

### 5.6 Incremental Drag due to Nozzle Configuration

Initial wind tunnel tests with a 1/20 scale nose supported, single balance propulsion model indicated little difference between nozzle "closed" (cruise and IRT operation) and nozzle "open" (AB operation) boattail drag. Subsequent tests with the 1/12 scale blade supported, twin balance (backend and nozzles) propulsion model discussed in Section 2.4 resulted in a considerable increase in "closed" nozzle interference drag at model test Reynolds numbers. Prior to this program, flight investigations of the effect of boattail nozzle drag in the United States have indicated a beneficial effect on nozzle drag with increasing Reynolds number. Therefore, the higher "closed" nozzle interference drag was not incorporated in the in-flight thrust calculation procedure. However, initial flight drag data calculated from quasi steady-state test maneuvers with nozzle "closed" (IRT climbs, accelerations, etc) and nozzle "open" (AB accelerations) would not generalize, indicating an improper accounting for nozzle open/closed interference drag. The nozzle "open" drag data consistently indicated a lower drag level. Incorporation of the updated wind tunnel increments for "closed" nozzle interference drag did generalize the in-flight drag measurement as shown in Figure 17. Figure 25 reflects the nozzle drag increment between "open" and "closed" nozzle operation through calculation of in-flight drag from steady-state test data using the original (same as nozzle "open") and revised cruise nozzle interference drag increments derived from wind tunnel tests.

### 5.7 Subsonic Skin Friction Drag Correction

The wind tunnel and flight boundary layer skin friction drag corrections were computed from the summation of the individual skin friction drag corrections for each airplane component (i.e., wing, fuselage, tail, etc.). The individual corrections were accomplished by traversing from the test Reynolds number to the reference condition Reynolds number (10,668 m, 35,000 ft) parallel to the isolated flat plate skin friction drag, for the fully turbulent incompressible case, as defined by Schlichting. Corrections for the effect of compressibility on skin friction drag were also incorporated. This method assumes a constant pressure or form drag variation with Reynolds number.

The validity of this procedure is verified in

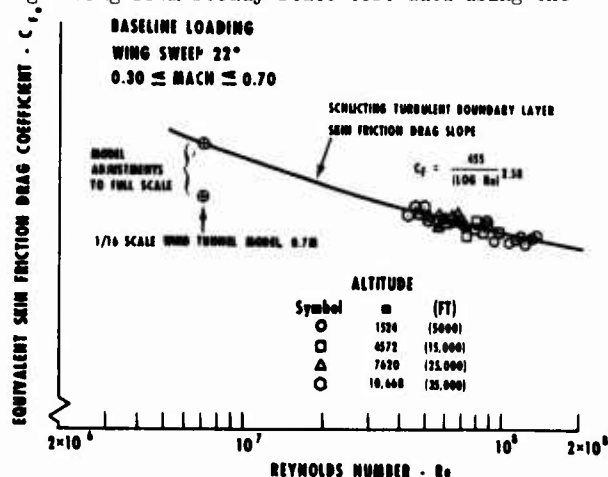


Figure 26 Subsonic Equivalent Skin Friction Drag

Figure 26, at least for the flight data Reynolds number range. The test data of Figure 16 for the No. 8 airplane, uncorrected for the Reynolds number effect on skin friction drag, cluster about the slope of the boundary layer skin friction drag variation with Reynolds number as defined by Schlichting. Prior to making this correction, the flight drag data would not generalize with altitude. The characteristic length for the full scale and model Reynolds number calculation of Figure 26 was based on a wetted area weighted average of the characteristic lengths of the individual airplane components.

Agreement between the estimated wind tunnel and full scale airplane drag levels, as discussed in Section 5.2, implies that the skin friction drag correction from wind tunnel to flight is also valid as shown in Figure 26. This conclusion is valid only if all other adjustments from wind tunnel to full scale are correct. Otherwise, any inaccuracies in these corrections could be masked by an equivalent error in the skin friction drag correction.

## 6. CONCLUSIONS

The inadequacies of airplane drag measurements by conventional techniques have been significantly improved. New techniques for in-flight engine thrust measurement; coupled with improved instrumentation accuracies, utilization of sensitive body axes accelerometers for evaluation of excess thrust and development of dynamic test methods, have produced drag data quantity, accuracy and repeatability not heretofore achievable. Random data scatter for steady-state test maneuvers is  $\pm 1\%$  and for quasi steady-state and dynamic test maneuvers is approximately  $\pm 2\%$  to  $\pm 4\%$  depending on Mach number. Drag determination from quasi steady-state and dynamic test maneuvers has resulted in a significant reduction in the amount of flight time required for aircraft drag evaluation. Dynamic test maneuvers have allowed assessment of induced drag characteristics to angles of attack not attainable by conventional test methods.

Comparison of in-flight measured airplane drag with predicted full scale drag from wind tunnel analyses has resulted in the following conclusions:

- a. Good to excellent agreement exists in subsonic minimum drag, drag rise Mach number, drag rise slope, external store drag increment (for the loading investigated) and high-lift configuration drag.
- b. Unexplained differences exist between airplane and wind tunnel estimates for minimum supersonic drag.
- c. The airplane induced drag characteristics are slightly degraded over wind tunnel estimates at most Mach numbers. This difference is caused by an increase in the amount of airplane trim stabilizer required for zero pitching moment over the wind tunnel model.
- d. The flight incremental drag due to nozzle configuration changes agrees with model measurements at wind tunnel test Reynolds numbers. No decrease in nozzle boattail drag at flight Reynolds numbers was observed.
- e. Subsonic skin friction drag corrections as a function of Reynolds number are verified.

## REFERENCES

1. A. A. Woodfield, Ann Cronin and Glynis Vorley, "Measurements of the Performance of a Turbo-jet Engine with Reheat (Rolls Royce RA28R Avon) in High Speed Flight and under Simulated Conditions in Test Beds," R. A. E. Technical Report 66060, Royal Aircraft Establishment, U.K., 1966.
2. F. W. Burcham, Jr., "An Investigation of Two Variations of the Gas Generator Method to Calculate the Thrust of the Afterburning Turbofan Engines Installed in an F-111A Airplane," NASA TN D-6297, Apr. 1971.
3. T. W. Davidson, "Measurement of Thrust in Flight" Journal of Aircraft, Vol I, No. 3, pp. 107-113, May-June 1964, American Institute of Aeronautics and Astronautics Inc., 1290 Avenue of the Americas, New York, N.Y. 10019.
4. M. H. Waters and P. A. Graham, "Evaluation of an Exhaust Nozzle Traversing Rake System as an In-Flight Thrust Measuring Device for an After-burning Turbofan Engine," NAPTC-ATD-150, Naval Air Propulsion Test Center, Trenton, N.J. 08628, Nov. 1968.
5. C. D. Perkins, Editor, "Advisory Group for Aeronautical Research and Development Flight Test Manual," Volume I, Performance Chapter 2:9. AGARD, NATO, Undated.
6. P. Poeschel, "Development of Dynamic Methods of Performance Flight Testing," Report No. ADR 07-01-70.1. Grumman Aerospace Corporation, Bethpage, N.Y. 11714, Aug. 1970.
7. E. J. Curtis, A. V. DaPuzzo and T. G. Davin, "F-14A Basic Aerodynamic Data Required for Substantiation of Standard Aircraft Characteristics Charts," GAC Conf. Rept A51-335-R-69-1, Grumman Aerospace Corporation, Bethpage, N.Y. 11714, Aug. 1969, revised May 1971.

## ACKNOWLEDGEMENT

This paper includes data obtained under U. S. Navy programs and contracts which have not yet resulted in documents suitable for referencing. The author, therefore, wishes to acknowledge the cooperation of personnel of the Aerodynamics, Propulsion and Flight Acceptance Departments of the Grumman Aerospace Corporation, the U. S. Naval Air Propulsion Test Center, the U. S. Naval Air Test Center and the Airframe and Propulsion Divisions of the Naval Air Systems Command who generously contributed their efforts and knowledge in the preparation of this paper.

REVIEW OF DRAG MEASUREMENTS FROM FLIGHT TESTS OF MANNED AIRCRAFT  
WITH COMPARISONS TO WIND-TUNNEL PREDICTIONS

25-1

Jon S. Pyle<sup>1</sup> and Edwin J. Saltzman<sup>2</sup>

NASA Flight Research Center  
P. O. Box 273  
Edwards, California 93523

SUMMARY

The NASA Flight Research Center has conducted in-flight studies of the overall and local components of drag of many types of aircraft. The primary goal of these studies was to evaluate wind-tunnel and semiempirical prediction methods. Some evaluations are presented in this paper which may be summarized by the following observations:

Wind-tunnel predictions of overall vehicle drag can be accurately extrapolated to flight Reynolds numbers, provided that the base drag is removed and that the boattail areas on the vehicle are small.

The addition of ablated roughness to lifting body configurations causes larger losses in performance and stability than would be expected from the added friction drag due to the roughness.

Successful measurements of skin friction have been made in flight to Mach numbers above 4.

A reliable inflatable deceleration device was demonstrated in flight which effectively stabilizes and decelerates a lifting aircraft at supersonic speeds.

NOTATION

A	cross-sectional area
$C_D$	drag coefficient
$C_f$	local skin friction coefficient
$C_m$	pitching moment coefficient
$C_{p_t}$	total pressure coefficient
d	diameter
h	base thickness (where step height = h/2)
L/D	lift-to-drag ratio
l	length behind towing body
M	Mach number
p	static pressure
R	Reynolds number based on appropriate body or test fixture length
T	absolute temperature
$\alpha$	angle of attack
$\Delta$	increment
$\theta$	boundary-layer momentum thickness
$\mu$	absolute viscosity
Subscripts:	
A	maximum cross-sectional area
b	base
i	incompressible
l	local

<sup>1</sup>Research Engineer, Performance Aerodynamics

<sup>2</sup>Research Engineer, Supervisor, Performance Aerodynamics Branch

25-2

min	minimum
r	equilibrium
w	wall
$\beta$	boattail
0	zero lift conditions

## Superscript:

( )' based on reference temperature method from references 1 and 2.

## 1. INTRODUCTION

The designers of modern aircraft depend on wind-tunnel-model data for estimating the performance of full-scale vehicles. The accuracy of the wind-tunnel results depends on the accuracy with which the geometry of the model, the support system, and the quality of the flow around the model simulate the full-scale flight flow conditions. The knowledge required to provide an accurate flight vehicle simulation in the wind tunnel has been acquired from many previous comparisons of wind-tunnel and flight data.

The NASA Flight Research Center has made such comparisons for a wide variety of configurations, including lifting bodies, supersonic and hypersonic airplanes, and military aircraft. Drag results from such vehicles are compared in this paper to corresponding wind-tunnel-model results or semiempirical predictions, or both, from subsonic Mach numbers to Mach numbers of above 4 and for flight Reynolds numbers between  $10^7$  and  $10^8$ .

These vehicle drag results can be separated into various components such as forebody drag and base drag. Consideration is given here to the methods of determining skin friction in flight, the effects of the ablation type of roughness, and the possibility of reducing base drag. In addition to the drag caused by different vehicle components, some discussion is included about the drag of large external stores and that of an inflatable towed decelerator.

## 2. VEHICLE DRAG CHARACTERISTICS

2.1 Wetted-area forebody drag

The usual flat-plate turbulent-boundary-layer extrapolation of zero lift drag from model to full-scale Reynolds numbers was adequate for simple, rigid configurations at subsonic and supersonic speeds. An example for each of these speed regions is shown in figure 1, which presents the zero lift drag coefficient for the YF-102 airplane (ref. 3) and the X-15 airplane (ref. 4) as a function of Reynolds number. The Kármán-Schoenherr variation of friction with Reynolds number (ref. 1) was used for this extrapolation, and the T' method was used to account for compressibility effects (refs. 1 and 2). The absence of variable geometry inlets and complicated jet exhausts, plus the rigidity of these configurations, made the simulation task relatively easy, resulting in very good agreement between the predictions and the full-scale flight results. However, the base area of the X-15 is large, so its base drag is a large percentage of the overall vehicle drag. Because the X-15 wind-tunnel base pressures did not agree with the flight base pressure measurements, an extrapolation of the X-15  $C_{D0}$  was not successful

until the base drag was subtracted from both the flight and wind-tunnel results. In addition, it was fortunate that the boattail areas on each of these vehicles was a small part of their total wetted areas, because this minimized the problems associated with the simulation of the flow over the boattail area. For aircraft with a large boattail angle or a large boattail area, or both, this method of extrapolation is not successful because of the inability to simulate the location of flow separation over these types of afterbody surfaces.

The M2-F3 lifting body vehicle shown in figure 2 is a good example of this problem. The configuration has a large boattail area with relatively large boattail angles. When the same extrapolation procedure that was applied to the YF-102 is applied to the M2-F3 (upper portion of fig. 3), the wind-tunnel results appear to agree with the forebody drag level at the flight Reynolds number. However, the wind-tunnel-model base drag values did not simulate the flight base drag values, and the M2-F3 base area is quite large. Therefore, if the comparison is made with the base drag subtracted (lower portion of fig. 3), as was done with the X-15, there occurs a disagreement of approximately 15 percent between the extrapolated drag level and the flight results. It is believed that this discrepancy is due to the difference in location of flow separation on the full-scale and model boattail areas.

It would be expected in figure 3 that the model boundary layer would be disproportionately thick because of the lower model Reynolds numbers. Separation would, therefore, occur at a different location over the boattail region than on the full-scale vehicle. In addition, model support and wall reflection effects are likely to modify the pressure over the aft sloping surfaces.

In a more recent comparison, some combination of the above factors also prevented adequate flow simulation over the fuselage afterbody. In this case a supercritical wing mounted on an F-8 fuselage was tested both in flight and in wind-tunnel facilities. A photograph of the F-8 airplane (fig. 4) shows that the boattail angles of the fuselage are relatively small. However, the large ratio of the model compared to the wind-tunnel test section and the model sting support influenced the boattail and base pressures of the model. These interference effects appear in the values for the F-8 fuselage base and boattail drag presented in figure 5 as the differences between the wind-tunnel predictions and the flight-measured data. Note that these differences are apparent at both the lower subsonic speeds as well as transonic speeds near  $M = 1$ , where some differences would be expected.

The supercritical wing is a concept to delay the drag rise Mach number of transport configurations. Wind-tunnel tests of this wing applied to a transport configuration indicated a significant increase in the drag rise

25-3

Mach number compared with conventional transport configurations (refs. 5 and 6). To verify these results in flight, a supercritical wing was carefully blended to the F-8 fuselage, as illustrated in figure 4. Although this configuration was not the optimum transonic transport design due to its relatively low fineness ratio, non-area-ruled fuselage, and smaller scale, the drag rise Mach number was significantly higher than exhibited by present day transports. The wind-tunnel drag rise Mach number was verified by the flight tests, the difference between the two sources being less than 0.01 Mach number. In addition, when the base and boattail drag differences (discussed previously) were subtracted from the flight and wind-tunnel results, the wetted-area forebody drag measured in flight at the design conditions agreed within 5 percent of the wind-tunnel predictions.

## 2.2 Base drag

The previous discussion of wetted-area forebody drag indicated that base drag is one of the major factors to be taken into account in the extrapolation of wind-tunnel performance data. The relative importance of an adequate simulation of base drag in wind-tunnel tests is particularly evident in cases where the base drag is a large portion of the overall drag, as shown in the examples in figure 6. The base drag for hypersonic and reentry configurations such as the X-15, HL-10 (ref. 7), and M2-F3 can constitute from 35 percent to as much as 70 percent of the overall vehicle drag. These results suggest that the different means of supporting wind-tunnel models or improved methods of predicting base pressure will be needed before accurate estimates of base drag can be obtained by the designer for development of new configurations.

Base drag also occurs on the aft-facing steps of lap joints, and in the shingle type of construction, which has been proposed for use in future airplanes that have hot surfaces. Prediction methods for this type of drag were adequate for subsonic and low supersonic speeds when the effects of boundary-layer thickness were included. An example is the aft-facing step that was installed 15 meters aft of the wing leading edge of the XB-70 airplane as shown in figure 7. The results of an experiment using this step (ref. 8) are presented in figure 8 in terms of the ratio of base pressure to ambient pressure as a function of the ratio of momentum thickness to step height. These data indicate some deficiencies in the prediction methods for Mach numbers above 2. The predicted curves were established from the wind-tunnel results of Hastings and Chapman (refs. 9 and 10). Note that the predictions for  $M = 2.0$  and  $2.4$  underestimate the drag for momentum-thickness-to-step-height ratios near 1, that is, for a relatively thick boundary layer. This suggests that for the larger and faster aircraft of the future the prediction discrepancy may be even larger.

For certain applications, there are a number of devices such as base bleed, boattailing, trailing disks, splitter plates, and vented cavities that show promise for reducing base drag at subsonic speeds. Typical of such devices are the splitter plate (ref. 11) and the vented cavity illustrated in figure 9. To evaluate the effectiveness of these two configurations, a special fin-like test fixture was installed and tested on an F-104 airplane. The results of this study (fig. 10) show that both devices reduce base drag by 35 to 40 percent at high subsonic Mach numbers. At low Mach numbers, the splitter plate effectiveness remains above 30 percent, whereas the vented cavity is only about half as effective.

## 2.3 Skin friction

Friction drag has been determined in flight by various means at the Flight Research Center, including use of force balances, Preston probes (refs. 12 and 13), and the Clauser-type determination, which is applied to boundary-layer-rake and traversing-probe data. In addition, a swinging wake probe is being developed for determining airfoil section drag coefficients.

A commercially available force balance with a special cooling jacket was used to successfully measure skin friction on the X-15 airplane at Mach numbers above 4. Flight results with this balance are compared in figure 11 with data from several other balance devices used in wind-tunnel tests (ref. 14). The wind-tunnel data were obtained at essentially equilibrium wall temperatures,  $T_w/T_r \approx 1.0$ . The flight values represent wall recovery temperature ratios from 0.5 to 1.25. The flight and wind-tunnel results generally agree with the compressibility effects predicted by the Sommer and Short  $T'$  relationship (ref. 2). However, the wall temperature effects measured in flight appear to be less than estimated.

The Clauser-type determination for estimating skin friction (refs. 15 and 16) has been used in flight with encouraging results. These data were transformed to incompressible conditions by using the charts in reference 16. Typical flight results from references 17 and 18 for Mach numbers from 0.5 to 2.1 are shown in figure 12 along with the Kármán-Schoenherr relationship (ref. 1) for turbulent flow over a flat plate. These data, which represent relatively low pressure gradient flow, agree well with the Kármán-Schoenherr relationship when transformed by the  $T'$  method to incompressible conditions. Also shown in figure 12 is a photograph of the traversing probe.

Another device which has been developed and flight checked recently is a swinging wake probe. This compact unit is shown in figure 13 with and without an aerodynamic fairing cover. Note in the uncovered view that the two transducers and the angular position sensor are all nested close to the motor and drive mechanism. The lightweight mechanism (1450 grams, including the fairing cover) permits easy and safe installation even near relatively thin wingtips.

Two profiles obtained with this device are shown in figure 13, one for attached flow and one for a separated boundary layer. These profiles were obtained with a probe travel rate of approximately 2 centimeters per second. Profiles such as these make possible the computation of the section drag coefficients. These examples demonstrate that well-defined profiles can be obtained with a compact and lightweight device.

## 2.4 Effect of ablated roughness

The marginal lift-drag ratio experienced during flight with the lifting body configurations indicated a need to assess the aerodynamic effects of rough ablated surfaces that would be likely to develop during reentry. Thus, as part of the X-24A lifting body aerodynamics study, the full-scale vehicle was tested with a sand coating in the full-scale wind tunnel at the NASA Ames Research Center. This coating was intended to simulate an actual ablated surface observed on a related unmanned subscale test vehicle that had been previously subjected to

heating during reentry into the earth's atmosphere. Photographs of selected areas of this ablated surface are compared in figure 14 to the simulated sand coating on the X-24A vehicle as tested in the full-scale wind tunnel. The simulation was intended to be of the first order so that any significant effects of the roughness could be noted.

Some of the force results obtained from the full-scale tests of the X-24A (ref. 19) are compared in figure 15 with wind-tunnel force results obtained on the related subscale vehicle. The most interesting results in this figure are the 20- to 30-percent losses in lift-to-drag ratio which were caused by the addition of roughness to the vehicle surface. These losses in lift-to-drag ratio are much greater than would be expected from the increased skin friction drag due to the roughness. It is believed that these large losses in performance were caused by a significant increase in separated flow over the aft sloping regions of the vehicles. This was verified by the presence of tufts on the X-24A vehicle surface. This conclusion is also substantiated by the noticeable loss in longitudinal stability for both vehicles when the roughened surface results are compared to the smooth surface results.

These significant losses in performance and stability were not anticipated. Designers of future low performance vehicles with ablated surfaces should be aware that the predicted increase in friction drag due to roughness may be only a small part of the actual roughness effects experienced by the vehicle.

### 3. EXTERNAL STORE DRAG

Although the Flight Research Center has not often evaluated external stores, the external fuel tanks used on the X-15 (ref. 20) to expand its performance capability were of special interest because of their large size. The cross-sectional area of the two tanks, as shown in figure 16, was 60 percent of the maximum cross-sectional area of the basic airplane. Because of the placement of the stores as shown in the photograph, significant interference drag was expected. For the Mach number range of these tests (1.6 to 2.3) the store drag was 70 percent of the basic airplane drag. A prediction of the store drag increment, which was composed of the several drag components without accounting for interference, indicated a store drag increment of 68 percent. Thus, in spite of the large size of these stores, supersonic interference drag appears to be negligible for cylindrical shapes close to and parallel with the primary vehicle.

### 4. INFLATABLE TOWED HIGH-SPEED DECELERATOR

The NASA Flight Research Center often conducts research on new unconventional aircraft. Therefore, it became desirable to flight qualify a drogue chute device which could rapidly decelerate or stabilize these unconventional vehicles, or both, if a problem arose. Although other drogue chutes and specialized parachutes are available for decelerating and stabilizing vehicles at subsonic speeds, a reliable supersonic decelerator had not been tested in the wake of a jet airplane.

Therefore, when an inflatable towed decelerator for supersonic and subsonic applications became available (fig. 17), it was flight tested in the asymmetric wake of an F-104 airplane. The drag results obtained from this decelerator are compared in figure 18 with wind-tunnel results for a solid model of the same geometry which was in the wake of a symmetrical body (ref. 21). Included also are the results from free-flight studies of an inflatable decelerator similar to the one used behind the F-104 but tested in the wake of a symmetrical body (ref. 22).

In the presence of the F-104 wake, the supersonic drag coefficient of the decelerator (based on the decelerator cross-sectional area) was near 1.0, whereas the results for symmetrical wakes generated by bodies of revolution showed higher supersonic drag. It is not known for certain whether these differences in drag are associated with the different types of wakes.

The stability of the decelerator in the asymmetric wake of the F-104 was excellent, although slight amounts of intermittent coning of the tow line and decelerator and some intermittent spinning were present. However, the presence of the coning and spinning did not deteriorate the performance of the decelerator.

### 5. CONCLUDING REMARKS

This paper presents a brief discussion of some of the studies of aircraft performance being conducted at the NASA Flight Research Center and includes a comparison of drag results from flight with those from wind-tunnel and semiempirical predictions. The following conclusions may be drawn from these studies:

Wind-tunnel predictions of vehicle overall drag can be accurately extrapolated to flight Reynolds numbers, provided that the base drag is removed and the boattail areas on the vehicle are small. This suggests that a need exists for a more reliable means of predicting drag for the base and boattail regions. This could be accomplished by improving the support system in the wind tunnel, reducing the interference from wall reflection effects, or by developing more realistic empirical formulas. This type of improvement will be especially important to the development of future aircraft such as hypersonic and reentry vehicles, which may be characterized by large boattail areas or blunt bases, or both.

The boattail regions are also cause for concern when the forebody is coated with ablated roughness. The addition of ablated surface roughness to lifting body configurations caused a larger loss in performance and stability than would be expected from the added friction drag caused by the roughness. The designer of future reentry vehicles should anticipate the boattail areas of the vehicle to have separated flow when subjected to ablated roughness.

Successful measurements of skin friction have been made on aircraft in flight to Mach numbers above 4.

A reliable inflatable deceleration device which effectively stabilizes and decelerates lifting aircraft has been demonstrated in flight at supersonic speeds.

## 6. REFERENCES

1. Peterson, John B., Jr.: A Comparison of Experimental and Theoretical Results for the Compressible Turbulent-Boundary-Layer Skin Friction With Zero Pressure Gradient. NASA TN D-1795, 1963.
2. Sommer, Simon C.; and Short, Barbara J.: Free-Flight Measurements of Turbulent-Boundary-Layer Skin Friction in the Presence of Severe Aerodynamic Heating at Mach Numbers From 2.8 to 7.0. NACA TN 3391, 1955.
3. Saltzman, E. J.; Bellman, D. R.; and Musialowski, N. T.: Flight-Determined Transonic Lift and Drag Characteristics of the YF-102 Airplane With Two Wing Configurations. NACA RM H56E08, 1956.
4. Saltzman, E. J.; and Garringer, D. J.: Summary of Full-Scale Lift and Drag Characteristics of the X-15 Airplane. NASA TN D-3343, 1966.
5. Braslow, Albert L.; and Ayers, Theodore G.: Application of Advanced Aerodynamics to Future Transport Aircraft. NASA Aircraft Safety and Operating Problems—Volume I. NASA SP-270, 1971, pp. 165-176.
6. Goodmanson, Lloyd T.: Transonic Transports. *Astronautics and Aeronautics*, vol. 9, no. 11, Nov. 1971, pp. 46-57.
7. Pyle, Jon S.; and Ash, Lawrence G.: Performance Characteristics of the Lifting Body Vehicles. Flight Test Results Pertaining to the Space Shuttlecraft, NASA TM X-2101, 1970, pp. 43-58.
8. Goecke, Sheryll A.: Flight-Measured Base Pressure Coefficients for Thick Boundary-Layer Flow Over an Aft-Facing Step for Mach Numbers From 0.4 to 2.5. NASA TN D-7202, 1973.
9. Hastings, R. C.: Turbulent Flow Past Two-Dimensional Bases in Supersonic Streams. *British R & M* No. 3401, 1965.
10. Chapman, Dean R.; Wimbrow, William R.; and Kester, Robert H.: Experimental Investigation of Base Pressure on Blunt-Trailing-Edge Wings at Supersonic Velocities. NACA Rept. 1109, 1952. (Supersedes NACA TN 2611.)
11. Saltzman, Edwin J.; and Hintz, John: Flight Evaluation of Splitter-Plate Effectiveness in Reducing Base Drag at Mach Numbers From 0.65 to 0.90. NASA TM X-1376, 1967.
12. Preston, J. H.: The Determination of Turbulent Skin Friction by Means of Pitot Tubes. No. 15,758, *British A.R.C.*, March 31, 1953.
13. Hopkins, Edward J.; and Keener, Earl R.: Study of Surface Pitots for Measuring Turbulent Skin Friction at Supersonic Mach Numbers—Adiabatic Wall. NASA TN D-3478, 1966.
14. Garringer, Darwin J.; and Saltzman, Edwin J.: Flight Demonstration of a Skin-Friction Gage to a Local Mach Number of 4.9. NASA TN D-3830, 1967.
15. Clauser, Francis H.: Turbulent Boundary Layers in Adverse Pressure Gradients. *J. Aeron. Sci.*, vol. 21, no. 2, 1954, pp. 91-108.
16. Allen, Jerry M.; and Tudor, Dorothy H.: Charts for the Interpolation of Local Skin Friction From Experimental Turbulent Velocity Profiles. NASA SP-3048, 1969.
17. Saltzman, Edwin J.: In-Flight Use of Traversing Boundary-Layer Probes. NASA TN D-6428, 1971.
18. Erlich, E.: Sondage de la Couche Limite en Vol Supersonique sur L'Avion "Mirage IV". O.N.E.R.A. paper presented at 3<sup>e</sup> Colloque Aerodynamique de l'A.F.I.T.A.E., Marseille, France, Nov. 8-10, 1966.
19. Pyle, Jon S.; and Montoya, Lawrence C.: Effect of Roughness of Simulated Ablated Material on Low-Speed Performance Characteristics of a Lifting-Body Vehicle. NASA TM X-1810, 1969.
20. Fisher, David F.: Flight-Measured Aerodynamic Drag of Two Large External Tanks Attached to the X-15-2 Airplane at Mach Numbers of 1.6 to 2.3. NASA TM X-1895, 1969.
21. Turk, Raymond A.: Pressure Measurements on Rigid Model of Ballute Decelerator at Mach Numbers From 0.56 to 1.96. NASA TN D-3545, 1966.
22. Usry, J. W.: Performance of a Towed, 48-Inch-Diameter (121.92-cm) Ballute Decelerator Tested in Free Flight at Mach Numbers From 4.2 to 0.4. NASA TN D-4943, 1969.

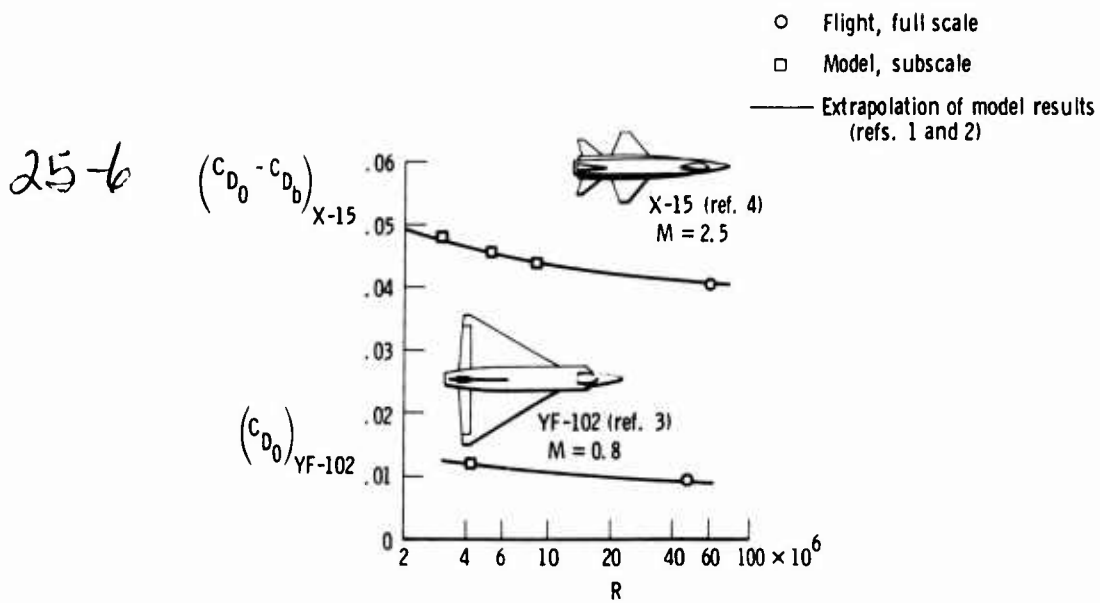


Figure 1. Comparison of extrapolated wind-tunnel-model drag coefficients with full-scale flight results.



Figure 2. Side view of the M2-F3 lifting body vehicle.

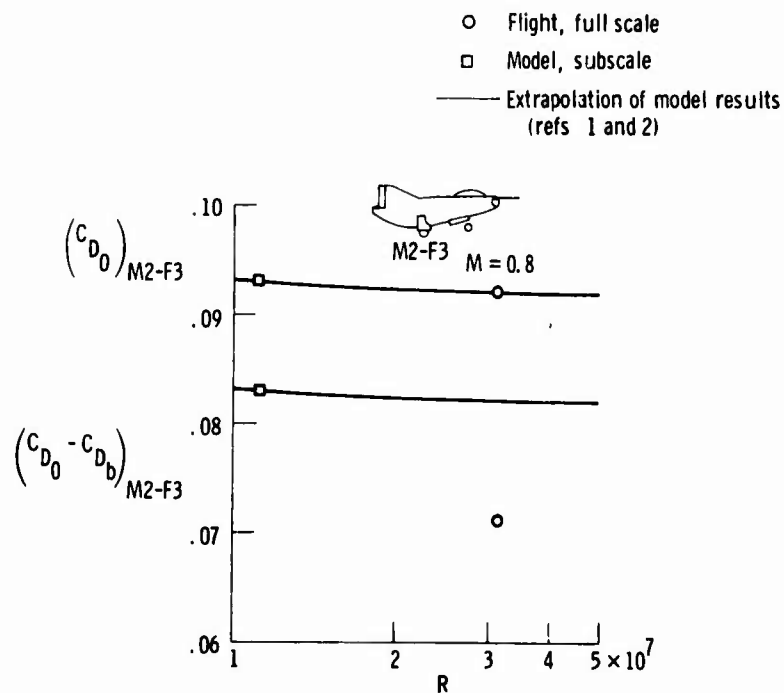


Figure 3. Comparison of M2-F3 lifting body model and flight drag with and without base drag.

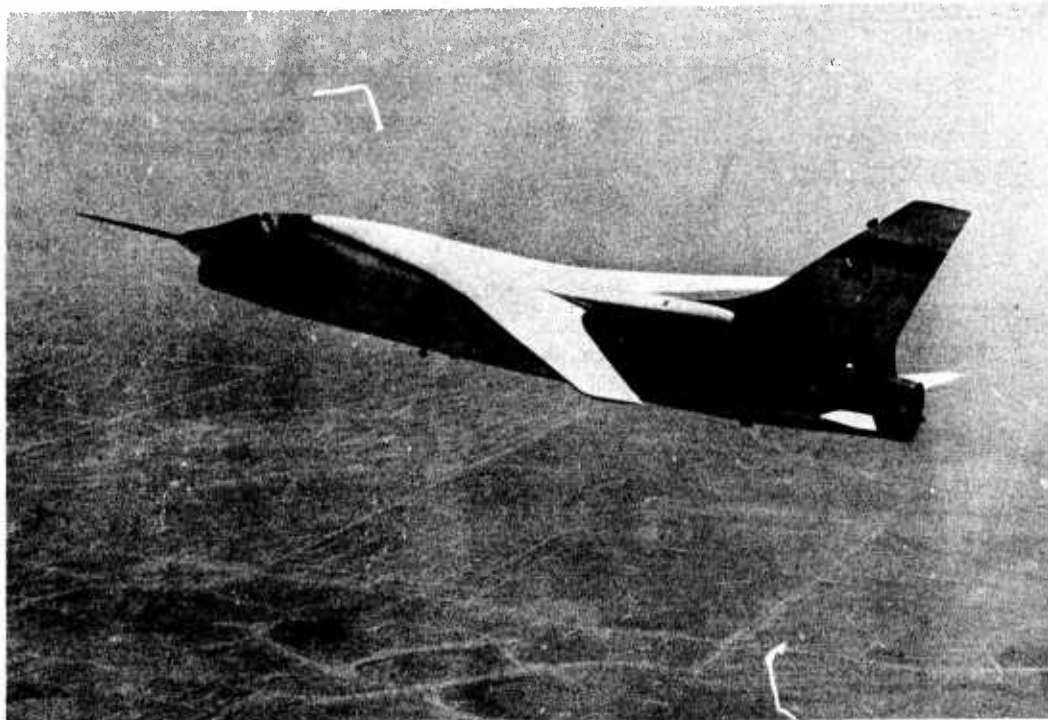


Figure 4. A supercritical wing adapted to the F-8 airplane.

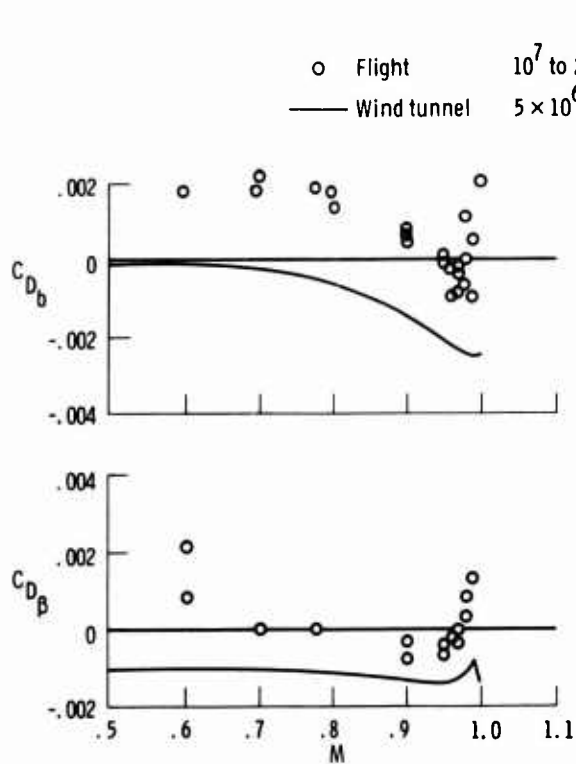


Figure 5. Fuselage base and boattail drag measured on the F-8 supercritical wing airplane compared to wind-tunnel results.

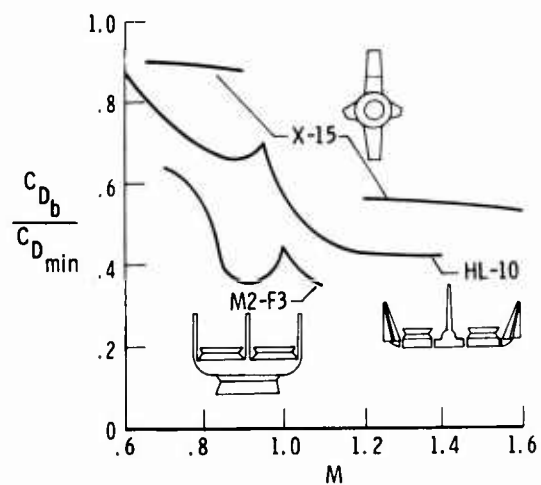


Figure 6. Ratio of base drag to minimum drag. Flight data.

25-8

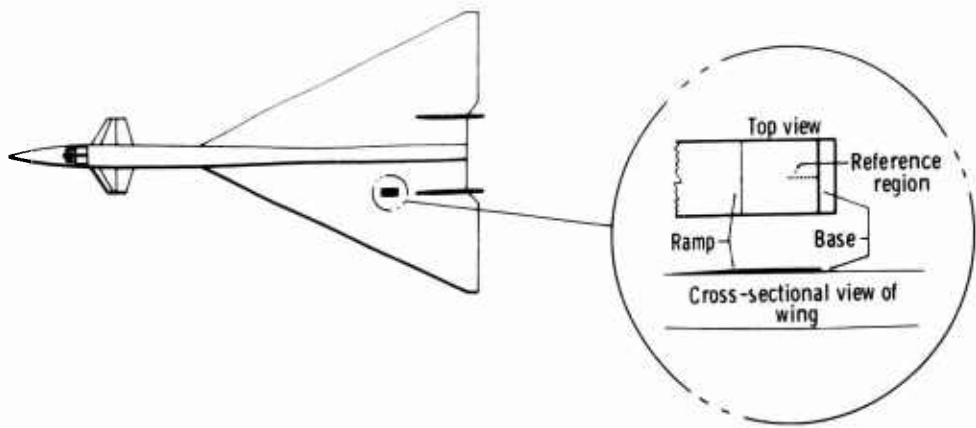


Figure 7. Aft-facing step experiment located on the wing of the XB-70 airplane.

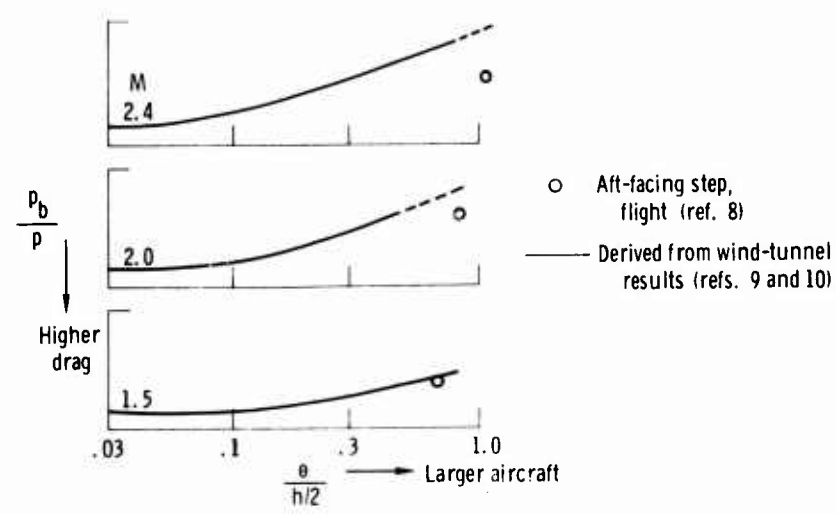


Figure 8. Base pressure ratio as a function of the ratio of momentum thickness to step height. From flight data and as predicted.

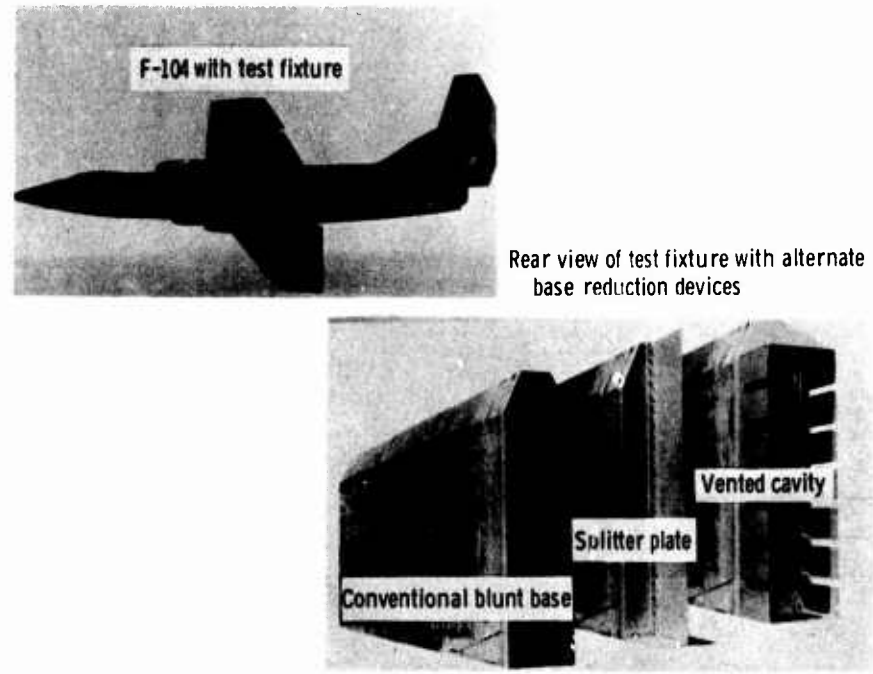


Figure 9. The test fixture used in the base drag reduction experiment and its installation under the fuselage of the F-104 airplane.

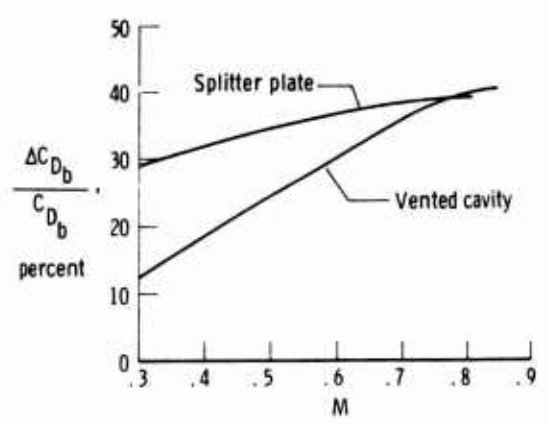


Figure 10. The reduction of base drag on the F-104 test fixture using a splitter plate and a vented cavity.

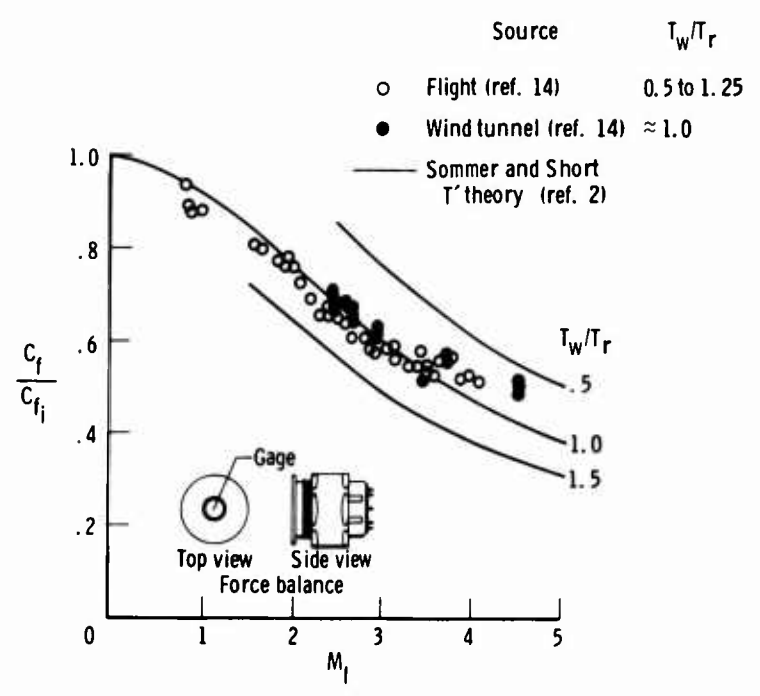


Figure 11. Normalized local skin friction coefficient from the X-15 airplane compared with wind-tunnel measurements and predictions.

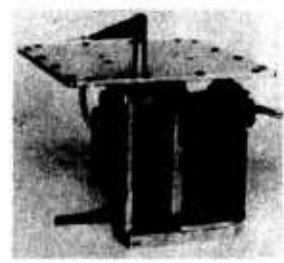
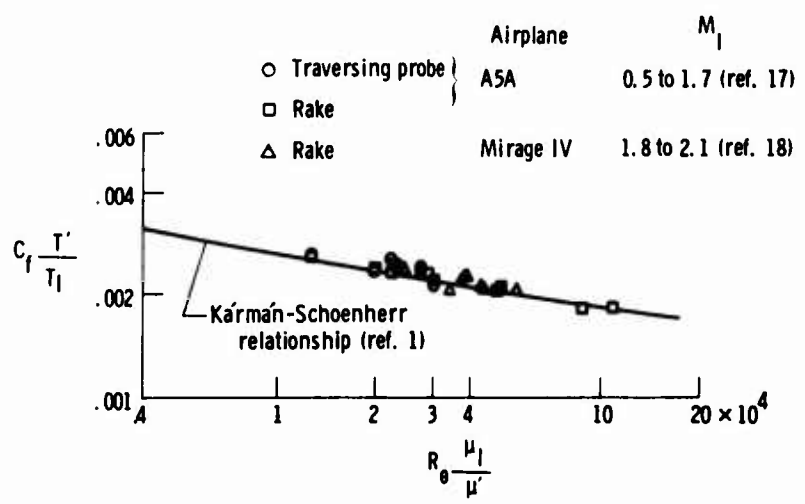


Figure 12. Local skin friction coefficients obtained in flight by the Clauser method, and the traversing probe which was used in flight.

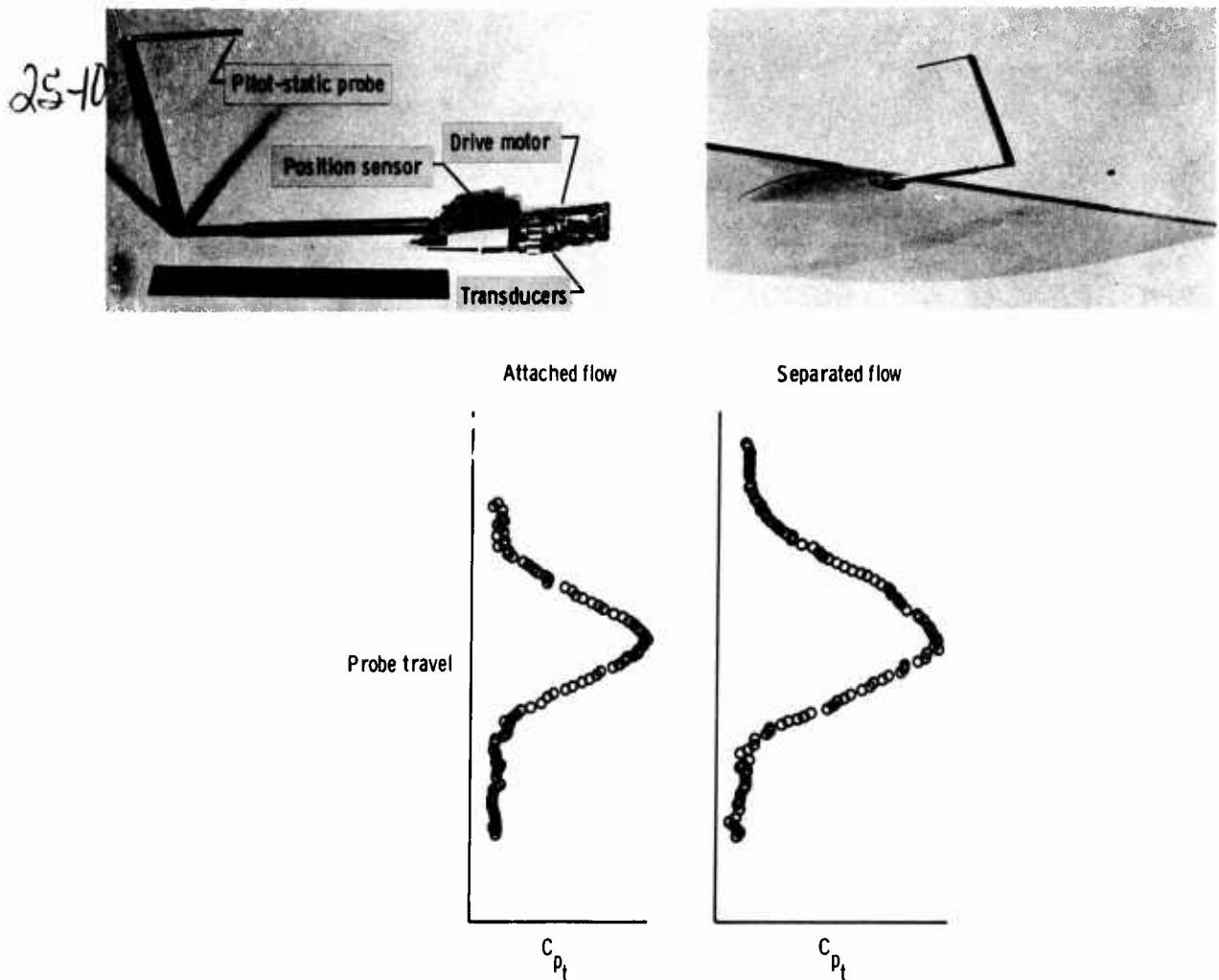


Figure 13. Swinging probe hardware and its installation on the trailing edge of a wing with some typical flight-measured profiles.

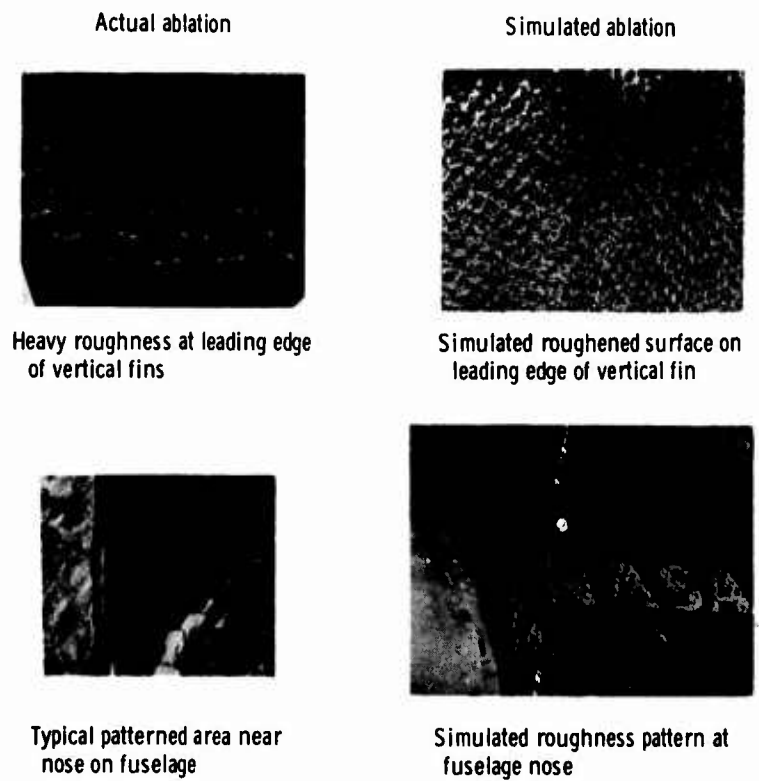


Figure 14. The actual ablated surface obtained from a reentry vehicle compared with a simulator by sand roughness.

	R	M	
—— X-24A	$30 \times 10^6$	0.2	(ref. 19)
- - - Related model	$3 \times 10^6$	0.3	

25-11

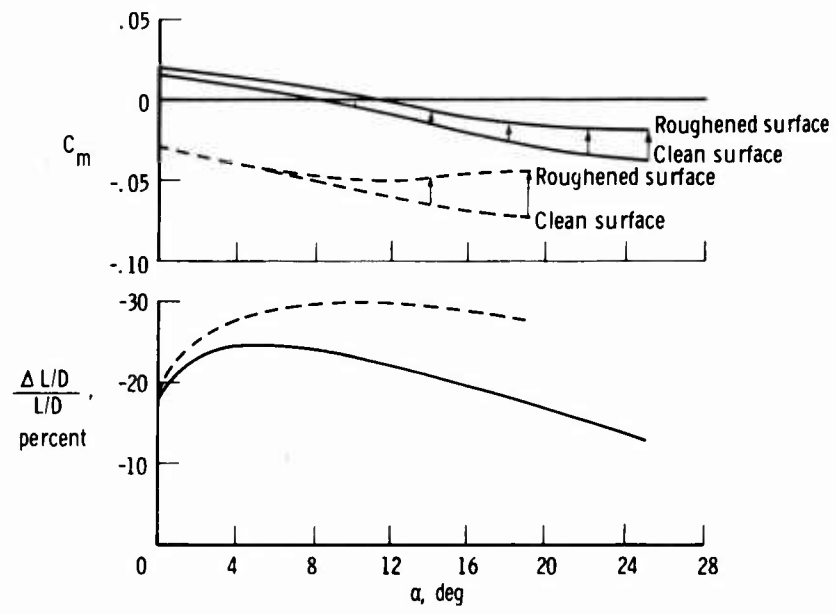
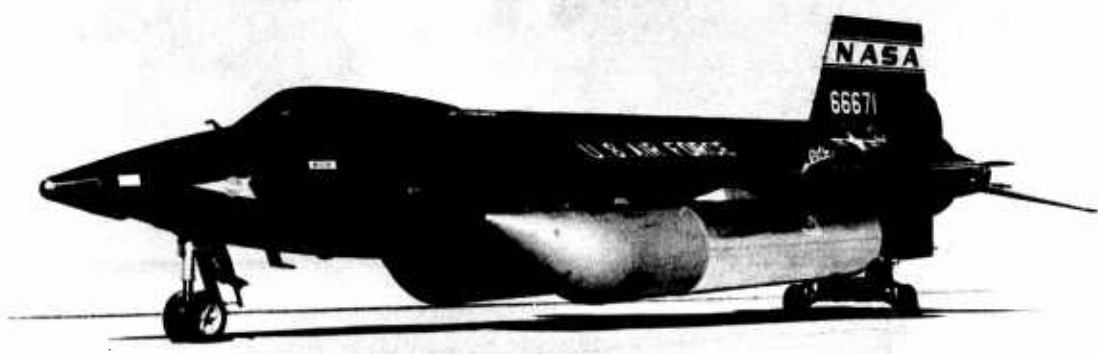


Figure 15. The effect of an ablated surface on the aerodynamic characteristics of two lifting body vehicles as determined from wind-tunnel tests.



$$\frac{\Delta A_{\text{stores}}}{A_{\text{aircraft}}} \approx 60\%$$

$$\left[ \frac{\Delta C_{D_{\text{stores}}}}{C_{D_{\text{aircraft}}}} \approx 70\% \right] \\ M = 1.6 \text{ to } 2.3$$

Figure 16. The effect of large external stores on the drag of the X-15 airplane (ref. 20).

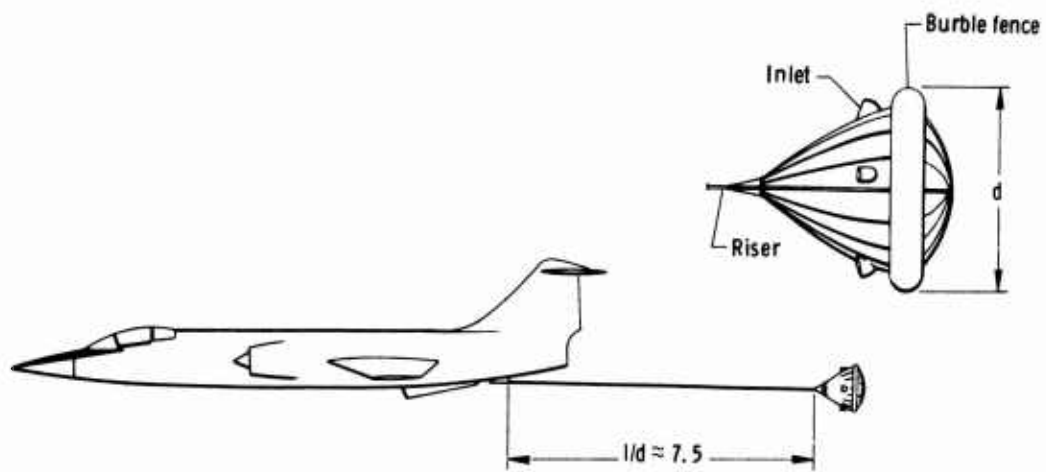


Figure 17. F-104 airplane towing a high-speed inflatable decelerator.

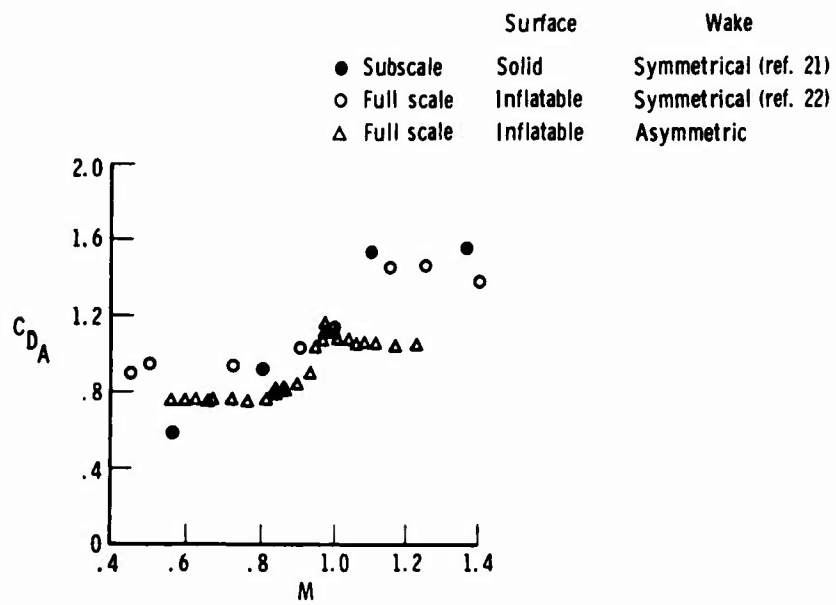


Figure 18. Drag coefficient of a high-speed decelerator towed within symmetric and asymmetric wakes.

AN ASSESSMENT OF THE ACCURACY OF TRANSONIC DRAG  
MEASUREMENT IN A LARGE MODERN WIND TUNNEL

by

26-1

R K Fancett B.Sc, Ph.D\*\*  
T Smith B.Sc, (Eng)

RARDE, Fort Halstead, Sevenoaks, Kent

SUMMARY

The aeroballistic coefficients of bodies of revolution are needed for the mathematical modelling of their trajectories. The most significant coefficient required is zero yaw drag and the accuracy required is about 0.5% for a perfect trajectory model, compared with about 5% for lift and overturning moment.

Lift, drag and overturning moment were measured over a range of yaw angles on two sting lengths in a 2.4 m x 2.7 m transonic wind tunnel. There was a marked difference in the measured drag values for these stings and a further investigation was made with five sting lengths.

From these tests an empirical correction for the support system was derived which agreed well with a subsonic theoretical estimate. At speeds above Mach 1.0 the irregularity of the tunnel axial pressure distribution dominated the effects due to the support system and a combined correction was derived. It was found that the difference in measured values after correction was very much less than before, over the whole Mach number range, thus supporting the correction procedure applied.

A statistical analysis of the residual coefficient errors has been summarized for the subsonic and transonic speed regions. The transonic percentage errors were generally less than the subsonic values, due to the larger coefficient values measured.

NOTATION

$C_D$	Drag coefficient = $\text{Drag} / \frac{1}{8} \rho V^2 d^2$	l	Length of parallel sting aft of model base
$C_{D0}$	Zero yaw drag coefficient	M	Mach number
$C_{Db}$	Base drag coefficient	V	Velocity
$C_{D\alpha^2}$	Yaw drag coefficient	$\alpha$	Yaw angle
$C_{La}$	Lift slope coefficient	$\Delta C_{pb}$	Incremental base pressure coefficient
$C_{Ma}$	Overturning moment slope coefficient	$\Delta C_{pf}$	Incremental forebody pressure coefficient
d	Maximum body diameter	$\rho$	Density
$d_b$	Base diameter		

1. INTRODUCTION

To date the most common means of studying the behaviour of free trajectory shells and missiles has been the ballistic range. Conversely to the wind tunnel this is a very accurate method for drag estimation but not so suitable for yaw forces and moments. It is however costly and time consuming and it is hoped that wind tunnels will be used increasingly for the determination of shell aerodynamics. Almost all the necessary parameters can be measured quickly and economically. The purpose of the tests discussed here was to check the accuracy of the wind tunnel measurement of the major static coefficients with particular emphasis on the drag function and to assess whether such a facility, backed up by empirical correction techniques, would be able to provide data with errors reduced to an admissible level for use in mathematical trajectory models able to accommodate inaccuracies of a few percent by fitting to a limited number of real firings. The aeroballistics of the shell chosen for the tests have already been well established from US tunnel and range firings thus providing the study with a set of data for comparison.

2. REVIEW OF COEFFICIENT ERRORS FROM MODERN FACILITIES

Operators of large modern wind tunnels claim that the repeatability of lift, drag and overturning moment measurements of a non-spinning projectile shape is probably better than 1% and with very good equipment may be as high as 0.1%. Hence the problem is not that of obtaining the required accuracy of instrumentation but of relating the wind tunnel measurements to full scale. This requires an extensive knowledge of the effect of Reynolds number, spin, model support and knowledge of the geometric shape of the shell after firing with the driving band engraved. The likely errors due to these effects are discussed below.

\* Senior Scientific Officer

\*\* Scientific Officer

26-2 2.1 Reynolds number

In general, wind tunnel tests are undertaken at Reynolds numbers significantly less than full scale although it is possible by use of large tunnels to test projectiles at full scale Reynolds numbers. However, the discrepancy between model and full scale is not likely to have a significant effect on the lift, overturning moment and forebody drag provided the boundary layer is artificially tripped such that turbulence occurs in a similar position to natural turbulence on the full size projectile in free flight. Most practical projectiles have a number of protruberances close to the nose which are likely to trip the boundary layer and for practical purposes the turbulent boundary layer may be assumed to start from the nose.

Skin friction does depend upon the value of Reynolds number but this dependence is well documented and since the skin friction is only about 10% of the total drag the small difference in skin friction between the model and full scale may be estimated within the required accuracy.

The base drag, which for a cylindrical afterbody may account for as much as 50% of the total drag, also depends upon Reynolds number and whilst there is ample data in the literature that may be used to correct for the effect of these differences at supersonic speeds it is doubtful if there is sufficient data at transonic Mach numbers to make the correction within the required accuracy.

2.2 Spin

Within the limits of experimental accuracy, balance measurements made with spinning models show that there is no discernible effect on lift and overturning moment. Thus these parameters may be obtained without spinning the model. However spark range studies carried out by Schmidt and Murphy (1) have shown variations of as much as 5% in the drag coefficient over the range of spin/velocity ratio encountered in the real environment. They ascribed this as being due to a rearward movement of transition with increasing spin which had the effect of decreasing the skin friction while increasing the base drag. These tests were for free transition, however if transition is fixed or occurs at the nose then the effect is likely to be smaller. The authors are not aware of any extensive data to confidently say that the consequent effect may be ignored or estimated, although it is thought that the error is likely to be around 1% for a cylindrical afterbody at moderate supersonic speeds.

2.3 Sting support

The standard method of supporting a model projectile in a wind tunnel is with a sting support. This support does not have an appreciable effect on measurements of lift and overturning moment but it does affect the base drag. The error introduced by the sting at M=2 was investigated by Reid and Hastings (2). Their experimental results showed that the base pressure with a sting is within 2% of the base pressure without a sting provided the sting diameter is less than 35% of the body diameter and also that any abrupt increase in size is located more than three body diameters downstream of the base.

2.4 Driving band

The driving band drag may be a significant part of the total drag. Although its presence probably reduces the base drag it is estimated that the overall effect is to enhance the total drag by about 4%. Thus, for drag measurements at least, the shape of the driving band after engraving must be reproduced. However, since the contribution is only 4%, the driving band probably need not be copied with high precision.

In summary there is little doubt that the lift and overturning moment results obtained from the tunnels are well within the accuracies required by the mathematical model (say 5 to 10%). The corrections which can be made for the above errors (and which mostly affect the base drag) really relate only to the supersonic region due to the data available. At the transonic Mach numbers there is insufficient data to make such reliable corrections particularly for the Reynolds number and sting effects. It was for this reason that the current study was carried out to estimate the residual errors in the static aerodynamic parameters at subsonic and transonic speeds. The evaluation was made for the tunnels at the Aircraft Research Association (ARA) which were selected as being best equipped for the study.

3. WIND TUNNELS

The facilities used were the 2.4 m x 2.7 m transonic and the 0.68 m x 0.76 m supersonic tunnels both of which are of the closed circuit, continuously operating type. Besides having smooth flow characteristics, they are well calibrated, and operate with good data acquisition equipment. (Mach number errors for the models tested were quoted as 0.25%). The tests were made on full scale and twice full scale unspun models in the supersonic (Mach 2.0 and 2.5) and transonic (Mach 0.5 to 1.4) speed ranges respectively (comprising fifteen Mach numbers in all). Tests were carried out both for constant Reynolds number conditions ( $1.2 \times 10^7$  and  $0.6 \times 10^7$  based on model length in the transonic and supersonic tunnels respectively) and also with a constant tunnel pressure of 76 cm of mercury in the transonic tunnel. The results of the tunnel tests, which have been fully reported (3) (4), are summarized below.

4. MODEL AND TEST DETAILS

Three configurations of the shell were tested each having a different driving band, one plain, one with streamwise engraving grooves, and one with grooves inclined at  $10^\circ$  to the model axis, which for brevity will be referred to as the "plain", the "streamwise" and the "inclined" respectively. All surface finishes were made to simulate the rough turned finish of the actual shell and the two keyways on the forebody were represented by a groove around the full circumference to allow for the spin in flight.

The sting to base diameter ratio was fixed at 35% on the evidence of (2) (which showed the measured base pressure at Mach 2 to be the same with and without the sting) and the length of the parallel sting ahead of the tapered section was chosen as 2.27 base diameters. Since the sting to base diameter ratio was considered optimum and the length of parallel sting after the base adequate, it was hoped that the base

pressures would be as close to the free flight values as it would be possible to predict. The drag discussed in this paper is therefore the total drag measured by the balance even though the base of each of the transonic models was fully pressure plotted. 26-3

The Acenaphthene sublimation technique was used to determine the state of the boundary layer. At transonic speeds (where the Reynolds number was comparable to that in free flight) the boundary layer was seen to be naturally turbulent and consequently no correction was considered necessary. For the supersonic tests however it was found necessary to trip the boundary layer with a transition strip of ballotini 0.18 to 0.20 mm in height. Schlieren photographs were taken in the supersonic tunnel and the yaw angle range was generally between  $\pm 20^\circ$ . Allowances were made for tunnel wall constraint, blockage and blockage buoyancy at transonic speeds. Forces and moments were all referenced to the maximum body diameter.

The aerodynamic forces and moments were measured for a set of yaw angles thought to give the best estimations (in the sense of minimum variance) of the four principal aeroballistic coefficients at each Mach number together with additional angles to guard against bias. The yaw angle pattern used for the plain configuration, (selected, for reasons described later, as the best for comparison with the US data) was much more extensive than those for the other two shells and included a series of replicate measurements. The yaw angle pattern was the same at each Mach number in the transonic region on the assumption that every Mach number was equally important. Also, the order in which the replications of each yaw angle were set up was randomised at each Mach number so as to control any unknown factors which might influence the shell's aerodynamic behaviour.

ARA showed that the drag results obtained from the preliminary test programme (3) may have been affected by sting leakage which led to a programme of repeat measurements on the plain configuration in the subsonic Mach number region. It was also found that the length of the original (or standard) sting strongly influenced the measured drag on the shell in the transonic wind tunnel, so the zero yaw measurements were repeated for the plain and streamwise groove configurations mounted on an extended sting having a total parallel length of 3.7 base diameters. The Mach numbers chosen for the second test programme (4) supplemented those in the earlier ARA study. Some of the Mach numbers, however, duplicated those included previously, so that the compatibility of the data sets could be checked.

The decision to use the balance measured drag was strengthened to some extent by the base pressure measurements which showed that the base pressure near zero yaw on shells of this type is very unsteady due to the unstable nature of the flow separation over the periphery of the shell base. This fluctuating base pressure is fundamental to the nature of the flow over this type of base and could be the source of small random variations in the measurements. However, it was considered that the filtered output of the axial force balance, which includes an integration of the fluctuating base pressures, is the most representative force to use.

#### 5. CORRECTION PROCEDURE

The corrections considered all related to errors in the measurement of the zero yaw drag coefficient due to the improper simulation of Reynolds number and spin and the presence of support interference. Corrections for roughness variations were ruled out on the grounds that there is little data in the literature describing the effect, which in any case is assumed to be small for properly simulated surface finishes.

Corrections for Reynolds number discrepancies between tunnel and full scale were applied to the early measurements to relate them to standard conditions at the muzzle. These corrections, which were for the skin friction and base drag components of the drag and obtained from well documented procedures (5), were found to be relatively small, the root-mean-square or RMS values averaged over the subsonic and transonic speed regions being 1.25 and 0.38% of the total measured drag respectively. The procedure however is rather tenuous as there is no unique representation of the real shell environment. In reality, as well as normal ground variations, there is a family of atmospheric conditions each relating to the particular values of muzzle velocity and quadrant elevation pertaining to the shell trajectory. On these grounds it was decided that no corrections should be applied.

The shell spin represents another area in which the wind tunnel does not simulate the trajectory conditions where the shell spin rate and velocity degrade with time. The empirical spin correction applied to the early shell-fixed measurements was taken as 1.4% from (1) to represent the muzzle spin condition. The small value of the correction has been substantiated by Sykes (6) who recently concluded a study at RARDE using spinning afterbodies. Following these results and the tenuous nature of the correction it was decided that the procedure should not be adopted for the more recent tunnel results.

The main correction applied to the drag measurements was for the effect of sting support interference which consists of two components, one due to the upstream pressure field caused by the sting, described as the "length effect" and the other due to the presence of the sting in the wake or the "diameter effect". No correction was applied for the latter mainly due to the lack of reliable data in the literature for transonic speeds. However a series of tests were carried out in the transonic tunnel using five different sting lengths to determine the length interference. At subsonic speeds the results agreed quite well with the approximate potential flow theory proposed by Tunnell (7) which predicts the variation of the incremental base pressure coefficient  $\Delta C_{pb}$  with sting length. Fig 1 shows that the theoretical and experimental pressure fields were best correlated with a sting flare of  $7^\circ$  compared with the actual value of  $6.5^\circ$ , a difference which might be explained by the boundary layer growth on the sting. Owing to the asymptotic nature of the predicted sting length effect it was necessary to define a practical "infinite sting" limit for  $\Delta C_{pb}$ . A value of 0.001 was chosen as it represented approximately 1% of the minimum total drag measured at subsonic speeds. It is seen that this value relates to a sting length of about 250 cm which would be quite impractical from the viewpoint of physical tunnel constraints and suggests that concepts of a "critical sting length" may be misleading.

Due to the presence of irregular pressure distributions in the working section at speeds above Mach 0.95 the total interference factors for this speed region were derived by adding a forebody correction term

$\Delta C_{Df}$  (allowing for these variations from the Mach number norm) to the theoretical estimate of  $\Delta C_{Df}$  due to the sting length effect on the base pressure. This process is shown diagrammatically in fig 2, and fig 3 illustrates the good correlation achieved for the balance measurements of the forebody drag ( $C_{D0} - C_{Df}$ ) over the Mach number range considered.

The correction factors that have been applied are tabulated in table 1 which shows that the corrections to the subsonic base drag for the standard sting reduce from about 9% to 5% of the total drag measured when it is replaced by the extended sting. At supersonic speeds the base drag correction decreases while the forebody correction, applied to the extended sting only, becomes more significant. It can also be seen that the difference in measurements for the two stings is significantly less after the corrections have been applied, which indicates the validity of the procedure used. The final column in the table shows the significant differences in measured drag between tests carried out on separate occasions, which are thought to be due to the sting leakage effects described earlier. Further experiments have been carried out by Sykes at RARDE on the effects of different base configurations on these corrections, the results of which suggest that, in general, the theoretical pressure field can be adjusted to agree with the experiment for a given base shape and base to sting diameter ratio.

The corrected and uncorrected estimates of the zero yaw drag coefficient for the plain shell are shown in fig 4 together with the US data set. The "ideal" coefficients were derived from the measured forces by standard curve fitting methods allowing for any bias error wherever possible. Table 2 shows the percentage variations of the zero yaw drag of streamwise and inclined models from that of the plain configuration. It is seen that the zero spin drag variations are significant (particularly around Mach 1.0) and tend to refute the earlier estimate of 4% as the likely effect of the driving band presence. However, this apart, it was felt that these variations would be significantly less in the real environment where the effect of the shell spin would be to make the driving band appear solid to the air flow thus tending to negate any perturbations due to design features within its external contour. It was for this reason that the plain configuration, properly matching the shape of the driving band after engraving, was selected as the best representation.

#### 6. COMPARISON OF ARA DATA WITH US SET

Fig 4 shows that the corrected tunnel zero yaw drag coefficient values agree very well with the US curve, thus lending confidence to the correction procedure applied. The main exception to this good agreement lies in the Mach number range 1 to 1.4 which includes the peak values of drag and where the effect of the correction is generally to enlarge the gap between the two sets of data. However it is worth noting that relatively little is known about the source and construction of the US data, thus discrepancies between it and the wind tunnel results do not necessarily mean that the latter is poor.

The tunnel values of the yaw drag coefficient were surprisingly less than half the corresponding US values. No obvious explanation can be given for this except to say that a value of  $C_{D\alpha^2} = 7.0/\text{rad}^2$ , derived from a model spark range at Mach 1.9, is in closer agreement with the current wind tunnel results. The tunnel measured lift coefficient showed the same good agreement with the US data as the zero yaw drag. For the lower part of the Mach number range however the tunnel values were less than the US equivalents as were the values for the overturning moment coefficient.

#### 7. ASSESSMENT OF THE WIND TUNNEL ERRORS

The coefficient errors comprised those inherent in the tunnel tests themselves and those arising from scaling the tunnel tests to real conditions. The former, which were ascribed to inaccuracies in instrumentation, the repeatability and regularity of the tunnel flow (referred to as the flow stability) and asymmetries between the flow and the model were determined to a 95% confidence limit whereas the scaling errors for drag and their correction (described earlier) were not. Both types of error have been expressed as percentages of the total measured coefficient and are listed in table 3 for the subsonic and transonic speed regions. RMS values of the component errors have been derived for those inaccuracy sources covered by a range of Mach number samples and these are tabulated together with the maximum deviation from the mean, the number of samples and the data points per sample.

The accuracy of the instrumentation was derived from the resolution of the data acquisition equipment given in (3) by converting the absolute values to percentages of the measured coefficients. This procedure yielded values of 1.2 and 0.4% for the drag measurements in the subsonic and transonic speed regions. The repeatability of the tunnel air flow in the working section was assessed from tests made under nominally identical conditions but in which the model was disturbed between successive measurements. Repeatability figures for drag of 0.7 and 0.8% were obtained for subsonic and transonic speeds respectively. Asymmetries between the model and the tunnel air flow were assessed from the difference in the drag measurements obtained for model roll orientations of 0 and 180° during the same test sequence. These differences amounted to errors for the drag measurements of 1.7% at subsonic speeds and 0.9% at transonic speeds.

The major error in the measurement of drag was due to the sting support. Although the semi-empirical corrections described earlier reduced the differences between measurements on the two stings there were still small differences remaining. These differences were used to determine the residual errors in the drag coefficient, the RMS values of which were 2.4 and 2.0% in the subsonic and transonic regions respectively.

The lift and overturning moment coefficients are not affected by the scaling errors and consequently the total error in their measurement is solely due to inaccuracies in the tunnel. The large model/tunnel flow asymmetry errors in  $C_{L\alpha}$  shown in table 3 are due, in some part, to the small values of the coefficients associated with the modest range of yaw over which measurements were made for the model in the 0 and 180° roll orientations.

Although the tunnel drag measurements have only been corrected for the effects of sting length and irregularities in the working section pressure distributions, table 3 attempts to summarize the total errors corresponding to (i) a full scale unspun model, uncorrected for Reynolds number or spin and (ii) a similar model corrected to full scale ground conditions. It is seen that the modest values of the total residual errors (around 2 to 3%) assessed for the latter case are compatible with the accuracy requirement of the mathematical model for both subsonic and transonic speeds. Indeed, the percentage errors at transonic speeds, which were generally less than the subsonic values due to the larger coefficients measured, are about the same level as earlier supersonic estimates. It must be emphasised however that the figures are optimistic as they do not include estimates for the component errors arising from sting diameter and roughness effects. The authors are aware of little data in the literature for these error sources and time did not permit a study although Sykes has recently carried out some sting support tests at RARDE using realistic shell models. The results however are regarded as both realistic and revealing as they include evaluations of inherent tunnel inaccuracies that are often assumed to be negligible.

## 8. CONCLUSIONS

An assessment has been made of the inaccuracies associated with measurements on bodies of revolution in large modern wind tunnels in order to examine the possibility of obtaining the coefficients required by mathematical trajectory models without recourse to extensive full scale firings.

A test programme was carried out using the transonic and supersonic tunnels of the Aircraft Research Association in which lift, drag and overturning moment were measured on a shell model having three driving band configurations. Although the lift and overturning moment results were shown to meet the required accuracy, marked differences were observed in the measured drag values obtained at subsonic and transonic speeds when using sting supports having similar diameters but different lengths.

An empirical correction for the support system was derived which agreed well with a subsonic theoretical estimate. At speeds above Mach 1.0 the irregularity of the tunnel axial pressure distribution dominated the effects due to the support system and a combined correction was derived. It was found that the difference in measured values after correction was very much less than before, over the whole Mach number range, thus supporting this technique.

The measured zero yaw base pressures were found to be unsteady due to the unstable nature of the flow separation over the periphery of the shell base. These fluctuations, which are probably fundamental to the nature of the flow over this type of base, were thought to be a source of small random variations in the measurements.

The corrected zero yaw drag coefficients agreed very well with an existing US set, thus lending confidence to the correction procedure applied.

A statistical analysis of the total residual coefficient errors due to those inherent in the tests themselves and those arising from the sting length effect yielded values of around 2 to 3% which were thought to be compatible with the accuracy requirement of the chosen mathematical model. Percentage errors at transonic speeds were generally less than subsonic values due to the larger measured coefficients.

## 9. REFERENCES

1. Schmidt L E  
Murphy C H "Effect of spin on aerodynamic properties of bodies of revolution", BRL Memo Report No 715, August 1953.
2. Reid J  
Hastings R C "Experiments on the axisymmetric flow over afterbodies and bases at  $M = 2.0$ ", FAE Report No Aero 2628, October 1959.
3. Fellows K A "Results of wind tunnel tests on two shells over the Mach number range 0.5 to 2.5", Unpublished ARA Report, May 1971.
4. Fellows K A "Results of wind tunnel tests on two shells over the Mach number range 0.5 to 2.5", Unpublished ARA Report, May 1972.
5. Engineering Society Data Sheets.
6. Sykes D M "Experimental investigation of base-pressure on a spinning cylinder and boattailed afterbody at subsonic speeds", RARDE Memorandum 32/72, November 1972.
7. Tunnell P J "An investigation of sting support interferences on base pressure and forebody chord force at Mach numbers from 0.60 to 1.30" NACA RM A54K16a, 1955.

## ACKNOWLEDGEMENTS

The authors would like to express their thanks to Mr E Carter and Mrs K Fellows of the Aircraft Research Association who were responsible for the tunnel programme. The paper is Crown copyright and is reproduced with the permission of the Controller, Her Majesty's Stationery Office.

**Table 1** Corrections applied for sting support interference

Mach Number	Corrections applied			Difference in drag measured on the two stings		Difference between original tests and recent series
	Extended sting		Standard sting	Before correction	After correction	
	Base drag	Forebody drag	Base drag			
0.5	4.9	-	8.8	2.4	1.3	6.5
0.7	4.8	-	9.0	6.3	2.5	7.7
0.8	4.8	-	9.2	8.5	4.6	8.5
0.85	4.6	-	9.1	10.1	5.9	-
0.9	4.1	-	7.9	8.1	4.7	16.4
0.95	2.8	-	-	-	-	-
1.0	2.9	1.1	4.9	6.8	3.3	-
1.05	2.0	0.3	-	-	-	-
1.1	0.9	3.5	1.1	0.1	2.8	-
1.15	2.5	2.7	-	-	-	-
1.3	1.4	4.1	2.2	2.3	1.2	-

NB The figures listed are expressed as percentages of the total measured drag for each Mach number

**Table 2** The percentage variation of the zero yaw drag of the grooved driving band models from that of the plain model:

Mach Number	Streamwise Grooves	Inclined Grooves
0.5	+ 2.0	+ 0.7
0.7	+ 1.0	+ 2.5
0.8	- 0.9	+ 1.1
0.9	+ 3.3	+ 4.4
0.95	- 2.5	+ 1.0
1.0	- 8.4	- 6.3
1.15	- 4.1	- 2.8
1.4	- 5.0	- 1.0

Table 3 Coefficient errors assessed from the Transonic Wind Tunnel results

Coefficient		$C_{D0}$		$C_{L\alpha}$		$C_{M\alpha}$		
Speed Region		Subsonic	Transonic	Subsonic	Transonic	Subsonic	Transonic	
Errors due to	Unrepresentative Reynolds Number	Mean RMS error	1.25	0.38				
		Maximum deviation	0.75	0.28				
		Number of samples	3/1	5/1				
	Unspun Model	Mean RMS error	1.40	1.40				
		Maximum deviation	-	-				
		Number of samples	3/1	5/1				
	Imperfect Sting Corrections	Mean RMS error	2.41	1.97				
		Maximum deviation	1.20	0.85				
		Number of samples	4/3	4/3				
	Model/Tunnel Asymmetry	Mean RMS error	1.72	0.87	3.90	3.59	1.21	0.91
		Maximum deviation	1.03	0.46	2.62	3.88	0.71	0.57
		Number of samples	3/2	5/2	3/4	5/4	3/4	5/4
	Instrumentation Inaccuracy	Mean RMS error	1.2	0.4	2.17	1.47	0.99	0.49
		Maximum deviation	-	-	-	0.67	-	0.04
		Number of samples	1/1	2/1	1/1	2/1	1/1	2/1
	Flow Instability	Mean RMS error	0.66	0.76	0.43	0.20	0.39	0.32
		Maximum deviation	-	-	-	-	-	-
		Number of samples	1/16	1/16	1/12	1/12	1/12	1/12
<b>TOTALS</b>	(i)	Mean RMS error	3.76	2.74	4.48	3.89	1.61	1.08
	(ii)	Mean RMS error	3.26	2.32				

- N.B. 1. The number of samples is expressed in the following manner:  
(Number of samples in mean) / (Number of readings in a sample)  
ie 3/12 is equivalent to 12 readings per Mach number and 3 Mach number samples in the mean.
2. The figures are expressed as percentages of the total measured coefficient. The model/tunnel asymmetry, instrumentation accuracy and flow stability results are given to 95% limits of confidence.

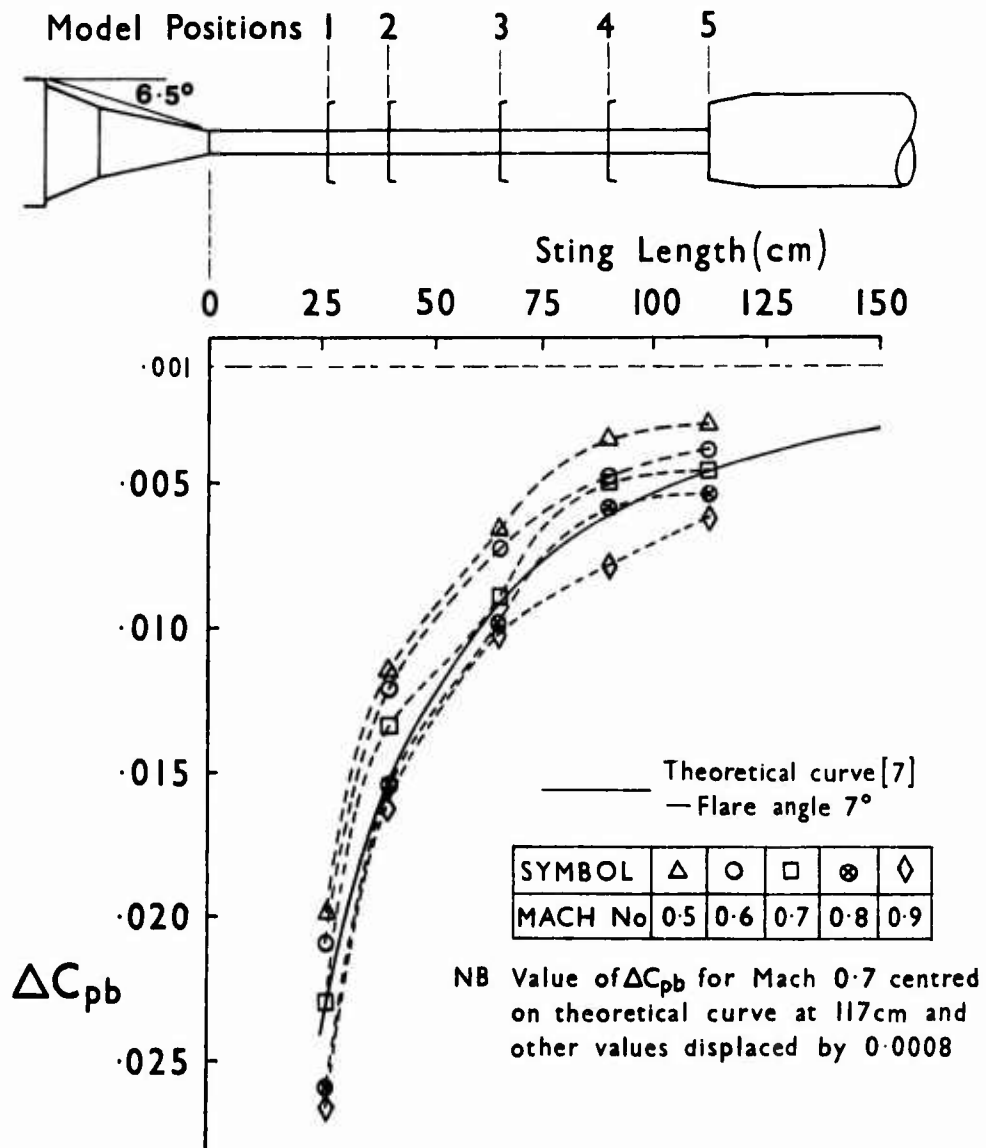


FIG1 THE VARIATION OF BASE PRESSURE WITH STING LENGTH

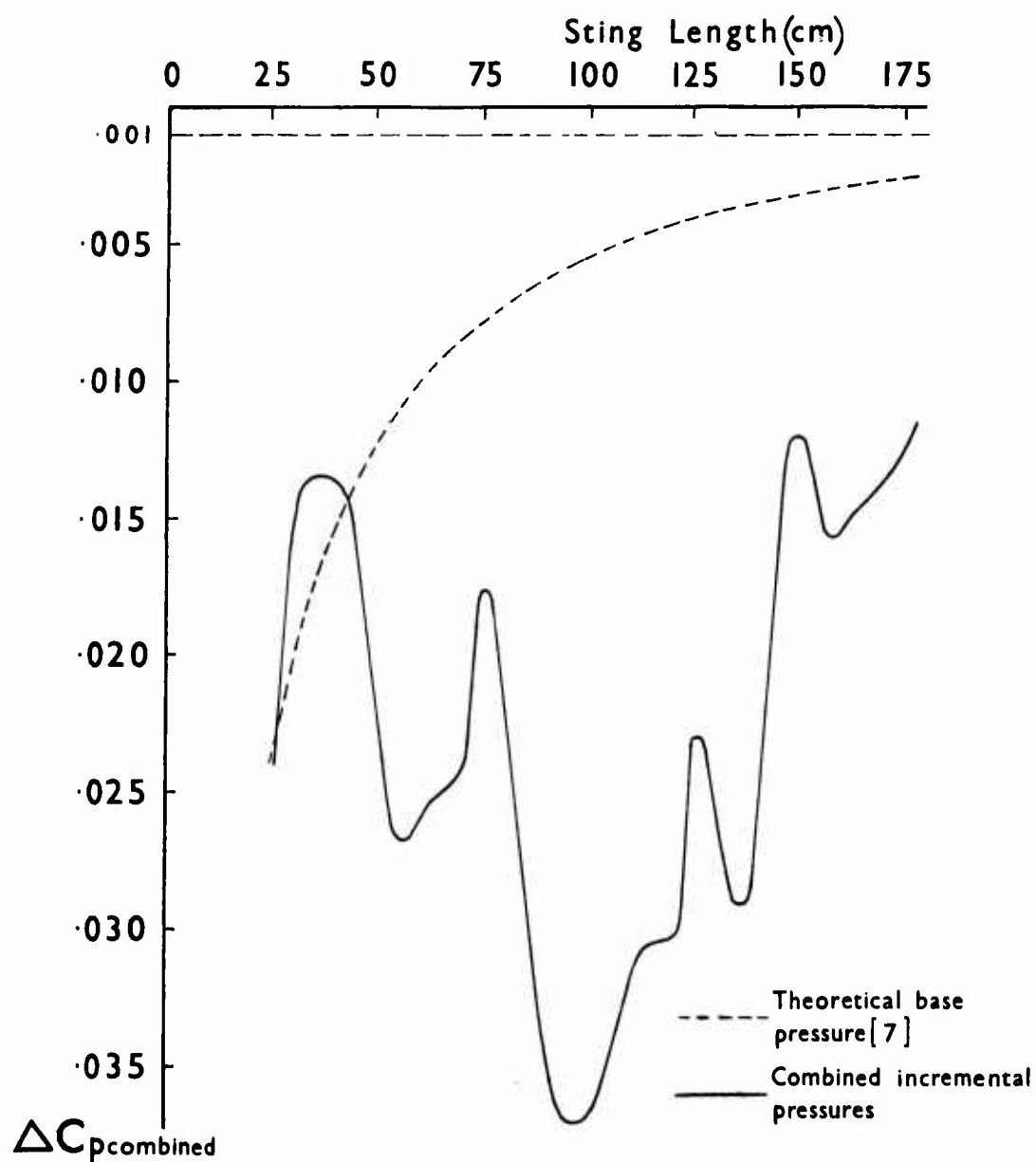


FIG2 COMBINED FOREBODY AND BASE  
INCREMENTAL PRESSURES AT MACH 1.4

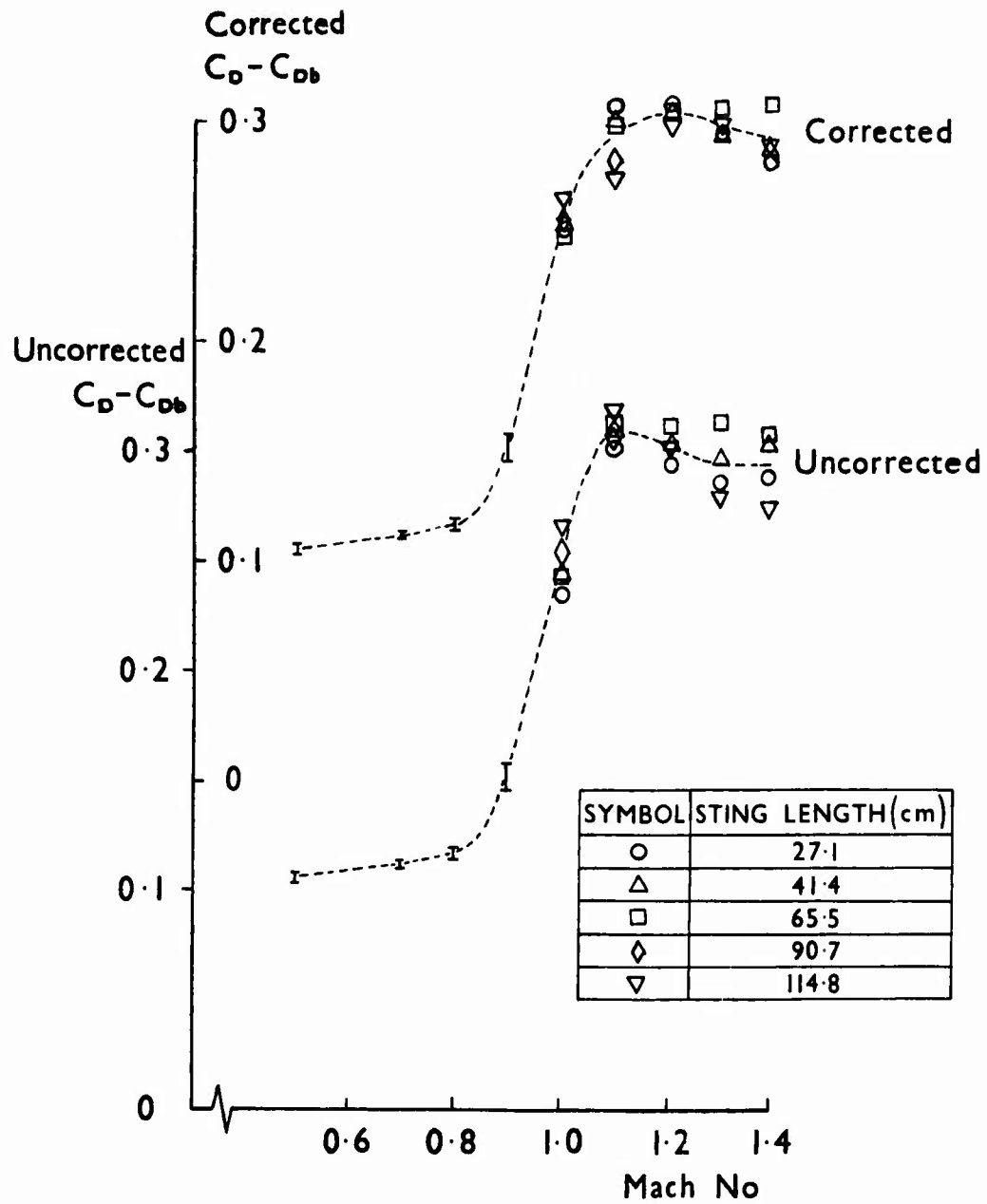


FIG 3 VARIATION OF FOREBODY DRAG  
WITH STING LENGTH

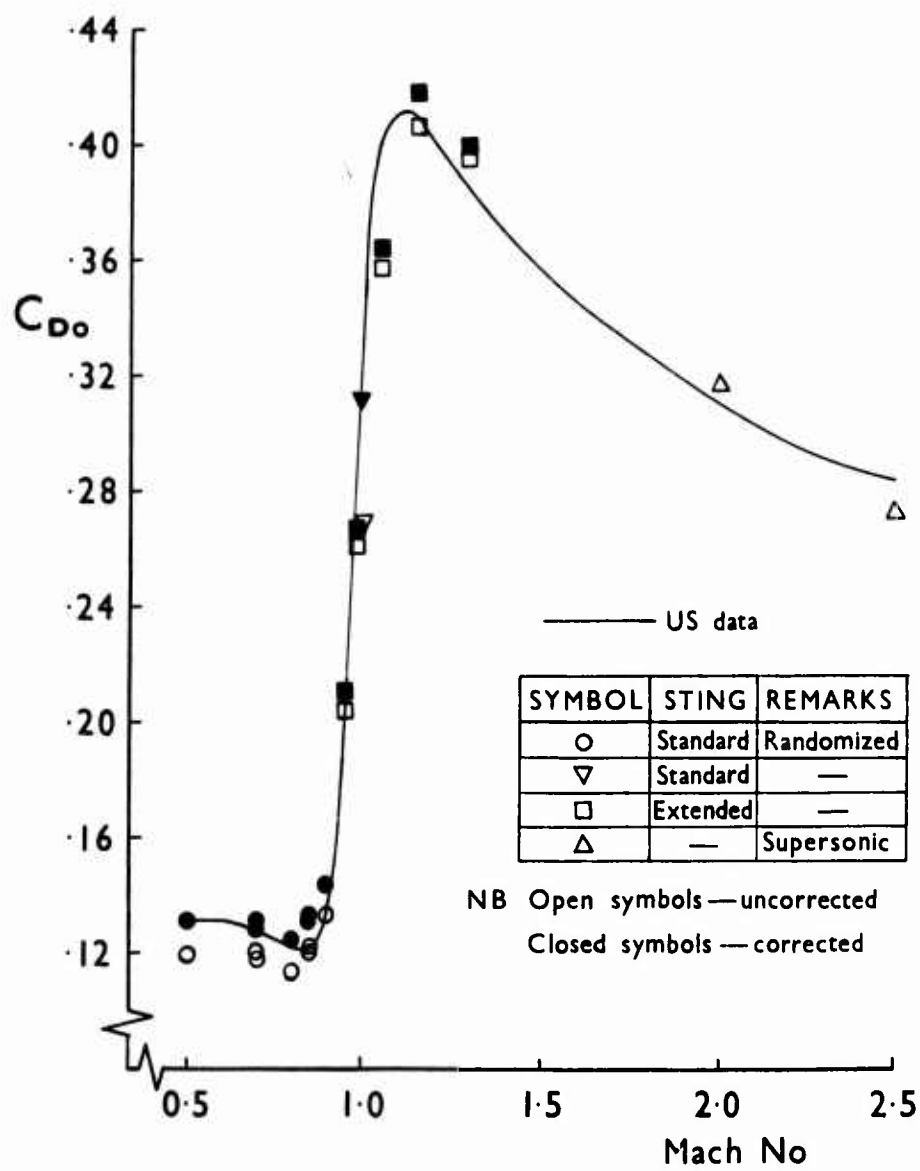


FIG 4 ZERO YAW DRAG COEFFICIENT  
FOR THE PLAIN SHELL

STING INTERFERENCE EFFECTS ON AFTERBODIES AT TRANSONIC SPEEDS

27-1

D. M. SYKES

Department of Aeronautics, The City University,  
St. John Street, London, EC1V 4PB, England

SUMMARY

The pressure distribution over the surface of three axisymmetric afterbodies at zero incidence has been measured and sting interference effects determined through the Mach number range from 0.70 to 1.15 in an octagonal, slotted wall wind tunnel.

The afterbodies tested were a simple cylinder and conical boat-tails  $\frac{1}{4}$  calibre long with  $7\frac{1}{2}^\circ$  angle and 1 calibre long with  $9^\circ$  angle, each carrying a representative driving band. Sting diameter effects were determined using 4 calibre long cylindrical stings of diameter  $\frac{1}{4}, \frac{1}{2}, \frac{3}{4}$  and 1 calibre, and sting-flare interference effects were determined for a  $10^\circ$  semi-angle cone on a  $\frac{1}{4}$  calibre sting.

The tests showed that the ratio of sting to base diameter was the main parameter for interference effects, but data for diameter effect from afterbodies with other geometries was not fully correlated using this parameter. Successful correlation with other data has been achieved for the proximity of conical flares of different angles for subsonic flow conditions.

NOTATION

$C_D$	pressure drag coefficient of afterbody	$\beta$	boat-tail angle
$C_{D_b}$	pressure drag coefficient of base	$\alpha$	flare cone semi-angle
$C_{D_\beta}$	pressure drag coefficient of boat-tail		
$C_p$	pressure coefficient $(p - p_\infty) / \frac{1}{2} \rho v_\infty^2$	Subsca. p's	
$D$	centrebody diameter	$b$	base
$d$	diameter	$f$	flare
$l$	length	$s$	sting
$M$	Mach number	$\beta$	boat-tail
$p$	pressure	$\infty$	free stream

1. INTRODUCTION

In the past the aerodynamic characteristics of shells, which are needed for trajectory and range calculations, have been determined mainly from range firing trials. A number of factors have combined over the last few years which make it desirable to reduce the number of such trials and Fancett and Smith (1) have re-examined the accuracy of transonic wind tunnel measurements of these properties.

One of the main sources of discrepancy between free flight and wind tunnel data is the presence of a sting support system which holds the model in position in the wind tunnel. McDonald and Hughes (2) presented a correlation of sting support interference effects, mainly on ogive boat-tailed afterbodies, but this is not really adequate for the conical boat-tail afterbodies which are generally found on shells. Recent tests by Fellows (3) on a shell model at full-scale Reynolds number showed the necessity for further investigation of sting interference effects on typical shell afterbodies. A series of conical boat-tail afterbodies has been tested at transonic speeds by Sykes (4) and the same facility and some of the models have been used in the present tests.

The sting support system under consideration typically consists of a length of a parallel cylindrical sting, one end of which enters the model at its base, and the other end expands as a conical flare which is generally attached to the incidence quadrant. Lee and Summers (5) showed that the interference effect consisted of a 'length' effect due to the proximity of the flare to the base, and a 'diameter' effect which was a function of sting to model base diameter ratio and which remained when the flare was so far from the base that it had no measurable effect. More recent tests of sting interference effects on afterbody drag have been made by Kurn (6) at fairly large sting to base diameter ratios on straight cylinder and ogive boat-tailed afterbodies.

The present tests have shown that there is a difference in the 'diameter' effect for a straight cylindrical afterbody compared to boat-tailed afterbodies. For the former geometry the base drag initially decreases, then increases to a local maximum and must then decrease again as the sting to base diameter ratio increases, whilst for the latter geometry the base (and afterbody) drag decreases steadily as sting to base diameter ratio increases. The 'length' effect has been found to be independent of sting diameter and a good correlation of data for conical flares with semi-angles between  $4^\circ$  and  $12^\circ$  at subsonic speeds has been achieved.

2. APPARATUS

The experiments were made using the RARDE continuous running closed return wind tunnel fitted with an octagonal slotted wall working section having 9% open area ratio. The working section is 457 mm long and the four pairs of parallel and opposite surfaces are each 184 mm apart. The stagnation pressure was approximately  $\frac{1}{2}$  atmosphere and Reynolds number/metre increased with Mach number from 7 to  $10 \times 10^6$ . Pressures were measured to the nearest 0.1 mm using a vertical multitube mercury manometer.

A hollow centrebody of 50.8 mm diameter passed into the working section from upstream and the various afterbodies were attached to the downstream end of the centrebody. The afterbodies tested were each 2

calibres long and consisted of a straight cylinder, and two conical boat-tailed models which had  $l/D = \frac{1}{2}$  with  $\beta = 7\frac{1}{2}^\circ$  and  $l/D = 1$  with  $\beta = 9^\circ$ , and the ratios of base diameter to body diameter were  $d_b/D = 1.000$ ,  $0.868$  and  $0.682$ , respectively. Each afterbody carried a model driving band and the model and driving band dimensions are shown in Figure 1.

The 'diameter' effect was determined by using straight cylindrical stings, each  $4D$  long and having diameter ratios  $d_s/D = \frac{1}{4}, \frac{1}{3}, \frac{1}{2}$  and  $\frac{1}{2}$ , which screwed into the base of the models. The work of Lee and Summers (5) indicated that afterbody pressures should not be affected by the changes in sting length to base diameter ratio  $l_s/d_b$ .

The 'length' effect was investigated using cylindrical stings with diameter ratios  $d_s/D = \frac{1}{2}$  and length ratios  $l_s/D = 4.87, 4.0, 3.0$  and  $2.0$  and a  $10^\circ$  semi-angle conical flare of length  $2.85D$  and base diameter  $1.26D$ . The upstream end of each sting located into the base of each model, whilst the base of the flare was mounted on a traverse gear which was attached to the roof of the wind tunnel downstream of the end of the slotted nozzle.

For the 'diameter' effect tests the base of the models was  $170$  mm ahead of the downstream end of the nozzle and the driving band carried streamwise grooves as shown in Figure 1. The boundary layer near the base was approximately  $0.09$  calibres thick, and turbulent with a power law exponent of  $6$ . For the 'length' effect tests it was necessary to fit a shortened centrebody which took the bases to  $345$  mm from the downstream end of the nozzle, the grooves in the driving band were filled, and the boundary layer thickness near the base was reduced. The positions of the models within the nozzle is shown in Figure 2.

The pressure distributions measured on the boat-tail surfaces and on the base were integrated to give boat-tail drag coefficient  $C_{D_b}$  and base drag coefficient  $C_{D_b}$  and the afterbody drag coefficient  $C_D$  was then found by addition.

### 3. RESULTS

#### 3.1 Sting diameter effect

Sting diameter effect tests were made through the range of Mach number from  $0.85$  to  $1.15$ . The pressures on the two boat-tailed models behaved in a similar manner whilst the cylinder model showed some differences. For the former, Figure 3 shows that for subsonic and through sonic speed, increasing sting diameter always decreased  $-C_{D_b}$  and thereby reduced base drag or increased base thrust, and there was little change in the Mach number for minimum base drag. Figure 4 shows that for the cylinder afterbody at subsonic and through sonic speeds the presence of the sting reduced the base pressure defect, but this effect was less with  $d_s/D = 0.500$  than with  $d_s/D = 0.375$ .

Figure 5 shows the change in base pressure coefficient at particular  $M_\infty$  values, plotted against  $d_s/d_b$ . For  $M_\infty \leq 1.05$  the 'diameter' interference effect was almost independent of  $M_\infty$  for the three afterbody geometries; on both boat-tail models the base pressure defect was consistently reduced as  $d_s/d_b$  increased. For the cylinder this occurred only for  $d_s/d_b < 0.3$  and then the interference effect began to fall away from the boat-tail curve, went through a local maximum at  $d_s/d_b \approx 0.4$  and extrapolation predicts zero interference effect at  $d_s/d_b \approx 0.58$ . It is expected that for larger  $d_s/d_b$  ratios the interference effect would again increase and tend to follow the boat-tail results. At  $M_\infty = 1.10$  all three afterbodies experienced differing interference effects for all  $d_s/d_b$  values, the cylinder behaving qualitatively as at lower Mach numbers. At  $M_\infty = 1.15$  there was no interference effect on the boat-tail bases for  $d_s/d_b \leq 0.4$ , but larger stings then produced different effects for the two models; the cylinder continued to behave qualitatively as at lower Mach numbers.

The effect of the presence of the sting was felt on the boat-tail surface and produced a change in boat-tail drag, as shown in Figure 6. For both boat-tailed afterbodies there was a consistent effect of increasing sting diameter decreasing the boat-tail drag coefficient, but when the interference change in  $C_{D_b}$  was plotted against  $d_s/d_b$  for various constant  $M_\infty$  it was found that the two geometries maintained their individual behaviour.

There was no detectable interference effect on the pressure on the cylinder model at either of the two side static pressure holes.

The interference effect was transmitted upstream from the base over the boat-tail surface for a distance which decreased as  $M_\infty$  increased. At the lowest Mach number the effect was carried right upstream to near but not ahead of the shoulder. As  $M_\infty$  increased, the flow around and for increasing distances downstream of the shoulder was supersonic and appeared to be unaffected by the presence of a sting.

The combination of base and boat-tail drag coefficient, the former evaluated assuming the base pressure acted uniformly over the full base area and not merely the annulus unobscured by the sting, yields afterbody drag coefficient  $C_D$ .

The sting interference effect on  $C_D$  as a function of  $d_s/d_b$  for the boat-tail afterbodies at various constant  $M_\infty$  is shown in Figure 7. For  $M_\infty \leq 1.00$  the data could be predicted reasonably well by a single curve. At  $M_\infty = 1.05$  there was a lesser decrease in  $C_D$  with increasing  $d_s/d_b$  than at the lower Mach numbers, but both afterbodies conformed to the same curve. At  $M_\infty = 1.10$  the results for the two afterbodies diverged for  $d_s/d_b > 0.3$  but  $C_D$  still decreased with an increase in  $d_s/d_b$ . When  $M_\infty = 1.15$  there was no interference effect for  $d_s/d_b < 0.4$  but then there was increasing  $C_D$  on the  $l/D = \frac{1}{2}, \beta = 7\frac{1}{2}^\circ$  boat-tail model, whilst the  $l/D = 1, \beta = 9^\circ$  boat-tail model showed decreasing  $C_D$  for  $d_s/d_b > 0.6$ . Since there is no boat-tail, the results for the cylinder afterbody are exactly as described when discussing the interference influence on base pressure.

### 3.2 Sting length effect

Sting length effect tests were made through the range of Mach number from 0.70 to 1.15 using a sting with  $d_s/D = 0.25$ . The shorter centrebody used for these tests brought the afterbodies just downstream of the throat of the nozzle and this caused small changes in the afterbody pressure distribution and also made the boundary layer on the afterbody somewhat thinner than in the 'diameter' tests; these effects slightly changed the base pressure on the models with no sting. This was not considered to be significant as these tests were to determine the changes in pressure due to the proximity of the conical flare. 27-3

The effect of shortening the distance between the base of the models and the conical flare is shown in Figures 8 and 9 and is seen to be similar to the effect of increasing sting diameter ratio  $d_s/d_b$ . A theoretical expression for the pressure perturbation at a point on a cylindrical sting due to a conical flare situated further downstream in a subsonic flow was given by Tunnell (7). For most practical sting geometries the expression may be written as

$$\Delta C_p = \frac{1}{2} \tan \theta \left( \frac{d}{l_s} - \frac{d_f}{(l_s + l_f)} \right)$$

which does not include the model base diameter or the stream Mach number. Experimental values of  $\Delta C_{pb}$ , the increase in base pressure due to flare proximity, appeared to be almost independent of Mach number for  $M_\infty < 1$  and showed a similar trend to the above expression with change of  $\theta$  and  $l_s$  but were clearly dependent on model base diameter  $d_b$ . The work of Tunnell (7) and Lee and Summers (5) has also shown that the relevant length scale for sting length effect is the model base diameter. The data for the present tests were plotted as  $\Delta C_{pb} \cot \theta$  against  $l_s/d_b$  and are shown in Figure 10, together with data of Lee and Summers (5) for a cylindrical model and further data from Fellows (8) for base pressure on a shell model with a boat-tail having  $l/D = \frac{1}{2}$ ,  $\beta = 90^\circ$ , mounted on a sting with a flare having effectively  $\theta = 6.5^\circ$ . It will be seen that all these results have correlated well despite the range of values of sting diameter to base diameter from 0.25 to 0.87 covered in these various tests. Thus it appears that the curve shown in Figure 10 can be used to predict sting length interference effect on base pressure on cylinder or conical boat-tail models from cylinder-flare stings in subsonic flows, and that this interference effect is negligible for  $l_s/d_b > 6$  at the largest flare angles, and for shorter lengths as the flare angle is reduced.

At supersonic speeds the effect of sting length on base pressure was less well defined and it is felt that this arose because, with the afterbody just downstream of the nozzle throat, the pressures were influenced by the larger Mach number gradients which are known to exist in this region of this tunnel at supersonic speeds.

The pressures on the two boat-tail surfaces were integrated and the boat-tail drag coefficients  $C_{D\beta}$  for the various sting lengths and Mach numbers were determined. The sting length effect was barely detectable on the  $l/D = 1$ ,  $\beta = 90^\circ$  boat-tail and for the  $l/D = \frac{1}{2}$ ,  $\beta = 7\frac{1}{2}^\circ$  model were only detectable for the shortest sting length at subsonic speeds; a reduction of  $C_{D\beta}$  of about 0.005 was measured. Thus for most practical situations it would appear that for stings with cylindrical lengths in the range  $3 < l_s/d_b < 6$  it is necessary to correct the base pressure for sting length or flare proximity interference effects at subsonic speeds using the curve given in Figure 10, and to correct afterbody drag for sting diameter effect using the curves given in Figure 7.

### 4. CONCLUSIONS

The pressure distribution has been measured at Mach numbers between 0.85 and 1.15 on three axisymmetric afterbodies consisting of a cylinder and two conical boat-tails of length 0.5 calibre with  $7\frac{1}{2}^\circ$  boat-tail angle and 1 calibre with  $90^\circ$  angle carrying simple cylindrical stings of  $\frac{1}{4}$ ,  $\frac{1}{2}$ ,  $\frac{3}{4}$  and 1 calibre diameter. The pressure distribution has also been measured at Mach numbers between 0.70 and 1.15 on the same afterbodies carrying a  $\frac{1}{2}$  calibre diameter sting with a  $10^\circ$  conical flare set at various distances from the base. These models were of typical shell afterbody configuration and each carried a representative driving band on the main body.

The results confirm previous work which showed that sting support interference effect for a cylinder-flare sting could be considered as consisting of a 'length' effect due to the proximity of the flare to the base of the model, which was additive to a sting 'diameter' effect. In both cases the relevant model length scale was found to be the base diameter.

Comparison of the results of the present 'length' interference tests with the data of Lee and Summers (5) showed that for subsonic speeds the presence of the flare had no detectable effect on the boat-tail or base pressure distribution if the flare commenced at a distance greater than about six base diameters downstream of the base. Even at shorter distances the interference effect on boat-tail drag was quite small, the maximum change measured being a decrease in drag coefficient of 0.005 for  $l_s/d_b = 2.3$ . The interference effect on base pressure was more significant with the presence of the flare tending to reduce base pressure defect, i.e. to reduce base drag. The changes in base pressure coefficient from the present tests and those measured by other workers using different flare angles  $\theta$  appeared to correlate well at subsonic speeds giving a single curve for  $\Delta C_{pb} \cot \theta$  as a function of length of the cylindrical sting to base diameter ratio. At the low supersonic speeds of the present tests the non-uniform velocity distribution in the region of the base of the model made the evaluation of the small changes in pressure over the afterbodies due to flare proximity open to doubt and no firm conclusions have been drawn.

Comparison of the results of the present sting diameter interference tests with the data of Kurn (6) raises a number of points of interest. Kurn's tests were made using truncated tangent ogive afterbody models mounted on a central support tube of 38 mm diameter in a 600 x 450 mm rectangular tunnel at a constant unit Reynolds number of  $8.8 \times 10^6/m$  over the Mach number range from 0.8 to 1.3, and so are at very closely comparable conditions to those of the present tests.

The variation of afterbody drag with sting diameter can be compared through the Mach number range for the  $l/D = 1$ ,  $\beta = 90^\circ$ ,  $d_b/D = 0.682$  model of the present tests, and the  $\beta = 9.6^\circ$ ,  $d_b/D = 0.703$  model of Kurn for the cases of no sting and with straight cylindrical stings having  $d_s/d_b = 0.73$  and 0.80 respectively. For these comparable geometries the data are in reasonable agreement for  $M_\infty \leq 1.05$  but for higher

Mach numbers the afterbody drags of the present tests reached greater maximum values than those of Kurn, although the latter results also included skin friction drag. From the results of the 'diameter' effects measured in the present tests and shown in Figure 7 the drag coefficient correction  $\Delta C_D = C_{D_{no\ sting}} - C_{D_{sting}}$  can be determined through the Mach number range of these tests. Such curves are shown in Figure 11 for sting to base diameter ratios  $d_s/d_b = 0.8$  and  $0.3$ ; also included in this figure is the correction curve for  $d_s/d_b = 0.8$  as given by Kurn for a straight cylindrical sting on the model with  $\beta = 9.6^\circ$ ,  $d_b/D = 0.703$ .

These results show that data from other afterbody geometries should not be used in detail for the correction of pressure distributions or drag of conical boat-tailed afterbodies for sting diameter effect.

#### REFERENCES

- 1 Fancett, R. K. and Smith, T. An assessment of the accuracy of transonic drag measurement in a large modern wind tunnel. Paper to be presented at AGARD Specialists Meeting on Aerodynamic Drag. 1973
- 2 McDonald, H. and Hughes, P. F. A correlation of high subsonic afterbody drag in the presence of a propulsive jet or support sting. AIAA Journal of Aircraft, 2, 3, 1965, p 202-207
- 3 Fellows, Mrs. K. A. Results of wind tunnel tests on two shells over Mach number range 0.5 to 2.5. Unpublished ARA Report. 1972
- 4 Sykes, D. M. Pressures on boat-tailed afterbodies in transonic flow with a low-thrust jet. AIAA Journal, 9, 6, 1970, p 1206-1208
- 5 Lee, G. and Summers, J. L. Effects of sting support interference on the drag of an ogive-cylinder body with and without a boat-tail at 0.6 to 1.4 Mach number. NACA RM A57 IO9, 1957
- 6 Kurn, A. G. Drag measurements on a series of afterbodies at transonic speeds showing the effect of sting interference. ARC CP 984. 1968
- 7 Tunnell, P. J. Investigation of sting support interference on base pressure and forebody chord force at Mach number from 0.6 to 1.3. NACA RM A54 K16a. 1954
- 8 Fellows, Mrs. K. A. Unpublished results of wind tunnel tests, 1972

#### ACKNOWLEDGEMENTS

This work was done whilst the author was acting as a Vacation Consultant and the author wishes to thank the Ministry of Defence (Army) for affording him the opportunity of working at RARDE. In particular the help and advice given by Mr. J. E. Bowman and Dr. R. K. Fancett is gratefully acknowledged.

The paper is Crown Copyright and is reproduced with the permission of The Controller, Her Majesty's Stationery Office.

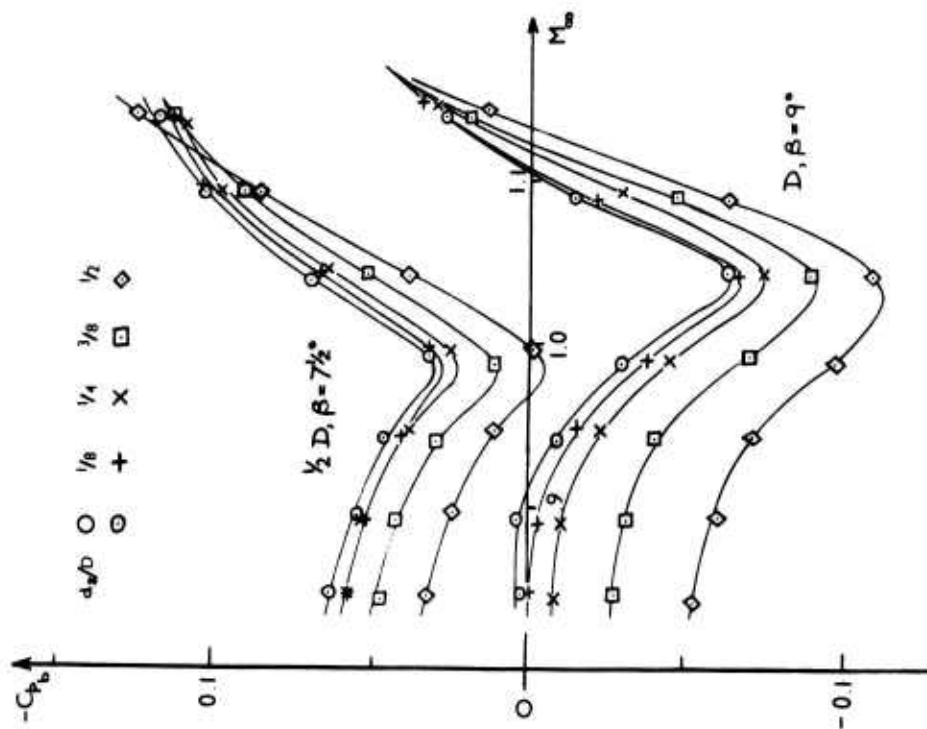


FIG 3 STING DIAMETER EFFECT ON BOAT TAIL BASE PRESSURE

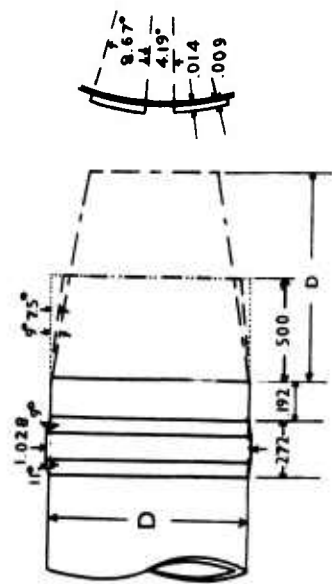


FIG 1 AFTERBODY GEOMETRY

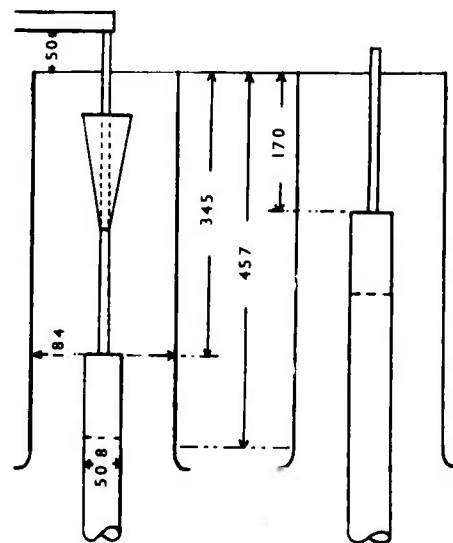


FIG 2 MODEL POSITION IN NOZZLE

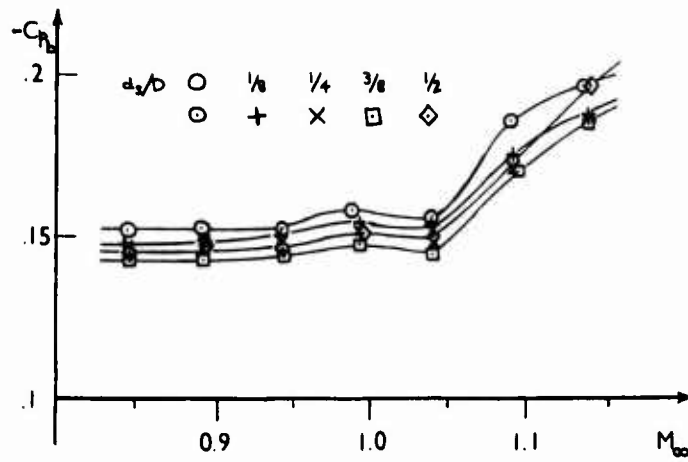


FIG 4 STING DIAMETER EFFECT ON CYLINDER BASE PRESSURE

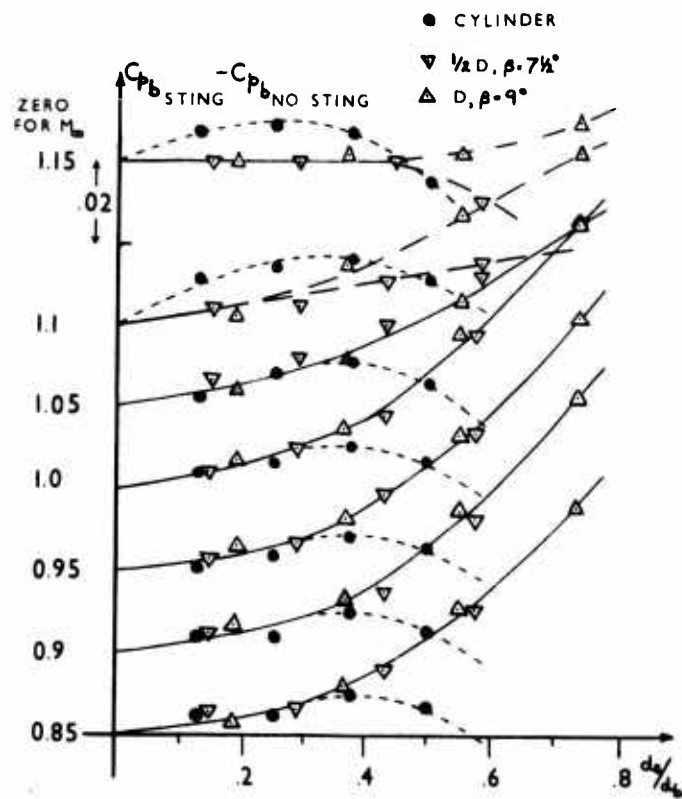


FIG 5 STING INTERFERENCE ON BASE PRESSURES

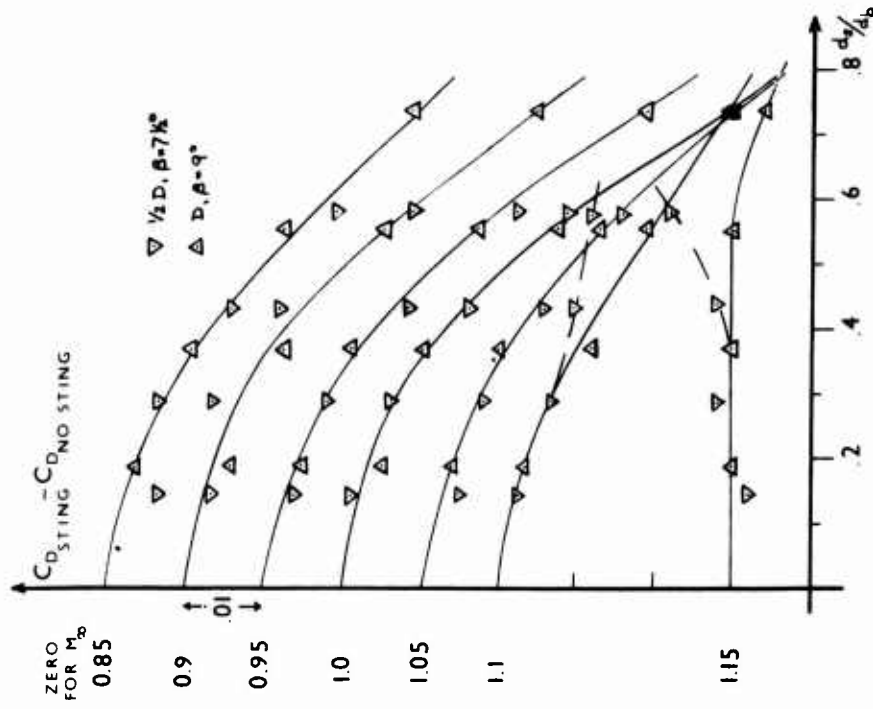


FIG 7 STING INTERFERENCE ON AFTERBODY DRAG

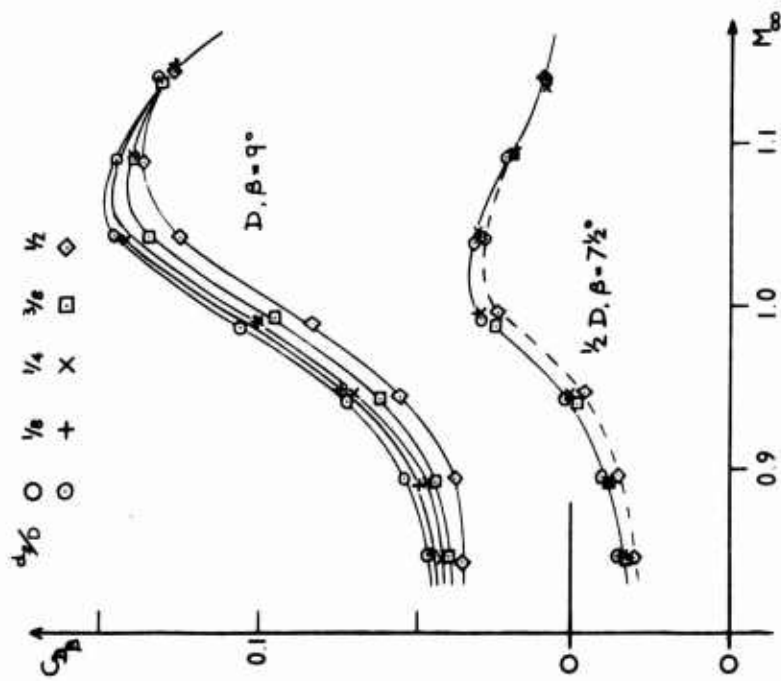


FIG 6 STING DIAMETER EFFECT ON BOAT-TAIL DRAG

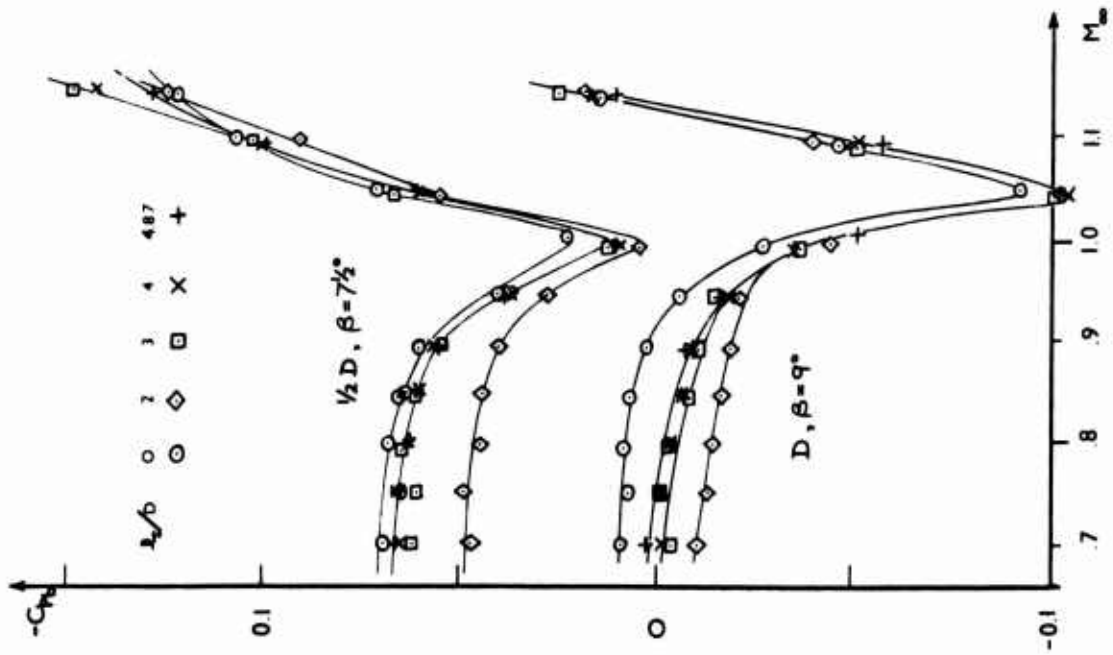


FIG 8 STING LENGTH EFFECT ON BOAT-TAIL BASE PRESSURE

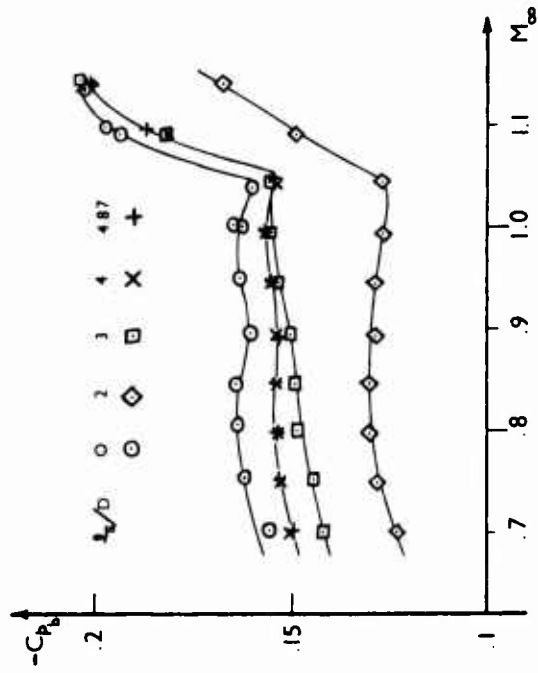


FIG 9 STING LENGTH EFFECT ON CYLINDER BASE PRESSURE

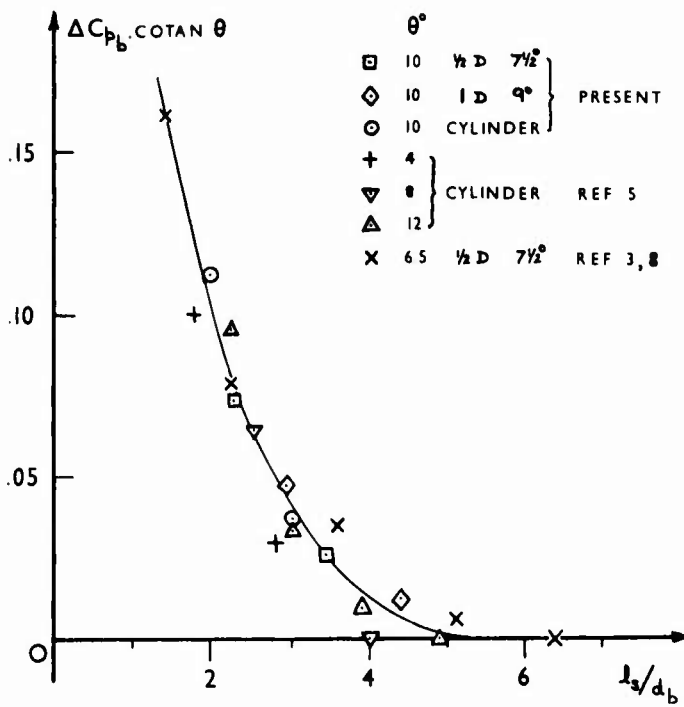


FIG 10 STING LENGTH INTERFERENCE ON BASE PRESSURE  $M_b < 1$

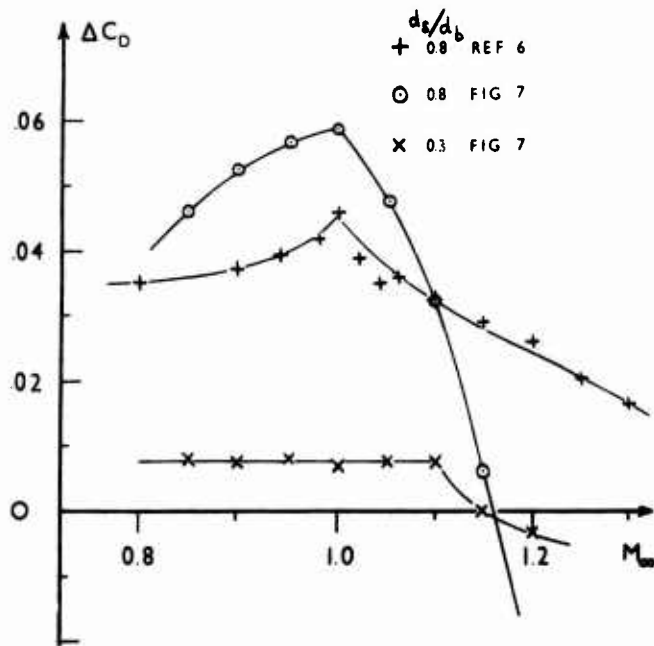


FIG 11 COMPARISON OF CORRECTIONS TO AFTERBODY DRAG

## MESURES DE TRAINEE EN TUNNEL DE TIR

par

Daniel BAHUREL

Alain DESGARDIN

LABORATOIRE DE RECHERCHES BALISTIQUES ET AERODYNAMIQUES

27207 VERNON - FRANCE

## R E S U M E

Après avoir rappelé sommairement le principe de la mesure de la traînée en tunnel de tir, on décrit les diverses méthodes d'exploitation actuellement utilisées :  $C_x$  constant -  $C_x$  fonction de l'incidence -  $C_x$  fonction du nombre de Mach, ainsi que leur domaine d'utilisation et la précision à en attendre.

On présente ensuite une série de résultats obtenus récemment au tunnel de tir du L.R.B.A. sur un projectile sphéro-conique et un projectile cylindro-conique à jupe dans une large gamme de nombre de Mach (0,7 à 14) et pour des incidences atteignant parfois 15°. Ces résultats sont complétés par des mesures obtenues au tunnel de l'Institut de Saint-Louis, essentiellement en transsonique sur des formes variées de projectiles allant du corps élané à la sphère.

## NOTATIONS

$x, y, z$  : Coordonnées du centre de gravité du projectile dans le trièdre lié au tunnel ( $x$  horizontale suivant l'axe de tir,  $y$  et  $z$  à 45° de la verticale).

$m$  : Masse du projectile

$\vec{V}$  : Vecteur vitesse de module  $V$

$S$  : Surface de référence égale au maître couple du projectile

$l$  : Longueur de référence égale à la longueur de la maquette

$L$  : Longueur de trajectoire étudiée

$t$  : Temps

$C_x, C_z$  : Coefficient de traînée et de portance dans des axes liés au vecteur vitesse

$$C_x \delta^2 = \frac{\partial C_x}{\partial (\delta^2)}$$

$V_R$  : Vitesse de référence en m/s prise égale à celle du milieu de la trajectoire

$\rho$  : Masse spécifique de l'atmosphère ambiante

$\delta^2$  : Carré de l'incidence globale =  $\lambda \bar{\lambda}$

$\lambda = \beta + i a$  avec  $\beta$  et  $a$  projections de l'angle d'incidence

$\psi, \theta$  : Angles de restitution de la position de l'axe de la maquette dans l'espace.

$$a_0^2 = \frac{1}{L} \int_0^L (\beta^2 + a^2) dx$$

$$x' = \frac{dx}{dt} \quad x'' = \frac{d^2x}{dt^2}$$

## 1. INTRODUCTION

L'étude du mouvement de maquettes en vol libre au tunnel de tir, dans de bonnes conditions de simulation du vol réel, apporte une contribution originale aux mesures de traînée aérodynamique. Si les méthodes d'essais sont maintenant bien classiques, les possibilités offertes par l'acquisition et le traitement moderne des mesures ont permis plus récemment d'affiner les méthodes d'exploitation et de fournir les résultats de traînée en vol, en fonction de l'incidence par exemple ou encore en fonction du nombre de Mach en transsonique.

La première partie de l'exposé est consacrée à une présentation des méthodes de mesure et d'exploitation en tunnel. Dans la seconde, après avoir présenté une série de résultats sur des corps de formes variées au tunnel classique de l'Institut de Recherches de Saint-Louis, on exposera les résultats obtenus récemment au tunnel de tir du L.R.B.A. sur deux projectiles, l'un sphéro-conique et l'autre cylindro-conique à jupe, pour des vitesses comprises entre Mach 0,7 et Mach 14 et pour des incidences atteignant parfois 15°.

## 2. DETERMINATION D'UNE TRAJECTOIRE DE VOL EN TUNNEL DE TIR

Le principe général utilisé pour la détermination de la loi de traînée d'un corps en vol libre est d'étudier le mouvement de son centre de gravité en fonction du temps. Il s'agit donc d'abord de restituer la trajectoire et ensuite de la traiter par une exploitation adéquate. La trajectoire est restituée à partir de photographies de la maquette en vol.

### 2.1. Visualisations

Dans le tunnel de tir du L.R.B.A. comme dans la majorité des installations analogues la trajectoire du projectile est obtenue par visualisation : le long du tunnel sont en effet disposées 24 sections de mesures équipées chacune de 2 chambres métriques de grande précision donnant deux ombroscopies dans des plans orthogonaux (planche I). Le tunnel étant tenu dans l'obscurité, les obturateurs des chambres sont maintenus ouverts pour le tir. Les sources lumineuses des 2 ombroscopies sont deux éclateurs ponctuels déclenchés par le signal d'un pont hyperfréquence travaillant en 3 cm de longueur d'onde et déséquilibré par le passage du projectile dans le champ des antennes. La durée du flash est de l'ordre  $1/20 \mu s$  et la précision des compteurs de temps est  $1/40 \mu s$ . Pour une vitesse de 5 000 m/s ces données correspondent à une erreur de restitution de l'ordre de 0,3 à 0,4 mm.

### 2.2. Restitution de la trajectoire

Pour obtenir la trajectoire à partir de la série des deux photographies, il est nécessaire de connaître par ailleurs les caractéristiques optiques des chambres métriques. Ces données constituent "la géométrie du tunnel" dont la détermination a fait l'objet d'études particulières citées en référence 1 et 2.

Les plaques photographiques sont lues à l'aide d'un agrandisseur muni d'une table X Y avec codeurs au  $1/20$  de mm. Les lois de l'optique sont utilisées en schématisant les objectifs photographiques par un centre fictif de projection conique. Les équations dans l'espace de l'axe de la maquette sont obtenues en recherchant l'intersection des plans bissecteurs des plans tangents aux contours apparents et passant par les centres de projections des chambres. La position du centre de gravité est ensuite recherchée sur cet axe en déterminant le centre de la sphère du nez dont le rayon est connu.

Tous les pointages sont effectués en nombre surabondant pour appliquer le principe des moindres carrés. Compte tenu des diverses imprécisions sur les données de la géométrie du tunnel, les incertitudes globales sur la restitution sont estimées à :

- 0,5 mm pour x : abscisse du centre de gravité G le long de l'axe de tir
- 0,2 mm pour y, z : coordonnées latérales de G
- 0,2 degré pour les angles.

## 3. METHODES D'EXPLOITATION DES MESURES EN TUNNEL

### 3.1. Equation générale de la traînée

Les conditions d'utilisation des tunnels de tir imposent des trajectoires tendues et l'abscisse curviligne du centre de gravité le long de la trajectoire peut être confondue sans grande erreur avec l'abscisse x le long de l'axe de tir. L'équation différentielle de la traînée d'un projectile de masse m s'écrit alors dans des axes liés à la vitesse  $\bar{V}$

$$(1) \quad m \frac{d^2 x}{dt^2} = - \frac{1}{2} \rho S V^2 C_x$$

Le problème posé est de déterminer les valeurs de  $C_x$  et de  $V_0$ , valeur de la vitesse à  $t = 0$ , compatibles avec les divers couples  $x_1, t_1$  mesurés.

Trois méthodes d'exploitation sont actuellement utilisables en fonction des caractéristiques du tir. On peut ainsi effectuer un dépouillement : à coefficient de traînée  $C_x$  constant  
à coefficient de traînée  $C_x$  variable en fonction de l'incidence  
à coefficient de traînée  $C_x$  variable en fonction de la vitesse

Les trois méthodes sont successivement présentées.

### 3.2. Résolution à $C_x$ constant

Si le coefficient  $C_x$  est supposé constant, l'équation (1) a pour solution formelle :

$$\begin{cases} V = V_0 e^{-\frac{\rho S}{2m} C_x \cdot x} \\ t = \frac{e^{-\frac{\rho S}{2m} C_x \cdot x} - 1}{-\frac{\rho S}{2m} C_x V_0} \end{cases}$$

avec  $x = 0$  ;  $V = V_0$  à  $t = 0$

La détermination des constantes  $V_0$  et  $C_x$  conduit alors à un pur problème de lissage dont la solution à l'aide du principe des moindres carrés est très aisément obtenue.

### 3.3. Résolution à $C_x$ variable en fonction de l'incidence

La maquette lancée en vol libre au tunnel de tir pendule autour de son centre de gravité ; l'incidence varie d'une manière continue le long de sa trajectoire ; en toute rigueur, le  $C_x$  ne peut pas être considéré comme constant. La loi de variation en fonction de l'incidence proposée pour la majorité des corps de révolution lancés au tunnel de tir est :

$$C_x = C_{x_0} + C_x \delta^2 \cdot \delta^2$$

Où  $\delta^2$  est le carré de l'incidence.

L'application de la théorie épicycloïdale peut donner une expression analytique approchant les variations du carré de l'incidence globale :

29-3

$$\delta^2 = \lambda \bar{\lambda} \quad \text{avec} \quad \lambda = \beta + i\alpha = K_1 e^{s_1 x} + K_2 e^{s_2 x} + K_3$$

où les coefficients  $K_j$  et  $s_j$  sont des quantités complexes

$$K_j = k_j + i k_j^* \quad \text{et} \quad s_j = \sigma_j + i \sigma_j^*$$

A l'aide d'un lissage préalable des angles de restitution  $\psi$ ,  $\theta$  et des coordonnées transversales  $y$  et  $z$ , les différents  $K_j$  et  $s_j$  peuvent être déterminés.

Malheureusement le report de  $\delta^2$  dans l'équation de traînée (1) conduit à la recherche de primitives compliquées et la solution formelle et rigoureuse de l'équation différentielle n'est pas connue :

$$V = V_0 \cdot e^{-\frac{PS}{2m} \left[ C_{x_0} \cdot (x-x_0) + C_x \delta^2 \int_{x_0}^x \delta^2(x) dx \right]}$$

Soit encore avec  $x = x_0 = 0$  et  $V = V_0$  pour  $t = 0$

$$t = \frac{1}{V_0} \int_0^x e^{-\frac{PS}{2m} \left[ C_{x_0} x + C_x \delta^2 \int_0^x \delta^2(x) dx \right]} dx$$

L'application du principe des Moindres carrés dont on trouvera des illustrations pour un tel traitement dans la référence 8, nécessitera aussi de calculer les différentes dérivées :

$$\frac{\partial t}{\partial C_{x_0}} = \frac{PS}{2m} \left[ t \cdot x - \int_0^x t dx \right]$$

$$\frac{\partial t}{\partial C_x} = \frac{PS}{2m} \left[ t \int_0^x \delta^2 dx - \int_0^x \delta^2 \cdot t dx \right]$$

$$\frac{\partial t}{\partial V_0} = -\frac{t}{V_0}$$

L'intégrale  $\int_0^x \delta^2 dx$  ne pouvant se calculer formellement, plusieurs approches de la solution vont être présentées en partant de solutions simples pour arriver à une solution "presque rigoureuse".

### 3.3.1 - Première méthode

On peut tenter de se ramener au cas précédent ( $C_x = Cte$ ) en considérant que  $C_x \delta^2 \cdot \delta^2$  n'est qu'un terme correctif dont la valeur peut être remplacée par une valeur moyenne en approchant

$$\int_0^x \delta^2 dx \quad \text{par la constante} \quad a_0^2 = \frac{1}{L} \int_0^L (\beta^2 + \alpha^2) dx$$

Il suffit alors d'effectuer un dépouillement à  $C_x$  constant et de considérer que le  $\bar{C}_x$  moyen correspond à la valeur moyenne  $a_0^2$  du carré de l'incidence du tir. Si on dispose de plusieurs tirs à incidences différentes, en portant les  $\bar{C}_x$  en fonction des  $a_0^2$  on doit trouver une droite dont la pente est  $C_x \delta^2$  et l'ordonnée à l'origine la valeur de  $C_{x_0}$ .

La droite peut évidemment être aussi recherchée par les moindres carrés mais pour chiffrer correctement les imprécisions sur les coefficients  $C_{x_0}$  et  $C_x \delta^2$  il est préférable de dépouiller directement tous les tirs à la fois en déterminant les valeurs de  $C_{x_0}$  et de  $C_x \delta^2$  qui minimisent la somme des carrés des écarts de tous les tirs.

### 3.3.2 - Deuxième méthode

Les résultats obtenus par la méthode précédente sont bons en eux-mêmes. Cependant ils nécessitent un grand nombre de tirs à incidences moyennes différentes alors qu'en vol libre on a la chance d'avoir une incidence variable dans un seul tir.

Aussi on peut calculer par des quadratures numériques les intégrales non calculables formellement. En effet la théorie épicycloïdale (référence 8) permet de calculer  $\delta^2$  et  $\int_0^x \delta^2 dx'$  et une méthode simple

de trapèze suffit pour traiter les 3 intégrales donnant :

$$t, \quad \int_0^x t dx \quad \text{et} \quad \int_0^x \delta^2 \cdot t dx$$

comme ci-dessus on peut traiter plusieurs tirs à la fois et les résultats obtenus sont très satisfaisants si l'incidence varie de façon appréciable sur la trajectoire.

### 3.3.3 - Troisième méthode

Un dernier pas est encore à franchir pour ne plus être tributaire de la théorie épicycloïdale non toujours

applicable. Dans le cas du transsonique par exemple les évolutions de l'incidence entraînées par un coefficient de moment variable en fonction du Mach ne peuvent être obtenues rigoureusement que par une intégration numérique de l'équation différentielle de pendulation. Aussi, à intégrer numériquement cette dernière, il est préférable dans la pratique d'intégrer aussi numériquement et simultanément l'équation de traînée. Si l'on explicite quelque peu les calculs concernant uniquement l'équation de traînée, le problème est d'intégrer :

$$\frac{d^2 x}{dt^2} = - \frac{PS}{2m} v^2 C_x$$

avec les conditions :  $C_x = C_{x_0} (1 + K \cdot \delta^2)$

$$\delta^2 = \beta^2 + a^2 \quad \text{qui est obtenu par une intégration numérique d'une ou plusieurs équations différentielles.}$$

Partant d'un lot de premières valeurs des inconnues et des conditions initiales, on peut toujours intégrer facilement cette équation et obtenir les résidus ou écarts entre les valeurs mesurées et calculées, à chaque section de mesure des grandeurs  $y, z, a, \beta$ .

On sait que la procédure de corrections différentielles demande en outre de connaître les valeurs des dérivées de la fonction  $x$  par rapport à toutes les inconnues appelées  $C_j$  pour la commodité. Ces valeurs peuvent être déterminées en remarquant qu'elles vérifient l'équation différentielle de traînée dérivée par rapport à  $C_j$ . Il suffit donc d'adjoindre à l'équation différentielle de traînée proprement dite, toutes celles obtenues en la dérivant par rapport à toutes les inconnues  $C_j$ , valeurs initiales comprises ( $x$  et  $\frac{dx}{dt}$  à  $t = 0$ )

$$\text{Ainsi } \left( \frac{\partial x}{\partial C_j} \right)' = - \frac{PS}{2m} \left[ 2v \frac{\partial v}{\partial C_j} C_x + v^2 \frac{\partial C_x}{\partial C_j} \right]$$

$$\text{avec } \frac{\partial C_x}{\partial C_j} = \frac{\partial C_{x_0}}{\partial C_j} \left[ 1 + K \delta^2 \right] + C_{x_0} \left[ \delta^2 \frac{\partial K}{\partial C_j} + K \frac{\partial \delta^2}{\partial C_j} \right]$$

Pour trouver les valeurs initiales de toutes les équations différentielles supplémentaires, l'approximation suivante a toujours donné satisfaction :

on développe  $x$  au voisinage de  $t = 0$

$$x = x_0 + x'_0 \cdot t + x''_0 \cdot \frac{t^2}{2} + \dots$$

$$\text{On a donc } \left( \frac{\partial x}{\partial x'_0} \right)_0 = (t)_0 = 0 \quad \frac{\partial^2 x}{\partial v_0 \partial t} = 1$$

$$\frac{\partial x}{\partial K} = \frac{\partial x}{\partial C_{x_0}} = \frac{\partial^2 x}{\partial K \partial t} = \frac{\partial^2 x}{\partial C_{x_0} \partial t} = 0$$

Le système présenté s'intègre facilement par la méthode de Runge-Kutta par exemple. Le détail de la procédure ainsi que des applications intéressantes sont présentés en références 3 et 4.

### 3.4. Résolution à $C_x$ variable en fonction de la vitesse

On sait qu'en faible supersonique et en transsonique le coefficient de traînée varie fortement en fonction de la vitesse. Même en limitant la trajectoire aux quarante premiers mètres du tunnel, on ne peut plus effectuer des dépouillements valables en considérant le  $C_x$  comme constant.

Une loi polynomiale en  $\frac{V_R - V}{V_R}$  où  $V_R$  est une vitesse de référence donnée, sensiblement celle du milieu de la trajectoire, a semblé intéressante car elle permet de reproduire, au moins par morceaux, la plupart des lois de traînée présentées dans la littérature. De plus l'expérience des dépouillements de tirs fictifs a montré que la détermination du coefficient  $C_{x_0}$  qui pour  $V = V_R$  correspond à celle de  $C_x$  est toujours obtenue avec une très bonne précision.

Dans la pratique une loi d'ordre 4 a été programmée

$$C_x = \sum_{i=0}^4 C_{x_i} \left( \frac{V_R - V}{V_R} \right)^i \quad \text{mais les ordres 1 ou 2 suffisent pour les tirs réels des corps}$$

de révolution d'érousement  $r_{\text{nez}} / r_{\text{culot}}$  voisin de 0,2.

La méthode de résolution qui est identique à la précédente a déjà été explicitée en détail à la référence 5. La procédure utilisée autorise même à cumuler les effets de variations d'incidence et de vitesse en traitant directement une loi de traînée de la forme :

$$C_x = C_{x_0} \delta^2 + \sum_{i=0}^4 C_{x_i} \left( \frac{V_R - V}{V_R} \right)^i \quad (2)$$

### 4. EVALUATION DES METHODES PROPOSEES PAR DES TIRS FICTIFS

Pour exploiter les méthodes de résolution rappelées ci-dessus, un programme de calcul appelé TRAIS (référence 5) a été écrit en langage Foftran. Il traite la loi de traînée générale :

$$C_x = C_{x_0} \delta^2 + \sum_{i=0}^4 C_{x_i} \left( \frac{V_R - V}{V_R} \right)^i \quad (2)$$

L'utilisateur fixe évidemment le nombre de termes à rechercher, en choisissant l'une des formulations :

$$C_x = C_{x_0} = \text{constante}$$

$$C_x = C_{x_0} + C_x \delta^2 \cdot \delta^2$$

$$C_x = \sum_{j=0}^n C_{x_j} \left( \frac{V_R - V}{V_R} \right)^j \quad \text{avec } n \leq 4$$

$$C_x = C_x \delta^2 \cdot \delta^2 + \sum_{j=0}^n C_{x_j} \left( \frac{V_R - V}{V_R} \right)^j \quad \text{avec } n \leq 4$$

Ce programme a été testé à l'aide de tirs fictifs calculés avec la loi de traînée tout à fait générale (2). On appelle tir fictif une trajectoire obtenue par intégration numérique des équations de la mécanique du vol en se donnant des conditions initiales et les lois aérodynamiques. La trajectoire ainsi obtenue peut ensuite être considérée comme provenant d'un tir réel et entrée dans les programmes de dépouillement dont l'exploitation finale doit permettre d'extraire les coefficients de la loi de traînée. Cette procédure permet de mettre en évidence les points délicats du traitement et les erreurs à minimiser dans l'acquisition. On a procédé en trois étapes. On a admis tout d'abord que la loi de traînée avait la même expression formelle que celle utilisée pour calculer la trajectoire fictive. Les couples  $(x_i, t_i)$  de la trajectoire sont alors utilisés comme données d'entrée du programme de dépouillement avec la précision des résultats du calcul précédent. On peut supposer dans un deuxième stade de simuler des erreurs de mesure en arrondissant les données d'entrée. On peut enfin admettre d'exploiter les résultats de la trajectoire fictive à l'aide d'une loi de traînée différente de celle qui a servi à la calculer. Les résultats obtenus avec la première procédure sont excellents quelle que soit la vitesse étudiée entre 200 et 5 000 m/s. Ceci signifie que les écarts résiduels à la convergence entre les couples  $(x_i, t_i)$  entrés et ceux calculés sont inférieurs à la précision des données d'entrée (6 décimales) et que les coefficients de la loi de traînée sont restitués avec une précision absolue équivalente. Le processus mathématique utilisé est donc correct. On a montré également que le programme TRAIS peut traiter jusqu'à 14 tirs à la fois. Ce nombre correspond à un cas réel de campagne existante sur une même maquette. Mais de bons résultats sont obtenus seulement sur 2 ou 3 tirs. Un premier pas pour s'approcher des tirs réels est d'appliquer une procédure d'arrondi simulant des erreurs de mesure. Avec des abscisses supposées connues à 0,5 mm près, les coefficients  $C_{x_0}$  et  $C_x \delta^2$  sont toujours convenablement restitués à 1 % près. Par contre en transsonique les imprécisions sur  $\delta^2$  les termes  $C_{x_1}$  et  $C_{x_2}$  peuvent atteindre 5 % suivant leur valeur. Enfin, le programme a été testé avec un tir fictif calculé par Giraud de l'Institut de Saint-Louis avec une autre formule de loi de traînée. Il s'agit d'un tir de sphère de 30 mm de diamètre et de masse 0,110 kg lancée dans une atmosphère d'air de masse spécifique 1,175 kg/m<sup>3</sup>. Les 20, 48 m de trajectoire étudiés ont été calculés à l'aide d'un polynôme de la forme

$$t = \sum_{j=1}^4 a_j x^j$$

ce qui correspond à une loi de traînée de la forme :

$$C_x = - \frac{\rho S}{2m} \times \frac{d^2 t / dx^2}{dt / dx}$$

qui s'écrit encore :

$$C_x = - \frac{\rho S}{2m} \times \frac{2a_2 + 6a_3 x + 12a_4 x^2}{a_1 + 2a_2 x + 3a_3 x^2 + 4a_4 x^3}$$

La vitesse au milieu de la trajectoire à 10, 24 m est de 411, 401 m/s. Cette vitesse a été prise comme vitesse de référence  $V_R$  pour les dépouillements.

Le tableau ci-après donne les résultats obtenus par le programme d'intégration numérique où l'on a pris  $C_x \delta^2 = 0$  et  $n = 4$ . On appelle  $C_{x_E}$  le coefficient de traînée calculé par la loi polynomiale en  $x$ . Le coefficient  $C_{x_C}$  est le coefficient restitué par la loi générale (2) avec les conventions précédentes.

Les écarts relatifs  $(C_{x_{calculé}} - C_{x_{exact}}) / C_{x_{exact}}$  obtenus après convergence n'atteignent pas 1 pour 1000, ce qui est tout à fait remarquable puisque la loi imposée dans le calcul de trajectoire ne correspond pas à celle du programme de dépouillement.

Giraud a, dans un deuxième temps faussé les temps des compteurs pour simuler des erreurs de mesure. Les erreurs introduites qui atteignent 3,2  $\mu$ s pour toutes les dernières tranches correspondent à des erreurs d'abscisses de l'ordre de 1,5 mm. Malgré ces erreurs élevées, le tableau des résultats montre que le coefficient de traînée est restitué à mieux que 1 % près sur les 14 mètres de trajectoire entourant la vitesse de référence. Par contre à chaque extrémité les erreurs atteignent 1,6 %, ce qui reste encore remarquable. On peut donc considérer que le programme de calcul donne toujours le terme constant  $C_{x_0}$  de la loi de traînée avec une précision supérieure à 1 % quelle que soit la vitesse. Les précisions sur les autres coefficients pouvant être moindres suivant l'incidence de la maquette, le nombre de mesures, pour une même gamme de vitesses ou les précisions de restitution.

## Résultats des tirs fictifs :

tranches	x m	temps exact $\mu$ s	$C_{xg}$ exact	$C_{xc}$	$\frac{C_{xc} - C_{xg}}{C_{xg}}$	temps faussés $\mu$ s	$C_{xc}$	$\frac{C_{xc} - C_{xg}}{C_{xg}}$
1	0	0		0,99464		0		
2	1,28	3 002,07		0,996387		3 002,80		
3	2,56	6 018,62	0,9955	0,9964	0,0009	6 020,25	0,9802	0,016
4	3,84	9 049,72	0,9940	0,9947	0,0007	9 052,11	0,9822	0,012
5	5,12	12 095,42	0,9908	0,9915	0,0007	12 098,275	0,9822	0,009
6	6,40	15 155,74	0,9859	0,9866	0,0007	15 158,755	0,9800	0,007
7	7,68	18 230,67	0,9796	0,9803	0,0007	18 233,65	0,9758	0,005
8	8,96	21 320,20	0,9717	0,9723	0,0006	21 323,105	0,9696	0,003
9	10,24	24 424,27	0,9623	0,9629	0,0006	24 427,205	0,9614	0,001
10	11,52	27 542,81	0,9513	0,9521	0,0008	27 545,89	0,9512	0,0001
11	12,80	30 675,72	0,9390	0,9397	0,0007	30 678,955	0,9391	0,0001
12	14,08	33 822,88	0,9251	0,9259	0,0009	33 826,155	0,9253	0,0002
13	15,36	36 984,15	0,9101	0,9107	0,0007	36 987,31	0,9098	0,0003
14	16,64	40 159,35	0,8933	0,8940	0,0008	40 162,32	0,8928	0,0006
15	17,92	43 348,29	0,8755	0,8760	0,0006	43 351,12	0,8744	0,0013
16	19,20	46 550,75		0,8567	-	46 553,57	0,8546	-
17	20,48	49 766,49		0,8361	-	49 769,32	0,8338	-

## 5. PRESENTATION DE RESULTATS EXPERIMENTAUX

Le succès d'une étude aérodynamique en tunnel de tir est liée d'une manière directe à la réalisation de la maquette. En effet, elle doit, comme pour un essai en soufflerie avoir une géométrie extérieure semblable à celle de l'engin à étudier, mais elle doit également être capable de résister sans dommage aux fortes accélérations du lancement ; elle doit de plus, supporter les contraintes thermiques du vol dans le tunnel de mesures où la simulation de nombres de Reynolds réalistes impose parfois des niveaux de pression engendrant des flux de chaleur élevés. Enfin la maquette doit être équipée pour le lancement d'un sabot dont la séparation doit apporter une perturbation minimale à la maquette pénétrant dans le tunnel.

Les techniques de conception et de réalisation de maquettes permettant en fait de répondre à ces contraintes pour une grande variété de formes, ce qui concourt à renforcer l'intérêt du tunnel de tir comme moyens d'essais aérodynamiques.

Pour illustrer les possibilités du tunnel de tir, on présente un ensemble de résultats aérodynamiques portant sur des mesures de traînée obtenues sur diverses formes. Deux corps, un sphéro-conique et un cylindro-conique ont été étudiés dans une gamme de vitesses variant entre 250 m/s et 4 500 m/s. Les résultats obtenus sur ces maquettes seront discutés d'une manière plus détaillée, à titre d'illustration des méthodes d'exploitation décrites dans la première partie de cette note.

## 5.1. Traînée globale de formes variées en transsonique et supersonique

Les premiers résultats présentés proviennent de l'Institut de Recherches de Saint-Louis et ont été obtenus dans un tunnel classique non pressurisé dont le Reynolds unitaire à Mach 1 est  $0,2 \cdot 10^6$  par cm.

Les projectiles concernés sont une sphère, une famille de corps cylindro-coniques avec jupe (têtes P), un projectile d'artillerie stabilisé par rotation et une famille de corps élancés (15 calibres) stabilisés par ailettes arrière.

La planche II donne la traînée globale en vol des divers projectiles en fonction du nombre de Mach. Elle met en évidence, en particulier, les possibilités du tunnel dans le domaine transsonique.

La comparaison des traînées des têtes PII à PV montre l'influence de l'angle de jupe dont la valeur est donnée ci-dessous :

maquette	Reynolds sur L	diamètre culot mm	longueur L mm	angle de jupe en degrés
PII	$1 \cdot 10^6$	32,9	84	40°
PIII	"			30°
PIV	"			20°
PV	"			15°

Au voisinage de Mach 1,2, la tête PII de 40° d'angle de jupe a une traînée globale supérieure à celle de la sphère étudiée dont le diamètre est de 20 mm. On peut expliquer ce phénomène par l'importance relative des traînées de frottement dont la contribution à la traînée totale est grande en transsonique.

On notera l'évolution particulière du  $C_x$  de la sphère entre Mach 1 et Mach 1,5. BAILEY et HIATT (référence 7) présentent une synthèse des résultats de traînée d'une sphère. Malheureusement le nombre de Reynolds ne dépasse pas 100 000 au lieu de 500 000 dans les tirs I.S.L., pour la zone de Mach intéressante et les résultats fortement dépendants du Reynolds dans cette gamme de vitesses ne peuvent pas être comparés à ceux de l'I.S.L.

### 5.2. Mesures de traînée globale d'un sphéro-conique entre 280 et 4 600 m/s

La planche III donne un schéma du projectile. Il s'agit d'un cône de  $12,5^\circ$ , de demi-angle au sommet et de rapport d'émoussement  $\frac{r_{nez}}{r_{culot}} = 0,2$ .

La planche IV donne l'allure du mouvement en y et z du centre de gravité de la maquette au cours d'un tir ; la planche V représente la variation des projections angulaires de l'axe de la maquette qui est en première approximation identique aux projections de l'angle d'incidence.

On présente les résultats obtenus sur ce corps en analysant séparément les tirs effectués au-dessus et en-dessous de 1 500 m/s. Les 2 zones de vitesses sont exploitées en effet de deux manières différentes. On discute également la précision des résultats en fonction des conditions imposées à la mesure.

#### 5.2.1. Résultats de traînée entre 1 500 et 4 600 m/s

Pour ce domaine de nombres de Mach élevés, les variations relatives de vitesse sur les quarante mètres de trajectoire étudiés sont très faibles et peuvent être négligées. Seule la variation de la traînée en fonction de l'incidence est donc à considérer.

$$C_x = C_{x_0} + C_{x_{\delta^2}} \cdot \delta^2$$

Le tableau suivant présente les résultats obtenus pour les cinq vitesses étudiées, à savoir 4 600, 3 900, 3 000, 2 500 et 1 500 m/s. On a tenu compte d'une variation du  $C_x$  en fonction de l'incidence :

- en remplaçant  $\delta^2$  par une valeur moyenne  $\alpha_0^2$  approchée, solution a.
- en calculant  $\int \delta^2 dx$  par une quadrature numérique, solution b.
- par intégration numérique directe de l'équation de traînée, solution c.

Tous les résultats présentés ont été obtenus en traitant à la fois l'ensemble des tirs effectués à une même vitesse quel que soit le centrage de la maquette.

Traînée globale du sphéro-conique  $12,5^\circ$  - Hypersonique (tableau I)

vitesse m/s	Reynolds sur la longueur de la maquette	nombre de tirs	$i_{max}$ en degrés	coef- ficients	solution		
					a	b	c
4 600	$4 \cdot 10^6$	10	7	$C_{x_0}$	$0,133 \pm 0,002$	$0,132 \pm 0,002$	$0,132 \pm 0,002$
				$C_{x_{\delta^2}}$	$3,1 \pm 0,4$	$3,3 \pm 0,4$	$3,3 \pm 0,4$
3 900	$5 \cdot 10^6$	10	8	$C_{x_0}$	$0,132 \pm 0,001$	$0,131 \pm 0,001$	$0,132 \pm 0,001$
				$C_{x_{\delta^2}}$	$4,4 \pm 0,5$	$4,28 \pm 0,45$	$4,3 \pm 0,4$
3 000	$10 \cdot 10^6$	12	8	$C_{x_0}$	$0,1394 \pm 0,0002$	$0,1400 \pm 0,0002$	$0,1397 \pm 0,0003$
				$C_{x_{\delta^2}}$	$4 \pm 0,1$	$4,1 \pm 0,1$	$4,2 \pm 0,1$
2 500	$8 \cdot 10^6$	11	7	$C_{x_0}$			$0,154 \pm 0,002$
				$C_{x_{\delta^2}}$			$2,35 \pm 0,3$
1 500	$5 \cdot 10^6$	5	5	$C_{x_0}$	$0,205 \pm 0,001$	$0,207 \pm 0,002$	$0,207 \pm 0,002$
				$C_{x_{\delta^2}}$	$2,8 \pm 0,1$	$2,8 \pm 0,2$	$2,9 \pm 0,1$

Comme prévu par la théorie, les résultats des solutions b et c sont équivalents. Quant à la solution a, elle donne toujours le bon  $C_{x_0}$  mais le  $C_{x_{\delta^2}}$  présente parfois un léger écart. Les résidus en y et z après convergence sont inférieurs au millimètre.

Les précisions obtenues sur le  $C_{x_0}$  sont excellentes : 7 pour mille à 3 900 m/s ; 2 pour mille à 3 000 m/s ; 1 % à 1 500 m/s. La campagne à 4 600 m/s donne une incertitude légèrement supérieure de 1,4 %, sans doute en raison des conditions sévères d'échauffement imposées à la maquette qui peuvent entraîner une légère déformation du nez de l'ogive.

Pour le gradient  $C_{x_{\delta^2}}$ , les incertitudes sont plus variables : dépendant essentiellement de l'incidence des tirs elles sont de  $\delta^2$  l'ordre de 3 à 4 % mais peuvent atteindre 10 %. Ces résultats pourraient être améliorés par des tirs à incidences plus élevées et en augmentant le nombre de compteurs de temps qui n'était que de 7 pour ces campagnes au lieu des 13 possibles.

#### 5.2.2. Résultats de traînée en transsonique

Il s'agit de résultats couvrant la gamme de Mach comprise entre 0,8 et 1,5 et encadrant le pic de traînée, centré vers Mach 1,1 ou 1,2. Le tableau ci-joint présente les résultats obtenus pour trois vitesses :

$$\begin{array}{l} 500 \text{ m/s} \quad (\approx M = 1,5) \\ 400 \text{ m/s} \quad (\approx M = 1,2) \\ 280 \text{ m/s} \quad (\approx M = 0,8) \end{array}$$

qui ont été exploitées avec la loi générale de traînée :

$$C_x = C_{x_{\delta^2}} \cdot \delta^2 + \sum_{i=0}^n \left( \frac{V_R - V}{V_R} \right)^i C_{x_i} \quad \text{avec } n = 0 \text{ et } 1$$

La planche VI donne la loi de traînée à incidence nulle pour toute la gamme de Mach balayée par l'ensemble de ces tirs transsoniques. Les imprécisions obtenues sur le  $C_{x_0}$  sont inférieures ou égales à 1 % ce qui est très correct pour des mesures en transsonique. Par contre les termes  $C_{x_{\delta^2}}$  et  $C_{x_1}$  ( $V_R - V$ ) /  $V_R$  ne sont jamais obtenus avec une bonne précision en raison des incidences trop faibles et du nombre restreint de compteurs utilisés (en moyenne 5 sur 18 m au lieu des 13 sections possibles).

Trainée globale du sphéro-conique - transsonique (tableau II)

V/réf m/s	Re <sub>1</sub>	nombre de tirs	i° max	V <sub>max</sub> m/s	V <sub>min</sub> m/s	coefficients calculés
500	1,6.10 <sup>6</sup>	10	4°	534	478	C <sub>x<sub>δ<sup>2</sup></sub></sub> = 4,10 ± 1,7 C <sub>x<sub>0</sub></sub> = 0,471 ± 0,004 C <sub>x<sub>1</sub></sub> = 0,4 ± 0,1
400	1,3.10 <sup>6</sup>	10	2°	428	375	C <sub>x<sub>0</sub></sub> = 0,595 ± 0,002 C <sub>x<sub>1</sub></sub> = 0,5 ± 0,1
280	1.10 <sup>6</sup>	12	5° pour 1 tir	300	265	C <sub>x<sub>δ<sup>2</sup></sub></sub> = 3,4 ± 0,6 C <sub>x<sub>0</sub></sub> = 0,340 ± 0,004 C <sub>x<sub>1</sub></sub> = - 0,5 ± 0,1

### 5.2.3. Récapitulation des résultats

L'ensemble des résultats précédents est récapitulé planche VII sur laquelle ont été portées en plus les prévisions pour le vol réel. On constate que malgré les différences d'échelle, les prévisions du vol coïncident avec les résultats obtenus au tunnel. Cet accord, naturel en hypersonique où les traînées de culot et de frottement sont négligeables ne peut s'expliquer en transsonique que par la coïncidence fortuite des traînées de frottement.

### 5.3. Mesures de traînée globale d'un cylindro-conique

La planche VIII donne un schéma du projectile qui comporte une jupe de 15°. Les planches IX et X fournissent un exemple du comportement des coordonnées transversales du centre de gravité et des projections angulaires de l'axe de la maquette

#### 5.3.1. Résultats de traînée en hypersonique

Deux vitesses seulement ont été étudiées : 4 600 m/s et 3 100 m/s. Le tableau suivant rapporte les résultats obtenus sous la même forme que précédemment (cf. 5.2.1) et avec les mêmes notations (solutions a, b, c) ; tous les tirs à même vitesse sont traités ensemble directement. Comme pour le sphéro-conique, les plages d'incertitude sont excellentes à 5 pour mille pour  $C_{x_0}$  et bonnes à 5 % pour  $C_{x_{\delta^2}}$ .

Trainée globale d'un corps cylindro-conique - hypersonique (tableau III)

vitesse m/s	Reynolds sur la longueur de la maquette	nombre de tirs	i <sub>max</sub> en degrés	coef- ficients	Solution :		
					a	b	c
4 600	3.10 <sup>6</sup>	14	13	C <sub>x<sub>0</sub></sub>	0,172 ± 0,001	0,172 ± 0,001	0,173 ± 0,001
				C <sub>x<sub>δ<sup>2</sup></sub></sub>	3,5 ± 0,2	3,5 ± 0,2	3,4 ± 0,2
3 100	12.10 <sup>6</sup>	9	6	C <sub>x<sub>0</sub></sub>	0,192 ± 0,002	0,1910 ± 0,0005	0,1909 ± 0,0004
				C <sub>x<sub>δ<sup>2</sup></sub></sub>	3,1 ± 0,2	3,0 ± 0,1	3,0 ± 0,1

Trainée globale d'un corps cylindro-conique - transsonique

vitesse m/s	Reynolds sur la longueur de la maquette	nombre de tirs	$i_{\max}$ en degrés	coefficients de la loi de trainée
520	$2,5 \cdot 10^6$	8	2	$C_{x_0} = 0,608 \pm 0,0009$ $C_{x_1} = 0,606 \pm 0,026$ $C_{x_2} = 1,282 \pm 0,207$ $C_{x_{\delta 2}} = \text{non déterminé}$
250	$3 \cdot 10^6$	8	5,5	$C_{x_0} = 0,3764 \pm 0,0009$ $C_{x_1} = -0,13 \pm 0,02$ $C_{x_{\delta 2}} = 2,5 \pm 0,2$

5.3.2. Résultats de trainée en transsonique

Une vitesse a été étudiée de part et d'autre du pic de trainée : 520 m/s en supersonique et 250 m/s en subsonique.

A 520 m/s, les incidences sont trop faibles pour déterminer le coefficient  $C_{x_{\delta 2}}$ . Par contre il a été nécessaire d'utiliser une loi de  $C_x$  de degré 2 en  $\frac{V_R - V}{V_R}$  :

$$C_x = \sum_{i=0}^2 C_{x_i} \left( \frac{V_R - V}{V_R} \right)^i$$

pour obtenir des résidus compatibles avec la précision estimée des mesures.

Compte tenu des difficultés rencontrées à ces bas nombres de Mach en soufflerie la précision obtenue sur le  $C_{x_0}$  est tout à fait remarquable : 1,5 pour mille.

A 250 m/s, il n'a pas été nécessaire d'utiliser un polynôme de degré 2 mais par contre les incidences étant plus élevées, le terme  $C_{x_{\delta 2}}$  a pu être déterminé avec une incertitude de 8 %.

Pour cette vitesse également, la précision obtenue sur le  $C_{x_0}$  est excellente à 2 pour mille.

La planche XI présente les lois de trainée trouvées dans la zone de nombres de Mach balayé par les tirs des deux campagnes transsoniques.

5.3.3. Récapitulation des résultats

La planche XII récapitule et extrapole les résultats obtenus pour proposer une loi de trainée globale à incidence nulle en fonction du nombre de Mach. L'étude d'autres vitesses serait nécessaire pour préciser le pic transsonique. Ici encore les résultats trouvés au tunnel sont proches des prévisions de vol : ce qui apparaît normal puisque l'on retrouve sensiblement les mêmes différences de Reynolds entre le vol et les essais en tunnel que pour le sphéro-conique étudié précédemment.

6. CONCLUSION

1. On a montré que des techniques évoluées de dépouillement de trainées aérodynamique en tunnel de tir sont maintenant disponibles. A condition de disposer d'un nombre de points de mesures suffisant sur la longueur de la trajectoire, avec la précision voulue, on peut rechercher une loi de trainée variable avec l'incidence ou avec la vitesse.

On déterminera les variations du  $C_x$  avec l'incidence d'autant plus facilement que l'incidence initiale de tir est plus élevée et la longueur de pendulation plus faible. De même la variation du  $C_x$  avec la vitesse, spécialement en transsonique sera trouvée plus aisément si la variation de la vitesse sur la trajectoire considérée est plus importante.

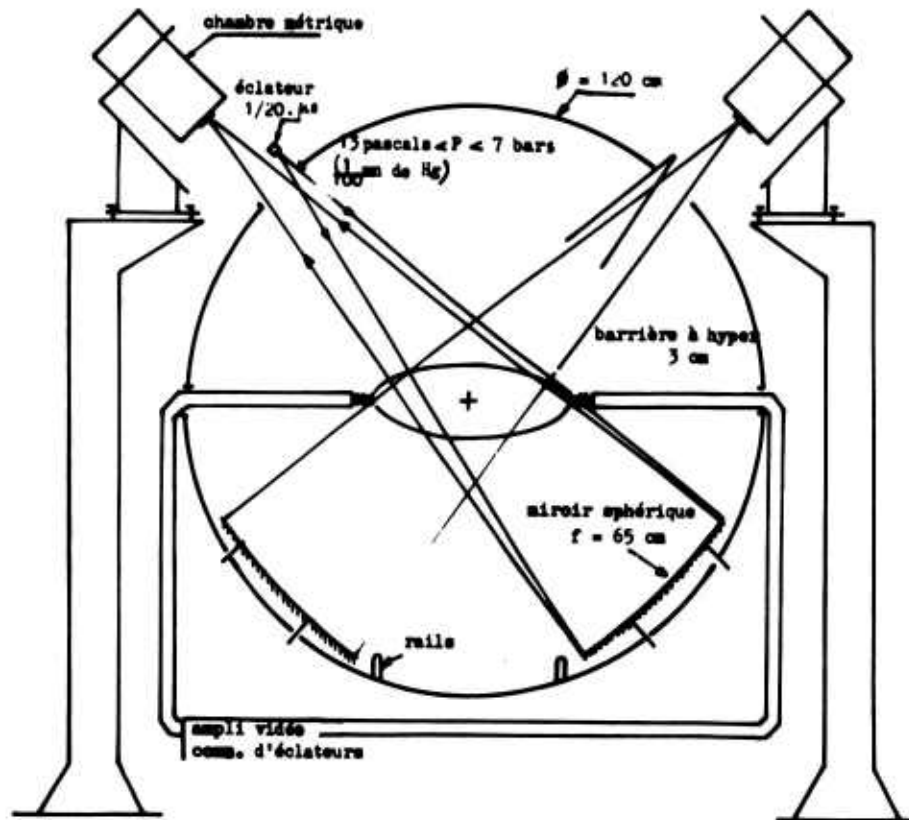
2. Les tirs réalisés au tunnel hyperballistique du L.R.B.A. dont les résultats complets ont été présentés pour 2 formes particulières de corps, ont été exploités à l'aide de ces nouvelles méthodes. On a montré que le coefficient de trainée peut être déterminé à 1 % près entre  $M = 0,7$  et  $M = 14$  dans une même installation.

3. La simulation d'un nombre de Reynolds réaliste vis à vis de celui du vol réel est souvent pénalisée par la petite taille de la maquette imposée par les moyens de lancement. Mais une simulation valable du nombre de Reynolds ou une étude de l'influence de ce paramètre peuvent être réalisées par des tirs dans des tunnels pressurisés à 2 ou 4 atmosphères. Ces conditions de tir sont d'ailleurs favorables à la détermination des lois de trainée variables avec l'incidence ou avec la vitesse en transsonique.

REFERENCES

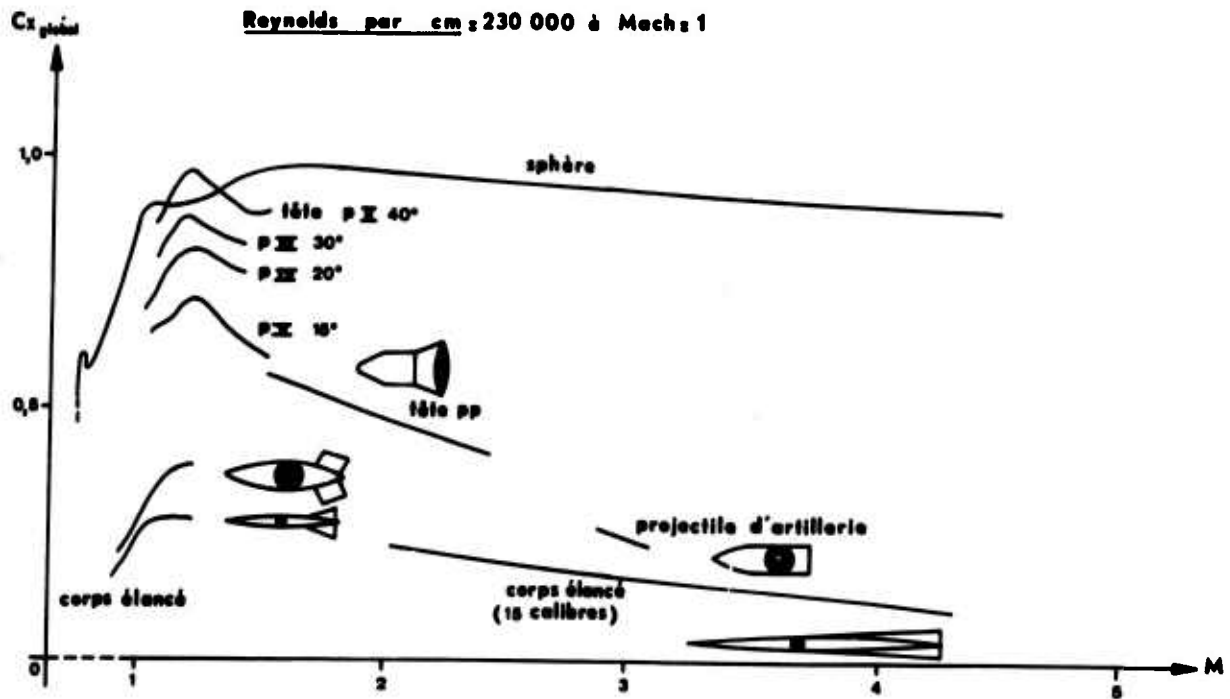
- 1 - L.R.B.A. E.1023 - NT.14 et 15/SAE : Géométrie des chambres métriques du tunnel hyperballistique
- 2 - L.R.B.A. E.1502 - NT.13/SAE : Contrôle du lecteur SFAT
- 3 - L.R.B.A. E.1502 - NT.12/SAE : Dépouillement de la trainée en fonction de l'incidence au tunnel hyperballistique.
- 4 - L.R.B.A. - Rapport-programme n° 23/SAE
- 5 - L.R.B.A. - R.P. n° 43/SAE : Détermination des lois de trainée en tunnel de tir
- 6 - I.S.L. - rapport 3/71 : Contribution à l'étude expérimentale de phénomènes aérodynamiques liés au vol transsonique décéléré.
- 7 - AIAA Jal - nov. 72 - Vol 10 - n° 11 - pp. 1436/1440 : Sphere Drag Coefficients for a Broad Range of Mach and Reynolds Numbers - A.B. Bailey et Hiatt
- 8 - Détermination des coefficients aérodynamiques en tunnel de tir - A. Desgardin. Thèse n° 40 8207 C.N.R.S.

( Tunnel hyperballistique )



**RESULTATS I.S.L EN TUNNEL CLASSIQUE**

Planche II



# SPHERO-CONIQUE

Planche III

29-11

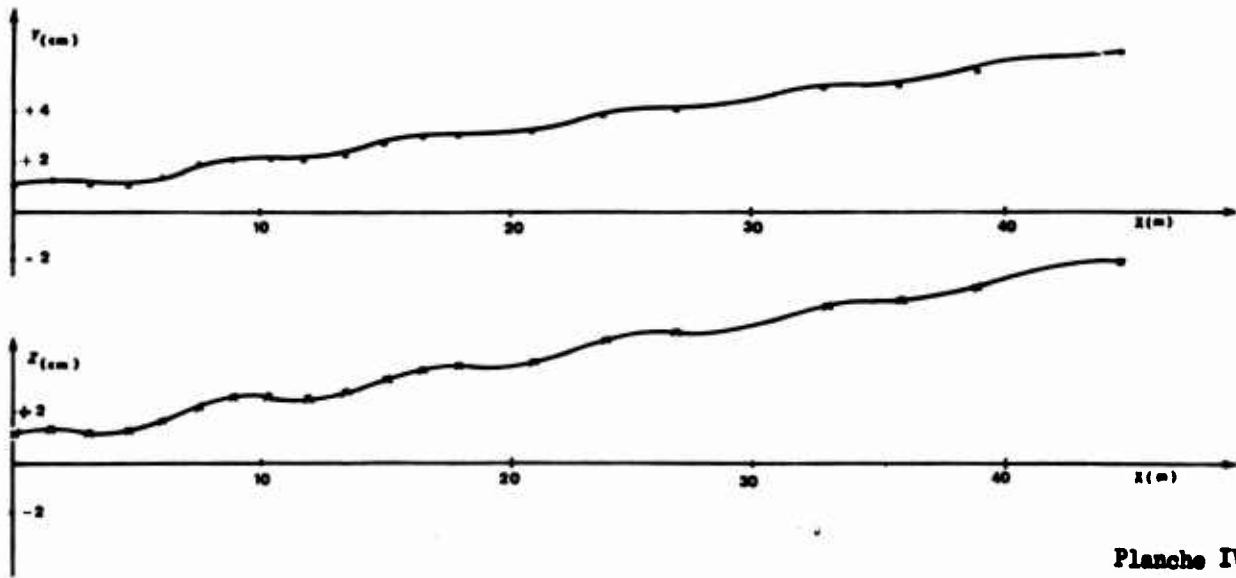
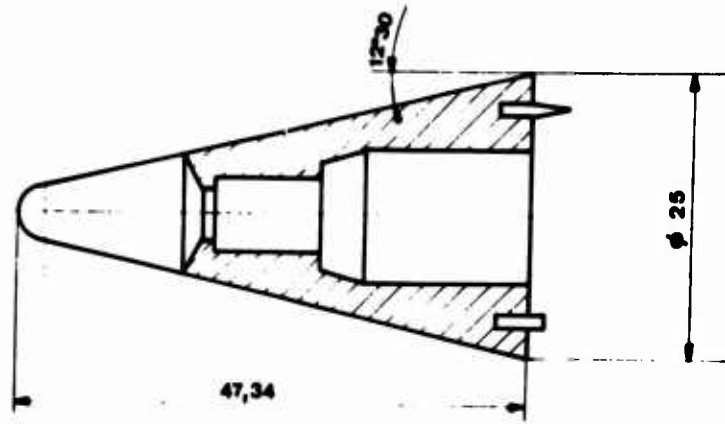


Planche IV

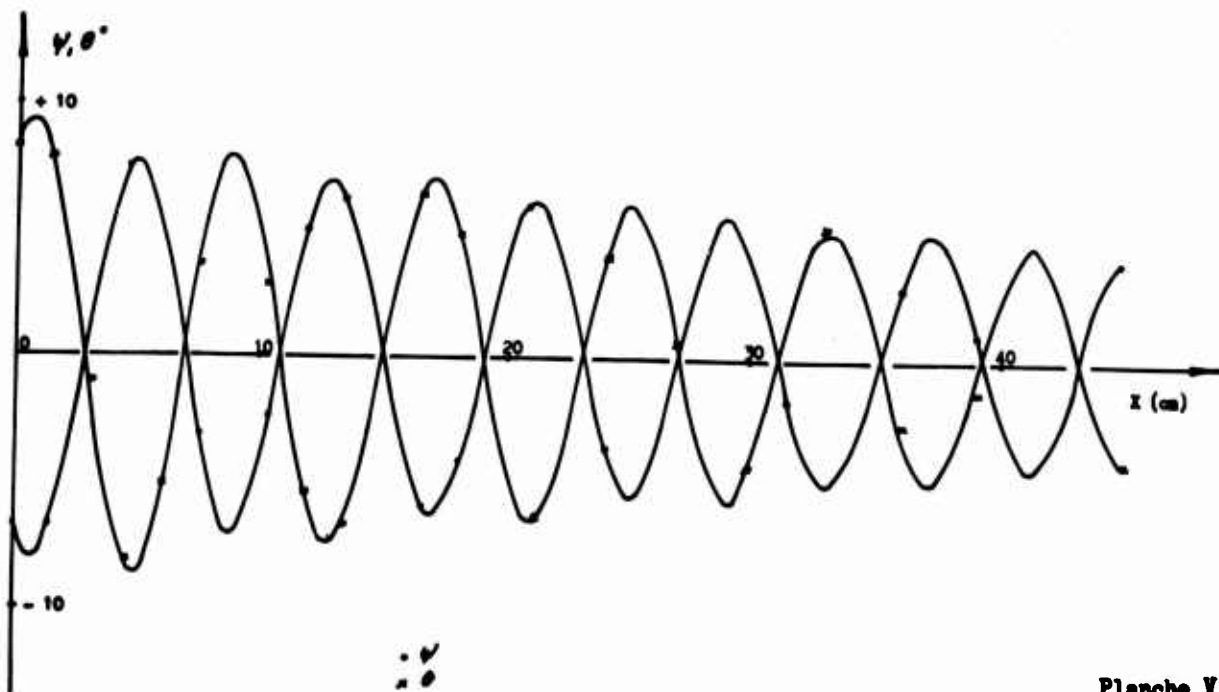
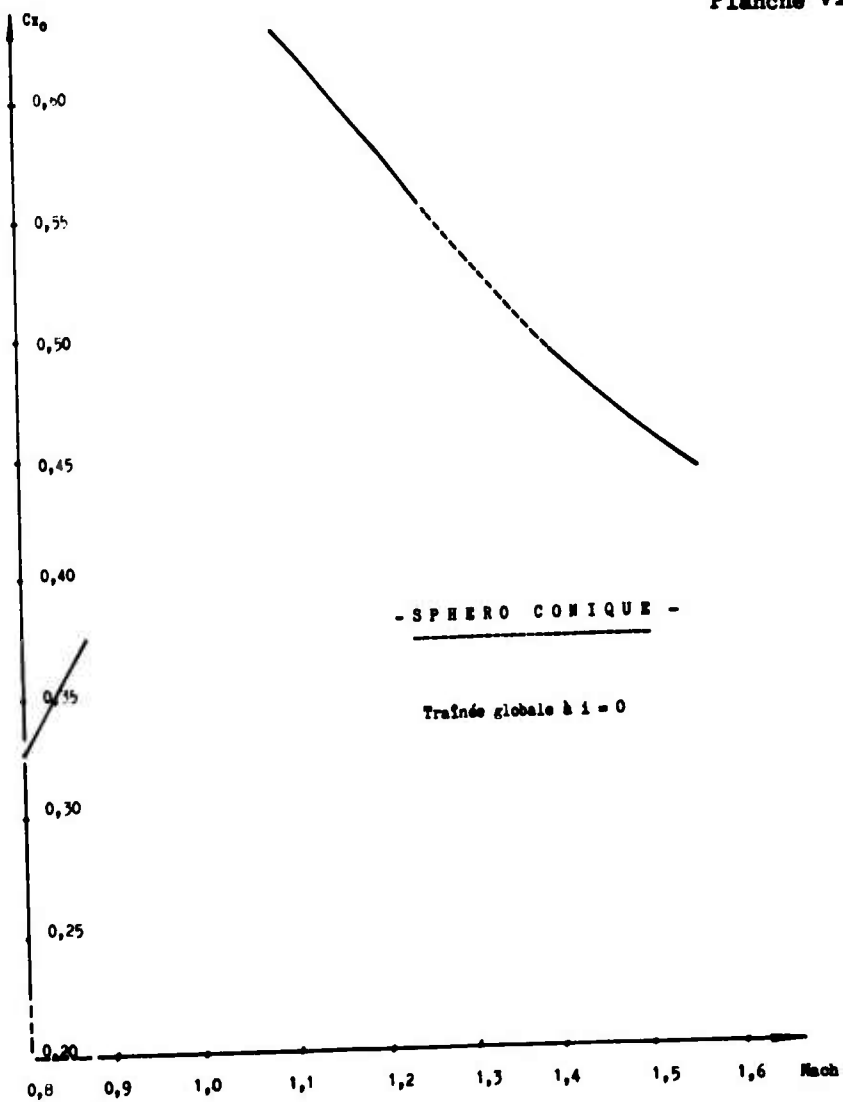


Planche V

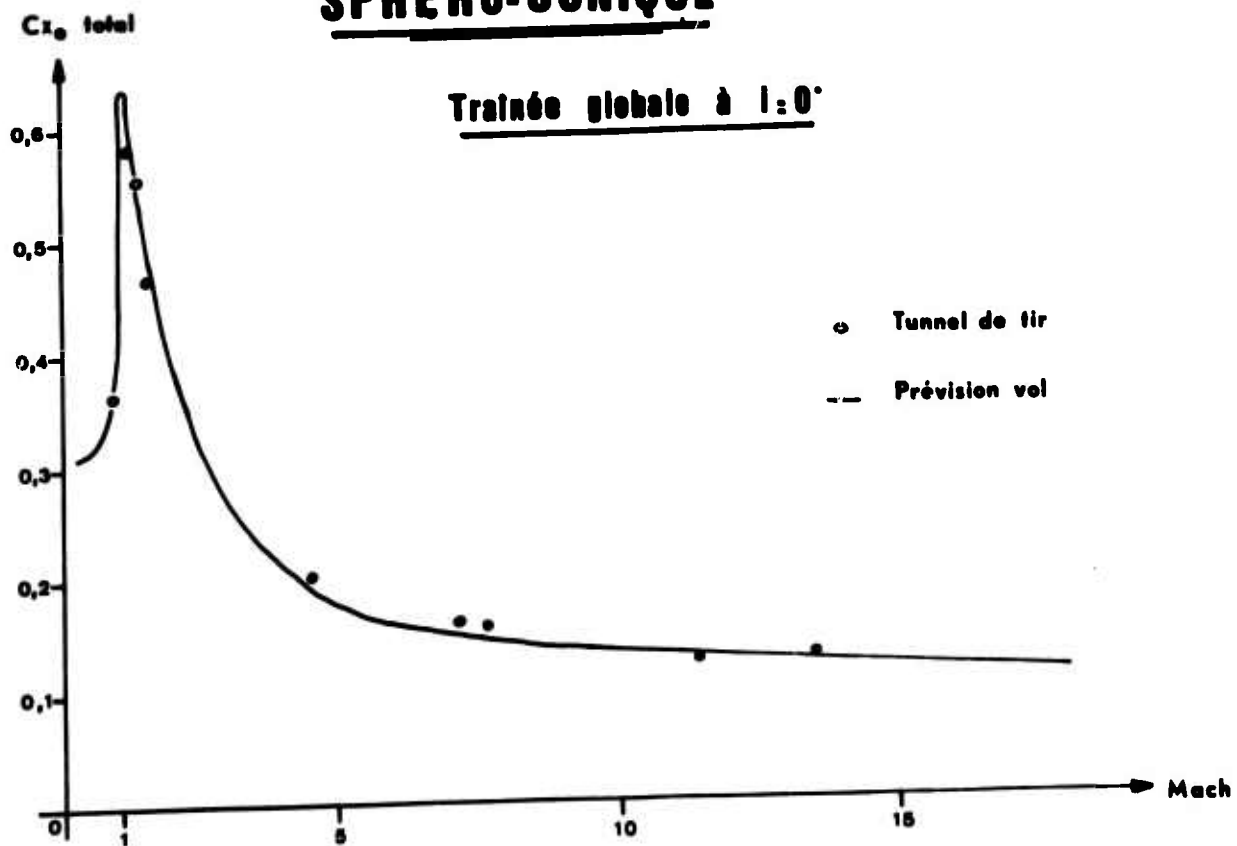
29-12

Planche VI



**SPHERO-CONIQUE**

Planche VII



# CYLINDRO-CONIQUE A JUPE

Planche VIII

29-13

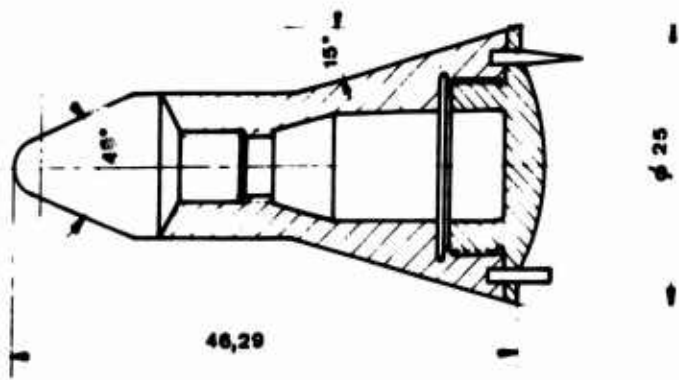


Planche IX

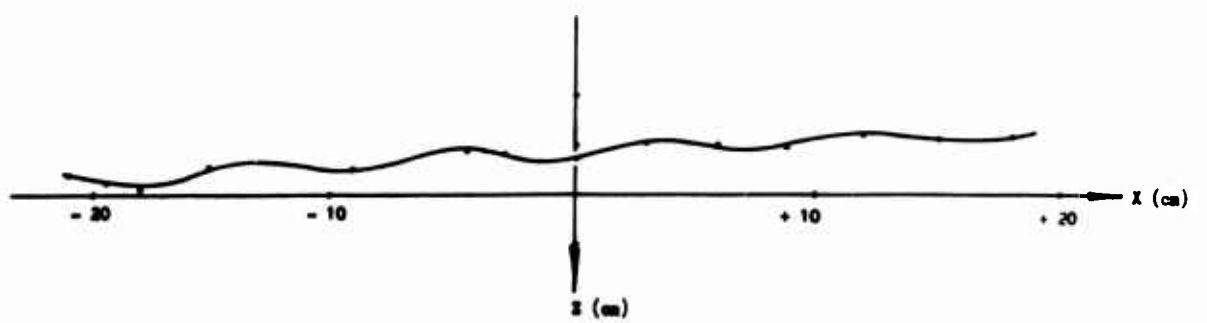
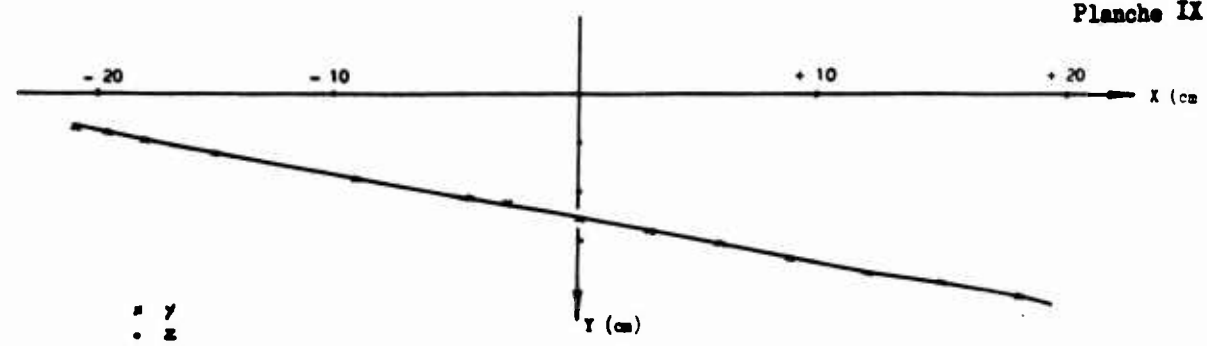
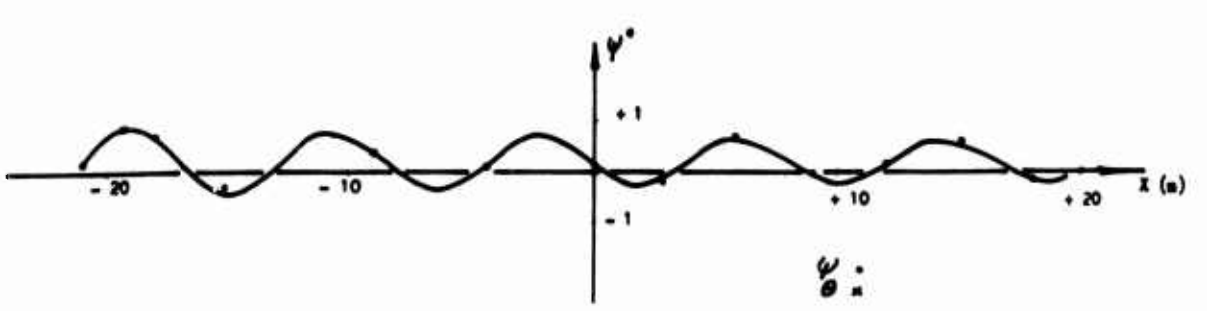
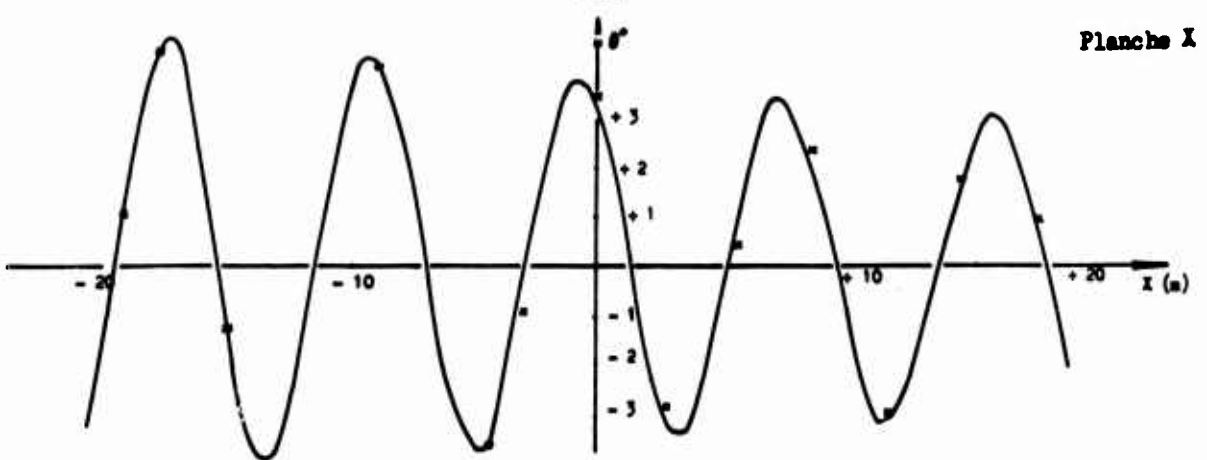
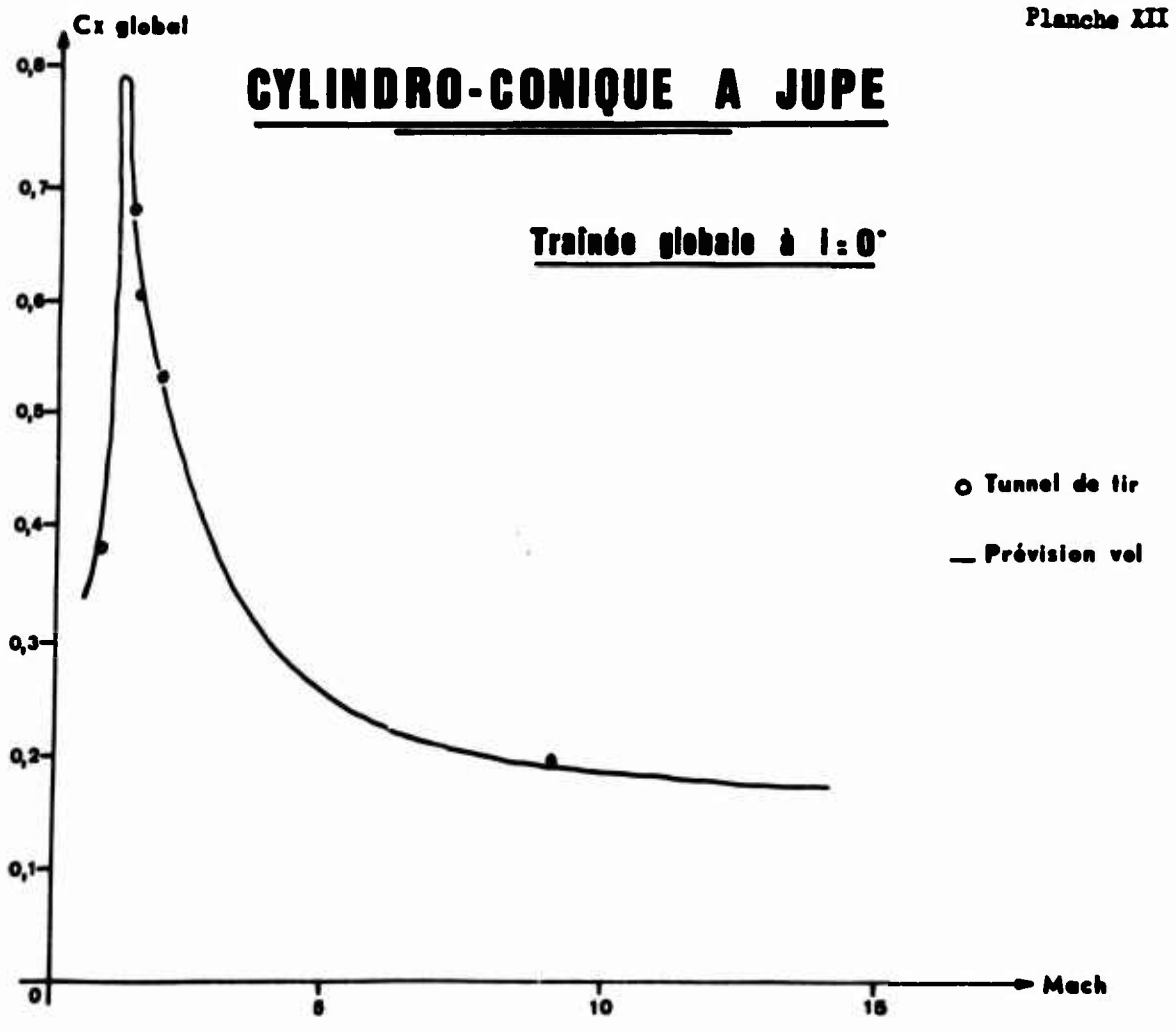
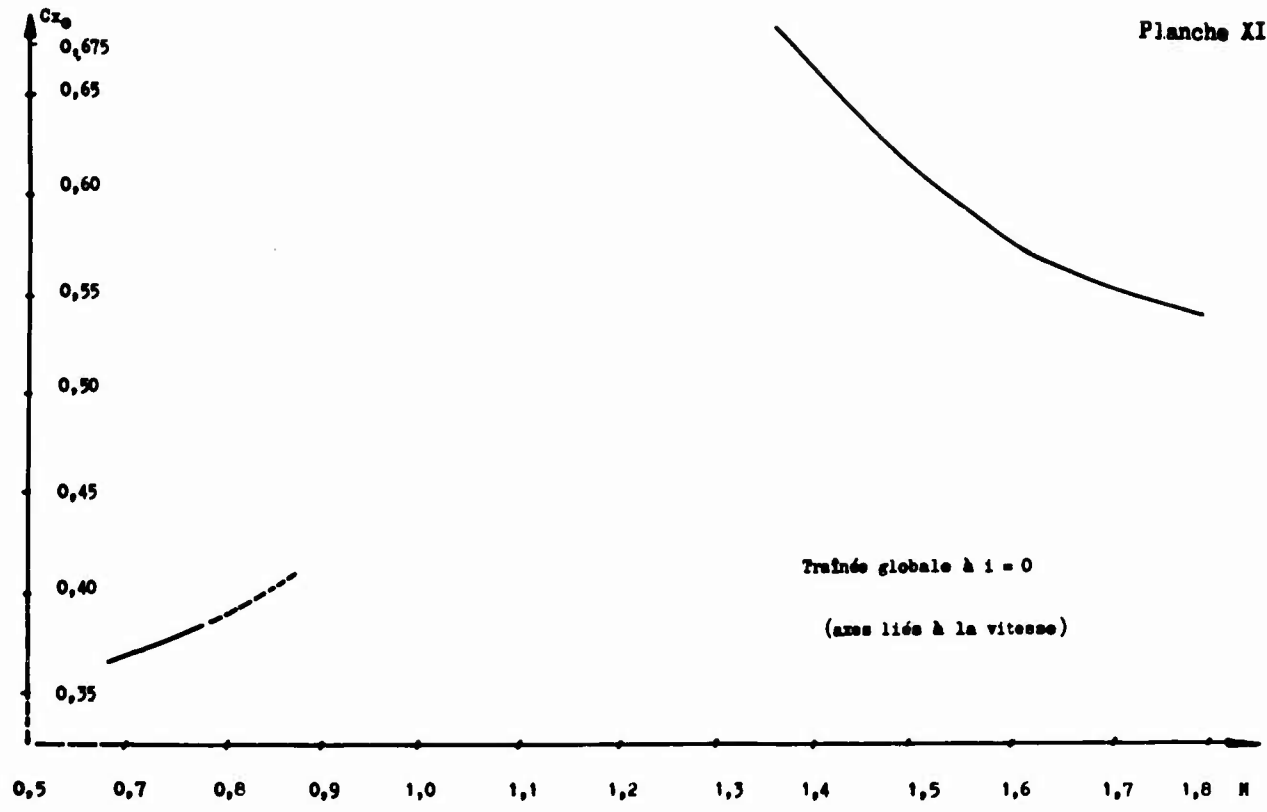


Planche X





## APPENDIX A

ROUND TABLE DISCUSSION HELD AFTER THE  
PRESENTATION OF PAPERS

Professor A.D.YOUNG (Chairman)	Department of Aeronautical Engineering Queen Mary College University of London UK
Mr J.H.PATERSON	C-5A Flight Sciences Manager Lockheed-Georgia Company USA
Mr S.F.J.BUTLER	Assistant Director Defence Policy Staff Ministry of Defence UK
M. M.SIRIEIX	Office National d'Etudes et de Recherches Aérospatiales France
Mr P.P.ANTONATOS	Director, Flight Mechanics Division, AFFDL, Wright-Paterson Air Force Base USA
Professor Dr W.WUEST	DFVLR Aerodynamische Versuchsanstalt Göttingen Germany

## ROUND TABLE DISCUSSION

**Professor A.D.Young:** Ladies and Gentlemen, we come now to the final session of our proceedings, namely, the Round Table Discussion, and as you will no doubt recognize, the people assembled on this platform are those who have prepared the major review lectures of this meeting. On my extreme left is Mr Paterson, next to him Mr Butler, next to him Mr Sirieix, then on my right is Mr Antonatos, and finally, at the end is Professor Wuest. What I would propose to do is to ask each of these gentlemen in turn to say very briefly what he thinks has emerged of importance from this meeting, and, in particular, what are the lines of future work which he sees as desirable, which this meeting has demonstrated. One hopes that as a result of this discussion there will be a number of basic points which will become clear and which people here who actually do the work will think about and, we hope, follow up in due course.

After each speaker has said his bit, I would like to open the discussion on the points which he raises and leave it to you, as members of this meeting, to contribute any additional points that you wish. We shall have to be fairly brief because we have at the most an hour and a half to devote to this discussion. Therefore, without more ado I will ask Mr Paterson to say what he feels are the important points that he would like people to bear in mind for the future.

**Mr J.H.Paterson:** It is obvious from the excellent material presented here this week that there are quite a number of areas for additional research. First, the current two-dimensional viscous flow theories require extension into the regime of the unsymmetrical trailing-edge boundary layers and into the high lift region to provide the designer with the capability to predict buffet onset and severe separation. In addition, the current methods need to be extended to the prediction of drag in supercritical flows. Second, the current methods of predicting drag rise Mach number in two-dimensional flow are generally conservative and can be improved by the development of suitable pressure distribution shape criteria. The third item requiring considerably more effort is that of three-dimensional viscous flow methods. Currently available methods for isolated components are both laborious and expensive, and methods of handling the complex flows of mutually interacting components remain to be developed. While such methods are under development, the designer will continue to rely on windtunnel development type tests using, among other things, various flow visualization techniques. The very complex nature of three-dimensional interacting viscous flows requires considerable study to develop better understanding of flow visualization results. Dr Peake and Professor Rainbird addressed this subject by presenting some of their boundary layer diverter work which shows what can be done by flow visualization techniques. The techniques developed by N.A.E., and others, not only provide a means by which three-dimensional flow problems can be solved during windtunnel development tests but can also be used to establish the understanding necessary to the development of better mathematical models of the flow phenomena.

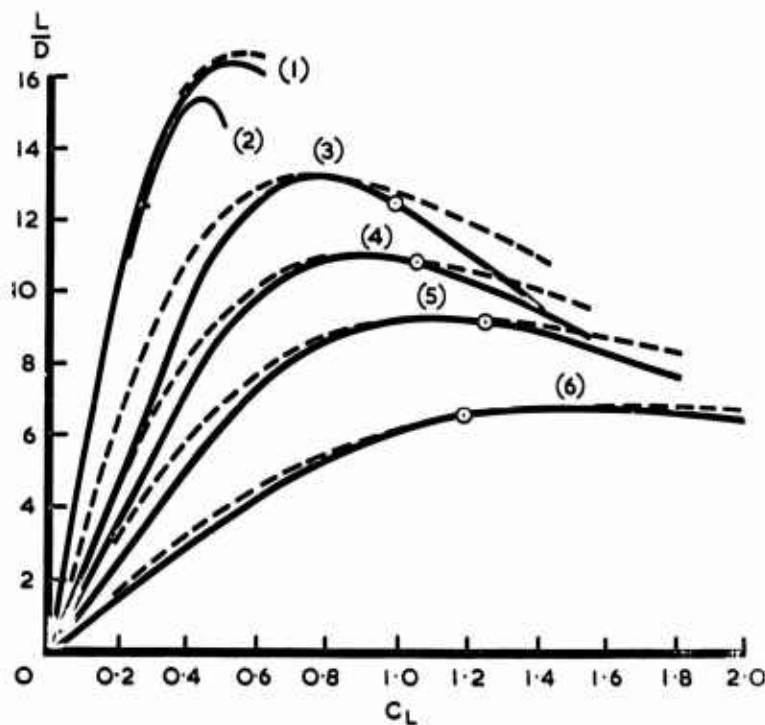
The fourth item I would mention is the perennial need for improvement of windtunnel testing techniques. Among these are, of course, the problems of wall interference, blockage, support system interference and the simulation of full scale mixed flow. The subject of support system interference has received considerable attention in recent years both in Europe and the United States. As a result of early windtunnel experience on the C-5A, a program to correlate the results of tests in a number of transonic windtunnels was initiated by the United States Air Force and NASA. This study, using a C-5A model, balance and sting arrangement, has led to the identification of a number of sources of error; however the study is still in progress and final results are not yet available. It is expected that the results will lead to a better understanding of some of the problems contributing to windtunnel data inaccuracies.

Finally, concerning the calculation of roughness drag, that is, the drag due to the manufacturing roughnesses, such as steps and gaps, there is a very great deficiency in the data that is currently available. Most of it is due to Weighardt's investigations and, as collated by Hoemer, is used to estimate the drag of manufacturing roughnesses and excrescences. In the US we establish very tight tolerances for the manufacturer. In the process of setting up these specifications, we are frequently doing it with tongue-in-cheek because we do not know how much drag avoidance we are achieving, and we do not know how much we are adding to the cost of the airplane when we impose these tight tolerances. It is an area where we are not going to get all the answers in a short span of time, but I was very glad to see that Mr Winter and his associates are doing some very fine work along this line. Of course, this work needs to be extended to the conditions of three-dimensional flows and to the type of configurations of today's airplanes. In other words, having established a base line for the drag of these excrescences on a wall, we need to expand the investigations to the conditions of, e.g., an airfoil shape; this may be approximated, of course, by superimposing a pressure gradient on such tests. All in all, I think that there is a great deal of excellent work going on in all the areas that we are concerned about, but I believe that roughness is perhaps the one thing that has been neglected in recent years.

A 2

**Professor A.D.Young:** Perhaps before discussing these points in a general way, I should ask if any other member of the panel wants to comment on the points that Mr Paterson has raised. This may eliminate some items that they have already prepared. Mr Butler, do you wish to say anything on these points? (Mr Butler replies, "No, I am content with what he said".) Well, can we take these points that Mr Paterson has raised. I will just remind you of them: the need for more reliable boundary layer prediction methods for wings at incidence, and in particular, with high lift in the approach to buffet onset and separation conditions and with particular reference to supercritical wings. More work needs to be done to improve our methods of predicting critical Mach numbers; three-dimensional methods of calculation need improvement and simplifying from the point of view of reducing costs and time involved; we do not understand anything really about three-dimensional separation, which is essentially empirical at present; our windtunnel testing techniques need improvement, a matter that has been considerably discussed by the LaWs Group; and finally, roughness drag calls for a lot more work than we have done up to the present. Would anyone like to pick on any of these points and add aspects which have not already been covered in the course of the meeting? I wonder if one or two of these areas are ones on which Prof. Küchemann would like to comment?

**Professor D.Küchemann:** I can only agree with what Mr Paterson has said, and on his selection of particular topics. What I would like to do, with your permission, is to do some very brief stocktaking of where we have got to, by showing you one example. We have heard a great deal about general frameworks for estimating drag, and we had also many papers concerned with individual drag components. How do they come together in the end? What I would like to show is just one slide where all the drags have been put together again, so these are drag curves for a complete aircraft.



LIFT-TO-DRAG RATIOS OF A SWEEP-WINGED  
TRANSPORT AIRCRAFT AT VARIOUS  
FLIGHT CONDITIONS

It is a contemporary transport aircraft, for short or medium ranges with a moderate angle of sweep. It is plotted in the form of lift-to-drag ratio against the  $C_L$  for various configurations. In the first place, it shows us that one aircraft has quite a number of different configurations, and we want to know the drag for every one of these configurations. Curve (1) is the cruise configuration, as measured at low speeds, so that it does not include compressibility effects. Curve (2) does include compressibility effects. Curve (3) shows what happens if some leading edge devices are put out at low speeds. You may not want to use that particular configuration in flight, so you go on to Curves (4) and (5), which are obtained when flaps are deflected, in Curve (4) by a relatively small angle,  $10^\circ$  to  $15^\circ$ , and in Curve (5) something between  $20^\circ$  and  $30^\circ$ . The last curve, Curve (6), is obtained when the flaps are deflected by a relatively large angle,  $45^\circ$  for example. These results give a good idea of what happens in any one of these configurations and we find that the differences are very large. I should like to add that  $L/D$  does matter, of course, in all flight conditions, from the performance aspect; even if you consider only noise, you always want  $L/D$  to be high. The operating points at low speeds are indicated by circles. They are somewhere around the  $L/D$  maximum. For the cruise configuration, you may go up and down the curve, depending on the range to be flown. What I have also drawn in this diagram, apart from the full lines which represent the actual

A-3

aircraft, are some dashed lines which are based simply on drag parabolas. It does not really matter what aircraft it is, or how they have been obtained. These estimates have been obtained by assuming that there is a zero-lift drag plus a lift-dependent drag which is simply a factor,  $K$ , divided by  $\Pi A$ , times  $C_L^2$ . They are fitted around the maximum values, and what you can see, when all these many drag components are added up, is that the outcome is still very much like a drag parabola. There are some deviations for the high-lift configurations, but only in those conditions we are not really interested in. It simply indicates that a high-lift design is fairly sensitive to off-design conditions, but one can make it fit, near the operating point, near  $(L/D)$  max. I think what matters in the context of what we are discussing here, are the values which go into the zero-lift drag and the lift-dependent drag factor. Consider that first, the lift dependent drag factor is about 1.2 for the cruise configuration (for the dashed lines) which is quite a usual value, and then it actually goes down. In Curve (6), for the approach, it is something like 1.0. The explanation must be that a non-planar trailing-vortex sheet is generated in some way, and that reduces the drag factor. The actual drag is, of course, still very high because it is multiplied into  $C_L^2$ , so it may well be more than half the total drag. Therefore, we are still interested in reducing the lift-dependent drag factor. I think the real lesson is in what is obtained for the zero-lift drag and, if I may, I will express that in drag counts which have been mentioned many times during this meeting. In these curves, the zero-lift drag in the cruise configuration is 165 drag counts. We have had many papers where people were arguing about just a few drag counts and every one is worth winning. As soon as a flap is deflected through only a small angle, it is up to 410, for Curve (4). If a flap is deflected a bit further, Curve (5), you have 605. And, in Curve (6), for the approach, it is 1160. I would conclude from that, that it is really the viscous effects, the viscous flows that we will have to concentrate on. I think that this agrees with what Mr Paterson has said. These are mainly threedimensional flows, and we have to know much more about viscous threedimensional flows and how they can be matched to the external inviscid stream. We must be able to take account of threedimensional flow separations, especially when it comes to mixed transonic flows and, again, these are threedimensional in order to be really useful in aircraft design. Therefore, I think the problems we have to tackle are fairly clear. Computers will be of some help, but most of the problems, for quite some time to come, will have to be sorted out experimentally. But again, in order to do sensible experiments, we still want a theoretical framework. So I would make a plea for establishing useful, physical frameworks which help us in designing sensible experiments which we need in order to answer all the questions which we have. In order to do sensible experiments, as the Chairman has said, we need suitable tools. That is where this question of providing a new generation of transonic windtunnels and low-speed windtunnels really comes in.

**Mr A.M.O.Smith:** There is one point that I would like to make. Over the past 10-15 years people have developed good methods of analysis of two-dimensional flows. There has really been lots of progress in that area. This, in turn, justifies a detailed experimental investigation of two-dimensional flows, and that is about the way things have been going. As I see it, that means that theory and experiment have been able to run hand in hand. Until we have real three-dimensional analysis, a great deal of experiment in three-dimensional flows is just in something of a vacuum, because it can not be tied in very well with three-dimensional theory. But three-dimensional theory is beginning to arrive, and in the next 5 to 10 years there is going to be a great deal of progress, so there is a point in looking hard and carefully at three-dimensional flows. That rather confirms your comments.

**Professor A.D.Young:** Thank you Dr Smith. That is very encouraging coming from Dr Smith knowing how much he has contributed in the analysis of flows in general. I will now pass on to Mr Butler and ask him if there are particular points that he wishes to draw to the attention of the meeting.

**Mr S.F.J.Butler:** I would like to start off with at least one area of omission. We touched on the tools needed to do the job, and I would refer you to the fact that, in the review paper which the UK provided, we included a section talking about general tunnel techniques for drag determination, mainly concentrating on transonic tunnels, coming to the conclusion that there really is not a transonic tunnel flow, be it for small experiments or large experiments, that can produce at present data of adequate accuracy. If this conclusion is correct, then this is something that we have got to home onto and sort out, quite apart from the very important problems of tunnel constraint effects. Is there a tunnel flow which is good enough to allow the rather delicate drag experiments that we need to do in the transonic flow range?

Having said that, the next point that I would like to stress is that we agree with the difficulties, going right to the other end, of flight test evaluation of thrust. You have got to assign the thrust before you can sort out the drag. At this conference we have been treated to some nice comparisons between flight and tunnel; encouraging comparisons which may tend to make us complacent. I might say here that the comparisons we have tried to do in the UK have not led us to complacency, quite the reverse. We think it is very difficult; particularly, if one is relying on the sort of quality of experiments that you may expect to achieve during a commercial development program. Here, I should stress that we have got an active group, working within the main UK Drag Analysis panel, on flight test techniques for the assignation of thrust, and hence drag, which is trying to prepare general guidelines specifying how to go about it for different types of engine arrangement. If there are any contributions on an international basis which you would like to put into the work of this panel, I am sure that they will be very gratefully received. Here is one area where we might with advantage have effective international collaboration.

## THEORETICAL METHODS FOR DRAG PREDICTION

<i>Theory feasible</i>	<i>No immediate prospect</i>
1. Viscid compressible flow about wing-body combinations.	1. Drag with extensive flow separations.
2. Optimised engine installations.	2. Inferior engine installations.
3. Datum streamlined aircraft (fully-turbulent flow)	3. Transition prediction for practical aircraft designs.
4. Wave drag for slender aircraft.	4. Wave drag for non-slender aircraft.
	5. Vortex drag for slender aircraft.
	6. Store installations.
	7. Drag of large excrescences.
	8. Drag at high lift.

Figure 1

To finish off, I would like to go back to one of the diagrams (Fig.1) that I showed you previously. It shows the present state of theory and tries to point out the areas where theory is strong, and where there seems to be not much likelihood of good theoretical developments in the immediate future. If we take the left-hand side, we have mainly been talking in the present discussion about Item 1, leading into Item 3. It would be of great help if we could take the datum, streamlined, swept-wing aircraft with supercritical flow, and calculate confidently the drag in its main cruising configurations. Obviously, you would like to be able to do this also at least in the take-off condition as well. I would have said that it was within the wits of man for us to do this in the next decade, if we collaborate and work together on this problem. Now, let us look at the right-hand side. There is a whole list there, and having come to this meeting, I rather hoped that I would get the answers to at least half of these. I do not think I have really got any answers at all. In some cases we are obviously going to have to rely on empirical correlations of data. In the engine intake and nozzle base flow areas that is all we can really hope for in the immediate future. Some work has been done in the UK by BAC and Rolls Royce and reported in the review paper. Look at the other problems you have; wave drag for non-slender aircraft, vortex drag for slender aircraft, quite apart from the drag of excrescences and the drag of store installations. I would like to stress the three-dimensional separation cases. Can we deal with boundary layer developments under three-dimensional conditions, either on a swept wing or at junctions of surfaces? If we could deal with those, including the effects of flow separations, then we would be making some real progress. Here, I would appeal to the theoreticians among you, that you do not only consolidate ground that has already been covered to a greater or lesser extent, but that you go out into uncharted areas. I would like to see one or two unsuccessful theoretical investigations pioneering new areas, rather than too much consolidation of areas which have already been treated by a first and, probably, second round of theoretical investigation.

**Professor A.D.Young:** Mr Butler has stressed the deficiencies of our existing transonic tunnels. That is not a new topic, but it needs stressing. He has expressed some degree of scepticism about the accuracy with which we can measure thrust at present; he would like to see more work done on the concept of a datum streamlined aircraft with fully attached flow. His list includes the topic of engine installations, but we will hear more about that later, I am sure. He drew attention to the fact that we do not know enough about such topics as wave drag of non-slender aircraft and vortex drag of slender aircraft. Does anybody wish to add to the points that he has raised?

**Mr K.G.Winter:** Both Mr Paterson and Mr Butler have mentioned aspects of tunnel techniques. One of the things that worries me is how you measure the drag of the backend of things. The sort of technique that Lockheed have used is to support a model on a blade, in order that the backend can be closed and not be distorted by the presence of a sting. I think, for many years to come, we are going to have to use sting supports of one sort or another in tunnels. It seems to me that the technique used is rather an article of faith of a particular organisation. In the US, the faith is in putting a blade at the front end of the aeroplane and hoping that the wake from the blade and the sting that comes forward to support the blade do not cause too much interference. In the UK, on the other hand, our faith is in using a combination of a single sting and twin stings; the twin stings we use to support the model from its wings. I do not think I have ever seen any measurements in which a given model has been taken, and comparisons made of different ways of obtaining the total drag of the aircraft. I think there is room for an experimental programme just investigating alternative sting supports.

**Mr J.H.Paterson:** I would like to say a couple words on that. For many, many years the rear sting was the standard arrangement for transonic tests. Because most transport configurations have upswept afterbodies, it was known for many years that the rear sting arrangement was inadequate. Consequently, numerous arrangements of stings have been investigated. In fact, in any windtunnel test of a new project, the first test includes an investigation of the sting tares. Various systems have been used to determine sting tares, with varying degrees of success. A-5

Continuing investigation of means of getting data free of sting interference led to the use of blade-mounts. The use of such mounts however, does not eliminate the need to determine sting tares but does permit the determination of valid tares, whereas the rear sting either provides erroneous tares or introduces a compromise in the shaping of the rear fuselage. This also introduces unknown errors. It is obvious that no single sting arrangement is appropriate to all aircraft configurations and that each case must be studied to determine a valid sting system. A good example of the method of obtaining reliable interference free data using a blade mount will be published shortly as a result of a study conducted by the Lockheed-Georgia Company under the sponsorship of NASA, Langley.

**Professor W.J.Rainbird:** I would like to strongly endorse the comments of Mr K.Winter, and warn that the problem of model support interference is going to get very much worse in the new high Reynolds number facilities being proposed. In reading, recently, that beautifully written final LaWs report, I note that stagnation pressures as high as 11 atmospheres are being suggested for the new transonic facilities. The consequent high loads will result in massive, yet highly stressed, stings and will aggravate the base interference problem. Moreover alternative means of support, at the same Reynolds number, will probably not be possible. This is a very important problem for these future facilities which requires some attention.

**Mr C.L.Bore:** Perhaps I could rub in a couple points made by Dr Küchemann and Mr Butler. What Dr Küchemann was pointing out really, was that well streamlined aeroplanes have got pretty low drag, compared to whatever you get whenever you put any sort of nasty bumps on. So, it is all the nasty bumps that are really our problem. These things amount to perhaps 20% of the drag of nice clean civil aeroplanes, and perhaps 150% of the drag of nasty dirty military aeroplanes. It seems to me that what we really have to concentrate on is finding out not quite how to measure the drag of these bumps with great precision, but much more how to make them far less draggy. There are many of these things which have very useful functions, for example, aials, probes, boundary layer diverters, boundary layer fences, vortex generators and then things which are, I am sure, much too roughly made; things like military stores and their pylons. In short we should have more work on making the nasty bits smooth.

**Mr F.Aulehla:** I quite agree that model support for afterbody drag measurements is far from ideal. Depending upon the purpose of the investigation, sting or blade support may be preferable. There are, however, two additional problems which, I think, need even more attention. I am referring to the problems of Reynolds number effects and the model split line.

In order to reduce the level of measured total forces and to increase the accuracy in afterbody drag measurements, usually the complete aircraft model is not put on the balance, but just the afterbody itself, sometimes even without tailplanes (as shown in one paper of this conference. See also AGARD Lecture Series 53, Chapter 4).

In such cases, where forces on only part of the model are measured, the displacement thickness of the boundary layer becomes most important: incorrect Reynolds number simulation in the windtunnel can then cause completely misleading results. Since correct boundary layer blowing or sucking is (1) difficult to achieve with afterbody models and, (2) may introduce additional simulation defects, the only solution seems to lie in a more accurate theoretical understanding of the actual flow field, including separation, for model conditions. The extrapolation to full scale Reynolds numbers and the definition of better measurement techniques (position of split line, interaction between fore and afterbody, etc.) should then be less problematic.

**Professor A.D.Young:** Thank you. I will now ask M. Sirieix to offer his views on the points of importance which have been raised during the course of this meeting.

**M. M.Sirieix:** Cette discussion concernera uniquement les problèmes de décollement dont l'importance sur le bilan de trainée a été soulignée par de nombreuses communications présentées ici. Il s'agit en fait de dégager les principales voies de recherche théorique et expérimentale qu'il paraît souhaitable d'aborder dans un avenir proche pour faire progresser cette question.

L'objectif le plus important, qui a d'ailleurs été mentionné par les 2 précédents animateurs est d'acquérir une connaissance beaucoup plus précise des phénomènes de décollement tridimensionnel et d'en développer les moyens de calcul. Ce point a été notamment souligné dans les contributions de Peake et Rainbird et de Surber; les zones décollées apparaissant sur les avions et les engins présentent en effet un caractère essentiellement tridimensionnel du fait de la géométrie et de l'incidence.

A-6

Il s'agit en particulier:

- d'améliorer les méthodes de calcul des couches limites turbulentes tridimensionnelles en vue notamment de prévoir les lignes de décollement,
- de tenir compte dans le calcul du couplage qui s'établit entre le développement des zones décollées et celui de l'écoulement extérieur, incluant notamment les effets d'enroulement tourbillonnaire.

Sur le plan des expériences fondamentales, l'effort de caractérisation des phénomènes de décollement tridimensionnel doit également porter sur la définition difficile de configurations typiques qui peuvent aider à l'élaboration de modèles de calcul.

Si l'étude des écoulements séparés tridimensionnels est essentielle, il n'en demeure pas moins que notre connaissance et notre maîtrise des décollements bidimensionnels est encore insuffisante sur bien des points.

En ce qui concerne le problème de la pression de culot, Addy, a montré ce que l'on pouvait actuellement attendre des méthodes de calcul existantes en supersonique. C'est ainsi que les calculs d'optimisation d'Arrière corps de propulseurs, peuvent être entrepris avec succès, lorsque les couches limites sont d'épaisseur modérée devant l'étendue du décollement.

Ces méthodes donnent bien le sens et la grandeur des variations de la trainée externe sous l'influence des facteurs géométriques et aérodynamiques intervenant dans la configuration traitée; elles permettent de prévoir avec assez d'exactitude les performances réelles à partir d'un minimum d'expériences sur maquette.

Toutefois Addy a signalé que lorsque le point de séparation n'est plus fixé à l'arête d'un culot mais se déplace sur le carenage extérieur de l'Arrière corps par suite de l'éclatement du jet interne par exemple, les méthodes de prévision actuelles des conditions de décollement d'une couche limite turbulente en écoulement supersonique sont très insuffisantes.

Les corrélations empiriques disponibles pour de tels calculs ne tiennent pas suffisamment compte de l'influence du nombre de Reynolds spécialement lorsque celui-ci est très élevé, ni plus généralement de l'état de la couche limite immédiatement en amont du décollement, la plupart des critères de décollement étant en effet établis à partir d'expériences effectuées en écoulement uniforme.

Les mêmes lacunes existent dans la prévision des phénomènes d'interaction couche limite - onde de choc en transsonique dont l'importance a été soulignée par Yoshihara. Dans ce cas, les recherches doivent être complétées par l'étude du comportement aval de la couche limite turbulente, fortement destabilisée par le choc et se développant en présence d'un gradient de pression défavorable.

Revenant au problème de la pression de culot, signalons comme l'a indiqué Pile, la nécessité de traiter le cas des couches limites de grande épaisseur relative. On peut toutefois penser que le développement des techniques de calcul dites de double-couche, entraîneront des progrès substantiels dans un avenir proche.

On peut également regretter l'insuffisance des moyens de prévision de la pression de culot: des corps de révolution en supersonique ainsi que dans des cas plus généraux, en écoulement subsonique et transsonique. Le seul recours à l'expérience pour traiter les problèmes de confluence d'écoulements et d'optimisation d'Arrière corps dans ces domaines constitue une grave lacune pour les applications pratiques.

Soulignons enfin comme application particulièrement importante des calculs d'écoulement de culot, la détermination des corrections des effets de support en dard, dans les essais en soufflerie subsonique. Si une évaluation théorique précise de cette correction était possible comme en supersonique, il en résulterait un progrès très net des mesures de trainée.

**Professor A.D.Young:** Mr Sirieix has affirmed the need for more knowledge on three-dimensional separations, but he also pointed out that for a number of cases we do not know enough about two-dimensional separated flow. I would strongly support that. He also emphasized the importance of being able to simulate high Reynolds numbers by proper simulation of boundary layer thicknesses. He raised the question of boundary layer-shock wave interactions and their effects; base pressures in the presence of very thick boundary layers; he pointed out that we have very little information on bodies of revolution, even at zero incidence, at transonic speeds; and finally, raised again the general question of support effects in measurement. Are there any further comments on these points?

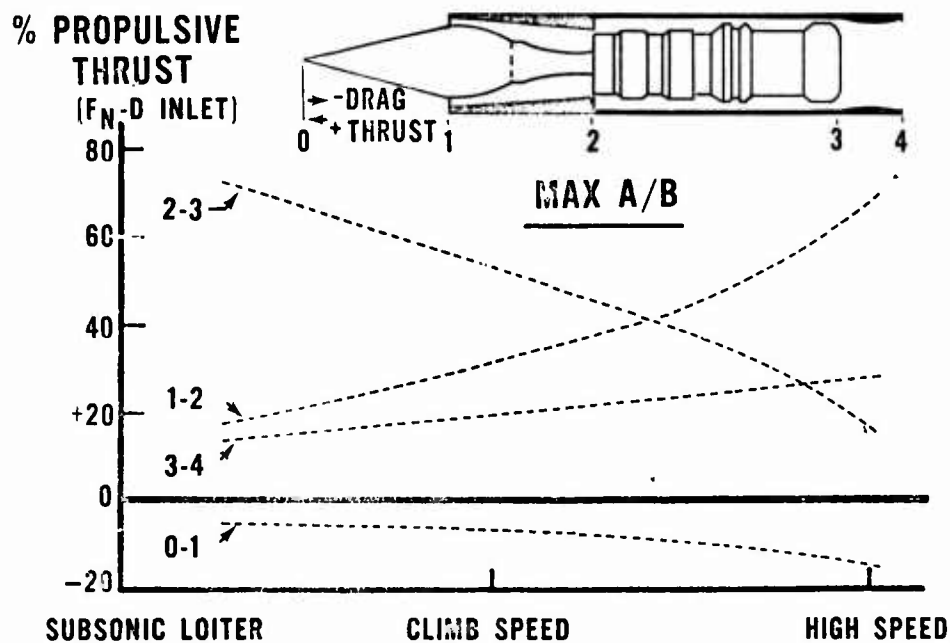
**Dr D.J.Peake:** It is most refreshing to see that at this meeting, the work at ONERA, and especially the "gospel" according to Eric Maskell of RAE, on the physical aspects of three-dimensional separations and attachments (which was published in 1955), are finally sinking in, after much tub thumping by RAE, ONERA and NAE. This is indeed rewarding!

With regard to the discussion on interference effects of sting supports, we should keep in mind another support problem, namely, the difficulties encountered with half-model testing. For example, the displacement effects of the tunnel wall boundary layer create a reflection plane that is often not a plane of symmetry. The wall boundary layer may also affect the flow in the wing root, thereby causing anomalous results. The methods of supporting the half model at the wall and the immersion of the model in the wall boundary layer therefore deserves close attention.

Professor A.D.Young: Are there no other points? In that case I shall ask Mr Antonatos to say what he thinks are the matters of importance which arise from our meeting.

Mr P.P.Antonatos: First, I would like to look at it from the preliminary designers viewpoint. We talked about these correlations today and during the last few days, I was quite heartened to see that, in some cases, the correlations were exceedingly good, indicating that with the proper attention to very exacting details in both the testing techniques and extrapolation of our analysis into those particular areas which are still not too well understood, we are able to obtain data to substantiate the windtunnel analysis. However, from the preliminary design viewpoint, you do not have this opportunity to look at the flight data and correct back. The problem here is to be able to design an airplane, especially a combat-type aircraft, and be able to establish its flight performance long before you have any really good substantial experimental data. Thus, the improvement in the correlation techniques, which then can feed back to further improving our analytical techniques, is quite important. Some of the presenters discussed some of the correlations, or let us say, the analysis that they are conducting presently in modifying some of the earlier techniques that were developed. It was quite interesting to see that everybody in this area had something to say about the Squire-Young methods, the important thing being that they are being reviewed in much more detail so as to be applicable to the problems that we have today. However, I have to agree with the discussion to date, that the windtunnel simulation techniques are still very critical, in that we do not develop the full simulation that is required, whether it is in the shock-boundary layer aspect, looking at the high Reynolds number effects; whether it is the development of the exact boundary layer in the aft body or the aft section of the aircraft, or even worse yet, the boundary layer conditions that exist at the inlet of the airplane, when you have a reduced-scale model in the windtunnel. Therefore, for example, something like the location of the diverter plate or the boundary layer diverter becomes a very strong argument and is subject to a lot of drag counts which can or cannot be explained, depending on what side of the fence you want to be on. For the sake of the aerodynamicist, I would like to show a rather simpleminded view of the effects looking at a nacelle on an extended Mach number aircraft.

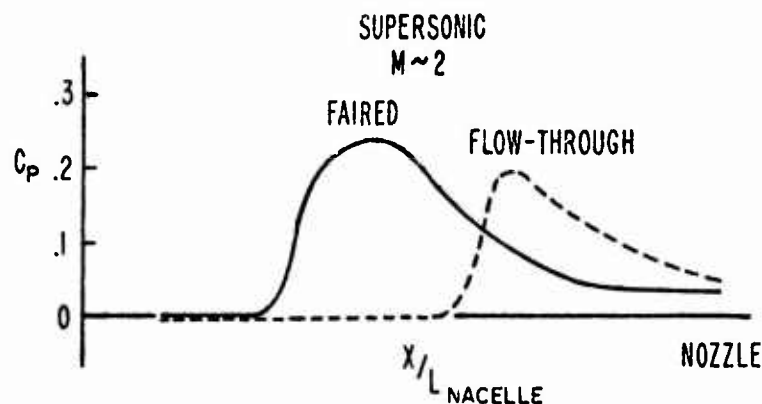
### THRUST & DRAG DISTRIBUTION vs Mo



From there, you can see the importance of the aerodynamics vs the combustion process, especially at transonic and supersonic speeds. I think most of you do not require any detailed explanation of this, but you can see that when you get above the climb speed, and here I am talking rather medium-high Mach numbers, the propulsive thrust basically depends on aerodynamic phenomena, either through the inlet or through the nozzle. This particular curve is a cumulative analysis. You can see that the propulsion unit itself, that is the combustion process, only provides something in the order of 20% of the thrust. The remainder of the thrust comes from the nozzle, and the inlet. The inlet, as you get up to high Mach numbers, provides about 80% of the thrust. Therefore, careful analysis of

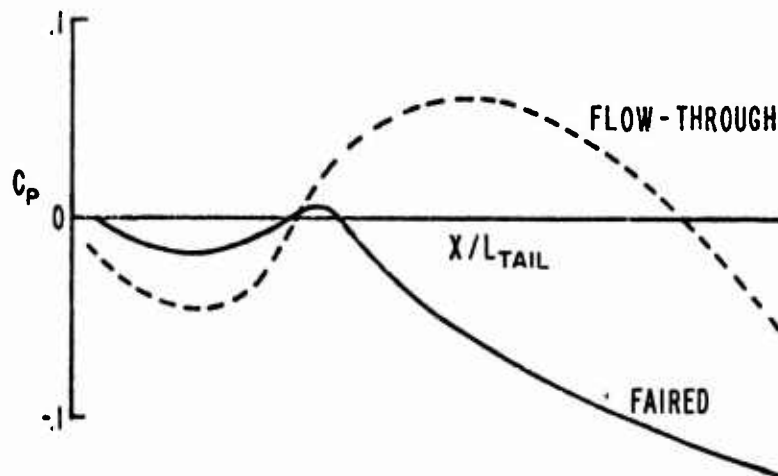
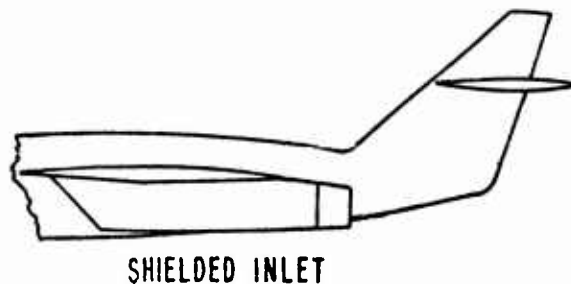
these phenomena is very critical in any new design because here you can very definitely get into rather gross errors where you can mistakenly tie them back to the combustion process, instead of an aerodynamic flow problem.

In reviewing some of the test data, I would like to take the opportunity also to show some of the effects on nacelle pressure distribution when in this particular case you fair the inlet, as compared with an unfaired inlet.



### EFFECT OF INLET FAIRING ON NACELLE PRESSURE DISTRIBUTION

This is for a high by-pass and for a supersonic case of Mach number 2. In some rather preliminary work that has been done lately, fairing the inlet shows a rather big discrepancy in the nacelle pressure distributions, as compared to looking at it in the flowthrough case. There are quite a few drag counts here, when you relate the pressure coefficient back to the performance of an airplane. Also, we have the effect of fairing the inlet vs a non-faired inlet on pressure distributions on the tail surface.



### EFFECT OF INLET FAIRING ON HORIZONTAL TAIL PRESSURE DISTRIBUTION

Here again, you can see on a particular test with a shielded inlet, the difference that occurred on the pressure distribution on the horizontal tail again affecting not only the lifting capability, but also the total pitching capability of the airplane.

In reviewing all the past data that has been available to us, we have developed a list of most critical items that we feel are not receiving focused attention to date.

A-9

#### MOST CRITICAL ITEMS NOT RECEIVING FOCUSED ATTENTION

- ASSESSMENT OF THE VALIDITY OF TRANSONIC WIND TUNNEL TESTING AND EXTRAPOLATION TECHNIQUES BY COMPARISONS BETWEEN EXTRAPOLATED WIND TUNNEL DATA AND FLIGHT DATA
- ASSESSMENT OF THE INFLUENCE OF TUNNEL GENERATED TURBULENCE AND NOISE ON DYNAMIC MEASUREMENTS
- DETERMINATION OF PRACTICAL LOWER LIMIT OF REYNOLDS NUMBER FOR TESTING OF AIRCRAFT AT TRANSONIC SPEEDS
- DEVELOPMENT OF EXPERIENCE IN THE USE OF LUDWIG TUBE FACILITIES FOR AIRCRAFT INVESTIGATIONS
- IMPROVEMENT OF WALL INTERFERENCE CORRECTIONS AT TRANSONIC SPEEDS FOR EXISTING TUNNEL DESIGNS
- DEVELOPMENT OF IMPROVED WALL DESIGN CONCEPTS TO PERMIT RELIABLE DATA TO BE OBTAINED AT NEAR SONIC SPEEDS FOR MODELS AT HIGH LIFT AND LARGER BLOCKAGES
- DEVELOPMENT OF NON-INTERFERING FLOW DIAGNOSTIC TECHNIQUES

Basically, it goes back to many of the comments that have been made by the other members of this roundtable, in addition to comments from the floor. It is quite an extensive list. Actually, in principle, it discusses the validity of transonic windtunnel testing and extrapolation of the data. These are the various items, that is the influence of the tunnel generated turbulence and noise, which I think a group in AGARD is now reviewing. Of course, looking at the Reynolds number effect, looking at developing experience in Ludwig tube facilities, but more importantly in the following items of the list looking at tunnel wall interference effects for present day windtunnels, because today those are the tunnels that we still have to use. In only a very few cases are the tunnels large enough to do any large scale model testing. Most of the time we have to resort to very small models. Wall correction procedures, which have been developed in the past, dealt basically with low  $C_L$ 's and slender bodies. The application of these correction procedures to high angles of attack in a closely coupled airplane, that is a fighter type that will pull a manoeuvring condition, with the inlets and nozzle all grouped together with the fuselage, makes it extremely difficult to have a reliable application of the correction procedures that exist today. Of course, there are possibilities of improving the present wall designs, porosity schedules and various methods of this sort to improve this validity.

In regards to one of the comments, it is too early to really assess many of the support systems. We are presently running a test on heavily instrumented models of three different scales, and also the airplane itself will be heavily instrumented, and the instrumentation will be matched between the windtunnel and flight. Hopefully, within a year, we will be able to obtain very exact correlations in the area of the inlet nozzle interference problem. At least, we will have masses of data to be able to look at. We will also use different support systems, that is we will have the half-scale model, we will have a sting support and a blade support, and in addition, we will have a very high strength model to be able to crank it up to extremely high angles of attack in the tunnel, hopefully, to be able to get data that can be correlated throughout the entire manoeuvring range of this particular airplane. Possibly next September (1974) we will be able to provide some preliminary reports on this.

**Professor A.D.Young:** Mr Antonatos has raised a number of new points in addition to those that have already been raised. He drew attention to a particularly important point; that is, at a certain stage in the design of an aircraft, when windtunnel and other test data are available, it is evidently possible, by considerable care and attention to detail, to make predictions in which one can be hopefully confident. At the preliminary design stage, however this is unfortunately not yet the case. He also re-emphasized the deficiencies existing in the techniques that we have. Windtunnel testing techniques and the like have a number of defects, and we saw a number of points listed on the slide shown on the screen. He emphasized the importance of inlet flow conditions in a very graphic and interesting way. He drew attention to the tremendous importance at transonic speeds of knowing a lot more than we do at present of all the possible sources of interference that there are.

**Mr P.P.Antonatos:** Some of these effects are due to the unusual spillage characteristics that occur, as compared to an inlet that takes in the entire flow. In the particular case of the first curve that we looked at just a few seconds ago, the by-pass flow is sufficient to give you more rolling moment and yawing moment on the airplane, depending on how you by-pass, than your aerodynamic control surfaces do.

**Professor A.D.Young:** I am glad that you mentioned that, because one of the lessons that became evident during the course of the meeting is that there are a number of new problems that have been introduced in achieving satisfactory techniques of testing by the advent of high by-pass ratio engines. It is clear that a lot more work has to be done on them.

A-10

**Dr D.J.Peake:** As I am sure Mr Antonatos is aware, one may compare the pressure distributions about a nacelle (and upon an adjacent wing surface) using either a blocked nacelle or a "through-flow" nacelle, but neither of these may be representative of the flight installation. At an earlier AGARD meeting on "Aerodynamic Interference", it was shown that especially with high by-pass ratio engine installations, one was forced to provide a more sophisticated model engine simulator with rotating machinery within the nacelle, to obtain a representative inflow as well as efflux, and to provide realistic static pressures on the aerodynamic surfaces in proximity to the powerplant.

**Mr P.P.Antonatos:** One of the questions that still remains is whether one needs a cold or hot efflux.

**Mr D.C.Leyland:** I am probably stepping back a little bit, but I am wondering if I can make a plea to the fluid dynamicists to help the engineers a little more by providing a link between the theories that they have produced and the engineering judgements that we have to make.

We have heard quite a lot about testing techniques in windtunnels, and of how one adds together various model measurements to produce a total drag. Yes, it is wholly logical that it is the thing to do, but unfortunately, as many of you will appreciate, in the design of aircraft you have to take decisions long before tunnel measurements can be made. Therefore, I wonder whether there is any hope of getting rather better basic drag estimating methods.

Maybe I should take some particular cases; for example, the supersonic drag of a bluff aircraft. I am not now referring to Concorde or to other aircraft that are fairly slender, because, going back to Harris and the supersonic area rule I think this gives reasonable estimates of supersonic drag. In contrast we find that when you look at a bluff aircraft you just cannot calculate its wave drag with any confidence and Mr Bore has already mentioned the problem. Taking a simple case; how do you calculate the supersonic drag of a rather short fuselage with a canopy? An asymmetric case. Is there any possibility of us getting some working rules that we can use as routine for practical design?

Another example is afterbody drag. I wonder again whether it is worthwhile someone in the fluid dynamics field taking a special interest. There is no doubt that the afterbody gives one of the largest numbers in a synthesis of aircraft drag. Is there something that can be done which will allow us to theoretically optimise the afterbody? Most of what has been done to date, in the US and elsewhere, has been completely empirical. We have had to use models in tunnels.

Maybe, as an instance, I could finish by asking Dr Smith a particular question. Could he offer some method that would allow us to calculate whether the F14 nozzle separation is the right arrangement to go for or not? We have had comparative data for tunnels, but is there a three-dimensional method of calculation available, even if it is restricted to non-separated flow? Can we have methods that will allow us to optimise by theory, or semi-empirical theory, rather than always having to rely upon tunnel tests?

**Mr A.M.O.Smith:** What I had in mind when I said we were making good progress in three-dimensional flow theory is more the idealized three-dimensional problem — not three dimensional with all sorts of corners and intersections, or even wing tips. The afterbody of something like the F14 is practically all intersections and I do not now see any solution. We should be thankful that we have windtunnels. Even though they are imperfect we will still have to depend on them.

**Mr E.C.Rooney:** I have some comments on F-14 afterbody drag since I am intimately familiar with it. The F-14 configuration, as I guess everyone here knows, was based on windtunnel tests of idealized afterbody/nozzle configurations conducted in the USA about five years ago. The design was essentially built around those tests. The flight data I presented this morning (I did not have time to discuss in detail the cruise condition) shows that we did not realize the drag reduction on the afterbody and nozzles for the cruise nozzle condition that was anticipated from those tests. We were able to duplicate the aircraft cruise nozzle drag later with a very detailed and sophisticated propulsion windtunnel model. Therefore, there needs to be some method developed to predict aircraft drag, especially the afterbody, for practical aircraft configurations prior to the design of the airplane because the design cannot be economically changed during the service life of the aircraft.

**Professor Dr K.Gersten:** I want to comment on Mr Smith's discussion regarding interference effects in corner flows and other complicated three-dimensional flows. The difficulty is that classical boundary layer theory does not apply

to those flows in which the boundary layer thickness is large compared with the local surface curvature radius. Classical boundary layer theory simply does not provide the appropriate theoretical framework for the analysis of such flows. It seems to me that one might consider new approaches for situations in which the boundary layer thickness exceeds the surface curvature radius by a large amount, as, e.g., in sharp corners. Because, in the latter case, the Reynolds number based on the radius of curvature is very small, classical boundary layer theory is clearly inappropriate and one should consider Stokes flow as an alternative. A-11

**Professor D.Küchemann:** I would like to come back to this question about making decisions in the design of an aircraft and the wish to do that before one has windtunnel results. This question was discussed at great length by the Large Windtunnel Working Group, which this panel has set up. It was also dealt with in a report by Dr Mitchell from the AEDC, who consulted many aircraft designers on this very point. I think the proceedings of this meeting have confirmed the conclusions we came to in the working group, and also what Dr Mitchell said, namely, that you have to wait in making decisions. You cannot freeze your aeroplane at an early stage. We are simply not good enough in predicting the performance. Even computers do not really help us enough, at least, at this stage. Roughly speaking, Mitchell recommends that at least 70% to 80% of the whole windtunnel testing should be completed before the design is frozen, and I think this is sound advice. You just can not come to a decision before that.

**Mr P.P.Antonatos:** I would like to remind Professor Küchemann that that is a very nice statement, I agree with it whole heartedly, but the people who are buying the airplanes do not always concur.

**Assoc. Professor C.Ciray:** I have listened very carefully to the discussion and the comments and the counter-comments. I will not try to summarize the discussion, since it is not my duty. An important point seemed to be missing among the problems that were discussed here. Indeed, one of the fundamental problems of fluid dynamics, that is non-linearity was somehow mentioned; the other fundamental problem, that is the difficulty of taking into consideration complex boundary conditions was somehow mentioned, perhaps under the general heading of "three-dimensional effects"; but the other one that has not been mentioned actually was turbulence. I wonder if anything about this problem has to be mentioned or does it not deserve any attention from either a practical point of view or from a fundamental point of view? I just wanted my mind clarified about this point.

**Professor A.D.Young:** When you mentioned turbulence, do you mean turbulence in the boundary layer or turbulence in the external stream?

**Assoc. Professor C.Ciray:** Precisely, one and the other one.

**Professor A.D.Young:** There was, of course, in the list that Mr Antonatos threw on the screen, a reference to the important effects of noise and turbulence in windtunnel measurements.

**Mr P.P.Antonatos:** There is an extensive program going on right now at AEDC examining this particular phenomenon, the effect of turbulence on so-called force measurements. They are just in the process of obtaining and reducing the data, so I really cannot give you any final comment on it at the present time. It is recognized as a critical problem, and there is a very extensive program. I believe also that NASA is carrying on similar type experiments.

**Professor A.D.Young:** Perhaps Professor Küchemann might confirm this, but I believe that one or two of the lectures that will appear shortly in an AGARD publication of a VKI lecture course deal with this problem — that of turbulence in windtunnel measurements.

If there are no further comments, I will now ask Professor Wuest to give us his contribution to our roundtable.

**Professor Dr W.Wuest:** We have heard from the papers presented at this meeting in the field of hypersonics that much progress has been made, especially in the last decade. Many experimental results have been obtained, especially for simple-shaped bodies such as spheres, cones or cylinders. These measurements have covered many decades of Reynolds number running from free molecular flow to continuum flow. Adequate theories have contributed to a better understanding of the flow processes. However, if we try to analyze measurements on more complicated bodies such as wing-body configurations or re-entry bodies, etc., we find that there are a lot of new problems which should be solved in the future. In view of the very low research capacity in the field of hypersonics, a selection of problems of main interest should be made. I would want to apply my opinion to which problems should be of priority in this field. If you begin with the free molecular range, we have learned that well established theories are now available for the calculation of the flow field for convex bodies or for concave bodies. I think

A-12

that we lack knowledge on gas surface interactions, especially if we consider surfaces with mono- or multi-molecular sheets, or if we consider molecules with excitation of internal degrees of freedom, and if we consider the reflection of such molecules on the surface. There is some lack of knowledge, if we go, for example, to the second field, i.e., the field of the transitional regime. I think that the main problems for more complicated bodies are the interaction effects. We have in rarefied flow a very strong viscosity action. For example, interaction of wing and body, we have also the leeside vorticity interaction which contributes to a large rise in heat transfer, for example, on the leeside of an afterbody. Much work should be done in these interaction problems. We have learned that different methods exist for calculating the flow on simple bodies, and these methods, even in these simple cases, are very complicated. There is little hope that in the near future, we will be able to calculate complicated three-dimensional flow fields on more complex bodies. Therefore, I think it is necessary to develop approximate semi-empirical theories, especially for engineering applications, to calculate the flow field on such configurations. Another research problem in the field of this transitional flow is a correct interpretation of windtunnel measurements. We have learned in these lectures that relaxation effects are very different in free flight and in the windtunnel simulation. This may be one part of corrections. In most facilities conical nozzles are used for the production of hypersonic flow. We know that the flow conditions are often very unsatisfactory, and I think that it is necessary to make the flow field in such windtunnels better, for example, by using contoured nozzles, or by strong cooling of the wall in order to reduce the viscosity effects, which may also influence the results in such windtunnels. To conclude, with the continuum regime, in my opinion, the most interesting problem in this field is laminar transition, i.e., transition to turbulent flow in rarefied continuum flow. I think the hypersonic Ludwig tube tunnel is well suited to study such problems, which are also very important for technical applications.

**Professor A.D.Young:** Thank you Professor Wuest. Would anyone like to add to this list of problems in hypersonic flow ranging from free molecular flow involving gas surface interactions to problems of transition in continuum flow?

**Professor Dr K.Gersten:** I want to comment on scaling hypersonic flows with relaxation, i.e., non-equilibrium flows. I am not certain if the similarity laws for non-equilibrium flow around a body have been established. It has been traditional to use those scaling parameters, the Reynolds number, Mach number and Knudsen number, which are clearly appropriate for equilibrium flows. However, since chemical reaction times are difficult to scale, scaling parameters such as, e.g., the ratio of relaxation length to the characteristic body dimension, must be included in the design and interpretation of the windtunnel experiments. It is not inconceivable that one might determine that a scaling factor of unity obtains and that only a full-scale model test is meaningful. Purposeful design of windtunnel experiments requires that the similarity laws for non-equilibrium flows be known.

**Professor Dr W.Wuest:** The first thing to be done is to investigate how large is the influence of these effects on the results in windtunnels, and perhaps to find out what corrections could be applied in order to make the results better. Full simulation is surely not possible, but it may be possible to correct the measurements for such effects.

**Professor Dr K.Gersten:** It may be that the scaling parameters such as the ratio of the relaxation length to the characteristic body dimension are much more important than the Reynolds number or the Mach number. In the past, most measurements have been scaled and correlated with Reynolds number and Mach number. My opinion is that theory can provide a better framework for the interpretation of windtunnel data and assist in the design of experiments which are physically meaningful.

**Professor Dr W.Wuest:** Yes. I think the next step must be done by theory.

**Professor A.D.Young:** It only remains for me to sum up. I am not going to attempt to list again all the points that have been raised. Of those that have been mentioned, the subjects that seem to me to stand out as particularly requiring further work are: the calculation of the drag of wings at angles of incidence, particularly those approaching stalling conditions; the particular problems of drag at transonic speeds associated with supercritical wings; separation presents problems that will be with us for a long time, and we must go on working away at them, both in two dimensions and three dimensions. I do not see the problems of separated flow as easy to solve, but I think we will gradually develop theoretical methods of dealing with them. High by-pass ratio engines and their simulation in windtunnels call for attention, as do the problems of thrust measurement with high by-pass ratio engines. Shock-boundary layer interaction presents problems which are perennials but which call for increasing attention, and we need to do a lot more work on them. Finally, we have heard from Professor Wuest of the major problems in hypersonic flow, which again I will not attempt to repeat. I think we have covered our subject fairly thoroughly. As always, one comes away with the feeling that there are now more problems as a result of our discussion than there were before. That is what we call progress. It only remains for me to thank you all for attending so diligently to the papers that have been presented, and to thank those people who have prepared papers. They were all extremely interesting and valuable and added considerably to our knowledge of the field. I would

like to thank particularly my fellow panel members for their excellent review papers. Every one of those review papers will stand on its own as a major contribution to the literature. I would like personally to thank our panel executive and his able assistant for all they have done towards making this meeting a success, which I hope it has been. Last but not least we should thank our host Professor Karhan and all his colleagues for all they have done to make our stay here a very happy one.

**APPENDIX B**

**A SELECTION OF  
AGARD PUBLICATIONS IN RECENT YEARS**

B-1

A SELECTION OF  
AGARD PUBLICATIONS IN RECENT YEARS

CATEGORY I – PUBLISHED BY TECHNIVISION SERVICES AND  
PURCHASABLE FROM BOOKSELLERS OR FROM:—

Technical Press Ltd  
112 Westbourne Grove  
London W.2  
England

Hans Heinrich Petersen  
Postfach 265  
Borsteler Chausee 85  
2000 Hamburg 61  
West Germany

Circa Publications Inc.  
415 Fifth Avenue  
Pelham  
New York 10803, USA

Diffusione Edizioni Anglo-Americaine  
Via Lima  
00198 Rome  
Italy

1969

AGARDograph 120      **Supersonic turbo-jet propulsion systems and components**  
Edited by J.Chauvin, August 1969.

1970

AGARDograph 115      **Wind effects on launch vehicles**  
By E.D.Geissler, February 1970.

AGARDograph 130      **Measurement techniques in heat transfer**  
By E.R.G.Eckert and R.J.Goldstein, November 1970.

Conference  
Proceedings 38      **New experimental techniques in propulsion and energetics research**  
Edited by D.Andrews and J.Surugue, October 1970.

CATEGORY II – NOT ON COMMERCIAL SALE – FOR  
AVAILABILITY SEE BACK COVER

1967

Report 558      **Experimental methods in wind tunnels and water tunnels, with special emphasis on the hot-wire anemometer**  
By K.Wieghardt and J.Kux, 1967.

Advisory Report 13      **Aspects of V/STOL aircraft development**  
(This report consists of three papers presented during the joint session of the AGARD FDP and FMP held in Göttingen, September 1967.)

AGARDograph 98      **Graphical methods in aerothermodynamics**  
By O.Lutz and G.Stoffers, November 1967.

AGARDograph 117      **Behaviour of supercritical nozzles under three-dimensional oscillatory conditions**  
By L.Crocco and W.A.Sirignano, 1967.

AGARDograph 119      **Thermo-molecular pressure effects in tubes and at orifices**  
By M.Kinslow and G.D.Arney, Jr, 1967.

AGARDograph 121      **Techniques for measurement of dynamic stability derivatives in ground test facilities**  
By C.J.Schueler, L.K.Ward and A.E.Hodapp, Jr, 1967.

B-2

- AGARDograph 124      **Nonequilibrium effects in supersonic-nozzle flows**  
By J.Gordon Hall and C.E.Treanor, 1967.
- Conference      **Fluid physics of hypersonic wakes**  
Proceedings 19      Specialists' Meeting, Fort Collins, Colorado, May 1967.  
(in two parts)
- Conference      **Fluid dynamics of rotor and fan supported aircraft at subsonic speeds**  
Proceedings 22      Specialists' Meeting, Gottingen, September 1967.
- Conference      As above – with supplement.  
Proceedings 22 – S 4
- 1968**
- AGARDograph 132      **The electron beam fluorescence technique**  
By E.P.Muntz, 1968.
- Conference      **Hypersonic boundary layers and flow fields**  
Proceedings 30      Specialists' Meeting, London, May 1968.
- Conference      Supplement to the above.  
Proceedings 30 Suppl.
- Conference      **Transonic aerodynamics**  
Proceedings 35      Specialists' Meeting, Paris, September 1968.
- Conference      Supplement to the above.  
Proceedings 35 Suppl.
- 1969**
- Advisory Report 17      **Technical Evaluation Report on AGARD Specialists' Meeting on Transonic aerodynamics**  
By D.Küchemann, April 1969.
- AGARDograph 134      **A portfolio of stability characteristics of incompressible boundary layers**  
By H.J.Obremski, M.V.Morkovin and M.Landahl, 1969.
- AGARDograph 135      **Fluidic controls systems for aerospace propulsion**  
Edited by R.J.Reilly, September 1969.
- AGARDograph 137      **Tables of inviscid supersonic flow about circular cones at incidence  $\gamma = 1.4$**   
(in two parts)      By D.J.Jones, November 1969.
- Conference      **Aircraft engine noise and sonic boom**  
Proceedings 42      Joint Meeting of the Fluid Dynamics and Propulsion and Energetics Panels, held in  
Saint-Louis, France, May 1969.
- Conference      **The aerodynamics of atmospheric shear flow**  
Proceedings 48      Specialists' Meeting, Munich, September 1969.
- 1970**
- Report 575      **Test cases for numerical methods in transonic flow**  
By R.C.Lock, 1970.
- Advisory Report 22      **Aircraft engine noise and sonic boom\***  
By W.R.Sears. (Technical Evaluation Report on AGARD FDP and PEP Joint Meeting on  
"Aircraft engine noise and sonic boom".) January 1970.
- Advisory Report 24      **The aerodynamics of atmospheric shear flows**  
By J.E.Cermak and B.W.Marschner, May 1970. (Technical Evaluation Report on AGARD  
Specialists' Meeting on "The aerodynamics of atmospheric shear flows".)
- Advisory Report 30      **Blood circulation and respiratory flow**  
By J.F.Gross and K.Gersten, December 1970. (Technical Evaluation Report on AGARD  
Specialists' Meeting on the above subject.)

\* See also Advisory Report 26 by J.O.Powers and M.Pianko, June 1970. AR26 has the same title as AR22 but was produced by the Propulsion and Energetics Panel of AGARD and deals primarily with engine noise.

- AGARDograph 138 **Ballistic range technology**  
By T.N.Canning, November 1970.
- AGARDograph 144 **Engineering analysis of non-Newtonian fluids**  
By D.C.Bogue and J.L.White, July 1970.
- AGARDograph 145 **Wind tunnel pressure measurement techniques**  
By D.S.Bynum, R.L.Ledford and W.E.Smotherman, December 1970.
- AGARDograph 146 **The numerical solution of partial differential equations governing convection**  
By H.Lomax, P.Kutler and F.B.Fuller, November 1970.
- AGARDograph 147 **Non-reacting and chemically reacting viscous flows over a hyperboloid at hypersonic condition**  
Edited by C.H.Lewis. (M.Van Dyke, J.C.Adams, F.G.Blottner, A.M.O.Smith, R.T.Davis and G.L.Keltner were contributors.) November 1970.
- Conference Proceedings 60 **Numerical methods for viscous flows**  
By R.C.Lock, November 1970. (Abstracts of papers presented at a Seminar held by the FDP of AGARD at the NPL, Teddington, UK, 18-21 September 1967.)
- Conference Proceedings 62 **Preliminary design aspects of military aircraft**  
March 1970, AGARD Flight Mechanics Panel Meeting held in The Hague, The Netherlands, September 1969.
- Conference Proceedings 65 **Fluid dynamics of blood circulation and respiratory flow**  
Specialists' Meeting, Naples, May 1970.
- Conference Proceedings 71 **Aerodynamic interference**  
Specialists' Meeting, Silver Spring, Maryland, USA, September 1970.
- 1971**
- Report 588 **Aerodynamic testing at high Reynolds numbers and transonic speeds**  
By D.Küchemann, 1971.
- Advisory Report 34 **Aerodynamic interference**  
By D.J.Peake, May 1971. (Technical Evaluation Report of the Specialists' Meeting on "Aerodynamic interference", September 1970.)
- Advisory Report 35 **Report of the high Reynolds number wind tunnel study group of the Fluid Dynamics Panel**  
April 1971
- Advisory Report 36 **Report of the AGARD Ad Hoc Committee on Engine-airplane interference and wall corrections in transonic wind tunnel tests**  
Edited by A.Ferri, F.Jaarsma and R.Monti, August 1971.
- Advisory Report 37 **Facilities and techniques for aerodynamic testing at transonic speeds and high Reynolds number**  
By R.C.Pankhurst, October 1971. (Technical Evaluation Report on Specialists' Meeting held in Göttingen, Germany, April 1971.)
- AGARDograph 137 (third volume) **Tables of inviscid supersonic flow about circular cones at incidence,  $\gamma = 1.4$**   
Part III, by D.J.Jones, December 1971.
- AGARDograph 148 **Heat transfer in rocket engines**  
By H.Ziebland and R.C.Parkinson, September 1971.
- Conference Proceedings 83 **Facilities and techniques for aerodynamic testing at transonic speeds and high Reynolds number**  
August 1971. Specialists' Meeting held in Göttingen, Germany, April 1971.
- Conference Proceedings 91 **Inlets and nozzles for aerospace engines**  
December 1971 Meeting held in Sandefjord, Norway, September 1971.

B-4

1972

- Report 598      **Experiments on management of free-stream turbulence**  
By R.I.Loehrke and N.M.Nagib, September 1972.
- Report 603      **Aerodynamic test simulation: Lessons from the past and future prospects**  
Edited by J.Lukasiewicz.
- Advisory Report 46      **Turbulent shear flows**  
By R.Michel, July 1972. (Technical Evaluation Report of the Specialists' Meeting on "Turbulent shear flows", September 1971.)
- Advisory Report 60      **The need for large wind tunnels in Europe**  
Report of the Large Wind Tunnels Working Group, December 1972.
- AGARDograph 156      **Planar inviscid transonic airfoil theory**  
By H.Yoshihara, February 1972.
- AGARDograph 161      **Ablation**  
By H.Hurwicz, K.M.Kratsch and J.E.Rogan, March 1972.
- AGARDograph 163      **Supersonic ejectors**  
Edited by J.J.Ginoux, November 1972.
- AGARDograph 164      **Boundary layer effects in turbo-machines**  
Edited by J.Surugue, December 1972.
- AGARDograph 165      **Heat transfer measurements in short-duration hypersonic facilities**  
By D.L.Schultz and T.V.Jones.
- Conference  
Proceedings 93      **Turbulent shear flows**  
January 1972. Specialists' Meeting held in London, England, September 1971.
- Conference  
Proceedings 102      **Fluid dynamics of aircraft stalling**  
November 1972. Specialists' Meeting held in Lisbon, Portugal, April 1972.
- Conference  
Proceedings 111      **The aerodynamics of rotary wings**  
February 1973. Specialists' Meeting held in Marseille, France, September 1972.
- Lecture Series LS42      **Aerodynamic problems of hypersonic vehicles. (Two volumes)**  
Edited by R.C.Pankhurst, July 1972.
- Lecture Series LS49      **Laser technology in aerodynamic measurements**  
Edited by R.C.Pankhurst, March 1972.
- Lecture Series LS53      **Airframe/engine integration**  
May 1972.
- Lecture Series LS57      **Heat exchangers**  
January 1972.
- 1973
- Report 601      **Problems in wind tunnel testing techniques**  
April 1973.
- Report 602      **Fluid motion problems in wind tunnel design**  
April 1973.
- Advisory Report 61      **Technical Evaluation Report on the Fluid Dynamics Panel Specialists' Meeting on Aerodynamics of rotary wings**  
By N.D.Ham, March 1973.
- Lecture Series LS56      **Aircraft performance - prediction and methods optimization**  
Edited by J.Williams, March 1973.

Lecture Series LS63    **Helicopter aerodynamics and dynamics**  
March 1973.

Lecture Series LS64    **Advances in numerical fluid dynamics**  
February 1973.

**FORTHCOMING PUBLICATION**

Report 600            **Problems of wind-tunnel design and testing**